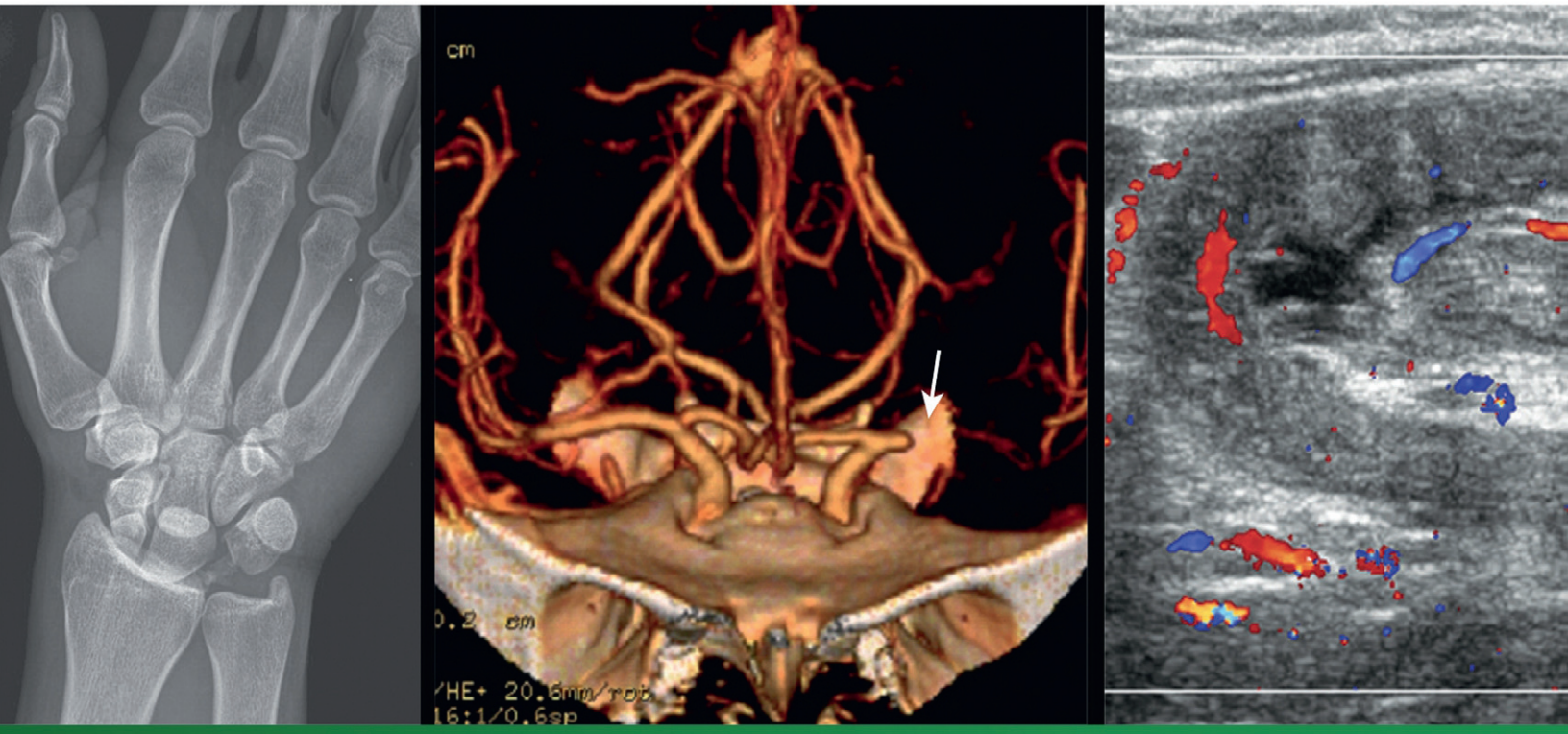
Get Full Access and More at ExpertConsult.com

JORGE SOTO | BRIAN LUCEY

EMERGENCY RADIOLOGY



THE REQUISITES

2nd EDITION

ELSEVIER

Expert CONSULT Built with inkling | E books

Any screen. Any time. Anywhere.



Activate the eBook version
of this title at no additional charge.

Expert Consult eBooks give you the power to browse and find content, view enhanced images, share notes and highlights—both online and offline.

Unlock your eBook today.

1. Visit **expertconsult.inkling.com/redeem**
2. Scratch off your code
3. Type code into "Enter Code" box
4. Click "Redeem"
5. Log in or Sign up
6. Go to "My Library"

It's that easy!

Scan this QR code to redeem your eBook through your mobile device:

For technical assistance:
email expertconsult.help@elsevier.com
call 1-800-401-9962 (inside the US)
call +1-314-447-8200 (outside the US)

ELSEVIER

Use of the current edition of the electronic version of this book (eBook) is subject to the terms of the nontransferable, limited license granted on expertconsult.inkling.com. Access to the eBook is limited to the first individual who redeems the PIN, located on the inside cover of this book, at expertconsult.inkling.com and may not be transferred to another party by resale, lending, or other means.

THE REQUISITES

Emergency Radiology

SERIES EDITOR

James H. Thrall, MD
Radiologist-in-Chief Emeritus
Department of Radiology
Massachusetts General Hospital
Distinguished Juan M.Taveras Professor of Radiology
Harvard Medical School
Boston, Massachusetts

OTHER VOLUMES IN THE REQUISITES RADIOLOGY SERIES

Breast Imaging
Cardiac Imaging
Gastrointestinal Imaging
Genitourinary Imaging
Musculoskeletal Imaging
Neuroradiology
Nuclear Medicine
Pediatric Radiology
Thoracic Radiology
Ultrasound
Vascular and Interventional Radiology

THE REQUISITES

Emergency Radiology

SECOND EDITION

Jorge A. Soto, MD
Professor of Radiology
Department of Radiology
Boston University School of Medicine;
Vice Chairman
Department of Radiology
Boston Medical Center
Boston, Massachusetts

Brian C. Lucey, MD
Associate Professor
Department of Radiology
Boston University School of Medicine
Boston, Massachusetts;
Clinical Director
Department of Radiology
The Galway Clinic
Doughiska, County Galway, Ireland

ELSEVIER

ELSEVIER

1600 John F. Kennedy Blvd.
Ste 1800
Philadelphia, PA 19103-2899

EMERGENCY RADIOLOGY: THE REQUISITES, SECOND EDITION ISBN: 978-0-323-37640-2

Copyright © 2017 by Elsevier, Inc. All rights reserved.

No part of this publication may be reproduced or transmitted in any form or by any means, electronic or mechanical, including photocopying, recording, or any information storage and retrieval system, without permission in writing from the publisher. Details on how to seek permission, further information about the Publisher's permissions policies and our arrangements with organizations such as the Copyright Clearance Center and the Copyright Licensing Agency, can be found at our website: www.elsevier.com/permissions.

This book and the individual contributions contained in it are protected under copyright by the Publisher (other than as may be noted herein).

Notices

Knowledge and best practice in this field are constantly changing. As new research and experience broaden our understanding, changes in research methods, professional practices, or medical treatment may become necessary.

Practitioners and researchers must always rely on their own experience and knowledge in evaluating and using any information, methods, compounds, or experiments described herein. In using such information or methods they should be mindful of their own safety and the safety of others, including parties for whom they have a professional responsibility.

With respect to any drug or pharmaceutical products identified, readers are advised to check the most current information provided (i) on procedures featured or (ii) by the manufacturer of each product to be administered, to verify the recommended dose or formula, the method and duration of administration, and contraindications. It is the responsibility of practitioners, relying on their own experience and knowledge of their patients, to make diagnoses, to determine dosages and the best treatment for each individual patient, and to take all appropriate safety precautions.

To the fullest extent of the law, neither the Publisher nor the authors, contributors, or editors, assume any liability for any injury and/or damage to persons or property as a matter of products liability, negligence or otherwise, or from any use or operation of any methods, products, instructions, or ideas contained in the material herein.

Previous edition copyright © 2009 by Mosby, Inc., an affiliate of Elsevier, Inc.

Library of Congress Cataloging-in-Publication Data

Soto, Jorge A., editor.
Lucey, Brian C., editor.
Emergency radiology / [edited by] Jorge A. Soto, Brian C. Lucey.
Emergency radiology (Soto) | Requisites in radiology. | Requisites series.
Second edition. | Philadelphia, PA : Elsevier, [2017] | Requisites |Requisites radiology series
Includes bibliographical references and index.
LCCN 2015037285
ISBN 9780323376402 (hardcover : alk. paper)
MESH: Diagnostic Imaging. | Emergency Medical Services.
LCC RC78 | NLM WN 180 | DDC 616.07/572–dc23 LC record available at http://lccn.loc.gov/2015037285

Executive Content Strategist: Robin Carter
Content Development Specialist: Amy Meros
Publishing Services Manager: Patricia Tannian
Project Manager: Stephanie Turza
Senior Book Designer: Amy Buxton

Printed in China

Last digit is the print number: 9 8 7 6 5 4 3 2 1

Working together to grow libraries in developing countries
www.elsevier.com • www.bookaid.org

To my parents, Jorge Sr. and Socorro, for their example and guidance, and to my wife, Ana, and children, Andrea and Alejandro, for their sustained support and patience as I devote my time to academic radiology.

J.A.S.

To my parents, James and Anne; sister, Suzanne; wife, Ciara; and son, James. Thanks for the unconditional support.

B.C.L.

This page intentionally left blank

Contributors

Carlos A. Anaya, MD
Medical Director
Cardiovascular Interventional Institute
Department of Radiology
Manati Medical Center
Manati, Puerto Rico

Stephan W. Anderson, MD
Associate Professor of Radiology
Boston University Medical Center
Boston, Massachusetts

Laura L. Avery, MD
Assistant Professor
Massachusetts General Hospital
Harvard Medical School
Boston, Massachusetts

Glenn D. Barest, MD
Assistant Professor of Radiology
Boston Medical Center
Boston, Massachusetts

Sarah D. Bixby, MD
Assistant Professor of Radiology
Harvard Medical School;
Pediatric Radiologist
Department of Radiology
Boston Children's Hospital
Boston, Massachusetts

Anna K. Chacko, MD
Adjunct Professor of Radiology
Boston University
Boston, Massachusetts;
Professor of Telemedicine
John A. Burns School of Medicine
University of Hawaii
Honolulu, Hawaii

Margaret N. Chapman, MD
Chief of Neuroradiology
Boston VA Healthcare System;
Assistant Professor of Radiology
Boston Medical Center
Boston University School of Medicine
Boston, Massachusetts

Luis E. Diaz, MD
Associate Chief of Radiology
VA Boston Health Care System;
Associate Professor of Radiology
Boston University
Boston, Massachusetts

Alejandra Duran-Mendicuti, MD
Department of Radiology
Brigham and Women's Hospital
Boston, Massachusetts

Ana Maria Gomez, MD
Department of Radiology
Manati Medical Center
Manati, Puerto Rico

Rathachai Kaewlai, MD
Instructor
Division of Emergency Radiology
Department of Diagnostic and Therapeutic Radiology
Ramathibodi Hospital
Faculty of Medicine
Mahidol University
Bangkok, Thailand

Russ Kuker, MD
Department of Radiology
University of Miami Hospital
Miami, Florida

Christina A. LeBedis, MD
Assistant Professor
Boston University Medical Center
Boston, Massachusetts

Brian C. Lucey, MD
Associate Professor
Department of Radiology
Boston University School of Medicine
Boston, Massachusetts;
Clinical Director
Department of Radiology
The Galway Clinic
Doughiska, County Galway, Ireland

Asim Z. Mian, MD
Assistant Professor of Radiology
Boston Medical Center
Boston University
Boston, Massachusetts

Sarah S. Milla, MD
Associate Professor
Department of Radiology and Imaging Sciences
Emory University;
Attending Pediatric Radiologist and Neuroradiologist
Children's Healthcare of Atlanta
Egleston Hospital
Atlanta, Georgia

Felipe Munera, MD
Department of Radiology
University of Miami Hospital
Miami, Florida

Rohini N. Nadgir, MD
Assistant Professor of Radiology and Radiological Science
Johns Hopkins Medical Institutions
Baltimore, Maryland

Osamu Sakai, MD, PhD
Chief of Neuroradiology
Professor of Radiology, Otolaryngology–Head and Neck Surgery and Radiation Oncology
Boston Medical Center
Boston University School of Medicine
Boston, Massachusetts

Rashmikant B. Shah, MD
Diagnostic Radiology
St. James Healthcare
Butte, Montana

Ajay Singh, MD
Department of Radiology
Massachusetts General Hospital
Boston, Massachusetts

Aaron D. Sodickson, MD, PhD
Department of Radiology
Brigham and Women's Hospital
Boston, Massachusetts

Jorge A. Soto, MD
Professor of Radiology
Department of Radiology
Boston University School of Medicine;
Vice Chairman
Department of Radiology
Boston Medical Center
Boston, Massachusetts

Michael Stella, MD
Department of Radiology
Brigham and Women's Hospital
Boston, Massachusetts

Joshua W. Stuhlfaut, MD
Beth Israel Deaconess Hospital
Plymouth, Massachusetts

Jennifer C. Talmadge, MD
Department of Radiology
Children's Hospital Boston
Boston, Massachusetts

Salvatore G. Viscomi, MD
Clinical Instructor
Harvard Medical School;
Attending Radiologist
Department of Radiology
Brigham and Women's Hospital
Boston, Massachusetts;
Chairman
Department of Radiology
Cape Cod Hospital
Hyannis, Massachusetts

Scott White, MD
Department of Radiology
Brigham and Women's Hospital
Boston, Massachusetts

Ryan T. Whitesell, MD
St. Paul Radiology
Regions Hospital
St. Paul, Minnesota

Foreword

Time passes quickly, and it is now time to introduce the second edition of *Emergency Radiology:* THE REQUISITES. Drs. Soto and Lucey, along with their coauthors, have once again created an excellent text that captures the fundamental building blocks of emergency radiology practice.

Drs. Soto and Lucey have maintained the logical division of their book by both body part and indication—trauma versus nontrauma with separate chapters for special considerations in children and for nuclear medicine applications. This allows the reader of *Emergency Radiology:* THE REQUISITES to go immediately to the material of interest. As a side note, only two or so decades ago, nontrauma emergency patients were not imaged nearly as often as they are today. Today, emergency applications for the nontrauma patient are just as important as the historic role of imaging in trauma. Imaging is truly the "guiding hand" of medical practice, making possible rapid diagnosis, triage, and disposition, which are vitally important given the time and resource constraints faced by busy emergency departments.

In the years between the preparation of the first edition and the current work, much has happened to enhance the role of radiology in the emergency department and to reshape our thinking. These changes affect every area of application and include, among many others, optimization of computed tomographic (CT) protocols in every organ system for lower radiation exposure, taking advantage of fast CT scanning capabilities to reduce contrast usage and an increasing appreciation for the potential roles of MRI for both traumatic and nontraumatic indications. Conventional radiography continues to play an important role, especially for extremity trauma and some thoracic imaging applications such as pneumonia and congestive heart failure. However, for most applications, radiography is being inexorably replaced by cross-sectional imaging.

Drs. Soto and Lucey have again assembled an outstanding team of coauthors to help ensure that *Emergency Radiology:* THE REQUISITES is as up to date as possible. Thanks to all the authors for their contributions.

Each chapter presents a different challenge in presenting material. All share a rich opportunity for illustrations, and *Emergency Radiology:* THE REQUISITES is extremely well illustrated. Otherwise the use of outline lists, boxes, and tables has been dictated by the material requiring presentation.

THE REQUISITES books have become old friends to imagers for over 25 years. We have tried to remain true to the original philosophy of the series, which was to provide residents, fellows, and practicing radiologists with a text that might be read within several days. From feedback I have received, many residents do exactly that at the beginning of each rotation. During first rotations this allows them to acquire enough knowledge to really benefit from their day-to-day exposure to clinical material and the conditions about which they have just read. During subsequent rotations, a rereading imprints the knowledge they will need subsequently for upcoming certification exams. For the practicing radiologist, it serves as a useful refresher, like a booster shot. At the workstation, the books in THE REQUISITES series are useful as a first reference source and guide to differential diagnosis.

THE REQUISITES books are not intended to be exhaustive. There are other large reference books to catalog rare and unusual cases and to present different sides of controversies. Rather, THE REQUISITES books are intended to provide information on the vast majority of conditions that radiologists see every day, the ones that are at the core of radiology practice. In fact, one of the requests to authors is to not look up anything they do not know but to put in the book what they teach their own residents at the workstation. Since the authors are experienced experts in their respective areas, this is predictably the most important material.

Drs. Soto and Lucey and their coauthors have again done an outstanding job in sustaining the philosophy and excellence of THE REQUISITES series and deserve congratulations. Their book reflects the contemporary practice of emergency imaging and should serve radiologists, emergency medicine specialists, and other physicians who deal with emergencies as a concise and useful foundation for understanding the indications for imaging and the significance of imaging findings in the emergency setting.

James H. Thrall, MD
Chairman Emeritus
Department of Radiology
Massachusetts General Hospital
Distinguished Taveras Professor of Radiology
Harvard Medical School

This page intentionally left blank

Preface

Emergency Radiology is a unique title in THE REQUISITES series. Although both the organ system–based and modality-based divisions of radiology have existed for some time, this REQUISITES title is the first to embrace a multimodality, multisystem approach to radiology. There is an ongoing paradigm shift in medical management over the past 25 years or so, away from inpatient-oriented health care toward an increasingly outpatient-based system. Nowhere is this more apparent than in emergency departments across the United States and around the world. The reliance on imaging for diagnosis and guiding management decisions throughout medicine has been increasing, and this is exemplified in the emergency setting. All imaging modalities are available to the emergency physician. More than in any other modality, the massive increase in the use of computed tomograpy (CT) has led to the development and growth of the specialty of emergency radiology. The value of CT in the setting of trauma, investigation of severe headache, abdominal pain, and the evaluation of patients with suspected pulmonary embolus forms the bedrock of emergency imaging, although there is an increasing role for MR and ultrasound imaging in the emergency setting, particularly for the rapid evaluation of musculoskeletal injury and emergent neurologic evaluation. The book is an attempt to collate all the radiology information required in today's emergency department setting into one succinct, practical, and current text that can be used by both residents in training and general radiologists in practice, as well as emergency department physicians and trauma surgeons.

The goal of this revision is to provide updates to address the rapid changes in emergency imaging requirements, including CT angiography in the emergency department for coronary, aorta, brain/neck, visceral, and extremity arteries, updated CT protocols in trauma and nontraumatic emergencies, and new and better quality images obtained with the latest imaging technology. Stepping away from the organ- and modality-based divisions, we acknowledge that there is potential for overlap among this text and others in THE REQUISITES series. However, to avoid this, we have endeavored to confine the text to medical and surgical conditions that commonly present through the emergency department rather than including every imaging possibility that may present. We apologize in advance if any overlap is identified—it was included for completeness—or for any deficiencies; some rare entities may have been omitted for the sake of brevity. The fundamental division of the book is in two parts, one dealing with acute trauma and the other with nontraumatic acute processes, and the division of the chapters reflects this. This makes it possible to easily select those chapters relevant to an individual radiology practice. Some departments, especially large academic departments with residency programs, will have trauma units, whereas some community practices may run an emergency department without dealing with acute trauma.

We are pleased with how this revision has developed from an abstract concept into reality and built upon the first edition. It has taken substantial effort, and we fully appreciate the contributions from the authors, all of whom have considerable experience in emergency imaging. We hope that the revision will be as well received as the first edition and will act as an integral resource for all radiology departments and training programs.

This page intentionally left blank

Acknowledgments

We would like to thank many people who helped transform the concept of this book into a reality. First, we owe thanks to innumerable individuals (staff, residents, fellows, technologists, and nurses) at the Boston University Medical Center who helped us and our colleagues build multidisciplinary groups for the care of the acutely ill patient. This was the principal driving force behind our growing interest in the field of emergency radiology. We would also like to thank Dr. James Thrall for insisting on the timeliness and necessity of this text to add to THE REQUISITES series. We would also like to extend a sincere thank you to the contributing authors, all of whom are experienced radiologists with extensive knowledge in the various aspects of emergency radiology. Each author has added his or her own subspecialty expertise to the chapters, which has resulted in the final product, a textbook that we believe they should all be proud of. Finally, thanks to all the staff at Elsevier, especially Amy Meros and Robin Carter, who waited patiently for us to deliver the various parts of the book, sometimes at a slower-than-hoped-for pace.

J.A.S.
B.C.L.

This page intentionally left blank

Contents

Chapter 1
Traumatic and Nontraumatic Emergencies of the Brain, Head, and Neck 1
Glenn D. Barest, Asim Z. Mian, Rohini N. Nadgir, and Osamu Sakai

Chapter 2
Chest Trauma 61
Ryan T. Whitesell and Laura L. Avery

Chapter 3
Abdomen Trauma 81
Joshua W. Stuhlfaut, Christina A. LeBedis, and Jorge A. Soto

Chapter 4
Extremity Trauma 115
Rathachai Kaewlai and Ajay Singh

Chapter 5
Extremities: Nontrauma 165
Luis E. Diaz

Chapter 6
Imaging Evaluation of Common Pediatric Emergencies 186
Jennifer C. Talmadge, Sarah S. Milla, and Sarah D. Bixby

Chapter 7
Traumatic and Nontraumatic Spine Emergencies 221
Glenn D. Barest and Margaret N. Chapman

Chapter 8
Nontraumatic Emergency Radiology of the Thorax 243
Alejandra Duran-Mendicuti, Scott White, Salvatore G. Viscomi, Michael Stella, and Aaron D. Sodickson

Chapter 9
Nontrauma Abdomen 281
Stephan W. Anderson, Brian C. Lucey, and Jorge A. Soto

Chapter 10
Pelvic Emergencies 316
Brian C. Lucey

Chapter 11
Vascular Emergencies 327
Russ Kuker, Carlos A. Anaya, Ana Maria Gomez, and Felipe Munera

Chapter 12
Emergency Nuclear Radiology 369
Anna K. Chacko and Rashmikant B. Shah

Index 395

This page intentionally left blank

THE REQUISITES

Emergency Radiology

This page intentionally left blank

Chapter 1

Traumatic and Nontraumatic Emergencies of the Brain, Head, and Neck

Glenn D. Barest, Asim Z. Mian, Rohini N. Nadgir, and Osamu Sakai

Imagine you are asked to create a list of the disorders of the brain, head, and neck that one might commonly expect to encounter at an emergency department (ED) and describe the typical imaging features. At first, this challenge seems straightforward enough. However, upon beginning the task, it soon becomes clear that almost every disorder within the realm of neuroradiology/head and neck radiology might at one time or another present as an acute emergency. Inclusion of certain diagnoses such as stroke, fractures, and epiglottitis is a must. Other diagnoses, such as oligodendroglioma or perhaps a slowly growing lesion, might seem less clear-cut. Ultimately, it is important to realize that a wide variety of processes will result in an alteration in mental status leading to an ED visit, with imaging playing a key role in diagnosis and appropriate management.

Upon admission, inpatient workups now occur on a 24/7 basis, with many complex examinations completed during the night shift. On-call radiologists (often residents or fellows) are expected to provide "wet readings" or complete interpretations for complex cases covering the full spectrum of medicine, pediatrics, surgery, and related subspecialties. It was not that many years ago that the radiologist was faced with a seemingly never-ending stack of plain films from the ED, inpatient wards, and intensive care units requiring rapid interpretations. This work was interrupted by an occasional computed tomography (CT) scan. In this new millennium, during a typical shift the radiologist must maintain a rapid pace to review thousands of cross-sectional CT and magnetic resonance images (MRI) with two-dimensional (2D) and three-dimensional (3D) reformats. For this reason, the majority of the discussion and most of the examples in this chapter are based on these modalities and the latest techniques.

The most daunting part of preparing this chapter was to boil down all of the disorders and details to a set of requisites. Division of this chapter into sections is not quite as neat as one might think. For example, it is not possible to separate the vascular system from discussion of the brain, head and neck, or spine, and the imaging methods applied to the extracranial vessels in the setting of stroke are similar to those used for blunt or penetrating trauma to the neck. One may therefore notice mention of similar techniques and findings in several places with examples appropriate to the context. All readers would do well to study the other volumes in the Requisites series (especially Neuroradiology, Musculoskeletal Imaging, and Pediatric Radiology), which cover this material in great detail. In this attempt at condensing so much material into one useful volume, important topics inevitably have been neglected. We hope that this volume can serve as a starting point for further study and become a valuable reference to on-call radiologists, emergency department physicians, and residents of both specialties.

INTRACRANIAL HEMORRHAGE AND TRAUMATIC BRAIN INJURY

Whether in the setting of head trauma, spontaneous development of headache, or alteration of mental status, the ability to diagnose intracranial hemorrhage (ICH) is of primary importance for all practitioners. These presentations are some of the most common indications for brain imaging in the emergency setting. Almost invariably, the requisition will read, "Rule out bleed." An understanding of traumatic and nontraumatic causes of ICH, the usual workup, and recognition of ICH is therefore important and seems like a natural starting point. A discussion of the important types of mass effect resulting from ICH and traumatic brain injury is also included in this section. An understanding of hemorrhage and herniation syndromes is central to the discussion of other topics that follow, such as stroke and neoplasms.

The word *hemorrhage* has Greek origins: the prefix *haima-,* meaning "blood," and the suffix *-rrhage,* meaning "to gush or burst forth." Incidence of ICH is approximately 25 to 30 per 100,000 adults in the United States, with a higher incidence in elderly hypertensive patients. ICH is typically more common in the African American and Asian populations. Bleeding may take place within the substance of the brain (intraaxial) or along the surface of the brain (extraaxial). Intraaxial hemorrhage implies parenchymal hemorrhage located in the cerebrum, cerebellum, or brainstem. Extraaxial hemorrhages include epidural, subdural, and subarachnoid hemorrhages, and intraventricular hemorrhage can be considered in this group as well. Hemorrhages can lead to different types of brain herniation, from direct mass effect and associated edema or development of hydrocephalus, causing significant morbidity and mortality.

TABLE 1-1 Usual Magnetic Resonance Signal Characteristics of Hemorrhage

Stage	Time	Component	T1	T2
Hyperacute	(0-12 h)	Oxyhemoglobin	Isointense	Hyperintense
Acute	(12 h-3 days)	Deoxyhemoglobin	Isointense	Hypointense
Early subacute	(3-7 days)	Methemoglobin (intracellular)	Hyperintense	Hypointense
Late subacute	(1 wk-1 mo)	Methemoglobin (extracellular)	Hyperintense	Hyperintense
Chronic	(>1 mo)	Hemosiderin	Hypointense	Hypointense

General Imaging Characteristics of Hemorrhage

The appearance of ICH on a CT scan can vary depending on the age of the hemorrhage and the hemoglobin level. The attenuation of blood is typically based on the protein content, of which hemoglobin contributes a major portion. Therefore the appearance of hyperacute/acute blood is easily detected on a CT scan in patients with normal hemoglobin levels (approximately 15 g/dL) and typically appears as a hyperattenuating mass. This appearance is typical because, immediately after extravasation, clot formation occurs with a progressive increase in attenuation over 72 hours as a result of increased hemoglobin concentration and separation of low-density serum. On the other hand, in anemic patients with a hemoglobin level less than 10 g/dL, acute hemorrhage can appear isoattenuating to the brain and can make detection difficult. Subsequently, after breakdown and hemolysis, the attenuation of the clot decreases until it becomes nearly isoattenuating to cerebrospinal fluid (CSF) by approximately 2 months. In the emergency setting, one should be aware of the "swirl" sign with an unretracted clot that appears to be hypoattenuating and resembles a whirlpool; this sign may indicate active bleeding and typically occurs in a posttraumatic setting. It is important to recognize this sign, because prompt surgical evacuation may be required. The amount of mass effect on nearby tissues will depend on the size and location of the hemorrhage, as well as the amount of secondary vasogenic edema that develops.

Use of an intravenous contrast agent usually is not necessary for CT detection of ICH. If a contrast agent is used, an intraaxial hemorrhage can demonstrate an enhancing ring that is usually due to reactive changes and formation of a vascularized capsule, which typically occurs 5 to 7 days after the event and can last up to 6 months. Subacute and chronic extraaxial hematomas also can demonstrate peripheral enhancement, usually because of reactive changes and formation of granulation tissue. Unexpected areas of enhancement should raise concern, because active bleeding can appear as contrast pooling. Refer to the section on aneurysms and vascular malformations in this chapter for a discussion of CT angiography in the setting of acute ICH.

MRI has greatly revolutionized the evaluation of ICH. The evolution of hemorrhage from the hyperacute to the chronic stage will have corresponding signal changes on T1-weighted images (T1WIs), T2-weighted images (T2WIs), fluid-attenuated inversion recovery (FLAIR) images, and gradient-echo sequences. These properties can assist in detection and understanding of the time course of the injury. Although it is beyond the scope of this chapter, a description of the physics of the signal characteristics of blood products on MRI is generally based on the paramagnetic effects of iron and the diamagnetic effects of protein in the hemoglobin molecule. The usual signal characteristics of hemorrhage and the general time course over which hemorrhages evolve are summarized in Table 1-1.

EXTRAAXIAL HEMORRHAGE

Extraaxial hemorrhage occurs within the cranial vault but outside of brain tissue. Hemorrhage can collect in the epidural, subdural, or subarachnoid spaces and may be traumatic or spontaneous. It is important to recognize these entities because of their potential for significant morbidity and mortality. Poor clinical outcomes are usually the result of mass effect from the hemorrhage, which can lead to herniation, increased intracranial pressure, and ischemia. Intraventricular hemorrhage will be considered with these other types of extracerebral hemorrhage.

Epidural Hemorrhage

Epidural hematoma is the term generally applied to a hemorrhage that forms between the inner table of the calvarium and the outer layer of the dura because of its mass-like behavior. More than 90% of epidural hematomas are associated with fractures in the temporoparietal, frontal, and parieto-occipital regions. CT is usually the most efficient method for evaluation of this type of hemorrhage. An epidural hematoma typically has a hyperdense, biconvex appearance. It may cross the midline but generally does not cross sutures (because the dura has its attachment at the sutures), although this might not hold true if a fracture disrupts the suture. Epidural hematomas usually have an arterial source, commonly a tear of the middle meningeal artery, and much less commonly (in less than 10% of cases) a tear of the middle meningeal vein, diploic vein, or venous sinus (Figs. 1-1 and 1-2). The classic clinical presentation describes a patient with a "lucid" interval, although the incidence of this finding varies from 5% to 50% in the literature. Prompt identification of an epidural hematoma is critical, because evacuation or early reevaluation may be required. Management is based on clinical status, and therefore alert and oriented patients with small hematomas may be safely observed. The timing of follow-up CT depends on the patient's condition, but generally the first follow-up CT scan may be obtained after 6 to 8 hours and, if the patient is stable, follow-up may be extended to 24 hours or more afterward.

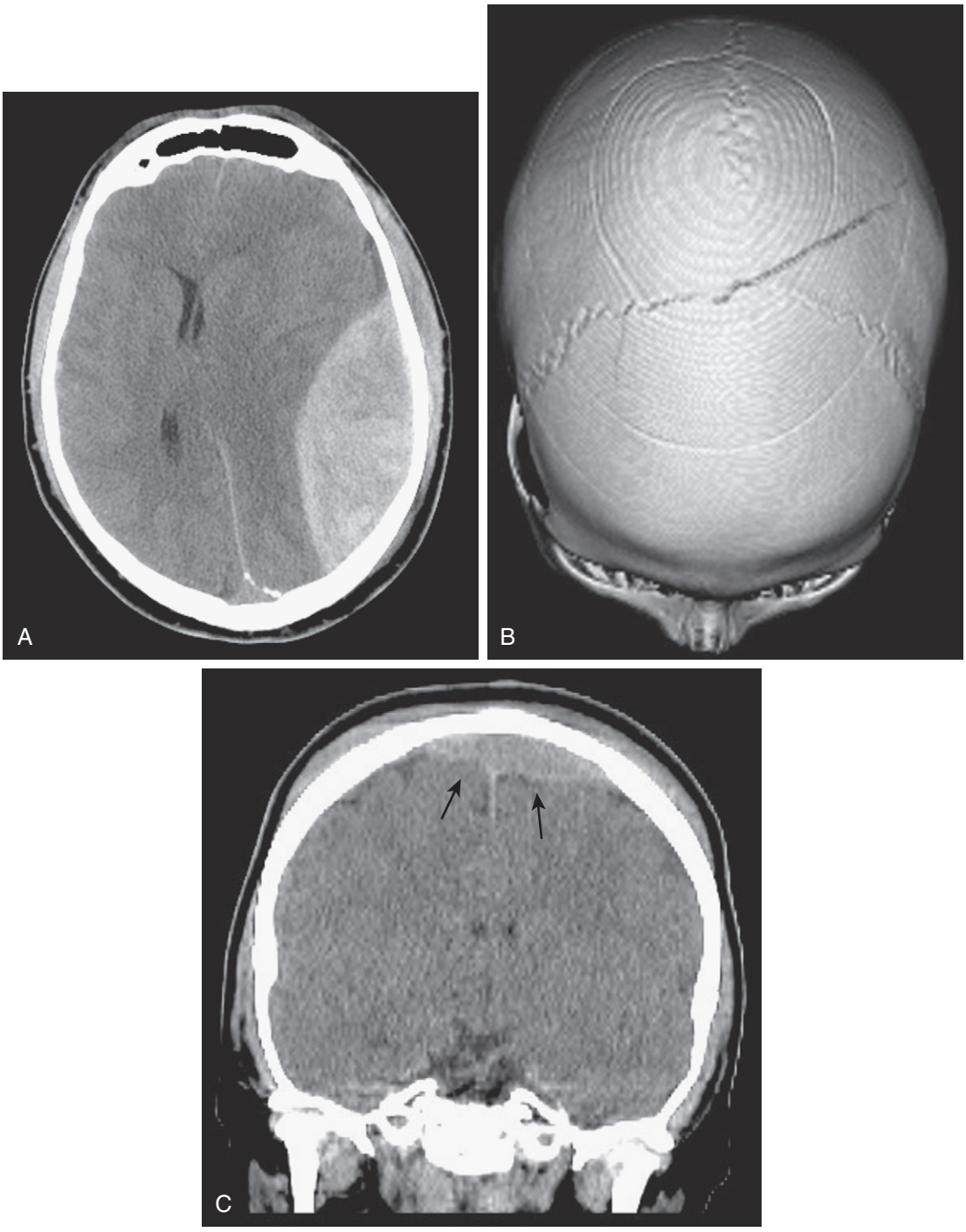


FIGURE 1-1 An epidural hematoma. **A,** Computed tomography (CT) shows a usual biconvex, hyperdense acute epidural hematoma causing effacement of sulci and lateral ventricles and shift of midline structures. **B,** A CT volume-rendered image shows a nondisplaced fracture at the vertex involving the coronal suture. **C,** Coronal multiplanar reconstruction shows a biconvex epidural hematoma crossing midline over the superior sagittal sinus *(arrows)*.

Subdural Collections

Subdural hematoma (SDH) is the term generally applied to a hemorrhage that collects in the potential space between the inner layer of the dura and the arachnoid membrane. It is typically the result of trauma (e.g., motor vehicle collisions [MVCs], assaults, and falls, with the latter especially occurring in the elderly population). An SDH causes a tear of the bridging vein(s) and has a hyperattenuating, crescentic appearance overlying the cerebral hemisphere (Fig. 1-3). These hemorrhages can cross sutures and may track along the falx and tentorium but do not cross the midline. Inward displacement of the cortical vessels may be noted on a contrast-enhanced scan. SDHs have a high association with subarachnoid hemorrhage. Acute SDHs thicker than 2 cm that occur with other parenchymal injuries are associated with greater than 50%

mortality. As the SDH evolves to the subacute stage (within 5 days to 3 weeks) and then to the chronic stage (after more than 3 weeks), it decreases in attenuation, becoming isodense to the brain and finally to CSF. A subacute SDH can have a layered appearance as a result of separation of formed elements from serum. Subacute hemorrhages may be relatively inconspicuous when they are isodense, and therefore it is especially important to recognize signs of mass effect, such as sulcal effacement, asymmetry of lateral ventricles, and shift of midline structures, as well as sulci that do not extend to the skull (Fig. 1-4). Bilateral isoattenuating SDHs can be especially challenging because findings are symmetric. One should beware of bilateral isoattenuating SDHs, particularly in elderly patients who do not have generous sulci and ventricles. At this stage, the SDH should be conspicuous on MRI, especially on FLAIR sequences. A subacute SDH also may be very conspicuous on T1WIs because of the hyperintensity of methemoglobin.

Chronic subdural hematomas are collections that have been present for more than 3 weeks. Even a chronic hematoma may present in the emergency setting, such as

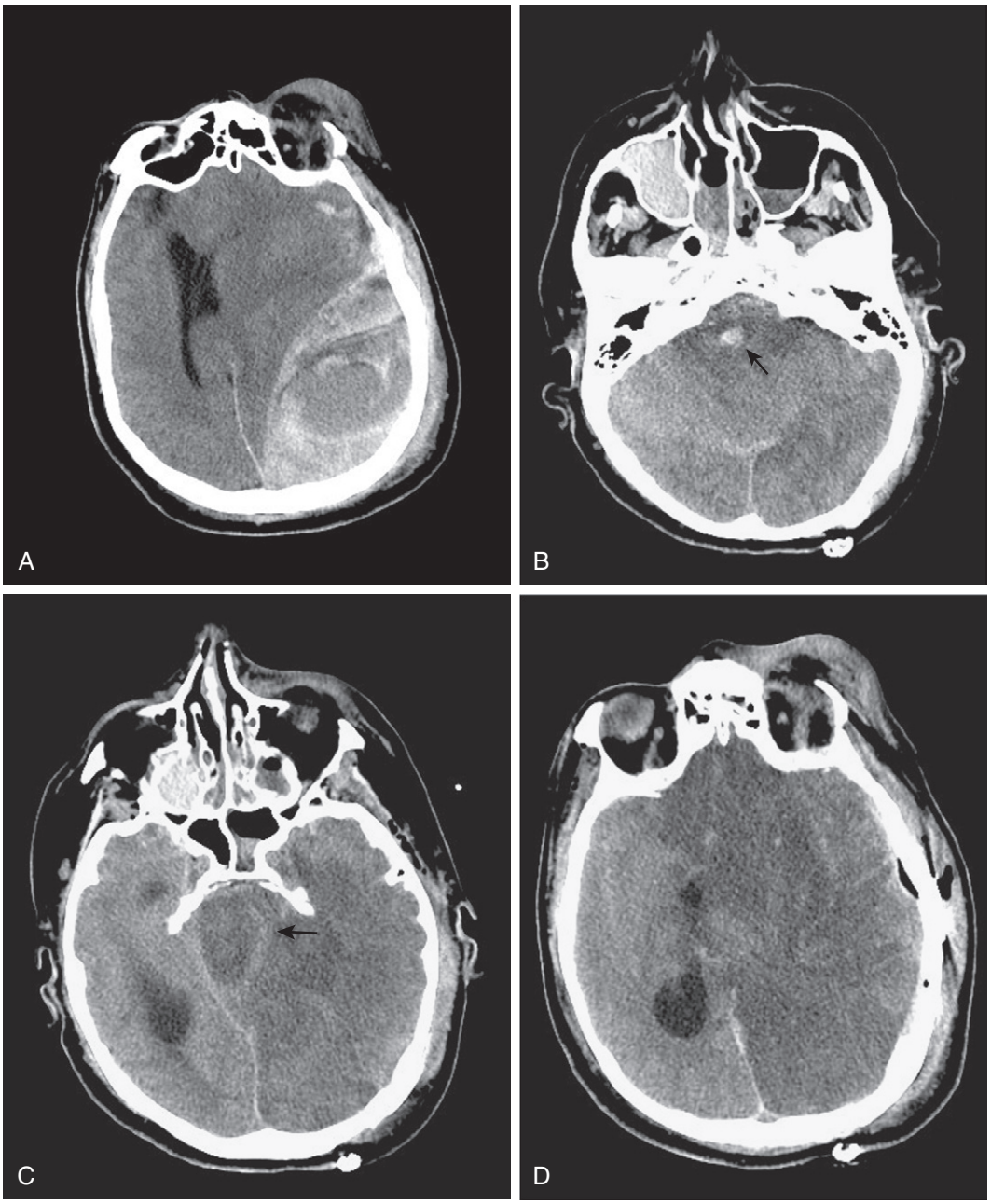


FIGURE 1-2 An epidural hematoma and complications demonstrate on noncontrast CT. **A,** The "swirl" sign in this large epidural hematoma suggests continued bleeding. **B,** A pontine (Duret) hemorrhage *(arrow)* and effacement of the basal cisterns as a result of downward herniation. **C,** Uncal herniation (the *arrow* shows the margin of the left temporal lobe) and a resultant left posterior cerebral artery territory infarct. The brainstem is distorted and also abnormally hypodense. **D,** Infarcts in bilateral anterior cerebral, left middle cerebral, and left posterior cerebral artery territories as a result of herniations.

in a patient prone to repeated falls who is brought in because of a change in mental status. On both CT and MRI, these collections typically have a crescentic shape and may demonstrate enhancing septations and membranes surrounding the collection after administration of a contrast agent. Calcification of chronic SDH can occur and may be quite extensive (Fig. 1-5). Areas of hyperdensity within a larger hypodense SDH may indicate an acute component due to recurrent bleeding, termed an "acute on chronic subdural hematoma." Mixed density collections also may be acute as a result of active bleeding or CSF accumulation as a result of tearing of the arachnoid membrane. A chronic SDH is usually isointense to CSF on both T1WIs and T2WIs, but the appearance can be variable depending on any recurrent bleeding within the collection. The FLAIR sequence is typically very sensitive for detection of chronic SDH as a result of hyperintensity based on protein content. Hemosiderin within the hematoma will cause a signal void because of the susceptibility effect, and "blooming" (i.e., the hematoma appears to be larger than its true size) will be noted on a gradient-echo sequence.



FIGURE 1-3 A subdural hematoma with a mixed density layered pattern due to recurrent hemorrhages. The image *(arrow)* shows one method of measuring midline shift.

A subdural hygroma is another type of collection that is commonly thought to be synonymous with a chronic subdural hematoma. The actual definition of a hygroma is an accumulation of fluid due to a tear in the arachnoid membrane, usually by some type of trauma or from rapid ventricular decompression with associated accumulation of CSF within the subdural space. Many persons still use this term interchangeably with chronic subdural hematoma. CT demonstrates a fluid collection isodense to CSF in the subdural space. MRI can be useful in differentiating CSF from a chronic hematoma based on the imaging characteristics of the fluid on all sequences. Occasionally hygromas are difficult to differentiate from the prominence of the extraaxial CSF space associated with cerebral atrophy. The position of the cortical veins can be a helpful clue. In the presence of atrophy, the cortical veins are visible traversing the subarachnoid space, whereas

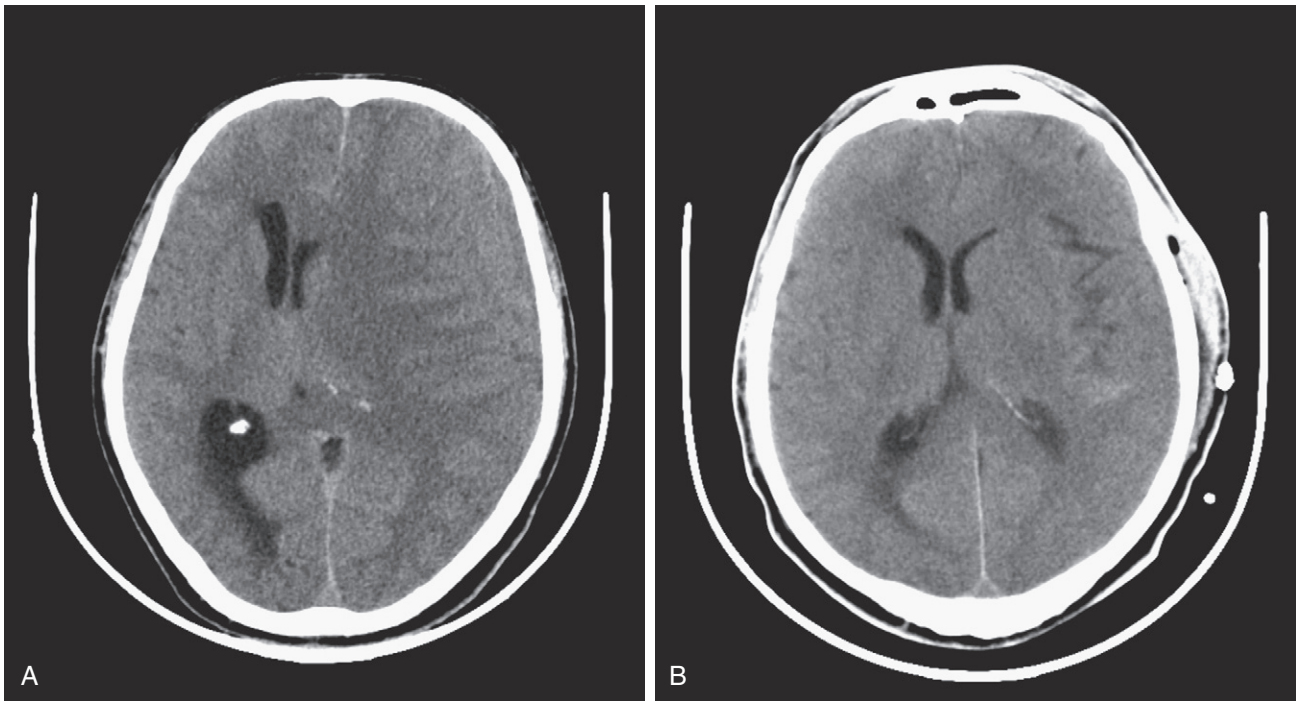


FIGURE 1-4 An isodense subdural hematoma. **A,** Sulcal effacement and a midline shift to the right are clues to the presence of a left-sided subdural hematoma. **B,** Reexpansion of the left Sylvian fissure and a reduction in midline shift after evacuation.

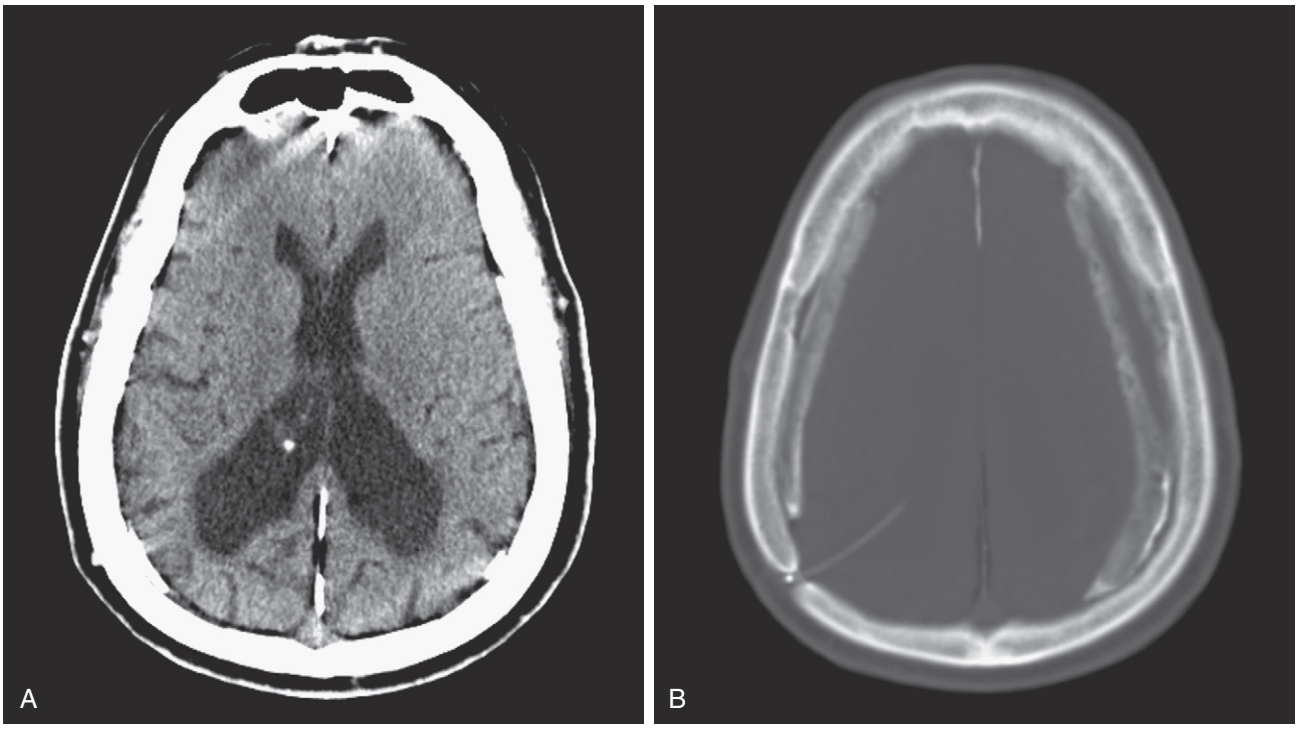


FIGURE 1-5 Calcified subdural hematomas. **A,** Colpocephaly configuration of the lateral ventricles. **B,** Bone window/level settings more clearly show the calcified subdurals in this adult patient who, as a child, had a shunt implanted because of congenital hydrocephalus.

with a hygroma, they are displaced inward along with the arachnoid membrane by the fluid in the subdural space.

Subarachnoid Hemorrhage

Subarachnoid hemorrhage (SAH) fills the space between the pia and the arachnoid membrane, outlining the sulci and basilar cisterns. SAH can be due to a variety of causes, including trauma, a ruptured aneurysm, hypertension, arteriovenous malformation, occult spinal vascular malformation, and hemorrhagic transformation of an ischemic infarction. SAH is often associated with overlying traumatic SDH. SAHs generally do not cause mass effect or focal regions of edema. However, in patients presenting with ominous signs on clinical grading scales, such as stupor or coma, diffuse cerebral edema may be evident. On CT, hyperdensity is seen within the sulci and/or basilar cisterns (Figs. 1-6 and 1-7).

Although MRI may be as sensitive as CT for the detection of acute parenchymal hemorrhage and SAH, CT generally remains the modality of choice (and the imaging gold standard). The sensitivity of CT for the detection of SAH compared with CSF analysis can vary from up to 98% to 100% within 12 hours to approximately 85% to 90% after 24 hours of symptom onset. Other factors affecting sensitivity are the hemoglobin concentration and the size and location of the hemorrhage. CT is widely available, can be performed rapidly, and is relatively inexpensive. In several small studies, MRI has demonstrated sensitivity equivalent to CT for detection of acute parenchymal hemorrhage and SAH. In some cases of "CT-negative" (subacute) hemorrhage, MRI has shown greater sensitivity. However, results may be confounded by artifacts from CSF pulsations, an elevated level of protein (meningitis), or oxygen concentration (i.e., a high fraction of inspired oxygen) in CSF on FLAIR images and the presence of blood products from previous microhemorrhages on gradient-echo images.

Intraventricular Hemorrhage

In the adult population, intraventricular hemorrhage (IVH) is typically caused by trauma. It can result from extension of a parenchymal hemorrhage into the ventricles or from redistribution of SAH. Primary IVH is uncommon and is usually caused by a ruptured aneurysm, an intraventricular tumor, vascular malformation, or coagulopathy (Fig. 1-8). Large IVHs are quite conspicuous on CT or MRI. They may occupy a majority of the ventricle(s) and may result in hydrocephalus and increased intracranial pressure. Small amounts of IVH may be difficult to detect; one must check carefully for dependent densities within the atria and occipital horns of the lateral ventricles. Normal choroid plexus calcifications in the atria of lateral ventricles, in the fourth ventricle, and extending through the foramina of Luschka should not be mistaken for acute IVH.

Another less common type of extracerebral ICH that may present acutely is a pituitary hemorrhage, which is usually associated with pituitary apoplexy due to pituitary necrosis that may become hemorrhagic. Presenting symptoms may include headache, visual loss, ophthalmoplegia, nausea, and vomiting. Other causes of pituitary hemorrhage include tumors (e.g., macroadenoma and germinoma) and, less commonly, trauma.

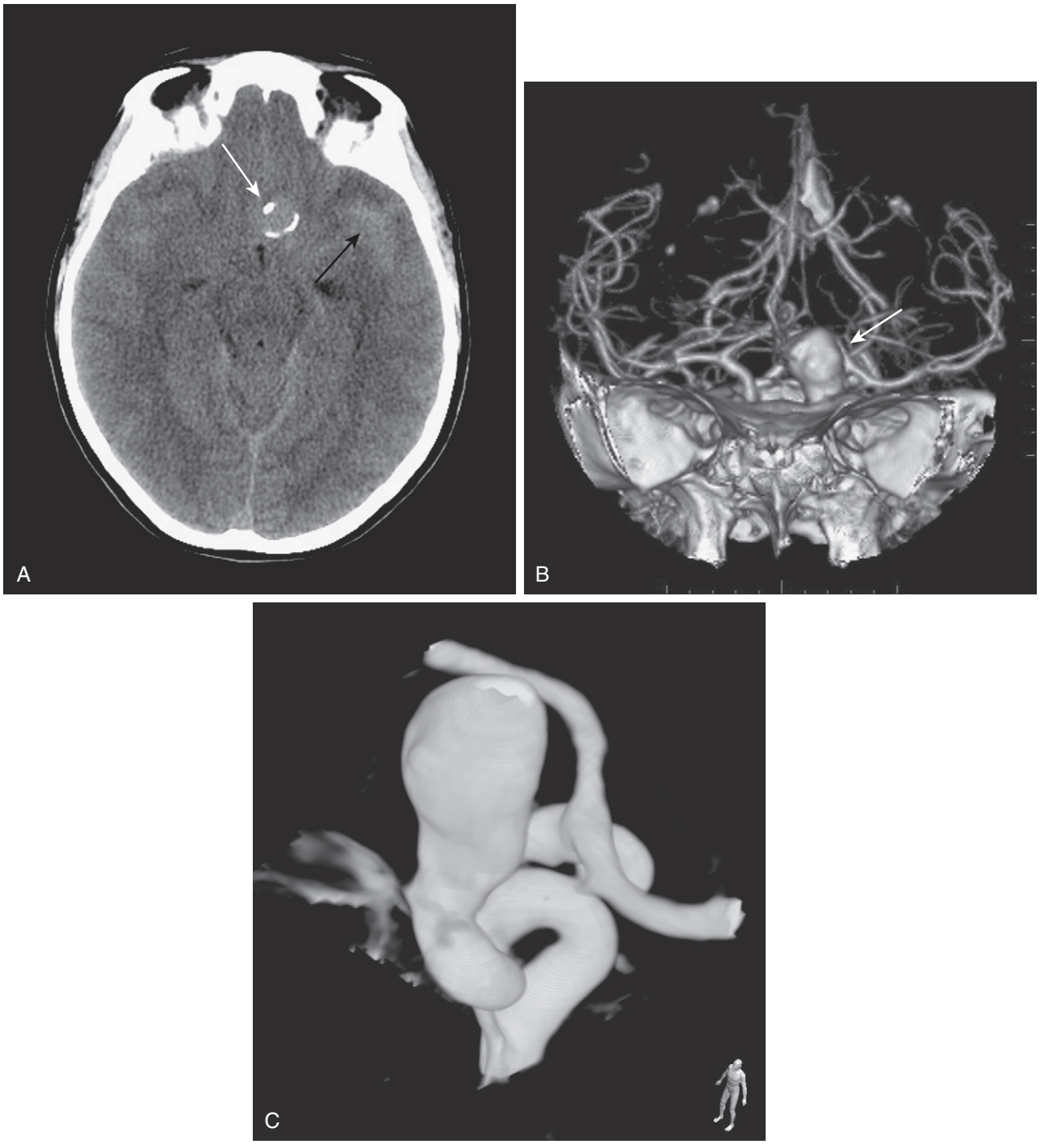


FIGURE 1-6 Subarachnoid hemorrhage from a ruptured aneurysm. **A,** Noncontrast computed tomography (CT) shows ill-defined hyperdense subarachnoid hemorrhage in the left Sylvian cistern *(black arrow)* and rim calcification in the wall of the aneurysm *(white arrow)*. **B,** A volume-rendered image from CT angiography shows a large aneurysm *(arrow)* projecting above the lesser sphenoid wing. **C,** Reconstruction from a three-dimensional rotational digital subtraction angiogram shows the carotid-ophthalmic aneurysm to the best advantage.

INTRAAXIAL HEMORRHAGE

The cause of intraaxial (parenchymal) hemorrhages can generally be categorized as spontaneous or traumatic. Traumatic causes include blunt injury from MVCs, assault, and penetrating injuries such as gunshot wounds. Intraaxial hemorrhages have many spontaneous causes, which are discussed in the section on hemorrhagic stroke.

Contusion

Parenchymal contusions result from blunt trauma and can occur in the cortex or white matter. Their locations are typically at the site of greatest impact of brain on bone, including the anterior/inferior frontal lobes and the temporal lobes. They can be considered coup (occurring at the site of impact) or contrecoup (opposite the site of

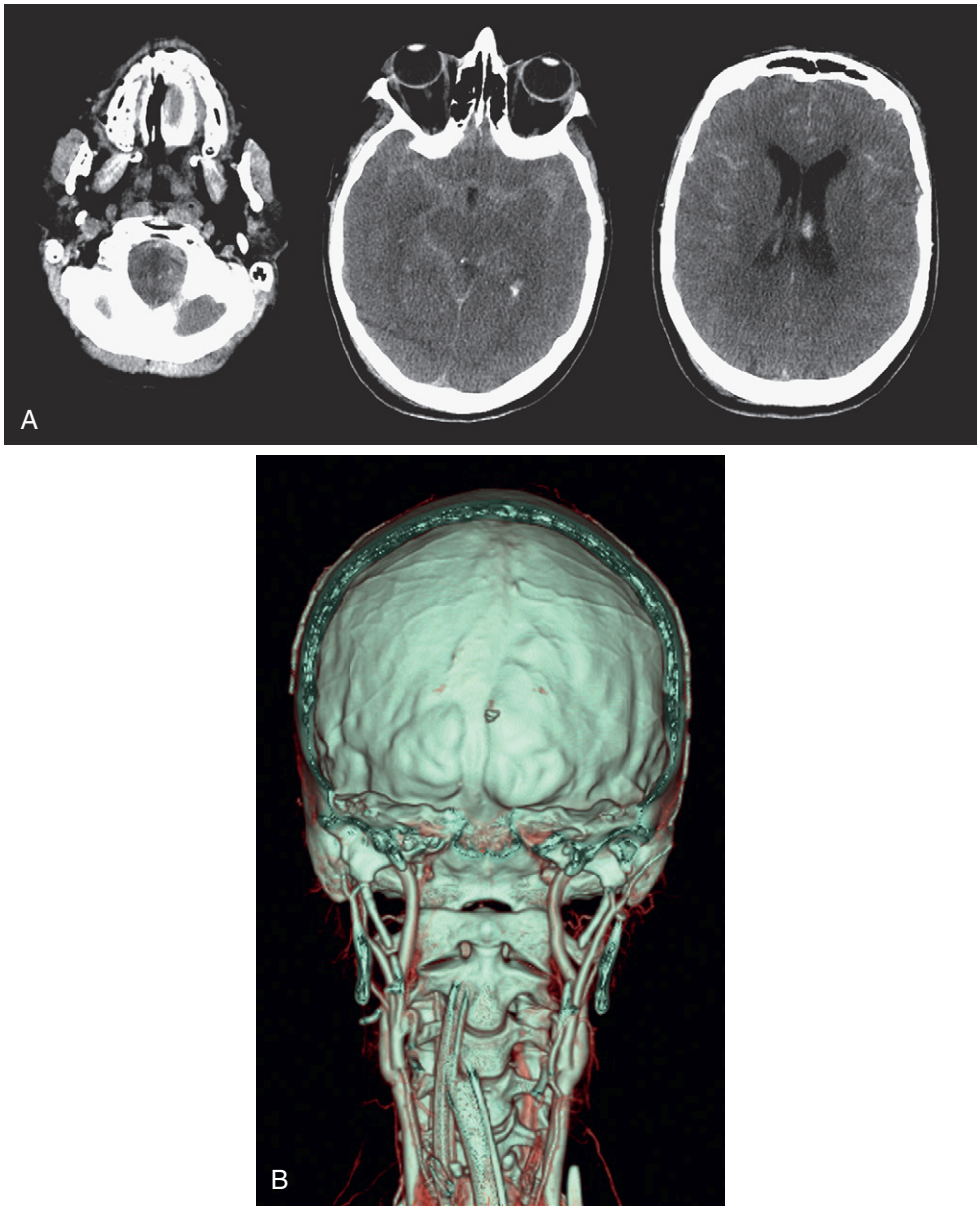


FIGURE 1-7 Subarachnoid hemorrhage and complications. **A,** Three computed tomography (CT) images show diffuse hyperdense subarachnoid hemorrhage filling basal cisterns and cerebral sulci bilaterally. Diffuse loss of gray–white differentiation and effacement of the sulci and cisterns probably preclude the need for further work-up. **B,** A volume-rendered image from CT angiography demonstrates lack of enhancement of intracranial vessels suggesting poor intracranial flow consistent with the expected elevation of intracranial pressure.

impact) types. On CT, a contusion typically appears as an area of hyperdensity with a surrounding rim of hypodense edema. A parenchymal contusion can initially appear as a focal area of subtle hypodensity and may blossom on follow-up examination at 12 to 24 hours with development of an obvious central area of hyperdensity and a larger surrounding zone of hypodense edema (Fig. 1-9). On MRI, signal characteristics reflect the hemorrhagic and edematous components. Over time, the density and signal characteristics of the hemorrhage will evolve in a fashion similar to a spontaneous hemorrhage. Parenchymal hemorrhage due to penetrating trauma, such as from a gunshot wound or impalement, will follow the same general pattern of evolution.

Diffuse Axonal Injury

Diffuse axonal injury (DAI) is another type of traumatic brain injury that may present with parenchymal hemorrhages and is distinct from a parenchymal contusion. DAI is an injury to the axons caused by acceleration/deceleration injury with a rotational component (usually from an MVC or other blunt trauma to the head). Complete transection of axons may occur with injury to the associated capillaries, or partial disruption of the axons may occur. DAI lesions typically occur at the interfaces of gray and white matter in the cerebral hemispheres, the body and splenium of the corpus callosum, the midbrain, and the upper pons. Lesions also may be seen in the basal ganglia.

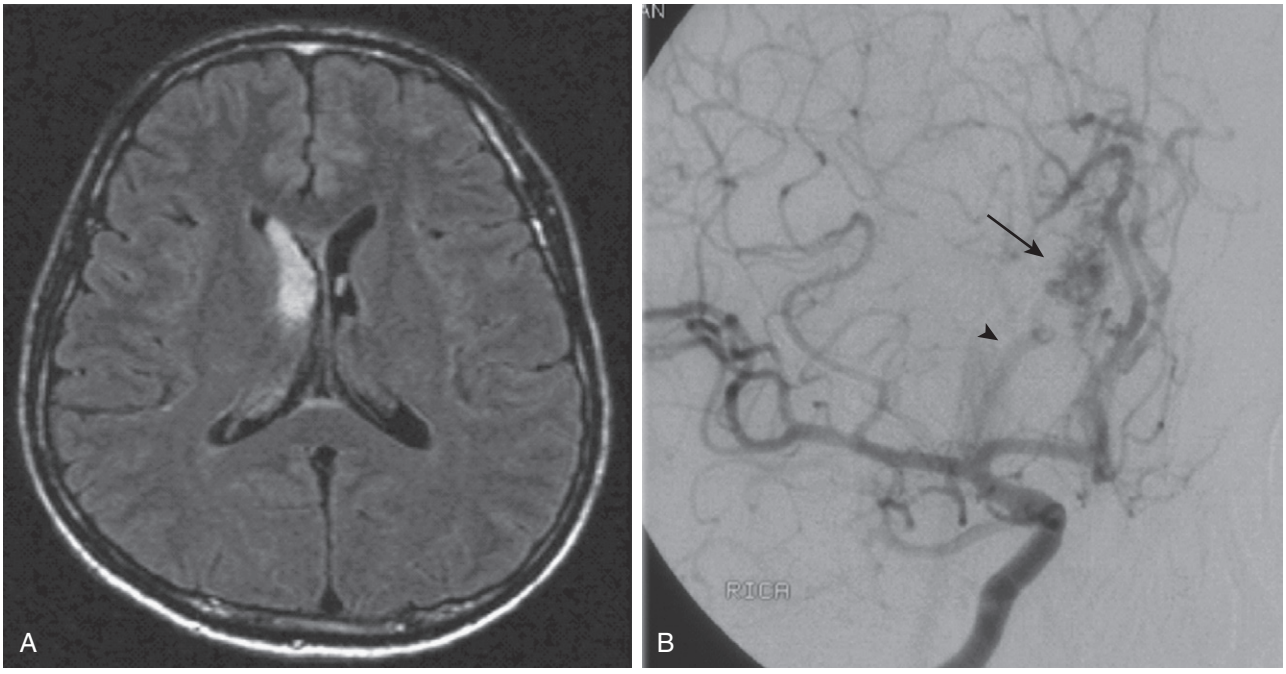


FIGURE 1-8 Intraventricular hemorrhage. **A,** A fluid-attenuated inversion recovery magnetic resonance image shows a hyperintense hemorrhage isolated to the frontal horn of the right lateral ventricle. **B,** An image from a right internal carotid artery digital subtraction angiogram in the late arterial phase shows a nidus *(arrow)* and an early draining vein *(arrowhead)* diagnostic of an arteriovenous malformation.

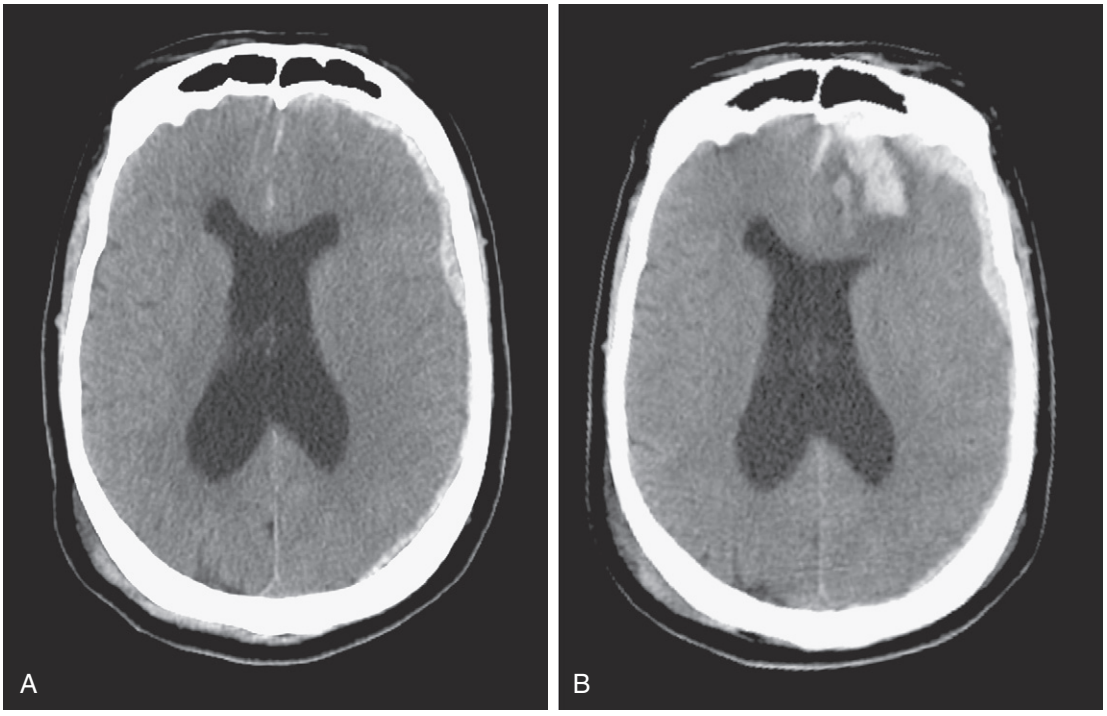


FIGURE 1-9 Blossoming of a contusion. **A,** Computed tomography (CT) shows a thin left frontoparietal subdural hematoma tracking along the anterior falx and mild sulcal effacement. **B,** A follow-up CT scan after 24 hours shows a hyperdense parenchymal hemorrhage and surrounding edema in left frontal lobe and a stable subdural hematoma. Notice the mass effect on the left lateral ventricle.

Patients sustaining DAI typically lose consciousness at the moment of impact. DAI may be suspected when the clinical examination is worse than expected based on the findings of an initial CT scan. Usually, the greater the number of lesions, the worse the prognosis. Persons who recover usually demonstrate lingering effects such as headaches and cognitive deficits. Initial CT scans in more than half of patients with DAI may be negative. CT findings include hypodense foci due to edema in areas of incomplete axonal disruption and hyperdense foci due

to petechial hemorrhage where complete transection of the axons and associated capillaries has occurred (Fig. 1-10). MRI is more sensitive than CT for detection of DAI. Approximately 30% of persons with negative CT findings will demonstrate abnormal findings on MRI. These findings include FLAIR and T2WI hyperintensities (edema) and gradient-echo hypointensities (hemorrhages) (Fig. 1-11). Lesions may appear hyperintense on diffusion-weighted images. It is estimated that more than 80% of DAI lesions are nonhemorrhagic. Generally, if imaging is repeated within 3 to 5 days, more lesions will become apparent as the process evolves.

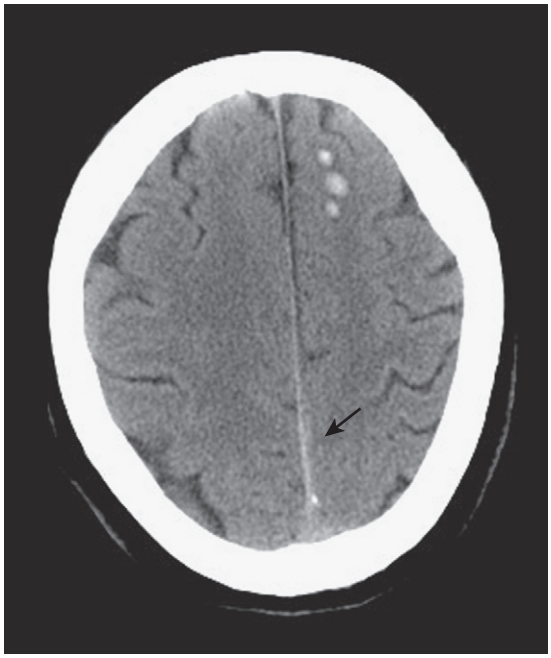


FIGURE 1-10 Shear hemorrhages of diffuse axonal injury. Noncontrast computed tomography shows three small hemorrhages in the left superior frontal gyrus after blunt head trauma. Note a subdural hematoma along the falx *(arrow)*.

A staging system for DAI based on locations of lesions on histopathology may be applied to MRI findings. Stage 1 is based on subcortical lesions in the frontal and temporal lobes. Stage 2 will also show lesions in the corpus callosum and lobar white matter, and stage 3 will have lesions in the midbrain and pons. Diffusion tensor imaging is well suited to the evaluation of white matter tracts and has been shown to be more sensitive than conventional MRI for detection of DAI and correlates more closely with clinical outcomes. Diffusion tensor imaging may be helpful for long-term diagnostic evaluation of patients with mild traumatic brain injury more so than in the initial emergency setting.

BRAIN HERNIATIONS

Brain herniation is a potentially devastating complication of increased intracranial pressure. The most common causes include ICHs, brain tumors, and cerebral edema from stroke or anoxic injury. To explain this concept, a common example from the literature describes the brain as being separated into multiple compartments within a rigid container. Any shift of the brain from one compartment to another is considered herniation. With shift of the brain, there can be mass effect on adjacent and contralateral parenchyma, the brainstem, major intracranial vessels, and cranial nerves. As a result, the feared complications of herniations include ischemic infarcts due to compression of the major intracranial vessels (commonly, the anterior and posterior cerebral arteries), cranial nerve

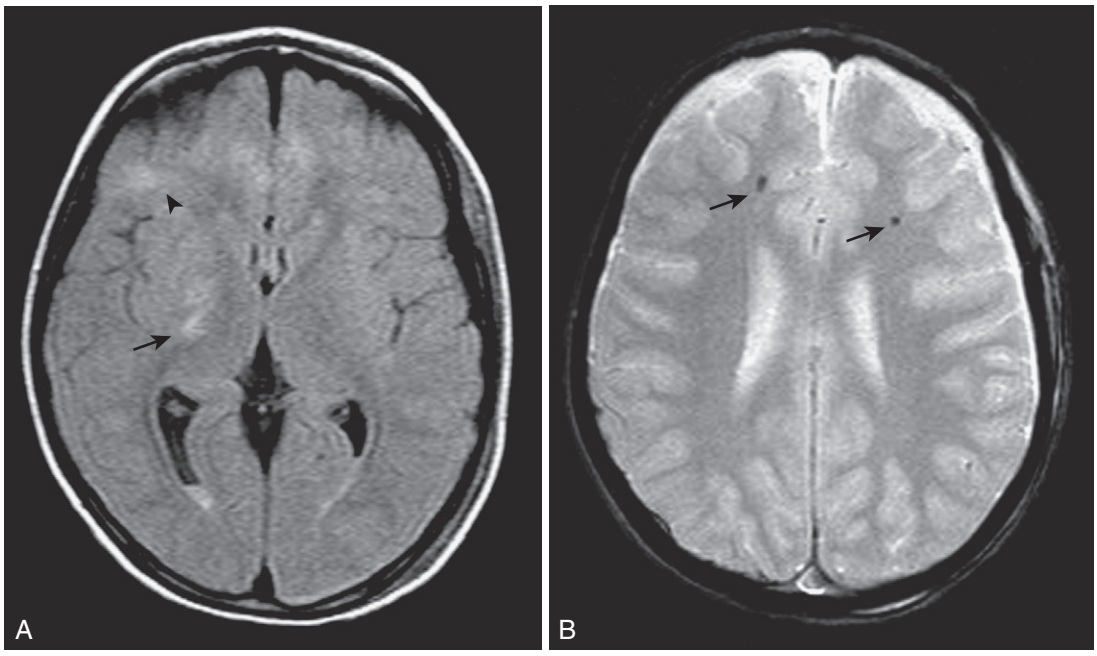


FIGURE 1-11 Diffuse axonal injury. **A,** Fluid-attenuated inversion recovery hyperintensities in the posterior limb of the internal capsule *(arrow)* and subcortical white matter *(arrowhead)*. **B,** Gradient-echo hypointensities in the subcortical white matter indicative of hemorrhages *(arrows)* were not evident on other sequences. Note intraventricular hemorrhage in the occipital horns of the lateral ventricles.

palsies, and "brain death" due to compression and infarction of the brainstem. The major types of intracranial herniations include subfalcine, transtentorial, tonsillar herniation through the foramen magnum, extracranial herniation (through a defect in the skull), and, less commonly, transalar herniation. Once the complications of herniation have developed, it is often too late to intervene. Thus it is best to recognize the signs of impending herniation, when prompt neurosurgical intervention may avert disaster.

Subfalcine Herniation

Subfalcine herniation occurs as a result of displacement and impingement of the cingulate gyrus underneath the falx. It is usually caused by mass effect on the frontal lobe and is associated with ipsilateral lateral ventricle compression and obstruction of the foramen of Monro with dilatation of the contralateral ventricle ("trapped ventricle"). The degree of midline shift (not synonymous with subfalcine herniation) can be estimated by drawing a line between the anterior and posterior attachments of the falx and measuring the shift of the septum pellucidum relative to this line (see Fig. 1-3). Anterior cerebral artery territory infarct(s) may result from this type of herniation.

Transtentorial Herniation

Transtentorial herniations include two major types: descending transtentorial herniation (DTH) and ascending transtentorial herniation (ATH). An early DTH is known as *uncal herniation*, in which the uncus (i.e., the anterior portion of the parahippocampal gyrus) is displaced medially and occupies the ipsilateral suprasellar cistern. A later-stage DTH is caused by continued mass effect with displacement of the remainder of the medial temporal lobe through the tentorial incisura, which completely occupies the suprasellar cistern (along with the uncus) and causes enlargement of the ipsilateral and effacement of the contralateral ambient cisterns. This phenomenon occurs because, as there is marked shifting of brain in the supratentorial compartment, the brainstem shifts in the same direction. Occasionally, when marked mass effect is present, there can be compression of the contralateral cerebral peduncle against the tentorium, or "Kernohan's notch," which leads to ipsilateral motor weakness (this phenomenon may be a false localizing sign). Other imaging findings include a "trapped" temporal horn of the lateral ventricle contralateral to the side of the mass and Duret hemorrhages—that is, hemorrhages of the midbrain and pons caused by stretching and tearing of the arterial perforators. In cases of bilateral mass effect, displacement of both temporal lobes and midbrain can occur through the incisura, leading to effacement of the basilar cisterns bilaterally. Complications of this type of herniation include compression of the posterior cerebral artery and penetrating basal arteries with associated infarcts in these vascular distributions (see Fig. 1-2). In addition, compression of the oculomotor nerve (cranial nerve [CN] III) can occur with an associated palsy. ATH is less common and is caused by superior displacement of the cerebellum and brainstem through the incisura. ATH is usually due to mass effect in the posterior fossa (as from hemorrhage, tumor, or infarct), and imaging shows compression on the posterolateral midbrain with associated effacement of the ambient and quadrigeminal plate cisterns. Hydrocephalus is usually present as a result of obstruction at the level of the cerebral aqueduct of Sylvius.

Tonsillar Herniation

Tonsillar herniation is caused by downward displacement of the cerebellar tonsils through the foramen magnum into the spinal canal (generally by more than 5 mm). Imaging shows a peg-like configuration to the tonsils with obliteration of the CSF space in the foramen magnum (Fig. 1-12). Complications include obstructive hydrocephalus from compression of the fourth ventricle. Mild tonsillar ectopia, Chiari I malformations, and sagging tonsils due to intracranial hypotension should not be mistaken for acute tonsillar herniation, but it should be considered seriously when downward mass effect is expected based on brain edema, mass, or hemorrhage.

Extracranial Herniation

An extracranial herniation is the displacement of brain parenchyma through a cranial and dural defect that is usually caused by trauma or a craniectomy (usually performed to prevent downward herniation from acute cerebral edema). Complications may include infarction of the herniated brain tissue.

Transalar Herniation

Transalar herniation is uncommon and, by itself, does not cause symptoms. It is usually associated with subfalcine and transtentorial herniations. This type of herniation is caused by displacement of the temporal lobe anteriorly or of the frontal lobe posteriorly across the sphenoid wing. One should look for anterior or posterior displacement of the middle cerebral artery to identify this type of herniation.

In the setting of severe head trauma, many of these different types of injuries may coexist. The mechanism of injury should correspond with the degree of injury. In cases when the reported mechanism is mild, nonaccidental trauma (e.g., "Trauma X" and "shaken-baby syndrome") should be considered. Infants, children, persons with mental or physical disabilities, and elderly persons are particularly at risk. Skull fractures, SAH, SDH, contusions, shear injuries, infarcts, vertebral compression fractures, and retinal hemorrhages constitute the usual neuroradiologic spectrum of abnormalities. Injuries of different ages, metaphyseal and rib fractures, and visceral injuries are other common findings of child abuse.

ACUTE CEREBROVASCULAR DISORDERS

Although acute cerebrovascular disorders usually do not occur as a result of trauma, they are treated with the same urgency as traumatic injuries or spontaneous ICH. According to the American Heart Association update for 2015, in the United States, approximately 800,000 strokes occur each year (on average, about one stroke occurs every 40 seconds, resulting in one death every 4 minutes). Almost 25% are recurrent, and 75% occur in persons older than

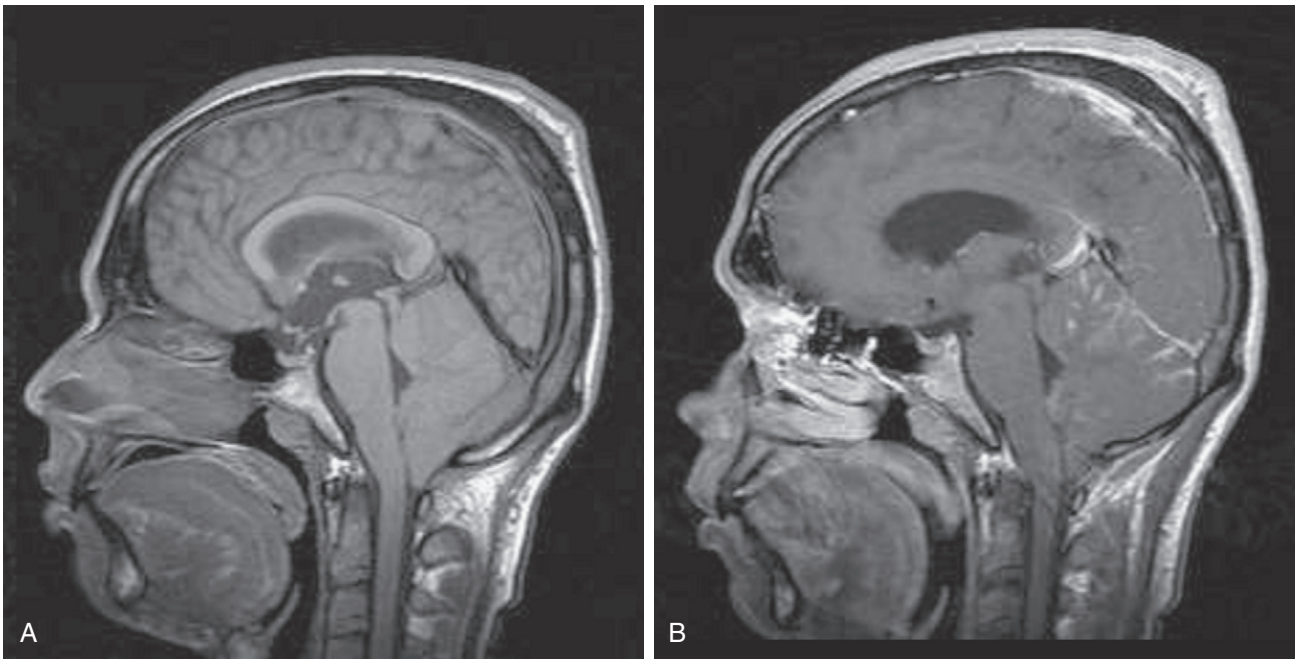


FIGURE 1-12 Tonsillar herniation. **A,** A sagittal T1-weighted image shows the pegged appearance of the cerebellar tonsils extending through the foramen magnum, simulating a Chiari I malformation (representing a dramatic change from a previous examination). **B,** A postgadolinium T1-weighted image shows cerebellar leptomeningeal enhancement due to cryptococcal meningoencephalitis in this patient with acquired immunodeficiency syndrome.

65 years. The 20% mortality rate is surpassed only by cardiac disease, cancer, and chronic lung disease. Stroke is the leading cause of severe, long-term disability and long-term care. Estimates of annual cost exceed $50 billion.

One clinical definition of stroke is a neurologic deficit caused by inadequate supply of oxygen to a region of the brain. Stroke can be due to a low flow state or rupture of a vessel and thus may be divided into ischemic and hemorrhagic varieties. The definition of stroke used for current clinical trials requires symptoms lasting more than 24 hours or imaging of an acute clinically relevant brain lesion in a patient with rapidly vanishing symptoms. In the past, a transient ischemic attack (TIA) implied resolution of the deficit within a 24-hour period. The current definition of TIA is a brief episode of neurologic dysfunction caused by a focal disturbance of brain or retinal ischemia, with clinical symptoms typically lasting less than 1 hour, and without evidence of infarction. Estimates of the annual incidence of TIA in the United States vary from 200,000 to 500,000. The 1-year mortality rate after TIA has been reported to be 12%. Evidence of acute infarction may be identified by MRI (tissue-based case definition) in up to 30% of patients who meet the clinical criteria for a TIA. Semantics can be unclear when an abnormality is detected on imaging in the absence of symptoms.



FIGURE 1-13 A spontaneous parenchymal hemorrhage as a result of uncontrolled hypertension. Noncontrast computed tomography in a patient with uncontrolled hypertension shows a large hyperdense parenchymal hemorrhage arising in the basal ganglia with intraventricular extension. Note the ventriculostomy catheter in the right lateral ventricle.

Hemorrhagic Stroke: Spontaneous Parenchymal Hemorrhage

Approximately 10% to 15% of strokes present with an acute parenchymal hemorrhage. The most common cause is hypertension (Fig. 1-13). Coagulopathies, hematologic disorders including hypercoagulable states, amyloid angiopathy, drugs, vascular malformations and aneurysms, vasculitides, and tumors round out the usual list of causes. (Refer to the section on aneurysms and vascular malformations in this chapter for a discussion of CT angiography in the setting of acute ICH.) Hemorrhages resulting from use of illicit drugs and vascular malformations are commonly found in young adults (Fig. 1-14). Sickle

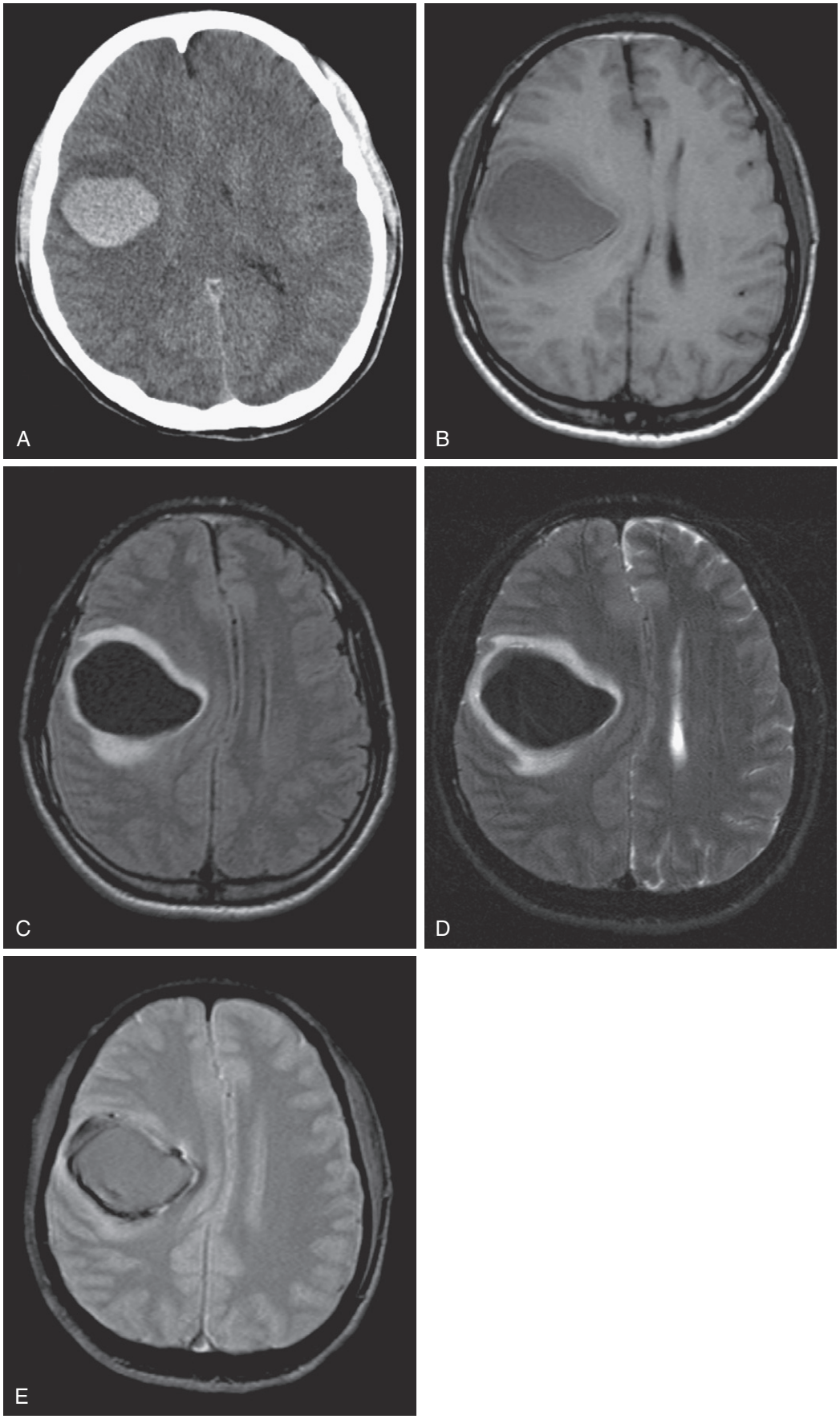


FIGURE 1-14 A parenchymal hemorrhage due to use of an illicit drug—Ecstasy (3,4 methylenedioxymethamphetamine). **A,** Computed tomography shows a hyperdense acute hemorrhage with minimal surrounding hypodense edema. **B,** A T1-weighted image shows iso- to mild hyperintensity with hypointense edema. Fluid-attenuated inversion recovery **(C)** and fat-suppressed T2-weighted gradient and spin echo **(D)** show hypointensity with surrounding hyperintense edema. **E,** Gradient echo shows a peripheral rim of signal loss and blooming. In summary, signal changes on T1- and T2-weighted images are consistent with deoxyhemoglobin, although the gradient echo suggests only a rim of deoxyhemoglobin.

cell disease and venous infarcts also may present with parenchymal hemorrhage. A ruptured intracranial aneurysm occasionally may cause a parenchymal hemorrhage in association with SAH. Hypertensive hemorrhages most commonly occur in the basal ganglia and thalamus but also may primarily arise within the cerebral hemispheres, brainstem, or cerebellum. Cerebral amyloid angiopathy (CAA) is another common cause of ICH in patients older than 65 years. CAA can be found in patients with mild cognitive impairment, Alzheimer-type dementia, and Down syndrome with extracellular deposition of β-amyloid occurring in the cortex and subcortical white matter. CAA can be hereditary (autosomal dominant, Dutch type), sporadic (with the presence of the Apoε4 allele), or acquired (as from hemodialysis). The lobar hemorrhages of CAA typically occur in the frontal and parietal regions. MRI is sensitive for the detection of hemosiderin deposition resulting from multiple microhemorrhages over the course of time that appear as small hypointense foci on gradient-echo sequences.

Imaging of Acute Ischemic Stroke

Computed Tomography

The role of imaging in acute stroke diagnosis and management continues to evolve. Since the mid 1970s, unenhanced CT has been the first-line modality to determine the cause of acute neurologic deficits. CT can offer the chance to detect an ischemic infarct, generally in the middle cerebral artery territory, within 3 hours in up to one third of cases based on findings of subtle parenchymal hypodensity, loss of gray–white matter differentiation (including loss of the insular ribbon or margins of basal ganglia; Fig. 1-15), and effacement of sulci. A hyperdense vessel sign may indicate the presence of an acute thrombus and support the diagnosis. The sensitivity for detection of acute stroke has been shown to increase with the use of the "acute stroke" window and level settings (see Fig. 1-15). A very narrow window width of 8 Hounsfield units (HUs) and a level of 32 HUs (compared with 80 and 40 HUs, respectively) may increase the sensitivity of CT to approximately 70% without a loss of specificity.

CT is currently used to screen patients who may be considered for treatment with intravenous recombinant tissue plasminogen activator (rt-PA). This medication is currently approved by the Food and Drug Administration for use within 3 hours of onset based on guidelines from the National Institute of Neurologic Disorders and Stroke rt-PA trial. Since 2013, its use within 4.5 hours of stroke onset in selected patients has been endorsed in a joint clinical policy statement of the American College of Emergency Physicians, American Academy of Neurology, and Neurocritical Care Society. Beyond this time, the risk of ICH due to intravenous thrombolysis was shown to outweigh potential benefits. An association between larger stroke volumes (greater than one third of the middle cerebral artery territory) and reperfusion hemorrhage was initially reported. This criterion for the use of 100 mL estimated infarct volume has commonly been applied in stroke trials. The Alberta Stroke Program early CT score, a 10-point topographic scoring system, was developed to try to more easily quantify initial stroke volumes. This score has been shown to correlate with the initial National Institutes of Health stroke score and is one piece of data that may be considered in determining patient management.

Magnetic Resonance: Diffusion-Weighted Imaging

MRI with diffusion-weighted imaging (DWI), which became widely available in routine clinical practice in the late 1990s, offers significantly greater sensitivity and specificity for the detection of acute stroke (greater than 90% compared with approximately 60% for CT). Energy depletion will trigger a cascade that alters the internal cellular milieu, such as the glutamate excitotoxic pathway, in which reduced energy-dependent glutamate reuptake within the synaptic clefts results in the development of cytotoxic edema. The restriction of water molecule diffusion appears as hyperintensity on diffusion-weighted images. The diffusion "experiment" can be performed with a variety of rapid imaging techniques, such as echo planar imaging, and can acquire images of the entire brain in half a minute. This approach minimizes the effects of patient motion, which is especially important when the clinical presentation includes alteration of mental status. The apparent diffusion coefficient (ADC) value is a quantitative measure that may be calculated from the diffusion-weighted images. Because diffusion-weighted images rely on both diffusion and T2 effects, it is wise to confirm that the ADC values are indeed reduced before diagnosing an acute infarct. This confirmation will reduce the number of false-positive results due to the "T2 shine-through" effect from old infarcts (gliosis) or other T2 hyperintense processes such as vasogenic edema.

Acute ischemic infarcts appear as hyperintense regions on DWI (see Fig. 1-15) as quickly as 30 minutes after onset. Up to 100% sensitivity has been demonstrated in clinical studies. However, in routine practice, small lesions in the brainstem may not be perceived initially, only to be detected on a follow-up examination prompted by persistent symptoms. It is also possible that a region of ischemia (prior to a completed infarction) may not be detected on an initial imaging study, thus providing a false-negative result. False-positive results on DWI can be due to processes that mimic stroke and also cause diffusion restriction, such as certain neoplasms, multifocal metastatic disease, and abscesses. The presence or absence of associated findings on conventional MRI sequences—such as loss of gray–white matter differentiation on T1WIs and hyperintense edema on FLAIR and T2WIs—may help with diagnosis, although these signs may be inconspicuous for 6 to 12 hours after stroke onset. Blooming on gradient-echo sequences due to intravascular thrombus and loss of expected vascular flow voids are other useful clues.

Lacunar infarcts are generally less than 1 cm in diameter and are presumed to be due to occlusion of small perforating branches as a result of embolic, atheromatous, or thrombotic lesions. Lacunar infarcts occur most commonly in the basal ganglia, internal and external capsules, immediate periventricular white matter (corona radiata), and, less frequently, in the centrum semiovale. Occlusion of basilar artery perforators will result in lacunes in the brainstem. Diffusion imaging offers the ability to identify very small, acute infarcts even in the background of chronic white

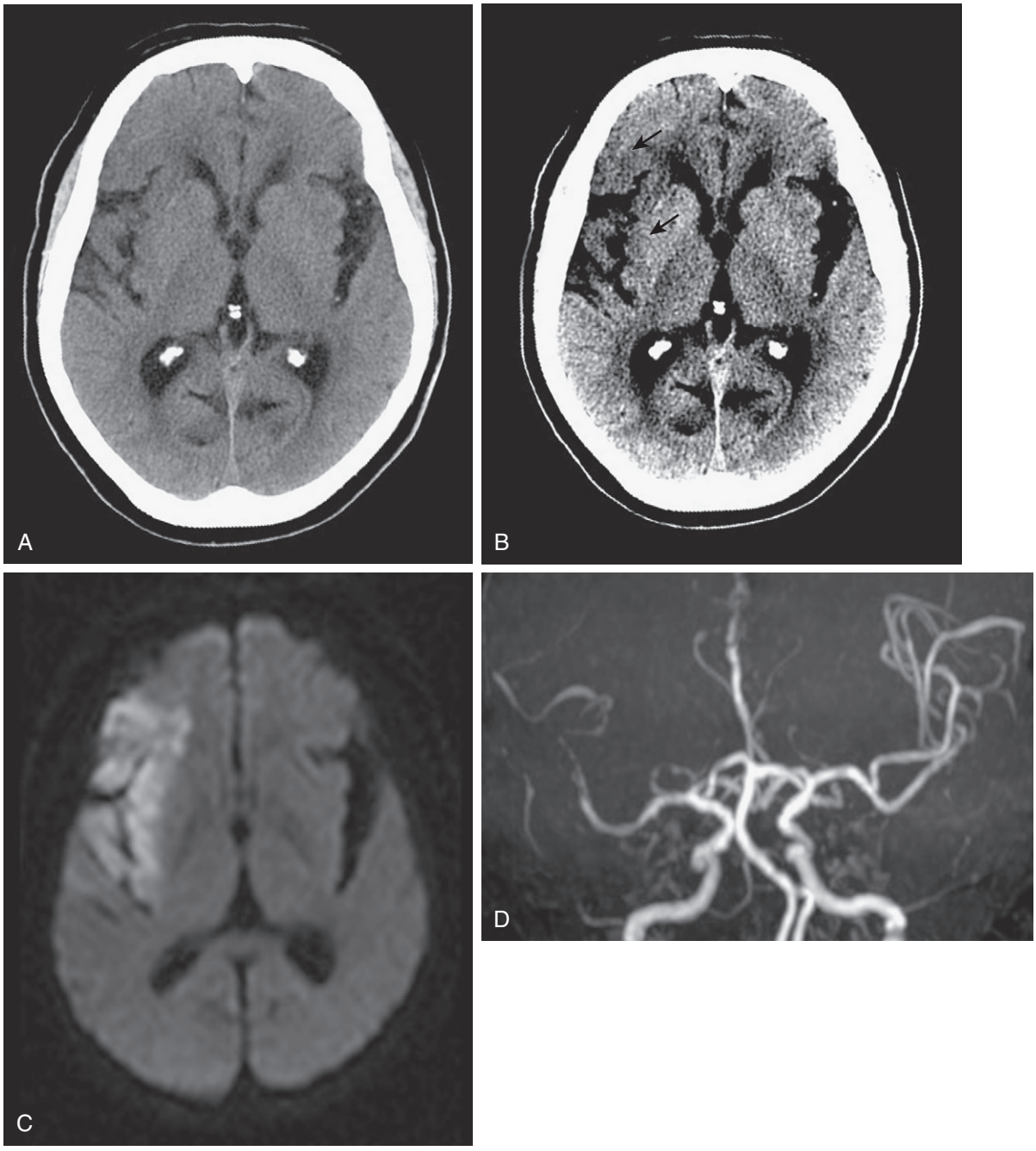


FIGURE 1-15 A hyperacute infarct. **A,** Noncontrast computed tomography with a window/level of 80/40 shows a subtle decrease in density of the right insular cortex. **B,** The insular "ribbon" sign is more conspicuous with a stroke window/level of 40/40 *(arrows)*. **C,** The infarct is much more conspicuous on a diffusion-weighted image. **D,** Time-of-flight magnetic resonance angiography shows attenuation of right middle cerebral artery distal branches.

matter disease and remote lacunes (Fig. 1-16). Although MRI is still considered a relatively expensive technique, it has the potential to reduce the number of unnecessary hospital admissions for recurrent small vessel infarcts in many patients. It also may assist in selecting the most appropriate pathway for patients with central embolic sources of infarcts based on the detection of infarcts in different vascular territories.

MRI is also valuable in the setting of neonatal hypoxic ischemic encephalopathy. Cranial ultrasonography and CT may be used to evaluate germinal matrix hemorrhages, periventricular leukomalacia, and hydrocephalus. Diffusion-weighted MRI is most sensitive for evaluating the different patterns of injury. In preterm infants subjected to mild hypotension, the periventricular regions are most often affected. With more severe hypotension, the basal ganglia, brainstem, and cerebellum may be involved. In full-term infants with mild hypotension, infarcts in the border zones between anterior and middle cerebral arteries or between middle and posterior cerebral arteries may result. Severe hypotension may result in infarcts of basal ganglia, hippocampi, corticospinal tracts, and sensorimotor cortex.

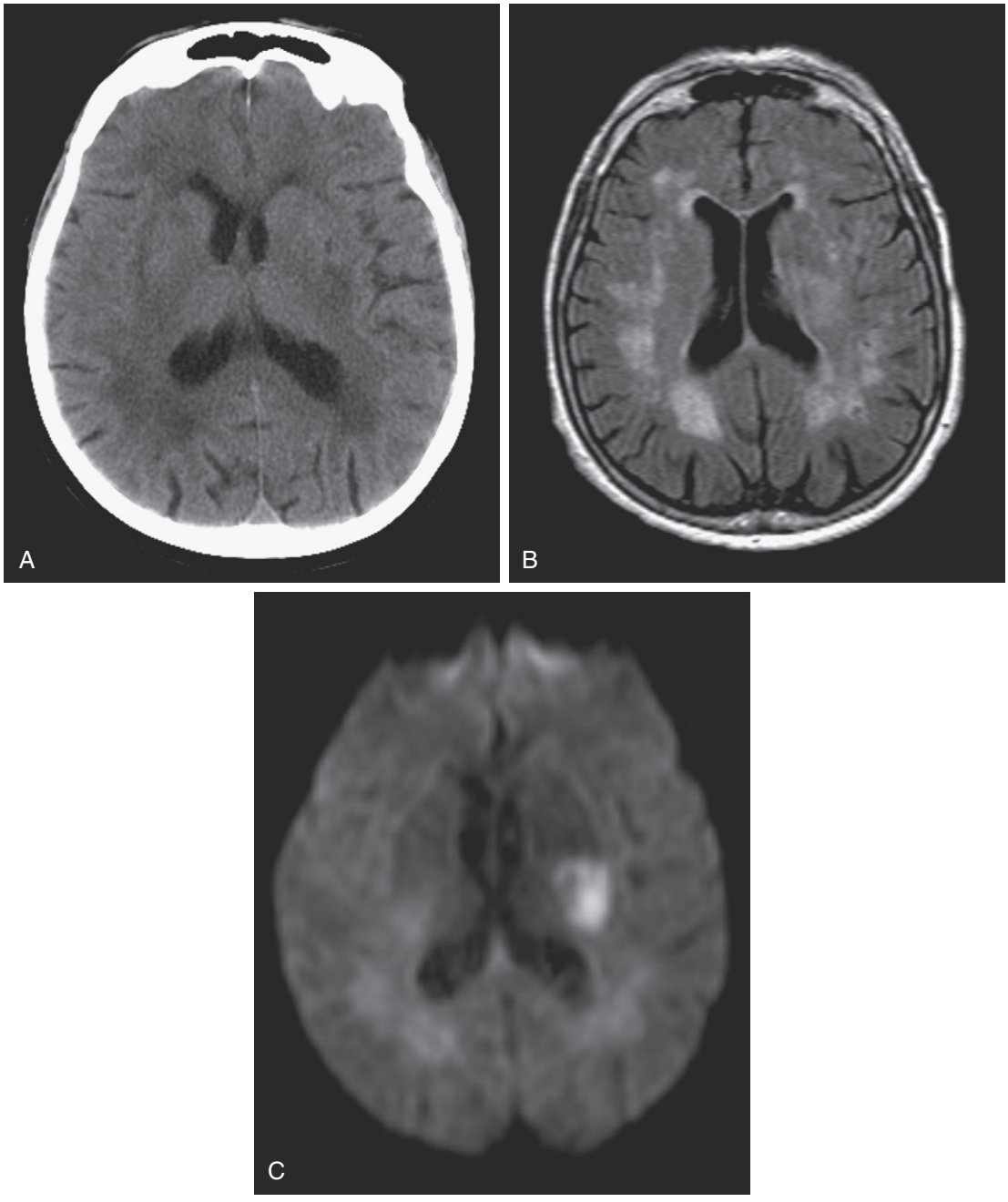


FIGURE 1-16 An acute lacunar infarct. **A,** Computed tomography shows multifocal hypodensities. **B,** A fluid-attenuated inversion recovery image shows corresponding hyperintensities due to chronic small vessel disease. **C,** A diffusion-weighted image shows the acute infarct in the left lentiform nucleus/posterior limb of internal capsule in a patient with acute onset of right-sided weakness. An apparent diffusion coefficient map (not shown) confirmed restricted diffusion. Other periventricular white matter mild hyperintensities are the result of "T2 shine-through."

Diffusion-weighted hyperintensity generally begins to decline after a few days, with the process of ADC pseudonormalization usually taking place during the next few weeks. Final ADC values will vary based on the degree of gliosis or cavitation of the infarct. It should be noted that infarct development depends on the magnitude and duration of ischemia and the metabolic demands of the affected tissue. Although diffusion restriction due to ischemia almost always results in infarction, rare cases of spontaneous reversible diffusion abnormalities have been reported, as well as those occurring in the setting of thrombolytic therapy.

Magnetic Resonance Angiography

Noninvasive imaging of the vessels of the head and neck with MR angiography (MRA) based on time-of-flight or phase-contrast MRA techniques can be used to locate stenoses and occlusions in the extracranial and intracranial arterial systems (see Fig. 1-15). Gadolinium-enhanced MRA has become the standard of care at some institutions; this procedure requires consideration of renal function. Complete brain MRI and head and neck MRA examinations can be acquired in less than 30 minutes and have become the routine standard of care; they are often performed immediately or soon after completion of CT. It must be stressed

that patient safety is a primary concern and therefore careful attention to screening for potential contraindications prior to MR scanning is a requisite at all times.

Magnetic Resonance: Perfusion Imaging

It became clear from imaging-based stroke trials that final infarct volumes were often larger than those identified by imaging at the time of admission. Advances in rapid scanning techniques soon led to the ability to obtain functional images of brain perfusion. By demonstrating an ischemic zone at the periphery of an acute infarct, salvageable tissue (the so-called *penumbra*) could be targeted with novel therapies. Dynamic gadolinium-enhanced T2* perfusion-weighted imaging (PWI) is one available technique that is based on the decrease in tissue signal intensity as a function of time during passage of a bolus of contrast material. Functional "maps" of different perfusion parameters may be calculated from the time-signal intensity curves obtained during a minute-long acquisition. Cerebral blood volume (CBV) and tissue mean transit time (MTT) can be estimated using different methods, most commonly deconvolution analysis. One limitation of MR-based techniques is that the blood volume estimate is a relative value. Cerebral blood flow (CBF) can be estimated by dividing CBV by MTT. A penumbra will be identified when a region of decreased CBF or prolonged MTT is larger than the infarct detected by DWI—a perfusion mismatch. Based on the extent of the mismatch, aggressive therapies may be pursued to limit the final infarct volume.

In some cases, the perfusion abnormality may exactly match the diffusion abnormality, and thus there is no penumbra. The final infarct volume is not expected to increase further. In other cases, when prompt reperfusion has occurred, such as from early vessel recanalization, the perfusion abnormality may be smaller than the diffusion abnormality. In both of these situations, the risk of aggressive treatment is probably not warranted. The potential of improved clinical outcomes from therapeutic strategies based on perfusion imaging may result from either salvage of tissue at risk or reduction of complications.

Arterial spin labeling (ASL) is an MR perfusion technique that does not require injection of a contrast agent. ASL uses paramagnetic labeling of water in blood flowing to the brain to produce measurements that are proportional to CBF. There are many varieties and technical limitations of ASL. Clinical utility will require determination of appropriate clinical perfusion thresholds. ASL is becoming increasingly available but is not yet used routinely at most centers.

Computed Tomography: Perfusion Imaging

The advent and wide availability of multidetector CT (MDCT) scanners has led to the use of CT angiography (CTA) and CT perfusion (CTP) imaging in the workup of suspected acute ischemic stroke. The ability to acquire a large 3D volume of data rapidly during administration of a bolus of contrast material combined with submillimeter spatial resolution results in CTA images that in many instances approach the diagnostic quality of more invasive digital subtraction angiograms. Large detector arrays and cine or shuttle modes of scanner operation allow for generous coverage of the brain during perfusion studies. Detector arrays with 64 rows are common now, and newer models with up to 320 rows are available. Analogous to PWI, CTP is based on measurement of tissue density as a function of time during a first pass of an intravenous contrast agent and commonly uses deconvolution analysis. In contrast to PWI, as a result of the proportionate increase in tissue attenuation due to iodine concentration, quantitative (rather than relative) estimation of CBV (and therefore CBF) can be obtained by CTP. Other parameters including time to maximum enhancement (Tmax) also may be measured.

CTP applied in the setting of acute stroke has been validated with clinical outcomes and follow-up imaging and also by comparison with DWI. Wintermark and colleagues initially proposed that regions with a CBV less than 2.5 mL/100 g be considered the "core infarct" and regions with a CBF reduction of more than 34% be defined as the penumbra. These values were based on correspondence with initial DWI abnormality and final infarct size. Schaefer and colleagues later proposed other absolute values and the use of normalized CBV and CBF ratios to help distinguish ischemic tissue likely to become infarcted from that likely to survive after intraarterial recanalization therapy. Perfusion maps can be visually compared to determine if a penumbra is present but may underestimate or overestimate the extent of tissue at risk (Fig. 1-17). Software packages are available that can automatically segment the processed perfusion maps into core infarct, penumbra, and normal regions based on thresholding techniques.

Therapeutic trials of desmoteplase, a novel thrombolytic drug, including the Desmoteplase in Acute Ischemic Stroke (DIAS) and Dose Escalation study of Desmoteplase in Acute Ischemic Stroke (DEDAS) trials, were based on demonstration of a perfusion mismatch. Although clinical outcomes were not promising, these trials demonstrated the value of advanced imaging compared with unenhanced CT and use of a strict time limit alone.

Thrombolysis with intravenous rt-PA is limited by a short time window after onset of symptoms and a recanalization rate of less than 50%. Stroke specialists had hoped that an endovascular approach to treatment of severe strokes would be a valuable addition or alternative to intravenous therapy. The paradigm of acute stroke imaging has continued to evolve with clinical trials.

Over the course of several trials without promising results, including randomized, controlled trials of intraarterial treatment (Interventional Management of Stroke III [IMS III], Synthesis, and Mechanical Retrieval and Recanalization of Stroke Clots Using Embolectomy [MR RESCUE]), many lessons were learned. Improved outcomes were demonstrated with enrollment of patients with severe strokes, proof of proximal vessel occlusion, early initiation of treatment, and use of modern thrombectomy devices (i.e., retrievable stents). The recently published results of the Multicenter Randomized Clinical Trial of Endovascular Treatment of Acute Ischemic Stroke in the Netherlands (MR CLEAN), which required demonstration of a proximal vessel occlusion, ended the long drought of negative results for endovascular treatment (Fig. 1-18).

In the Extending the time for Thrombolysis in Emergency Neurological Deficits–Intra-Arterial (EXTEND-IA) trial, the imaging inclusion criteria were a proximal intracranial occlusion, a perfusion mismatch (CTP Tmax >6-second delay perfusion volume compared with CT-CBF or DWI

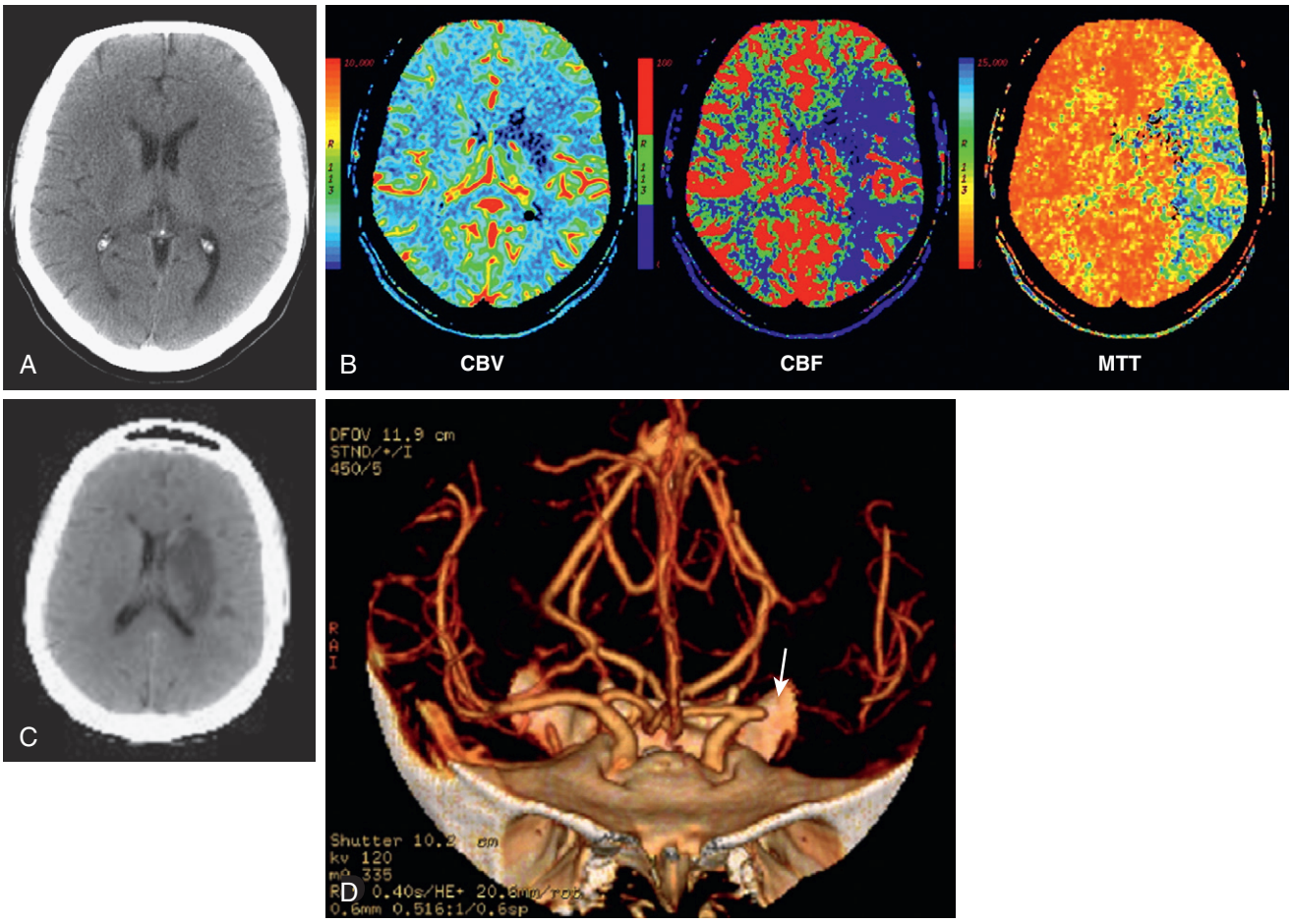


FIGURE 1-17 Perfusion computed tomography (CT)—large mismatch. **A,** Noncontrast CT shows decreased density of the left caudate head and putamen. **B,** Cerebral blood flow (CBF) and mean transit time (MTT) abnormalities are much larger than core infarct (cerebral blood volume [CBV] abnormality). **C,** CT follow-up 1 week after conservative management shows that the final infarct volume closely matches the initial CBV abnormality. **D,** An initial CT angiogram showed abrupt occlusion of the left middle cerebral artery stem *(arrow)* but with filling of distal branches as a result of robust leptomeningeal collateral circulation.

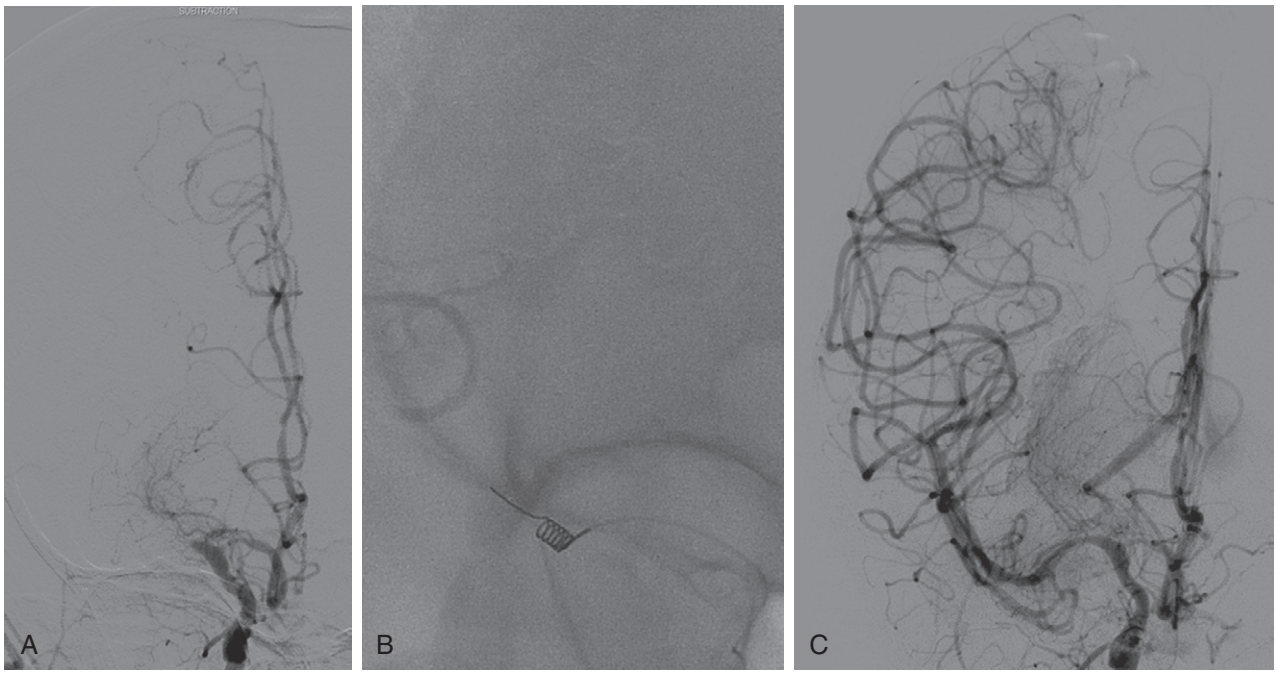


FIGURE 1-18 Mechanical thrombectomy. **A,** An acute right middle cerebral artery occlusion. **B,** A Merci retriever is deployed distal to the thrombus. (Note that newer stent retrievers, such as the Solitaire revascularization device, have supplanted use of this device.) **C,** Recanalization of the right middle cerebral artery after clot retrieval.

infarct core), and infarct core lesion volume less than 70 mL.The study demonstrated that early thrombectomy with a stent retriever in this setting improved reperfusion, early neurologic recovery, and functional outcome.

Another consideration in penumbral imaging is based on assessment of collateral circulation by CTA, MRA, or digital subtraction angiography (DSA). Good collateral circulation has been associated with improved clinical outcomes after treatment even when reperfusion was achieved. Different methods of grading collaterals have been described based on single or multiphase CTA techniques. In the multicenter Endovascular Treatment for Small Core and Anterior Circulation Proximal Occlusion with Emphasis on Minimizing CT to Recanalization Times (ESCAPE) trial, imaging inclusion/exclusion criteria were based on CTA identification of the location of the occlusion, the extent of collateral vessels, and the extent of CTP mismatch (CBV and CBF). Rapid endovascular thrombectomy improved functional outcomes and reduced mortality in patients with acute strokes who had proximal vessel occlusion, a small infarct core, and moderate to good collateral circulation.

A recent mismatch-based penumbral imaging paradigm takes into consideration venous outflow based on MR susceptibility-weighted imaging (SWI). An increase in brain tissue demand for oxygen leads to an increase in concentration of deoxyhemoglobin in capillaries and veins and signal loss on SWI. Perfusion mismatch may be graded by the ratio of SWI abnormality to the DWI infarct core volume.

Thus current paradigms may be based on identification of tissue-based, collateral, or venous outflow–based mismatches. Continued outcomes-based research will be necessary to determine the best imaging protocol to identify the subset of patients who might benefit from aggressive treatment with a reduced risk of symptomatic hemorrhage. It should be noted that great variety exists in the application of these techniques in routine clinical practice. Some authors have proposed that CT and MR perfusion techniques should be limited to research patients and that clinical decisions regarding pursuit of endovascular treatment should be based on results of noncontrast CT, CTA, and DWI examinations.

Hemorrhagic Transformation

Hemorrhagic transformation of an ischemic infarct that is thought to result from reperfusion injury can be a dreaded complication of therapy or may happen spontaneously within hours or after a period of several weeks (Fig. 1-19). If a large hematoma is present at the time of initial imaging, it may not be possible to distinguish a primary parenchymal hemorrhage from hemorrhagic transformation. The blood products generally cause substantial artifacts on DWI. However, if the hemorrhage is confined within a larger zone of restricted diffusion, the cause may be clear. Petechial hemorrhages occur very commonly within an ischemic infarct, are best detected by gradient-echo imaging, and do not usually lead to increased morbidity.

Cortical Laminar Necrosis

A pattern of gyriform T1-weighted hyperintensity developing a week or two after an ischemic infarct may be attributed to cortical laminar necrosis (Fig. 1-20). It seems that gray matter is more vulnerable to ischemic necrosis than white matter (especially the third layer of the six cortical layers), and although the signal changes may lead one to diagnose hemorrhage or calcification, in one histologic study neither was detected.The exact cause of the T1



FIGURE 1-19 Hemorrhagic transformation of an ischemic infarct. Noncontrast computed tomography 24 hours postictus shows a hyperdense hemorrhage within a large left middle cerebral artery territory infarct.

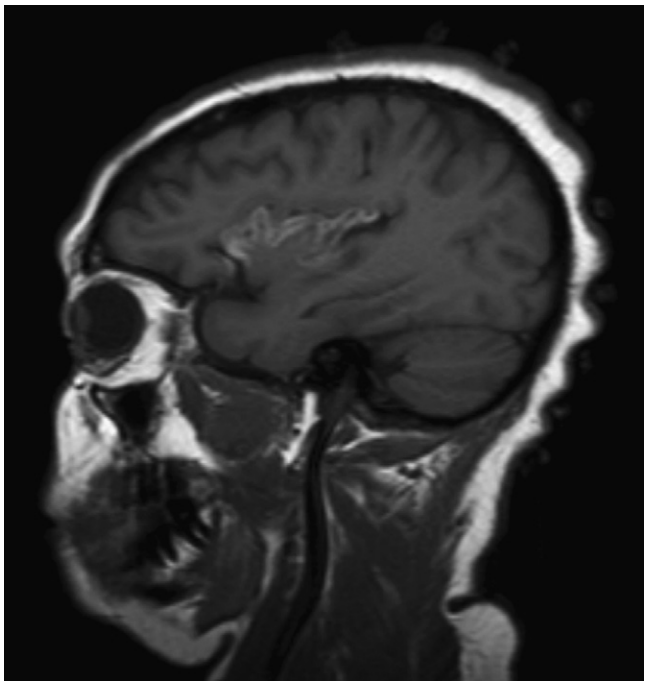


FIGURE 1-20 Cortical laminar necrosis. A T1-weighted image shows gyriform hyperintensity in a peri-sylvian distribution 1 week after a middle cerebral artery infarct.

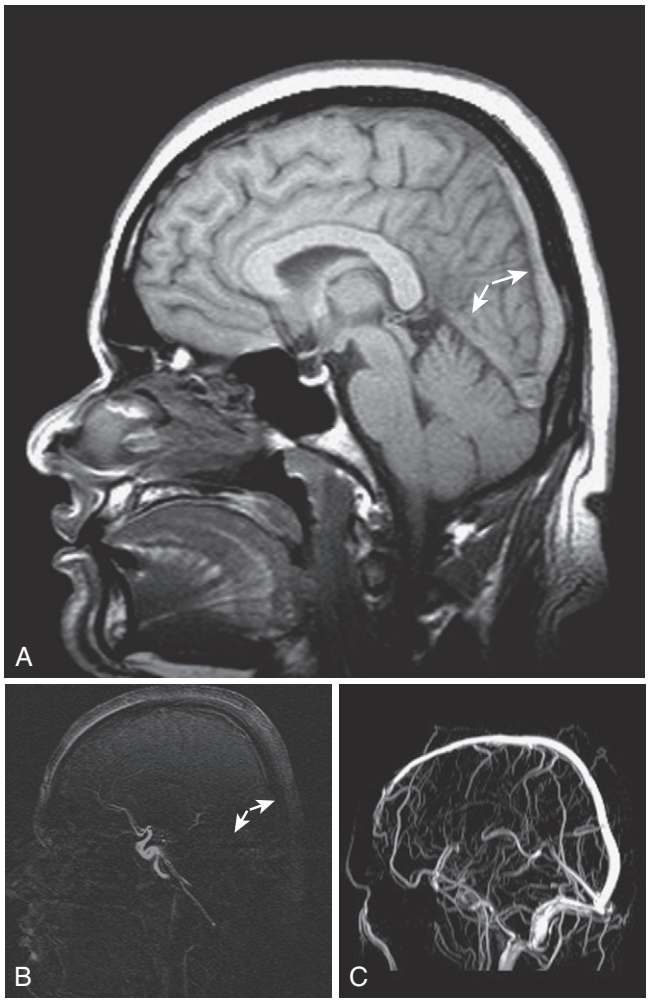


FIGURE 1-21 Venous sinus thrombosis. **A,** T1-weighted image shows loss of usual flow voids in the superior sagittal and straight sinuses *(arrows)*. **B,** Two-dimensional phase contrast magnetic resonance (MR) venography shows a corresponding lack of flow-related signal. **C,** Three-dimensional phase contrast MR venography 1 week after systemic anticoagulation shows recanalization.

shortening is uncertain, but it may be due to high concentrations of proteins and macromolecules related to tissue necrosis.

Cerebral Venous Infarction and Sinus Thrombosis

An uncommon (with annual incidence estimates of less than 1 case per 100,000 population) but important cause of hemorrhage is cerebral venous thrombosis (Fig. 1-21), which may affect cortical veins and other portions of the superficial and deep venous drainage systems. Hypercoagulable states due to pregnancy and the postpartum period or oral contraceptive use, dehydration, regional infections, and trauma are relatively common. Common presenting symptoms include headache, seizure, and focal neurologic deficits. Fluctuating symptoms and intracranial hypertension are common as well. Bilateral parenchymal hemorrhages or infarcts that do not obey usual arterial territory borders can be clues to diagnosis. A working knowledge of the normal anatomy of the major venous structures and the common variants is necessary to avoid diagnostic pitfalls, especially false-positive results. On unenhanced CT, normal venous structures may appear denser than usual as a result of dehydration or elevated hematocrit, whereas thrombosis should appear hyperdense relative to arteries. A filling defect or occlusion may be detected on contrast-enhanced CT. CT venography can be performed with a thin-section, volumetric technique that allows the creation of 2D and 3D reconstructions. Normal and thrombosed venous sinuses take on many different appearances on MRI depending on scan parameters, flow velocity, and turbulence. Unexpected hyperintensity, loss of usual flow voids, and blooming on gradient-echo sequence are clues that flow-sensitive MR venography (MRV) should be performed. Time-of-flight MRV may be less sensitive than phase contrast technique because of shine-through of methemoglobin in a thrombosed sinus, simulating flow in the vessel. Contrast-enhanced MRV may be more sensitive, although enhancement of chronic thrombus can be misleading. Associated findings of edema, hemorrhage, or ischemic infarct may help one arrive at the correct diagnosis, but brain swelling without signal changes has been reported in up to approximately 40% of patients. Cavernous sinus thrombosis is discussed in relation to complex sinus and orbit infections in the section on head and neck imaging in this chapter. Prompt diagnosis of cerebral venous thrombosis is critical, because many of the parenchymal changes may be reversible. Systemic anticoagulation and local catheter-based thrombolytic, mechanical, or rheolytic (hydrodynamic) clot dissolution are treatment considerations. Intracranial hypertension and collateral formation leading to dural arteriovenous malformations are possible long-term sequelae.

Imaging of the cerebral venous sinuses is also often performed in the workup of patients with papilledema or suspected idiopathic intracranial hypertension (IIH). Many patients with IIH have venous hypertension and stenosis of either the dominant or both transverse sinuses. One retrospective study reported cure of IIH symptoms in 49 of 52 patients after transverse sinus stent placement.

ANEURYSMS, VASCULAR MALFORMATIONS, AND VASCULAR INJURIES

Aneurysms and cerebral vascular malformations present in various ways in the emergency setting. SAH resulting from a ruptured aneurysm and parenchymal hemorrhage related to an arteriovenous malformation are dramatic examples of disorders that may present with headache as the chief complaint. Presenting symptoms of nausea and vomiting are common with hemorrhages that arise in the posterior fossa. On routine noncontrast CT, large unruptured aneurysms may simulate other mass lesions and displace or compress adjacent structures. Arteriovenous malformations also may be conspicuous on routine CT based on abnormally enlarged feeding arteries and draining veins or internal calcifications (Fig. 1-22).

The traditional gold standard for diagnostic evaluation of vascular lesions, both spontaneous and traumatic, is DSA. The risk of major complication from this invasive procedure is low in experienced hands, and treatment (complete or partial) with endovascular techniques is possible for many types of aneurysms and other vascular lesions. That

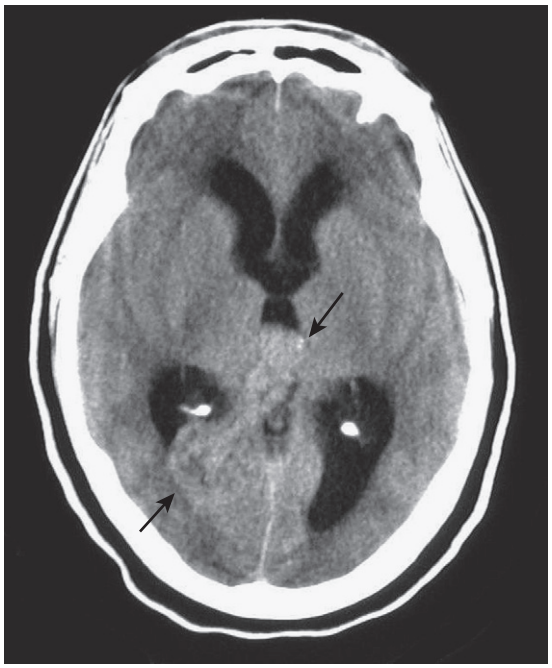


FIGURE 1-22 An arteriovenous malformation. Noncontrast computed tomography shows a hyperdense lesion extending from the third ventricle to the right occipital lobe and associated hydrocephalus *(arrows)*.

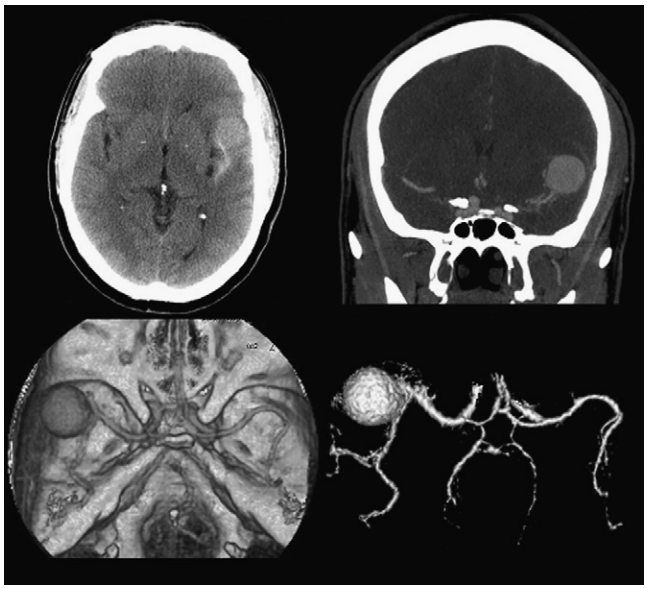


FIGURE 1-23 Subarachnoid hemorrhage due to a ruptured aneurysm. Noncontrast computed tomography (CT) *(upper left)* shows subarachnoid hemorrhage in the left Sylvian fissure and a round hyperdense mass. Images from a CT angiogram (coronal multiplanar reconstruction, volume-rendered volume of interest, and volume created from a seed point) confirm a large left middle cerebral artery bifurcation aneurysm.

being said, the constantly improving technology and clinical experience with CTA have led to a substantial decrease in the number of diagnostic angiograms. CTA is commonly applied in the setting of spine, facial, and skull base fractures. One study of CTA in 2004 in the setting of acute SAH reported a sensitivity of 89% and a specificity of 100% for detection of aneurysms. Dual-energy CT may provide benefits compared with standard techniques. A more recent study with 320-detector technique found overall sensitivity of 96%, specificity of 100%, and accuracy of 95%. Many centers have adopted immediate CTA in their protocol for the workup of spontaneous SAH (Fig. 1-23). If a ruptured aneurysm is detected by this method, detail may be adequate for treatment planning in certain situations. However, other investigators have offered the opinion that the gold standard of DSA (with 3D rotational angiography) provides greater sensitivity and should not yet be replaced by CTA. This opinion is based on reports of a 10% false-negative rate of CTA for aneurysm detection and the belief that the greater spatial resolution of DSA is necessary to accurately determine proper triage to surgery versus endovascular coiling. Both of these reasons support the use of DSA regardless of a negative or positive result from CTA. Given its availability and lack of invasive risks, CTA will probably continue to be used as a diagnostic tool in this setting.

In the setting of SAH, a negative result of a CTA or DSA examination often requires a repeat examination, depending on the pattern of hemorrhage. DSA offers evaluation of cerebral hemodynamics, which is important for the diagnosis of brain and dural vascular malformations. This type of detail is still not available with most current CTA techniques, but because of continued technical improvements, time-resolved (multiphase, four-dimensional) CTA is expected to be commonly available in the near future. On occasion, arteriovenous shunting may be inferred from the presence of dilated draining veins or from asymmetric opacification of the cavernous sinuses, although this shunting might just as well be due to normal physiologic variation. Evaluation of the smallest arteries is necessary for the evaluation of cerebral vasculitis. Improvements in spatial and temporal resolution and reconstruction techniques will certainly reduce the number of false-negative aneurysm hunts and increase the clinical utility of CTA for evaluation of arteriovenous malformations and vasculitis. Use of CTA in the setting of spontaneous parenchymal hemorrhage has become routine. Since the initial study of CTA in the setting of acute intracerebral hemorrhage that demonstrated that tiny enhancing foci (extravasation) within the hematoma (CTA spot sign) is an independent predictor of hematoma expansion, many other studies have evaluated this sign. An underlying vascular lesion may be found in up to 15% of patients with spontaneous ICH, potentially affecting acute management. Some authors recommend spot sign evaluation during CTP imaging. In addition to its clinical predictive value, the spot sign will continue to be of interest in trials of hemostatic therapy.

CERVICOCEREBRAL ARTERIAL INJURIES

Spontaneous Cervical Dissection

Spontaneous cervical arterial dissection used to be considered a rarity, but since the 1980s, largely as a result of improvements in imaging, awareness of this cause of stroke has increased. It is estimated that up to 25% of strokes in young and middle-aged adults occur on this basis. Community-based studies have found that the annual incidence of internal carotid artery dissection is 3 per 100,000 per year, and that of vertebral artery dissection is 1.5 per 100,000 per year. A history of a trivial

precipitating event, such as minor movement of the neck, is commonly reported. Chiropractic manipulation of the cervical spine has become recognized as a potential cause of dissection, but estimates of the rate of occurrence vary widely. Many different types of triggering events associated with hyperextension or rotation of the neck—including sport and recreational activities, painting of ceilings, coughing, sneezing, and vomiting—have been reported. A higher incidence in the autumn suggests inflammation or an excess amount of sneezing and coughing related to upper respiratory tract infections as predisposing factors. The effect of genetics has not yet been completely determined, but approximately half of patients show mild ultrastructural connective tissue alterations similar to Ehlers-Danlos syndrome. Traditional vascular risk factors have not been systematically studied, but atherosclerosis is generally not found in patients with spontaneous dissections. Migraine has been suggested as an independent risk factor.

Traumatic Cervicocerebral Injuries

The evaluation of vascular injuries of the neck and head has undergone a dramatic transformation as a result of the capabilities of helical and MDCT angiography. Since 2000, favorable results from the use of CTA in the setting of penetrating trauma have supported its clinical application on a routine basis. High sensitivity and specificity for the detection of vascular injuries have been reported in a number of studies. CTA has essentially replaced DSA, which is still the gold standard, as the initial screening modality of choice for penetrating neck injuries at many institutions. In many cases it has been used as a complementary technique to surgical exploration of the neck, but more recently, a normal CTA may avert the need for surgical exploration. CTA has been applied to the setting of blunt trauma with similar results and has resulted in a decrease in the number of DSA examinations performed. Abnormalities that may be detected include stenosis, occlusion, dissection, pseudoaneurysm formation, and contrast extravasation from vessel rupture. Vascular evaluation is generally limited to the common carotid, internal carotid, and vertebral and proximal branches of the external carotid arteries. With currently available equipment, submillimeter, subsecond imaging is possible, and even minor abnormalities of the distal external carotid branches are now being diagnosed prospectively. Nondiagnostic examinations may occur as a result of technical deficiencies such as extravascular contrast infiltration from intravenous catheters or patient motion. Use of a contrast test bolus or bolus tracking techniques helps reduce the number of poor-quality scans due to arrhythmias or compromised cardiac output. Because an intravenous contrast bolus may be impeded by transient compression of the left brachiocephalic vein as a result of pulsations of the great vessels, a right-sided antecubital injection site is preferred. Streak artifacts from dental fillings and hardware and beam-hardening effects also take their toll on image quality. Positive findings on CTA help guide therapeutic decisions toward medical, surgical, or endovascular intervention; however, well-defined pathways do not yet exist for most vascular injuries. It is the clinical expectation that with prompt diagnosis and implementation of antithrombotic or other vascular treatments, the incidence of stroke will be reduced. Because more subtle injuries will be detected with advances in CT technology, outcomes research will be necessary to help determine the most appropriate therapy. It is well known that a certain (small) percentage of patients will present with delayed formation and rupture of a posttraumatic pseudoaneurysm, yet recommendations for and timing of follow-up examination remain rather dubious (Fig. 1-24).

Dissection of the internal carotid and vertebral arteries may be the direct result of blunt trauma, with a reported incidence of less than 1% in some series. As might be expected, the risk of vascular injury in the setting of spine fracture is substantially higher. Another mechanism of carotid injury is intraoral trauma, such as from a fall with a pencil in the mouth or from iatrogenic causes. Basilar skull fracture, especially involving the carotid canal, is also included in this category in most studies of traumatic dissection. The indications for CTA continue to broaden. Because of the potential for devastating neurologic consequences of cerebrovascular injuries, some trauma centers follow a liberalized screening approach—including not only patients with symptoms referable to vascular injury but also asymptomatic patients undergoing CT for head and cervical spine trauma. In such a study reported by Biffl and colleagues in 2006, 5.4% of patients had blunt cerebrovascular injuries. In a 2-year retrospective review of patients at our center, 8% of 106 patients with fractures of the cervical spine and skull base (involving the foramen transversarium or near the carotid canal) had vascular injuries detected by CTA. Of 161 trauma patients without fractures who also underwent CTA, 2% had vascular injuries detected. Therefore the presence of a fracture yielded an odds ratio for vascular injury of approximately 4 to 1 in this population. False-positive and false-negative results are generally considered few, with the expectation that they will continue to decline as technology advances and experience with the technique increases.

Some authors propose mandatory imaging in the following instances: (1) arterial bleeding from the mouth, nose, ears, or wound; (2) expanding cervical hematoma; (3) bruit in patients older than 50 years; (4) acute infarct; (5) unexplained neurologic defect or TIA; and (6) Horner syndrome or neck or head pain. In one angiographic study of asymptomatic patients with skull base fractures, up to 60% had abnormal angiogram findings. Other studies have reported significantly lower rates of serious injury. One recent series found a 4% incidence of traumatic carotid-cavernous fistula in patients with skull base fractures. Although prompt diagnosis and treatment of carotid-cavernous fistula are desirable, diagnosis at the time of admission is not as critical as it is for dissection with its inherent risk of stroke.

Whether performed for screening or based on symptoms, the workup and treatment of dissection continue to evolve. As with other vascular disorders, catheter angiography was once the only method available and is still used for confirmation if other studies are equivocal. The most common finding is a smoothly or mildly irregular tapered mid-cervical narrowing. Dissections that result in occlusion may show a "rat tail" or "flame-shaped" lumen, which may help distinguish other causes such as

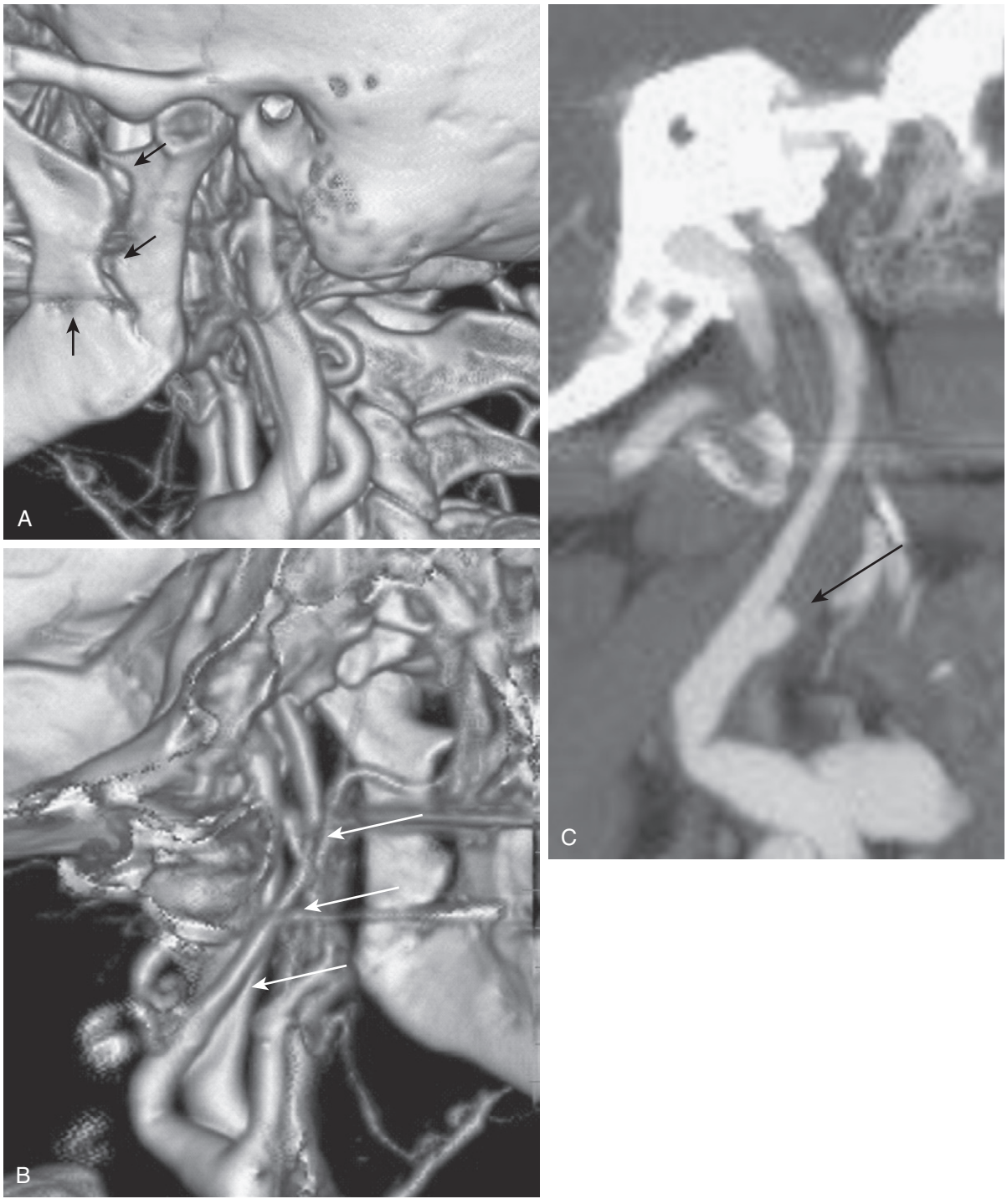


FIGURE 1-24 An arterial dissection resulting from blunt trauma. **A,** A volume-rendered image from a computed tomography (CT) angiogram shows a comminuted mandibular fracture *(arrows)*. The internal jugular vein obscures the internal carotid artery. **B,** A 180-degree rotation and application of an anterior cutting plane reveal tapered contour of the internal carotid artery *(arrows)* as a result of dissection. **C,** Multiplanar reconstruction from a follow-up CT angiogram 1 week later shows development of a small pseudoaneurysm *(arrow)* with residual, mild, distal stenosis.

thromboembolism or atherosclerotic disease from dissection (Fig. 1-25). Saccular or fusiform aneurysmal dilatation (pseudoaneurysm) also may be identified. The presence of an intimal flap or a false or double lumen is unusual in the cervicocerebral vessels. In the internal carotid artery, the dissection is typically found a few centimeters beyond the carotid bifurcation or a few centimeters below the skull base. The most common sites of vertebral artery dissection are at the entry into the C6 foramen transversarium and at the C1-C2 level.

Ultrasound assessment of cervical internal carotid and vertebral artery dissections is possible, but many pitfalls exist. The pathognomonic finding is a membrane in the longitudinal and axial views. In addition to the findings that may

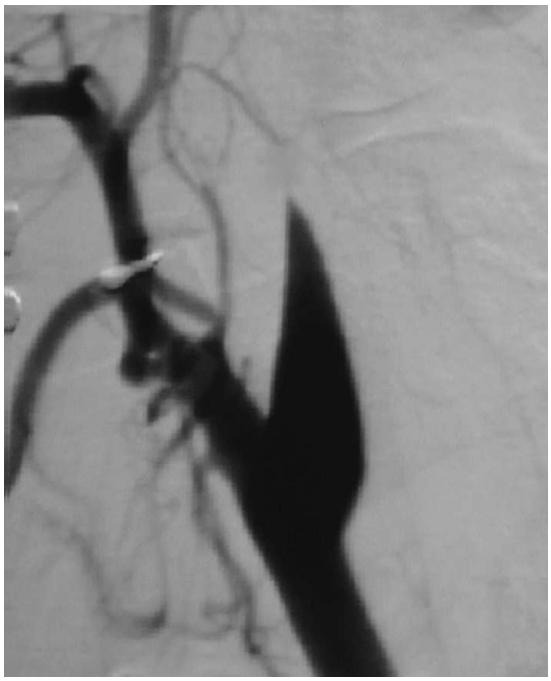


FIGURE 1-25 Acute dissection. A digital subtraction angiogram shows sharply tapered occlusion of the internal carotid artery as a result of spontaneous dissection.

be demonstrated by angiography, a thickened, hyperechoic vessel and high-resistance spectral waveform or absence of flow may be noted. However, Doppler analysis may be normal in cases of low-grade carotid stenosis, and ultrasound sensitivity of only 20% has been reported in such cases. Ultrasound evaluation of vertebral artery dissection is limited by the transverse processes of the cervical spine.

The combination of MRI and MRA is considered by many to be the preferred technique. MRA should be able to demonstrate the morphologic features of the vessel in a fashion similar to DSA. In addition, MRI may demonstrate an eccentrically located narrowed lumen, a crescentic or circumferential intramural hematoma, and an increase in the external artery diameter. Fat-suppressed T1WIs are recommended to improve sensitivity for detection of the intramural hematoma (Fig. 1-26). However, in the acute setting, the clot should not be expected to appear hyperintense, because it may take a few days for conversion to methemoglobin to take place. The reported sensitivity and specificity for detection of carotid dissection are very high—approximately 95% and 99%, respectively. Sensitivity is lower for vertebral dissection (approximately 60%) because of the smaller size of the native vessel and the relatively high incidence of hypoplasia. One must remember that lack of flow-related signal due to slow flow in a vessel may simulate occlusion. These noninvasive techniques are very useful for follow-up of dissection as a result of the lack of ionizing radiation or the need for injection of a contrast agent.

CTA shares many of the advantages of MRA and provides higher spatial resolution. Another specific sign reported by CTA is the "target" sign, which is composed of a thickened wall and a narrowed eccentric lumen surrounded by a thin rim of contrast enhancement. CTA is certainly the fastest way to screen patients in the emergency setting and is often performed immediately after or at the time of imaging of the head and cervical spine.

CTA has also become the initial method for evaluation of stable patients with penetrating trauma to the neck, face, and head based on availability, efficiency, and similar profiles of sensitivity and specificity as in blunt trauma. The high sensitivity of CT for the detection of small amounts of contrast extravasation or air in the soft tissues helps to localize subtle injuries to major vessels that otherwise might not be noticed. An understanding of the expected trajectory of bullets or knives based on skin entry and exit wounds may increase the likelihood of the detection of injury. Detection of dissection, transection, pseudoaneurysm, and arteriovenous fistula formation can help guide treatment—that is, medical versus open surgical versus endovascular. Posttraumatic vasospasm may lead to a false-positive diagnosis of dissection or transection, appearing normal on immediate follow-up angiography. Definitive characterization of an injury in cases of segmental arterial narrowing or occlusion may be challenging in neck CTA, as well as in other areas, given the overlap in imaging findings for traumatic dissection, occlusion, and vasospasm. Retained bullets and shrapnel often cause substantial artifacts that limit the diagnostic value of CTA. DSA can usually overcome this limitation through the use of multiple oblique projections.

Spontaneous Intracranial Dissection

Intracranial arteries lack an external elastic lamina and have thinner media and adventitia compared with extracranial vessels, and thus intracranial dissections may behave differently. If the dissection occurs between the intima and media, then luminal stenosis or occlusion may lead to ischemia or infarct, similar to the extracranial setting. If the dissection plane is between the media and adventitia, then (dissecting) pseudoaneurysm formation is likely. Because of the thin media and adventitia, rupture and SAH may occur. SAH is reported in approximately 20% of intracranial internal carotid dissections and more than 50% of intracranial vertebral dissections. The supraclinoid segment of the internal carotid artery and the segment of the vertebral artery near the posterior inferior cerebellar artery (V4) are the most common sites of intracranial dissection. The cause of intracranial dissection remains unknown, with some instances related to trauma or underlying connective tissue disorders (such as fibromuscular dysplasia, Marfan, and Ehlers-Danlos types). It may not be possible to differentiate traumatic stenosis or occlusion from atherosclerosis or thromboembolism by any imaging technique. The only truly diagnostic findings of dissection are the presence of a dissecting pseudoaneurysm and a double lumen.

Treatment options vary depending on stenosis versus pseudoaneurysm configuration and the presence of an infarct or SAH. Endovascular intervention with stent placement may be considered when medical therapy for stenosis has failed. Aneurysm coiling, proximal occlusion, and trapping of an abnormal segment are other possible techniques.

OTHER NONTRAUMATIC INTRACRANIAL EMERGENCIES

As with ischemic stroke and spontaneous hemorrhage, the indication for workup of other nontraumatic emergencies

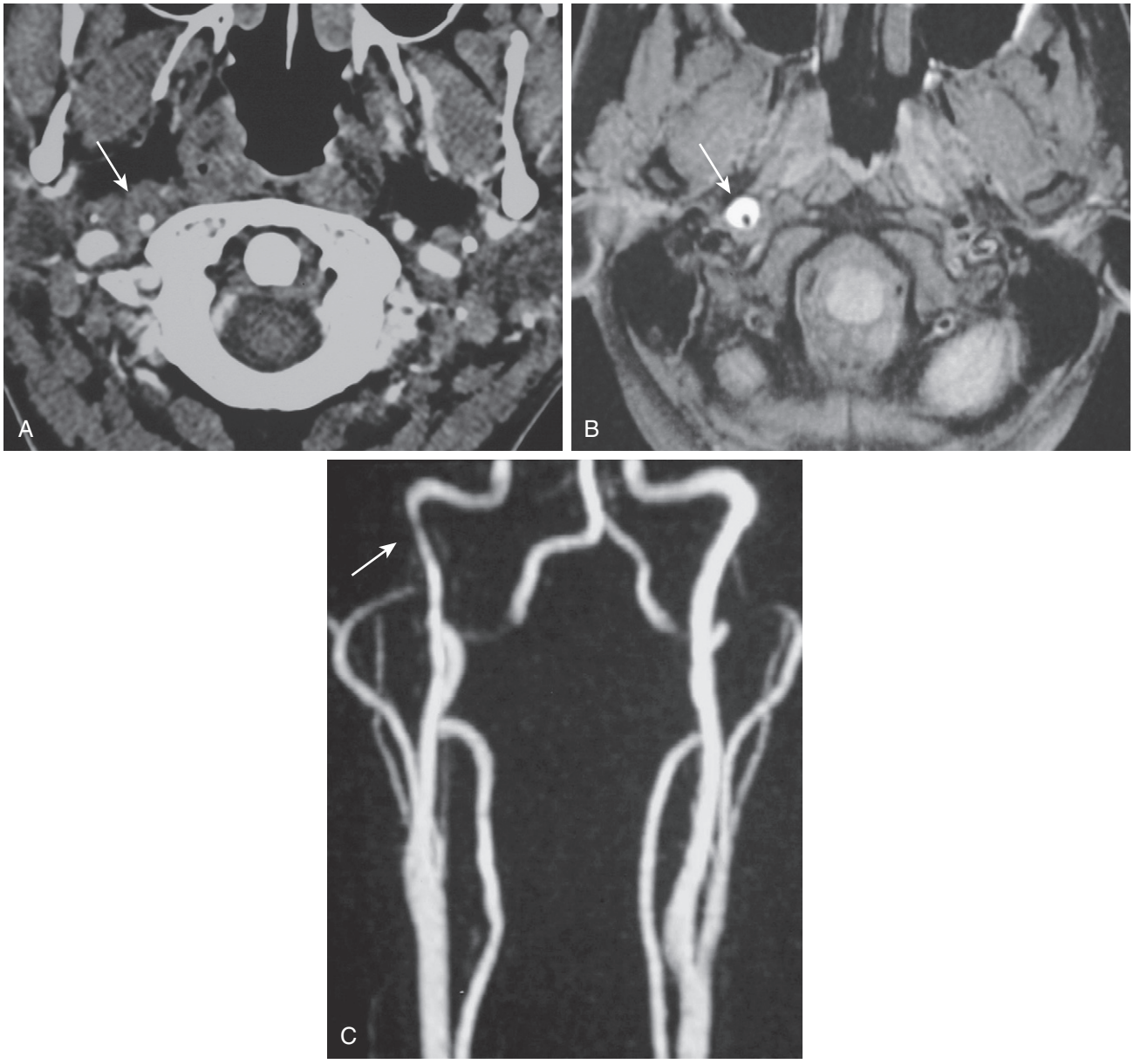


FIGURE 1-26 Internal carotid artery dissection as seen on computed tomography (CT) and magnetic resonance (MR) angiogram. **A,** A CT angiogram source image shows a narrowed upper cervical right internal carotid artery lumen with an increase in the external caliber of the vessel *(arrow)*. **B,** A fat-suppressed T1-weighted image shows corresponding narrowed flow void with a hyperintense eccentric intramural hematoma *(arrow)*. **C,** A time-of-flight MR angiogram shows a narrowed segment of the right internal carotid artery *(arrow)*.

affecting the brain will be based on an acute change in mental status or onset of headache, seizure, or a focal neurologic deficit. Delirium, or acute confusional state, is a common indication for brain imaging in concert with a search for other causes such as hypoxia, cerebral hypoperfusion, systemic or regional infection, intoxication, and other metabolic causes. Noncontrast head CT offers rapid noninvasive detection of lesions producing mass effect or brain edema. Spontaneous and subacute hemorrhages have been addressed in previous sections of this chapter. Other causes run the gamut of infection, inflammation, tumors, and other causes of encephalopathy. The following sections illustrate a few of the more commonly seen entities from these categories.

Hydrocephalus

Disturbance of the usual pattern of CSF flow or production/absorption may result in dilatation of the ventricular system. Hydrocephalus may occur acutely or may be of chronic duration, and the distinction between the two forms may not be entirely clear based on imaging alone. Hypodensities/T2-weighted hyperintensities in the periventricular white matter of the frontal and periatrial regions may be a sign of interstitial edema—often described as transependymal flow of CSF—and may be seen with acute hydrocephalus. Chronically compensated hydrocephalus is less likely to demonstrate this finding. Terminology can be confusing; obstruction at the



FIGURE 1-27 Hydrocephalus as a result of shunt malfunction. Severe hydrocephalus is shown. Portions of the bilateral ventriculoperitoneal shunts are visible. Abdominal computed tomography (not shown) demonstrated a pseudocyst as a cause of the malfunction.

level of the foramen of Monro, cerebral aqueduct of Sylvius, or foramina of Magendie and Luschka is considered noncommunicating hydrocephalus, whereas obstruction at the level of the arachnoid granulations is considered communicating hydrocephalus. One should always remember the value of prior examinations, because longstanding, compensated hydrocephalus is generally not a cause for alarm even if encountered in the emergency setting. Ventricular obstruction may develop as a result of SAH, IVH, intraventricular mass, aqueductal stenosis, and any lesion that may cause extrinsic mass effect. Analysis should include evaluation of basal cisterns and a search for possible complications that may result from herniation. Ideally, treatment of hydrocephalus will prevent such complications. Recurrence of symptoms due to ventricular shunt malfunction is a common problem that may result from catheter/tubing obstruction (intrinsic or in the peritoneal cavity), disconnection, or migration (Fig. 1-27).

Classification is complicated further by normal pressure hydrocephalus. The cause of this disorder in which intracranial pressure is not elevated is unknown. In the setting of ventriculomegaly out of proportion to sulcal prominence, the presence of the classic triad of dementia, abnormal gait, and urinary incontinence can help to make this diagnosis. However, by the time the classic symptoms are evident, treatment may be ineffective. The fourth ventricle may be relatively spared, and periventricular edema may be absent in normal pressure hydrocephalus.

A related disorder is IIH (pseudotumor cerebri), which may be due to poor CSF absorption such as from venous sinus thrombosis or stenosis. The incidence is highest in obese females of child-bearing age, and it may present with headache and visual loss due to papilledema. Although intracranial pressure may be severely elevated in this disorder, the ventricular system is generally small. Progressive visual loss may be an indication for emergent, fluoroscopic-guided, diagnostic, and therapeutic lumbar puncture. As described in the section on cerebral sinus thrombosis, CT or MR venography is commonly requested in this setting.

Colpocephaly is the term applied to enlarged occipital horns of the lateral ventricles as a result of a developmental structural abnormality of the brain, and it sometimes may be mistaken for acute hydrocephalus. Other congenital abnormalities such as agenesis of the corpus callosum will also present with abnormal ventricular configuration and should be recognized as one of the expected constellation of findings. *Benign external hydrocephalus* or *benign extracerebral fluid collections* are two of the terms commonly applied to the pattern of mild ventriculomegaly and generous subarachnoid spaces in neonates and infants. It is associated with macrocephaly and usually resolves spontaneously by 1 to 2 years of age.

Infections

Meningitis

Suspected meningitis is a very common cause for imaging, not necessarily for diagnosis, but as a precaution prior to performance of a lumbar puncture. In adults with suspected meningitis, clinical features can be used to identify those who are unlikely to have abnormal findings on CT of the head. However, many practitioners still rely on CT prior to lumbar puncture to exclude unsuspected mass effect and lesions that might result in rapid increases in intracranial pressure; this is especially true for patients who are immunocompromised or older than 60 years. Findings of the majority of examinations are normal, but the detection of findings such as brain edema possibly leading to herniation, hydrocephalus, or other complications will alter management. On FLAIR images, sulci may appear hyperintense as a result of proteinaceous exudates; however, SAH or a high concentration of inspired oxygen also may cause the same appearance. In the vast majority of cases, meningitis is aseptic (generally of viral origin, commonly enteroviruses) and is self-limited. Bacterial meningitis is more likely to result in severe disease, and in some cases the source of meningitis may be evident on imaging, such as a sinus or ear infection. On intravenous contrast-enhanced CT and MR examinations, diffuse enhancement within the sulci (leptomeningeal) may be detected. Imaging is also indicated for patients who do not respond to antibiotic treatment in the hope of detecting a drainable source, such as a subdural empyema or parenchymal abscess. Gadolinium-enhanced MR is generally preferred to CT because of its relatively higher soft tissue contrast. Neonatal meningitis due to *Citrobacter* species is another indication for imaging because brain abscess develops in 80% to 90% of cases. Meningoencephalitis (encephalomeningitis) is the term applied to brain parenchymal infection in association with meningitis. Other complications of meningitis include infarcts, venous thrombosis, subdural empyema

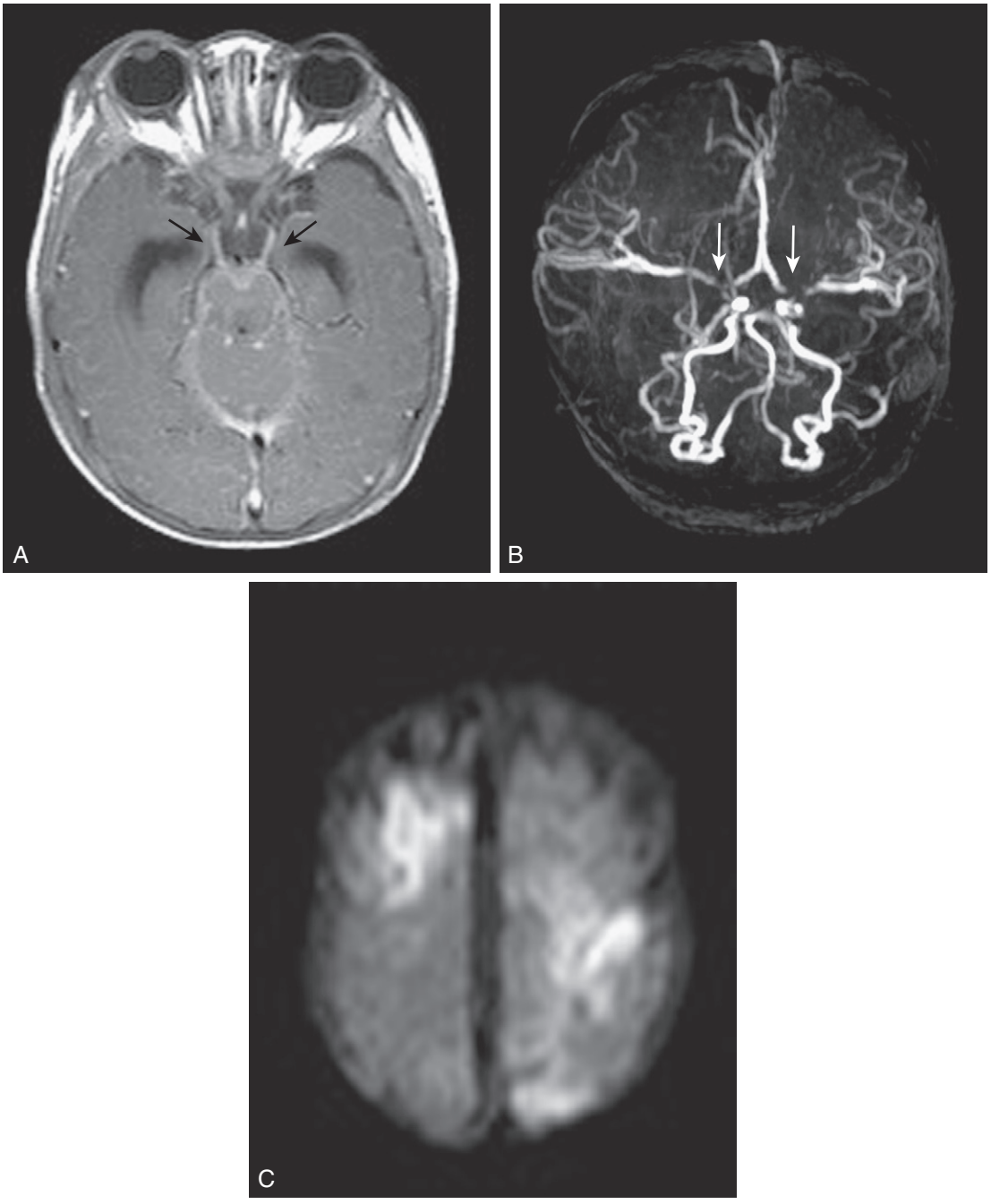


FIGURE 1-28 Meningitis caused by group B streptococcus in a 4-year-old. **A,** A postgadolinium T1-weighted image shows mild diffuse leptomeningeal enhancement and abnormal enhancement of the bilateral cranial nerve III *(black arrows)*. **B,** A magnetic resonance angiogram shows the bilateral internal carotid artery terminus and anterior cerebral artery and middle cerebral artery origin stenoses *(white arrows)*. **C,** A diffusion-weighted image shows resultant infarcts.

or hygroma, and obstructive or communicating hydrocephalus (Fig. 1-28). Subdural empyema and epidural abscess are illustrated in the section on head and neck imaging.

Many other infectious agents may cause meningitis, including Lyme disease (*Borrelia*) and, especially in the immunocompromised setting, human immunodeficiency virus (HIV), toxoplasmosis, cryptococcosis, tuberculosis, syphilis, cytomegalovirus, and a variety of fungi (see Fig. 1-12).

Diffuse thickened enhancement of the dura is a sign of pachymeningitis, which can be due to carcinomatous, granulomatous, and noninfectious causes, including idiopathic intracranial hypotension (Fig. 1-29). Tuberculosis has a predilection for causing basal meningitis with resultant stroke due to involvement of arteries at the base of the brain.

Brain Parenchymal Infection

The term encephalitis refers to inflammation of the brain and is usually applied in the setting of viral infection.

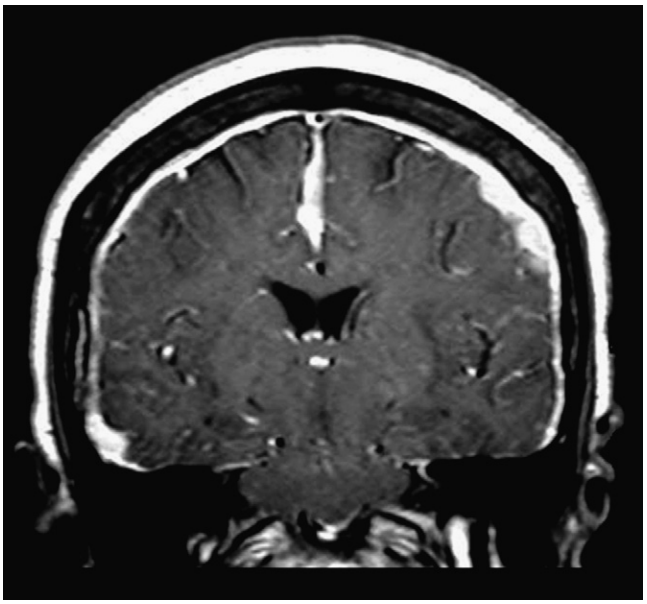


FIGURE 1-29 Pachymeningitis. A postgadolinium T1-weighted image shows diffuse, pachymeningeal, thickened enhancement due to neurosarcoidosis.

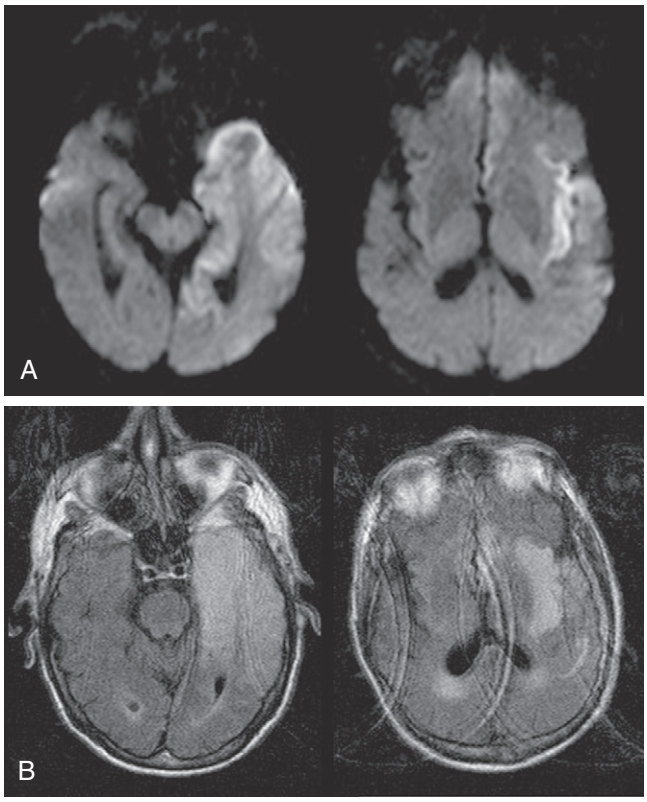


FIGURE 1-30 Herpes encephalitis. Diffusion-weighted **(A)** and fluid-attenuated inversion recovery **(B)** images show corresponding hyperintensities in the left temporal lobe and insula as a result of herpes simplex virus type I infection. Note the motion artifact so commonly encountered in patients evaluated for a change in mental status.

Cerebritis is often used interchangeably; however, it should be reserved for the cerebrum with cerebellitis added when necessary. Usually the findings are nonspecific, with simultaneous involvement of various structures. A certain pattern may suggest a particular organism, such as the classic findings of T2WI hyperintensity, restricted diffusion, and minimal enhancement within the temporal lobe(s) and limbic system as a result of herpes simplex type 1 infection (Fig. 1-30). Nonspecific patchy T2 hyperintensities, variable diffusion, and enhancement characteristics may lead to a differential diagnosis including infarction, infiltrating neoplasm, status epilepticus, and toxic/metabolic causes. Rather than identify the exact agent, imaging findings may be able to suggest infection and exclude other possibilities.

Abscess

An abscess is a focal parenchymal infection due to bacteria, fungi, or parasites. The imaging characteristics reflect the phase of the infection as it evolves from early cerebritis to late cerebritis, then to early and finally late encapsulated stages. If diagnosed early, it often appears as a low-density (on CT), T2-weighted hyperintense region with faint enhancement and a mild amount of surrounding edema. Once in the capsule stage, a typical fluid collection with a thin rim of enhancement and larger amount of edema becomes evident (Fig. 1-31). Over time (with treatment), the lesion may decrease in size and develop a thicker rim of enhancement, and surrounding edema will wane. The rim is typically T2 hypointense and thinner along the deep margin, which may predispose cerebral lesions to rupture into the ventricular system, leading to ventriculitis and a dramatic clinical decline. A bacterial abscess typically shows diffusion-weighted hyperintensity, which may help to distinguish a bacterial abscess from a necrotic tumor. Lesions in the differential diagnosis other than neoplasm might include demyelination, subacute infarct, and subacute hematoma. In the setting of immune suppression, a fungal abscess should be considered. In the setting of acquired immunodeficiency syndrome (AIDS), the differential diagnosis for single or multiple ring-enhancing lesions includes toxoplasmosis versus lymphoma (Fig. 1-32). Also prevalent in the AIDS population are *Mycobacterium tuberculosis* and *Cryptococcus,* which can present as either meningitis or focal parenchymal lesions. To further complicate matters, another classic presentation of cryptococcosis is that of nonenhancing, gelatinous pseudocysts that distend the perivascular spaces.

Single or multiple abscesses may develop from septic emboli as a result of endocarditis. Initially, these abscesses appear similar to other cardioembolic infarcts but in time develop relatively more surrounding edema and enhancement as a result of the inflammatory response (Fig. 1-33). If cardiac valve replacement is considered, screening for mycotic aneurysms may be requested prior to surgery.

Neurocysticercosis is an intracranial infection by the pork tapeworm, *Taenia solium*, which is endemic in many parts of the world. It is the leading cause of seizures worldwide and has a unique life cycle and imaging characteristics. After ingestion of contaminated food or water, larvae migrate from the gastrointestinal tract to the brain and skeletal muscle. Once intracranial, the larvae develop into

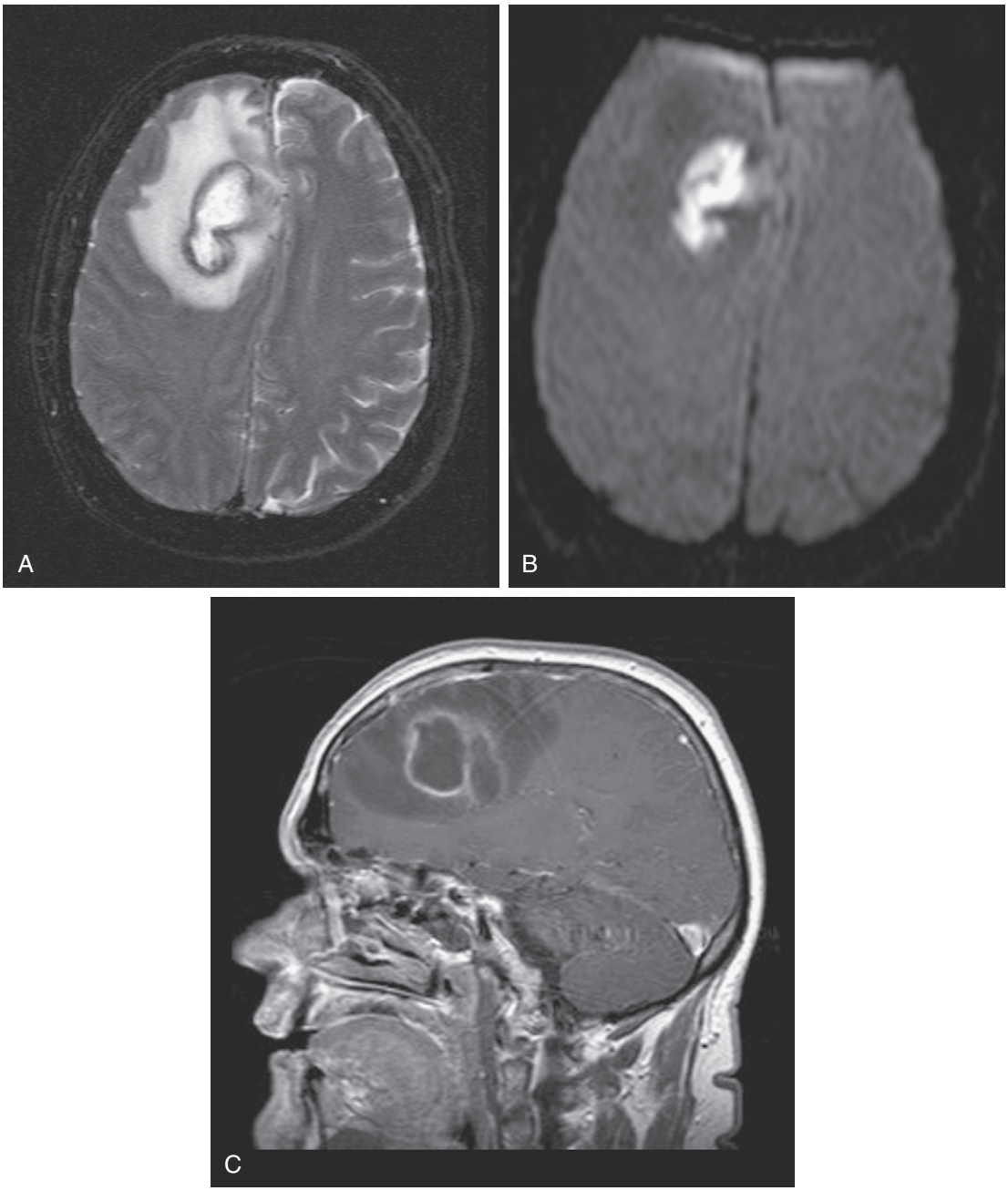


FIGURE 1-31 A pyogenic abscess. **A,** A T2-weighted image shows hyperintense fluid collection in the right frontal lobe with a hypointense rim and extensive surrounding edema. **B,** Corresponding hyperintensity on a diffusion-weighted image. **C,** A postgadolinium T1-weighted image shows a relatively thin rim along the deeper portion of the abscess adjacent to the lateral ventricle.

cysticerci, and these cysts may be located in the subarachnoid spaces, brain parenchyma, or ventricular system. The cysts then progress through four stages with distinct imaging features based on the lesion and the host response. In the vesicular stage, the lesions appear as thin-walled, fluid-filled cysts, possibly with mild rim enhancement, but without surrounding edema. Lesions are generally small (less than 1 cm), and often an eccentric scolex of a few millimeters can be detected. In the colloidal vesicular stage, in which the larva starts degenerating, a thicker rim of enhancement and surrounding edema develop. It is in this stage that the appearance is similar to that of any other brain abscess. Next is the granular nodular stage in which the cyst involutes, the wall thickens, the lesion begins to calcify, and edema decreases. In the final nodular calcified stage, only a small calcification persists and the edema resolves completely. Because lesions may progress at different rates, it is not uncommon to find more than one type of lesion. Identification of cysts in different compartments (parenchymal, subarachnoid, and intraventricular), the presence of a scolex, variable amounts of edema, and small calcifications in the same patient offer great sensitivity and specificity. It is not often that the radiologist can show such confidence in diagnosis, and therefore

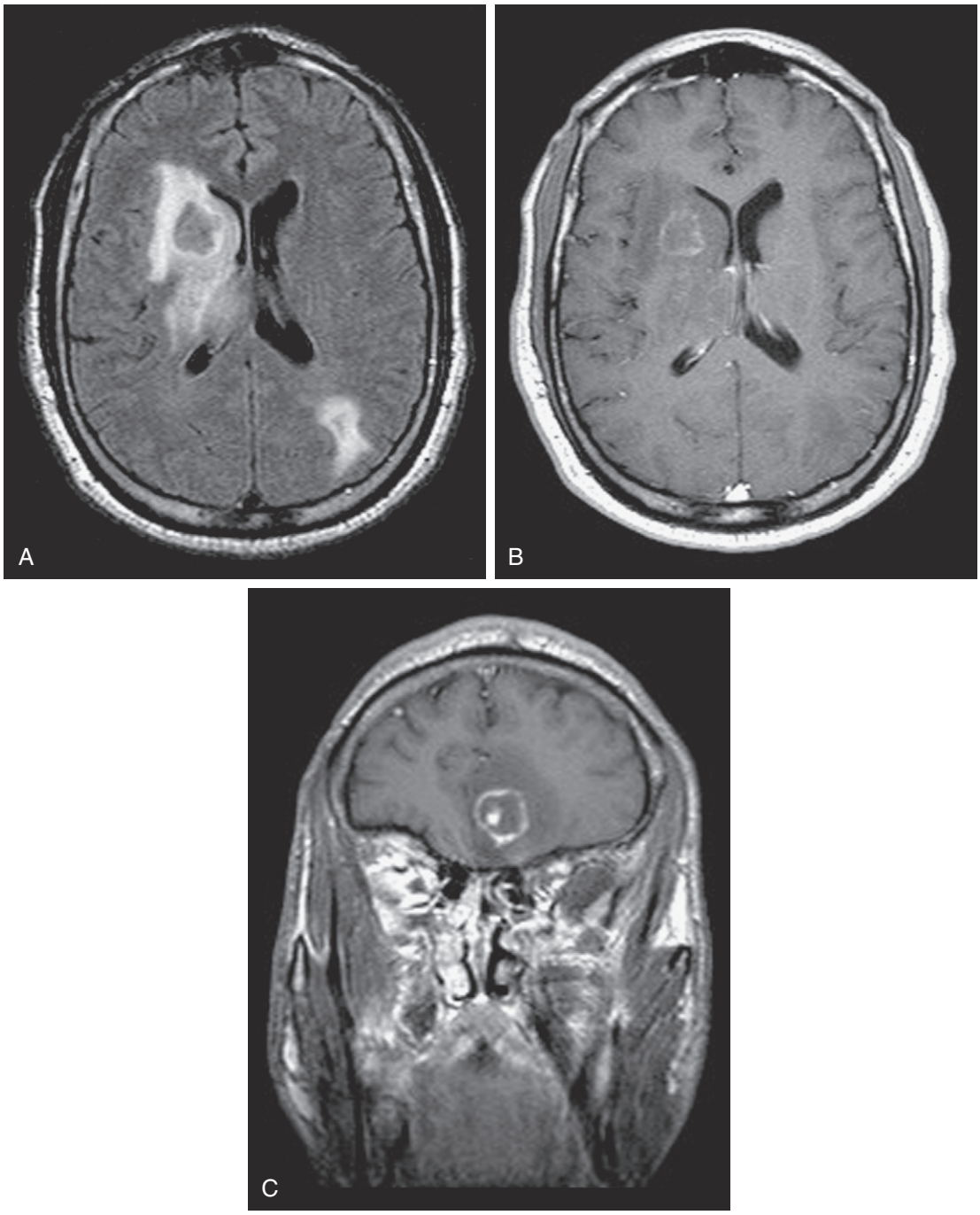


FIGURE 1-32 Toxoplasmosis. **A,** A fluid-attenuated inversion recovery image shows isointense lesions in the right basal ganglia and left parietal lobe with surrounding edema. **B,** A postgadolinium T1-weighted image shows faint rim enhancement of right basal ganglia lesion. **C,** A postgadolinium T1-weighted image shows a typical "target" sign in a left frontal lobe lesion.

neurocysticercosis deserves special recognition (Fig. 1-34). One might not expect this infection to be common in the United States; however, because of travel and immigration, it presents fairly commonly in patients presenting to U.S. EDs with new or recurrent seizures.

Tumors

As with infection, it is not possible to review all of the myriad entities in this category. Within the scope of this chapter it is possible to provide only a limited framework and describe some of the more common lesions.

Metastases account for approximately half of all intracranial neoplasms in adults. They may present as multiple small enhancing lesions at the gray–white junction or as a single large lesion with extensive surrounding edema. Lesions are usually found in the cerebral hemispheres and may be solid, cystic, calcified, or hemorrhagic, and approximately 50% will present as a solitary lesion. The most common primary tumors are lung, breast, and melanoma.

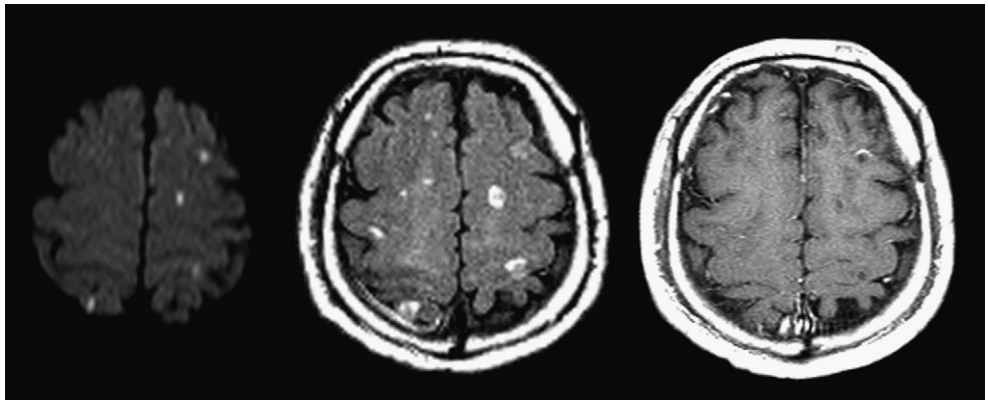


FIGURE 1-33 Septic emboli. Diffusion *(left)*, fluid-attenuated inversion recovery *(middle)*, and postgadolinium T1-weighted *(right)* images show multiple small lesions with surrounding edema and faint rim enhancement.

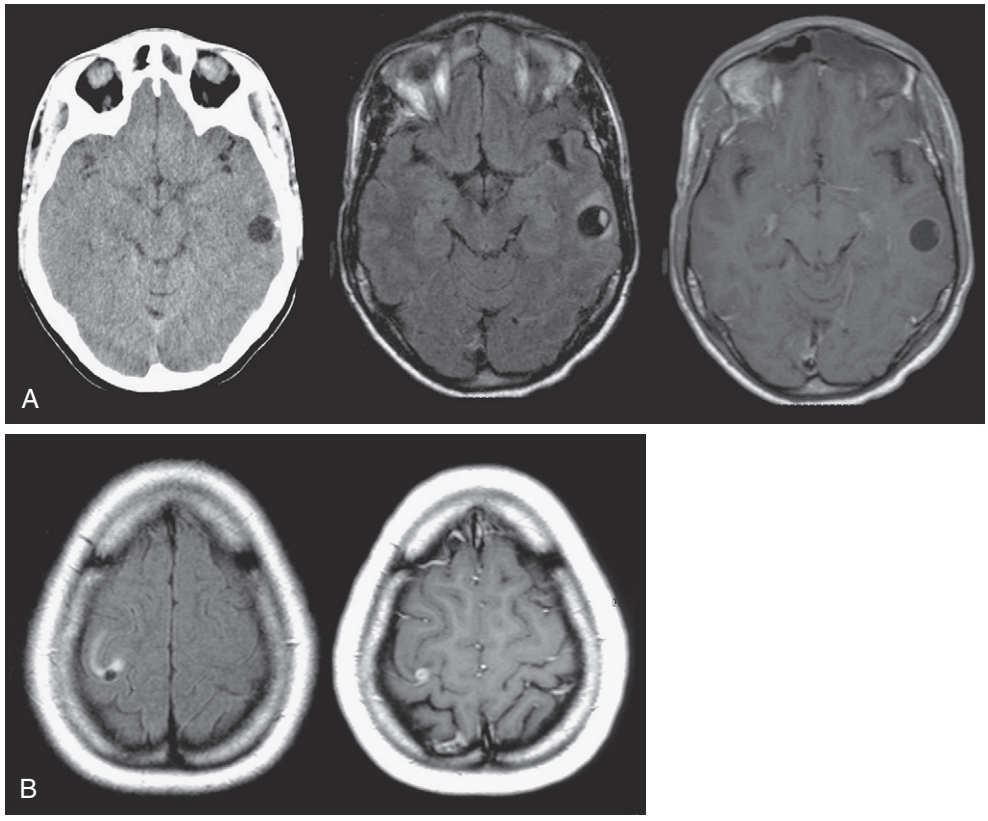


FIGURE 1-34 Neurocysticercosis. **A,** Computed tomography *(left)*, fluid-attenuated inversion recovery (FLAIR) *(middle)*, and postgadolinium T1-weighted *(right)* images demonstrate a cyst with scolex, thin rim of enhancement, and surrounding edema in the vesicular stage. **B,** FLAIR *(left)* and postgadolinium T1-weighted *(right)* images showing signal loss related to calcification, a small amount of edema, and rim enhancement in the granular nodular stage.

Calcification may imply a tumor of mucinous origin (gastrointestinal tract), and hemorrhage may indicate hypervascular primaries such as choriocarcinoma, renal, or thyroid in addition to the other more common cancers. The World Health Organization classification of primary central nervous system neoplasms is generally based on either cell type of origin or other location (e.g., sellar). Knowledge of this classification system is important for accurate communication among clinicians from different subspecialties, especially pathology, neurooncology, and neurosurgery. In addition, the radiologist should be familiar with the typical imaging characteristics, locations, and demographics of the common lesions in each category. As in any field, expertise requires effort and experience. Although it may be very satisfying to correctly identify the tumor histology (or at least narrow the differential diagnosis to a select few), the major goal in the emergency setting is to recognize subtle lesions, bring attention to those that may soon result in significant complications, and provide reassurance when intervention is not indicated. Perhaps the first step in this process should be to try to determine whether a mass is intraaxial or extraaxial. Although not always clear, this

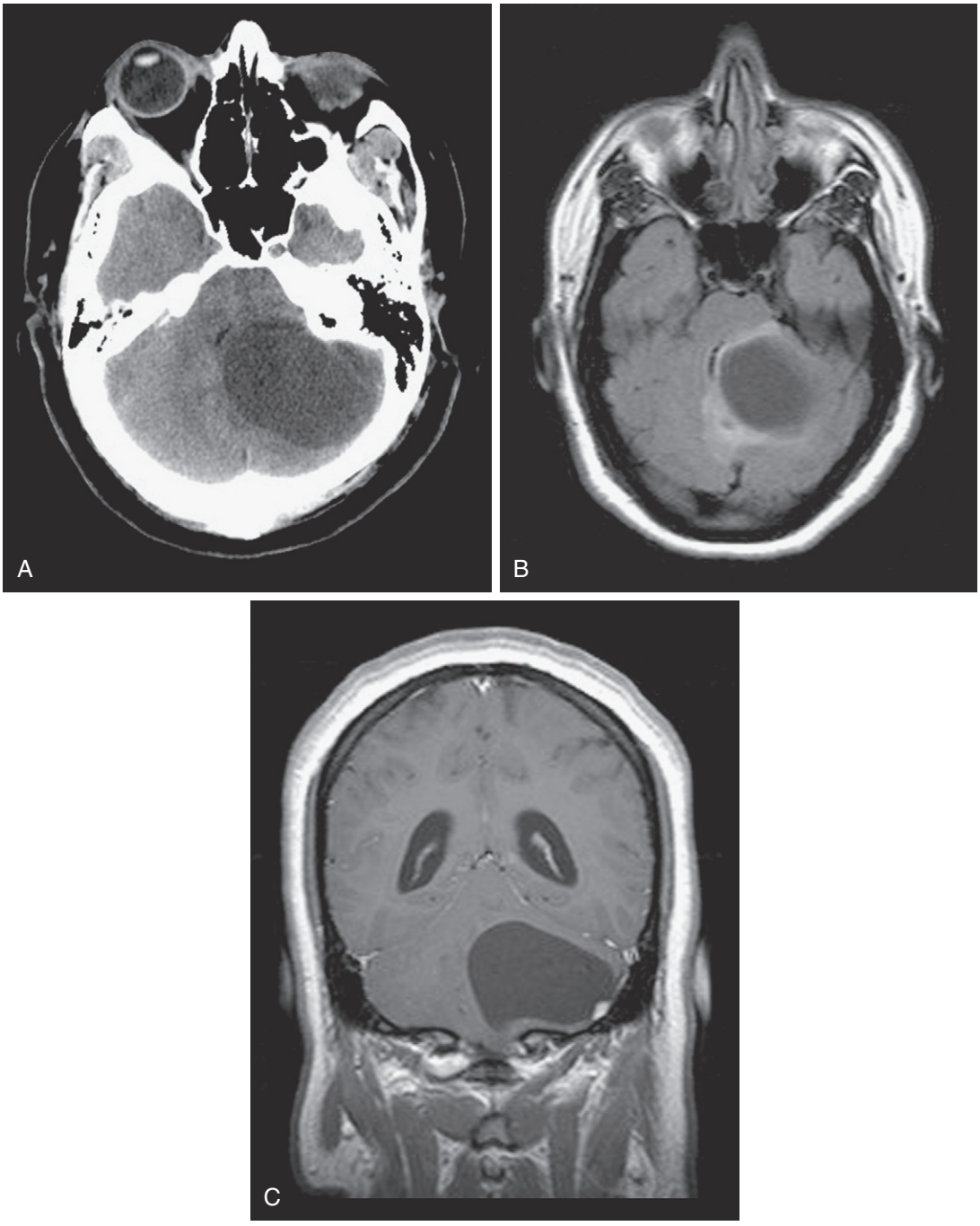


FIGURE 1-35 Hemangioblastoma. **A,** Computed tomography shows a fluid density mass in the cerebellum and surrounding edema resulting in compression of the fourth ventricle. **B,** On a fluid-attenuated inversion recovery image, the signal is relatively hyperintense to cerebrospinal fluid, suggesting protein content. **C,** A postgadolinium T1-weighted image shows a small enhancing mural nodule within the cystic mass. Note dilated lateral ventricles due to obstructive hydrocephalus.

distinction helps guide the differential diagnosis toward the proper category. The location of the lesion (supratentorial vs. infratentorial) and relation to the skull base and cisterns (e.g., anterior or middle fossa, sellar/parasellar, pineal region, cerebellopontine angle cistern, or intraventricular), along with multiplicity, are also important details. Demographics and clinical presentation may be equally important. One must also be aware that the differential diagnosis for many primary neoplasms includes metastasis, as well as infection, infarct, demyelination, inflammatory conditions, and congenital/developmental anomalies. Although space limitations preclude even the most basic description of each of the intracranial tumors, a few examples are presented to illustrate common imaging features to be recognized during the workup of patients in the emergency setting (Figs. 1-35 to 1-39).

Disorders of White Matter

No review of nontraumatic emergencies could be complete without mention of the following set of loosely related disorders. The common bond may be that they do

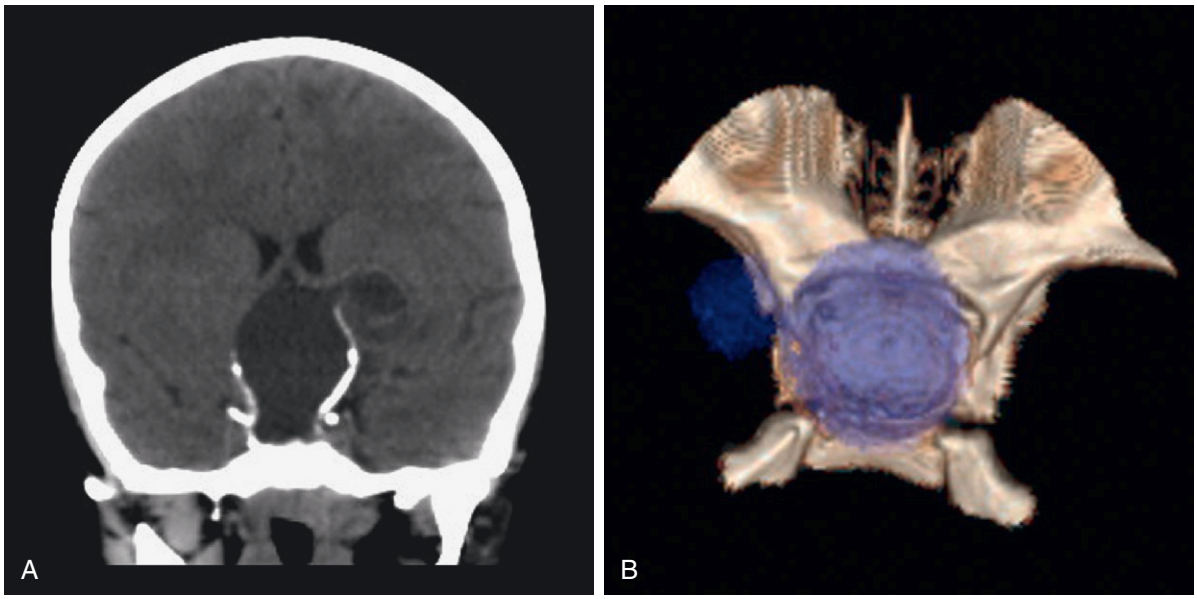


FIGURE 1-36 Craniopharyngioma. **A,** Coronal reformat of noncontrast computed tomography (CT) shows a large cystic sellar/suprasellar mass with peripheral calcifications. **B,** A volume-rendered image shows the cystic components of the lesion as a semitransparent surface. By varying the transparency of the mass, the remodeled sella is easily demonstrated. This 5-year-old girl was sent by her ophthalmologist for urgent CT because of worsening visual acuity.

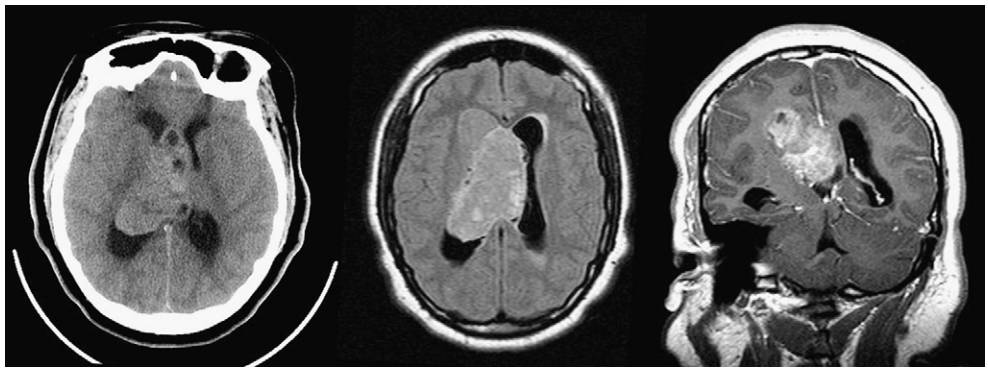


FIGURE 1-37 Central neurocytoma. Noncontrast computed tomography *(left)*, fluid-attenuated inversion recovery *(middle)*, and postgadolinium T1-weighted *(right)* images show a large, enhancing intraventricular mass related to the septum pellucidum causing hydrocephalus. This 22-year-old woman presented to the emergency department with worsening headaches.

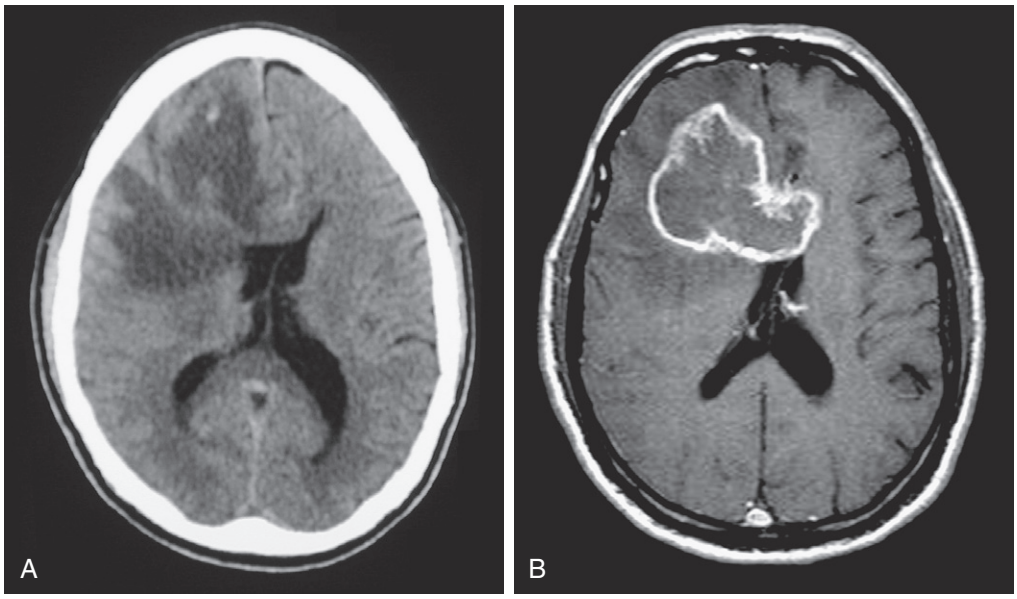


FIGURE 1-38 Glioblastoma multiforme (astrocytoma World Health Organization grade IV/IV). **A,** On noncontrast computed tomography the mass cannot be clearly separated from the edema. **B,** A postgadolinium T1-weighted image shows an irregular rim of enhancement of this mass that crosses the midline via the corpus callosum. This 50-year-old man presented with altered mental status.

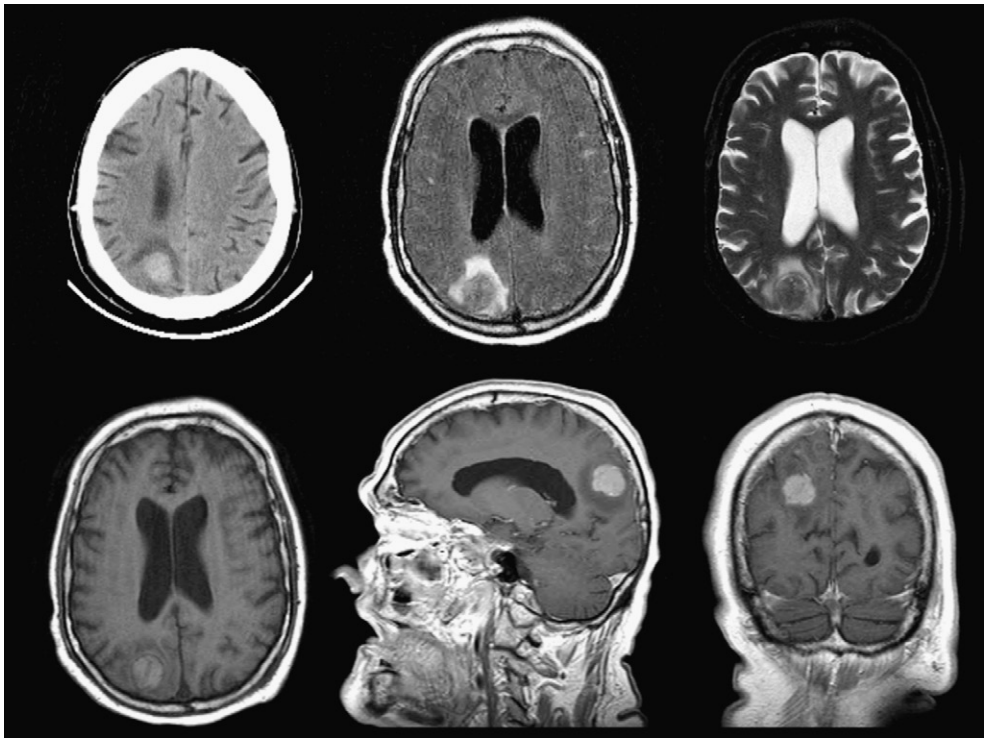


FIGURE 1-39 Metastatic lung carcinoma as shown on noncontrast axial computed tomography, fluid-attenuated inversion recovery (FLAIR), T2-weighted, T1-weighted, and sagittal and coronal postgadolinium T1-weighted images. This single lesion is hyperdense, FLAIR/T2 isointense, T1 mildly hyperintense, and homogeneously enhancing. A moderate amount of edema is present relative to the size of the lesion.

not fall into the infectious or neoplastic categories. Some are quite common and the others are being diagnosed more frequently because of the relatively classic imaging features and recognized clinical associations.

Multiple Sclerosis

Patients presenting with a clinically isolated syndrome (first episode of neurologic dysfunction) often undergo imaging in the emergency setting mainly to exclude infarction or other processes. White matter lesions detected by CT or MRI may raise the suspicion of a demyelinating disorder. The diagnosis of multiple sclerosis (MS) can be complex, requiring dissemination of lesions in time and space and exclusion of other causes such as Lyme disease, vasculitis, neurosarcoidosis, lupus, and others. The McDonald Diagnostic Criteria for MS imaging (originally published in 2001, with revisions in 2005 and 2010) are a standardized set of diagnostic guidelines that are applied clinically and within clinical trials. These criteria are based on identifying lesions that are disseminated in space and time on the basis of number, location (periventricular, juxtacortical, infratentorial, and spinal cord), and enhancement. Classically, hypodense/T2 hyperintense lesions are located in a periventricular distribution, in the corpus callosum (callosal-septal interface), and also in the brainstem, cerebellum, and spinal cord. Transient disruption of the blood-brain barrier will lead to solid or rim enhancement of active plaques (Fig. 1-40). Active demyelination may appear hyperintense on DWI. Magnetization transfer and MR spectroscopy techniques may demonstrate abnormalities even in white matter that appears normal. Genetic and environmental factors and female to male ratios of almost 2 to 1 (adults) and greater than 5 to 1 (children) have been found. As the name implies, the rare tumefactive variety simulates a neoplasm, often leading to biopsy. Another autoimmune-mediated disorder that is generally monophasic is acute disseminated encephalomyelitis (ADEM), and it may be indistinguishable from MS on initial imaging (Fig. 1-41). Another presumably autoimmune disorder that mimics MS and ADEM is Susac syndrome. This rare syndrome has a clinical triad of encephalopathy, branch retinal artery occlusions, and hearing loss.

Progressive Multifocal Leukoencephalopathy

In the immunocompromised host (especially due to AIDS), nonenhancing T2 hyperintensities (often confluent) in the parietal and occipital lobes should raise suspicion of progressive multifocal leukoencephalopathy (Fig. 1-42). This demyelinating process due to infection with the John Cunningham (JC) virus was originally thought to affect only white matter, but cases with both gray and white matter lesions and variable enhancement have been reported. The progressive nature of the disorder is also less certain because of current, highly active, antiretroviral therapy (HAART) regimens. Progressive multifocal leukoencephalopathy (PML) has also been reported in patients with MS or psoriasis treated with immune-modulating medications such as natalizumab or dimethyl fumarate (Tecfidera).

A related disorder is central nervous system–immune reconstitution inflammatory syndrome (CNS-IRIS). In HIV-positive patients with severe immunosuppression that responds rapidly to the start of HAART therapy, an enhanced inflammatory response may lead to worsening neurologic

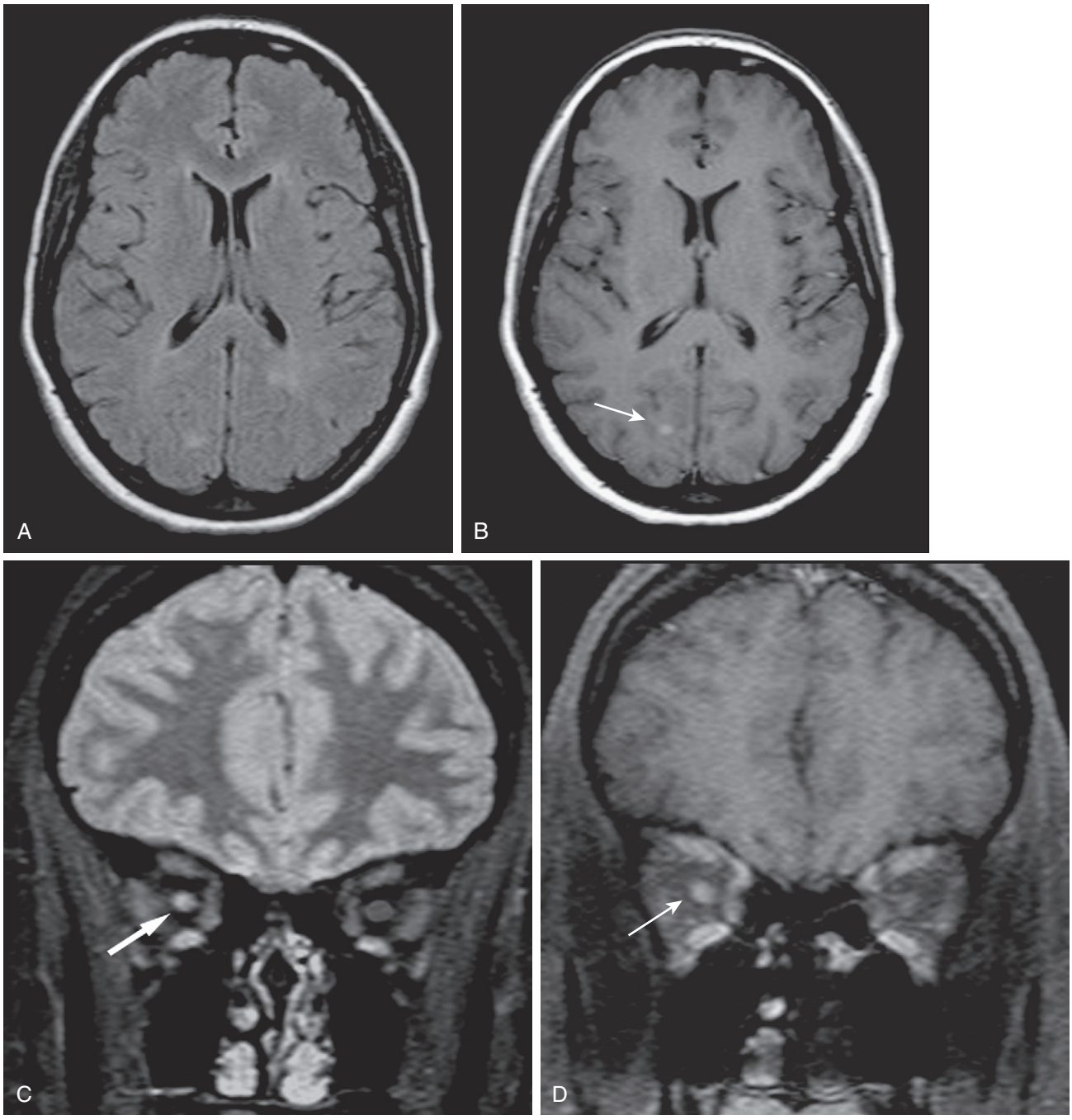


FIGURE 1-40 Multiple sclerosis—optic neuritis. **A,** A fluid-attenuated inversion recovery image shows a few white matter hyperintensities. **B,** One enhancing lesion *(arrow)* is detected on a postgadolinium T1-weighted image. **C,** A coronal short tau inversion recovery (STIR) image shows asymmetric hyperintensity of the right optic nerve *(arrow)*. **D,** Asymmetric enhancement of the right optic nerve *(arrow)* is shown on a postgadolinium, fat-suppressed, T1-weighted image.

symptoms. In a patient with known PML, new enhancement of FLAIR hyperintense lesions, and development of interstitial edema, mass effect and restricted diffusion would support the diagnosis of PML-IRIS. Among the organisms most commonly associated with CNS-IRIS are the JC virus and *Cryptococcus*. Similarly, the inflammatory response could be directed toward other infections such as HIV, *Mycobacteria, Toxoplasma,* cytomegalovirus (CMV), varicella-zoster virus (VZV), and *Candida* with varied imaging findings. CNS-IRIS may develop in the absence of an infectious agent and even at long intervals after initiation of HAART. If the inflammation responds to steroid treatment, long-term outcome may be improved.

Posterior Reversible Encephalopathy Syndrome

Posterior reversible encephalopathy (and seizure) syndrome (PRES) has a number of common causes such as (pre)eclampsia, hypertensive crisis, lupus and other causes of nephropathy, and drug toxicity (including immunosuppressants and erythropoietin). In the workup of

new seizures, the classic features of T2 hyperintensity in a rather symmetric distribution within the occipital, parietal, and posterior frontal lobes should bring this diagnosis to mind (Fig. 1-43). Although white matter is primarily affected, gray matter structures in the basal ganglia, brainstem, and cerebellum also may be involved. Diffusion imaging is most helpful to differentiate this process from acute infarction; ADC values will be elevated in lesions of PRES. Small amounts of hemorrhage (and infarcts) may occur within the background of vasogenic edema resulting from abnormal vascular autoregulation. Differentiation from acute or subacute stroke is important in directing the search toward an offending agent rather than initiating the stroke clinical pathway.

Toxic Encephalopathy

Whether due to accidental or intentional exposure/ingestion, a variety of well-known toxins may cause encephalopathy. Symmetric bilateral hypodensities/T2 hyperintensities in the globus pallidus are the hallmark of hypoxic damage due to carbon monoxide poisoning; hemispheric white matter also may be involved. Methanol toxicity typically affects the putamen and can be hemorrhagic. In addition to cerebellar degeneration, chronic alcoholism may lead to the development of Wernicke encephalopathy. It can also be the result of thiamine deficiency and a variety of other less common systemic conditions, presenting with lesions of the hypothalamus, mammillary bodies, dorsal medial thalamus, and periaqueductal gray matter.

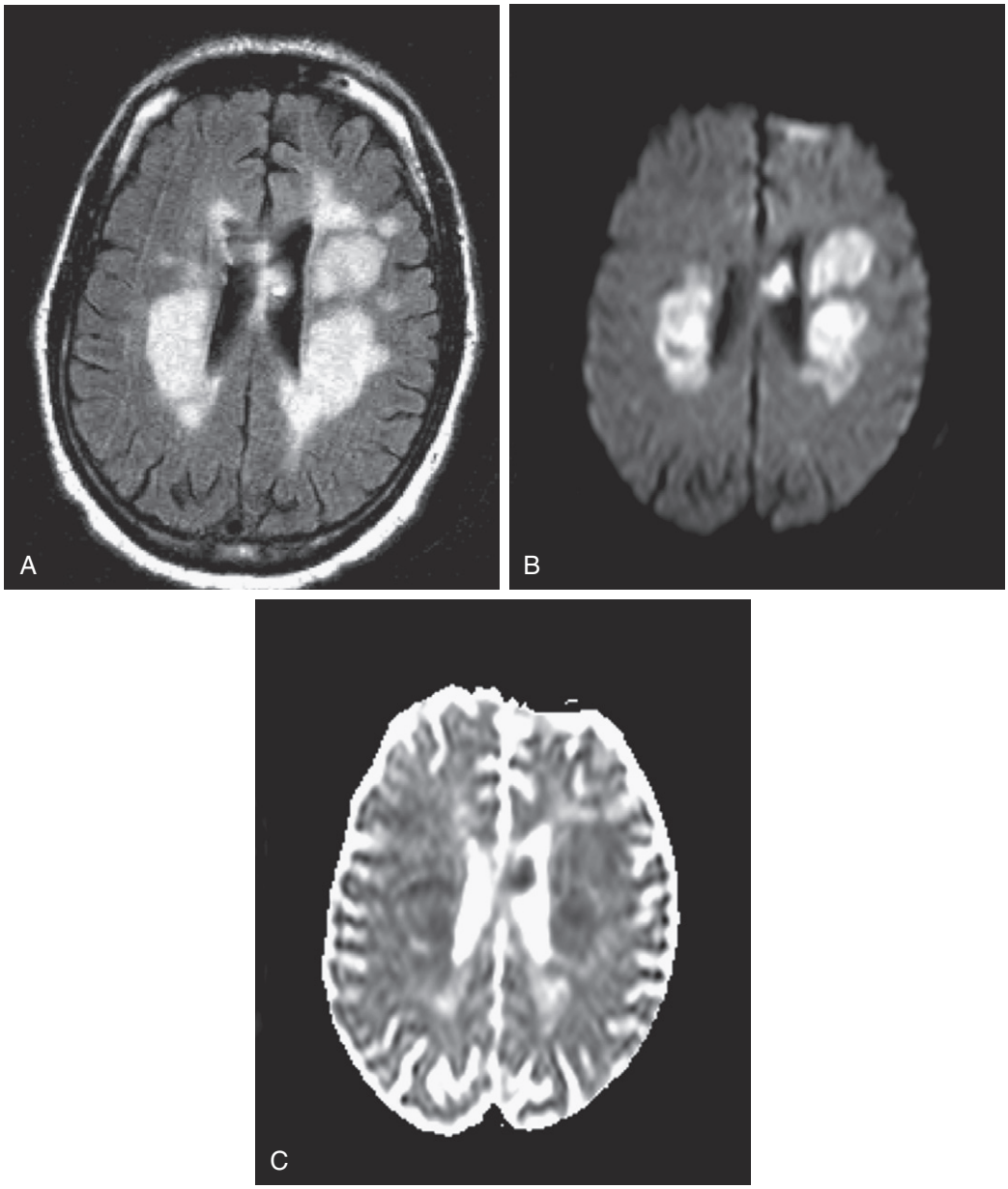


FIGURE 1-41 Acute disseminated encephalomyelitis. **A,** A fluid-attenuated inversion recovery image shows nonspecific periventricular and subcortical white matter hyperintensities. A diffusion-weighted image **(B)** and apparent diffusion coefficient map **(C)** show central areas of restricted diffusion and surrounding vasogenic edema ("T2 shine-through"). This acute demyelinating process mimics acute stroke. The distribution of the lesions is not typical of an acute infarct.

Ischemic and hemorrhagic complications related to use of illicit drugs have already been discussed. Toxic encephalopathy may also result from drug abuse. The pattern of white matter abnormality that results from inhalation of heroin vapor (known as "chasing the dragon") can be quite dramatic (Fig. 1-44). Encephalopathy may also be iatrogenic and related to chemotherapy (e.g., methotrexate) or radiation therapy and generally affects the periventricular white matter in a diffuse fashion. Another potentially iatrogenic disorder may result from the rapid correction of hyponatremia, leading to the classic central pontine or extrapontine varieties of demyelination (myelinolysis).

HEAD AND NECK TRAUMA

According to statistics from the 2014 American College of Surgeons National Trauma Data Bank survey (based on more than 6 million records from the United States and Canada), injuries resulting from MVCs accounted for 27% of all cases. Other cases were due to falls (42%), being struck (7%), and gunshot wounds (4%). Bicyclists were involved in 2% of cases. The largest percentage of fatalities (almost half) were due to falls, followed by MVCs and firearms. A large percentage of the injuries involve the head, face, and neck. Diagnostic imaging plays an important role in decision making for immediate patient management, as well as surveillance for potential long-term complications. Osseous injuries including facial, skull, and skull base fractures and soft tissue injuries to orbits, vessels, the airway, and the pharynx should be considered in the routine workup performed in the settings of blunt and penetrating trauma.

Acute traumatic injuries in the head and neck region are best evaluated by CT. At our institution, we use 64-row detector helical scanners with 0.625-mm detector size. Depending on the protocol, images may be prospectively processed as contiguous 1.25-mm and 5-mm sections for review of the brain, 1.25-mm sections for the facial bones, calvarium, and cervical spine, or 0.625-mm sections of the skull base. Images are processed using both soft tissue and bone algorithms, and coronal and sagittal reformats are routinely created. Images through any region can be retrospectively processed at 0.625-mm section thickness if finer detail is necessary based on a review of the initial images. Three-dimensional volume-rendered reconstructions are often created to present an overview for referring physicians and for surgical planning. Noncontrast head CT, followed immediately by CTA of the neck and head performed with 0.625-mm contiguous sections during bolus intravenous injection of low-osmolar, nonionic contrast material, will allow for simultaneous screening for vascular injuries.

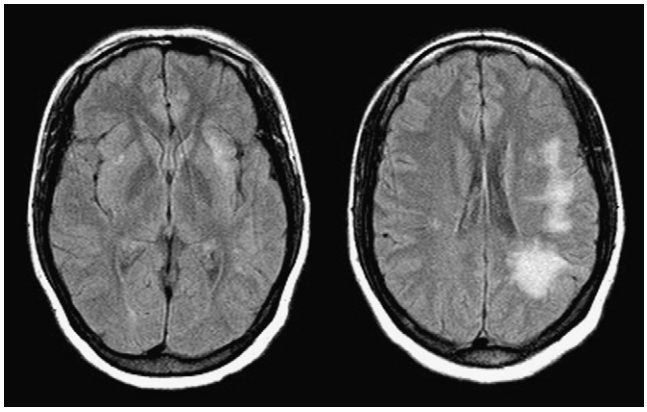


FIGURE 1-42 Progressive multifocal leukoencephalopathy. Fluid-attenuated inversion recovery images show asymmetric white matter hyperintensities involving predominantly the left external capsule and periventricular and subcortical white matter. No enhancement or mass effect was present. This patient with acquired immunodeficiency syndrome presented with a rapid decline in mental status.

Skull Fractures

In the past, the workup of head trauma included skull radiographs, but those days are gone. The use of CT has become the standard of care for rapid assessment of the skull and intracranial contents. In the early days of CT, it was estimated that more than half of skull fractures were not detected because they were oriented almost parallel to the imaging plane and therefore volume averaged with adjacent normal bone. With recent decreases in section thickness and use of the multidetector-row technique, this

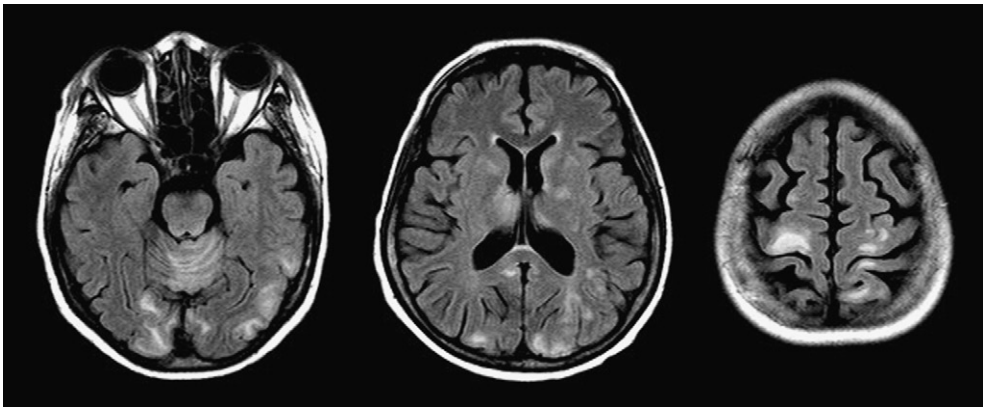


FIGURE 1-43 Posterior reversible encephalopathy syndrome. Fluid-attenuated inversion recovery images demonstrate slightly asymmetric hyperintensities primarily involving the cerebellum, thalami, and posterior frontal, parietal, and occipital lobes. Note involvement of both gray and white matter structures. This patient presented with new-onset seizures. Signal abnormalities resolved completely within 1 month.

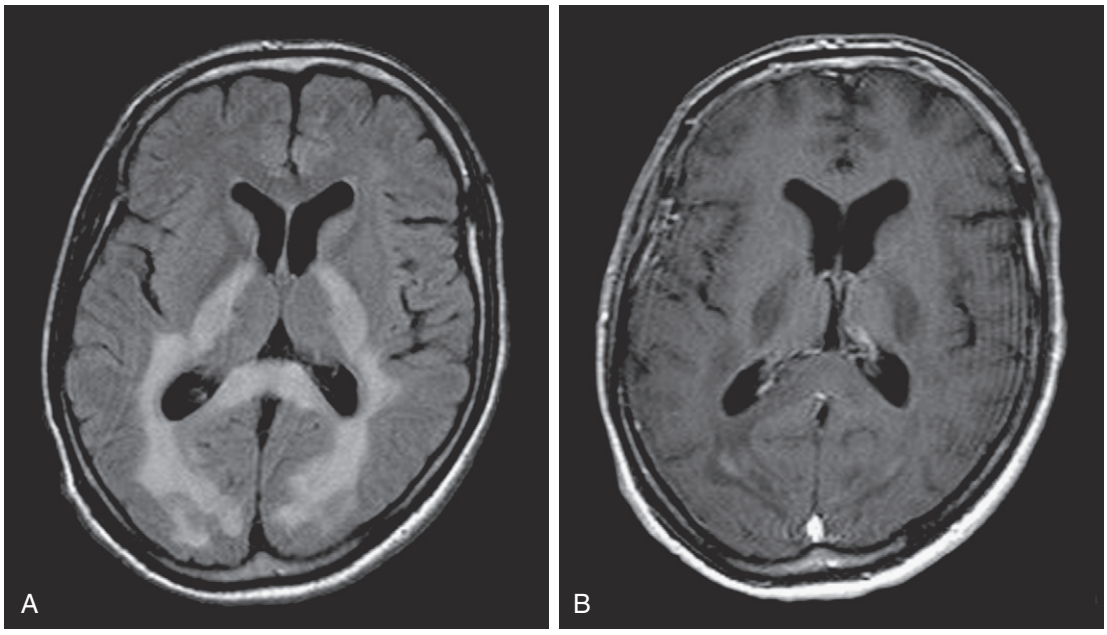


FIGURE 1-44 Toxic encephalopathy. **A,** A fluid-attenuated inversion recovery image shows symmetric, confluent, primarily white matter hyperintensities. **B,** A postgadolinium T1-weighted image shows minimal enhancement. The key to the diagnosis is the association with inhalation of heroin vapor—"chasing the dragon."

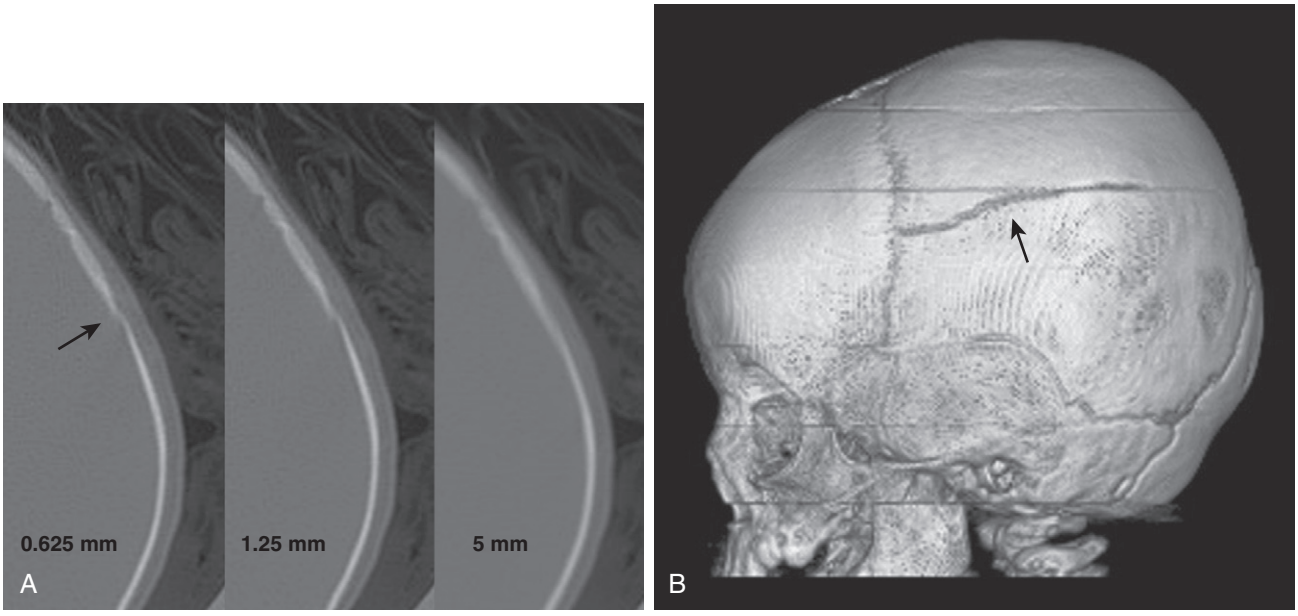


FIGURE 1-45 Skull fracture. **A,** Nondisplaced skull fracture is occult on routine 5-mm–thick section due to volume averaging. Fracture is most conspicuous on 0.625-mm section although with an increase in noise. **B,** Volume-rendered image shows fracture is nearly parallel to axial imaging plane.

limitation has effectively been overcome (Fig. 1-45). Careful review of millimeter or submillimeter thickness sections and 3D volume-rendered images and familiarity with normal sutural anatomy and variants may be necessary to accurately detect fractures. The radiologic evaluation should start with the scalp, because soft tissue swelling and scalp hematoma are very helpful indicators of possible underlying fracture. Skull fractures may be linear or comminuted, and either type may be depressed. Diastasis is the term applied to separation of linear fracture fragments or sutures. Diastatic fractures occur more commonly in children. If the arachnoid membrane gets trapped within a diastatic fracture, a "growing fracture" (leptomeningeal cyst) may develop over time.

Bullet wounds may leave behind a wake of comminuted bone and metallic fragments and burst fractures at the point of exit. Identification of a fracture should lead to the dedicated search for other important findings, such as ICH. Fractures through the skull base may lead to other complications such as vascular or cranial nerve injuries or CSF leak. The presence of intracranial air should prompt the search for fracture through an aerated paranasal sinus or pneumatized portion of the temporal bone, because antibiotic therapy may be indicated for prophylaxis against

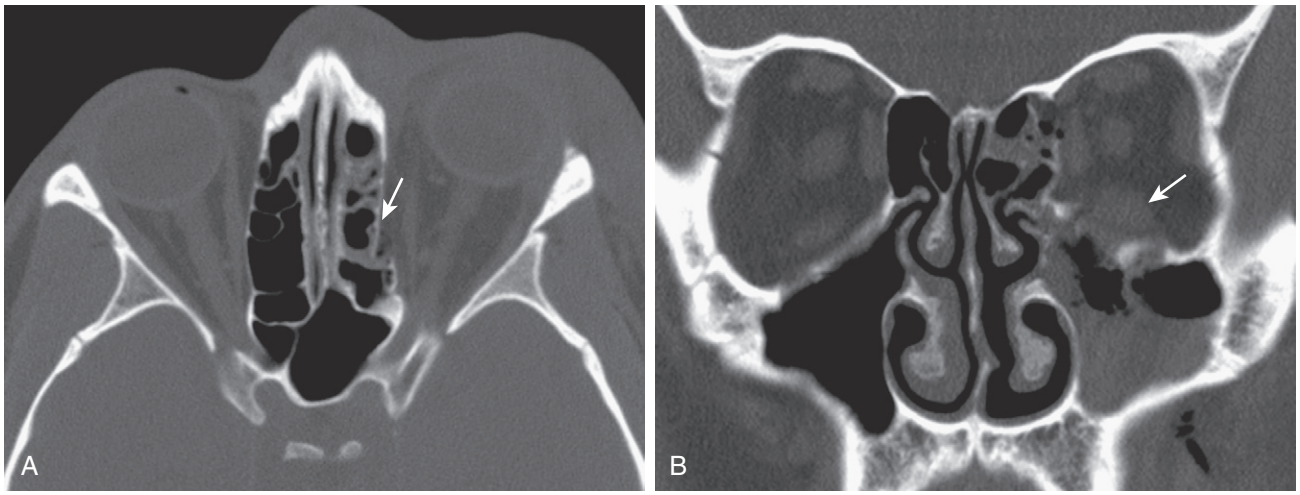


FIGURE 1-46 Orbital blow-out fractures. **A,** Axial computed tomography (CT) shows a displaced fracture of medial wall of the left orbit (lamina papyracea; *arrow*). **B,** A direct coronal CT image shows a displaced left orbital floor fracture with an air–fluid level in the maxillary sinus. (This is of historical value, because most coronal images are now obtained by reformation.) The inferior rectus muscle is swollen *(arrow)*. This patient was hit in the eye with a baseball.

meningitis. One should not be alarmed by all bubbles of air, because reflux into the cavernous and other dural sinuses often occurs after insertion of intravenous catheters and injections of saline solution, medications, or contrast material with lax technique. The presence of fluid within the sphenoid sinuses, middle ear cavities, or mastoid air cells should also prompt a search for fractures through these regions. Temporal bone fractures may result in damage to the facial nerve, ossicles, and otic capsule. Screening for potential vascular injury in the setting of fracture of the central skull base may be accomplished with CTA, which was discussed in the section on cerebrovascular emergencies (see also Fig. 1-54).

Maxillofacial Fractures

MDCT has also revolutionized the workup of facial fractures. Once within the realm of plain film radiography, these injuries now are almost exclusively evaluated with CT. The general principles of fracture detection are often taken for granted but warrant quick mention. An unexpected linear lucency, the disappearance or displacement of a normal structure, and a double density from abnormal overlap of adjacent structures are classic radiographic findings of facial fractures. A cortical defect, separation of a suture, and presence of subcutaneous, orbital, or periorbital air are findings that apply equally to radiographic and CT examinations. Likewise, soft tissue swelling and fluid levels in the paranasal sinuses are equally important clues to recognize, although these clues are less specific and may occur without fractures. Whereas in the past several CT scans were necessary to evaluate the brain and face (including both thin-section axial and direct coronal scans), complete evaluation of the head and facial skeleton now can be performed with a single exposure. As an example, our 64-detector scanner offers the prospective creation of routine 5-mm-thick contiguous sections processed with a soft tissue algorithm to evaluate the brain and 0.625- or 1.25-mm–thick contiguous sections processed with a bone algorithm for evaluation of the face and skull. The thinner sections are routinely reformatted in coronal and sagittal planes, and, if desired, 3D volume-rendered images may be created at the CT console or other workstation. Depending on clinical examination findings, imaging of the head may begin at the level of the dental occlusal plane or include the chin and continue to the vertex. This method improves detection and characterization of facial fractures and reduces the amount of additional radiation exposure and scan time. Comprehension of the fracture may be improved by illustrating its relationship to normal anatomic landmarks. This technique helps the radiologist apply the most appropriate terminology or classification and it helps the surgeon to determine the need for operative reduction and fixation, usually with titanium plates and screws. Sometimes an implant is necessary to repair a large defect, as in the orbital floor.

The facial skeleton can be considered to be composed of several vertical and horizontal buttresses of thickened bone that support the functions of the face, eyes, mouth, and airway. The buttresses are linked to each other and act as attachments of the face to the calvarium and skull base. The individual components of this system and the sutures are important anatomic landmarks for the radiologist and the surgeon but are beyond the scope and space limitations of this chapter. A brief overview of common facial fractures and associated injuries follows.

Orbital Blow-Out Fractures

Isolated trauma to the orbit, a common cause of ED visits, plays a role in many cases of head trauma. Nontraumatic orbital emergencies are discussed later in this chapter. Fractures and injuries to the orbital soft tissues come in many different varieties. A blow to the eye causes an increase in intraorbital pressure, which is transmitted to the thin walls of the orbit. Blow-out fractures may involve the orbital floor, the medial wall, or both; the orbital rim should not be involved (Fig. 1-46). Even though the medial wall (lamina papyracea) is thinner, the network of ethmoid sinus septations acts as a support, and therefore

isolated orbital floor fractures are more common. In up to about half of floor fractures, medial wall fractures also occur. Orbital emphysema and herniation of orbital contents are possible associated findings. Coronal images are very useful to assess the degree of displacement of fracture fragments. Sagittal reformatted images help define the anteroposterior extent of orbital floor fractures. Fragment size and displacement help determine conservative versus operative management. Numbness of the upper cheek due to injury to the infraorbital nerve and diplopia may be presenting symptoms. Persistent diplopia and enophthalmos are possible long-term complications. Fractures that affect the orbital apex may be surgical emergencies. A bone fragment or hematoma can compress the optic nerve, leading to acute decrease in visual acuity. An afferent papillary defect should also prompt careful review of this region with bone and soft tissue algorithms and display settings. Although extraocular muscle entrapment is a clinical diagnosis, certain imaging features may offer guidance to the surgeon. If the inferior rectus muscle is displaced and does not retain its normal flattened shape on coronal images, then the fascial sling of the globe may be disrupted. Herniation of the muscle into the maxillary sinus can occur in the absence of a visible defect in the floor, implying that a "trapdoor" fragment has sprung back into place, and clearly, prompt repair will be necessary. Hematomas within the orbital soft tissues may occur in association with fractures, including retrobulbar and subperiosteal locations.

Although orbital decompression results from the blow-out fracture mechanism, up to 25% have an associated ocular injury. Imaging findings can signal the need for an ophthalmologic examination that may be overlooked in the setting of multitrauma. A ruptured globe, caused by either blunt or penetrating trauma, is small, often with a flattened contour. Hemorrhage within the eye appears relatively hyperdense and can occur in several different compartments, including subretinal, subchoroidal, and subhyaloid. The distinction between these compartments can often be made based on shape and limits of the hemorrhage but is best made by physical examination. Dislocation of the lens, whether partial or complete, is not usually a subtle finding but can be easily overlooked if it is not included in the usual search pattern. Rupture of the capsule of the lens results in lens edema, appearing as a decrease in attenuation of this usually high density (proteinaceous) structure. Intraorbital and intraocular foreign bodies may be detected by CT; however, certain materials, such as wood, are better detected by ultrasound or MRI. Calcifications of the trochlear apparatus, the sclera, and optic drusen are common and should not be misinterpreted as foreign bodies. The shrunken, calcified globe (phthisis bulbi) resulting from past trauma or infection should not be mistaken for an acute injury. Likewise, intraocular silicone oil or gas and scleral buckles (both high- and low-density silicone) for treatment of retinal detachments, as well as other devices (such as aqueous shunts for treatment of glaucoma), also should be properly recognized and not become causes of concern.

Orbital roof fracture is an uncommon injury that may extend to the frontal or ethmoid sinuses. This fracture is best appreciated with coronal and sagittal reformatted images. With a "blow-in" type of fracture, as from pressure phenomenon due to a gunshot wound to the head, progressive herniation of the frontal lobe into the orbit may result from cerebral edema. A blow-out fracture of the orbital roof is an uncommon occurrence.

Nasal Fractures

Although nasal fractures commonly occur in isolation, they are also often associated with other fractures of the midface. Nasal fractures account for approximately half of all facial fractures. Radiographs occasionally may be requested for isolated nasal trauma, and therefore one should be aware that fractures are usually oriented perpendicular to the nasal bridge and will cross the normal nasomaxillary suture and groove for the nasociliary nerve. These fractures can be of cosmetic importance or may result in airway obstruction. Attention must be directed to the nasal septum because treatment of a septal hematoma might be necessary to avoid possible complications of ischemic necrosis, saddle deformity, and abscess formation.

As the name implies, naso-orbitoethmoid fractures are more complex and involve the nasal bones, as well as the central upper midface. Impaction of the nose and disruption of the medial canthal regions, medial orbital walls, and ethmoid sinuses will result in widening of the intercanthal distance and the need for repair. Involvement of the nasofrontal duct or nasolacrimal canal may lead to significant morbidity and also may require surgical attention to reduce the chance of frontal sinus mucocele development.

Zygomaticomaxillary Complex Fractures

The zygoma has four sutural attachments, two to the skull and two to the maxilla. The zygoma is the second most commonly fractured facial bone. Isolated arch fractures account for a minority of zygomatic fractures and can be easily demonstrated with the traditional submentovertex view ("bucket handle") radiograph. More commonly, 3D volume-rendered images from an MDCT dataset are used to arrive at the same impression. This injury may require repair for cosmetic reasons or because impaction of fracture fragments against the coronoid process of the mandible or temporalis muscle may result in trismus.

The more common injury to the zygoma involves the three major attachments (zygomaticomaxillary, zygomaticofrontal, and zygomaticosphenoid) and therefore has acquired the term *tripod fracture*. The preferred term may be zygomaticomaxillary complex (ZMC) fracture because it is more aptly considered a quadripod fracture as a result of involvement of the posteriorly located zygomaticotemporal attachment. Specific components include the inferior orbital rim, orbital floor, and lateral wall, as well as the attachments to the skull base (sphenoid and temporal bones). Impaction and rotation of a large fracture fragment will result in significant deformity of the cheek and orbit (Fig. 1-47). Fractures of the pterygoid plates or greater wing of the sphenoid may sometimes be seen with severe ZMC fractures.

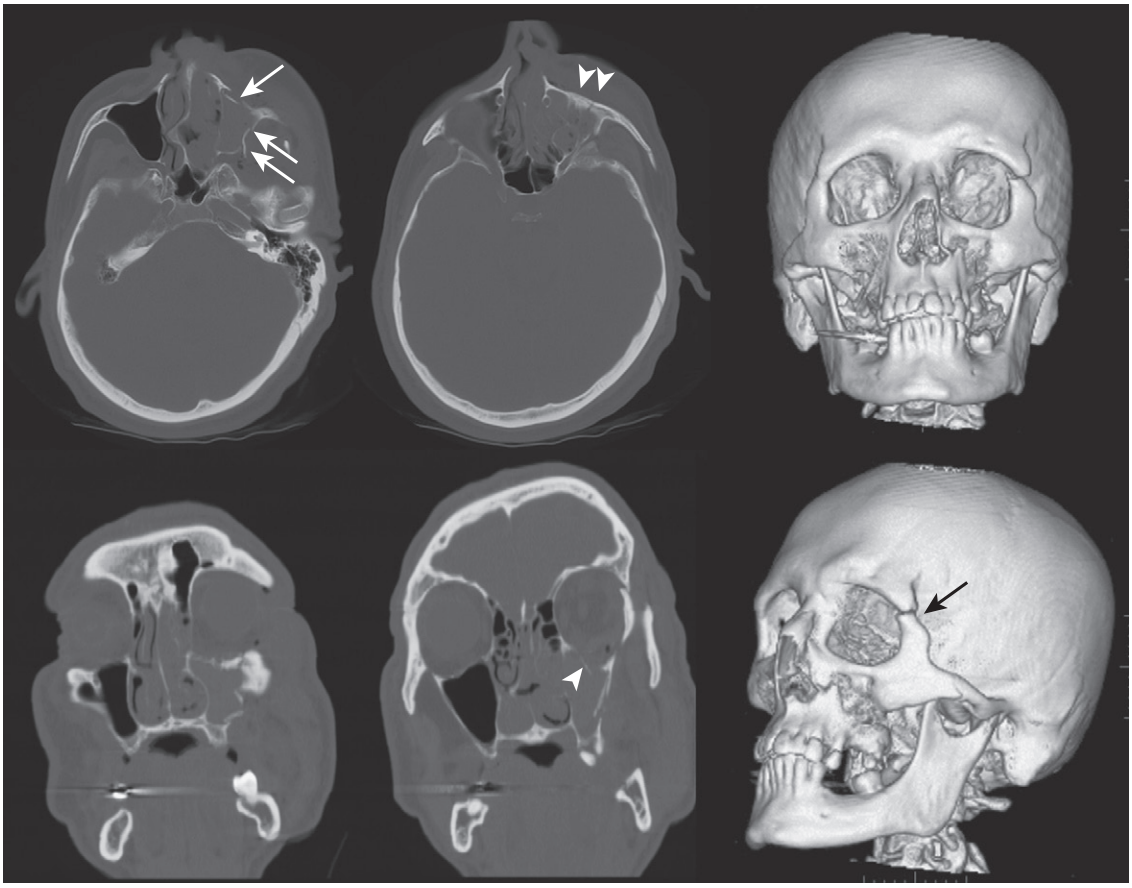


FIGURE 1-47 Zygomaticomaxillary complex fracture. Composite images show fractures of the left maxillary sinus anterior wall *(white arrow)* and posterolateral wall *(double arrows)*, orbital floor *(arrowhead)*, and inferior orbital rim *(double arrowheads)*. Volume-rendered images demonstrate diastasis of the zygomaticofrontal suture *(black arrow)* and degree of impaction of the malar eminence.

Le Fort Fractures

The Le Fort classification of midface fractures applies to separations of the maxilla from the skull base. The three-tier classification was developed by Le Fort in 1901 based on cadaveric experiments. These fractures rarely occur in their pure forms, and although originally they were described as being bilateral, common usage allows for unilateral and combined bilateral types. The Le Fort I fracture involves the maxillary antra, crossing midline above the hard palate. If it is unilateral, a sagittally oriented fracture of the palate will be present. Fractures of the pterygoid plates may occur, although some persons consider this to be a requirement by definition. With this injury, the hard palate will be allowed to separate from the remainder of the face, and it often is diagnosed by physical examination. Le Fort II fractures involve both maxillary antra and inferior orbital rims crossing at the nasion (either at the nasofrontal junction or the frontal process of the maxilla). The maxilla will be separated from the remainder of the face. In Le Fort III fractures, also termed *craniofacial dissociations*, the inferior orbital rims are intact but the lateral orbital walls and zygomatic arches are fractured, allowing separation of the face from the remainder of the skull. Variations and combinations of Le Fort and ZMC fractures are common (Fig. 1-48).

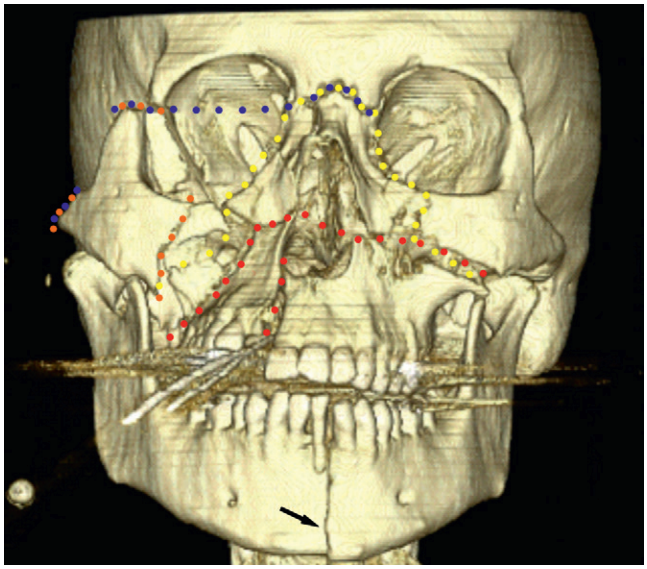


FIGURE 1-48 Le Fort fractures. A volume-rendered image from an unrestrained driver involved in a rollover motor vehicle collision shows multiple displaced fractures. Components: *red dots,* Le Fort I; *yellow dots,* Le Fort II; and *blue dots,* unilateral Le Fort III. *Orange dots* may be considered the zygomaticomaxillary complex. The *arrow* shows a fracture of the mandibular symphysis.

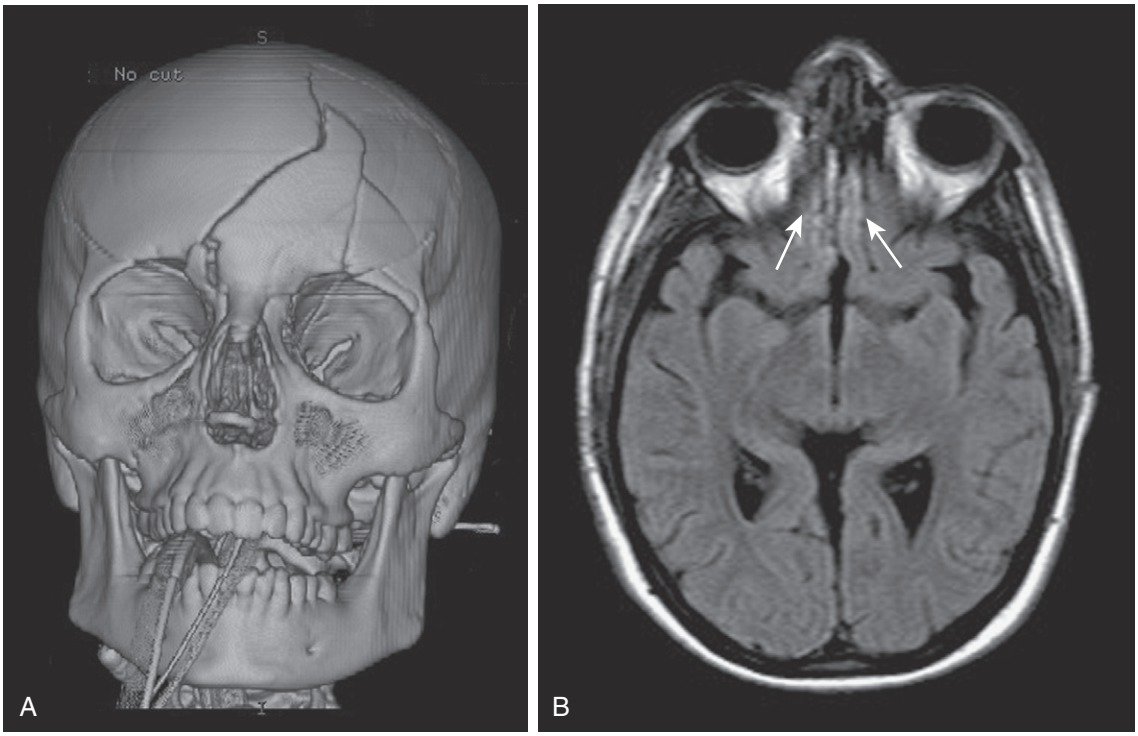


FIGURE 1-49 Smash fracture. **A,** A volume-rendered image shows the complexity of a comminuted frontal smash fracture that involves the frontal sinuses and both orbits. **B,** A fluid-attenuated inversion recovery image months later shows residual signal abnormality involving the gyrus rectus of both frontal lobes as a result of prior contusions.

Smash Fractures

The term *facial smash* is a general term applied to severely comminuted fractures of the facial bones that generally occur in association with fractures of the calvarium. ICH and traumatic brain injury occur commonly with these types of fractures. The frontal type commonly involves the anterior and posterior walls of the frontal sinus (Fig. 1-49). The naso-orbitoethmoid complex can be considered in this category. Central skull base types include fractures of the sphenoid bone. Vascular injuries related to skull base fractures are discussed in the sections on temporal bone fractures and cerebrovascular emergencies.

Mandibular Trauma

Fractures of the mandible are common and are classified by location—alveolar, symphyseal, parasymphyseal, body, angle, ramus, subcondylar (neck), or condylar. The mandible may be considered a ring structure, but with some flexibility due to the temporomandibular joints. Therefore, one, two, or more fractures may occur depending on the magnitude and direction of the applied force.

Bilateral temporomandibular joint dislocation without fracture is an uncommon injury resulting from a blow to the symphysis. The mandibular condyles should normally be seated symmetrically in the glenoid fossae. On occasion, the condyles may be anteriorly displaced, simply a reflection of normal open mouth position at the time of image acquisition. However, in a true dislocation, the glenoid fossae are empty, with condyles positioned anterior to the glenoid tubercles and the jaw locked in the open position.

If the styloid process is disrupted in the setting of mandibular fracture, air may be seen in the infratemporal fossa, possibly related to oral or Eustachian tube laceration. Mandibular fractures may be associated with hematomas within the masticator space.

Airway compromise may result from bilateral parasymphyseal fractures because the symphysis becomes a free fragment, allowing the tongue to obstruct the oral cavity. Fractures across the mandibular canal may cause injury to the inferior alveolar nerve (branch of mandibular division of the trigeminal nerve) and result in paresthesia of the chin. Fractures affecting the teeth are considered open and require antibiotic prophylaxis. Fractured or avulsed teeth can pose a risk for aspiration, particularly in the unresponsive patient. A dedicated search for radiopaque foreign bodies in the airway on all other imaging studies is therefore necessary. Muscular forces may act favorably or unfavorably, resulting in nondisplaced or displaced fractures, respectively. Displacement may occur in either the vertical or horizontal direction. Reduction with maxillomandibular fixation or open reduction and internal fixation may be required to restore occlusion and allow proper masticatory function, speech, and facial contour. As with other facial fractures, multiplanar reconstruction and 3D volume-rendered images are helpful in comprehending the injury, especially the orientation of fracture fragments

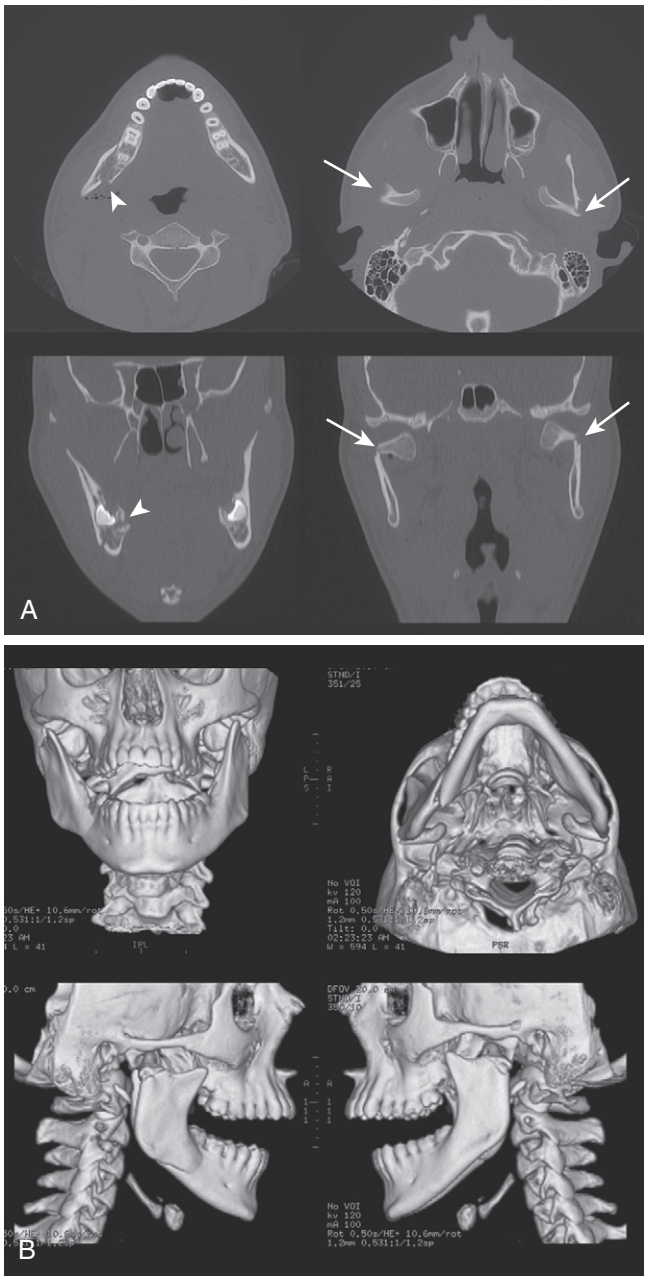


FIGURE 1-50 Mandibular fractures. **A,** Axial and reformatted coronal computed tomography images show bilateral mandibular subcondylar fractures *(arrows)* and fracture of right ramus *(arrowheads)*. **B,** Volume-rendered images provide a clear overview of the fractures.

and relationships to the coronoid processes and condyles, and they aid in surgical planning (Figs. 1-50 and 1-51).

Temporal Bone Fractures

Temporal bone fracture should always be suspected when opacification of the mastoid air cells and/or middle ear compartments is present in the trauma setting. Slice thickness of 1 mm or less may be necessary to clearly identify and fully characterize the fracture.Temporal bone fracture usually occurs as a result of blunt head injury and is classically characterized as either longitudinally or transversely oriented relative to the long axis of the petrous bone. The other components of the temporal bone, namely, the mastoid, styloid, squamous, and tympanic, can be involved as well. Temporomandibular joint dislocation and styloid process fracture are discussed with mandibular fractures in the section on facial trauma. In practice, however, fractures through this region tend to be complex, and more typically than not they demonstrate both longitudinal and transverse fracture characteristics (Fig. 1-52). Furthermore, characterization of the fracture plane does not provide much prognostic insight. It is now recognized that it is more important to characterize whether the otic capsule (the bony housing of the inner ear structures including cochlea and semicircular canals) and internal auditory canal are involved and whether adjacent critical vascular structures (the internal carotid artery and sigmoid sinus) are at risk for injury.

Temporal bone fractures parallel to the long axis of the petrous bone are more common than transversely oriented fractures (Fig. 1-53). Fracture components can secondarily involve the external auditory canal, tympanic cavity, and squamosal portions of the temporal bone. Blood and fracture fragments in the external auditory canal and tympanic cavity and ossicular disruption can account for the common clinical presentation of conductive hearing loss. Longitudinally oriented fracture planes tend to extend anteriorly toward the Eustachian tube and middle cranial fossa, avoiding the bony labyrinth (anterior subtype). The glenoid fossa can be involved, and disruption of the middle meningeal artery can result in a concomitant epidural hematoma. Less often the fracture plane may extend posteriorly behind the bony labyrinth to involve the jugular foramen and posterior fossa (posterior subtype). In these instances, careful attention is required to evaluate for involvement of foramen lacerum or the sphenoid bone, which put the traversing internal carotid artery at risk for traumatic injury. If the fracture plane approximates or involves the carotid canal, CTA or conventional angiography can be performed to evaluate for possible internal carotid artery injury at the skull base (Fig. 1-54).

Injury to the facial nerve is not uncommon in the setting of temporal bone fractures. A careful search for fractures along the entire course of the facial nerve from the internal auditory canal to the stylomastoid foramen is necessary. Focal swelling or a hematoma developing within an otherwise intact facial nerve may manifest clinically as partial facial weakness in a delayed rather than immediate fashion. This presentation is associated with better long-term prognosis for facial nerve function because the nerve is not disrupted.

Transversely oriented fractures are perpendicular to the long axis of the petrous bone and can be further classified into medial and lateral subtypes, depending on the position of the fracture plane relative to the arcuate eminence.The medial subtype transgresses at or medial to the lateral-most aspect of the internal auditory canal, whereas the lateral subtype transgresses the bony labyrinth. As with longitudinal fractures, careful attention must be directed to the relationship of the fracture plane to the carotid canal, because injury to the internal carotid artery can be seen in this setting. Both transverse subtypes can be associated with acute and permanent sensorineural



FIGURE 1-51 Mandible fracture. Axial, reformatted coronal, and sagittal images show a comminuted displaced fracture of the mandible with involvement of the alveolar ridge. A volume-rendered image clearly demonstrates the relationship of the mobile teeth.

hearing loss as a result of acute transection of the vestibulocochlear nerve. Facial nerve paralysis, if present, is also immediate and complete because of transection of the facial nerve.

Given the complex anatomy of the temporal bone, normal sutures and channels often can be mistaken for fracture planes. Normal petro-occipital, temporo-occipital, and occipitomastoid sutures can demonstrate irregular, coarse margins, raising concern for possible fracture (Fig. 1-55). Diastasis of sutures (equivalent to a fracture) can be seen without apparent fracture. Intrinsic sutures to the temporal bone itself, including tympanosquamous, tympanomastoid, and petrotympanic sutures, also can be confused with acute fractures (Fig. 1-56). Small channels in the middle and inner ear such as the cochlear and vestibular aqueducts, singular canal, and subarcuate fossa also can convey an appearance similar to fracture planes. An understanding of normal temporal bone anatomy is essential to avoid these errors. Symmetry, lack of opacification of mastoid air cells and middle ear compartments,

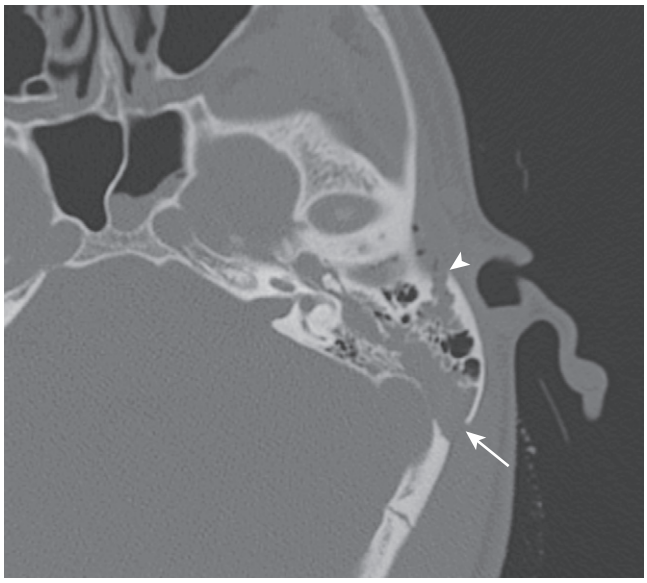


FIGURE 1-52 Complex temporal bone fracture. Longitudinal *(arrow)* and transverse *(arrowhead)* components are shown. The ossicles and otic capsule were not disrupted in this case.



FIGURE 1-53 Longitudinal temporal bone fracture. The fracture *(arrowhead)* extends parallel to the long axis of the petrous bone. Note partial opacification of mastoid air cells.

absence of overlying soft tissue swelling, and the clinical context also can provide reassurance that no fracture is present.

In addition to varied severity of facial weakness and conductive and sensorineural hearing loss, complex temporal bone fractures can have long-term complications. Squamous epithelial proliferation along fracture planes can result in cholesteatoma without concurrent mastoid disease. CSF leak can result from disruption of the epitympanic roof; this frank communication of the intracranial CSF space and middle ear can present as otorrhea if the tympanic membrane is disrupted or as rhinorrhea if the tympanic membrane is intact. Although otorrhea and rhinorrhea may resolve in the early posttraumatic setting, persistent leakage must be surgically managed because of the increased risk of meningitis. Cephalocele is also possible if the bony defect is large enough. A posttraumatic perilymphatic fistula between the inner and middle ear can occur with disruption of the oval or round windows or fractures through the otic capsule and may present with hearing loss and vertiginous symptoms. Perilymphatic fistulas are difficult to demonstrate radiographically but can be suspected based on clinical manifestations.

Airway and Pharyngeal Injuries

Acute trauma to the airway and pharynx typically occurs in the setting of penetrating trauma (stab wounds and gunshot wounds) or can be iatrogenic (as with traumatic intubation). Injury to the aerodigestive tract should be suspected in the setting of unexplained gas in the soft tissues adjacent to the airway or pharynx. It is important to keep in mind that lack of associated soft tissue gas does not exclude injury to these structures. Soft tissue gas adjacent to the aerodigestive tract could be a result of superior tracking of pneumomediastinum and pneumothorax from a penetrating chest wound or could be related to the tract of the penetrating object itself. Tracheal diverticula are often seen at the thoracic inlet level on the right and represent a common normal variant. The presence of air along the aerodigestive tract can be idiopathic or related to asthmatic pneumomediastinum. Correlation with clinical presentation is necessary to avoid unnecessary imaging studies.

If an injury is suspected, endoscopic evaluation with direct visual inspection is essential. A single contrast radiographic swallow study with a water-soluble contrast agent may be helpful in the initial evaluation of a hypopharyngeal injury; however, in a patient with potential concomitant airway injury or poor airway control, it may not be safe to perform such an examination given the risk of aspiration and possible complication of chemical pneumonitis.

Injuries to the airway may be accompanied by injury to the larynx and vocal cords. The presence of a laryngeal hematoma and vocal cord injury should be suspected if asymmetry is present in these regions when comparing right and left (Fig. 1-57). Patients with such an injury typically present with hoarseness soon after the acute event. Again, if such an injury is suspected, direct visualization by endoscopy is indicated. It should be remembered that patient phonation or phase of respiration can result in apposition of the vocal cords, creating an appearance of airway obstruction. Lack of associated soft tissue swelling and clinical correlation can help in minimizing the false-positive diagnosis of laryngeal injury in these cases.

INFECTIONS

Infections in the head and neck region are commonly seen in the ED setting. Usually the diagnosis is clear based on the physical examination and history. The role of imaging is to define the extent of infection and to provide information that is critical to immediate patient management.

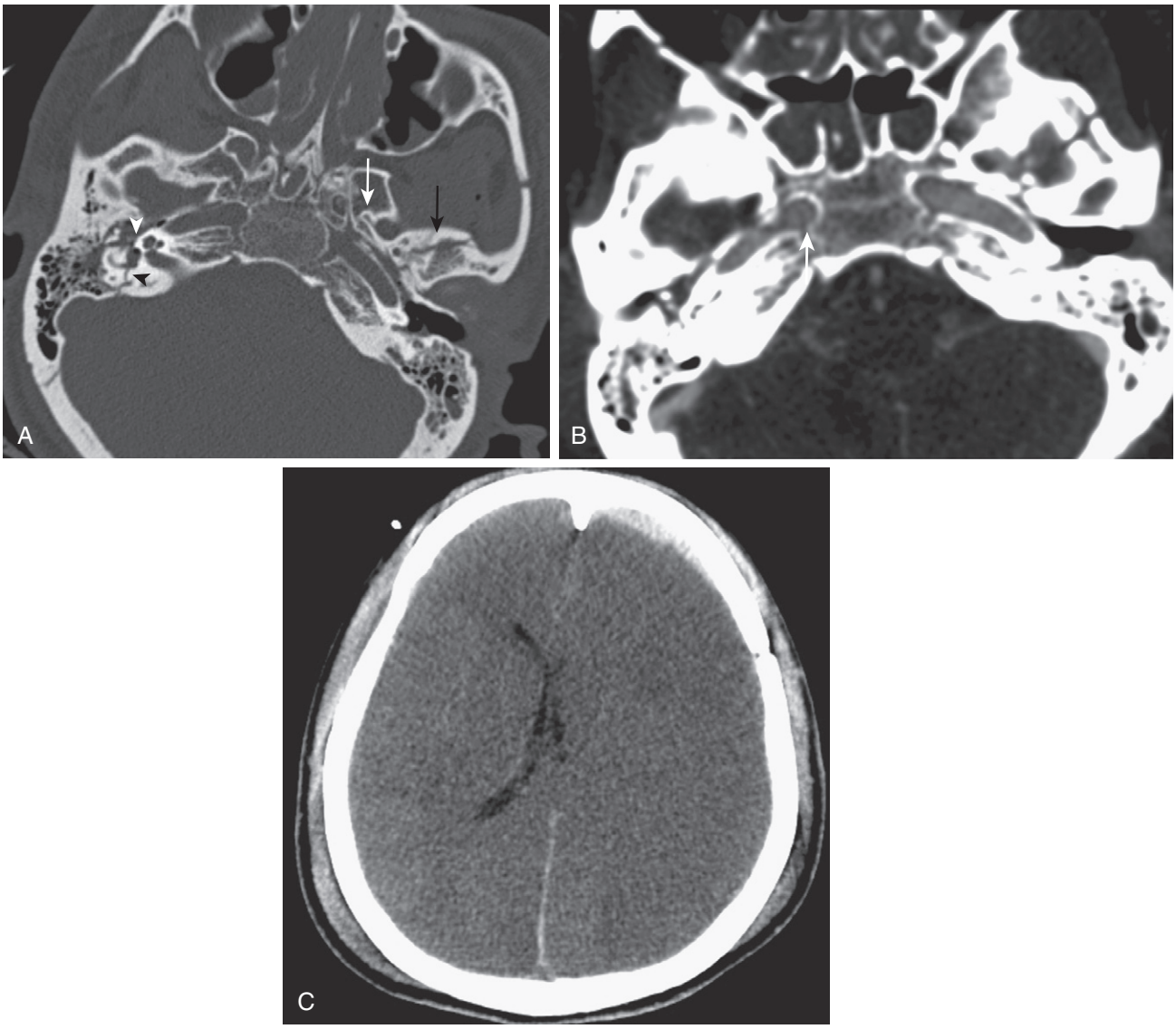


FIGURE 1-54 Skull base fractures and associated vascular injuries. **A,** This patient sustained bilateral temporal bone fractures after a motor vehicle collision. A nondisplaced transverse temporal bone fracture, lateral subtype *(black arrowhead)* and associated air in the vestibule of the semicircular canals *(white arrowhead)* were identified. A nondisplaced fracture through the left temporal bone perpendicular to the carotid canal *(black arrow)* was also identified. Incidental note was made of the foramen of Vesalius *(white arrow)*—normal anatomy seen in up to 80% of patients. **B,** Given concern about the possibility of the fracture plane extending to the carotid canal, a computed tomography (CT) angiogram was performed and demonstrated an intimal flap within the petrous portion of the right internal carotid artery *(arrow)*. Left petrous internal carotid artery dissection also was suspected on the basis of multiple contiguous images. **C,** A noncontrast head CT scan 6 days after the trauma occurred demonstrates diffuse loss of the gray–white differentiation and sulcal and ventricular effacement consistent with bilateral hemispheric infarcts.

Peritonsillar Abscess

Pharyngitis is typically a clinical diagnosis, but imaging may be performed upon clinical suspicion of complications. Imaging findings of tonsillar or peritonsillar soft tissue asymmetric enlargement with adjacent fat stranding may signal inflammation. A peritonsillar abscess, often seen in pediatric and immunocompromised patients, is a peripherally enhancing fluid collection formed in the potential space between the fibrous capsule of the tonsil and pharyngeal constrictor muscles.The patient typically presents with dysphagia, odynophagia, ear pain, and trismus after improvement of acute symptoms of tonsillitis. Infection extending beyond the pharyngeal constrictor muscles into the parapharyngeal space may cause mycotic aneurysms and thrombophlebitis. A discrete abscess identified by imaging may require immediate incision and drainage. Associated reactive lymphadenopathy is usually present.

Retropharyngeal Infection

Spread of pharyngeal infection to the medial or lateral (Rouvière) retropharyngeal nodes may lead to cellulitis or development of suppurative adenitis (an enlarged, rim-enhancing

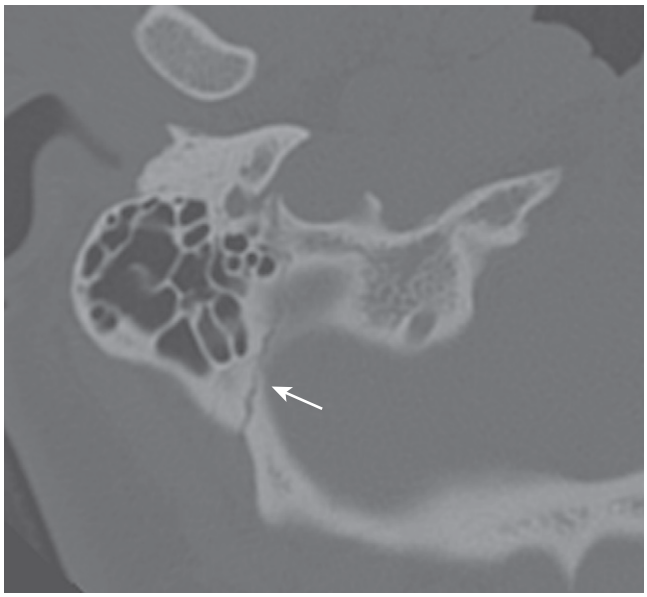


FIGURE 1-55 Normal occipitomastoid suture. Note the jagged but well-corticated margins of the suture plane *(arrow)*.

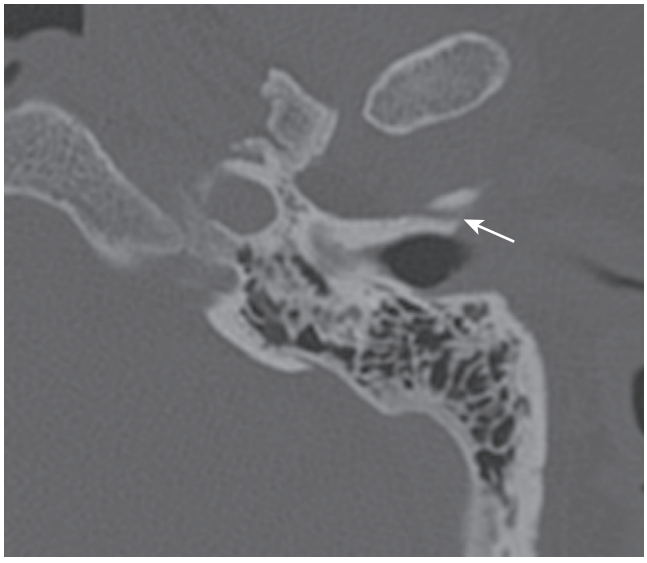


FIGURE 1-56 Normal tympanosquamous suture. A suture is present at the anterior bony wall of the external auditory canal *(arrow)*.

node). Associated edema of the retropharyngeal soft tissues is quite common, noted by expansion and diffusely increased density of the retropharyngeal fat. Extracapsular spread of nodal infection may result in a true retropharyngeal abscess typically identified as a rim-enhancing bow tie–shaped fluid collection. Retropharyngeal space infections may quickly spread into the mediastinum (Fig. 1-58), which is a serious complication with high mortality and morbidity. Immediate surgical drainage of a retropharyngeal abscess may be indicated. Imaging plays an important role in determining the indication and access route for surgical drainage. Vascular complications of infection include spasm, arteritis, and mycotic aneurysm of the internal carotid artery and thrombophlebitis of the internal jugular vein (Lemierre syndrome). The latter condition was more common in the preantibiotic era, with rare cases still encountered in the present day. On postcontrast CT or MRI, a filling defect in the

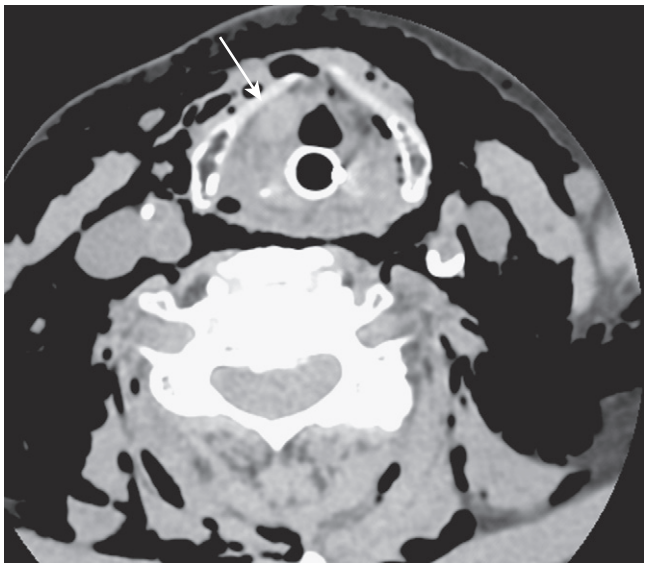


FIGURE 1-57 Laryngeal fracture. Extensive subcutaneous and deep space emphysema was due to extension of pneumothoraces in this patient after a motor vehicle collision. However, because of soft tissue density in the right supraglottic larynx (arrow), a laryngeal hematoma was suspected. This hematoma was confirmed with endoscopy.

internal jugular vein with enhancement of the vessel wall can be demonstrated. Early diagnosis is critical, because the untreated thrombus can propagate systemically, resulting in septicemia and pulmonary emboli/infarcts.

In the setting of peritonsillar and retropharyngeal infections, careful examination of the airway is vital. Prophylactic intubation should be considered if the airway is significantly compromised.

Prevertebral Infection/Inflammation

Prevertebral collections in the neck typically occur in the setting of discitis and osteomyelitis of the cervical spine (Fig. 1-59). An associated prevertebral abscess can progress in size to potentially compromise the airway. In these cases, urgent intubation and surgical drainage may have to be considered. Retropharyngeal inflammation often occurs as a result of prevertebral space infection. Identification of the primary site of infection is important for appropriate patient management.

Salivary Gland Disorders

Inflammation of the submandibular or parotid glands demonstrated by glandular enlargement and associated surrounding fat stranding could be related to distal obstruction of Wharton or Stensen ducts, respectively, often as a result of obstructing calculus. Of the salivary glands, the submandibular gland is most prone to sialolithiasis, in part because of stasis from the descending then ascending course of its duct and the relatively more alkaline nature of its glandular secretions. Bacterial and viral infections can also result in salivary gland inflammation. Bacterial inflammation is most commonly seen in debilitated patients or neonates, caused by localized *Staphylococcus aureus* infection, and is typically unilateral. Viral inflammation occurs in children, tends

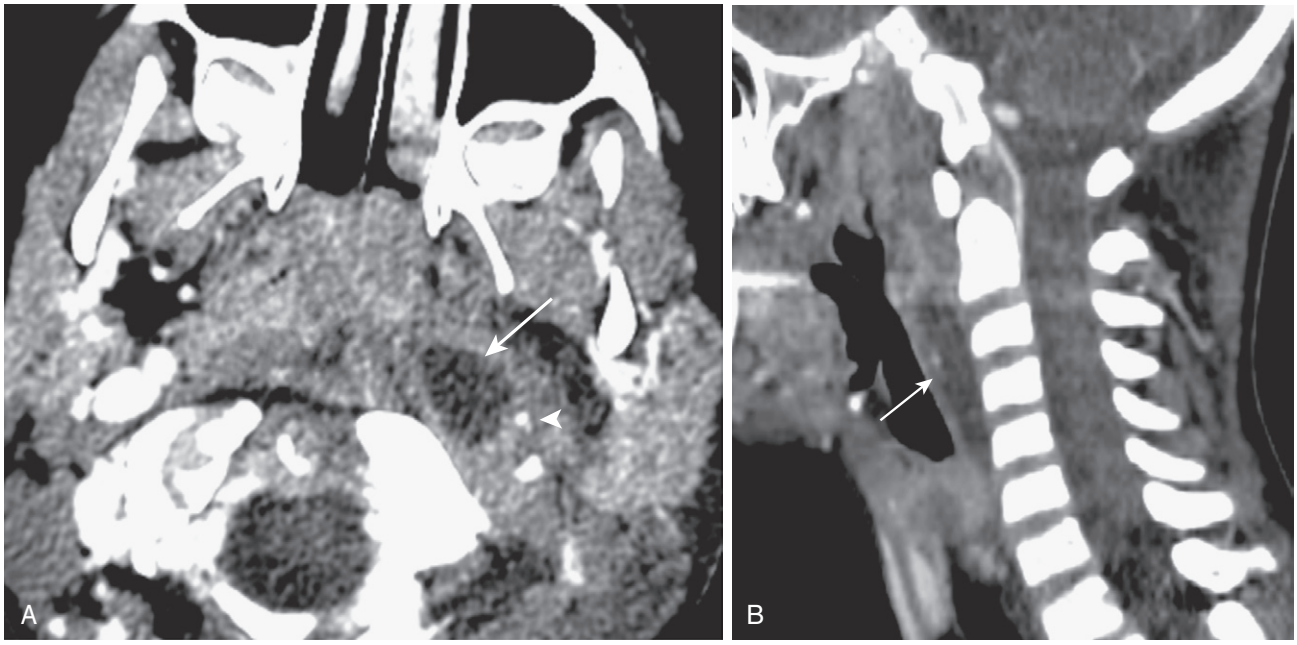


FIGURE 1-58 Retropharyngeal abscess. **A,** An abscess *(arrow)* is demonstrated within the lateral retropharyngeal node (of Rouvière) in a young patient presenting with painful swallowing. Note the associated smaller caliber of the cervical left internal carotid artery as a result of vasospasm *(arrowhead)*, which is common in pediatric patients with an intranodal abscess. **B,** Sagittal reformat demonstrates associated retropharyngeal fluid extending to the C5 level *(arrow)*. A lack of peripheral enhancement suggested that this fluid was reactive, rather than a discrete abscess. Because the patient's condition did not improve with intravenous antibiotics, incision and drainage were required.

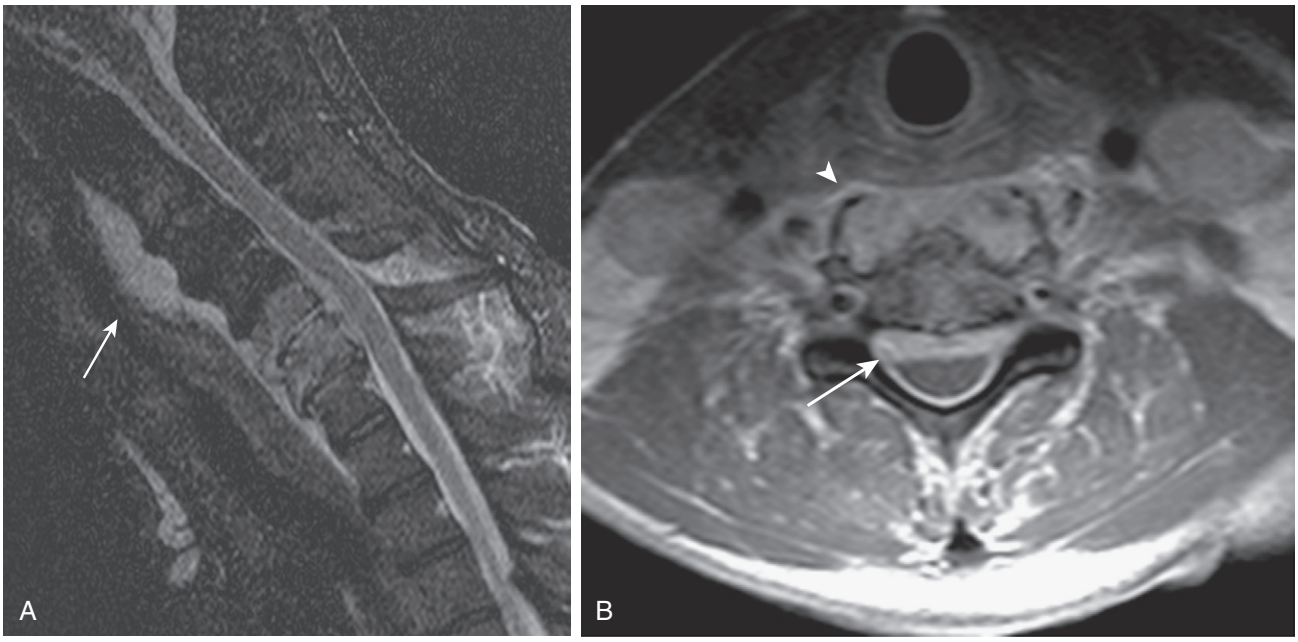


FIGURE 1-59 Discitis/osteomyelitis resulting from intravenous drug use. **A,** A sagittal fat-suppressed T2-weighted image shows abnormal signal hyperintensity in the C5-6 disk and adjacent vertebral bodies and a large associated prevertebral process *(arrow)*. **B,** A postgadolinium axial T1-weighted image shows enhancement of prevertebral phlegmon *(arrowhead)* and circumferential epidural extension *(arrow)* resulting in spinal cord compression.

to be related to systemic infection, most commonly mumps, and is usually bilateral. The inflamed gland is enlarged and hyperenhancing, with stranding of adjacent fat reflecting cellulitis, or it may contain a discrete abscess (Fig. 1-60). Enlarged heterogeneous parotid glands with solid and cystic changes may reflect lymphoepithelial lesions seen in the setting of HIV disease. Similar lesions can be seen in Sjögren syndrome and other autoimmune disorders. In the chronic phase of this condition, atrophy of the parotid gland with parenchymal calcifications can be seen.

Thyroid-Related Disorders

When inflamed, the thyroid gland can appear diffusely enlarged or relatively hypoenhancing, and it may demonstrate an associated fluid collection. Suppurative thyroiditis is

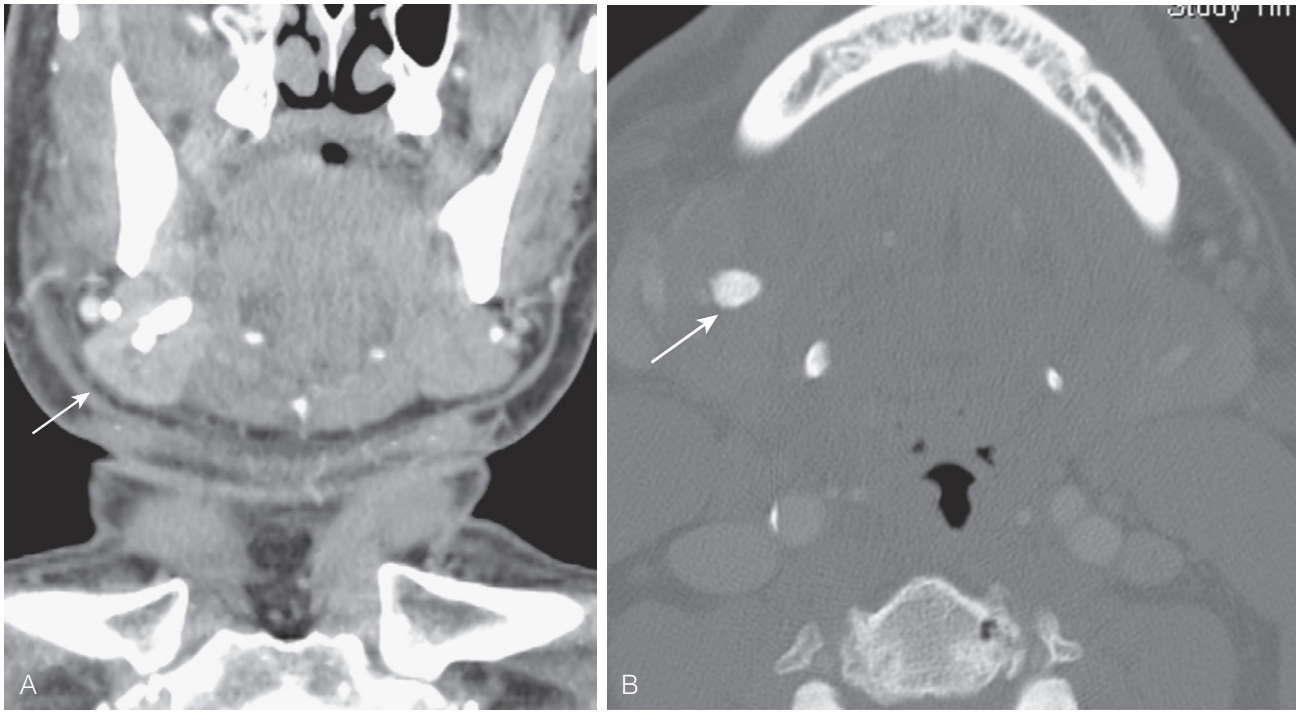


FIGURE 1-60 Salivary gland inflammation. **A,** In this patient with acute right facial swelling, computed tomography coronal reformat demonstrates an enlarged, hyperenhancing, right submandibular gland *(arrow)* with stranding of the subcutaneous fat. **B,** An axial image with bone window/level settings confirms a sialolith *(arrow)* within the gland.

rare because of its iodine content. In such cases, pyriform sinus fistula, or third or fourth branchial pouch anomaly, should be considered as an underlying cause. Most cases involve the left lobe of the thyroid. Such patients require a barium swallow test after completion of antibiotic therapy to identify the fistulous tract.

A thyroglossal duct cyst is a remnant of the thyroglossal duct and can be found in a midline or paramidline location between the foramen cecum at the base of the tongue and the thyroid bed. The cyst is classically embedded within the strap muscles, which helps distinguish this lesion from other midline neck masses, such as dermoid and epidermoid cysts. Although thyroglossal duct cysts are found most commonly at the level of the hyoid bone, they also can be suprahyoid or infrahyoid. If the cystic lesion exhibits peripheral rim enhancement, superinfection should be suspected in the appropriate clinical setting. The cyst is usually lined by respiratory or squamous epithelium and occasionally contains thyroid tissue, which carries the potential for development of malignancy, most commonly papillary carcinoma. For this reason, any enhancing soft tissue within a thyroglossal duct cyst should be reported, and surgical excision should be strongly considered.

Branchial Cleft Cysts

Branchial cleft cysts are congenital epithelial-lined cystic lesions in the neck originating anywhere from the level of the mandible (first branchial cleft) to the supraclavicular region (fourth branchial cleft). These cysts can become superinfected and present as an acutely enlarging neck mass. The second branchial cleft cyst is most common, present in the submandibular region, anteromedial to the sternocleidomastoid muscle and anterolateral to the carotid vessels (Fig. 1-61). An infected branchial cleft cyst will demonstrate peripheral rim enhancement. Necrotic infectious and metastatic lymphadenopathy may present similarly and should be considered in the differential diagnosis, particularly in adult patients.

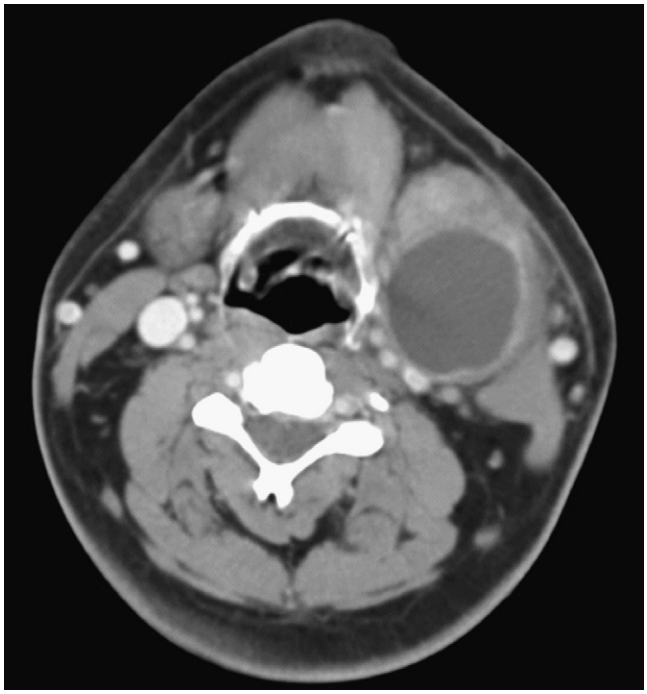


FIGURE 1-61 Second branchial cleft cyst. This second branchial cleft cyst is in the classic location, that is, the submandibular region, anteromedial to the sternocleidomastoid muscle and anterolateral to the carotid vessels.



FIGURE 1-62 Neck abscess. **A,** In this patient who sustained infection in a graft soon after a carotid endarterectomy, a postcontrast axial computed tomography image demonstrates organized fluid collection *(arrowhead)* adjacent to abnormal enhancing inflammatory tissue surrounding the carotid bifurcation on the right *(arrow)*. **B,** Slightly inferiorly, a fistulous tract between the collection and the inflammatory tissue is identified *(arrow)*. **C,** Coronal reformat demonstrates that the inflammatory tissue encasing the carotid bifurcation extends superiorly along the internal carotid artery *(arrow)*, causing focal critical stenosis.

Superficial Abscesses

Multiple bilateral superficial neck abscesses can be seen in intravenous drug abusers or "skin poppers." Occasionally, retained fragments of needles may be present in the soft tissues. After routine operations on the neck, fluid collections may develop in the superficial or deep soft tissues. In these cases, careful evaluation of adjacent vascular structures is warranted to assess for potential injury (pseudoaneurysm, dissection, thrombosis, or occlusion) or extension of inflammation (Fig. 1-62).

Lymphadenopathy

Cervical lymphadenopathy can present clinically as diffuse neck swelling and may be related to an inflammatory process or underlying neoplasm.The presence of necrosis

within normal-sized or enlarged cervical lymph nodes can be due to intranodal abscess formation but should raise suspicion for metastatic disease, especially from squamous cell carcinoma. If it is metastatic, the primary tumor typically arises from the base of the tongue, tonsils, nasopharynx, and pyriform sinus or from papillary thyroid cancer. This form of thyroid cancer often affects relatively young women. Certainly, necrotic adenopathy can be seen in the setting of infection such as tuberculosis and atypical mycobacterial infections such as *Mycobacterium avium-intracellulare* complex, particularly in immunocompromised patients. Large conglomerations of necrotic lymph nodes can be seen in these settings. Careful evaluation of the lung apices for an inflammatory process is necessary, because this finding can support the diagnosis of tuberculous adenitis. Imaging can play an important role in raising the possibility of tuberculosis in patients not suspected of having this disease. In such a case, the referring service should be notified immediately, because isolation may be required. Interestingly, calcifications related to tuberculosis are not typically found in the cervical lymph nodes.

Croup

In the pediatric patient population, laryngotracheobronchitis, or "croup," presents clinically with a characteristic cough. The condition usually occurs in children younger than 3 years and is thought to be most often caused by parainfluenza virus, although other respiratory viruses and *Mycoplasma* have also been implicated. Croup is the most common pediatric infection causing stridor, accounting for approximately 15% of clinic and ED visits for pediatric respiratory infections. The cough is a consequence of subglottic edema and manifests classically on plain radiographs with symmetric, subglottic narrowing, the so-called "steeple" sign (Fig. 1-63). Coronal CT reformats can now replicate this appearance, although cross-sectional imaging is typically not necessary for this particular indication.

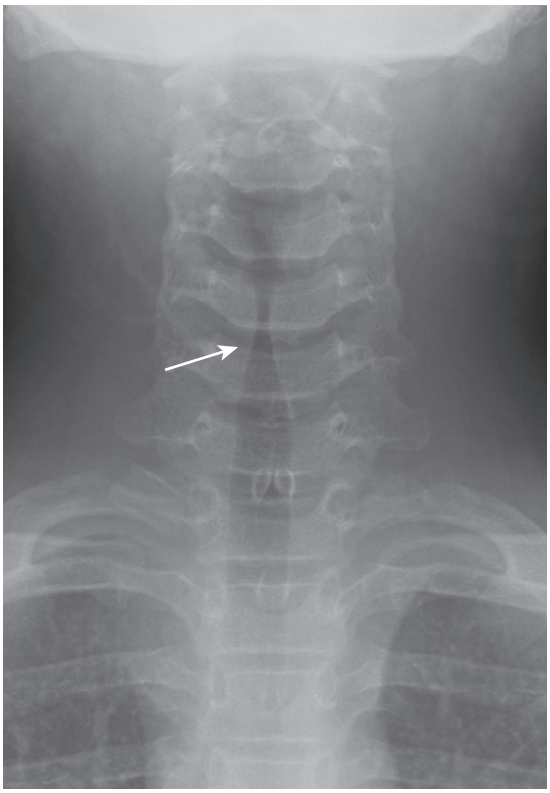


FIGURE 1-63 Croup. In this patient who presented acutely with a barking cough, a frontal radiograph of the neck demonstrates the classic "steeple" sign *(arrow)* representing concentric subglottic edema.

Epiglottitis

Epiglottitis is now less commonly seen in the pediatric ED setting as a result of childhood immunization against the offending agent, *Haemophilus influenzae*. However, epiglottitis can occur at any age, and recently an increase in incidence has occurred in the adult population, which is often underappreciated. Patients who have not been immunized can present with acute airway compromise and may require urgent intubation. On a lateral radiograph, the classic "thumb" (or "thumbprint") sign is produced by the thickened, inflamed epiglottis (Fig. 1-64). The clinical picture and radiographic imaging are usually so characteristic that cross-sectional imaging is generally unnecessary. CT imaging can provide greater diagnostic detail and can demonstrate the inflamed epiglottis along with symmetrically thickened and inflamed aryepiglottic and pharyngoepiglottic folds. However, management should be based on clinical and radiographic findings because obtaining a CT examination might delay proper treatment.

Angioedema

Although angioedema is not due to infection, it is included in this section on airway disorders. It can be hereditary or acquired and may be idiopathic, manifesting as acute narrowing of the airway, possibly resulting in airway compromise. Angioedema due to allergic reactions is often associated with urticaria. Although clinical diagnosis should be straightforward, CT imaging can be useful for further evaluation. Imaging can show diffuse mucosal and submucosal swelling involving the hypopharynx and larynx, with infiltration of the subcutaneous fat and deep tissue planes of the neck.

Sinus and Orbital Infections

Uncomplicated acute sinusitis is typically clinically diagnosed and managed. On imaging, findings of acute sinusitis are not very specific. An air–fluid level within a sinus can suggest acute sinusitis; however, lack of this finding does not mean that a patient does not have acute sinusitis. Occasionally, hyperdense opacification in the paranasal sinuses can be seen; the hyperdensity can reflect hemorrhage related to trauma, trapped proteinaceous debris, or fungal infection. Fungal infection is an important diagnostic consideration, because steroids probably should be incorporated into the treatment regimen if the cause is related to allergic disease (Fig. 1-65).

When advanced sinus disease is of concern, imaging plays a more definitive role. Complicated sinus disease should be clinically suspected if the patient presents with visual changes, altered mental status, or seizures. Initial imaging for workup of complicated sinusitis can begin with CT. At our institution, axial images through the facial bones are routinely acquired at 1.25-mm intervals with coronal and sagittal reformats using bone and soft tissue algorithms. If

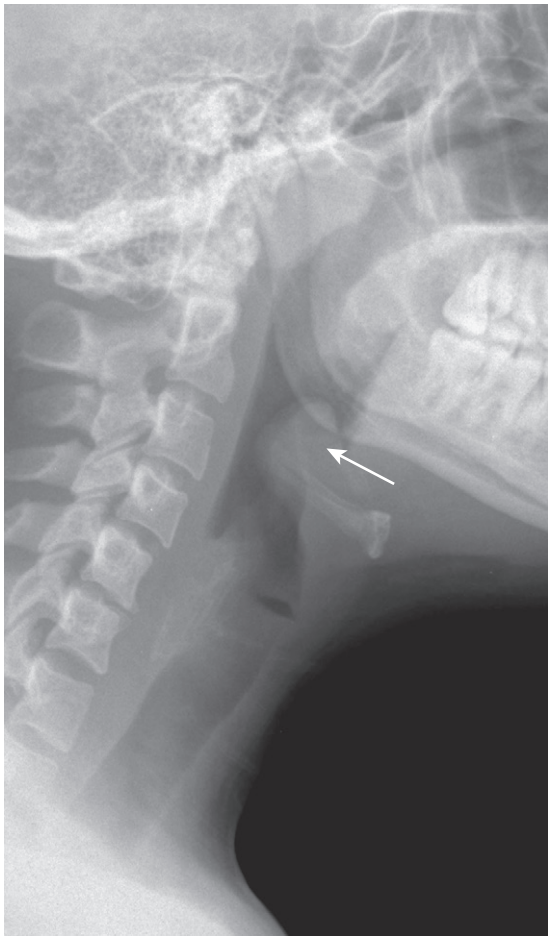


FIGURE 1-64 Epiglottitis. In this young child who presented with difficulty breathing, a lateral neck radiograph demonstrates the classic "thumbprint" sign *(arrow)* of the inflamed epiglottis.

concern exists regarding intracranial or orbital extension of infection, contrast-enhanced CT using similar imaging parameters can provide additional critical information. If clinical concern exists regarding intracranial extension, the entire brain should be imaged. Because complicated sinus infection usually warrants close follow-up imaging, MRI is the preferred imaging modality to minimize radiation exposure, especially in the pediatric setting. Typical brain MRI protocol includes sagittal T1-weighted, axial FLAIR, fat-suppressed T2-weighted, gradient echo, and diffusion-weighted images, followed by multiplanar postcontrast T1WIs of the brain. If orbital extension is of clinical concern, high spatial resolution T2WIs with and without fat suppression through the orbits and axial and coronal pre- and postcontrast T1WIs can provide excellent diagnostic detail.

CT is particularly useful in establishing the integrity of paranasal sinus walls and can effectively demonstrate areas of bony dehiscence. Intracranial or orbital spread of infection can occur directly through areas of bony dehiscence or indirectly by perivascular extension, most commonly as a result of frontal or ethmoid sinus disease. Perivascular spread more commonly occurs in the pediatric setting. Intracranial extension is usually seen in the setting of frontal sinus infection, with involvement of the anterior cranial fossa and frontal lobes (Fig. 1-66). Imaging can demonstrate associated dural enhancement, epidural or subdural collections, and meningoencephalitis with abscess formation. The patient may have concomitant swelling of the overlying soft tissues of the forehead, known as Pott's puffy tumor (Fig. 1-67). This finding does not imply neoplastic involvement but rather describes osteomyelitis with extracranial soft tissue abscess formation. The presence of pachymeningeal enhancement does not necessarily imply that brain parenchyma is involved and may only reflect dural reaction. Epidural and subdural collections can be

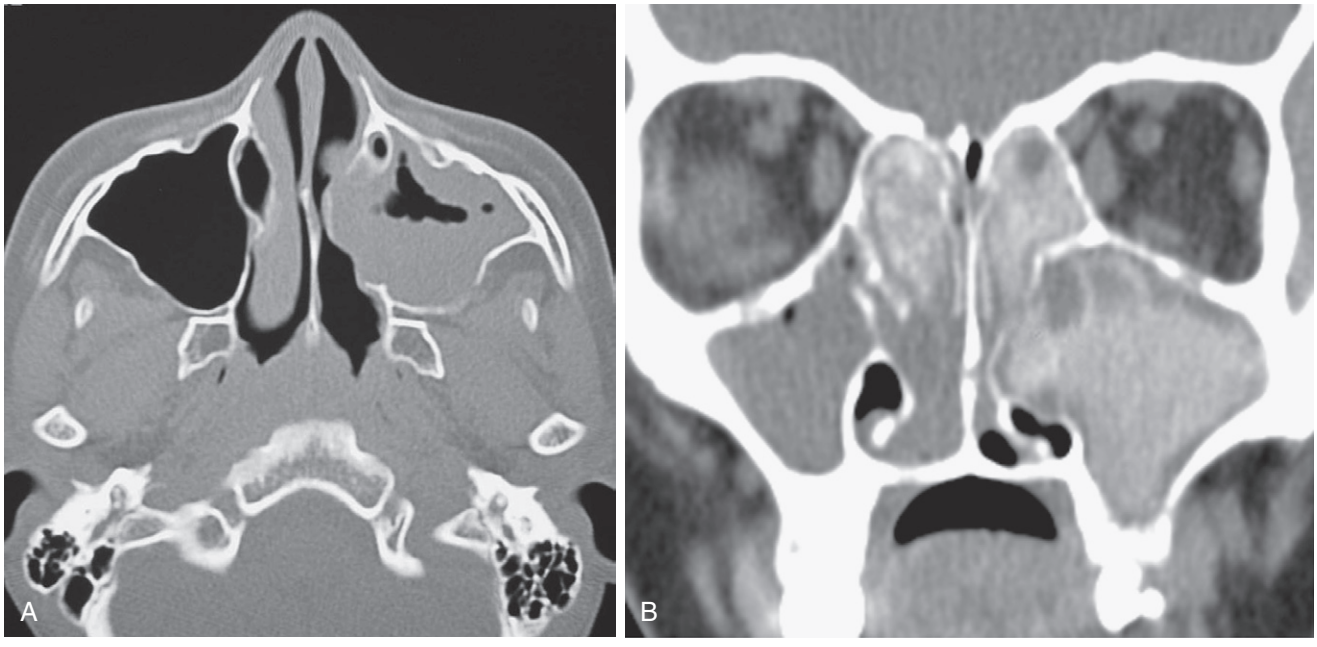


FIGURE 1-65 Sinusitis. **A,** Mucosal thickening in the left maxillary sinus is accompanied by an air–fluid level due to acute sinusitis in this patient presenting with sinus pressure, pain, and headache. **B,** In a different patient, coronal reformat in soft tissue window/level settings demonstrates hyperdense material in most of the paranasal sinuses as a result of allergic fungal sinusitis.

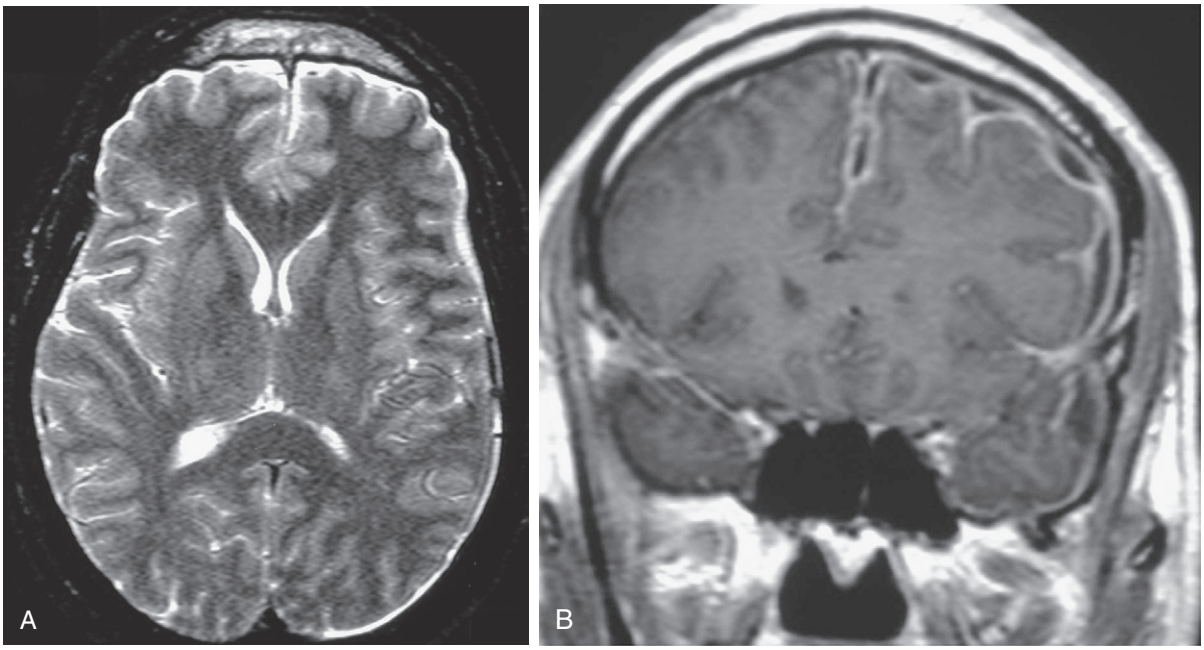


FIGURE 1-66 Sinusitis—subdural empyema and infarct. **A,** An axial T2-weighted image shows proteinaceous material within the frontal sinuses. **B,** A postgadolinium coronal T1-weighted image demonstrates an associated subdural abscess and leptomeningeal enhancement.

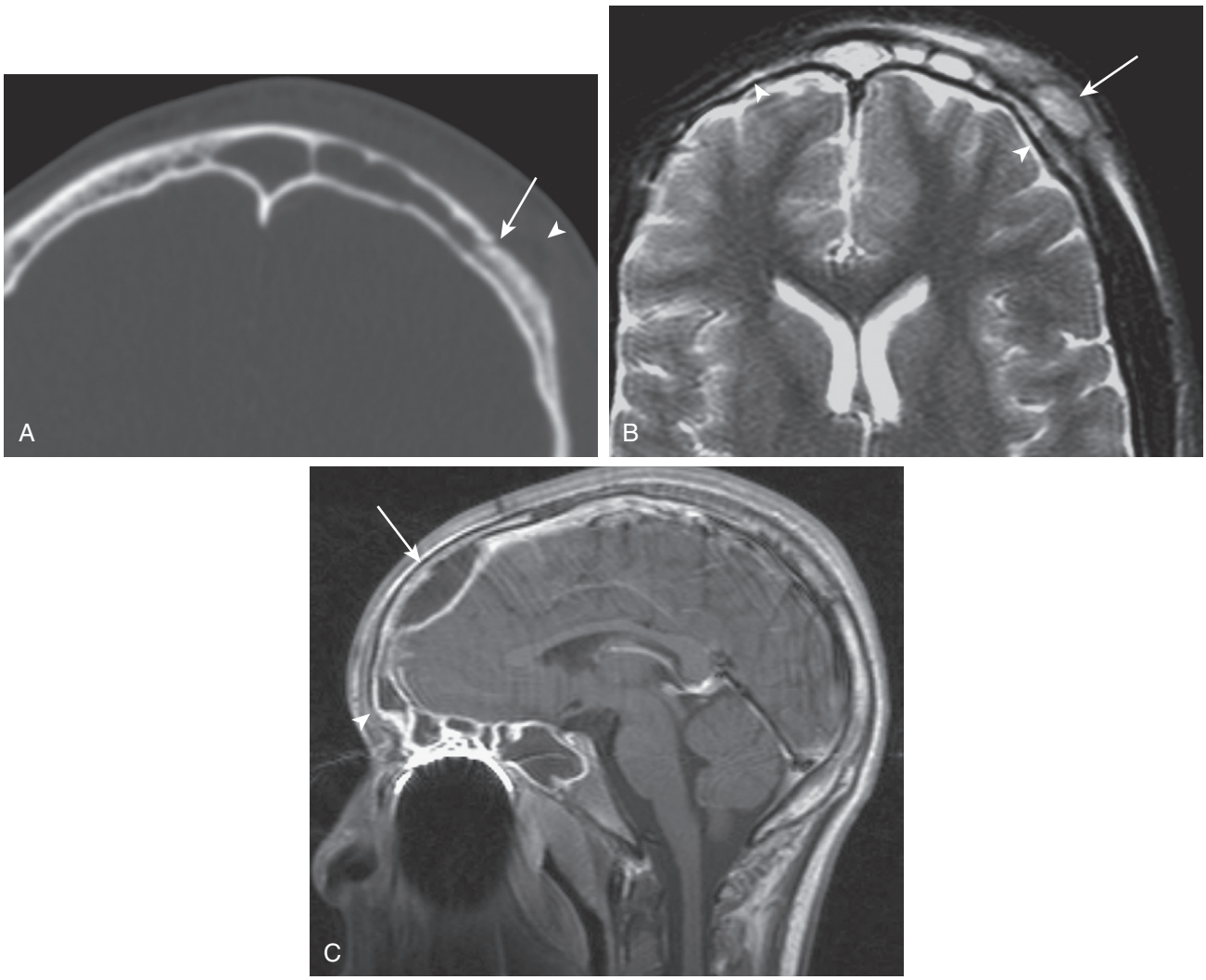


FIGURE 1-67 Sinusitis—Pott's puffy tumor and epidural abscess. **A,** An axial computed tomography image shows opacification of the frontal sinuses and overlying soft tissue swelling. A tract from the anterior table of the frontal sinus *(arrow)* and adjacent fluid collection *(arrowhead)* are shown. **B,** An axial T2-weighted image demonstrates abnormal hyperintensity of marrow in the frontal bone *(arrowheads)* and overlying soft tissue swelling, including small scalp fluid collection *(arrow).* **C,** A postgadolinium sagittal T1-weighted image shows an epidural abscess *(arrow)* and fluid-filled paranasal sinuses with inflamed mucosa *(arrowhead)*.

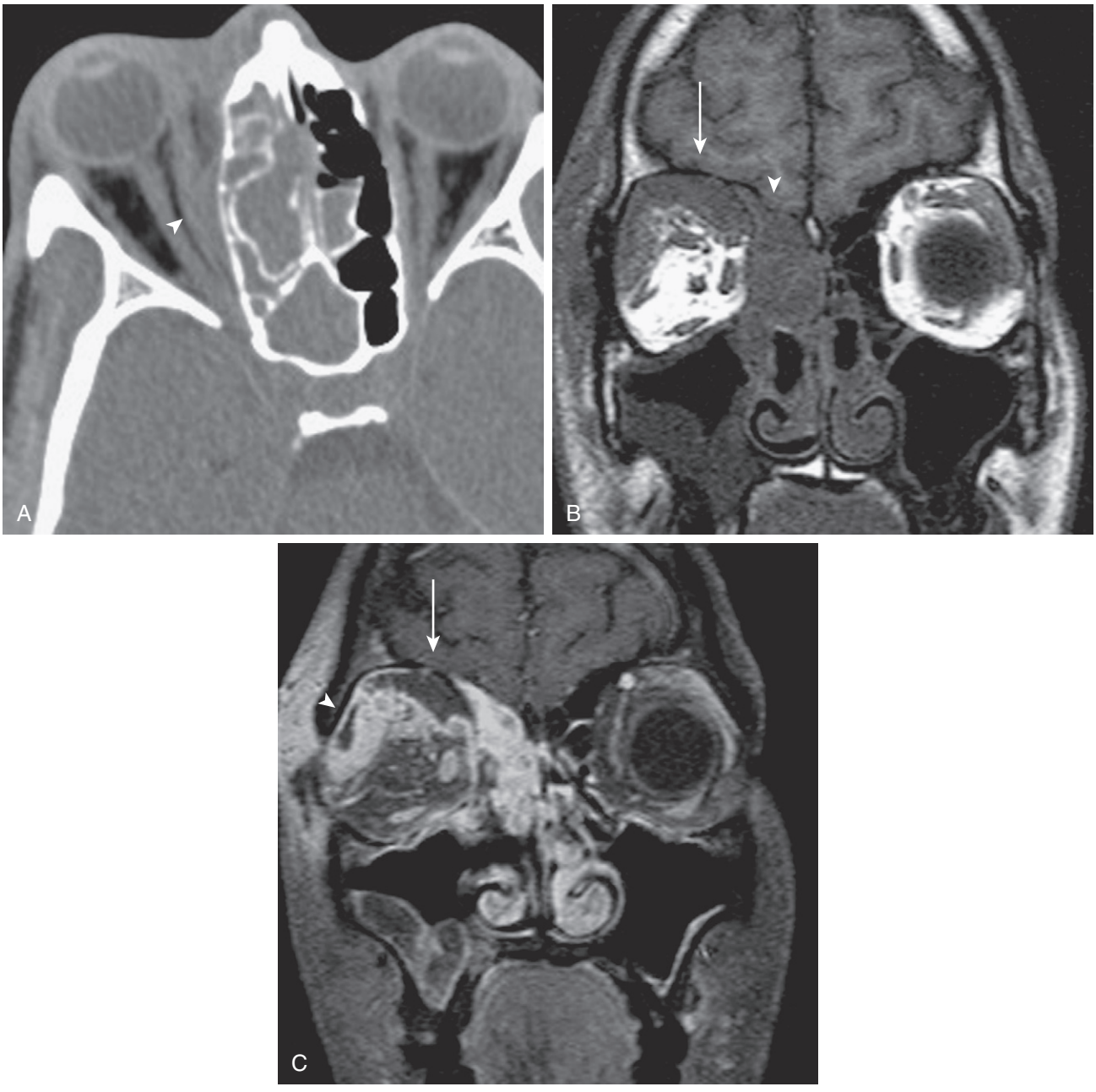


FIGURE 1-68 Complications of sinusitis. **A,** Axial computed tomography in a young patient with mild acute proptosis demonstrates opacification of the right ethmoid air cells with abnormal soft tissue in the medial aspect of the right orbit *(arrowhead)*, displacing the medial rectus muscle. Normally, this space should contain orbital fat, but in this case, there has been perivascular extension of inflammation into the orbit; note that the lamina papyracea is intact. **B,** A coronal T1-weighted image demonstrates extensive collection extending from the sinuses *(arrowhead)* into the orbit *(arrow)*, displacing extraocular muscles and the optic nerve inferiorly. **C,** A postgadolinium coronal T1-weighted image shows that much of the abnormal soft tissue in the orbit *(arrow)* is due to subperiosteal abscess *(arrowhead)*.

demonstrated on either CT or MRI as extraaxial fluid, possibly compressing the subjacent brain parenchyma. Subdural collections can cross sutures and generally maintain a crescentic shape, whereas epidural collections are restricted by sutures and may have a biconvex shape. Whereas a reactive subdural effusion may be associated with smooth pachymeningeal enhancement, an infected subdural or epidural collection can demonstrate restricted diffusion and thickened, more irregular dural enhancement on MRI. Leptomeningeal involvement is demonstrated as curvilinear enhancement extending into sulci. This manifestation may be accompanied by FLAIR hyperintensity in a corresponding distribution, which is a sensitive but nonspecific finding. Parenchymal involvement can be demonstrated by FLAIR hyperintensity and enhancement. Frank abscess formation can be demonstrated by CT or MRI as a peripherally enhancing fluid collection. Restricted diffusion in the collection can support this impression.

Although posterior ethmoid disease can also lead to intracranial involvement, more commonly, untreated ethmoid sinusitis can extend into the medial aspect of the orbit (Fig. 1-68). Infection can spread in a subperiosteal

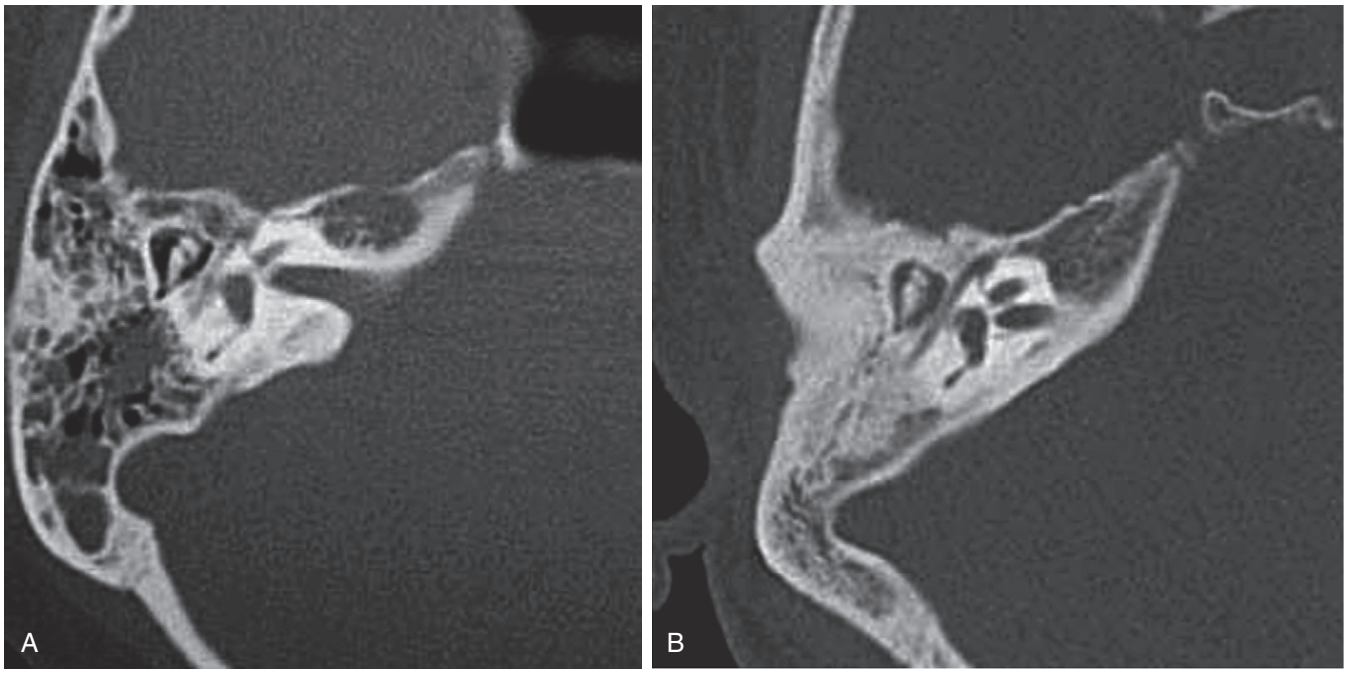


FIGURE 1-69 Mastoiditis. **A,** Opacification of mastoid air cells without bony changes in a patient with symptoms of acute mastoiditis. **B,** Opacification of the middle ear with sclerotic changes of the mastoid bone in a patient with a history of chronic otomastoiditis.

fashion along the medial wall of the orbit, appearing as an elliptical phlegmon or fluid collection, and may cause displacement of extraocular muscles. Without treatment, the phlegmon or abscess can then break through the periosteum and extend directly into the orbit and into the extraocular muscles. Depending on the size of the inflammatory process, displacement of extraocular muscles and the globe can occur, along with distortion, stretching, and compression of the optic nerve. Such findings constitute an ophthalmologic emergency, because prolonged mass effect on the optic nerve can result in permanent blindness.

Other possible critical complications of orbital infection include extension of infection and involvement of the contents of the orbital apex (CN II), superior orbital fissure (CNs III, IV, V_1, and VI and the superior ophthalmic vein), and inferior orbital fissure (V2, infraorbital nerve). Idiopathic inflammation involving the cavernous sinus, known as Tolosa-Hunt syndrome, can manifest clinically as palsies of the cranial nerves that traverse the cavernous sinus, namely, CNs III, IV, V_1, V2, and VI.

Venous sinus thrombosis can result from ethmoid or sphenoid sinus or orbital infection, and careful attention to the cavernous sinuses on postcontrast images is necessary. Facial soft tissue, dental, and ear infections are other possible causes. Direct signs of septic cavernous sinus thrombosis, also termed *cavernous sinus thrombophlebitis (CST)*, include an enlarged sinus with a convex border and a single large filling defect or multiple irregular filling defects. Normal neural structures and intracavernous fat deposits should not be mistaken as true filling defects. Indirect signs include dilation of the superior ophthalmic vein, exophthalmos, soft tissue edema, thrombi in the superior ophthalmic vein, superior and inferior petrosal, or sigmoid sinuses, and a decrease in the caliber of the internal carotid artery. Thin-section, contrast-enhanced CT with coronal reformats may be equivalent to MRI for the detection of these findings. However, once venous sinus thrombosis is suspected, MRI of the brain may confirm the diagnosis and evaluate for possible complications of meningitis, subdural empyema, cerebritis, and even pituitary necrosis. Postcontrast T1-weighted coronal and axial images are generally sufficient to make the diagnosis. Contrast-enhanced MR venography also may offer support in diagnosis. (Phase contrast MR venography is generally limited for this evaluation. Contrast-enhanced CT [CT venography] and MRI with thin slices are generally more helpful to diagnose CST.) Prior to the antibiotic era, CST was almost always fatal. In the modern era, mortality in the range of 20% to 30% may still be expected. In addition to antibiotics, early institution of anticoagulant therapy may reduce mortality. Morbidity may result from cranial nerve dysfunction including blindness, pituitary insufficiency, and hemiparesis.

Ear Infections

Much like uncomplicated paranasal sinus disease, external and middle ear infections can be diagnosed and followed up clinically. Occasionally acute and chronic otomastoiditis can be picked up on imaging and should be reported, because these conditions may not be suspected clinically (Fig. 1-69). If clinical concern exists regarding a more complicated infectious process, CT and MRI can be very useful adjuncts in diagnosis. CT imaging of the temporal bone includes the entire auditory system. At our institution this imaging is performed with overlapping 0.625-mm–thick sections with coronal and sagittal reformats in bone and soft tissue algorithms. If clinical concern exists regarding intracranial

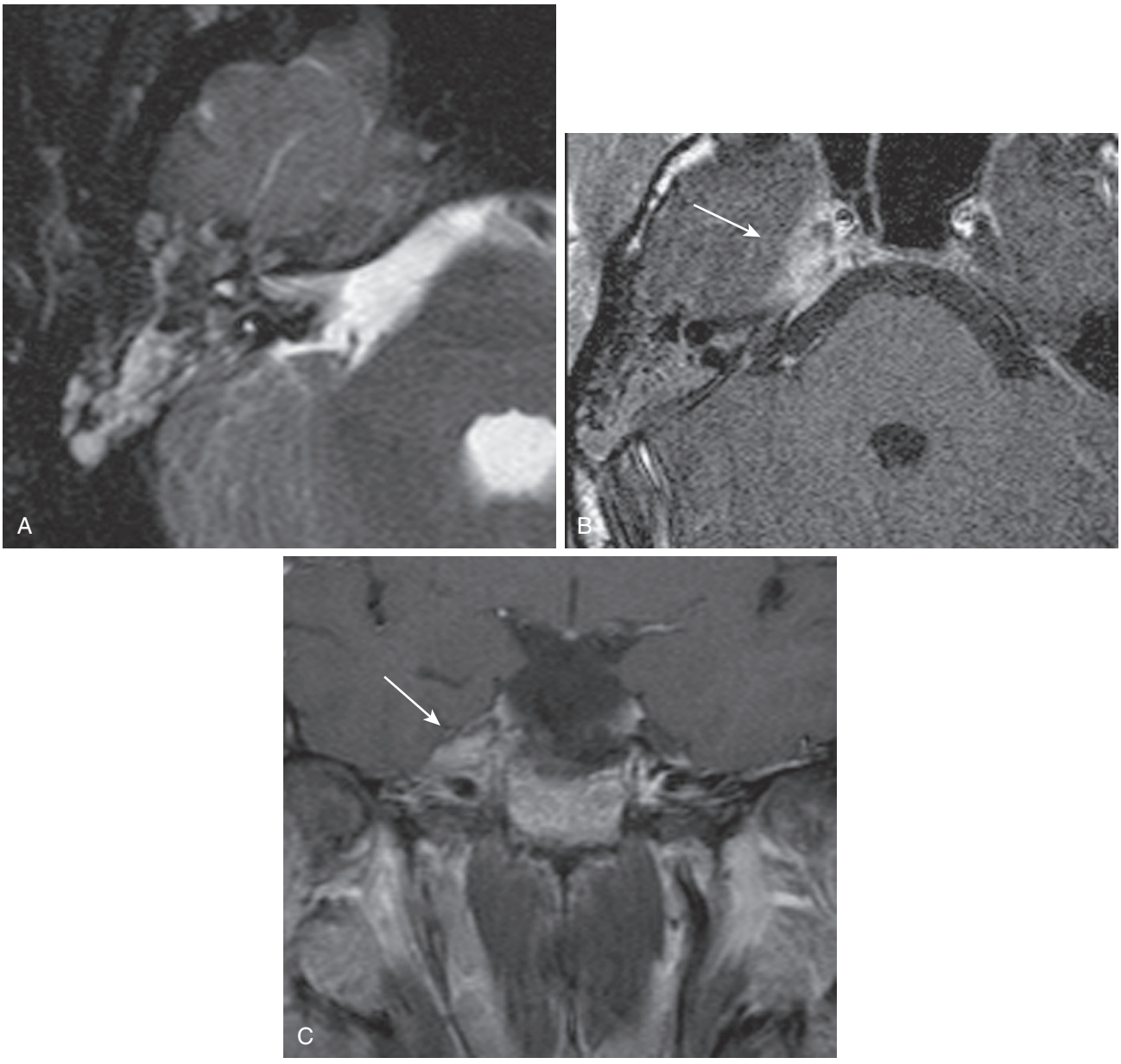


FIGURE 1-70 Gradenigo syndrome. **A,** In this patient with mastoiditis and facial pain, an axial fat-suppressed T2-weighted image demonstrates bright signal in the right mastoid air cells. Axial **(B)** and coronal **(C)** postgadolinium T1-weighted images demonstrate abnormal enhancement within Meckel's cave on the right side *(arrows)*. This patient reported new facial pain in the setting of chronic mastoid disease.

involvement, contrast-enhanced CT using the same imaging parameters can provide additional diagnostic detail. MRI can be particularly useful in the setting of cranial nerve involvement. Our technique includes high spatial resolution T2WIs and pre- and postcontrast axial and coronal images from the level of the orbits to the base of the brain, in addition to routine brain imaging.

Malignant otitis externa, which is typically seen in diabetic and immunocompromised patients, is a rare but serious complication of external ear infection. The inflammation can quickly progress to involve the entire ear, external auditory canal, and middle and inner ear structures. Evaluation of the stylomastoid foramen for extension of inflammation with fat stranding is important, particularly in patients with facial nerve symptoms. Associated osteomyelitis is seen as a locally aggressive destructive process of the temporal bone. Urgent treatment is indicated, usually with surgical debridement, because intracranial extension of infection can develop rapidly. Cranial nerve involvement from untreated middle ear infection can occur secondarily by spread of inflammation into the cavernous sinus, typically involving CN V within Meckel's cave and CN VI within the cavernous sinus (Gradenigo syndrome) (Fig. 1-70). Additional cranial nerve involvement can quickly ensue. Intracranial extension can result from dehiscence of the temporal bone, with direct spread into the middle cranial fossa. As with complicated paranasal sinus infection, extension into the middle cranial fossa can result in epidural abscess, subdural empyema, meningoencephalitis, or brain abscess. Transverse sinus,

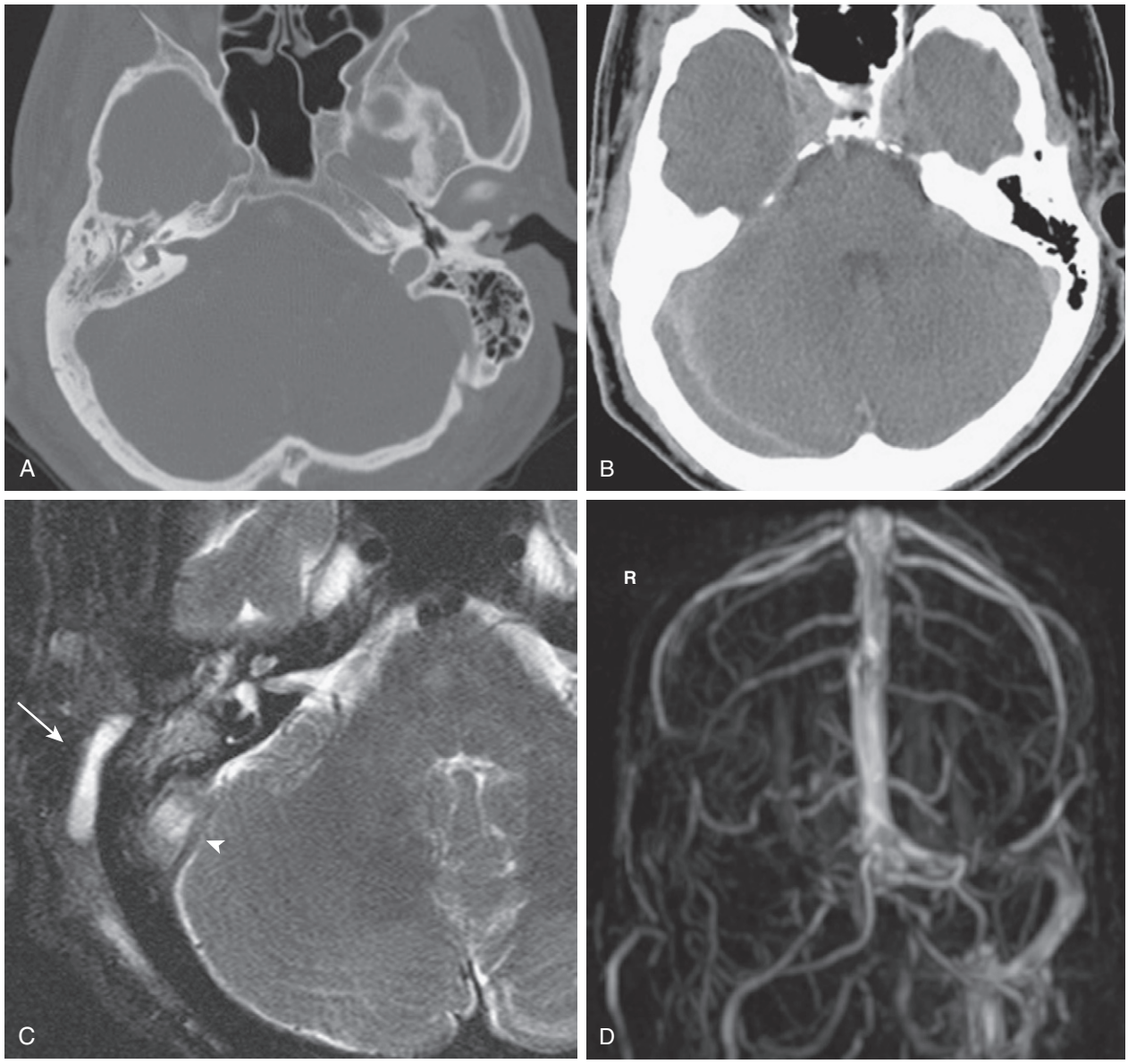


FIGURE 1-71 Mastoiditis—septic thrombophlebitis. **A,** Initial noncontrast computed tomography (CT) in a patient with headache demonstrates chronic right otomastoiditis. **B,** Based on clinical examination and findings on the noncontrast examination, a contrast-enhanced CT study was performed, demonstrating a large filling defect within the right transverse sinus. **C,** A T2-weighted image shows a hyperintense subperiosteal abscess *(arrow)*. There is also abnormal T2 hyperintensity in the expanded sigmoid sinus *(arrowhead)* rather than the expected flow void. **D,** Maximum intensity projection reconstruction from three-dimensional phase contrast magnetic resonance venography demonstrates lack of flow-related signal in the right transverse and sigmoid sinuses and right internal jugular vein, consistent with venous sinus thrombosis.

sigmoid sinus, and jugular vein thrombosis are other possible complications (Fig. 1-71).

Complicated Dental Disease

Periapical lucencies around individually infected teeth are often incidentally detected on routine CT images of the mandible and maxilla performed for other reasons. Occasionally the infection can progress to the medullary bone, eventually breaking through the overlying buccal or lingual cortex. In these cases, this sinus tract acts as a conduit for spread of infection into the adjacent soft tissues (Fig. 1-72). With time, an abscess can develop, and the patient may present to the ED with pain, swelling, and an elevated white blood cell count. Fluid collections in the face therefore should be carefully evaluated for a possible dental source, because the soft tissue infection will not be cured by drainage alone. Rapid progression of infection into other spaces, including the orbit and intracranial compartment, is a serious and potentially life-threatening complication. Ludwig angina is characterized by extensive facial swelling and hardened cellulitis centered in the submandibular space, classically bilateral, related to periodontal disease (Fig. 1-73).

In the case of a suspected dental-related facial abscess, maxillofacial CT with thin (1.25-mm) axial sections and coronal

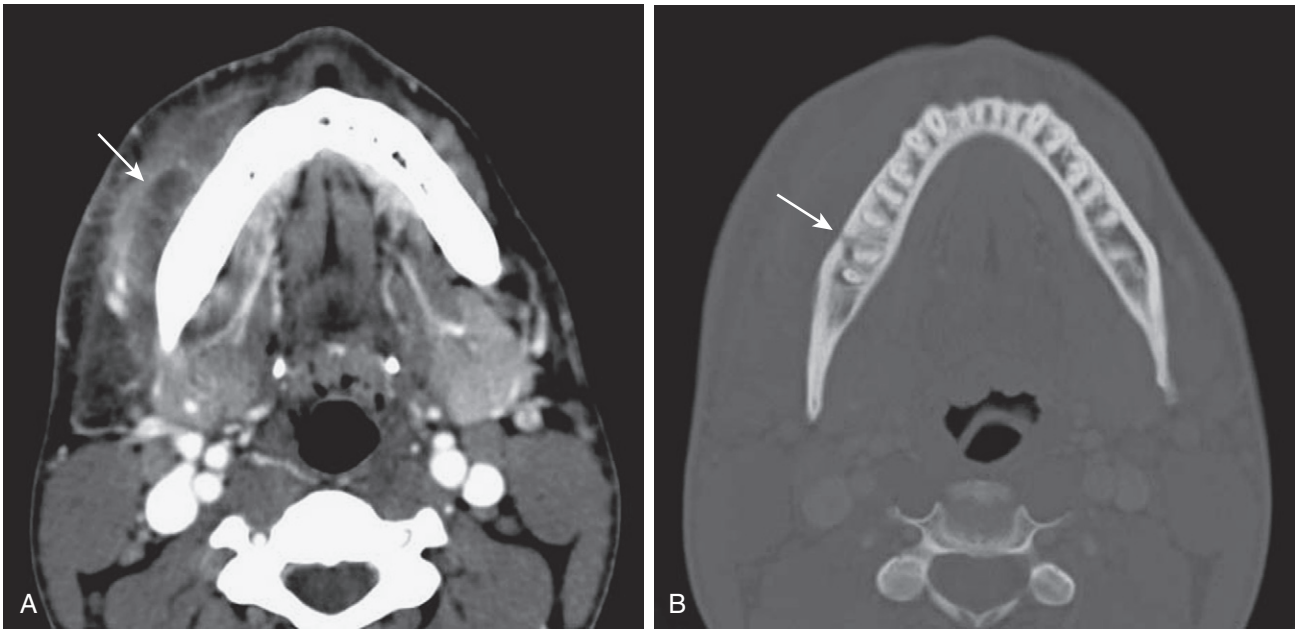


FIGURE 1-72 Perimandibular abscess. **A,** In this patient with right facial pain and swelling, contrast-enhanced computed tomography demonstrates a fluid collection *(arrow)* and subcutaneous stranding along the buccal surface of the right body of the mandible. **B,** Within the mandible at the same level is a periapical lucency related to a molar tooth with a cortical defect *(arrow)* consistent with a sinus tract.

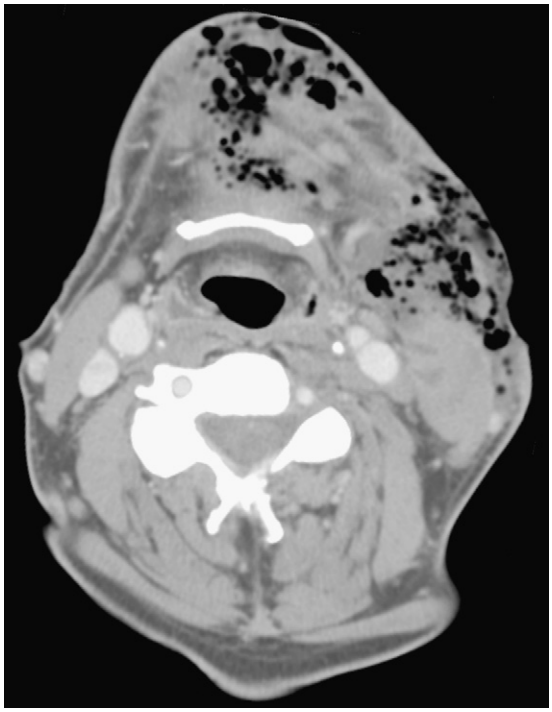


FIGURE 1-73 Ludwig angina. This patient presented with massive neck swelling, and upon imaging the inflammation extended from the upper face to the axilla. Extensive emphysema throughout the neck was of concern for necrotizing fasciitis. Upon surgical exploration, the source of inflammation was suspected to be dental disease, but the dentition was so poor and inflammation was so extensive that the causative tooth could not be determined. Cultures from the neck grew mixed flora, including fusobacterium, commonly found in oral flora.

and sagittal reformats in bone and soft tissue algorithms should be performed. Intravenous contrast-enhanced examination increases the sensitivity for detection of an abscess based on peripheral rim enhancement. CT is particularly useful in identifying areas of cortical disruption of the mandible or maxilla, whereas MRI may identify the fluid collection but could easily miss the source of the infection, namely, the affected tooth, because of artifacts inherent to MRI.

SUMMARY: HEAD AND NECK

A wide variety of disease may present as emergencies in the head and neck region. Although many conditions can be diagnosed and managed clinically, imaging plays an important role in diagnosis and management when more complicated disease and acute traumatic injuries are encountered. A clear understanding of the history and physical findings based on communication between the radiologist and referring clinician will guide selection of the most appropriate imaging modality and protocol. As with all other parts of the body, a working knowledge of the anatomy and variants, as well as the disorders specific to the region, is necessary to provide excellent patient care.

ACKNOWLEDGMENT

We thank Keith Begelman, MD, for his assistance with the section on facial trauma.

SUGGESTED READINGS: BRAIN

Adams JH, Doyle D, Ford I, et al. Diffuse axonal injury in head injury: definitions, diagnosis and grading. *Histopathology*. 1989;15:49–59.

Ahmed RM, Wilkinson M, Parker GD, et al. Transverse sinus stenting for idiopathic intracranial hypertension: a review of 52 patients and of model predictions. *AJNR Am J Neuroradiol*. 2011;32(8):1408–1414.

Al-Nakshabandi NA. The swirl sign. *Radiology*. 2001;218:433.

Allmendinger AM, Tang ER, Lui YW, et al. Imaging of stroke: Part 1, Perfusion CT—overview of imaging technique, interpretation pearls, and common pitfalls. *AJR Am J Roentgenol*. 2012;198(1):52–62.

Almekhlafi MA. On the search for the perfect mismatch!. *AJNR Am J Neuroradiol*. 2014;35(11):2068–2069.

Arfanakis K, Haughton VM, Carew JD, et al. Diffusion tensor MR imaging in diffuse axonal injury. *AJNR Am J Neuroradiol*. 2002;23:794–802.

Berkhemer OA, Fransen PS, Beumer D, et al. A randomized trial of intraarterial treatment for acute ischemic stroke. *N Engl J Med*. 2015;372(1):11–20.

Biffl WL, Egglin T, Benedetto B, et al. Sixteen-slice computed tomographic angiography is a reliable noninvasive screening test for clinically significant blunt cerebrovascular injuries. *J Trauma*. 2006;60:745–752.

Bivard A, Krishnamurthy V, Stanwell P, et al. Arterial spin labeling versus bolus-tracking perfusion in hyperacute stroke. *Stroke*. 2014;45(1):127–133.

Broderick JP, Palesch YY, Demchuk AM, et al. Endovascular therapy after intravenous t-PA versus t-PA alone for stroke. *N Engl J Med*. 2013;368(10):893–903.

Caceres JA, Goldstein JN. Intracranial hemorrhage. *Emerg Med Clin North Am*. 2012;30(3):771–794.

Campbell BC, Mitchell PJ, Kleinig TJ, et al. Endovascular therapy for ischemic stroke with perfusion-imaging selection. *N Engl J Med*. 2015;372(11):1009–1018.

Casey SO, Sampaio RC, Michel E, et al. Posterior reversible encephalopathy syndrome: utility of fluid-attenuated inversion recovery MR imaging in the detection of cortical and subcortical lesions. *AJNR AM J Neuroradiol*. 2000;21:1199–1206.

Chao CP, Zaleski CG, Patton AC. Neonatal hypoxic-ischemic encephalopathy: multimodality imaging findings. *Radiographics*. 2006;26:S159–S172.

Chen M, Caplan L. Intracranial dissections. In: Baumgartner RW, ed. *Handbook on Cerebral Artery Dissection*. Basel (Switzerland): Karger; 2005:160–173.

Ciccone A, Valvassori L, Nichelatti M, et al. Endovascular treatment for acute ischemic stroke. *N Engl J Med*. 2013;368(10):904–913.

Copen WA, Schaefer PW, Wu O. MR perfusion imaging in acute ischemic stroke. *Neuroimaging Clin N Am*. 2011;21(2):259–283.

Copen WA, Schwamm LH, Gonzalez RG, et al. Ischemic stroke: effects of etiology and patient age on the time course of the core apparent diffusion coefficient. *Radiology*. 2001;221:27–34.

Davis PC. Expert Panel on Neurologic Imaging. Head trauma. *AJNR Am J Neuroradiol*. 2007;28:1619–1621.

Delgado Almandoz JE, Kelly HR, Schaefer PW, et al. CT angiography spot sign predicts in-hospital mortality in patients with secondary intracerebral hemorrhage. *J Neurointerv Surg*. 2012;4(6):442–447.

Dimmick SJ, Faulder KC. Normal variants of the cerebral circulation at multidetector CT angiography. *Radiographics*. 2009;29(4):1027–1043.

Eastwood JD, Lev MH, Azhari T, et al. CT perfusion scanning with deconvolution analysis: pilot study in patients with acute middle cerebral artery stroke. *Radiology*. 2002;222:227–236.

Edlow JA, Smith EE, Stead LG, et al. Clinical policy: use of intravenous tPA for the management of acute ischemic stroke in the emergency department. *Ann Emerg Med*. 2013;61(2):225–243.

Filley CM, Kleinschmidt-DeMasters BK. Toxic leukoencephalopathy. *N Engl J Med*. 2001;345:425–432.

Given CA, Burdette JH, Elster AD, et al. Pseudo-subarachnoid hemorrhage: a potential imaging pitfall associated with diffuse cerebral edema. *AJNR Am J Neuroradiol*. 2003;24:254–256.

Goyal M, Demchuk AM, Menon BK, et al. Randomized assessment of rapid endovascular treatment of ischemic stroke. *N Engl J Med*. 2015;372(11):1019–1030.

Gupta RK, Nath K, Prasad A, et al. In vivo demonstration of neuroinflammatory molecule expression in brain abscess with diffusion tensor imaging. *AJNR Am J Neuroradiol*. 2008;29:326–332.

Hacke W, Kaste M, Bluhmki E, et al. Thrombolysis with alteplase 3 to 4.5 hours after acute ischemic stroke. *N Engl J Med*. 2008;359(13):1317–1329.

Hennerici M, Daffertshofer M, Jakobs L. Failure to identify cerebral infarct mechanisms from topography of vascular territory lesions. *AJNR Am J Neuroradiol*. 1998;19:1067–1074.

Huang BY, Castillo M. Hypoxic-ischemic brain injury: imaging findings from birth to adulthood. *Radiographics*. 2008;28(2):417–439.

Huang YC, Liu HL, Lee JD, et al. Comparison of arterial spin labeling and dynamic susceptibility contrast perfusion MRI in patients with acute stroke. *PLoS One*. 2013;8(7):e69085.

Huisman TA, Schwamm LH, Schaefer PW, et al. Diffusion tensor imaging as potential biomarker of white matter injury in diffuse axonal injury. *AJNR Am J Neuroradiol*. 2004;25:370–376.

Johnston SC. Clinical practice. Transient ischemic attack. *N Engl J Med*. 2002;347 :1687–1692.

Jones KM, Seeger JF, Yoshino MT. Ipsilateral motor deficit resulting from a subdural hematoma and a Kernohan notch. *AJNR Am J Neuroradiol*. 1991;12:1238–1239.

Jovin TG, Chamorro A, Cobo E, et al. Thrombectomy within 8 hours after symptom onset in ischemic stroke. *N Engl J Med*. 2015;372(24):2296–2306.

Katramados AM, Burdette D, Patel SC, et al. Periictal diffusion abnormalities of the thalamus in partial status epilepticus. *Epilepsia*. 2009;50(2):265–275.

Keogh CF, Andrews GT, Spacey SD, et al. Neuroimaging features of heroin inhalation toxicity: "chasing the dragon." *AJR Am J Roentgenol*. 2003;180:847–850.

Kidwell CS, Jahan R, Gornbein J, et al. A trial of imaging selection and endovascular treatment for ischemic stroke. *N Engl J Med*. 2013;368(10):914–923.

Koculym A, Huynh TJ, Jakubovic R, et al. CT perfusion spot sign improves sensitivity for prediction of outcome compared with CTA and postcontrast CT. *AJNR Am J Neuroradiol*. 2013;34(5):965–970. S1.

Laine FJ, Shedden AI, Dunn MM, et al. Acquired intracranial herniations: MR imaging findings. *AJR Am J Roentgenol*. 1995;165:967–973.

Leach JL, Fortuna RB, Jones BV, et al. Imaging of cerebral venous thrombosis: current techniques, spectrum of findings, and diagnostic pitfalls. *Radiographics*. 2006;26:S19–S43.

Lev MH, Segal AZ, Farkas J, et al. Utility of perfusion-weighted CT imaging in acute middle cerebral artery stroke treated with intra-arterial thrombolysis. Prediction of final infarct volume and clinical outcome. *Stroke*. 2001;32:2021–2028.

Liang L, Korogi Y, Sugahara T, et al. Detection of intracranial hemorrhage with susceptibility-weighted MR sequences. *AJNR Am J Neuroradiol*. 1999;20:1527–1534.

Lonergan GJ, Baker AM, Morey MK, et al. From the Archives of the AFIP: Child abuse: radiologic-pathologic correlation. *Radiographics*. 2003;23:811–845.

Lou M, Chen Z, Wan J, et al. Susceptibility-diffusion mismatch predicts thrombolytic outcomes: a retrospective cohort study. *AJNR Am J Neuroradiol*. 2014;35(11):2061–2067.

Maudsley AA, Govind V, Levin B, et al. Distributions of magnetic resonance diffusion and spectroscopy measures with traumatic brain injury. *J Neurotrauma*. 2015;32(14):1056–1063.

Menon BK, d'Esterre CD, Qazi EM, et al. Multiphase CT angiography: a new tool for the imaging triage of patients with acute ischemic stroke. *Radiology*. 2015;275(2):510–520.

Mozaffarian D, Benjamin EJ, Go AS, et al. Heart disease and stroke statistics—2015 update: a report from the American Heart Association. *Circulation*. 2015;131(4):e29–e322.

Munera F, Soto JA, Palacio DM, et al. Penetrating neck injuries: helical CT angiography for initial evaluation. *Radiology*. 2002;224(2):366–372.

Munera F, Soto JA, Palacio D, et al. Diagnosis of arterial injuries caused by penetrating trauma to the neck: comparison of helical CT angiography and conventional angiography. *Radiology*. 2000;216(2):356–362.

Nadgir RN, Loevner LA, Ahmed T, et al. Simultaneous bilateral internal carotid and vertebral artery dissection following chiropractic manipulation: case report and review of the literature. *Neuroradiology*. 2003;45:311–314.

American College of Surgeons. *National Trauma Data Bank 2014 Annual Report*. Chicago, IL: American College of Surgeons; 2014.

Noguchi K, Seto H, Kamisaki Y, et al. Comparison of fluid-attenuated inversion-recovery MR imaging with CT in a simulated model of acute subarachnoid hemorrhage. *AJNR Am J Neuroradiol*. 2000;21:923–927.

Nunez DB, Torres-Leon M, Munera F. Vascular injuries of the neck and thoracic inlet: helical CT-angiographic correlation. *Radiographics*. 2004;24:1087–1100.

O'Connor KM, Barest G, Moritani, et al. "Dazed and diffused": making sense of diffusion abnormalities in neurologic pathologies. *Br J Radiol*. 2013;86(1032):20130599.

Osborn AG, Salzman KL, Barkovich J. *Diagnostic Imaging: Brain*. 2nd ed. Salt Lake City, UT: Amirsys; 2009.

Packard AS, Kase CS, Aly AS, et al. "Computed tomography-negative" intracerebral hemorrhage. *Arch Neurol*. 2003;60:1156–1159.

Pelkonen O, Tikkakakoski T, Pyhtinen J, et al. Cerebral CT and MRI findings in cervicocephalic artery dissection. *Acta Radiol*. 2004;45:259–265.

Pexman JH, Barber PA, Hill MD, et al. Use of the Alberta Stroke Program Early CT Score (ASPECTS) for assessing CT scans in patients with acute stroke. *AJNR Am J Neuroradiol*. 2001;22(8):1534–1542.

Polman CH, Reingold SC, Banwell B, et al. Diagnostic criteria for multiple sclerosis: 2010 revisions to the McDonald criteria. *Ann Neurol*. 2011;69(2):292–302.

Pond JB, Suss RA, Scott HD, et al. CT angiography of the cerebral venous system: anatomic structure, pathologic features, and pitfalls: resident and fellow education feature. *Radiographics*. 2015;35(2):498–499.

Post MJD, Thurnher MM, Clifford DB, et al. CNS–immune reconstitution inflammatory syndrome in the setting of HIV infection, part 1: overview and discussion of progressive multifocal leukoencephalopathy–immune reconstitution inflammatory syndrome and cryptococcal–immune reconstitution inflammatory syndrome. *AJNR Am J Neuroradiol*. 2013;34(7):1297–1307.

Post MJ, Thurnher MM, Clifford DB, et al. CNS–immune reconstitution inflammatory syndrome in the setting of HIV infection, part 2: discussion of neuro-immune reconstitution inflammatory syndrome with and without other pathogens. *AJNR Am J Neuroradiol*. 2013;34(7):1308–1318.

Pulli B, Schaefer PW, Hakimelahi R, et al. Acute ischemic stroke: infarct core estimation on CT angiography source images depends on CT angiography protocol. *Radiology*. 2012;262(2):593–604.

Rodallec MH, Krainik A, Feydy A, et al. Cerebral venous thrombosis and multidetector CT angiography: tips and tricks. *Radiographics*. 2006;26:S5–S18.

Saver JL, Jahan R, Levy EI, et al. SOLITAIRE™ With the Intention for Thrombectomy (SWIFT) trial: design of a randomized, controlled, multicenter study comparing the SOLITAIRE™ flow restoration device and the MERCI retriever in acute ischaemic stroke. *Int J Stroke*. 2014;9(5):658–668.

Saver JL, Goyal M, Bonafe A, et al. Stent-retriever thrombectomy after intravenous t-PA vs. t-PA alone in stroke. *N Engl J Med*. 2015;372(24):2285–2295.

Schaefer PW, Roccatagliata L, Ledezma C, et al. First-pass quantitative CT perfusion identifies thresholds for salvageable penumbra in acute stroke patients treated with intra-arterial therapy. *AJNR Am J Neuroradiol*. 2006;27(1):20–25.

Shenton M, Hamoda H, Schneiderman J, et al. A review of magnetic resonance imaging and diffusion tensor imaging findings in mild traumatic brain injury. *Brain Imaging Behav*. 2012;6(2):137–192.

Siskas N, Lefkopoulos A, Ioannidis I, et al. Cortical laminar necrosis in brain infarcts: serial MRI. *Neuroradiology*. 2003;45(5):283–288.

Srinivasan A, Goyal M, Al Azri F. State-of-the-art imaging of acute stroke. *Radiographics*. 2006;26:S75–S95.
Stuhlfaut JW, Barest G, Sakai O, et al. Impact of MDCT angiography on the use of catheter angiography for the assessment of cervical arterial injury after blunt or penetrating trauma. *AJR Am J Roentgenol*. 2005;185:1063–1068.
Susac JO, Murtagh FR, Egan RA, et al. MRI findings in Susac's syndrome. *Neurology*. 2003;61:1783–1787.
Tomandl BF, Kostner NC, Schempershofe M, et al. CT angiography of intracranial aneurysms: a focus on postprocessing. *Radiographics*. 2004;24:637–655.
Uyeda JW, Anderson SW, Sakai O, et al. CT angiography in trauma. *Radiol Clin North Am*. 2010;48(2):423–438.
van der Vorp HB, van Gijn J. Acute ischemic stroke. *N Engl J Med*. 2007;357:572–579.
Vertinsky AT, Schwartz NE, Fischbein NJ, et al. Comparison of multidetector CT angiography and MR imaging of cervical artery dissection. *AJNR Am J Neuroradiol*. 2008;29(9):1753–1760.
Vo KD, Lin W, Lee J-M. Neuroimaging in acute ischemic stroke. In: Medina LS, Blackmore CC, eds. *Evidence-Based Imaging: Optimizing Imaging in Patient Care*. New York, NY: Springer Science + Business Media; 2006:160–179.
Wada R, Aviv RI, Fox AJ, et al. CT angiography "spot sign" predicts hematoma expansion in acute intracerebral hemorrhage. *Stroke*. 2007;38:1257–1262.
Wang H, Li W, He H, et al. 320-detector row CT angiography for detection and evaluation of intracranial aneurysms: comparison with conventional digital subtraction angiography. *Clin Radiol*. 2013;68(1):e15–e20.
Wintermark M, Reichhart M, Cuisenaire O, et al. Comparison of admission perfusion computed tomography and qualitative diffusion- and perfusion-weighted magnetic resonance imaging in acute stroke patients. *Stroke*. 2002;33:2025–2031.
Woo K, Magner DP, Wilson MT, et al. CT angiography in penetrating neck trauma reduces the need for operative neck exploration. *Am Surg*. 2005;71:754–758.
Yeo LL, Paliwal P, Teoh HL, et al. Assessment of intracranial collaterals on CT angiography in anterior circulation acute ischemic stroke. *AJNR Am J Neuroradiol*. 2015;36(2):289–294.
Yousem DM, Grossman RI. *Neuroradiology: The Requisites*. 3rd ed. Philadelphia, PA: Elsevier; 2010.
Zhang LJ, Wu SY, Niu JB, et al. Dual-energy CT angiography in the evaluation of intracranial aneurysms: image quality, radiation dose, and comparison with 3D rotational digital subtraction angiography. *AJR Am J Roentgenol*. 2010;194(1):23–30.

SUGGESTED READINGS: HEAD AND NECK

Al-Dajani N, Wootton SH. Cervical lymphadenitis, suppurative parotitis, thyroiditis, and infected cysts. *Infect Dis Clin North Am*. 2007;21:523–541.
Alvi A, Bereliani A IV: Trauma to the temporal bone: diagnosis and management of complications. *J Craniomaxillofac Trauma*. 1996;2:36–48.
Battista RA, Baredes S, Krieger A, et al. Prevertebral space infections associated with cervical osteomyelitis. *Otolaryngol Head Neck Surg*. 1993;108:160–166.
Bentsianov BL, Parhiscar A, Azer M, et al. The role of fiberoptic nasopharyngoscopy in the management of the acute airway in angioneurotic edema. *Laryngoscope*. 2000;110:2016–2019.
Caruso PA, Watkins LM, Suwansaard P, et al. Odontogenic orbital inflammation: clinical and CT findings—initial observations. *Radiology*. 2006;239:187–194.
Chapman MN, Nadgir RN, Akman AS, et al. Periapical lucency around the tooth: radiologic evaluation and differential diagnosis. *Radiographics*. 2013;33(1):E15–E32.
Clary RA, Cunningham MJ, Eavey RD. Orbital complications of acute sinusitis: comparison of computed tomography scan and surgical findings. *Ann Otol Rhinol Laryngol*. 1992;101:598–600.
Conlin JL, Mian AZ, Sakai O. Unilateral mass-like pharyngeal and laryngeal angioedema. *Emerg Radiol*. 2011;18(5):441–443.
Dolan KD, Jacoby CG, Smoker WR. Facial fractures. *Radiographics*. 1984;4:577–663.
Freeman J. Temporal bone fractures and cholesteatoma. *Ann Otol Rhinol Laryngol*. 1983;92:558–560.
Ginsberg LE, Pruett SW, Chen MY, et al. Skull-base foramina of the middle cranial fossa: reassessment of normal variation with high-resolution CT. *AJNR Am J Neuroradiol*. 1994;15:283–291.
Harris JH, Harris WH. The Radiology of Emergency Medicine;1-30. 4th ed. Philadelphia, PA: Lippincott Williams and Wilkins; 2000:49–134.
Hopper RA, Salemy S, Sze RW. Diagnosis of midface fractures with CT: what the surgeon needs to know. *Radiographics*. 2006;26:783–793.
Ishman SL, Friedland DR. Temporal bone fractures: traditional classification and clinical relevance. *Laryngoscope*. 2004;114:1734–1741.
Kinoshita T, Ishii K, Naganuma H, et al. Acute suppurative thyroiditis arising from a piriform sinus fistula: CT diagnosis. *Radiat Med*. 1998;16:217–219.
Koesling S, Kunkel P, Schul T. Vascular anomalies, sutures and small canals of the temporal bone on axial CT. *Eur J Radiol*. 2005;54:335–343.
LeBedis CA, Sakai O. Nontraumatic orbital conditions: diagnosis with CT and MR imaging in the emergent setting. *Radiographics*. 2008 Oct;28(6):1741–1753.
Little SC, Kesser BW. Radiographic classification of temporal bone fractures: clinical predictability using a new system. *Arch Otolaryngol Head Neck Surg*. 2006;132:1300–1304.
Ludwig BJ, Foster BR, Saito N, et al. Diagnostic imaging in nontraumatic pediatric head and neck emergencies. *Radiographics*. 2010;30(3):781–799.
Ludwig BJ, Wang J, Nadgir RN, et al. Imaging of cervical lymphadenopathy in children and young adults. *AJR Am J Roentgenol*. 2012;199(5):1105–1113.
Lyos AT, Marsh MA, Jenkins HA, et al. Progressive hearing loss after transverse temporal bone fracture. *Arch Otolaryngol Head Neck Surg*. 1995;121:795–799.
McKennan KX, Chole RA. Post-traumatic cholesteatoma. *Laryngoscope*. 1989;99:779–782.
Mian AZ, Saito N, Sakai O. Rhabdomyolysis of the head and neck: computed tomography and magnetic resonance imaging findings. *Dentomaxillofac Radiol*. 2011;40(6):390–392.
Ogura I, Kaneda T, Sasaki Y, et al. Prevalence of temporal bone fractures in patients with mandibular fractures using multidetector-row CT. *Clin Neuroradiol*. 2015;25(2):137–141.
Peralta R, Hurford WE. Airway trauma. *Int Anesthesiol Clin*. 2000;38:111–127.
Rafferty MA, McConn Walsh R, Walsh MA. A comparison of temporal bone fracture classification systems. *Clin Otolaryngol*. 2006;31:287–291.
Reynolds SC, Chow AW. Life-threatening infections of the peripharyngeal and deep fascial spaces of the head and neck. *Infect Dis Clin North Am*. 2007;21:557–576.
Rhea JT, Rao PM, Novelline RA. Helical CT and three-dimensional CT of facial and orbital injury. *Radiol Clin North Am*. 1999;37:489–513.
Rodt T, Bartling SO, Zajaczek JE, et al. Evaluation of surface and volume rendering in 3D-CT of facial fractures. *Dentomaxillofac Radiol*. 2006;35:227–231.
Saigal K, Winokur RS, Finden S, et al. Use of three-dimensional computerized tomography reconstruction in complex facial trauma. *Facial Plast Surg*. 2005;21:214–220.
Saito N, Hito R, Burke PA, et al. Imaging of penetrating injuries of the head and neck: current practice at a level I trauma center in the United States. *Keio J Med*. 2014;63(2):23–33.
Saito N, Nadgir RN, Flower EN, et al. Clinical and radiologic manifestations of sickle cell disease in the head and neck. *Radiographics*. 2010;30(4):1021–1034.
Saito N, Watanabe M, Liao J, et al. Clinical and radiologic findings of inner ear involvement in sickle cell disease. *AJNR Am J Neuroradiol*. 2011;32(11):2160–2164.
Schuknecht B, Graetz K. Radiologic assessment of maxillofacial, mandibular, and skull base trauma. *Eur Radiol*. 2005;15:560–568.
Shah S, Sharieff GQ. Pediatric respiratory infections. *Emerg Med Clin North Am*. 2007;25:961–979.
Sherman SC, Buchanan A. Gradenigo syndrome: a case report and review of a rare complication of otitis media. *J Emerg Med*. 2004;27:253–256.
Simons JP, Branstetter BF IV, Mandell DL: Bilateral peritonsillar abscesses: case report and literature review. *Am J Otolaryngol*. 2006;27:443–445.
Singh AK, Buch K, Sung E, et al: Head and neck injuries from the Boston Marathon bombing at four hospitals [published online ahead of print May 12, 2015]. Emerg Radiol. 25962489.
Smith JA, Danner CJ. Complications of chronic otitis media and cholesteatoma. *Otolaryngol Clin North Am*. 2006;39:1237–1255.
Snow JB. Jr: Diagnosis and therapy for acute laryngeal and tracheal trauma. *Otolaryngol Clin North Am*. 1984;17:101–106.
Stassen NA, Hoth JJ, Scott MJ, et al. Laryngotracheal injuries: does injury mechanism matter? *Am Surg*. 2004;70:522–525.
Sung EK, Nadgir RN, Fujita A, et al. Injuries of the globe: what can the radiologist offer? *Radiographics*. 2014;34(3):764–776.
Takao M, Ido M, Hamaguchi K, et al. Descending necrotizing mediastinitis secondary to a retropharyngeal abscess. *Eur Respir J*. 1994;7:1716–1718.
Watanabe M, Saito N, Nadgir RN, et al. Craniofacial bone infarcts in sickle cell disease: clinical and radiological manifestations. *J Comput Assist Tomogr*. 2013;37(1):91–97.

Chapter 2

Chest Trauma

Ryan T. Whitesell and Laura L. Avery

Thoracic injuries account for approximately 25% of trauma deaths, second in number only to head trauma. In the United States each year, more than 300,000 patients are hospitalized and more than 25,000 die as a result of chest trauma. Blunt trauma accounts for 90% of chest trauma cases. The most common causes of blunt trauma are motor vehicle collisions and falls.

The imaging protocol of patients with suspected thoracic injuries usually begins with a supine portable anteroposterior chest radiograph. Many obvious thoracic injuries such as displaced rib fractures, large pneumothoraces, and hemothoraces may be detected quickly with this examination. Chest radiographs are also useful in confirming the correct positioning of an endotracheal tube or nasogastric tube. Other traumatic conditions such as a small pneumothorax, a small hemothorax, a parenchymal lung laceration, aortic trauma, a tracheobronchial injury, a cardiac injury, a diaphragm rupture, and a thoracic spine injury usually require further imaging with computed tomography (CT). Multidetector CT (MDCT) scanners can quickly and accurately diagnose a wide variety of thoracic injuries. The use of multiplanar and volumetric images derived from the acquired axial or helical data may not only aid in diagnostic evaluation but also better display the extent of the injuries, which may assist in optimal treatment planning.

MDCT PROTOCOL FOR SUSPECTED THORACIC INJURY

Chest CT scans for suspected thoracic trauma should be performed with an intravenous contrast agent to opacify key anatomic structures such as the heart, aorta, and thoracic blood vessels and demonstrate vascular injuries such as a pseudoaneurysm or active bleeding. CT scanning of the chest after trauma is best performed in the arterial phase after a 25- to 30-second delay. Scans should be acquired at thin detector configurations so that high-quality multiplanar volumetric reformations and a CT arteriogram can be produced from the thin axial images. Routine coronal and sagittal reformations of the chest are recommended for all patients with chest trauma to better demonstrate injuries, particularly injuries to the major vessels, diaphragm, or spine. A detector configuration of 16 • 1.25 mm is preferable for 16-slice scanners, whereas 64-slice scanners would utilize axial slices having less than 1-mm thickness. The thin slices may be reformatted to 2.5 mm for viewing axial slices and transmitted to the Picture Archival Computer System along with the coronal and sagittal reformations for formal examination interpretation. Thick-slice maximum intensity projection images also may be helpful in evaluating vascular injuries. All axial and multiplanar images should be reviewed on soft tissue, lung, and bone windows.

INJURIES OF THE PLEURAL SPACE

A hemothorax—that is, blood in the pleural space—may result from injury to the chest wall, diaphragm, lung, or mediastinal structures. CT may confirm a hemothorax when the pleural fluid collection in a trauma patient measures blood density, greater than 35 to 40 Hounsfield units (HUs) (Fig. 2-1). A pneumothorax—that is, air in the pleural space—may result from a lung injury, tracheobronchial injury, or esophageal rupture. The most common cause is lung injury associated with a rib fracture. A pneumothorax occurs in about 15% to 40% of patients with acute chest trauma. Many small and even moderate-sized pneumothoraces that are not visible on the supine chest film can easily be identified on CT. A pneumothorax seen on CT that cannot be identified on a supine chest film is referred to as an "occult" pneumothorax. Studies estimate that up to 50% of pneumothoraces seen on CT are not evident on the supine anteroposterior film. Radiographic signs of pneumothorax may be subtle. In the supine patient, air collects in nondependent locations such as the anterior costophrenic sulcus. This region extends from the seventh costal cartilage to the eleventh rib in the midaxillary line. The air collection appears as an abnormal lucency in the lower chest or upper abdomen, frequently referred to as the "deep sulcus" sign. Additional signs of pneumothorax in a supine patient include a sharply outlined cardiac or diaphragmatic border and depression of the hemidiaphragm (Fig. 2-2). Detection of even a small pneumothorax is important because it may enlarge during positive-pressure ventilation or induction of general anesthesia. A tension pneumothorax, which results from a lung or airway injury associated with a one-way accumulation of air within the pleural space, is a clinical emergency. As intrapleural pressure rises, the mediastinal structures are compressed, decreasing venous return to the heart and leading to hemodynamic instability. Radiography and CT will show a mediastinal shift to the contralateral hemithorax, hyperexpansion of the ipsilateral thorax, and depression of the ipsilateral hemidiaphragm.

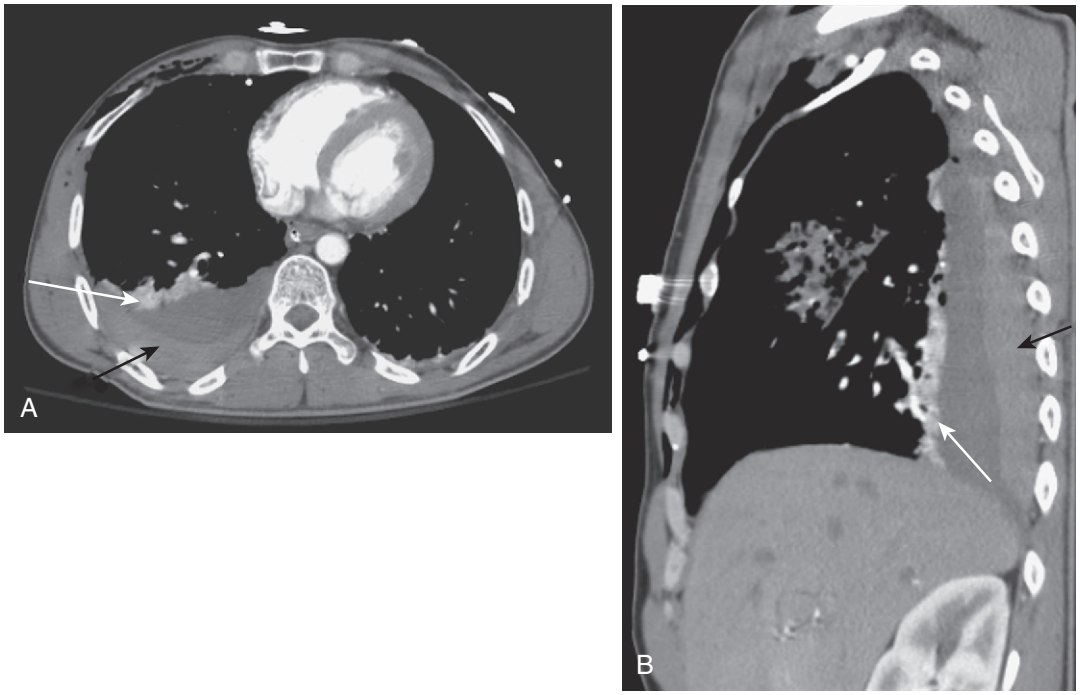


FIGURE 2-1 **A,** Axial computed tomography shows high-density blood layering within the pleural space consistent with a hemothorax *(black arrow)*. The *white arrow* indicates the adjacent opacified lung. **B,** A sagittal image shows both hemothorax *(black arrow)* and opacified lung *(white arrow)*.

ESOPHAGEAL INJURIES

Blunt trauma to the esophagus is extremely rare because this structure is well protected in the posterior mediastinum. Most esophageal injuries occur from penetrating or iatrogenic trauma. Blunt trauma may result in rupture or an intramural hematoma. These injuries normally involve the upper thoracic esophagus or the lower esophagus just above the gastroesophageal junction. The most commonly accepted theory regarding the pathophysiology of rupture is similar to the mechanism in Boerhaave syndrome in that an increase in intraluminal pressure against a closed glottis results in a tear at the weakest point of the esophageal wall, usually the distal third of the esophagus on the left where there is less protection from the pleural lining and the heart. Other causes of injury include disruption of the esophageal blood supply, resulting in ischemia and late perforation, and a blast effect caused by a concomitant tracheal injury. Direct injury also may result from adjacent thoracic spine fractures or compression between the sternum and thoracic spine, as observed in high-speed road traffic collisions. Esophageal injuries are often associated with clinical symptoms such as hemoptysis or dysphagia. CT may suggest the diagnosis of traumatic esophageal perforation with the presence of pneumomediastinum, mediastinitis, hydropneumothorax, or leakage of oral contrast medium into the mediastinum or the pleural space. Water-soluble contrast esophagography, followed by flexible esophagoscopy, may be required to fully evaluate the injury site.

CARDIAC INJURIES

Cardiac and pericardial injuries are uncommon with blunt thoracic trauma but do occur with severe blows to the anterior chest. The diagnosis of blunt cardiac injury relies on a high clinical suspicion. Cardiac injuries often occur in conjunction with sternal fractures. The anterior aspect of the heart that abuts the sternum is most vulnerable to injury. Patients with cardiac injuries may have an abnormal electrocardiogram and elevated cardiac enzymes. Cardiac injuries include cardiac contusion, cardiac rupture, pneumopericardium, hemopericardium, cardiac tamponade, and cardiac valve injury. Hemopericardium from a cardiac injury or cardiac rupture may quickly produce cardiac tamponade with hemodynamic compromise (Fig. 2-3). A chest radiograph may demonstrate enlargement of the cardiac silhouette, which can be confirmed as representing hemopericardium by CT or cardiac sonography.

AORTIC AND GREAT VESSEL INJURIES

Injuries of the aorta account for a significant number of fatalities after blunt trauma. Seventy percent of all thoracic aortic injuries are fatal at the trauma scene. Of patients who are transported to the hospital, 90% of aortic ruptures occur at the aortic isthmus, located at the junction of the posterior aortic arch and descending aorta, just distal to the origin of the left subclavian artery. The proposed mechanism of injury is rapid deceleration that produces a shear injury at the site where the rate of deceleration of the mobile aortic arch differs from that of the relatively fixed descending aorta. In addition, bending stress occurs because the aorta is flexed over the left pulmonary artery and left mainstem bronchus. Only 5% of aortic injuries in clinical series involve the ascending aorta, and these injuries may be associated with life-threatening cardiac and pericardial injuries. Rarely,

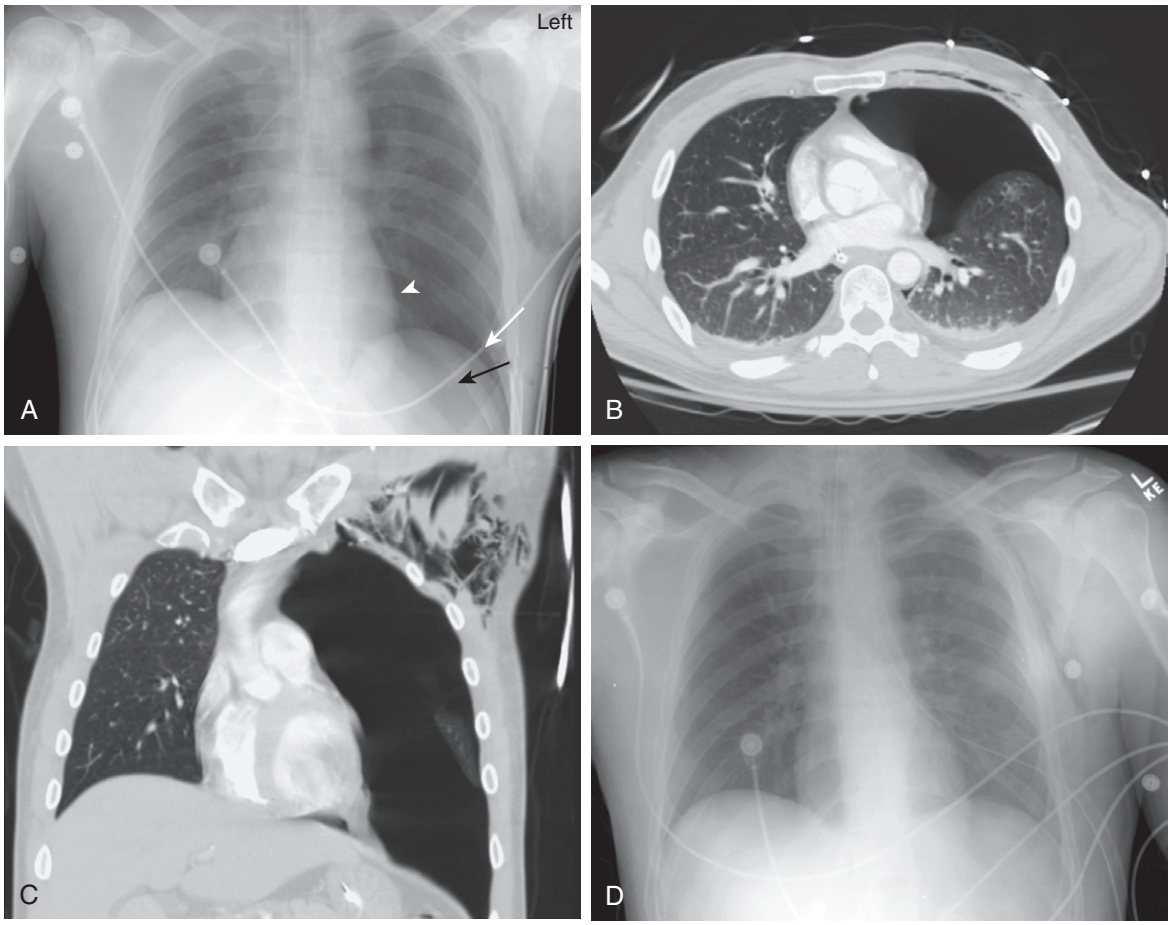


FIGURE 2-2 **A,** Anteroposterior chest radiograph findings of tension pneumothorax including the "deep sulcus" sign *(black arrow),* sharply outlined cardiac and diaphragmatic border *(arrowhead),* and depression of the hemidiaphragm *(white arrow).* Note rightward deviation of the mediastinum consistent with tension. **B,** An axial image from multidetector computed tomography demonstrates air collecting nondependently in the anterior costophrenic sulcus. Note rightward deviation of the heart, indicating developing tension. **C,** A coronal image demonstrates depression of the hemidiaphragm and rightward deviation of the mediastinum. **D,** Chest tube placement results in normal positioning of the hemidiaphragm and mediastinum.

aortic injuries may involve the descending aorta at the level of the diaphragmatic hiatus.

A chest radiograph with normal findings has a high negative predictive value (98%) but a low positive predictive value for aortic injury. The chest film findings suggestive of aortic injury include mediastinal widening greater than 8 cm, loss of the normal aortic arch contour, a left apical pleural cap, displacement of the nasogastric tube to the right, widened paraspinal lines, and loss of the descending aortic line. Most of the plain film findings of aortic injury are nonspecific, and some signs can be replicated by technical factors such as anteroposterior imaging of a supine patient, hypoventilation, and patient rotation. Traditionally the gold standard for the diagnosis of aortic injury has been aortography; however, at most trauma centers today, aortography has been replaced with MDCT.

The sensitivity and specificity of CT has been reported to be 92% to 100% and 62% to 100%, respectively, for the detection of aortic injury. The accuracy of aortic trauma detection with CT has been improving in parallel with technologic improvements in CT scanning. Current fast MDCT scanners decrease motion artifact and provide higher quality two- and three-dimensional reformations for diagnosis and treatment planning.

The CT findings of aortic trauma include indirect signs, such as mediastinal hematoma surrounding the posterior aortic arch and proximal descending aorta, as well as the direct signs of intimal tear/flap, aortic contour abnormality, thrombus protruding into the aortic lumen, false aneurysm formation, pseudocoarctation, and extravasation of intravenous contrast material. If only direct signs are used, the sensitivity and negative predictive value remain at 100%, but the specificity increases to 96% (Fig. 2-4).

A common aortic injury is a traumatic false aneurysm resulting from disruption of the vessel intima and media while the adventitia remains intact. The intravascular blood confined by only the adventitia bulges outward, forming a pseudoaneurysm. In many cases, the aortic injury may be limited to a partial circumferential tear. CT findings typically consist of a saccular outpouching demarcated from the aortic lumen by torn intima, which

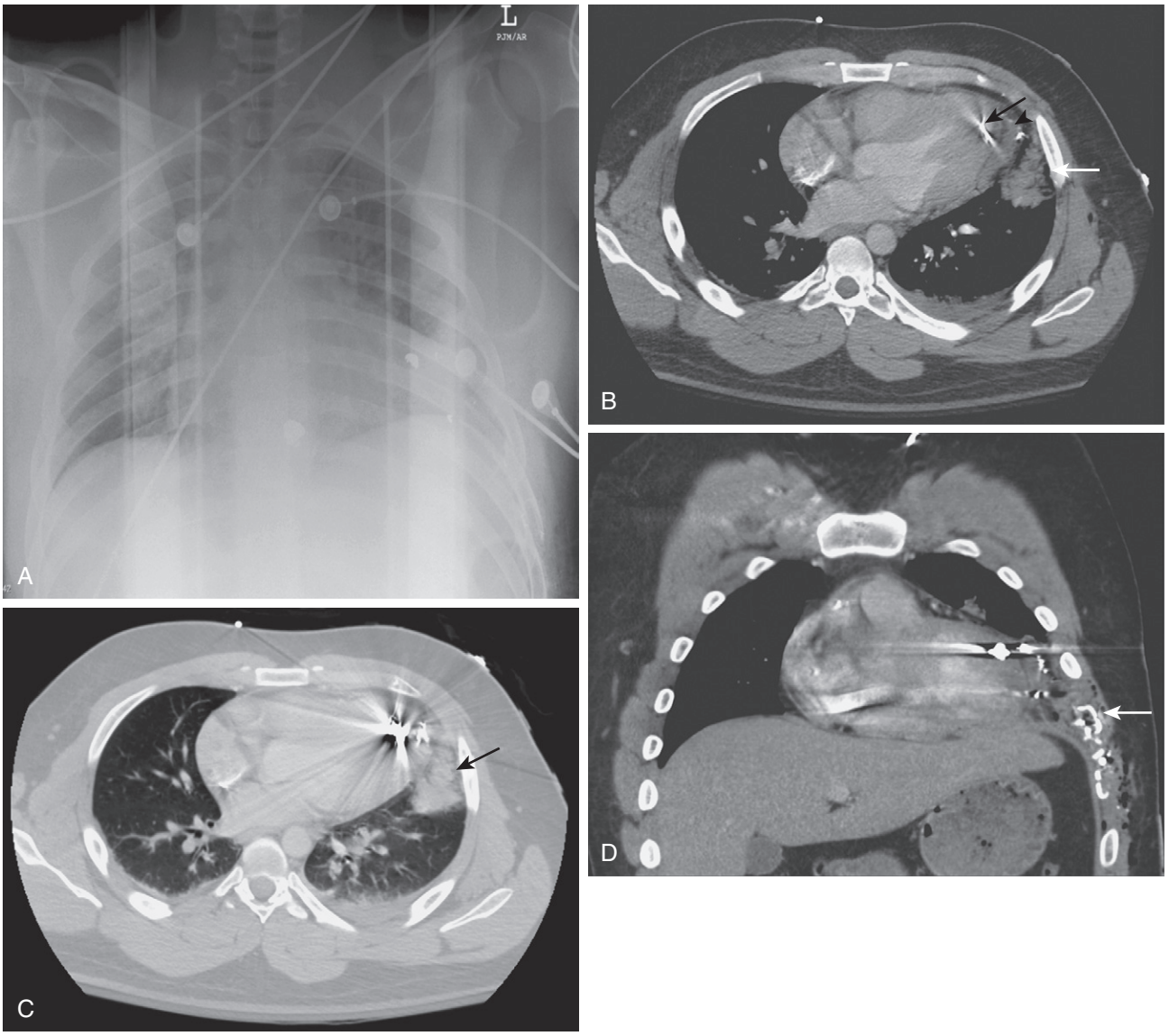


FIGURE 2-3 A 28-year-old man with a gunshot injury. **A,** The anteroposterior view of the chest demonstrates bullet fragments projecting over the cardiac silhouette. **B,** Axial computed tomography (CT) demonstrates a bullet fragment in the myocardium of the left ventricle *(black arrow)*. Note hemopericardium *(black arrowhead)* and adjacent lung contusion *(white arrow)*. **C,** Axial CT in lung windows better demonstrates the adjacent lung contusion *(arrow)*. **D,** Coronal CT demonstrates multiple rib fractures resulting from the penetrating injury *(arrow)*.

frequently results in hemomediastinum. Contemporary treatment of pseudoaneurysms often consists of intravascular stent grafting. False-positive examinations may be related to a prominent ductus diverticulum or an ulcerated atheromatous plaque. A traumatic pseudoaneurysm is usually surrounded by mediastinal blood, unlike a ductus diverticulum and an ulcerated atheromatous plaque (Figs. 2-5 to 2-7).

LUNG INJURIES AND LUNG CONTUSION

Lung contusion results from traumatic extravasation of blood and accumulation of edema in the pulmonary interstitium and air spaces as a result of disruption of alveolar-capillary integrity but without significant disruption of the pulmonary parenchyma. The injury is caused by energy transmitted directly to the lung from an impact to the overlying chest wall. On radiographs, the contusion appears as patchy areas of consolidation (Fig. 2-8). When the contusion is extensive, radiographs may show diffuse dense homogeneous lung consolidation. These opacities resulting from lung contusion are said to differ from those of bronchopneumonia and aspiration in that they are not confined to the anatomic limits of various segments or lobes, which may be difficult to definitively ascertain on an initial anteroposterior chest radiograph. A contusion may not be visualized on the initial chest film but usually becomes evident within 6 hours of injury. CT can usually detect a pulmonary contusion immediately after injury. Contusions usually resolve in a few days.

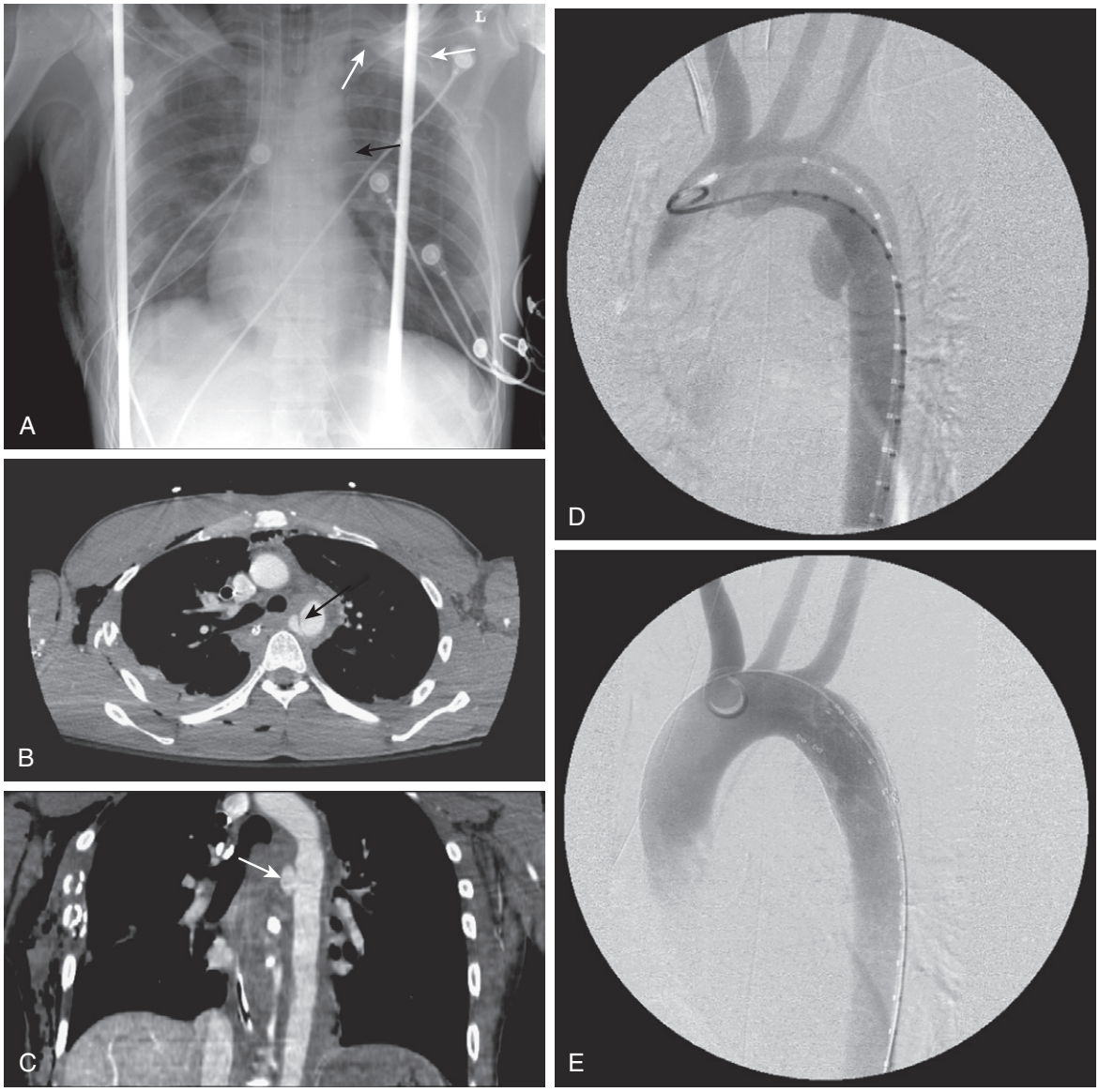


FIGURE 2-4 **A,** A portable chest radiograph shows an enlarged indistinct aortic arch *(black arrow),* a left apical pleural cap, and upper rib fractures *(white arrows).* **B,** Axial computed tomography demonstrates a mediastinal hematoma, an intimal flap, and a pseudoaneurysm *(arrow).* **C,** Oblique coronal reformation shows the extent of the pseudoaneurysm *(arrow).* **D** and **E,** Thoracic aortography before and after treatment with an aortic stent.

CT may show areas of consolidation often directly beneath the site of injury in a nonsegmental distribution and often sparing 1 to 2 mm of the subpleural lung parenchyma. The opacities may be single or multiple, and both coup and contracoup contusions may be identified. Contusions are often seen surrounding pulmonary lacerations.

LUNG LACERATION

Pulmonary lacerations are tears of the lung parenchyma that fill with air, blood, or both. If the laceration fills with air, the injury is termed a traumatic pneumatocele. If it fills with blood, a spherical hematoma or hematocele forms. If both air and fluid are present, an air–fluid level may be identified. The spherical shape of intraparenchymal lacerations has been attributed to normal elastic recoil of the lung parenchyma pulling centrifugally in all directions on the disrupted region (Fig. 2-9).

On a chest radiograph, lacerations initially may be obscured by surrounding lung contusions; however, the lacerations become visible once the contusions clear. In contrast, acute lung lacerations are nearly always detected on CT imaging. Four types have been described with blunt trauma (Fig. 2-10):

- Type 1, a compression rupture laceration, resulting from sudden compression of a pliable chest wall wherein the air-containing lung is ruptured
- Type 2, a compression shear laceration, which occurs in a paravertebral lower lobe of the lung (the mechanism occurs when the more pliable lower chest wall is acutely compressed, causing the lower lobe to shift suddenly across the vertebral body in a shearing-type injury [Fig. 2-11])

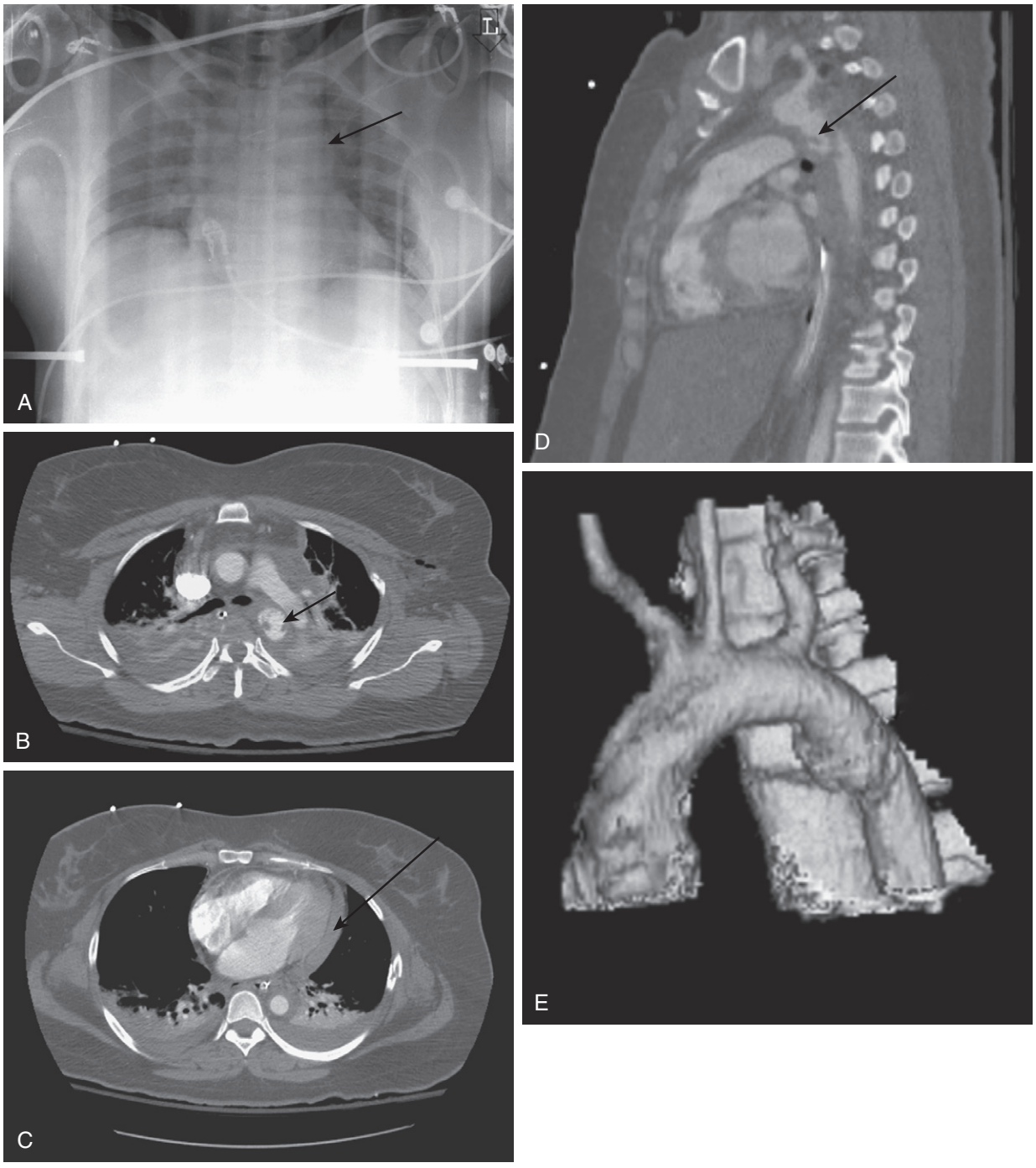


FIGURE 2-5 A 39-year-old woman involved in a rollover motor vehicle accident. **A,** A portable chest radiograph demonstrates a widened superior mediastinum *(arrow)*. **B,** An axial computed tomography section shows an intimal flap and pseudoaneurysm formation with the extraluminal extension of contrast material *(arrow)*. **C,** A lower axial section shows the hemopericardium; the patient had cardiac enzyme elevation consistent with cardiac contusion *(arrow)*. **D,** A sagittal volume-rendered image shows the pseudoaneurysm more clearly *(arrow)*. **E,** Three-dimensional images demonstrate pseudoaneurysm formation.

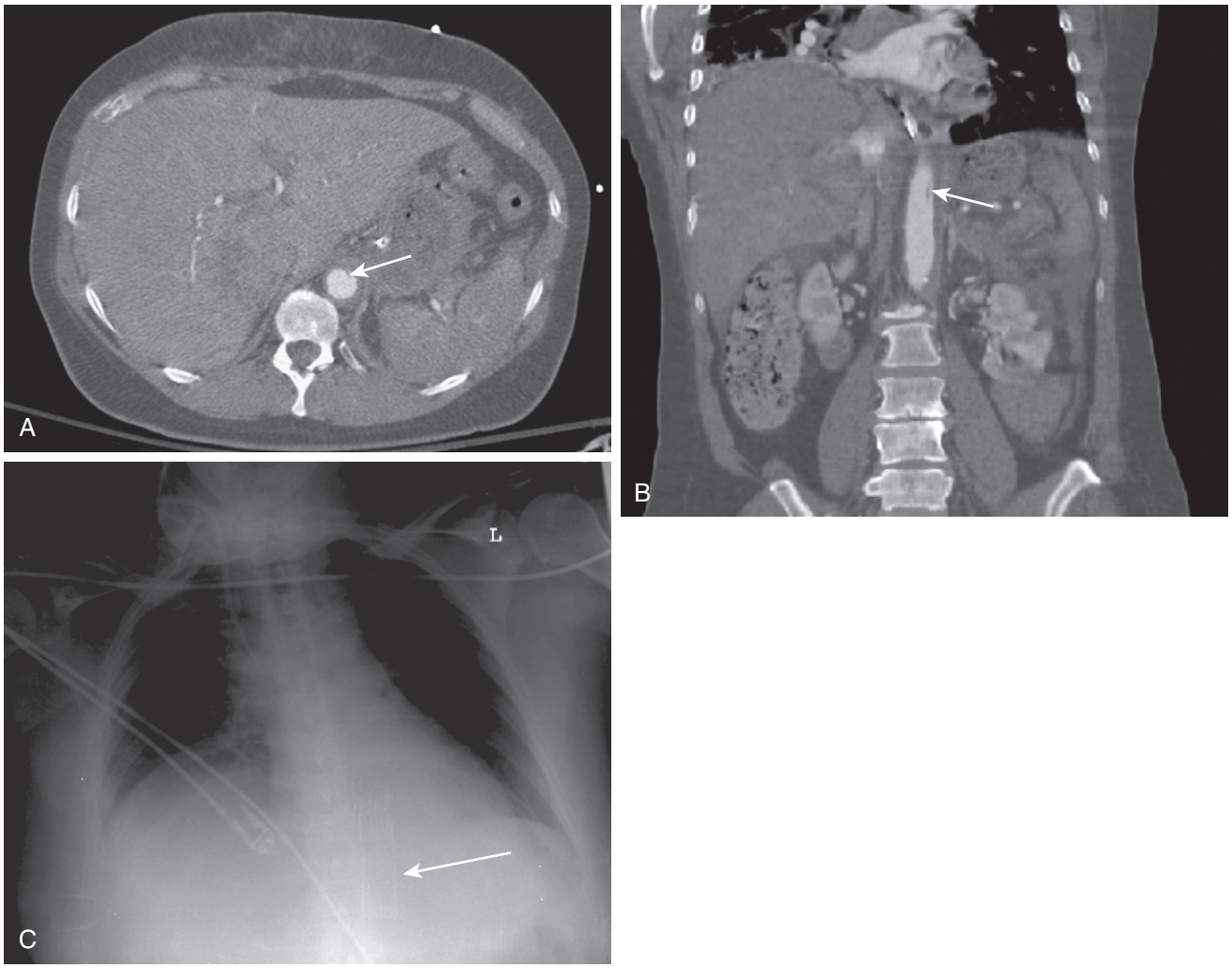


FIGURE 2-6 A 53-year-old woman after a motor vehicle accident. **A** and **B,** Axial and coronal sections at the level of the diaphragm demonstrate intimal flap formation *(arrow)* within the aortic lumen in conjunction with a periaortic hematoma. **C,** The patient after stent graft repair of the aorta *(arrow)*.

- Type 3, a rib penetration tear, causing a peripheral injury adjacent to a rib fracture (a pneumothorax is generally associated with this type of injury because it represents a penetrating injury)
- Type 4, an adhesion tear, which results from tearing of prior pleural-pulmonary adhesions, causing the lung to tear when the overlying chest wall is violently moved inward or fractured

Lung lacerations also may result from penetrating trauma, most frequently from stab wounds and gunshot wounds. Pulmonary lacerations are better shown and more extensively evaluated with CT than with plain films. Unlike pulmonary contusions, lung lacerations may take weeks or months to heal and may result in residual lung scarring. Frequently, as lacerations resolve they appear as lung nodules (Fig. 2-12).

TRACHEOBRONCHIAL INJURIES

Injuries to the airways are uncommon, occurring in approximately 1.5% of blunt trauma cases. Tears and fractures of the tracheobronchial tree frequently are not recognized on initial imaging, and a delayed diagnosis is common. Eighty percent of tracheobronchial injuries occur within 2 cm of the carina. Rupture of the left and right mainstem bronchi occur with equal frequency. Chest radiograph findings most commonly include pneumomediastinum and subcutaneous emphysema (Fig. 2-13). Air continuously leaks through the rupture and flows into the surrounding mediastinal soft tissues with superior extension into the neck. Pneumomediastinum is an anticipated accompaniment of tracheobronchial injury. Large volumes of pneumomediastinum are easy to identify on plain radiographs but may not be visible on the initial portable chest radiograph. The presence of mediastinal air should initiate a search for a possible tracheobronchial injury; however, other causes of pneumomediastinum exist, including complications of dyspnea, aggressive mechanical ventilation, and esophageal rupture. In the presence of a tracheobronchial laceration, air dissects into fascial planes as a consequence of the continuous air leak. Hence, on sequential radiographs,

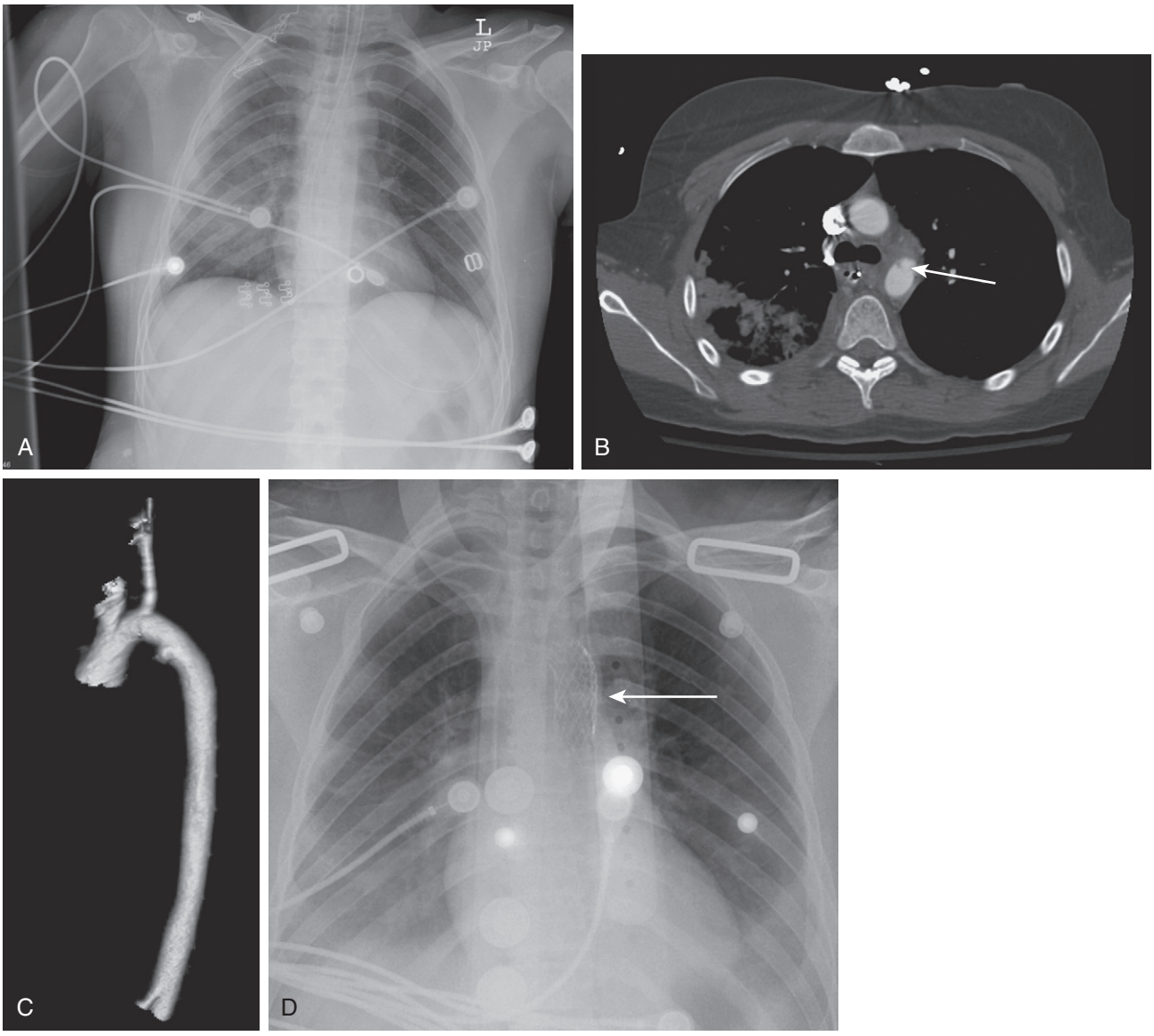


FIGURE 2-7 A 21-year-old patient after a high-speed motor vehicle accident. The patient was an unrestrained driver. **A,** A portable anteroposterior chest radiograph showing patchy opacity in the right lung representing a pulmonary contusion. **B,** An axial computed tomography section demonstrates a mediastinal hematoma with intimal flap formation *(arrow)* and contour irregularity of the aortic lumen. **C,** Three-dimensional reformation demonstrates a small pseudoaneurysm. **D,** Note stent graft placement for treatment of a pseudoaneurysm *(arrow)*.

the subcutaneous emphysema is expected to persist or increase (Fig. 2-14).

Tracheal lacerations are usually longitudinal and located at the junction of the cartilaginous and membranous parts of the trachea. Tears of the trachea or proximal left main bronchus normally cause central dissection of air with mediastinal and cervical emphysema but without pneumothorax. In bronchial injuries, the majority of cases also have an associated pneumothorax. Pneumothorax in patients with tracheobronchial transection is the result of rupture of the mediastinal pleura or injury to the right mainstem bronchus or distal left bronchus. Air is allowed to enter the pleural space on the ipsilateral side. The classic clinical feature of this condition is a pneumothorax that does not resolve despite chest tube suction as a result of a continuous leakage of air through the airway rupture. However, resolution of a pneumothorax after chest tube placement does not exclude the diagnosis. Another pathognomonic finding is that of a "fallen lung," which is a sign of complete bronchial transection and occurs when the lung collapses toward the lateral chest wall or diaphragm, rather than toward the pulmonary hilum, which is the usual situation.

Other signs of tracheobronchial injury include a sharply angulated bronchus, bronchial discontinuity, and bronchial "cutoff." Abnormalities of an endotracheal tube balloon also may be noted with tracheal laceration. The balloon may appear overinflated or more spherical as it actually herniates through a vertical laceration of the trachea. An extratracheal location of the endotracheal tube might be seen, but it is rare. All of these findings are better depicted on CT than on plain radiography. CT can reveal the exact site of tracheal injury by directly

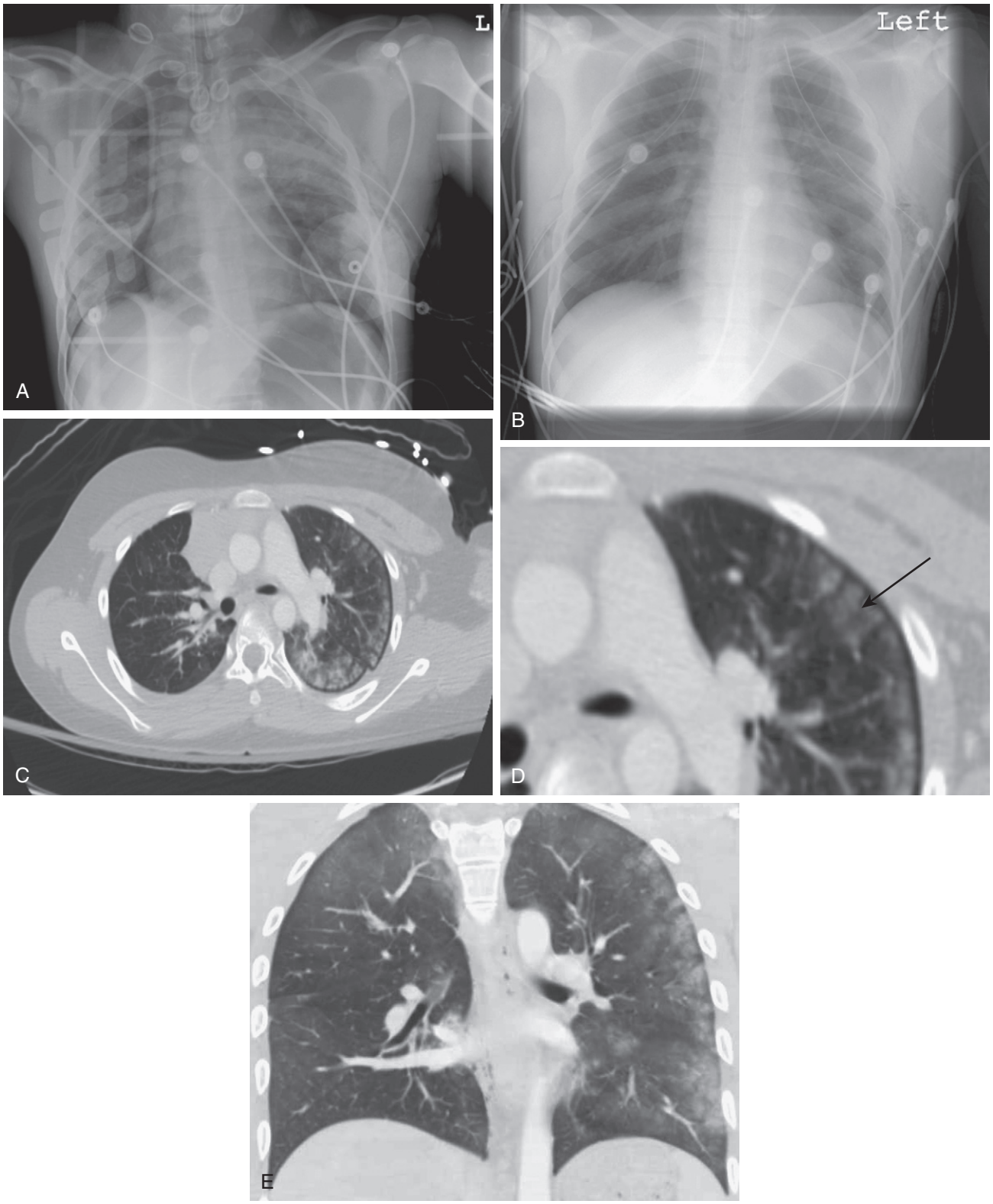


FIGURE 2-8 A 19-year-old male patient after a motor vehicle accident. **A,** The initial chest radiograph demonstrates left upper lung patchy consolidation consistent with a contusion. **B,** A chest radiograph 3 days later demonstrates rapid resolution of the pulmonary contusion. **C,** An axial section through a computed tomography scan demonstrates a left-sided contusion affecting both the upper and lower lobes, not confined to a single lobe. **D,** There is sparing of 1 to 2 mm of subpleural space *(arrow)*. **E,** A coronal image demonstrates the extent of the lung contusion.

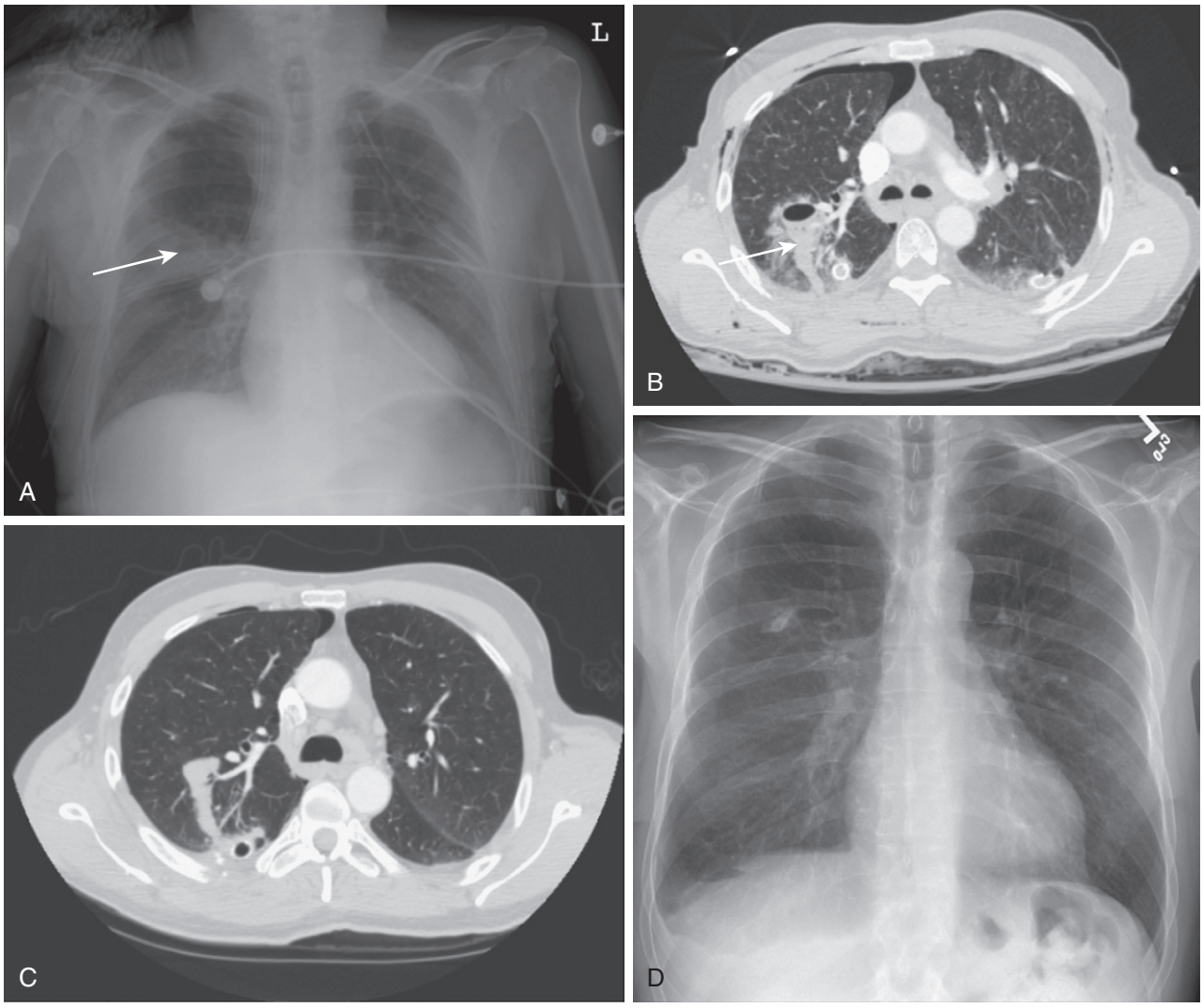


FIGURE 2-9 A 55-year-old patient stabbed in the chest. **A,** An anteroposterior chest radiograph demonstrates patchy opacities surrounding a lucent cavity lesion *(arrow)* consistent with a pulmonary pneumatocele with surrounding contusion resulting from a penetrating stab injury. **B,** An axial computed tomography (CT) image demonstrates a lung laceration *(arrow)* with a track to the skin surface. **C,** A follow-up chest CT scan 6 days after injury demonstrates resolution of the contusion with involution of the hematocele. **D,** A remote follow-up chest radiograph demonstrates scarring related to the laceration.

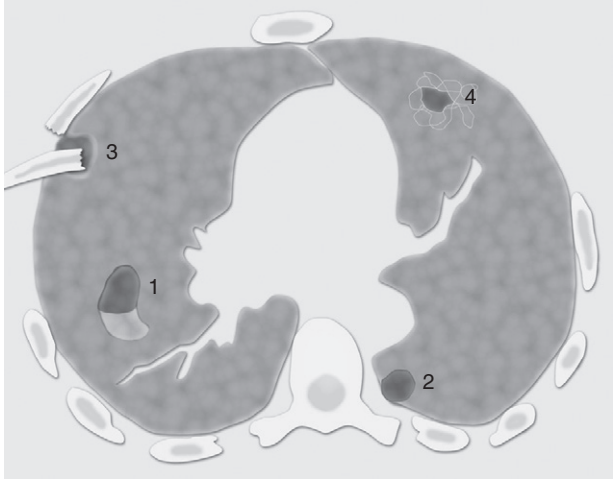


FIGURE 2-10 Four types of pulmonary lacerations. *(1)* Compression rupture injury, *(2)* compression shear injury, *(3)* rib penetration injury, and *(4)* adhesion tear injury.

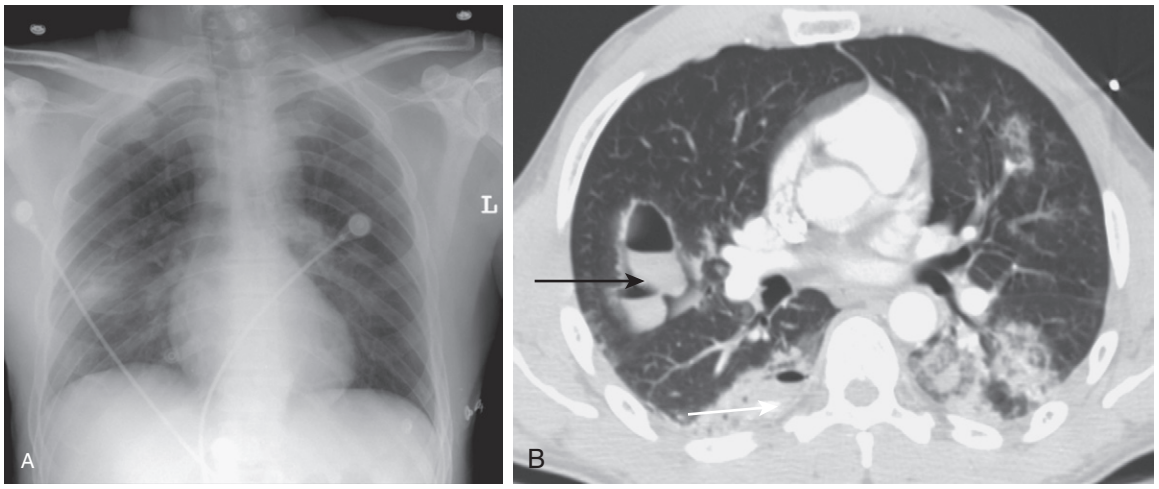


FIGURE 2-11 A 41-year-old man with a history of multiple suicide attempts and polysubstance abuse who fell from the second story of a burning building. **A,** A chest film demonstrates patchy opacification of the right hemithorax consistent with a contusion. **B,** An axial image demonstrates both a compression rupture *(black arrow)* and compression shear-type lacerations *(white arrow)*.

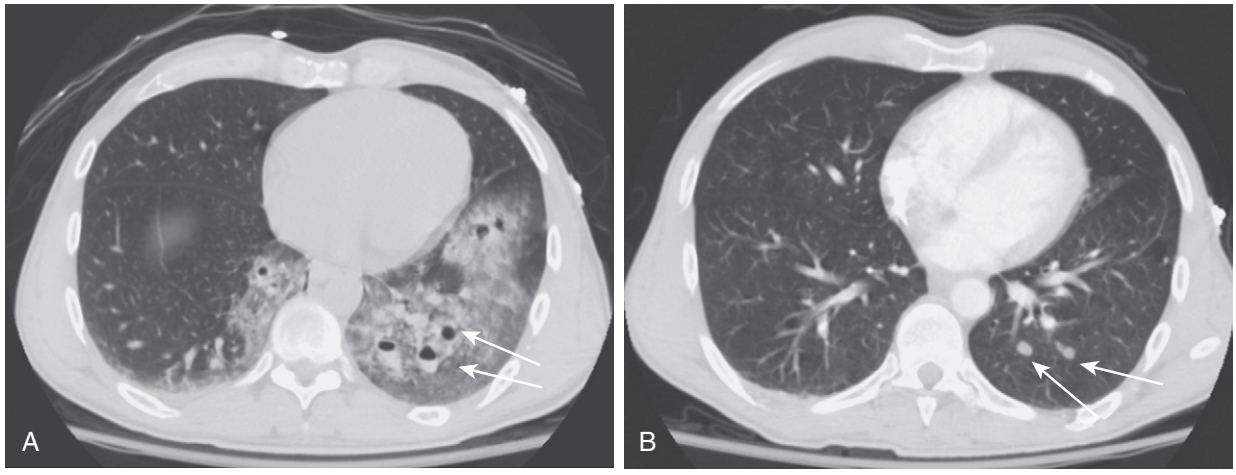


FIGURE 2-12 A 40-year-old man after a fall from a third-floor window. **A,** The initial axial computed tomography (CT) image demonstrates multiple lung lacerations *(arrows)* with surrounding contusions. **B,** A follow-up CT scan 3 weeks after the initial event demonstrates involution of hematoceles, which now have the appearance of pulmonary nodules *(arrows)*.

showing focal defects or the circumferential absence of the tracheal wall, a contour deformity, or abnormal communication with other mediastinal structures. CT can also show more subtle secondary signs, such as smaller volumes of pneumomediastinum, than can the chest radiograph.

The diagnosis of tracheobronchial injury should be confirmed by flexible bronchoscopy. Late complications of untreated tracheobronchial injury include bronchial stenosis, recurrent pneumonia, and bronchiectasis. Prompt diagnosis and treatment generally lead to good functional recovery.

DIAPHRAGMATIC INJURIES

Diaphragmatic rupture is an uncommon injury seen in about 5% of patients undergoing a laparotomy or thoracotomy for trauma. The postulated mechanism for blunt diaphragmatic injuries is a lateral blow causing shearing of the diaphragm and disruption of the attachments to the chest wall with a concomitant increase in intraabdominal pressure resulting from a frontal impact. Hence diaphragm rupture is more common with lateral impact motor vehicle collisions. Early diagnosis of diaphragmatic rupture is clinically important, because complications related to visceral herniation through the lacerated diaphragm may result in respiratory compromise as a result of impairment of lung inflation. Additionally, visceral incarceration may lead to strangulation and possible perforation.

Left-sided injuries are more common, having a reported left-to-right ratio of 3:1. Bilateral and central tendon ruptures are uncommon. The increased frequency of left-sided

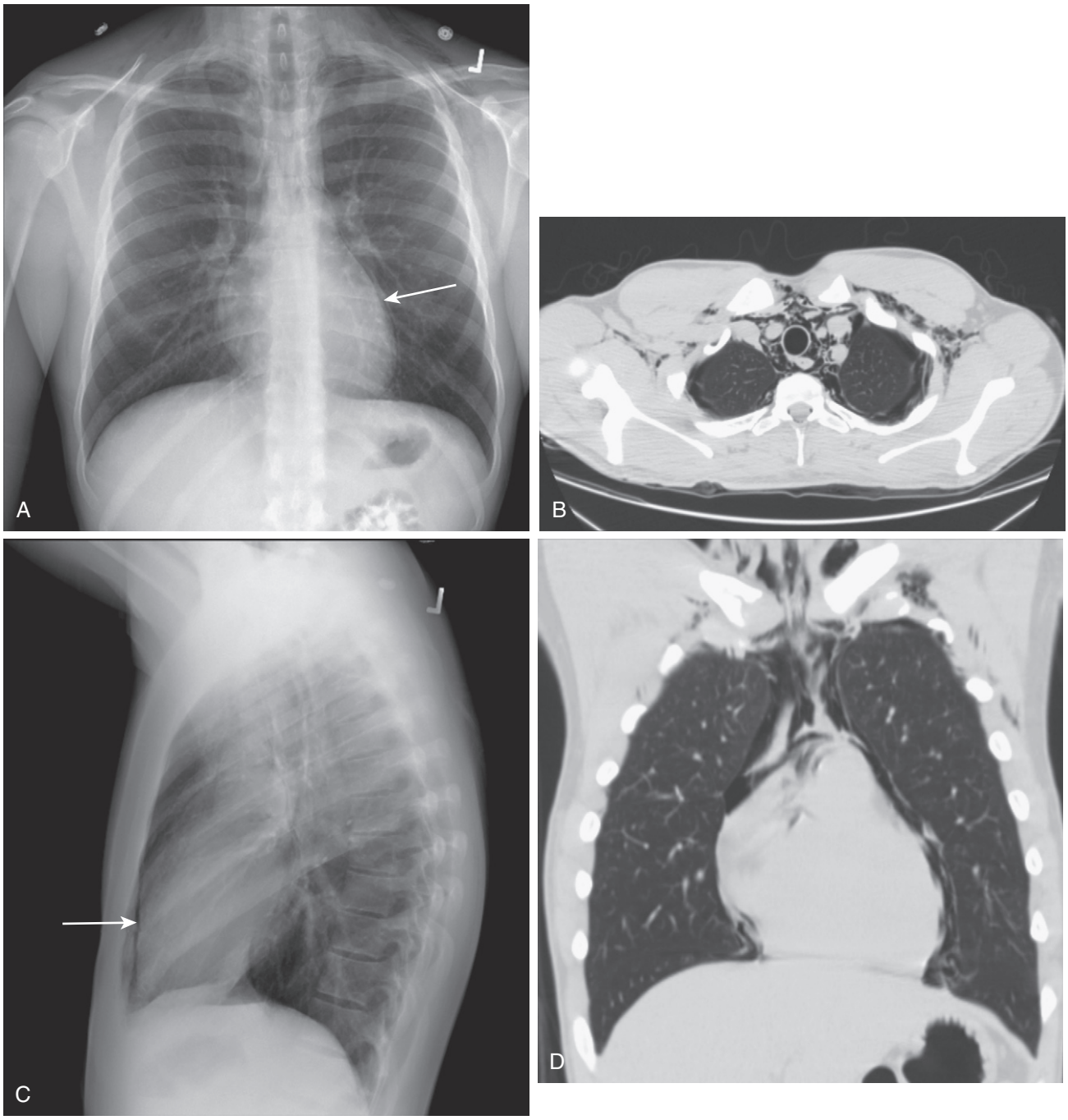


FIGURE 2-13 A 22-year-old man after a motor vehicle accident. **A** and **C,** Posteroanterior and lateral views of the chest demonstrate both pneumomediastinum *(arrow)* and subcutaneous emphysema. **B** and **D,** Axial and coronal computed tomography images demonstrating extensive pneumomediastinum.

injury has been attributed to an area of congenital weakness in the posterolateral diaphragm with central radiation of the tear. Right-sided injuries are thought to be less frequent because of the inherent increased strength of the right hemidiaphragm and the protective effect of the liver (Fig. 2-15).

Imaging of a diaphragmatic rupture may be difficult because of the great variation in the normal diaphragm. These normal variants include incidental posterolateral diaphragmatic defects (Bochdalek hernia), localized diaphragmatic thinning (i.e., eventration), and areas of diaphragmatic discontinuity. These defects advance with age and are uncommon in younger age groups.

The chest radiograph is usually the initial imaging examination used for trauma patients. The supine positioning and portable technique may limit the ability to evaluate for diaphragmatic integrity. The chest radiograph may show an intrathoracic location of abdominal viscera with possible focal constriction known as the "collar" sign (Fig. 2-16). A nasogastric tube tip may be visible above the

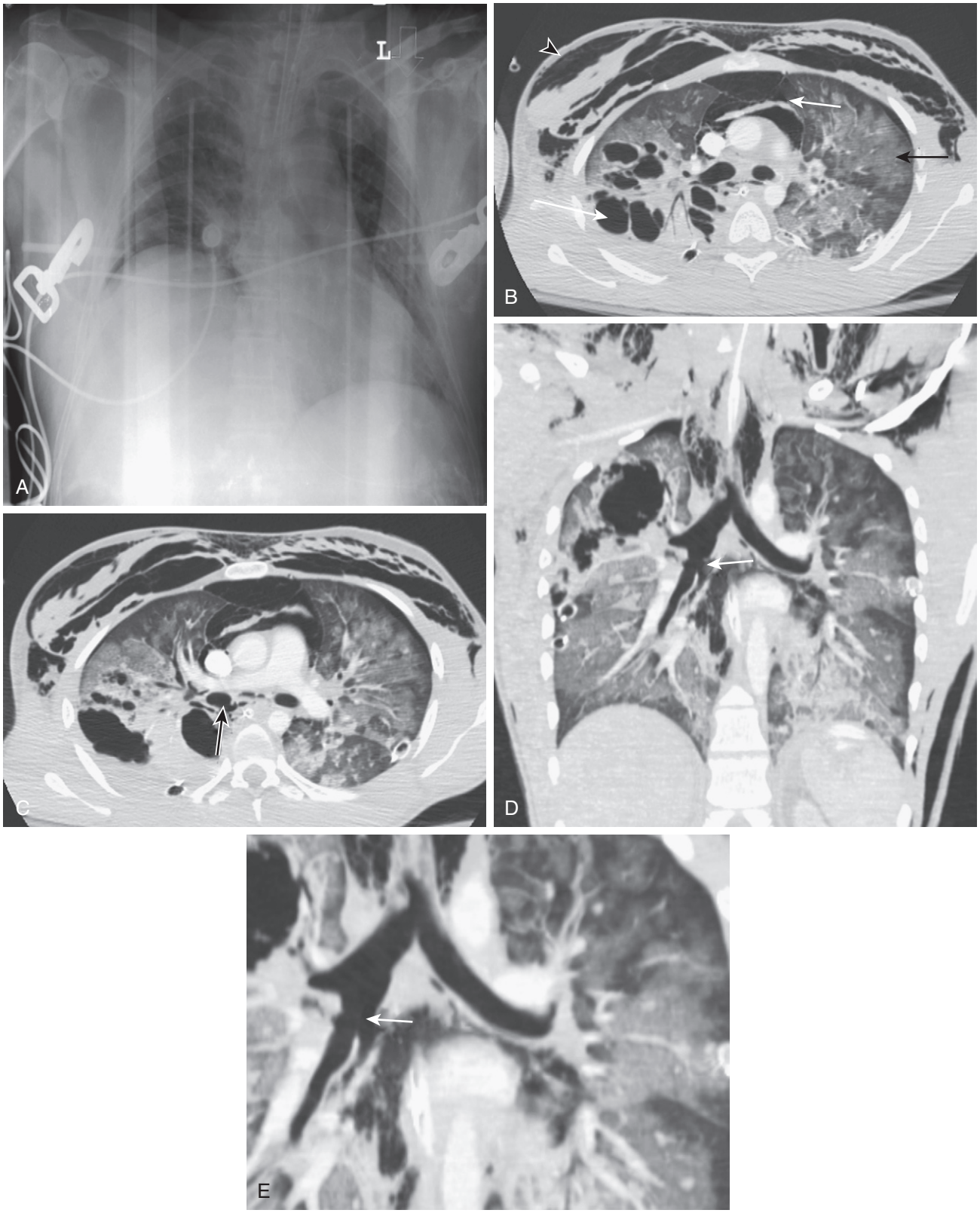


FIGURE 2-14 An 18-year-old patient after a motor vehicle crash involving a manhole cover, which blew from the street and acted as a projectile into the front window of a moving truck. The patient, an unrestrained passenger, was struck by the manhole cover and sustained maxillofacial, right humerus, right clavicle, and upper thoracic injuries, among others. **A,** A portable anteroposterior image of the chest demonstrates extensive subcutaneous emphysema and patchy opacification of the lungs consistent with contusions. **B,** An axial image demonstrates lung contusions and lacerations with extensive subcutaneous emphysema *(arrowhead)* and pneumomediastinum. **C,** An axial image demonstrates a laceration in the posterior aspect of the right bronchus intermedius *(arrow)*. **D,** A coronal image demonstrates a bronchial laceration in the bronchus intermedius *(arrow)*. **E,** Thick-section maximal intensity projection improves visualization of the laceration *(arrow)*.

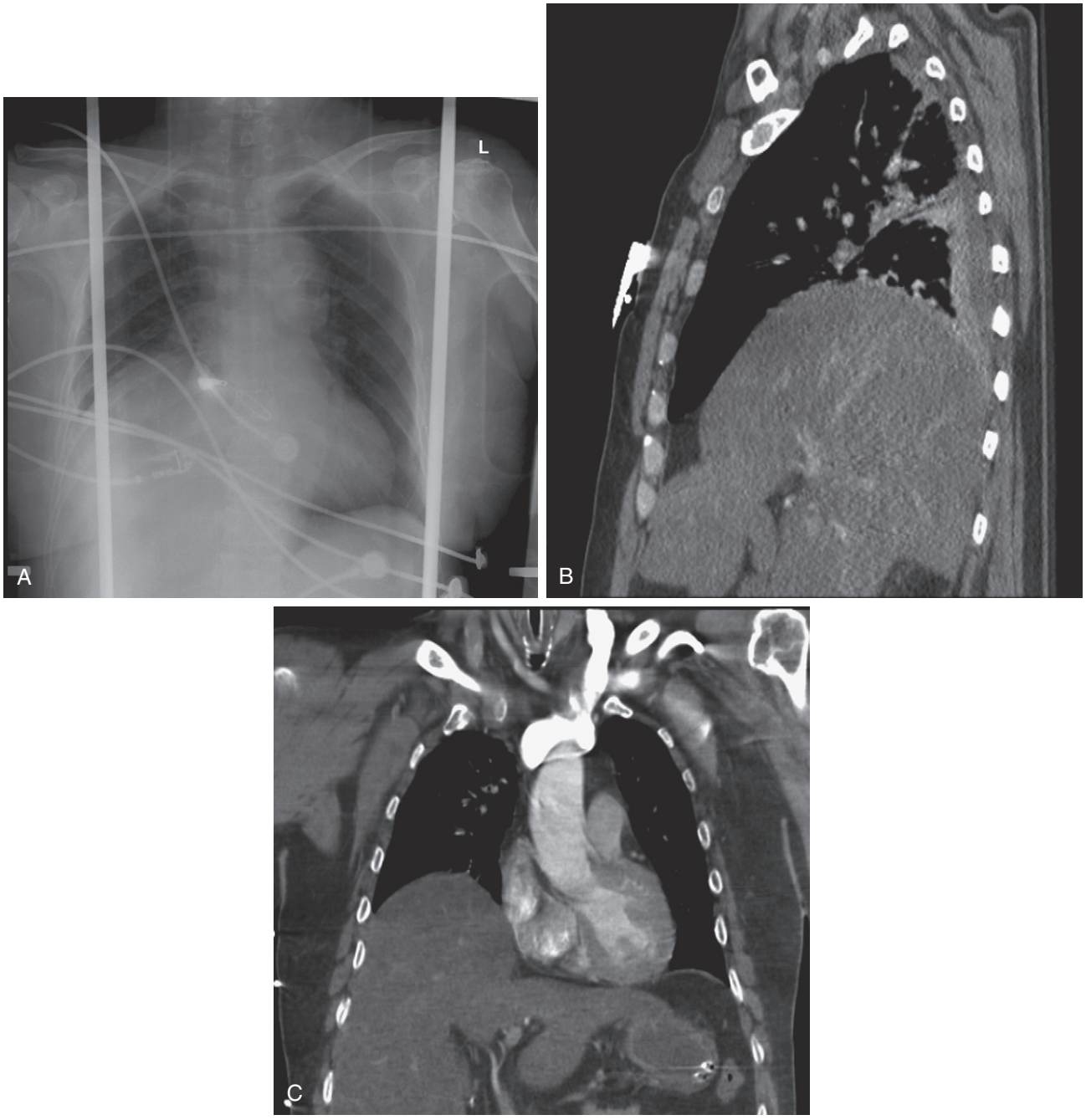


FIGURE 2-15 A 19-year-old man after a fall. **A,** The anteroposterior view of the chest demonstrates elevation of the right hemidiaphragm. **B,** A sagittal computed tomography (CT) image demonstrates that a portion of the upper third of the liver abuts the posterior chest wall, consistent with the "dependent viscera" sign. **C,** A coronal CT image shows elevation of the liver through a diaphragmatic defect.

left hemidiaphragm. Significant elevation of the hemidiaphragm without associated atelectasis may be a sign of a diaphragm rupture (Fig. 2-17).

Today, MDCT axial scans combined with high-quality coronal and sagittal reformations may show both large and small ruptures of the diaphragm, in addition to showing any abdominal organs herniated across the rupture. CT signs of diaphragm injury include the direct visualization of injury, intrathoracic herniation of viscera with a "collar" sign, the "dependent viscera" sign, and peridiaphragmatic active contrast extravasation. Additional findings of hemothorax, hemoperitoneum, and adjacent visceral injury may increase the suspicion of a diaphragm injury. Of particular note, intrathoracic herniation of viscera is highly sensitive (up to 90.9%) when limited to left-sided injury. When abdominal viscera herniate through a diaphragm tear, the edges of the diaphragm may constrict the herniated organ, resulting in the "collar." The "dependent viscera" sign is diagnostic of diaphragm rupture (Fig. 2-18). An intact diaphragm prevents the upper abdominal viscera from directly contacting the posterior chest wall in the supine patient. Conversely, when the diaphragm is torn, the viscera may lie dependently against the posterior chest wall.

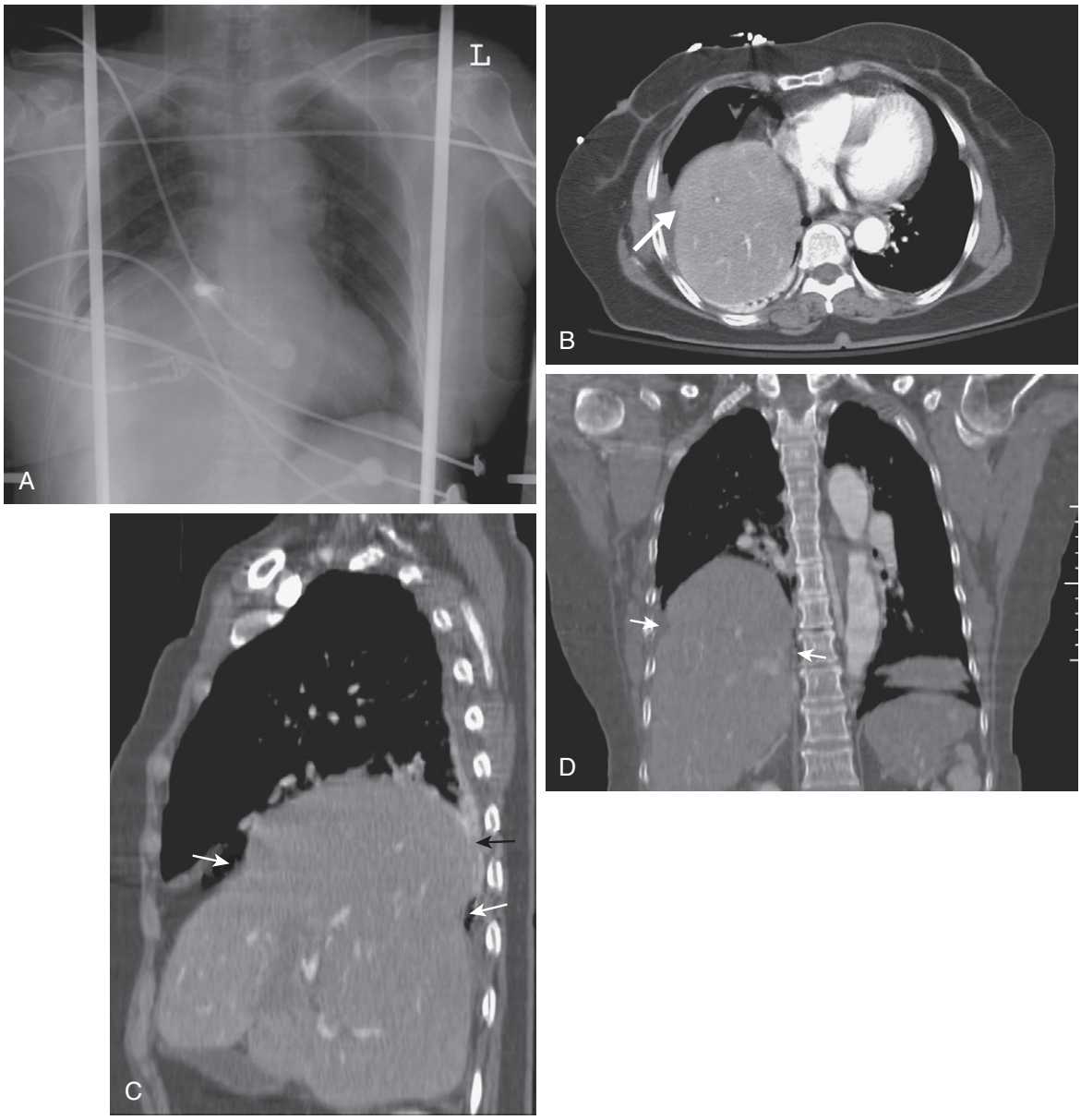


FIGURE 2-16 A 52-year-old man after a motor vehicle accident. **A,** The anteroposterior view of the chest demonstrates elevation of the right hemidiaphragm. **B,** An axial computed tomography image shows the liver in contact with the posterior chest wall. Note the impression on the liver from the diaphragm *(arrow)*. **C** and **D,** Sagittal and coronal images demonstrate the "dependent viscera" sign with a portion of the upper third of the liver in contact with the posterior chest wall *(black arrow)*. The "collar" sign can also be appreciated with the ruptured diaphragm, causing constriction of the liver *(white arrows)*.

INJURIES OF THE THORACIC SKELETON

Skeletal injuries of the thorax may be apparent on initial portable chest radiograph imaging. Therefore, a careful evaluation for rib fractures should be performed. Knowledge of the presence of rib fractures may result in a CT scan for further evaluation given that the fractures may be a harbinger of a more extensive underlying injury. Fractured ribs may lacerate the pleura or lung. Upper rib fractures indicate "high-energy" trauma, because these ribs are relatively well protected by the shoulder girdle and adjacent musculature. Upper rib fractures may be associated with injuries of the aorta, great vessels, or brachial plexus. Lower rib fractures may be associated with injuries to the liver, spleen, or kidneys. "Flail chest" occurs when five contiguous simple or three contiguous segmental rib fractures occur and result in paradoxical movement of the chest wall (Fig. 2-19). Flail chest may lead to altered chest wall mechanics and interfere with ventilation, and it may lead to respiratory failure. Older patients have a much greater incidence of rib fractures because their ribs are fairly inelastic, compared with children, in whom the incidence of fracture is low because they have more pliable and resilient ribs. The utility of chest radiographs is limited because they may show only 40% to 50% of rib fractures. Nearly all skeletal injuries are better shown with CT.

Rarely, a segment of lung may herniate through a defect in the chest wall created by a rib or costochondral

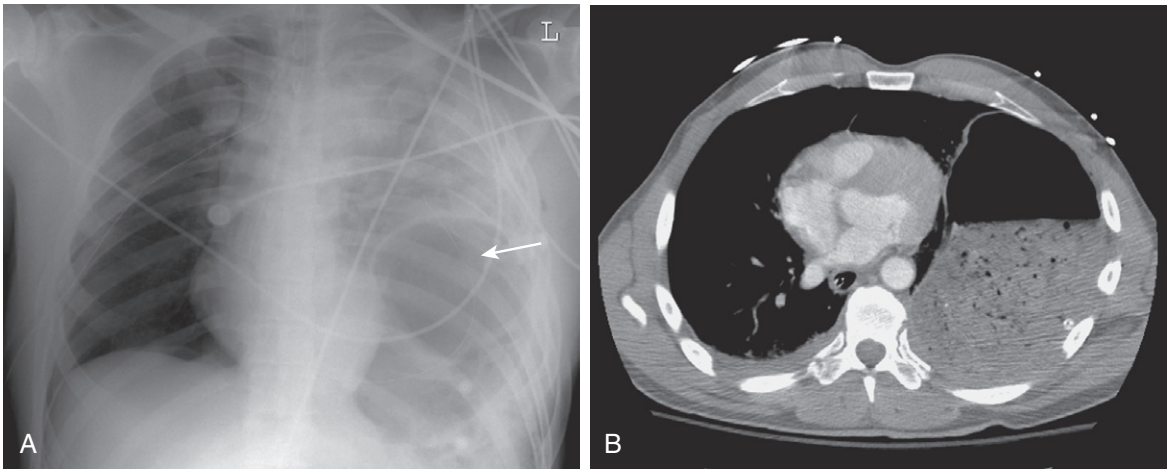


FIGURE 2-17 A 25-year-old male patient ejected from a motor vehicle after a crash. **A,** The anteroposterior view of the chest demonstrates a nasogastric tube within the lumen of the stomach, which is located in the left chest *(arrow)*. **B,** An axial computed tomography image shows the stomach abutting the posterior chest wall. Note the shift of the mediastinum to the right.

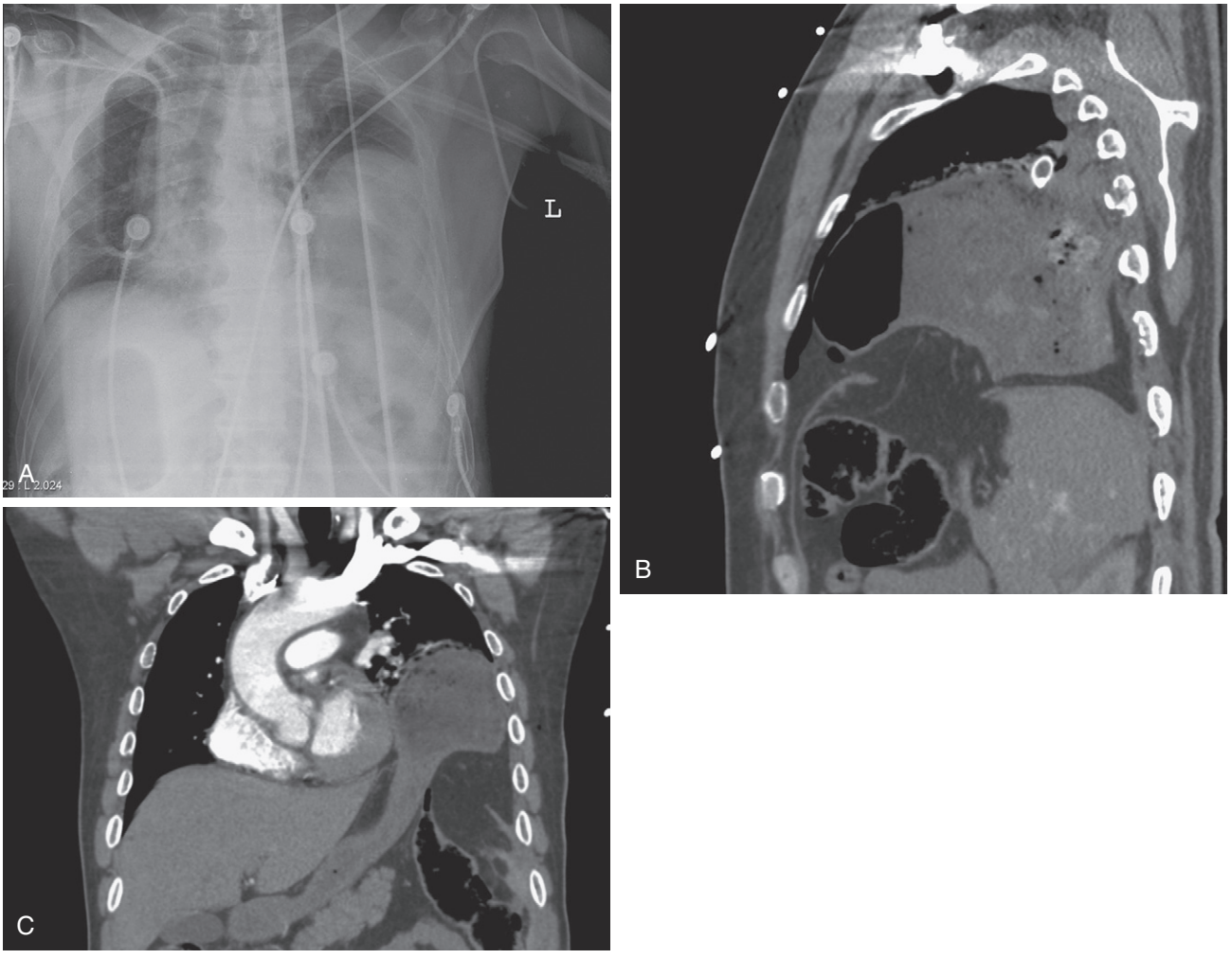


FIGURE 2-18 A 42-year-old man after a motor vehicle collision. **A,** The anteroposterior view of the chest demonstrates elevation of the left hemidiaphragm. **B** and **C,** Sagittal and coronal computed tomography images demonstrate herniation of the stomach through a defect in the diaphragm. Again, note that the "dependent viscera" and "collar" signs are present.

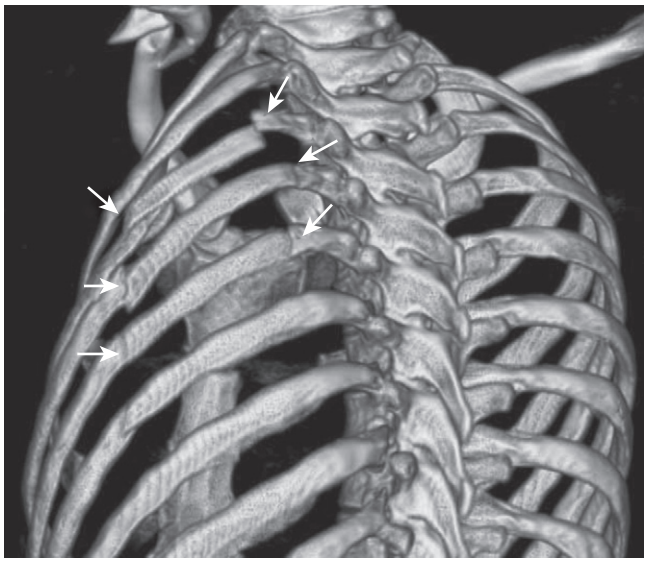


FIGURE 2-19 Three-dimensional reformation from a chest computed tomography image demonstrates segmental fractures of three posterior ribs *(arrows),* resulting in a flail chest.

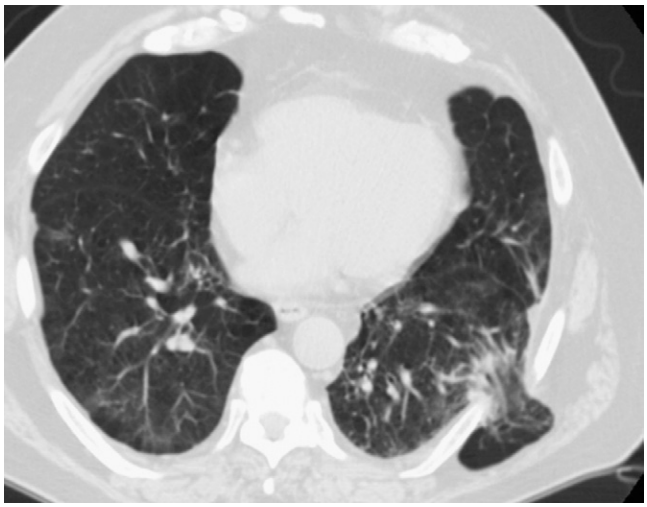


FIGURE 2-20 An axial computed tomography image demonstrates herniation of lung parenchyma through the chest wall after ejection from a motor vehicle.

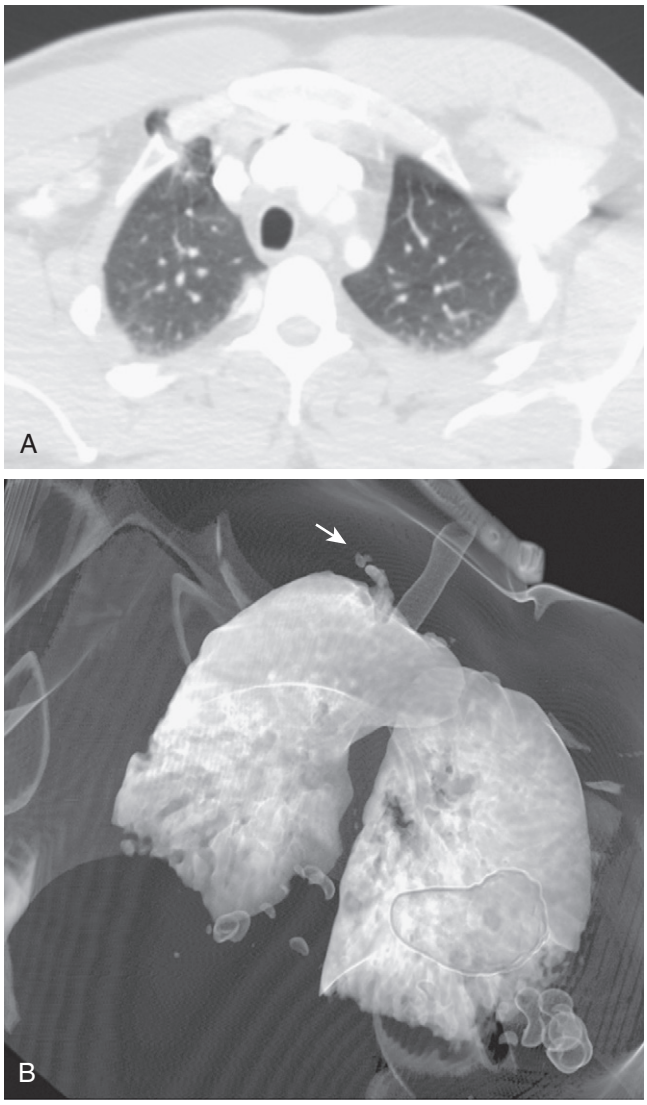


FIGURE 2-21 **A,** An axial computed tomography image demonstrates herniation of the lung through a fracture at the costochondral junction. **B,** Three-dimensional reformation shows the herniated portion of the lung *(arrow)*.

fracture (Figs. 2-20 and 2-21). The incidence of transthoracic lung herniation increases with the use of positive-pressure ventilation. Lung herniation may occur as a result of blunt chest trauma or iatrogenic surgical trauma. The herniated lung may become entrapped or strangulated. Because lung herniation may increase with positive-pressure ventilation, it may require treatment before use of mechanical ventilation and induction of general anesthesia.

Other common injuries of the thoracic skeleton include scapular fractures, sternal fractures, sternoclavicular dislocation, and thoracic spine injuries. Posterior sternoclavicular dislocation typically results from a posterior blow to the shoulder or a blow to the medial clavicle; the latter results in a posteriorly displaced clavicular head relative to the manubrium (Fig. 2-22). Serious morbidity and even death have been associated with posterior dislocation of the clavicle at the sternoclavicular joint, because the displaced clavicle head may impinge on or injure the trachea, esophagus, great vessels, or major nerves in the superior mediastinum. Anterior sternoclavicular dislocations usually result from an anterior blow to the shoulder. Anterior dislocations are more common than posterior dislocations and typically are less dangerous because there is no significant risk of great vessel injury. Sternoclavicular dislocation is generally well visualized by CT.

Sternal fractures are usually not seen on an anteroposterior portable chest radiograph and may be difficult to see on a lateral chest radiograph. However, nearly all sternal fractures are visible on CT, especially with sagittal reformations (Fig. 2-23). CT also shows associated retrosternal hematomas. Sternal fractures have a high association with both aortic and cardiac injuries. Most patients with sternal fractures are monitored for a myocardial contusion with serial enzyme analysis and telemetry monitoring (Fig. 2-24).

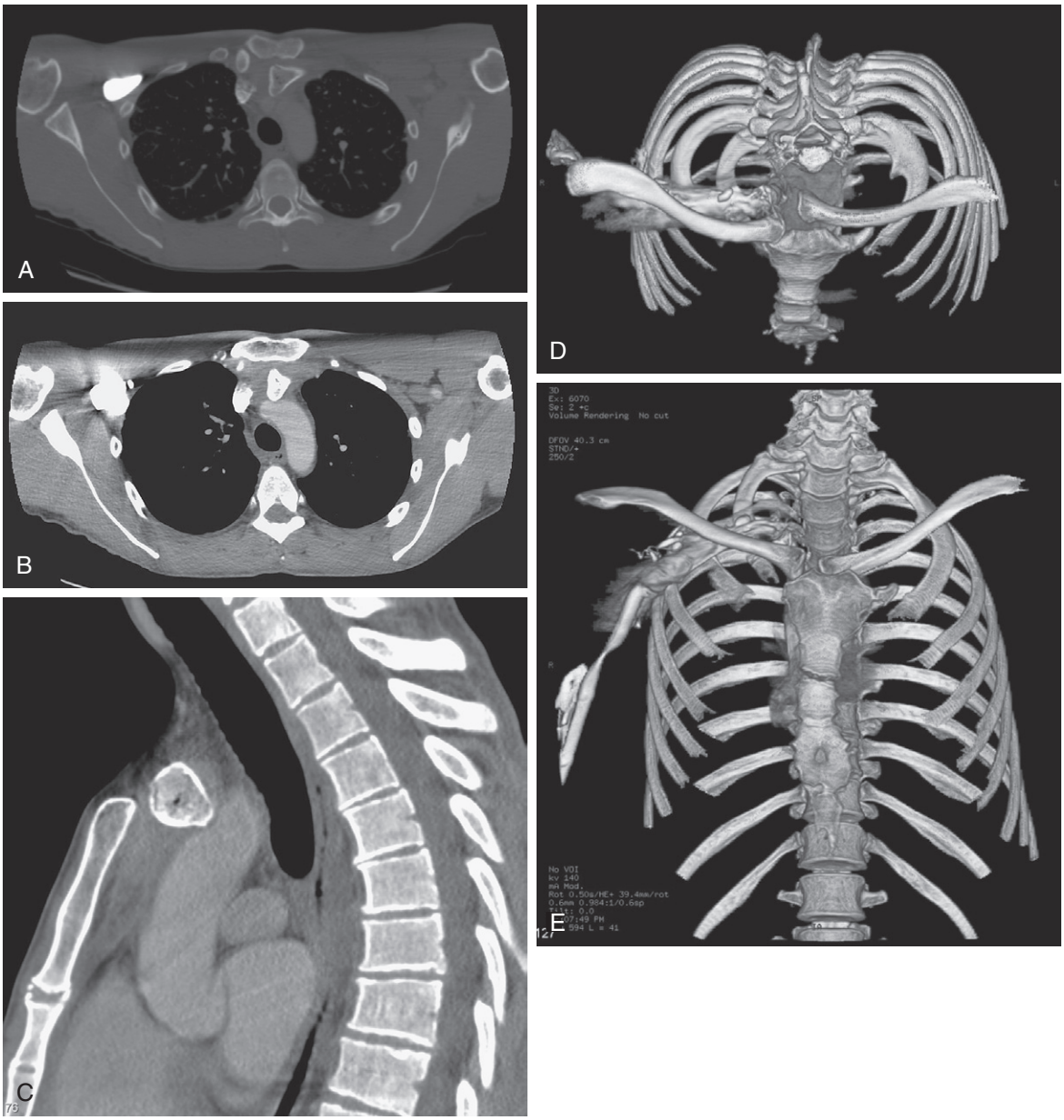


FIGURE 2-22 **A** and **B,** Axial computed tomography (CT) images demonstrate posterior displacement of the clavicular head with impingement on the underlying aorta. **C,** A sagittal CT image with posterior dislocation of the sternoclavicular joint. An adjacent hematoma is present. **D** and **E,** Three-dimensional images beautifully demonstrate the relationship of the sternoclavicular joints.

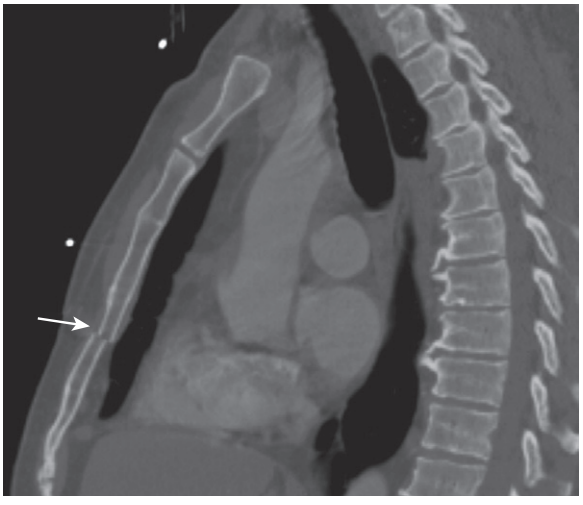


FIGURE 2-23 A sagittal computed tomography image demonstrates a fracture of the sternum *(arrow).*

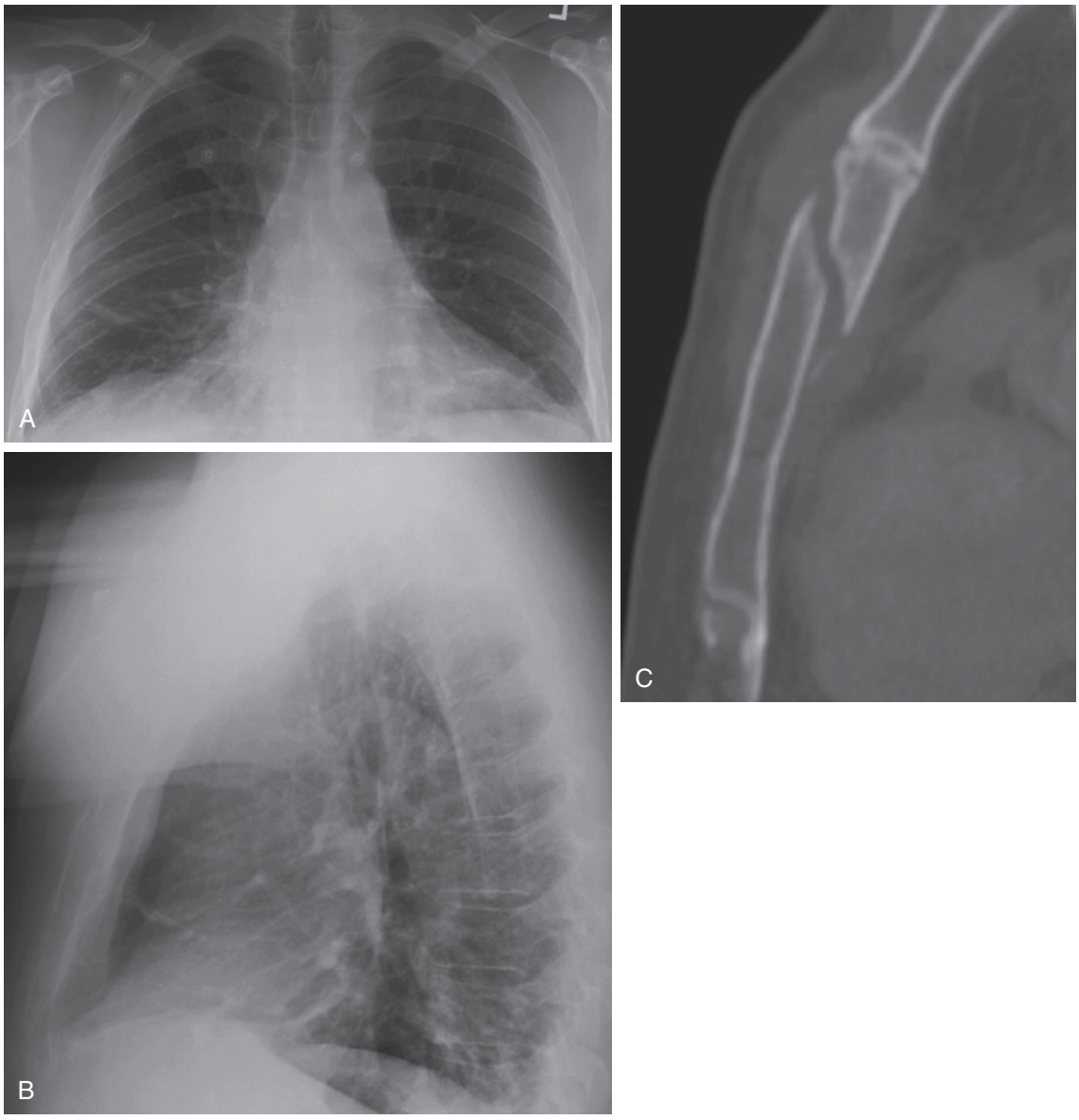


FIGURE 2-24 Anteroposterior (**A**) and lateral (**B**) radiographs of a 32-year-old male patient after a motor vehicle collision. No sternal injury can be appreciated on these images. **C,** Sagittal reconstructed images through the sternum clearly show a minimally displaced sternal fracture that was not seen on plain radiographs.

Fractures of the thoracic spine account for 15% to 30% of all spine fractures. These fractures often result from hyperflexion or axial loading forces. The most vulnerable segment of the thoracic spine is at the thoracoabdominal junction from T9 to T12. The most common fractures are anterior wedge compression and burst fractures. Multiple fractures, which often are present, are frequently at noncontiguous levels, which highlights the need to evaluate the entire spine. The thoracic spinal cord is particularly susceptible to injury because of the tapering circumference of the spinal canal, and it is easily injured by displaced bone fragments or disk material. Moreover, the blood supply of the midthoracic spinal cord is tenuous. Only 12% of patients with fracture-dislocation of the thoracic spine are neurologically intact; 62% of patients with thoracic spine fracture or dislocation have complete neurologic deficits.

Thoracic spine fractures are occasionally detected on a portable chest radiograph. The radiographic signs might include a flattened vertebral body, increased intrapedicular distance, and loss of vertebral body height. A possible sign on a plain radiograph of thoracic spine fracture is widening of the right or left paravertebral stripe, which results from a paraspinal hematoma. Between 10% and 30% of thoracic spine fractures are not visible on portable radiographs. A CT scan with coronal and sagittal reformations can both diagnose fractures with greater accuracy and better define the relationship of osseous fragments to the spinal cord. Magnetic resonance imaging is a better choice for defining spinal cord or nerve root injury.

SUGGESTED READINGS

Bergin D, Ennis R, Keogh C, et al. The "dependent viscera" sign in CT diagnosis of blunt traumatic diaphragmatic rupture. *AJR Am J Roentgenol*. 2001;177:1137–1140.

Blaisdell F, Trunkey D. *Trauma Management III: Cervicothoracic Trauma*. 2nd ed. New York, NY: Thieme; 1994.

Caskey CI, Zerhouni EA, Fishman EK, et al. Aging of the diaphragm: a CT study. *Radiology*. 1989;171:385–389.

Collins J, Primack SL. CT of non-penetrating chest trauma. *Appl Radiol Online*. 2001;30:1–10.

Dyer DS, Moore EE, Mestek MF, et al. Can chest CT be used to exclude aortic injury? *Radiology*. 1999;213:195–202.

Gavant ML, Menke PG, Fabian T, et al. Blunt traumatic aortic rupture: detection with helical CT of the chest. *Radiology*. 1995;197:125–133.

Gelman R, Mirvis SE, Gens E. Diaphragmatic rupture due to blunt trauma: sensitivity of plain chest radiographs. *AJR Am J Roentgenol*. 1991;156:51–57.

Groskin SA. Selected topics in chest trauma. *Semin Ultrasound CT MR*. 1996;17:119–141.

Iochum S, Ludig T, Walter F, et al. Imaging of diaphragmatic injury: a diagnostic challenge? *Radiographics*. 2002;22(suppl):S103–S118.

Kaewlai R, Avery LL, Asrani AV, Novelline RA. Multidetector CT of blunt thoracic trauma. *Radiographics*. 2008;28:1555–1570.

Kearney PA, Rouhana SW, Burney RE. Blunt rupture of the diaphragm: mechanism, diagnosis, and treatment. *Ann Emerg Med*. 1989;18:1326–1330.

Mazurek A. Pediatric injury patterns. *Int Anesthesiol Clin*. 1994;32:11–25.

Mirvis SE, Bidwell JK, Buddemeyer EU, et al. Value of chest radiography in excluding traumatic aortic rupture. *Radiology*. 1987;163:487–493.

Mirvis SE, Shanmuganathan K, Miller BH, et al. Traumatic aortic injury: diagnosis with contrast-enhanced thoracic CT—five-year experience at a major trauma center. *Radiology*. 1996;200:413–422.

Mueller CF, Pendarvis RW. Traumatic injury of the diaphragm: report of seven cases and extensive literature review. *Emerg Radiol*. 1994;1:118–132.

Rhea JT, Sheridan RL, Mullins ME, Novelline RA. Can chest and abdominal CT eliminate the need for plain films of the spine? *Emerg Radiol*. 2001;8:99–104.

Sangster GP, Gonzâlez-Beicos A, Carbo AI, et al. Blunt traumatic injuries of the lung parenchyma, pleura, thoracic wall, and intrathoracic airways: multidetector computer tomography imaging findings. *Emerg Radiol*. 2007;14:297–310.

Sevitt S. The mechanisms of traumatic rupture of the thoracic aorta. *Br J Surg*. 1977;64:166–173.

Shah R, Sabanathan S, Mearns AJ, et al. Traumatic rupture of diaphragm. *Ann Thorac Surg*. 1995;60:1444–1449.

Shettry VR, Bolman RM. Chest trauma. Assessment, diagnosis, and management. *Clin Chest Med*. 1994;15:137–146.

Spencer JA, Rogers CE, Westaby S. Clinico-radiological correlates in rupture of the major airways. *Clin Radiol*. 1991;43:371–376.

Steenburg SD, Ravenel JG, Ikonomidis JS, et al. Acute traumatic aortic injury: imaging evaluation and management. *Radiology*. 2008;248:748–762.

Wegner R, Crawford W, Schimpf P. Classification of parenchymal injuries of the lung. *Radiology*. 1988;167:77–82.

Williams JS, Graff JA, Uku JM, et al. Aortic injury in vehicular trauma. *Ann Thorac Surg*. 1994;57:726–730.

Wintermark M, Wicky S, Schnyder P. Imaging of acute traumatic injuries of the thoracic aorta. *Eur Radiology*. 2002;12:431–442.

Wiot JF. The radiologic manifestations of blunt chest trauma. *JAMA*. 1975;231:500–503.

Chapter 3

Abdomen Trauma

Joshua W. Stuhlfaut, Christina A. LeBedis, and Jorge A. Soto

Blunt and penetrating abdominal trauma are two of the more common indications for radiologic investigation in the emergency department setting and are common causes of morbidity and mortality among patients admitted to trauma centers. Many of these patients have multisystem injuries resulting from high-velocity mechanisms, and the full extent of these injuries is often difficult to detect clinically. A variety of imaging and nonimaging methods have been used to aid the clinician in the evaluation of patients with abdominal trauma, but in recent years ultrasonography (US) and computed tomography (CT) have become the cornerstones of diagnosis and management. The almost universal use of CT, and of US in specific settings or circumstances, has modified the diagnostic approach of the polytrauma patient and has relegated diagnostic peritoneal lavage to virtually a historical procedure. This state-of-the-art imaging allows rapid detection of potentially life-threatening injuries that can be difficult or impossible to detect clinically, especially when the presence of associated injuries may mask overt clinical manifestations or divert the attention of the admitting physician away from major intraabdominal bleeding.

BLUNT TRAUMA

Blunt trauma mechanisms leading to significant intraabdominal injuries often include compression and deceleration forces. Motor vehicle collisions are the leading cause of injury, both in the United States and throughout the world. Other common mechanisms include falls from high altitudes, assaults, projectile injuries, and sports-related trauma. Although the likelihood of injuring an individual organ depends on the specific mechanism of trauma and the vulnerability of the patient at the time of the event, the data in the trauma literature have repeatedly demonstrated that the liver and spleen are the most frequently injured organs. Other potentially injured organs include the kidneys, bowel and mesentery, pancreas, adrenals, diaphragm, intraabdominal vessels, and bladder.

During the past 2 decades, improvements in imaging technology have considerably improved our ability to detect intraabdominal injuries from blunt trauma. Of the available imaging modalities, CT and US are the two most commonly used imaging techniques when evaluating for acute traumatic abdominal injury. Other modalities such as plain film radiography, magnetic resonance imaging (MRI), nuclear scintigraphy, and catheter angiography are typically used in specific circumstances for further characterization of injuries, detection of complications from the initial injury, and treatment of such injuries.

Focused Abdominal Sonography for Trauma

Typically, US is used during the initial assessment of the patient who has sustained polytrauma, and CT images are obtained once the patient has been stabilized. Rapid assessment of the trauma patient can be performed at the bedside by experienced sonographers as part of the focused abdominal sonogram for trauma (FAST). Such scans can readily identify free fluid within the abdomen or pelvis and can help triage patients at the time of initial assessment. FAST evaluation consists of visualization of the following five spaces:

1. Pericardium (subxiphoid view)
2. Splenorenal and hepatorenal (i.e., the Morison pouch)
3. Right paracolic gutter (Fig. 3-1)
4. Left paracolic gutter (see Fig. 3-1)
5. The Douglas pouch

Multiple studies have demonstrated the benefit of a FAST study in the emergent decision-making process for acutely traumatized patients. FAST is mainly used to detect free fluid (acute hemorrhage in this setting) in the peritoneal, pericardial, or pleural spaces to direct immediate therapeutic interventions by the trauma surgeons in unstable or marginally stable patients. More recently, the development of contrast-enhanced US has improved detection of solid organ injuries and active bleeding. This technique, although not commonly used in the United States, has potential as a means of evaluating trauma patients without the use of ionizing radiation.

Computed Tomography Technique

Once the patient with abdominal trauma is stabilized, more complete imaging can be obtained with a CT examination. With multidetector CT (MDCT) scanners, imaging of the head, cervical spine, chest, abdomen, and pelvis is performed as a single examination ("panscan"). Although adequate evaluation is possible with 4- and 8-row detector scanners, most large trauma centers now use 64-row or higher detector scanners for trauma and other emergency department applications. Specific protocols regarding slice thickness, volume of the intravenous contrast material administered, timing of image acquisition, and use of an oral contrast agent are continually reconfigured and vary between institutions.

In general, optimal evaluation of the abdomen and pelvis is performed by acquiring the axial dataset of CT images after intravenous injection of iodinated contrast material during the portal venous phase of hepatic enhancement. Intravenous contrast material—100 mL injected at a rate of 3 to 5 mL per second—is routinely used for CT imaging of trauma patients. If a dual syringe power injector (the

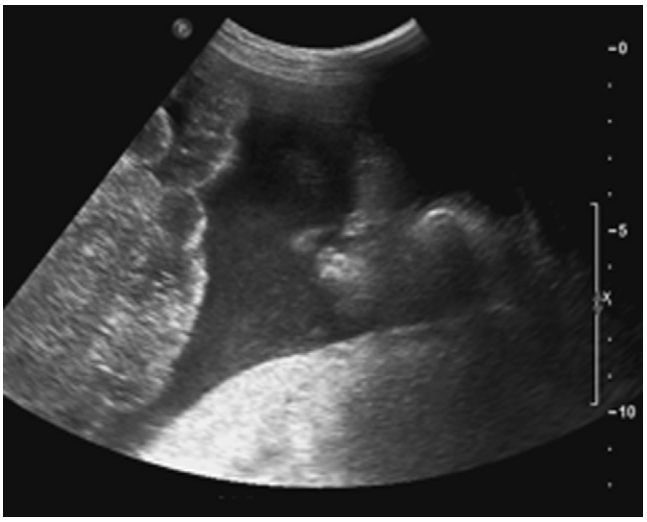


FIGURE 3-1 Intraperitoneal hemorrhage due to blunt abdominal trauma. A focused abdominal sonogram for trauma of the abdomen shows complex free fluid in the left lower quadrant in this patient after a motor vehicle collision.

preferred system) is used, the contrast bolus is followed by a 30- to 50-mL bolus of normal saline solution, typically injected at the same rate as the contrast material. This saline "chaser" ensures delivery of the complete contrast bolus into the circulation so that it doesn't remain in the tubing or the veins of the upper extremities or mediastinum.

Regardless of the scanning protocol used, modern 64-row detector (or higher) scanners provide several definite advantages compared with earlier generation scanners. The most important of these advantages is their markedly improved temporal resolution. With the development of these multidetector-row scanners, thin images (1 to 2 mm) can be acquired easily while still keeping the scan time at 8 seconds or less per body part. To facilitate review at the interpretation workstations, it is advisable to reconstruct a separate set of thicker axial images by "fusing" the thin sections. For example, images acquired with 0.625- or 1.25-mm thickness can be reconstructed at 3.75- or 5-mm thickness. In addition, sagittal and coronal reformations are now routinely generated, taking advantage of the rapid scan times that nearly eliminate motion artifact. These sagittal and coronal reformations are ideal for adequate evaluation of the diaphragm, long vascular territories, and thoracic and lumbosacral spine, and they reduce the need for lumbosacral and thoracic spine radiographs in the vast majority of patients. All series are sent to the Picture Archival Computer System and are available at the time of interpretation and for further postprocessing, if necessary. Other benefits include the ability to combine routine protocols with CT angiograms of multiple body parts while still using a single bolus of contrast material. This procedure is possible because of the increased scanner table length (2 m) available with many of the 64-row MDCT scanners. With use of scout images of the entire body, multiple complex CT examinations (including CT angiograms of the neck or extremities) are planned and combined in succession into one scan using a single injection of contrast material (Fig. 3-2).

The increased temporal resolution and decreased scan times of 64-row or higher detector scanners have resulted in a modification in the time intervals applied between the start of contrast injection and image acquisition. To ensure that all body parts are scanned at the optimum peak of contrast enhancement, it is preferable to scan the chest (30 to 35 seconds) independently from the abdomen and pelvis (65 to 75 seconds), rather than with a continuous scan encompassing all three regions and starting at approximately 60 seconds. The split-scan method avoids the potential need for rescanning the chest to obtain true CT angiography images of the thoracic aorta, essentially eliminating the need for catheter angiography for suspected thoracic aortic injury. The scan time for each body part is approximately 4 to 8 seconds (for 64-row detector scanners), with a pause of 30 to 35 seconds between scans of the chest and abdomen. The only drawback of separating the thorax from the abdomen and pelvis is in the generation of multiplanar reformations. These acquisitions are, for all intents and purposes, two different studies and necessitate separate multiplanar reformats, which makes image analysis slightly more tedious. However, the benefits of an optimal study of the aortic arch and great vessels outweigh this drawback. Some centers advocate for the use of whole-body CT angiography when imaging traumatically injured patients to detect vascular injuries and to differentiate between arterial and venous hemorrhage—important findings that can reduce morbidity and mortality when detected early. In fact, certain injuries, including contained vascular injuries of the spleen, which have unfavorable outcomes with conservative management given their propensity to lead to active extravasation, can only be seen with arterial-phase imaging.

In addition to portal venous-phase imaging, the judicious acquisition of delayed images has become an increasingly important part of the trauma CT evaluation. Delayed images can be useful in evaluating vascular injuries, as well as injuries to both the solid organs and the bowel and mesentery. Delayed CT acquisitions allow for improved characterization of solid organ injuries by helping to differentiate contained injuries (such as arterial pseudoaneurysms and arteriovenous fistulas) from uncontrolled active extravasation of contrast-enhanced blood. On delayed images, areas of active extravasation persist as hyperattenuating foci (relative to the aorta) and change configuration as blood (with contrast material) diffuses into a potential space (Fig. 3-3), whereas pseudoaneurysms show an attenuation coefficient that remains similar to the aorta, with no change in overall size or shape. Delayed images also improve detection and characterization of bladder and renal injuries, as discussed later in this chapter. Finally, delayed scans can help in the characterization of findings seen on portal venous-phase images that potentially represent foci of extravasation and could be related to the acute injury (Fig. 3-4). However, the routine use of delayed images is unnecessary and should be discouraged, because the majority of trauma CT scans performed in emergency departments today show no evidence of abdominal injury, and the additional radiation dose is unnecessary. As an alternative, delayed images can be acquired selectively and used only when solid organ or bowel injury is detected or suspected on the initial CT acquisition. Additionally, because the sole purpose of this delayed scan is to characterize an injury seen or suspected on the initial scan, techniques using a reduced radiation dose are employed, including

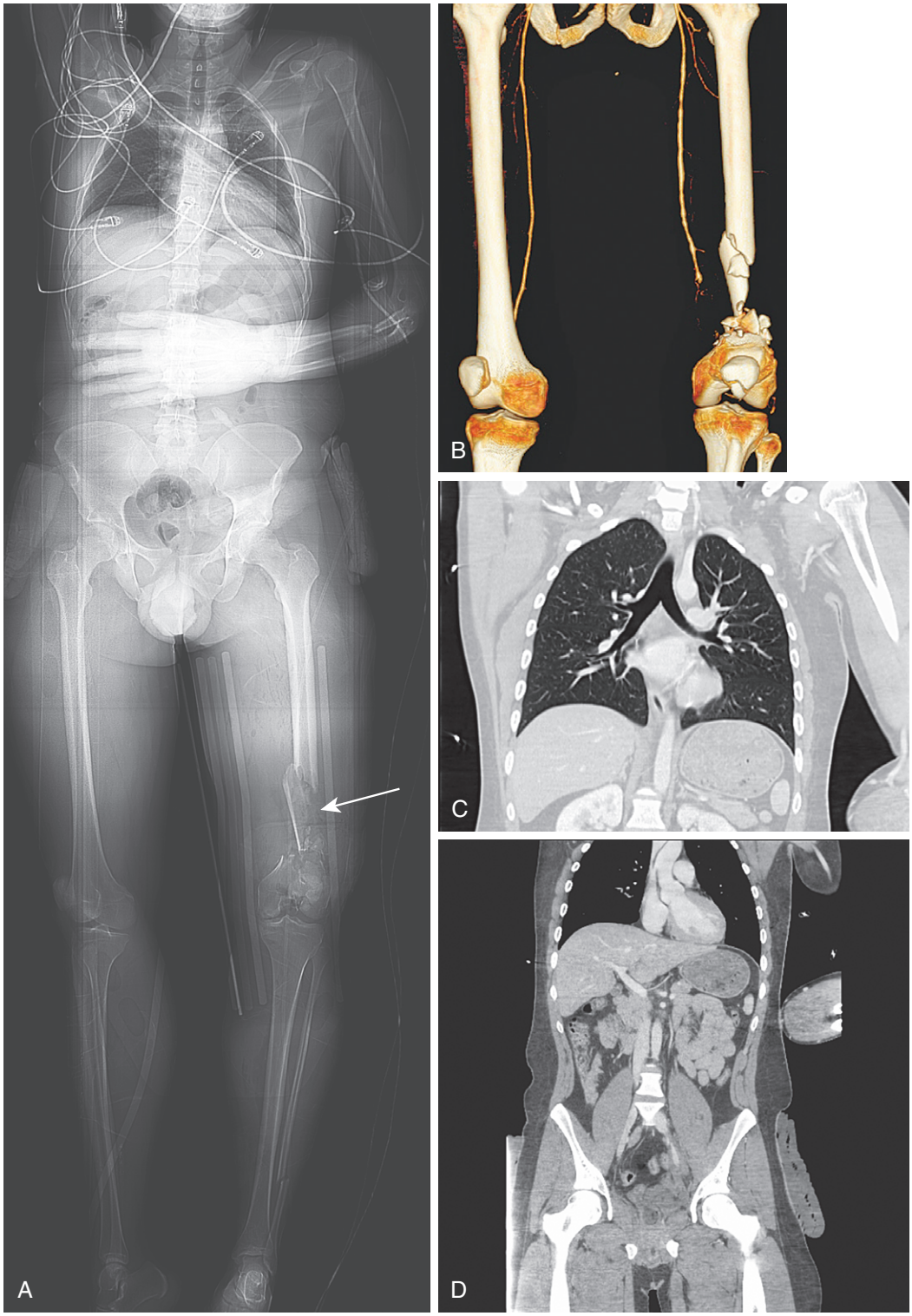


FIGURE 3-2 A 22-year-old man who was in a motor vehicle collision. **A,** A scout image obtained on a 64-detector computed tomography (CT) scanner. With use of a single scout image, multiple CT studies can be planned, including dedicated CT angiographic studies of focal areas of injury. Note the presence of a distal left femur fracture *(arrow)* in this patient who sustained significant blunt trauma. **B,** In this case, CT angiography of the extremities was requested to evaluate the peripheral arteries of the lower extremity. Maximum intensity projection reconstruction demonstrates diffuse vasospasm of the left superior femoral artery with occlusion at the level of the distal femoral fracture. Thoracic (**C**) and abdominal-pelvic (**D**) CT scans were obtained at the same time as the CT angiography. These coronal images reconstructed from the axial dataset were acquired during the arterial and portal venous phases of contrast enhancement, respectively.

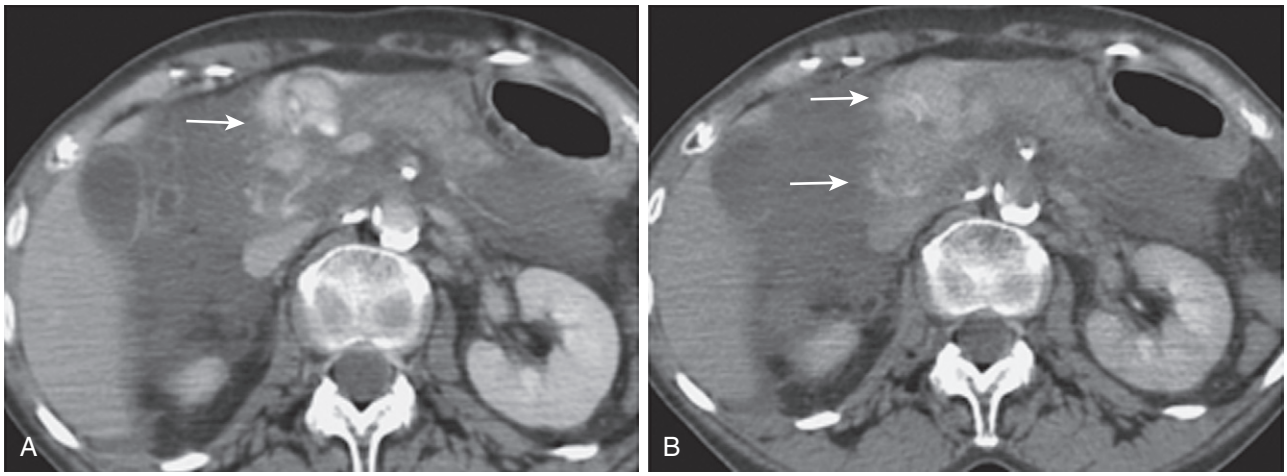


FIGURE 3-3 Active extravasation of contrast material after blunt abdominal trauma. **A,** Computed tomography (CT) obtained during the portal venous phase shows extravasation of contrast material into the peripancreatic region as a result of an acute vascular injury *(arrow)*. **B,** On the 5-minute delay CT, the contrast material continues to diffuse into the soft tissue at the site of injury *(arrows)*.

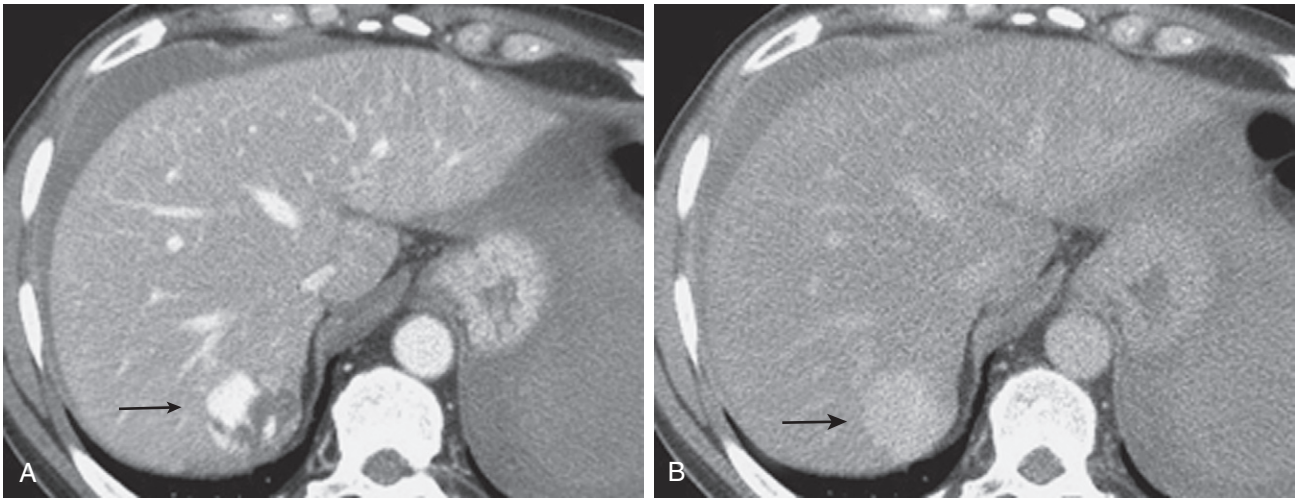


FIGURE 3-4 A hemangioma in a young female patient detected during trauma computed tomography (CT). **A,** Portal venous-phase CT shows focal puddling of contrast material in the posterior segment of the right lobe of the liver *(arrow)*. Initially, there was some question as to the presence of a focal liver injury with active bleeding. Free fluid is present adjacent to the liver margin. **B,** The 5-minute delay CT shows retention of contrast material within a focal liver lesion *(arrow)*, which excludes a focal liver injury. Instead, the diagnosis of a benign hemangioma was confirmed.

reducing the milliamperes and increasing the noise index. Iterative reconstruction techniques have led to substantial advancements in radiation dose reduction with use of CT.

In the past, oral contrast material was considered a mandatory component of trauma CT protocols. However, reports in the radiologic and surgical literature have concluded that imaging by MDCT without use of oral contrast material is similarly accurate for the detection of bowel and mesenteric injuries at the time of the initial CT evaluation. Occasionally, the initial scan may be inconclusive with regard to the presence of a bowel injury. In this case, and if there is a specific question of bowel injury on the initial scan, a follow-up CT (typically 12 hours later) with oral contrast material can be performed at the discretion of the interpreting radiologist. If oral contrast material is used to opacify the bowel in the setting of acute trauma, patients generally receive water-soluble contrast agents because of the potential for contrast extravasation into the peritoneal cavity from an acute bowel injury. Oral contrast material can be given by mouth or inserted into an indwelling nasogastric tube. The method chosen depends on the level of consciousness of the patient and associated injuries. CT imaging should not be delayed while waiting for the contrast material to migrate into the distal small bowel.

With isotropic voxel scanning, CT has truly become a multiplanar modality. As previously described, sagittal and coronal reformations have become a common component of trauma CT protocols. As the number of images generated for trauma patients increases, review of multiplanar images is one possible solution for improving interpretation efficiency. Coronal and sagittal reformations are also a useful, intuitive tool for communicating with clinical colleagues, because large amounts of information are represented on fewer images. Multiplanar image review is particularly

useful for several trauma applications, including evaluation of potential spine injuries, a more complete appreciation of often-complex injuries of solid organs, hollow viscera, and the diaphragm, and for CT angiography, where longer segments of vessels may be visualized in sagittal and coronal planes.

HEPATIC TRAUMA

The liver is one of the most commonly injured organs in the abdomen, with the prevalence of injury in patients who have sustained multiple blunt trauma between 1% to 8%. Despite the wide array of hepatic injuries that occur, including extensive lacerations and parenchymal hematomas, the vast majority of hemodynamically stable patients are treated conservatively with observation and supportive measures alone, without the need for direct therapeutic intervention. This advancement has led to significant improvements in mortality from severe liver trauma; however, nonoperative management is associated with morbidity such as bleeding, infection, abdominal compartment syndrome, and complications from biliary injury. Endovascular therapy with embolization is reserved for definitive treatment of patients with significant vascular injury and active bleeding. The growing trend toward successful nonsurgical management of liver injuries is in part related to major advances in imaging technology and CT techniques in the past decade. Specifically, the focus is to rapidly demonstrate areas of potentially life-threatening active bleeding that require immediate attention. MDCT and US are the main modalities used for the initial detection and characterization of hepatic injuries. Other modalities, such as MRI with MR cholangiopancreatography (MRCP), hepatobiliary scintigraphy, and endoscopic retrograde cholangiopancreatography (ERCP), are reserved for detecting subacute or delayed complications, such as bile duct leaks, bilomas, and biliary strictures. Because CT with proper technique is sufficient to demonstrate the extent and significance of essentially all liver injuries, catheter angiography is reserved for confirmation of CT findings that suggest major vascular injury and, especially, as a means to treat lesions that require intervention via embolization.

Ultrasonography

Sonographic evaluation of hepatic injuries is mostly limited to screening the trauma patient for indirect signs of injury, such as free fluid adjacent to the liver (as part of the FAST scan). When fluid is detected along the margin of the liver, it can appear complex and can contain an echogenic clot because of its hemorrhagic nature. Although a careful inspection of the liver can demonstrate lacerations and contusions as focal areas of parenchymal distortion, various factors limit the use of US beyond the search for free peritoneal fluid. These factors include technical limitations such as difficult access to appropriate sonographic windows and the variability in operator experience and availability. However, advances in US technology and the development of sonographic contrast agents has led to increased use of this modality for direct evaluation of the solid parenchymal organs, including the liver, especially in European countries. On noncontrast US examinations, hepatic parenchymal injuries can produce three different morphologic patterns. The most common pattern is a focal area of increased echogenicity with respect to the background liver, which is thought to correspond to the focal lacerations or hematomas seen on CT. The other two patterns are a more diffuse area of increased echogenicity and focal areas of decreased echogenicity. Liver lacerations can be difficult to detect on initial examinations; they often appear more prominent in the days after the initial injury (Fig. 3-5). The advent of sonographic contrast agents has increased the ability of ultrasound to detect acute hepatic injuries. Generally, the contrast agent is given in a bolus and the area of interest is scanned continuously for 4 to 6 minutes. On contrast-enhanced US, liver injuries are best seen during the portal venous phase of imaging. Liver lacerations can also appear as focal linear or branching hypoechoic areas, often oriented perpendicular to the liver surface. Contusions may appear as geographic areas of decreased echogenicity, often with ill-defined borders. Similar to active contrast extravasation on CT, active bleeding can be detected by the presence of microbubbles (contrast material) extending into a hematoma. In general, despite recent advances in technology, US is still considered an adjunctive test.

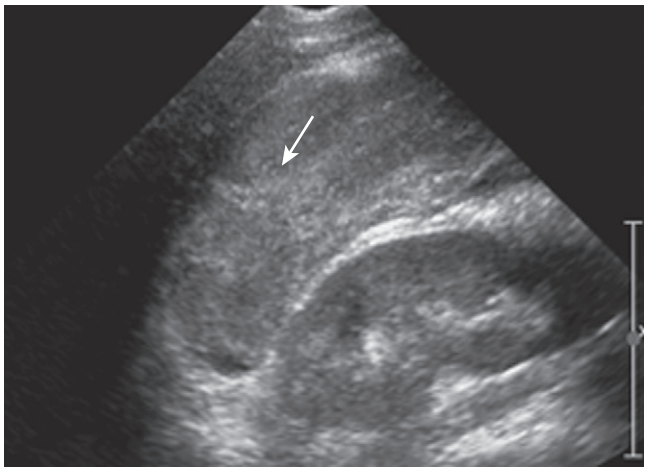


FIGURE 3-5 A liver laceration detected by ultrasound. A sagittal image of the right upper quadrant demonstrates a focal linear echogenic abnormality in the liver, compatible with an acute liver laceration *(arrow)*.

Computed Tomography

CT is the dominant imaging modality in emergency departments in the United States and most other Western countries. Improvements in the rate of CT detection of liver injuries, as well as in the proper characterization of most injuries, are some of the reasons that support the trend toward conservative management of such injuries. As previously mentioned, liver injuries are optimally seen on CT that is performed during the portal venous phase of contrast enhancement. Once liver injuries are identified, it is important to document the type and location of such injuries. In addition, it is especially important to note the presence of active extravasation of contrast-enhanced blood and the potential for injury to central hepatic vessels such as the hepatic veins and inferior vena cava. Hepatic injuries are typically characterized as either lacerations or hematomas (subcapsular or parenchymal). Although many

radiologists rely exclusively on morphologic descriptors in their report, it is useful to understand the liver injury scale that has been developed by the American Association for the Surgery of Trauma (AAST; Table 3-1). This grading scale takes into account features such as the size of subcapsular or parenchymal hematomas and lacerations, as well as evidence of active extravasation and major vascular injuries of the liver; these findings are all readily identified on well-performed CT examinations. The value of this scale lies more in the ability to communicate properly with trauma surgeons about the extent of the injury than in the ability to predict individual patient prognosis or the type of therapy necessary.

TABLE 3-1 American Association for the Surgery of Trauma Classification of Traumatic Liver Injury

Grade	Description
I	Hematoma: Subcapsular, <10% surface area Laceration: Capsular tear, <1 cm in parenchymal depth
II	Hematoma: Subcapsular, 10%-50% surface area; intraparenchymal, <10 cm in diameter Laceration: 1-3 cm in parenchymal depth, <10 cm in length
III	Hematoma: Subcapsular, >50% surface area or expanding or ruptured subcapsular hematoma with active bleeding; intraparenchymal, >10 cm or expanding or ruptured Laceration: >3 cm in parenchymal depth, <10 cm in length
IV	Hematoma: Ruptured intraparenchymal hematoma with active bleeding Laceration: Parenchymal disruption involving 25%-75% of a hepatic lobe or 1 to 3 Couinaud segments within a single lobe
V	Laceration: Parenchymal disruption involving >75% of a hepatic lobe or more than 3 Couinaud segments within a single lobe Vascular: Juxtahepatic venous injuries (i.e., retrohepatic vena cava or central major hepatic veins)

A subcapsular hematoma is typically hypodense to the enhancing liver parenchyma and appears elliptical, conforming to the confines of the liver capsule. Such collections are usually easily distinguished from perihepatic fluid. An intraparenchymal hematoma appears as an ill-defined hypoattenuating region within the liver. When seen on noncontrast CT, hematomas are typically hyperdense to the background liver parenchyma. Liver lacerations appear as hypoattenuating linear, often branching, and complex regions within the parenchyma of the liver (Fig. 3-6). Extension to the hepatic surface is very common. Even small lacerations can be associated with perihepatic blood. It is important to identify lacerations that extend to the periportal region, because patients with these injuries are at an increased risk for the development of delayed bile leaks as a result of injury of the biliary ductal system.

CT can also readily identify hepatic vascular injuries. Active extravasation of intravenous contrast material, when seen during routine portal venous phase images, suggests ongoing hemorrhage from a hepatic arterial or portal venous source. Active extravasation may be confined to the hepatic parenchyma or may be seen as hyperattenuating collections of contrast-enhanced blood accumulating in the perihepatic spaces. On delayed CT images, the focus of active extravasation typically increases in size as the material continues to diffuse throughout the area of the expanding hematoma (Fig. 3-7). In the past, active extravasation was considered an indication of the need for prompt surgical management. Currently, the demonstration of a sizable focus of active extravasation is more likely to trigger a response from the vascular interventional team for catheter angiography and coil embolization (see Fig. 3-7). Even patients with high-grade injuries can be managed conservatively using such techniques.

Injuries to major hepatic vessels also may be directly depicted with CT. For example, direct evidence of portal venous injury may be seen as abrupt termination of a branch of an intrahepatic portal vein. Parenchymal injuries may extend centrally to involve the hepatic veins and inferior vena cava, seen on CT as abrupt termination of the hepatic

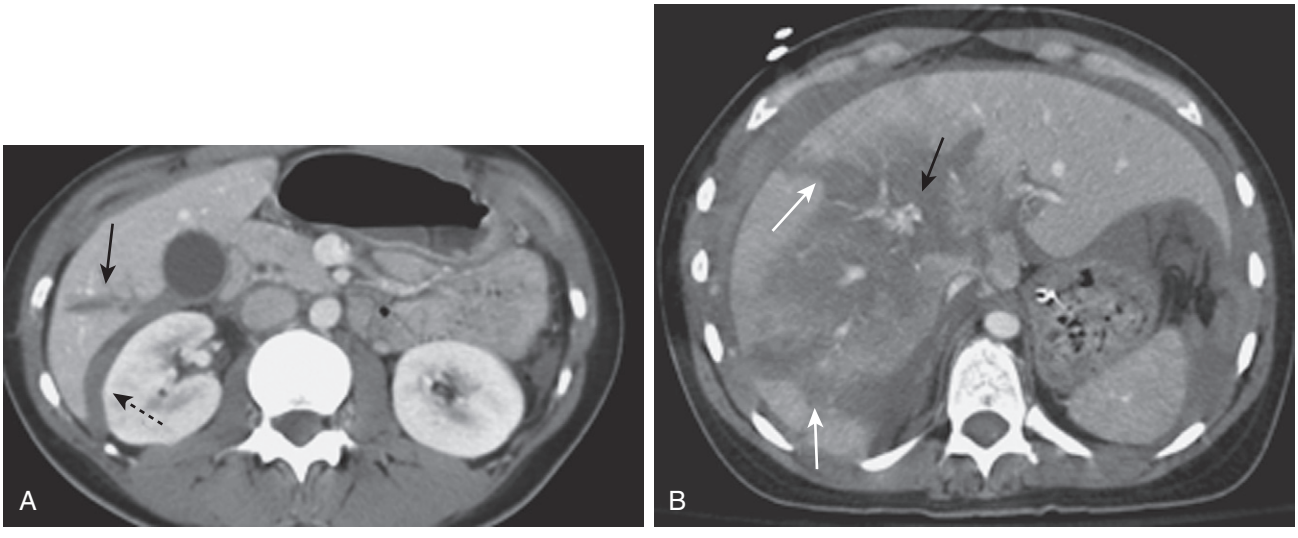


FIGURE 3-6 Computed tomography (CT) depiction of liver lacerations after blunt abdominal trauma. **A,** A portal venous-phase axial CT image demonstrates a focal liver laceration in the right lobe of the liver *(solid arrow)* with perihepatic blood in the Morison pouch *(dashed arrow)*. **B,** Portal venous-phase CT in a different patient after a motor vehicle accident shows a more complex liver laceration *(white arrows)* with a focal area of active contrast extravasation *(black arrow)*.

veins, which may just begin to enhance during routine portal venous phase images. Such major venous injuries are more likely to require surgical management, because they can cause continued bleeding and hemodynamic instability and are not readily treated by interventional radiology techniques (Fig. 3-8). Major venous injuries are also commonly associated with hepatic arterial trauma. Complications of hepatic vascular injuries include traumatic fistulas between various hepatic structures, including arterioportal structures; fistulas between hepatic arteries and biliary ducts; and, rarely, fistulas between a hepatic artery and adjacent bowel. Hepatic pseudoaneurysms also can occur as a result of hepatic injury and are extremely important to detect and document because they are at risk for delayed rupture, a potentially lethal complication. Hepatic artery pseudoaneurysms used to be considered rare, but they are now detected more frequently as a result of improvements in the spatial resolution of CT and the ability to routinely scan at the peak of contrast enhancement throughout the scan (Fig. 3-9). Pseudoaneurysms appear as hyperattenuating foci on early-phase images and demonstrate washout on delayed-phase images.

If delayed rupture and hemorrhage are suspected on the basis of clinical or laboratory parameters, CT is also the best method for detecting a subacute hemorrhage. On follow-up CT, a delayed hemorrhage presents as an increase in the size of a previous hematoma. The more acute hemorrhage appears as focal hyperattenuating material in a previously documented hematoma or along the margin of the liver, the so-called "sentinel clot" sign. In addition to pseudoaneurysm formation and delayed hemorrhage, other complications of hepatic trauma result from associated

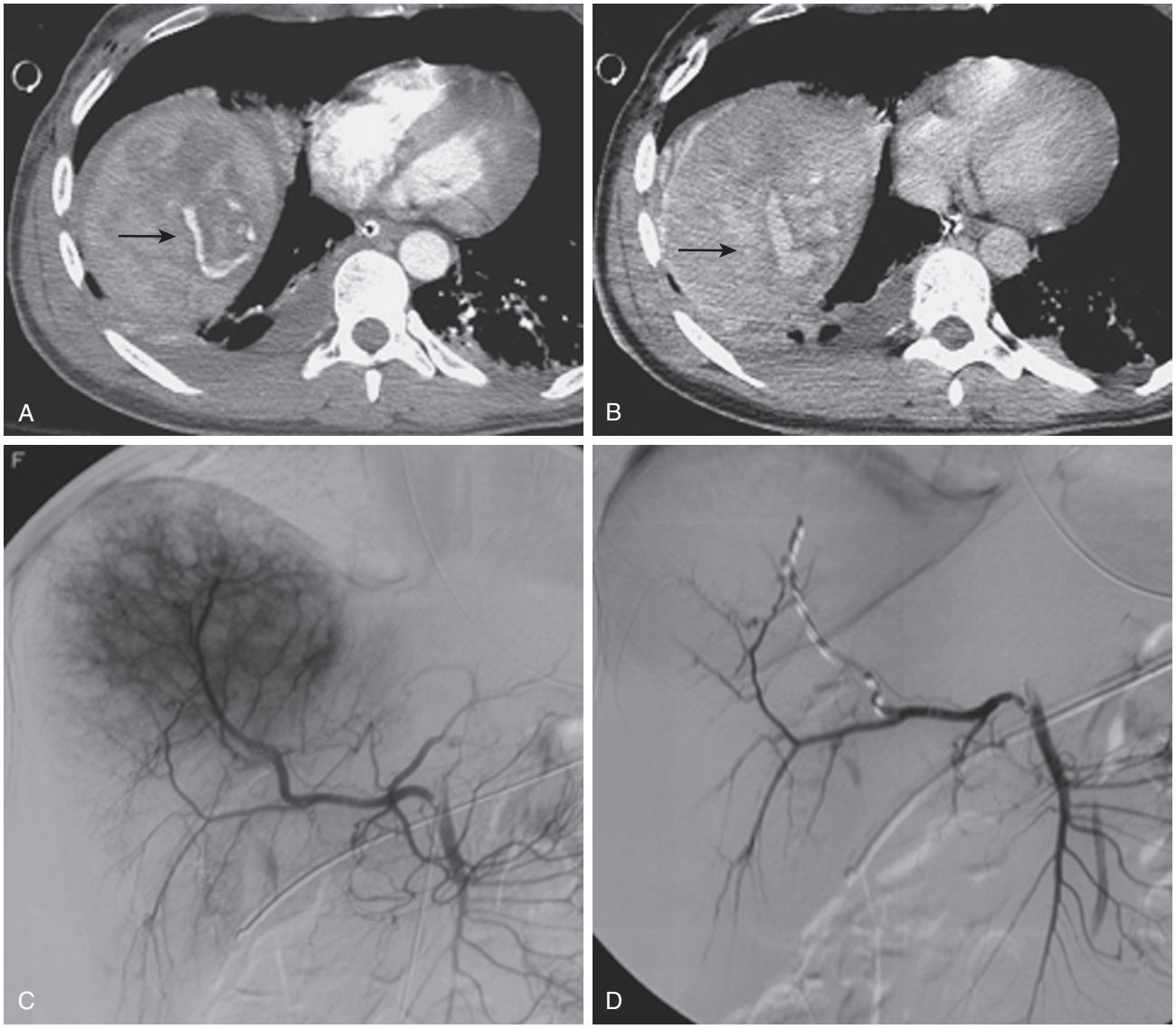


FIGURE 3-7 Active contrast extravasation after acute abdominal trauma. **A,** Axial computed tomography (CT) obtained during the portal venous phase shows a complex liver laceration with active extravasation of contrast material *(arrow)*. **B,** The 5-minute delay CT shows ongoing bleeding with contrast material continuing to diffuse into the area of injury *(arrow)*. **C,** Selective catheterization of the superior mesenteric artery (due to a replaced right hepatic artery) shows active bleeding as a large blush of contrast material in the right lobe of the liver. **D,** After embolization, the postprocedure angiogram shows resolution of the contrast blush with adequate control of active bleeding.



FIGURE 3-8 A portal venous injury after blunt abdominal trauma. An axial computed tomography scan obtained during the portal venous phase shows a complex injury involving the left lobe of the liver with active contrast extravasation. At surgery, a laceration of the left portal vein was detected that required surgical repair.

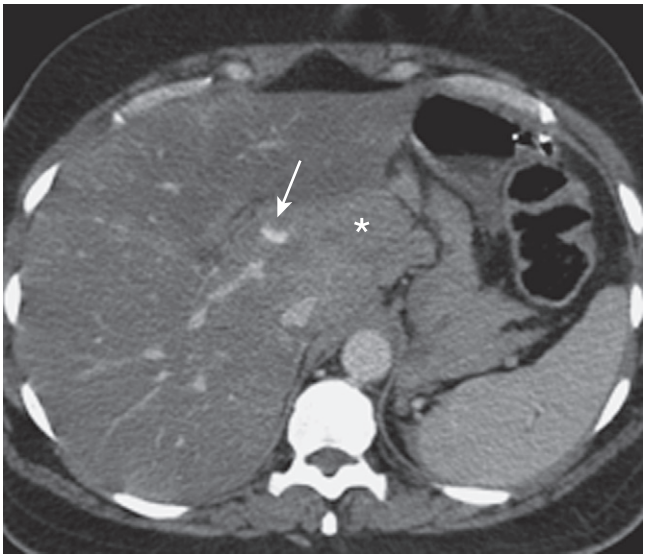


FIGURE 3-9 A hepatic arterial pseudoaneurysm after a motor vehicle accident. An axial computed tomography scan obtained during the portal venous phase shows a large hematoma in the porta hepatis *(asterisk)* with a small pseudoaneurysm of the left hepatic artery *(arrow)*. Surgical intervention was required to repair a laceration of the left hepatic artery.

bile duct injury and include the development of bilomas and abscess collections, persistent bile leaks with bile peritonitis, and bile duct strictures.

GALLBLADDER AND BILE DUCT TRAUMA

Blunt trauma may result in injury to the biliary tract, including the gallbladder and intrahepatic or extrahepatic bile ducts. The gallbladder and extrahepatic ducts are protected by the liver, which may explain the low frequency of injury to these structures with blunt trauma. The most common location of extrahepatic biliary tract injuries is the gallbladder, followed by the common bile duct. Gallbladder injury is almost invariably associated with additional significant injuries. Liver, splenic, and duodenal injuries are most common, occurring in up to 91%, 54%, and 54% of cases, respectively. Extrahepatic bile duct injuries are very rare and also are usually associated with injuries to other organs.

Gallbladder and bile duct injury may occur as a result of torsion, shearing, or compression forces. Certain factors may predispose to gallbladder injury, such as distention of the gallbladder in a preprandial state, which makes the gallbladder more vulnerable to compression injury. Injuries to the gallbladder are classified into three main categories: contusion, laceration/perforation, and complete avulsion. In general, contusions are considered to represent intramural hematomas, are the mildest form of gallbladder injury, and are treated conservatively. Lacerations and perforations are full-thickness wall injuries that require a cholecystectomy. Avulsion of the gallbladder may involve variable portions of the gallbladder and cystic duct. Any of these lesions can be associated with transection of the cystic artery and major blood loss.

Extrahepatic duct injuries may occur at sites of anatomic fixation, such as the intrapancreatic portion of the common bile duct, and are frequently caused by blunt impact or acute deceleration, possibly with compression against the spine. Elevation of the liver after blunt trauma may cause stretching of the relatively fixed common duct. Injuries to the intrahepatic bile ducts are seen in patients with severe liver lacerations.

Delayed complications of gallbladder or bile duct injury, such as sepsis, may result from leakage of bile into the peritoneal cavity and subsequent infection. Sterile bile within the peritoneum undergoes continuous peritoneal reabsorption and initially may lead to surprisingly few symptoms. Because bile in the peritoneum usually does not cause symptoms until infection occurs, bile leakage may occur for weeks or months before it is detected clinically. When signs and symptoms are present, they are nonspecific and include vague abdominal pain, nausea, vomiting, and occasionally jaundice. With an extrahepatic bile duct injury, diagnosis may be particularly difficult; up to 20% of such injuries are not detected at surgery. Injury to either extra- or intrahepatic bile ducts may also result in biliary strictures. Patients may present weeks, months, or even years later with signs of biliary obstruction or infection as a result of focal strictures that have developed at the site of the injury.

Ultrasonography

Acute gallbladder trauma is only rarely detected by US. Gallbladder wall thickening or complex echogenic fluid within the gallbladder may be present, which might suggest the presence of intraluminal blood. However, sonographic examination may be limited by underdistention of the gallbladder in a nonfasting patient. Ultrasound plays only a very small role in the detection of acute injuries of the biliary system.

Computed Tomography

Gallbladder injuries are usually diagnosed at the time of the initial trauma CT scan. Contusions appear as diffuse

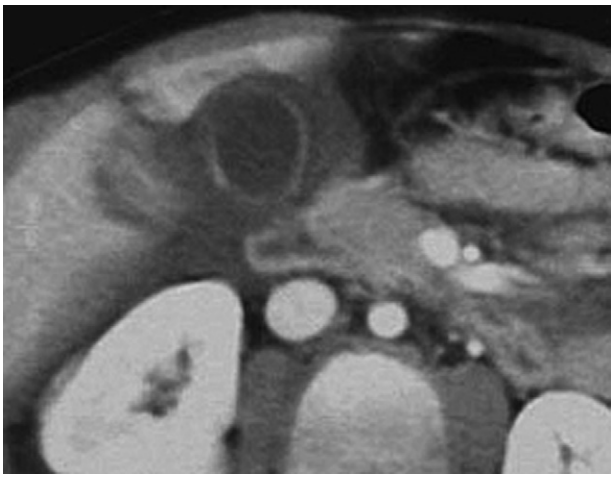


FIGURE 3-10 Avulsion of the gallbladder due to blunt trauma. Computed tomography (CT) obtained during the portal venous phase shows incomplete enhancement of the gallbladder wall with blood adjacent to the gallbladder. The gallbladder appeared inferiorly displaced at the time of CT. At surgery, avulsion of the gallbladder was confirmed, requiring cholecystectomy. *(Reprinted with permission from Gupta A, Stuhlfaut JW, Fleming KW, et al. Blunt trauma of the pancreas and biliary tract: a multimodality imaging approach to diagnosis.* Radiographics. *2004;24:1381-1395.)*

gallbladder wall thickening. The presence of pericholecystic fluid is not specific but may be an associated finding. High-attenuation fluid within the gallbladder lumen suggests hemorrhage and is a good indicator of acute injury. However, differentiation between high-attenuation sludge and blood may be difficult. Lacerations of the gallbladder wall are seen as focal disruption of the normal mural enhancement of the gallbladder wall. The presence of dense contrast material in the gallbladder lumen or in the gallbladder fossa suggests active bleeding from injury to the cystic artery. If the gallbladder is avulsed from its pedicle, it may be displaced from the gallbladder fossa (Fig. 3-10). Injury of the extrahepatic bile ducts can be difficult to diagnose with CT, because perihepatic fluid is often caused by injury to other organs in the abdomen. An intrahepatic biliary ductal injury may be suggested on follow-up CT by the development or persistence of low-attenuation perihepatic fluid collections, usually with an obvious associated hepatic injury.

Hepatobiliary Scintigraphy

Once a patient with complex liver trauma has survived the acute phase of hepatic trauma, when bleeding and possible exsanguination are the main concerns, the possibility of the development of bile leaks with complicating abscesses and sepsis must be considered and treatment provided. A recent study evaluating patients who had sustained either blunt or penetrating trauma demonstrated a high incidence of bile leaks in the setting of liver laceration (31%). An increased propensity for bile leaks was seen in these patients with increasing AAST liver injury grade and central location of the liver laceration. Free bile leaks in the setting of hepatic trauma are important because they portend a higher morbidity, with these patients undergoing more imaging studies and therapeutic procedures while having longer lengths of hospital stay when compared with posttraumatic patients who have either no biliary injury or contained bile leaks. Persistent perihepatic fluid collections and increasing low-attenuation intraperitoneal fluid are common indicators of bile leaks that require direct therapy.

Biliary scintigraphy is a simple and useful method for detecting and characterizing bile duct injuries. Hepatobiliary radiopharmaceutical agents are taken up by hepatocytes and excreted into the bile ducts. Sequential imaging over 1 to 2 hours identifies extraluminal collections that develop as the radiotracer is excreted into the biliary system and drains into the small bowel lumen. In some cases, images delayed 4 hours are necessary when no evidence of injury is found on the initial image acquisition. With hepatobiliary scintigraphy, accumulation of the radiopharmaceutical agent outside the bile ducts is indicative of a bile leak, which can be either contained (see Fig. 3-12) or free if it extends into the peritoneal cavity.

Small bilomas can be treated conservatively and monitored, whereas larger collections may require percutaneous drainage, especially in the presence of superimposed infection. Early detection of bile leaks allows proper treatment through the use of either percutaneous drainage or ERCP with a sphincterotomy and placement of a stent (Fig. 3-11). A possible delayed complication of bile duct injury is the development of a bile duct stricture with obstruction and infection. MRCP is an ideal method for following up on hepatobiliary injuries to assess for the possible development of strictures. An emerging tool for biliary imaging in trauma patients is MRI with use of hepatobiliary agents such as gadoxetic acid (Eovist), which provides both anatomic and functional evaluation of the hepatobiliary system.

SPLENIC TRAUMA

The spleen is the most commonly injured organ in the abdomen when blunt trauma is sustained. In the past, an exploratory laparotomy with a splenectomy was the dominant treatment for splenic injuries. However, improvements in our understanding of the natural history of splenic injuries and in the quality of and access to imaging methods have modified treatment algorithms. Nonoperative management is now used initially for the vast majority of splenic injuries. Splenectomy is reserved for the most complex injuries in unstable patients who do not respond to resuscitative efforts and for patients in whom conservative therapy fails. Patients who would otherwise be candidates for conservative management but who require a laparotomy for other abdominal injuries may still undergo a splenectomy.

Splenic trauma is typically difficult to detect clinically. Patients can present with left upper quadrant pain, although associated severe injuries may confound the clinical picture or distract attention from the spleen or abdomen. Instead, most injuries are detected with either US or CT imaging studies performed in these trauma patients. The portable radiograph performed upon admission may demonstrate left rib fractures and alert trauma surgeons to the possibility of an underlying splenic injury. However, plain film radiographs have no role in the direct demonstration of splenic injury. Once an injury is detected, and while the resuscitation process is ongoing, the interventional

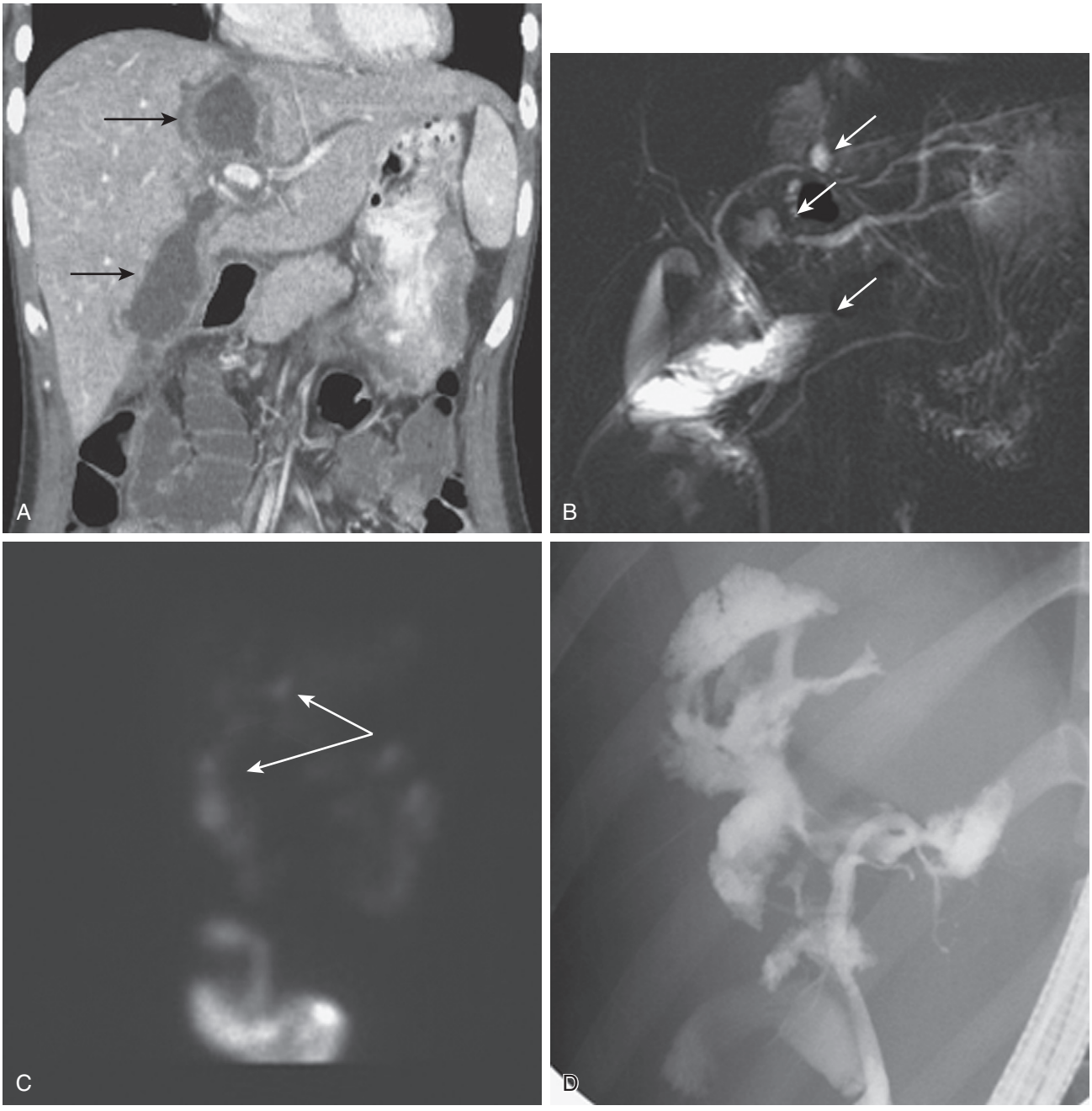


FIGURE 3-11 A biliary leak with biloma after blunt abdominal trauma. **A,** A coronal computed tomography image obtained several days after the initial trauma demonstrates two focal fluid collections in the intrahepatic and perihepatic regions *(arrows)*. **B,** Coronal thick slab magnetic resonance cholangiopancreatography also demonstrates the presence of several extraluminal fluid collections as focal areas of increased signal on this fluid-sensitive sequence *(arrows)*. **C,** A hepatobiliary scan obtained in the anterior projection confirms the presence of bilomas with radiotracer located outside the expected lumen of the biliary tree *(arrows)*. **D,** Endoscopic retrograde cholangiopancreatography was performed to further characterize the injury and for possible stent placement and confirms the presence of a bile duct injury.

radiology team should be alerted, because catheter angiography may become necessary for treating vascular injuries, thus avoiding the need for a splenectomy. However, a splenectomy may still become necessary if the injury is severe and bleeding cannot be controlled by nonoperative means.

Splenic injuries are characterized as either hematomas or lacerations. As with the liver, the AAST has developed a scale for grading splenic trauma that is still commonly used for describing specific patterns of injury (Table 3-2). The prognostic implications of this scale are limited, because even complex injuries can heal without specific therapy. It is important to describe the type of injury, the location (parenchymal vs. subcapsular), the size of the hematoma or laceration, and all associated complications. Severe injuries can affect the hilar vascular structures, leading to total or subtotal organ devascularization. Injuries to the splenic

TABLE 3-2 American Association for the Surgery of Trauma Classification of Traumatic Splenic Injury

Grade	Description
I	Hematoma: Subcapsular, <10% of surface area Laceration: Capsular tear, <1 cm of parenchymal depth
II	Hematoma: Subcapsular, 10%-50% of surface area; intraparenchymal hematoma, <5 cm in diameter Laceration: 1-3 cm in parenchymal depth not involving a parenchymal vessel
III	Hematoma: Subcapsular, >50% of surface area or expanding or ruptured subcapsular or parenchymal hematoma; intraparenchymal hematoma, >5 cm in diameter Laceration of >3 cm parenchymal depth or involving trabecular vessels
IV	Laceration of segmental or hilar vessels producing major devascularization (>25% of the spleen)
V	Completely shattered spleen Vascular hilar injury with devascularized spleen

artery or branch vessels can cause active bleeding, which can be easily demonstrated with current MDCT examinations. Finally, splenic injuries can lead to the development of contained vascular injuries that are often seen only in an arterial phase; these injuries are extremely important to note, because patients with such injuries have an increased risk of delayed morbidity and mortality as a result of rupture.

Ultrasonography

Splenic injuries can be detected by US evaluation of the abdomen and may be suspected based on the results of the initial FAST scan. However, the parenchymal injury can be difficult to detect. Instead, indirect evidence of injury is often identified, including a hemoperitoneum and a focal echogenic clot adjacent to the spleen. Splenic hematomas are heterogeneous and hypoechoic compared with the background spleen (Fig. 3-12). The borders are ill defined, and no associated mass effect or vessel displacement is present. Lacerations appear as linear or branching areas of decreased echogenicity compared with the normal spleen and often extend to the splenic surface. Although they are not commonly used in many countries, sonographic contrast agents have been shown to improve the ability to detect splenic injuries. The spleen can be readily imaged with contrast-enhanced US because it retains the contrast agent for up to 5 to 7 minutes after intravenous injection. If the vascular pedicle is injured, there may be total or subtotal loss of enhancement in the spleen. Active contrast extravasation can be identified as a hyperechoic collection that develops in the early phase after injection of the contrast agent.

Computed Tomography

MDCT is the main imaging modality used to detect, characterize, and monitor splenic trauma. Most splenic injuries are optimally detected on portal venous-phase images of the abdomen after intravenous injection of contrast material. Splenic hematomas appear as focal areas of decreased attenuation compared with the background-enhancing

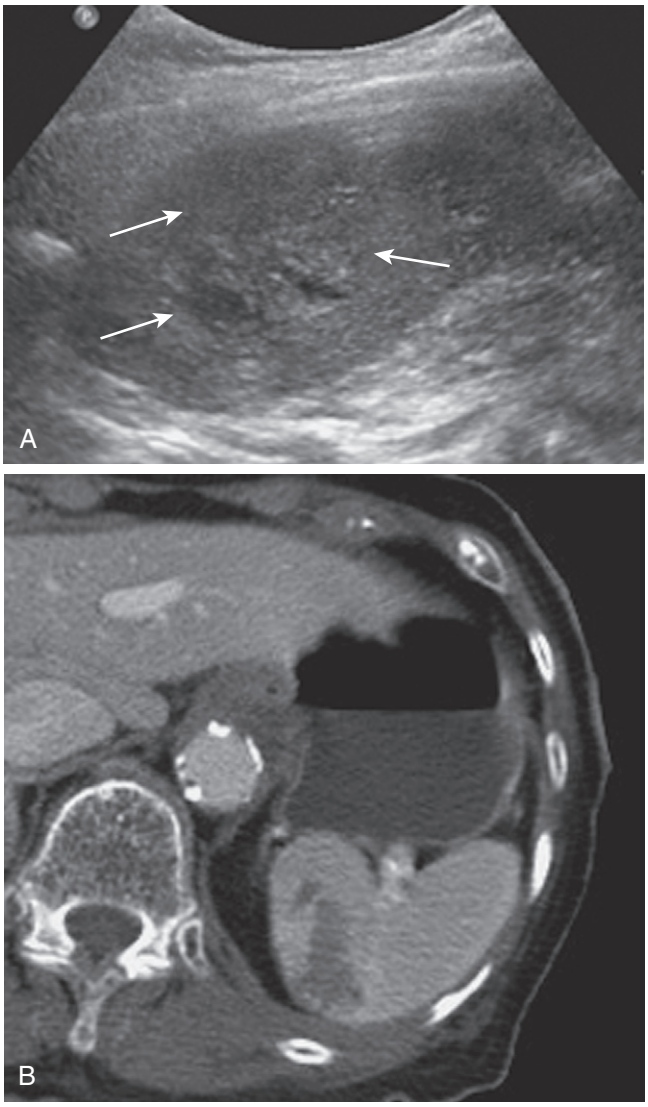


FIGURE 3-12 A splenic hematoma. **A,** A focused ultrasound of the left upper quadrant demonstrates a focal region of heterogeneity in the spleen *(arrows),* suggestive of an acute splenic injury. **B,** Computed tomography performed after the initial ultrasound confirms the presence of an acute splenic hematoma.

splenic tissue (Fig. 3-13). Hematomas can be intraparenchymal or subcapsular. Lacerations appear as linear, irregular, and often branching areas of decreased attenuation (Fig. 3-14). Higher-grade injuries tend to be larger and involve more of the total volume of the spleen (Fig. 3-15). Injuries of the vascular pedicle lead to focal wedge-shaped areas of decreased enhancement, whereas severe injuries of the vascular pedicle may produce a markedly decreased or absent enhancement of most or all of the spleen on CT. In addition to describing the type of injury, it is important to note the presence of either active contrast extravasation or contained vascular injury. Active contrast extravasation in the spleen is characterized on CT by contrast density outside the expected lumen of the vessel that is similar or higher in attenuation compared with the adjacent vessels (Fig. 3-16). The shape is often irregular, with poorly defined margins as a result of the diffusion of the contrast material into the site of the injury. Typically, contrast extravasation is identified within the splenic parenchyma



FIGURE 3-13 A splenic hematoma after a motor vehicle collision. Axial computed tomography during the portal venous phase demonstrates a wedge-shaped hypodense region in the spleen *(arrow),* consistent with a subcapsular hematoma and characterized as a grade II injury according to the American Association for the Surgery of Trauma trauma scale (see Table 3-2).



FIGURE 3-14 A splenic laceration after a motor vehicle accident. An axial computed tomography image obtained during the portal venous phase of contrast enhancement demonstrates a focal linear laceration in the spleen *(arrow)* that extends from the anterior to posterior surface, fracturing the spleen into two fragments. A perisplenic hematoma *(asterisk)* is evident posterior to the area of the injury.



FIGURE 3-15 A shattered spleen is shown on an axial computed tomography image obtained during the portal venous phase of contrast enhancement after a motor vehicle injury. No definable splenic tissue is present in the left upper quadrant. Instead, the shattered splenic tissue is surrounded by a large amount of perisplenic hematoma that extends to the midline. Blood is also present along the surface of the right lobe of the liver. The patient required an emergent splenectomy to control the severe blood loss from this acute splenic injury.

or in a hematoma adjacent to the site of laceration in the perisplenic spaces. In contrast, contained vascular injuries of the spleen are contained extraluminal collections that often have a more round or ovoid appearance (Fig. 3-17). These injuries are usually confined to the splenic parenchyma. Recent literature reports that contained vascular injuries of the spleen are often only seen on an arterial phase. On delayed CT images, active contrast extravasation shows a change in shape and usually an increase in size as the material continues to diffuse into the site of injury (see Figs. 3-16 and 3-17). On the other hand, a contained vascular injury does not change in size or shape at different points in time, and the attenuation of the contained vascular injury tends to follow that of adjacent arteries such as the splenic artery or aorta (see Figs. 3-18 and 3-19). Of note, some contained vascular injuries of the spleen can only be detected on arterial phase images (Fig. 3-18).

Other focal vascular injuries include the development of arteriovenous fistulas. Such injuries can be difficult to distinguish by CT alone and are better characterized with catheter angiography. Once active contrast extravasation or a focal vascular injury such as a pseudoaneurysm is detected, the need for catheter angiography and possible endovascular therapy should be carefully assessed. Although practices vary among institutions, patients with proved active extravasation are more likely to undergo a splenectomy, whereas contained vascular injuries are more amenable to endovascular therapy with coil embolization.

PANCREATIC INJURY

Traumatic injuries of the pancreas are much less common than injuries of the liver and spleen. In fact, pancreatic injury is reported to occur in less than 1% of all patients who experience blunt abdominal trauma. However, detection of such injuries is critical, because a delay in diagnosis can be a cause of significant morbidity and mortality. Unlike

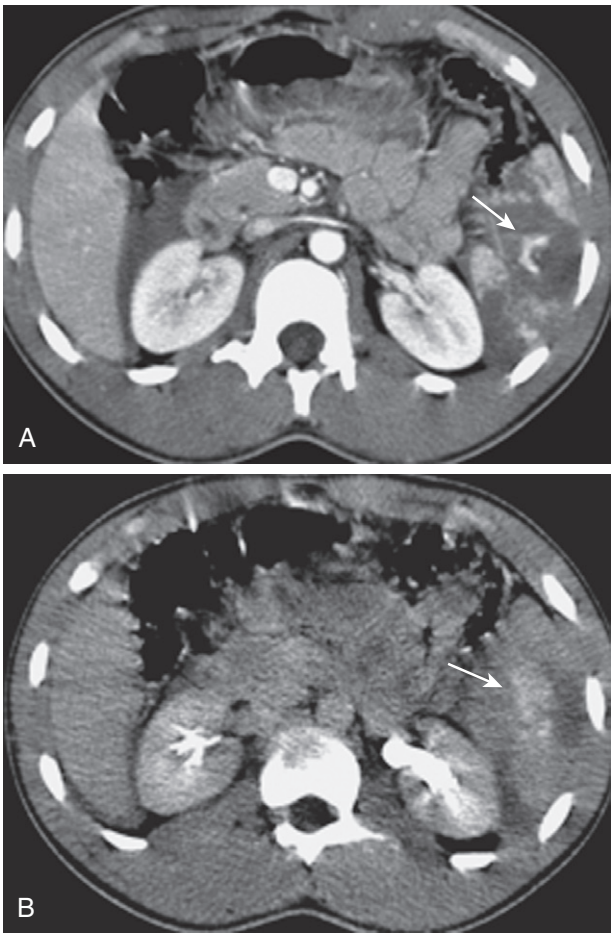


FIGURE 3-16 A splenic injury after blunt abdominal trauma. **A,** An axial computed tomography image obtained during the portal venous phase of contrast enhancement demonstrates a complex splenic injury containing both complex lacerations and parenchymal hematoma. Active extravasation of contrast material is present *(arrow)*. **B,** A delayed image obtained 5 minutes later with a decreased radiation dose (100 mA) confirms the presence of active extravasation (as opposed to a contained vascular injury) by demonstrating continued diffusion of the contrast material into the surrounding parenchymal hematoma *(arrow)*.

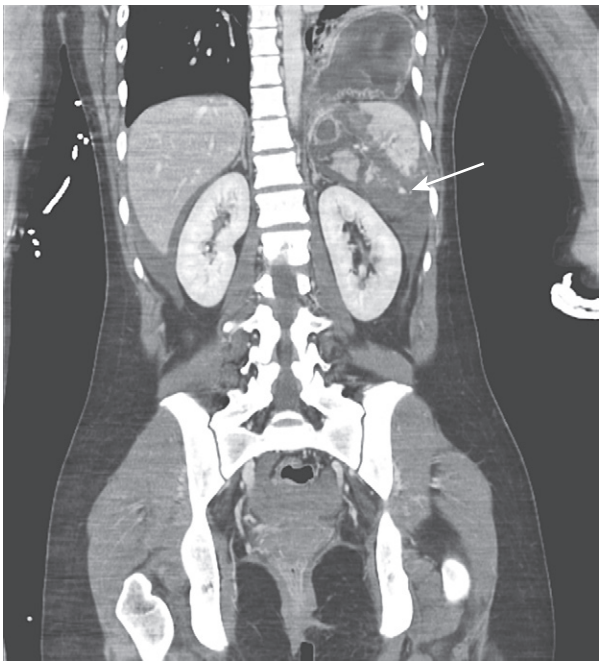


FIGURE 3-17 An 18-year-old woman who had been in a motor vehicle collision. A coronal contrast-enhanced computed tomography image demonstrates a shattered spleen with active extravasation of intravenous contrast *(arrow)* and a left diaphragmatic rupture with the stomach in the left hemithorax.

most injuries to the liver and spleen, injuries of the pancreas can be extremely difficult to detect and require a careful evaluation of MDCT images and the use of complementary studies, such as MRCP and ERCP.

The pancreas is vulnerable to crushing injury from impact against the adjacent vertebral column. Two thirds of pancreatic injuries occur in the pancreatic neck (i.e., the junction of the body and head) and body, and the remainder are equally distributed between the head and tail. Isolated pancreatic injuries are rare; injuries to other organs, especially the liver, stomach, duodenum, and spleen, occur in more than 90% of cases. Not uncommonly, three or more organs are involved. In adults, more than 75% of blunt injuries to the pancreas are due to motor vehicle collisions. In children, a bicycle-related injury is a common mechanism. Child abuse should be suspected in cases of infants with pancreatic trauma. Clinical findings are not very helpful in detecting such injuries; more often the injury is suspected when amylase and lipase levels are found to be elevated. However, CT is still the mainstay for diagnosing pancreatic injuries in trauma patients.

Injuries to the pancreatic head are almost twice as likely to be fatal (28%) than are injuries to the tail (16%) because of associated involvement of the inferior vena cava, superior mesenteric vein, or portal vein in the latter. In addition, the location of the injury influences the surgical approach. Removal of more than 50% of the gland may lead to glucose regulation abnormalities or frank diabetes, and thus pancreas-sparing procedures are often attempted. Duct injuries occurring in the tail of the pancreas may be treated successfully by partial pancreatectomy with little risk of endocrine or exocrine dysfunction.

The main source of delayed morbidity and mortality from pancreatic trauma is disruption of the main pancreatic duct. The risk of abscess and fistula formation in patients with disruption of the pancreatic duct approaches 25% and 50%, respectively. Conversely, abscess or fistula formation occurs in patients without duct injuries in less than 10% of cases. Disruption of the pancreatic duct is treated surgically or by therapeutic endoscopy with stent placement, whereas injuries without duct involvement are usually treated nonsurgically. As such, it is critical that imaging focus on determining the integrity of the pancreatic duct directly or on indirect findings that suggest damage to the duct.

The imaging appearance of pancreatic trauma usually mimics the type of injury present. The role of ultrasonography is limited, but gland lacerations and transection can be seen as hypoechoic linear defects within the pancreatic parenchyma. CT diagnosis of pancreatic injury is often difficult, with a reported sensitivity of 65% to 75% (although the sensitivity with newer MDCT scanners may be higher). Pancreatic injuries are typically detected on portal

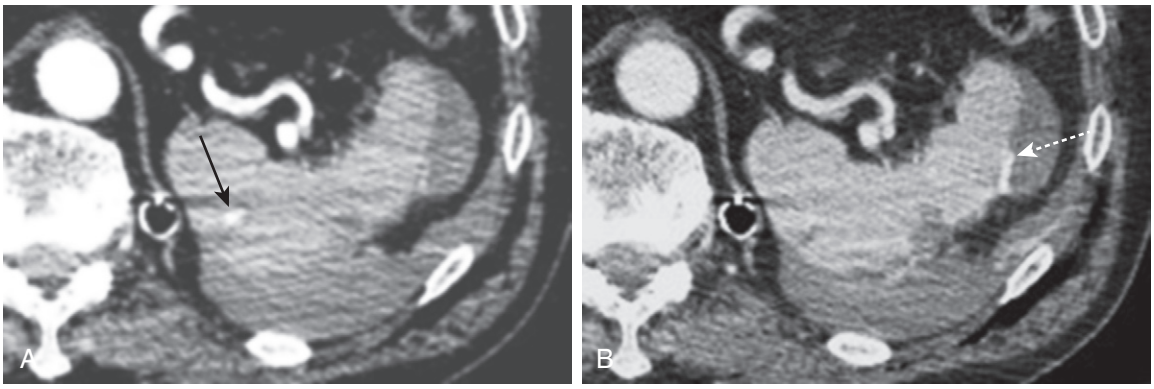


FIGURE 3-18 A 30-year-old woman with a splenic laceration who was in a motor vehicle collision. An axial computed tomography image in the arterial phase (**A**) demonstrates a splenic-contained vascular injury *(arrow),* and an image in the portal venous phase (**B**) also demonstrates active extravasation *(dashed arrow)*. Note that the contained vascular injury is only seen on the arterial phase. The patient underwent coil embolization of these splenic vascular injuries.

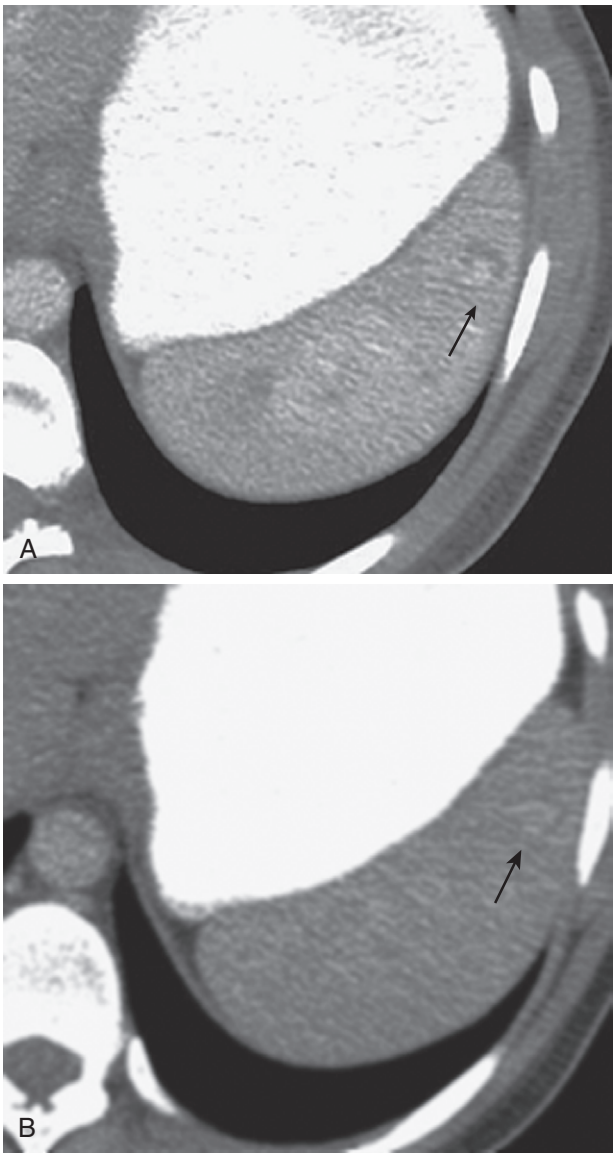


FIGURE 3-19 A contained vascular injury of the spleen, likely a pseudoaneurysm. **A,** Axial computed tomography obtained during the portal venous phase demonstrates a focal collection of contrast material in the spleen *(arrow)* with enhancement similar to the aorta. **B,** The collection of contrast material is contained on the 5-minute delay CT and has decreased in density similar to the aorta *(arrow),* consistent with the presence of a focal splenic pseudoaneurysm.

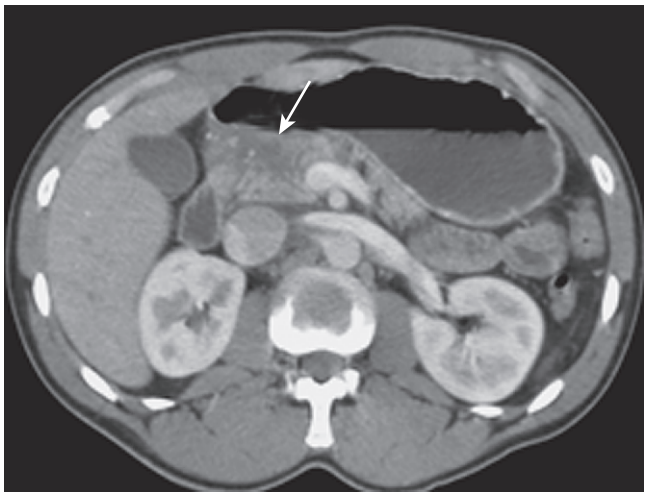


FIGURE 3-20 Pancreatic trauma after a blunt rugby injury. Axial computed tomography during the portal venous phase shows a contusion of the pancreatic head *(arrow).* This patient was managed conservatively without the need for surgical intervention.

venous-phase CT images of the abdomen. It is important to closely inspect the pancreas on thin-section images with liberal use of multiplanar reconstruction when available, because the many clefts of the pancreas can mimic or hide subtle injuries.

On contrast-enhanced CT, crush injuries such as contusions and hematomas may show focal or diffuse enlargement and edema within the pancreas, characterized by areas of low or high attenuation extending through the planes of tissue within the gland, respectively (Figs. 3-20 and 3-21). Lacerations are detected as focal low-attenuation lines, most often perpendicular to the plane of the gland and duct (Fig. 3-22), and may extend completely through the pancreas (termed *pancreatic transection*; Fig. 3-23). Additional indirect signs of injury include peripancreatic fluid/stranding, as well as retroperitoneal hematoma in the peripancreatic region. A crucial part of the imaging characterization of pancreatic injury is to determine the depth of a laceration and any possible involvement of the main pancreatic duct. With modern MDCT technology, the pancreatic duct can be seen directly in the majority of patients. The depth of a laceration is also a useful predictor of main duct involvement: involvement of more than 50% of the anteroposterior thickness of the

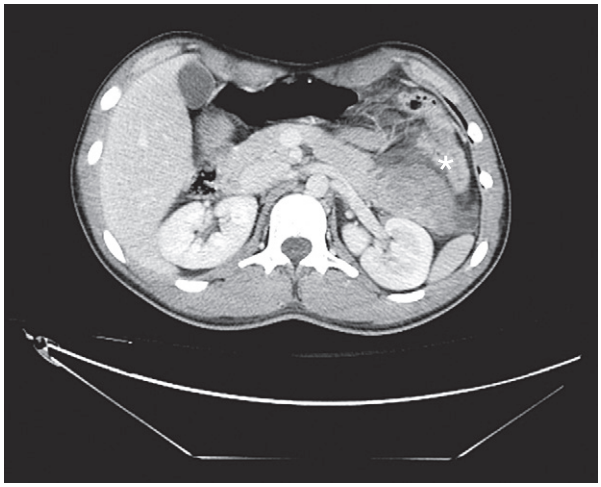


FIGURE 3-21 A 22-year-old male pedestrian who was struck by a motor vehicle. An axial contrast-enhanced computed tomography image demonstrates a pancreatic tail hematoma *(asterisk)*.

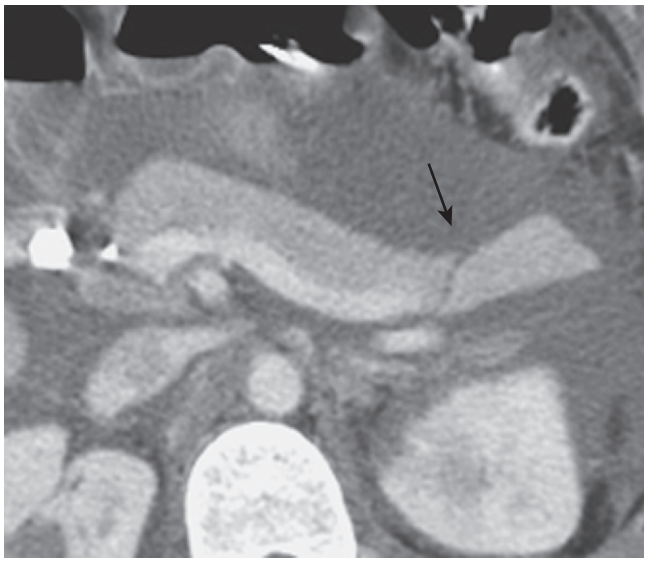


FIGURE 3-22 A pancreatic laceration. Computed tomography obtained in the portal venous phase demonstrates a focal low attenuation line *(arrow)* running through the pancreatic parenchyma in the tail of the pancreas, consistent with a focal pancreatic laceration.

gland is often associated with duct transection (Fig. 3-24). Although it is not commonly used, at least one CT grading system that parallels the surgical classification of Moore has been suggested: grade A, pancreatitis or superficial laceration (less than 50% pancreatic thickness); grade B1, deep laceration (greater than 50% pancreatic thickness) of the pancreatic tail; grade B2, transection of the pancreatic tail; grade C1, deep laceration of the pancreatic head; and grade C2, transection of the pancreatic head. Delayed complications, such as arterial pseudoaneurysms, abscesses, and pseudocysts, are all readily imaged by CT. Pseudoaneurysms typically appear as focal collections of contrast material that enhance similarly to the aorta on all phases of imaging (Fig. 3-25). Pseudocysts and abscesses appear as focal pancreatic fluid collections of varying size. Percutaneous sampling under imaging guidance is very useful to confirm the diagnosis of superimposed infection.

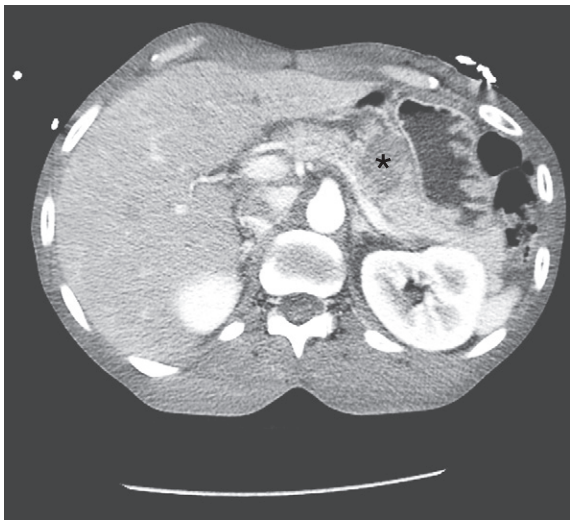


FIGURE 3-23 A 47-year-old man who fell down the stairs. An axial contrast-enhanced computed tomography image demonstrates a pancreatic body contusion and possible laceration *(asterisk)*.

One potential pitfall to be avoided is the misinterpretation of isolated low-attenuation fluid around the pancreas, without direct evidence of parenchymal trauma, as evidence of a pancreatic injury (Fig. 3-26). In the trauma population, this finding can be the result of accumulation of fluid in the retroperitoneum from rapid or excessive administration of fluids for resuscitation. If the nature of the finding is in question, a repeat CT scan 24 to 48 hours later is advisable. Fluid related exclusively to exogenously administered replacements will decrease or resolve, whereas true pancreatic injuries lead to growing fluid collections and hematomas. In addition, pancreatic lacerations may be very subtle on initial CT scans. Thus, if the patient experiences abdominal pain after admission, a repeat CT scan with special attention to the pancreas is indicated.

Once injury to the pancreas is identified, MR and MRCP can help in further assessing the status of the main pancreatic duct, especially for follow-up of pancreatic injuries in these typically young patients for whom unnecessary radiation should be avoided if possible (Fig. 3-27). Common MR pulse sequences acquired include fat-suppressed T1- and T2-weighted sequences and MRCP, which are performed by using heavily T2-weighted breath-hold or non–breath-hold sequences. Fast spin echo (two-dimensional or three-dimensional) and rapid acquisition with relaxation enhancement sequences performed in the coronal and axial planes are usually sufficient. In addition to evaluating the pancreatic duct, MR can be used to assess for pancreatic fluid collections that may have developed as a result of the pancreatic ductal injury (Fig. 3-28). Hemorrhagic components are also easily detected with MR. Although MRCP is useful for evaluating the pancreatic duct, ERCP is important because of its potential to definitively confirm communication of an apparently interrupted duct with surrounding fluid collections (see Fig. 3-23). In addition, ERCP provides a means for possible endoscopic therapy of pancreatic duct leaks and fluid collections.

BOWEL AND MESENTERIC INJURY

Injuries to the bowel and mesentery are uncommon but potentially devastating because they are difficult to diagnose

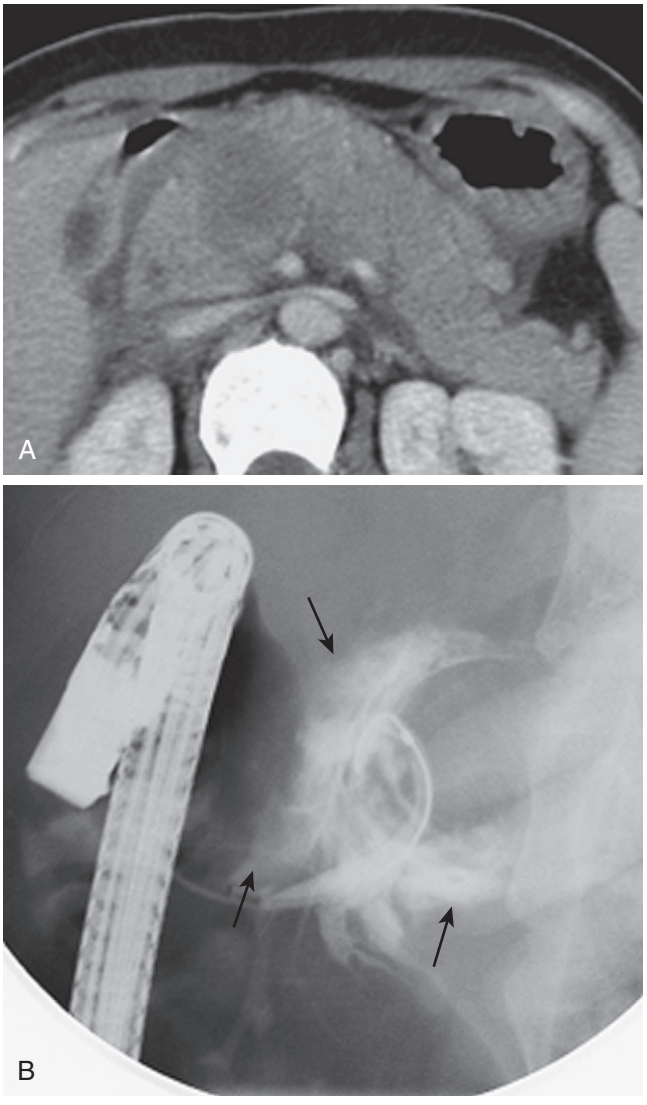


FIGURE 3-24 A pancreatic laceration with a main duct injury. **A,** Axial computed tomography obtained at the time of the initial evaluation demonstrates a complex laceration of the pancreatic head–neck junction with near-complete transection. Injury of the main pancreatic duct was suspected. **B,** Endoscopic retrograde cholangiopancreatography obtained to evaluate the extent of the injury demonstrates extravasation of contrast material at the site of injury *(arrows),* confirming the presence of an injury to the main pancreatic duct.

both clinically and with imaging. Most blunt injuries are a consequence of motor vehicle collisions, although other mechanisms, including assaults and sports-related trauma, can produce such injuries. Injury of the small bowel is much more common than injury of the colon or stomach in the setting of blunt trauma (Box 3-1).

Although bowel and mesenteric injuries can occur in isolation, most patients present with injuries to other organ systems, typically the liver or spleen. Three different mechanisms have been described. The first type of injury, a crush injury, generally occurs as a result of impaction of the bowel between the anterior abdominal wall and the spine or another solid organ. This type of injury leads to bowel wall contusions, mural hematomas, and lacerations, and it often involves the duodenum and transverse colon. The second type of injury, a shearing injury, occurs at the sites of fixed anatomic structures, such as at acquired adhesions or at normal points of bowel fixation (such as the ligament of Treitz and the ileocecal valve). During brief periods of rapid deceleration, mobile loops of bowel are pulled away from points of fixation, leading to shearing-type injuries, which include bowel or mesenteric lacerations, mesenteric vascular injuries, and degloving injuries in which the serosa is stripped away from the remainder of the wall. The third type of injury, the burst injury, is due to sudden increases in intraluminal pressure that lead to focal bowel perforation or laceration.

Delayed diagnosis of bowel or mesenteric injuries is a leading cause of morbidity and mortality in persons who sustain blunt trauma. The clinical diagnosis of a focal injury to the bowel or mesentery can be extremely challenging. Trauma patients are often intoxicated and have distracting injuries, altered levels of consciousness, or closed head injuries that preclude the accurate detection of physical symptoms and may mask the clinical manifestations of a bowel injury. In the past, trauma surgeons relied on invasive tests such as diagnostic peritoneal lavage as a means of detecting intestinal contents or blood in the peritoneal cavity. However, this test is invasive and not specific and often led to a large number of nontherapeutic exploratory laparotomies. Peritoneal lavage has been replaced by CT as the main diagnostic modality. Improvements in technology and increased awareness of the many (often subtle) CT signs of bowel and mesenteric injuries have resulted in earlier detection. Ultrasonography is not reliable for direct demonstration of the bowel injury, although the finding of free peritoneal fluid on the initial FAST scan may serve as indirect evidence of injury and heighten clinical suspicion.

CT diagnosis of injuries to the bowel and mesentery is not always straightforward. Unlike with most solid organ injuries, which are often obvious, the radiologist must carefully inspect the images for direct and indirect signs, each having varying ranges of sensitivity and specificity. Numerous CT signs have been reported to occur in the setting of bowel and mesenteric trauma (Box 3-2).

Because the detection of bowel and mesenteric injuries is challenging and so many reported CT signs must be carefully sought, it may be more useful to consider the types of injury and the possible appearance of such injuries on trauma CT scans. According to the AAST injury scale for the bowel (including the stomach, duodenum, small intestine, and colon), injuries tend to vary from mild grade I injuries such as bowel wall hematomas to severe grade V injuries, including devascularization and complete bowel wall transection. Mesenteric vascular injuries vary from grade I distal branch vessel injury to grades III and IV superior mesenteric trunk and celiac axis injuries, with grade V injury reserved for major abdominal vessel (aortic, caval, or extrahepatic portal vein) injury. Thus the frequency of individual CT signs found in bowel and mesenteric injuries depends on the type and severity of the injury that has occurred.

Bowel wall hematomas and contusions, when visible by CT, typically present with focal thickening of the bowel wall. The area of thickening may appear to be hyperattenuating relative to the normal bowel wall because of the acute presence of blood (Fig. 3-29). Depending on the severity of the injury, the hematoma may be eccentric or concentric in appearance. More severe injuries, which include

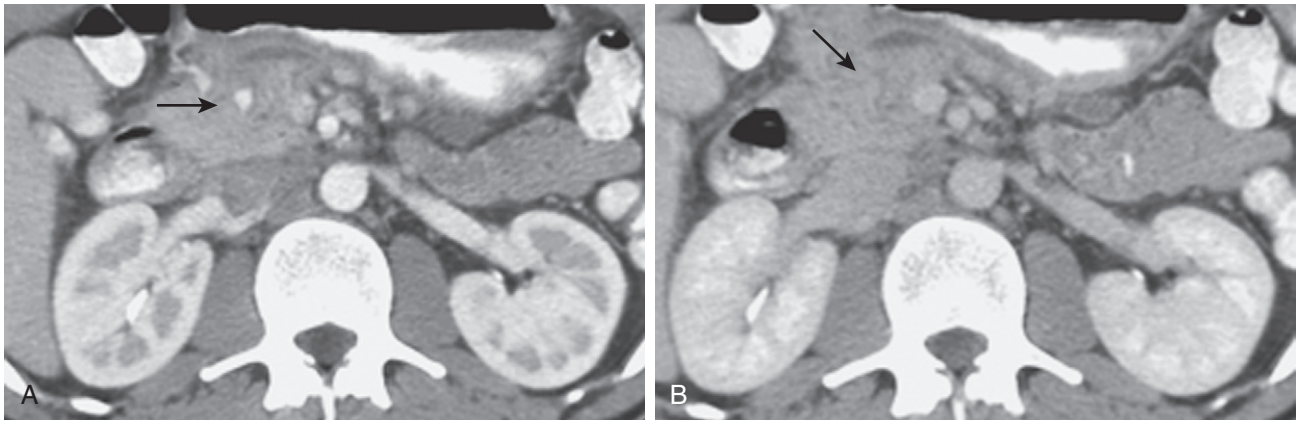


FIGURE 3-25 A pancreatic pseudoaneurysm after blunt trauma. **A,** Axial computed tomography (CT) performed during the portal venous phase demonstrates a focal contained collection of contrast material in the pancreatic head/neck region *(arrow)* at the site of previous pancreatic laceration with enhancement similar to the aorta. **B,** A delayed CT image obtained 5 minutes after the initial injection of contrast material confirms the presence of a pseudoaneurysm, with the focal collection *(arrow)* now decreased in attenuation as it mirrors enhancement characteristics of the adjacent vessels (including the aorta). This pseudoaneurysm resolved several days later and did not require further intervention.

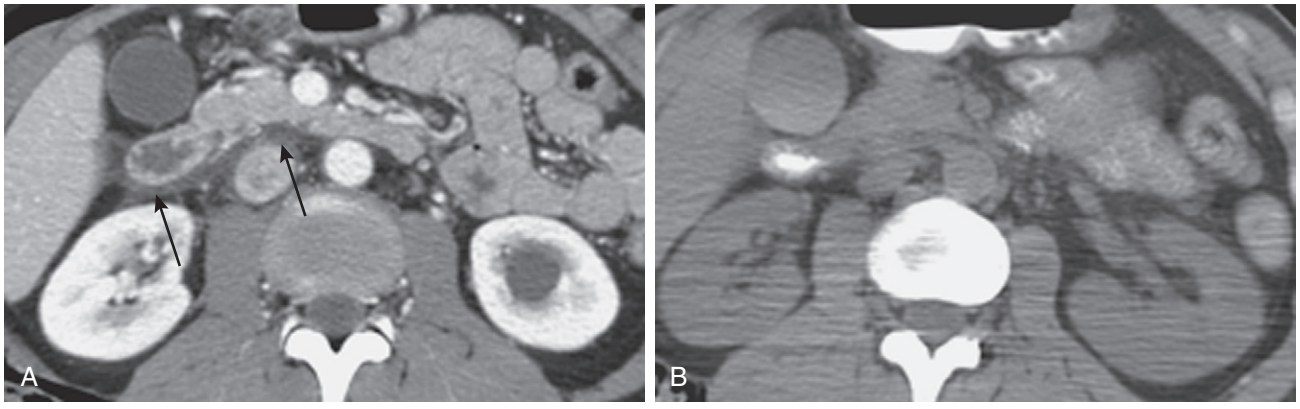


FIGURE 3-26 Retroperitoneal fluid mimicking a pancreatic injury. **A,** An axial computed tomography (CT) image during the portal venous phase after a motor vehicle accident shows low-density fluid *(arrows)* in the retroperitoneum posterior to the pancreas tracking anterior to the inferior vena cava and posterior to the duodenum. The possibility of pancreatic or duodenal injury was initially raised, although the patient did not exhibit clinical signs of either injury, and thus follow-up CT was requested. **B,** An axial CT image with use of oral and intravenous contrast material obtained 24 hours later shows that the fluid has nearly resolved, suggesting that the initial CT findings were due to fluid resuscitation and not to a pancreatic or bowel injury.

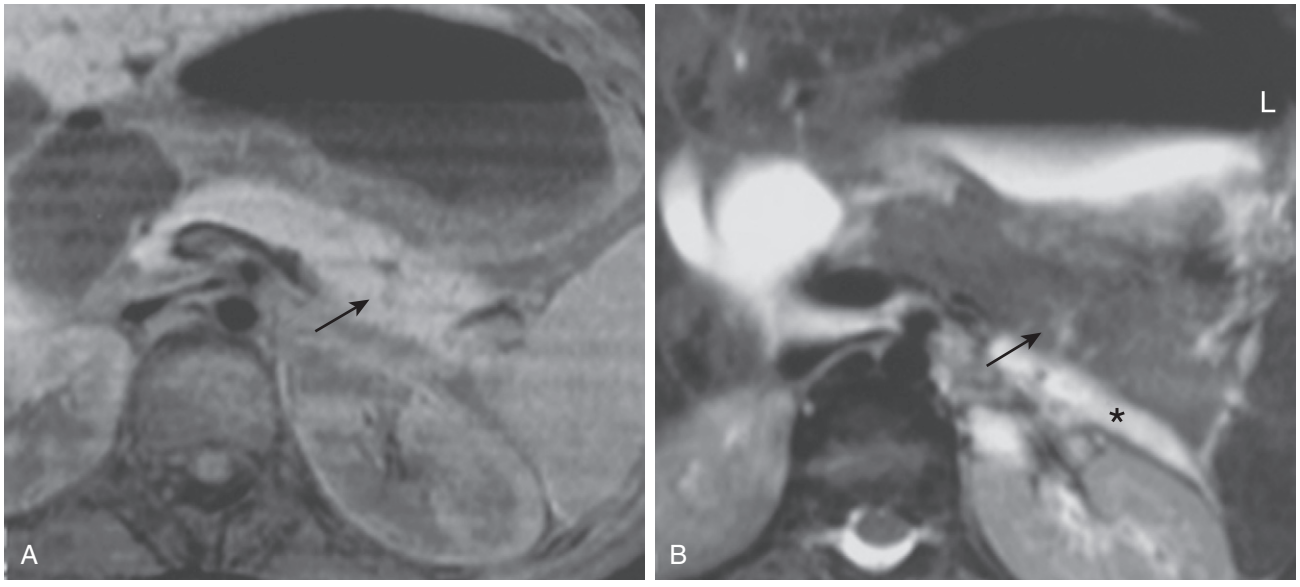


FIGURE 3-27 Magnetic resonance appearance of a pancreatic injury. **A,** An axial T1-weighted image with chemical fat saturation demonstrates a focal laceration *(arrow),* which appears as low signal intensity on this pulse sequence. **B,** An axial fat-saturated T2-weighted sequence shows the laceration as a focal linear increased signal in the tail of the pancreas *(arrow).* The fluid-sensitive T2 sequence also shows the presence of peripancreatic fluid *(asterisk).*

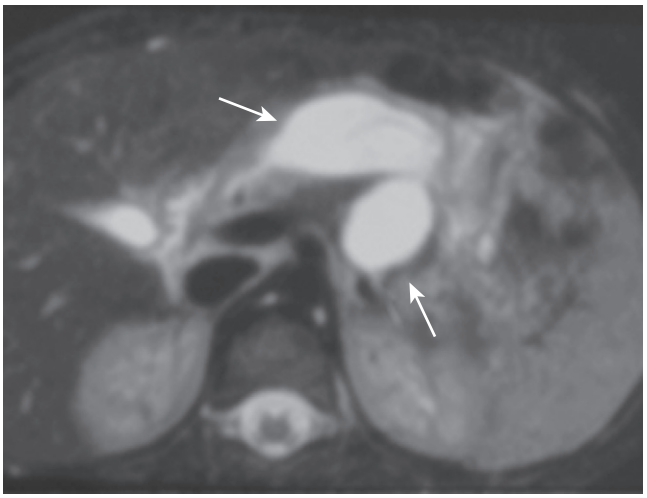


FIGURE 3-28 Magnetic resonance appearance of pancreatic fluid collections. An axial fat-saturated T2-weighted pulse sequence demonstrates two distinct fluid collections *(arrows)* as high signal intensity. The collections developed as a result of a pancreatic laceration with a ductal injury that occurred at the time of the initial trauma.

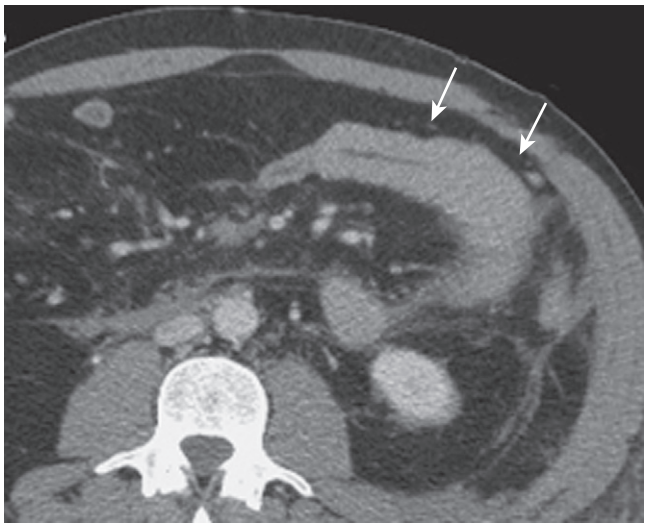


FIGURE 3-29 A bowel wall hematoma. Axial computed tomography without use of oral contrast material demonstrates focal bowel wall thickening *(arrows)* in this patient after a motor vehicle collision. The bowel wall is thickened and increased in density compared with the adjacent muscle.

BOX 3-1 Typical Locations of Bowel Injuries Due to Blunt or Penetrating Trauma

STOMACH

Anterior wall > greater curve > lesser curvature > posterior wall

SMALL INTESTINE

Duodenum (second and third segment injuries are most common)
Jejunum (near the ligament of Treitz)
Ileum (distal near the ileocecal valve)

COLON

Left colon (more common in blunt trauma)
Right colon and transverse colon (more common in penetrating trauma)
Rectum (more common in penetrating trauma; rare in blunt trauma)

BOX 3-2 Computed Tomography Signs of Injury

CT SIGNS OF BOWEL INJURY

Intramural hematoma
Intramural gas
Bowel wall disruption
Bowel wall transection
Abnormal bowel wall enhancement
Free intraperitoneal air
Free retroperitoneal air
Free intraperitoneal fluid
Free retroperitoneal fluid
Extravasated extraluminal oral contrast material
Bowel wall thickening

CT SIGNS OF MESENTERIC INJURY

Mesenteric hematoma
Mesenteric vascular beading
Mesenteric active contrast extravasation

CT, Computed tomography.

lacerations of the bowel wall, are only rarely directly seen on CT as focal wall interruptions or frank discontinuity. Instead, other secondary signs of bowel laceration may be present to suggest such an injury. Free intraperitoneal air is one of the more common findings in patients with focal bowel wall lacerations (Fig. 3-30). However, the overall sensitivity of this finding varies between 20% and 75%. Free air may be found locally, adjacent to the site of perforation, or remotely in the upper abdomen near the surface of the liver or along the undersurface of the peritoneum. The presence of free air is not 100% specific for bowel injury, and other benign iatrogenic and traumatic causes (such as bladder rupture and air introduced at the time of Foley catheter placement) must be considered (Box 3-3).

Free intraperitoneal fluid is another sign associated with bowel and mesenteric trauma. In fact, it has been reported as the most common individual finding. This fluid can be seen adjacent to the site of the injury within the leaves of the mesentery or diffusely throughout the abdomen and pelvis. Although it is often present in combination with other CT findings, the significance of isolated free fluid on trauma CT scans is controversial, but it appears to be less commonly associated with bowel and mesenteric injuries than was once thought (see the discussion on free fluid later in this chapter). However, isolated small puddles of free fluid trapped within the mesentery, seen on CT as small triangles outlining the mesenteric leaves (Fig. 3-31), should prompt a very careful review of the bowel loops for direct evidence of injury.

In addition to extraluminal air and fluid, oral contrast material also may escape into the peritoneal cavity when a bowel laceration is present (Fig. 3-32). Unfortunately, this finding is uncommon, with reported sensitivities as low as 6%, and it is highly unlikely to be present as an isolated finding. This is the main reason why the mandatory use of an oral contrast agent in patients who have sustained blunt trauma has been questioned, and the trend toward use of nonoral contrast CT for this indication is now growing. It should be noted that focal lacerations of the duodenum

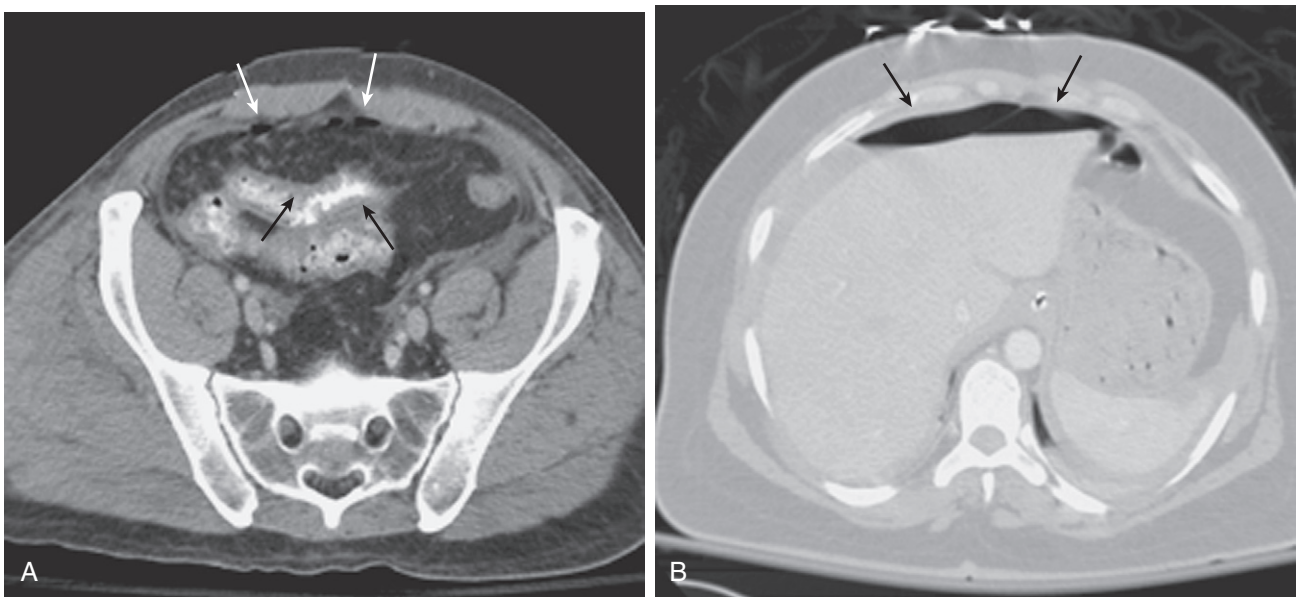


FIGURE 3-30 Free intraperitoneal air due to a bowel injury. **A,** Axial computed tomography (CT) performed with oral and intravenous contrast material shows focal wall thickening of the distal ileum *(black arrows)* with small bubbles of free air in the lower abdomen *(white arrows).* A focal 1-cm ileal perforation was confirmed at surgery. **B,** Axial CT performed during the portal venous phase shows a large collection of free air in the upper abdomen *(arrows).* A sigmoid laceration was detected at surgery.

BOX 3-3 Causes of Free Intraperitoneal Air on Trauma Computed Tomography Examinations

TRAUMATIC CAUSES

Bowel injury
Bladder injury

NONTRAUMATIC CAUSES

Penetrating injury without organ damage
Iatrogenic
Diagnostic peritoneal lavage
Pneumothorax
Pneumomediastinum
Mechanical ventilation

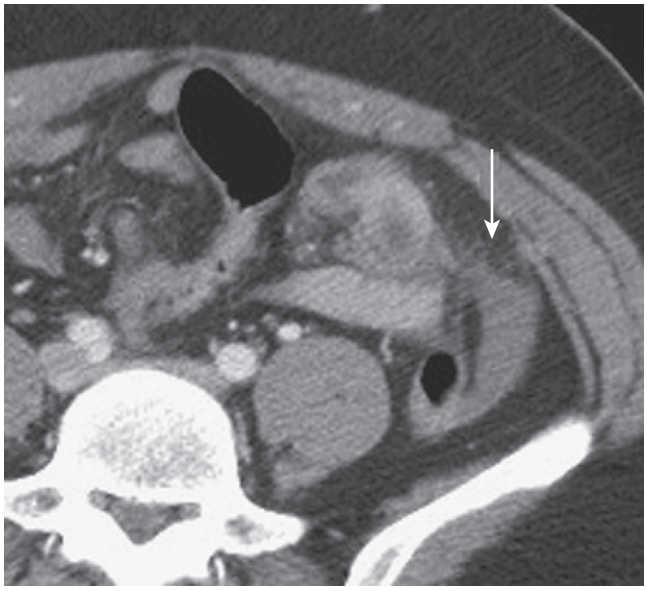


FIGURE 3-31 A mesenteric hematoma. Axial computed tomography in this patient demonstrates a focal triangular-shaped hematoma in the bowel mesentery *(arrow).* Mesenteric hematomas are often subtle, and thus careful inspection of the mesentery is required to exclude the presence of injury. The presence of a mesenteric hematoma should raise the index of suspicion for an associated bowel injury.

may produce free air and free fluid that is isolated to the retroperitoneum (Fig. 3-33). Close inspection of the duodenal wall should be made when such findings are present.

Bowel injuries also may produce focal changes in the appearance of the bowel wall itself that can be readily detected with MDCT. Partial-thickness injuries may allow air to escape into the bowel wall, producing focal pneumatosis. Other findings include focal wall thickening and focal abnormal wall enhancement after intravenous administration of contrast material (Fig. 3-34). Enhancement may be increased or decreased, as occurs with severe devascularization from degloving injuries. Focal abnormal wall enhancement almost always indicates that an injury requiring surgical intervention has occurred. Colonic injuries also may manifest as focal wall thickening, usually with a surrounding mesenteric hematoma (Fig. 3-35).

Blunt trauma can result in significant injuries that are isolated to the mesentery, such as lacerations and vascular injuries. Mesenteric lacerations cannot be directly seen; however, they often produce indirect CT signs, such as mesenteric "stranding" (a focal ill-defined increase in attenuation) or the formation of a frank mesenteric hematoma as a result of a small vessel injury (Fig. 3-36). When larger vessels are injured, active extravasation of contrast material may be present (Fig. 3-37). Additionally, mesenteric lacerations can lead to the development of internal hernias. Close clinical follow-up of a mesenteric injury is mandatory, because even small hematomas associated with small vessel injury can produce vascular compromise

of the associated segment of bowel. The resulting bowel ischemia may be seen as a focal hypoenhancing segment on CT; however, delayed presentation of such injuries, such as bowel obstruction as a result of an ischemic stricture, is possible.

FREE PERITONEAL FLUID

Previous studies have shown that isolated free fluid is present in approximately 3% of all trauma CT scans. In the past, trauma surgeons often elected to surgically explore this subset of patients to fully evaluate the bowel for the presence of injury. However, increasingly these patients are being managed nonoperatively. Often such patients are



FIGURE 3-32 A bowel wall laceration involving the jejunum. An acute bowel wall injury in this patient was confirmed by the presence of oral contrast material outside the expected lumen of bowel *(arrow).*

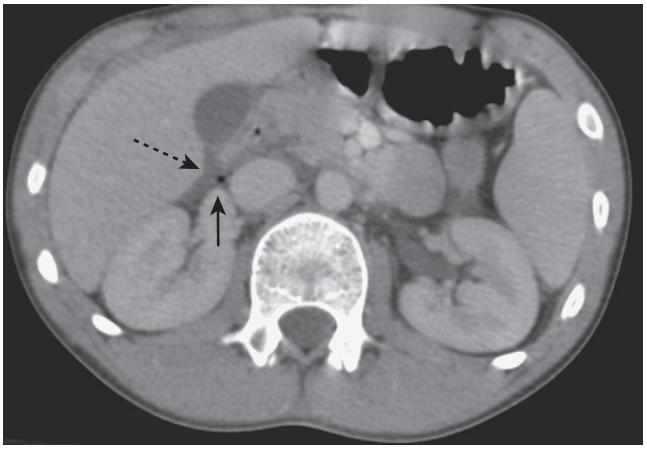


FIGURE 3-33 A duodenal laceration after a motor vehicle accident. An axial computed tomography (CT) image during the portal venous phase demonstrates a small bubble of air in the retroperitoneum *(solid arrow)* with associated retroperitoneal fluid *(dashed arrow).* A duodenal injury was suspected based on the CT findings, and a focal laceration was confirmed at the time of surgery.

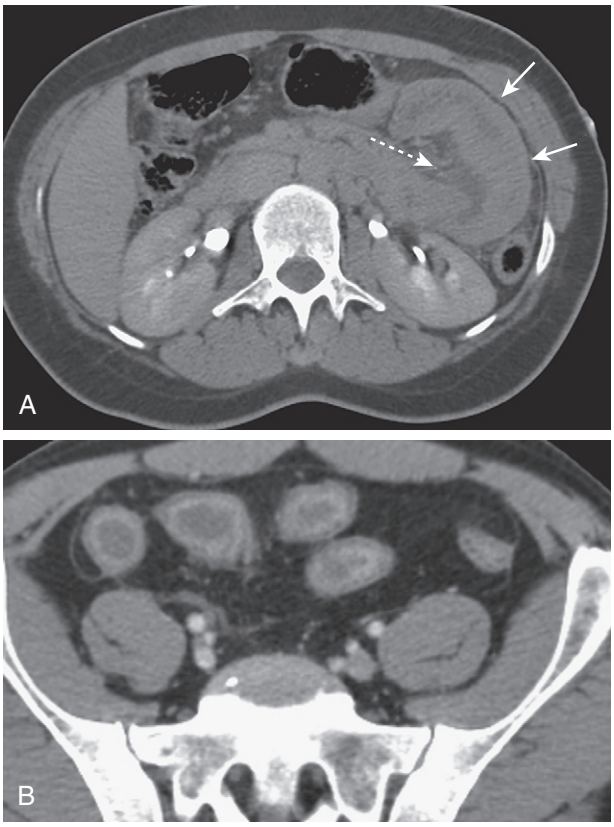


FIGURE 3-34 Computed tomography (CT) findings suggestive of a focal bowel wall injury. **A,** Axial CT obtained at 5-minute delay shows focal thickening of the jejunum *(solid arrows)* with fluid in the mesentery *(dashed arrow)* due to a focal jejunal laceration that required surgical repair. **B,** Axial CT in another patient with a distal ileum laceration shows abnormal enhancement of the bowel wall greater than the adjacent psoas muscle. *(B, From Stuhlfaut JW, Lucey BC, Varghese J, et al. Blunt abdominal trauma: utility of 5-minute delayed CT with a reduced radiation dose.* Radiology. *2006;238:473-479.)*

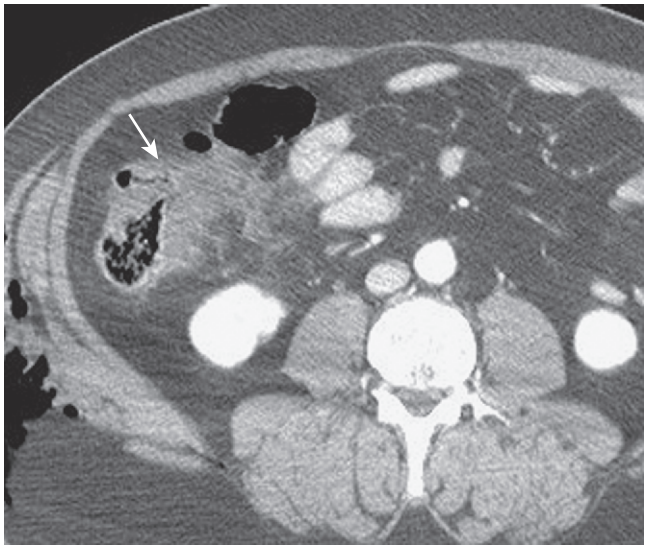


FIGURE 3-35 A focal colon injury after blunt trauma. Axial computed tomography demonstrates focal bowel wall thickening of the ascending colon *(arrow)* with an adjacent mesenteric hematoma. This patient required surgery to repair a focal laceration.

managed expectantly unless other clinical criteria are present to suggest an acute bowel injury. The appearance and location of free fluid are often helpful in selecting patients for nonoperative management. Isolated free pelvic fluid in female patients is often of no clinical significance; a growing amount of evidence also suggests that small amounts of low-attenuation fluid in male patients may be a benign finding that is not associated with significant bowel or mesenteric injury (Fig. 3-38). However, large amounts of free fluid in male or female patients (especially if high in attenuation), focal mesenteric fluid, and free fluid in more than one space or location (Fig. 3-39) may be indicative of an underlying injury and may warrant surgery, close clinical observation, or CT follow-up.

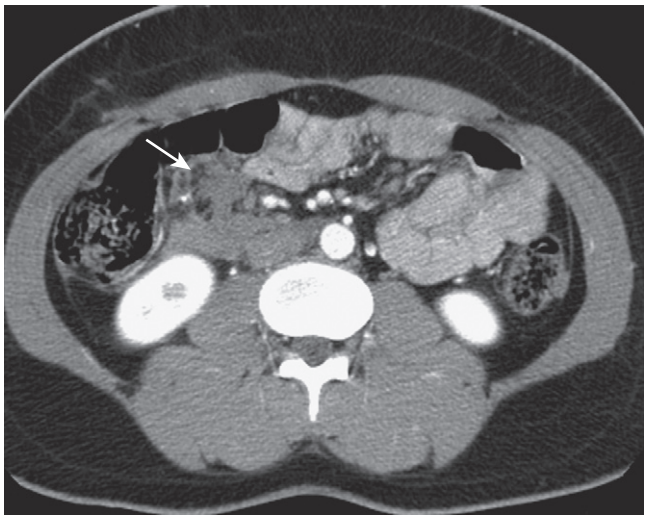


FIGURE 3-36 A mesenteric hematoma after motor vehicle–related blunt trauma. An axial computed tomography image after administration of intravenous contrast material demonstrates a focal hematoma in the mesentery *(arrow)* without evidence of a bowel injury. A mesenteric laceration that required repair was identified at surgery; no bowel injury was detected.

Unfortunately, the surgeon and radiologist are often faced with patients whose clinical evaluation and CT examination, although not entirely normal, do not conclusively confirm the presence of a bowel injury that warrants a laparotomy. These examinations include findings such as questionable focal wall thickening, small isolated mesenteric hematomas, or isolated free intraperitoneal fluid. These patients should be admitted for close clinical observation. If the patient exhibits signs or symptoms consistent with peritoneal irritation, surgical intervention is then advised. Otherwise, a repeat CT with a water-soluble oral contrast agent 12 to 24 hours after the admission CT should be considered before discharging the patient. Given the high morbidity associated with a delayed diagnosis of a bowel injury, this careful approach is recommended.

Finally, in addition to focal bowel injury, the initial trauma CT may show a diffuse abnormality of the bowel that can be seen in patients with hypovolemic shock (so-called "shock bowel"). Typically the small intestine is diffusely thickened and increased enhancement of the small bowel mucosa is present (Fig. 3-40). The cause of the intense mucosal enhancement is not completely understood, although it is thought to be due to increased vascular permeability of the bowel mucosa due to hypoperfusion. Occasionally the bowel may appear dilated. This appearance is fairly classic and is usually reversible once the patient

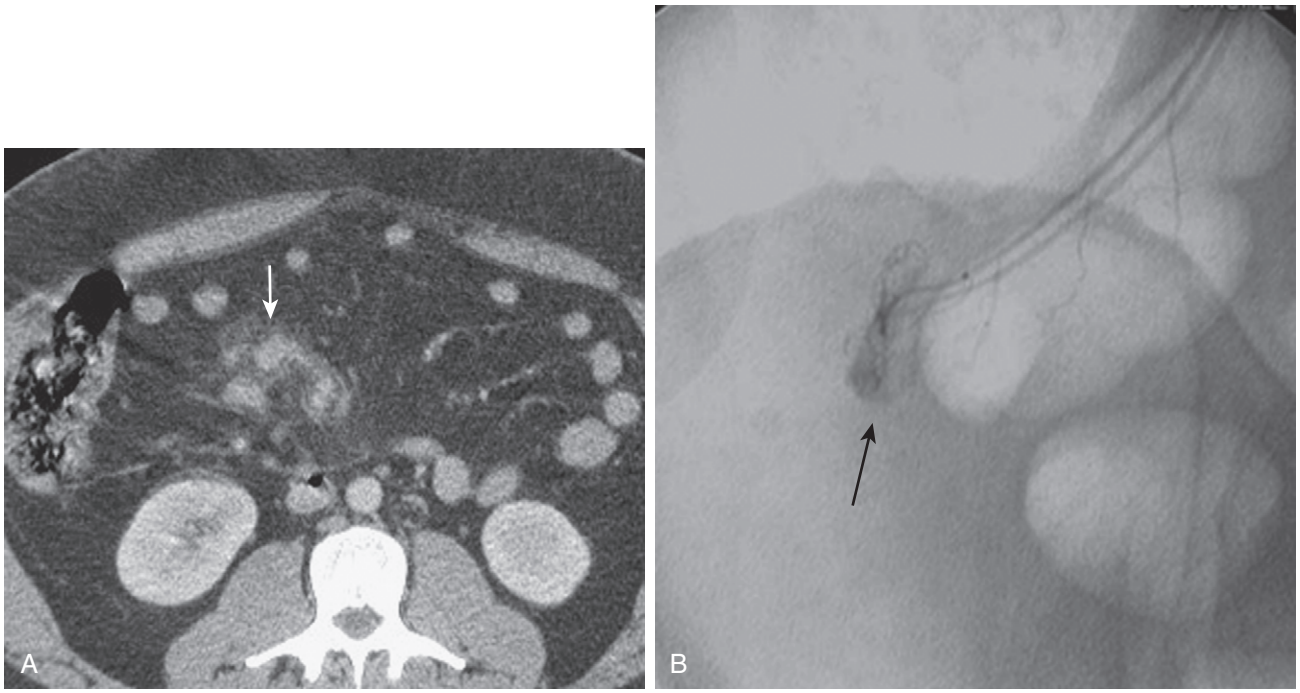


FIGURE 3-37 A mesenteric injury with active bleeding. **A,** Axial computed tomography obtained during the portal venous phase demonstrates mesenteric stranding with a focal collection of extraluminal contrast material *(arrow)* consistent with active extravasation. **B,** Catheter angiography was requested. A single digital subtraction image after selective injection of superior mesenteric artery branch vessels demonstrates a focal blush of contrast material *(arrow)* that confirms the presence of active bleeding. This patient was treated with coil embolization.

is appropriately resuscitated. In addition to small bowel abnormalities, profound hypovolemia is also associated with flattening of the inferior vena cava, a decrease in the caliber of the abdominal aorta, pancreatic swelling, and increased enhancement of the adrenal glands (typically greater than adjacent vascular structures), which maintain normal size and shape.

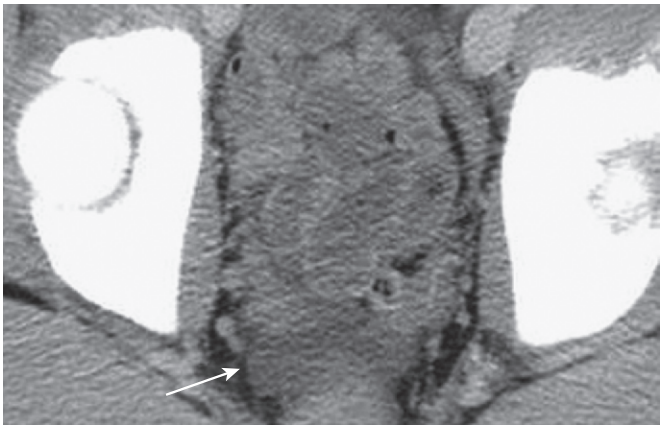


FIGURE 3-38 Free pelvic fluid in a male patient after blunt trauma. Axial computed tomography demonstrates a small amount of free fluid in the rectovesicle space *(arrow)* in this male patient after a motor vehicle collision. No solid organ injury or bowel injury was detected, and the patient recovered without the need for further imaging or intervention.



FIGURE 3-39 Free intraperitoneal fluid. A sagittal reformatted image in this male patient after a motor vehicle collision demonstrates a large amount of dense fluid in the left lower quadrant and in the perisplenic region *(arrows)*. Although no injury to the bowel, mesentery, or solid organs was identified, the patient was taken to surgery based on the computed tomography findings. A laceration of the middle colic artery was found and repaired at the time of exploration.

RENAL AND URETERAL TRAUMA

Renal Injury

Injuries of the genitourinary system involve the kidney, adrenal gland, ureter, bladder, and urethra. The most commonly injured organ is the kidney, which accounts for approximately 90% of all injuries to the genitourinary system. Most renal injuries occur as a result of blunt trauma, such as motor vehicle collisions or sports-related injuries. The main clinical finding leading to suspected renal trauma is gross or microscopic hematuria, although many patients are asymptomatic or may have associated injuries that confound the clinical presentation. In addition, up to 14% of patients with trauma to the kidneys may present without hematuria, including some patients with severe injuries. CT and, less often, US are used to identify renal injuries. If a renal or ureteral injury is suspected prior to imaging, or if the initial images show signs of injury, delayed images should be obtained to better evaluate the integrity of the collecting system and to determine the need for further intervention.

The types of injuries that can affect the kidneys include renal contusions, hematomas, lacerations, fractures, a shattered kidney, and a renal vascular pedicle injury. Again, the AAST has developed a grading system for renal

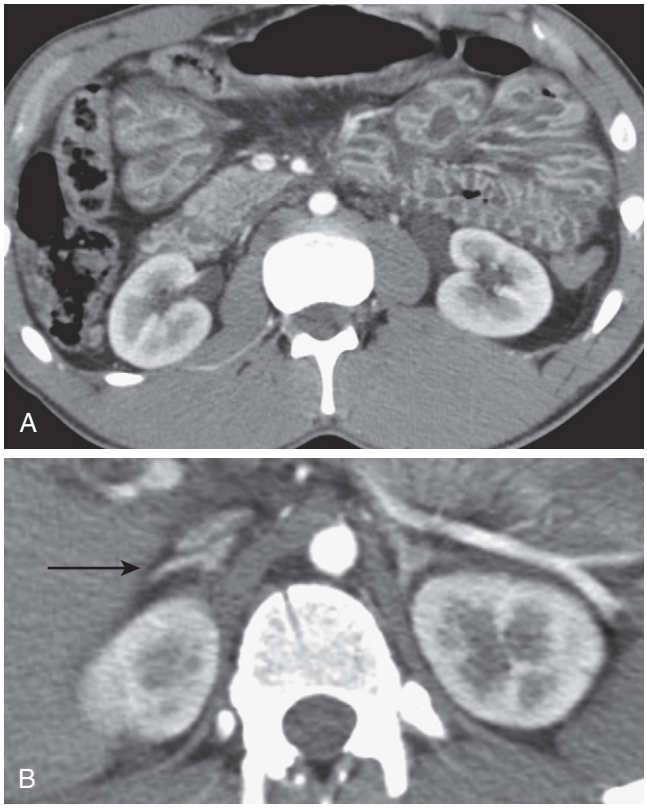


FIGURE 3-40 Computed tomography (CT) appearance of hypovolemic shock. **A,** Axial CT obtained in the portal venous phase demonstrates diffuse mural thickening and intense enhancement of the small bowel mucosa in this patient with profound hypovolemic shock after a motor vehicle accident. **B,** In addition to the bowel findings in **A,** this patient has a flat inferior vena cava and small-caliber aorta, and enhancement of the adrenal glands is increased (the *arrow* depicts an abnormal right adrenal; the left is partially imaged at this level), all signs of hypovolemic shock.

injury that can serve as a guideline for characterizing injuries at the time of CT interpretation (Table 3-3). Overall, most renal injuries fall into one of two categories: contusion and laceration. These injuries may appear severe upon CT because of the associated lack of enhancement of the traumatized segment, but they are often stable and require no further intervention or follow-up. Contusions represent parenchymal injuries that produce interstitial edema and hemorrhage. The contused kidney is often swollen and hypofunctioning, either focally at the site of injury or diffusely with more severe injury. Lacerations represent focal tears in the parenchyma. If a laceration is present, the patient is at risk of the development of a perirenal urinoma and hematoma. Only about 5% of traumatic lesions are classified as renal fractures, shattered kidneys, or vascular pedicle injuries. These injuries may be unstable and usually require further intervention, either by catheter angiography or surgical repair.

TABLE 3-3 American Association for the Surgery of Trauma Classification of Traumatic Renal Injury

Grade	Description
I	Contusion Subcapsular hematoma
II	Nonexpanding perinephric hematomas confined to the retroperitoneum Superficial cortical lacerations <1 cm in depth without collecting system injury
III	Renal lacerations >1 cm in depth that do not involve the collecting system
IV	Renal lacerations extending through the kidney into the collecting system Injuries involving the main renal artery or vein with contained hemorrhage Segmental infarctions without associated lacerations Expanding subcapsular hematomas compressing the kidney
V	Shattered or devascularized kidney Ureteropelvic avulsions Complete laceration or thrombus of the main renal artery or vein

Ultrasonography

Sonography is particularly limited for evaluation of the kidneys after blunt trauma. Acute hematomas are typically hyperechoic and difficult to differentiate from the echogenic renal sinus or perirenal fat (Fig. 3-41). Although early experience suggests that detection of parenchymal injuries is enhanced with the use of ultrasound contrast agents, their use in practice is limited, as is the case for most trauma applications. When they are seen, renal lacerations appear as linear hypoechoic defects within the parenchyma and may extend to the renal capsule. Injury to the vascular pedicle may be identified by a total lack of enhancement of the kidney after injection of contrast material.

Computed Tomography

On CT, renal contusions appear to be hypoattenuating relative to the surrounding enhanced parenchyma and are optimally seen on the nephrographic phase of contrast enhancement, which typically occurs 90 to 120 seconds after initiation of intravenous contrast infusion. However, most injuries are also well visualized in the portal venous phase of hepatic contrast enhancement, which is the timing used for most abdominal trauma CT scans. A contused kidney is often hypofunctioning, and CT demonstrates a delay in enhancement relative to the normal-functioning contralateral kidney or the ipsilateral noncontused areas (Fig. 3-42). On later phases, the contused kidneys may show a persistent nephrogram with delayed excretion of contrast material into the collecting system. A renal laceration represents a tear in the parenchyma and manifests as a focal area of linear low attenuation on CT. The laceration typically extends to the surface and often is associated with a perirenal hematoma or fluid collection (Fig. 3-43). Once a laceration is identified, delayed images are extremely important for

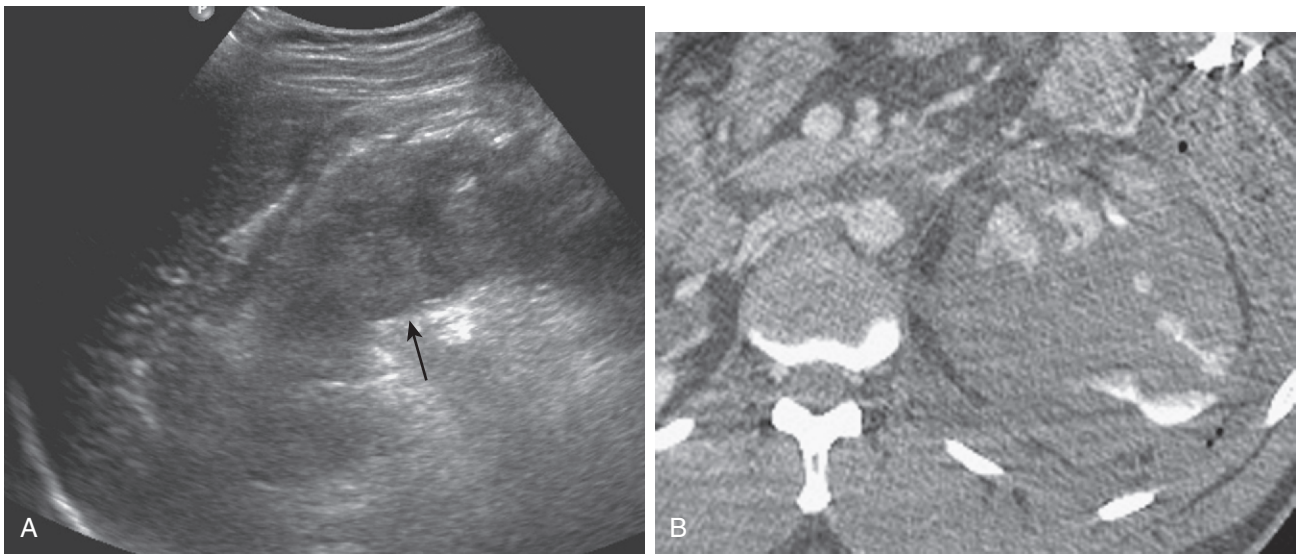


FIGURE 3-41 A shattered kidney. **A,** Ultrasound of the left flank demonstrates increased echogenicity in the expected location of the left kidney *(arrow),* without readily identifiable renal parenchyma. **B,** Computed tomography (CT) performed after the initial ultrasound confirms the presence of a shattered kidney. The increased echotexture on ultrasound corresponds to a hematoma, which appears as low density on this CT image.



FIGURE 3-42 Renal contusion. An axial computed tomography image obtained after a blunt abdominal injury during the portal venous phase of contrast enhancement. A focal area of hypodensity *(arrow)* is present in the upper portion of the right kidney with minimal stranding as a result of blood in the perirenal fat. This injury is typical of a renal contusion and typically requires no further management.

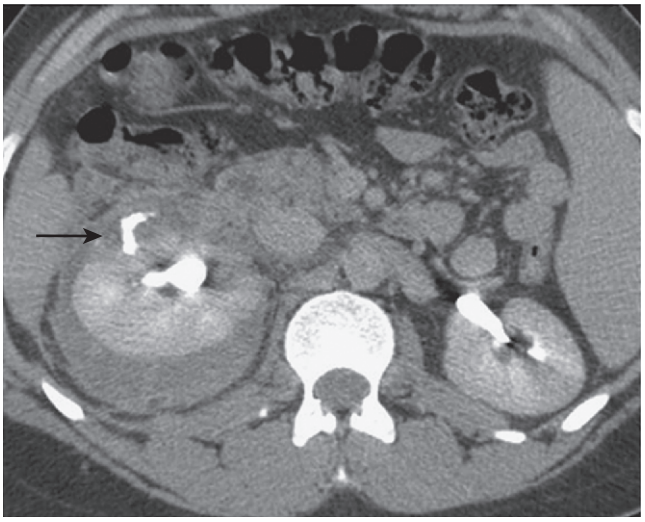


FIGURE 3-44 A renal laceration. Axial computed tomography in this patient was obtained at a 5-minute delay to assess the integrity of the collecting system. In addition to a small laceration with perinephric hematoma, a focal collection of contrast *(arrow)* is present in the perinephric space, consistent with a small urine leak.



FIGURE 3-43 A renal laceration. Axial computed tomography in a patient after a motor vehicle collision demonstrates a focal low density line *(arrow)* in the renal cortex diagnostic of a focal renal laceration. A perinephric hematoma is present in the fat adjacent to the injury.

demonstrating a potential leak of urine containing dense contrast material into the perinephric space (Fig. 3-44). In addition, some lacerations are associated with active extravasation of contrast-enhanced blood (Fig. 3-45). Unless an associated major vascular injury is present, most lacerations will heal without any specific therapy.

A renal fracture represents a severe form of laceration in which the kidney is separated into at least two complete independent fragments. If the kidney is fractured into more than three parts, the injury is typically described as a "shattered kidney." This injury is often easier to characterize with the help of multiplanar reformations, which afford the opportunity to identify fracture lines running in different planes. Once detected, any significant perirenal hematoma or focus of active contrast extravasation should be noted because patients with these findings may require further intervention. If the patient is stable and surgery can be avoided, catheter angiography is often helpful to identify isolated arterial injuries that may benefit from embolization. Shattered kidneys more often require surgical intervention and nephrectomy to control bleeding from multiple injured branch vessels.

Finally, injury of the vascular pedicle typically represents either an acute traumatic dissection or transection of the renal artery or vein (Fig. 3-46). When such an injury occurs, the kidney will show an absence or near absence of contrast enhancement on the portal venous phase CT examination, and an associated perirenal hematoma may be present. This injury is severe, and patients may present in hypovolemic shock as a result of profound blood loss. This injury may be treated by surgical revascularization if it is detected early (typically within the first 6 hours after the initial trauma); otherwise, a nephrectomy is indicated because the kidney is not salvageable if the diagnosis is delayed or if the patient presents too long after the time of the initial injury.

Ureteral Injury

The ureter is the least commonly injured segment in the genitourinary system, accounting for less than 1% of all injuries. Most ureteral injuries are penetrating injuries such as gunshot wounds. The injury can occur anywhere along the course of the ureter and most often is confined to one side of the body. Similar to other organs of the genitourinary system, ureteral injuries often present clinically with gross or microscopic hematuria. However, hematuria may

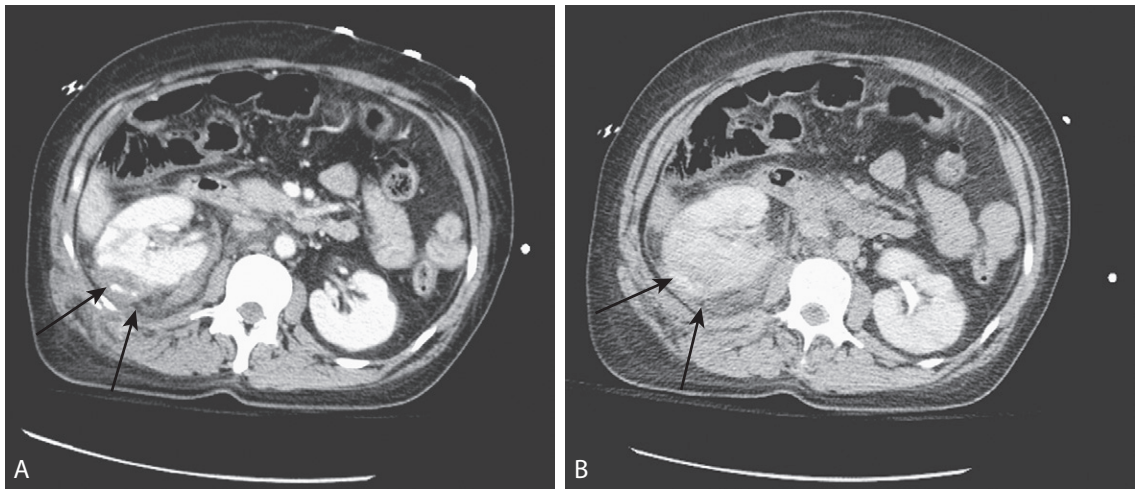


FIGURE 3-45 A 42-year-old woman pedestrian who was struck by a car and then fell off a bridge. Axial contrast-enhanced images in the arterial (**A**) and portal venous (**B**) phases demonstrate active extravasation *(arrows)* from the right kidney.

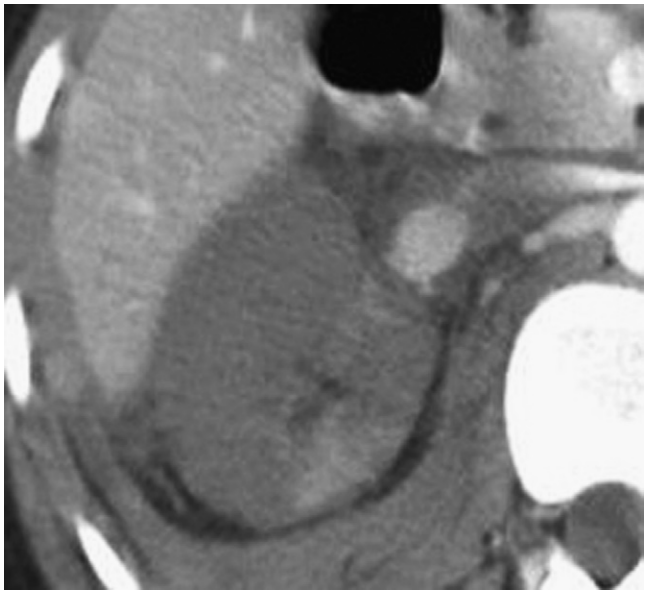


FIGURE 3-46 A renal vascular pedicle injury. An axial computed tomography image in this patient after a high-speed motor vehicle collision demonstrates diminished enhancement in a large portion of the right kidney as a result of this vascular pedicle injury.

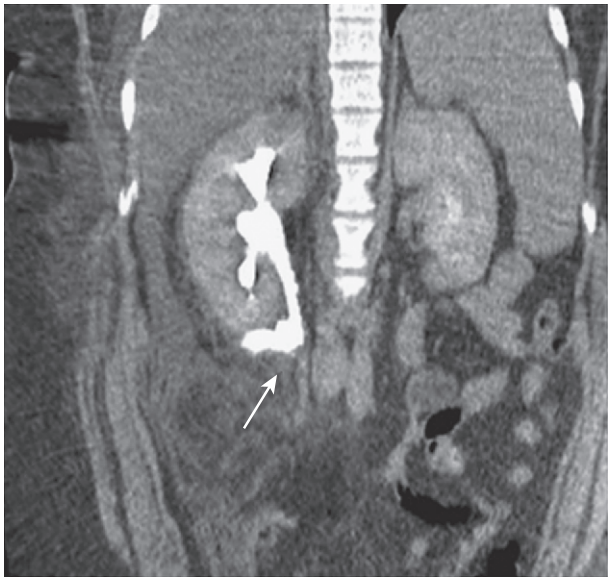


FIGURE 3-47 Ureteral trauma. A coronal reformatted image obtained at a 5-minute delay demonstrates abrupt termination of the proximal right ureter with extraluminal contrast material just lateral to the site of injury, adjacent to the lower pole of the right kidney *(arrow)*. This patient required placement of a stent to treat the injury. *(Reprinted with permission from Stuhlfaut JW, Soto JA, Lucey BC, et al. Blunt abdominal trauma: performance of CT without oral contrast material.* Radiology. *2004;233:689-694.)*

not be present in up to 25% of patients with ureteral trauma, and thus these injuries may not be suspected at the time of abdominal CT or exploratory surgery (especially in the case of penetrating trauma). In the past, intravenous urography was the imaging test of choice for detecting ureteral injuries; however, CT has essentially replaced intravenous urography in that setting.

When a focal injury of the collecting system or ureter is suspected, delayed CT images are mandatory. These images typically are obtained 5 to 7 minutes after injection of contrast material to avoid unnecessary delay in patient care while the patient is undergoing diagnostic imaging evaluation. Early portal venous-phase images may show abnormal fluid or stranding adjacent to the ureter; delayed images show extravasation of urine with contrast at the site of the injury (Fig. 3-47). Multiplanar reformations are useful in highlighting the site of injury and may aid the urologist in treatment planning.

ADRENAL TRAUMA

Injury of the adrenal gland is uncommon, occurring in approximately 1% of all patients who sustain abdominal trauma. An isolated adrenal injury is even rarer, occurring in less than 5% of all patients with adrenal trauma. Instead, most patients with adrenal injuries also have sustained an injury to one or more other solid organs in the abdomen, most commonly the liver, spleen, or kidney. Ipsilateral rib fractures are also common. Adrenal injuries typically occur

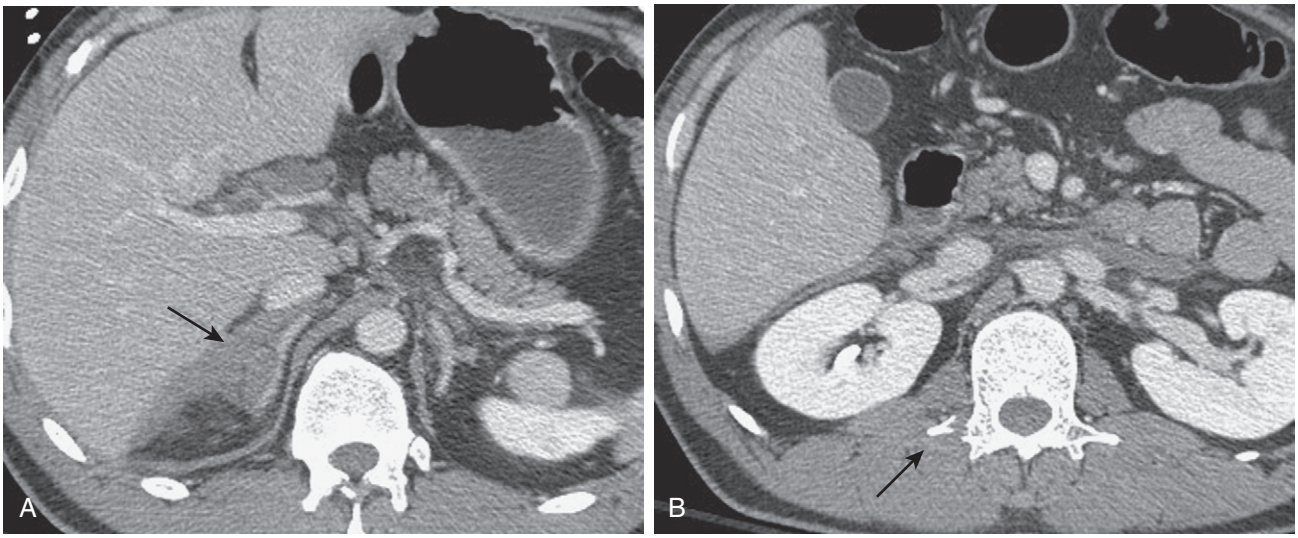


FIGURE 3-48 Adrenal injury. **A,** A transverse computed tomography image in this patient after blunt trauma depicts a right adrenal hematoma *(arrow)* with stranding of soft tissue in the periadrenal region. **B**, Adrenal injuries are often associated with fractures of the transverse process, as was evident in this patient at a level below the site of adrenal injury *(arrow)*.

on the right side and are much less commonly seen in isolation in the left adrenal gland. Possible explanations for this discrepancy that have been offered include the position of the right adrenal gland in relatively tight quarters between the spine and the liver and the fact that the right adrenal gland is subject to higher venous pressure than the left adrenal gland when increased abdominal pressure occurs at the time of injury. The right adrenal gland might see relatively higher venous pressures transmitted from the vena cava, whereas venous pressures are filtered by the left renal vein before reaching the left adrenal gland. Regardless, injury to the adrenal gland can be readily identified on routine trauma CT imaging. Typically, adrenal injuries appear as round or ovoid nodules replacing the normal adrenal gland. Not uncommonly, there is a fracture of an ipsilateral transverse process (Fig. 3-48). These hematomas can be associated with surrounding periadrenal fat stranding on CT. It is important to distinguish adrenal hematomas from incidental adrenal nodules, which are commonly seen in the trauma population (and in the general population). It is helpful to measure the attenuation of the lesion. Most adrenal hematomas have attenuation coefficients higher than 50 Hounsfield units (HUs). Adrenal injuries typically have a higher HU than other adrenal lesions such as adenomas, which often have attenuation measurements of less than 10 HUs. If they are available, delayed images (10 to 15 minutes after injection of contrast material) can help characterize the lesion by determining the washout characteristics. If there is any question, follow-up imaging can be obtained to assess for interval change in the suspected adrenal injury. On follow-up CT, adrenal hematomas typically regress or calcify. In addition, pseudocysts can develop as sequelae of adrenal injury. Rarely, clinical manifestations of adrenal insufficiency can develop in patients with a bilateral adrenal injury.

PELVIC TRAUMA

Although the pelvis communicates with the peritoneal and extraperitoneal compartments of the abdominal cavity and is imaged concomitantly with the abdomen at the time of admission CT, the unique anatomic disposition of the pelvic ring and the types of injuries encountered deserve a separate discussion in this chapter. In most settings, a portable radiograph of the pelvis is obtained upon arrival at the trauma bay of a patient who has sustained multiple traumas. If a displaced (and possibly unstable) fracture of the pelvic ring is demonstrated, the pelvic cavity should be investigated carefully for associated injuries to the vascular structures, rectum, bladder, or urethra. Strong forces are necessary to disrupt the osseous pelvic ring; the radiographic evaluation of trauma to the bony pelvis is discussed in detail in Chapter 4.

The possibility of vascular injury and major (sometimes life-threatening) bleeding should be considered in every patient with a disruption of the pelvic ring. CT has been shown to be valuable in evaluating for vascular injury in patients with pelvic trauma. Large hematomas and foci of active extravasation are the main findings that may prompt a consultation with the interventional radiology service for possible endovascular therapy via embolization. Multiphasic CT imaging provides a temporal assessment of change in the size of the hematoma and an indirect means of estimating the rate of bleeding (Fig. 3-49).

Bladder Trauma

Bladder injuries result from blunt (70% to 80%) or penetrating (20% to 30%) trauma. Common causes of bladder rupture include direct impact with the steering wheel or seat belt in motor vehicle accidents and assaults to the lower abdomen by a kick or blow. The likelihood of bladder trauma is directly related to the degree of distention at the time of the injury, with a full bladder more likely to rupture than an empty one. A high clinical suspicion and timely diagnosis are the keys to successful medical or surgical treatment. Approximately 10% of patients with pelvic fractures have bladder injuries, and the likelihood of bladder injury is directly related to the severity of the fracture.

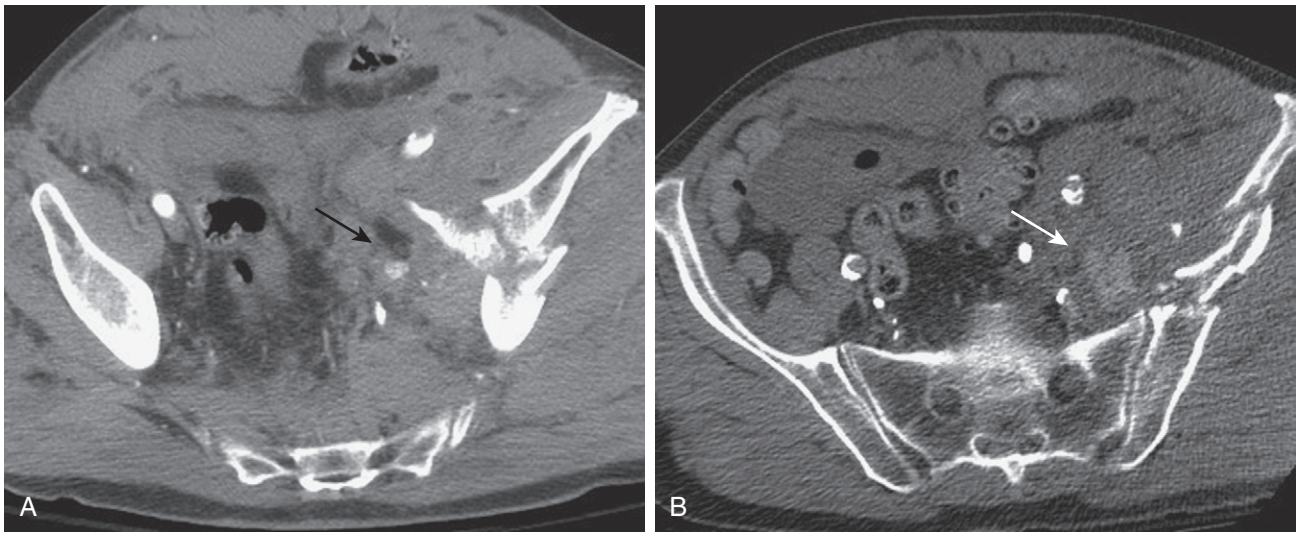


FIGURE 3-49 A complex pelvic fracture with active bleeding. **A,** A transverse computed tomography (CT) image obtained as part of a CT angiogram demonstrates a complex fracture of the left ilium with a large pelvic hematoma and active extravasation of contrast material *(arrow)*. **B,** A CT image obtained at 5-minute delay shows an increase in the size of the hematoma with continued diffusion of blood and contrast material *(arrow)* into the site of the injury.

A high association also exists between bladder rupture and urethral disruption.

Patients with signs and symptoms suggestive of a bladder injury typically have a history of pelvic trauma, often with a fracture evident on the admission radiograph. Although the clinical signs of bladder injury are nonspecific, a triad of symptoms is often present: suprapubic pain, gross hematuria, and an inability to void or difficulty in doing so. The hallmark of a bladder rupture is hematuria, which is almost invariably present. More than 95% of bladder ruptures are associated with gross hematuria, and 5% are associated with microscopic hematuria. Because some patients can still void, the ability to urinate does not exclude bladder injury or perforation. Whenever a bladder injury is suspected, the patient should be further evaluated with conventional cystography or CT cystography, and the threshold for performing these tests should be very low.

Cystography

A well-performed cystogram begins with an abdominal radiograph (scout view). This radiograph serves to evaluate the pelvic bones and determine if any displaced fracture is present that could limit the patient's ability to position properly. Subsequently, a Foley catheter should be placed into the bladder. However, it is mandatory to carefully inspect the urethral meatus for evidence of gross blood before attempting to catheterize the bladder. Blood at the urethral meatus is an absolute indication for retrograde urethrography to assess urethral integrity before attempting to blindly pass a Foley catheter. Approximately 10% to 20% of men with a posterior urethral injury have an associated bladder injury. Blind passage of a urethral catheter may convert a partial disruption of the urethra into a complete tear. If a posterior urethral injury is present, placement of a percutaneous suprapubic catheter may be necessary to evaluate bladder integrity.

Once the lumen of the bladder has been catheterized, diluted water-soluble contrast material is slowly instilled by gravity (approximately 75 cm above the pelvis). The examination should be performed under continuous fluoroscopic observation. If gross extravasation is noted, no further distention is necessary. If extravasation is absent, the remainder of the contrast material is infused (to 300 to 400 mL total) until full distention is achieved. Spot fluoroscopic images should be obtained as necessary. Standard static projections include anteroposterior and oblique views of the bladder filled with contrast material, along with another anteroposterior film obtained after drainage. Oblique films are often difficult to obtain in a patient with pelvic fractures and may be omitted in selected cases. The total volume of contrast material administered is less important than ensuring that adequate bladder distention is achieved, in order to demonstrate small injuries that otherwise may not be detected. Some superficial lacerations may seal temporarily by wall edema or by an overlying hematoma, omentum, or adjacent segment of large or small bowel. Full distention helps prevent this false-negative result. Also, the postdrainage film is a critical part of the study because it may disclose small foci of extravasation that may be hidden by the distended bladder. The accuracy of a well-performed cystogram ranges between 90% and 98%.

CT Cystography

Most patients with bladder injuries have sustained multiple trauma and require abdominal or pelvic CT scans as part of their evaluation. The CT scan of the pelvis provides information on the status of the pelvic organs and osseous pelvis. Occasionally, bladder rupture is shown on the initial pelvic CT images, with urine that contains contrast material accumulating in the perivesical space or peritoneal cavity (Fig. 3-50). However, bladder integrity is not confirmed until full distention of the bladder with homogeneously opacified fluid is achieved. A CT cystogram is performed after the abdominopelvic CT is completed. With a Foley catheter secured in the bladder, water-soluble contrast material is instilled to achieve full distention (typically 300 to 400 mL). CT images limited to the pelvis are then obtained.

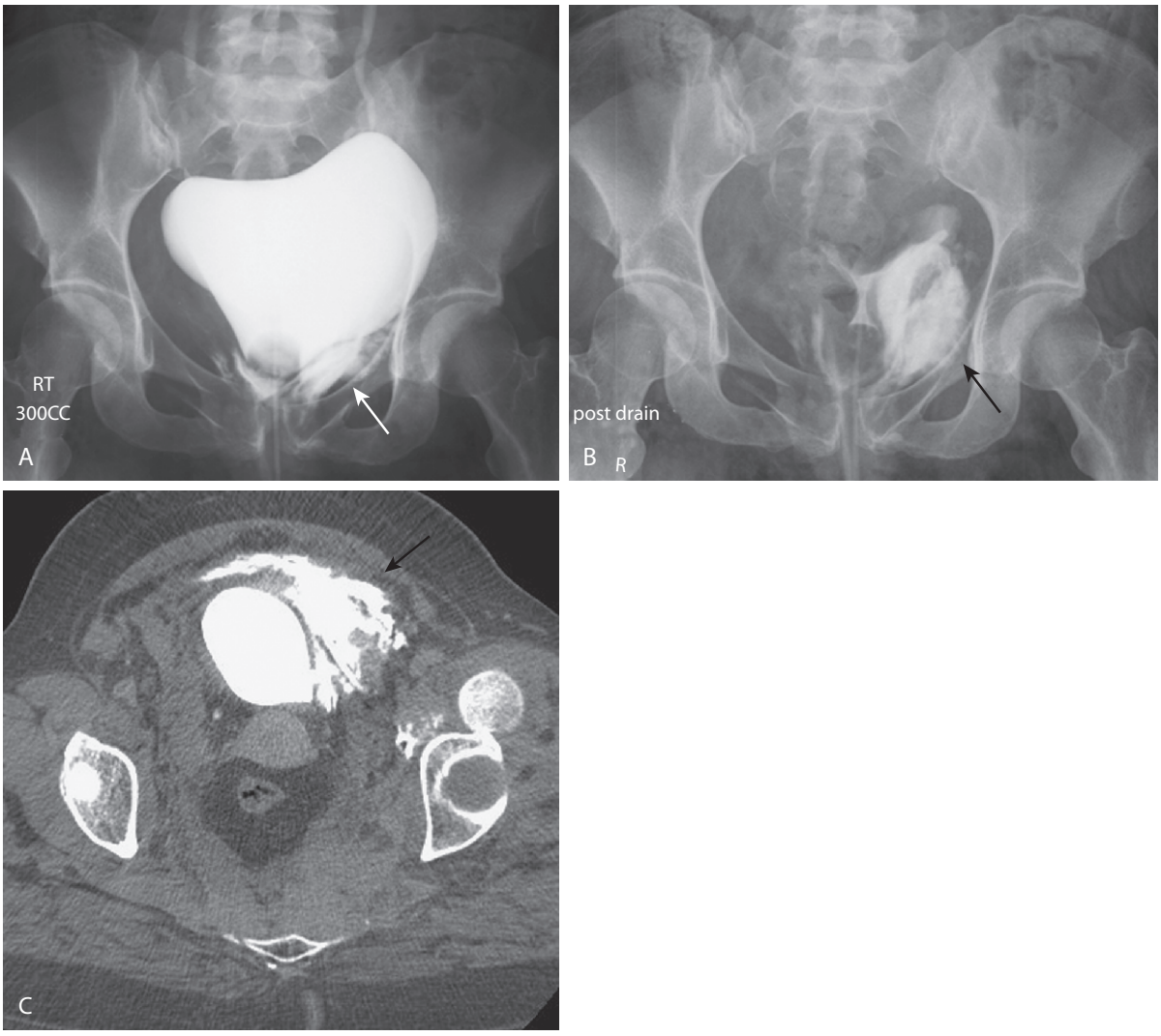


FIGURE 3-50 Cystographic and computed tomography (CT) appearance of an extraperitoneal bladder rupture. **A,** An anteroposterior image of the pelvis obtained after gravity-assisted bladder distention demonstrates contrast material outside the expected lumen of the bladder *(arrow).* **B,** This finding is better depicted on the postdrainage film *(arrow),* which clearly depicts the extraperitoneal nature of this injury. **C,** On CT cystography, extraluminal contrast due to a bladder injury is also readily identified *(arrow).*

Although CT cystography lacks the temporal, dynamic information provided by fluoroscopy, the superior contrast resolution compensates for this limitation, often showing small accumulations of extravesical contrast material. In the majority of major trauma centers, CT cystography has replaced conventional cystography as the most widely used method to assess bladder integrity.

Types of Bladder Rupture

Bladder ruptures are classified as extraperitoneal, intraperitoneal, or combined (intra- and extraperitoneal). This distinction is critical, because management varies considerably: intraperitoneal ruptures require immediate surgical therapy, whereas extraperitoneal ruptures are usually managed with bladder drainage and delayed reconstruction, when necessary. Extraperitoneal injuries account for approximately 70%, intraperitoneal injuries account for approximately 20%, and combined perforations account for approximately 10% of all injuries. The proportion of intraperitoneal ruptures is considerably higher in children because of the predominantly intraabdominal location of the bladder in this age group; usually the bladder descends into the pelvis by the age of 20 years.

In blunt trauma, extraperitoneal bladder ruptures are almost invariably associated with pelvic fractures. Rupture may occur either from a direct perforation by a bony fragment (as with fractures of the anterior pubic arch) or from a burst injury or sudden shearing force from the pelvic ring at the time of the impact. The classic finding on cystography or CT cystography is contrast extravasation around the base of the bladder confined to the peri- and prevesical space (of Retzius); flame-, starburst-, or molar tooth–shaped areas of contrast extravasation are characteristic (see Figs. 3-50 and 3-51). An associated pelvic hematoma may give the bladder a teardrop shape. With a more complex injury, the contrast material extends to the thigh, scrotum (or labia), penis, or perineum, or into the anterior abdominal wall (Fig. 3-52). Extravasation will reach the scrotum when the superior fascia of the urogenital diaphragm or the urogenital diaphragm itself has been

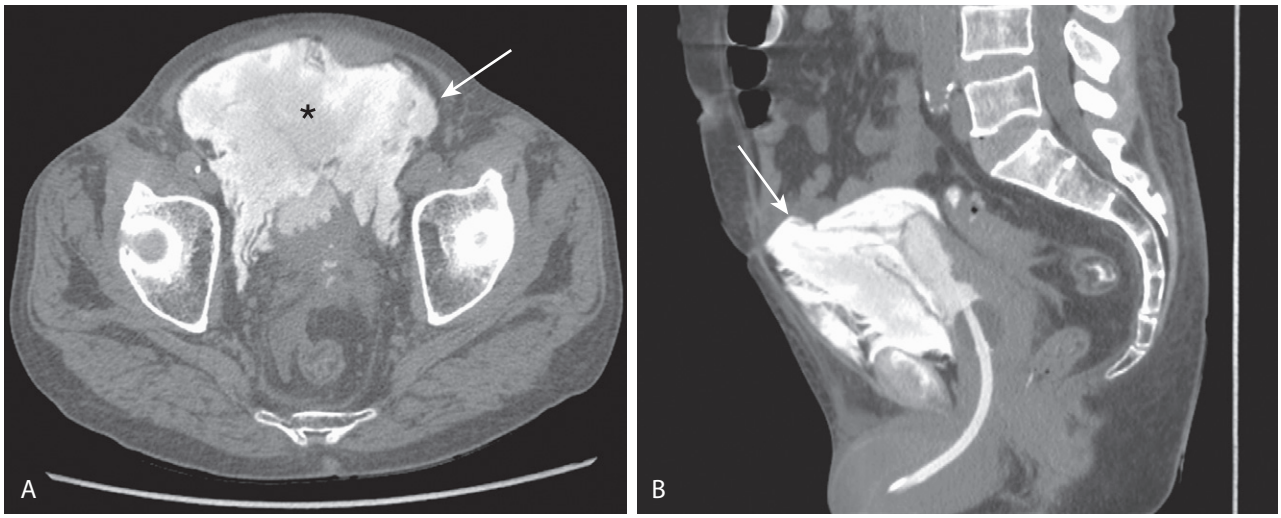


FIGURE 3-51 A 55-year-old man who was in a motor vehicle collision. Axial (**A**) and sagittal (**B**) images from a computed tomography cystogram demonstrate an extraperitoneal bladder rupture with instilled bladder contrast material pooling in the space of Retzius *(arrow)*, causing the classic "molar tooth" sign on the axial image *(asterisk)*.



FIGURE 3-52 An extraperitoneal bladder injury. An axial image from a computed tomography cystogram demonstrates extraluminal contrast within the prevesicle space due to an acute extraperitoneal bladder injury. In addition, contrast material has tracked inferiorly and laterally in the left inguinal region.

disrupted. If the inferior fascia of the urogenital diaphragm is violated, the contrast material will reach the thigh and penis (contained by Colles fascia).

A typical intraperitoneal rupture results from a horizontal tear occurring in the dome of the bladder (Fig. 3-53). The dome is the weakest and least supported area and the only portion of the adult bladder covered by peritoneum. The mechanism of injury is usually a direct blow to a fully distended urinary bladder. Initial CT images often demonstrate low-attenuation fluid within the peritoneal cavity, as well as gas if a Foley catheter has been introduced. On cystography, contrast material accumulates in the peritoneal cavity, outlines loops of bowel, and fills the paracolic gutters, pouch of Douglas, and other peritoneal spaces, including the subphrenic spaces (Fig. 3-53). In combined intraperitoneal and extraperitoneal ruptures, cystography reveals contrast material outlining the abdominal viscera and perivesical space. Combined ruptures are common after penetrating injuries from a high-velocity bullet or a knife traversing the bladder.

Urethral Injury

Early recognition of urethral injuries is necessary to prevent serious long-term sequelae such as strictures that require recurrent interventions to prevent infectious complications. The vast majority of urethral injuries occur in men. Most urethral injuries are associated with major blunt trauma such as that caused by motor vehicle accidents or falls, but penetrating injuries, although rarely, may be the cause as well. Given the severity of the traumatic event that caused the urethral injury, many of these men have associated neurologic and orthopedic injuries that further complicate therapy. Iatrogenic causes, such as traumatic catheter placement or transurethral dilation, also can occur.

Urethral injuries are usually classified as belonging to one of two types, based on the anatomic site of the tear: posterior urethra or anterior urethra. Posterior urethral injuries are more common and usually occur at the junction of the prostatic and membranous segments, where the urethra is fixed by the attachments of the puboprostatic ligaments. Thus posterior urethral injuries are typically caused by severe blunt trauma with fractures of the anterior pelvis; displacement of the bone fragments overstretches the short membranous segment. Male patients with pelvic fractures have a 5% to 10% incidence of posterior urethral injury.

Anterior urethral injuries affect the bulbar or penile segments and are usually the result of trauma to the perineum, such as straddle injuries. Relatively minor trauma can injure the bulbar urethra, but the diagnosis may be delayed by months or even years, when patients present with urethral strictures. Occasionally, tears of the penile urethra are seen in the setting of a penile fracture.

Diagnosis Retrograde Urethrogram

The possibility of a urethral injury should be considered in every patient with a pelvic fracture before blindly

inserting a Foley catheter into the bladder. Other potential antecedent history, such as traumatic catheterization, straddle injury, or any penetrating injury near the urethra, should also raise suspicion. Symptoms include hematuria and an inability to void. However, these symptoms are rarely useful in the setting of major acute trauma, when patients are intubated and sedated or unconscious. Upon physical examination, the hallmark finding is the presence of blood at the meatus or a high-riding prostate gland upon rectal examination.

The diagnosis is confirmed with a retrograde urethrogram, which must be performed prior to insertion of a catheter into the bladder to avoid further injury to the urethra. For the retrograde urethrogram, a Foley catheter is generally preferred rather than the Brodney clamp. A 16-French catheter is placed into the distal urethra, and the balloon (3 mL) is inflated within the fossa navicularis; 30 to 60 mL of water-soluble contrast material is then injected under fluoroscopic guidance using a 60-mL piston syringe. Oblique views (when possible) are usually the most helpful.

Urethrography serves to assess integrity and to localize and characterize tears as complete or incomplete. In posterior urethral injuries, contrast material accumulates outside the urethra in the retropubic extraperitoneal space (Fig. 3-54). At least some continuity is present in a partial rupture, which allows partial filling of the bladder, in addition to the extravasated contrast material. Complete tears are shown as an interruption of the urethra. Involvement of the urogenital diaphragm is assumed when contrast material accumulates in the perineum. Partial tears of the posterior urethra usually heal uneventfully, whereas complete tears may heal with formation of a stricture. Other long-term symptoms associated with severe urethral injuries include impotence and, rarely, incontinence. These sequelae are more likely a reflection of the severity of the initial trauma rather than being caused by the urethral injury itself. In anterior urethral injuries, contrast material may fill the corpora cavernosa or corpus spongiosum, or it may reflux into the draining veins.

Rectal Injury

The rectum is rarely injured as a result of blunt trauma. When it is injured, there is often a history of direct perineal force at the time of the traumatic event, and patients often have associated pelvic fractures. A rectal injury can be difficult to detect clinically, although some patients present with bright red blood in the rectum. Physical examination may detect the presence of blood or bone fragments in the rectal vault, indicating a high likelihood of injury. Often, patients with suspected injury are evaluated directly with a rigid sigmoidoscope. However, rectal injuries are increasingly diagnosed at the time of diagnostic CT imaging. CT

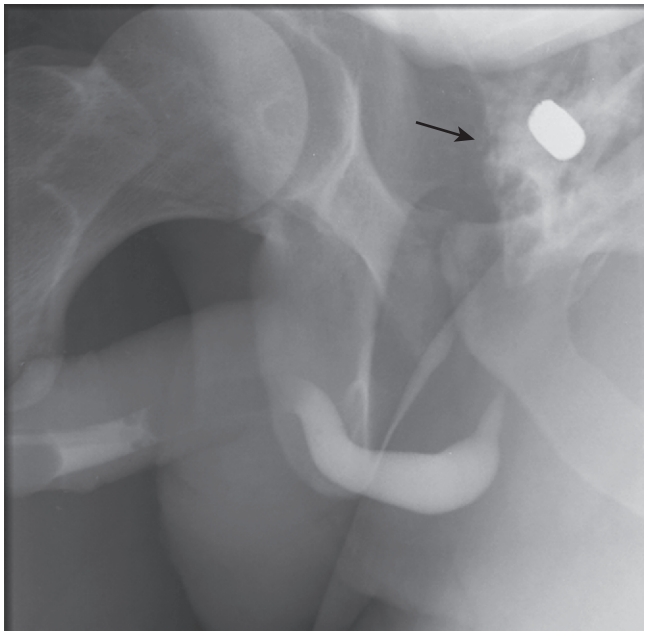


FIGURE 3-54 A posterior urethral injury after acute trauma. The image, obtained at the time of retrograde urethrography, demonstrates extravasation of contrast material into the retropubic space *(arrow)* from a posterior urethral injury.

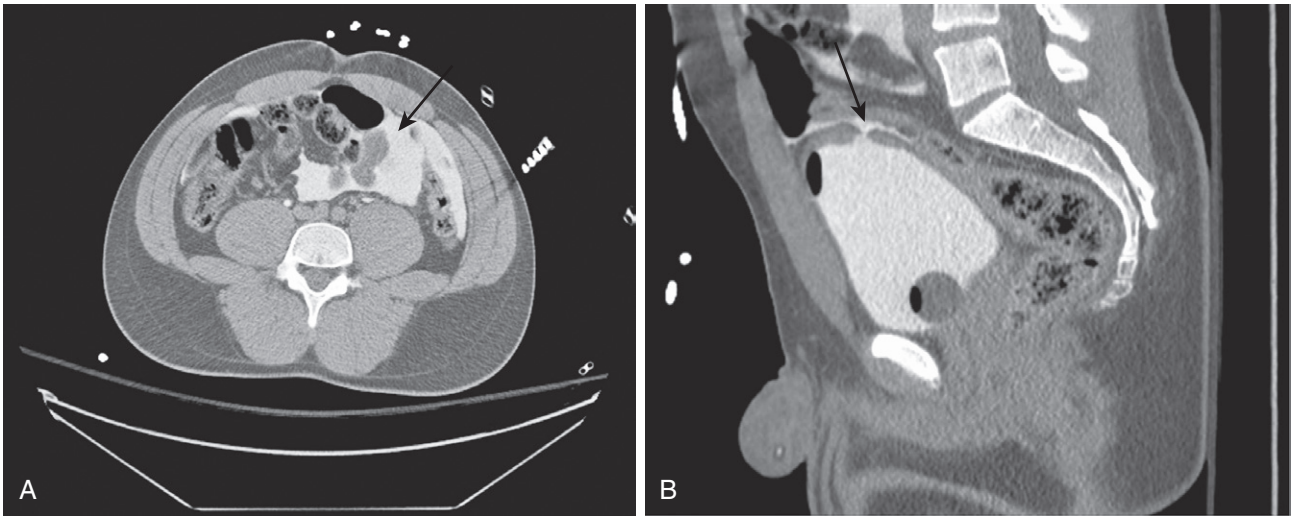


FIGURE 3-53 A 30-year-old man who was in a motor vehicle collision. Axial (**A**) and sagittal (**B**) images from a computed tomography cystogram demonstrate an intraperitoneal bladder rupture. On the axial image, instilled bladder contrast material is seen within the peritoneum interdigitating between loops of bowel *(arrow)*. On the sagittal image, instilled bladder contrast material is seen flowing through a defect in the dome of the bladder into the peritoneal cavity *(arrow)*.

imaging may show focal rectal wall thickening (Fig. 3-55) or localized free air in the perirectal fat. In addition, a hematoma may be present in the perirectal fat as a result of such an injury. Water-soluble contrast material administered as an enema may be necessary to demonstrate the site of perforation in questionable cases (Fig. 3-56).

PENETRATING ABDOMINAL TRAUMA

Penetrating abdominal trauma caused by stab or gunshot wounds is a frequent cause of admission to emergency departments in large urban centers. The pathophysiology involved in penetrating trauma is unpredictable, and the pattern of injuries differs from blunt abdominal trauma. Compared with blunt trauma, injuries to the bowel, mesentery, and diaphragm are more common with penetrating trauma. Bowel injuries may remain clinically occult for several hours after trauma occurs, and thus early detection of bowel injuries is a major concern in this patient group. In the past, an exploratory laparotomy was considered mandatory for diagnosis and treatment of all patients with confirmed penetration of the peritoneum. This surgical approach is based on the following assumptions: a laparotomy is necessary to exclude intraabdominal injuries; a diagnostic laparotomy is associated with little morbidity; and increased morbidity and mortality are associated with delayed treatment of injuries to the hollow viscera. An immediate laparotomy is still mandated when the penetrating injury is associated with definite signs of peritoneal irritation, hemodynamic instability, gastrointestinal bleeding, or evisceration. However, if all penetrating abdominal injuries are managed with surgery, even without clinical evidence to suggest visceral involvement, the frequency of negative or nontherapeutic laparotomy varies between 20% and 40%. The rate of complications is also high, in the range of 5% to 20%, for patients with negative or nontherapeutic laparotomy findings.



FIGURE 3-55 An acute rectal injury. A sagittal reformat obtained after trauma computed tomography shows focal thickening of the posterior rectal wall *(arrow)* with fluid in the presacral space. A rectal laceration was confirmed at surgery.

The high proportion of negative laparotomy findings and the relatively high frequency of complications led some surgeons to question the need for mandatory surgical exploration in this setting. Knowledge gained from conservative or nonsurgical treatment of blunt trauma has resulted in an extension of this alternative treatment to some victims of penetrating stab injuries and, more recently, to select groups of victims of gunshot wounds. With a conservative approach, patients who have sustained penetrating trauma and do not have an indication for immediate laparotomy at presentation are admitted to the hospital and observed for 24 hours or longer. During the period of clinical observation, laparotomy becomes necessary if abdominal pain (which is almost invariably present at admission) worsens progressively or if the patient experiences rebound tenderness, generalized abdominal guarding, hypoperistalsis, unexplained shock, or gastrointestinal

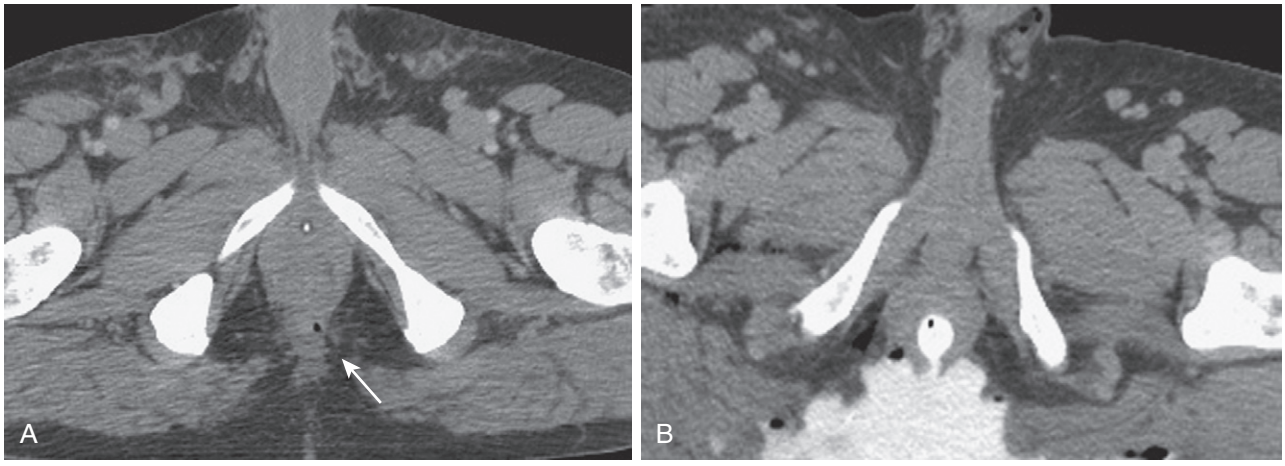


FIGURE 3-56 An acute rectal injury after a blunt injury. **A,** An axial computed tomography (CT) image obtained during the initial trauma CT demonstrates stranding in the soft tissue posterior to the distal rectum *(arrow)*, which is suspicious for an acute injury. **B,** After administration of water-soluble rectal contrast material, a posterior laceration with contrast extravasation is readily identified.

bleeding. The downside is that the delay generated by the period of observation may increase the severity of peritoneal involvement and cause a longer postoperative course if a laparotomy is eventually required and a hollow viscus injury is found. Thus this conservative approach has resulted in a growing interest in using diagnostic procedures and imaging tests such as peritoneal lavage, laparoscopy, US, and CT to identify patients with occult injuries that require operative management before they become clinically apparent, including injuries to the hollow viscera, mesentery, large vessels, and diaphragm.

Peritoneal lavage has high sensitivity but low specificity. Use of an elevated cell count as a criterion for the need for laparotomy is not uniform and has not been adjusted to the modern concept of nonsurgical treatment of wounds to the solid viscera. In general, patients with occult hollow viscus injury are not well evaluated by means of diagnostic peritoneal lavage. Laparoscopy is useful for diagnosis of peritoneal violation and wounds of the diaphragm and, in some patients, therapeutic procedures can be performed at the same time. The downside is that laparoscopy is an invasive procedure that requires general anesthesia, evaluation of the retroperitoneum is limited, and visualization of all the hollow viscera is incomplete.

Ultrasonography

As previously mentioned, the main use of US in blunt trauma is for detecting (and grossly quantifying) free intraperitoneal fluid. US has also been proposed for stable patients who have penetrating torso injuries caused by gunshots or by sharp objects. Unfortunately, the finding of free fluid is not a specific indicator of an occult gastrointestinal tract or major vascular injury. Furthermore, when the results of US are negative, injuries to the hollow viscera or diaphragm are not excluded, and other diagnostic studies must be performed. Thus US findings are of very little help in the decision-making process, and the method is not particularly useful for the evaluation of penetrating abdominal trauma.

Computed Tomography

Although not widely used in the setting of penetrating trauma, CT increasingly is being used in hemodynamically stable patients who have sustained a penetrating trauma. Initial reports on the use of CT for penetrating trauma were limited to asymptomatic patients with injuries in the back and flank, because they infrequently have associated injury to critical retroperitoneal viscera as a result of the good protection provided by the ribs, spine, and large paraspinal muscles. Given the higher frequency of hollow viscus injuries that occurs in penetrating trauma, it is mandatory that patients receive intravenous, oral, and rectal contrast material (a "triple-contrast" CT) to maximize the diagnostic potential of CT for penetrating trauma. Typically, patients receive 600 to 800 mL of diluted (2% to 3% concentration) water-soluble (iodinated) contrast material orally and a 1- to 1.5-L enema of similarly diluted water-soluble contrast material. Oral contrast material should be administered within 30 minutes of CT data acquisition. Rectal contrast is typically administered on the CT table, immediately prior to CT scanning. Several studies have found this approach to be highly sensitive and specific for detecting and ruling out hollow viscus injuries. As for patients with blunt trauma, delayed images (3 to 5 minutes after the initiation of intravenous contrast material injection) should be acquired for a complete evaluation of the renal collecting system and ureters and for characterization of extravascular collections of contrast-enhanced blood. The diagnostic criteria used for interpretation of blunt trauma CT scans cannot be applied to patients with penetrating trauma. The presence of free intraperitoneal air or free peritoneal fluid is a sign of peritoneal violation but is not definitive evidence of a bowel injury, because air can be introduced into the peritoneal cavity by a bullet or knife wound, and free fluid can be the result of bleeding from the peritoneal lining itself (Fig. 3-57). The only unequivocal sign of a hollow viscus injury is the presence of extraluminal collections of oral or rectal contrast material (Fig. 3-58).

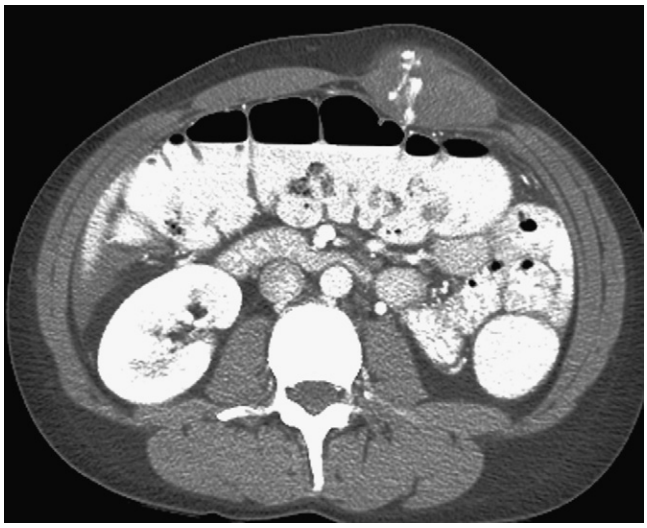


FIGURE 3-57 A penetrating injury with a rectus abdominis hematoma. Axial computed tomography obtained to evaluate a stab wound to the anterior abdomen demonstrates thickening of the left rectus muscle with active contrast extravasation. Free fluid is present in the right abdomen, but the bowel appeared completely normal. This patient recovered without need for exploratory surgery.

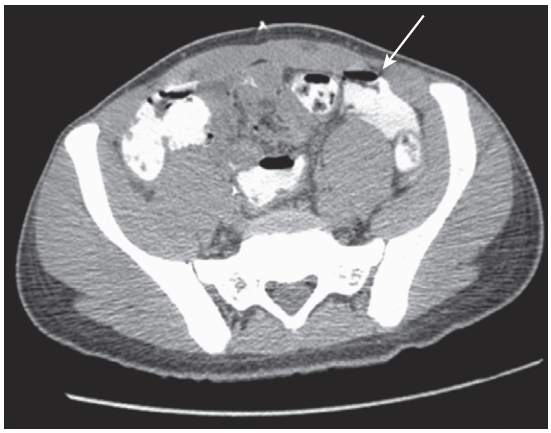


FIGURE 3-58 A bowel injury after penetrating trauma. Axial computed tomography with use of a rectal contrast agent obtained to evaluate a gunshot wound demonstrates extraluminal contrast *(arrow)* from an acute, full-thickness, colonic injury.

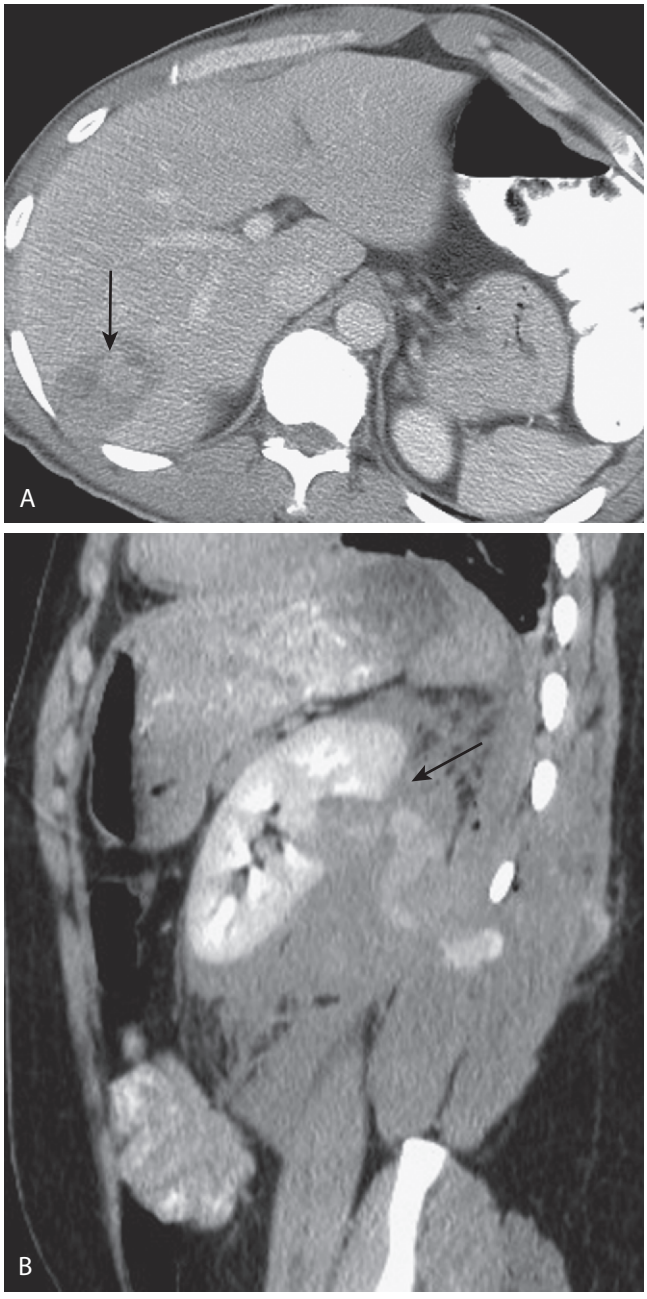


FIGURE 3-59 A solid organ injury after an acute gunshot injury. **A,** Axial computed tomography obtained after the acute injury demonstrates a focal liver laceration in segment 7 *(arrow).* **B,** A sagittal reformat also demonstrates a focal renal laceration with a large perinephric hematoma *(arrow).*

Other CT findings considered highly indicative of bowel injury include the presence of focal bowel wall thickening or discontinuity and a bowel wall hematoma. Mesenteric injuries are confirmed by finding active extravasation of contrast material, as shown by the portal venous and delayed phase scans, or a focal mesenteric hematoma. Injuries to solid organs resulting from penetrating injuries

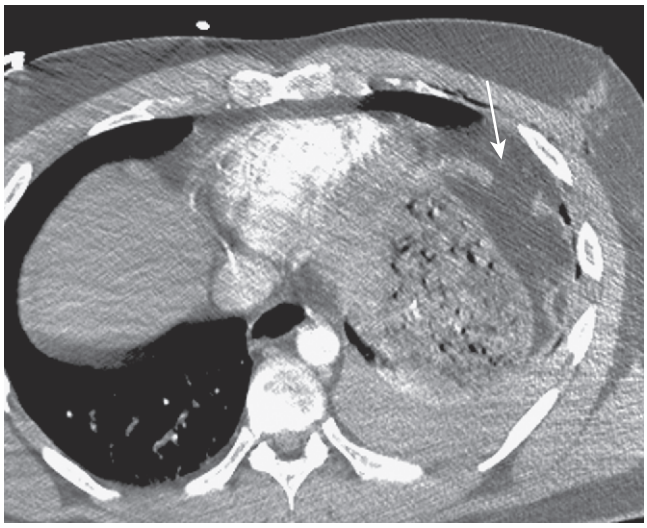


FIGURE 3-60 A diaphragmatic injury. Axial computed tomography obtained after a gunshot injury demonstrates a focal rent in the diaphragm *(arrow).* The stomach has herniated into the left side of the chest through the defect.

are similar in appearance to those from blunt trauma (Fig. 3-59). Injury to the diaphragm is suspected when the trajectory of the missile or sharp object appears to extend toward or to the diaphragm. More specific signs, however, include finding herniated abdominal content into the chest through the diaphragmatic rent (Fig. 3-60), the CT "collar" sign (focal constriction of herniated abdominal fat or viscera at the site of the diaphragmatic defect), and the finding of injured organs on either side of the diaphragm when only one injury was inflicted (thoracoabdominal injury). CT findings of potential diaphragm injury include a penetrating injury tract that extends to the diaphragm, thickening of the diaphragm, and an isolated focal defect in the normal continuity of the diaphragm without adjacent hemorrhage. If a question concerning the presence of peritoneal penetration persists during the period of clinical observation, a laparoscopy should be performed as a definitive test.

CT is also increasing being used after an emergent exploratory laparotomy in search of missed injuries at the time of surgery. Commonly missed injuries in the peritoneal cavity at exploratory laparotomy include the esophagogastric junction, proximal jejunum (at the ligament of Treitz), mesenteric border of small bowel, and the posterior wall of the transverse colon. Commonly missed injuries in the retroperitoneum at an exploratory laparotomy include the retroperitoneal duodenum, ureters, and extraperitoneal rectum and bladder. Frequently encountered findings on the postexploratory laparotomy CT include an open abdomen with towel clips or a vacuum dressing, retained surgical equipment, visceral hemostasis with gauze pads, foreign bodies such as bullet fragments, bowel ligation without anastomosis, and CT findings of hypovolemic shock (Fig. 3-61).

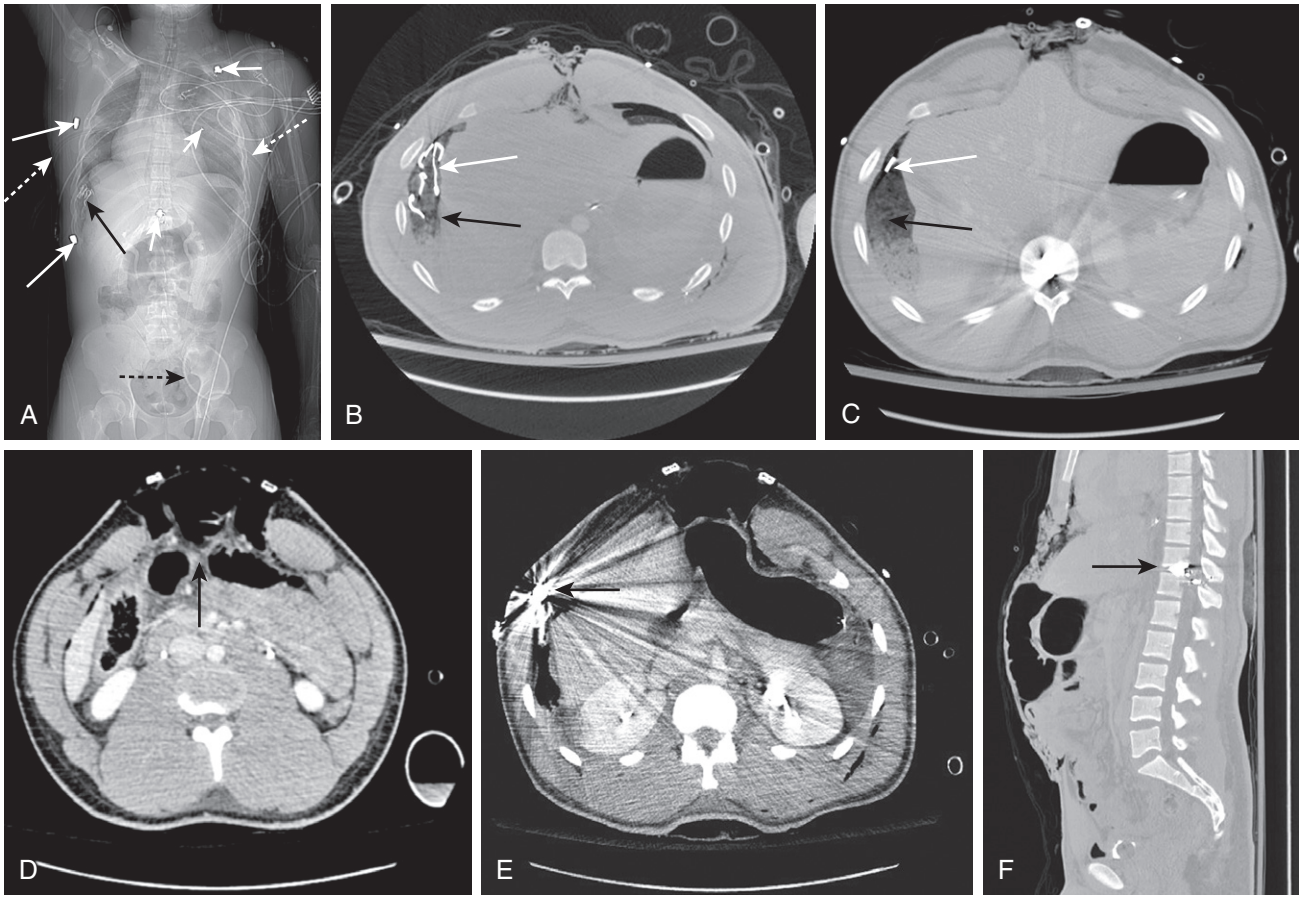


FIGURE 3-61 A 20-year-old man who sustained multiple gunshot wounds and underwent an emergent exploratory laparotomy. **A,** A scout image from a postexploratory laparotomy computed tomography (CT) scan demonstrates multiple bullet fragments *(white arrows)*, bilateral chest tubes *(dashed white arrows)*, packing material adjacent to the liver in the right upper quadrant *(black arrows)*, and a wound vacuum device *(black dashed arrow)* over the open abdomen. **B** and **C,** Axial CT images through the upper abdomen illustrate the appearance of surgical packing material with its linear hyperdense ribbon *(white arrow)* and intervening foci of air *(black arrow)*. **D,** An axial CT image showing the wound vacuum overlying bowel loops that herniate through the open laparotomy defect *(arrow)*. **E** and **F,** Radio-opaque bullet fragments are seen in the right upper quadrant soft tissues and traversing the lower thoracic spinal canal *(arrows)*.

SUGGESTED READINGS

Atri M, Hanson JM, Grinblat L, et al. Surgically important bowel and/or mesenteric injury in blunt trauma: accuracy of multidetector CT for evaluation. *Radiology*. 2008;249:524–533.

Boscak AR, Shanmuganathan K, Mirvis SE, et al. Optimizing trauma multidetector CT protocol for blunt splenic injury: need for arterial and portal venous phase scans. *Radiology*. 2013;268:79–88.

Bouras AF, Truant S, Pruvot FR. Management of blunt hepatic trauma. *J Visc Surg*. 2010;147:e351–e358.

Carter JW, Falco MH, Chopko MS, et al. Do we really rely on fast for decision-making in the management of blunt abdominal trauma? *Injury*. 2015;46:817–821.

Drasin TE, Anderson SW, Asandra A, et al. MDCT evaluation of blunt abdominal trauma: clinical significance of free intraperitoneal fluid in males with absence of identifiable injury. *AJR Am J Roentgenol*. 2008;191:1821–1826.

Dreizin D, Munera F. Blunt polytrauma: evaluation with 64-section whole-body CT angiography. *Radiographics*. 2012;32:609–613.

Gordon RW, Anderson SW, Ozonoff A, et al. Blunt pancreatic trauma: evaluation with MDCT technology. *Emerg Radiol*. 2013;20:259–266.

Higashi H, Kanki A, Watanabe S, et al. Traumatic hypovolemic shock revisited: the spectrum of contrast-enhanced abdominal computed tomography findings and clinical implications for its management. *Jpn J Radiol*. 2014;32:579–584.

Holmes JF, McGahan JP, Wisner DH. Rate of intra-abdominal injury after a normal abdominal computed tomographic scan in patients with blunt trauma. *Am J Emerg Med*. 2014;30:574–579.

LeBedis CA, Anderson SW, Mercier G, et al. The utility of CT for predicting bile leaks in hepatic trauma. *Emerg Radiol*. 2015;22:101–107.

LeBedis CA, Anderson SW, Soto JA. CT imaging of blunt traumatic bowel and mesenteric injuries. *Radiol Clin North Am*. 2012;50:123–136.

Lee CH, Haaland B, Earnest A, et al. Use of positive oral contrast agents in abdominopelvic computed tomography for blunt abdominal injury: meta-analysis and systematic review. *Eur Radiol*. 2013;23:2513–2521.

Lozano JD, Munera F, Anderson SW, et al. Penetrating wounds to the torso: evaluation with triple-contrast multidetector CT. *Radiographics*. 2013;33:341–359.

MacLean AA, Durso A, Cohn SM, et al. A clinically relevant liver injury grading system by CT, preliminary report. *Emerg Radiol*. 2005;12:34–37.

Melamud K, LeBedis CA, Anderson SW, et al. Biliary imaging: multimodality approach to imaging biliary injuries and their complications. *Radiographics*. 2014;34:613–623.

Panda A, Kumar A, Gamanagatti S, et al. Evaluation of diagnostic utility of multidetector computed tomography and magnetic resonance imaging in blunt pancreatic trauma: a prospective study. *Acta Radiol*. 2015;56:387–396.

Petrosoniak A, Engels PT, Hamilton P, et al. Detection of significant bowel and mesenteric injuries in blunt abdominal trauma with 64-slice computed tomography. *J Trauma Acute Care Surg*. 2013;74:1081–1086.

Saksobhavivat N, Shanamuganathan K, Chen HH, et al. Blunt splenic injury: use of a multidetector CT-based splenic injury grading system and clinical parameters for triage of patients at admission. *Radiology*. 2015;274:702–711.

Soto JA, Anderson SW. Multidetector CT of blunt abdominal trauma. *Radiology*. 2012;265:678–693.

Stuhlfaut JW, Lucey BC, Varghese JC, et al. Blunt abdominal trauma: utility of 5-minute delayed CT with a reduced radiation dose. *Radiology*. 2006;238:473–479.

To'o KJ, Duddalwar VA. Imaging of traumatic adrenal injury. *Emerg Radiol*. 2012;19:499–503.

Uyeda JW, LeBedis CA, Penn DR, et al. Active hemorrhage and vascular injuries in splenic trauma: utility of the arterial phase in multidetector CT. *Radiology*. 2014;270:99–106.

Vaccaro JP, Brody JM. CT cystography in the evaluation of major bladder trauma. *Radiographics*. 2000;20:1373–1381.

Wittenberg A, Minotti AJ. CT diagnosis of traumatic gallbladder injury. *AJR Am J Roentgenol*. 2005;185:1573–1574.

Yoon W, Jeong YY, Kim JK, et al. CT in blunt liver trauma. *Radiographics*. 2005;25:87–104.

Yu J, Fulcher AS, Wang DB, et al. Frequency and importance of small amount of isolated pelvic free fluid detected with multidetector CT in male patients with blunt trauma. *Radiology*. 2010;256:799–805.

Chapter 4

Extremity Trauma

Rathachai Kaewlai and Ajay Singh

The use of medical imaging for evaluation of patients with orthopedic trauma has contributed to accurate diagnosis and subsequent management. In the era of modern medical technology, a wide range of imaging modalities are available for assessment of orthopedic trauma. Availability, invasiveness, cost-effectiveness, and image resolution dictate the use of each modality.

Conventional radiography is the primary diagnostic modality for assessment of fractures and dislocations. Routine radiography includes two orthogonal views supplemented by additional projections. Most fractures and dislocations are sufficiently identified and managed through use of conventional radiographs alone. In addition, radiographs are useful for assessing limb length and overall alignment and for monitoring fracture healing. *Computed tomography (CT)* is helpful for evaluation of complex extremity fractures and spine injuries. Typical indications for CT in extremity trauma include fractures of the proximal humerus, wrist, scapula, pelvis, hip, tibial plateau, tibial plafond, calcaneus, and midfoot. Postoperative evaluation of fracture reduction and monitoring of fracture healing are increasingly assessed by CT scans. *Magnetic resonance imaging* (MRI) plays a leading role in the detection of soft tissue injuries, bone contusions, and occult trabecular fractures.

Knowing the important steps for interpretation of skeletal trauma and always keeping them in mind is useful to increase diagnostic accuracy (Box 4-1). Fracture terminology and a guide to fracture description are summarized in Boxes 4-2 and 4-3. Figures 4-1 and 4-2 show common fractures in the upper and lower extremities. Along with direct visualization of the fracture line, secondary or indirect signs that are diagnostic clues for the presence of fractures include the presence of soft tissue swelling, obliteration or displacement of fat stripes, periosteal and endosteal reactions, joint effusion, lipohemarthrosis, a double cortical line, and buckling of the cortex.

FRACTURES OF THE SCAPULA

The scapula provides a strong support to the upper extremity through its articulation with the humerus. Fractures of the scapula (Box 4-4) often occur as a result of severe direct blunt trauma. These fractures are commonly associated with other significant injuries in up to 80% to 90% of cases, including thoracic, glenohumeral joint, brachial plexus, and axillary artery injuries. Attention is generally diverted to these concomitant injuries, resulting in delayed diagnosis of scapular fractures. Scapular fractures are classified according to their location: body, spine, neck, glenoid, acromion process, and coracoid process. Approximately 80% of fractures of the scapula involve either the body see Fig. 4-1 or the neck. Glenoid and neck fractures have the potential to threaten the function of the shoulder girdle because malalignment of these fractures can contribute to instability of the glenohumeral joint, arthrosis, and dysfunction of the rotator cuff and girdle musculatures. They may require open reduction and internal fixation. Fractures that pass through the suprascapular notch or spinoglenoid notch are at risk of neurovascular bundle injury. Glenoid rim fractures are usually associated with subluxation or dislocation of the glenohumeral joint. On imaging, one should assess the entire bone and the glenohumeral, acromioclavicular (AC), coracoclavicular (CC), and scapulothoracic joints. When a fracture is identified, it is crucial to rule out glenoid fossa involvement and determine the degree of displacement, the comminution, and the angular relationship between the glenoid and the body. Early recognition may lead to a change of treatment planning in polytrauma patients.

FRACTURES OF THE CLAVICLE

The primary mechanism causing a fracture of the clavicle (Box 4-5) is a fall onto the superolateral shoulder. Because of the strength of the sternoclavicular ligament, the force exits the clavicle in the midshaft, resulting in the most common pattern of clavicle fracture—fracture of the middle third. The most widely used classification system (by Allman) divides clavicle fractures into three groups by their location: medial third, middle third, and lateral third. The lateral third fractures are further divided into three distinct types by Neer classification (type I with an intact CC ligament, type II with a detached CC ligament from the medial segment but an intact lateral segment, and type III with intraarticular extension into the AC joint).

The middle third of the clavicle (group 1 fracture; see Fig. 4-2, *A, B,* and *C*) is involved in 65% to 85% of all fractures. Complete fractures typically result in superior displacement of the medial fragment (as a result of the pull of the sternocleidomastoid muscle) and inferior displacement of the lateral fragment (as a result of gravity pull of the shoulder joint). Overriding of fragments is common, with the lateral fragment underlying the medial fragment.

The lateral third of the clavicle (group 2 fracture) is involved in 15% to 30% of all fractures. In this group, the integrity of CC ligaments influences the severity of the displacement. The fracture may extend between the two portions of the CC ligaments (medial conoid and lateral trapezoid ligaments) without causing ligamentous disruption, or it may involve the conoid ligament. The latter is a type II fracture that is more prone to delayed union and nonunion. A stress radiograph is often useful to make an accurate determination. Rarely, the fracture line involves only the joint margin and extends into the AC joint.

BOX 4-1 Important Steps to Increase Accuracy in Interpretation of Skeletal Trauma

1. Having a high index of suspicion
2. Knowing where the patient hurts
3. Obtaining optimal radiographs
4. Knowing the frequent sites of injury and looking specifically for them
5. Knowing what is commonly missed
6. Once a fracture is identified, not forgetting to look at the rest of the image(s)

BOX 4-2 Fracture Terminology

Fracture = complete disruption in continuity of a bone
Incomplete fracture = disruption of the bone trabeculae while others are bent or remain intact
Open fracture = a fracture that communicates with the outside environment such as ambient air; fractures caused by gunshot wounds or shrapnel and traumatic amputations are always open fractures
Segmental fracture = a segment of a shaft isolated by proximal and distal lines of fracture
Butterfly fragment = a triangular fragment of bone detached from two other larger fragments of a long bone
Fatigue fracture = fracture of a normal bone due to abnormal stress
Insufficiency fracture = fracture of an abnormal bone due to a normal stress
Stress fracture = a group of fractures made up of fatigue and insufficiency fractures
Avulsion fracture = fracture entailing a fragment that is pulled away from the bone at the ligamentous or tendinous insertion
Pathologic fracture = fracture resulting from a preexisting bone abnormality
Dislocation = complete disruption of a joint such that there is no contact of articular surfaces
Subluxation = minor disruption of a joint where some articular contact remains

BOX 4-3 Fracture Description

- Anatomic site and extent: use anatomic landmarks for description; in the long bone, divide the shaft into thirds
- Type: complete or incomplete, simple or slightly/moderately/markedly comminuted, presence of a butterfly fragment, segmental fracture
- Alignment: displacement, angulation, rotation, foreshortening, and distraction
- Direction of the fracture line in relation to the longitudinal axis of the bone: transverse, oblique, spiral, and longitudinal
- Special features: impaction, depression, or compression
- Status of adjacent joints: normal, subluxation, dislocation, diastasis, and intraarticular extension of the fracture line
- Special type of fractures: stress fracture, pathologic fracture, and avulsion fracture
- Open or closed fracture: preferably determined by clinical examination

Fractures of the medial third of the clavicle (group 3 fracture) are rare, accounting for only 5% of all clavicular fractures. These fractures are easily overlooked on conventional radiographs because of their nondisplacement and because of the overlapping ribs and spines. A serendipity

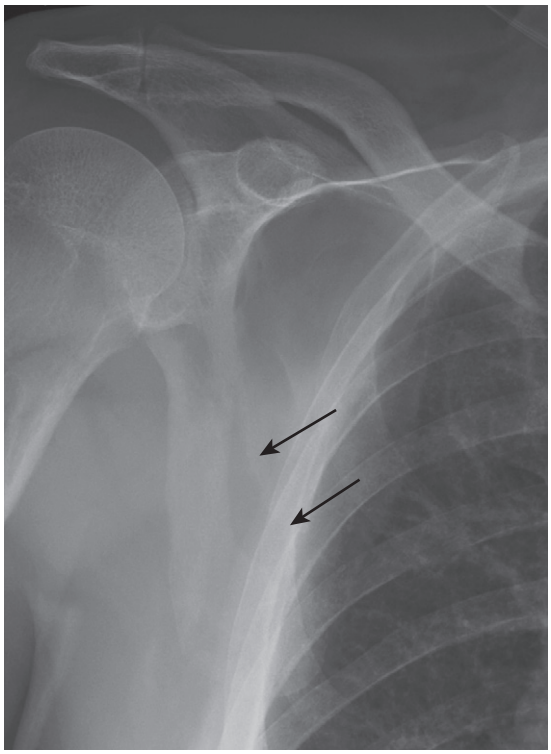


FIGURE 4-1 Fracture of the scapula. An anteroposterior radiograph of the shoulder demonstrates a fracture *(arrows)* in the body of the scapula.

view (a 40-degree cephalic angle in the supine position) can be helpful to assess this area, and CT should be obtained when a question remains of injury to the medial third of the clavicle or the sternoclavicular joint. Unusual patterns of clavicle fractures that usually occur in children and young adults include medial physeal separation and a periosteal sleeve fracture that occurs in the most medial and most lateral portions of the clavicle.

ACROMIOCLAVICULAR JOINT INJURIES

AC injuries (Box 4-6) commonly result from direct injury, such as a fall on the lateral aspect of the shoulder with an adducted arm during athletic activities. The initial injury is directed to the AC joint capsule, and with greater force, disruption of the CC ligaments occurs, along with detachment of the trapezius and deltoid muscles surrounding the joint. The name understates the status of the CC ligament, which is the most important ligament in maintaining the clavicle and scapula. Radiographic evaluation of the AC joint injury typically includes a standard anteroposterior (AP) view of the AC joint with the beam directed 15 degrees cephalad in the upright position. Both shoulders should be included in the same image. A stress radiograph may be performed with 10- to 15-lb weights attached to each wrist if the initial radiograph without the addition of weight is normal. However, the increasing trend toward nonoperative management of type II and III injuries has made stress radiographs potentially clinically irrelevant.

Six types of AC joint injuries are identified. In a *type I injury* (an AC ligament sprain with an intact CC ligament), a normal AC joint space is seen in radiographs with and

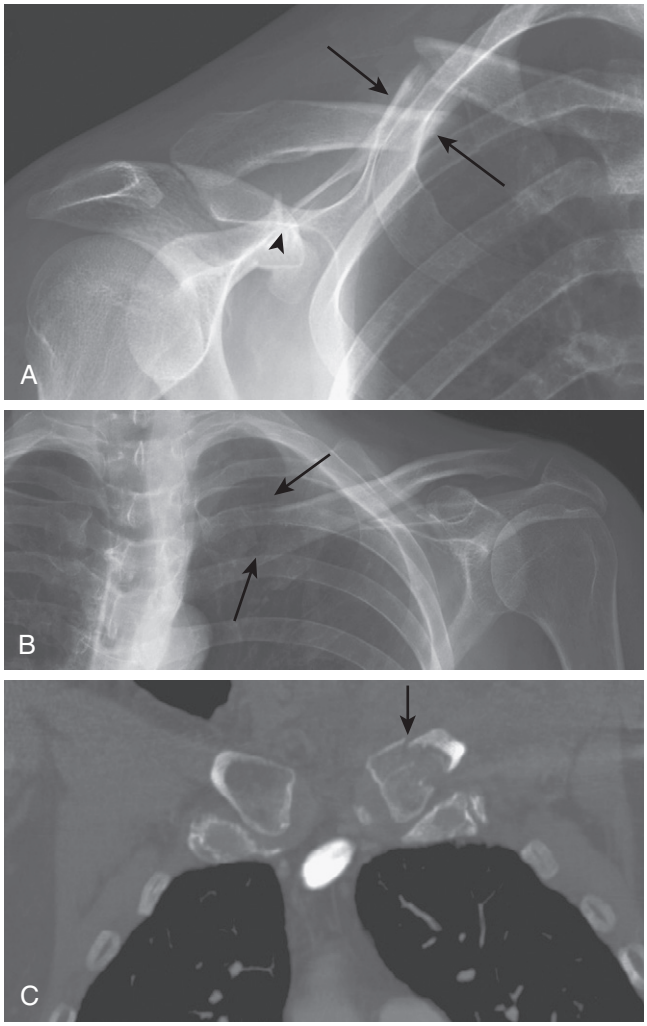


FIGURE 4-2 Fractures of the clavicle. **A,** A segmental fracture of the middle third *(arrows)* is shown in the anteroposterior radiograph of the clavicle. This pattern is the most common, with a classic superior displacement of the medial fracture fragment and inferior displacement of the lateral fragment. A coexisting fracture of the superior border of the scapula is present *(arrowhead)*. **B**, An anteroposterior radiograph of the clavicle demonstrates a fracture of the medial third of clavicle *(arrows)* with displacement. **C,** A coronal reformatted computed tomography image shows a fracture of the medial third of the clavicle *(arrow)* in a different patient.

without the use of weights. In a *type II injury* (Fig. 4-3, *A*), the AC joint may be slightly widened, and the lateral end of the clavicle may be slightly elevated on nonstress radiographs. On a stress view, the AC joint is wide, which implies a partial or complete AC ligament tear. In a *type III injury* (Fig. 4-3, *B* and *C*), complete disruption of both AC and CC ligaments has occurred, resulting in a widened AC and CC distance on nonstress radiographs. The distal clavicle is displaced superiorly. In a *type IV injury*, the clavicle is displaced posteriorly, which is best visualized on axillary projection. *Type V and type VI injuries* display partial separation of the sternoclavicular (SC) joints. Marked elevation of the distal clavicle occurs in a type V injury. A type VI injury displays a unique inferior displacement of the distal clavicle, either into subacromial or subcoracoid regions. This type of injury is usually a result of severe trauma with other accompanying fractures.

BOX 4-4 Fractures of the Scapula

Standard views: Anteroposterior and lateral views of the scapula
Frequent sites of injury: Body, spine, and neck of the scapula
Frequently missed injuries: Fractures of the acromion process and coracoid process
Fracture mimics:
- Os acromiale—an unfused acromial ossification center with smooth, straight, and uniformly sclerotic margins, distinguishing it from a true fracture
- Scapular foramen—a well-circumscribed hole in the center of the scapular body
- Nutrient foramina/canals—in the neck and body of the scapula

BOX 4-5 Fractures of the Clavicle

Standard views: Straight posteroanterior (PA), and PA with a 15-degree caudad angle; if the patient cannot lie prone, straight anteroposterior (AP) and AP with a 15-degree cephalad angle is acceptable
Frequent sites of injury: Middle third
Frequently missed injuries: Medial third, associated subluxation of acromioclavicular and sternoclavicular joints
Relevant normal anatomy:
- Sternocleidomastoid muscle distal attachment—inner surface of medial third of the clavicle
- Coracoclavicular ligaments consist of trapezoid (lateral) and conoid (medial) ligaments

BOX 4-6 Acromioclavicular Joint Injuries

Standard views: Anteroposterior with the beam directed 15 degrees cephalad in the upright position without use of weights (both shoulders on the same image)
Relevant normal anatomy: The coracoclavicular ligament is the most important ligament in stabilizing the clavicle and scapula
- Normal acromioclavicular (AC) joint space <8 mm, with the right and left differing <2-3 mm
- Distal inferior cortical margin of the clavicle and acromion are at the same plane
- Coracoclavicular distance <11 mm, with the right and left differing <5 mm

Frequently missed injuries: Coracoid fracture
Mimics AC injuries:
- Distal clavicular physeal separation—childhood equivalent of AC separation, representing separation of the distal clavicular metaphysis from the epiphysis
- Nontraumatic laxity of the AC joint
- Unilateral erosion of the distal clavicle—posttraumatic osteolysis, gout, or a neoplasm such as multiple myeloma
- Bilateral erosions of the distal clavicle—rheumatoid arthritis, hyperparathyroidism, and scleroderma

FLOATING SHOULDER

Floating shoulder is a rare injury that represents disruption in two places (double disruption) of the superior shoulder suspensory complex. The complex represents a combination of soft tissues (the AC ligament and CC ligament) and bony structures (the glenoid process, coracoid process, distal clavicle, and acromion) that form a ring suspending

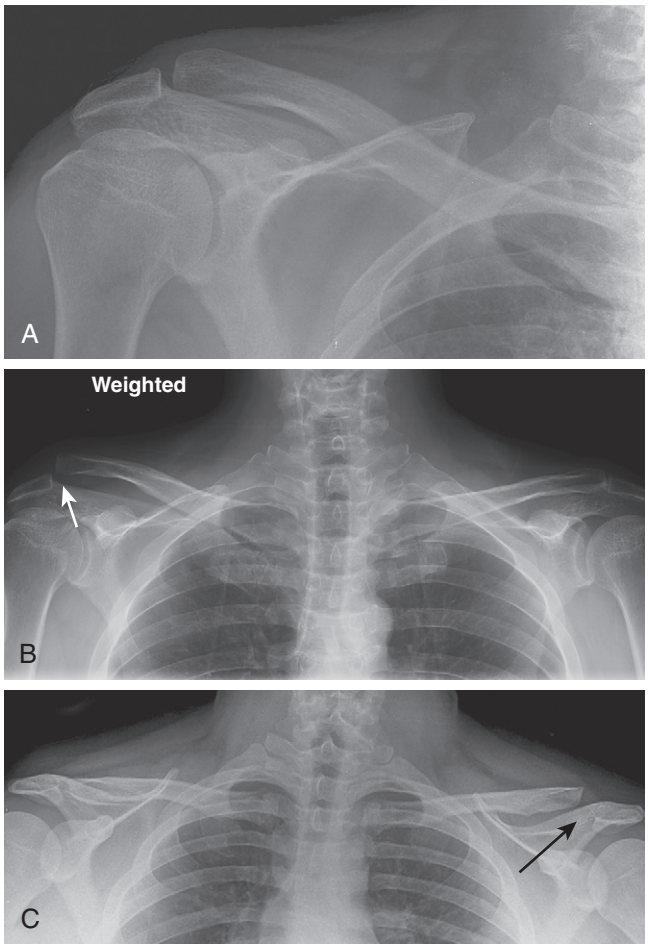


FIGURE 4-3 An acromioclavicular (AC) joint (type II) injury. An anteroposterior radiograph of the AC joint, without weight. **A,** A normal AC space. **B,** With weight bearing, widening of the joint space occurs *(arrow)*. **C,** An anteroposterior radiograph of both AC joints demonstrates a type III injury *(arrow)*. Differentiation between these two types may not be clinically relevant because of a trend toward nonoperative management in both categories.

the upper extremity to the thorax. Injuries in two places, classically fractures of the distal clavicle and the glenoid neck, may create a potentially unstable condition. If it is associated with significant bony displacement or AC and/or CC ligamentous injuries, a floating shoulder may result in a healing problem and long-term functional difficulties. Fractures of the glenoid neck and clavicle are easily detected on routine radiography, but CT can be helpful to define the exact nature of the fractures. One should look for evidence of AC/CC ligamentous disruption on both radiography and CT.

SUBLUXATIONS AND DISLOCATIONS AROUND THE GLENOHUMERAL JOINT

The glenohumeral joint (Box 4-7) is the most frequent site of dislocation of any joint in the body. Most commonly they are posttraumatic dislocations, although nontraumatic etiologies such as seizure and voluntary dislocations also occur. The types of dislocations are determined by the final resting place of the humeral head relative to the glenoid: anterior, posterior, superior, or inferior.

BOX 4-7 Subluxations and Dislocations Around the Glenohumeral Joint

Standard views: Anteroposterior (AP) in external rotation and axillary views of shoulder; Neer view or transthoracic view if an axillary view cannot be obtained
Relevant normal anatomy: On a routine AP view of the shoulder, the articular surface of the humeral head should overlap the glenoid shadow
Frequent types of injury: Anterior dislocation, Hill-Sachs fracture
Frequently missed injuries: Posterior dislocation, Bankart lesion

Anterior Dislocation

The vast majority of glenohumeral dislocations are anterior dislocations (Fig. 4-4, *A*). The dislocation usually occurs as a result of indirect force applied to the arm in abduction, extension, and external rotation. Subcoracoid anterior dislocation is the most common subtype, followed by subglenoid, subclavicular, and intrathoracic. The dislocation is readily diagnosed on clinical examination and a frontal radiograph as a medially and inferiorly located humeral head relative to the glenoid. The common associated injuries are a Hill-Sachs fracture and a Bankart lesion as a result of impact of the soft base of the humeral head onto the relatively hard anterior glenoid during dislocation. A *Hill-Sachs fracture* (Fig. 4-4, *B* and *C*) is a large defect or groove in the posterolateral aspect of the humeral head that is present in up to 68% of initial anterior dislocations. *Bankart lesions* (Fig. 4-4, *B*) may consist of a soft tissue (e.g., fibrocartilaginous or cartilaginous labrum) or a piece of bone avulsed from the anteroinferior portion of the glenoid rim. Bankart lesions are less common than Hill-Sachs fractures. Internally rotated AP projection is probably the best option for showing the Hill-Sachs fracture. The Stryker notch view is helpful to identify both Hill-Sachs and bony Bankart lesions. Neither of these lesions are signs of a recurrent or previous dislocation because they do occur at the initial dislocation.

Posterior Dislocation

Posterior dislocation of the glenohumeral joint (Fig. 4-5) is uncommon and usually presents with violent muscle contractions that occur during a seizure or electric shock. Dislocation can be subacromial, subglenoid, or subspinous. It frequently coexists with an impacted fracture of the anterior humeral head (a reverse Hill-Sachs lesion) because of impaction of the humeral head on the glenoid fossa during dislocation. In obese or muscular persons, posterior dislocation can be difficult to detect clinically. On frontal radiographs, it is not recognized in up to 50% of cases. Subtle signs on this view include (1) a greater than 6 mm distance between the articular cortex of the humeral head and the anterior glenoid rim (positive rim sign); (2) a humeral head fixed in internal rotation (the light bulb sign); and (3) a curvilinear dense line parallel to the articular margin of the humeral head (the trough line), representing an impacted fracture of the anterior aspect of the humeral head that coexists with dislocation. Posterior dislocation is clearly identified on a true lateral (axillary) and transcapular views.

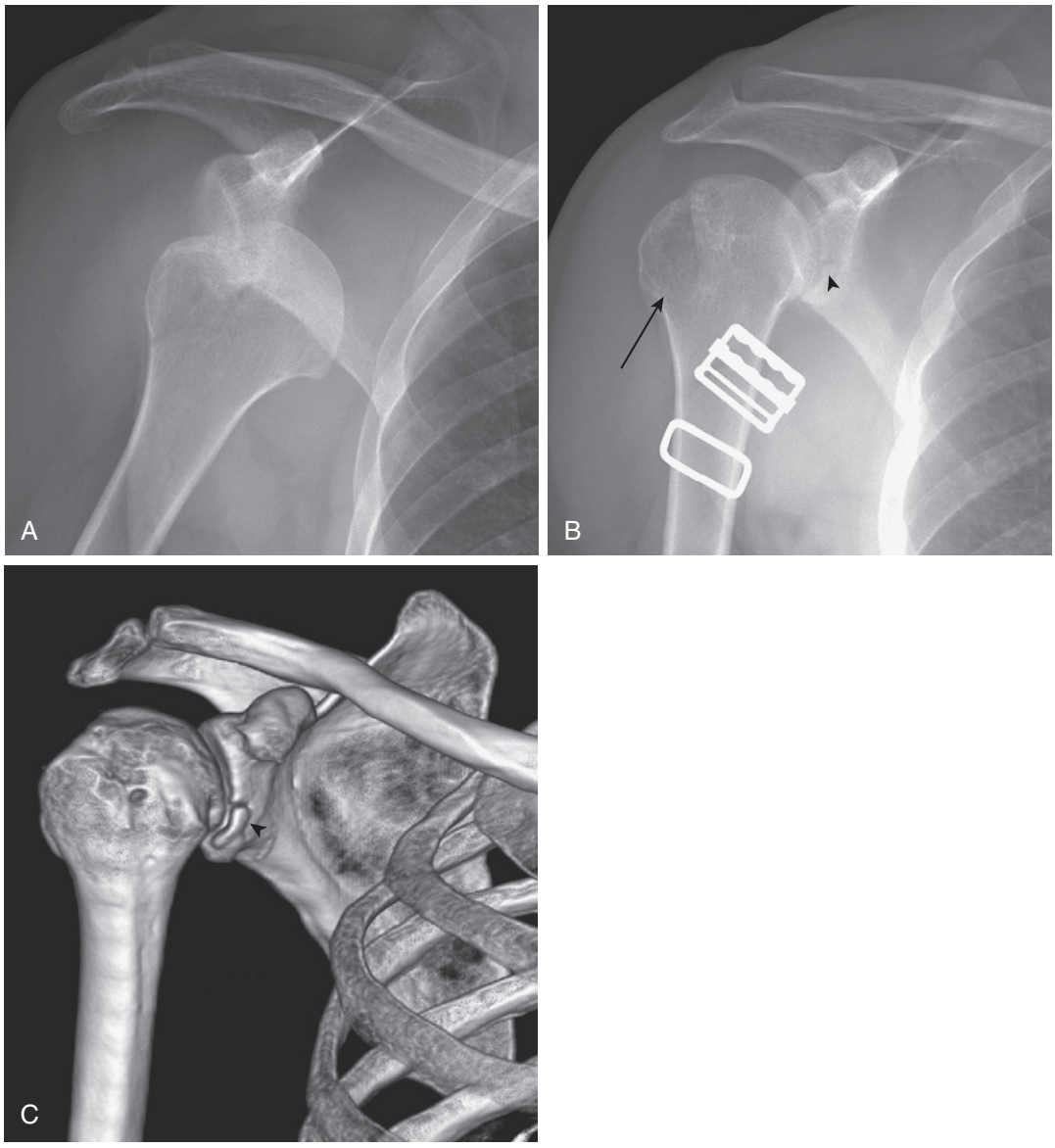


FIGURE 4-4 Anterior shoulder dislocation. **A,** An anteroposterior radiograph of the shoulder demonstrates a classic subcoracoid anterior shoulder dislocation. The humeral head is located medial to the glenoid fossa and inferior to the coracoid process. **B,** A postreduction radiograph reveals an impacted fracture of the posterolateral aspect of the humeral head, consistent with a Hill-Sachs fracture *(arrow)*. A linear lucency at the anterior glenoid rim is a bony Bankart fracture *(arrowhead)*. **C,** A volumetric (three-dimensional) computed tomography image confirms the Bankart fracture *(arrowhead)*.

Inferior Subluxation (Luxatio Erecta)

Luxatio erecta is a rare type of subglenoid inferior dislocation in which the arm is severely hyperabducted and the humerus is directed superiorly so that the long axis of the humeral shaft is perpendicular to the lateral chest wall. This rare entity is associated with Hill-Sachs fractures, other humeral head fractures, and occlusion of the axillary artery.

Pseudosubluxation

Pseudosubluxation describes drooping of the humeral head with respect to the glenoid, which is usually apparent only on the erect examination. This condition is not a true dislocation. It is a result of joint distension of traumatic or nontraumatic etiologies from fluid (e.g., hemarthrosis and lipohemarthrosis) or disruption of the joint capsule in chronic or recurrent dislocation. In acute trauma, an upright shoulder radiograph may demonstrate lipohemarthrosis.

FRACTURES OF THE PROXIMAL HUMERUS AND THE SHAFT OF THE HUMERUS

Fractures of the Proximal Humerus

The proximal humerus (Box 4-8) consists of the head, anatomical neck, greater tuberosity, lesser tuberosity, surgical neck, and proximal shaft. The anatomical neck represents an old epiphyseal plate, whereas the surgical neck, located

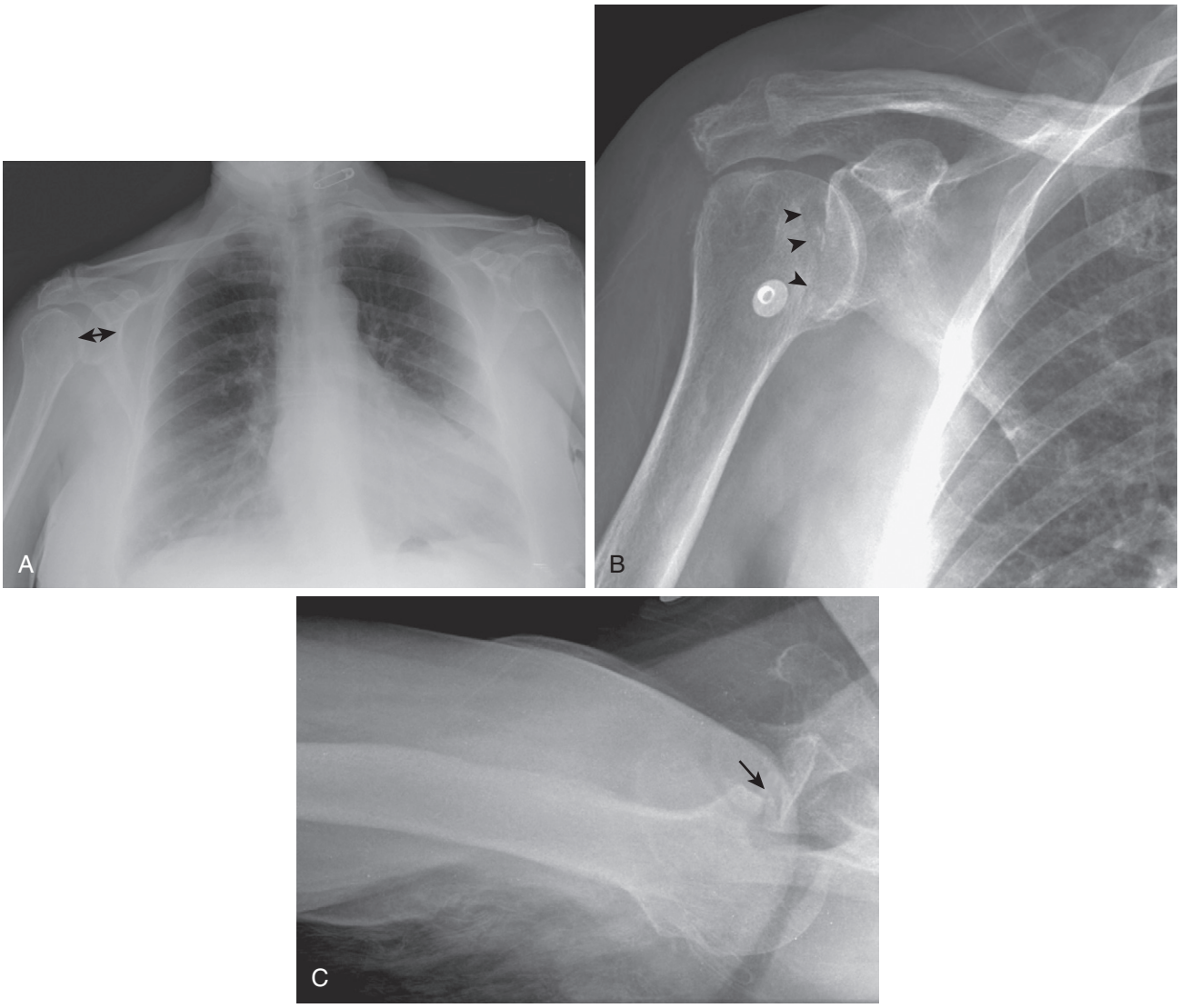


FIGURE 4-5 Posterior shoulder dislocation. **A,** A chest radiograph shows increased distance between the articular cortex of the humeral head and the anterior glenoid rim *(double-headed arrow)*. An anteroposterior shoulder radiograph **(B)** of the same patient shows a "trough line" sign as a curvilinear density *(arrowheads)* consistent with an impacted reverse Hill-Sachs fracture, confirmed in the axillary projection (**C,** *arrow*).

BOX 4-8 Fractures of the Proximal and Shaft of the Humerus

Standard views: Anteroposterior, lateral (transthoracic) of the shaft of the humerus

Frequent sites of injury: Fractures of the surgical neck

Relevant normal anatomy: The anatomical neck is a narrow groove separating the head from the tuberosities; it is an attachment site for the glenohumeral joint capsule

- Surgical neck is a constriction below the greater and lesser tuberosities
- Pectoralis major insertion—outer bicipital ridge of the humerus (anterior aspect of the upper third)
- Deltoid insertion—outer aspect of the middle third of the humerus

approximately 2 cm distal to it, is a weakened area below the tuberosities and head. Fractures of the proximal humerus are associated with the presence of osteoporosis. Most fractures are a result of indirect force, such as a fall onto an outstretched arm. The pattern of fracture and displacement is dictated by the position of the humerus at the time of injury, bone quality, and muscular pull on humeral fracture fragments. By counting the number of major displaced fragments and defining specific parts of involvement (the head, greater tuberosity, lesser tuberosity, and shaft), Neer classifies fractures of the proximal humerus into one-, two-, three-, and four-part fractures. Each of the four fracture sites results in a potential fragment, or "part." A fragment is considered a "part" if it is displaced more than 1 cm or rotated more than 45 degrees. The lesser degree of displacement is considered to be minimal regardless of the number of the fracture line. One-part fractures (Fig. 4-6, *A* and *B*) are nondisplaced or minimally displaced fractures. Muscles inserting on the proximal humerus

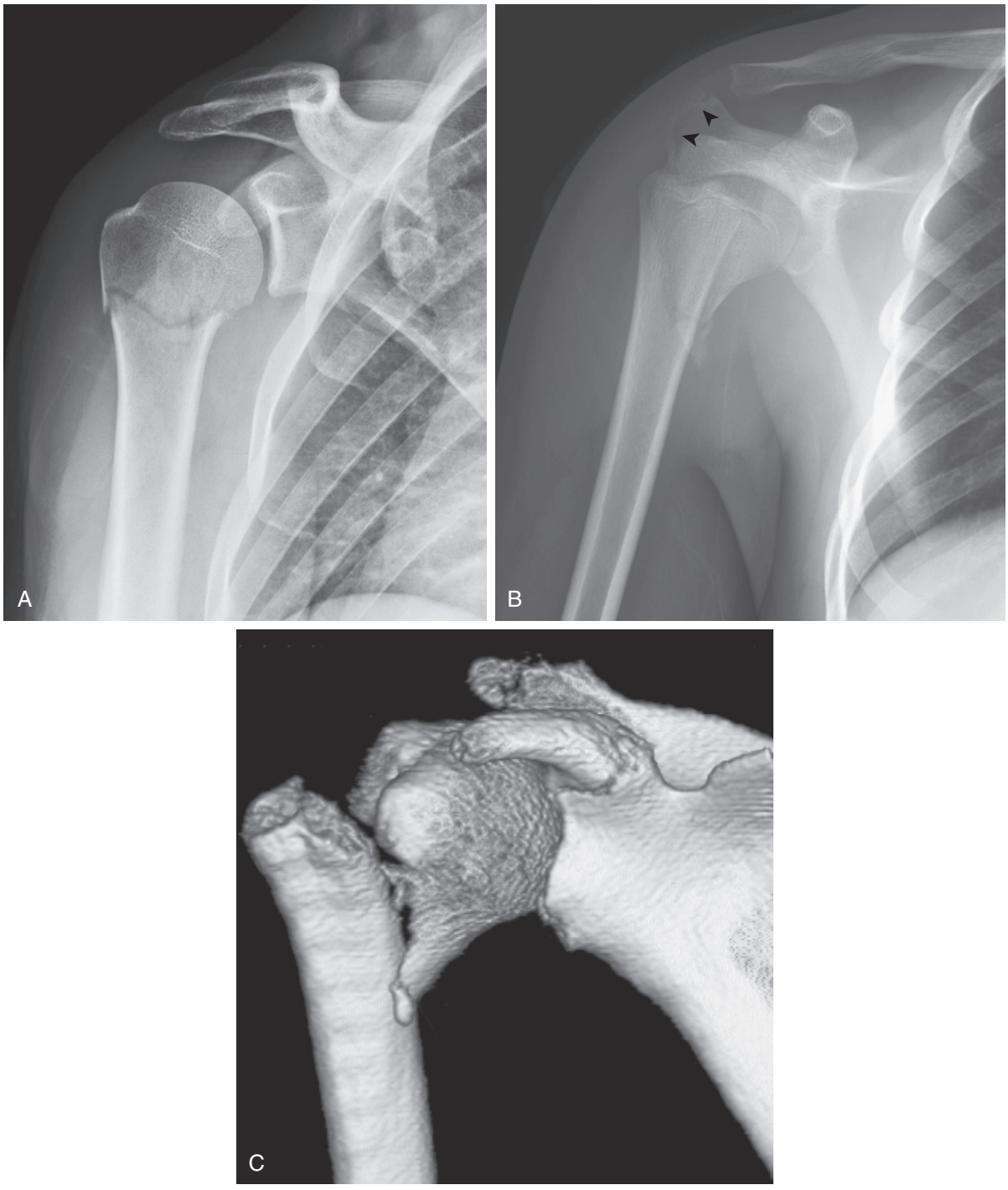


FIGURE 4-6 Fracture of the proximal humerus. **A,** An anteroposterior radiograph of the shoulder demonstrates a nondisplaced ("one-part") fracture of the surgical neck of the humerus. **B** and **C,** An anteroposterior radiograph and volumetric (three-dimensional [3D]) computed tomography (CT) reformation of the shoulder reveal a comminuted fracture of the surgical neck. This fracture is a "two-part" fracture (proximal articulating part and shaft); only two fragments are considered "parts" because they are displaced more than 1 cm. In addition, a nondisplaced fracture of the acromion process is present (**B,** *arrowheads*).

influence the directions of displaced fragments. The pectoralis major muscle pulls the humeral shaft anteromedially. Supraspinatus and infraspinatus muscles pull the greater tuberosity posterosuperiorly, and the subscapularis muscle pulls the lesser tuberosity medially. When describing the fractures of the proximal humerus, specify the type (one-, two-, three-, or four-part; surgical or anatomical neck) and the involved fragments (shaft, greater tuberosity, or lesser tuberosity).

According to the Neer description, 80% of fractures of the proximal humerus are one-part fractures, and most are *impacted fractures of the surgical neck.* Nondisplaced surgical neck fractures usually have a good prognosis because blood supply to the humeral head is

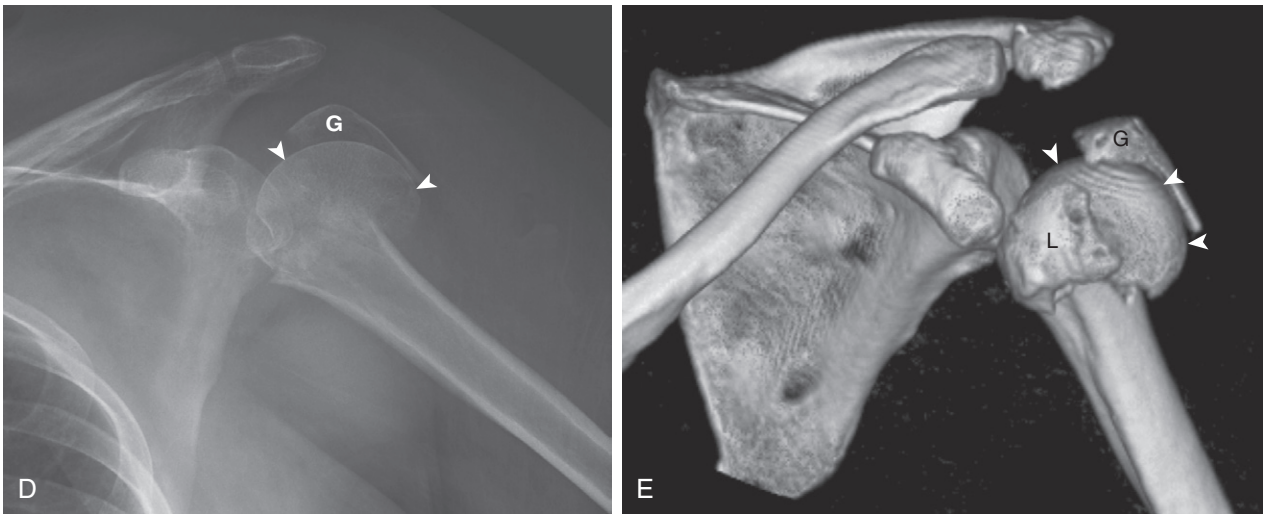


FIGURE 4-6, cont'd **D** and **E,** A four-part fracture with valgus impaction is shown in an anteroposterior radiograph and a volumetric (3D) CT reformation. The greater tuberosity *(G)* and articulating part of the humeral head *(arrowheads)* and shaft are separated from each other by more than 1 cm. The letter "L" indicates lesser tuberosity.

preserved. On the contrary, *fractures of the anatomical neck* are often displaced and considered a two-part fracture. These fractures heal poorly because the vascular supply is completely disrupted, which results in avascular necrosis and secondary osteoarthritis. Two-part fractures (Fig. 4-6, *C* and *D*) accounted for 10% of all proximal humeral fractures. Displaced fractures of the surgical neck may injure the brachial plexus and axillary artery, which lie immediately anterior to it. Isolated fractures of the greater or lesser tuberosities are uncommon and are frequently associated with anterior and posterior glenohumeral dislocations, respectively. *Three-part fractures* often combine a tuberosity fragment (either the greater or lesser tuberosity) with a displaced surgical neck fragment. The humeral shaft is pulled superiorly, whereas the glenohumeral articular surface rotates and faces posterior, resulting in a rounded appearance of the articular fragment. In *four-part fractures* (Fig. 4-6, *E*), the articular fragment is isolated from both tuberosities and the humeral shaft, becoming devoid of all soft tissues. This fragment can be seen on an AP radiograph as a small crescent of bone detached from the anatomical neck. In addition to healing problems seen with three-part fractures, the risk of avascular necrosis is increased. Another important variant of a four-part fracture is a "valgus-impacted" fracture that has a better prognosis as a result of maintained residual vascularity. *Fracture-dislocation* of the shoulder is a combination of glenohumeral dislocation with any of the two-, three-, or four-part proximal humeral fractures.

Fractures of the Shaft of the Humerus

A humeral shaft fracture is defined as a fracture with the main fracture line distal to the surgical neck and proximal to the supracondylar ridge. Fractures of the humeral shaft are common. Bending force produces a transverse fracture, whereas torsion will result in a spiral fracture. A combination of both forces can result in an oblique fracture with or without a butterfly fragment. The location of the fracture line affects the way the fragments are displaced. With fractures above the pectoralis major insertion, the distal fragment is displaced anteromedially by the pull of the pectoralis major. Fractures between the insertion of the pectoralis and deltoid (Fig. 4-7) are associated with lateral displacement of the distal fragment. Fractures distal to the deltoid insertion result in abduction of the proximal fragment by the deltoid and shortening of the arm by the pull of the brachialis and biceps attached to the distal fragment. Associated injuries of the radial nerve are common, especially with fractures located at the junction of the middle and distal thirds. Pathologic fractures of the humerus are common in adults as a result of metastatic disease, myeloma, and lymphoma. Indeed, the humerus is the second most common site of long-bone metastases, after the femur. In children, they usually occur through a simple bone cyst of the proximal humerus.

FRACTURES AND DISLOCATIONS AROUND THE ELBOW

The Fat Pad Sign

Normal thin layers of fat lie between the synovium and the joint capsule of the elbow anteriorly and posteriorly. In a normal flexed elbow, the anterior fat pad is visible and the posterior fat pad is hidden in the intercondylar depression on the posterior surface of the humerus. In the presence of a joint effusion, the posterior fat pad (Fig. 4-8, *A*; see Fig. 4-11, *A*) is displaced posteriorly and the anterior fat pad is elevated. They become visible on the lateral radiograph of a flexed elbow, seen as the fat pad sign and the sail sign, respectively. In an acute trauma setting, elbow joint effusion can be a result of an intraarticular fracture or traumatic synovitis. This sign is usually present in children and adolescents, in which 70% to 90% prove to have a fracture on an initial or subsequent examination. The sign is less frequently seen in adults, and its absence cannot be used to exclude a fracture. Because the

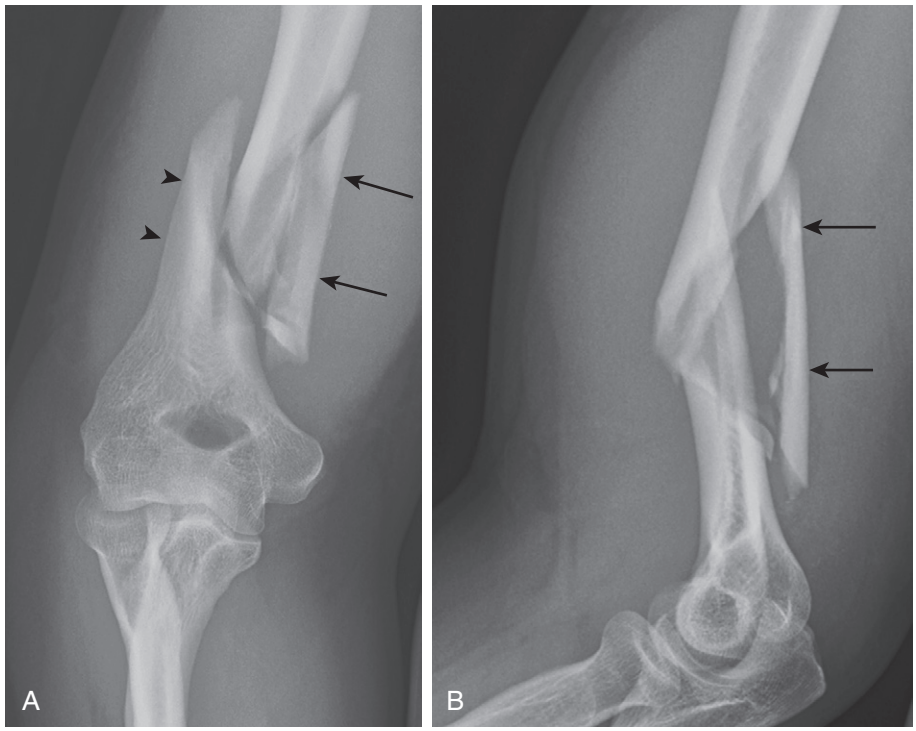


FIGURE 4-7 Fracture of the shaft of the humerus. **A** and **B,** Anteroposterior and lateral radiographs demonstrate a comminuted fracture of the distal third of the humerus with a large butterfly fragment *(arrows)*. The butterfly fragment is pulled medially and posteriorly, whereas the distal fragment *(arrowheads)* is retracted proximally because of the pull by the deltoid muscle.

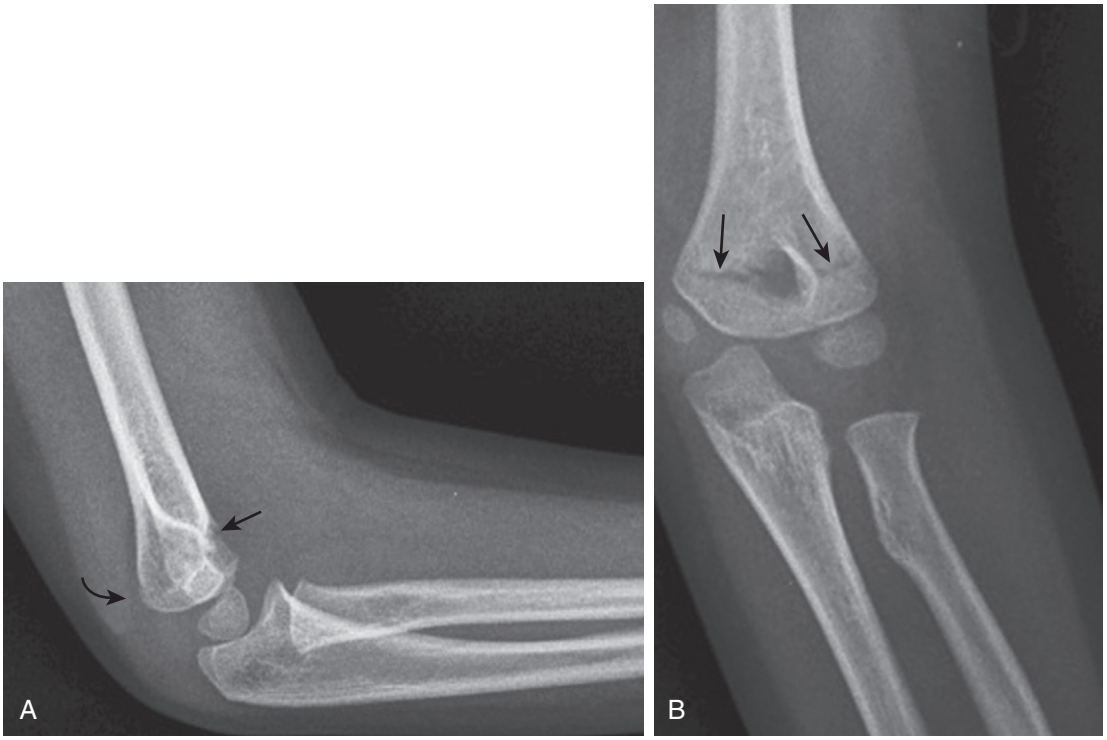


FIGURE 4-8 A supracondylar fracture in a child. **A,** A lateral radiograph of the elbow demonstrates a posterior fat pad sign *(curved arrow)*, indicating the presence of an intraarticular fracture. A subtle cortical break is seen on this view *(arrow)*. **B,** an anteroposterior view confirms the fracture line *(arrows)*.

synovium must be intact to ensure that the effusion does not mix with extrasynovial fat, this sign is not present in elbow dislocation, displaced intraarticular fractures with a torn joint capsule, and fracture-dislocation of the elbow. An optimal lateral radiograph of the elbow is essential for evaluation of the fat pad sign. The image is taken when the elbow is flexed at 90 degrees with the hand in the lateral position. On the radiograph, three concentric arcs of the distal humerus (the trochlear groove, capitellum, and medial trochlea) should be visualized.

Fractures Around the Elbow in Children

Supracondylar fracture is the most common elbow fracture in children (Box 4-9), with the peak age between 6 and 7 years. Its typical mechanism is a fall onto an outstretched hand, causing hyperextension of the arm in which the olecranon acts as a fulcrum. The thin and slender cortex of the supracondylar region at this age predisposes it to fracture, which is usually extraarticular. The distal fragment displaces posteriorly in most cases. When they are completely displaced and when cortical contact is lacking, the fractures (Fig. 4-8, *A* and *B*) are easily recognized. To help detect nondisplaced fractures and fractures with angulation but an intact posterior cortex, one should search for the fat pad sign. The Baumann angle and the anterior humeral line are commonly used to identify change of the carrying angle and subtle posterior displacement. The Baumann angle is created by the intersection of a humeral shaft axis and a line drawn along the growth plate of the lateral condyle of the elbow. In patients with a supracondylar fracture, the Baumann angle is increased, related to varus deviation, and the anterior humeral line passes anterior to the capitellum. The presence of abnormal cubitus valgus or varus should be assessed because either of these findings may alter the therapy. The Volkmann ischemic contracture is the most serious complication of this type of fracture that causes diminished blood flow to the remainder of the arm. Because subtle fractures are difficult to visualize directly, the presence of the posterior fat pad sign and an abnormal anterior humeral line is most helpful in this circumstance.

Lateral condylar fracture (Fig. 4-9, *A* and *B*) is the second most common fracture around the elbow in children. This fracture is caused by a lateral blow to the forearm that results in varus stress across the elbow. Typically the fracture line runs across or along the physis, with or without a small metaphyseal fragment. Fractures may terminate in the physis (incomplete, Salter-Harris type II, or Milch type II) or beyond the physis through the ossified capitellum or unossified cartilage (complete, Salter-Harris type IV, or Milch type I), with the former being more common. Oblique or lateral radiographs can better demonstrate a fracture line just above the capitellum than can the AP projection. However, differentiation between incomplete and complete fractures can be difficult because most of the

BOX 4-9 Fractures and Dislocations Around the Elbow

Standard views: Anteroposterior (AP), lateral (elbow flexed 90 degrees with the hand in the lateral position), both oblique views; in children, only AP and lateral views

- Optional—radial head view (must be accompanied by a full elbow series)

Frequent sites of injury:

- Children—supracondyle, lateral condyle of distal humerus
- Adults—radial head, olecranon

Relevant normal anatomy: The distal humerus consists of the supracondylar region, medial and lateral condyles, and medial and lateral epicondyles

- Anterior humeral line: downward extension of the anterior cortex of the distal humeral shaft; on a lateral radiograph, it intersects the capitellum near the junction of its anterior and middle thirds
- Radiocapitellar line: a line bisecting the proximal radial shaft that should pass through the capitellum on every radiographic view
- Normal carrying angle of the elbow (valgus) = 165 degrees

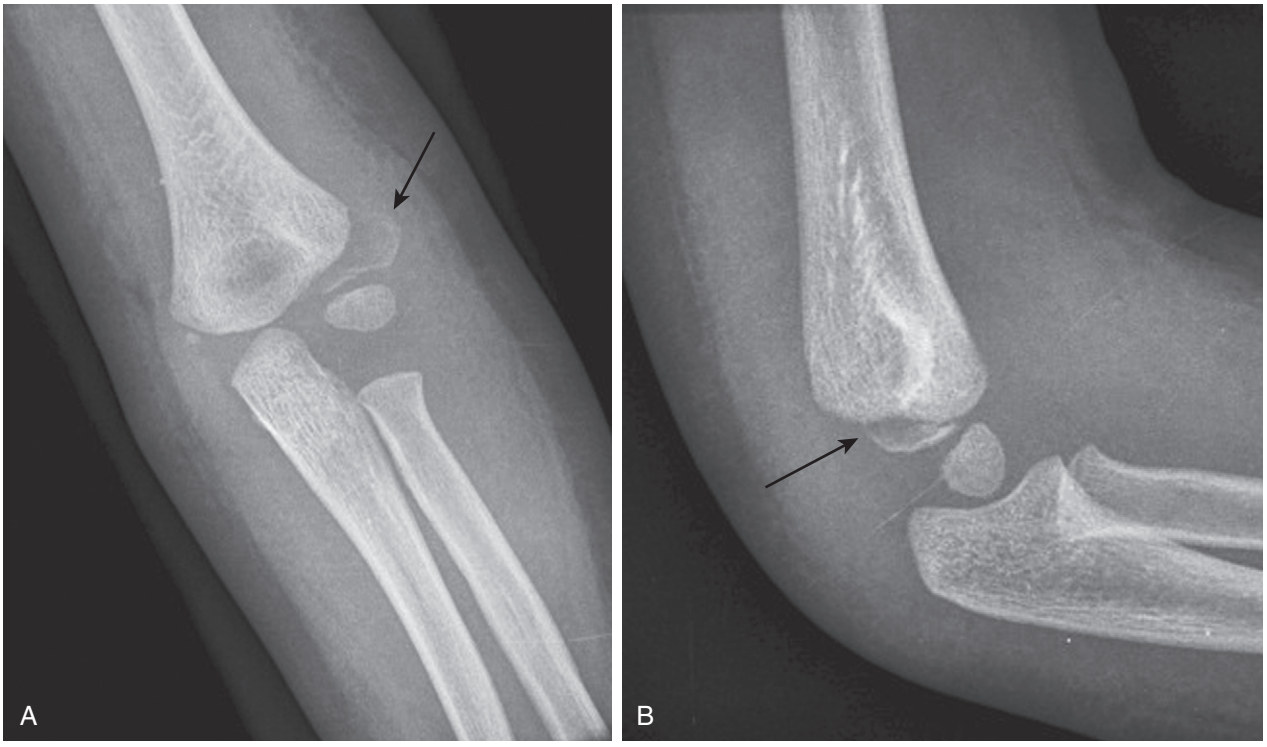


FIGURE 4-9 A lateral condylar fracture in a child. Anteroposterior and lateral radiographs (**A** and **B,** respectively) of the elbow demonstrate a displaced lateral condylar fracture *(arrows)*, which is the second most common fracture around the elbow in children.

fractures extend through the unossified cartilage. Because many fractures require surgery to prevent displacement and healing problems, additional imaging with MRI or intraoperative assessment with arthrography to determine the exact type is often needed.

Fractures of the Distal Humerus

The distal humerus consists of two columns of medial and lateral epicondylar ridges of the distal humeral metaphysis and a central articulating axis of trochlea. The most distal part of the lateral column is the capitellum, and that of the medial column is the nonarticular medial epicondyle. Between the two columns lies the trochlea, which serves as a "tie-arch." Although the column anatomy is not important to stability of the elbow, it is essential in the determination of surgical reconstruction. An increasing trend toward operative treatment of these fractures requires a comprehensive classification system. The AO/OTA (Orthopedic Trauma Association) classified distal humeral fractures into three types. Type A is an extraarticular fracture, type B is a partial articular fracture, and type C is a complete articular fracture. Approximately 95% of distal humeral fractures in adults are intraarticular.

Type A: extraarticular fractures (Fig. 4-10, *A* and *B*) are apophyseal avulsion fractures (i.e., avulsion of the lateral epicondyle and medial epicondyle) and simple and complex nonarticular metaphyseal transcolumn fractures.

Type B: partial articular fractures (Fig. 4-10, *C* and *D*) are intraarticular fractures that involve only one column (either medial or lateral) with one or more sites of intraarticular extension (capitellum, trochlear, or both). They are further categorized into lateral sagittal, medial sagittal, and frontal fractures. Sagittal fractures can be transcapitellar or transtrochlear fractures. Frontal fractures are an isolated fracture of the capitellum, trochlear, or both without metaphyseal extension. *Fracture of the capitellum,* which accounts for 10% of all distal humeral fractures in adults, results from a shearing force transmitted by the radial head or trochlear groove. The fragment is visualized on the lateral radiograph of the elbow and is characteristically displaced proximally above the radial head and coronoid process.

Type C: complete articular fractures (Fig. 4-10, *E* and *F*) are fractures that involve both medial and lateral columns with articular extension. There are three subtypes: articular and metaphyseal simple; articular simple and metaphyseal complex; and multifragmentary. The subtypes are classified according to the nature (simple or complex) of the column fractures and intraarticular fracture.

Fractures of the Proximal Radius

Radial head fractures (Fig. 4-11, *A, B,* and *C*), which are the most common type of elbow fractures in adults, are intraarticular and usually produce hemarthrosis. They can be subtle and are mostly seen on only one projection. Two patterns of fractures are usually seen: a single longitudinal fracture through the proximal articular surface of the radial head, or impaction of the intact radial head into the radial neck. The former pattern presents as a step-off or abrupt angulation of the joint surface or a depression of the fragment (double line of cortical bone). The latter pattern creates an abrupt step-off between the normally gentle concave curve of the radial head and neck. Three types of radial head fractures were described by Mason and later modified by Morrey to include a type IV fracture. Type I is a nondisplaced fracture, which accounts for 50% of cases. Type II is a displaced but not comminuted fracture, and type III is a comminuted fracture. Type IV is a radial head fracture-dislocation. The fracture is considered displaced if the fragment involves 30% or more of the articular surface or is displaced more than 2 mm. Radiography often underestimates the true degree of comminution, articular involvement, and displacement. Open reduction with internal fixation is sometimes used to correct this fracture, especially with a large displaced fragment.

The presence of comminuted radial head and neck fractures due to high-energy trauma should raise a suspicion for additional elbow and forearm injuries, such as capitellar and coronoid process fractures, elbow dislocation, and the Essex-Lopresti fracture. The Essex-Lopresti fracture is a combination of a comminuted fracture of the radial head and neck and proximal migration or subluxation of the distal radioulnar joint (DRUJ) that leads to an acute tear of the interosseous ligament of the forearm. This fracture is unstable, and if the DRUJ component is not recognized, resection of the radial head and neck fragments may result in further proximal migration of the radial shaft and abnormal wrist alignment.

Fractures of the olecranon account for 20% of elbow fractures in adults. They can be a result of a high-energy direct injury, resulting in comminution, distracted fragments, and possible concomitant ulnar shaft fracture. Low-energy olecranon fractures are caused by an indirect injury (e.g., a fall on the forearm), which results in a simple fractures. If the periosteum is completely torn, traction by the triceps will pull the proximal fragment proximally, resulting in a wide fracture gap. Fractures are considered displaced if the gap is widened upon flexion of the elbow to 90 degrees or the displacement is greater than 2 mm. Although the fractures are usually obvious on lateral radiographs, soft tissue swelling in the olecranon bursa and elbow joint effusion are an important clue to the presence of a subtle fracture.

Fractures of the coronoid process (Fig. 4-12) are caused by a shearing mechanism, commonly from posterior elbow dislocation. Therefore, in every posterior dislocation, the coronoid process should be examined closely to exclude a fracture. The fracture fragment may be small. It can occur at the tip, with or without comminution. A severely comminuted fracture near the coronoid base is associated with posterior dislocation and increased risk of instability.

Dislocations of the Elbow

Elbow dislocation, which is one of the most frequent major joint dislocations, usually results from a fall onto an extended elbow. It usually occurs in young persons, with a peak between 5 and 25 years of age. Dislocation of both the radius and ulna together, with respect to the distal end of the humerus, is the most common type. More than 80% are posterior or posterolateral dislocations (Fig. 4-12). Less commonly, the radius and ulna dislocate in divergent directions. Radial head fracture is most frequently associated with a complex elbow dislocation. "*Terrible triad" fracture dislocations* describe

the elbow dislocation, in combination with radial head fracture and coronoid process fracture.This condition is prone to early recurrent instability and posttraumatic arthritis. Other associated injuries include fractures of the medial epicondyle of the distal humerus, as well as brachial artery and ulnar nerve injuries. The brachial artery damage occurs more frequently in open dislocations.

FRACTURES OF THE SHAFTS AND DISTAL RADIUS AND ULNA

Abnormal Pronator Quadratus Sign

The pronator quadratus is a thin flat muscle located on the volar aspect of the interosseous membrane at the level of distal radioulnar joint. It is seen on a normal lateral



FIGURE 4-10 Fractures of distal humerus. **A** and **B,** Anteroposterior and lateral radiographs of the elbow show a comminuted transverse extraarticular metaphyseal fracture (type A) *(arrows)* with medial and volar displacement of the distal fragment. **C** and **D,** A transtrochlear fracture (partial articular, type B) *(arrows)* with mild displacement. The fracture extends from the trochlea to the lateral column of the distal humerus.

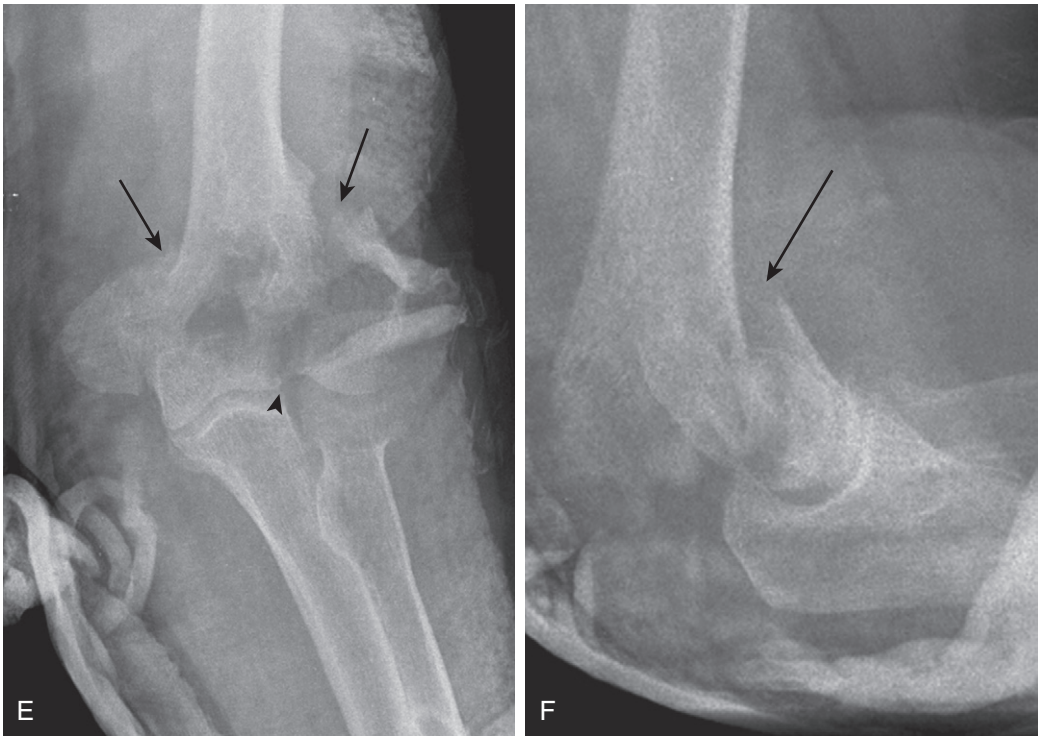


FIGURE 4-10, cont'd **E** and **F,** A complete articular fracture (type C) with marked displacement. The fracture lines extend to both medial and lateral columns *(arrows)* of the distal humerus, as well as to the articular surface of the elbow *(arrowhead)*. The distinction between type B and type C is based on the number of columns involved.

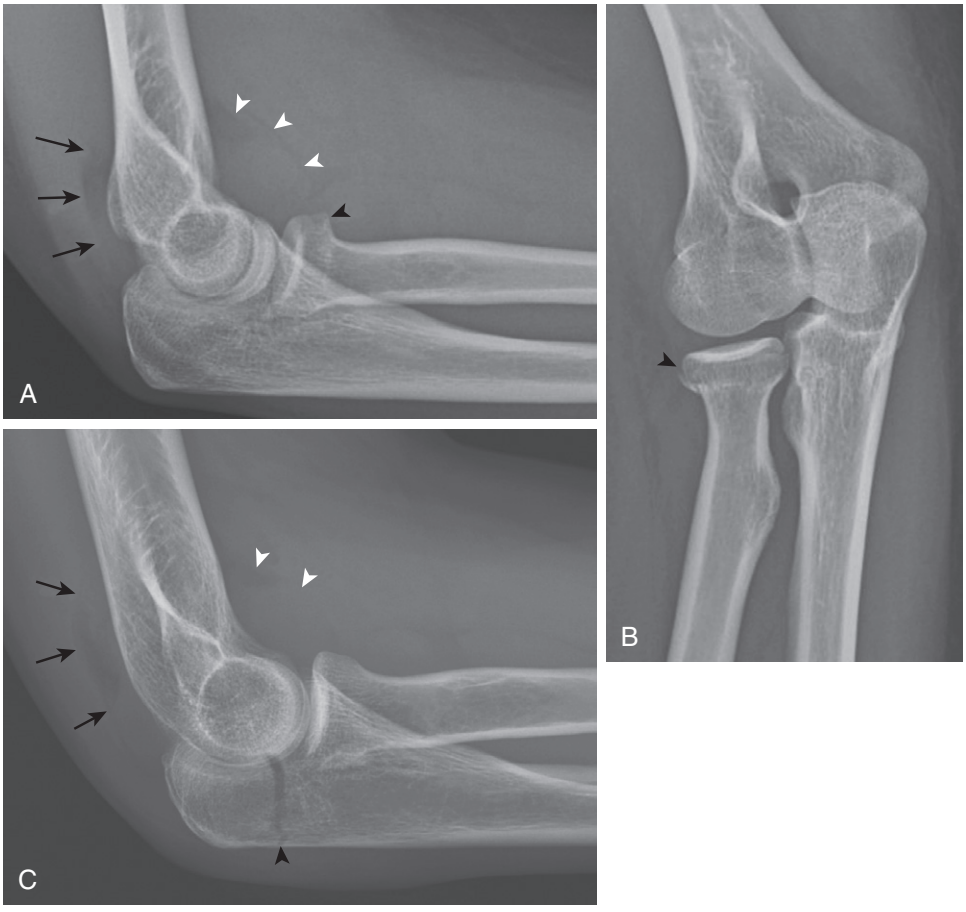


FIGURE 4-11 Fractures of the radial head and olecranon process. **A,** A lateral radiograph of the elbow demonstrates a classic posterior fat pad sign *(arrows)* produced by the posterior bulge of the extrasynovial fat. In addition, an elevated anterior fat pad is present *(white arrowheads)*. The cause of the joint effusion is a radial head fracture *(black arrowhead)*. **B,** The *black arrowhead* demonstrates a nondisplaced fracture of the radial head. **C,** A lateral radiograph of the elbow shows a transverse fracture of the olecranon process *(black arrowhead)*, a posterior fat pad sign *(arrows)*, and an elevated anterior fat pad *(white arrowheads)*.

radiograph in 90% of cases and is outlined anteriorly by a thin radiolucent fat stripe beneath the flexor digitorum profundus muscle. When a hemorrhage occurs beneath or in the muscle, the muscle bulges anteriorly and can displace/efface the fat plane. This phenomenon could present as a volar bulge of the thin fat stripe superficial to the muscle or a loss of definition of the lucent fat stripe overlying the muscle itself. It is usually caused by injuries to the distal thirds of the radius and ulna.



FIGURE 4-12 Elbow dislocation and fracture of the coronoid process. A lateral radiograph of the elbow demonstrates a posterior dislocation of the radius and ulna with respect to the distal humerus. A coronoid process fracture is noted *(arrowheads)*.

Monteggia Fracture-Dislocation

Monteggia fracture-dislocation (Fig. 4-13) is a combination of a fracture of the proximal ulna shaft and subluxation or dislocation of the radial head. "Monteggia lesion" describes a number of traumatic lesions having common disruption of the radial head and fracture of the ulna at any level. Four types of Monteggia fracture-dislocation (per the Bado classification) are described according to the direction of the displaced ulnar fracture and the dislocated radial head. *Type I,* the most common type, is a fracture-dislocation with volar angulation at the fracture site and volar dislocation of the radial head. *Type II,* or reverse Monteggia fracture-dislocation, is more likely to be seen in adults; it has dorsal angulation at the fracture site and dorsal dislocation of the radial head. *Type III* is the most severe of all the Monteggia fracture-dislocations; the fractures are laterally displaced with lateral or anterolateral dislocation of the radial head. *Type IV* is a fracture-dislocation that includes a fracture of the proximal radius along with the proximal ulna and volar dislocation of the radial head. In the presence of an isolated ulnar shaft fracture, one must always anticipate the possibility of the injuries to the radius and vice versa. Dislocation of the radial head may be subtle but can be diagnosed by abnormal alignment of the radiocapitellar line. However, in young children with a nonossified radial head, diagnosis of radial head dislocation with radiography can be difficult. Ultrasound or MR imaging may be helpful in this circumstance.

Galeazzi Fracture-Dislocation

Galeazzi fracture-dislocations (Fig. 4-14) account for 3% to 6% of all forearm fractures. They consist of a fracture of the distal third of the radial shaft and dislocation or subluxation of the DRUJ. The fracture of the distal radial shaft is usually transverse with apex anterior angulation, and it is almost always located superior to the proximal border of the pronator quadratus. When one is faced with an isolated radial shaft fracture, injury of the DRUJ should be sought. The following signs suggest traumatic disruption of the DRUJ: fracture of the ulnar styloid at its base,

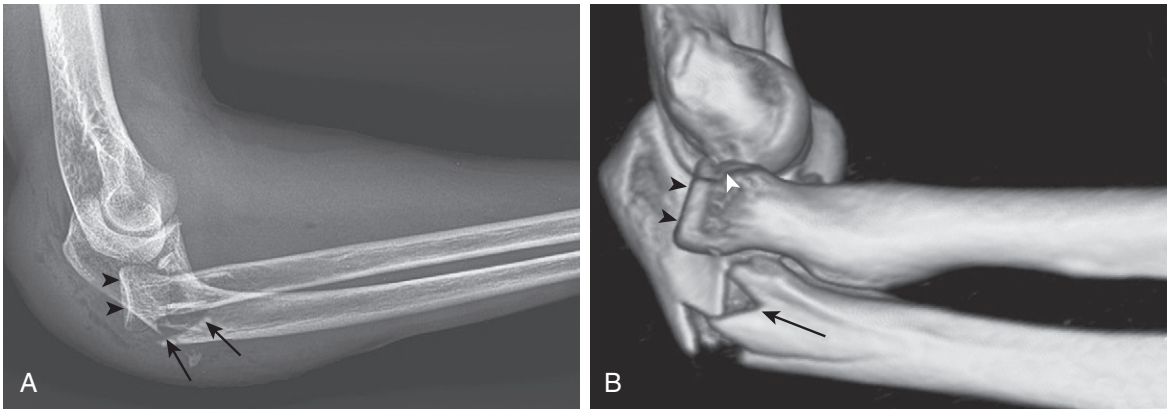


FIGURE 4-13 Monteggia fracture-dislocation. **A,** A lateral radiograph of the forearm demonstrates dorsal dislocation of the radial head *(black arrowheads),* along with an angulated comminuted fracture of the proximal third of the ulna *(arrows)*. Soft tissue gas indicates an open injury. This injury is a type II Monteggia fracture-dislocation. **B,** Volumetric (three-dimensional) computed tomography reformation reveals an impacted fracture of the radial head *(white arrowhead)* along with the Monteggia fracture-dislocation *(black arrowheads and arrow)*.

a widened DRUJ space on a frontal radiograph, dislocation of the radius relative to the ulna on a lateral radiograph, and radial shortening. Entrapment of the extensor tendons, especially extensor carpi ulnaris, may complicate this fracture-dislocation.

Fractures of the Distal Radius

Fractures of the distal radius are very common. They affect women more than men, and the incidence increases with advancing age. The injuries are usually the result of low-energy trauma. Classification of these fractures as Colles, Smith, or Barton continues in clinical practice and the medical literature. However, most distal radial fractures do not fall into one of these categories. The more clinically useful way to describe fractures of the distal radius is to use the number of the fracture "parts" and define whether the fracture is intra- or extraarticular. *Extraarticular fractures* do not affect either the radiocarpal joint or the DRUJ. Characteristically, they occur in the distal 3 to 4 cm of the radius and consist of two parts. *Intraarticular fractures* can be two, three, four, or more parts. They extend into the radiocarpal joint or DRUJ. Barton and chauffeur fractures fall into this category. The degree of intraarticular incongruity is the most clinically significant predictor of functional outcome and future degenerative changes of the radiocarpal joint, especially if incongruity of 2 mm or more is present. Instability of these fractures is determined by the degree of angulation, comminution of the dorsal metaphysis, the presence of an intraarticular portion, and the patient's age.

Colles fracture (Fig. 4-15, *A* and *B*) is a transverse extraarticular fracture of the distal inch of the radius with dorsal displacement of the distal fragment together with the bones of the wrist and hand. It usually occurs as a result of a fall on an outstretched hand in older persons with osteoporosis. The dorsal surface of the distal radius undergoes compression, while the volar surface undergoes tension. Initially the fracture line is often on the volar side and appears as a single line. Extensive comminution, radial shortening, dorsal angulation, and radiocarpal articular extension with a greater than 2-mm articular step-off are findings associated with failure of nonoperative management. It is commonly associated with an ulnar styloid process avulsion fracture, scapholunate dissociation, and other carpal dislocations or fractures.

Fractures of the ulnar styloid (Fig. 4-15, *C*) occur in approximately 60% to 70% of distal radius fractures. The majority of them are small avulsion fractures involving the tip of the ulnar styloid. Treatment remains controversial, although the injury may well produce symptoms as a result of the fracture itself or injury to the triangular fibrocartilage complex. Treatment may be indicated if the fracture involves the base of the ulnar styloid with significant displacement and/or gross translation of the radius relative to the ulna.

Smith fracture (Fig. 4-15, *D*) is a transverse fracture of the distal radius with volar displacement of the distal fragment together with the carpus and hand, the so-called "garden spade deformity." It can be extraarticular, intraarticular (extending into the radiocarpal joint, similar to a volar Barton fracture), or juxtaarticular (extending to the dorsal articular surface).

Barton fracture (Fig. 4-16, *A, B,* and *C*) is an intraarticular oblique coronal fracture of the dorsal or volar margins (dorsal vs. volar Barton) of the distal radius resulting from a

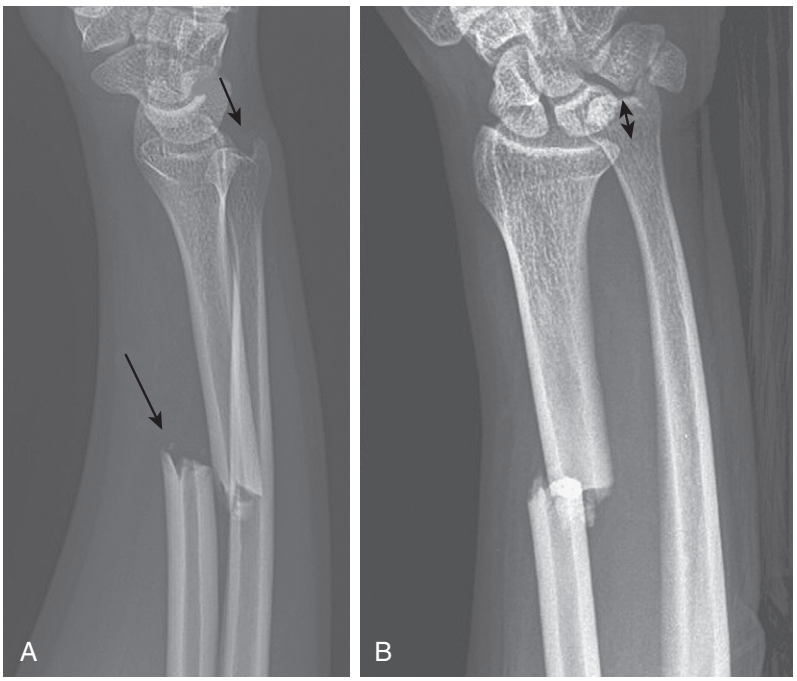


FIGURE 4-14 A Galeazzi fracture-dislocation. **A** and **B,** Lateral and anteroposterior radiographs of the forearm show a displaced transverse fracture *(long arrow)* of the radial shaft at the junction of the middle and distal thirds, along with dislocation *(short arrow)* of the distal radioulnar joint (DRUJ). Dislocation of the radius relative to the ulna on the lateral radiograph and radial foreshortening *(double-headed arrow)* are clues suggesting DRUJ disruption.

die-punch mechanism. The distal fragment displaces volarly or dorsally and proximally along with the carpus and hand, which is the main feature differentiating Barton from Colles and Smith fractures. They can be comminuted and involve the anterior, posterior, radial, or ulnar cortex of the distal radius. The volar Barton fracture is more common than the dorsal Barton fracture. The latter fracture frequently occurs with a radial styloid fracture. Most Barton fractures require operative treatment.

Chauffeur fracture (Hutchinson fracture) (Fig. 4-16, *C*) is an intraarticular fracture of the base of the radial styloid process. The name was coined in the era when hand



FIGURE 4-15 Fractures of the distal radius *(arrows)*. **A** and **B,** Posteroanterior and lateral wrist radiographs demonstrate a transverse extraarticular fracture of the distal end of the radius *(arrows)* with dorsal displacement of the distal fracture fragment, producing a "dinner fork" deformity. This injury is a classic Colles fracture. **C** and **D,** A Smith, or reverse Colles, fracture is demonstrated and characterized by volar displacement of the distal fracture fragment. An arrowhead denotes a non-displaced fracture of the ulnar styloid process.

cranking was required to start motor vehicles. At present, it is most frequently caused by a fall on an outstretched hand, resulting in an avulsion of the radial collateral ligament, or by a direct blow to the radial styloid process. The styloid process may be displaced from the radius but typically maintains alignment with the carpus as a result of strong ligamentous attachments. This fracture is associated with scapholunate dissociation (SLD), perilunate dislocation, and dorsal Barton fracture. The chauffeur fracture itself is best seen on a semipronated view; however, to visualize the SLD, a clenched fist semisupinated view is most helpful.

Among pediatric distal radial fractures, *torus fracture (buckle fracture)* (Fig. 4-16, *E*) is the most common fracture in young children. It is usually caused by a fall



FIGURE 4-16 Fractures of the distal radius *(arrows)*. **A** and **B,** Frontal and lateral radiographs of the wrist demonstrate an oblique coronal fracture of the distal radius with intraarticular extension. The fracture line extends to the volar aspect of the distal radius (volar Barton fracture). **C,** A frontal radiograph of the wrist shows a nondisplaced transverse fracture of the radial styloid process, or a chauffeur fracture.

Continued

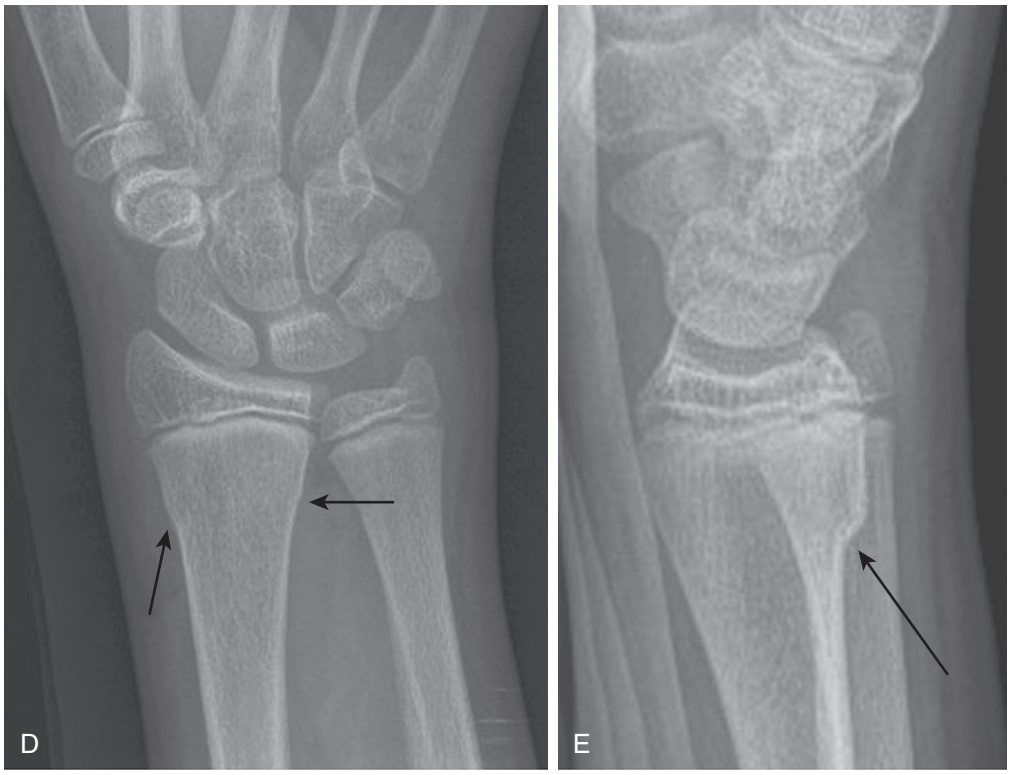


FIGURE 4-16, cont'd **D** and **E,** A torus fracture. Posteroanterior and lateral radiographs of the wrist of a child reveal a subtle undulation in the distal radial metaphysis *(arrows)*, which is a classic location for a fracture of the dorsal cortex of the distal radial metaphysis.

on an outstretched hand that causes compression on one side—mostly the dorsal cortex. Characteristically the fracture involves only the compression side, usually 2 to 3 cm proximal to the physis. The periosteum and cortex are intact on the side opposite to the fracture, and hence this fracture has a good prognosis. Careful evaluation of the tension side (volar cortex) is important to ensure its integrity because the fracture on this side (greenstick fracture) constitutes a different pattern and treatment. *Greenstick fracture* represents an incomplete long bone fracture with failure of the cortex on the tension side and plastic deformation on the compression side. *Distal radial physeal fractures* can be seen as a result of a similar mechanism of injury. Most of them are Salter-Harris type I and II fractures. The pronator quadratus sign is helpful to identify type I fractures (Box 4-10).

BOX 4-10 Fractures of the Shafts and Distal Radius and Ulna

Standard views: Anteroposterior (supination) and lateral views of the forearm (with the elbow flexed 90 degrees and the hand in a lateral position); the distal radius is imaged with wrist protocol
Frequent sites of injuries: Distal end of radius, ulnar styloid process
Frequently missed injuries: Distal radioulnar joint injury; when only one bone of the forearm is broken, the distal radioulnar joint and elbow joint should always be assessed

FRACTURES AND DISLOCATIONS OF THE CARPUS

Scaphoid Fractures

Scaphoid fracture (Fig. 4-17) is the most common fracture of the carpal bone. It almost exclusively occurs in young adults as a result of falls on the outstretched hand, athletic injuries, or motor vehicle accidents. A strong index of suspicion is the key to early diagnosis because scaphoid fractures may produce little pain, swelling, or limited motion. Scaphoid fractures are classified by their anatomic location: proximal third (proximal pole), middle third (waist), distal articulating portion, and tubercle. The most common location of fracture is at the waist (80%), followed by proximal pole (15%), tubercle (4%), and distal articular fracture (1%). The location of the fractures provides prognostic implications because of characteristic blood supply to the scaphoid. The scaphoid is supplied by two major vascular pedicles: one entering the tubercle, supplying the distal one third and accounting for 20% to 30% of blood flow, and the other entering the foramina on the spiral groove at and distal to the waist. The latter pedicle gives 70% to 80% of the blood supply to the scaphoid in the retrograde fashion from the waist to the proximal pole. The more proximal the fracture line is, the greater the incidence of avascular necrosis. Most fractures run in a plane transverse to the long axis of the scaphoid. The dorsal sulcus fracture, however, runs obliquely along the line of the dorsal sulcus that is 45 degrees to the scaphoid waist. Four or five radiographic views of the wrist supplement each other



FIGURE 4-17 A scaphoid fracture. **A,** A posteroanterior radiograph of the wrist in ulnar deviation reveals a subtle cortical disruption at the waist of the scaphoid *(curved arrow)*. **B,** A coronal reformatted computed tomography image of the same patient performed subsequently confirms a scaphoid fracture *(arrow)*. **C,** In a different patient, a coronal T1-weighted magnetic resonance image reveals a scaphoid waist fracture *(arrow)*. T1 hypointensity is present in the proximal pole of the scaphoid *(arrowhead)*, indicating development of avascular necrosis in this nonacute fracture.

in identifying and characterizing scaphoid fractures. A semipronated view is best to detect dorsal sulcus fractures, whereas a semisupinated view is helpful for proximal pole fractures and assessing humpback deformity (i.e., dorsal angulation of the proximal pole/lunate complex and flexion of the distal pole). The scaphoid waist is best seen on the ulnar-deviated posteroanterior (PA) view, especially if it is performed with 20-degree angulation toward the elbow. Although a series of wrist radiographs is usually sufficient for diagnosis, up to 30% of scaphoid fractures are radiographically occult. The presence of snuffbox tenderness and a history of trauma, even with negative radiographs, necessitate immobilization or further imaging with CT or MR. If immobilization is used, radiographs obtained after 10 days usually reveal abnormalities—either resorption of the fracture line (a clearly visible lucent line) or faint sclerosis around the fracture. CT is becoming a more common investigation for acute wrist trauma because of its wide availability and rapid scanning time. CT can be performed on the day of the injury to detect occult fractures if the diagnosis is essential, for example, in athletes. It can also characterize known fractures, particularly in the determination of humpback deformity. Stability of the fractures depends on the presence of displacement, the degree of comminution, and associated injuries.

Triquetral Fractures

Triquetral fractures (Fig. 4-18, *A* and *B*) are the second most common fractures of the carpal bone. They commonly involve the dorsal surface as a result of a shear or chisel injury from impingement of the ulnar styloid on the dorsal aspect of the triquetrum when the wrist is forcibly dorsiflexed and ulnarly deviated. Pain and tenderness are localized to the dorsolateral portion of the wrist. A flake of bone fragment is best visualized in lateral or pronated oblique projections. Transverse fracture of triquetral body can be identified on a standard PA view. However, CT may be required to detect and assess the extent of the injury.

Hamate Fractures

Fractures of the hamate (Fig. 4-18, *C*) are rare and frequently missed on radiographs. They can involve the body or the hook of the hamate. The latter fracture is more common and can produce significant disability. Either a direct blow to the hook or avulsion of the transverse carpal ligament and pisohamate ligament can result in this fracture. The hamate hook fracture is best visualized on a carpal tunnel view or CT scan. The absence or indistinctness of an "eye sign" (an oval dense cortical ring shadow over the hamate) is described as a sign of fracture of the hook of hamate on a frontal radiograph.



FIGURE 4-18 Other carpal fractures. **A** and **B,** A lateral radiograph of the wrist and a sagittal reformatted computed tomography (CT) image, respectively, demonstrate a small dorsal triquetral fracture *(arrows)* with overlying soft tissue swelling. **C,** A hook of hamate fracture. An axial CT image shows a nondisplaced fracture of the hook of the hamate *(arrow)*.

Lunate Fractures

Lunate fractures are the fourth most common carpal fracture after scaphoid, triquetrum, and trapezium fractures. Most patients have a hyperextension injury or repetitive stress of the wrist. Isolated acute lunate fractures are frequently not recognized on radiographs because of nondisplacement and superimposed structures. CT and MR imaging provide more precise detail and accurate diagnosis. Fragmentation of the lunate occurs in Kienböck disease (idiopathic avascular osteonecrosis of the lunate). This condition is sometimes confused with lunate fractures. It is predisposed by multiple causes: primary fracture, repetitive trauma, injury to the ligament carrying blood to the lunate, and the presence of ulnar negative variance. In an early stage, the lunate may appear normal on radiographs. Later, sclerosis, loss of lunate height, fragmentation, and eventually wrist collapse and arthritis ensue.

Carpal Dislocations

The mechanism responsible for carpal dislocations is an axial compression-hyperextension injury, usually from a fall onto an outstretched hand. Failure of the connecting structures bridging the proximal and distal rows of the carpus results in dorsal displacement of the distal row (perilunate dislocation). If the force is more severe, complete lunate dislocation may occur. These injuries can be diagnosed with use of lateral radiographs.

Perilunate dislocation (Fig. 4-19, *A* and *B*) is the most common type of all wrist dislocations. A dorsal dislocation of the carpal bones (scaphoid, triquetrum, and other carpal bones) is present around the lunate, while the lunate itself remains in a normal position with respect to the distal radius. Loss of congruity of the three carpal arcs, along with abnormal triangular configuration of the lunate with the apex pointing distally, are signs on frontal radiographs.



FIGURE 4-19 Carpal dislocations and instabilities. **A** and **B,** Perilunate dislocation. A posteroanterior radiograph of the wrist (**A**) shows a wide scapholunate space, loss of congruity of the three carpal arcs, and triangular configuration of the lunate *(L)*. A lateral radiograph (**B**) confirms dislocation of the carpal bones *(curved arrow)* with the lunate *(L)* remaining in the normal position with respect to the distal radius. **C** and **D,** Lunate dislocation. A lateral view (**D**) demonstrates a dislocated lunate with respect to the distal radius and other carpal bones, giving the appearance of a "spilled teacup" *(curved arrow)*. **E,** Scapholunate dissociation is shown as widening of the scapholunate space *(arrow)* to more than 5 mm (the "Terry Thomas" sign).

On lateral projections, the relationship of the lunate and distal radius is normal, but all other carpal bones are located posterior to the lunate. When the dislocation occurs with a scaphoid waist fracture, it is called a *transcaphoid perilunate dislocation*.

In *lunate dislocation* (Fig. 4-19, *C* and *D*), the lunate is dislocated volarly with respect to the distal radius, and all other carpal bones lie dorsal to the lunate, producing a radiographic "spilled teacup sign" on lateral radiographs. The capitate migrates proximally and sits in the lunate fossa. It is the most severe type of carpal instability. On frontal projections, the congruity of the three carpal arcs is lost, and superimposition of the base of the capitate and lunate is present. Lunate dislocations commonly occur with scaphoid fractures.

Carpal Instabilities

Radiographic signs of carpal instabilities include disruption of one or all of the three carpal arcs (arcs of Gilula), alteration of symmetric intercarpal joint spaces, and changes in contour of an individual carpal bone.

Scapholunate dissociation (rotatory subluxation of the scaphoid) (Fig. 4-19, *E*) is a spectrum of injuries caused by an interruption of the scapholunate ligament and extrinsic ligaments that stabilize this articulation, resulting in abnormal motion between the scaphoid and lunate. It is the most common pattern of carpal instability. Because of normal compressive forces across the wrist that tend to force the scaphoid into further palmar flexion, disruption of the scapholunate ligament seen in scapholunate dissociation will allow an abnormal degree of palmar flexion of the scaphoid. Thus the key finding on the lateral radiograph is an increased scapholunate angle of more than 60 degrees. On frontal radiographs, there is widening of the scapholunate space of more than 2 mm measuring at or distal to the midpoint of the joint space (4 mm is considered to be pathognomonic), the so-called "Terry Thomas sign." If in doubt, comparison between the scapholunate space and lunotriquetral space should reveal a significant widening of the former in case of scapholunate dissociation. The "cortical ring sign" is another radiographic finding of this condition that describes the cortex of the distal pole of palmar-flexed scaphoid as seen end-on on the frontal radiograph. This type of injury can be isolated or associated with distal radial fractures. Without treatment, this injury leads to scapholunate advanced collapse.

Dorsal intercalated segmental instability (DISI; dorsiflexion instability), which is usually associated with scapholunate dissociation, is a derangement of the radial side of the wrist and is often associated with radial-sided symptoms. On lateral radiographs, the lunate tilts dorsally, resulting in an increased capitolunate angle of greater than 20 or 30 degrees. Lateral fluoroscopy of the wrist in flexion is more definitive because the static radiographic configuration of DISI occasionally can be seen as a normal variant. DISI is most frequently observed with displaced scaphoid fractures and scapholunate dissociation.

Volar intercalated segmental instability (volar flexion instability) is much less common than DISI, although it is the most common pattern of carpal stability seen in patients with rheumatoid arthritis. It is a result of ulnar-sided ligament derangement. The lunate tilts volarly, and the capitolunate angle is greater than 20 or 30 degrees (Box 4-11).

BOX 4-11 Fractures and Dislocations of the Carpus

Standard views: Posteroanterior, lateral, internal, and external oblique views; the scaphoid view, if performed, must be accompanied by a full wrist series
Frequent sites of injury:
Children: Torus fractures
Adolescents/young adults: Carpal fractures (e.g., scaphoid and triquetrum)
Adults: Colles fractures
Frequently missed injuries: Nondisplaced scaphoid fractures, hook of hamate fractures, perilunate dislocations
Relevant normal anatomy: A normal fat stripe anterior to the pronator quadratus is thin and smooth, without volar bulge; this is abnormal when the distance between the distal radius and the fat plane is greater than 7 mm in women or 10 mm in men
Normal radiocarpal angle: 15 degrees ulnar inclination (frontal projection) and 15 degrees volar inclination (lateral projection)
Ulnar variance (radial length): At the site of articulation with the lunate, the radius and ulna are normally on the same level; negative ulnar variance occurs when the articular surface of the ulna projects 5 mm proximal to the radiolunate articulation; positive ulnar variance occurs when the articular surface of the ulna projects 8 mm distal to the site of radiolunate articulation
Normal carpal bone alignment (frontal projection) (three smooth arcs of Gilula): Arc I joins the proximal articular surfaces of the scaphoid, lunate, and triquetrum; arc II is formed by distal convexities of the scaphoid, lunate, and triquetrum; arc III is formed by proximal convexities of the capitate and hamate
Normal carpal bone alignment (lateral projection): In the long axis of the distal radius, the lunate and capitate are linear; the long axis of the scaphoid is at an angle of 30 to 60 degrees to the axis of the distal radius, lunate, and capitate (scapholunate angle)
Three carpal columns: Central (radius-lunate-capitate), ulnar (ulna-triquetrum-hamate), and radial (radius-scaphoid-trapezoid-trapezium)

BOX 4-12 Fractures and Dislocations of the Hand

Standard views:
Hand—Posteroanterior (PA), lateral, internal oblique
Thumb—Anteroposterior, lateral, oblique
Fingers—PA, lateral, oblique
Frequent sites of injuries: Phalanges, base of the thumb metacarpal
Frequently missed injuries: Fourth and fifth carpometacarpal dislocations, volar plate fractures, Mallet fingers, Bennett fractures
Relevant normal anatomy: The volar plate is a dense fibrous band forming the volar aspect of the thumb's metacarpophalangeal and the finger's proximal interphalangeal joints
Sesamoid—two constant sesamoids are at the first metacarpophalangeal
Fracture mimics: Nutrient artery canals: the oblique lucent line located near the middle third of shafts of the phalanges and metacarpal bones should not be mistaken for fractures

FRACTURES AND DISLOCATIONS OF THE HAND

Thumb Fractures and Dislocations

Fractures of the base of the thumb metacarpal constitute 80% of thumb fractures (Box 4-12). They usually result from an axial load to the partially flexed thumb metacarpals (e.g., during fistfights) and include four types: epibasal (extraarticular; Fig. 4-20, *A*), Bennett, Rolando, and comminuted fractures. Bennett fractures (Fig. 4-20, *B* and *C*) are intraarticular oblique fractures through the proximal articular surface of the thumb metacarpal, resulting in two separate fragments. The triangular fragment is attached to the trapezium, whereas the distal fragment and metacarpal are displaced proximally as a result of an act of the abductor pollicis tendon that inserts on the dorsal surface of the thumb metacarpal. Rolando fractures (Fig. 4-20, *D*) are intraarticular comminuted fractures consisting of three major fragments. In Rolando and comminuted fractures,

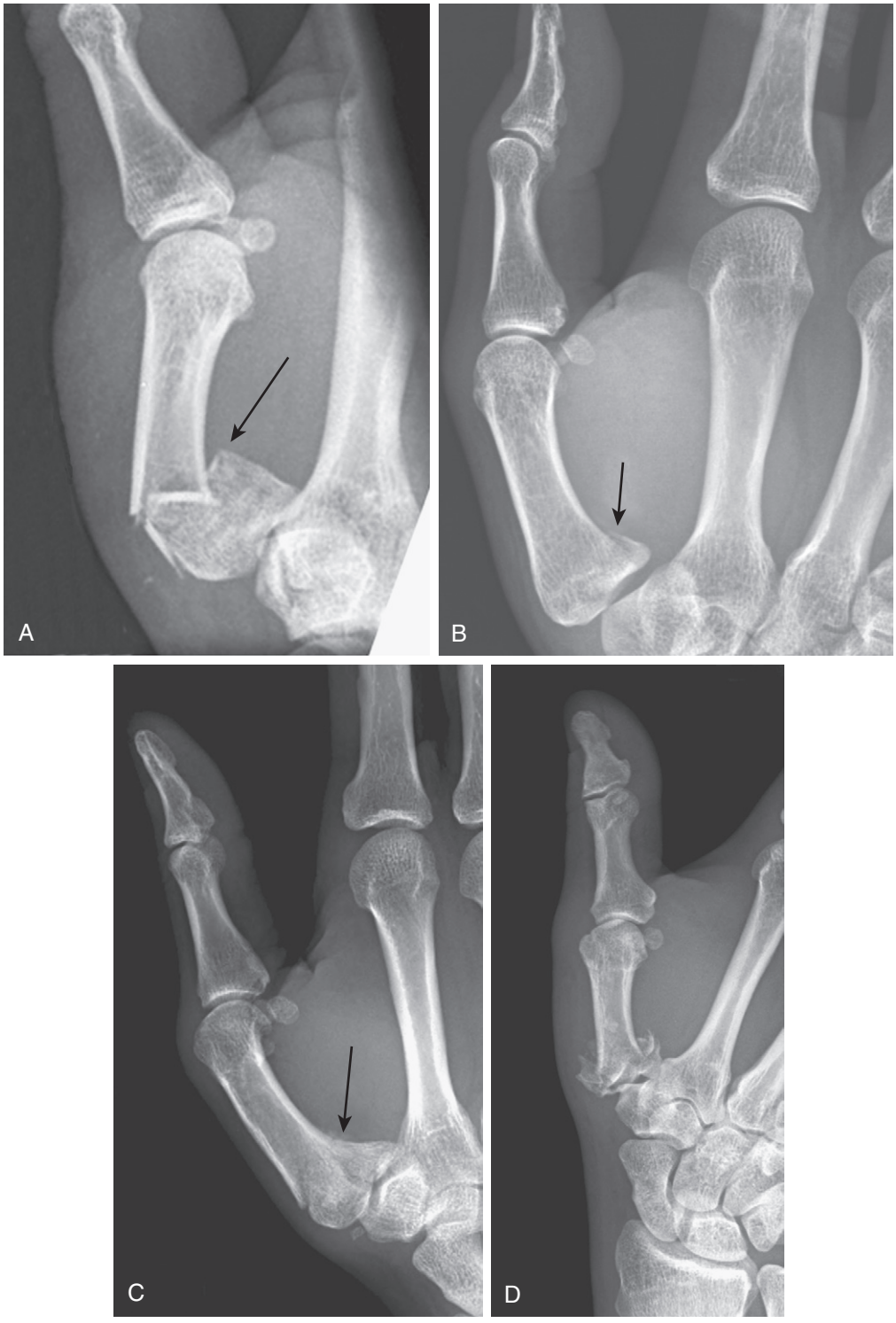


FIGURE 4-20 Fractures of the base of the first metacarpal. Four types of fractures *(arrows)* are shown. **A,** Epibasal extraarticular type. **B,** A Bennett or intraarticular oblique fracture with two separate fragments. **C,** A Rolando fracture—a comminuted fracture with three separate fragments. **D,** A comminuted fracture.

the large distal fragment is impacted into the two smaller fragments instead of being retracted.

Gamekeeper's or skier's thumb (Fig. 4-21) signifies an injury to the ulnar collateral ligament of the thumb metacarpophalangeal (MCP) joint as a result of forceful abduction of the thumb proximal phalanx. The spectrum of injuries ranges from a pure ligamentous injury to an avulsion of the ulnar aspect of the distal attachment site of the ligament or a transverse fracture of the base of the proximal phalanx.

Dislocations of the Carpometacarpal Joints

A very complex network of dense carpometacarpal (CMC) and intermetacarpal ligaments holds CMC joints, and thus a major force is required to cause injuries to this region.



FIGURE 4-21 Gamekeeper's or skier's thumb. An avulsion fracture *(curved arrow)* of the ulnar aspect of the base of the proximal phalanx of the thumb is shown.

Dislocation at the first CMC joint usually occurs with high-energy trauma, with concomitant neurovascular injuries. Pure thumb CMC dislocation is mostly dorsal and results from axial loading on a partially flexed thumb. Of other CMC joints, fractures and dislocations frequently occur at the fourth and fifth CMC joints (Fig. 4-22, *A* and *B*) because of their greater flexibility and mobility.

Metacarpal Fractures

Fractures of the metacarpal bones are classified according to the location: base, shaft, neck, or head. They are commonly oblique (Fig. 4-23) or spiral rather than transverse in configuration and are usually obvious. The exception is nondisplaced fractures at the base of the lateral metacarpal bones, which are frequently occult because of the bony configuration, superimposition in this region, and minimal displacement of the fragments. *Boxer's fracture* is a metacarpal neck fracture with angulation of the distal fragment as a result of a direct impact on the metacarpal head with fists clenched. It is most commonly seen in the fifth metacarpal. The description of boxer's fracture is somewhat misleading because professional fighters are more likely to sustain a second or third metacarpal neck fracture. *Fractures of the base of the metacarpals* are divided into four types: epibasal, two-part (reverse Bennett), three-part, and comminuted. In the reverse Bennett type, flexor and extensor carpi ulnaris muscles usually retract the larger distal fragment proximally.

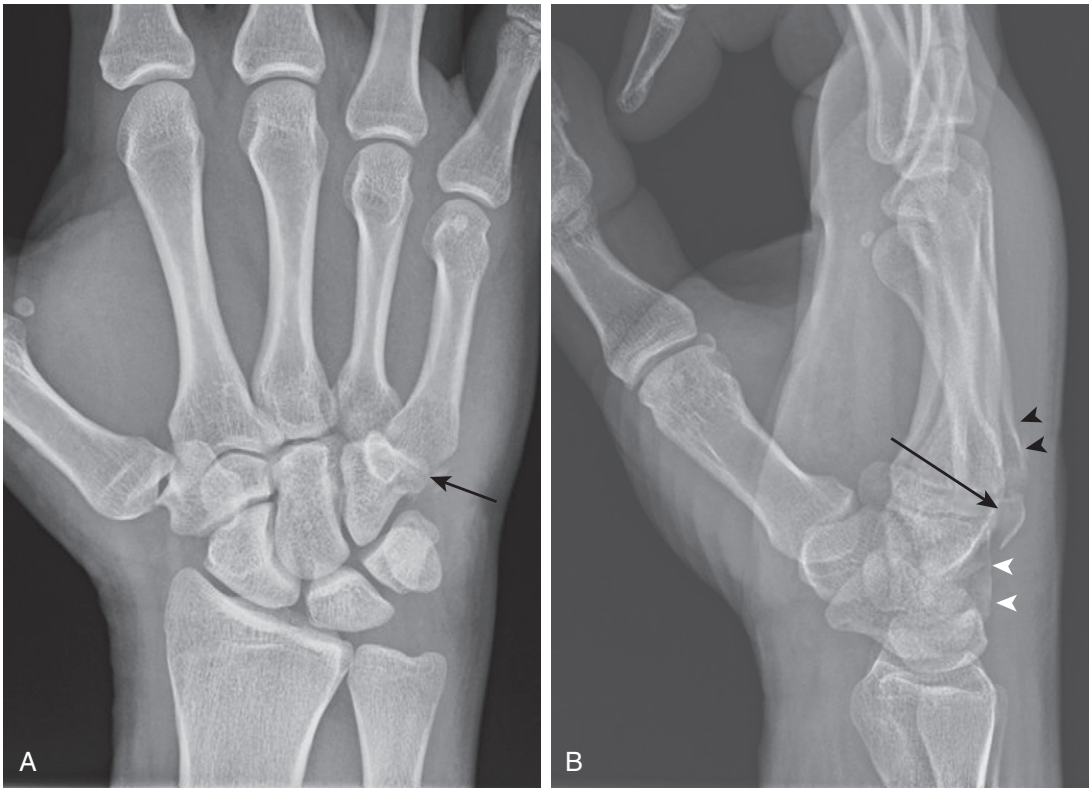


FIGURE 4-22 A carpometacarpal dislocation. **A,** A posteroanterior radiograph of the hand demonstrates a subtle overlap *(arrow)* of the proximal end of the fifth metacarpal and the hamate. **B,** A lateral radiograph reveals dorsal dislocation of the fifth metacarpal *(black arrowheads)* with respect to the carpal bones *(white arrowheads)*. A fracture of the body of the hamate is also visualized *(arrow)*.

Dislocations of the Metacarpophalangeal Joints

The most common type of MCP joint dislocation is dorsal dislocation. Volar dislocation is rare but potentially unstable. When a fracture is clinically irreducible, it is called a *complex dislocation* and is most often due to volar plate interposition. A radiographic sign of complex dislocation is the appearance of a small piece of bone in the joint space, representing an interposed volar plate.



FIGURE 4-23 Boxer's fracture. A posteroanterior radiograph of the hand demonstrates a metacarpal neck fracture *(arrow)* with volar angulation of the distal fragment.



FIGURE 4-24 A transverse fracture of the distal phalanx. This fracture is commonly associated with nail bed injuries.

Phalangeal Fractures

Phalangeal fractures are more common than metacarpal fractures. They may be classified as either extraarticular (involving shafts) or intraarticular (involving proximal or distal margins of the phalanges). The distal phalanx is most commonly involved, accounting for more than half of hand fractures. These fractures vary from a comminuted, longitudinal split, or transverse fracture, and frequently are associated with lacerations of the nail bed. Fractures of the proximal phalanx (P1), middle phalanx (P2), and distal phalanx (P3; Fig. 4-24) are described according to their location (head, neck, shaft, and base) and appearance. A phalangeal neck fracture with volar spike of bone from the proximal fragment may impinge onto the subcapital recess, resulting in a complication of limited movement of the interphalangeal joint.

Baseball or mallet finger (Fig. 4-25, *A*) is a flexion deformity at the distal interphalangeal (DIP) joint. The injury occurs when an extended DIP joint is forcibly flexed, resulting in avulsion of the extensor tendon from the dorsal lip at the base of the distal phalanx. A small piece of bone may or may not be avulsed along with the tendon. Radiographs may reveal no fracture but only flexion deformity of the DIP joint.

Volar plate injury (Fig. 4-25, *B*) is an avulsion injury at the proximal interphalangeal (PIP) joint. It occurs at the insertion of the volar plate on the volar surface of the base of



FIGURE 4-25 Fractures and dislocations involving the interphalangeal joint. **A,** Mallet finger. A lateral radiograph of the finger shows an avulsion fracture *(arrow)* at the dorsal lip of the base of the distal phalanx, resulting in flexion deformity of the distal interphalangeal joint. **B,** A volar plate fracture. A lateral radiograph of the finger demonstrates an avulsion fracture of the volar lip of the base of the middle phalanx *(arrow)*. These fractures are common fractures of the lower extremity.

the middle phalanx as a result of a hyperextension injury. A volar plate injury can occur with or without bony avulsion. In the latter, a small, avulsed bony fragment is usually nondisplaced. The fragment is often a thin sliver of bone, which is minute and easily overlooked. It is best visualized on lateral or oblique projections of the radiograph of an involved finger.

Jersey finger is an avulsion injury at the DIP joint resulting from a pull of the flexor digitorum profundus tendon from the volar base of the distal phalanx. Forced extension while the DIP joint is in flexion, such as when grabbing a jersey of an escaping football player, is the mechanism of injury. This type of fracture is similar to the volar plate injury.

Boutonniere deformity is a flexion deformity of the PIP joint with hyperextension of the DIP joint. It is caused by a tear or avulsion of the middle slip of the extensor mechanism that allows the PIP joint to flex while the DIP is extended. The site of avulsion is on the dorsal surface of the base of the middle phalanx. At the initial injury, the patient may report only pain and swelling around the PIP joint. The characteristic deformity develops subsequently.

Dislocations of the Interphalangeal Joints

Dislocations of the interphalangeal joints are the result of a hyperextension injury. Most of them are dorsal dislocations; the affected phalanx is displaced dorsally. They are associated with a volar plate rupture that manifests as an avulsion with or without a small flake of bone from the volar margin of the base of the phalanx. Irreducible dorsal dislocations are usually due to a trapped volar plate, a trapped flexor digitorum profundus, a buttonholed P2 through the volar plate, or a rent in the flexor digitorum profundus. On a rare occasion, an irreducible dislocation is caused by interposition of the sesamoid bone within the joint.

LOWER EXTREMITY FRACTURES OF THE PELVIC RING

The pelvic ring (Box 4-13) is a round or oval plane of pelvic inlet that includes the sacral promontory, the inferior margin of sacroiliac joints, the iliopectineal line to the superior margin of the superior pubic rami, and the pubic symphysis. The pelvic ring is divided into anterior and posterior portions by an imaginary line connecting the ischial spines. Two main types of injury to the bony pelvis are classified according to the presence or absence of the disruption to the pelvic ring.

BOX 4-13 Fractures of the Pelvic Ring

Standard views: Anteroposterior, inlet and outlet views of the pelvis
Frequent sites of injuries: Pelvic ring disruption (LC and APC)
Frequently missed injuries: Sacrum, pubic ramus, avulsion injuries
Relevant normal anatomy:
- Anterior arch of pelvic ring-weaker; pubic rami, symphysis
- Posterior arch of pelvic ring-stronger; sacrum, SI joints, posterior ilium
- Sacral arcuate line-arch of the superior surface of sacral foramina that is tangential to the x-ray beam; it is normally sharply defined, smooth, and bilaterally symmetrical
- Inlet view-anterior/posterior translation of bony pelvic structures, rotation of hemipelvis, sacral arch/crush injuries
- Outlet view-sacral fracture, SI widening, elevation of hemipelvis
- Radiographic instability-cephalic displacement of posterior sacroiliac complex >5-15 mm on inlet and outlet views

Fracture mimics: Chronic avulsions may mimic bone/soft tissue tumors

Isolated Injuries Without Disruption of the Pelvic Ring

Avulsion injuries (Fig. 4-26) are a result of sudden muscular contractions or abrupt change of speed or direction that usually occur during athletic activities. They occur frequently in adolescents before the apophyseal closure because the muscles and tendons are stronger than the apophyseal attachments. Typical locations are at the anterior superior iliac spine, anterior inferior iliac spine, ischial tuberosity, and inferior margin of the pubic body. The muscles and tendons responsible for these injuries are the sartorius, rectus femoris, biceps femoris, and adductor group, respectively. The fractures are displaced as a result of the pull from the muscles and are usually obvious on radiographs at the initial injury. The contour of the displaced fragments mirrors the adjacent portions of the pelvis. These injuries, if not detected at the initial presentation, may heal extensively and mimic bone tumors on radiography.

Isolated fractures of the pelvic bones that do not disrupt the pelvic ring include a fracture of the iliac wing (Duverney fracture) and transverse fracture of the lower sacral and coccygeal segments. Sacrococcygeal dislocations and coccygeal fractures are also in this category.

Pelvic Ring Disruption

The most common cause of pelvic ring disruption is a motor vehicle accident. It has a high mortality rate, varying from 5% to 50%, depending on the Injury Severity Score and the age of the patient. Interruption of the pelvic ring at two or more sites on the opposite side, either by fractures or diastasis, indicates a potentially unstable injury. The rule of thumb is that an injury at one site of the pelvic ring must accompany another on the other side of the ring. Therefore, when one encounters a pelvic ring disruption, one must search for a fracture or separation of the other

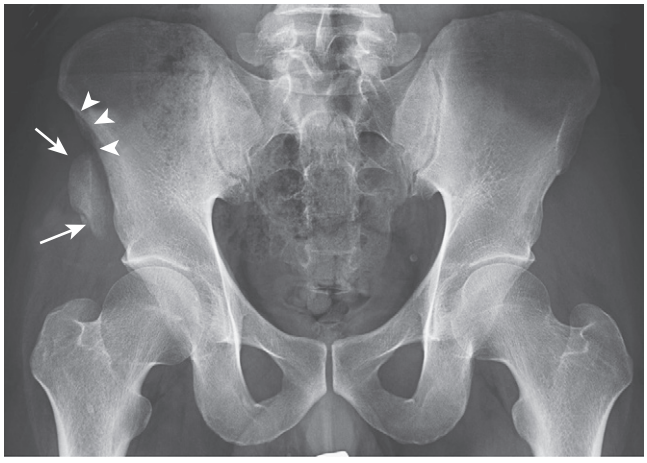


FIGURE 4-26 A pelvic fracture without pelvic ring disruption. An anteroposterior radiograph of the pelvis demonstrates an avulsed right anterior superior iliac spine *(arrows)* due to a sudden muscular contraction of the sartorius. *Arrowheads* indicate the donor site.

side of the ring. The exceptions are in pediatric patients before the fusion of the triradiate cartilage and in stress or insufficiency fractures. It should be noted that acetabular fractures do not constitute any components of pelvic ring disruption. Pelvic classification schemes are helpful in defining the injuries, allowing optimal communication, and assisting in treatment planning. However, the ability to predict associated injuries, morbidity, or mortality of these classifications has not been rigorously tested.

The most widely accepted classification of pelvic ring disruption is the Young-Burgess system. This system divides the pelvic ring disruption into four types according the direction of forces to the pelvis: lateral compression (LC), anteroposterior compression (APC), vertical shear (VS), and combined mechanism. *LC injuries* (Fig. 4-27, *A*) are the most common form of pelvic ring disruption. The force of injury is from the side (e.g., from a side impact motor vehicle collision), causing the pelvic ring to collapse and rotate medially toward the midline. Characteristic imaging features are transverse (horizontally oriented) fractures of the pubic rami with ipsilateral or contralateral posterior ring injury. In LC-I injuries, a sacral compression fracture occurs, which can be seen as discontinuity of the sacral foramina on the inlet radiographic view. LC-II injuries have a crescent iliac fracture on the impact side, which usually extends laterally from the sacroiliac joint. LC-III injuries represent a windswept pelvis, having an LC pattern on one hemipelvis and an APC pattern on the other.

APC injuries (Fig. 4-27, *B* and C) result from a direct blow to the anterior pelvis or forced external rotation of the legs (e.g., as in a motorcycle crash), with symphyseal diastasis or longitudinal fractures of the pubic rami. APC-I

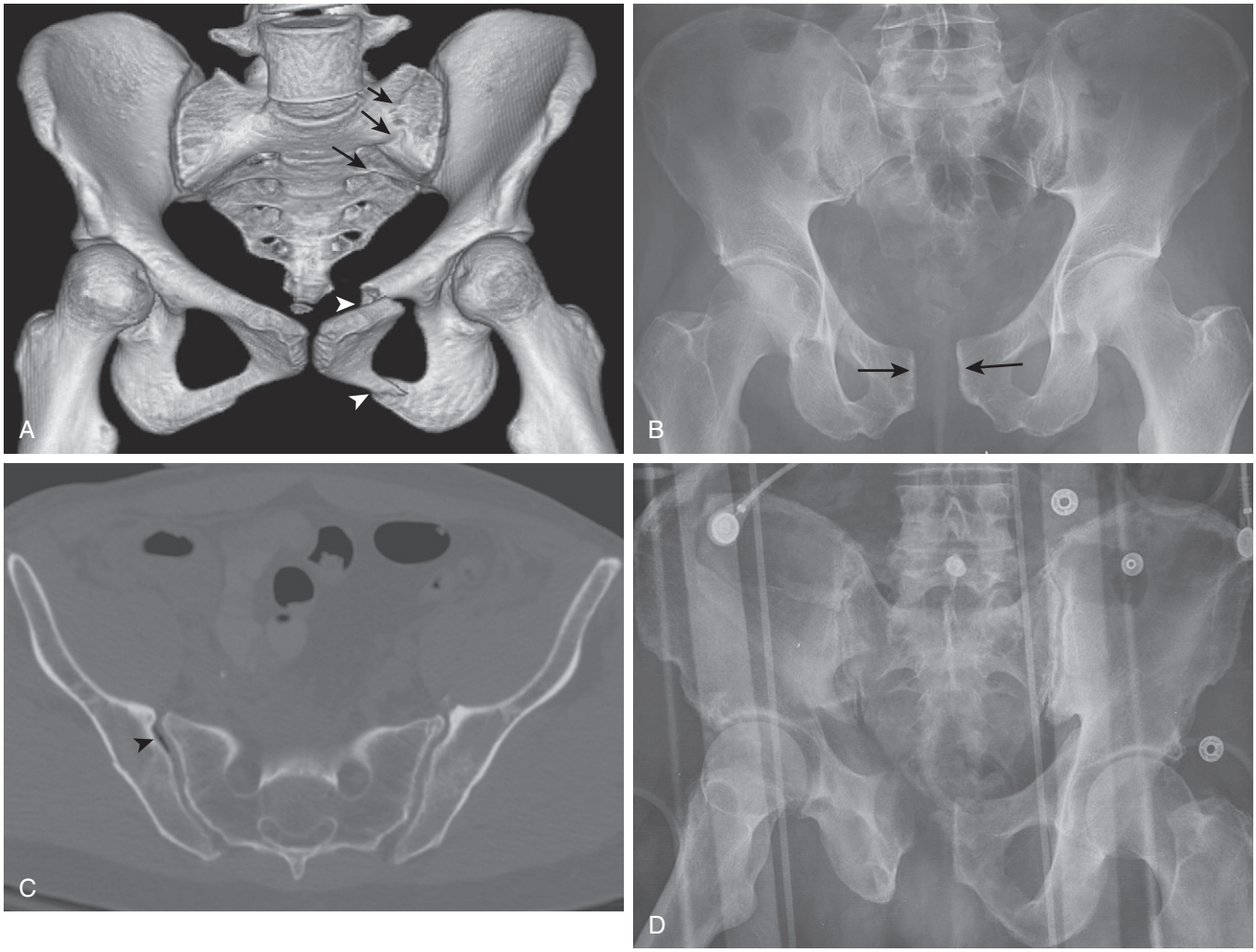


FIGURE 4-27 Pelvic fractures with pelvic ring disruption. **A,** A volumetric (three-dimensional) computed tomography (CT) reformation demonstrates a lateral compression type of pelvic ring disruption. Vertical fractures of the left superior and inferior pubic rami (anterior ring disruption, *white arrowheads*) with overlap of medial and lateral fragments are shown. A vertical fracture of the left ala of the sacrum through its neural foramina is present *(black arrows)*. **B** and **C,** Anteroposterior compression. An anteroposterior radiograph of the pelvis (**B**) and an axial CT image (**C**) at the level of the midsacrum demonstrate diastasis of the symphysis pubis (anterior ring disruption, *arrows*). The radiograph fails to provide information about a posterior ring abnormality. The axial CT image reveals mild widening of the right sacroiliac joint *(arrowhead)*, indicating an injury to the posterior ring. **D,** Vertical shear. An anteroposterior radiograph of the pelvis demonstrates diastasis of the pubic symphysis (anterior ring disruption) and vertical fracture of the right iliac wing involving the pelvic inlet (posterior ring disruption). Vertical displacement, with foreshortening, of the entire right lower extremity is present, indicating a vertical shear injury.

injuries have slight widening of the pubic symphysis. The anterior sacroiliac (SI) ligament (bounding the SI joint) is intact. APC-II injuries are an open-book injury. The force further disrupts the anterior SI joint and sacrotuberous and sacrospinous ligaments, resulting in even wider pubic symphysis (usually greater than 1 to 2 cm) and widening of the anterior SI joint. Complete separation of the hemipelvis without vertical offset is considered an APC-III injury. The anterior and posterior SI ligaments, as well as the sacrospinous and sacrotuberous ligaments, are disrupted, causing lateral displacement of the hemipelvis. The pelvis is rotationally and vertically unstable. Straddle injuries are a subset of APC, in which there is a free-floating symphysis from fractures of bilateral pubic rami. They are highly associated with bladder and urethral injury.

VS injuries (Fig. 4-27, *D*), or Malgaigne fractures, are a result of a strong vertical force (e.g., a fall from a height onto the lower limbs). Rupture of the entire pelvic floor occurs, including the posterior SI ligaments and the sacrospinous and sacrotuberous ligaments. Injuries of the anterior ring include vertically oriented fractures of the pubic rami of at least one side, symphyseal disruption, or a combination of both. In the posterior ring, there may be fracture of the iliac bone, fracture/dislocation of the SI joint, and fractures of the fourth/fifth lumbar transverse processes. Superior displacement of the lateral fragment of the pelvis is seen.

The forth type is the *combined mechanism,* in which the most frequent combination is a combined LC/VS injury.

Determination of the stability of the pelvic fractures relies mainly on a clinical ground. In general, a single break in the pelvic ring is a stable injury (e.g., single pubic ramus, unilateral pubic rami, Duverney fracture, and transverse sacral fracture), and two or more breaks in the pelvic ring are considered unstable. Superior displacement of the posterior sacroiliac complex of greater than 1.5 cm has been used as a radiologic criterion for instability as defined by Tile. It should be noted that the initial radiographic examinations might not demonstrate instability when the pelvis is indeed unstable.

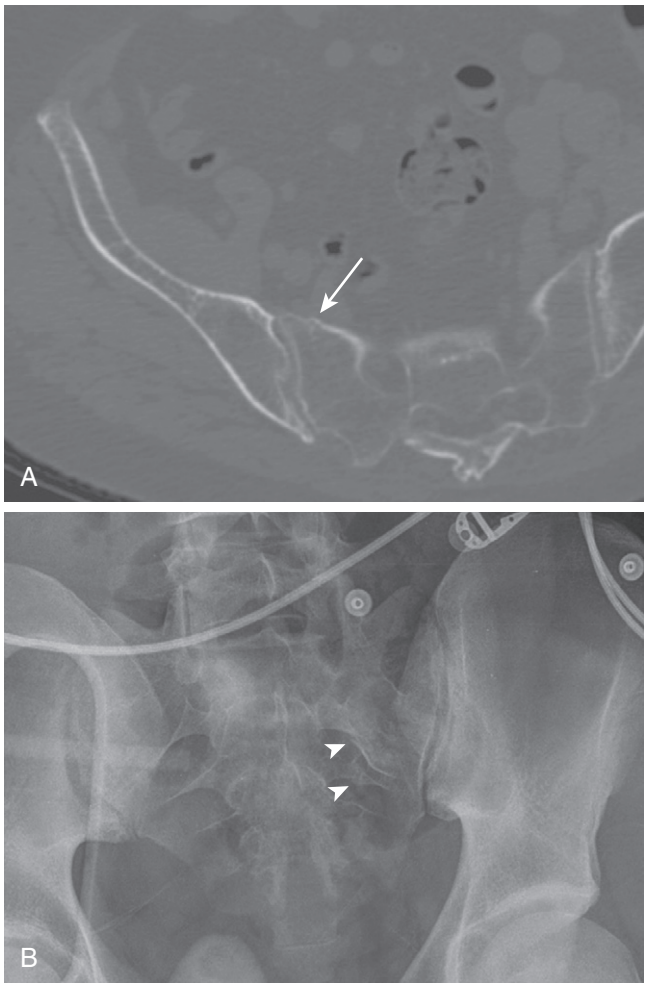


FIGURE 4-28 Sacral fractures. **A,** A zone I injury. An axial computed tomography image at the level of the midsacrum demonstrates a subtle irregularity of the anterior cortex of the right sacral wing, indicating a nondisplaced fracture *(arrow)*. The fracture is located lateral to the sacral neural foramina. **B,** A zone II injury. An anteroposterior radiograph of the pelvis shows abnormal disrupted concavities of multiple left sacral neural foramina, indicating a vertical fracture *(arrowheads)*.

Sacral Fractures

The majority of sacral fractures are associated with pelvic or lumbar spine fractures. They are frequently vertically oriented (only 5% to 10% are transverse). Denis classification divides the sacrum into three zones relative to the sacral foramina and describes the risk of neurologic deficits associated with the fractures in each zone. Zone I fracture (Fig. 4-28, *A* and *B*) is lateral to the sacral foramina, and thus it rarely causes neurologic injuries. Zone II fracture occurs through the sacral foramina (transforaminal), with approximately a 28% chance of neurologic injuries. Zone III fracture is through the sacral body with a high chance of cauda equina injury and neurogenic bladder. There is a 57% chance of neurologic injuries. Because the sacrum is a part of the pelvic ring, when one diagnoses a sacral fracture, the anterior pelvic ring should be thoroughly checked for potential injuries. An impacted sacral alar fracture can be a part of LC injuries, and a displaced vertical sacral fracture can be a part of VS injuries.

Associated Pelvic Injuries

Pelvic hemorrhage is the primary concern in patients with pelvic ring disruption. Patient manipulation and movement should be restricted until conditions are stabilized to reduce the risk of bleeding. The initial radiographic examinations are restricted to the AP view of the pelvis (and/or outlet view on a CT scan) for this reason. Even though as the injury severity increases, the risk of hemorrhage rises—the injury pattern defined by Young-Burgess—classification cannot be used to guide hemorrhage control in individual cases.

Urinary tract injury is more common with the specific types of pelvic fractures that include symphyseal diastasis and pubic rami fractures. Clinically, gross hematuria is the most obvious sign of urinary tract injury associated with pelvic fractures. The presence of microscopic hematuria is rarely associated with a urinary tract injury requiring surgical intervention. If indicated, complete evaluation of the urinary tract requires CT, cystography (conventional or CT), and urethrography.

Direct injury to the gastrointestinal tract is usually due to fracture fragments lacerating the anus or rectum. The injury often extends to the perineum.

FRACTURES OF THE ACETABULUM

Acetabular fractures (Box 4-14) are commonly associated with pelvic fractures. They are usually a result of motor vehicle accident. Radiographic evaluation aims to answer the questions of whether the fracture involves the column, wall, or dome, if any bone fragments are entrapped in the joint, or if an associated femoral head fracture is present. CT is better than radiography with regard to defining the degree of rotational displacement and denoting the presence of intraarticular fragments, articular impaction, and femoral head injury. The Judet-Letournel system classifies fractures of the acetabulum into 10 different types: 5 elementary and 5 associated types. The elementary type is a simple fracture that runs in one main direction, including the fractures of the anterior wall, anterior column, posterior wall, posterior column (Fig. 4-29, *A* and *B*), and transverse fracture. The elementary fractures are less common than column fractures. The column fractures involve the acetabulum and its corresponding pubic ramus. The anterior column fracture at least has acetabular and superior pubic ramus involvement, whereas the posterior column fracture at least has acetabular and inferior pubic ramus involvement. It should be noted that no anatomic boundary of anterior and posterior columns exists. Acetabular column fractures are named according to the portion of the acetabulum that is separated from the intact ilium by the fracture. Wall fractures are differentiated from column fractures in that the latter separates only a portion of the column's articular surface. The associated type is a complex fracture that runs in more than one main plane. It includes an "associated both column" (ABC) fracture, a T-shaped fracture, a transverse fracture plus posterior wall, a posterior column fracture plus wall, and an anterior column fracture plus posterior hemitransverse. Because of the complexity of the acetabular anatomy and the fracture classification, it is easier to define a fracture as one of the three main types: wall fracture, column fracture, or transverse fracture. Ninety percent of acetabular fractures can be identified as one of five common types: ABC fracture, T-shaped fracture, transverse fracture plus posterior wall, transverse fracture, and posterior wall fracture.

An imaging algorithm can be used to help correctly diagnose these five fracture types. First, one should observe the integrity of the obturator ring. If the obturator ring is disrupted, two possibilities are ABC fracture and T-shaped fracture. The ABC fracture has a fracture line extending into the iliac wing, which is not the case with the T-shaped fracture. If the obturator ring is not disrupted, one should determine if the ilioischial and iliopectineal lines are disrupted. If these lines are not disrupted and a posterior wall fracture is present, it is an isolated posterior wall fracture. If these lines are disrupted, possibilities include transverse fractures and transverse plus posterior wall fractures, which can be distinguished by the presence of the posterior wall fracture.

Posterior Wall Fractures

Posterior wall fractures (Fig. 4-29, *C*) are the most common type of acetabular fractures, accounting for one third of all fractures. Disruption of a variable amount of the posterior wall of the acetabulum occurs. The fracture may have one single fragment or multiple fragments; the latter presentation is more common.

Transverse Fractures

A transverse fracture line separates the innominate bone and acetabulum into two segments: the superior iliac segment (containing the acetabular roof and intact ilium) and the ischiopubic segment (containing both rami) without disrupting the obturator ring. They disrupt both iliopectineal and ilioischial lines and cross the acetabulum horizontally or obliquely. A lack of obturator ring involvement makes them different from the T-shaped fracture. They account for 5% to 19% of all acetabular fractures.

Transverse Plus Posterior Wall Fractures

A combination of transverse and posterior wall fractures (Fig. 4-29, *D*) accounts for 20% of all acetabular fractures. In up to 96% of cases, associated hip dislocations are present.

BOX 4-14 Fractures of the Acetabulum

Standard views: Anteroposterior (AP) view of the pelvis and AP and Judet views of the hip

Frequent sites of injuries: Associated both column (ABC), T-shaped, transverse plus posterior wall, transverse, posterior wall

Relevant normal anatomy: The acetabulum is located in the concavity of an arch formed by two columns of bone: anterior and posterior columns in an inverted V-shaped configuration

- Anterior column—the longer, larger portion from the superior pubic ramus to the iliac wing
- Posterior column—the ischium to the posterior ilium
- Iliopectineal line—from the sciatic notch to the pubic tubercle; a break indicates an anterior column fracture
- Ilioischial line—from the sciatic notch, quadrilateral plate to the internal cortex of the ischium; a break indicates a posterior column fracture
- Anterior lip—a break indicates an anterior column or wall fracture
- Posterior lip—a break indicates a posterior column or wall fracture; on AP projection, it is slightly lateral to the anterior lip
- Roof—a break indicates a superior articular surface fracture
- Radiographic teardrop—a composite U-shaped shadow at the anteroinferior portion of the acetabular fossa

Fracture mimics: Os acetabuli: secondary ossification center on the superior aspect of the posterior acetabular lip (mimics a posterior wall fracture)

Making the distinction:

- Integrity of the obturator ring—breaks indicate two common possibilities: ABC and T-shaped fractures
- Iliopectineal line—a break indicates an anterior column fracture
- Ilioischial line—a break indicates a posterior column fracture
- Posterior lip—a break indicates a posterior wall fracture
- Oblique fracture of the iliac bone—indicates an ABC or anterior column fracture
- Spur sign—pathognomonic for an ABC fracture
- Fracture plane on computed tomography—a column fracture is shown as a coronally oriented fracture

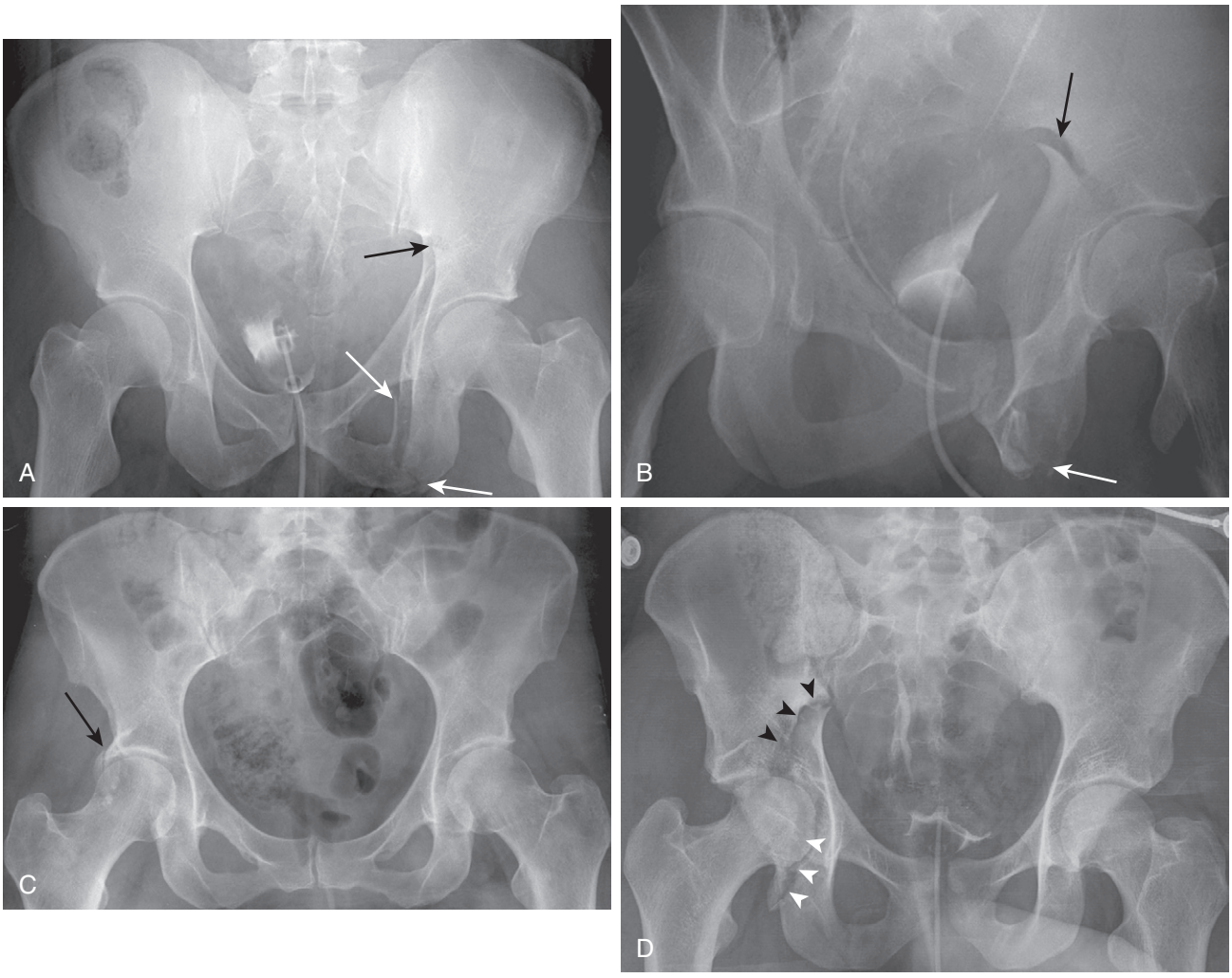


FIGURE 4-29 Acetabular fractures. **A** and **B,** A posterior column fracture. An anteroposterior radiograph of the pelvis shows a break in the obturator ring at the inferior pubic ramus *(white arrows)*. A fracture through the posterior border of the innominate bone *(***B,** *black arrow)* is better visualized on the oblique view of the left hip. **C,** A posterior wall fracture *(arrow)* is visualized with no associated disruption of the iliopectineal or ilioischial lines or obturator ring. **D,** A transverse wall fracture. An anteroposterior radiograph of the pelvis demonstrates a transverse fracture of the innominate bone *(black arrowheads)* and a posterior wall fracture *(white arrowheads)*.

Associated Both Column Fractures

ABC fractures are the most common associated-type fractures of the acetabulum and the second most common (23%) of all acetabular fractures. No portion of the articular surface of the acetabulum remains in contact with the innominate bone, and a split occurs between the anterior and posterior column components. The *spur sign* represents an external cortex of the most caudal portion of the intact ilium. It is visualized because the femoral head is displaced medially with all portions of the acetabular surface. This sign is pathognomonic for ABC fracture and is best demonstrated on Judet's obturator oblique projection.

T-Shaped Fractures

T-shaped fractures represent 7% of all acetabular fractures. They are transverse fractures with an associated vertical fracture line running across the quadrilateral plate and disrupting the obturator foramen. Identification of a fracture of an ischial ramus leads to recognition of the T-shaped fracture.

HIP DISLOCATIONS AND FRACTURES OF THE PROXIMAL FEMUR

Hip Dislocations

Posterior dislocation of the hip (Fig. 4-30, *A* and *B*) is the most common type of hip dislocation (Box 4-15). It is a result of an abrupt deceleration injury such as in motor vehicle accidents when a knee strikes the dashboard and is commonly associated with fractures of the posterior rim or wall of the acetabulum. In adolescents, this injury may cause separation of the capital femoral epiphysis. On a frontal radiograph, the femoral head is dislocated from the acetabulum and lies in the superolateral position. The involved femoral head appears smaller than the contralateral hip because it is placed closer to the radiographic plate (or film), and internal rotation of the femur is present. The injury is obvious on a true lateral projection. Postreduction radiographs are performed to assess for any widening of the joint space, which suggests the possible presence of intraarticular fragments, a fractured femoral head, or soft tissue interposition.

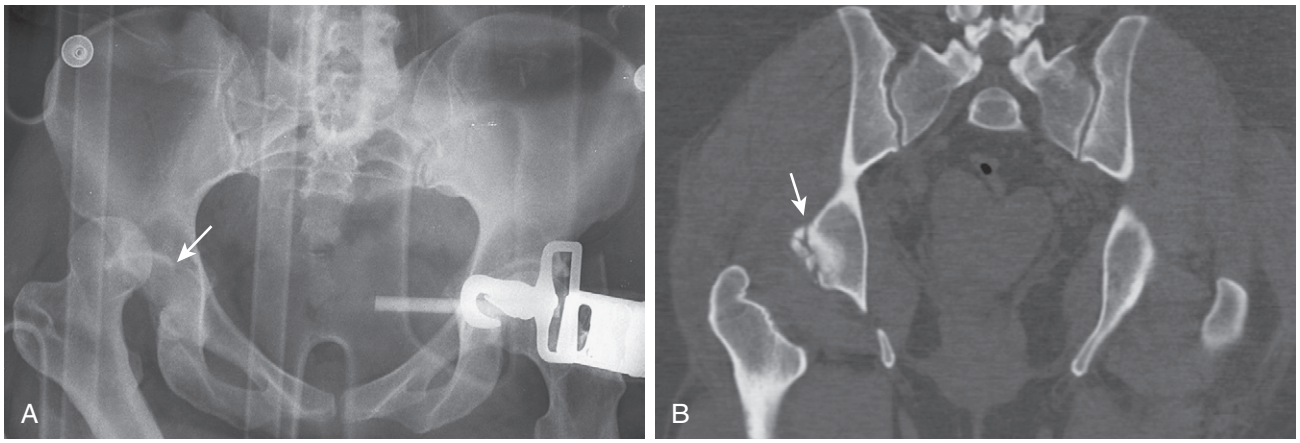


FIGURE 4-30 Dislocations of the hip. **A,** An anteroposterior radiograph of the pelvis demonstrates a superolaterally dislocated right femoral head relative to the acetabulum *(arrow)*, demonstrating a classic appearance of a posterior dislocation, in contrast to anterior dislocations in which the femoral head lies anteromedial to the acetabulum. **B,** A coronal reformatted computed tomography image at the level of the posterior acetabulum reveals a comminuted fracture of the posterior wall *(arrow)*, an injury commonly associated with posterior hip dislocation.

BOX 4-15 Hip Dislocations and Fractures of the Proximal Femur

Standard views: Anteroposterior (AP) and inlet views of the pelvis and true lateral and AP views of the injured hip with the foot inverted 15 degrees
Frequent sites of injuries: Subcapital femoral neck
Frequently missed injuries: Isolated greater trochanter fracture
Relevant normal anatomy: The sweep of cortex extending from the neck to the head of the femur is smooth and symmetric
- An asymmetric femoral head with respect to the neck, even if seen only in one projection, is abnormal
- Fovea centralis—an insertion site of the ligamentum teres carries 10% of the blood supply to the femoral head
- Calcar femorale—a vertical ridge of dense bone originating from the posteromedial endosteal surface of the proximal femoral shaft (near the lesser trochanter) to the posterior portion of the femoral neck (toward the greater trochanter)
- The capsule of the hip joint attaches to the intertrochanteric line of the femur anteriorly, above the intertrochanteric crest posteriorly, and above the lesser trochanter medially.

CT is performed to differentiate these conditions and also to assess for an associated posterior wall fracture. Osteonecrosis of the femoral head and secondary osteoarthritis of the hip joint are known complications.

Anterior dislocation of the hip accounts for 10% to 15% of all hip dislocations and is caused by forced abduction and external rotation of the hip. The femoral head is displaced either anteromedially toward the superior pubic ramus or toward the obturator foramen. Usually it is a simple dislocation without associated injury. Impacted fracture of the femoral head as a result of impaction of the head on the dense acetabular rim (a Hill-Sachs type of fracture) may occur. On a frontal radiograph, the femoral head is medially, superiorly, or inferiorly displaced with respect to the acetabulum. It appears larger than the contralateral head, and the lesser trochanter is seen in profile. The lateral view is diagnostic.

Central hip dislocation (protrusio) is always associated with acetabular fractures either of the inner wall, superior dome, or both (known as a *bursting fracture*). The femoral head protrudes into the pelvic cavity through the fractures of the acetabulum. This dislocation is associated with retroperitoneal hemorrhage and sciatic nerve injury.

Fractures of the Proximal Femur

Fractures of the proximal femur are classified on the basis of their geographic location into femoral head, neck, trochanteric, intertrochanteric, and subtrochanteric regions. These fractures also can be categorized by their relationship to the joint capsule into two groups: intracapsular or extracapsular. Fractures of the femoral head and femoral neck (subcapital and transcervical types) are considered intracapsular. The trochanteric, intertrochanteric, and subtrochanteric fractures are extracapsular. Basicervical femoral neck fractures are generally acknowledged as extracapsular. The distinction between intra- and extracapsular fractures is important in the determination of treatment and the prediction of outcome. Intracapsular fractures have a significantly increased incidence of avascular necrosis. Extracapsular fractures usually heal well but are more prone to be unstable. In the elderly population, proximal femoral fractures can be very subtle and may occur in the setting of minor trauma as a result of the presence of osteoporosis. CT or MRI should be strongly considered for evaluation of the hip in this age group, even when findings of plain radiographs are negative.

Fractures of the femoral head occur during the dislocations and appear as impaction or shear injury.

Fractures of the Femoral Neck

Femoral neck fractures are common in the elderly population, particularly in women, because of the high prevalence of osteoporosis. These fractures are divided into subcapital, transcervical, and basicervical types. The more proximal the fracture and the more displaced the fracture, the higher the incidence of the development of avascular necrosis and nonunion. Fractures with posterior comminution, which can be assessed on a lateral radiographic projection, have a higher prevalence of abnormal healing.

Subcapital fracture (Fig. 4-31, *A, B,* and *C*) is the most common type and is commonly extremely subtle. A disruption and angulation are present at the junction of

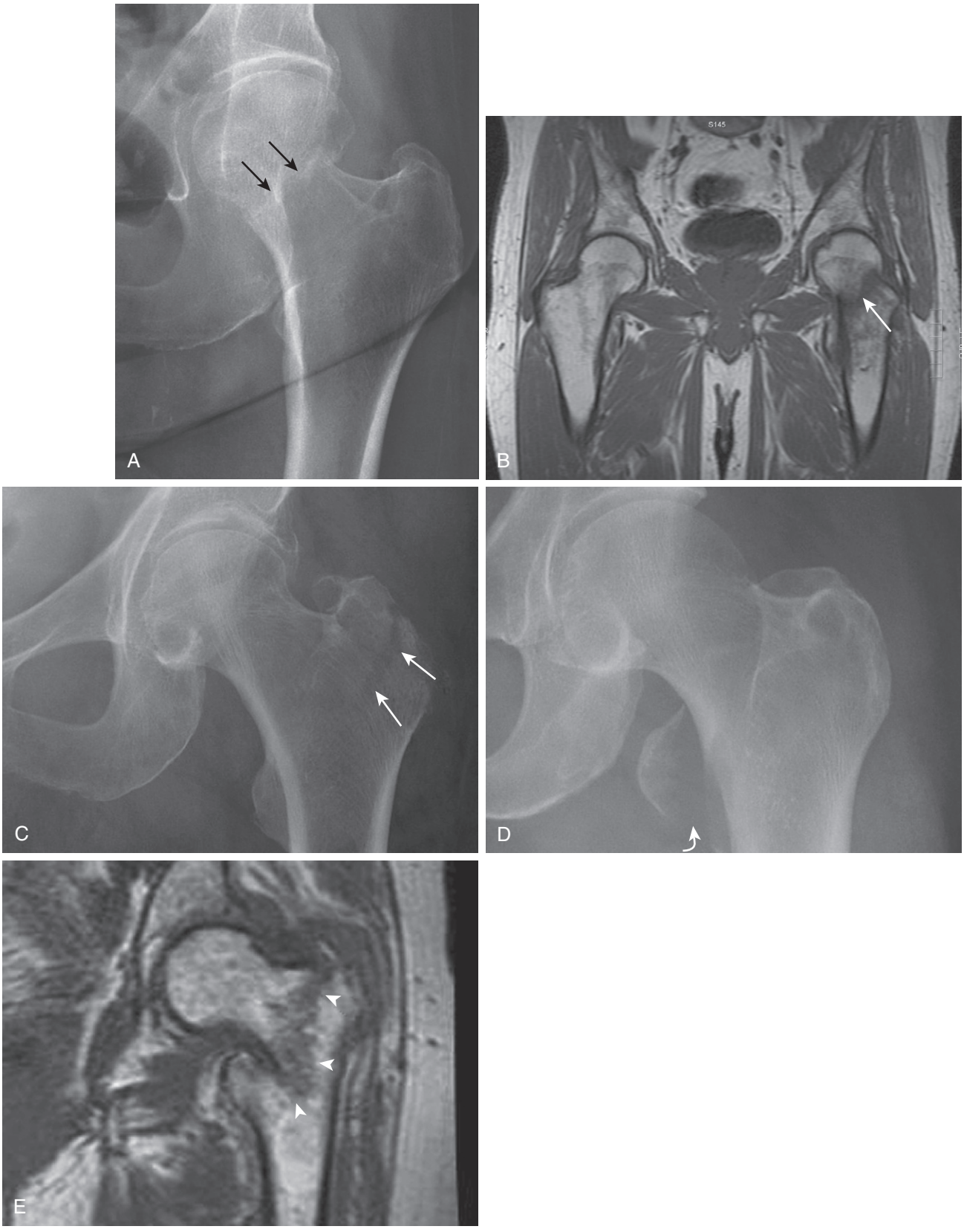


FIGURE 4-31 Fractures of the proximal femur. **A** and **B,** A subcapital femoral neck fracture. An anteroposterior radiograph of the left hip (**A**) demonstrates a subcapital femoral neck fracture. The fracture line itself is visualized as a band of apparent sclerosis *(black arrows)*. A coronal T1-weighted magnetic resonance image (MRI) (**B**) confirms the presence of a fracture line *(arrow)* in the femoral neck. **C,** An isolated fracture of the greater trochanter. An anteroposterior radiograph of the left hip demonstrates a fracture of the greater trochanter *(white arrows)*. **D,** An isolated pathologic fracture of the lesser trochanter due to plasmocytoma. An anteroposterior radiograph of the left hip reveals an avulsion fracture of the lesser trochanter *(curved arrow)* in an adult patient with multiple myeloma. **E,** An intertrochanteric fracture. A T1-weighted MR image reveals an intertrochanteric fracture line *(white arrowheads)* in a patient in whom the plain radiographs (not shown) were interpreted as normal.

the superior cortex of the femoral neck with the femoral head. The Garden classification categorizes the subcapital fractures into four stages based on the position of the principal (medial) compressive trabeculae of the femoral head and neck and acetabular trabeculae on frontal radiographs. Stage I fractures are incomplete or impacted fractures that spare the inferior femoral neck trabeculae. The principal compressive trabeculae of the head and neck are aligned in mild valgus position. Stage II fractures are complete fractures without displacement. The principal compressive trabeculae of the femoral head and neck are aligned in mild varus or near anatomic position, distinguishing them from stage I fractures. Stage I and stage II fractures are generally stable and have a good prognosis if treated promptly. However, when this fracture is subtle and impacted in the near anatomic position, it may permit ambulation and may be relatively painless, and thus clinical and radiologic diagnosis may be equivocal. Stage III fractures are complete fractures with partial displacement and feature more severe varus alignment of the trabeculae of the femoral head and neck. In addition, the trabeculae of the femoral head are not aligned with the acetabular trabeculae. Shortening and external rotation of the distal fragment are common. Stage IV fractures are complete fractures with total displacement. The femoral shaft is not only externally rotated but also telescoped. However, the femoral head is in the anatomic alignment with the acetabulum, and therefore the trabecula of the femoral head and the acetabulum are parallel.

Transcervical and basicervical fractures are rare. The transcervical fractures are usually apparent on frontal projection, and a varus deformity is present at the fracture site. Basicervical fractures are located at the base of the femoral neck, just proximal to the intertrochanteric crest. It is generally acknowledged that basicervical fractures are extracapsular, although this may not always be true. Basicervical fractures have a greater incidence of avascular necrosis than do the more distal intertrochanteric fractures.

Trochanteric Fractures

Isolated fractures of the greater trochanter (Fig. 4-31, *D* and *E*) are common in osteoporotic women who fell onto the lateral side. The normal irregularity in this region makes it difficult to detect this type of fracture, especially when it is nondisplaced.

Isolated fractures of the lesser trochanter in children and adolescents are usually due to avulsion injuries of the apophysis from the pull of the iliopsoas tendon, which inserts on the lesser trochanter. In adults, an isolated lesser trochanter fracture is unusual and should raise the suspicion of underlying disease, especially metastatic disease.

Intertrochanteric Fractures

Intertrochanteric fractures are the most common type of extracapsular fracture of the proximal femur. These fractures more often occur in older persons than do femoral neck fractures. Men and women are equally affected. These fractures may involve the lesser or greater trochanters, or both. The main fracture line is usually an oblique line extending along the line joining the greater and lesser trochanters. The most frequent pattern is a comminuted fracture consisting of a proximal fragment, a distal fragment, and both trochanters. The status of the lesser trochanter is a very important component of the intertrochanteric fractures because, if it is fractured, it typically includes a large fragment of the cortex of the femoral neck. Comminution of the posteromedial cortex (calcar femorale), subtrochanteric extension, or a reverse obliquity pattern (when the main fracture line runs perpendicular to the line joining the greater and lesser trochanters) makes the fractures unstable. These unstable fractures, if untreated, will collapse into varus and retroversion.

Subtrochanteric Fractures

The subtrochanteric region is the area between the lesser trochanter and 5 cm distal to it in the shaft of the femur. Fractures in this region may or may not coexist with intertrochanteric fracture. They are distinguished from the intertrochanteric fractures by the presence of a fracture line in the proximal femoral shaft. Subtrochanteric fractures are frequently comminuted and markedly displaced as a result of various muscle attachments.

Fractures of the Femoral Shaft

Femoral shaft fractures are the most common long bone fractures in patients with multiple injuries. A violent, severe, high-energy trauma must occur to cause these fractures because the femur is the strongest and heaviest bone in the body. Radiographic evaluation must include the region of the hip and tibia to assess for potential associated injuries such as proximal femoral fractures, acetabular fractures, and tibial fractures.

FRACTURES AND DISLOCATIONS AROUND THE KNEE

Hemarthrosis/Lipohemarthrosis

The appearance of knee hemarthrosis is similar to that of other types of joint effusion—that is, an oval-shaped density obliterating the lucent space anterior to the femoral cortex (suprapatellar recess). If the effusion is large, it will cause anterior displacement of the quadriceps femoris muscle, quadriceps tendon, and patella.

On the other hand, the presence of blood mixed with liquid fat in the knee joint or *lipohemarthrosis* (Fig. 4-32, *A* and *B*) has a significant meaning because it suggests the presence of an intraarticular fracture of the distal femur or proximal tibia. The fracture permits a flow of blood and liquid fat from the medullary cavity into the joint space. The sign is visualized in a horizontal-beam lateral radiograph (lateral cross-table) obtained with the patient supine. The joint capsule is distended with a layering fat-blood interface that resembles an air-fluid level, the so-called "fat-blood interface sign." The presence of lipohemarthrosis is very useful because it leads to identification of a minimally displaced intraarticular fracture. *Pneumolipohemarthrosis or pneumohemarthrosis* has a very similar radiologic characteristic, except that air is more lucent than fat. It signifies an open, intraarticular fracture of the distal femur or proximal tibia.

Fractures of the Distal Femur

Fractures of the distal femur are caused by severe axial load with either varus, valgus, or rotational force. In younger persons, these fractures are usually a result

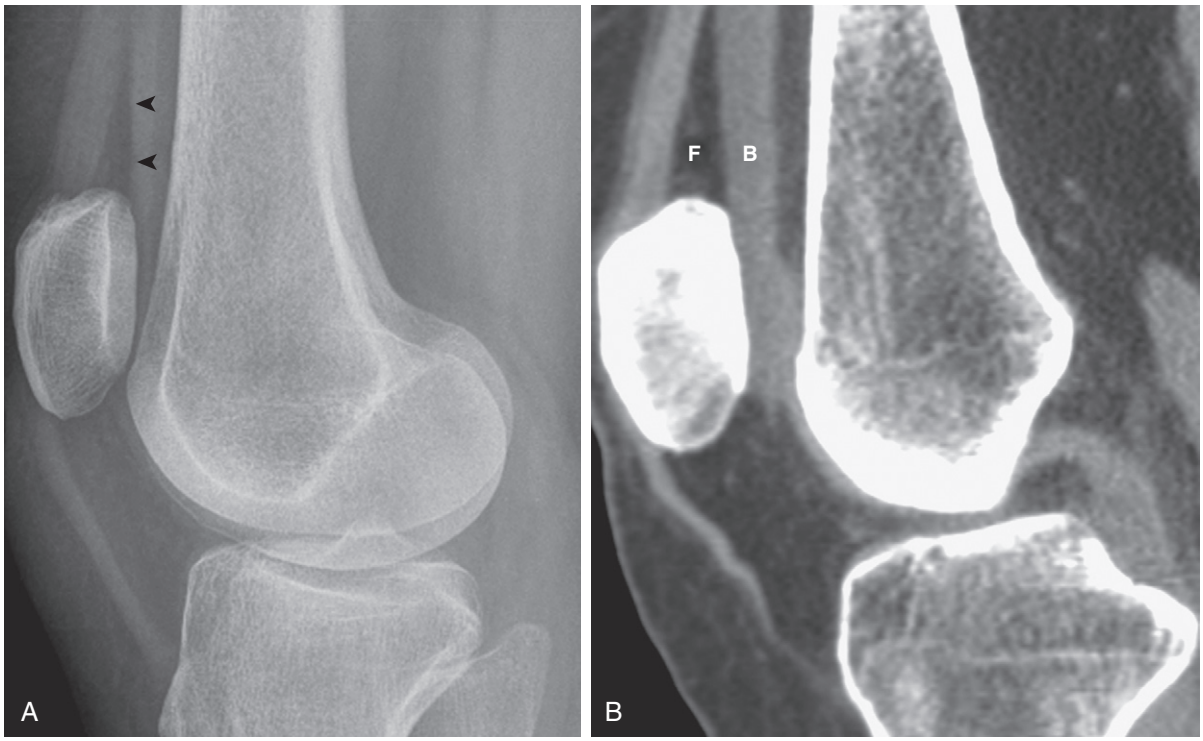


FIGURE 4-32 Lipohemarthrosis. **A** and **B,** Lipohemarthrosis. A lateral cross-table radiograph of the knee shows a fat fluid level *(arrowheads)* in the suprapatellar bursa. A sagittal reformatted computed tomography image of the same patient depicts the same finding. The fat *(F)* blood *(B)* interface sign of lipohemarthrosis is shown.

of motor vehicle collision. In the elderly population, a minor slip and fall on a flexed knee can result in these types of fractures. The supracondylar area of the femur is a zone between the femoral condyles and the junction of metaphysis and diaphysis of the femoral shaft. According to the AO/OTA classification, fractures of the distal femur can be supracondylar, unicondylar, or bicondylar. The former fracture is extraarticular, whereas the latter two fractures are intraarticular. Intraarticular extension to the knee joint frequently appears sagittal/vertical through the intercondylar component. If it is in a coronal plane, it is called a *Hoffa fragment*. CT is helpful to identify the intercondylar osteochondral fragment and Hoffa fragment. "Floating knee" (Fig. 4-33, *A, B,* and *C*) is a term used when these fractures are associated with tibial shaft fractures, creating a free large segmental fragment consisting of the knee joint. The incidence of arterial injury is low (2% of all supracondylar fractures).

Knee Dislocations

Knee dislocations are a rare injury. They can be anterior, posterior, medial, lateral, or rotational, describing the tibia in relation to the femur. Anterior dislocations (Fig. 4-34, *A, B,* and *C*) are the most common type and result from severe hyperextension. The incidence of vascular injuries in knee dislocations varies from 7% to 64% on different series, depending on the mechanism of injury (high vs. low velocity). Clinical evidence of vascular injuries should be sought in every knee dislocation. They are also commonly associated with avulsion fractures of the tibial articular surface and tears of the cruciate ligaments, joint capsule, and extracapsular ligaments.

Patellar Dislocations

The patella is normally located in the sulcus of the anterior distal femur (Box 4-16). Dislocations of the patella (Fig. 4-34, *D*) are caused by internal rotation of the femur on a fixed foot and are usually relocated prior to clinical presentation. The dislocations are invariably lateral, with disruption of the medial retinaculum. The preferential lateral dislocation occurs because the lateral femoral condyle arc is more shallow than the medial condyle, and there is a shallow angle of inclination of the lateral facet of the posterior surface of the patella. The dislocations may be associated with chondral or osteochondral fractures, which arise from the lateral margin of the lateral femoral condyle or articular surface of the medial patellar facet. The presence of fragments in the joint space may impair joint motion and lead to a locking or degenerative change of the knee. A high-riding patella (patella alta) and osteochondral fracture can be seen on lateral radiography. An axial view of the patella is performed to assess for fracture of the medial patellar facet. Classic MRI findings of recent prior patellar dislocation include hemarthrosis, disruption of the medial patellar retinaculum, lateral patellar tilt, and bone contusions in the lateral femoral condyle and medial patellar facet.

Fractures of the Patella

Most fractures of the patella are the result of a direct blow to the patella from a fall or motor vehicle accident. Most

Text continued on p. 151

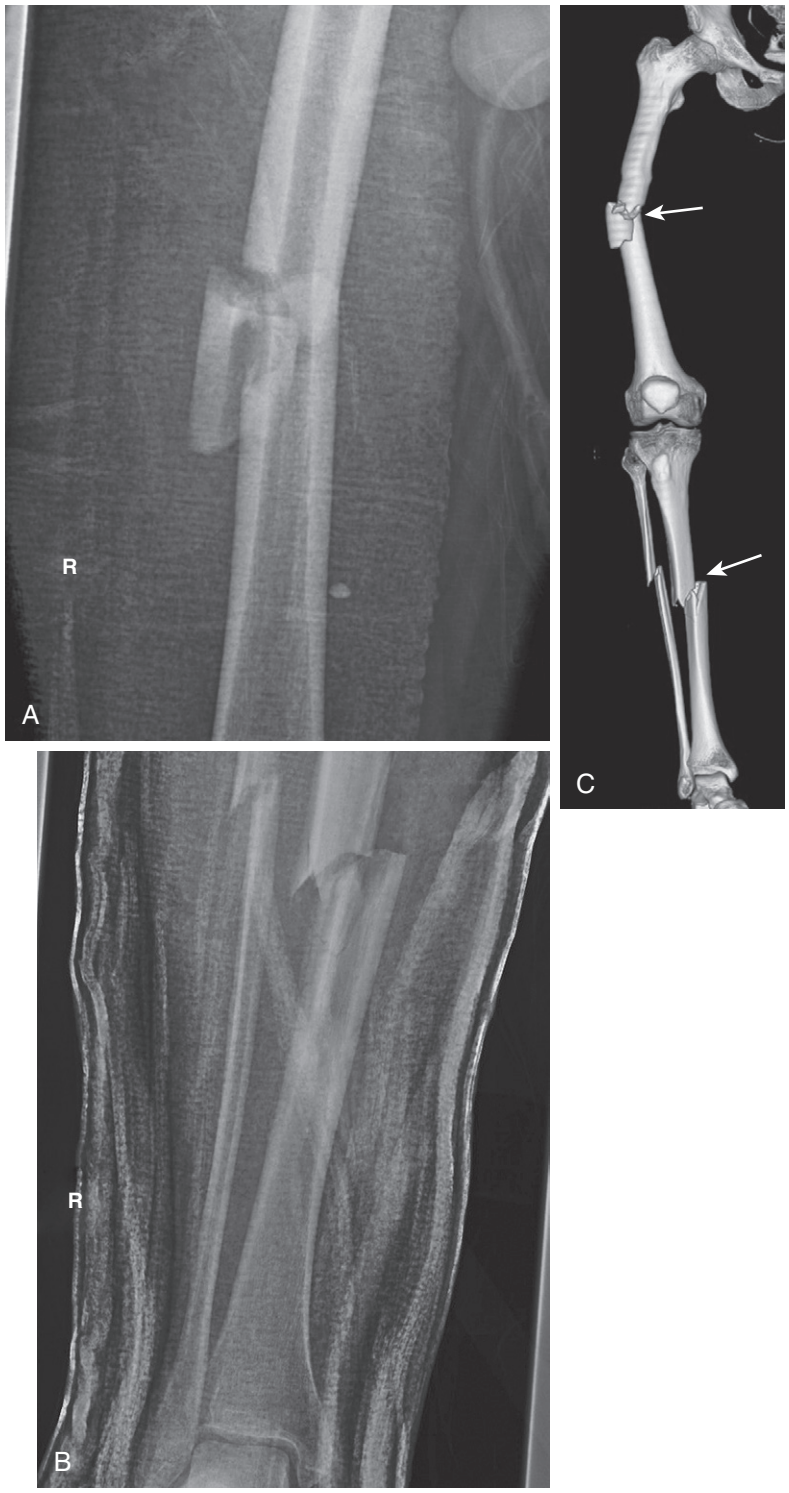


FIGURE 4-33 Floating knee. **A** and **B,** Frontal radiographs of the femur, tibia, and fibula of the right *(R)* leg reveal a segmental fracture of the midshaft of the femur and midshaft fractures of both bones of the leg. This combination of fractures results in a free, large segmental fragment consisting of the knee joint. **C,** Volumetric (three-dimensional) computed tomography reformation beautifully displays the long bone fracture sites *(arrows)*.

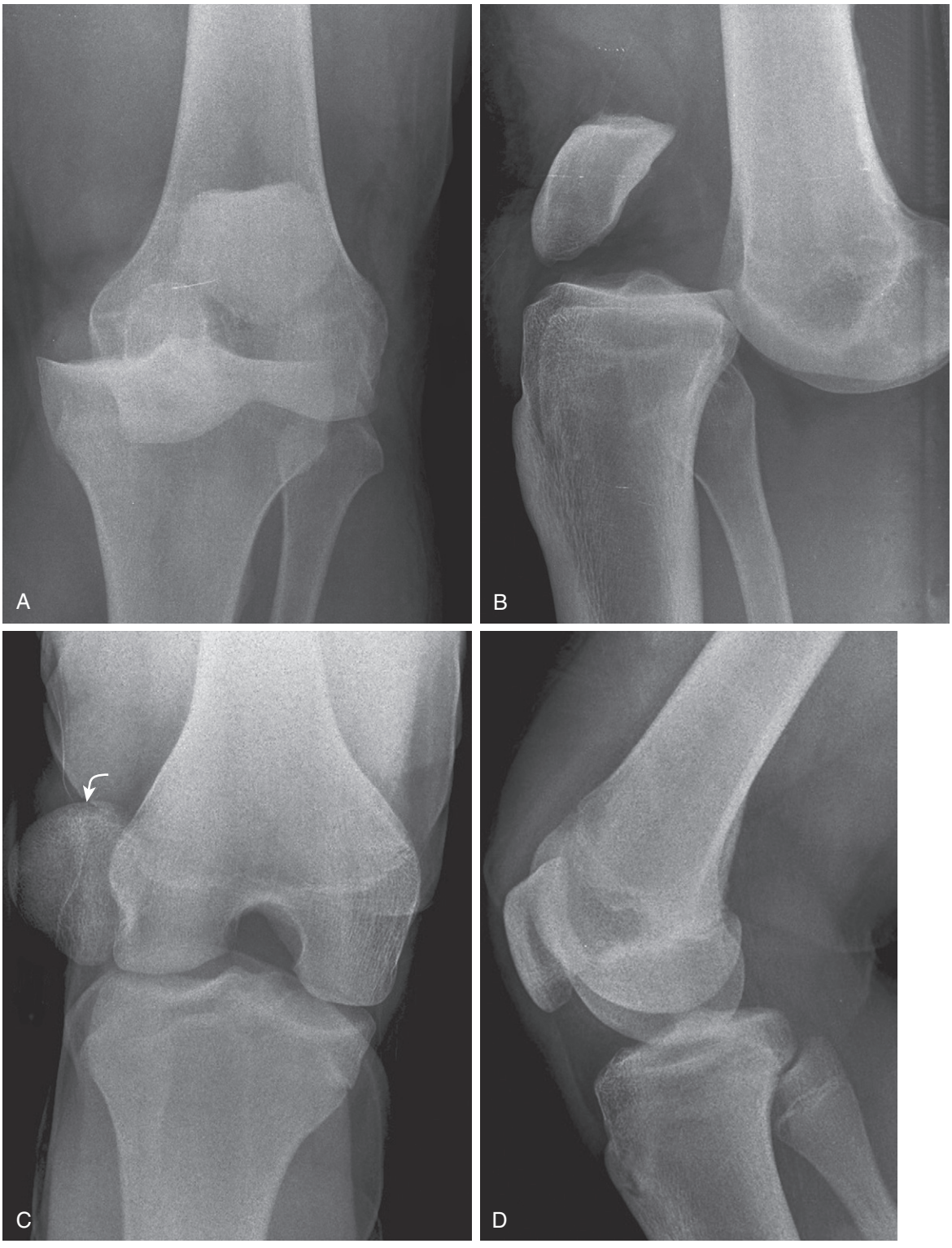


FIGURE 4-34 Dislocations around the knee. **A** and **B,** Frontal and lateral radiographs of the knee demonstrate an anteriorly dislocated tibia relative to the femur, representing a classic anterior knee dislocation with a complete bicruciate ligament tear subsequently confirmed with magnetic resonance imaging (not shown). Anterior knee dislocation is frequently associated with a traction injury of the popliteal artery. **C** and **D,** Lateral patellar dislocation *(curved arrow)* is depicted on frontal and lateral radiographs of the knee.

BOX 4-16 Fractures and Dislocations Around the Knee

Standard views:
- Knee—Anteroposterior (AP), lateral (20-degree flexion of the knee), both oblique views
- Patella—skyline view and full knee series
- Femur—AP and lateral views
- Frequent sites of injuries: Tibial plateau

Relevant normal anatomy: The medial femoral condyle is larger and more prominent than the lateral condyle, which helps when viewing the knee on lateral or axial patellar projections
- Suprapatellar recess—the recess between the suprapatellar tendon and the anterior cortex of the femur; it is normally relatively radiolucent
- Anterior cruciate ligament distal attachment—medial spine of the intercondylar eminence of the tibia
- Normal patellar length—approximately equal to the length of patellar tendon, variation not exceed 20%
- Normal location of patella—on the frontal view, the inferior pole should lie within 2 cm of a plane formed by the distal femoral condyles; on the lateral view with 90 degrees flexion, the superior pole of the patella should lie inferior to the anterior surface of the femoral shaft

Frequently missed injuries: Avulsions of ACL, PCL, Segond fracture" before the Fracture mimics

Fracture mimics: Bipartite patella: an unfused ossification center at the superolateral aspect of the patella, well corticated and usually bilateral

fractures involve the midbody and are transverse fractures (60%; Fig. 4-35, *A* and *B*). Twenty-five percent of fractures are stellate or comminuted, and 10% are vertical (Fig. 4-35, *C* and *D*). Displacement is defined when there is separation of the fragments of more than 3 mm or articular incongruity of 2 mm or greater. The displaced fractures may occur at the proximal or distal poles. The former fracture may cause a low-lying patella as a result of unopposed pull from the patellar tendon inferiorly (patella baja; Fig. 4-35, *E*). Alternatively, patella baja is seen in patients with a quadriceps tendon tear. A high-riding patella (Fig. 4-35, *F*) may be seen in the distal pole fractures or in patients with a patellar tendon tear. Use of lateral radiographs is best to assess the fracture pattern and patellar location. Peripheral fractures may be confused with bipartite patella.

Fractures of the Tibial Plateau

Fractures of the tibial plateau are severe injuries caused by high-speed motor vehicle collisions and falls from heights. Axial loading, valgus stress, or both are the usual mechanisms. The fractures may involve the medial plateau, the lateral plateau, or both, with extension into the metadiaphysis of the tibia. Fractures of the lateral plateau are the most common type because of stronger cancellous trabeculae of the medial plateau. As a result, an isolated medial plateau fracture is the least frequent type. The Schatzker classification, which is the most widely used classification system, categorizes tibial plateau fractures into six types according to the fracture appearance, location, and extension. Type

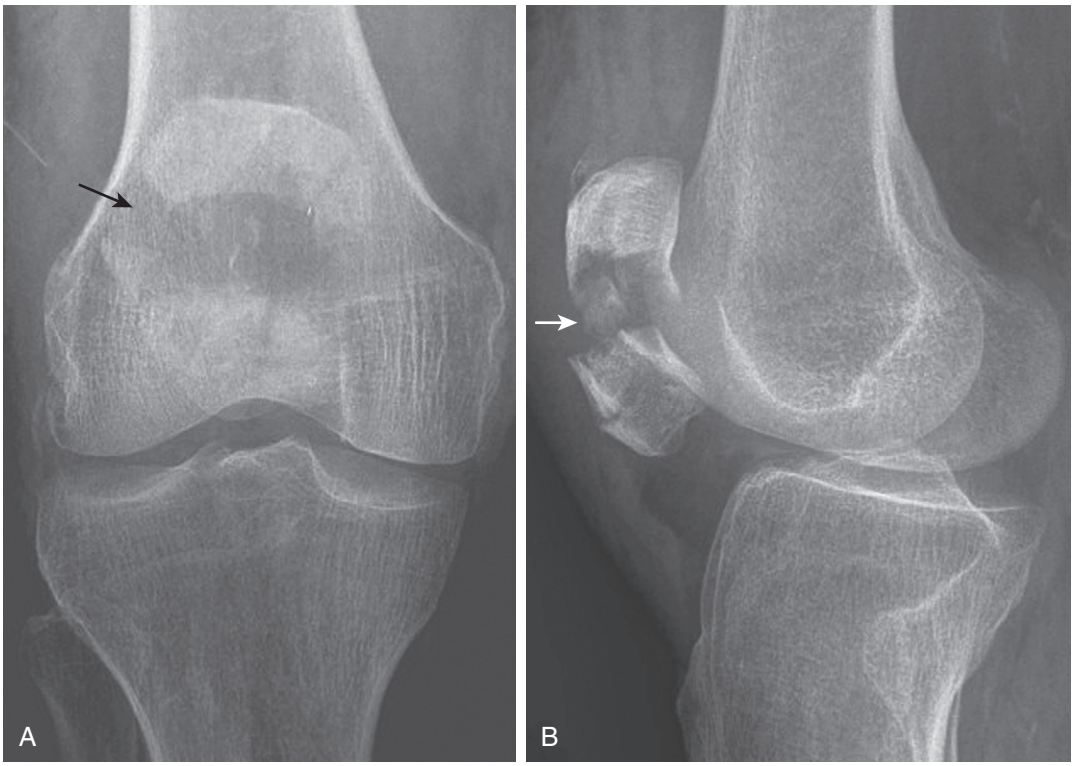


FIGURE 4-35 Fractures of the patella. **A** and **B,** Frontal and lateral radiographs of the knee demonstrate a comminuted fracture of the patella with the main transverse fracture line *(arrows)* traversing through its midbody. Separation of the proximal and distal fragments is present as a result of traction from the quadriceps superiorly and patellar tendon inferiorly.

Continued

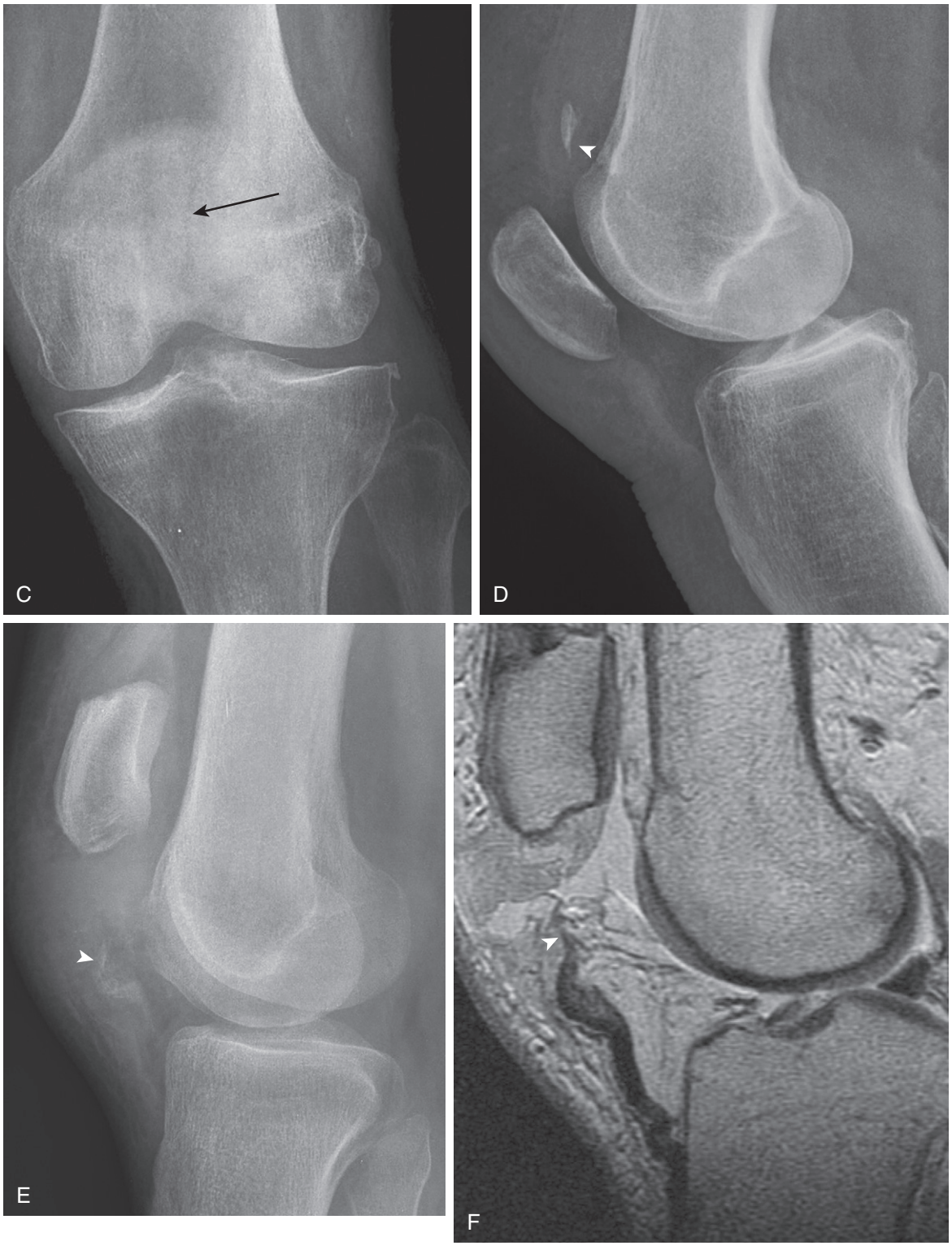


FIGURE 4-35, cont'd **C,** A vertical nondisplaced fracture *(arrow)* of the patella is barely seen on the frontal radiograph, emphasizing the need to routinely obtain four views of the knee in patients with an acute knee injury. **D,** A lateral radiograph of the knee shows an avulsion fracture of the proximal pole of the patella *(arrowhead)*, which causes a low-lying patella as a result of unopposed pull from the patellar tendon (patella baja). **E** and **F,** A high-riding patella (patella alta) is due to unopposed action of the quadriceps in this patient with distal pole fracture of the patella *(arrowhead)*. A sagittal magnetic resonance image **(F)** confirms a complete disruption with retraction of the patellar tendon *(arrowhead)*.



FIGURE 4-36 Fractures of the tibial plateau. **A** and **B**, Volumetric (three-dimensional [3D]) computed tomography (CT) images demonstrate a fracture of the lateral tibial plateau that has two components of a split *(arrows)* and depression *(arrowheads)* (type II) fracture. CT accurately depicts the fragments, degree of depression, amount of joint space involved, and displacement. **C**, An oblique radiograph of the knee shows a pure depression fracture of the lateral tibial plateau *(arrowheads)* (type III). **D** and **E,** An oblique radiograph of the knee and a volumetric (3D) CT image demonstrate a comminuted fracture of both medial and lateral tibial plateaus *(arrowhead)* with dissociation between the tibial metaphysis and diaphysis *(arrows)*. An avulsion fracture of the tibial spine is noted *(short arrows)* on the CT reformation **(E)**.

I is a split fracture of the lateral plateau. The fracture line causes a wedge-shaped fracture fragment of the plateau. Type II (Fig. 4-36, *A* and *B*) is a split-depression fracture of the lateral plateau. In addition to the presence of a cleavage fracture of the lateral plateau, the articular surface is depressed into the metaphysis. Type III (Fig. 4-36, *C* and *D*) is a pure depression fracture of the lateral plateau with an intact osseous rim. Type IV is a medial plateau fracture, subdivided into IVA (split) and IVB (depressed) subtypes. Type V is a bicondylar fracture in which the fracture line often forms an inverted "Y." The metaphysis and diaphysis remain intact. Type VI (Fig. 4-36, *E*) is a tibial plateau fracture with dissociation between the tibial metaphysis and diaphysis. These fractures may involve either one or two plateaus and have a varying degree of comminution. The goal of imaging is to show the number of fracture

fragments, degree of displacement, degree of depression, location, and type of plateau fractures. Meniscal injuries, especially of the lateral meniscus, are seen in up to 50% of cases of tibial plateau fractures. Injuries to the medial collateral ligament and anterior cruciate ligament (ACL) are common.

Avulsions Around the Knee

Avulsion of ACL insertion usually occurs in children or adolescents and involves the medial spine of the intercondylar eminence of the tibia (the distal attachment of the ACL). Radiographs show a fracture at the base of the intercondylar eminence or medial tibial spine (Fig. 4-37, *A*). It should be noted that isolated fracture of the lateral tibial spine does not involve either cruciate ligament. In some cases, a bony fragment in the joint may be indistinguishable from a loose body or an osteochondral fracture.

Avulsion of posterior cruciate ligament (PCL) insertion occurs at the posterior aspect of the plateau where the PCL attaches to the tibial plateau. It is best visualized on lateral radiographs (Fig. 4-37, *B* and *C*).

Segond fracture is an avulsion fracture at the lateral aspect of the lateral proximal tibia just below the level of the tibial plateau (Fig. 4-37, *D*) as a result of lateral capsular ligament pull. A small sliver of bone can be found adjacent to the lateral tibial plateau in the midcoronal section near the joint line, along with widening of the lateral tibiofemoral compartment of the knee joint and joint effusion. A Segond fracture is caused by forceful internal rotation of a flexed knee. ACL and meniscal injuries are frequently associated with this fracture. On radiography this fracture may mimic an iliotibial band avulsion of the Gerdy tubercle, which is located more anteriorly, and fibular head avulsion.

FRACTURES AND DISLOCATIONS AROUND THE ANKLE

Fractures of the Ankle

Ankle fractures (Box 4-17) are most commonly classified by their appearance on radiographs. Certain radiographic features can be used to determine the mechanism and to understand these complex injuries. Two major mechanisms responsible for ankle fractures are rotational and axial-loading injuries. Rotational malleolar fractures are less severe injuries than axial-loading tibial plafond or pilon fractures.

Rotational Malleolar Fractures

A combination of different forces, namely supination, pronation, external rotation, adduction, and abduction, causes *rotational malleolar fractures*. These forces result in either impaction injury or avulsion injury to the malleoli. Characteristic of impaction injury is an oblique fracture line, whereas the horizontal fracture line is typical of an avulsion injury. These fractures are described by the location of malleolar fracture lines (medial, lateral, or posterior malleoli, or more than one of these). Bimalleolar or trimalleolar fractures are injuries that involve more than one structure. A detailed description should include the level of the fibular fracture, orientation of the fracture line (horizontal or oblique), possibility of syndesmosis disruption, involvement of the tibial plafond, and size of the fragments. Several classifications are used in the assessment of the ankle fractures. The Weber (AO) classification is simple to use and correlates well with treatment and prognosis. The level of fibular fracture determines the extent of injury to the syndesmotic complex and is used to categorize fractures in this classification. In general, the higher the fibular fracture, the more extensive the damage to the syndesmosis and the greater the risk of ankle instability. Type A (Fig. 4-38, *A*) is an infrasyndesmotic injury, in which the fibular fracture is transverse and located below the syndesmosis. This injury results from a supination-adduction force described in Lauge-Hansen classification. The transverse fibular fracture (or its equivalent: lateral collateral ligament rupture) may occur in isolation (stage 1) or with fracture of the medial malleolus (stage 2). Type B (Fig. 4-38, *B*) is the most common type of ankle fracture, describing a transsyndesmotic injury. This injury results from a supination-external rotation force. The initial stage (stage 1) involves the anterior syndesmostic tear, which features normal-appearing radiographs. The fracture of the fibula occurs in a later stage (stage 2 and higher), which is oblique and located at the level of the syndesmosis. The oblique fibular fracture may occur in isolation (stage 2), with fracture of the posterior malleolus (stage 3), or with a horizontal fracture of the medial malleolus or deltoid ligament rupture (stage 4). Partial disruption of the syndesmosis occurs. Type C is a suprasyndesmotic injury, resulting from pronation-external rotation force. The injury starts medially with avulsion of the medial malleolus or deltoid ligament rupture (stage 1) and continues with rupture of the anterior syndesmotic ligament (stage 2). Progressive injuries are a fracture of the fibula above the level of the syndesmosis (stage 3) and the avulsion of the posterior malleolus (stage 4). Type C (Fig. 4-38, *C*) is usually treated with syndesmosis fixation in addition to stabilization of the lateral malleolus. When reviewing ankle radiographs, use the Weber/AO classification because of its simplicity and then combine it with the trauma mechanism described in the Lauge-Hansen system. Because these injuries occur in a stepwise fashion, applying the trauma mechanism in the diagnostic approach is helpful to detect subtle injuries.

Maisonneuve fracture (Fig. 4-38, *D* and *E*) is a part of the spectrum of Weber/AO type C (pronation-external rotation) injuries, in which the fibular fracture is more proximal and there is a tear of the full length of the interosseous membrane. Fractures of the proximal fibula are easily overlooked because of the distracting painful injuries at the ankle. The diagnosis of Maisonneuve fracture should be considered in the following situations: isolated fracture of the posterior lip of the tibia, isolated displaced fracture of the medial malleolus, and widening of the medial or lateral clear space without evident fracture of the lateral malleolus or fibula. In these circumstances, full-length views of the tibia and fibula should be obtained to identify associated fracture of the proximal fibula.

Tibial Plafond (Pilon) Fractures

Axial loading to the ankle joint drives the talus against the distal tibial articular surface, resulting in tibial plafond

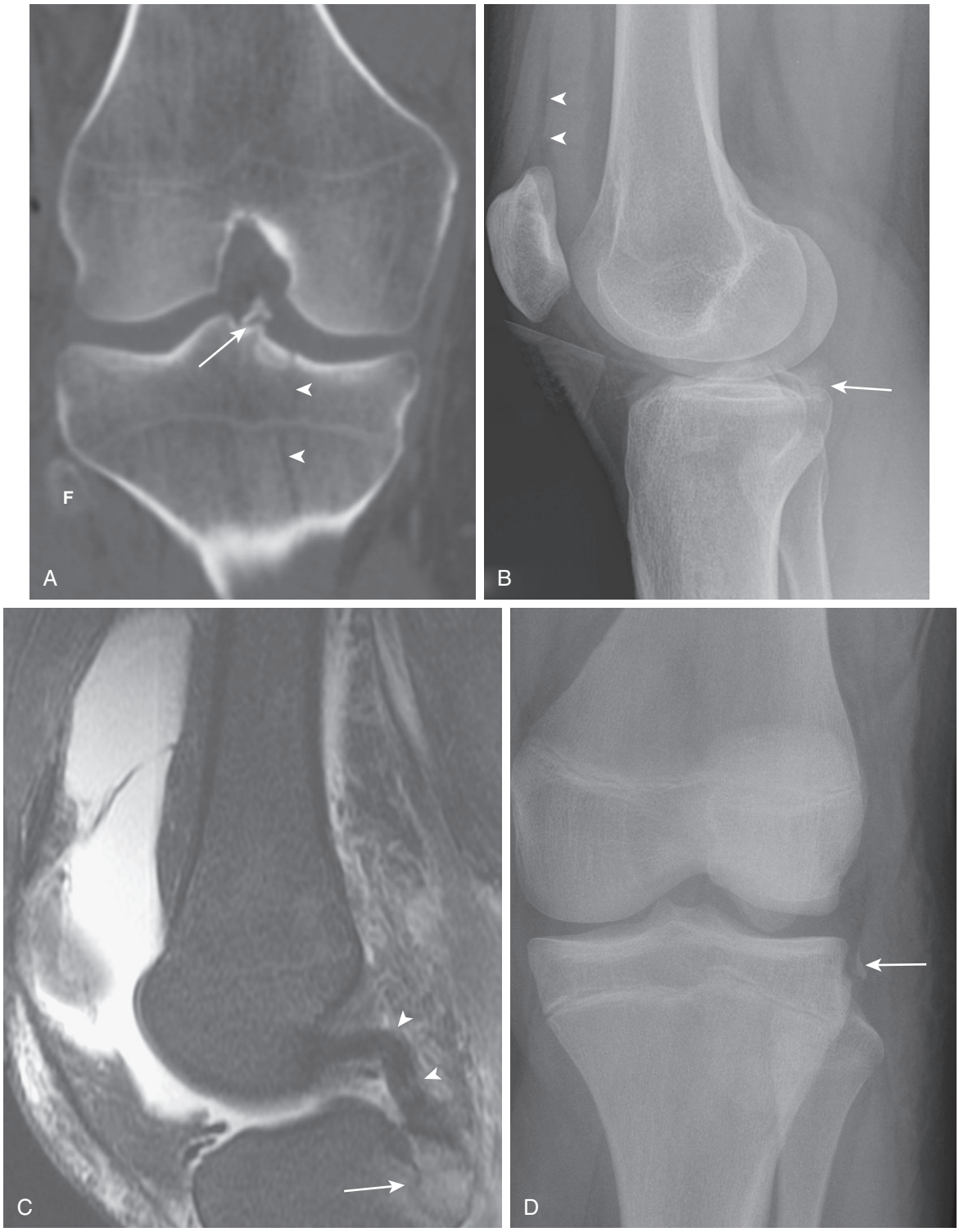


FIGURE 4-37 Avulsions around the knee. **A,** Anterior cruciate ligament (ACL) avulsion. A coronal reformatted computed tomography (CT) image of the knee shows an avulsion fracture of the medial tibial spine *(arrow)*, the attachment site of the ACL. In addition, a nondisplaced split fracture *(arrowheads)* of the medial tibial plateau is present. **B** and **C**, Posterior cruciate ligament (PCL) avulsion. A lateral cross-table radiograph **(B)** of the knee demonstrates a lipohemarthrosis *(arrowheads)*. A subtle bone fragment *(arrow)* is visualized at the tibial attachment of the PCL. A sagittal fat-suppressed T2-weighted magnetic resonance image **(C)** confirms the fracture site *(arrow)* at the distal attachment of the PCL *(arrowheads)*. **D,** A Segond fracture. An avulsion fracture *(arrow)* of the lateral tibial plateau is shown in a frontal radiograph of the knee. ACL and meniscal injuries are commonly associated with Segond fractures.

BOX 4-17 Fractures and Dislocations Around the Ankle

Standard views:
- Ankle: anteroposterior (AP), lateral, and mortise (10 degrees internal rotation) views (include the base of the fifth metatarsal)
- Lower leg: AP and lateral views
- Frequent sites of injuries: Malleoli

Frequently missed injuries: Fracture of lateral process of talus

Relevant normal anatomy: The ankle mortise consists of the medial malleolus, lateral malleolus, and horizontal plate of the distal articular surface of the tibia (tibial plafond)
- Ankle joint—the joint between the ankle mortise and the superior articular surface of the talus
- Ligamentous complex of the ankle—medial collateral (deltoid) ligament, lateral collateral ligaments, and distal tibiofibular complex (most important for ankle stability)
- Medial clear space—on either mortise or AP views, the space of the medial ankle joint space should be equal to superior joint space and less than 4 mm wide; widening indicates a lateral talar shift
- Tibiofibular clear space—the distance between the medial wall of the distal fibula and the incisural surface of the tibia should be less than 6 mm on both AP and mortise views; widening indicates syndesmosis disruption
- Superior clear space—normally the articular surface of distal tibia is parallel to that of the talus; superior clear space should be equal between the medial and lateral side of the joint (difference of less than 2 mm); widening indicates talar tilt
- Tibiofibular line—on the mortise view, a line drawn along the tibial articular surface should be continuous with the medial aspect of the fibula; incongruity suggests fibular shortening, rotation, or lateral displacement
- Talocrural angle—on the mortise view, the angle between a line drawn on the tibial articular surface and a line connecting the tip of malleoli should be 8 to 15 degrees; a smaller angle suggests fibular shortening
- Syndesmotic integrity—on the AP view, a normal distal tibia overlaps with the distal fibula; the normal width of this overlap is greater than 10 mm; a smaller value suggests injury to the syndesmosis

fractures (Fig. 4-38, *F*). The malleoli usually maintain anatomic relationships with the talus, although associated fibular fractures are common. Tibial plafond fractures are comminuted, intraarticular fractures of the distal tibia, which are more severe than rotational malleolar fractures. They are distinguished by profound comminution of the distal tibia, intraarticular extension of the tibial fracture to involve the dome of the plafond, common association with the talar fractures, and preservation of the tibiofibular syndesmosis. The Ruedi-Allgower classification separates axial loading fractures of the distal tibia into three types, based on the degree of comminution of the articular surface. Type I is a nondisplaced cleavage fracture. Type II is a displaced but minimally comminuted fracture with incongruity of the articular surface. Type III is a displaced and highly comminuted fracture with gross comminution of the articular surface. Posttraumatic arthritis is a common complication.

Avulsions Around the Ankle

Tillaux fracture (Fig. 4-39, *A*) is an avulsion of the anteroinferior tibiofibular ligament from the lateral distal tibial margin that is created by an external rotation of the foot. A vertical fracture line extends from the distal articular surface of the tibia superiorly to the lateral tibial cortex. When lateral displacement of more than 2 mm or step-off of the articular surface of the distal tibia occurs, surgery is usually required. In children, this fracture is a Salter-Harris type III because the medial growth plate fuses earlier than that of lateral growth plate. In adults, it is usually a ligamentous injury or "Tillaux lesion." An avulsion fracture of the medial margin of the fibula at the attachment of the anterior tibiofibular ligament is known as the *Wagstaffe–Le Fort fracture*. Isolated Tillaux fractures and Wagstaffe–Le Fort fractures do occur but are more commonly parts of more extensive injuries to the ankle mortise and are associated with malleolar fractures.

Triplane fractures (Fig. 4-39, *B* and *C*) are distinct fractures of the distal tibial epiphysis that are caused by plantar flexion and external rotation. Fracture lines occur in three planes: a horizontal plane within the growth plate or physis, a sagittal plane through the epiphysis, and an oblique vertical plane in the posterior distal metaphysis. Two distinct types of triplane fractures exist: two-fragment and three-fragment fractures. The two-fragment fracture is more common and represents a Salter-Harris type IV fracture. The appearance is quite similar to that of Tillaux fractures, except that there is a metaphyseal component of the fracture on the lateral view. In the three-fragment fracture, the entire epiphysis is usually displaced posteriorly. It is seen as a Salter-Harris type III fracture on the AP view and as a type II fracture on the lateral view. Distinguishing the two is important because the three-fragment fractures usually require open reduction and internal fixation to preserve the joint.

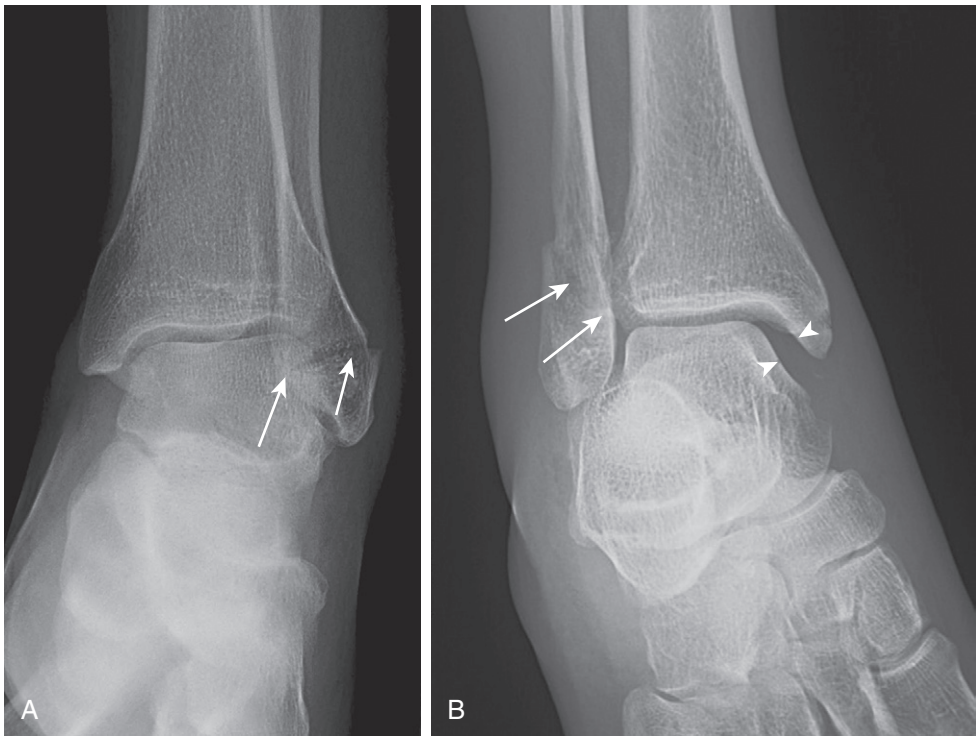
FRACTURES AND DISLOCATIONS OF THE FOOT

Injuries to the Hindfoot

Subtalar or peritalar dislocation (Fig. 4-40, *A* and *B*) is a rare injury. A concomitant dislocation occurs at the talocalcaneal and talonavicular joints, with a normal tibiotalar relationship. This dislocation is obvious on lateral radiographs, because of the absence of the talar head in the cup of the navicular. Medial subtalar dislocation is far more common and is often called "basketball foot." It is a result of an inversion injury. On radiography, medial displacement of the foot and calcaneus is noted. The navicular is displaced medially and dorsally to the talar head. *Total talar dislocation* is a complete dislocation of both tibiotalar (ankle joint) and subtalar joints and is the most serious of all talar injuries.

Fractures of the Talus

The talus is the second most common site of fractures involving the tarsal bones. These fractures are caused by a forced dorsiflexion. Fractures are classified by anatomic location: head, neck, body, posterior process, and lateral process. *Fractures of the talar head* are uncommon and difficult to diagnose on radiography. In most cases, the fractures involve the talonavicular joint and often are associated with talonavicular subluxation. There is a low incidence of avascular necrosis because vascularity is adequate.



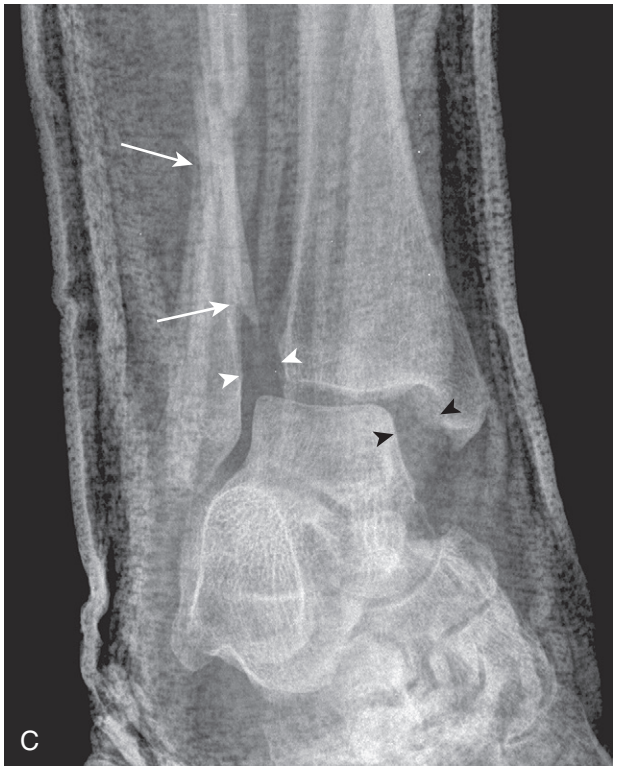


FIGURE 4-38 Fractures of the ankle. Three types of rotational malleolar fracture. **A**, Type A. The fibular fracture line *(arrows)* is located completely below the level of the syndesmosis. **B**, Type B. The fibular fracture *(arrows)* begins at the level of the syndesmosis. Widening of the medial mortise *(arrowheads)* is present, indicating a deltoid ligament injury. **C**, Type C. A fibular fracture *(arrows)* is above the level of syndesmosis. There is disruption of the syndesmosis (widening of the tibiofibular space, *white arrowheads*) up to the level of the fibular fracture, as well as a deltoid ligament injury with a widened mortise *(black arrowheads)*.

Continued

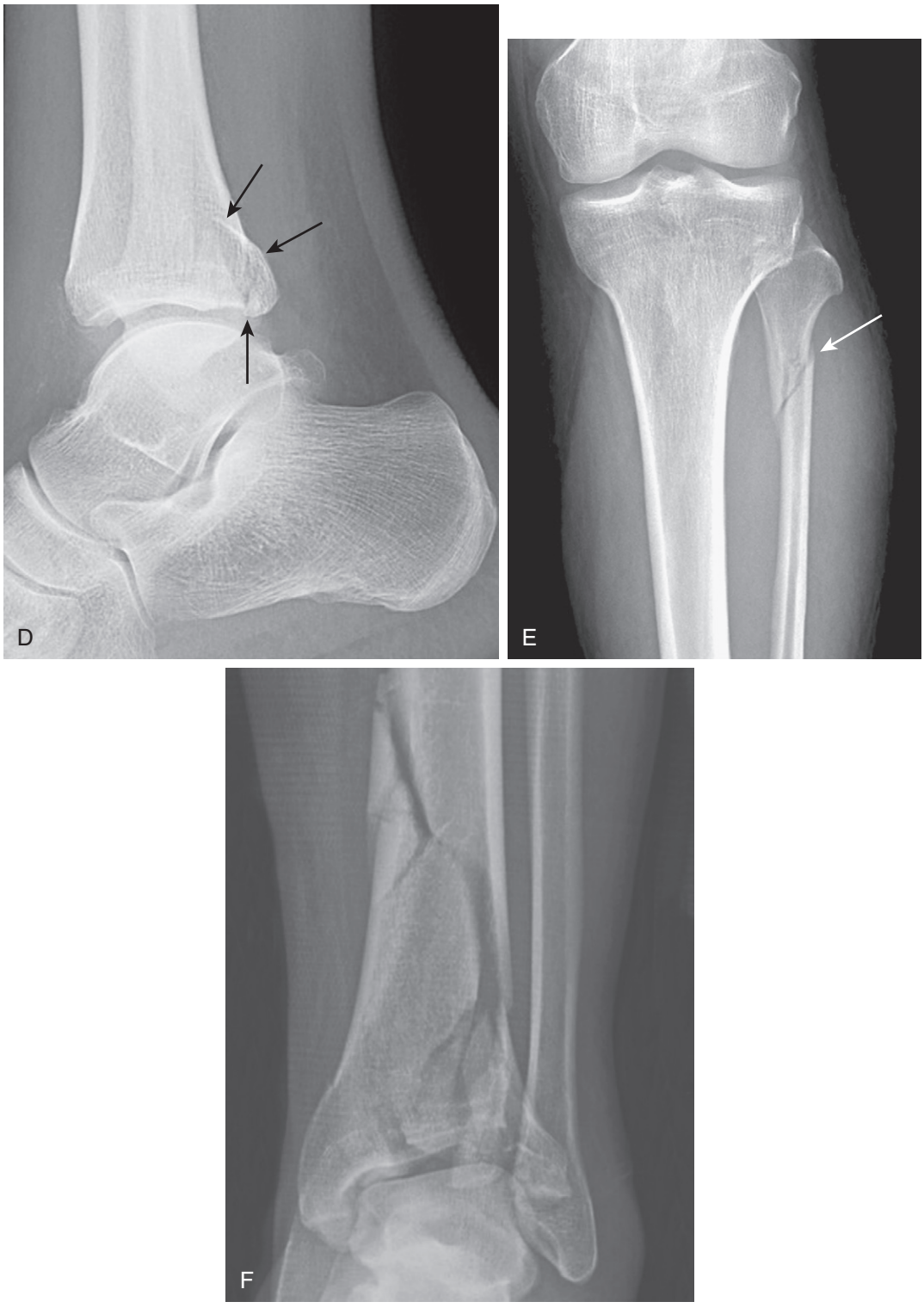


FIGURE 4-38, cont'd **D** and **E**, A Maisonneuve fracture. A frontal radiograph of the ankle shows an isolated posterior malleolar fracture *(arrows)* that prompted a request for an additional radiograph to include the entire length of the fibula. An oblique fracture *(arrow)* of the proximal fibula is revealed. **F,** A tibial plafond (pilon) fracture. An anteroposterior radiograph of the ankle demonstrates a severely comminuted intraarticular fracture of the distal tibia extending to the tibial plafond. The malleoli are in anatomic alignment.

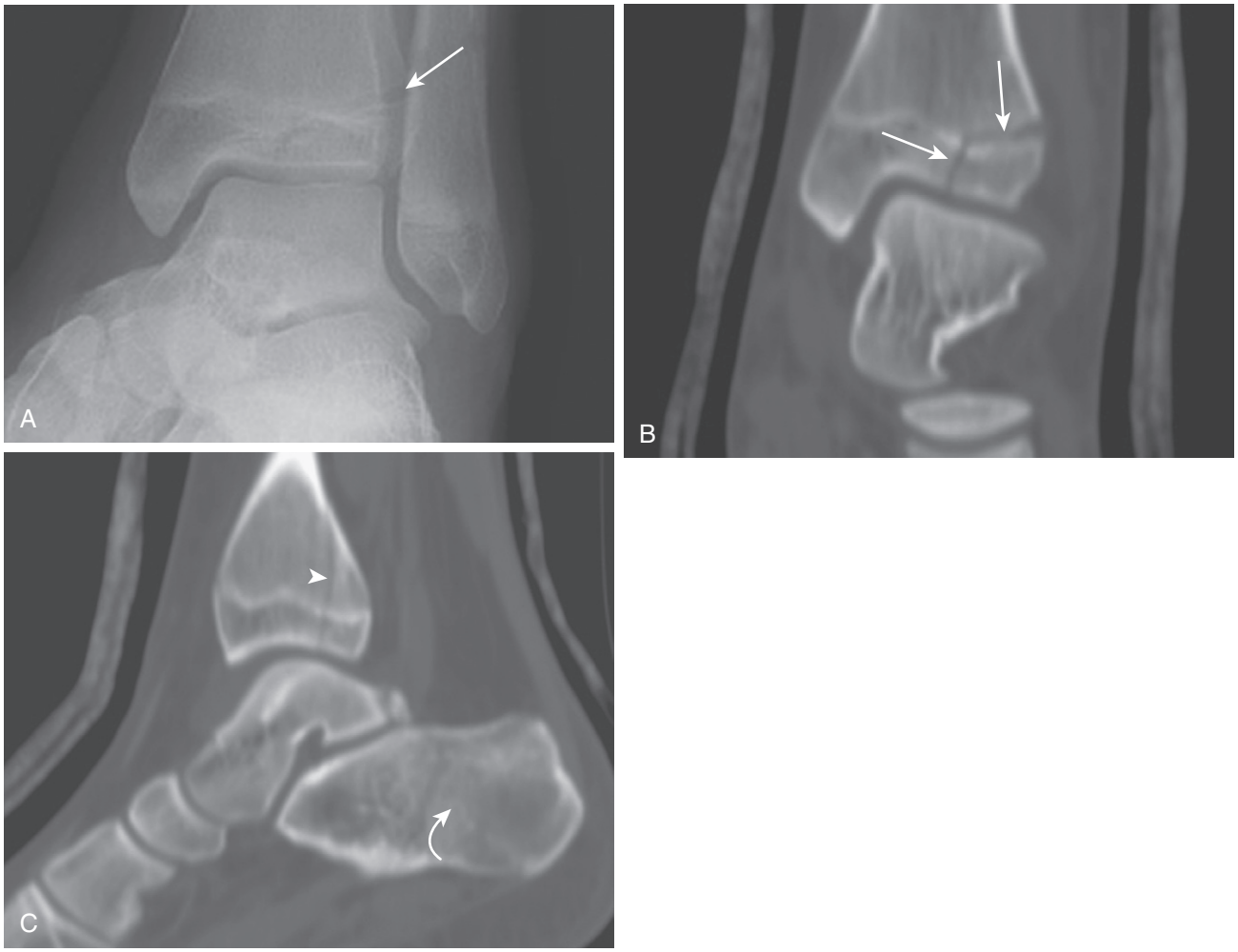


FIGURE 4-39 Fractures of the ankle. **A,** A Tillaux fracture. A mortise view of the ankle shows a vertical fracture of the distal articular surface of the tibia extending to the lateral tibial cortex (*arrow;* Salter-Harris type III in this case). **B** and **C**, A triplane fracture. A coronal reformatted computed tomography image **(B)** demonstrates the typical findings of a Tillaux fracture *(arrows)*. On the sagittal reformation **(C)** there is a coronally oriented vertical metaphyseal component of the fracture *(arrowhead)*, thereby completing the three components of a triplane fracture. Note also a nondisplaced fracture of the calcaneus. A triplane fracture is a combination of a fracture line extending in three planes (sagittal epiphysis, axial physis, and coronal metaphysis). Note a nondisplaced fracture of the calcaneus *(curved arrow)*.

The talar neck lies anterior to the lateral process. It is the most vulnerable site to fracture, mostly in a vertical plane. The *fractures of the talar neck* (Fig. 4-40, *C* and *D*) are divided into four types (Hawkins classification). Type I is a nondisplaced fracture. Type II is a fracture with subtalar subluxation or dislocation. Type III is a fracture with subtalar dislocation and tibiotalar dislocation. Type IV is a fracture with subtalar subluxation and dislocation of the talonavicular joint. The risk of avascular necrosis is 15%, 40% to 50%, and 100% for type I, type II, type III, and type IV, respectively. These fractures can be seen with fractures of the medial malleolus, sustentaculum tali, and metatarsal head. Aviator's astragalus is an eponym for a displaced fracture of the talar neck that results in medial displacement and rotation of the distal fragment, together with the bones of the foot. The Hawkins sign, which is best appreciated on the mortise view, represents normal subchondral bony resorption that occurs in the talar dome 6 to 8 weeks after the injury. Its presence indicates adequate vascular supply and also indicates that expected healing is ongoing. Fractures extending into or posterior to the lateral process of talus are defined as *fractures of the talar body*. By definition, these fractures are intraarticular. A high rate of avascular necrosis is observed. *Fracture of the posterior process of the talus,* either medial or lateral tubercle, is best seen on a lateral view. In fact, fracture of the entire posterior process is uncommon. Os trigonum is the main differential diagnosis, although it usually has a well-corticated edge and appears smooth. *Fracture of the lateral process of talus* is frequently overlooked and misinterpreted as a severe sprain. This fracture is usually an avulsion associated with ankle injury and is best visualized on the mortise view.

Fractures of the Calcaneus

The calcaneus is the most common site of tarsal bone fractures. Fractures are classified by the location and the presence of subtalar joint involvement. *Calcaneal fractures with subtalar joint involvement* (Fig. 4-40, *E*) are more common (75% of all calcaneal fractures) as a result of an axial-loading force to the body of the calcaneus through

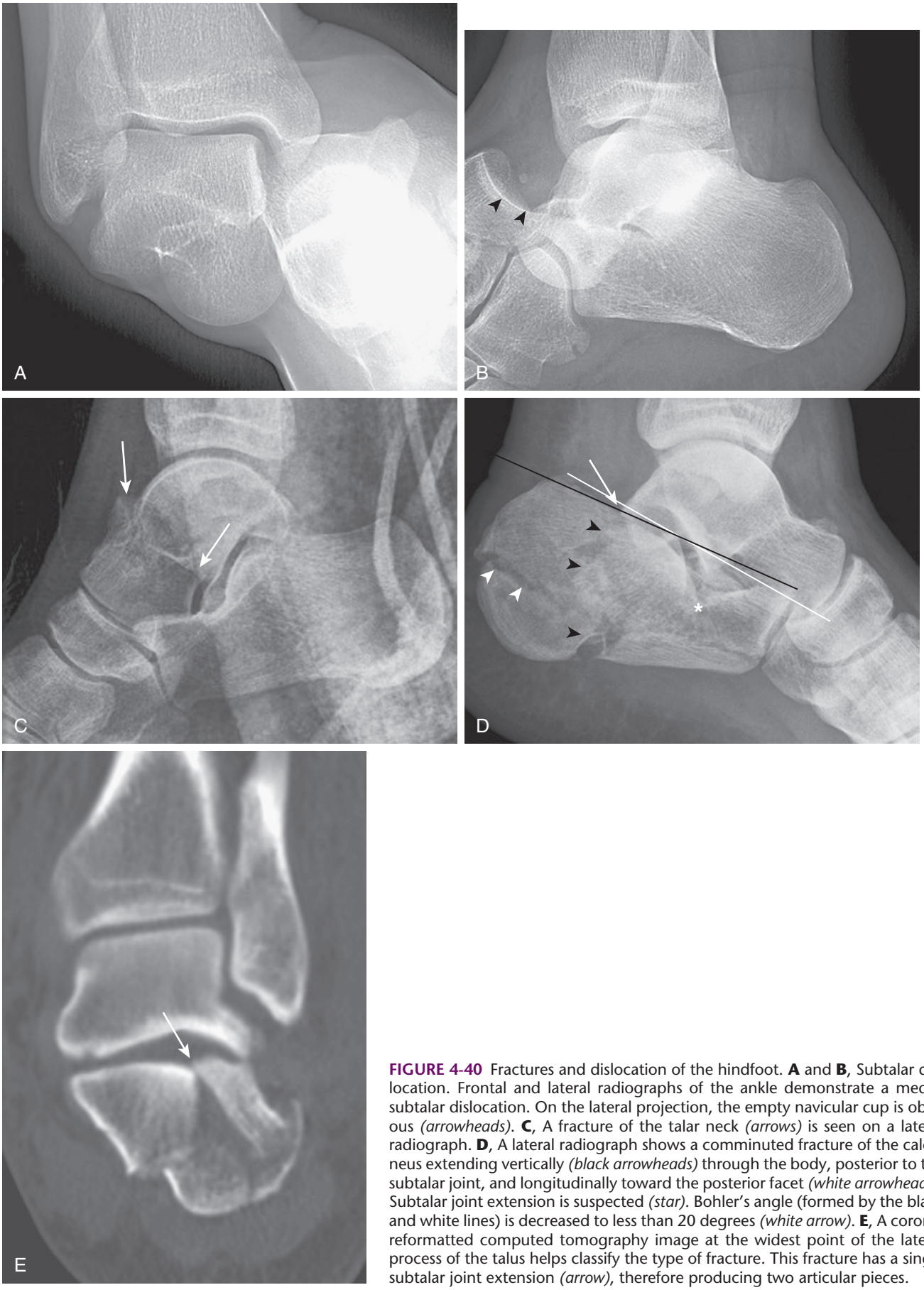


FIGURE 4-40 Fractures and dislocation of the hindfoot. **A** and **B**, Subtalar dislocation. Frontal and lateral radiographs of the ankle demonstrate a medial subtalar dislocation. On the lateral projection, the empty navicular cup is obvious *(arrowheads)*. **C**, A fracture of the talar neck *(arrows)* is seen on a lateral radiograph. **D**, A lateral radiograph shows a comminuted fracture of the calcaneus extending vertically *(black arrowheads)* through the body, posterior to the subtalar joint, and longitudinally toward the posterior facet *(white arrowheads)*. Subtalar joint extension is suspected *(star)*. Bohler's angle (formed by the black and white lines) is decreased to less than 20 degrees *(white arrow)*. **E**, A coronal reformatted computed tomography image at the widest point of the lateral process of the talus helps classify the type of fracture. This fracture has a single subtalar joint extension *(arrow)*, therefore producing two articular pieces.

the talus. Typically on the lateral view, a loss of calcaneal height, decreased Boehler angle, increased angle of Gissane, and disruption of the facet of the subtalar joint are noted. On the axial calcaneal projection, widening of the calcaneus is observed. The direction of the primary fracture line, involvement of the posterior talocalcaneal joint, and lateral comminution of the fracture can be assessed on this view. The axial loading force produces two separate fracture lines: shear and compression lines. A shear fracture line is a sagittal plane fracture through the posterior facet, dividing it into sustentacular (anteromedial) and tuberosity (posterolateral) fragments. The sustentacular fragment is constantly attached to the talus by strong ligaments. The tuberosity fragment is usually impacted, rotated, and displaced laterally, resulting in loss of calcaneal height and increased calcaneal width. The compression fracture line is a coronal plane fracture that split the middle facet and anteromedial fragment. When viewed from the lateral side, this line has a shape of an inverted Y. If the posterior limb extends horizontally toward the tuberosity, it is called a *tongue-type fracture*; if not, it is a joint depression type. Sander classification relies on the numbers of articular pieces of the posterior facet of the subtalar joint, as visualized on reformatted CT images. Type I fractures are nondisplaced. Type II fractures (two articular pieces), type III fractures (three articular pieces), and type IV fractures (four or more articular pieces) are displaced fractures. The more pieces that are involved, the poorer the prognosis. In addition, CT is helpful to assess the amount of remaining attachment of the sustentaculum tali to the posterior facet, involvement of calcaneocuboid joint, and impingement of the lateral border of the calcaneus on the lateral malleolus with potential tendon/nerve entrapments. Occasionally ligament entrapment between the fragments or sinus tarsi involvement are present. These fractures are frequently bilateral, and 10% are associated with fractures of the thoracolumbar spine.

The remainder of the fractures that do not involve the posterior facet are in the *calcaneal fractures without subtalar joint involvement* category, including fractures of the anterior process, midcalcaneus (body, sustentaculum tali, peroneal tubercle, and lateral calcaneal process), and posterior calcaneus (tuberosity and medial calcaneal tubercle). They account for 25% of all calcaneal fractures. Fractures of the midcalcaneus are usually the result of axial loading mechanisms, whereas avulsive forces or inversion injuries cause the other fractures.

Injuries to the Midfoot

The midfoot is defined as the section of the foot distal to the Chopart joint and proximal to the Lisfranc joint. The navicular, cuboid, and medial, middle, and lateral cuneiforms constitute the bones of the midfoot (Box 4-18). The midfoot does not have any bony weight-bearing contact with the ground but is a connection between the forefoot and hindfoot. *Navicular fractures* are commonly due to an indirect force that occurs in a sports-related injury, a fall, or a motor vehicle accident. Less likely, it is a result of a direct blow that causes an avulsion of the talonavicular or naviculocuneiform ligaments. The fractures can be cortical avulsions of the tuberosity (the medial prominence of the navicular, most commonly), or they can be body or dorsal lip fractures. Body and dorsal lip fractures are best seen on a lateral radiograph. The presence of an accessory navicular (os tibiale externum) can be mistaken for a cortical avulsion fracture of the tuberosity. This accessory ossicle is present in up to 25% of the general population and is bilateral in 90% of cases. *Cuboid and cuneiform injuries* are commonly seen with other injuries to the midfoot/forefoot and Lisfranc joint.

BOX 4-18 Fractures and Dislocations of the Foot

Standard views:
- Foot—dorsoplantar, lateral, and oblique views
- Calcaneus—lateral and Harris (tangential 45 degree) views
- Toe—dorsoplantar, lateral, and oblique views

Frequent sites of injuries: Phalanges

Frequently missed injuries: Fracture of the lateral process of the talus, Lisfranc injury

Relevant normal anatomy: Three parts of the foot—hindfoot (calcaneus and talus), midfoot (navicular, cuboid, and cuneiforms), and forefoot (metatarsals and phalanges)
- Chopart joint—transverse tarsal joint between the hindfoot and midfoot
- Lisfranc joint—tarsometatarsal joint between the midfoot and forefoot
- Boehler angle—normal is 20 to 40 degrees (the angle is formed by the intersection of lines drawn tangentially to the anterior and posterior elements of the superior calcaneal surface)

Fracture mimics:
- The sesamoid bone on the plantar aspect of the first metatarsal
- The os trigonum (mimics fracture of the posterior process of the talus)
- Nutrient artery canal—midshaft of metatarsal
- Calcaneal apophysis—fragmented, irregularly dense, and more dense than the calcaneus
- Normal apophysis of the base of the fifth metatarsal—parallel to the shaft of the metatarsal along the inferolateral margin; it does not extend into the joint
- Os peroneum—proximal to the tip of the fifth metatarsal base, lateral to the cuboid in the peroneus longus tendon, well corticated

Tarsometatarsal (Lisfranc) Injuries

Injuries to the tarsometatarsal joint range from a stable sprain to a gross unstable deformity. These injuries can result in prolonged recovery and significant long-term morbidity, and therefore it is important to recognize and treat them early. Up to 20% of these injuries are missed on initial presentation. They commonly result from indirect forces that cause hyperplantarflexion across the long axis of the foot, which can occur with minimal trauma (e.g., foot entrapment on the car break pedal or a minor fall) and as a sports-related injury (e.g., an opponent falls on the foot in fixed equinus). A key anatomic structure related to this type of injury is the Lisfranc ligament, which is the strongest and largest ligament of this joint complex, originating from the plantar lateral aspect of the medial cuneiform and inserting on the plantar medial aspect of the second metatarsal base. It is an indirect link between the first and second metatarsals and the only ligamentous support between the medial portion of the forefoot with the rest of the lateral portion of the forefoot. The nidus of Lisfranc injuries is typically at the



FIGURE 4-41 A Lisfranc injury. An anteroposterior radiograph of the foot demonstrates homolateral lateral dislocation of the tarsometatarsal joints. The Lisfranc ligament is completely torn, as indicated by the complete lateral dislocation of the second metatarsal with respect to the medial and middle cuneiforms.

medial cuneiform and the base of the second metatarsal, where a Lisfranc ligament is located. This ligament may be torn (e.g., no fracture of the medial cuneiform or base of the second metatarsal) or intact (e.g., with fracture of the base of the second metatarsal). On radiography, fractures at the base of the second metatarsal or the anterior aspect of the cuboid should raise concern about the possibility of a Lisfranc injury. A standing AP view (stress view) or CT can be used to assess the first/second joint space. Two major types of these injuries are described. The *homolateral type* (Fig. 4-41) is a lateral dislocation of the four lateral metatarsals or all metatarsals. The *divergent type* is a less common but more severe injury. In this type, a lateral displacement of the second through fifth metatarsals occurs with medial displacement of the first metatarsal. Rarely, an isolated medial dislocation of the first metatarsal and medial cuneiform may occur. The most common fractures associated with these dislocations are fractures at the base of the second metatarsal. Chip fractures of the distal margin of the cuboid and the bases of other metatarsals are frequent.

Injuries to the Forefoot

Metatarsal Fractures

Most injuries to the fifth metatarsal are related to sports or athletic activities. These fractures are separated into two groups: proximal base fractures and distal spiral or dancer's fractures. Three distinct fracture patterns of the *proximal fifth metatarsal* exist as defined by the location of the fracture line. Zone 1 injury (Fig. 4-42, *A*) is an avulsion fracture at the base of the fifth metatarsal that usually

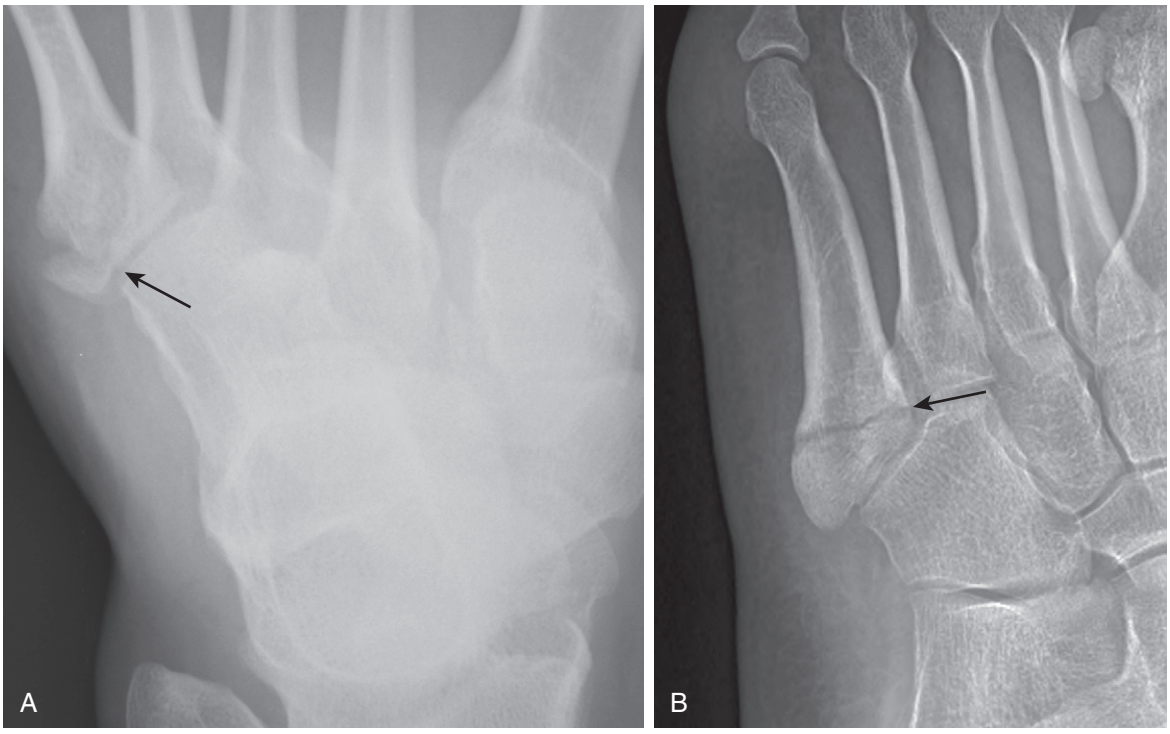


FIGURE 4-42 Fractures of the proximal fifth metatarsal bone. **A,** A zone 1 injury is an avulsion fracture at the base of the fifth metatarsal *(arrow)*. It is the most common type of fracture of the proximal fifth metatarsal. **B,** A zone 2 injury, or "true Jones fracture," involves the metadiaphyseal junction *(arrow)*.

occurs from an indirect load. Tension was produced along the insertion of the lateral band of the plantar aponeuroses during sudden inversion of the hindfoot, causing disruption of the bony cortex in a transverse orientation to the joint. Zone 2 injuries (Fig. 4-42, *B*) are true Jones fractures that involve the metadiaphyseal junction of this bone. The fracture line propagates from the lateral aspect of the proximal metatarsal toward the four-five articular surface and may progress into the metatarsocuboid joint. It is a result of tensile stress along the lateral border of the metatarsal. Zone 3 injuries are seen in the proximal fifth metatarsal and are referred to as *proximal diaphyseal stress fractures*. They are relatively rare and occur in the proximal 1.5 cm of the shaft of the metatarsal. Relative frequencies of these fractures are 93% in zone 1, 4% in zone 2, and 3% in zone 3. *Dancer's fracture* is a spiral, oblique fracture of the distal fifth metatarsal caused by rolling over the outer border of the foot.

Metatarsophalangeal Injuries

Injuries to the metatarsophalangeal (MTP) joint complex can occur in isolation or as a part of a multiple trauma. Most commonly, it involves the first MTP joint that normally provides stable load sharing between the metatarsal head and the toe. The *dislocations of the first MTP joint* can be complicated by avulsion injuries of the medial or lateral collateral ligaments or displacement of the sesamoid structures. Sesamoids function within the first MTP joint complex as shock absorbers and fulcrums in supporting the weight-bearing function of the first toe. The spectrum of *sesamoid injuries* is wide, ranging from sesamoiditis to stress fracture to acute fracture. Acute fractures are a result of a direct blow, axial loading, or hyperpronation. The fractures can be transverse, comminuted, or stellate, depending on the mechanism of injury. The medial sesamoid is injured more often than the lateral sesamoid. A partite sesamoid can be distinguished from a fracture by its smooth sclerotic edge, and the sum of a partite sesamoid's parts makes it larger than a normal sesamoid. Injury to the partite sesamoid can be diagnosed by a stress radiograph with the toe in dorsiflexion.

Phalangeal fractures are the most common injury to the forefoot. Fractures of the proximal phalanx are more common than those of the middle and terminal phalanx. Of these, the proximal phalanx of the fifth toe is most often involved. Two major mechanisms result in fractures: a direct blow (e.g., when a heavy object is dropped onto the foot) and axial loading (a stubbing injury). The former mechanism usually causes a comminuted or transverse fracture. The latter mechanism tends to produce more deformity as a result of secondary valgus or varus force and results in spiral or oblique fractures.

Interphalangeal dislocations are a result of axial loading applied to the terminal end of the unprotected digit. The proximal interphalangeal joint is most commonly injured, usually in the dorsal direction. A radiograph of the dislocation of the halluxed, partially spontaneously reduced interphalangeal joint can be as subtle as minimal widening of the joint.

SPECIAL CONSIDERATIONS

CT Angiography of the Extremities in Trauma

Traumatic arterial injuries to the extremities may occur with either blunt or penetrating trauma. Clinical signs of arterial injuries are divided into two categories: hard and soft signs. The hard signs include the presence of pulsatile bleeding, expanding hematoma, pulse deficit, bruit/thrill, and distal limb ischemia. Patients with hard signs usually require immediate surgical intervention. Soft signs are stable hematoma, hypotension, neurologic deficit, or injuries in proximity to the major artery. CT angiography (CTA) has largely replaced conventional catheter angiography for evaluation of possible peripheral arterial injury in trauma patients because of its fast acquisition, allowing rapid assessment, high spatial resolution, increased anatomic coverage, and high-quality multiplanar reformations and volumetric reconstructions. When CTA is diagnostic, its sensitivity and specificity are between 94% and 98% and 97% and 100%, respectively. Direct signs of arterial injuries on CT angiography are extravasated collection of contrast medium, wall irregularity, abrupt change in arterial caliber, enhancement difference, and intimal flap. Other indirect signs include perivascular hematoma, bullet trajectory through the artery, and a fragment adjacent to the artery. Known pitfalls that render the examinations uninterpretable or indeterminate are examinations with poor arterial opacification, motion artifacts, or streak artifacts (especially in penetrating missile injuries). Slow blood flow distal to an arterial injury may limit the evaluation of the runoff vessels. Detection of injuries to the distal, small arteries below the ankle or elbow is limited by the spatial resolution of CTA. CTA should be performed only if immediate surgery is not indicated. Stable patients with a diminished pulse, expanding hematoma, bruit/thrill, and an anatomically susceptible injury site may benefit from this study.

Volumetric (Three-Dimensional) Reconstruction and Image Postprocessing

A combination of multidetector CT and volumetric (three-dimensional [3D]) reconstruction has proved to be valuable in the diagnosis of complex orthopedic injuries and in treatment planning. CT scan techniques for this purpose include the helical (spiral) acquisition, narrow collimation, and lower pitch with small reconstruction increments. The raw data of axial images are interpolated to create isotropic voxels and then mapped with the appropriate rendering algorithm into a 3D volume. Shaded surface rendering and volume rendering are major reconstructive algorithms for 3D musculoskeletal imaging. The former technique beautifully displays the gross relationships of the structures. The latter technique conveys information about the lesions hidden beneath the bone surface and is less likely to register interference by stair-step artifacts. Routine use of multiplanar (two-dimensional) reformations and volumetric (3D) reconstructions is a critical part of the CT examination of musculoskeletal trauma because they potentially lead to a change in management decision.

SUGGESTED READINGS

Court-Brown CM, Heckman JD, McQueen MM, Ricci WM, Tornetta P III, eds. *Rockwood and Green's Fractures in Adults*. 8th ed. Philadelphia, PA: Lippincott Williams & Wilkins; 2014.

Daftary A, Haims AH, Baumgaertner MR. Fractures of the calcaneus: a review with emphasis on CT. *Radiographics*. 2005;25:1215–1226.

Durkee NJ, Jacobson J, Jamadar D, et al. Classification of common acetabular fractures: radiographic and CT appearances. *AJR Am J Roentgenol*. 2006;187:915–925.

Falchi M, Rollandi GA. CT of pelvic fractures. *Eur J Radiol*. 2004;50:96–105.

Fishman EK, Horton KM, Johnson PT. Multidetector CT and three-dimensional CT angiography for suspected vascular trauma of the extremities. *Radiographics*. 2008;28:653–667.

Geijer M, El-Khoury GY. MDCT in the evaluation of skeletal trauma: principles, protocols, and clinical applications. *Emerg Radiol*. 2006;13:7–18.

Greenspan A, Beltran J. *Orthopedic Imaging: A Practical Approach*. 6th ed. Philadelphia, PA: Lippincott Williams & Wilkins; 2014.

Kaewlai R, Avery LL, Asrani AV, et al. Multidetector CT of carpal injuries: anatomy, fractures, and fracture-dislocations. *Radiographics*. 2008;28:1771–1784.

Lee P, Hunter TB, Taljanovic M. Musculoskeletal colloquialisms: how did we come up with these names? *Radiographics*. 2004;24:1009–1027.

Manaster BJ, May DA, Disler DG. *Musculoskeletal Imaging: The Requisites*. 4th ed. Philadelphia, PA: Elsevier Saunders; 2013.

Markhardt BK, Gross JM, Monu JUV. Schatzker classification of tibial plateau fractures: use of CT and MR imaging improves assessment. *Radiographics*. 2009;29:585–597.

Pope TL Jr, Harris JH Jr. *The Radiology of Emergency Medicine*. 5th ed. Philadelphia, PA: Lippincott Williams & Wilkins; 2012.

Rogers LF, West OC. *Imaging Skeletal Trauma*. 4th ed. Philadelphia, PA: Elsevier Saunders; 2014.

Chapter 5

Extremities: Nontrauma

Luis E. Diaz

Most true emergencies of the musculoskeletal system are traumatic in nature. Musculoskeletal trauma is reviewed in other chapters. Neck and back pain are the most common nontraumatic musculoskeletal conditions leading to emergency department visits (National Hospital Ambulatory Medical Care Survey—Emergency Department 2010; data obtained from the U.S. Department of Health and Human Services, Centers for Disease Control and Prevention, National Center for Health Statistics).

Shoulder pain, a painful hip, and musculoskeletal infection are three common clinical problems in patients presenting to the emergency department with minimal, unrecognized, or no acute trauma. This chapter discusses the clinical presentations and imaging findings that can be expected with these conditions, with a detailed description of conventional radiographic and advanced imaging features. Because cross-sectional imaging studies continue to be acquired with increasing frequency in the emergency setting, a comprehensive knowledge of imaging findings for these modalities is necessary.

SHOULDER PAIN

Evaluation of "nontraumatic" shoulder pain in the acute setting is challenging for clinicians and radiologists alike. The imaging features of the most common conditions presenting with shoulder pain in clinical practice are reviewed in an effort to assist radiologists and clinicians who perform radiographic assessment of the shoulder in the emergency department setting. However, some of these entities may be the result of minor, remote, or unrecognized trauma.

Conventional radiographs should be obtained as the initial examination in most patients presenting with shoulder pain. Two standard views of the shoulder are performed in the anteroposterior projection with the humerus in external and internal rotation. The external rotation view is easily recognized as the one in which the greater tuberosity is seen in profile on the lateral aspect of the humerus. With internal rotation, the bicipital groove of the humerus translates medially, leaving the lesser tuberosity partially in profile. The glenohumeral joint is oriented obliquely approximately 30 degrees in the axial plane (with the anterior glenoid medially situated relative to the posterior glenoid), and thus it is not seen in profile on the standard anteroposterior view. Additional radiographic views of the shoulder include the axillary view and the scapular "Y" view. The axillary view is preferable if the patient can tolerate this position. When properly performed, the axillary view provides excellent visualization of the acromion, coracoid process, and glenohumeral joint. Although an "impingement radiographic series" may be requested by the orthopedic surgeon, these radiographs are only rarely obtained in the emergency setting.

Careful evaluation of shoulder radiographs requires a detailed review of the periarticular and intraarticular soft tissues for abnormal mineral deposits, the osseous structures for alignment and bone mineralization (regional and general), and the acromioclavicular joint, glenohumeral joints, and subacromial space.

Calcium Hydroxyapatite Deposition Disease

Hydroxyapatite deposition disease is a common entity characterized by pain and periarticular deposition of calcium phosphate crystals. The soft tissues around the shoulder are the most common locations for deposits occurring in tendons, the joint capsule, ligaments, and bursae. Although this disease process has been assigned multiple names, it is mostly known as calcific bursitis/tendinitis. Middle-aged patients are most commonly affected, and the condition is slightly more common in men than in women. More than 30% of persons with calcific deposits in the area of the shoulder are asymptomatic. When the deposits are clinically apparent, patients present with varying degrees of pain and disability, which may last for weeks or months if the condition is untreated. It is important to note that the finding of hydroxyapatite deposits within the rotator cuff tendons ("calcific tendinitis") has no relationship with the subsequent development of rotator cuff tears.

Calcific deposits are more easily identified and characterized with use of radiographs, computed tomography (CT), and ultrasonography (US) than with magnetic resonance imaging (MRI). On radiographs, most calcific deposits appear as homogeneous and amorphous densities that are ovoid, linear, or triangular in shape, with and without internal trabeculations (Fig. 5-1, *A*). The precise appearance and location varies with the phase of the disease process and specific anatomic structure involved. The supraspinatus is the most frequently affected tendon. US is highly sensitive for detecting even very small calcific deposits and may be used to guide puncture, aspiration, and lavage as therapeutic options. Hyperechoic foci with minimal or no significant posterior shadowing are identified, sometimes as ill-defined and fluffy or as discrete, well-defined calcifications that are linear or rounded (Fig. 5-1, *B*). Calcific deposits may be seen on MRI as nodular foci of low signal intensity in all pulse sequences (Fig. 5-1, *C*) and may be easier to identify on gradient-echo sequences, because they may induce a blooming artifact. Inflammatory changes in surrounding soft tissues may be present and identified as heterogeneous hyperintensity in fluid-sensitive (T2-weighted and short T1 inversion recovery [STIR]) sequences.

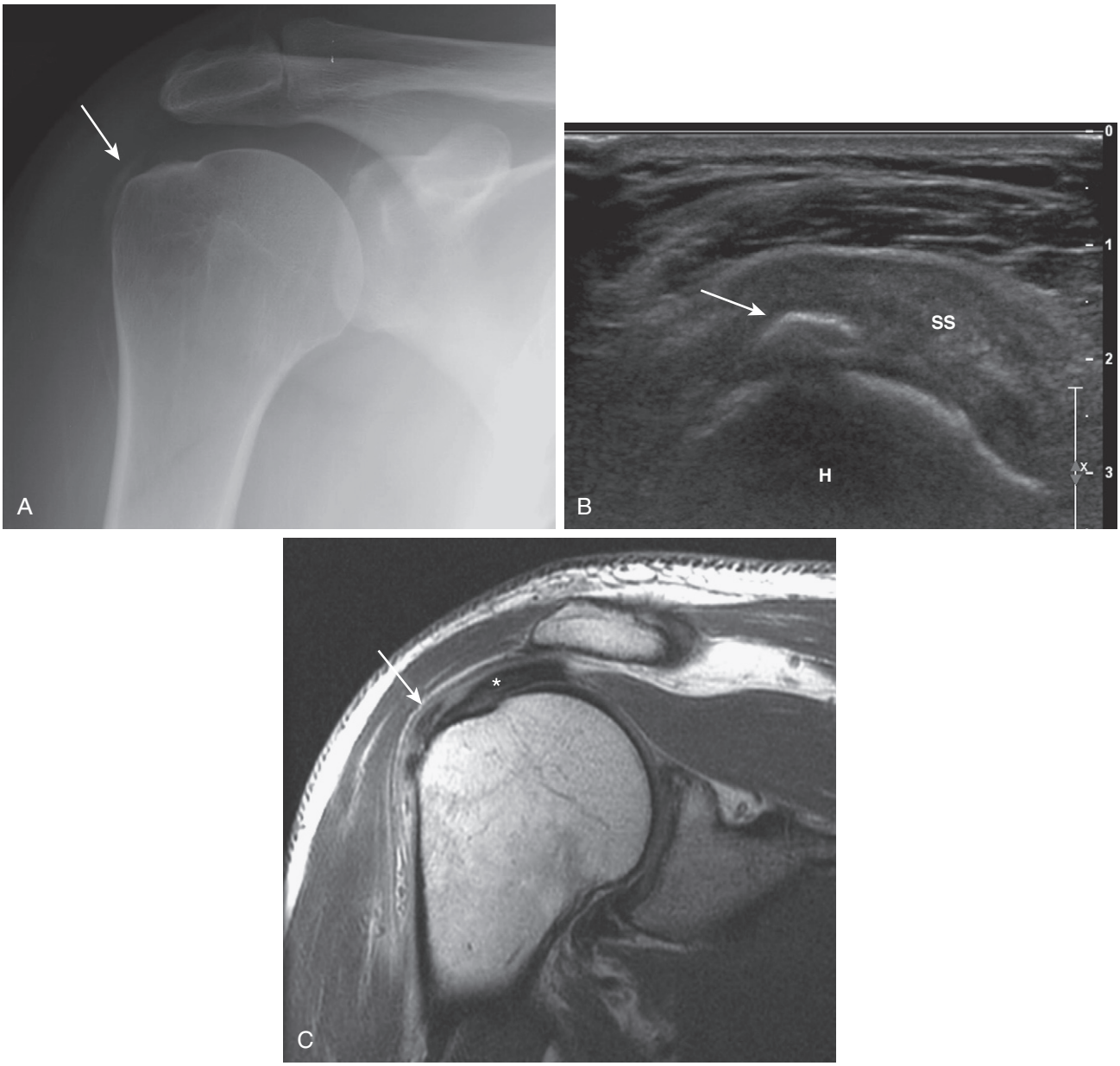


FIGURE 5-1 Calcific bursitis. **A,** An external rotation view of the right shoulder in an adult patient presenting to the emergency department with acute exacerbation of right shoulder pain demonstrates periarticular mineralization *(arrow)* adjacent to the greater tuberosity of the humerus. **B,** An oblique longitudinal ultrasound image of the shoulder in a different patient also presenting with shoulder pain shows a curvilinear hyperechoic focus *(arrow)* within the supraspinatus *(SS)* tendon near its humeral *(H)* insertion. **C,** An oblique coronal proton density magnetic resonance image in the same patient as **A** shows an amorphous focus of low signal intensity in the subacromial-subdeltoid bursa *(arrow)* superficial to the SS tendon *(asterisk)*.

Rotator Cuff Abnormalities and Impingement

The concept of extrinsic subacromial impingement was initially described by Neer in 1972 and continues to be a very controversial topic even today. The notion of impingement is based on the anatomic arrangement of the shoulder joint (fixed component) and on the motion of the humeral head relative to the other components of the shoulder joint (dynamic component). In essence, the rotator cuff tendons (primarily the supraspinatus) and muscles, as well as the subacromial-subdeltoid bursa, located between the coracoacromial arch and the humeral head, may be impinged with motion of the arm. It is thought that this repetitive microtrauma from friction will lead to tendon degeneration, bursal inflammation, and, ultimately, a tear of the cuff. The "critical zone" is particularly susceptible to this pathophysiologic process; this critical zone has been described as a hypovascular area located on the anterior aspect of the supraspinatus tendon, approximately 1 cm from its insertion. Other factors described as potential contributors to the impingement process are narrowing of the subacromial space by enthesophytes arising from the undersurface of the acromion, advanced acromioclavicular joint osteoarthritis with hypertrophic changes, a type III acromion (anteriorly hooked), and the presence of an os acromiale (i.e., a secondary ossification center at the tip of the acromion that persists after skeletal maturity as a

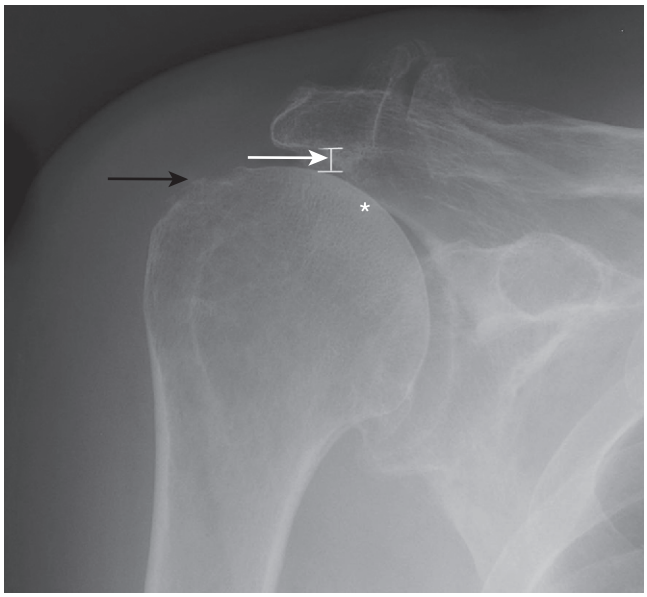


FIGURE 5-2 Chronic rotator cuff tear indirect signs. An external rotation view of the shoulder shows superior subluxation of the humeral head with decreased subacromial space to 4 mm *(white arrow),* sclerosis of the humeral head *(asterisk),* and surface irregularity at the greater tuberosity *(black arrow)*.

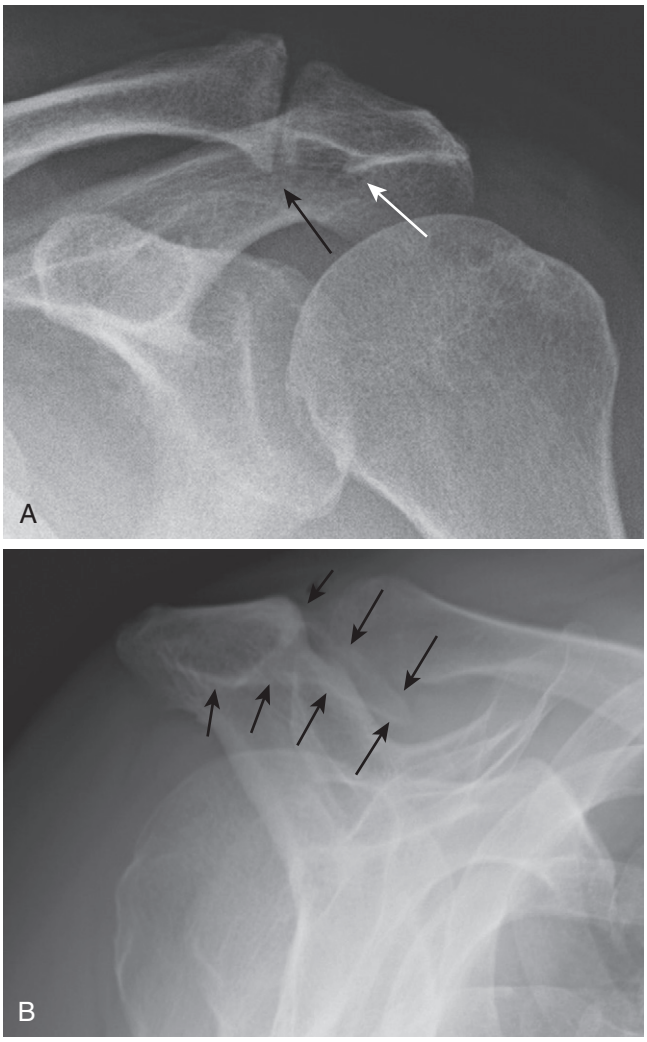


FIGURE 5-3 Potential anatomic sources of impingement. **A,** An internal rotation view of the shoulder shows an enthesophyte at the undersurface of the acromion *(white arrow)* and hypertrophic changes at the acromioclavicular joint *(black arrow)*. **B,** A Y-view of the shoulder reveals a type III (anteriorly hooked) acromion *(arrows)*.

separate bone). However, impingement can occur without any visible anatomic predisposing factor, and the presence of anatomic variations does not necessarily indicate that impingement is occurring. Thus the diagnosis of shoulder impingement is made mainly on clinical grounds rather than on the basis of radiographs alone. The radiologist should focus on describing, characterizing, and grading rotator cuff disease, as well as on identifying potential contributing sources to the impingement process.

The spectrum of rotator cuff disease includes tendinopathy or tendinosis, partial- and full-thickness tendon tears, and subacromial-subdeltoid bursitis. Most rotator cuff tears are chronic and occur as the result of repetitive microtrauma. Acute rotator cuff tears are rare but do occur, especially in older patients with preexisting chronic impingement and degenerative tendon changes. It is not unusual, however, for patients with acute or chronic rotator cuff tears to seek care at the emergency department on an urgent basis because of severe or acutely worsening shoulder pain.

Radiographs should always be performed initially for evaluation of shoulder pain. However, they often are not contributory to a diagnosis. The presence of gas from the vacuum phenomenon in the glenohumeral joint strongly suggests the absence of a full-thickness rotator cuff tear. The rotator cuff tendons cannot be directly seen on radiographs; rather, a number of radiographic findings serve as indirect evidence of cuff disease and impingement (Fig. 5-2). These findings include superior subluxation of the humerus with a decreased subacromial space (less than 8 mm) and secondary changes in the humeral head, such as sclerosis, flattening, surface irregularity, and cystic changes. Radiographs also may demonstrate potential anatomic causes of impingement (Fig. 5-3).

Direct visualization of the rotator cuff tendons is achieved with MRI or US. One of these two methods is usually required to accurately diagnose and characterize rotator cuff tears. Selection of the modality depends on availability, individual expertise, and preference of the interpreting radiologist. Both offer relative advantages and disadvantages, which determine preference, and practice trends vary among different world countries. For example, in the United States, MRI is used more commonly than US, perhaps because of its faster learning curve and because the method is easily reproducible and less operator dependent than US. On the other hand, US is a great cost-effective alternative in experienced hands and is the first alternative in many institutions throughout the world.

Rotator cuff tendinopathy (tendon degeneration) is characterized on MRI by increased signal within the tendon on low echo time (TE) sequences (T1 and proton density). The tendon may demonstrate associated focal or diffuse thickening, but this finding is not consistent (Fig. 5-4, *A*). Abnormal signal within the rotator cuff tendons in low TE sequences may be seen in a variety of normal situations, and thus the need exists for close clinical correlation—most commonly, magic angle artifact as an area of increased signal at 55 degrees from the main magnetic field, which, on oblique coronal planes, coincides with the

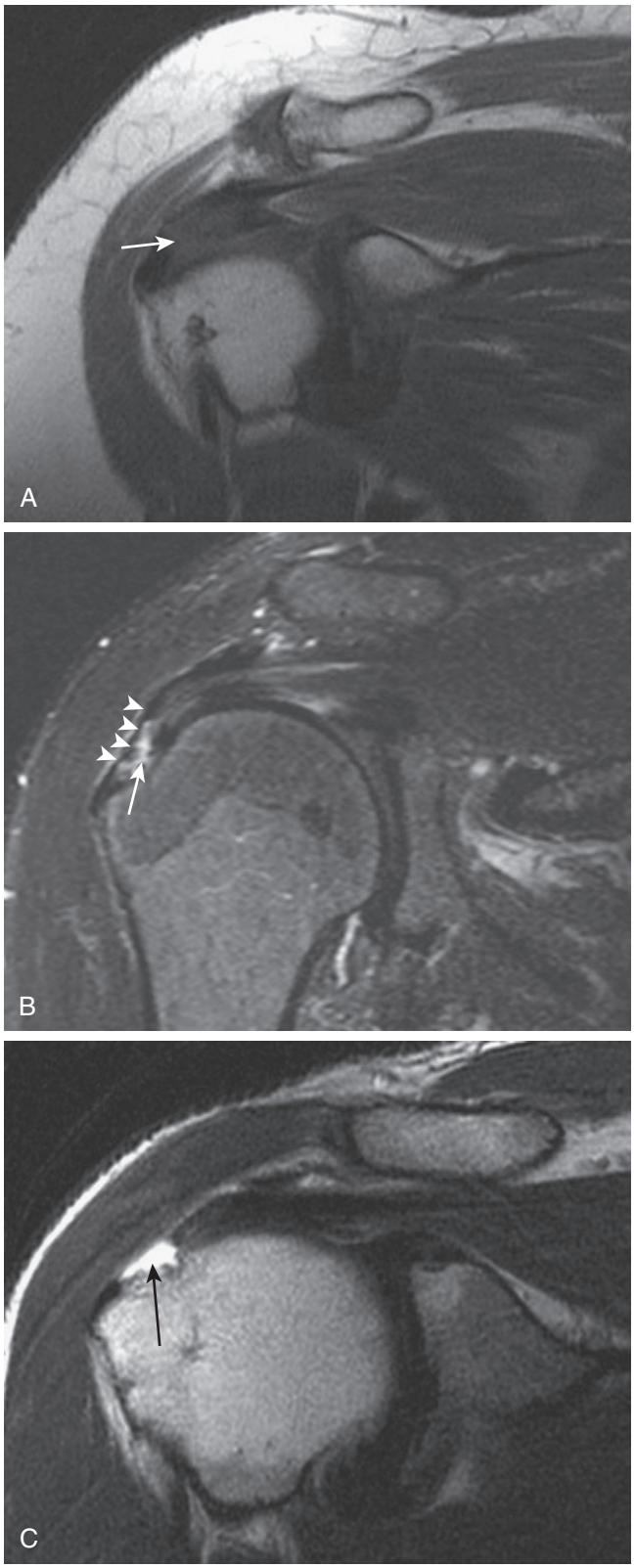


FIGURE 5-4 The spectrum of rotator cuff disease seen on magnetic resonance. **A,** Tendinopathy or tendinosis is characterized in this proton-density image as increased signal and thickening *(arrow)* of the supraspinatus (SS) tendon. **B,** A partial-thickness, articular surface tear of the SS tendon on an oblique coronal short T1 inversion recovery (STIR) image characterized by fluid signal *(arrow)* between the disrupted articular surface and interstitial fibers and the intact bursal surface fibers *(arrowheads)*. **C,** A full-thickness tear of the SS tendon seen on an oblique coronal T2-weighted sequence as fluid signal *(arrow)* extending across the entire thickness of the tendon.

supraspinatus "critical zone." Cuff tendon tears present as disruption (interruption) of fibers and may be either partial thickness or full thickness in the craniocaudal plane. High signal fluid is seen separating the disrupted fibers. This fluid may extend from the articular (inferior) surface superiorly in varying degrees to the bursal (superior) surface (Fig. 5-4, *B*). Partial-thickness tears affecting the articular surface are more common than isolated bursal surface tears. In full-thickness tears, fluid invariably extends across the tendon (Fig. 5-4, *C*) into the subacromial-subdeltoid bursa. Subacromial-subdeltoid bursitis may occur in isolation or in conjunction with rotator cuff tears.

Figure 5-5, *A,* shows an intact supraspinatus and its relation to the humeral head and deltoid muscle. The primary or direct signs of a full-thickness supraspinatus tear in US include nonvisualization of the tendon and a hypoechoic or anechoic full-thickness defect filling the gap of the torn tendon (Fig. 5-5, *B*). Secondary or indirect signs that are helpful to correlate with the primary signs include sagging of the peribursal fat, cortical irregularity at the greater tuberosity, fluid in the subacromial-subdeltoid bursa, and muscle atrophy. Partial-thickness tears manifest sonographically as focal areas of hypoechoic or anechoic tendon defects involving the bursal or articular surface (Fig. 5-5, *C*). An adequate examination requires evaluation of the extension of the defect on two orthogonal planes to confirm the findings. Tendon degeneration is demonstrated as internal heterogeneous echogenicity.

Acromioclavicular Joint Disease (Osteolysis and Osteoarthritis)

The incidence of acromioclavicular joint disease as a cause of shoulder pain is higher than generally realized. The acromioclavicular joint is often ignored, to the point that it has been termed the "forgotten" or "overlooked" joint. Osteolysis and osteoarthritis are two of the most common causes of shoulder pain arising from the acromioclavicular joint.

Osteolysis

Destruction of bone (osteolysis) may be seen as the result of multiple localized or generalized conditions. Destruction of the distal end of the clavicle is not uncommon and may be idiopathic, posttraumatic, or caused by rheumatoid arthritis, hyperparathyroidism, metastatic disease, multiple myeloma, primary osteolysis syndromes, and infection.

Posttraumatic osteolysis deserves special attention because of its relative frequency as a cause of debilitating pain and painful shoulder motion and because very often it is unrecognized. This entity can occur after a single or multiple episodes of minimal or major injury to this region. Most important is the recognition that posttraumatic osteolysis can occur without an obvious acute or known traumatic episode, and in those situations it is thought to be due to repetitive stress, as seen in weightlifters, judo practitioners, and pneumatic tool workers. The pathogenesis is poorly understood, and several theories have been formulated, including a neurologic and/or vascular mechanism, hyperemia, and autonomic phenomenon. More recently it has been proposed that osteolysis may be the result of a reactive process originating in the synovium or a subchondral fracture.

When it is advanced, resorption of the distal clavicle may be easily recognized radiographically (Fig. 5-6), with loss of up to 3 cm of bone and widening of the acromioclavicular

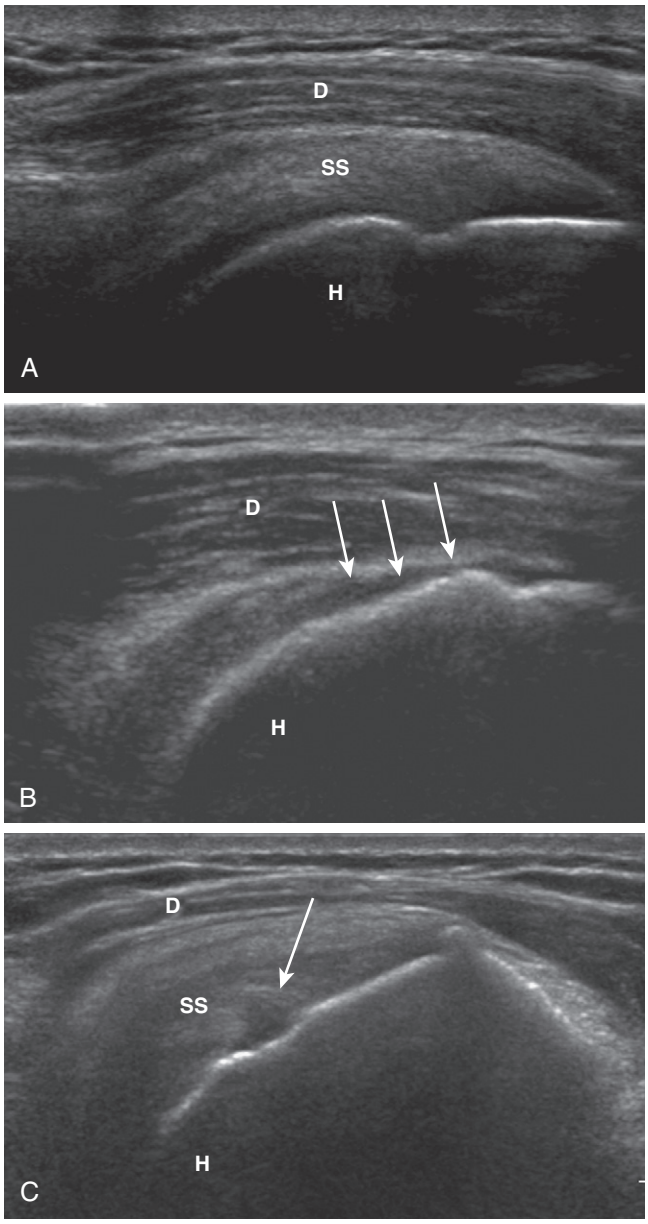


FIGURE 5-5 The spectrum of rotator cuff disease on ultrasound (US). **A,** A normal longitudinal image of the left shoulder demonstrating an intact supraspinatus *(SS)* and its relation to the humeral head *(H)* and deltoid muscle *(D)*. **B,** A longitudinal US image of the left shoulder with nonvisualization of a fully torn and retracted SS tendon. A gap is present in the expected location of the tendon *(arrows)*. **C,** A longitudinal US image of the left shoulder demonstrating a partial-thickness articular surface tear of the SS tendon as a focal hypoechoic area at its insertion *(arrow)*. (Courtesy Alda Cossi, MD.)

joint. However, the radiologist should focus on identifying early signs, because immobilization seems to diminish the amount of bone loss and shorten the natural course of the lytic phase. Early radiographic signs include soft tissue swelling, demineralization, and loss of the subarticular sclerotic cortex at the distal end of the clavicle. MRI findings usually precede radiographic findings. Initially periarticular soft tissue swelling/edema is present, and a bone marrow edema pattern may be evident. The marrow signal abnormality can be limited to the distal end of the clavicle or involve the acromion as well, albeit to a lesser degree. An associated joint effusion may be present, although this

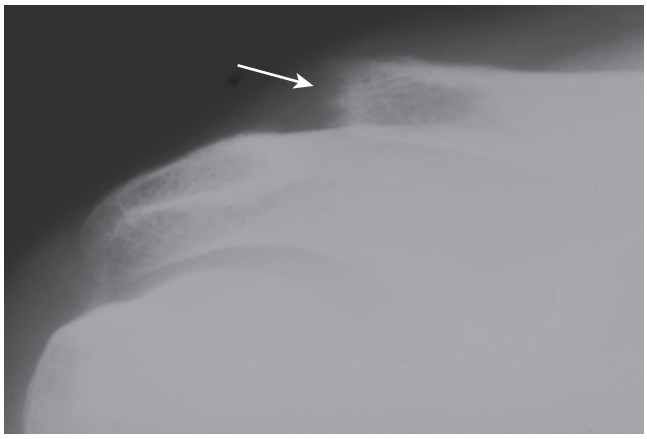


FIGURE 5-6 Posttraumatic osteolysis. A 28-year-old weightlifter with no recognizable acute trauma presented with acute shoulder pain. An anteroposterior radiograph of the right shoulder revealed a widened acromioclavicular joint and resorption of the distal end of the clavicle *(arrow)*.

finding is variable. The disease process then progresses to bone erosion and frank destruction. Other MRI findings include cortical irregularity, subchondral erosion or cystic changes, and a subchondral line suggestive of a subchondral fracture.

Osteoarthritis

Any arthropathy can involve the synovial acromioclavicular joint. However, osteoarthritis is the condition most commonly found in clinical practice and is a very important cause of disability and loss of work hours. The acromioclavicular joint is almost universally affected in the elderly population with osteoarthritis. Shoulder pain caused by osteoarthritis can be severe and incapacitating and can cause affected patients to seek emergency medical attention.

The radiographic hallmarks of osteoarthritis include joint space narrowing, subchondral sclerosis ("eburnation"), subchondral cyst formation, osteophytes, deformity, and malalignment. Although MRI is not necessary to detect acromioclavicular osteoarthritis, the acromioclavicular joint should be included in the field of view of all shoulder MR examinations. All imaging findings described on radiographs can be seen on MRI. Additionally, MRI may depict joint effusions, capsular hypertrophy, and a subchondral bone marrow edema pattern. The clinical significance of MRI and radiographic findings is poorly understood, because these abnormalities are present in both symptomatic and asymptomatic patients. Some studies suggest that the presence of a bone marrow edema pattern and an effusion is associated with pain and that the thickness of the capsule (greater than 3 mm) may be a predictor of a good response to intraarticular injections.

Glenohumeral Joint Disease (Arthropathy and Adhesive Capsulitis)

The glenohumeral joint may be affected by a multitude of conditions. The discussion in this section is limited to adhesive capsulitis, because of its frequency and complexity, and to rheumatoid arthritis, which is a very common arthropathy affecting this joint. Only osteoarthritis is more common, and the imaging features of osteoarthritis have already been described for the acromioclavicular joint.

Rheumatoid Arthritis

Rheumatoid arthritis is a symmetric inflammatory arthropathy affecting predominantly the small joints of the hand, wrist, and feet. Involvement of the glenohumeral joint is not infrequent and occurs later in the disease course. Approximately half of patients with rheumatoid arthritis have shoulder symptoms during the first 2 years of their disease.

Conventional radiographs are still important for diagnosis and classification of rheumatoid arthritis. Classically, patients have uniform joint space narrowing, periarticular demineralization, subchondral cystic changes, and marginal erosions. Erosions in the shoulder have a predilection for the lateral portion of the humeral head and may resemble a Hill-Sachs deformity (Fig. 5-7). Characteristically, productive bone changes are lacking. Superior subluxation of the humeral head also can be seen, because chronic rotator cuff tear or cuff atrophy occurs frequently in patients with rheumatoid arthritis. The role of other imaging tests for rheumatoid arthritis is still evolving. US and MRI are more sensitive for detection of erosions and soft tissue findings. A role for these modalities may exist in early detection and for evaluation of disease activity or response to therapy. MRI can demonstrate erosions earlier than plain radiographs, along with subchondral cystic changes on both sides of the joint. Erosions are commonly located in the humeral head near the insertion of the rotator cuff tendons. MRI can also show common findings not identifiable in radiographs, such as joint effusion, signs of synovitis, tears or atrophy of the rotator cuff muscles and tendons, synovial cysts, bursitis, and rice bodies. Routine MRI is limited for evaluation of glenohumeral articular cartilage.

Adhesive Capsulitis

Also known as a "frozen shoulder," adhesive capsulitis is a commonly recognized but poorly understood disorder that causes severe shoulder pain, stiffness, and disability. Even though the diagnosis of this condition is made clinically, rather than on the basis of imaging findings, radiographs and other tests are often performed to exclude other conditions that can cause shoulder pain and to identify features that may support the diagnosis. Although most imaging is performed on a nonemergent basis, patients with adhesive capsulitis often present in an urgent care setting with significant shoulder pain.

Adhesive capsulitis is a synovitis that may be idiopathic or the result of other conditions, including multiple arthropathies and trauma. Pathologically, it is shown to be a synovial inflammation with preferential involvement of the rotator interval, axillary pouch, and subscapularis recess. Imaging findings parallel histologic findings. Radiographs are not contributory, as might be expected from the description of the underlying disease. Likewise, MRI examinations may show no abnormalities. Findings that support the diagnosis include synovial prominence at the rotator interval with obliteration of the subcoracoid fat, thickening of the coracohumeral and/or superior glenohumeral ligaments, and capsular thickening at the axillary pouch. After intravenous administration of gadolinium chelates, enhancement of the rotator interval and/or axillary recess may be demonstrated. MR arthrography has been advocated because of the added information obtained from estimating the volume of fluid necessary to achieve joint distention (typically decreased in adhesive capsulitis), and the potentially decreased capacity of the axillary pouch and bicipital tendon sheath. However, these findings have not been reproduced consistently, and added value from MR arthrography as a diagnostic tool for this condition is probably limited.

THE PAINFUL HIP

Similar to shoulder pain, evaluation of the painful hip in the absence of recognizable acute trauma is challenging and often a diagnostic quandary. Hip pain is also a very common source of emergent and nonemergent medical visits. The causes of hip pain are multiple, and pain

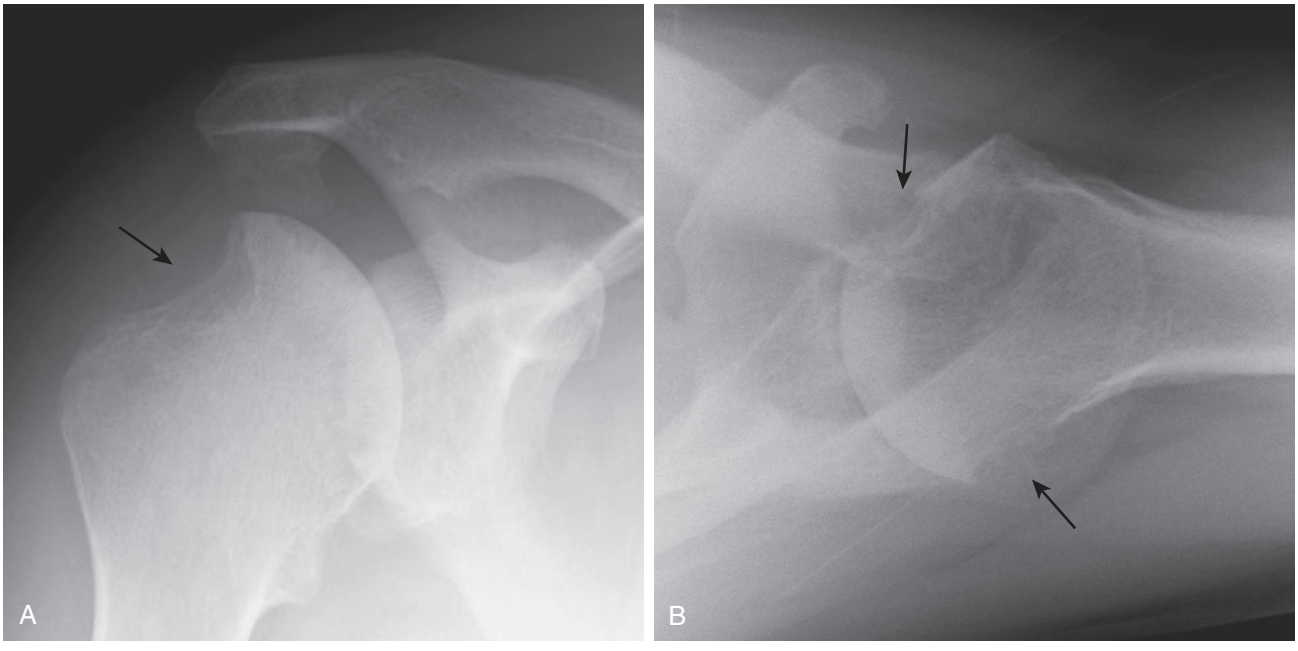


FIGURE 5-7 Rheumatoid arthritis of the glenohumeral joint. Anteroposterior (**A**) and axillary (**B**) views of the right shoulder demonstrate uniform joint space narrowing and large humeral head erosions *(arrows)*.

may be due to localized abnormalities in the soft tissues, synovium, cartilage, bone, or bone marrow, or it may come from distant causes, such as referred pain from the spine or knee. This section is dedicated to discussing the imaging features of the most common conditions presenting with hip pain, excluding infectious causes, which are described later in this chapter.

As with most other joints, the imaging evaluation of hip pain typically begins with conventional radiographs, even in the absence of a history of trauma. The routine examination should include an anteroposterior and a frog-leg lateral view of the hip along with an anteroposterior view of the pelvis. The view of the pelvis is essential for comparison with the opposite hip and for detection of subtle abnormalities. The anteroposterior view should be obtained with internal rotation to optimally evaluate the femoral neck. Unfortunately, most patients with hip pain tend to flex and externally rotate the hip for pain relief. This position tends to shorten the femoral neck and makes the evaluation more difficult. The frog-leg lateral radiograph is obtained with the hip in abduction and provides a tangential view of the anterior and posterior surfaces of the femoral head.

A systematic evaluation of the radiographs should begin with the soft tissues for swelling, displacement of fat pads, and calcifications. Overall bone alignment, including the acetabular coverage of the femoral head, should be assessed. The width of the symptomatic joint space, as well as symmetry with the contralateral hip, may provide clues about the presence of an articular process. The pattern of bone mineralization and trabeculation is also important. Finally, it is mandatory to carefully evaluate the radiographs for preservation of the pelvic lines and bony contours, particularly of the femoral neck.

Insufficiency Fractures

Insufficiency fractures are a type of stress fracture that occurs when a usual strength or physiologic force is applied to an abnormal or weakened bone. Most insufficiency fractures are caused by osteoporosis. In the pelvis, subcapital neck fractures (Fig. 5-8) are by far the most common. However, these fractures are usually associated with some degree of trauma. Common locations in the pelvis not usually associated with trauma include the sacrum, pubic rami, and supraacetabular region. Undisplaced insufficiency fractures are very difficult to diagnose on conventional radiographs. Good radiographic technique and a high index of suspicion, especially when evaluating demineralized bones, are essential. If a stress fracture is suspected clinically and radiographs are not diagnostic, an MRI examination should be obtained if available. MRI is more accurate than scintigraphy. Additionally, MRI may demonstrate coexisting conditions or alternative diagnoses that may influence management.

Radiographic findings may be occult or very difficult to detect and depend on the site of the fracture. Most commonly, a sclerotic band or line is evident. This finding is usually subtle and often is the only indication of a stress fracture. Evaluation for symmetry on the anteroposterior view of the pelvis is essential. Other potential findings include a fracture line, cortical disruption, and periosteal reaction. Supraacetabular insufficiency fractures should be considered in elderly women with hip pain and no history of trauma. Particular attention should be directed to the distinct trabecular pattern of the acetabulum. Dense trabeculae outline a more lucent triangular area immediately above the sclerotic acetabular roof. A band of sclerosis

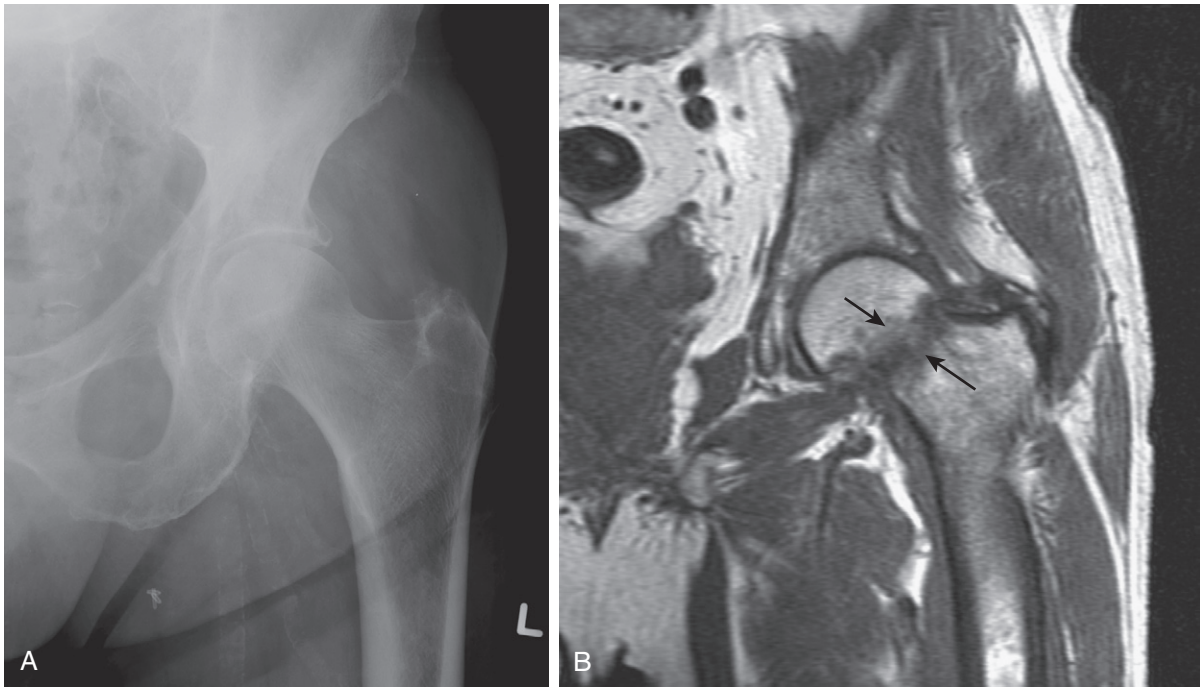


FIGURE 5-8 A radiographically occult insufficiency subcapital femoral neck fracture in a 74-year-old man presenting to the emergency department with left hip pain and no history of trauma. The anteroposterior view (**A**) of the left hip demonstrates mild demineralization of the bones but no evidence of fracture. A coronal T1-weighted image of the left hip (**B**) revealed an undisplaced subcapital femoral neck fracture characterized by a dark linear band *(arrows)*.

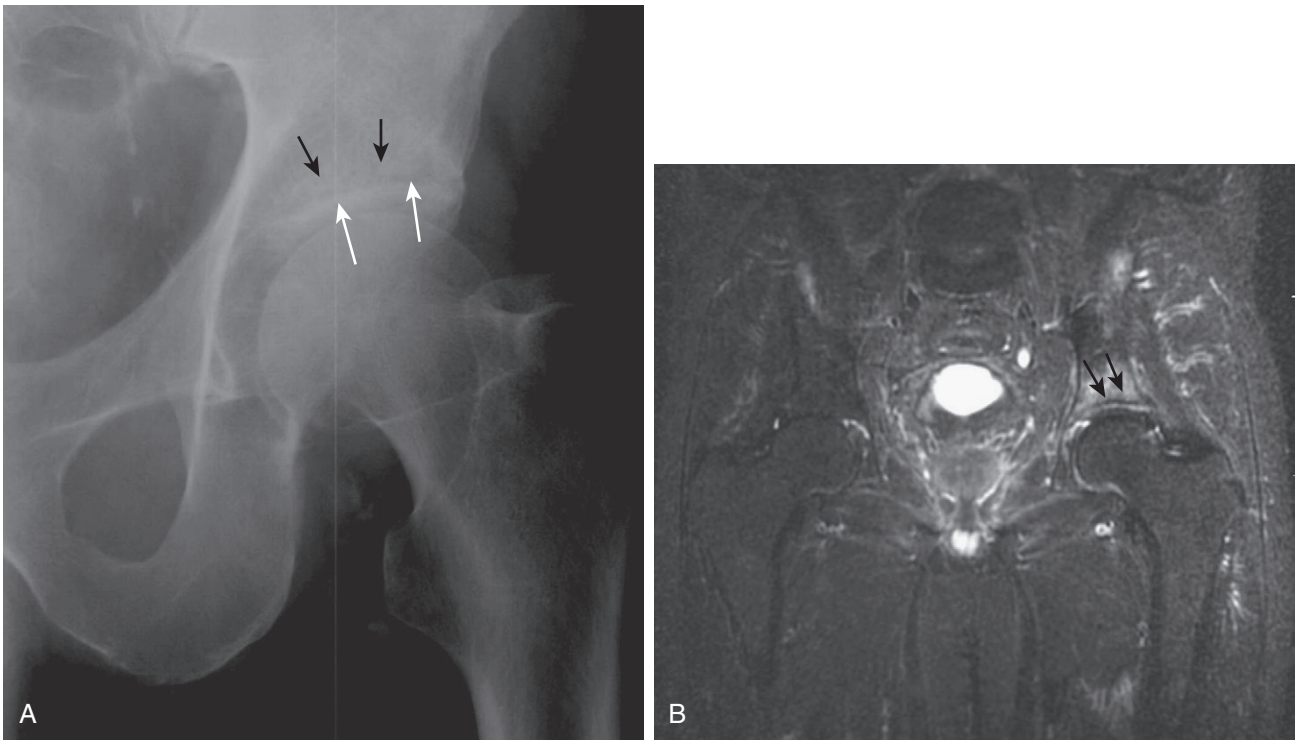


FIGURE 5-9 An insufficiency fracture of the left acetabulum in an elderly man with a history of prostate cancer, left hip pain, and no history of trauma. An anteroposterior radiograph of the left hip (**A**) demonstrates a band of sclerosis *(black arrows)* parallel and immediately superior to the sclerotic acetabular roof *(white arrows)*. A coronal short T1 inversion recovery image of the pelvis (**B**) reveals a bone marrow edema pattern and a low-signal line parallel and just superior to the acetabular roof *(arrows)*.

within this triangular lucent region, parallel to the roof of the acetabulum, is characteristic and should be diagnostic of a stress fracture in most cases (Fig. 5-9).

MRI is a highly sensitive and accurate tool for the diagnosis of insufficiency fractures. T1-weighted images may identify the fracture line itself as a serpiginous line of low signal intensity. On T2-weighted images with fat saturation and STIR sequences, the fracture line (high or low signal) may be obscured by the surrounding marrow edema in the acute setting. Linear low-signal intensity on both T1- and T2-weighted sequences located in the supraacetabular region running parallel to the acetabular roof is the characteristic finding of an insufficiency fracture (see Fig. 5-9).

Bone scintigraphy is also a sensitive modality for the diagnosis of insufficiency fractures. Often, however, it lacks specificity, demonstrating increased uptake of tracer in the area of fracture.

Transient Bone Marrow Edema and Transient Osteoporosis of the Hip

Transient bone marrow edema describes a painful condition of the hip that eventually resolves without treatment. Transient osteoporosis of the hip is a related condition in which, additionally, transient demineralization is evident radiographically. Some authors refer to these conditions interchangeably, whereas other authors (those who are more purist) treat them separately and reserve the term "osteoporosis" for cases in which demineralization is documented. It is unclear whether the high sensitivity of MRI for detecting marrow edema pattern enables the diagnosis of the same condition earlier, before demineralization is evident on radiographs. Transient osteoporosis was first described in pregnant women during the third trimester. It is now recognized more commonly in middle-aged men. Complete resolution of symptoms and imaging findings occurs an average of 6 months after onset. The condition may reappear in the same or other joints after a short interval, and the condition is then called "regional migratory bone marrow edema syndrome" or "regional migratory osteoporosis." The underlying cause of transient bone marrow edema is unknown. Many theories, including aborted osteonecrosis, synovitis, reflex sympathetic dystrophy, and occult trauma, have been proposed.

Transient bone marrow edema or osteoporosis of the hip remains a diagnosis of exclusion. Differential considerations for bone marrow edema affecting only the femoral side of the hip joint include fractures, osteonecrosis, osteomyelitis, and neoplasms.

Conventional radiographs are normal initially and, over time, show variable degrees of demineralization involving the femoral head and neck regions (Fig. 5-10, *A*). The acetabulum may occasionally be involved, but to a lesser degree. The joint space is preserved. Loss of the subchondral cortex of the femoral head is characteristic. Bone scintigraphy is abnormal before radiography. Increased, often extensive and homogeneous uptake is evident in the femoral head and neck (Fig. 5-10, *B*). MRI shows a bone marrow edema pattern in the head and neck of the femur, sometimes extending into the intertrochanteric region (Fig. 5-10, *C*). Mild involvement of the acetabulum is an inconsistent finding. Heterogeneous low-signal intensity on T1-weighted sequences and high signal intensity on fluid-sensitive sequences are noted.

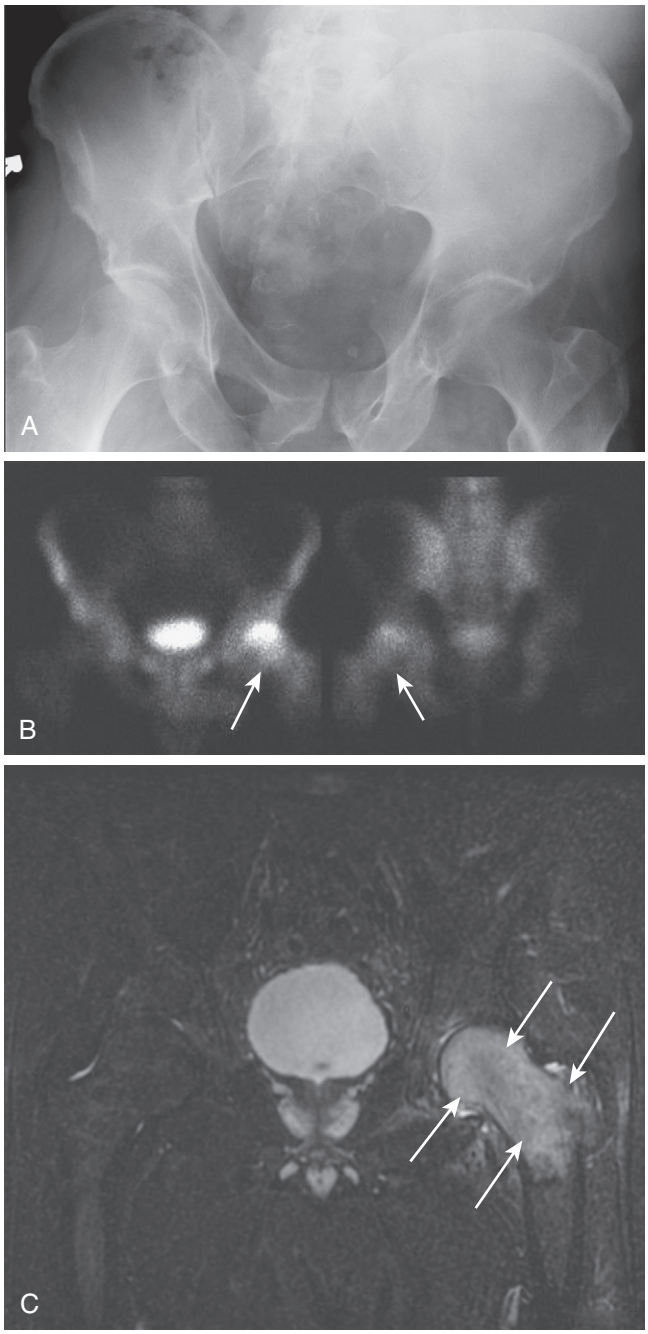


FIGURE 5-10 Transient osteoporosis of the hip in a 55-year-old man with sudden, severe onset of left hip pain. **A,** An anteroposterior view of the pelvis demonstrates demineralization of the left femoral head and neck. **B,** Anterior and posterior planar bone scintigraphy images of the pelvis demonstrate increased tracer uptake in the left femoral head and neck *(arrows)*. **C,** A coronal short T1 inversion recovery image of the pelvis reveals a diffuse bone marrow edema pattern involving the left femoral head and neck extending into the intertrochanteric region *(arrows)*.

A joint effusion is frequently present. The surrounding soft tissue and the contralateral side are normal.

Osteonecrosis of the Femoral Head

Avascular necrosis can be defined as ischemic necrosis of bone affecting the epiphyseal or subarticular locations. Histopathologic findings are identical to bone infarcts, but by convention the term "bone infarct" is reserved for ischemic necrosis occurring in the metaphyseal or diaphyseal locations. Osteonecrosis, a more descriptive term, can be used for any location. Potential causative factors are multiple and include trauma, medications (especially steroids), alcoholism, pancreatitis, hemoglobinopathies, radiation therapy, dialysis, hypercoagulable states, barotrauma, and storage diseases (such as Gaucher disease). Often, however, a specific predisposing factor cannot be identified (termed *idiopathic avascular necrosis*). Regardless of the cause, the patterns of bone injury, reactive response, and imaging findings are very similar.

TABLE 5-1 Osteonecrosis: Ficat Classification

Stage	Pain	Radiography
0	–	Normal
I	+	Normal
II	+	Cysts and/or sclerosis
III	++	Collapse ("crescent" sign, step-off in contour, flattening of articular surface)
IV	+++	Osteoarthrosis (joint space narrowing, acetabular disease)

Even though no universally satisfactory therapy exists for early stage disease, diagnosis of this entity before the joint is affected leads to an improved long-term prognosis. The Ficat classification, described in the 1980s, describes five stages based on clinical and radiographic findings (Table 5-1). Additional classification systems incorporating MRI findings have also been developed. Imaging plays a pivotal role for the diagnosis, the determination of prognosis, and planning of appropriate treatment. The size of the osteonecrosis lesion is an essential parameter for determining prognosis. The presence of bone collapse and joint involvement influences potential treatment options.

Initially, conventional radiographs are normal. In the reparative phase, both lytic and sclerotic areas are identified in the femoral head (Fig. 5-11, *A*). Next, a subchondral fracture may develop. This fracture manifests on radiographs as a subchondral crescent lucency (the "crescent" sign) and is best seen on the frog-leg lateral view (Fig. 5-11, *B*). As the disease progresses, subarticular collapse may follow, which is seen as a loss of the normal rounded contour and flattening of the femoral head (Fig. 5-11, *D*). Ultimately, severe collapse and destruction of the femoral head will lead to secondary osteoarthritis with joint space narrowing, osteophytes, subchondral cyst formation, and involvement of the acetabulum (Fig. 5-11, *C*).

MRI is more sensitive and specific than radiography and scintigraphy (Fig. 5-12). MRI provides an accurate estimation of the size of the lesion and demonstrates early subarticular collapse and secondary osteoarthritis. It is essential that the MRI examination include both hip joints, because osteonecrosis is bilateral in more than 50% of cases. The superoanteromedial quadrant of the femoral head is most frequently involved. A focal abnormality is seen, outlined by a low-signal intensity margin. This margin represents the reactive interface between necrotic and viable bone and extends to the subchondral bone. The characteristic "double line" sign is seen on T2-weighted images and consists of an inner rim or band of high signal intensity outlined by

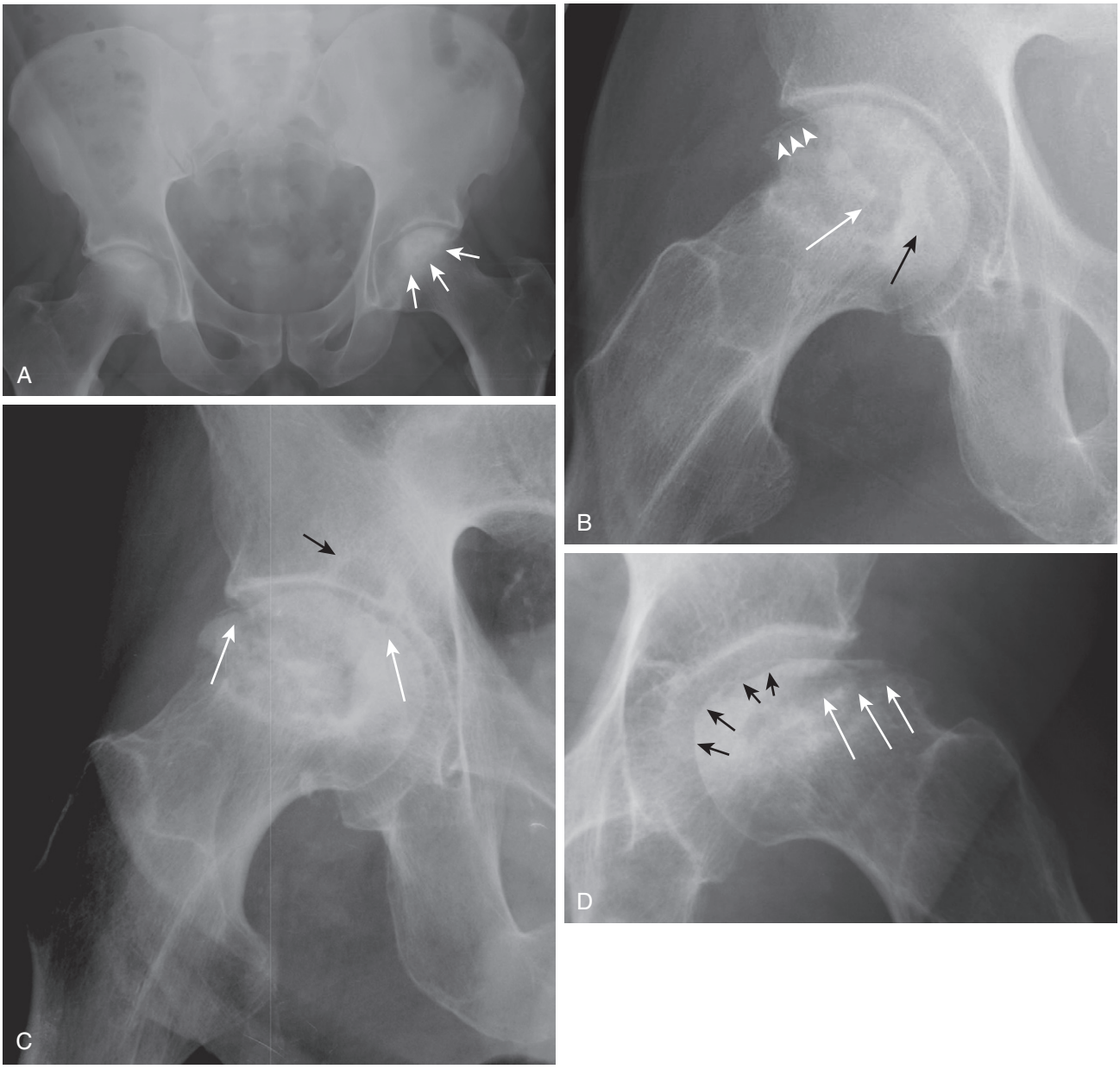


FIGURE 5-11 The radiographic spectrum of osteonecrosis of the femoral head. **A,** An anteroposterior radiograph of the pelvis in a patient with left hip pain demonstrates sclerosis of the left femoral head *(arrows)* and a radiographically normal-appearing right side. Magnetic resonance imaging (not shown) showed findings of osteonecrosis bilaterally (Ficat stage 0 on the right and stage II on the left). **B,** A frog-leg lateral view of the right hip in a different patient showing more advanced osteonecrosis with sclerotic *(black arrow)* and lytic *(white arrow)* areas, as well as a subchondral crescentic lucency *(arrowheads)* consistent with a subchondral fracture (Ficat stage III). **C,** A frog-leg lateral view of the right hip for the same patient as in part **B** 6 months later shows more advanced subarticular collapse with new loss of the normal rounded contour of the femoral head *(white arrows),* as well as joint space narrowing and involvement of the acetabulum (*black arrow*; Ficat stage IV). **D,** A frog-leg lateral view of the left hip in a different patient with advanced collapse of the femoral head *(black arrows)* also shows a subchondral fracture *(white arrows)* but preservation of the hip joint (Ficat stage III).

an outer low signal margin. A subchondral fracture appears as a high-signal subchondral crescent on fluid-sensitive sequences. Identification of subchondral collapse, when present, is crucial. Flattening of the articular surface is often seen earlier on the sagittal plane. The MRI appearance of late osteonecrosis with severe joint destruction is confusing and may be misinterpreted as neuropathic arthropathy or septic joint. Prior history and prior imaging are of utmost importance for making the differential diagnosis.

Arthropathies

Different types of arthropathies commonly affect the hip joint and can be the source of debilitating and acute pain. Imaging findings may be very subtle. When evaluating the hip joint for a possible arthropathy, the radiologist must carefully evaluate the width of the joint space. The joint space may be widened if a sizable joint effusion is present; this effusion is an important finding of septic arthropathy, which is discussed later in this chapter. Most arthropathies

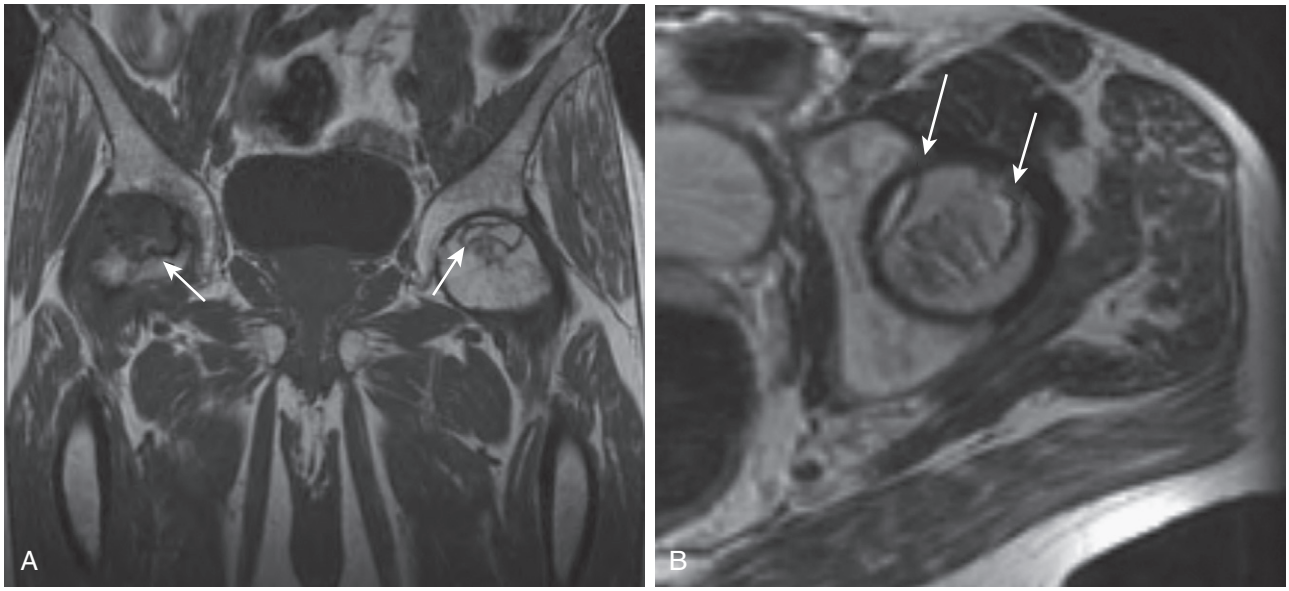


FIGURE 5-12 Magnetic resonance imaging spectrum of osteonecrosis of the femoral head. **A,** A T1-weighted coronal image of both hips demonstrates abnormal bone marrow signal in both femoral heads in a distribution pattern consistent with bilateral osteonecrosis. Note focal bone marrow abnormality outlined by a low signal margin *(arrows)*. **B,** The double line sign *(arrows)* on an axial T2-weighted image of the left hip. Linear increased signal is outlined by a dark signal characteristic of osteonecrosis.

cause joint space narrowing. The pattern of joint space narrowing provides clues for classifying the arthropathy and limiting the differential diagnosis. Uniform narrowing is typical of inflammatory arthropathies, whereas a nonuniform joint space narrowing is characteristic of degenerative arthropathy. Depositional arthropathies present with preservation of the joint space, but degenerative changes may ensue as the disease progresses, with consequent narrowing of the joint space. Conventional radiographs are usually sufficient to diagnose and categorize hip arthropathies. MRI may allow earlier detection of some articular findings and might be useful for evaluating the soft tissue findings that accompany some arthritides.

Osteoarthritis is by far the most common arthropathy affecting the hip. Nonuniform joint space narrowing most commonly occurs superiorly, with the femoral head migrating superomedially or, more commonly, superolaterally. Buttressing (thickening of bone) of the femoral neck is a characteristic but not pathognomonic finding. The classic findings of osteoarthritis—namely, marginal osteophytes, subchondral cyst formation, and eburnation—can also be found in the hip (Fig. 5-13, *A*). Occasionally, acetabular protrusio can be a result of osteoarthritis. In this condition, medial (rather than superior) migration of the femoral head occurs (Fig. 5-13, *B*). Other causes of protrusio include Paget disease, rheumatoid arthritis, osteomalacia, trauma, ankylosing spondylitis, radiation, and infection.

A particularly destructive but rare form of osteoarthritis can be seen with a rapid progression of disease, mainly in elderly persons. Awareness of rapidly destructive osteoarthritis is important to avoid misdiagnosis as a more aggressive or infectious arthropathy (Fig. 5-13, *C*). In osteoarthritis, MRI directly demonstrates loss of articular cartilage earlier than other modalities and also may identify synovial cysts. MRI is particularly useful in the differential diagnosis of osteoarthritis in cases with a confusing clinical presentation and nonspecific radiographic findings.

Rheumatoid arthritis can affect the hip joint and causes uniform joint space narrowing. Characteristic radiographic findings include bilateral and symmetric periarticular demineralization, erosions, and lack of proliferative changes (Fig. 5-14). Acetabular protrusion, if bilateral and symmetric, should favor the diagnosis of rheumatoid arthritis. Additional findings seen on MRI examinations include joint effusion, trochanteric or iliopsoas bursitis, tendon ruptures, pannus, and rice bodies.

The seronegative spondyloarthropathies commonly affect the hip joint. This group of joint conditions includes ankylosing spondylitis, reactive arthritis (e.g., Reiter syndrome), psoriatic arthritis, arthritis associated with inflammatory bowel disease, and undifferentiated spondyloarthropathies. The joint space appears uniformly narrowed with productive bone changes. Bone mineralization is relatively preserved. Enthesophytes (i.e., proliferative bone changes that occur at the insertions of ligaments and tendons) commonly occur. Late-stage complications include acetabular protrusion and ankylosis. Careful attention must be directed to the sacroiliac joints, which often reveal bilateral symmetric involvement in the presence of ankylosing spondylitis (Fig. 5-15) and unilateral or bilateral asymmetric involvement in the other spondyloarthropathies.

Other arthropathies that may involve the hip and may occasionally present with acute pain are synovial chondromatosis and pigmented villonodular synovitis (PVNS). These entities are proliferative diseases of the synovium characterized clinically by joint pain and limited motion. Radiographic appearance is similar for both, with pressure erosion usually along the neck of the femur, periarticular demineralization, and late joint space narrowing. Subchondral cystic changes favor PVNS. The intraarticular deposits of synovial osteochondromatosis often calcify, whereas those of PVNS typically do not calcify. MRI typically demonstrates the hemosiderin content on PVNS as focal areas of low signal in all imaging sequences. MRI findings on

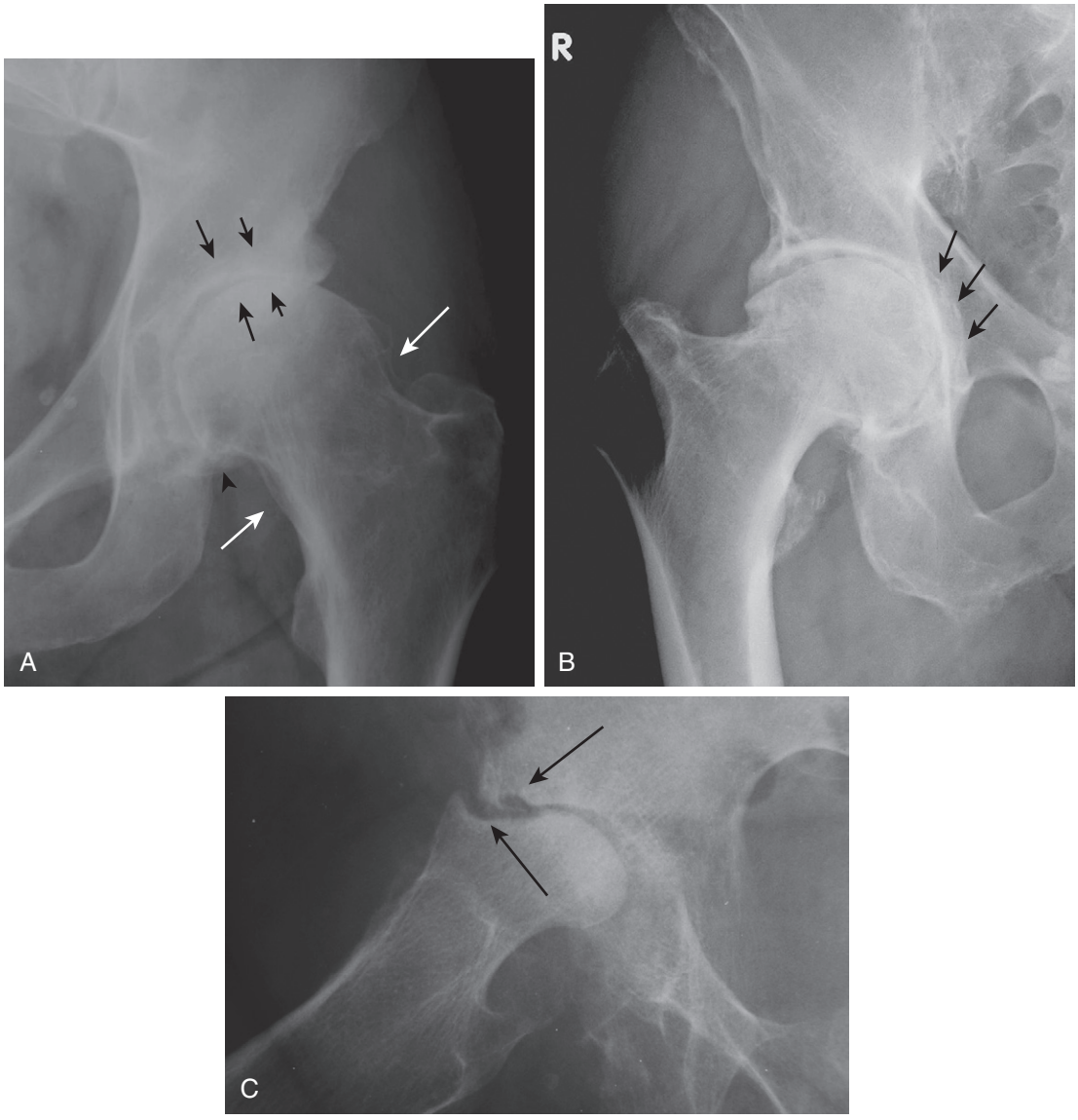


FIGURE 5-13 Osteoarthritis. **A,** An anteroposterior radiograph of the left hip with classic osteoarthritis manifested by nonuniform, superolateral hip joint narrowing, subchondral eburnation *(black arrows)*, marginal osteophytes *(arrowhead)*, and buttressing *(white arrows)*. **B,** An anteroposterior radiograph of the right hip in a patient with protrusio defined as intrapelvic displacement of the medial wall of the acetabulum *(arrows)*. **C,** Rapidly destructive osteoarthritis. A lateral frog-leg view of the right hip in a 72-year-old woman with severe right hip joint pain demonstrates rapidly progressing destruction compared with near-normal radiographs 6 months earlier (not shown). Note the destructive changes on both sides of the joint *(arrows)*.

synovial chondromatosis are variable depending on the degree of mineralization of the intraarticular deposits, but most commonly they reveal intraarticular areas of low to intermediate signal on T1-weighted images and very high signal on T2-weighted images with areas of hypointense calcifications. Similar radiographic and MRI findings can be expected with involvement of other joints with PVNS or synovial chondromatosis.

APPENDICULAR MUSCULOSKELETAL INFECTION

Musculoskeletal infection is a common clinical problem. Even though clinical and laboratory findings are of paramount importance, imaging always plays a critical role in the diagnosis and evaluation of the extent of the infectious process. Frequently, imaging identifies involvement of additional sites and other tissues that may not be evident clinically. Early detection and accurate determination of extension are essential to prescribe the appropriate treatment regimen, decrease morbidity, avoid complications, and improve prognosis. This section discusses the imaging features of infections involving the soft tissues, bones, and joints.

Conventional radiographs should always be performed initially despite the lack of sensitivity for soft tissue and early bone infection. The demonstration of bone involvement with radiographs may obviate the need for more expensive imaging tests in some cases. Radiographs may clarify confusing findings of other imaging modalities and may narrow potential differential diagnoses. US is a great tool for appendicular soft tissue infections. Sonography can

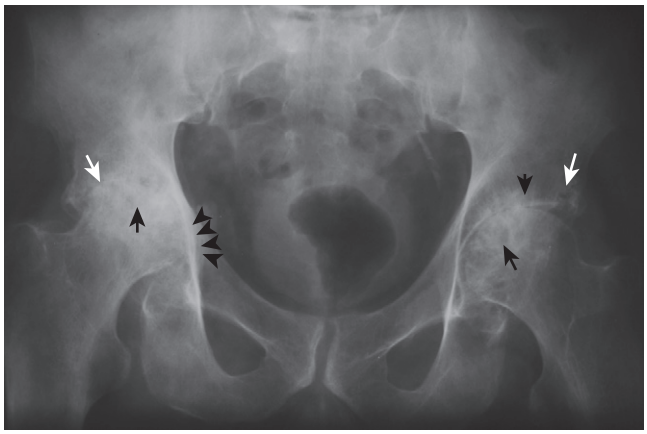


FIGURE 5-14 Rheumatoid arthritis with hip involvement. An anteroposterior radiograph of the pelvis demonstrates bilateral, symmetric, uniform joint space narrowing. The radiograph shows mild right protrusio *(arrowheads)*, erosions *(white arrows)*, and subchondral cystic changes *(black arrows)*.

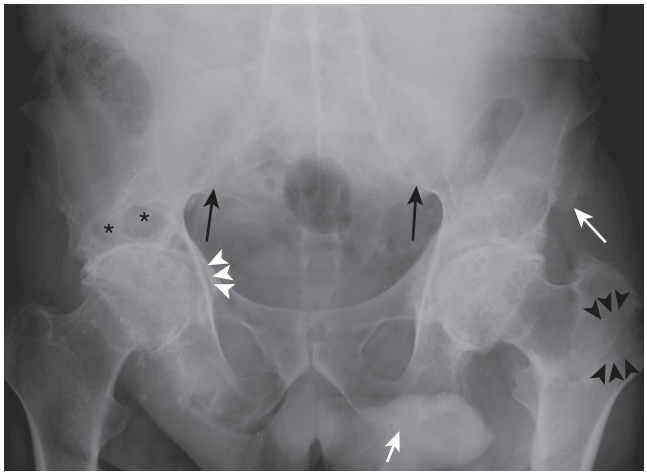


FIGURE 5-15 Ankylosing spondylitis in a 62-year-old patient presenting to the emergency department with an intertrochanteric fracture after a fall. An anteroposterior view of the pelvis demonstrates a mildly displaced left intertrochanteric fracture *(black arrowheads)*. Also note the symmetric, uniform joint space narrowing of the hips with large subchondral cystic changes *(asterisks)*, enthesophytes *(white arrows)*, ankylosis of the sacroiliac joints *(black arrows)*, and right acetabular protrusio *(white arrowheads)*.



FIGURE 5-16 Foot cellulitis. A lateral radiograph of the left *(L)* foot shows swelling, increased density, and gas *(black arrows)* within the plantar and dorsal soft tissues. Note an ulcer at the plantar aspect of the forefoot *(white arrow)*.

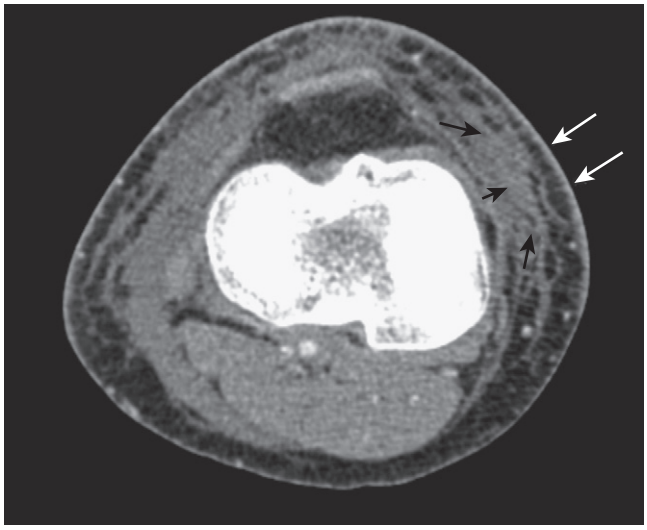


FIGURE 5-17 Leg cellulitis shown on a computed tomography (CT) image. An axial image at the level of the proximal tibia demonstrates skin thickening *(white arrows)*, septations, and inflammatory stranding of the subcutaneous fat *(black arrows)*. These findings, however, are nonspecific and may be seen in multiple conditions that cause subcutaneous edema. CT can demonstrate extension to the deeper tissues and formation of organized fluid collections (abscess).

be performed quickly, is readily available, and is highly sensitive for detecting fluid collections that often accompany focal infections. It also may be used to guide interventional procedures such as needle aspirations. The roles of CT and scintigraphy have decreased with the advent and wide use of MRI. MRI is far more sensitive than both CT and scintigraphy for early detection of soft tissue and bone infection.

Soft Tissue Infection

Cellulitis, an acute suppurative infection of the dermis and subcutaneous tissues, is usually the result of contiguous spread of infection from skin breakdown and is the initial step in the development of deep soft tissue infections. Findings on radiographs are minimal and nonspecific: increased soft tissue density, soft tissue swelling, and infiltration of the subcutaneous fat. Small radiolucent foci may be seen if gas is present (Fig. 5-16). CT may demonstrate thickening of the skin, subcutaneous tissues, and fascia (Fig. 5-17). US demonstrates increased echogenicity of the involved tissues and anechoic bands traversing the subcutaneous tissues, giving them a cobblestone appearance (Fig. 5-18). Findings on MRI are similar, with decreased T1-weighted signal and increased T2-weighted signal in the thickened and infiltrated skin, subcutaneous tissues, and fascia (Fig. 5-19). Enhancement is variable. In clinically confusing cases, the finding of intense enhancement favors the diagnosis of cellulitis rather than noninfectious causes of subcutaneous edema that otherwise could have the same imaging findings. Three-phase bone scintigraphy demonstrates increased blood flow (initial phase) and blood pool (early phase) activity. Delayed images (third phase) are normal or demonstrate only mild increased uptake of the involved soft tissues.

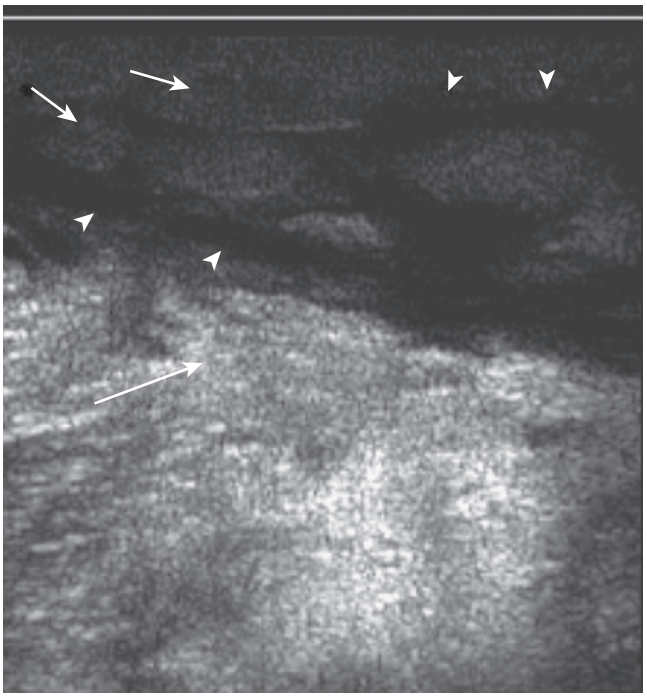


FIGURE 5-18 Leg cellulitis shown on an ultrasound image. A longitudinal image of the leg shows thickening and increased echogenicity of the subcutaneous tissues *(arrows)* with intermixed anechoic bands *(arrowheads)*, giving a cobblestone appearance.

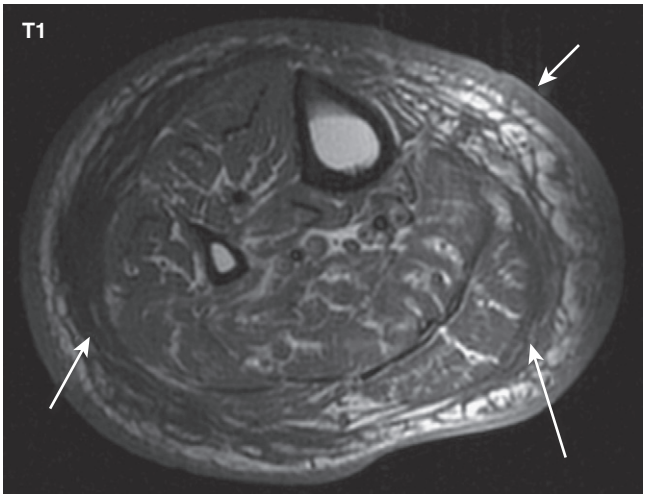


FIGURE 5-19 Leg cellulitis shown on a magnetic resonance image. A T1-weighted, fat-saturated image of the right lower extremity shows decreased signal in the thickened, infiltrated skin and subcutaneous tissues *(arrows)*.

Necrotizing fasciitis is a rare but very aggressive and often fatal condition characterized by necrosis of subcutaneous and deep fascial tissues. Patients with underlying conditions leading to decreased immunity, such as elderly persons, those with human immunodeficiency virus (HIV) infection and leukemia, drug abusers, alcoholics, and persons taking immunosuppressive medication, are all at increased risk of the development of this lethal disease. The infection is most commonly polymicrobial, with both aerobic and anaerobic organisms. The disease is a surgical emergency requiring fasciotomy and extensive debridement of the necrotic tissue. Rapid diagnosis and prompt surgical intervention are essential. Cellulitis has clinical and imaging characteristics similar to those of necrotizing fasciitis, but the treatment is not surgical. The clinical dilemma always lies between acting rapidly and waiting for imaging test results that may or may not be helpful. If imaging cannot be performed expeditiously, delaying surgical intervention is not justified. Radiographic and sonographic findings are similar to those of cellulitis but with more severe involvement (Fig. 5-20). The presence of soft tissue gas on radiographs is an ominous sign. Severe asymmetric thickening, with air and fluid collections, is the hallmark of necrotizing fasciitis on CT. However, this constellation of findings occurs inconsistently. CT often demonstrates nonspecific thickening and enhancement of the superficial and deep fascial layers. MRIs show thickening, high T2-weighted signal, and abnormal enhancement in the subcutaneous tissues and deep fascial planes. However, when necrosis is established, only minimal or peripheral enhancement surrounding the area of necrosis may be present. MRI overestimates the extent of deep fascial involvement compared with findings at the time of surgery. The absence of deep fascial involvement on MRI virtually excludes the diagnosis of necrotizing fasciitis.

An abscess is defined as a localized collection of pus (necrotic tissue, inflammatory debris, and bacteria). An earlier stage in the development of an abscess, before liquefaction and organization ensue, is called a *phlegmon*. An abscess can occur anywhere in the soft tissues, and when it is located in a skeletal muscle (which is relatively resistant to infection), the term *pyomyositis* is used. Radiographs may be noncontributory, showing only diffuse or focal increased soft tissue density, focal prominence of the affected soft tissues, and displacement of fat pads. The sonographic appearance of abscesses is variable. Most commonly, a complex hypoechoic, predominantly fluid-containing mass with increased through-transmission is identified. The margins of the mass may be well or ill defined, depending on the stage of evolution. Internal septations and amorphous internal echoes are additional common findings (Fig. 5-21). Often, dynamic evaluation of the area with gentle compression is necessary to reveal the liquid nature of the contents. Color or power Doppler demonstrates absent internal flow and hyperemia of the wall and adjacent tissues. CT reveals an organized low attenuation fluid collection with an enhancing wall of variable thickness (Fig. 5-22), internal septations, and high-attenuation internal foci. Surrounding edema or findings of cellulitis are common. MRI depicts abscesses and adjacent soft tissue changes to greater advantage (Fig. 5-23). Focal fluid collections demonstrating low or intermediate signal on T1-weighted sequences and high signal on T2-weighted sequences surrounded by reticulated, edematous soft tissue are characteristic. Administration of intravenous contrast material increases the conspicuity of the lesion with intense peripheral (wall) enhancement.

Infectious Arthritis

Infectious arthritis is a common clinical problem with devastating consequences if it is not diagnosed and treated early. Infectious arthritis is classified as pyogenic (septic) or nonpyogenic. Pyogenic causes are divided into gonococcal

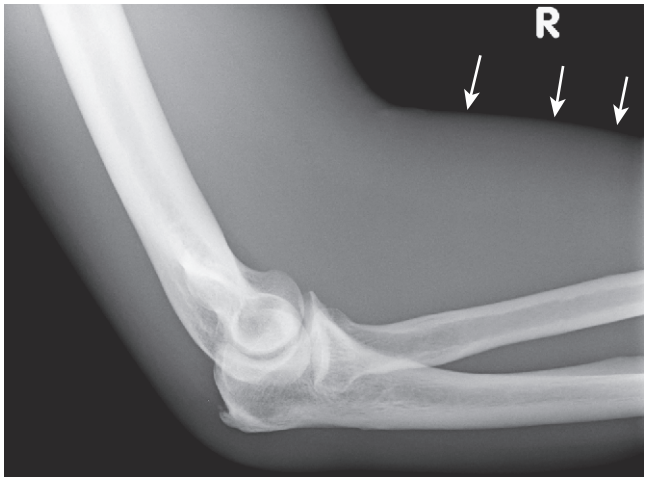


FIGURE 5-20 Forearm necrotizing fasciitis. A lateral radiograph of the elbow demonstrates nonspecific soft tissue swelling and increased soft tissue density *(arrows)*. Necrotizing fasciitis was found at surgery.

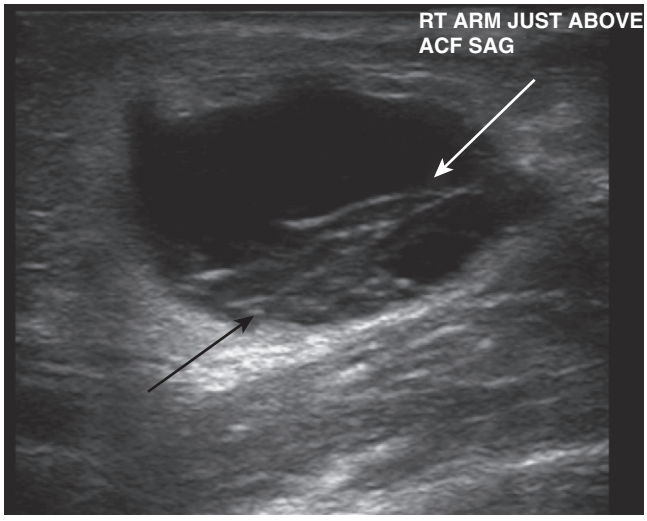


FIGURE 5-21 An arm abscess shown on an ultrasound (US) image. A single longitudinal US image of the right *(RT)* arm just superior to the antecubital fossa *(ACF)* in a patient with soft tissue infection demonstrates a complex, hypoechoic, predominantly cystic fluid collection with increased through-transmission internal septations *(white arrow)* and dependent debris *(black arrow)*. *SAG*, Sagittal.

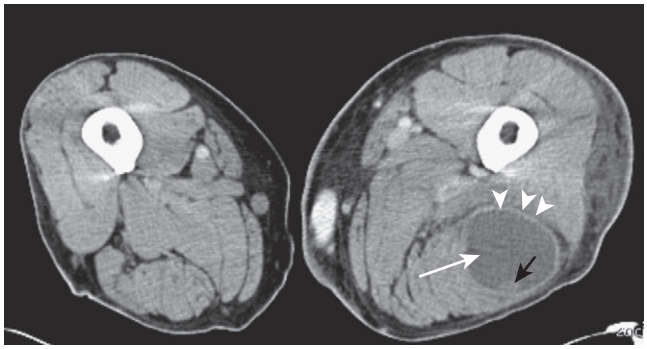


FIGURE 5-22 A computed tomography (CT) image of a posterior thigh abscess. An axial image of a contrast-enhanced CT scan of the thigh shows a well-defined low-attenuation fluid collection *(white arrow)* with a thick enhancing wall *(arrowheads)* and an internal focus of high attenuation *(black arrow)*.

and nongonococcal. Staphylococcus and streptococcus species are the most common pathogens causing nongonococcal septic arthritis. Nonpyogenic pathogens include mycobacteria, fungi, and viruses. Synovial involvement occurs first and may be the result of hematogenous spread, spread from a contiguous focus, direct implantation, or postsurgical contamination. Septic arthritis is monoarticular in the majority of cases and can affect any joint. The prevalence of the specific joint affected depends on the mechanism of infection and the patient population studied. Risk factors include advanced age, diabetes, underlying rheumatoid arthritis, recent joint surgery, presence of soft tissue infection, intravenous drug abuse, infection with HIV, and other immunosuppression states. Although the imaging findings of septic arthritis are discussed in this section, it should always be kept in mind that the most rapid and definitive test for making a diagnosis of septic arthritis is arthrocentesis and microbiologic evaluation of the aspirated joint fluid.

Early findings on conventional radiographs include periarticular demineralization, joint widening/effusion, and soft tissue swelling. Later, the following conditions may occur: joint space narrowing, periosteal reaction, erosions (both marginal and central), destruction of the subchondral bone, subluxations and dislocations, and, ultimately, ankylosis (Figs. 5-24 and 5-25). Intraarticular gas is a rare finding. The diagnosis of septic joint superimposed on known rheumatoid arthritis or other inflammatory arthropathy is very challenging. Infection should be suspected if widening of the joint space is present along with rapid articular destruction and significant soft tissue asymmetry.

Sonography is very sensitive for demonstrating a joint effusion and is an excellent tool for aspiration guidance. Synovial thickening is seen consistently in infectious and inflammatory arthropathies. Bone scintigraphy demonstrates increased blood flow, prominent blood pool, and increased delayed activity in the distribution of the affected joint. The use of gallium citrate as a marker of inflammation has been largely replaced by imaging with labeled leukocytes, either with indium-111 or technetium 99m hexamethylpropyleneamine oxime. Increased tracer uptake of these agents in the joint improves specificity for the diagnosis of infectious arthritis (see Fig. 5-24).

CT is rarely used for imaging patients with suspected joint infection, except for patients with orthopedic hardware. All findings described in conventional radiographs may be seen on CT, both more easily and earlier (see Fig. 5-24). Additionally, synovial thickening may be identified. Synovial and periarticular soft tissue enhancement is variable.

MRI is highly sensitive and more specific than other imaging modalities for the detection of septic arthritis. MRI easily demonstrates even a small joint effusion, which is often the first sign of an infected joint. However, an effusion does not necessarily indicate the presence of infection. Other MRI findings include synovial thickening and perisynovial edema, seen as periarticular areas of increased signal on fluid-sensitive sequences. Focal abnormal bone marrow signal in the adjacent bone is not diagnostic of superimposed osteomyelitis, because it may be a reactive change. The diagnosis of superimposed osteomyelitis is favored when the bone marrow signal abnormality is diffuse and is seen mostly as decreased signal on T1-weighted images.

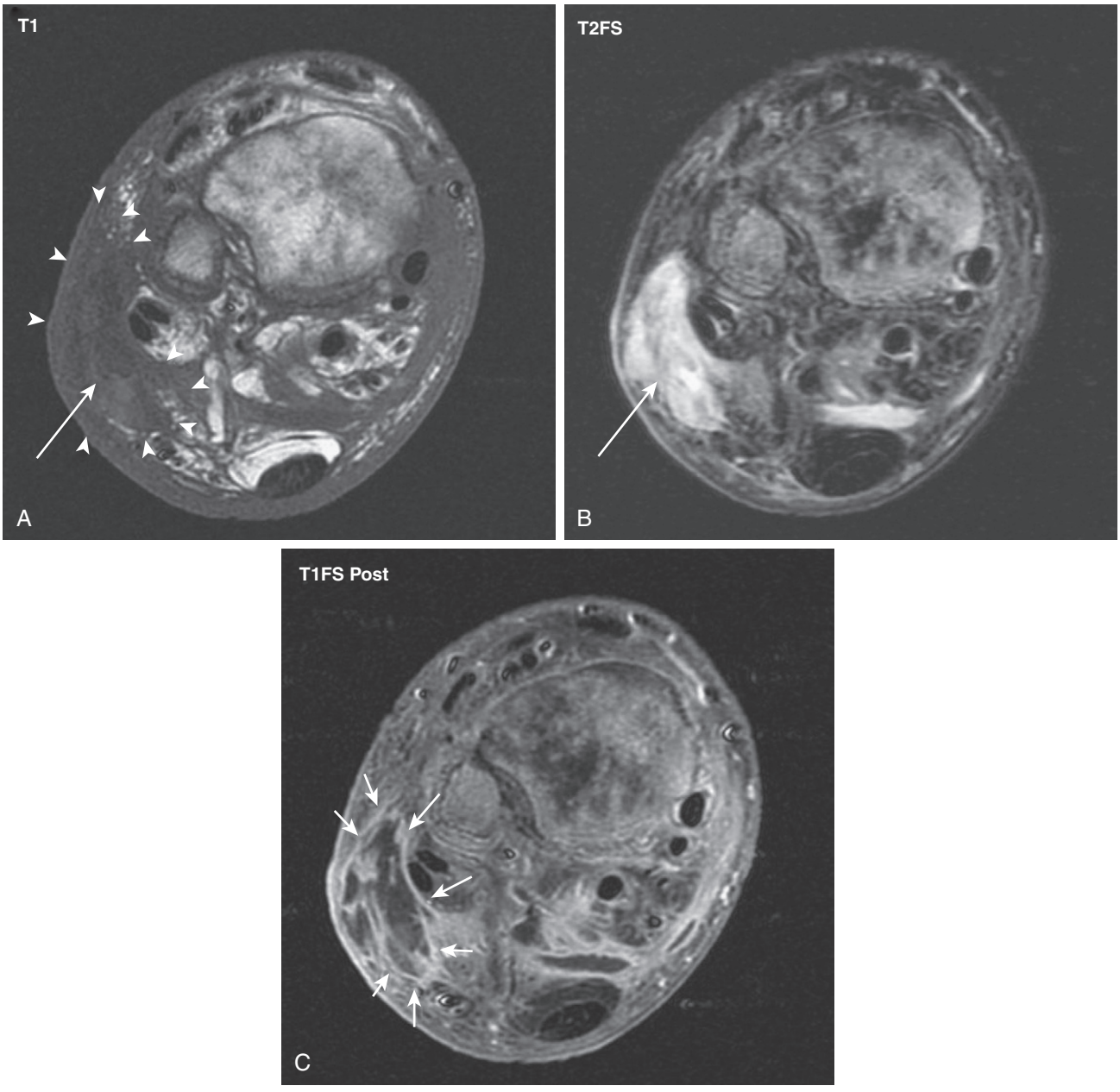


FIGURE 5-23 A subcutaneous abscess at the posterolateral ankle. T1-weighted (**A**), fat-suppressed T2-weighted (**B**), and fat-suppressed, postcontrast T1-weighted (**C**) axial images of the ankle demonstrate a focal complex fluid collection with heterogeneous foci of low T1-weighted and high T2-weighted signal (**A** and **B**, *arrows*). Note the peripheral enhancement (**C,** *arrows*) and adjacent edematous soft tissues (**A**, *arrowheads*).

After intravenous administration of gadolinium chelates, synovial and perisynovial soft tissue enhancement occurs. Intense synovial enhancement is not a normal finding in a healthy joint.

Acute Osteomyelitis

A proper use of pertinent terms is important when discussing imaging of osteomyelitis. Osteomyelitis indicates infectious involvement of the bone marrow. Infective osteitis is infection of the bone cortex and infective periostitis infection of the periosteum. These entities are often seen together, because the infectious process may extend outward from the marrow or inward from the soft tissues. As with infectious arthritis, multiple mechanisms can cause the inoculation of an infectious agent into the bone. Hematogenous spread is rarely the source of acute primary osteomyelitis in the adult appendicular skeleton. More commonly, osteomyelitis in the adult occurs from direct spread or surgery. Contiguous spread from ulcerations is most common in patients with foot ulcers (such as the diabetic foot), patients who sustained a spinal cord injury, and bedridden patients.

The overall sensitivity of conventional radiographs for early osteomyelitis is poor. The appearance of radiographic findings may be delayed for weeks after the initial infection. The earliest sign is usually swelling of the deep soft tissues. Early radiographic findings in the bone itself include focal demineralization and periosteal reaction. However, periosteal reaction may be absent in small bones, such as

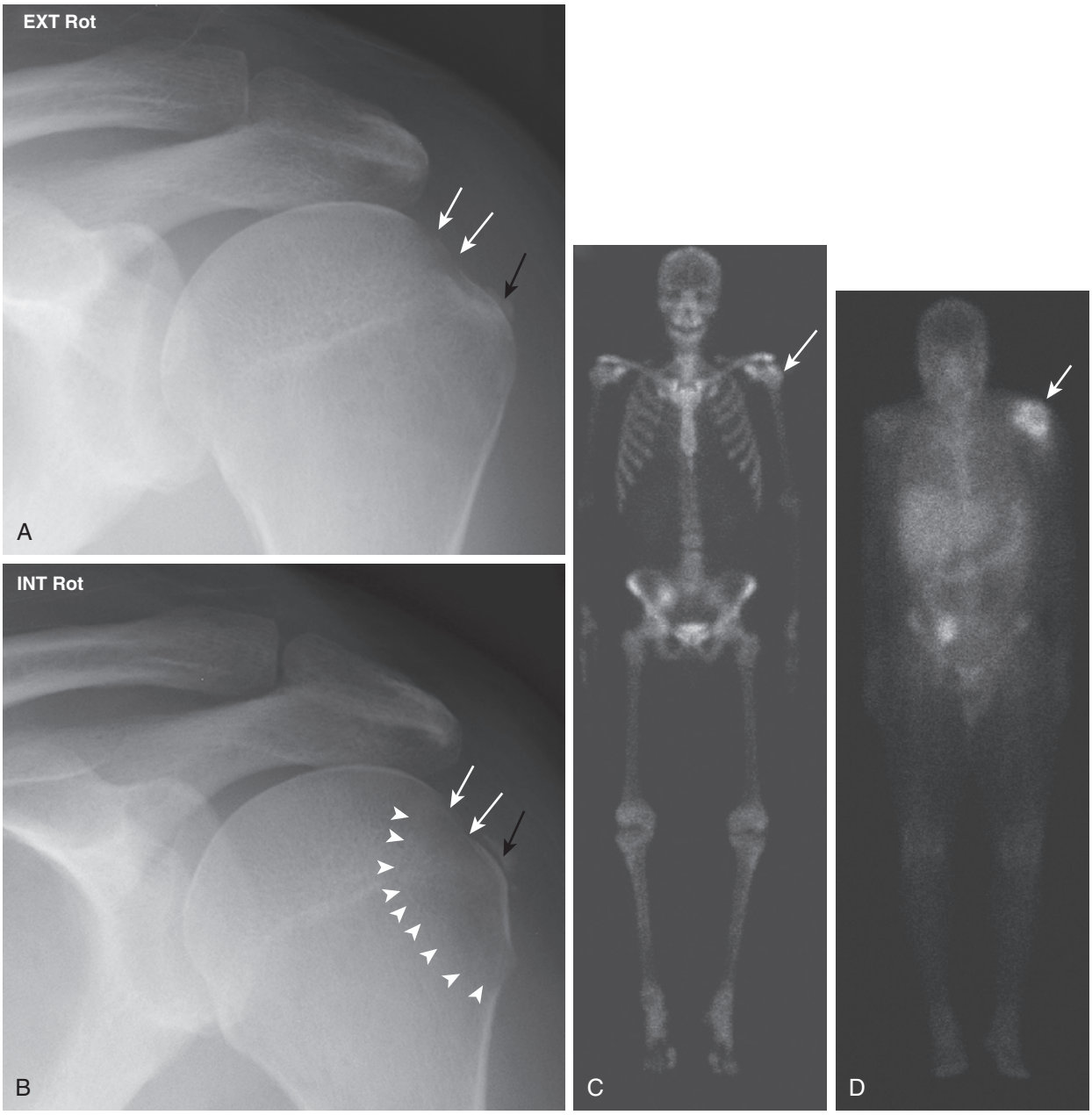


FIGURE 5-24 Septic arthritis of the left shoulder and humeral head osteomyelitis in a 36-year-old intravenous drug–addicted male patient presenting to the emergency department with left shoulder pain. External rotation *(EXT Rot)* (**A**) and internal rotation *(INT Rot)* (**B**) anteroposterior radiographs of the left shoulder show cortical irregularity and destruction of the subchondral bone *(white arrows)*, as well as well-demarcated focal osteopenia *(arrowheads)*. Incidental calcific bursitis is also noted *(black arrows)*. A total body anterior bone scintigram (**C**) and anterior total body gallium scan (**D**) demonstrate abnormal increased uptake in the left shoulder region *(arrows)*. Note that the extent of involvement is much greater in the gallium scan, suggesting additional involvement of the soft tissues.

those of the feet. Later, cortical lucency and frank bone destruction occur (see Fig. 5-25). Sonography is limited for the diagnosis of acute osteomyelitis. Deep soft tissue swelling, adjacent to the bone, may be seen, but this finding is nonspecific. A fluid collection immediately adjacent to the bone in the proper clinical setting is highly suggestive of osteomyelitis but is rarely observed. CT is helpful in select cases of acute osteomyelitis, although osseous findings may be detected to greater advantage and earlier than in radiographs. These findings include focal demineralization of the affected bone, cortical destruction, periosteal reaction, and hyperattenuation of the bone marrow. Soft tissue findings associated with osteomyelitis also can be demonstrated.

Three-phase bone scintigraphy is a highly sensitive test for the diagnosis of osteomyelitis. There is increased focal or regional uptake in the initial blood flow and early blood pool images. Focal increased activity in the affected area of the bone is noted on delayed images. A normal bone scan excludes the diagnosis of osteomyelitis, unless severe underlying vascular disease is present. Unfortunately, the specificity of bone scintigraphy is low, because many other

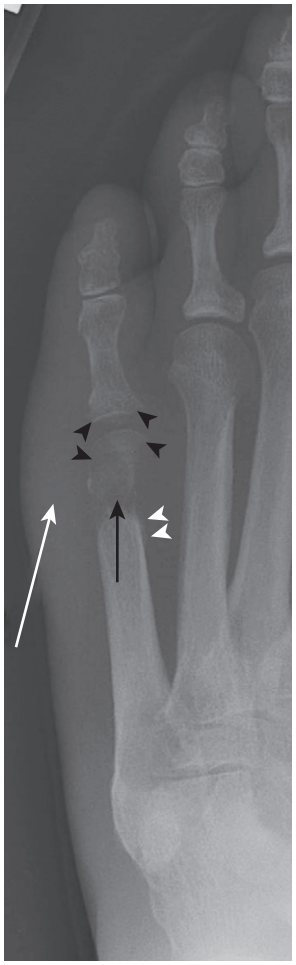


FIGURE 5-25 Osteomyelitis. An anteroposterior radiograph in a patient with diabetes with osteomyelitis of the left fifth metatarsal head and septic arthritis of the metatarsophalangeal joint demonstrates focal soft tissue swelling *(white arrow)*, focal demineralization *(black arrow)*, frank bone destruction, and minimal periosteal reaction *(white arrowheads)*. Note widening of the metatarsophalangeal joint and marginal erosions at both sides of the joint *(black arrowheads)*.

conditions, such as trauma, prior surgery, or underlying arthropathy, can present with similarly abnormal findings. Labeled white blood cell scintigraphy or a gallium scan may be performed in conjunction with a bone scan to increase specificity. Focal accumulation of radiotracer paralleling bone scan findings is consistent with osteomyelitis.

MRI is the imaging test of choice that should be obtained whenever osteomyelitis is suspected and radiographs show normal findings. Furthermore, MRI may be indicated even in the presence of abnormal radiographs for evaluation of extent of infection and for planning potential surgical interventions. MRI also may be helpful in limiting the differential diagnosis of patients with complex radiographic abnormalities or whenever the presence of underlying bone disease limits the specificity of plain radiographs. MRI findings of osteomyelitis can be divided into those affecting the osseous structures and those affecting the soft tissues.

Soft tissue findings are almost invariably seen in patients with osteomyelitis. Soft tissue findings include ulcers, sinus tracts, cellulitis, and abscess formation (Fig. 5-26). The MRI features of most of these conditions have already been described in this chapter. An ulcer presents on MRI as a cutaneous and soft tissue defect with granulation tissue at its base, which usually enhances avidly after administration of gadolinium chelates. Sinus tracts may extend outward from the bone to the superficial soft tissues and skin or inward from an ulcer toward the bone. Sinus tracts appear as linear areas of increased signal on fluid-sensitive sequences, but they are much more easily identified after contrast administration as parallel linear areas of enhancement in a "tram–track" pattern.

Osseous findings include abnormal bone marrow signal and enhancement, cortical interruption or destruction, and periosteal reaction. A focus demonstrating low signal intensity on T1-weighted sequences, high signal intensity on T2-weighted or STIR sequences, and enhancement is highly consistent with the diagnosis of osteomyelitis. However, these findings are not completely specific and should be analyzed in the context of the clinical presentation,

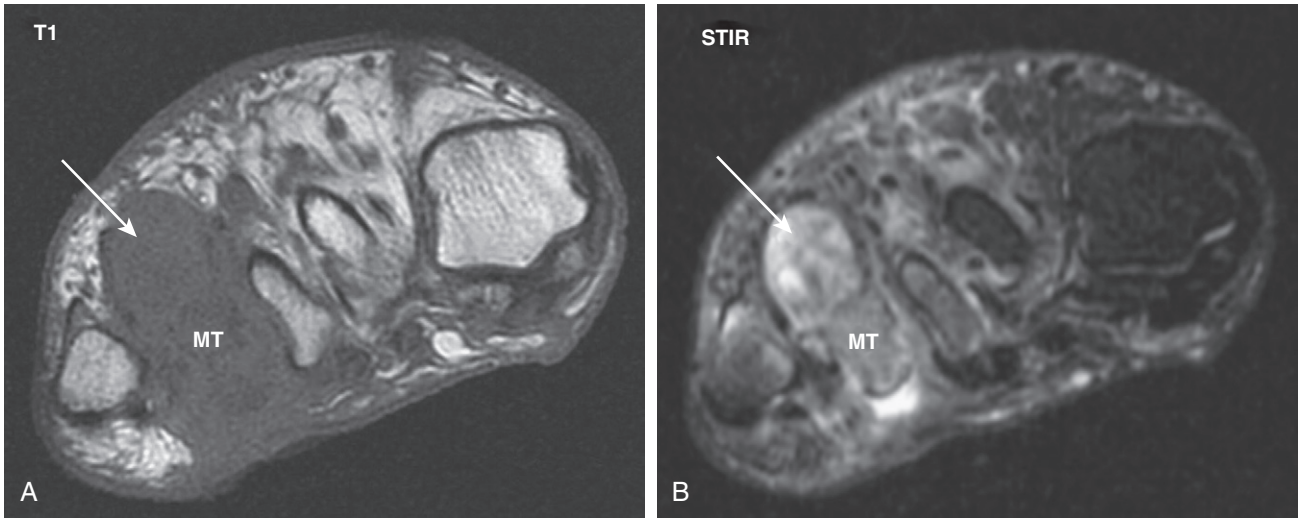


FIGURE 5-26 Osteomyelitis. Short axis T1-weighted (**A**) and short T1 inversion recovery (STIR) (**B**) magnetic resonance images of the forefoot reveal a periosteal abscess *(arrows)* at the fourth metatarsal head *(MT)* as a heterogeneous low T1-weighted and high STIR signal fluid collection. Note the replacement of the MT marrow signal consistent with osteomyelitis.

underlying osseous or articular disease, and soft tissue involvement. The negative predictive value of a normal STIR sequence is very high, approaching 100%. Periosteal reaction appears as a thin linear edema-like pattern and enhancement paralleling or surrounding the bone cortex.

Foreign Bodies

Puncture wounds and suspected retained foreign bodies (FBs) are a common cause of emergency department visits. Retained FBs are frequently overlooked initially, leading to inflammatory and infectious complications that are often severe, and thus prompt detection and removal are imperative. Precise localization of the object is extremely useful because it may minimize the extent of surgical dissection and shorten surgical time. A high clinical suspicion is always necessary, especially in patients with neuropathy who may be unaware of a prior puncture and present with a soft tissue infection (Fig. 5-27, *A* and *B*). Wood, glass, and metal account for the vast majority of retained FBs encountered. On conventional radiographs, metal is almost always visible. Glass is seen radiographically in more than 90% of cases. On the other hand, wood is identified in only a minority of patients (approximately 15% or less).



FIGURE 5-27 A foreign body in the right hand. An adult patient with diabetes presented to the emergency department with a red and swollen right hand after working in his garden. An anteroposterior radiograph at initial presentation (**A**) shows soft tissue swelling and diffuse increased density in the region of the thenar eminence *(arrow)*. An anteroposterior radiograph of the hand 8 weeks later (**B**), obtained after a second visit to the emergency department for worsening swelling and erythema, demonstrates periosteal reaction *(white arrows)* and sclerosis *(black arrows)* of the second metacarpal bone. No radio-opaque foreign body was identified. A transverse ultrasound image (**C**) shows a linear hyperechoic foreign body *(arrows)* adjacent to the second metacarpal (MC) with posterior shadowing and a surrounding hypoechoic rim *(arrowheads)*. An axial short T1 inversion recovery image (**D**) of the right hand demonstrates the foreign body *(arrow)* as a low-signal structure surrounded by a rim of high signal, adjacent to the second metacarpal bone. At surgery, a thorn was extracted.

Ultrasound is highly sensitive and specific in the detection of retained FBs. US can be performed rapidly, is inexpensive and accessible, and does not entail use of ionizing radiation. It should be the modality of choice for radiographically occult FBs in the superficial soft tissues. All FBs are hyperechoic with acoustic posterior shadowing (see Fig. 5-27, *C*). The degree of acoustic shadowing is variable and depends on the surface characteristics rather than the composition of the FB. Flat, smooth surfaces often encountered in metal and glass produce a reverberation artifact or "dirty" shadowing, whereas irregular surfaces usually produce "clean" shadowing. Sonographic detection may be enhanced by the presence of a hypoechoic rim surrounding the FB. This rim may be seen after at least 24 hours, when an inflammatory reaction has developed. US also allows examination of the surrounding tissues for infectious complications and associated soft tissue injuries.

MRI is rarely used in the acute setting for the detection of FBs. More commonly, FBs may be detected incidentally on MRI scans performed for the workup of musculoskeletal infection. Foreign bodies exhibit low signal intensity on all pulse sequences and may show magnetic susceptibility artifact. Conspicuity on MRI depends on size, location, and composition. Small FBs are difficult to distinguish from adjacent low-signal structures such as tendons, scars, and calcifications. Foreign objects may incite an inflammatory reaction, seen as surrounding areas of low signal intensity on T1-weighted images and high signal intensity on T2-weighted images. MRI is highly accurate for identifying infectious musculoskeletal complications (see Fig. 5-27, *D*). Not infrequently, small FBs may become chronically embedded within the soft tissues and form foreign body granulomas. These lesions generate variable degrees of inflammatory response but often present with little or no T2-weighted signal changes. They should be suspected when an area of magnetic susceptibility or signal void with peripheral enhancement is noted.

Infected Orthopedic Hardware

Important improvements have occurred in orthopedic surgical technique and preoperative and postoperative care, leading to a considerable decrease in overall postsurgical infections. The frequency of hardware infections has been reduced from nearly 10% in the early years to somewhere between 0.5% and 2% currently. Nonetheless, postoperative infection continues to be an important cause of morbidity and mortality. Prompt detection and localization of hardware infection are essential for appropriate patient management and to avoid even more serious consequences.

Approximately one third of arthroplasty-related infections occur within the first 3 months after the operation. The remainder occur beyond this period and are considered late infections. Late infections are more indolent and can be difficult to diagnose. Differentiating between late infection and other causes of hardware failure is challenging clinically, radiographically, and histopathologically. In most (but not all) cases, the diagnosis of hardware infection is made by isolating organisms from the fluid or tissues around the hardware. Occasionally, organisms are not found around hardware that is later proven to be infected. Pain, increased white cell count, elevated C-reactive protein, and increased erythrocyte sedimentation rate are often present but lack specificity in the postoperative period. Clinicians must utilize a combination of clinical, laboratory, and imaging data to confirm or exclude the diagnosis of hardware infection. Imaging plays an important role and helps guide the clinical management of these patients.

Radiographs should be performed initially for suspected hardware infection. Most often, there are no radiographic findings suggestive of infection, especially in the patients with acute presentations. Radiographic findings include periosteal reaction, osteolysis, cortical irregularity, erosions, and frank bone destruction. Chronic infections can produce areas of bone sclerosis. Additionally, radiographs may serve to suggest or exclude other causes of postoperative pain and hardware failure. The temporal evolution is extremely useful when prior radiographs are available. Rapid development of the previously discussed radiographic abnormalities should be viewed as highly suspicious for infection. Cross-sectional imaging studies such as CT and MRI can also help when evaluating potentially infected hardware. Unfortunately, image quality with both modalities is degraded by the presence of metallic hardware. With the advent of multidetector CT, the severity of beam hardening artifact from metal has been reduced. CT exquisitely depicts osseous findings of hardware infection: periosteal reaction, cortical erosion, cortical tracts, osseous fistulae, bony sequestrae, and areas of osteolysis. MRI depicts the soft tissue findings to greater advantage.

Radionuclide imaging plays an important role in the evaluation of orthopedic hardware infection and is used in many centers as the second line of imaging after radiographs. Multiple radionuclides have been used for the detection of musculoskeletal infection, and all show areas of increased tracer activity in the infected tissue, albeit via different mechanisms of uptake. Nuclear scintigraphy studies currently being used for the detection of musculoskeletal infection include technetium 99m methylene diphosphonate (MDP), radionuclide-labeled white blood cells (WBCs), and gallium-67 citrate imaging. More recently, fluorodeoxyglucose F 18 positron emission tomography (FDG PET) has emerged as an alternative for imaging infection and inflammation.

Technetium 99m MDP localizes in areas of increased bone turnover. The sensitivity of bone scintigraphy is very high, and the lack of accumulation virtually excludes bone infection. The overall specificity for bone infection is low, and it is even worse in the postoperative period when bone uptake related to the surgical procedure itself can be seen to variable degrees within the first year, which is also when most infections occur. Additionally, uptake may be abnormally high in persons with multiple noninfectious postoperative complications.

Radionuclide-labeled WBCs can be performed using indium-111 or technetium 99m hexamethylpropyleneamine. These tracers accumulate in areas of neutrophil-mediated inflammation and infection. The sensitivity is similar to and the specificity is better than that of bone scintigraphy. Labeled WBC scans are more useful for acute hardware infections than for chronic, low-grade cases. In the past, gallium-67 citrate was a popular agent used to image infection, although the mechanism of tracer localization in infection is poorly understood. In view of the lower accuracy, unfavorable imaging characteristics,

and long wait prior to imaging, gallium has been largely replaced by other agents. Although initial reports suggested that FDG PET could differentiate between infection and other causes of hardware failure (specifically aseptic loosening), more recent data are less convincing. Advantages of FDG PET compared with other modalities include faster imaging times, higher spatial resolution, and increased sensitivity for low-grade infections. Cost and availability also limit its utilization.

SUGGESTED READINGS

Ahmadi ME, Morrison WB, Carrino JA, et al. Neuropathic arthropathy of the foot with and without superimposed osteomyelitis: MR imaging characteristics. *Radiology*. 2006;238:622–631.

Anderson MW, Brennan C, Mittal A. Imaging evaluation of the rotator cuff. *Clin Sports Med*. 2012;31:605–631.

Andrews CL. From the RSNA refresher courses: evaluation of the marrow space in the adult hip. *Radiographics*. 2000;20(suppl):S27–S42.

Bauer TW, Parvizi J, Kobayashi N, Krebs V. Diagnosis of periprosthetic infection. *J Bone Joint Surg Am*. 2006;88:869–882.

Berquist TH. Imaging of joint replacement procedures. *Radiol Clin North Am*. 2006;44:419–439.

Bigliani LU, Levine WN. Current concepts review: subacromial impingement syndrome. *J Bone Joint Surg Am*. 1997;79:1854–1868.

Bigoni BJ, Chung CB. MR imaging of the rotator cuff interval. *Magn Reson Imaging Clin North Am*. 2004;12:61–73.

Bock GW, Garcia A, Weisman MH, et al. Rapidly destructive hip disease: clinical and imaging abnormalities. *Radiology*. 1993;186:461–466.

Boyse TD, Fessell DP, Jacobson JA, et al. US of soft tissue foreign bodies and associated complications with surgical correlation. *Radiographics*. 2001;21:1251–1256.

Brower AC, Kransdorf M. Imaging of hip disorders. *Radiol Clin North Am*. 1990;28:955–974.

Bureau NJ, Chhem RK, Cardinal E. Musculoskeletal infections: US manifestations. *Radiographics*. 1999;19:1585–1592.

Cahill BR. Osteolysis of the distal part of the clavicle in male athletes. *J Bone Joint Surg Am*. 1982;64:1053–1058.

Chen AL, Joseph TN, Zuckerman JD. Rheumatoid arthritis of the shoulder. *J Am Acad Orthop Surg*. 2003;11:12–14.

Connell D, Padmanabhan R, Buchbinder R. Adhesive capsulitis: role of MR imaging in differential diagnosis. *Eur Radiol*. 2002;12:2100–2106.

Cooper KL, Beabout JW, McLeod RA. Supraacetabular insufficiency fractures. *Radiology*. 1985;157:15–17.

del Cura JL, Torre I, Zabala R, Legorburu A. Sonographically guided percutaneous needle lavage in calcific tendonitis of the shoulder: short- and long-term results. *AJR Am J Roentgenol*. 2007;189:W128–W134.

Erdman WZ, Tamburro F, Jayson HT, et al. Osteomyelitis: characteristics and pitfalls of diagnosis with MR imaging. *Radiology*. 1991;180:533–539.

Erickson SJ, Kneeland JB, Komorowski RA, et al. Post-traumatic osteolysis of the clavicle: MR features. *J Comput Assist Tomogr*. 1990;14:835–837.

Fang C, Teh J. Imaging of the hip. *Imaging*. 2003;15:205–216.

Fayad LM, Carrino JA, Fishman EK. Musculoskeletal infection: role of CT in the emergency department. *Radiographics*. 2007;27:1723–1736.

Fridman R, Bar-David T, Kamen S, Leung DK, Rasiej MJ. Imaging of diabetic foot infections. *Clin Podiatr Med Surg*. 2014;31:43–56.

Fugitt JB, Puckett ML, Quigley MM, Kerr SM. Necrotizing fasciitis. *Radiographics*. 2004;24:1472–1476.

Hayes CW, Conway WF. Calcium hydroxyapatite deposition disease. *Radiographics*. 1990;10:1031–1048.

Hayes CW, Conway WF, Daniel WW. MR imaging of bone marrow edema pattern: transient osteoporosis, transient bone marrow edema syndrome or osteonecrosis. *Radiographics*. 1993;13:1001–1011.

Jordan LK, Kenter K, Griffiths HL. Relationship between MRI and clinical findings in the acromioclavicular joint. *Skeletal Radiol*. 2002;31:516–521.

Karachalios T, Karantanas AH, Malizos K. Hip osteoarthritis: what the radiologist wants to know. *Eur J Radiol*. 2007;61:36–48.

Karantanas AH. Acute bone marrow edema of the hip: role of MR imaging. *Eur Radiol*. 2007;17:2225–2236.

Karchevsky M, Schweitzer ME, Morrison WB, Parellada JA. MRI findings of septic arthritis and associated osteomyelitis in adults. *AJR Am J Roentgenol*. 2004;182:119–122.

Kassarjian A, Bencardino JT, Palmer WE. MR imaging of the rotator cuff. *Magn Reson Imaging Clin North Am*. 2004;12:39–60.

Kassarjian A, Llopis E, Palmer WE. Distal clavicular osteolysis: MR evidence for subchondral fracture. *Skeletal Radiol*. 2007;36:17–22.

Levine AH, Pais MJ, Schwartz EE. Posttraumatic osteolysis of the distal clavicle with emphasis on early radiologic changes. *AJR Am J Roentgenol*. 1976;127:781–784.

Love C, Thomas MB, Tronco GG, Palestro CJ. FDG PET of infection and inflammation. *Radiographics*. 2005;25:1357–1368.

Malizos KN, Karantanas AH, Varitimidis SE, et al. Osteonecrosis of the femoral head: etiology, imaging and treatment. *Eur J Radiol*. 2007;63:16–28.

Manaster BJ. From the RSNA refresher courses. Adult chronic hip pain: radiographic evaluation. *Radiographics*. 2000;20(suppl):S3–S25.

Manton GL, Schweitzer ME, Weishaupt D, Karasick D. Utility of MR arthrography in the diagnosis of adhesive capsulitis. *Skeletal Radiol*. 2001;30:326–330.

Mengiardi B, Pfirrmann CW, Gerber C, et al. Frozen shoulder: MR arthographic findings. *Radiology*. 2004;233:486–492.

Miller TT. Imaging of hip arthroplasty. *Eur J Radiol*. 2012;81:3802–3812.

Mitchell M, Howard B, Haller J, et al. Septic arthritis. *Radiol Clin North Am*. 1988;26:1295–1313.

Moosikasuwan JB, Miller TT, Burke BJ. Rotator cuff tears: clinical, radiographic and US findings. *Radiographics*. 2005;25:1591–1607.

Morag Y, Jacobson JA, Miller B, et al. MR imaging of rotator cuff injury: what the clinician needs to know. *Radiographics*. 2006;26:1045–1065.

Morrison WB, Ledermann HP. Work-up of the diabetic foot. *Radiol Clin North Am*. 2002;40:1171–1192.

Ohashi K, El-Khoury G, Bennett DL, et al. Orthopedic hardware complications diagnosed with multi-detector row CT. *Radiology*. 2005;237:570–577.

Otte MT, Helms CA, Fritz RC. MR imaging of supra-acetabular insufficiency fractures. *Skeletal Radiol*. 1997;26:279–283.

Peh WC, Khong PL, Yin Y, et al. Imaging of pelvic insufficiency fractures. *Radiographics*. 1996;16:335–348.

Peterson JJ, Bancroft LW, Kransdorf MJ. Wooden foreign bodies: imaging appearance. *AJR Am J Roentgenol*. 2002;178:557–562.

Rahmouni A, Chosidow O, Mathieu D, et al. MR imaging in acute infectious cellulitis. *Radiology*. 1994;192:493–496.

Rogers LF, Hendrix RW. The painful shoulder. *Radiol Clin North Am*. 1988;26:1359–1371.

Sadro C. Current concepts in magnetic resonance imaging of the adult hip and pelvis. *Semin Roentgenol*. 2000;35:231–248.

Siegel DS, Wu JS, Del Cura JL, Hochman MG. Calcific tendinitis: a pictorial review. *Can Assoc Radiol J*. 2009;60:263–272.

Steinbach LS. Rotator cuff disease. In: Steinbach LS, Tirman PFJ, Peterfy CG, Feller JF, eds. *Shoulder Magnetic Resonance Imaging*. Philadelphia, PA: Lippincott Williams & Wilkins; 1988:99–133.

Steinberg DR, Steinberg ME, Garino JP, et al. Determining lesion size in osteonecrosis of the femoral head. *J Bone Joint Surg Am*. 2006;88(suppl 3):S27–S34.

Stiles RG, Otte MT. Imaging of the shoulder. *Radiology*. 1993;188:603–613.

Strobel K, Pfirrmann CW, Zanetti M, et al. MRI features of the acromioclavicular joint that predict pain relief from intraarticular injection. *AJR Am J Roentgenol*. 2003;181:755–760.

Tamai K, Akutsu M, Yano Y. Primary frozen shoulder: brief review of pathology and imaging abnormalities. *J Orthop Sci*. 2014;19:1–5.

Tang JS, Gold RH, Bassett LW, Seeger LL. Musculoskeletal infection of the extremities: evaluation with MR imaging. *Radiology*. 1988;166:205–209.

Tehranzadeh J, Wong E, Wang F, Sadighpour M. Imaging of osteomyelitis in the mature skeleton. *Radiol Clin North Am*. 2001;39:223–250.

Turecki MB, Taljanovic MS, Stubbs AY, et al. Imaging of musculoskeletal soft tissue infections. *Skeletal Radiol*. 2010;39:957–971.

Turpin S, Lambert R. Role of scintigraphy in musculoskeletal and spinal infections. *Radiol Clin North Am*. 2001;39:169–189.

Watson RM, Roach NA, Dalinka MK. Avascular necrosis and bone marrow edema syndrome. *Radiol Clin North Am*. 2004;42:207–219.

Weishaupt D, Schweitzer ME. MR imaging of septic arthritis and rheumatoid arthritis of the shoulder. *Magn Reson Imaging Clin North Am*. 2004;12:111–124.

Winalski CS, Aliabadi P, Wright RJ, et al. Enhancement of joint fluid with intravenously administrated gadopentetate dimeglumine: technique, rationale and implications. *Radiology*. 1993;187:179–185.

Wysoki MG, Santora TA, Shah RM, Friedman AC. Necrotizing fasciitis: CT characteristics. *Radiology*. 1997;203:859–863.

Zanca P. Shoulder pain: involvement of the acromioclavicular joint (analysis of 1000 cases). *Am J Roentgenol Radium Ther Nucl Med*. 1971;112:493–506.

Chapter 6

Imaging Evaluation of Common Pediatric Emergencies

Jennifer C. Talmadge, Sarah S. Milla, and Sarah D. Bixby

Imaging in children differs from imaging in adults because of the unique illnesses of children and their wide range of size, varying ability to hold still and cooperate, and relative sensitivity to ionizing radiation. The primary goal of the pediatric radiologist is to acquire diagnostic images while limiting patient morbidity, cost, and radiation exposure in this vulnerable population. Image Gently, a campaign initiated in 2006, raises awareness of opportunities to lower radiation dosage in pediatric imaging Lowering radiation dosage should always be considered when choosing and implementing the appropriate imaging test in the emergency setting. The imaging evaluation of common pediatric emergencies relies heavily on plain radiographs, fluoroscopy, and ultrasound (US). Computed tomography (CT) is often reserved for cases in which US and plain films are nondiagnostic. Magnetic resonance imaging (MRI) is increasingly relied upon as a problem-solving tool in the emergency setting, especially in centers where new technology allows for faster imaging and specially trained staff help young children hold still for examinations without requiring sedation. An advantage of MRI compared with some other types of imaging studies is that it involves no ionizing radiation. This chapter illustrates the imaging manifestations of some of the most common pediatric emergencies.

GASTROINTESTINAL

Abdominal pain and vomiting are common presentations in children who come to the emergency department. The differential diagnosis of abdominal pain depends on the patient's age. Neonates may present in the first few days of life with intestinal obstruction or failure to pass meconium. Premature infants and neonates with congenital heart disease are at risk of the development of necrotizing enterocolitis and may present with abdominal distension. In young infants who are otherwise healthy, a history of vomiting invokes a relatively short differential diagnosis that includes hypertrophic pyloric stenosis and intestinal malrotation. In older children, a history of emesis, especially bilious emesis, invokes a more lengthy differential diagnosis that includes intussusception, appendicitis, bowel obstruction, gastroenteritis, and many other conditions. Imaging investigation largely depends on the patient's age, clinical signs and symptoms, and laboratory markers.

Neonatal Intestinal Obstruction

Intestinal obstruction is one of the most common neonatal abdominal emergencies. The obstruction is classified as either a high or low obstruction depending on whether it occurs above or below the level of the mid ileum. Infants typically present with abdominal distention, vomiting, and failure to pass meconium within 24 to 48 hours. The distinction between a high and a low obstruction is often made on the basis of plain abdominal radiographs. If the radiograph demonstrates one or only a few dilated loops of bowel, the obstruction is likely a high obstruction. If the radiograph reveals multiple dilated loops of bowel, the obstruction is a low obstruction (Fig. 6-1). In an infant with intestinal obstruction, the correct interpretation of the plain film is critical in directing the most appropriate next course of action.

High Obstruction

A high intestinal obstruction may be the result of duodenal atresia or stenosis, jejunal atresia or stenosis, or malrotation with volvulus. Esophageal atresia will be discussed separately. An upper gastrointestinal (UGI) examination is often requested to identify the level of obstruction. The UGI examination also assists the surgeon in determining the urgency of surgery. In children with duodenal atresia or stenosis, the obstruction almost always occurs at the level of the ampulla of Vater. Abdominal radiographs in children with duodenal atresia often reveal the classic "double bubble" sign in an abdomen in which gas is otherwise absent (Fig. 6-2). The dilated gas-filled "bubbles" represent the stomach and duodenal bulb. This sign is virtually diagnostic of duodenal atresia in the correct clinical setting. More than 50% of babies with duodenal atresia will have additional associated anomalies, and approximately 30% will have trisomy 21. In cases of incomplete duodenal obstruction, radiographs reveal gas in the distal bowel loops. In this case a UGI examination would show a focal area of narrowing within the duodenum through which a tiny amount of contrast material may pass. In some cases the stenosis may be the result of a duodenal web, which appears as a curvilinear filling defect extending across the duodenal lumen (Fig. 6-3). Annular pancreas also can coexist with duodenal stenosis and may result in luminal narrowing of the proximal duodenum. Jejunal atresia and stenosis are less common but should be included in the

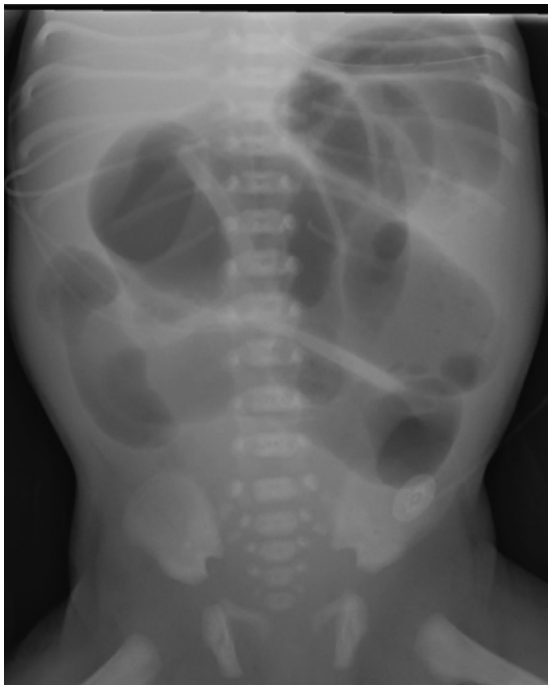


FIGURE 6-1 A plain radiograph of the abdomen in a full-term newborn infant with bilious vomiting demonstrates multiple dilated loops of bowel.

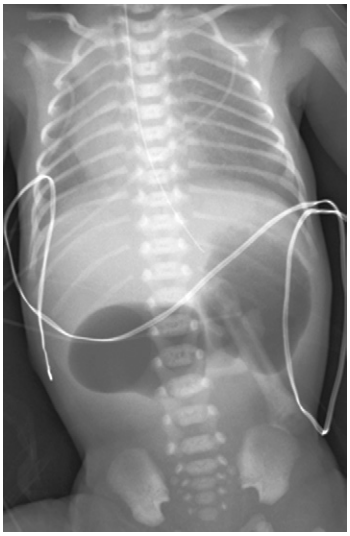


FIGURE 6-2 An abdominal radiograph in this newborn with duodenal atresia demonstrates the "double bubble," in which there is gaseous distension of the stomach and duodenal bulb within an otherwise gasless abdomen.

differential diagnosis of congenital high intestinal obstruction. Malrotation with volvulus is a surgical emergency and will be discussed later in this chapter.

Low Obstruction

Low intestinal obstruction may be a result of meconium ileus, ileal atresia, functional immaturity of the colon, colonic atresia, and Hirschsprung disease. A contrast enema is the study of choice to confirm the diagnosis. Meconium ileus almost always occurs in infants with cystic fibrosis. When a contrast enema is performed, a microcolon is present (Fig. 6-4). A microcolon is a colon of universally small

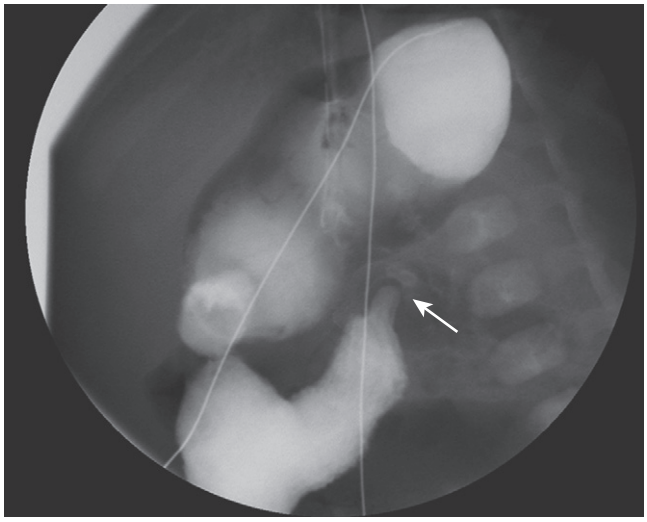


FIGURE 6-3 A fluoroscopic spot image acquired during an upper gastrointestinal examination in a newborn infant with bilious vomiting demonstrates dilated duodenum proximal to a partially obstructing duodenal web *(arrow)*.

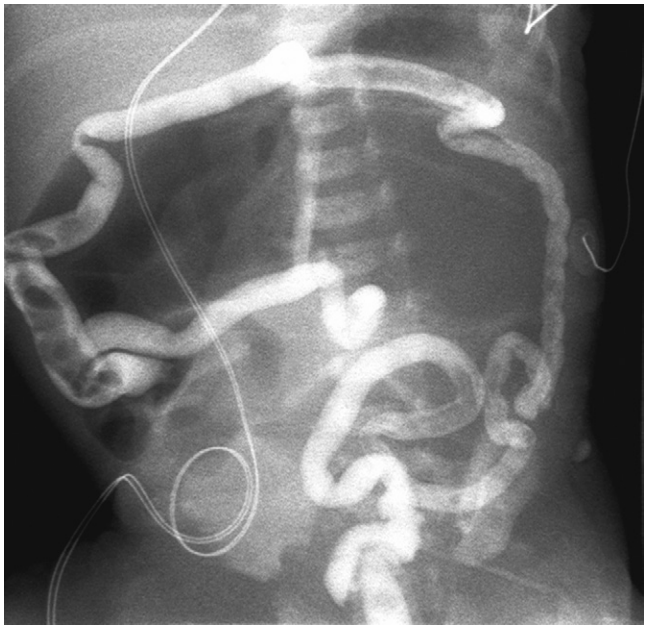


FIGURE 6-4 A contrast enema in a newborn with low intestinal obstruction as a result of ileal atresia demonstrates a microcolon—that is, is a colon of universally small caliber (1 cm or less in diameter).

caliber (1 cm or less in diameter). Its presence implies that the colon has never been used. Bowel atresia proximal to the distal ileum does not lead to a microcolon because the succus entericus produced by distal small bowel allows the colon to achieve a normal caliber. In patients with meconium ileus, refluxed contrast material in the distal ileum reveals multiple filling defects within the distal small bowel. These filling defects represent inspissated meconium and help distinguish meconium ileus from ileal atresia.

In functional immaturity of the colon, previously known as "small left colon syndrome" or "meconium plug syndrome," the descending colon and sigmoid colon are small in caliber compared with the normal ascending and transverse colon.

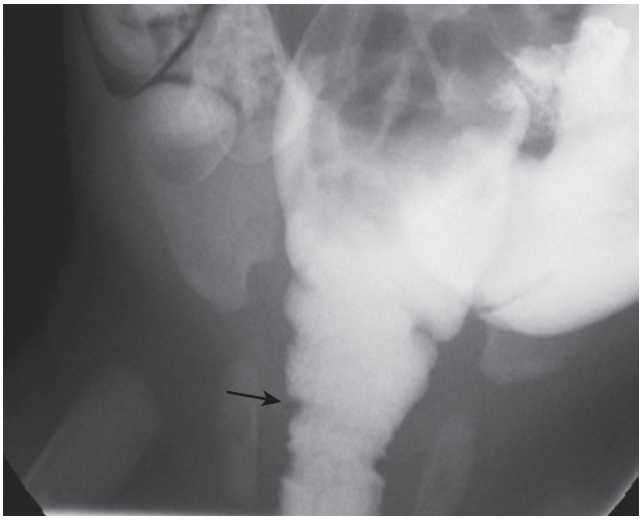


FIGURE 6-5 An anteroposterior fluoroscopic spot image during contrast enema in a newborn baby with bowel obstruction reveals a "saw-tooth" mucosal pattern in the rectum *(arrow)*. The rectosigmoid relationship is reversed. This child had Hirschsprung disease.

The incidence of functional immaturity of the colon is increased in infants of mothers with diabetes and of mothers who received magnesium sulfate. Functional immaturity of the colon will resolve on its own without intervention.

Colonic atresia results in complete obstruction of a segment of colon, likely as a result of an ischemic event in utero. As such, a contrast enema will reveal a microcolon distal to the atresia, the inability to pass contrast material into the proximal colon, and multiple dilated bowel loops proximal to the obstruction.

In infants with Hirschsprung disease, a transition occurs from normal bowel that is of normal caliber to aganglionic bowel that is small in caliber (Fig. 6-5). Classically, this transition occurs at the level of the rectosigmoid. In healthy infants the rectal diameter should be greater than the sigmoid diameter, although in infants with Hirschsprung disease, this relationship is reversed. Boys are affected four times as often as girls. Allergic colitis related to milk allergy occasionally can mimic Hirschsprung disease. Ultimately a biopsy is required to confirm the diagnosis. Total colonic aganglionosis is a rare form of Hirschsprung disease that occurs in approximately 2% to 13% of cases. Total colonic aganglionosis is often familial, affects boys and girls equally, and can be difficult to diagnose radiographically because of the diffuse nature of the disease.

Esophageal Atresia

Congenital atresia of the esophagus is a rare abnormality that may occur as an isolated abnormality or as part of a larger spectrum of abnormalities—for instance, in children with vertebral, anal, cardiac, tracheal, esophageal, renal, and limb (VACTERL) association. In most cases an associated fistula to the trachea is present. The diagnosis is almost always suspected clinically when an infant has difficulty feeding or when difficulty is encountered in passing a nasogastric tube into the stomach. Radiographs help confirm the diagnosis when no gas is identified within any bowel loops in the abdomen. If a tracheal-esophageal fistula is present, a normal bowel gas pattern may occur in the abdomen. If placement of a nasogastric tube has been attempted, the tube will be identified above the diaphragm on the radiograph, often in a dilated, gas-filled, esophageal pouch (Fig. 6-6). An esophagram with use of contrast material or a UGI examination is not necessary to make the diagnosis of esophageal atresia.

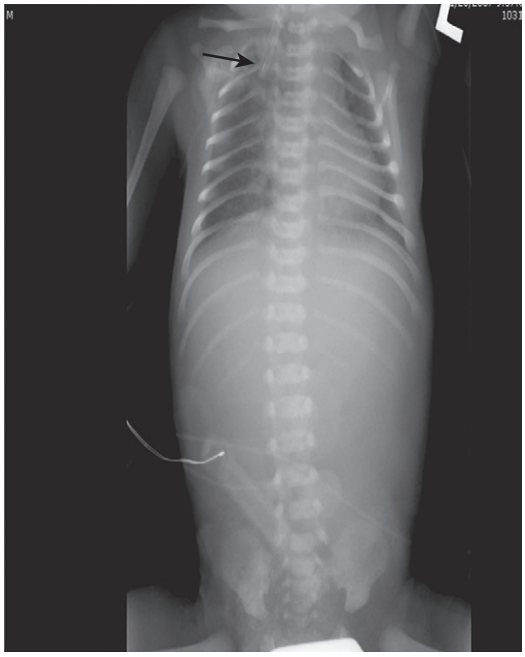


FIGURE 6-6 A babygram performed on a newborn demonstrates a nasogastric tube within a dilated esophageal pouch in this infant with esophageal atresia *(arrow)*. There is no gas within the abdomen to suggest a tracheoesophageal fistula.

Necrotizing Enterocolitis

Necrotizing enterocolitis (NEC) is a gastrointestinal condition that occurs in 2% to 3% of neonates, most commonly in premature or very low birth weight infants. In term infants, NEC is associated with congenital heart disease, such as aortic coarctation, which results in intestinal hypoxia. Mortality rates in infants with NEC range from 15% to 40%. The pathogenesis of the disease is thought to be related to relative immaturity of intestinal motility and barrier function, as well as abnormal bacterial colonization. Neonates with NEC often present within the first 2 weeks of life with feeding intolerance, vomiting, abdominal distention, blood in the stool, and/or generalized lethargy. Abdominal radiographs are the modality of choice for the initial evaluation of neonates with suspected NEC and to monitor its progression. An early sign of NEC is a mildly dilated and fixed loop (or loops) of bowel on serial abdominal radiographs. Although this finding is sensitive, it is not specific. Pneumatosis intestinalis, or air within the wall of the bowel, is considered a hallmark of NEC (Fig. 6-7). Pneumatosis represents by-products of metabolism of bacteria within the intestinal wall. Occasionally the bubbly lucencies of pneumatosis can be mistaken for stool on an abdominal radiograph. It is important to know if the baby is being fed, because stool is not expected in babies who are receiving total parenteral nutrition. Portal venous gas appears on abdominal radiographs

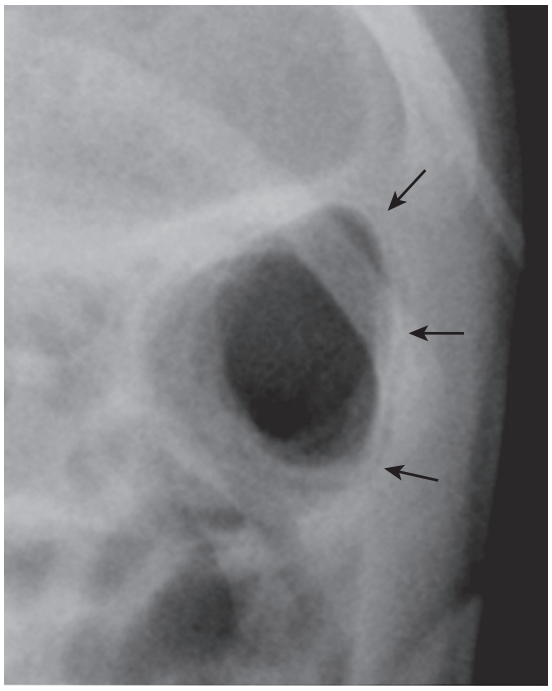


FIGURE 6-7 An abdominal radiograph of a premature infant with necrotizing enterocolitis demonstrates circumferential lucencies surrounding a bowel loop in the left upper quadrant consistent with pneumatosis intestinalis *(arrows)*.

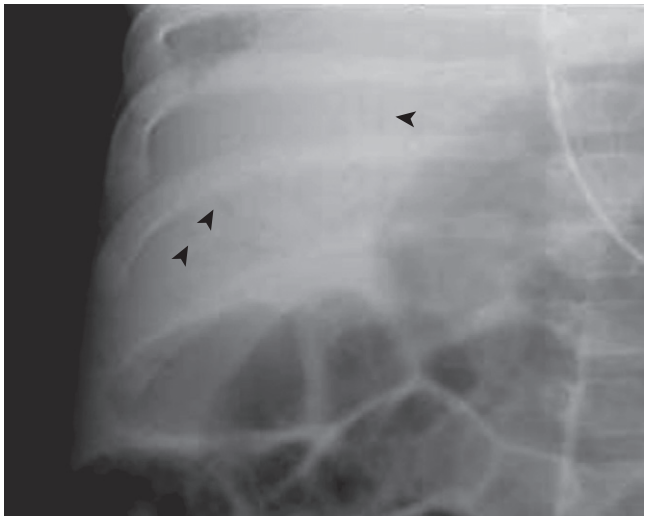


FIGURE 6-8 An abdominal radiograph in a male infant with severe bowel ischemia as a result of congenital heart disease reveals branching lucencies in the liver consistent with portal venous gas *(arrowheads)*.

as lucent, branching, linear structures within the liver (Fig. 6-8). The presence of pneumoperitoneum indicates perforation of the bowel. When pneumoperitoneum is present in a supine infant, the falciform ligament is visualized on a supine radiograph as a result of the presence of air around it, also known as the "football sign" (Fig. 6-9). Both sides of the bowel wall are also visible, which is called the Rigler sign (Fig. 6-10). The abdomen may appear abnormally lucent when large amounts of gas collect anteriorly within the abdomen on a supine film (Fig. 6-11). A cross-table lateral or lateral decubitus view of the abdomen is helpful in confirming the presence of free air (Fig. 6-12).

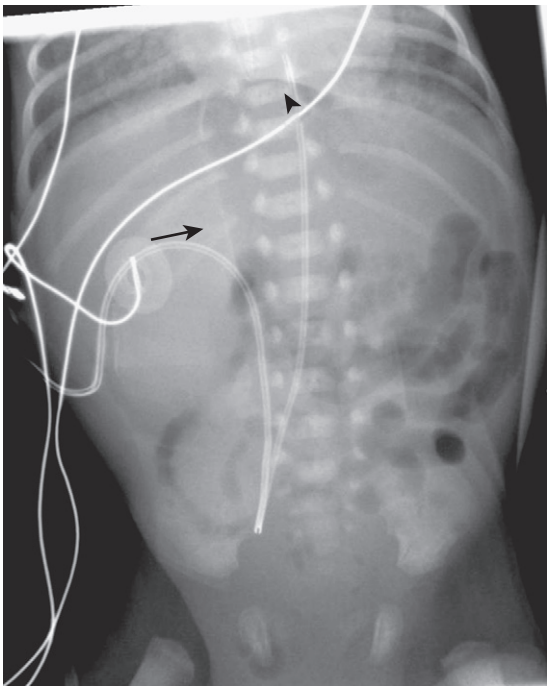


FIGURE 6-9 An abdominal radiograph of a premature infant with clinical necrotizing enterocolitis demonstrates air outlining the falciform ligament *(arrow),* as well as air outlining the undersurface of the diaphragm *(arrowhead)*. At surgery, it was found that this child had a perforation in his ileum.

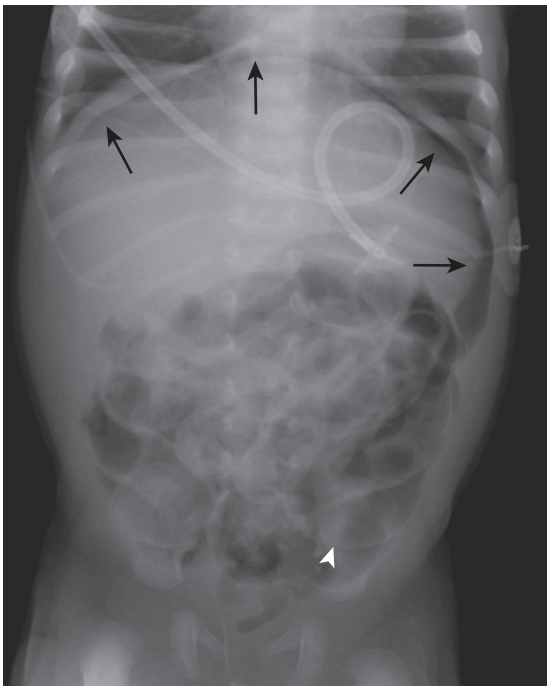


FIGURE 6-10 An abdominal radiograph in a premature infant with perforated necrotizing enterocolitis demonstrates air beneath the diaphragm *(arrows)* and outlining the bowel wall *(arrowhead)*.

Most cases of NEC are treated medically, usually with bowel rest, gastric suction, antibiotics, and hydration. Surgery is indicated if evidence is found of bowel perforation. Plain radiographs are critical in evaluating the progression of the disease. A changing bowel gas pattern, as opposed

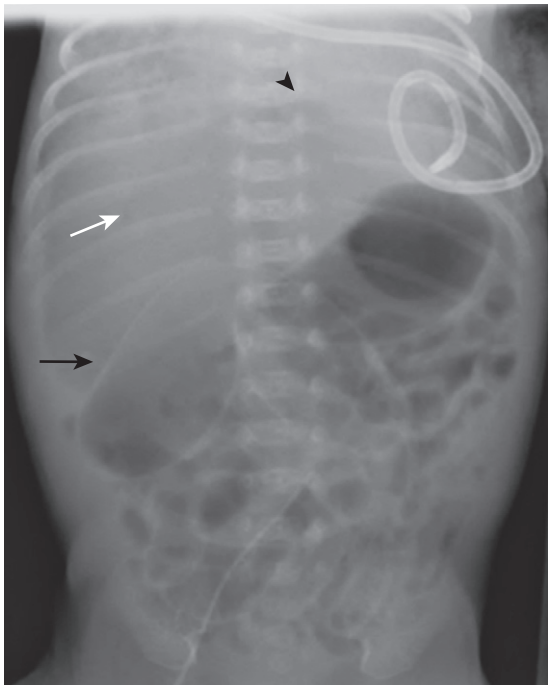


FIGURE 6-11 An abdominal radiograph of same patient as in Figure 6-10 taken several hours later demonstrates hyperlucency of the liver *(white arrow)*, free air under the diaphragm *(arrowhead)*, and air outlining loops of bowel *(black arrow)*.

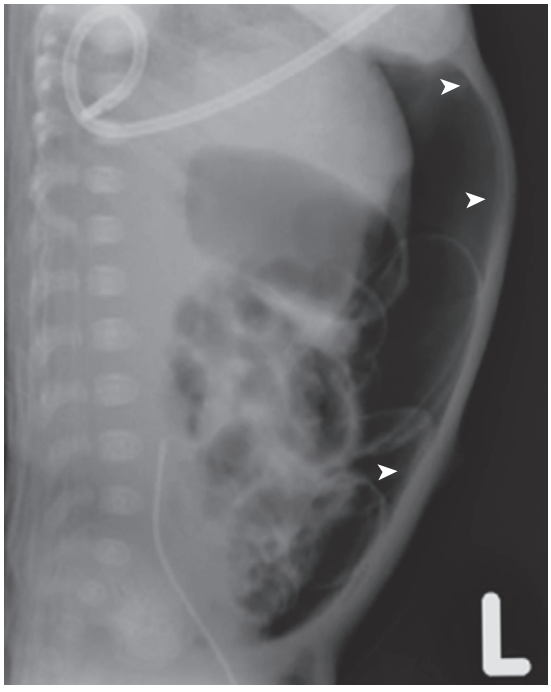


FIGURE 6-12 A cross-table lateral abdominal radiograph in an infant with perforated bowel demonstrates a large amount of free intraabdominal air *(arrowheads)*.

to dilated bowel loops that remain fixed on serial abdominal radiographs, is an important radiographic sign, because this changing pattern often coincides with clinical improvement. Sequelae of NEC include short gut syndrome and intestinal strictures, which typically present 3 to 8 weeks after the acute illness.

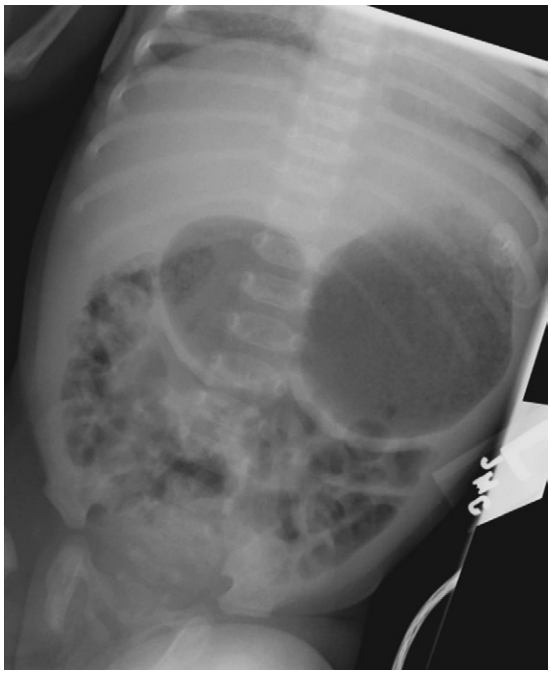


FIGURE 6-13 An abdominal radiograph in a 1-month-old infant with pyloric stenosis demonstrates a dilated stomach. A wave of peristalsis gives the stomach the appearance of a caterpillar.

Hypertrophic Pyloric Stenosis

Hypertrophic pyloric stenosis (HPS) is a condition that affects young infants, usually between 3 to 12 weeks of age, with 4 weeks the peak age at diagnosis. Although these infants are normal at birth, they display the gradual onset of nonbilious emesis during the first several weeks of life, commonly described as projectile in quality. In severe cases, dehydration and malnourishment ensue, which may be accompanied by marked electrolyte imbalances. The disease is caused by overgrowth of the muscularis layer of the pylorus. The mucosal layer also becomes hypertrophied and redundant, which causes obstruction of the lumen. The precise cause of HPS is unclear, although there is a familial predisposition. Males are affected four times as frequently as females.

US is the imaging study of choice for the diagnosis of HPS, and use of a high-resolution linear array transducer is recommended. When HPS is present, the pyloric channel is nearly always visualized and appears both thickened and elongated (Fig. 6-13). The hypertrophied pyloric channel fails to relax despite vigorous peristaltic contractions in the stomach. The hyperechoic mucosa is redundant and crowded and often protrudes into the antrum, a finding termed the "nipple sign." The length of the hypertrophic pyloric channel is variable and can range between 14 to 20+ mm. Measurements of muscle thickness are more reliable for the diagnosis of HPS. A muscle thickness greater than 3 mm is consistent with pyloric stenosis. Occasionally transient pylorospasm can mimic hypertrophic pyloric stenosis, and therefore it is important to assess for the passage of fluid from the gastric antrum into the duodenal bulb. In healthy patients the normal pyloric ring bridges these two structures (Fig. 6-14). Careful observation of this region over the course of the examination reliably allows differentiation between a normal and an abnormal study. If the US findings

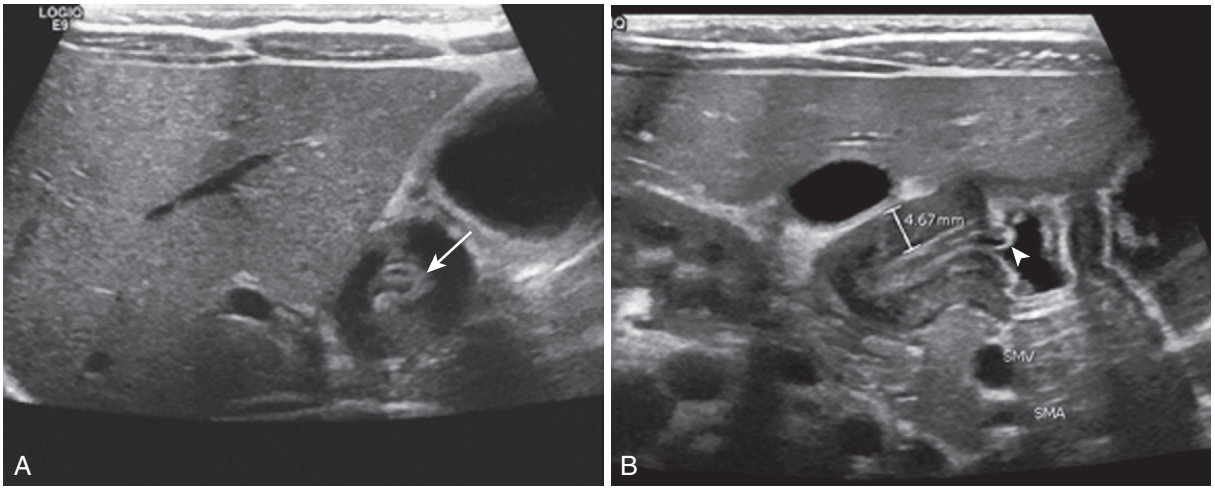


FIGURE 6-14 **A,** A transverse ultrasound image of a 5-week-old infant demonstrates thickening of the pylorus and redundancy of the mucosa in the pyloric channel *(white arrow)*. This patient was found to have hypertrophic pyloric stenosis at surgery. **B,** A longitudinal image of the pylorus in the same infant demonstrates the mucosa projecting into the antrum, a finding called the "nipple sign" *(arrowhead)*.

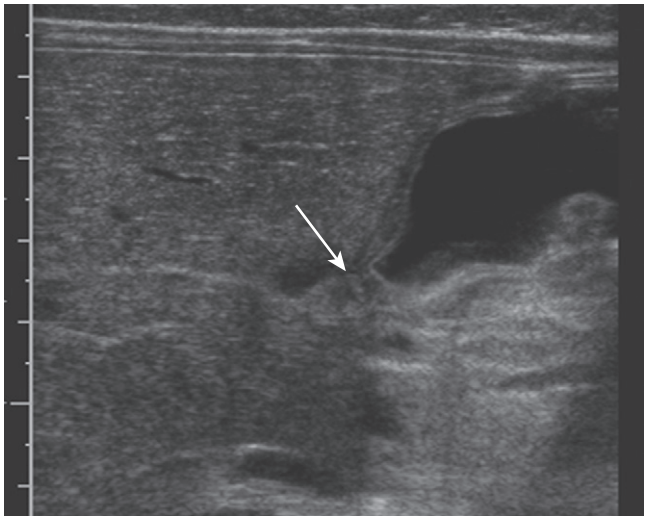


FIGURE 6-15 A longitudinal ultrasound image through a normal pylorus *(arrow)*, which appears as a cleft separating the stomach antrum and the duodenal bulb.

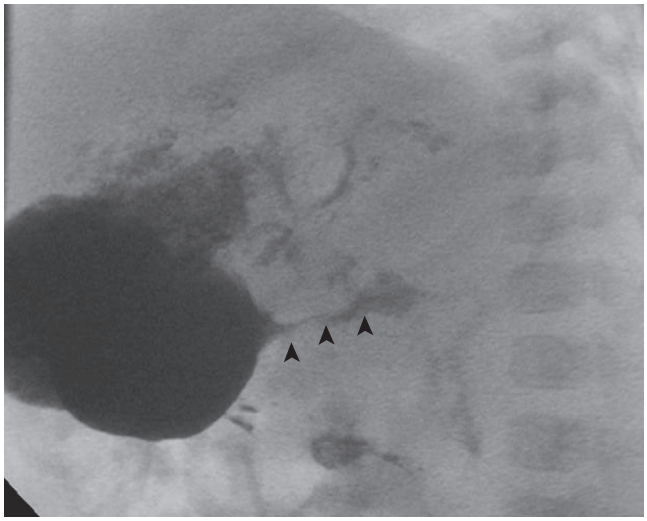


FIGURE 6-16 A fluoroscopic spot image from an upper gastrointestinal examination of a 1-month-old boy with reported bilious emesis. The pyloric channel is elongated, and only a small trickle of contrast material is able to pass through *(arrowheads)*. Hypertrophic pyloric stenosis was confirmed upon a subsequent ultrasound.

are negative or borderline but the patient's symptoms progress, a follow-up US examination may be necessary to evaluate for interval development of pyloric stenosis. Abdominal radiographs are not necessary to make the diagnosis of HPS but typically demonstrate a dilated, gas-filled stomach (unless the stomach has been decompressed with a nasogastric tube). Peristaltic contractions within the stomach give the appearance of a "caterpillar stomach" (Fig. 6-15).

In the past, UGI examination was performed to confirm the diagnosis of HPS. Although the thickness of the pylorus muscle is not discernable at UGI examination, other imaging signs suggest the diagnosis. The pyloric channel appears elongated at UGI examination as wispy, linear tracts of contrast material pass through the canal, a finding called the "string sign" (Fig. 6-16). The "shoulder sign" is the name given to the appearance of the thickened impression of the pylorus upon the dilated stomach antrum. Vigorous peristaltic contractions in the stomach occur without associated relaxation of the pyloric channel. Imaging over time allows reliable diagnosis of pyloric stenosis because contrast material is never able to pass through the channel in more than tiny wisps at a time.

The current treatment for HPS is a pyloromyotomy, which can be performed laparoscopically. In this procedure the hypertrophied muscularis is divided and the mucosa is allowed to bulge through the incision (i.e., suturing is not performed over the muscle). This procedure has been extremely effective at reducing the mortality rate in infants with HPS, which is now well below 1%.

Malrotation

"Malrotation" is a term used to describe an arrest in the development of the midgut that may occur at various stages of embryologic growth. This developmental arrest

leads to a spectrum of abnormal rotation patterns of the intestinal tract. In patients with malrotation, peritoneal or "Ladd" bands form as a result of disorganized embryologic attempts to fixate the malrotated bowel. These bands may lead to bowel obstruction by crossing over a loop of bowel and compromising the integrity of its lumen. The malfixated intestines have a propensity to twist around the mesentery, leading to a midgut volvulus. The compromised blood supply to the bowel can lead to bowel infarction, sepsis, and eventually death. In a previously healthy infant presenting with bilious emesis, midgut volvulus is a primary clinical concern. Although symptoms related to malrotation theoretically may occur at any age, they are more likely to occur in the first month of life. In most cases malrotation is an isolated defect with no predisposing genetic susceptibility or associated syndromes. Some conditions, however, are nearly universally associated with malrotation, including gastroschisis, congenital diaphragmatic hernia, and omphalocele. The heterotaxy syndromes also are associated with malrotation.

Abdominal radiographs and gastrointestinal contrast studies (UGI) are paramount in making the diagnosis of malrotation and must be performed on an emergent basis. The bowel gas pattern is often normal in the presence of malrotation. Normal findings of an abdominal radiograph should not preclude further investigation in a child with clinical concern for malrotation. A UGI examination evaluates the course of the duodenum and the position of the duodenojejunal junction (DJJ). In healthy patients the duodenum has a characteristic C-sweep that consists of four portions: the duodenal bulb and the descending, transverse, and ascending portions (Fig. 6-17). The descending through ascending portions of the duodenum are fixed in the retroperitoneum. The DJJ is normally located to the left of midline at the level of the duodenal bulb. When the DJJ is inferior or medial to this position, it is considered abnormal (Fig. 6-18). A few rare exceptions to this rule exist, including previous surgery in the abdomen, abdominal masses that displace bowel, and marked gastric or colonic distention. A "corkscrew" configuration of the duodenum implies that a midgut volvulus is present (Fig. 6-19). Midgut volvulus causes a closed loop bowel obstruction. The bowel may appear tapered or "beaked" at the level of

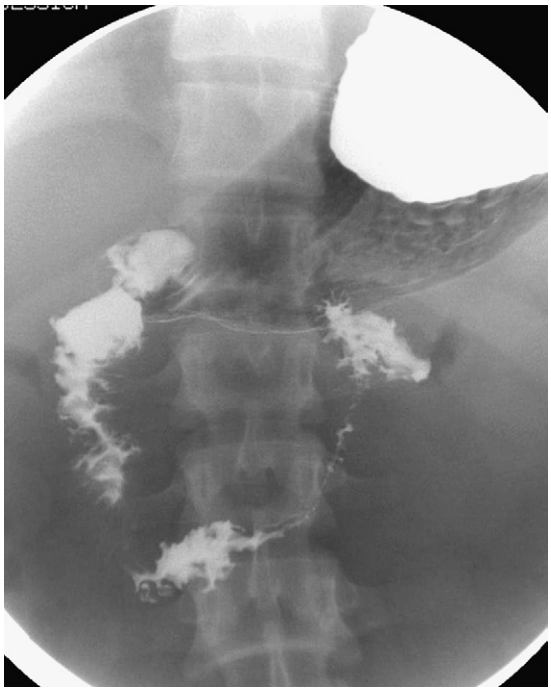


FIGURE 6-17 A fluoroscopic spot image from a normal upper gastrointestinal examination. The duodenal C-sweep has a characteristic course, and the duodenojejunal junction is located to the left of midline at the level of the pylorus.

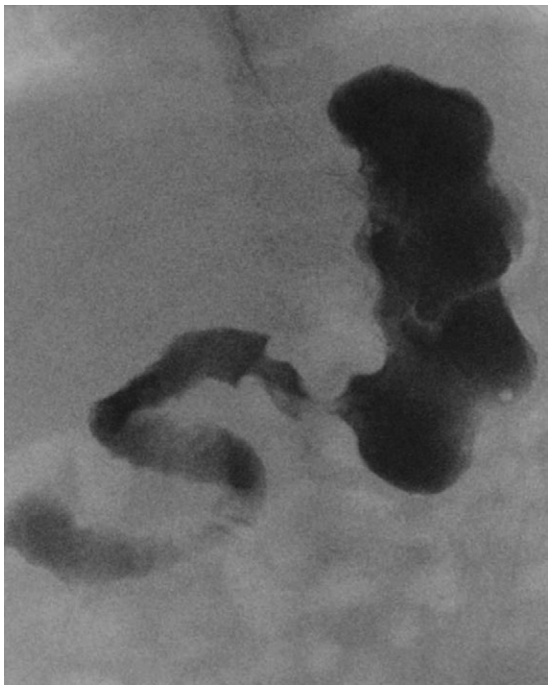


FIGURE 6-18 An upper gastrointestinal examination of a newborn baby with gastroschisis repair demonstrates malrotation.

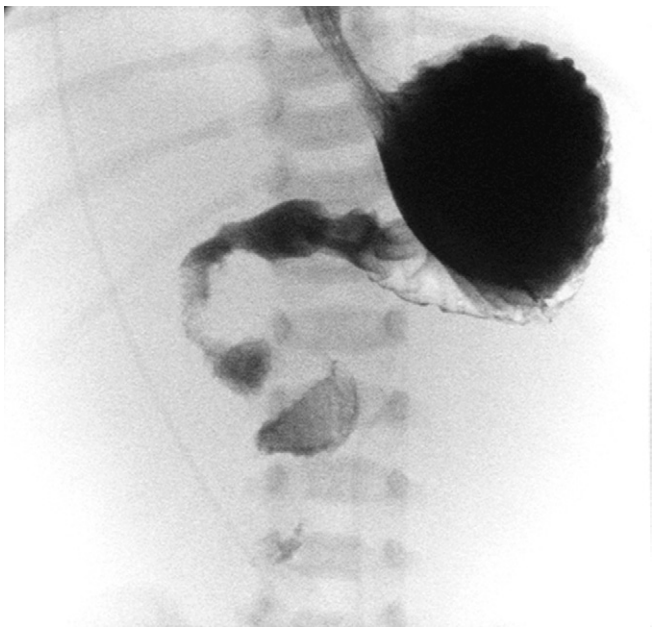


FIGURE 6-19 An upper gastrointestinal examination of a newborn baby who presented with bilious emesis and was found to have malrotation with midgut volvulus. The patient was taken to the operating room for emergent surgical correction.

obstruction, with proximally dilated bowel loops. Midgut volvulus is a surgical emergency. Despite all of these findings, the diagnosis of malrotation (without midgut volvulus) remains difficult to make with certainty in up to 30% of cases because of the subtlety of the findings and the overlap with normal anatomy. If the course of the duodenum is not straightforward, serial abdominal radiographs can be performed to follow the contrast material distally to the colon. When malrotation is present, the small bowel is commonly located on the right side of the abdomen, and the cecum also may be abnormally positioned.

The preferred treatment for infants or children with malrotation is a Ladd procedure. This surgery, often performed laparoscopically, entails reduction of a midgut volvulus, division of obstructing peritoneal bands, placement of the bowel in a position of nonrotation, and appendectomy. The urgency of surgery depends on whether a midgut volvulus is present at the time of diagnosis. Because all patients with malrotation are at risk of volvulus, even patients without a volvulus proceed to surgery semiurgently. Recurrence of volvulus after a Ladd procedure has been performed is rare but can occur.

Intussusception

Intussusception is one of the most common causes of bowel obstruction in young children. Intussusception occurs when one segment of the bowel (the intussusceptum) telescopes into the bowel immediately distal to it (intussuscipiens). This phenomenon occurs most often in children between 6 months and 3 years of age. Common presenting symptoms are vomiting, lethargy, and bouts of irritability in which the child draws his or her legs to the chest. The more classic symptoms of a palpable abdominal mass and "red currant jelly stool" are present in only a minority of cases and should not be relied upon to suggest the diagnosis. Bloody stool is a manifestation of sloughed intestinal mucosa, which is a late finding in the disease and is present in fewer than half of all cases. Delayed diagnosis may lead to bowel ischemia and perforation. Most intussusceptions in children are idiopathic, and approximately 5% of cases are the result of the presence of a pathologic lead point (PLP). PLPs include Meckel diverticulum, colonic polyps, lymphoma, duplication cyst, or underlying diseases of the bowel such as Henoch-Schönlein purpura. PLPs should be considered in children younger than 1 month or older than 5 years or who have had multiple recurrent intussusceptions. The most common site for intussusception to occur is at the hepatic flexure, of which ileocolic intussusceptions are the most common type. Small bowel intussusceptions also may occur. Small bowel intussusceptions are usually transient phenomena that may not cause symptoms. They are likely to reduce spontaneously, and an air reduction enema is not therapeutic.

Imaging evaluation of the child with suspected intussusception begins with abdominal radiographs. Supine and left lateral decubitus views are recommended. The decubitus film, by allowing the cecum and ascending colon to assume a nondependent position in the abdomen, allows air to fill the cecum when an ileocolic intussusception is not present or if the cecum is not filled with stool. The sigmoid colon is often located within the right lower quadrant in young children, and one should be careful when excluding intussusception based on gas-filled bowel loops in this location. The "meniscus sign" and "target sign" are terms used to describe the radiographic appearance of a soft tissue mass in the colon (Fig. 6-20). Small bowel dilatation and air-fluid levels may be present, signifying the presence of a small bowel obstruction (Fig. 6-21).

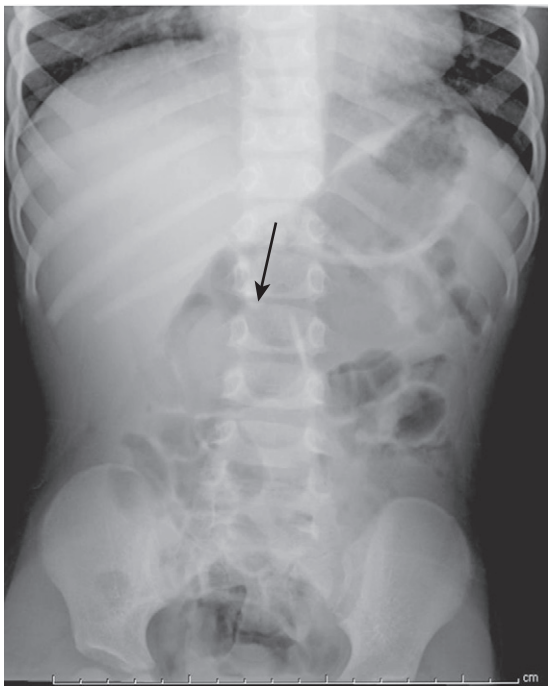


FIGURE 6-20 An abdominal radiograph of a 2-year-old boy with abdominal pain reveals a soft tissue mass within the right upper quadrant in the region of the hepatic flexure *(arrow)*. Ultrasound confirmed that this mass represented an ileocolic intussusception.

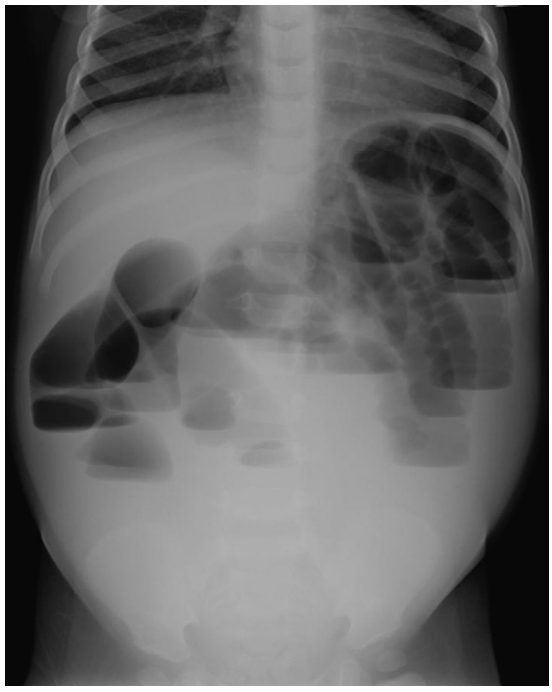


FIGURE 6-21 An abdominal radiograph in a 1-year-old boy demonstrates multiple air fluid levels and dilated loops of bowel. Ultrasound confirmed that this child had an ileocolic intussusception.

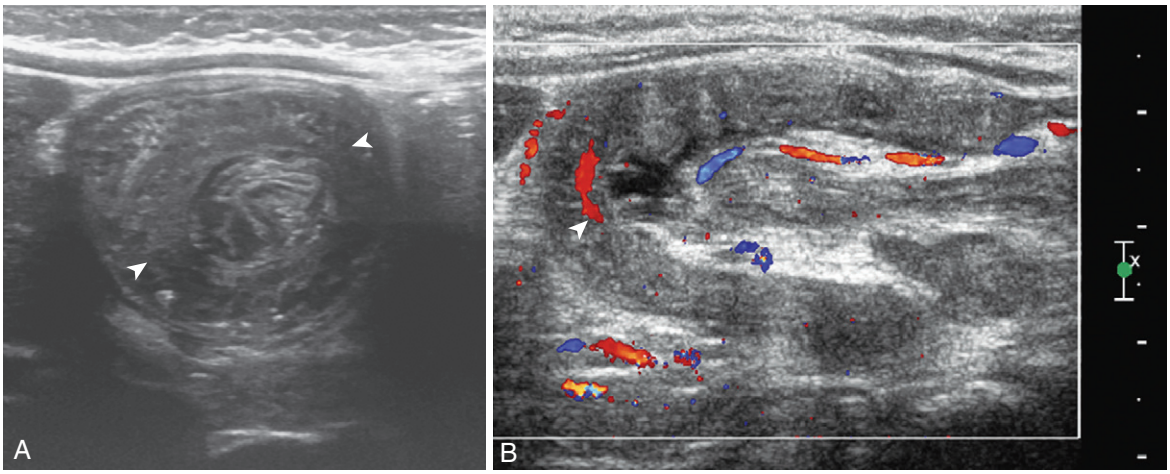


FIGURE 6-22 **A,** A transverse ultrasound image in a 1-year-old child with crampy abdominal pain demonstrating the "target" appearance of an ileocolic intussusception. The "intussuscipiens" is delineated by *arrowheads*. **B,** A sagittal ultrasound image of the right lower quadrant in the same patient demonstrates the presence of color Doppler flow to the intussuscipiens *(white arrowhead)*.

For confirmation of intussusception, US is the preferred modality. When the sonographer is familiar with its imaging appearance, intussusception is identified in all cases. Intussusception has a characteristic appearance in both transverse and sagittal planes. In transverse planes, an intussusception appears as a mass, usually between 3 to 5 cm in diameter, that has a "target" or "doughnut" configuration of alternating hypo- and hyperechoic layers (Fig. 6-22, *A*). In the sagittal plane the mass assumes a "pseudokidney" configuration. Color Doppler imaging is used to evaluate the vascularity of the bowel and is a promising predictor of bowel viability (Fig. 6-22, *B*). Enlarged mesenteric lymph nodes may be present at the site of intussusception, which may function as a lead point. Imaging pitfalls in the diagnosis of intussusception include stool in the cecum, thickened loops of small bowel in the right lower quadrant, and the normal psoas muscle. Each of these structures may be mistaken for an intussusception. It is also important to appreciate the difference between small bowel intussusceptions and ileocolic intussusception. Small bowel intussusceptions are usually treated conservatively, whereas ileocolic intussusceptions are treated with enema reduction or surgery. The diagnosis of small bowel intussusception is suggested by the location of the intussusception (outside of the right lower quadrant), small diameter (<2 cm), and short-segment involvement (<5 cm).

Fluoroscopically guided air reduction enema is a widely accepted and utilized method of treatment for ileocolic intussusception. Contraindications to performing an enema include shock, peritonitis, or radiographic evidence of perforation. Although contrast enema reductions can be performed, air is generally preferred. After inserting a rectal catheter into the buttocks with the patient in the prone position, air is insufflated into the colon, ensuring a tight seal at the level of the buttocks to prevent an air leak. The intussusception is visualized fluoroscopically as it is reduced back through the colon (Fig. 6-23). A successful reduction involves the reduction of the intussusception beyond the ileocecal valve (often with a visible "pop"), with reflux of air into the small bowel. Air reduction enema procedures are successful in more than 80% of cases. When the enema is not successful, surgery is curative. A rare but serious complication of the air reduction enema is bowel perforation leading to tension pneumoperitoneum, which necessitates emergent needle decompression. Perforation occurs in approximately 1.5% of cases.

Acute Appendicitis

Acute appendicitis is the most frequent condition in children that requires emergent abdominal surgery. Acute appendicitis is caused by obstruction of the appendiceal lumen, which leads to the accumulation of fluid and secondary inflammation and infection. Luminal obstruction can be the result of the presence of a fecalith, lymphoid hyperplasia, foreign bodies (FBs), or mass lesions (e.g., lymphoma). Perforation is common in pediatric patients. The frequency of perforation increases as the age of the patient decreases. Children who are suspected of having acute appendicitis warrant imaging evaluation that is both expeditious and accurate to avoid complications of perforation, such as abscess formation, bowel obstruction, and sepsis.

Graded-compression sonography is the imaging modality of choice for the initial evaluation of children suspected of having acute appendicitis. Advantages of US include the lack of ionizing radiation, lack of the need for patient preparation, and lack of sedation. The patient often is able to precisely localize the site of pain to direct the sonographer to the appropriate area. On US, the inflamed appendix will appear as a blind-ending tubular structure with bowel signature (Fig. 6-24). When pressure is applied, the inflamed appendix is noncompressible. On transverse images the appendix will have a "target sign" configuration that is made up of the alternating layers of the appendiceal wall. Although no exact measurement defines an acutely inflamed appendix, in general practice an appendix with a diameter greater than 6 mm with compression is considered abnormal. Secondary signs of appendicitis include hyperemia, increased echogenicity

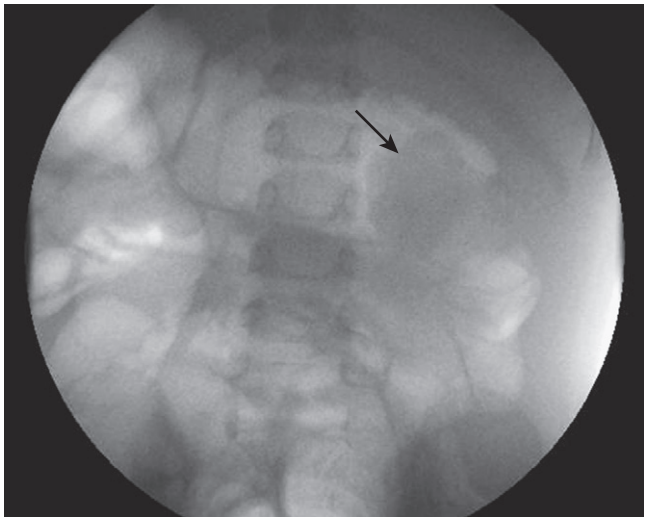


FIGURE 6-23 A fluoroscopic image obtained during air reduction enema in a child (who is prone) demonstrates the soft tissue mass at the hepatic flexure *(arrow)*. Later images demonstrated complete reduction of this ileocolic intussusception.

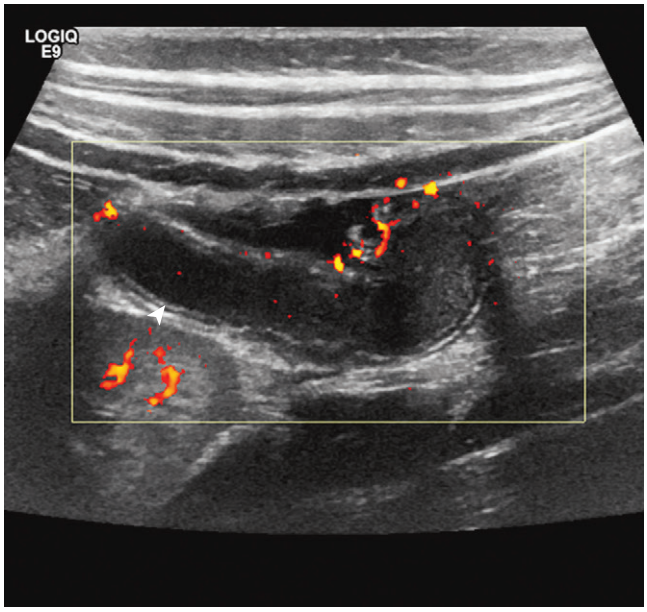


FIGURE 6-24 A longitudinal ultrasound image of the appendix *(arrowhead)* in a teenage boy with right lower quadrant pain and fever. The appendix measured 10 mm and was noncompressible. The patient had a laparoscopic appendectomy, which confirmed acute appendicitis.

of the periappendiceal fat, suggesting inflammation, free fluid in the abdomen or pelvis, and fluid collections adjacent to the appendix that may represent abscesses and suggest perforation. Disadvantages of US are that it is highly operator dependent, the accuracy of the study is largely affected by the body habitus of the patient, and the appendix can be difficult to locate, particularly if it is in a retrocecal position.

CT examination is highly sensitive for the diagnosis of acute appendicitis and can be used if US is nondiagnostic and there is strong clinical concern for appendicitis. Complications from a ruptured appendix, such as the development of abscesses, will also be visible on CT. At our

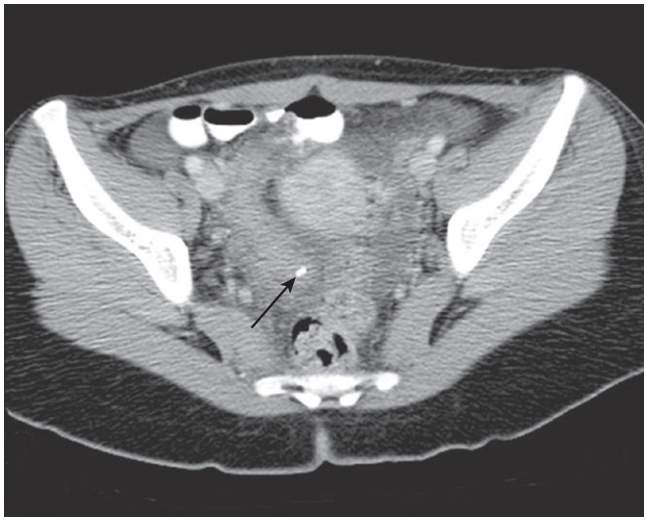


FIGURE 6-25 An axial image from a computed tomography examination performed with intravenous contrast material demonstrated a dilated, inflamed appendix in the right lower quadrant, extending into the pelvis. An appendicolith *(arrow)* is present. This patient underwent surgery and an inflamed, nonperforated appendix was removed.

institution, CT for appendicitis is performed with intravenous contrast material only, and the field of view is restricted to below L3 to perform the examination without delay while minimizing radiation exposure.

CT findings of acute appendicitis include an enlarged (greater than 6 mm in diameter), fluid-filled appendix with or without an appendicolith, with periappendiceal inflammatory changes (Fig. 6-25). Nonspecific associated findings include enlarged mesenteric lymph nodes, free fluid, and inflammatory changes in the adjacent bowel. The presence of free air and abscess formation are important signs that the appendix is likely perforated.

Although appendicitis is common, its imaging features are not always straightforward. Given the variability in the location and position of the appendix, the clinical symptoms can be misleading. If the appendix is located within the pelvis in a young woman, appendicitis may simulate an ovarian process such as torsion of the ovary or a hemorrhagic ovarian cyst. Likewise, a subhepatic appendix may present with right upper quadrant pain simulating gallstones or flank pain, representing a concern for pyelonephritis. Imaging the uterus and ovaries in female patients at the time of their appendix US is important to exclude ovarian causes of acute pain. This imaging is best achieved by imaging through a full bladder to provide a window to the uterus and ovaries, because transvaginal US in not an option in most pediatric patients who are not sexually active.

Meckel Diverticulum

Meckel diverticulum, the most common congenital anomaly of the gastrointestinal tract, is found in 2% to 3% of the general population. A Meckel diverticulum is a true diverticulum along the antimesenteric border of the distal ileum that results from incomplete atrophy of the omphalomesenteric duct in fetal development. Its lining consists of normal small bowel mucosa, although in some cases ectopic gastric or pancreatic mucosa may

be present. It is most often located in the right lower quadrant. No known association with other congenital malformations exists. Asymptomatic Meckel diverticulum occurs with nearly equal frequency in boys as in girls, although symptomatic Meckel is more common is males.

Approximately 40% of children with vitelline duct anomalies such as Meckel diverticulum are symptomatic. The most common symptoms are abdominal pain, nausea, vomiting, and rectal bleeding. Hemorrhage and obstruction are the most common complications. In patients presenting with hemorrhage related to a Meckel diverticulum, ectopic gastric mucosa is almost always present. The bleeding is caused by peptic ulceration within the gastric mucosa and/or the adjacent ileal mucosa, and it is typically painless. The presence of ectopic gastric mucosa serves as the basis for the "Meckel scan," or technetium 99m pertechnetate scintigraphy. Given the relatively low sensitivity of this examination, however, a negative result often has little impact on clinical management when a Meckel diverticulum is strongly suspected. Arteriography and contrast studies may be helpful in these instances, although these evaluations may be superseded by colonoscopy or laparoscopy.

Bowel obstruction as a result of Meckel diverticulum can occur as a result of either volvulus, intussusception, inversion of the diverticulum into the bowel lumen, inclusion of the diverticulum into a hernia, or diverticulitis. Persistent attachments of the diverticulum to the umbilicus may be the cause of bowel obstruction. A transition point may be identified on CT where proximal, dilated bowel loops abruptly change caliber to collapsed, distal loops, although the obstructing band itself is not visible. The diverticulum also can serve as a lead point for intussusception and should be suspected in any child presenting with intussusception who is outside the typical age range for idiopathic intussusception (Fig. 6-26). Acute Meckel diverticulitis may mimic acute appendicitis in a child presenting with abdominal pain, fever, and vomiting. Visualization of a normal appendix is helpful in distinguishing these two entities and identifying the ileum at the base of the diverticulum. This assessment is much more easily made with CT than with US. Identification of an enterolith on abdominal radiographs or CT is useful for suggesting the diagnosis of Meckel diverticulum in the setting of obstruction, especially when it is located in the right lower quadrant. Mixed-attenuation fecal material may be entrapped within the blind-ending diverticulum.

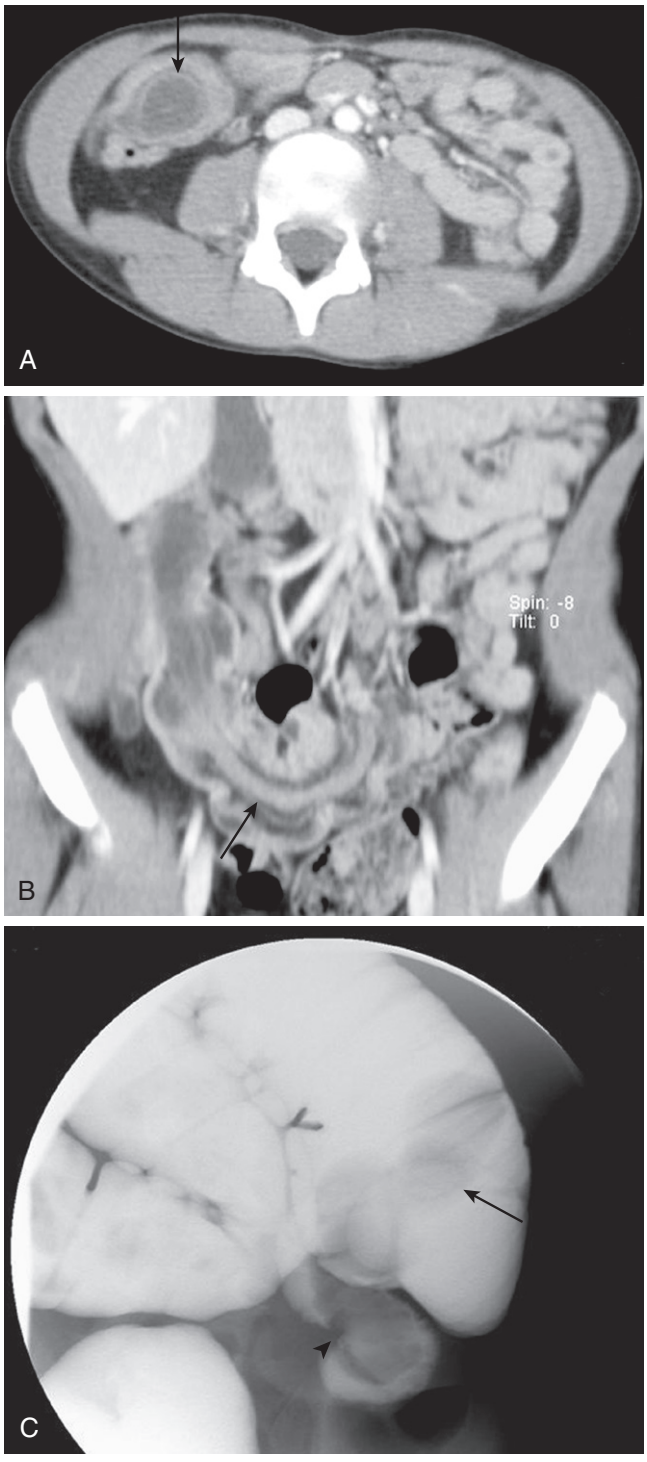


FIGURE 6-26 **A,** Axial computed tomography with intravenous contrast in a 6-year-old boy with right lower quadrant pain reveals a cystic mass *(arrow)* within the ascending colon. **B,** A coronal reformatted image demonstrates the presence of an ileocolic intussusception *(arrow)* with an intraluminal cystic mass as a pathologic lead point. **C,** A subsequent contrast enema demonstrates a Meckel diverticulum intussuscepting into the ascending colon *(arrow)*. Contrast material was not able to be refluxed past the base of the diverticulum *(arrowhead)*.

Mesenteric Adenitis

Not all children presenting to the emergency department with abdominal pain have an abnormality requiring emergent diagnosis and treatment. In the absence of other abnormalities, a child's symptoms are often attributed to an entity called "primary mesenteric lymphadenitis." Enlarged mesenteric lymph nodes on CT or US may be the only imaging abnormality present. The cause of the lymphadenopathy is unclear, although a nonspecific gastrointestinal inflammation may be the underlying cause. Although no precise size criteria define an abnormally enlarged mesenteric lymph node in children, a node with a short-axis diameter greater than 8 mm is considered enlarged. Although these measurements are based on data acquired with CT, the diagnosis also may be made on the basis of US findings.

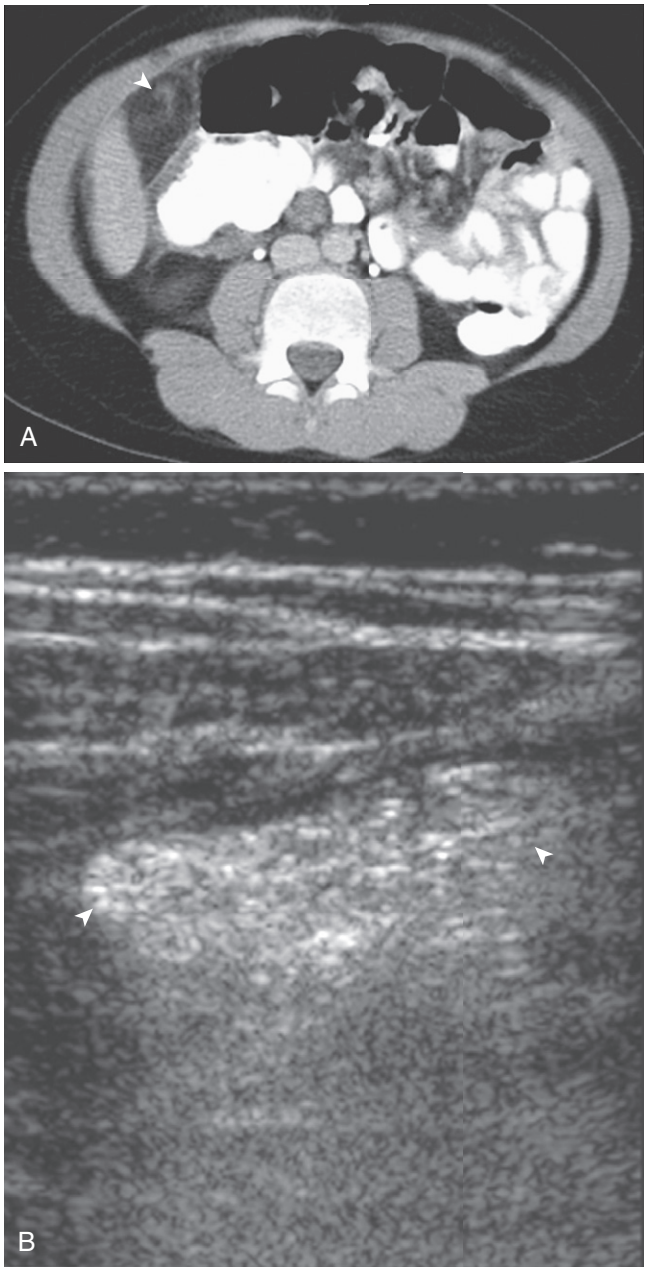


FIGURE 6-27 A, An axial image from a computed tomography scan on an obese 6-year-old boy performed with oral and intravenous contrast material demonstrated a central focus of increased attenuation within the omentum in the right lower quadrant *(arrowhead)*. **B,** A transverse ultrasound image from the same patient demonstrates an echogenic lesion in the right lower quadrant *(arrowheads)*. This patient was treated conservatively with a presumptive diagnosis of omental infarction.

Omental Infarction

Omental infarction most often occurs in obese children. This entity is best recognized with CT, although it also can be detected with US. Patients often present with right lower quadrant or diffuse abdominal pain, and often fever and an elevated white blood cell count are not present. Imaging studies (CT and US) demonstrate a normal-appearing bowel, including the appendix. The presence of hazy, increased attenuation within the anterior abdomen in the region of the omentum is a hallmark of this diagnosis (Fig. 6-27, *A*). The diagnosis also may be suggested at US by detection of an echogenic, masslike structure just deep to the anterior abdominal wall in the area of pain (Fig. 6-27, *B*). If no other abnormalities are appreciated, this entity can be treated conservatively with prophylactic antibiotic and analgesic drugs.

GENITOURINARY

Posterior Urethral Valves

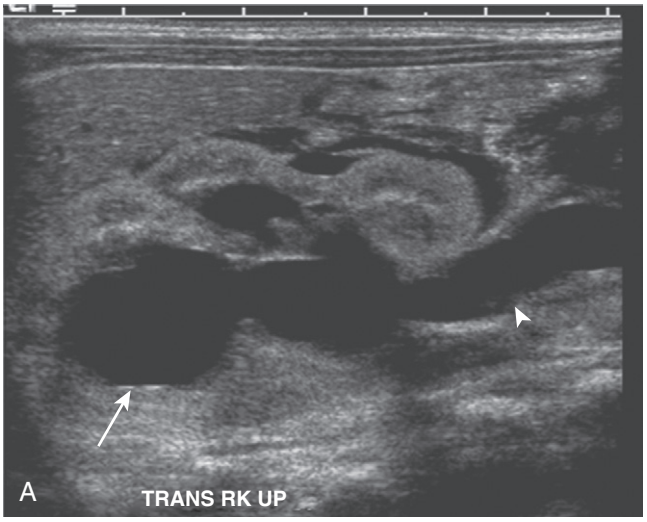
Posterior urethral valves (PUVs) are the most common congenital cause of *bilateral* renal obstruction. Their embryologic development is complex and has been previously described in the literature. Briefly, PUVs consist of an obstructing membrane, or persistent urogenital membrane, at the level of the verumontanum in the posterior urethra of male infants. This membrane causes varying degrees of bladder outlet obstruction and bilateral hydroureteronephrosis. The diagnosis is often made in utero. The presence of PUVs is associated with oligohydramnios, which can result in pulmonary hypoplasia if it is severe.

US examination of patients with PUVs reveals dilated renal collecting systems and ureters bilaterally (Fig. 6-28). The bladder is often greatly distended, and the bladder wall may appear sacculated, thickened, or trabeculated. The dilated posterior urethra has a "keyhole" configuration at US. A voiding cystourethrogram (VCUG) is the standard of care for the diagnosis of PUVs. The bladder is usually of large caliber and may require a larger than expected volume of contrast material to reach capacity. Bladder wall trabeculations and diverticula are often present. When reflux is present, the refluxed contrast material will be diluted by the preexisting urine within the dilated ureter and renal collecting system. The degree of hydronephrosis is often massive. Images of the urethra acquired during voiding demonstrate an abrupt change in caliber between the dilated posterior urethra and the normal-caliber anterior urethra (Fig. 6-29). In some cases the obstructing membrane is identified at the point of transition. The verumontanum is often enlarged and is identified as an intraluminal filling defect along the posterior wall of the urethral just proximal to the valves.

The PUVs are treated with ablation. Even after the valves are ablated, the long-term sequelae of the bladder outlet obstruction in utero can be catastrophic, with renal failure developing by early childhood. Ultimately, the degree of renal function is of primary importance in determining patient outcome, because massive vesicoureteral reflux (VUR) in utero may cause severe renal dysplasia that leads to renal failure. In utero, calyceal rupture and urinoma formation is protective of renal function. PUVs must be differentiated from other causes of bilateral hydroureteronephrosis in infancy, including prune-belly syndrome, bilateral ureterovesicular junction obstruction, transient bilateral VUR, and the rare "megacystis-microcolon-intestinal hypoperistalsis-syndrome." The findings at VCUG should readily differentiate PUVs from these other entities.

Urinary Tract Infection

The diagnosis of a urinary tract infection (UTI) in children is based on symptoms, bacterial growth in the urine, and



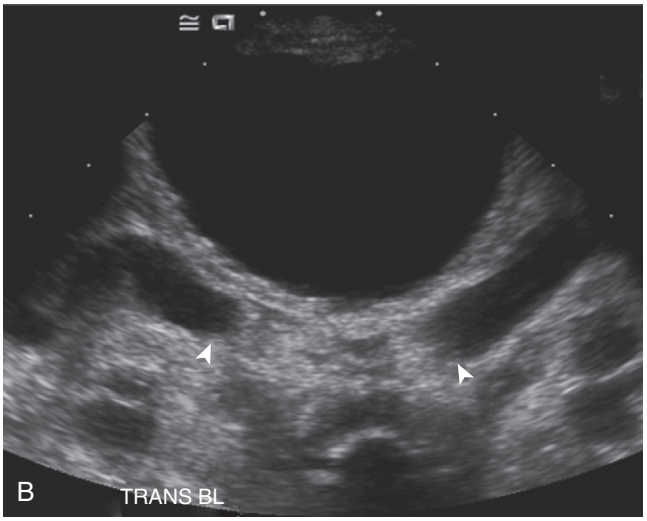


FIGURE 6-28 **A,** A sagittal ultrasound image of the right kidney in a male infant with posterior urethral valves demonstrates dilated renal calyces *(arrow)* and a dilated proximal ureter *(arrowhead)*. **B,** A transverse ultrasound image of the bladder in the same patient demonstrates a distended urinary bladder. Dilated distal ureters can be appreciated posterior to the bladder *(arrowheads)*.

other laboratory markers. Distinguishing between upper tract infection (i.e., pyelonephritis) and lower tract infection (i.e., cystitis) is based on clinical criteria such as the presence of a fever. The goal of imaging in children with a UTI is to exclude an underlying structural abnormality that predisposes the child to develop infection, evaluate for an obstructed urinary system or other disease that would require urgent intervention (e.g., an abscess), and evaluate for evidence of renal damage such as scarring. Ultrasonography of the kidneys and bladder is recommended to assess for any underlying anatomic abnormality. Although cortical renal scintigraphy is the most sensitive imaging technique for the detection of acute pyelonephritis, it is rarely performed emergently. Pyelonephritis in children can be a result of VUR. Therefore, many young children with a febrile UTI are evaluated for VUR with a VCUG or radionuclide cystogram. Depending on the severity of reflux, the child may warrant treatment with prophylactic antibiotics to decrease the risk of renal scarring related to pyelonephritis. Currently, the American Academy of Pediatrics recommends VCUG in the setting of an abnormal

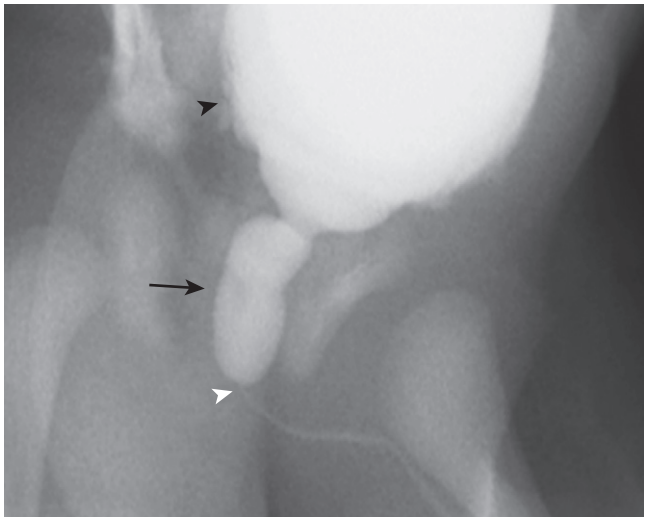


FIGURE 6-29 A lateral-oblique voiding fluoroscopic image acquired during a voiding cystourethrogram in same patient as in Figure 6-28 demonstrates a distended urinary bladder with several small diverticulae *(black arrowhead)*. An abrupt change in caliber from the dilated posterior urethra to the anterior urethra *(white arrowhead)* is noted. The enlarged verumontanum can be identified as a filling defect in the posterior urethra *(arrow)*.

renal US or recurrent febrile UTI, but not after a single febrile UTI. VCUG can be performed several days or weeks after the initial infection. Children presenting to the emergency department with a complicated UTI (i.e., persistent fevers despite administration of antibiotic or clinical signs and symptoms that cause concern for severe illness or sepsis caused by a UTI) warrant evaluation with US.

In patients with acute pyelonephritis, US may reveal focal areas of decreased attenuation. These same areas demonstrate decreased vascularity with color Doppler US. Urothelial thickening is often present. Complications of pyelonephritis include acute focal bacterial nephritis (AFBN) and, rarely, renal or perinephric abscess formation. AFBN is a pseudotumoral inflammatory mass that can be mistaken for a tumor. On imaging it may be heterogeneous with areas of both enhancement and necrosis, but it should decrease in size over time with treatment. A frank abscess will appear as a hypoechoic or anechoic mass with increased through-transmission (Fig. 6-30, *A*). A renal abscess may simulate a solid mass at US. At CT an abscess will appear as a focal, hypoattenuating mass (Fig. 6-30, *B*) with peripheral but no central enhancement. A perinephric abscess is suggested by fluid or soft tissue attenuation within the perinephric space. These collections may penetrate through Gerota fascia and involve surrounding structures, such as the psoas muscle. Urine cultures in patients with renal abscess are negative in up to 20% of cases.

Hydronephrosis

Hydronephrosis refers to dilatation of the urinary collecting system caused by an obstruction to the normal flow of urine. The obstruction may occur anywhere along the urinary tract from the renal calyces to the urethra. Stasis of urine and increased pressures within the collecting system may have deleterious effects on the kidney over time and lead to progressively worsening renal function. A dilated urinary collecting system is not always obstructed. VUR, for

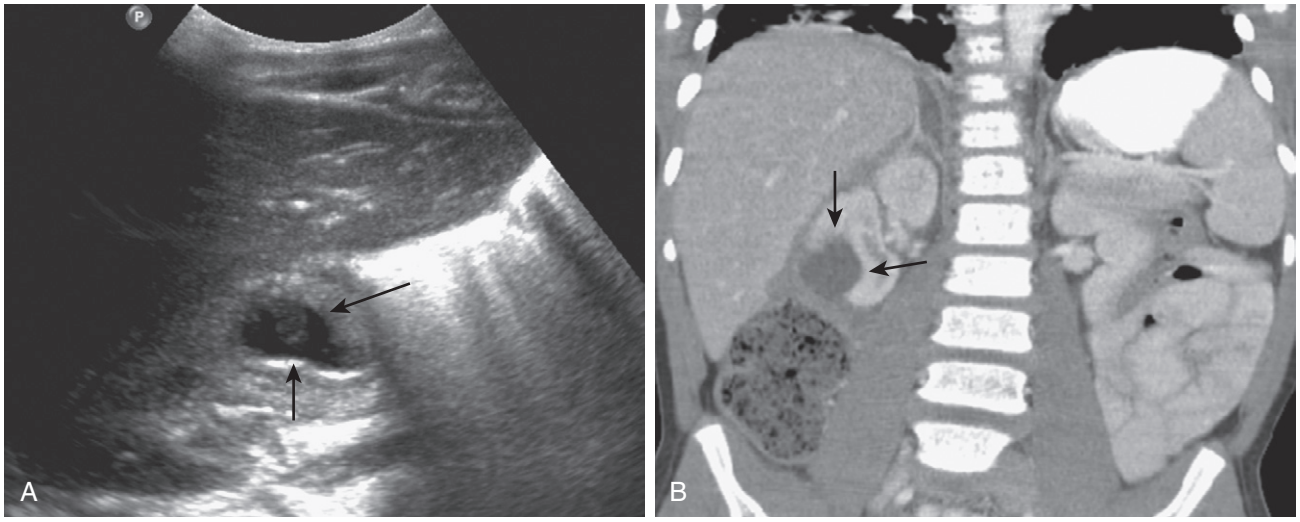


FIGURE 6-30 **A,** A transverse ultrasound image through the kidney in an 8-year-old boy 1 day after a negative appendectomy was performed. A hypoechoic collection is present at the lower pole of the right kidney *(arrows)*. **B,** A coronal reformatted image from a computed tomography scan performed with oral and intravenous contrast material demonstrates a hypoattenuating collection at the right lower pole that does not enhance *(arrows)*. This collection was later found to represent a renal abscess, and a drainage catheter was inserted. Incidentally, this child had negative urine cultures.

example, causes transient dilatation of the urinary collecting system. An obstructing ureteral calculus or stricture may lead to proximal hydroureteronephrosis (dilatation of both the renal collecting system and the ureter), which is indistinguishable from VUR. Determining the cause for a dilated collecting system is not always straightforward. Often other clinical parameters are necessary to make this determination, along with additional imaging evaluation.

US is the modality of choice for evaluating for hydronephrosis. Communication between multiple cystic-appearing, dilated renal calyces and the renal pelvis is an important finding at US. If these cystic spaces do not communicate with each other or with the renal pelvis, it is more likely that the patient has cystic renal disease rather than a dilated collecting system. Color Doppler US is helpful in demonstrating prominent vessels in the renal hilum so that they are not mistaken for a dilated renal pelvis. The ureters are not typically visualized at US unless they are dilated. A dilated distal ureter often can be visualized posterior to the bladder as the level of the ureterovesicular junction (UVJ). If a single ureter is dilated at this level, the obstruction is likely at the UVJ; if both ureters appear dilated at this level, the obstruction is likely within or below the bladder (although bilateral UVJ obstruction can occur). Imaging of the bladder may reveal wall thickening and/or trabeculations in patients with an underlying abnormality, such as a neurogenic bladder. Intraluminal debris or calculi may be present within the bladder of patients with concurrent UTI.

Ureteropelvic Junction Obstruction

A common cause of hydronephrosis in children is ureteropelvic junction obstruction (UPJO). UPJO may be the result of either intrinsic or extrinsic factors. In many children prenatal US detects intrinsic UPJO, and therefore approximately half of all children presenting later in childhood with intermittent UPJO have an extrinsic abnormality such as a crossing vessel. UPJO is often an intermittent

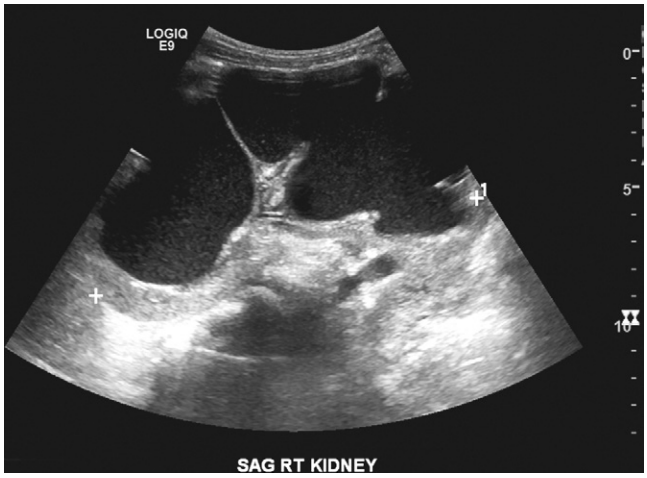


FIGURE 6-31 A sagittal (SAG) ultrasound image through the right (RT) kidney in a child with ureteropelvic junction obstruction. Severe hydronephrosis is present with thinning of the renal cortex. Debris is present within the fluid in the renal pelvis.

phenomenon. Children with intermittent UPJO present with episodic abdominal pain, nausea, and vomiting. The severity of pain correlates with the rapidity of the onset of symptoms rather than the degree of distention of the collecting system. Hematuria is present in approximately half of patients and aids in elucidating the urinary system, rather than other abdominal organs, as the source of symptoms. UPJO is more common in males and occurs most often on the left side.

The US appearance of UPJO is a dilated renal collecting system on the patient's symptomatic side during the acute pain crisis (Fig. 6-31). The proximal ureter appears dilated with an abrupt tapering at the level of the crossing vessel. US should be performed during the pain crisis because the hydronephrosis is present only when the patient is experiencing symptoms. Unilateral hydronephrosis is not specific for UPJO, nor does US evaluate the functional status of the kidney. Although additional investigation is often

required before treatment can be initiated, US is critical in the preliminary imaging of patients with suspected urinary tract obstruction.

Urolithiasis

Although less common in children than in adults, urinary tract calculi are an important cause of flank pain and UTI. The majority of urinary tract calculi in children are located in the kidneys or ureters. Boys and girls are affected with nearly equal frequencies. Abdominal or flank pain is the most common presenting symptom but is present in fewer than half of children with renal stones. Other signs and symptoms include pyuria, hematuria, nausea, vomiting, fever, and urinary retention. Smaller children who are not able to verbalize their symptoms more commonly present with symptoms of infection rather than specific complaints of pain. Most pediatric patients with urolithiasis have an underlying predisposition to forming stones. These predisposing conditions include congenital structural disorders of the urinary system (e.g., UPJO or horseshoe kidney), metabolic disorders (e.g., hypercalciuria or cystinuria), prolonged states of immobilization leading to urinary stasis, enteric disease causing intestinal malabsorption, or recurrent UTIs.

The imaging evaluation of a child with suspected urolithiasis is performed with US, CT, or both. US is an appealing first-line imaging modality because it detects complications of urolithiasis such as hydronephrosis or perinephric fluid without the use of ionizing radiation. At US, renal calculi appear as echogenic foci with posterior acoustic shadowing (Fig. 6-32). US also has the advantage of evaluating the renal parenchyma for changes of medical renal disease or evidence of scarring. US is less sensitive than CT for detection of urinary tract calculi and is limited in diagnosing calculi that are confined to the ureter. CT is often performed in children who have persistent urolithiasis symptoms despite normal results of a US examination.



FIGURE 6-32 A sagittal (SAG) ultrasound image through the right kidney (RK) in a teenage girl with known renal calculi. Echogenic calculi demonstrating posterior acoustic shadowing are present, the largest of which is in the upper pole.

Unenhanced CT is highly sensitive for the detection of urolithiasis in pediatric patients. CT protocols that include a lower dose of radiation have been developed, thus minimizing radiation risk to patients. Phleboliths, which often mimic ureteral calculi in older patients, are rarely encountered in children, which facilitates diagnosis of urolithiasis on CT. Secondary CT signs of urolithiasis are helpful in confirming the diagnosis and include proximal ureteral dilatation, renal enlargement, hydronephrosis, decreased renal attenuation, the tissue rim sign, and perinephric stranding. The tissue rim sign refers to the circumferential rim of soft tissue attenuation surrounding a ureteral calculus (Fig. 6-33). These secondary signs of urinary tract calculi are less commonly encountered in pediatric patients than in their adult counterparts. Proximal ureteral dilatation and renal enlargement are the most commonly detected secondary signs and occur in approximately half of patients. Perinephric or periureteral stranding is rarely encountered in the pediatric patient, which may be a result of the decreased amount of perinephric fat in this population.

Scrotal Hernia

If the testes have not descended into the scrotum by 1 year of age, cryptorchidism (failure of the testes to descend into the scrotal sac), inguinal-scrotal hernias, and hydroceles may result. Although these conditions are most often detected on physical examination, it is not uncommon to make the diagnosis with US. Plain films are diagnostic of scrotal hernias in infants when the finding of bowel gas in the scrotum is noted (Fig. 6-34). Because the presence of bowel gas in the scrotum is not a common finding, US is the imaging modality of choice for evaluation of a scrotal hernia when the physical examination is inconclusive. Herniated omentum appears as an echogenic structure outside of the testis and epididymis. Bowel loops containing both air and fluid also may be visualized within the scrotum. Visualization of bowel peristalsis during imaging is an important finding to note when herniated bowel is identified within the scrotum.

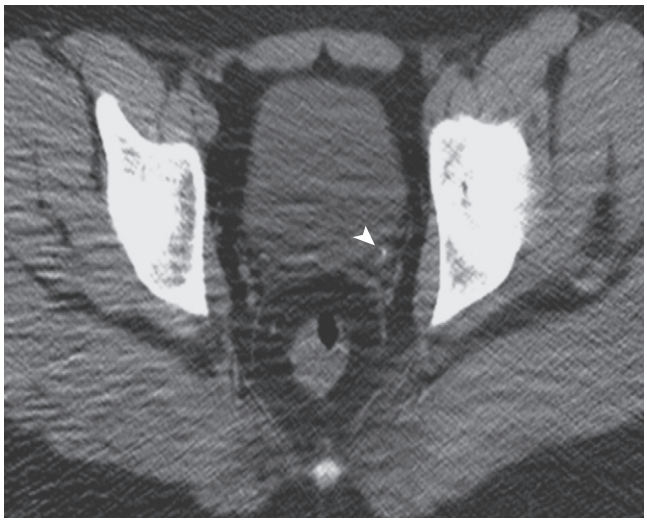


FIGURE 6-33 An axial image from a noncontrast computed tomography scan performed in a 17-year-old boy with left groin pain and a negative scrotal ultrasound. A tiny calculus is present at the left ureterovesicular junction *(arrowhead)* with periureteral stranding.

If bowel is identified within the scrotum but no peristalsis is visualized during the entire examination, the bowel may be strangulated. An akinetic, dilated loop of bowel observed at US in a hernia sac is a highly sensitive and specific sign of bowel strangulation. A strangulated scrotal hernia is an indication for urgent surgery.

Epididymitis

Epididymitis, or epididymo-orchitis, is an infection of the epididymis and/or testis and is a common cause of acute-onset scrotal pain in children. Typically, scrotal pain associated with epididymitis or epididymo-orchitis is relieved when the testes are elevated over the symphysis pubis, a maneuver called *the Prehn sign.* In contradistinction, pain associated with testicular torsion is not relieved by this maneuver. Although the causative agent in epididymitis is usually not identified in young children, the infection usually originates in the prostate gland or bladder and spreads to the epididymis and testis via the vas deferens and spermatic cord lymphatics. A congenital anomaly of the urinary tract may be present. In adolescents the cause is most often a sexually transmitted infection.

US examination of a child with epididymitis demonstrates enlargement of the epididymis (primarily the head) with heterogeneous echotexture. Color Doppler evaluation reveals increased blood flow to the epididymis and/or testis (Fig. 6-35). A reactive hydrocele may be an associated finding. When the entire testis is involved, it is often enlarged and has altered echogenicity. On gray-scale imaging findings alone, the appearance of the testis may mimic a diffusely infiltrative disease such as leukemia or lymphoma, although the clinical presentation should suggest the correct diagnosis.

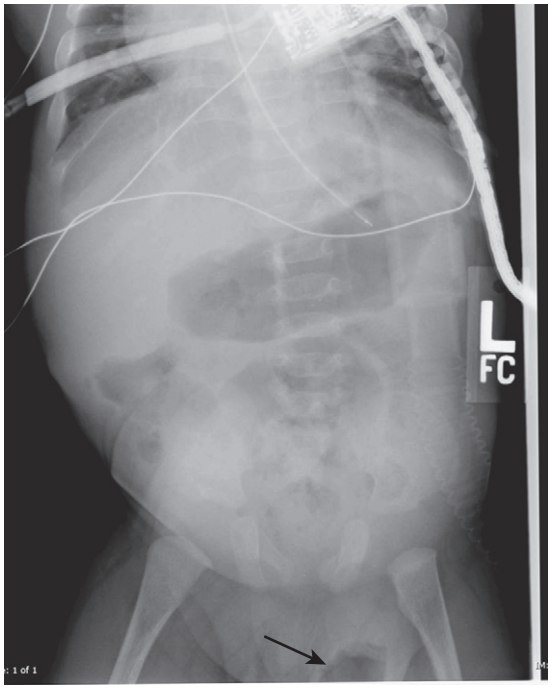


FIGURE 6-34 An abdominal radiograph of a newborn infant with several loops of mildly dilated bowel reveals gas projecting over the scrotum at the inferior aspect of the image *(arrow)*. This infant has a scrotal hernia.

Torsion of the Testicular Appendages

Although there are four testicular appendages, only two are commonly visible at US: the appendix testis and appendix epididymis. These appendages are remnants of embryonic ducts and serve no real function. Because they are attached by a small pedicle, they are prone to torsion. Torsion of these appendages is one of the most common causes of acute scrotal pain in children. The appendix testis is more commonly affected than the appendix epididymis, although it is often difficult to identify the offending appendage. Patients are usually young, prepubertal boys who report having acute-onset scrotal pain. Clinical examination may reveal a bluish discoloration of the skin at the site of pain, which is called the "blue dot" sign and is pathognomonic. At US the twisted appendix is often identified as a round, extratesticular, extraepididymal mass lacking

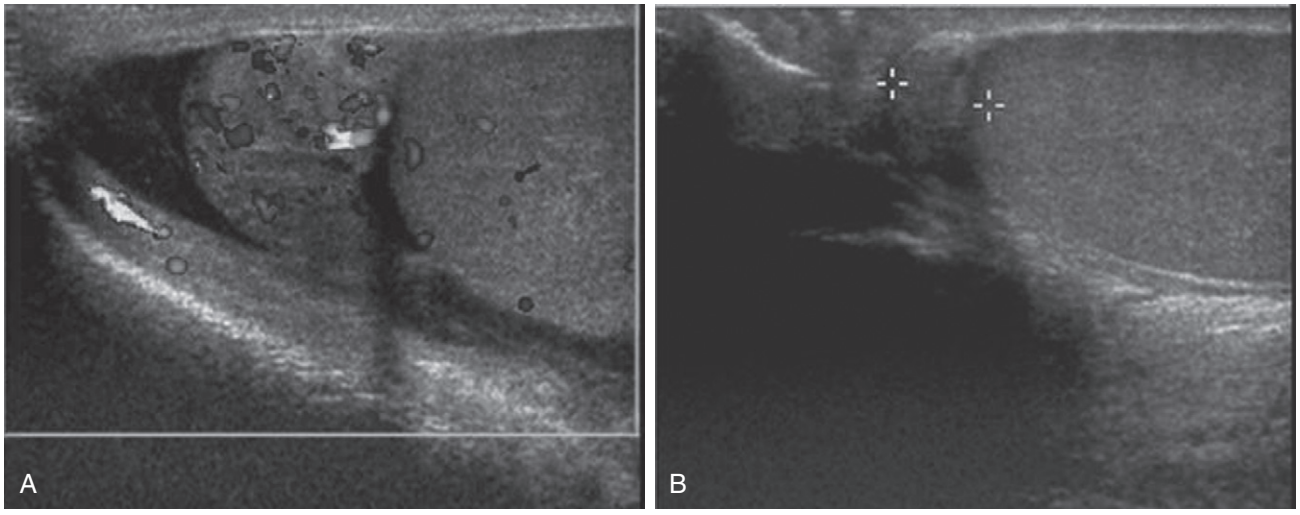


FIGURE 6-35 **A,** A sagittal ultrasound image through the left testis in a 17-year-old male patient with left scrotal pain. The left epididymis is enlarged and hyperemic. **B,** A sagittal ultrasound image from the same patient demonstrating the normal right testicle for comparison.

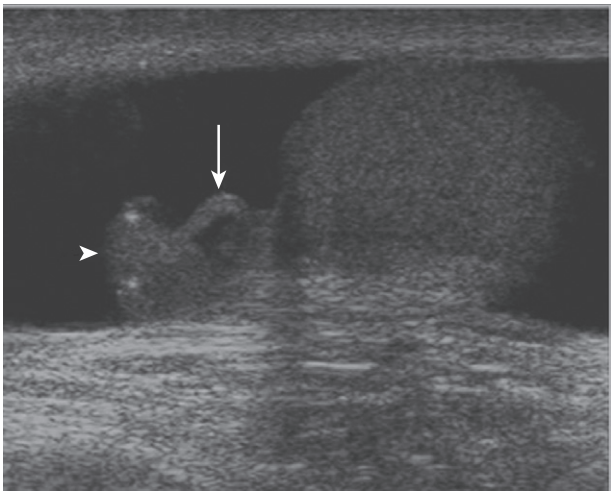


FIGURE 6-36 A transverse ultrasound image through the testis of a teenage boy with scrotal pain. A mixed echogenicity structure *(arrowhead)* is connected to the testis by a thin stalk *(arrow)*. Color Doppler ultrasound failed to demonstrate flow within this structure. The teen was given a presumed diagnosis of torsed testicular appendage and was treated conservatively.

color Doppler flow (Fig. 6-36). A reactive hydrocele may be present, along with scrotal wall skin thickening.

Testicular Torsion

The testis and epididymis attach to the inner scrotal wall by a broad attachment. When this attachment is too narrow, it may function as a pedicle around which the testis may twist. This twisting, or torsion, compromises the blood supply to the testis, which may lead to infarction of the testis. Scrotal pain is often the presenting symptom in boys with testicular torsion, a condition that requires emergent treatment to maintain viability of the affected testis. Testicular salvage rates are greatest when surgery is performed within 6 hours of the onset of symptoms and range from 90% to 100%. The salvage rate drops to 20% to 50% after 12 hours. After 24 hours the testis is usually no longer salvageable.[63] Patients with the "bell clapper" deformity, in which the tunica vaginalis joins high on the spermatic cord, are more prone to testicular torsion compared with the general population.

US is the preferred imaging examination for the diagnosis of testicular torsion because of its high sensitivity and specificity. Gray-scale US findings are often completely normal when torsion is present, and the testes may appear symmetric with respect to both size and echogenicity. A small hydrocele may be present on the affected side. Within a few hours of the onset of symptoms, the scrotal wall will appear thickened, and the testis and epididymis appear enlarged and hypoechoic (as a result of inflammation and/or hemorrhage). Color Doppler imaging is crucial for the diagnosis of torsion. The lack of demonstrable blood flow to the affected testis (assuming appropriate US settings are used) is virtually pathognomonic for torsion (Fig. 6-37). In prepubertal patients it is often difficult to demonstrate the presence of blood flow even in normal testes. Testicular scintigraphy is rarely used as an adjunct to US when a diagnosis of torsion cannot be made with certainty. Given the added delay of scintigraphic examinations,

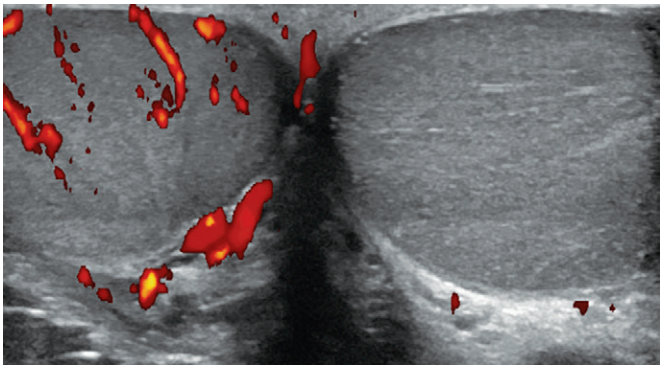


FIGURE 6-37 A transverse ultrasound image of bilateral testes in a teenage boy with left testicular pain. The left testis has no color Doppler flow. This patient had testicular torsion, which was confirmed at surgery.

however, some surgeons will operate on the basis of an equivocal US. The treatment for testicular torsion is detorsion of the affected testicle and orchiopexy, a procedure in which the testis is affixed to the scrotal wall to prevent torsion from recurring.

Adnexal Torsion

Acute onset of adnexal pain in a young or adolescent female is concerning for adnexal or ovarian torsion. The fallopian tubes are long in children and the ovaries are hypermobile, which increases their susceptibility to torsion. Although normal ovaries may twist, most often an ovarian or paraovarian cyst or mass predisposes the ovary to torsion by functioning as a fulcrum around which the ovary can twist. The ovary becomes twisted around its pedicle, leading to various degrees of hemorrhagic infarction. If surgery is not performed expeditiously, future fertility and hormonal regulation may be compromised. There is a slight predilection for torsion to involve the right ovary. When the right ovary is affected, the diagnosis is more difficult to establish given the number of other conditions that present with right lower quadrant or pelvic pain, such as appendicitis, Meckel diverticulitis, and inflammatory bowel disease. The median age of patients with ovarian torsion is 11 years.

Pelvic US is the study of choice for evaluation of ovarian torsion. Normal ovaries often appear hypoechoic relative to the adjacent pelvic tissue and have an ovoid or ellipsoid shape. Although the size of normal ovaries varies, mean ovarian volumes are approximately 1.2 cm^3 in prepubertal girls and 5.8 cm^3 in pubertal girls. Microcystic follicles are routinely identified in normal ovaries. When the ovaries demonstrate normal gray-scale imaging characteristics and have a normal size and shape, color Doppler evaluation is usually not necessary. However, if one ovary appears abnormally large relative to the other side, torsion may be present. In nearly all cases of ovarian torsion, the affected ovary is massively enlarged and has a round or globular configuration. In neonates and young girls, ovarian torsion is commonly seen as a large cystic mass with fluid-debris levels. In young or adolescent girls the more classic imaging appearance is an enlarged, echogenic ovary with multiple enlarged peripheral follicles. In other cases, the ovary may appear as a complex cystic mass resulting from the

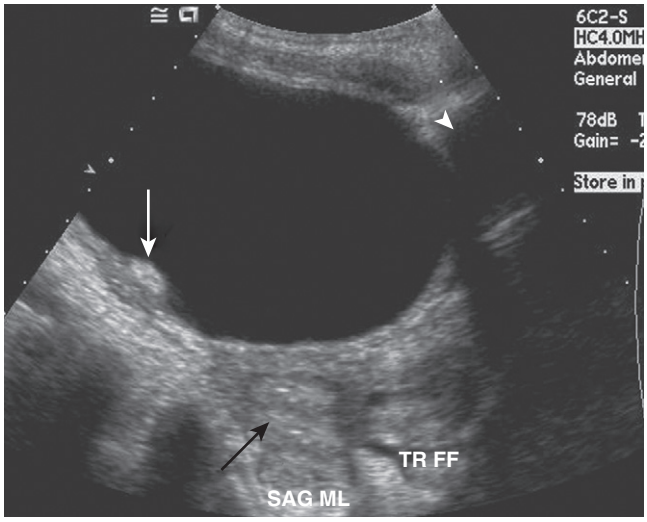


FIGURE 6-38 A sagittal ultrasound image of the pelvis in a 15-year-old girl with right lower quadrant pain. The bladder is nearly empty *(arrowhead)* and a large, complex cystic mass present within the pelvis contains a mural nodule *(white arrow)*. The uterus is posterior to this mass *(black arrow)*. Color Doppler imaging revealed no convincing flow to this mass. At surgery the patient was found to have a right ovarian teratoma that had twisted.

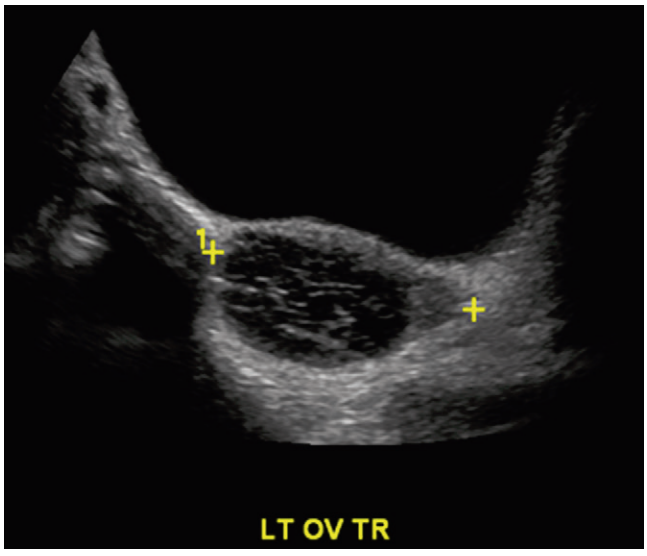


FIGURE 6-39 An ultrasound image from a 15-year-old adolescent female with left pelvic pain demonstrates a 6-cm hemorrhagic cyst on the left ovary. The fine, reticular septations resembling a fishnet pattern are typical for a hemorrhagic cyst. A follow-up ultrasound 6 weeks later demonstrated resolution of the cyst.

presence of an underlying cyst or tumor (Fig. 6-38). Color Doppler evaluation of the ovary often reveals an absence of blood flow, a finding that is classically associated with ovarian torsion. However, torsion may be present even if arterial waveforms are demonstrated because the ovary has a dual blood supply (from both the uterine and ovarian arteries). The presence of arterial waveforms within the ovary should not sway the diagnosis away from ovarian torsion if the grayscale imaging findings and physical examination are consistent with torsion.

Hemorrhagic Ovarian Cyst

Although hemorrhagic ovarian cysts are common, their imaging appearance is widely variable. Hemorrhagic cysts are almost exclusively encountered in menstruating, adolescent females. Hemorrhagic cysts develop at the time of ovulation when vessels surrounding a corpus luteal cyst rupture, giving rise to hemorrhage within the corpus luteum. As the cyst evolves over time, the sonographic features change with the stage of clot retraction. Patients may present with acute-onset adnexal pain that may be severe.

Physiologic ovarian follicles measure less than 3.0 cm in diameter. Most hemorrhagic cysts have a thin outer wall, demonstrate posterior acoustic through-transmission, and can be variable in size but often measure 3 to 3.5 cm in diameter. Fine, reticular septations resembling a fishnet pattern are a common finding at US (Fig. 6-39). These septations represent fibrin strands that contain no blood flow. In some patients the hemorrhagic cyst contains a retracting clot. Although a large portion of the cyst appears anechoic, the retracting clot appears as an adherent, echogenic structure within the cyst that contains no blood flow. In rare cases, when the clot becomes very small, it can simulate a mural nodule and raise concern for an ovarian neoplasm. Fluid-fluid or fluid-debris levels also can be demonstrated within a hemorrhagic cyst. Hemorrhagic cysts can be complicated by rupture, with free spill of hemorrhagic contents into the pelvis. When rupture occurs, echogenic fluid will be demonstrated within the pelvis surrounding the uterus and adnexa. In some cases, the hemoperitoneum may be massive. If the diagnosis of hemorrhagic cyst is uncertain, a 6-week follow-up US can be obtained. Hemorrhagic cysts change throughout the menstrual cycle and typically will resolve or decrease in size at follow-up.

Other causes of adnexal pain include a tubo-ovarian abscess, ectopic pregnancy, and pelvic inflammatory disease. In patients who are sexually active, these diagnoses should also be considered within the differential diagnosis. Human chorionic gonadotropin results are critical for the accurate interpretation of a pelvic US examination in a sexually active female with pelvic pain.

Hematocolpos/Hematometrocolpos

Patients with imperforate hymen, transverse vaginal septum, or lower vaginal agenesis usually present at the time of adrenarche with cyclic bouts of pelvic pain that correspond to menstruation episodes. The patient may not be aware that she has begun menstruating because of the lack of passage of blood products from the obstructed vagina. The diagnosis of hematocolpos is often made on the basis of physical examination, because the hymen may appear to be bulging outward as a result of accumulated secretions. In some cases US may suggest the diagnosis when a thorough physical examination has not been performed. In rare cases, the patient may have a congenital uterine anomaly with an obstructed hemivagina. In these cases the diagnosis is clinically more confusing because the patient will appear to menstruate normally given the presence of an unobstructed hemivagina.

US examination in these patients reveals a round or oblong-shaped midline or paramidline pelvic mass that compresses the bladder anteriorly and the rectum posteriorly. The mass appears hypoechoic with posterior acoustic transmission. Internal echoes will be present within the

mass, reflecting the complex nature of its contents (hemorrhage). If only the vagina is involved (hematocolpos), the uterus will be visualized separately from this mass (Fig. 6-40). When the uterus is also affected (hematometrocolpos), only a thin rind of normal uterine tissue may be visualized. Patients usually experience relief of symptoms once the obstruction is corrected.

CHEST AND AIRWAY

Neonatal Respiratory Distress

Common respiratory illnesses encountered in the neonatal intensive care unit include surfactant deficiency disease (SDD) and/or its complications, transient tachypnea of the newborn (TTN), neonatal pneumonia, and meconium aspiration syndrome (MAS). Neonates with these conditions are commonly evaluated with chest radiographs. The patient's clinical information, including gestational age, prenatal history, method of delivery, and presence of meconium at birth, is critical for the correct interpretation of the radiographs.

Surfactant Deficiency Disease

SDD, also termed "hyaline membrane disease" and "respiratory distress syndrome," almost exclusively affects premature infants (i.e., younger than 36 to 38 weeks gestation) and increases in prevalence as gestational age decreases. The lack of surfactant in the lungs of a premature infant causes collapse of pulmonary alveoli, which leads to poor oxygenation. Infants with SDD demonstrate signs and symptoms of respiratory distress at birth, manifested by grunting, nasal flaring, retracting, and tachypnea. The radiographic findings of SDD may be present at birth, although in some cases the findings evolve after 12 to 24 hours. Classic radiographic findings of SDD are low lung volumes with diffuse, bilateral, granular opacities (Fig. 6-41). These opacities improve after treatment with exogenous surfactant. Infants with SDD are often in severe respiratory distress and require mechanical ventilation.

Air Block Complications

Infants connected to mechanical ventilators are at risk of experiencing complications as a result of barotrauma or volutrauma. This risk is especially true for infants with underlying lung disease such as SDD as a result of diminished pulmonary compliance. Air may rupture outside of the alveoli entering the perivascular or peribronchiolar spaces, giving rise to interstitial lucencies termed "pulmonary interstitial emphysema" (Fig. 6-42). The air also may dissect into the mediastinum, pleural space, or pericardium. On a supine chest radiograph, a pneumothorax tends to collect anteriorly along the heart border or inferiorly above the

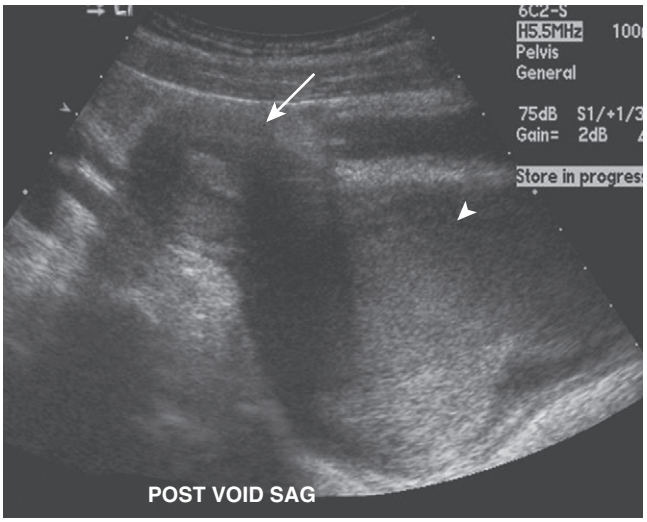


FIGURE 6-40 A sagittal (SAG) ultrasound image through the pelvis in a 13-year-old girl with severe, crampy abdominal pain. Inferior to the uterus *(arrow)* is an oblong-shaped mass *(arrowhead)* with low-level internal echotexture. The mass is within the vagina. At surgery this patient was found to have hematocolpos.

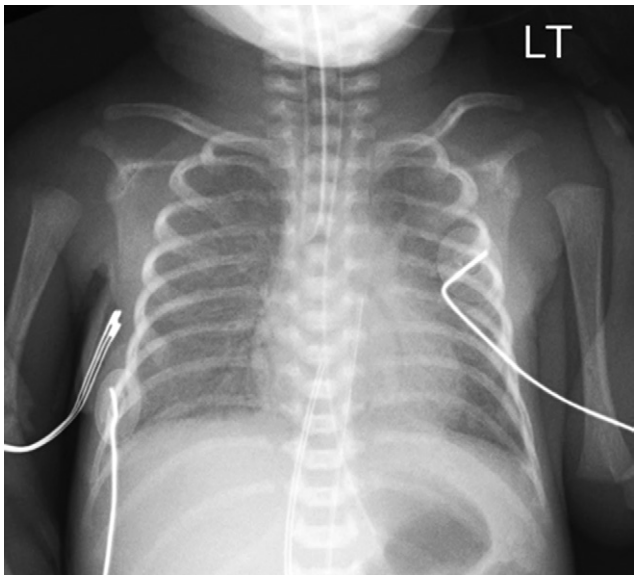


FIGURE 6-41 A chest radiograph in a premature infant with surfactant deficiency demonstrates an endotracheal tube in place. Bilateral, diffuse granular opacities can be seen within the lungs with air bronchograms. Note the high positioning of the umbilical artery catheter and umbilical venous catheter in the heart.

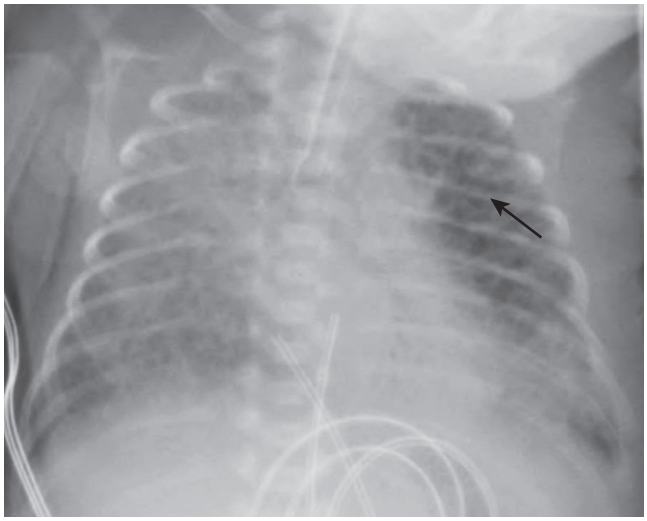


FIGURE 6-42 A chest radiograph in a premature male infant demonstrates an endotracheal tube in place. Branching cystic lucencies within the left upper lobe *(arrow)* are consistent with pulmonary interstitial emphysema.

diaphragm (Fig. 6-43) and is manifested as a paracardiac lucency (for a medial pneumothorax) or a deep costophrenic sulcus (for an inferior pneumothorax). A cross-table lateral view is often necessary to demonstrate the anterior location of the air (Fig. 6-44). Pneumomediastinum causes anterior and superior displacement of the thymus in a "spinnaker sail" configuration (Fig. 6-45). Pneumopericardium outlines the heart border without extending superior to the great vessels (Fig. 6-46).

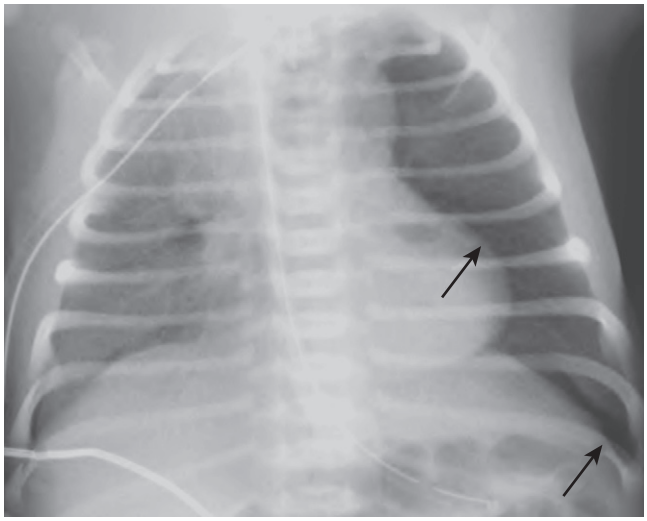


FIGURE 6-43 In this premature infant, lucency adjacent to the left heart border and projecting over the left hemidiaphragm *(arrows)* indicates the presence of a pneumothorax.

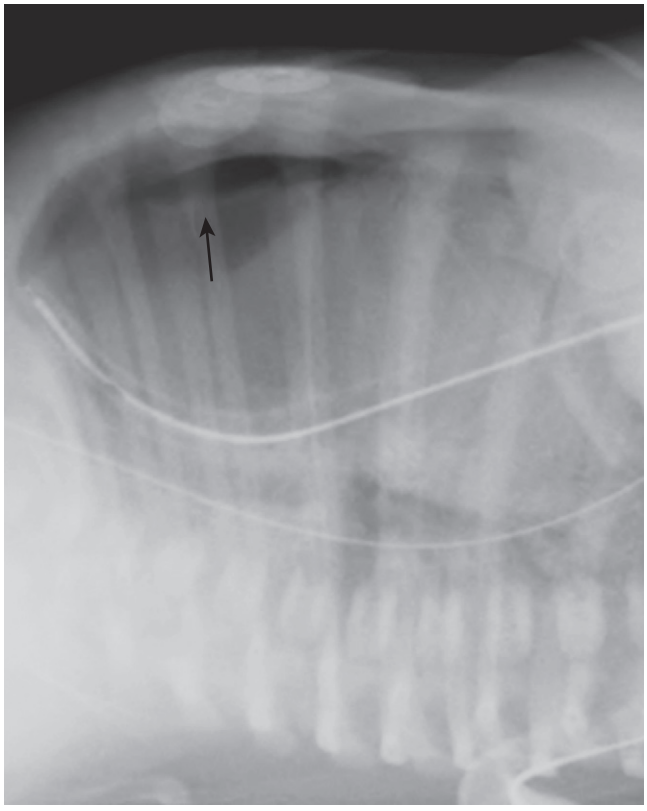


FIGURE 6-44 A cross-table lateral chest radiograph in the same infant as in Figure 6-43 demonstrates the anterior location of the pneumothorax *(arrow)*.

Transient Tachypnea of the Newborn

Infants with TTN are often full-term infants delivered via cesarean section. The course of delivery does not effectively clear the fetal lung fluid, which is why this entity is also referred to as "retained fetal lung fluid." Coarse interstitial opacities on chest radiographs are often present, indicative of underlying pulmonary edema. A pleural effusion and/or fluid tracking along the fissures is commonly present. The hallmark of TTN is return of the radiograph to normal in 24 to 48 hours, which coincides with resolution of tachypnea. Lung volumes are normal or increased.

Neonatal Pneumonia

Neonatal pneumonia is usually a result of an ascending vaginal infection; the most common infectious agent is group B streptococcus. A major risk factor for neonatal pneumonia is prolonged rupture of the amniotic membranes. The most common finding on chest radiographs in neonates with pneumonia is bilateral alveolar densities

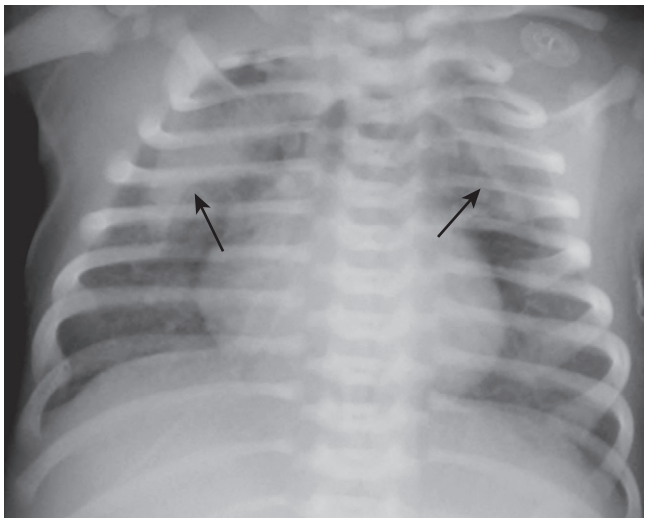


FIGURE 6-45 A chest radiograph in a premature baby demonstrates the thymus displaced anteriorly by pneumomediastinum *(arrows)*.

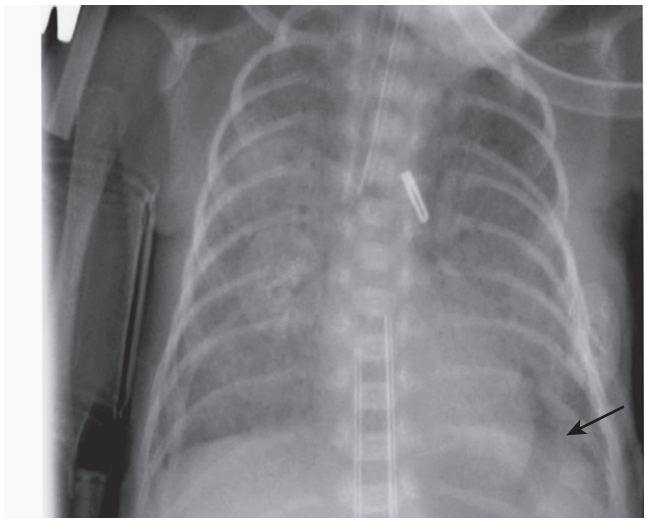


FIGURE 6-46 A chest radiograph in a premature infant who had a patent ductus arteriosus ligation demonstrates a lucency projecting adjacent to the cardiac apex *(arrow)*, consistent with pneumopericardium.

with air bronchograms. The radiographic findings often are difficult to distinguish from other conditions, such as SDD or MAS. Serial films and clinical history are most helpful in distinguishing between these entities.

Meconium Aspiration Syndrome

MAS is diagnosed by the presence of meconium below the level of the vocal cords at birth. Infants with MAS are usually post-dates or have experienced intrauterine stress. The thick, tenacious meconium causes obstruction of small and medium-sized airways, which leads to areas of both atelectasis and overinflation. The meconium can cause a chemical pneumonitis and also inactivates surfactant within lung alveoli. Chest radiographs in infants with MAS reveal coarsened interstitial densities and bilateral parenchymal opacities interspersed with areas of hyperaeration (Fig. 6-47). MAS is the most common respiratory disease to cause a pleural effusion in the first few days of life.

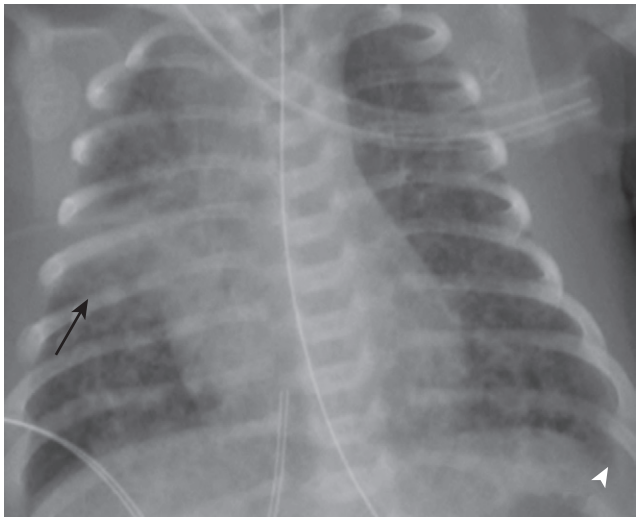


FIGURE 6-47 A chest radiograph in a full-term baby girl with meconium aspiration demonstrates coarse interstitial lung markings, a focal opacity projecting over the right mid-lung *(arrow)*, and a small left pleural effusion *(arrowhead)*.

Respiratory Emergencies in Children

Stridor

Stridor is a term used to describe a high-pitched sound caused by partial obstruction of the airway. Stridor can have an inspiratory, expiratory, or biphasic pattern (both inspiratory and expiratory). An inspiratory pattern suggests an upper airway cause (e.g., epiglottitis). An expiratory pattern suggests a lower airway etiology (e.g., tracheomalacia). A biphasic pattern suggests a glottic or subglottic obstruction (e.g., subglottic hemangioma). Imaging evaluation of the child with stridor is commonly performed with neck and/or chest radiographs, depending on the pattern of stridor and associated clinical findings.

Retropharyngeal Abscess

In addition to stridor, patients with a retropharyngeal abscess typically also present with symptoms of neck pain and fever. Radiographs of the neck are often requested to evaluate the retropharyngeal soft tissues. Because of the wide range of ages and sizes within the pediatric population, precise measurements of the retropharyngeal soft tissues are not as reliable for determining the presence of soft tissue swelling as are relative measurements. The thickness of the retropharyngeal/prevertebral soft tissues should not be greater than the anteroposterior (AP) diameter of the adjacent vertebral body (Fig. 6-48). False thickening of the retropharyngeal/prevertebral soft tissues can occur if the

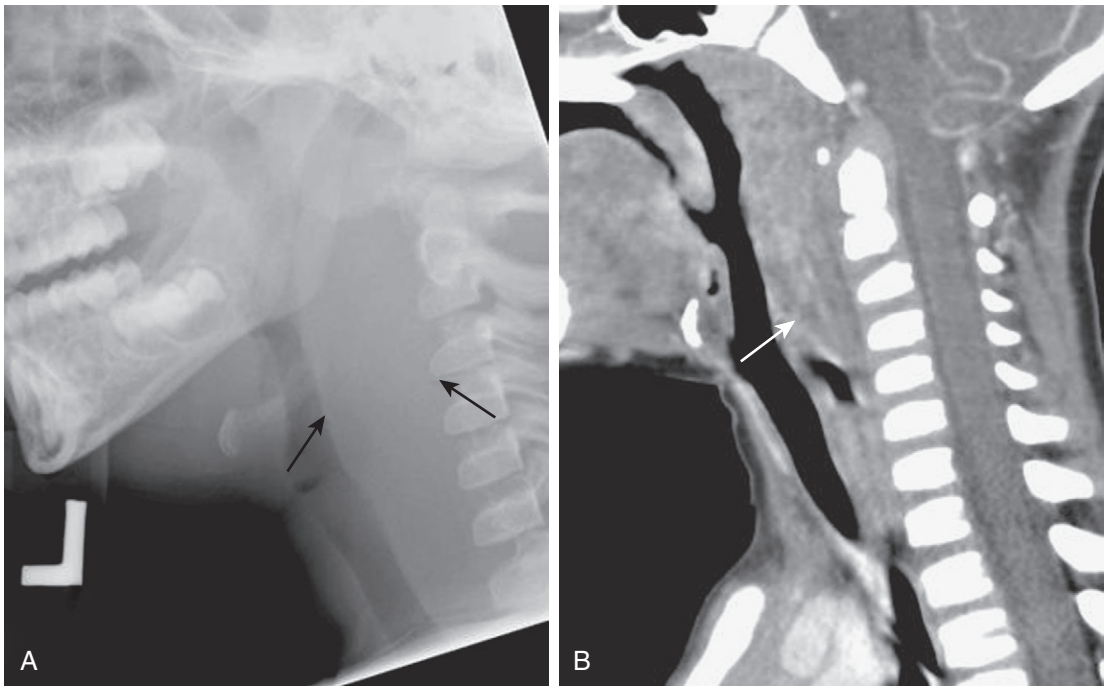


FIGURE 6-48 **A,** A lateral neck radiograph in a 3-year-old child with fever and neck pain reveals thickening of the retropharyngeal soft tissues (denoted by *arrows*). **B,** A sagittal reformatted image obtained from subsequent computed tomography of the neck demonstrates evidence of retropharyngeal cellulitis *(arrow)*.

child's neck is in flexion or if the film was acquired with the child in end-expiration. Although CT can be used to further evaluate positive findings on neck radiographs, it is often prudent to repeat the lateral radiograph of the neck with the patient in a more exaggerated extension or in full inspiration when the initial radiographs are believed to be falsely positive. Alternatively, airway fluoroscopy can be performed to distinguish true retropharyngeal soft tissue thickening from pseudothickening.

Another common cause of acute stridor within the nasopharynx and oropharynx is enlargement of the tonsils and adenoids. This diagnosis can be readily differentiated from retropharyngeal abscess on the basis of findings of a lateral radiograph of the neck (Fig. 6-49). Enlarged adenoids and tonsils cause encroachment on the nasopharyngeal and oropharyngeal airway, without associated thickening of the retropharyngeal soft tissues.

Epiglottitis

Epiglottitis is inflammation and enlargement of the epiglottitis, aryepiglottic folds, and supraglottic tissue. Epiglottitis is a life-threatening condition with both viral and bacterial causes. Haemophilus influenza B has historically been the most common cause of epiglottitis, although its incidence has decreased dramatically since the development of the *Haemophilus influenzae* type B vaccine. The epiglottis can be identified at the level of the hyoid bone on lateral radiographs of the neck. On lateral neck radiographs, "thumblike" enlargement of the epiglottis and thickening of the aryepiglottic folds are findings consistent with epiglottitis (Fig. 6-50). Children with high clinical and radiographic concern for epiglottitis are often examined in the operating room with the presence of an anesthesiologist, because airway compromise may be precipitated by manipulation of the hypopharynx and urgent intubation or tracheostomy may be necessary.

Croup

Viral croup (laryngotracheobronchitis) is the most common cause of acute stridor in children. Findings on chest or neck radiographs include narrowing of the subglottic airway. This condition is best visualized on the AP projection as the "steepling" or loss of the normal shouldering in the subglottic region (Fig. 6-51). Bacterial tracheitis, also known as *membranous croup*, is another serious upper airway infection that is seemingly becoming more common as viral croup and epiglottitis have decreased in incidence. The diagnosis of bacterial tracheitis can be suggested on radiographs if subglottic narrowing is seen in conjunction with tracheal irregularity or a soft tissue membrane.

Glottic/Subglottic Masses

Subglottic masses may present in an emergent setting when a superimposed viral or bacterial illness causes exacerbation and acuity of symptoms. The most common glottic mass is a papilloma, and the most common subglottic mass is a hemangioma. Extrinsic mass effect from mediastinal or neck masses can cause airway compromise. Bronchogenic cysts, foregut duplication cysts, and vascular rings can cause airway narrowing and acute symptoms when coexistent with an acute respiratory infection. Any abnormal deviation of the trachea (besides the mild contour deformity from the normally positioned left-sided aortic arch) should be investigated (Fig. 6-52). Fluoroscopy and a contrast esophagram can be performed to confirm the presence of mass effect on the airway and adjacent esophagus. CT or MRI can better visualize the abnormality if these initial studies demonstrate an abnormality.

Foreign Body

The majority of patients with an aspirated FB are between the ages of 1 and 3 years. The FB may become embedded

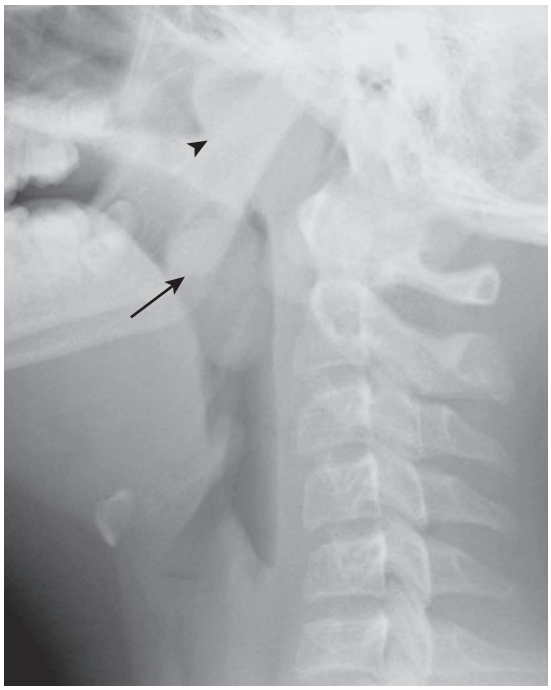


FIGURE 6-49 A lateral radiograph of the neck in an 11-year-old girl with difficulty breathing demonstrates enlarged adenoids *(arrowhead)* and palatine tonsils *(arrow)*.

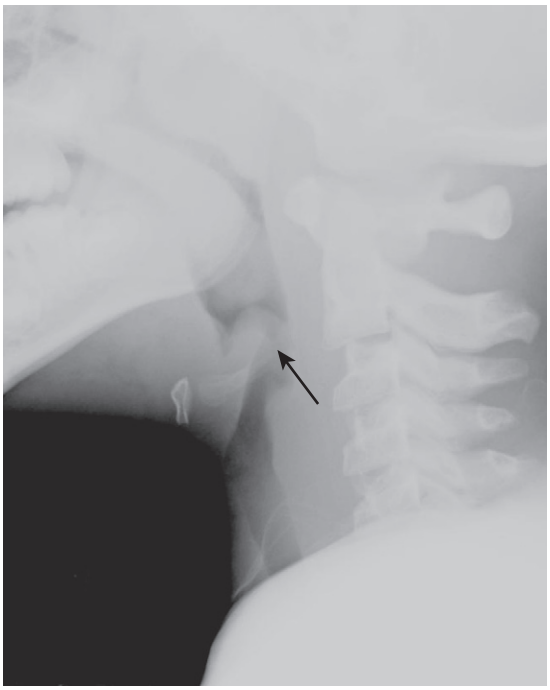


FIGURE 6-50 A lateral neck radiograph in a 6-year-old boy with fever, sore throat, and drooling demonstrates thumblike enlargement of the epiglottitis *(arrow)*. This child had epiglottitis.

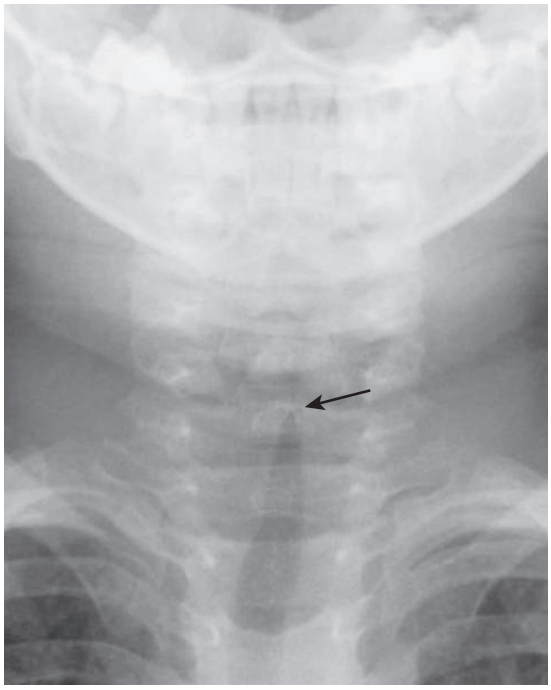


FIGURE 6-51 An anteroposterior radiograph of the neck in a 2-year-old child with stridor demonstrates "steepling" of the subglottic airway *(arrow)* as a result of viral croup.

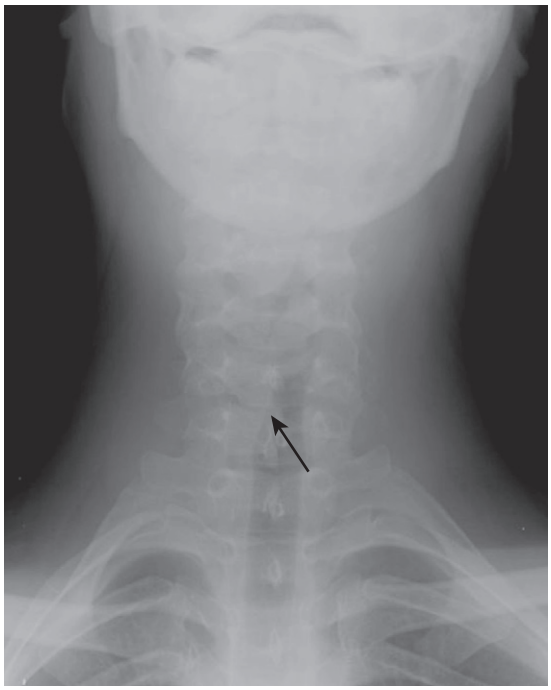


FIGURE 6-52 An anteroposterior radiograph of the neck in a teenage boy with trisomy 21 demonstrates a right lateral impression on the subglottic trachea *(arrow)* as a result of a mass that was later found to be a spindle cell tumor.

anywhere along the airway in children. Symptoms of an aspirated FB include choking, wheezing, coughing, and dyspnea. Patients with an aspirated FB require bronchoscopy for removal of the object. Clinical history, radiography, and fluoroscopy can all be used to determine if a FB has been aspirated. If the FB is caught at the level of the vocal cords, the pharynx may appear hyperinflated on neck radiographs. Aspirated FBs are likely to settle into the right mainstem bronchus given that it typically has a more vertical orientation than the left mainstem bronchus.

The majority of aspirated FBs are not radio-opaque. In children with a history of suspected aspirated FB, inspiratory and expiratory chest radiographs evaluating for areas of air trapping are performed. Bilateral decubitus views can be performed in place of expiratory films in younger patients who are not able to cooperate for inspiratory and expiratory imaging. In a normal patient, both lungs should collapse equally on an expiratory film, and the dependent lung should collapse on a lateral decubitus film while the nondependent lung expands. When the dependent lung does not collapse on decubitus films, air trapping is implied, and an aspirated FB must be suspected (Fig. 6-53). Chest fluoroscopy also can be performed to assess for symmetric movement of the diaphragm with inspiration and expiration. If one hemidiaphragm remains depressed on expiration, air trapping on that side suggests obstruction due to an FB. Radiographs cannot exclude the presence of an aspirated FB, and false-negative radiographs are common. Negative radiographs should not preclude bronchoscopy in a child with a convincing history or physical examination consistent with an aspirated FB. Occasionally, when the diagnosis of FB aspiration is delayed, postobstructive pneumonia may develop. In some cases, plain films may reveal that the FB has not been aspirated but rather is lodged within the esophagus (Fig. 6-54).

Pneumonia

Lower respiratory tract infections are one of the most common indications for imaging the chest in pediatric patients. Bacterial pneumonia is manifested on a chest radiograph as an area of focal air space opacity without associated volume loss (Fig. 6-55). Pneumonia may be complicated by a pleural effusion or parenchymal necrosis. Lobar pneumonias are the most common presentation of a bacterial pneumonia in children. Radiographs are often repeated after completion of antibiotic therapy to assess the resolution of the consolidation. If no significant improvement has occurred after appropriate treatment, additional imaging with CT is warranted. If a patient has had multiple appropriately treated recurrent pneumonias in the same location, a CT scan of the chest may be warranted to assess for an underlying anomaly predisposing the patient to recurrent illnesses, such as pulmonary sequestration. In young children, bacterial pneumonia also may present on chest radiographs as a round mass, aptly called "round pneumonia."

Patients with sickle cell disease are prone to acute infiltrates on radiographs, termed "acute chest syndrome." Although these patients are often treated with antibiotics, not all of them truly have an infection. Pulmonary infarctions can have a similar appearance to infection, and studies suggest that evaluation of the location and age of the patient may be helpful to predict whether there is an underlying infection in these patients with an "acute chest."

Bronchiolitis

Viral bronchiolitis is one of the most frequent causes of infant hospitalization during the winter. Infants with bronchiolitis present with wheezing, cough, and respiratory distress. Nontoxic-appearing infants with classic symptoms usually require no imaging. Chest radiographs are

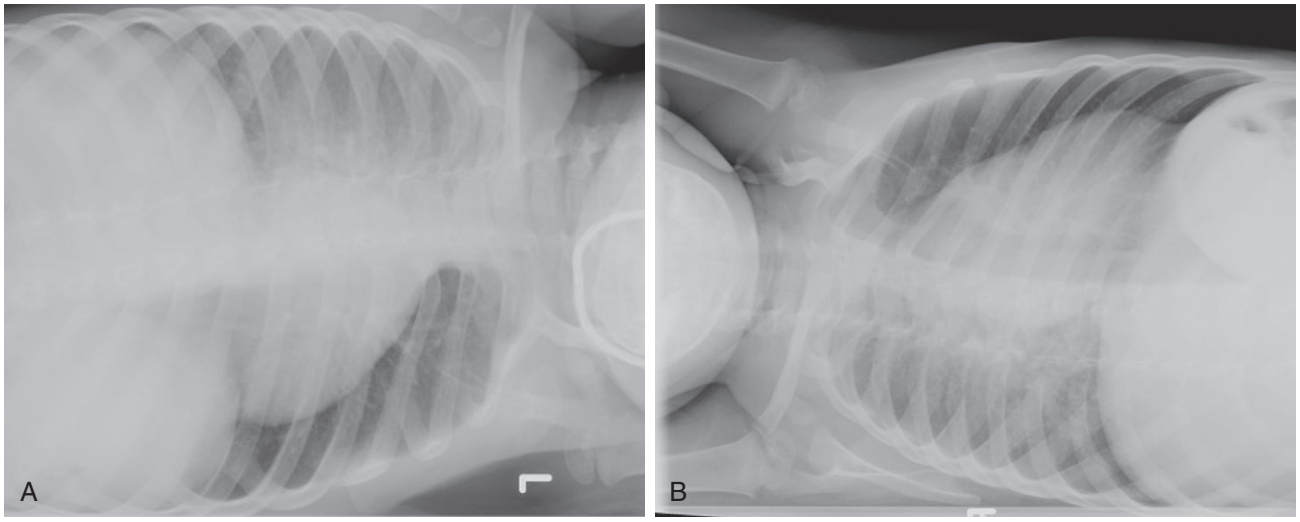


FIGURE 6-53 **A,** A left lateral decubitus chest radiograph in a 22-month-old with cough and suspected foreign body aspiration fails to demonstrate normal collapse of the dependent left lung. **B,** A right lateral decubitus film in the same patient demonstrates normal collapse of the right lung. This patient was found to have a peanut in the left mainstem bronchus at bronchoscopy.



FIGURE 6-54 A lateral radiograph of the neck in a child demonstrates an ingested radio-opaque foreign body lodged within the esophagus posterior to the trachea.

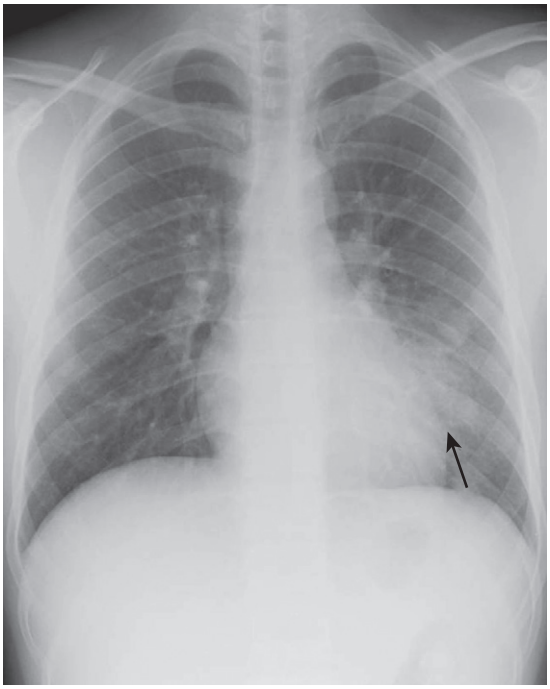


FIGURE 6-55 An anteroposterior chest radiograph of a teenager with symptoms of pneumonia demonstrates a focal opacity in the lingula *(arrow),* consistent with pneumonia.

often obtained when the diagnosis is unclear or when an underlying bacterial pneumonia is suspected. Chest radiographs often reveal evidence of airway disease, which include areas of atelectasis, air trapping, and bronchiolar wall thickening (Fig. 6-56). Atelectasis and air trapping are findings related to underlying bronchial obstruction caused by edema and secretions. Bronchiolar wall thickening is most prominent in the perihilar regions on chest radiographs.

Pneumothorax

Acute shortness of breath in an older child may be a result of a spontaneous pneumothorax. Pneumothoraces in this age group are often caused by rupture of a small subpleural bleb, typically located at the lung. Chest radiographs reveal variable degrees of collapse of the affected lung, and the visceral pleura will be identified as a discrete line paralleling the chest wall. Shifting of the heart and mediastinum to the opposite hemithorax is consistent with a tension pneumothorax, which requires immediate decompression (Fig. 6-57). Patients with an underlying parenchymal bleb often will have recurrent pneumothoraces if the bleb is not resected or if pleurodesis is not performed. CT is more sensitive than plain radiographs for visualizing tiny blebs. CT is often performed after reexpansion of the affected lung has occurred to best visualize the peripheral lung parenchyma.



FIGURE 6-56 An anteroposterior chest radiograph in an infant with wheezing reveals hyperinflated lungs with areas of atelectasis and air trapping, as well as peribronchiolar wall thickening. This child was treated for bronchiolitis.

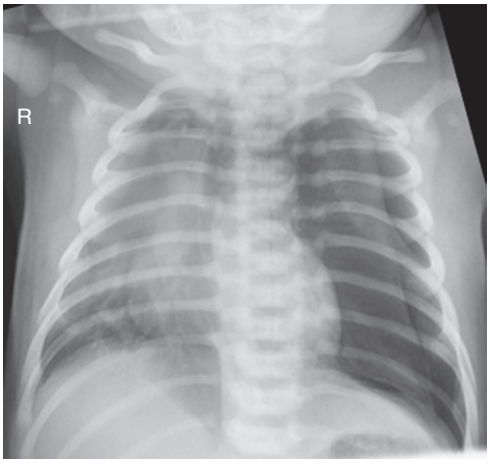


FIGURE 6-57 An anteroposterior chest radiograph performed on a newborn baby girl who required positive pressure ventilation demonstrates a large left tension pneumothorax resulting in rightward shift of the heart and thymus and downward shift of the left hemidiaphragm. The patient was treated emergently with needle decompression.

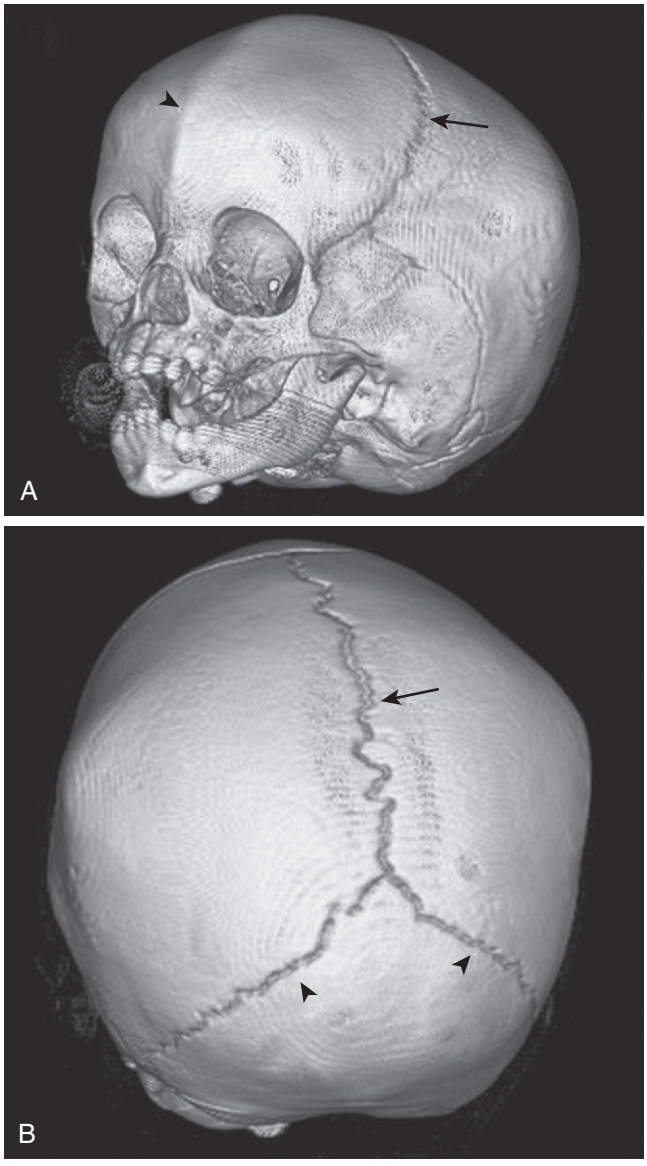


FIGURE 6-58 Three-dimensional reconstructed images of the calvarium from a head computed tomography scan of an infant demonstrate normal sutural anatomy. **A,** The metopic suture has fused *(arrowhead)*. A normal coronal suture is shown *(arrow)*. **B,** Normal sagittal *(arrow)* and lambdoid sutures *(arrowheads)*.

Patients with underlying pulmonary disorders, such as cystic fibrosis and Langerhans cell histiocytosis, are at higher risks for spontaneous pneumothoraces because of the presence of blebs and cysts.

CENTRAL NERVOUS SYSTEM

Skull Fractures

The leading cause of death in the pediatric population is traumatic brain injury. Patterns of acute intracranial injury are similar to those of the adult population and are further discussed in other chapters. However, certain special considerations must be kept in mind when evaluating the pediatric brain. Plain skull radiographs are useful for evaluating fractures in certain situations, although CT has largely supplanted plain radiographs for this diagnosis because of the superior capability of CT to evaluate complications of fracture, such as intracranial hemorrhage. The detection of skull fractures can be subtle even on CT. Skull fractures must be distinguished from the normal sutures (Fig. 6-58). Cranial sutures are usually symmetric and lack overlying soft tissue swelling, in contrast to skull fractures (Fig. 6-59). Accessory and anomalous sutures also can be mistaken for skull fractures. Because of the axial plane of CT imaging, skull fractures oriented along the plane of the scan may not be visible on the axial images. It is critical to evaluate the scout image so that these fractures are detected. Coronal, sagittal, and three-dimensional bony reformatted images also greatly improve our ability to detect subtle fractures. The degree of comminution of the fracture, depression or displacement of fragments, and additional intracranial findings such as hemorrhage, mass effect, and edema are all important associated findings. Bilateral fractures, complex



FIGURE 6-59 A lateral skull radiograph of a 6-month-old boy who was a victim of nonaccidental injury demonstrates a right parietal skull fracture *(arrow)*.

fractures, or fractures that cross a suture line, especially in patients without an appropriately significant traumatic history, may be signs of nonaccidental injury (NAI). NAI should be suspected when the history does not support the radiographic findings. Although subdural hematomas may be present in victims of NAI, hemorrhage of different ages does not necessarily equate with abuse, especially in children with underlying enlargement of the extraaxial spaces.

Hypoxic Ischemic Injury

Young children may present to the emergency department after a history of near-drowning or choking with subsequent hypoxic ischemic injury of the brain as a result of profound asphyxiation. The resultant cerebral edema and infarction can be subtle on CT, especially in the early stages after the event. Lack of visualization of normal sulci, an abnormally dense cerebellum, and loss of normal gray/white matter differentiation should suggest underlying cerebral edema. These patients are often followed up clinically with imaging repeated during the next several days to further evaluate the extent of hypoxic ischemic injury. MRI is more sensitive in the detection of early hypoxic ischemic injury.

Hydrocephalous

Hydrocephalus refers to the overaccumulation of cerebrospinal fluid (CSF) within the ventricular system. Children with hydrocephalus often present with headache, vomiting, and lethargy. Hydrocephalus may be a result of congenital or acquired factors. Congenital hydrocephalus may be a result of in utero infection, aqueductal stenosis, or malformations of the brain (Chiari or Dandy-Walker). Acquired causes of hydrocephalus include infection, hemorrhage, and obstructing mass lesions. The ventricles will appear dilated on CT, and hypoattenuating areas adjacent to the ventricles represent sites of transependymal CSF absorption. Abnormal dilatation of the ventricles may be defined by several criteria, including visualization of the temporal horns of the lateral ventricles (usually not visible), upward bowing of the corpus callosum, and enlargement of the frontal horns of the lateral ventricles compared with the calvarial diameter measured from the inner tables (greater than 50%). Depending on the cause of the hydrocephalus, all of the ventricles may not be equally dilated. In aqueductal stenosis, for example, the third and lateral ventricles will appear dilated, whereas the fourth ventricle is normal.

Assessing the size of the ventricular system and extraaxial spaces can be challenging in infants. Prominence of the extraaxial spaces in infants is often benign and self-resolving. Often infants are found to have an enlarging head circumference at a routine visit to the pediatrician. This phenomenon typically occurs between 3 and 9 months of age, with expected resolution by the age of 2 years.

Venous Sinus Thrombosis

Venous sinus thrombosis (VST) can be caused by a variety of different factors, both local and systemic. Local processes include mastoiditis and intracranial neoplasm, whereas systemic processes include genetic predisposition to hypercoagulopathy, underlying malignancies, or medications. In young children, severe dehydration can lead to venous stasis and thrombosis. These patients usually present with lethargy, irritability, and/or seizures.

VST can be detected on the basis of findings made on head US, CT, and MRI. On US, images obtained through the anterior fontanelle of young infants will demonstrate the lack of Doppler flow within the superior sagittal sinus. On noncontrast CT, thrombus within a venous sinus will appear abnormally dense (Fig. 6-60, *A*). This finding may also be seen in dehydrated patients with an elevated hematocrit level. If this is the case, the attenuation of the arteries and veins should appear similar, whereas in patients with VST, the sinus will appear denser than the arteries. With contrast-enhanced CT, the "empty delta" sign describes the appearance of an intraluminal filling defect (i.e., thrombus) within the dural envelope. MRI is more sensitive for detection of venous thrombosis. Findings on MRI consistent with VST include absence of normal flow voids and abnormal signal intensity within the sinus (Fig. 6-60, *B*). Indirect signs of deep venous thrombosis include collateral venous channels, cerebral hemorrhage, and signs of increased intracranial pressure. VST may lead to venous infarction and hemorrhage in the cortex and/or basal ganglia, depending on the sinuses involved.

Meningitis/Encephalitis

Meningitis is a clinical diagnosis that is often made on the basis of history and laboratory markers, including CSF analysis. Imaging of patients with meningitis is usually not performed unless complications are suspected such as encephalitis, epidural abscess, or VST. In these instances, contrast-enhanced MRI is the most appropriate imaging

evaluation, although the diagnosis also can be suggested based on findings made at CT. In a child with clinical and laboratory findings consistent with intracranial infection, the effacement of sulci and subtle differences in attenuation of the cortical gyri on a CT scan suggests parenchymal infection such as encephalitis. On MRI, the involved brain parenchyma will appear abnormally increased in signal on fluid-sensitive sequences (Fig. 6-61). Cerebellitis, or inflammation of the cerebellum, may be suggested on noncontrast head CT by areas of abnormal hypointense foci within the cerebellum, often in a pattern mimicking the longitudinal pattern of the cerebellar folia (Fig. 6-62).

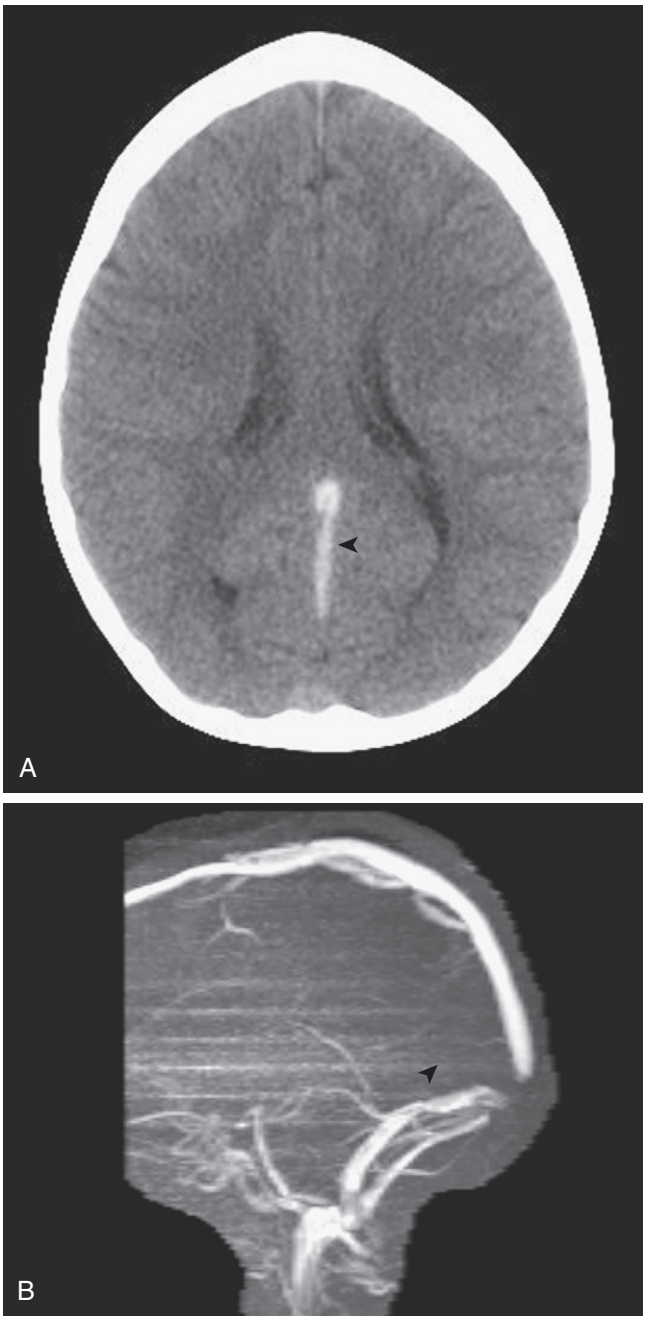


FIGURE 6-60 **A,** An axial computed tomography image through the brain demonstrates hyperattenuation within the straight sinus *(arrowhead)*. **B,** Magnetic resonance venography confirms the absence of flow within the straight sinus *(arrowhead)*, consistent with sinus thrombosis.

Often a recent history of a viral infection or immunization can be recalled. Cerebellitis may be suggested by CT, but abnormalities may be subtle, and MRI is usually the diagnostic study.

Cervical Spine Injury

Pediatric cervical spine injury is relatively uncommon, with an incidence between 1% and 2%. Younger children (<8 years) are more apt to injure the upper cervical spine (C1-C2) than are older adolescents (>8 years), who are more apt to injure the lower cervical spine (C3-C7). This pattern of injury is thought to be due to the mechanics and structure of the maturing cervical spine. The multiple synchondroses in the upper cervical spine are points of relative instability. The relatively large size of the head in a child in comparison with that of adults places increased stress on the upper cervical spine. The causes of cervical spine trauma are also different in the two age groups, with motor vehicle accidents being the primary cause of injury in the younger group and sports/recreation injuries the leading cause in the older group.

Despite the widespread availability of CT scanners in many emergency departments, plain radiographs of the cervical spine are still the mainstay for evaluating pediatric cervical spine trauma. Many imaging pitfalls exist in the evaluation of the cervical spine in children. Knowledge of the multiple synchondroses of C2 is important for the accurate diagnosis of injury. The presence of a fracture at the synchondrosis of the dens should be raised if anterior angulation or displacement of the dens in relation to the body of C2 is present. The ring apophyses of the vertebral bodies are normal structures that may be mistaken for avulsion or chip fractures. The normal pseudosubluxation at C2-C3 (as a result of ligament laxity in young children) may raise concerns in clinicians unfamiliar with this common appearance. Patient cooperation is often limited in the younger age group, and it may be difficult to impossible to obtain odontoid views.

Algorithms to direct the most judicious use of radiology in clearing the cervical spine have been suggested. In an effort to limit the radiation exposure to pediatric patients, limited use of CT for cervical spine evaluation is recommended. Initial evaluation of the pediatric cervical spine should be performed with plain radiographs. If concern for occult fracture persists after initial radiographs are obtained, focused CT can be performed through the levels of concern. If a cervical spine fracture is present, CT may then be performed through the entire cervical spine to exclude additional fractures. A small subset of patients with injury to the cervical spine do not have radiographic abnormalities. This presentation more commonly occurs in younger patients (<8 years). Consideration should be given to using MRI rather than CT as a troubleshooting tool in younger patients because of their increased risk of ligamentous injury without fracture.

Mastoiditis

Fever and ear pain are common symptoms of otitis media (OM) in young children. OM is diagnosed on the basis of physical examination findings, and it is commonly treated with antibiotics. Imaging is not indicated for

uncomplicated OM. Lack of response or progression of symptoms while taking antibiotics may prompt further evaluation to evaluate for complications of OM or other causes for the patient's symptoms. When mastoiditis or other complications of OM are clinically suspected, a CT through the temporal bones should be performed with use of intravenous contrast material. Fluid within the middle ear on a CT scan is consistent with OM. Mastoiditis is often associated with OM and represents extension of infection from the middle ear into the mastoid air cells, because these structures are contiguous. When evidence exists of bony erosion or intracranial extension of infection (such as a subperiosteal abscess), this condition is called *coalescent mastoiditis*, and surgical intervention may be required (Fig. 6-63). Given the proximity of the dural venous sinuses to the temporal bone, particular attention should be directed to excluding secondary venous thrombosis. Additional complications of otitis media include petrous apicitis, or spread of infection into the petrous apices, epidural abscess, meningitis, and, rarely, carotid artery involvement.

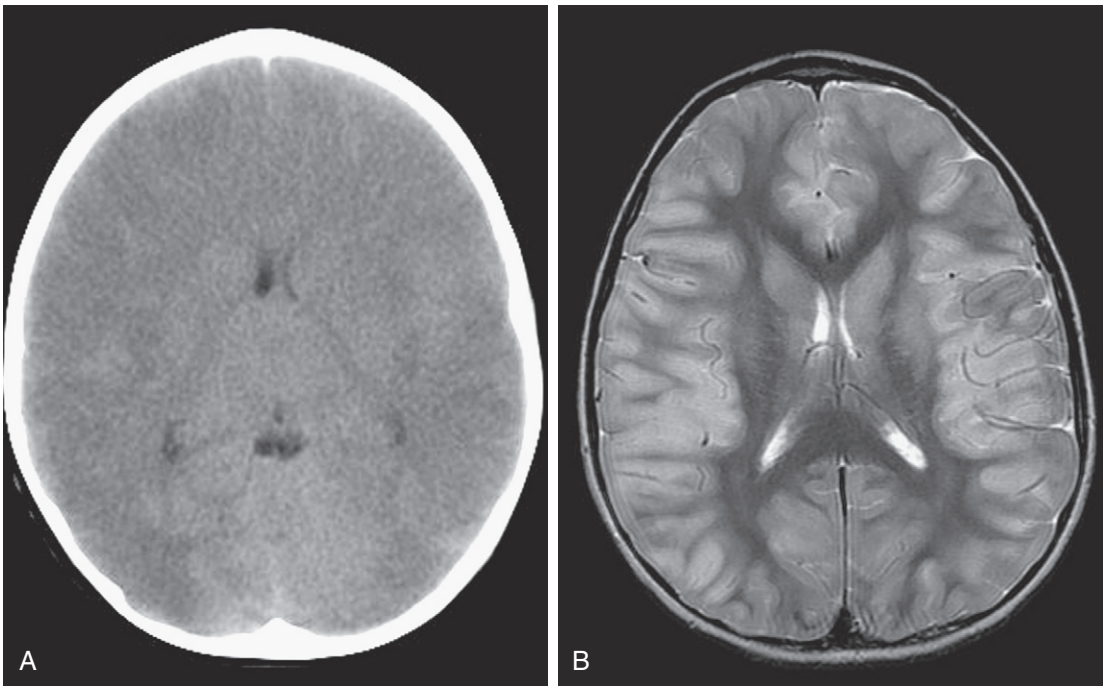


FIGURE 6-61 **A,** An axial computed tomography image through the brain in a 4-year-old boy with a history of otitis media followed by changes in mental status reveals loss of normal gray-white differentiation and effacement of sulci. **B,** A T2-weighted magnetic resonance image reveals diffusely abnormal signal intensity throughout the cerebellar hemispheres. This child had encephalitis.

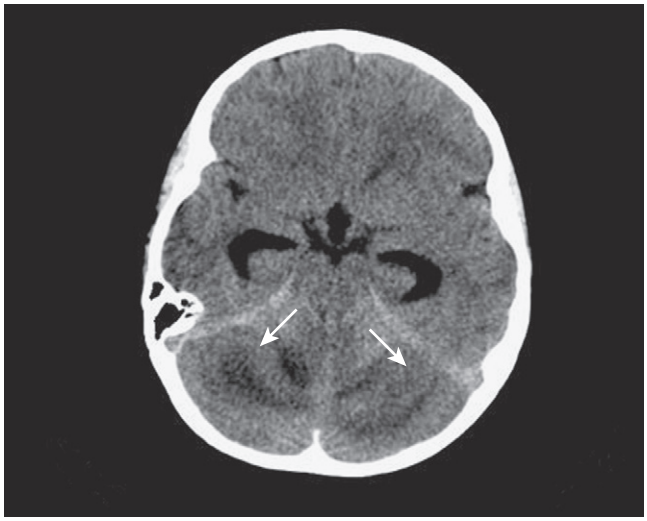


FIGURE 6-62 An axial computed tomography image obtained in a young girl presenting with ataxia reveals abnormal hypoattenuating lesions within the cerebellum *(arrows)*, consistent with cerebellitis. This diagnosis was later confirmed with magnetic resonance imaging.

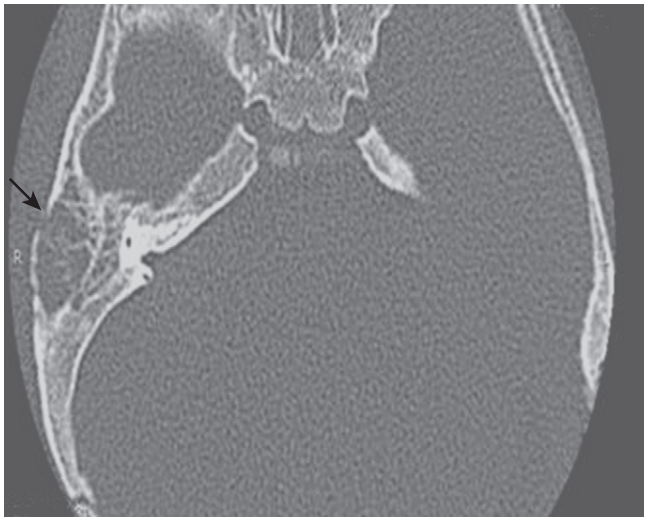


FIGURE 6-63 An axial computed tomography image through the temporal bones in a young child with complicated otitis media demonstrates abnormal fluid attenuation within the mastoid air cells on the right with osseous destruction *(black arrow)* consistent with coalescent mastoiditis.

These potential complications should be considered when reviewing a CT for complicated OM.

Cervical Adenitis

Children presenting to the emergency department with enlarged cervical lymph nodes, fever, and an elevated white blood cell count often have a diagnosis of cervical adenitis. Cervical adenitis is a nonspecific inflammation of the lymph nodes that can be the result of a bacterial or viral infection. Imaging is performed in cases in which abscess formation is a concern. US is often performed initially to evaluate the superficial, or palpable, lymph nodes. US is excellent at differentiating between solid and cystic masses and can identify abscesses or fluid collections that are amenable to drainage. Although US evaluation may be sufficient for evaluating superficial lymph nodes, signs and symptoms of a tonsillar infection such as trismus, drooling, and sore throat may prompt an evaluation with contrast-enhanced CT. CT can identify a potential peritonsillar abscess, assess the mass effect on the airway, and assess for displacement, compression, or thrombosis of adjacent vessels. Thrombosis of the internal jugular vein or a tributary vein in association with peritonsillar abscess is termed *Lemierre syndrome*. Lemierre syndrome is usually caused by the bacterium *Fusobacterium.* Nontuberculous mycobacterial infection can be suggested in a child with low-density lymphadenopathy, particularly when a draining sinus tract is present. In the absence of a draining sinus tract or signs/symptoms of infection, the differential diagnosis for multiple enlarged lymph nodes in a child includes lymphoproliferative disorders, such as lymphoma.

Anterior midline neck infections should suggest an underlying congenital abnormality such as thyroglossal duct cyst or dermoid. Abscesses along the anterior border of the sternocleidomastoid may represent sequela from lymphadenitis or may represent superinfection of a second brachial cleft cyst. If CT of an "acute onset" neck mass demonstrates a multicystic collection with internal fluid/fluid levels, the diagnosis may be a lymphatic malformation. This diagnosis becomes even more likely if the multicystic collection crosses compartments within the neck.

MUSCULOSKELETAL

The adage "children are not little adults" is particularly true for the evaluation of the pediatric musculoskeletal system. The pediatric skeleton responds to traumatic forces with different patterns of injury than does the skeleton of adult patients. In addition to having open physes, pediatric bones are surrounded by a thick periosteum that is a vascular fibrous sheath. Pediatric bones are more plastic and can remodel relatively quickly compared with the adult skeleton. In all fractures, the underlying bone should be assessed to exclude an underlying benign or malignant lesion, such as a unicameral bone cyst (Fig. 6-64) or osteosarcoma.

Salter-Harris Fractures

One of the most well-known fracture classification systems is the Salter-Harris (SH) classification of fractures that occur at the physis of young children. SH1 fractures solely involve the growth plate (physis; Fig. 6-65). SH2 fractures extend through the metaphysis into the growth plate (Fig. 6-66). SH3 fractures extend through the epiphysis into the



FIGURE 6-64 An anteroposterior radiograph of the left humerus in an adolescent demonstrates a comminuted fracture through a lucent, mildly expansile lesion in the proximal diaphysis, consistent with a pathologic fracture through a unicameral bone cyst.



FIGURE 6-65 An anteroposterior radiograph through the wrist demonstrates widening of the distal radial physis *(arrow)*. The patient was focally tender at this site. This finding is consistent with a Salter-Harris 1 fracture.

growth plate. SH4 fractures extend from the metaphysis, through the growth plate, into the epiphysis. SH5 fractures are crush injuries to the growth plate. Fractures that occur at the physis may cause early fusion of the physis and lead to growth disturbance. Two distinct SH fractures at the ankle are the triplane and juvenile Tillaux fractures, which typically occur in older adolescents. The triplane fracture is a complex SH4 injury of the tibia that has a vertical component through the epiphysis, a horizontal component through the growth plate, and an oblique component through the metaphysis (Fig. 6-67). The Tillaux fracture is a SH3 injury involving fracture of the anterolateral aspect of the growth plate and epiphysis (Fig. 6-68). Fusion of the tibial growth plate begins centrally, proceeds medially, and completes laterally. The Tillaux pattern is a result of injury after the medial distal tibial growth plate has fused. When Tillaux or triplane injuries are suspected or diagnosed by radiographs, CT is typically performed because decisions for orthopedic repair hinge on the appearance of the fractures and measurements of distraction.

Plastic Bending Fractures

Plastic bending fractures are seen in the long bones of children who have sustained axial load injuries. These fractures appear as bowing contour deformities. Buckle or torus fractures are seen as minimal disruptions or irregularities in the cortical contours, which are particularly common in the long bones of the forearm (Fig. 6-69). Greenstick fractures demonstrate cortical continuity along one aspect of the bone and obvious fracturing or splintering of the opposite cortical margin. Toddler's fractures are hairline cortical tibial fractures seen in walking older infants and young children (Fig. 6-70). These pediatric fractures are often initially overlooked because of the subtle differences in angulation or cortical continuity. Certain buckle fractures, plastic fractures (bowing deformities), hairline fractures, subtle SH1 fractures, and impaction fractures can be subtle and are more evident if



FIGURE 6-66 A radiograph of the right hand demonstrates a Salter-Harris 2 fracture through the base of the first metacarpal.

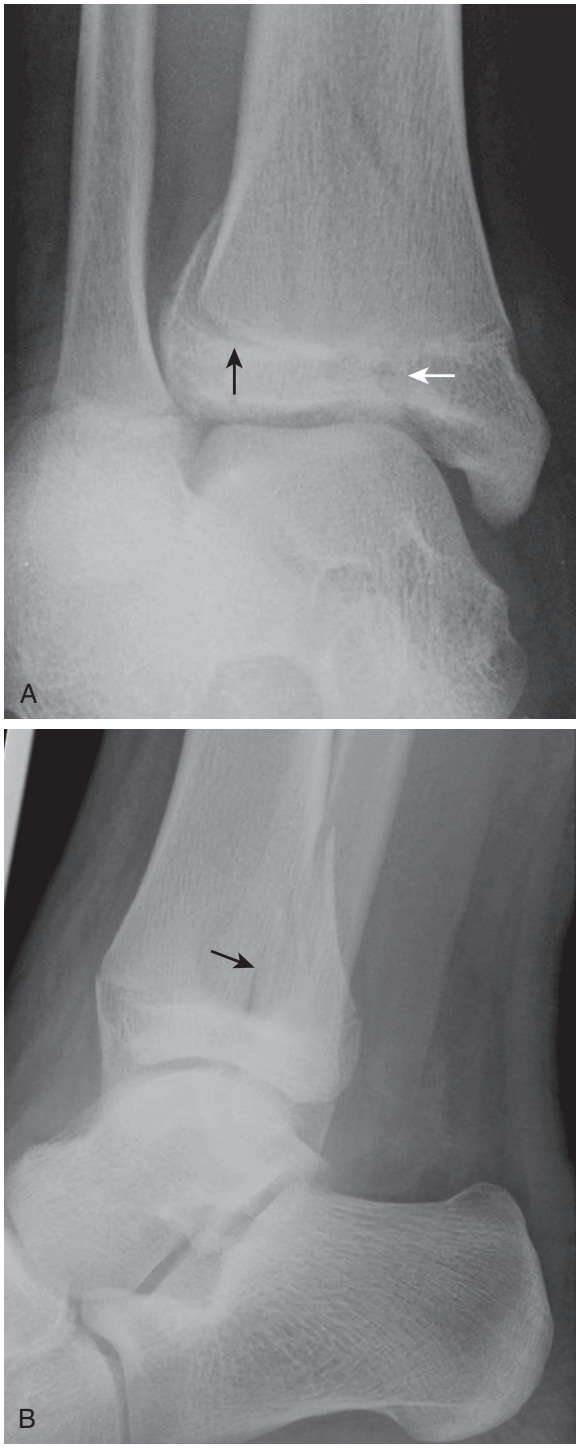


FIGURE 6-67 **A,** An anteroposterior radiograph through the ankle in a teenage boy after a sporting injury reveals a fracture through the tibial epiphysis *(white arrow)* that extends through the lateral portion of the physis *(black arrow)*. **B,** A lateral radiograph of the ankle reveals the obliquely oriented metaphyseal component of this triplane, Salter-Harris 4, fracture *(arrow)*.

a contralateral view is obtained. When initial radiographs appear normal but clinical suspicion for fracture is high, follow-up radiographs in 10 to 14 days may be useful. The presence of periosteal reaction, sclerosis, or increased conspicuity of the fracture line on a follow-up radiograph is indicative of a healing injury that may have been occult in the acute stage.

Elbow Fractures

The elbow is a challenging joint to evaluate in the pediatric skeleton because of the multiple ossification centers and predominance of radiolucent cartilage. Given that elbow fractures in children are common injuries and many portions of



FIGURE 6-68 A coronal reformatted image obtained from a computed tomography examination through the ankle in a teenage boy who sustained an injury to his ankle reveals a fracture through the distal tibial epiphysis *(arrow)* that extends through the lateral portion of the physis *(arrowhead)*. This fracture is called a *Tillaux fracture*, which is a specific type of Salter-Harris 3 injury.

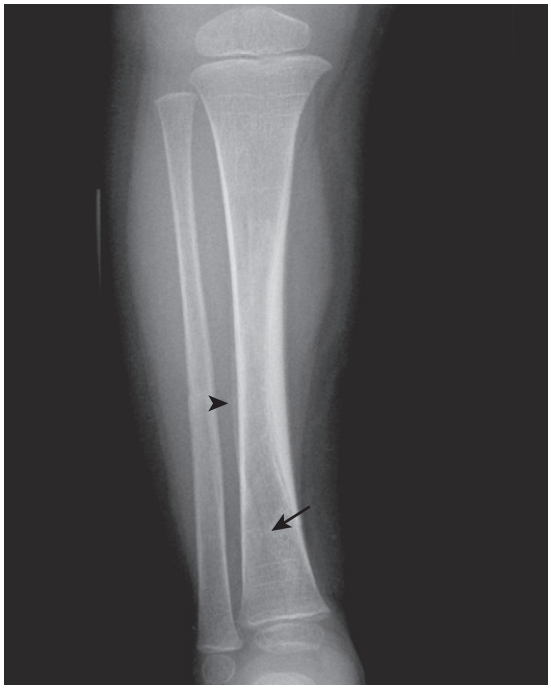


FIGURE 6-70 An anteroposterior radiograph of the tibia in a toddler demonstrates a subtle lucency within the shaft of the distal tibia *(arrow)*, as well as periosteal reaction along the lateral cortical surface of the bone *(arrowhead)*. This child sustained a toddler's fracture of her tibia.

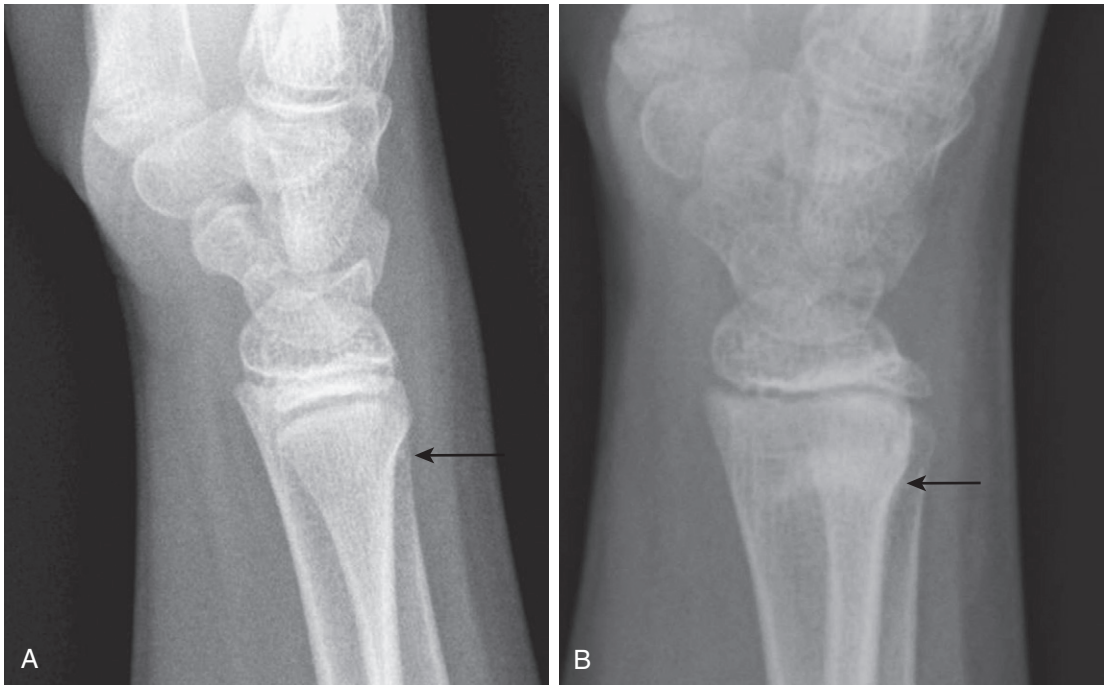


FIGURE 6-69 **A,** An initial lateral radiograph of the wrist obtained at the time of injury in a young girl with wrist pain demonstrates a subtle buckle fracture of the distal radius *(arrow)*. **B,** A follow-up radiograph performed 10 days later reveals linear sclerosis at the fracture site *(arrow)*, indicative of healing.

the joint are not radiographically visible, elbow fractures are particularly prone to false-negative plain film interpretations. Knowledge of the normal anatomic alignment of the elbow, as well as the appearance and timing of the ossification centers, is essential when evaluating the elbow. "CRITOE" (capitellum, radial head, internal epicondyle, trochlea, olecranon, and external epicondyle) is a common mnemonic that describes the typical order in which the ossification centers appear. Bowing of the anterior fat pad ("sail sign") and visualization of the posterior fat pad indicates a joint effusion (Fig. 6-71). The presence of an effusion does not necessarily connote a fracture, although it reflects significant traumatic injury to the joint. The radiocapitellar line drawn through the midshaft of the radius should always intersect the capitellum. Distortion of this relationship represents subluxation or dislocation of the radial head from its normal anatomic articulation with the capitellum. The anterior humeral line drawn along the anterior cortex of the humerus should intersect the middle third of the capitellum. If the line intersects the anterior third of the capitellum or passes anterior to the capitellum, a supracondylar fracture should be suspected. This line can lead to false-positive assessments in nonlateral projections. Care also should be used in the extremely young patients with minimal ossification of the capitellum. A mnemonic device such as FOOL (*F*at pads, cortical *O*utlines, *O*ssification centers, and anterior humeral and radiocapitellar *L*ines) can remind the busy radiologist to look for the presence of effusions, subtle buckle fractures, avulsed or "missing" ossification centers, and radial head dislocations or subtle supracondylar fractures. If the medial epicondylar ossification center is absent in a child who has visible ossification of the trochlea or lateral epicondyle, it may be avulsed and displaced into the joint space (Fig. 6-72). In addition to supracondylar fractures, the most common pediatric elbow fractures include lateral condylar and medial epicondylar fractures.

Hip Pain

Patients presenting with hip pain may have septic arthritis of the hip joint, a diagnosis that requires emergent diagnosis to avoid permanent joint damage. The presence of a hip effusion can be suggested on AP radiographs of the pelvis by asymmetric widening of the femoral head-acetabular teardrop distance on the affected side, although radiographs are not sensitive for this diagnosis. US is an excellent tool for evaluating for the presence of a hip effusion. Using a high-frequency linear transducer along the long axis of femoral metaphysis, an effusion will appear as a hypoechoic collection ballooning outward from the cortex of the femoral head and neck (Fig. 6-73). Imaging the

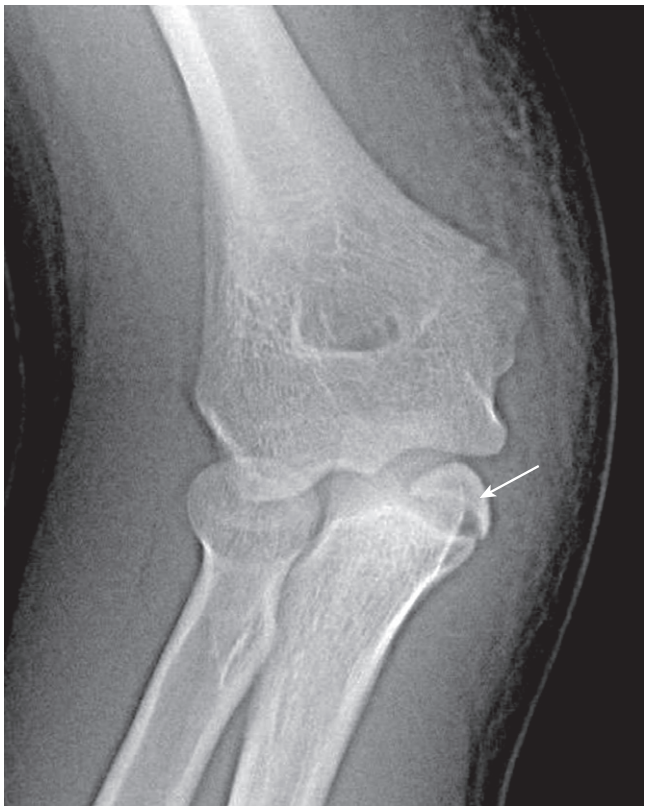


FIGURE 6-72 An anteroposterior oblique radiograph of the elbow in a 15-year-old boy with elbow pain after a football injury demonstrates an avulsed medial epicondyle within the joint *(arrow)*.



FIGURE 6-71 A lateral radiograph of the elbow demonstrates the "sail sign" of an elbow effusion *(arrow)*. The posterior fat pad is also visible *(arrowhead)*. This child was treated for an occult supracondylar fracture.

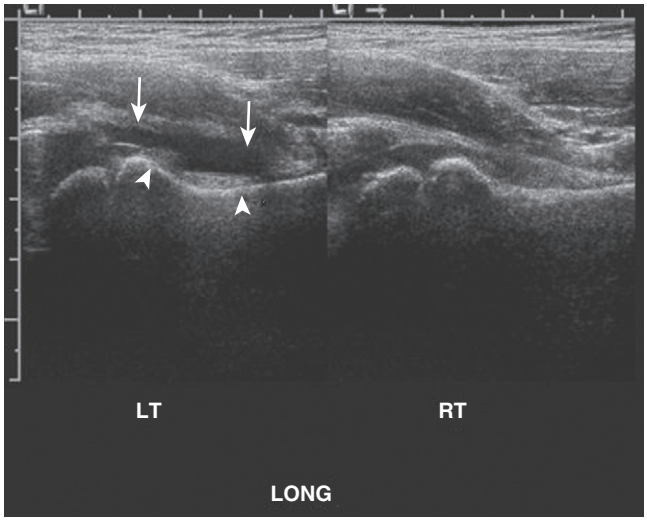


FIGURE 6-73 Ultrasound images obtained along the long axis of the hips bilaterally demonstrate evidence of a hip effusion on the left *(arrows)*, the patient's symptomatic side. The cortical surface of the femur is denoted by the *arrowheads*.

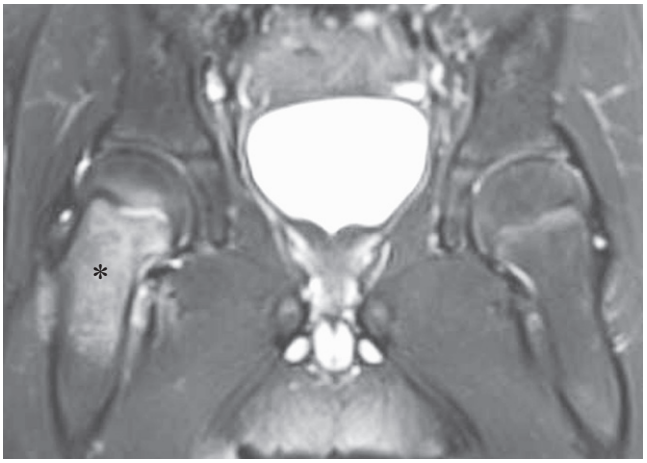


FIGURE 6-74 A coronal T2-weighted magnetic resonance image through the hips with fat suppression demonstrates increased signal within the right proximal femoral metaphysis *(asterisk)* in this child with right hip pain, elevated c-reactive protein, and fever. The findings are consistent with osteomyelitis.

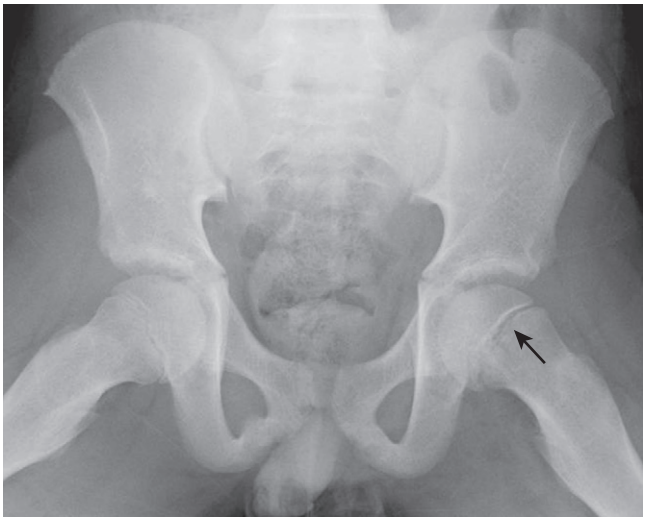


FIGURE 6-75 Frog-leg lateral views of bilateral hips reveal widening of the physis on the left *(arrow)* and posteromedial displacement of the left femoral epiphysis, consistent with slipped capital femoral epiphysis.

normal asymptomatic side will demonstrate the asymmetry in the amount of fluid in the symptomatic joint. Transient synovitis cannot be differentiated from a septic hip sonographically. The diagnosis is determined by the histopathologic evaluation of the aspirated fluid. In a child with hip pain, the presence of fever, elevated white blood cell count, increased erythrocyte sedimentary rate, and elevated C-reactive protein should help direct any decision to perform hip aspiration. MRI is recommended if osteomyelitis is a potential concern; MRI would show decreased signal on T1-weighted images and increased signal on T2-weighted images within the bone marrow, usually centered at the metaphysis or metaphyseal equivalent (Fig. 6-74).

Other causes of hip pain in children include Legg-Calvé-Perthes (LCP) disease and slipped capital femoral epiphysis (SCFE). LCP is idiopathic avascular necrosis of the hip. Most commonly occurring in 4- to 8-year-olds, the early radiographic signs of LCP may be subtle. Subcortical lucency along the proximal femoral epiphysis may be the first imaging sign of the disease. Cortical collapse, sclerosis, and deformity of the head and neck is seen in more advanced disease. SCFE is often diagnosed in the slightly older age group (ages 8-12 years) and is more common in overweight children. On AP radiographs, early SCFE can be seen as subtle asymmetry of the growth plates, whereas more advanced SCFE will have lateral displacement of the proximal femoral metaphysis with respect to the epiphysis. Often the slip is better seen on the frog-leg lateral view, where the offset of the epiphysis and metaphysis is better demonstrated (Fig. 6-75).

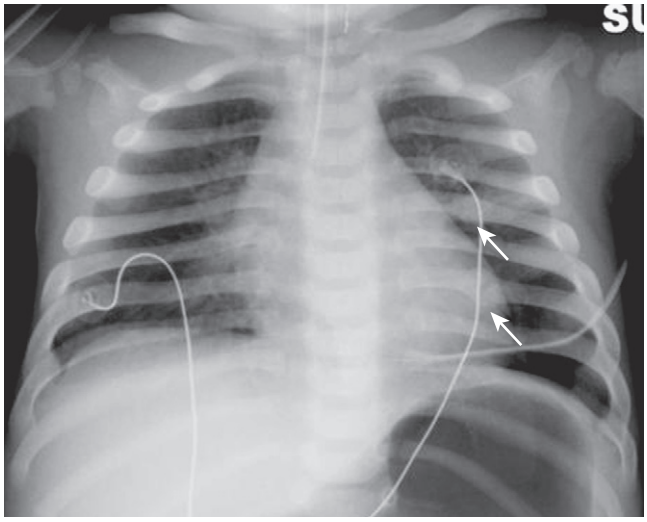


FIGURE 6-76 An anteroposterior radiograph of the chest in a 6-month-old boy who was a victim of nonaccidental injury reveals healing left posterior rib fractures *(arrows)*.

Nonaccidental Injury

When interpreting pediatric imaging studies, one must be constantly on the lookout for signs of NAI. Certain types of osseous injuries have a high specificity for NAI. Posterior rib fractures, for example, are highly specific for NAI and may be detected on chest or abdominal radiographs obtained for unrelated history, such as cough or vomiting (Fig. 6-76). Other fractures highly suggestive of child abuse are classic metaphyseal lesions, sometimes referred to as *corner* or *bucket-handle fractures* (Fig. 6-77). Although relatively uncommon, scapular fractures, spinous process fractures, and sternal fractures also have a high specificity for abuse.

In general, long bone fractures in children are common and have a low specificity for abuse. However, spiral fractures of the long bones in infants who are not ambulatory are worrisome for NAI. When clinical concern is raised or when a radiographic finding is suggestive of NAI, a full skeletal survey should be performed with high-quality small field of view technique. Multiple fractures, particularly if they are of varying ages, should alert radiologists to the possibility of abuse. A follow-up skeletal survey in 2 weeks can be suggested to assess for additional injuries that may not be visible on initial radiographs.



FIGURE 6-77 An anteroposterior radiograph of the femur in the same child as in Figure 6-76 reveals a metaphyseal fracture of the distal tibia *(arrow)*.

A few metabolic disorders can mimic the osseous injuries seen in NAI, with the most common being osteogenesis imperfecta. These disorders are very rare, and often there will be other clinical findings or a family history to suggest the diagnosis.

SUGGESTED READINGS

Agrons GA, Harty MP. Lung disease in premature neonates: impact of new treatments and technologies. *Semin Roentgenol*. 1998;33(2):101–116.

Anderson RCE, Scaife ER, Fenton SJ, et al. Cervical spine clearance after trauma in children. *J Neurosurg*. 206;105(5 suppl):361–364.

Artz GJ, Reilly JS, Mattei P. Stridor in an infant. *Clin Pediatr*. 2006;45:578–581.

Atabaki SM. Pediatric head injury. *Pediatr Rev*. 2007;28(6):215–223.

Atkinson Jr GO, Patrick LE, Ball Jr TI, et al. The normal and abnormal scrotum in children: evaluation with color Doppler sonography. *Am J Roentgenol*. 1992;158:613–617.

Bixby SD, Lucey BC, Soto JA, et al. Perforated versus nonperforated acute appendicitis: accuracy of multidetector CT detection. *Radiology*. 2006;241(3):780–786.

Blanch AJ, Perel SB, Acworth JP. Paediatric intussusception: epidemiology and outcome. *Emerg Med Australas*. 2007;19(1):45–50.

Booth TN. Cervical spine evaluation in pediatric trauma. *AJR Am J Roentgenol*. 2012;198:417–425.

Bruce J, Huh Y, Cooney D, et al. Intussusception; evolution of current management. *J Pediatr Gastroenterol Nutr*. 1987;6:663–664.

Buonomo C. Neonatal gastrointestinal emergencies. *Radiol Clin North Am*. 1997;35(4):845–864.

Choi H, Snyder III HM, Duckett JW. Urolithiasis in childhood: current management. *J Pediatr Surg*. 1987;22(2):158–164.

Choudhary AK, Sellars MEK, Wallis C, et al. Primary spontaneous pneumothorax in children: the role of CT in guiding management. *Clin Radiol*. 2005;60:508–511.

Choudy MS, Rahman N, Boyd P, et al. Duodenal atresia: associated anomalies, prenatal diagnosis and outcome. *Pediatric Surg Int*. 2009;25(8):727–730.

Cleveland RH. A radiologic update on medical diseases of the newborn chest. *Pediatr Radiol*. 1995;25:631–637.

Cogley J, O'Connor S, Houshyar R, et al. Emergent pediatric US: what every radiologist should know. *Radiographics*. 2012;32:651–665.

Daneman A, Navarro O. Intussusception part 1: a review of diagnostic approaches. *Pediatr Radiol*. 2003;33:79–85.

Daneman A, Navarro O. Intussusception part 2: an update on the evolution of management. *Pediatr Radiol*. 2004;34:97–108.

Donnelly LF. Traumatic elbow effusions in children are not synonymous with occult fracture—even with evaluation by MR imaging. *AJR Am J Roentgenol*. 2002;179(2):531–532.

Donnelly LF, Emery KH, Brody AS, et al. Minimizing radiation dose for pediatric body applications of single-detector helical CT: strategies at a large children's hospital. *AJR Am J Roentgenol*. 2001;176:303–306.

Eich GF, Superti-Furga A, Umbricht FS, et al. The painful hip: evaluation of criteria for clinical decision-making. *Eur J Pediatr*. 1999;158(11):923–928.

Ein SH, Alton D, Palder SB. Intussusception in the 1990's: has 25 years made a difference? *Pediatr Surg Int*. 1997;12(5-6):374–376.

Ellis H, Kumar R, Kostyra B. Neonatal small left colon syndrome in the offspring of diabetic mothers—an analysis of 105 children. *J Pediatr Surg*. 2009;44(12):2342–2346.

Epelman M, Daneman A, Navarro OM, et al. Necrotizing enterocolitis: review of state-of-the-art imaging findings with pathologic correlation. *Radiographics*. 2007;27(2):285–305.

Evans ED, Kramer SS, Kravitz RM. Pediatric diseases of the lower airways. *Semin Roentgenol*. 1998;33(2):136–150.

Fassett DR, McCall R, Brockmeyer DL. Odontoid synchondrosis fractures in children. *Neurosurg Focus*. 2006;20(2):E7 (1-4).

Findlay RD, Taeusch HW, Walther FJ. Surfactant replacement therapy for meconium aspiration syndrome. *Pediatrics*. 1996;97(1):48–52.

Fiorella DJ, Donnelly LF. Frequency of right lower quadrant position of the sigmoid colon in infants and young children. *Radiology*. 2001;219:91–94.

Ford EG, Senac MO, Srikanth MS, et al. Malrotation of the intestines in children. *Ann Surg*. 1992;215(2):172–178.

Fragoso AC, Pereira JM, Estevao-Costa J. Nonoperative management of omental infarction—a case report. *J Pediatr Surg*. 2006;41(10):1777–1779.

Freed HA, Shields NN. Most frequently overlooked radiographically apparent fractures in a teaching hospital emergency department. *Ann Emerg Med*. 1984;13(10):900–904.

Garel L, Dubois J, Grignon A, et al. US of the pediatric female pelvis: a clinical perspective. *Radiographics*. 2001;21(6):1393–1407.

Godbole P, Stringer MD. Bilious vomiting in the newborn: how often is it pathologic? *J Pediatr Surg*. 2002;6:909–911.

Goodman TR, McHugh K. The role of radiology in the evaluation of stridor. *Arch Dis Child*. 1999;81:456–459.

Graif M, Itzchak Y. Sonographic evaluation of ovarian torsion in childhood and adolescence. *AJR Am J Roentgenol*. 1988;150(3):647–649.

Greason KL, Thompson WR, Downey EC, et al. Laparoscopic pyloromyotomy for infantile hypertrophic stenosis: report of 11 cases. *J Pediatr Surg*. 1995;30(11):1571–1574.

Guthrie SO, Gordon PV, Thomas V, et al. Necrotizing enterocolitis among neonates in the United States. *J Perinatol*. 2003;23(4):279–285.

Haney PJ, Bohlman M, Sun CC. Radiographic findings in neonatal pneumonia. *Am J Roentgenol*. 1984;143(1):23–26.

Hernanz-Schulman M. Infantile hypertrophic pyloric stenosis. *Radiology*. 2003;227:319–331.

Hernanz-Schulman M, Sells LL, Ambrosino MM, et al. Hypertrophic pyloric stenosis in the infant without a palpable olive: accuracy of sonographic diagnosis. *Radiology*. 1994;193(3):771–776.

Hertzberg BS, Kliewer MA, Paulson EK. Ovarian cyst rupture causing hemoperitoneum: imaging features and the potential for misdiagnosis. *Abdom Imaging*. 1999;24:304–308.

Hopkins A, Lahiri T, Salerno R, et al. Changing epidemiology of life-threatening upper airway infections: the reemergence of bacterial tracheitis. *Pediatrics*. 2006;118:1418–1421.

Huang B, Castillo M. Hypoxic-ischemic brain injury: imaging findings from birth to adulthood. *Radiographics*. 2008;28(2):417–439.

Ifergan J, Pommier R, Brion M, et al. Imaging in upper urinary tract infections. *Diagn Interv Imaging*. 2012;93(6):509–519.

Jagannathan J, Dumont AS, Prevedello DM, et al. Cervical spine injuries in pediatric athletes: mechanisms and management. *Neurosurg Focus*. 2006;21(4):E4 (1-5).

Jain KA. Sonographic spectrum of hemorrhagic ovarian cysts. *J Ultrasound Med*. 2002;21(8):879–886.

Karmazyn B, Werner EA, Rejaie B, et al. Mesenteric lymph nodes in children; what is normal? *Pediatr Radiol*. 2005;35(8):774–777.

Kawashima A, Sandler CM, Goldman SM. Imaging in acute renal infection. *BJU Int*. 2000;86(suppl 1):70–79.

Kleinman PK. Differentiation of child abuse and osteogenesis imperfect: medical and legal implications. *AJR Am J Roentgenol*. 1990;154(5):1047–1048.

Kleinman PK, Nimkin K, Spevak MR, et al. Follow-up skeletal surveys in suspected child abuse. *AJR Am J Roentgenol*. 1996;167(4):893–896.

Ko HS, Schenk JP, Tröger J, et al. Current radiological management of intussusception in children. *Eur Radiol*. 2007;17(9):2411–2421.

Kocher MS, Mandiga R, Zurakowski D, et al. Validation of a clinical prediction rule for the differentiation between septic arthritis and transient synovitis of the hip in children. *J Bone Joint Surg Am*. 2004;86-A(8):1629–1635.

Kornecki A, Daneman A, Navarro O, et al. Spontaneous reduction of intussusception; clinical spectrum, management, and outcome. *Pediatr Radiol*. 2000;30(1):58–63.

Kosloske AM, Musemeche CA, Ball WS, et al. Necrotizing enterocolitis: value of radiographic findings to predict outcome. *Am J Roentgenol*. 1988;151(4):771–774.

Krishnan A, De Souza A, Konijeti R, et al. The anatomy and embryology of posterior urethral valves. *J Urol*. 2006;175:1214–1220.

Lavocat MP, Granjon D, Allard D, et al. Imaging of pyelonephritis. *Pediatr Radiol*. 1997;27(2):159–165.

Lee SE, Kim HY, Jung SE, et al. Situs anomalies and gastrointestinal abnormalities. *J Pediatr Surg*. 2006;41(7):1237–1242.

Liang T, Metcalfe P, Sevcik W, et al. Retrospective review of diagnosis and treatment in children presenting to the pediatric department with acute scrotum. *AJR Am J Roentgenol*. 2013;200:444–449.

Lim HK, Bae SH, Lee KH, et al. Assessment of reducibility of ileocolic intussusception in children: usefulness of color Doppler sonography. *Radiology*. 1994;191(3):781–785.

Lin PW, Stoll BJ. Necrotizing enterocolitis. *Lancet*. 2006;368(9543):1271–1283.

Lonergan GJ, Baker AM, Morey MK, et al. From the archives of the AFIP: child abuse: radiologic-pathologic correlation. *Radiographics*. 2003;23(4):811–845.

Long FR, Kramer SS, Markowitz RI, et al. Intestinal malrotation in children: tutorial on radiographic diagnosis in difficult cases. *Radiology*. 1996;198:775–780.

Long WA, Lawson EE, Harned HS, et al. Pleural effusion in the first days of life: a prospective study. *Am J Perinatol*. 1984;1(2):190–194.

Ludwig BF, Foster BR, Saito N, et al. Diagnostic imaging in nontraumatic pediatric head and neck emergencies. *Radiographics*. 2010;30:781–799.

Lumerman J, Gershbaum MD, Hines J, et al. Unenhanced helical computed tomography for the evaluation of suspected renal colic in the adolescent population: a pilot study. *Urology*. 2001;57(2):342–346.

Macpherson RI, Leithiser RE, Gordon L, et al. Posterior urethral valves: an update and review. *Radiographics*. 1986;6(5):753–791.

Martin L, Buonomo C. Acute chest syndrome of sickle cell disease: radiographic and clinical analysis of 70 cases. *Pediatr Radiol*. 1997;27(8):637–641.

Mazeh H, Kaliner E, Udassin R. Three recurrent episodes of malrotation in an infant. *J Pediatr Surg*. 2007;42(4):E1–E3.

McCall R, Fassett D, Brockmeyer D. Cervical spine trauma in children: a review. *Neurosurg Focus*. 2006;20(2):E5 (1-8).

McNeely PD, Atkinson JD, Saigal G, et al. Subdural hematomas in infants with benign enlargement of the subarachnoid spaces are not pathognomonic for child abuse. *Am J Neuroradiol*. 2006;27(8):1725–1728.

Merten DF, Goetxman BW, Wennberg RP. Persistent fetal circulation: an evolving clinical and radiographic concept of pulmonary hypertension of the newborn. *Pediatr Radiol*. 1984;6(2):74–80.

Meservy CJ, Towbin R, McLaurin RL, et al. Radiographic characteristics of skull fractures resulting from child abuse. *AJR Am J Roentgenol*. 1987;149:173–175.

Milliner DS, Murphy ME. Urolithiasis in pediatric patients. *Mayo Clin Proc*. 1993;68(3):241–248.

Montenegro MA, Santos SL, Li LM, et al. Neuroimaging of acute cerebellitis. *J Neuroimaging*. 2002;12(1):72–74.

Moore S. Total colonic agangliosis in Hirschsprung disease. *Semin Pediatr Surg*. 2012;12(4):302–309.

Moore TC. Omphalomesenteric duct malformations. *Semin Pediatr Surg*. 1996;5(2):116–123.

Nance ML, Adamson WT, Hedrick HL. Appendicitis in the young child: a continuing diagnostic challenge. *Pediatr Emerg Care*. 2000;16(3):160–162.

Navarro O, Daneman A. Intussusception part 3: diagnosis and management of those with an identifiable or predisposing cause and those that reduce spontaneously. *Pediatr Radiol*. 2004;34:305–312.

Offiah A, Van Rijn RR, Perez-Rossello JM, et al. Skeletal imaging of child abuse (non-accidental injury). *Pediatr Radiol*. 2009;39:461–470.

Ogata M, Imai S, Hosotani R, et al. Abdominal ultrasonography for the diagnosis of strangulation in small bowel obstruction. *Br J Surg*. 1994;81(3):421–424.

Özokutan BH, Küçükaydin M, Gündüz Z, et al. Urolithiasis in childhood. *Pediatr Surg Int*. 2000;16:60–63.

Palmer JS, Donaher ER, O'Riordan MA, et al. Diagnosis of pediatric urolithiasis: role of ultrasound and computerized tomography. *J Urol*. 2005;174(4 pt 1):1413–1416.

Patriquin HB, Yazbeck S, Trinh B, et al. Testicular torsion in infants and children: diagnosis with Doppler sonography. *Radiology*. 1993;188:781–785.

Platzer P, Jaindl M, Thalhammer G, et al. Cervical spine injuries in pediatric patients. *J Trauma*. 2007;62:389–396.

Rao PM, Rhea JT, Novelline RA. Helical CT technique for the diagnosis of appendicitis: prospective evaluation of a focused appendix CT examination. *Radiology*. 1997;202(1):139–144.

Romano C, Brown T, Frewen TC. Assessment of pediatric near-drowning victims: is there a role for cranial CT? *Pediatr Radiol*. 1993;23(4):261–263.

Rooks VR, Lebowitz RL. Extrinsic ureteropelvic junction obstruction from a crossing renal vessel: demography and imaging. *Pediatr Radiol*. 2001;31:120–124.

Rosado WM, Trambert MA, Gosink BB, et al. Adnexal torsion: diagnosis by using Doppler sononography. *AJR Am J Roentgenol*. 1992;159(6):1251–1253.

Rudman DT, Elmaraghy CA, Shiels WE, et al. The role of airway fluoroscopy in the evaluation of stridor in children. *Arch Otolaryngol Head Neck Surg*. 2003;129:305–309.

Rushton HG. Urinary tract infections in children. Epidemiology, evaluation, and management. *Pediatr Clin North Am*. 1997;44(5):1133–1169.

Sadow KB, Atabaki SM, Johns CMS, et al. Bilious emesis in the pediatric emergency department: etiology and outcome. *Clin Pediatr*. 2002;41:475–479.

Schuh S, Lalani A, Allen U, et al. Evaluation of the utility of radiography in acute bronchiolitis. *J Pediatrics*. 2007;150:429–433.

Servaes S, Zurakowski D, Laufer MR, et al. Sonographic findings of ovarian torsion in children. *Pediatr Radiol*. 2007;37(5):446–451.

Shah RK, Roberson DW, Jones DT. Epiglottitis in the Haemophilus influenza type B vaccine era: changing trends. *Laryngoscope*. 2004;114:557–560.

Sharma R, Hudak M. A clinical perspective of necrotizing enterocolitis: past, present, and future. *Clin Perinatol*. 2013;40(10):27–51.

Skibo L, Reed MH. A criterion for a true lateral radiograph of the elbow in children. *Can Assoc Radiol J*. 1994;45(4):287–291.

Smergel E, Greenberg SB, Crisci KL, et al. CT urograms in pediatric patients with ureteral calculi: do adult criteria work? *Pediatr Radiol*. 2001;31:720–723.

Stark KE, Siegel MJ. Ovarian torsion in prepubertal and pubertal girls: sonographic findings. *AJR Am J Roentgenol*. 1994;163(6):1479–1482.

Stoodley N. Controversies in non-accidental head injury in infants. *Br J Radiol*. 2006;79:550–553.

Strouse PJ. Disorders of intestinal rotation and fixation ("malrotation"). *Pediatr Radiol*. 2004;34:837–851.

St-Vil D, Brandt ML, Panic S, et al. Meckel's diverticulum in children: a 20-year review. *J Pediatr Surg*. 1991;26(11):1289–1292.

Subcommittee on Urinary Tract Infection, Steering Committee on Quality Improvement and Management. Urinary tract infection: clinical practice guideline for the diagnosis and management of the initial UTI in febrile infants and children 2-24 months. *Pediatrics*. 2011;128(3):595–610.

Swaniker F, Soldes O, Hirschi RB. The utility of technetium 99m pertechnetate scintigraphy in the evaluation of patients with Meckel's diverticulum. *J Pediatr Surg*. 1999;34(5):760–764.

Swischuk LE, Hernandez JA. Frequently missed fractures in children (value of comparative views). *Emerg Radiol*. 2004;11(1):22–28.

The Alliance for Radiation Safety in Pediatric Imaging. Image Gently. imagegently.org.

Thornbury JR. Acute renal infections. *Urol Radiol*. 1991;12:209–213.

Tsai JD, Huang FY, Lin CC, et al. Intermittent hydronephrosis secondary to ureteropelvic junction obstruction: clinical and imaging features. *Pediatrics*. 2006;117:139–146.

Tung GA, Kumar M, Richardson RC, et al. Comparison of accidental and nonaccidental traumatic head injury in children on noncontrast computed tomography. *Pediatrics*. 2006;118:626–633.

Vane DW, West KW, Grosfeld JL. Vitelline duct anomalies. Experience with 217 childhood cases. *Arch Surg*. 1987;122(5):542–547.

Verschelden P, Filiatrault D, Garel L, et al. Intussusception in children: reliability of US diagnosis-a prospective study. *Radiology*. 1992;8:343–347.

Vogl TJ, Bergman C, Villriner A, et al. Dural sinus thrombosis: value of venous MR angiography for diagnosis and follow-up. *Am J Roentgenol*. 1994;162(5):1191–1198.

Wells J, Mukerji S, Chandran H, et al. Urinomas protect renal function in posterior urethral valves—a population based study. *J Pediatr Surg*. 2010;45(2):407–410.

Zerella JT, Dimier M, McGill LC, et al. Foreign body aspiration in children: value of radiography and complications of bronchoscopy. *J Pediatr Surg*. 1998;33(11):1651–1654.

Chapter 7

Traumatic and Nontraumatic Spine Emergencies

Glenn D. Barest and Margaret N. Chapman

TRAUMATIC SPINE INJURY

Background and Imaging Algorithms

Spine injuries are quite common, with more than 137,000 cases entered into the American College of Surgeons National Trauma Data Bank in 2014. Major causes include motor vehicle collisions or pedestrian strikes, falls, acts of violence, and participation in sports. Of these cases, 35,000 had an abbreviated injury score of serious or higher, and almost 3000 fatalities occurred. According to the National Spinal Cord Injury Statistical Center, approximately 12,500 spinal cord injuries occur each year, resulting in 7500 new cases of quadriplegia. Imaging is liberally applied with a positive yield of 1% to 3% of all examinations, resulting in an estimated annual national cost of approximately $3 billion. The lifetime cost to individuals and society is enormous. Understandably, attempts have been made to develop evidence-based diagnostic algorithms in this area of medicine.

Multivariate analysis of data derived from two major clinical research initiatives, the National Emergency X-Radiography Utilization Study (NEXUS) and the Canadian C-Spine Study, have provided the basis for acute spine trauma imaging pathway development. Decision rules have been created that allow for discrimination of patients in need of imaging and those for whom imaging can be safely avoided, thereby reducing costs when possible. Once the decision to perform imaging has been made, the next step is to select the most appropriate modality. Plain film radiography traditionally has been the initial examination to evaluate for possible fracture or malalignment because it is readily available, relatively inexpensive to perform, and highly sensitive. It continues to be a cost-effective option for patients with a low probability of injury. However, it has been supplanted by computed tomography (CT) in the setting of moderate to high probability of injury, based on cost-effectiveness analysis that takes into account the high medical and legal costs of the rare missed fracture that leads to severe neurologic deficit. Studies of CT as the initial modality have demonstrated higher sensitivity for the detection of fractures; however, the clinical significance of many of the radiographically occult injuries is uncertain because of the lack of studies addressing outcomes. Another clinical prediction rule that has been developed, based on data from the Harborview study, may be used to stratify risk based on the injury mechanism and other clinical parameters. This type of approach is supported by trauma surgery societies and is commonly applied at trauma centers.

Multidetector-row CT (MDCT) has become the standard of care, even for patients with a low probability of injury. A zero-tolerance (for missed injury) approach to diagnosis using the fastest, most accurate examination rather than an outcome-based approach is easily adopted by the emergency department or trauma team. It used to be that for patients who had negative cervical radiographs but persistent pain, tenderness, or limited range of motion, symptomatic treatment with analgesics, cervical collar application, and clinical follow-up were the rule. At the follow-up visit, if symptoms had not resolved, flexion-extension radiographs were obtained to evaluate for the possibility of ligamentous injury or instability. Flexion-extension views have been shown to have little utility in the acute setting, primarily because of limited range of motion as a result of muscle spasm. In low-probability settings, this approach may still be followed, but more commonly, CT is requested to exclude occult fracture. The higher direct cost of CT may be offset by the increase in emergency department throughput, albeit at a higher radiation exposure. On some occasions, after a negative CT examination, magnetic resonance imaging (MRI) may be pursued to screen for signs of potential ligamentous injury before allowing the patient to be discharged.

The cost-effectiveness of MR for the detection of clinically significant ligamentous injuries has not yet been definitively determined. This is another instance in which technology is being applied because of its availability and perhaps for theoretical limitation of liability. Clearly, when a neurologic deficit is present and CT fails to identify a cause, MRI may offer additional sensitivity for the detection of soft tissue injuries, including disk extrusion, hematoma within the spinal canal, cord compression or contusion, and unstable ligamentous injury. Other injuries such as unsuspected bone marrow edema (microfractures) and vascular injuries also may be detected. One study that correlated MRI and intraoperative findings found that MRI had moderate to high sensitivity for detection of injury to specific ligamentous structures but suggested that it may overestimate the extent of disruptive injury. The increased sensitivity of MRI is accompanied by a small false-positive rate that may lead to added costs related to treatment/workup of clinically insignificant or unrelated abnormalities, such as thyroid lesions and lymphadenopathy. Special consideration has been given to the obtunded patient, because some studies have shown a 2% incidence of unstable cervical spine injuries that were not detected by radiography and CT because of the lack of an associated fracture or

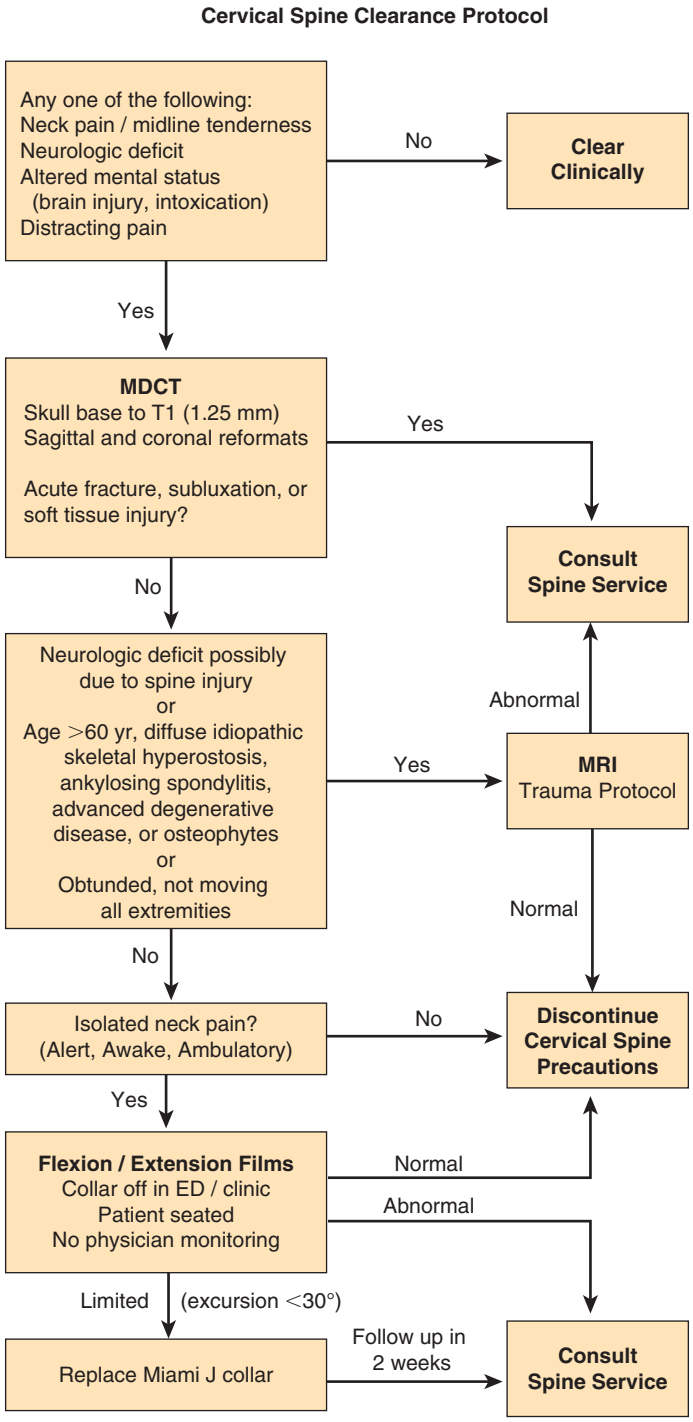


FIGURE 7-1 Cervical spine clearance protocol. *ED,* Emergency department; *MDCT,* multidetector computed tomography; *MRI,* magnetic resonance imaging.

malalignment. However, many authors have recently suggested that MRI "clearance" of the cervical spine is not necessary in this setting. At our institution, we generally adhere to the practice management guideline from the Eastern Association for the Surgery of Trauma as outlined in Figure 7-1. This approach, which no longer advocates MRI for obtunded patients with negative results of a high-quality CT scan, is from an evidence-based, meta-analysis approach using a 0.3% upper acceptable limit for missed unstable cervical spine injury.

Regarding the thoracolumbar spine, clinical prediction rules have been evaluated but provide only a very small decrease in the number of examinations performed. In patients with blunt trauma who undergo CT of the chest, abdomen, and pelvis with thin-section imaging (2.5 mm or less), sagittal and coronal reformats have been shown to be more sensitive and specific for detection of fractures, and therefore radiography can be avoided. When the viscera are not in need of examination, the role of CT for screening the spine is not as clear. The mechanism of injury is an

important determinant for further workup in this category of patients. Similar to the logic applied to the cervical spine, screening is warranted if a high-energy mechanism of injury is known or suspected, including falls from significant height (greater than 10 feet), a motor vehicle or bicycle crash, pedestrians who have been struck, assault, a sports-related or crush accident, and a concomitant cervical spine fracture. Other valid indications are altered mental status, evidence of intoxication with ethanol or drugs, painful distracting injuries, neurologic deficits, and spine pain or tenderness to palpation.

For patients with neurologic deficits referable to a thoracolumbar spine injury, current Eastern Association for the Surgery of Trauma guidelines recommend obtaining an MRI examination as soon as possible after admission to the emergency department. Early decompression of a mass lesion, such as a traumatic herniated disk or epidural hematoma, is more likely to improve the neurologic outcome.

It is somewhat counterintuitive that the absence of symptoms does not exclude injury to the thoracolumbar spine. In one study, only 60% of trauma patients with a confirmed fracture were symptomatic. In a review from Maryland's Shock Trauma Center of 183 fractures in 110 patients who were neurologically intact with a Glasgow Coma Scale score between 13 and 15 and who were considered amenable to clinical examination, 31% were recorded as having no pain or tenderness. The evidence would suggest that many of these fractures were not truly asymptomatic but rather occult as a result of intoxication or an unreliable physical examination. It is clear from the literature that no imaging modality is accurate 100% of the time. Most studies have found that radiographs of the thoracolumbar spine are commonly inadequate, especially in obese patients, and provide a sensitivity and specificity of only 60% to 70%.

Studies to develop specific guidelines for imaging of pediatric trauma patients are ongoing. The increasing use of MDCT and the long-term effects of radiation exposure are topics of special concern in this population.

Patterns of Cervical Spine Injury and Imaging Findings

In this section we include a brief review of the many different types of spine injuries that one must be familiar with when evaluating victims of trauma. Many texts are devoted solely to the imaging of spine trauma, with a few that truly reward the reader with insight into the anatomy, physiology, biomechanics, and pathology of this extensive topic. This section should serve as a valuable aid to the radiologist on call and can be used as a starting point for further study. Rather than taking a how-to approach to the interpretation of spinal imaging, in this section we rely on a working knowledge of the normal anatomy and basic principles of plain film, CT, and MR analysis. The general classifications of injuries are covered through a review of classic examples, using primarily CT with important plain film and MR correlations where appropriate.

Imaging of the spine can be thought of as a continuum, with radiography providing an overview of alignment and soft tissues, CT adding greater detail regarding fractures, and MR yielding finer detail with respect to soft tissues, including the spinal cord. Attention must be directed to the technical factors necessary to achieve a satisfactory (and safe) examination, including patient immobilization and positioning, image acquisition parameters, and multiplanar analysis.

Lateral, anteroposterior, and open-mouth odontoid views are the minimum requirement for plain films. A "swimmer's" view may be necessary to adequately demonstrate the cervicothoracic junction. Thin-section CT (with a section thickness of 2 mm or less) with sagittal and coronal reformats of similar thickness is generally sufficient. However, anecdotal cases have arisen in which hairline fractures that were not detected prospectively with the standard technique were detected on scans performed with submillimeter thickness. Clearly a trade-off exists between the level of anatomic detail and the number of images that must be reviewed. With isotropic voxel size now possible with modern scanners, some radiologists have proposed a primary review of sagittal and coronal reformats to increase patient throughput. Thankfully, many of the missed fractures will be clinically insignificant because of their small size and inherent stability. In addition to the standard T1- and T2-weighted sequences used to evaluate the cervical spine, fat-suppressed T2-weighted sequences, with chemical selective or short tau inversion recovery (STIR) technique and gradient-echo sagittal sequence, are useful in the trauma setting. MR angiographic sequences may be indicated in certain circumstances.

Careful analysis of the structures (vertebrae, intervertebral disks, spinal cord, and other soft tissues) and their normal and abnormal attributes (size, shape, alignment, density, and signal intensity) requires an understanding of mechanisms of injury, including magnitude and acuity, and underlying diseases. The mechanisms generally can be grouped into hyperflexion, hyperextension, rotation, axial loading, lateral flexion, and others. Box 7-1 attempts to categorize the injuries of the cervical spine based on these mechanisms. Combined mechanisms, such as flexion and rotation, are common and may lead to multiple injuries at different sites and vertebral levels within the same patient. Rather than relaxing one's vigilance after detecting an injury, the examiner should intensify the search for other lesions.

The determination of instability, which may be associated with or have the potential to progress to neurologic injury, major deformity, or incapacitating pain, is an important part of this process. General principles may apply based on specific imaging findings, but the final determination is probably best made by an expert in the treatment of spine injuries. One should note that the classifications of these injuries are constantly being revised based on new treatment techniques and clinical outcomes.

The following sections provide a top-down review of the major types of injuries and the mechanisms that cause them. It is not possible to describe all of the features of each injury in this abbreviated format; however, the general principles and commonly used classifications are described.

Injuries of the Cervicocranium

The cervical spine can be subdivided into the cervicocranium (including the basiocciput, craniocervical junction, atlas [C1], and axis [C2]) and the subaxial spine

(C3 through C7), with each region including associated supporting ligaments.

Injuries of the cervicocranium are usually the result of blunt trauma and often are associated with high morbidity and mortality. Accurate rapid diagnosis is essential for appropriate management and satisfactory outcomes but is challenging because of the subtlety of imaging findings, the low incidence of disease, satisfaction of search (stopping after finding the first injury) in cases of multitrauma, and lack of familiarity with this anatomic region. Patients are often unresponsive or have altered mental status at the time of presentation, thus compounding the difficulty of injury assessment.

Although the relationship of the skull to the cervical spine has always been part of the usual evaluation, findings on radiographs are often subtle or obscured by overlapping structures. Reassessment of formerly relied upon radiographic measures to diagnose craniocervical injuries (including the Power ratio, X-line, and basion-posterior axial line) has shown limited sensitivity and specificity of these methods. Many authors have studied the relationships of the craniocervical junction in healthy subjects and in patients with clinically evident abnormalities and have derived myriad normal CT measurements, some of which differ from traditional radiographic measurements. As in radiography, abnormalities of the prevertebral soft tissues also provide important clues to diagnosis. Familiarity with and working knowledge of the CT measurements and prevertebral soft tissue findings will prepare the radiologist to identify clinically important injuries of the cervicocranium.

Considerable differences exist among authors because of various study methods and the expected variance within a population. Normal variation of the anterior atlantodental interval with age has been accepted for many years. Small variations in the other atlantoaxial relationships have also been reported based on MDCT studies. Therefore, it is not possible to define an absolute value for the upper limit of normal for these measurements. Use of the most conservative measurements may be the safest approach. When in doubt, based on CT, MRI should be considered for further evaluation of potential injury to ligaments and other soft tissues. Table 7-1 provides reasonable limits (based mainly on the work of Chang et al., Radcliff et al., and Rojas et al.—see the Suggested Readings). Based on logistic regression analysis of a series of proven injuries, Chang et al. suggested that an abnormal sum of occipital condylar displacements or C1-C2 spinolaminar widening resulted in a 95% detection rate of craniocervical distractions. Overall, the measurements should be considered with appropriate judgment to avoid missing clinically significant injuries. Occasionally the change from a patient's previous examination will provide a clue to the diagnosis.

BOX 7-1 Categories of Injuries of the Cervical Spine Based on Mechanism

HYPERFLEXION
- Anterior subluxation (including C1-C2)
- Compression fracture
- Clay shoveler fracture
- Facet fracture-dislocation
- Flexion teardrop
- Interfacetal dislocation (unilateral or bilateral)

HYPEREXTENSION
- Articular mass fracture
- Avulsion of anterior arch of C1
- Extension teardrop
- Fracture of posterior arch of C1
- Hangman fracture (C2 spondylolysis/spondylolisthesis)
- Hyperextension dislocation
- Hyperextension fracture-dislocation
- Laminar fracture
- Pedicolaminar fracture-separation

AXIAL LOADING
- Burst fracture
- Jefferson fracture (C1 burst)

LATERAL FLEXION
- C1 lateral mass fracture
- Occipital condyle fracture
- Transverse process fracture
- Uncinate process fracture

OTHER OR UNKNOWN MECHANISMS
- Atlantoaxial rotatory subluxation
- Atlanto-occipital and atlantoaxial dissociation (distraction)
- Odontoid fracture

TABLE 7-1 Computed Tomography Measurements to Evaluate the Cervicocranium

Parameter	Distance Between	Limit*	Notes
Anterior atlantodental interval	Anterior cortex of the dens and posterior cortex of the anterior arch of C1	Adult: 2.5-3 mm Child: 5 mm	On sagittal reformats at the midportion of the C1 arch
Atlanto-occipital interval	Occipital condyle and C1	1-2.5 mm* 1 mm	On sagittal reformats On coronal reformats
Condylar sum	Sum of bilateral atlanto-occipital intervals	Sum: 4 mm	On sagittal reformats
Basion-dens interval	Basion and tip of odontoid process	8 mm	
C1-C2 posterior interval	C1 posterior tubercle and spinous process of C2	8 mm	
Atlantoaxial interval	Lateral masses of C1 and C2	Adult: 3 mm Child: 4 mm	
Mid occiput to mid C2	Occipital condyle and lateral mass of C2	20 mm	

*Published measurements vary considerably based on reference methodology and the sample. Measurements also may vary by plane of section. For example, to measure the atlanto-occipital interval perpendicular to articular surfaces, an appropriately angled coronal image may be best. A straight coronal or sagittal reformat may overestimate this distance in a normal case, hence a larger range. However, abnormal anterior or posterior displacement will be better assessed on a sagittal reformat.

Assessment of the Prevertebral Soft Tissues

Evaluation of the prevertebral soft tissues (PVSTs) is an important component of the radiologic assessment of the cervical spine because subtle alterations in contour and thickness may be a harbinger for adjacent osseous and/or ligamentous injury.

In 2001, Harris described alteration of the normal PVST contour as an important secondary sign of injury. Such analysis increased detection of clinically important abnormalities with high sensitivity (less than 1% false-negative results) but was not very specific (84% false-positive results).

In 2009, Rojas et al. evaluated the PVST utilizing MDCT and established a range of normal values at the various cervical levels (upper limits): 8.5 mm at C1, 6 mm at C2, 7 mm at C3, and 18 mm at C6 and C7. Values were not determined at the C4 and C5 levels because of the varying position of the esophagus and larynx. In the setting of trauma, thickened prevertebral soft tissues may be due to edema and hemorrhage. Anterior displacement of the usually thin stripe of fat between the soft tissue densities of the pharyngeal mucosa/constrictor muscles and the prevertebral ligaments is another clue to injury. As with other measurements, none is perfect or absolute and should be considered with other findings and the clinical setting. Without a history or other signs of trauma, alternate differential diagnoses should be considered.

Specific Injuries by Site

Occipital Condyle

Occipital condyle fractures are relatively rare and often are classified into three types. Type I is a longitudinal fracture from axial loading. Type II is a continuation of a fracture from the flat part of the occipital bone. Type III is the most serious—an avulsion of the condyle at the attachment of the alar ligament—and may be unstable (Fig. 7-2).

Atlanto-occipital Dislocation

Atlanto-occipital dislocation refers to disruption of the articulations of the skull and spine. Atlanto-occipital dissociation (synonymous with craniocervical dissociation) is a broader term encompassing partial (subluxation) and complete (dislocation) disruption of the articulations. After high-speed motor vehicle collisions, this injury is more often diagnosed at autopsy than at the trauma center (Fig. 7-3). See Table 7-1 for measurements to consider.

C1 Fractures

The classic Jefferson burst fracture of the atlas (C1) is due to disruption of the anterior and posterior arches (with several possible variations). Lateral displacement of the lateral masses of C1 with respect to C2 is seen on the open mouth view radiograph or the CT coronal reformatted image (Fig. 7-4). Isolated anterior arch fractures (which goes against the pretzel ring theory) or lateral mass fractures also may occur at this level.

Atlantoaxial Dissociation

Atlantoaxial dissociation includes partial (subluxation) and complete (dislocation) disruptions of the articulations of C1 and C2. Disruption of the transverse atlantal ligament, the horizontal component of the cruciform ligament complex, allows for widening of the anterior atlantodental interval (Fig. 7-5). Generally, greater than 2.5 to 3 mm in adults or greater than 5 mm in children is considered abnormal. Conditions that may predispose to atlantoaxial dissociation include rheumatoid arthritis, Down syndrome, neurofibromatosis, and other syndromes and congenital anomalies. A distraction injury will result in widened lateral atlantoaxial joints (Fig 7-6). See Table 7-1 for measurements to consider.

Rotatory dissociation (fixation) is rare and has been subdivided into four types based on the extent and direction

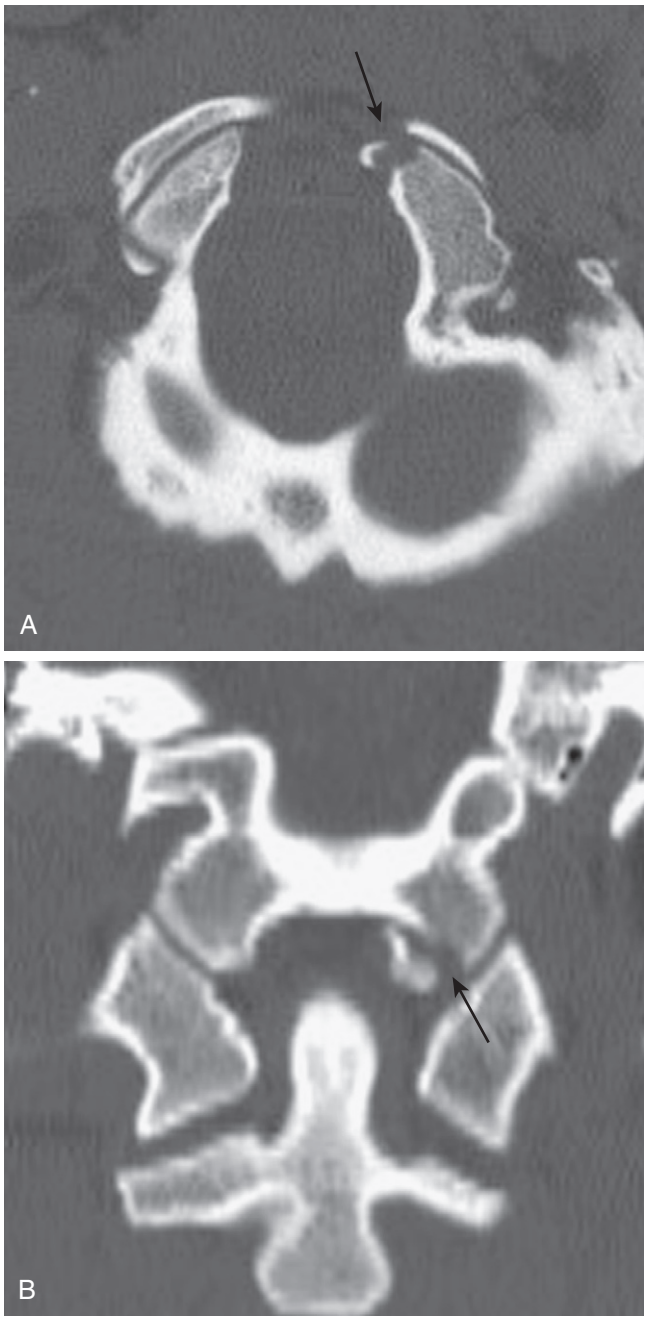


FIGURE 7-2 An occipital condyle fracture *(arrows)*. **A,** Axial computed tomography. **B,** A coronal reformat image shows an avulsion fracture of the left occipital condyle at the attachment of the alar ligament (type III).

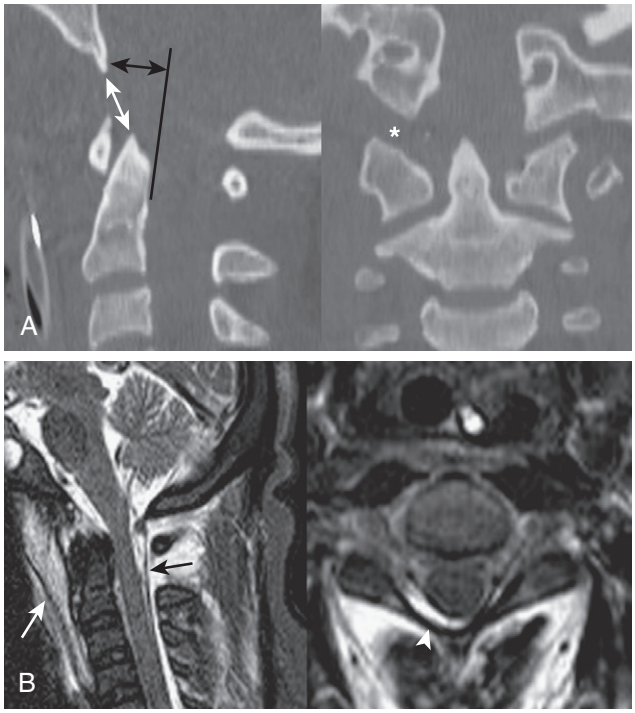


FIGURE 7-3 An atlanto-occipital dislocation. **A,** A computed tomography sagittal reformat shows a widened basion-dens interval *(white double arrow)* and basion-posterior axial line interval (BAI) *(black double arrow).* Note that the BAI is a relatively insensitive measure, but in this case it is grossly abnormal. A coronal reformat shows a widened right atlanto-occipital joint *(asterisk).* **B,** A magnetic resonance short tau inversion recovery sagittal image shows a prevertebral hematoma *(white arrow), a* hyperintense interspinous ligament, and displacement of the dura *(black arrow)* by a posterior epidural hematoma. An axial T2-weighted image shows the crescentic hyperintense epidural hematoma *(white arrowhead).*

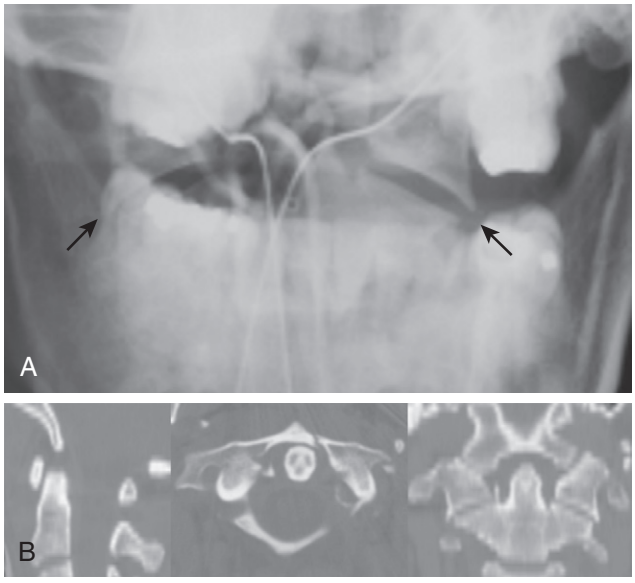


FIGURE 7-4 A C1 Jefferson fracture. **A,** An odontoid view shows overhanging margins of lateral masses of C1 *(arrows).* **B,** A computed tomography sagittal reformat shows normal relationships. The axial source image shows fractures of anterior and posterior arches of C1. A coronal reformat shows overhanging margins of C1 as seen on a plain radiograph.

of displacement of the atlas. Type I may appear similar to physiologic rotation. Therefore, to confirm the diagnosis, CT may be repeated after voluntary contralateral rotation of the head to assess for a locked position. Torticollis refers to simultaneous lateral tilt and rotation of the head and may be caused by disorders that affect either the atlanto-axial joint or the sternocleidomastoid muscle. Because it may produce the same imaging findings as type I rotatory fixation, diagnosis may rely on clinical judgment and a trial of conservative treatment. Types II, III, and IV are determined based on the direction and extent of displacement of the cranium.

C2 Fractures

Approximately 20% of cervical fractures involve the axis (C2). Of these, more than half are traumatic spondylolysis/spondylolisthesis—fracture between the superior and inferior facets (pars interarticularis) of C2—often described as the "hangman" fracture (Fig. 7-7). Because of the unique shape of C2, this fracture involves the pedicles, whereas a pars fracture of the subaxial spine is termed the "pillar" fracture. Aside from the mechanism implied by the name, other forms of hyperextension, such as motor vehicle dashboard impact, are usually to blame. At least three types have been described, based on degree of fragment distraction, angulation at the fracture site, and disruption of the C2-3 disk.

The dens (odontoid process) may be involved in approximately 25% of C2 fractures. The classification system of Anderson and D'Alonso is commonly applied. Type I—avulsion of the tip by the alar ligament—is uncommon and may be associated with atlanto-occipital dislocation. Type II is the most common (occurring in about 60% of cases) and involves the base of the dens (Fig. 7-8). Operative repair via transoral screw fixation or posterior arthrodesis of C1 and C2 is often necessary. Type III involves the dens and body of C2. Because of the larger surface area, this type of fracture is more likely to heal without the need for instrumentation (Fig. 7-9). Because the plane may be nearly horizontal, dens fractures may be quite subtle on axial CT. Sagittal reformats therefore demand careful review. Beware of misregistration artifact of axial CT as a result of patient movement between adjacent images, although this phenomenon has become less of a problem since the advent of helical and MDCT techniques. Because the scanning process is so fast with these techniques, a different type of artifact—motion blur—can occur. Distorted images should signal the need to repeat the scan. For uncooperative patients, a lateral plain film may provide complementary demonstration of proper alignment.

Injuries of the Subaxial Cervical Spine

Injury of the subaxial spine generally follows a set of patterns based on the mechanism and degree to which the spine has been stressed beyond physiologic limits.

Hyperflexion

Of the injuries caused by hyperflexion, the simple wedge compression fracture (involving the anterior column; see following section on thoracolumbar injuries for a description of the three-column system) and the isolated spinous process (clay shoveler) fracture are relatively straightforward

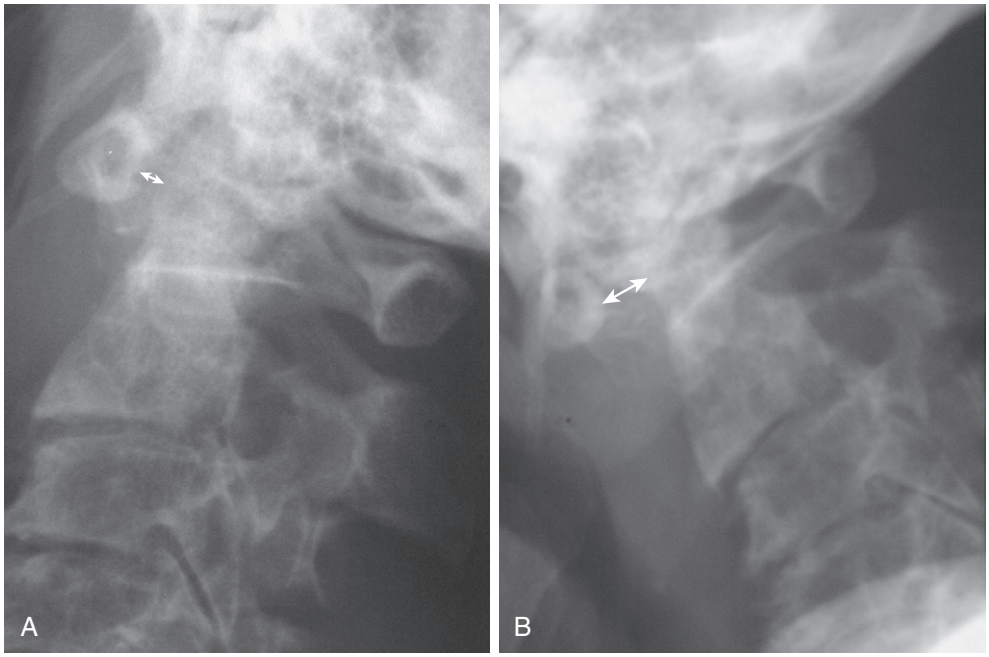


FIGURE 7-5 Atlantoaxial dissociation. **A,** An extension view shows a normal anterior atlantodental interval (AADI, *double arrow*). **B,** The AADI *(double arrow)* is abnormally widened on flexion view, confirming disruption of the transverse atlantal ligament. The abnormal atlantoaxial relationship was incidentally noted on a routine head computed tomography scan performed after a minor fall at the nursing home. The patient had a history of mild chronic neck pain, without exacerbation reported.

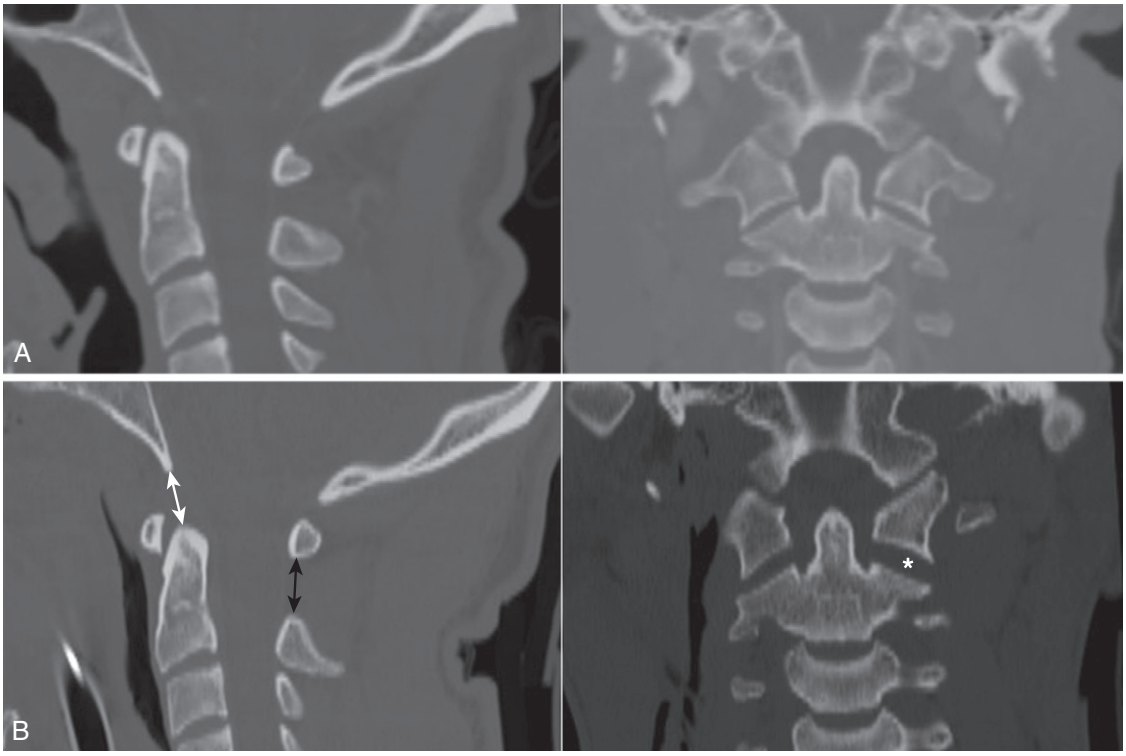


FIGURE 7-6 Atlantoaxial dissociation and atlanto-occipital dissociation. **A**, Normal craniocervical relationships on sagittal and coronal reformats from a previous neck computed tomography performed for evaluation of a tonsillar abscess. **B**, After a motorcycle collision in which the rider's helmet was dislodged, distraction injuries are present. The basion-dental interval *(double white arrow)* increased from 7 to 14 mm; the C1-C2 posterior interval *(double black arrow)* increased from 7 to 14 mm; both lateral atlantoaxial intervals increased from 3 to 5 mm *(asterisk)*; and atlanto-occipital intervals increased from <1 to 1.7 mm (not indicated). Air tracking in the prevertebral and paravertebral soft tissues was due to extension of pneumothorax.

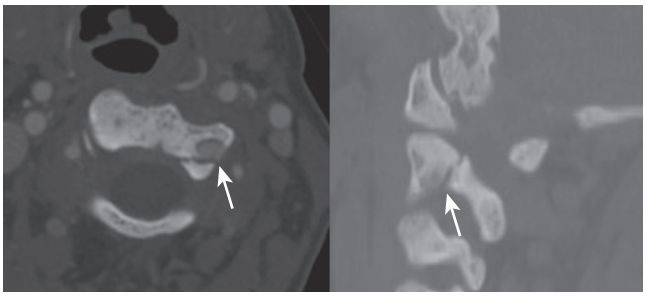


FIGURE 7-7 A C2 hangman fracture. Contrast-enhanced axial computed tomography *(left)* shows a fracture *(arrow)* through the body of C2 involving the left transverse foramen. A sagittal reformat *(right)* shows the oblique course of the fracture *(arrow)* that separates the superior and inferior articulating facets of C2.

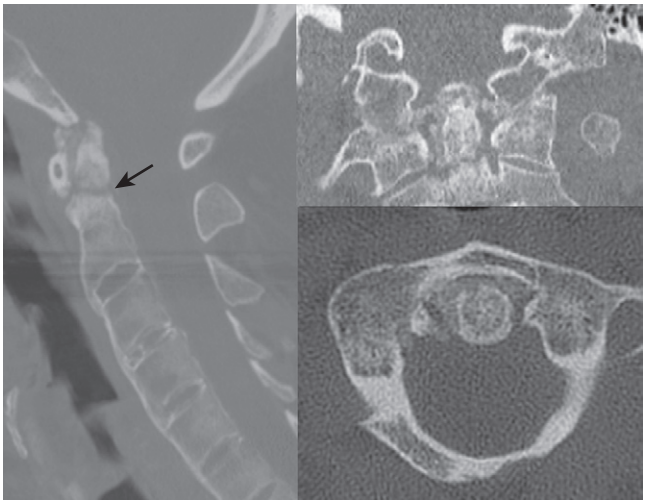


FIGURE 7-8 Ankylosing spondylitis—C2 fracture. A computed tomography sagittal reformat *(left)* shows a dens fracture *(arrow)* and ankylosis of C2 through C6 vertebral bodies. A coronal reformat *(upper right)* and axial source image *(lower right)* show extensive hypertrophic bone formation resulting in ankylosis of the occiput to C1 and C1 to the tip of the dens. The altered biomechanics are a setup for a dens fracture.

in terms of diagnosis. Although generally considered stable injuries, they can occur in association with other, more insidious injuries, and therefore flexion/extension radiographs or MRI may be indicated. Anterior subluxation (or hyperflexion sprain) is indicative of injury to the posterior ligamentous structures. It can be quite subtle, presenting with focal kyphotic angulation, very mild malalignment of facets, and widening of the posterior margin of the disk space and interspinous distance. Failure to diagnose and treat this injury may result in delayed instability in up to 50% of cases. As the degree of anterior vertebral body translation, facet joint distraction, and "fanning" of spinous processes increases, the signs of instability become more obvious. Facets may become perched or jumped (complete dislocation). Anterior translation of a vertebral body by more than 50% relative to the subjacent body is a sign of bilateral interfacetal dislocation (Figs. 7-10 and 7-11). With perched facets, the "naked facet" sign will be seen on axial CT. With bilateral interfacetal dislocation, the convex surfaces of the articular masses will be apposed rather than the usual concave articular surfaces. Anterior, middle, and posterior ligamentous structures will be disrupted, and the extent of soft tissue injuries (including cord compression and contusion) will be best assessed by MRI. If the mechanism of injury has any rotational component, unilateral interfacetal dislocation or a combination of perched and jumped facets may occur. Fractures of the subjacent vertebral body or articular masses will result in a fracture-dislocation. The flexion teardrop fracture is thought to result from a combination of hyperflexion and axial loading. It is feared because of the high incidence of permanent neurologic damage resulting from the more complex variety, which usually includes fractures of the posterior elements. Although it can be difficult to distinguish this fracture from the hyperextension teardrop fracture based on the configuration of the vertebral body fracture alone, kyphosis and posterior element distraction can be useful clues.

Hyperextension

The types of injuries to the subaxial spine resulting from hyperextension mechanisms are analogous to those sustained by hyperflexion, but with a few differences. Hyperextension sprain, dislocation, and fracture-dislocation encompass a spectrum that may result from a blow to the face, as from impact against the dashboard during a motor vehicle collision, an assault, or a fall. Soft tissue structures are involved in a progressive fashion from anterior to posterior, including prevertebral muscles, anterior longitudinal ligament, anterior portion of annulus, intervertebral disk, and the posterior longitudinal ligament. A sprain usually leaves the middle and posterior columns intact. A dislocation also disrupts the middle and possibly posterior ligaments. A fracture-dislocation may result in fractures of the posterior aspect of the vertebral body and any of the posterior elements as a result of impaction forces. When underlying ankylosis is present, such as in diffuse idiopathic skeletal hyperostosis or ankylosing spondylitis, a relatively mild hyperextension force may result in fracture-dislocation (see Fig. 7-8). This outcome is due to the loss of normal ligamentous laxity, a lever arm up to several spinal segments long, and coexistent osteoporosis. An extension teardrop fracture fragment is the result of avulsion by the anterior longitudinal ligament. The vertical dimension of the fragment is generally greater than the horizontal dimension (Fig. 7-12).

Extension combined with rotation and lateral or tilting forces may result in articular mass (also known as *pillar*) fractures (Fig. 7-13). A fracture of the pedicle and ipsilateral lamina may result in a freely mobile articular mass (pedicolaminar separation). Occasionally, isolated fracture(s) of the lamina(e) will be occult on anteroposterior and lateral films, which is one advantage of oblique radiographs. Another advantage is confirmation of unilateral facet dislocation, but, alas, MDCT has made these films nearly obsolete. It is the rare technologist who can still obtain perfect trauma oblique views that are taken without removing the cervical collar or turning the patient's head. It seems that most centers have abandoned oblique views from the routine cervical spine series. The extra clues provided by oblique views may still have value in centers where trainees interpret plain film examinations on call.

Axial Loading

Axial loading as a result of diving injuries, falls, or ejections from vehicles may result in a burst fracture, with comminuted fractures of the vertebral body and often displaced fractures of the posterior elements. As pressure is transmitted

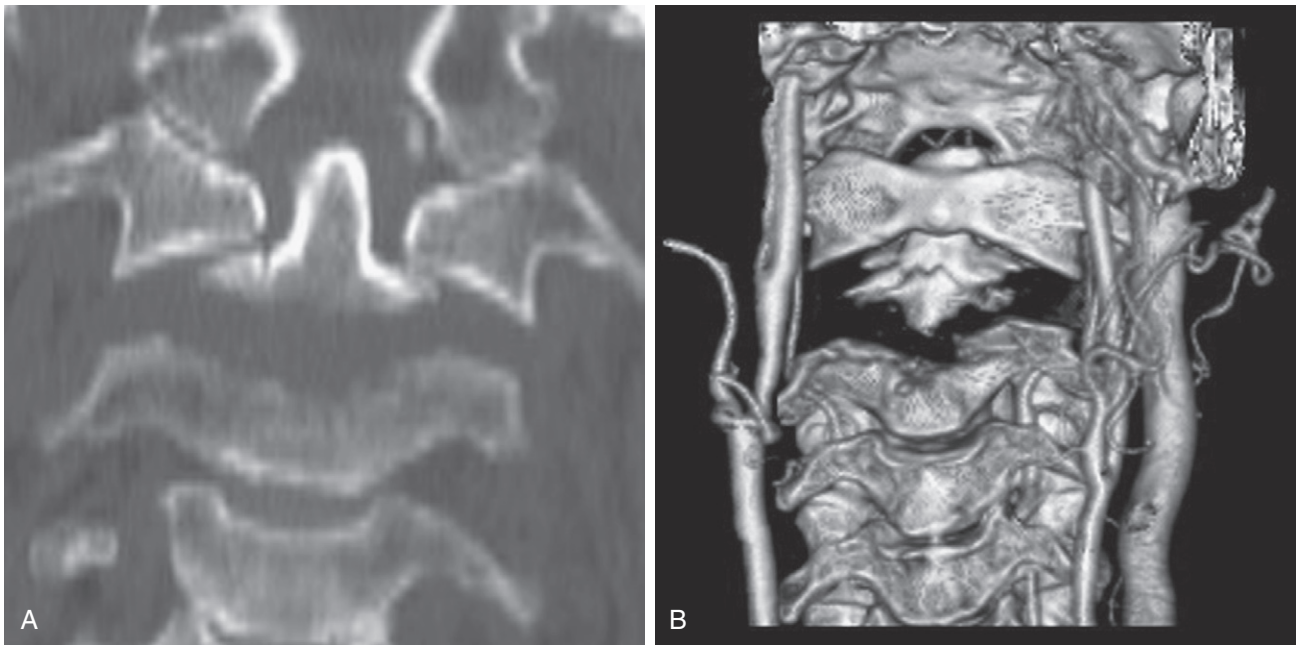


FIGURE 7-9 Dens fracture—type III. A computed tomography (CT) coronal reformat **(A)** and volume-rendered image from a CT angiogram **(B)** show fracture of the dens involving the body of C2 and distraction of fragments.

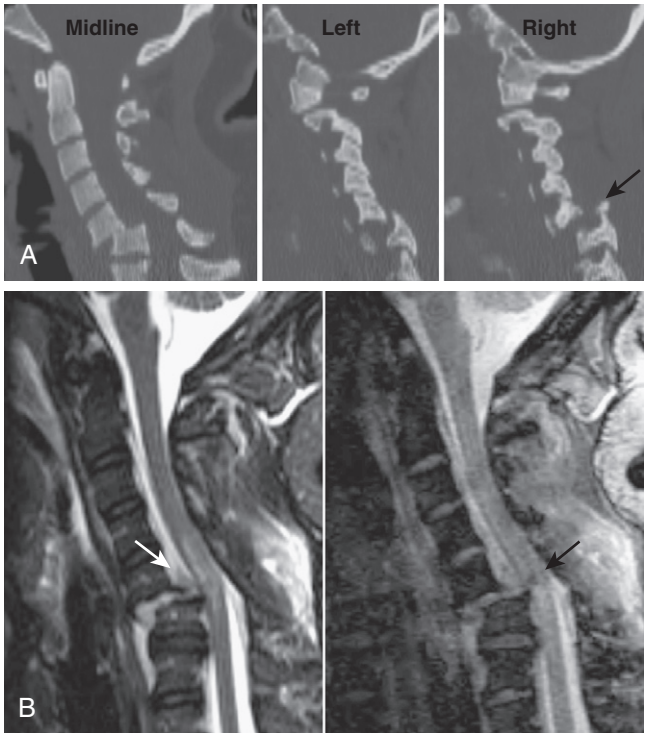


FIGURE 7-10 Hyperflexion—bilateral interfacetal dislocation. **A,** Computed tomography sagittal reformats show greater than 50% offset of C5 on C6, jumped left facet, and fracture of the right C5 inferior facet *(black arrow)* with dislocation. **B,** Sagittal short tau inversion recovery and gradient-echo images show associated small epidural hematoma versus C5-6 disk extrusion *(white arrow)*. Also note hemorrhage in the disk space extending inferiorly in the prevertebral region. Hyperintense signal in the spinal cord is consistent with edema. The central isointense region is noted to be hypointense on gradient-echo image *(black arrow)*, indicating hemorrhage (cord contusion). The Subaxial Cervical Spine Injury Classification and Severity Scale (SLIC) score is >5 (surgical) based on morphology (4 points for rotation/translation), discoligamentous disruption (2 points), and 2 to 3 points dependent on the clinical extent of the cord injury.



FIGURE 7-11 Hyperflexion—anterior subluxation. A lateral radiograph shows complete subluxation of C5 on C6 (spondyloptosis). This patient with previous C3 through C5 laminectomies for canal stenosis was the unfortunate victim of an accidental gas main explosion.

through the intervertebral disk, the body may be split in a sagittal plane, or the disk may lose vertical height, causing retropulsion of the posterior portion of the body into the spinal canal.The latter form clearly has a higher potential to result in spinal cord injury (SCI). Involvement of the anterior and middle columns is generally considered an unstable injury and requires operative fixation.

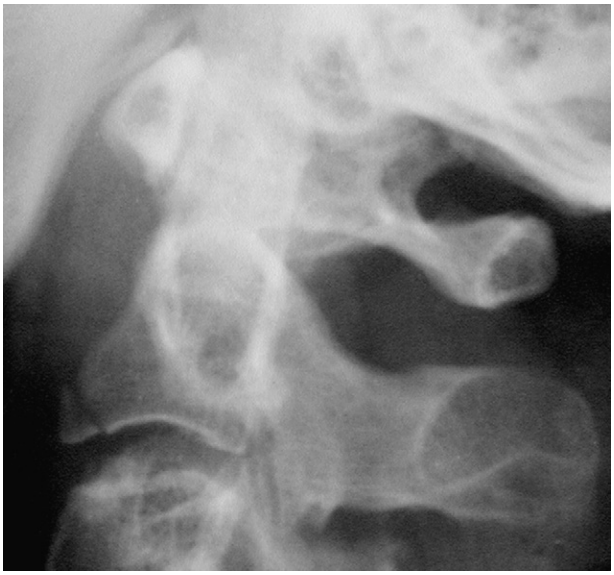


FIGURE 7-12 An extension teardrop fracture. A lateral radiograph shows that the height of the fracture fragment is greater than the width.

Many of the injuries previously described may present with relatively preserved alignment as a result of the rebound of structures after traumatic displacement. The snapshot provided by imaging after stabilization and transport to the trauma center may provide clues to the cause of a neurologic deficit. In many cases, the cause will still be evident—for example, cord compression as a result of severe canal stenosis, malalignment, displaced bone fragment, hematoma within the spinal canal, cord contusion, or edema.

Lateral Bending

Injuries due to lateral bending do not seem to be very common, but an occasional uncinate process or transverse process fracture may be detected by CT. Fracture involving the foramen transversarium brings a risk of dissection or occlusion of the vertebral artery and the possibility of stroke.

Extreme flexion, extension, and blunt trauma to the neck also carry risk of vascular injuries. Therefore, screening CT angiography has become a common part of the initial evaluation of trauma patients. Diagnosis of vascular injuries is discussed in Chapter 1 (brain, head, and neck) and Chapter 11 (vascular emergencies).

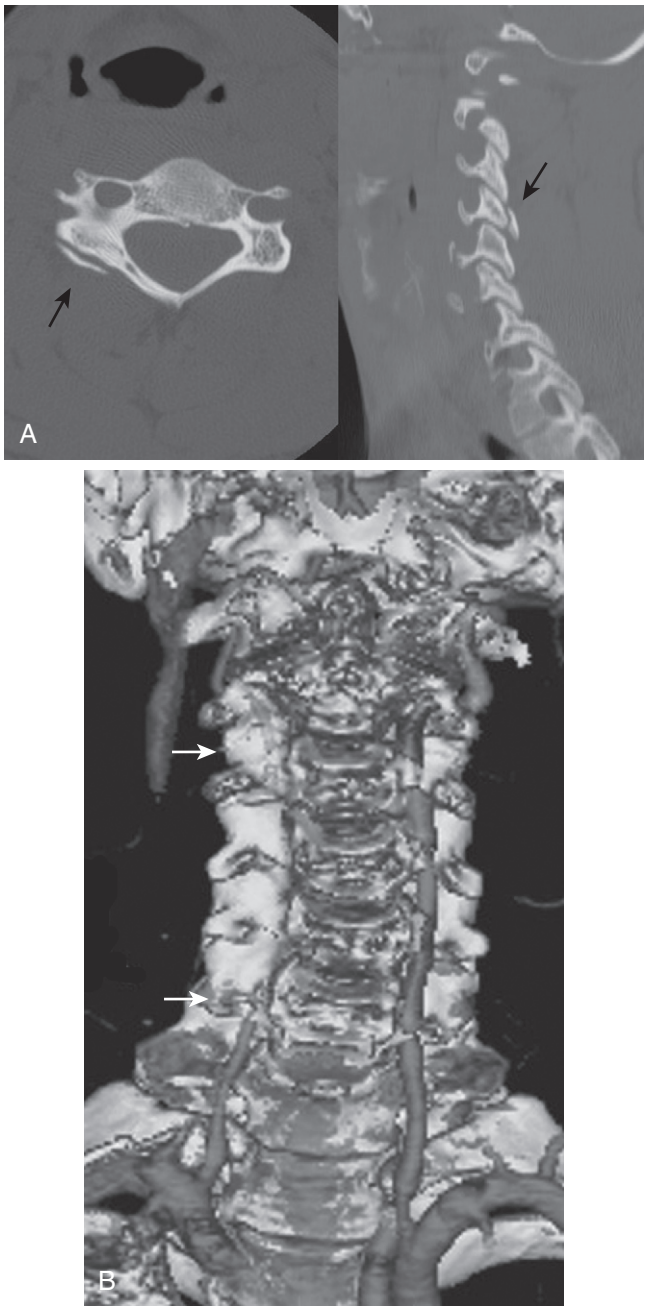


FIGURE 7-13 Articular facet fracture—vascular injury. **A,** Computed tomography (CT) axial and sagittal reformats show a C4 right pillar fracture *(black arrows)*. **B,** A volume-rendered image from a CT angiogram shows segmental occlusion *(white arrows)* of the right vertebral artery. Reconstitution via muscular collaterals is a common finding in vertebral artery injuries.

Injury Severity, Stability, and Treatment Decisions

Treatment decisions have always been formulated by consideration of clinical examination and the severity of injury based on imaging—extent of fractures, degree of malalignment, and expected mechanism.

The Subaxial Cervical Spine Injury Classification and Severity Scale (SLIC) was developed in 2007 based on a similar system used for thoracolumbar spine injuries. This scale was intended to unify spine injury classification, improve communication between health care providers, and help guide treatment decision making. The overall severity score is the sum of three components—injury morphology, integrity of the discoligamentous complex, and neurologic status.

The morphology score (0 to 4) is assigned based on assessment from radiographs, CT, and/or MRI as follows: no abnormality (0); compression fracture (1); burst fracture (2); distraction injury (3); or rotation/translation (4).

The discoligamentous score (0 to 2) is a measure of the integrity of the disk, anterior and posterior longitudinal ligaments, ligamentum flavum, interspinous and supraspinous ligaments, and the facet joint capsules. Loss of integrity of these structures will result in

instability. A score of 2 is assigned for disruption of these tissues, which is inferred from malalignment/abnormally widened anatomic relationships. On MR, abnormal T2 hyperintensity related to the discoligamentous complex with normal anatomic relationships is assigned an indeterminate score (1).

The neurologic status score (0 to 4) may be the single most influential predictor of treatment. The highest score (4) is assigned to an incomplete cord injury with continued cord compression because of the highest potential for benefit. Other scores in this category are incomplete cord injury (3); complete cord injury (2); root injury (1); or intact (0). Although spinal cord hemorrhage predicts a poor chance for complete recovery, it is not considered within this scoring system.

The sum of these three component scores may be used as a guide to determine surgical versus nonsurgical treatment. For a total of 5 points or more, operative management is recommended consisting of correction of alignment, possible decompression, and stabilization. For scores of 3 or less, nonoperative management may be considered. A score of 4 is indeterminate.

Pitfalls in Spine Imaging

One must become familiar with the normal pattern of development and congenital anomalies in children, such as os odontoideum, incomplete ossification of the neural arches, and pseudosubluxation in order to avoid false-positive diagnoses (Fig. 7-14).

It is often helpful to realize that abnormalities must be evaluated in context. For example, not every malalignment is acute. Mild subluxations of the cervical spine are quite common as a result of chronic osteoarthritis. Therefore, analysis of the pattern of facet hypertrophy may provide confidence that the deformity is chronic. Dynamic testing with flexion-extension radiographs may support such a conclusion; however, an understanding of the normal segmental motion of the spine is necessary. On the other hand, sometimes it is necessary to call attention to a clearly chronic finding detected serendipitously. An os odontoideum that is well corticated but chronically unstable provides just one such example (Fig. 7-15).

Injuries of the Thoracolumbar Spine

Although similar mechanisms of injury apply, differences in biomechanics between the cervical and thoracolumbar spine result in different patterns of findings. Compression fractures due to flexion are very common (Fig. 7-16). Osteoporotic compression fractures are common, with more than 700,000 occurring annually in the United States, with costs from treatment approaching $1.5 billion. Although the majority may be considered stable, medical therapies required to treat the associated pain may lead to other serious complications. The increase in age-adjusted 5-year mortality approaches 25% for female patients. Use of alcohol and certain medications, including steroids, anticonvulsants, cytotoxic drugs, thyroid hormones, and heparin, all may be associated with osteoporotic compression fractures. Metastatic disease may predispose to the development of pathologic compression fractures. One fracture also increases the risk

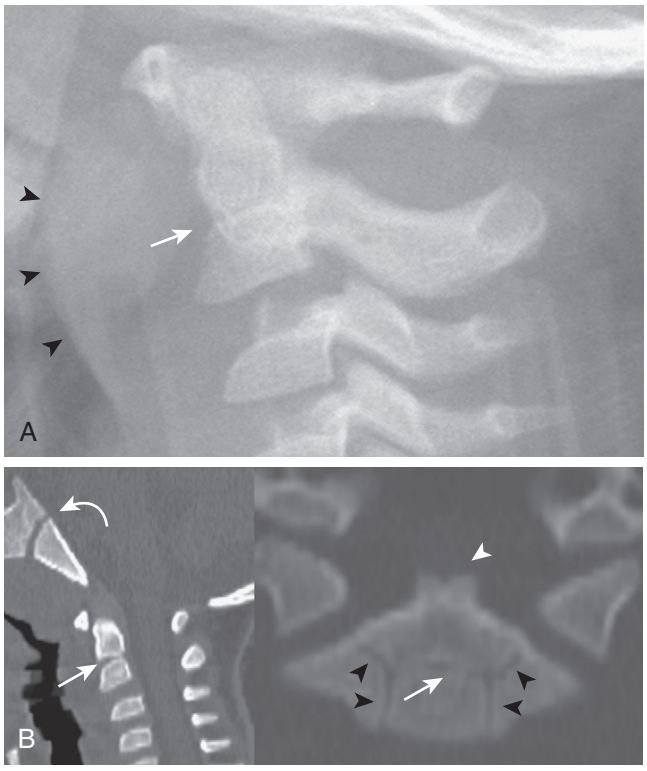


FIGURE 7-14 Normal developmental anatomy—C2. **A,** A lateral radiograph in a small child was interpreted as prevertebral soft tissue swelling *(arrowheads)* and dens fracture *(white arrow)*. **B,** Computed tomography sagittal and coronal reformats show normal developmental anatomy—subdental synchondrosis *(white arrows)* and neurocentral and neurodental synchondroses *(black arrowheads)*. The tip of the dens ossification center (ossiculum terminale) is not yet visible *(white arrowhead)*. The apparent soft tissue swelling was due to normally lax tissues and phase of respiration. Note also the normal spheno-occipital synchondrosis *(curved arrow)*.

for development of other fractures as a result of altered biomechanics of the kyphotic spine. Vertebroplasty and kyphoplasty are minimally invasive spine procedures that are possible treatments for patients who do not respond to an appropriate trial of conservative therapies. With more than 50% loss of anterior vertebral body height, disruption of the posterior longitudinal ligament may occur, leading to the possibility of instability.

An axial loading mechanism may result in a burst fracture. These fractures occur most commonly near the thoracolumbar junction but also may affect the mid and lower lumbar levels. The extent of retropulsion of the posterior portion of the vertebral body, the relative size of the spinal canal, and the position of the conus medullaris are factors affecting the risk of neurologic injury. Screening examination of the thoracolumbar spine should be performed when calcaneal fractures result from a jump or fall from a height because of the high association of these injuries (Fig. 7-17).

The combination of flexion and distraction, which is common in lap belt deceleration injuries, results in a rather unique pattern of findings. A horizontally oriented fracture plane through the intervertebral disk and posterior elements has come to be called the "Chance" fracture. Because many variations exist in terms of bony and ligamentous components, the term "Chance-type

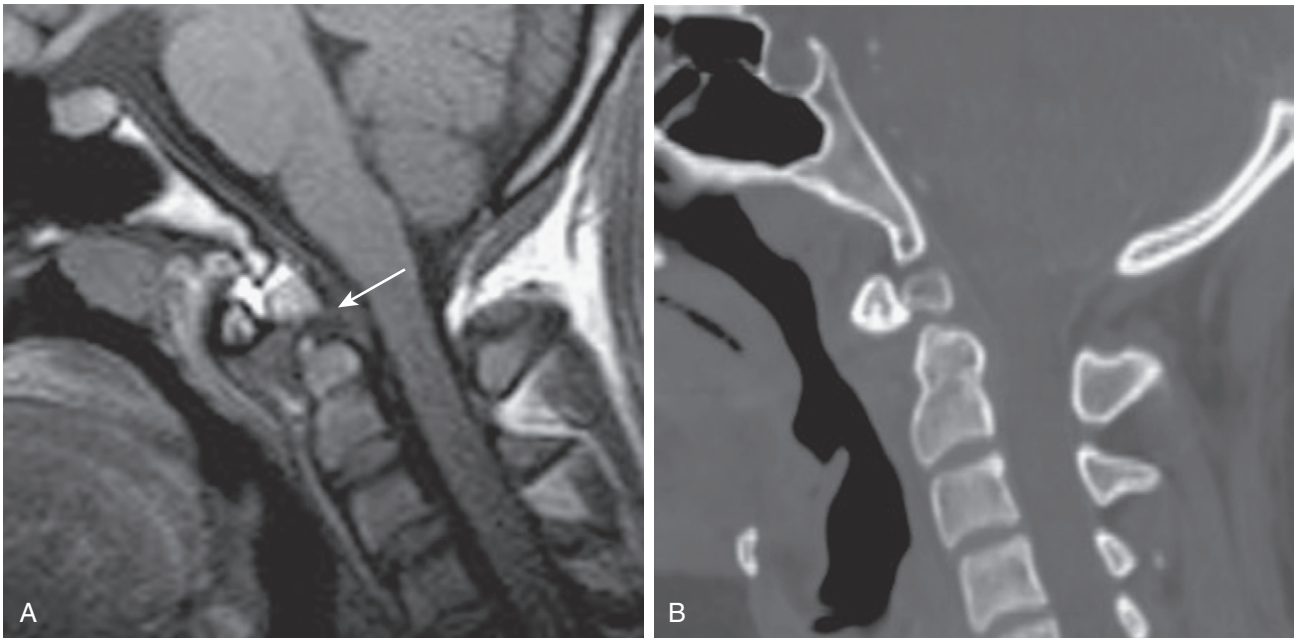


FIGURE 7-15 Os odontoideum—unstable. **A,** A sagittal T1-weighted image of a teenager with headaches and visual scotomata revealed an anomaly of the cervicocranium *(white arrow)*. **B,** A sagittal reformat of cervical spine computed tomography confirmed an os odontoideum and incomplete posterior arch of C1 variants. Flexion-extension radiographs demonstrated instability (not shown). Transient compression of the basilar artery related to instability was thought to be responsible for the visual changes. The patient is asymptomatic after C1-C2 fusion.

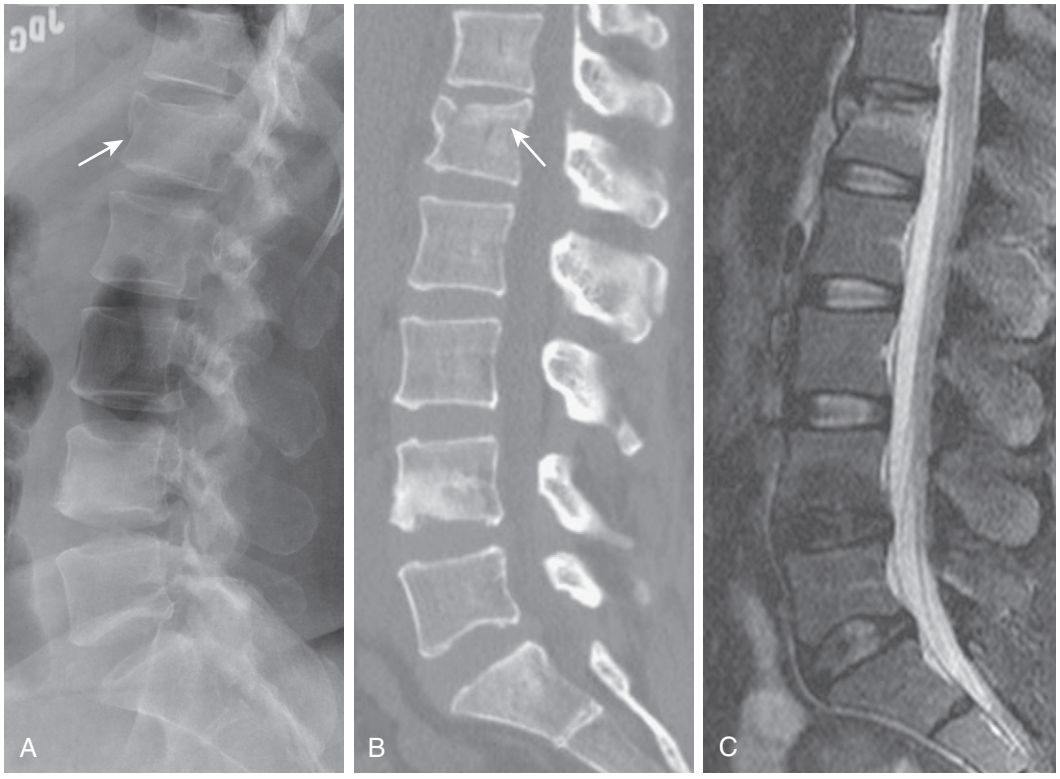


FIGURE 7-16 Lumbar compression fracture. **A,** A lateral radiograph in a patient with calcaneal fractures after jumping from a roof. Slight anterior wedging of the L1 vertebral body with a triangular fragment *(arrow)*. **B,** A computed tomography sagittal reformat shows increased density of the impaction zone *(arrow)*. **C,** A magnetic resonance short tau inversion recovery sagittal image shows a fracture fragment, marrow edema in the impaction zone, and a small prevertebral hematoma. Contrast these findings with the endplate irregularity and sclerotic changes at the inferior aspect of L4 vertebral body as a result of chronic degenerative disease.



FIGURE 7-17 Thoracic burst fracture. A sagittal T1-weighted image *(left)* and T2-weighted image *(right)* show retropulsion of the posterior portion of the T11 vertebral body, resulting in cord compression. Cord T2 hyperintensity is consistent with edema. A contusion should be suspected based on the degree of compression; however, no T2 or gradient-echo hypointensity is present to confirm the presence of hemorrhage. Thoracolumbar Injury Classification and Severity Score (TLICS): 4; burst fracture morphology (2), posterior ligamentous complex intact (0), and neurologic status (2 points because this patient had a complete cord/conus medullaris deficit). In indeterminate cases such as this, immediate surgery might be offered to relieve the continued cord compression in hopes of improving the chance for partial neurologic recovery.

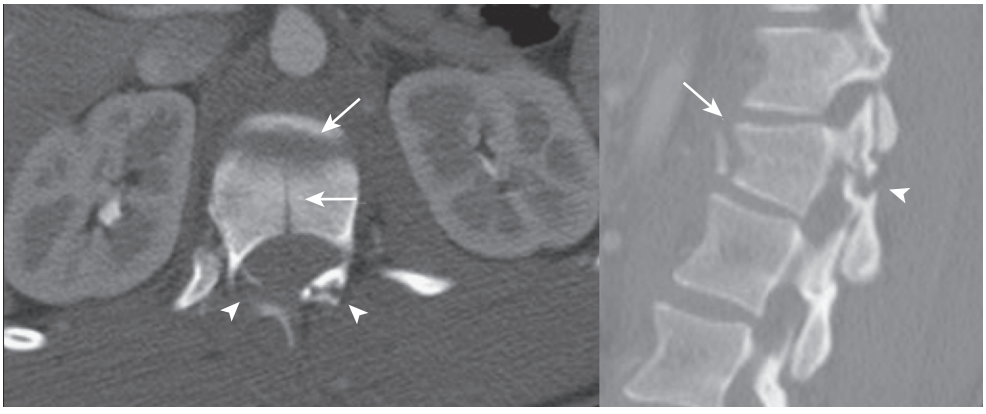


FIGURE 7-18 A Chance-type fracture. Axial *(left)* and sagittal reformatted *(right)* images from contrast-enhanced computed tomography of the abdomen after a motor vehicle collision. Images show anterior wedge deformity of a lower thoracic vertebra. Note longitudinal *(arrows)* and horizontal *(arrowheads)* fracture planes and distraction of the posterior elements.

fracture" may be applied to these horizontal fractures that most commonly affect the upper lumbar spine (Fig. 7-18). The abdominal viscera should be carefully evaluated in patients with Chance-type fractures, because association with intestinal and solid organ injuries is strong.

Hyperextension injuries may result in disk and anterior ligamentous injury or impaction fractures of the posterior elements. Patients with ankylosing spondylitis are particularly prone to extension injuries and also may develop horizontally oriented fractures through the vertebral bodies.

The classic three-column approach to stability proposed by Denis divides the spine into the anterior column (the anterior longitudinal ligament, annulus, and anterior two thirds of the vertebral body and disk), the middle column (the posterior third of vertebral body and disk, annulus, and posterior longitudinal ligament), and the posterior column (the posterior elements, ligamentum flavum, joint capsules, and intertransverse, interspinous, and supraspinous ligaments). In this system, instability is generally based on disruption of two of the three columns.

The Thoracolumbar Injury Classification and Severity Score (TLICS) predated the previously described system for the subaxial cervical spine (SLIC). Fracture morphology (1 to 4), integrity of the posterior ligamentous complex (PLC) (0 to 3; PLC does not include the anterior and posterior longitudinal ligaments or the disk), and neurologic status (0 to 3) are tallied. Recommendation for or against surgery is based on the total score in a fashion similar to the SLIC. Integrity of the PLC and neurologic status influence the surgical approach—anterior and/or posterior. Other important considerations include the degree of angulation, open fractures, associated burns or rib fractures, and comorbidities.

A type of injury unique to the thoracic region is rib dislocation, which usually is not found as an isolated injury. Spinal cord transection as a result of the guillotine effect of a displaced rib has been reported but is exceedingly rare.

Lumbar transverse process fractures as a result of avulsions by the paraspinal muscles are commonly detected in association with visceral injuries, sacral fractures, and pelvic fractures. When detected on plain films, CT of the abdomen and pelvis may be in order as a result of this association. Sacral fractures and sacroiliac joint disruptions are easily diagnosed by pelvic CT when gross displacement is present. As with any other portion of the spine, subtle displacements may be easily overlooked. Insufficiency fractures of the sacrum are common in the setting of osteoporosis. Attention to the arcuate lines of the sacrum is important when reviewing plain films of the pelvis. Coccygeal fractures may be a source of persistent pain, with patients thus presenting to the urgent care clinic. Plain film radiography is generally sufficient to assess this site of injury. The angulation of the coccyx can be quite varied, and often presumably is the result of prior trauma.

Evaluation of Spinal Soft Tissue Injuries

Spinal Cord Injury

In some of the cases illustrated thus far, findings of SCI have been present. In each of these cases, injuries to the spinal column were noted as well. SCIs may also occur in the absence of injury to the spinal column. The acronym SCIWORA (spinal cord injury without radiographic abnormality) was coined in 1982. SCIWORA may be due to longitudinal distraction of the cord; in some cases, MR imaging may demonstrate evidence of the cause of spinal cord dysfunction as a result of hemorrhage or edema within the cord or from extrinsic compression or transection. SCI may be complete (with complete loss of motor and sensory function) or incomplete (with partial loss of sensory and/or motor function). Different constellations of neurologic dysfunction may result because of the topographic organization of pathways, including anterior cord, central cord, Brown-Séquard, and conus medullaris syndromes. Cauda equina syndrome results from injury to spinal nerve roots. Spinal cord concussion is analogous to the cerebral transient ischemic attack.

Spinal cord edema appears as a zone of T2 hyperintensity almost immediately upon injury. Gross swelling of the cord may be very subtle. In many cases it may be possible to detect hemorrhage located centrally within the region of edema (a true contusion). This hemorrhage may appear relatively isointense or hypointense to normal cord, with greater sensitivity on gradient echo, usually because of the presence of deoxyhemoglobin. Within a few days, T1 hyperintensity, and still later T2 hyperintensity, may develop as a result of the conversion to methemoglobin. Many authors have attempted to develop classification systems to predict functional outcomes based on MRI findings, and these systems have worked to varying degrees. Detection of a hemorrhage larger than 1 cm in longitudinal dimension and lack of resolution of signal abnormalities on follow-up imaging generally indicate the poorest prognosis for recovery. Normal cord signal intensity or edema alone are more likely to be associated with better clinical outcomes. A newly proposed system, the Brain and Spinal Cord Injury Center (BASIC) score, assesses the severity of acute cervical spinal cord injury with axial T2-weighted findings. It should be noted that cord compression by bone fragments, disk, or hematoma is predictive of the development of hemorrhage and is therefore the basis for early decompression by many spine surgeons.

Diagnosis of injury to any of the other soft tissue structures listed in the following sections can be based on T2 hyperintensity. In addition, anterior and posterior longitudinal ligaments may be displaced (elevated) or disrupted. Disks may be widened or extruded. Facet capsules may be widened and fluid-filled, or facets may be dislocated. Ligamentum flavum and interspinous ligaments may be disrupted. Cervical root avulsion as a cause of brachial plexopathy may present with abnormal enlargement of nerve root sleeve(s)—that is, pseudomeningocele (Fig. 7-19).

Although MRI is indicated primarily for evaluation of soft tissues, the STIR sequence is especially well suited for the detection of bone marrow edema. Fractures may be detected as changes in shape of the vertebrae or linear hypointensities but are generally more easily detected using CT.

Spinal Hematomas

Hemorrhage within the spinal cord is most often the result of trauma. Spontaneous hemorrhage within the spinal cord (intramedullary hemorrhage) can result from intrinsic cord lesions, such as ependymoma or cavernous malformation, and may present with sudden onset of weakness of the extremities.

Hemorrhage can occur within the other compartments of the spinal canal, usually as a result of trauma but, on occasion, without provocation. The spinal epidural, subdural, and subarachnoid spaces are contiguous with their intracranial counterparts. Hematoma/hemorrhage can collect in these areas by extension or occur primarily within the spine. As seen in many of the figures demonstrating spine fractures and subluxations, epidural hematomas arise commonly in the setting of trauma, and if they are causing cord or conus compression, emergent evacuation may prove beneficial. Emergency surgical evacuation is generally considered the standard treatment for patients with

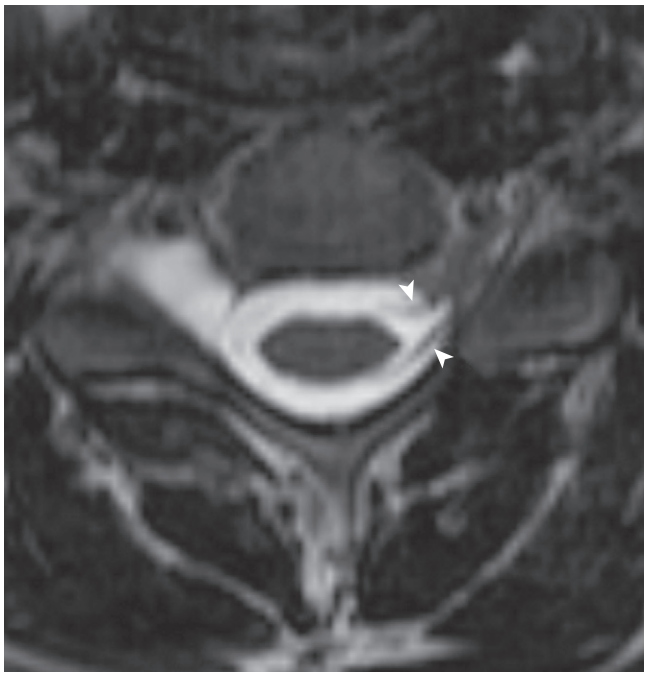


FIGURE 7-19 Cervical root avulsion. An axial T2-weighted image in a patient with right brachial plexopathy after a motorcycle collision. Note the right-sided pseudomeningocele and nonvisualization of ventral and dorsal roots. Normal roots are indicated on the left side *(arrowheads)*.

disabling and/or persistent neurologic deficit. A conservative approach under close neurologic observation may be suitable for patients with mild deficits, patients who show early and continuous clinical improvement, and patients with noncompressive epidural hematomas. Reported cases of spontaneous remission are very rare.

MRI features of spinal epidural hematoma include variable, often heterogeneous T1- and T2-weighted signal intensity; capping of epidural fat; direct continuity with the adjacent osseous structures; compression of epidural fat, the subarachnoid sac, and the spinal cord; and usual posterolateral location in the spinal canal. A tapered appearance of the cerebrospinal fluid space as a result of extrinsic hematoma is usually apparent.

On the other hand, hemorrhage confined by the thecal sac must be within either the subdural or subarachnoid space. Differentiation of the three types of extramedullary spinal hemorrhage sometimes can be quite difficult. Extension into the neural foramen, beyond the expected confines of the thecal sac, is a sure indication that the hemorrhage is in the epidural space. Subarachnoid hemorrhage often collects in a uniform circumferential configuration around the spinal cord, mixes uniformly with cerebrospinal fluid, intermingles with the roots of cauda equina, and seeks a dependent position in the spinal canal. Spinal subdural hematoma is easiest to differentiate when the arachnoid mater and roots are displaced by a hematoma confined to the thecal sac (Figs. 7-20 to 7-22).

Advanced MR techniques are now being applied to spine imaging, with much research in the field of SCI.

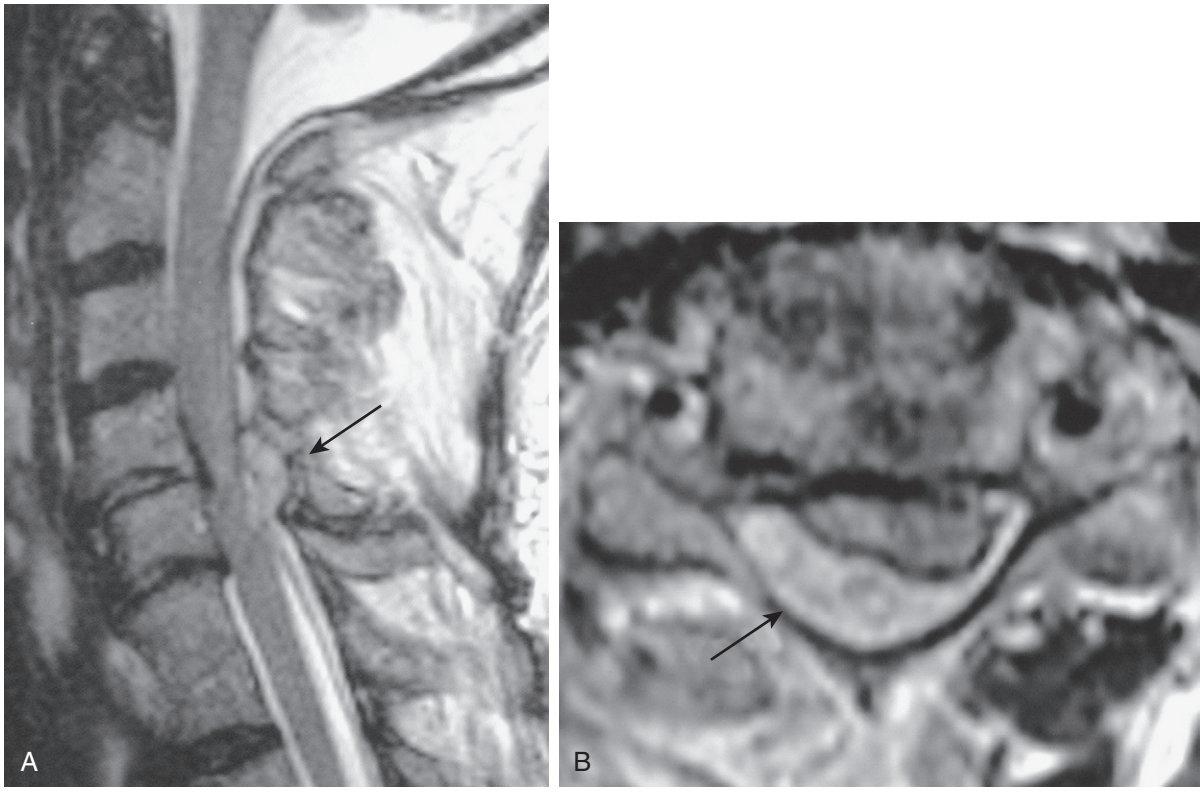


FIGURE 7-20 Spinal epidural hematoma—cord compression. This patient sustained an isolated C4 lamina fracture after a fall from a loading dock and experienced right hand weakness after undergoing computed tomography. **A,** A sagittal T2-weighted image and **B,** an axial gradient echo T2-weighted image show an intermediate intensity posterior epidural hematoma *(arrows)* causing cord compression.

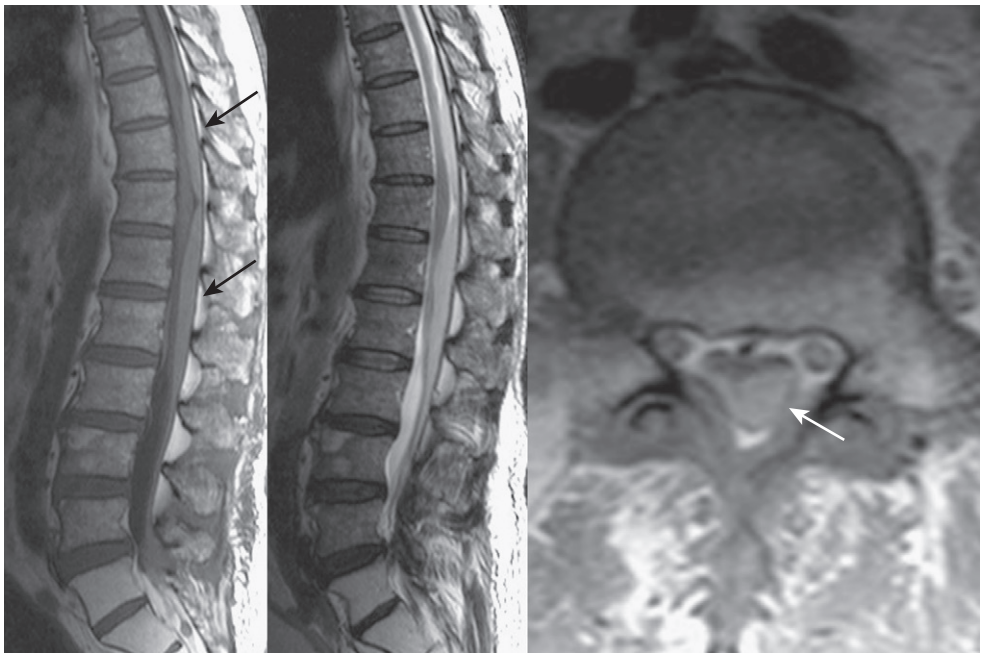


FIGURE 7-21 A spinal subdural hematoma. A sagittal T1-weighted image and T2-weighted image and axial T1-weighted image demonstrate a long, lobulated intradural hematoma *(arrows)* that displaces the roots of the cauda equina. The hematoma is limited by the displaced arachnoid membrane.

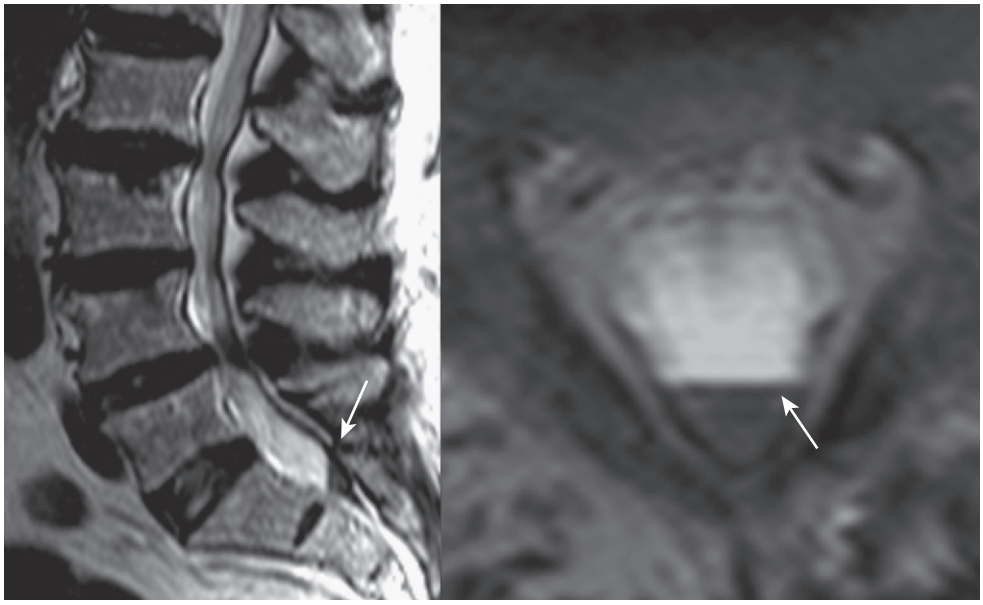


FIGURE 7-22 Spinal subarachnoid hemorrhage. Sagittal and axial T2-weighted images show a hypointense fluid level *(arrows)* within the subarachnoid space.

Diffusion-weighted and diffusion tensor imaging, MR spectroscopy, and functional imaging have great potential for future clinical applications. These techniques are not yet widely available. Many technical limitations still must be overcome before they can be applied routinely.

Vascular Injuries of the Neck Associated with Spine Trauma

The spectrum of traumatic vascular injuries of the neck related to spine trauma and the imaging features are reviewed in Chapters 1 and 11.

NONTRAUMATIC SPINE EMERGENCIES

The spontaneous development of limb weakness, pain or paresthesia, and progressive inability to ambulate may be causes for presentation to the emergency department. In many cases, the history and physical examination localize the abnormality to the spine and prompt imaging is required to evaluate for the possibility of cord or root compression or an intrinsic process of the spinal cord. MRI is generally the modality of choice; the addition of gadolinium-enhanced sequences, especially with fat

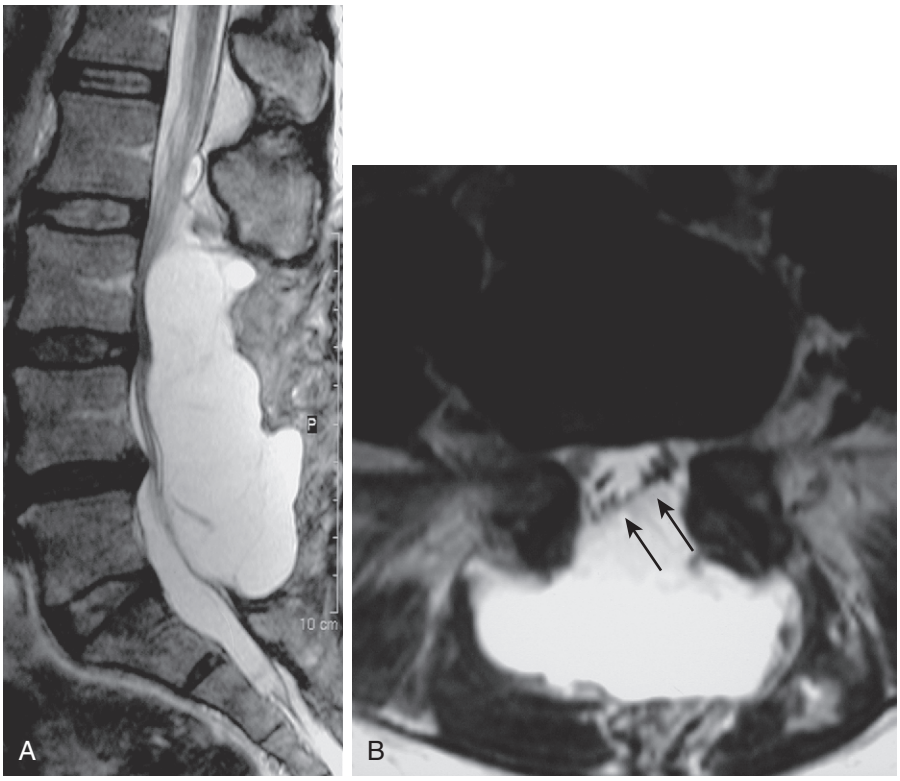


FIGURE 7-23 Postoperative pseudomeningocele—root compression. This patient experienced progressive weakness 1 week after decompressive laminectomies for spinal stenosis. Sagittal (**A**) and axial (**B**) T2-weighted images show large fluid collection with signal isointense to cerebrospinal fluid, which causes root displacement *(arrows)* and compression. Neurologic improvement occurred after repair of the leak.

suppression, to the routine protocols is often useful. The following brief review illustrates the spectrum of nontraumatic disorders and the common differential diagnoses to be considered.

Congenital Disorders

Although congenital/developmental anomalies and abnormalities are not likely to present emergently, they may be unknown until an unrelated acute event occurs. Occasionally, a Chiari I malformation may be found during a trauma workup. A preexisting syrinx should not be mistaken for an acute SCI. A tethered cord or lipoma of the filum terminale might be found in the process of workup for an acute episode of sciatica.

Degenerative Disease/Arthropathy

As mentioned in the section on spine trauma, underlying conditions resulting in narrowing of the spinal canal are often found in patients who present with SCIs, sometimes resulting from rather minor trauma. Many causes of canal stenosis exist, including routine spondylosis, ossification of the posterior longitudinal ligament, ossification of ligamentum flavum, a synovial cyst, and epidural lipomatosis. Underlying disorders such as these are often discovered in the setting of an acute disk extrusion that results in a new neurologic deficit. Degenerative disk disease is ubiquitous, and the imaging findings are generally straightforward. One should not be fooled by the T2 hyperintensity of a disk extrusion that simulates fluid or by a sequestered fragment displaced a considerable distance from the remainder of the disk. Gadolinium-enhanced images may help to identify root inflammation or arachnoiditis and differentiate granulation tissue (scar) from a recurrent disk extrusion in the setting of a postoperative patient presenting with recurrent symptoms. Familiarity with expected routine postoperative findings is important, but one also must be able to analyze features in a systematic fashion, for example, to determine if a cerebrospinal fluid leak/pseudomeningocele might be causing root compression (Fig. 7-23).

Patients with rheumatoid arthritis may show a variety of findings, including laxity of the transverse atlantal ligament and atlantoaxial subluxation, vertical subluxation or erosion of the odontoid, or development of granulation tissue around the odontoid (pannus). Spinal cord compression can result from acute trauma or the combination of pannus and chronic instability.

Other arthritides such as amyloidosis or crystal pyrophosphate deposition may present with mass lesions or destructive changes of the spine, mimicking malignancy or infection (Fig. 7-24).

Neoplasms and Tumorlike Conditions

Tumors of the spine may be divided into intramedullary, extramedullary intradural, and extramedullary extradural categories. The development of symptoms is usually slowly progressive, but acute presentations due to the inability to ambulate, incontinence, or in relation to hemorrhage are not uncommon.

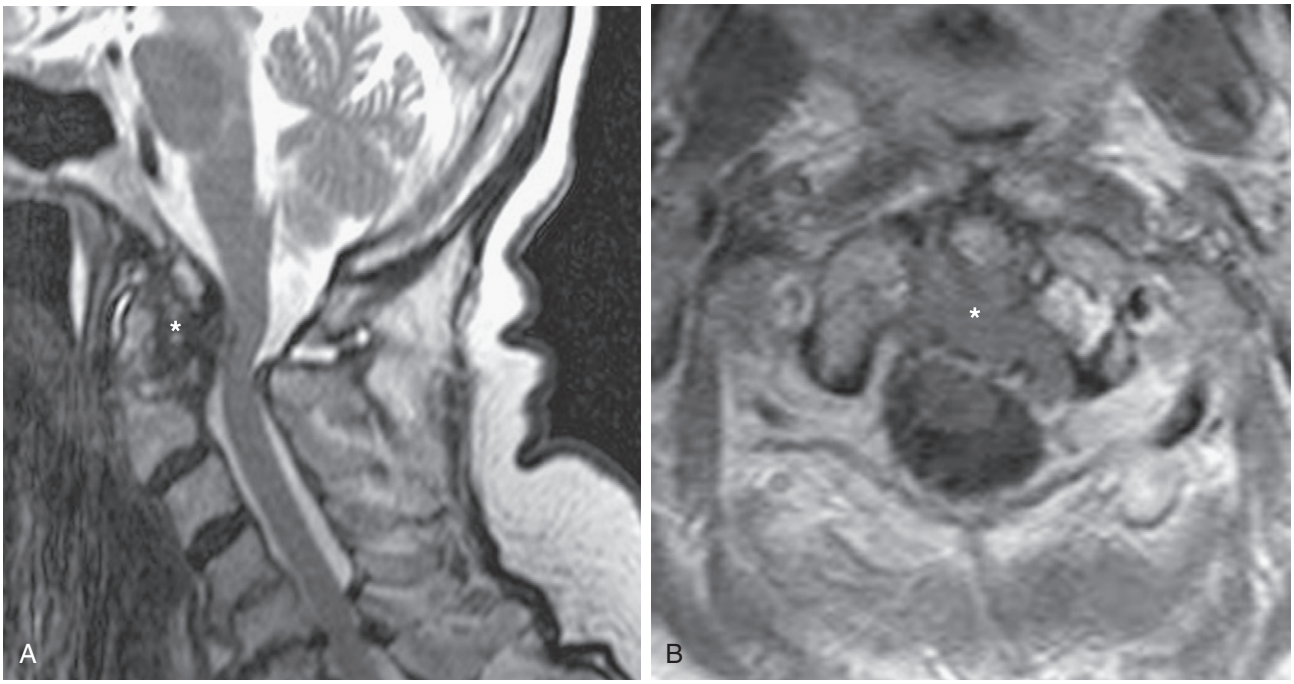


FIGURE 7-24 Calcium pyrophosphate disease—cord compression. A sagittal (**A**) T2-weighted image and axial (**B**) T1-weighted image show a soft tissue pannus related to the dens *(asterisk)* in a patient with "pseudogout" who experienced symptoms of myelopathy as a result of chronic cord compression.

Extradural lesions, which are encountered most commonly, include disk herniations and degenerative changes from arthritis and traumatic conditions, as already discussed. Metastatic disease makes up the majority of the neoplastic extradural masses, usually from carcinomas of the lung, breast, and prostate. Although metastasis to the bone with extradural extension is typical, metastasis to or primary involvement of the extradural soft tissues also may result in neural compromise. Lymphoma may present this way or by extension from the retroperitoneum through the neural foramen (Fig. 7-25). Vertebral involvement by multiple myeloma may present with an extradural mass or pathologic compression fracture (Fig. 7-26). Common osseous lesions such as aneurysmal bone cyst, osteoblastoma, osteochondroma, and Paget disease occasionally may present with symptoms related to cord compression. Chordoma, a destructive bone tumor arising from notochord rests, accounts for approximately 5% of primary bone tumors. Most commonly occurring in the sacrum, a chordoma also may arise in the clivus, cervical or lumbar regions. A large soft tissue mass, calcifications, and residual bone fragments are typical features.

Many tumorlike lesions may affect the spine. Hemangiomas are commonly found in the vertebral bodies on routine examinations and generally are not a cause for concern. Composed of thin-walled blood vessels and a variable amount of adipose tissue within the bony trabeculae, these lesions have signal characteristics determined by the relative amounts of vascular, bone, and fat components. They are usually slow-growing, benign lesions, but occasionally, expansion of the vertebral body and extension of the lesion into the epidural space may compromise the spinal canal. Thoracic cord compression due to extramedullary hematopoiesis occurs rarely in patients with hematologic disorders, such as thalassemia. Notice of diffuse signal abnormality of the vertebral marrow may be important to making this diagnosis.

Extramedullary intradural masses include meningiomas, tumors of nerve sheath origin, metastases, and others. Meningiomas and nerve sheath tumors (schwannomas and neurofibromas) account for approximately half of all intraspinal neoplasms. These three lesions may be associated with neurofibromatosis (types I and II), but details of the patterns of occurrence are beyond the scope of this review. Like their intracranial counterparts, spinal meningiomas are more commonly found in women, especially in the thoracic region. Schwannomas are found equally in males and females and occur throughout the spine. Secondary signs of bone remodeling may be seen as a result of these slow-growing lesions. Combined intradural-extradural or isolated extradural involvement of nerve sheath tumors and meningiomas occurs much less commonly than the usual intradural extramedullary form. Lipomas, dermoids, and epidermoids may occur in this compartment and occasionally have combined intramedullary involvement as well.

Extramedullary intradural metastatic disease more commonly arises from tumors of the central nervous system via cerebrospinal fluid dissemination. These tumors include ependymomas, pineal tumors, and choroid plexus tumors. Seeding generally results in nodular lesions in the lumbosacral subarachnoid space. The majority of metastases via hematogenous spread are the result of lung and breast carcinoma and melanoma.

Intramedullary tumors account for approximately 10% of primary intraspinal tumors; the majority of these are gliomas (approximately 70% are ependymomas and the remainder are astrocytomas). These tumors may be indistinguishable by imaging; both may show enlargement of the cord and irregular T2 hyperintensity and enhancement

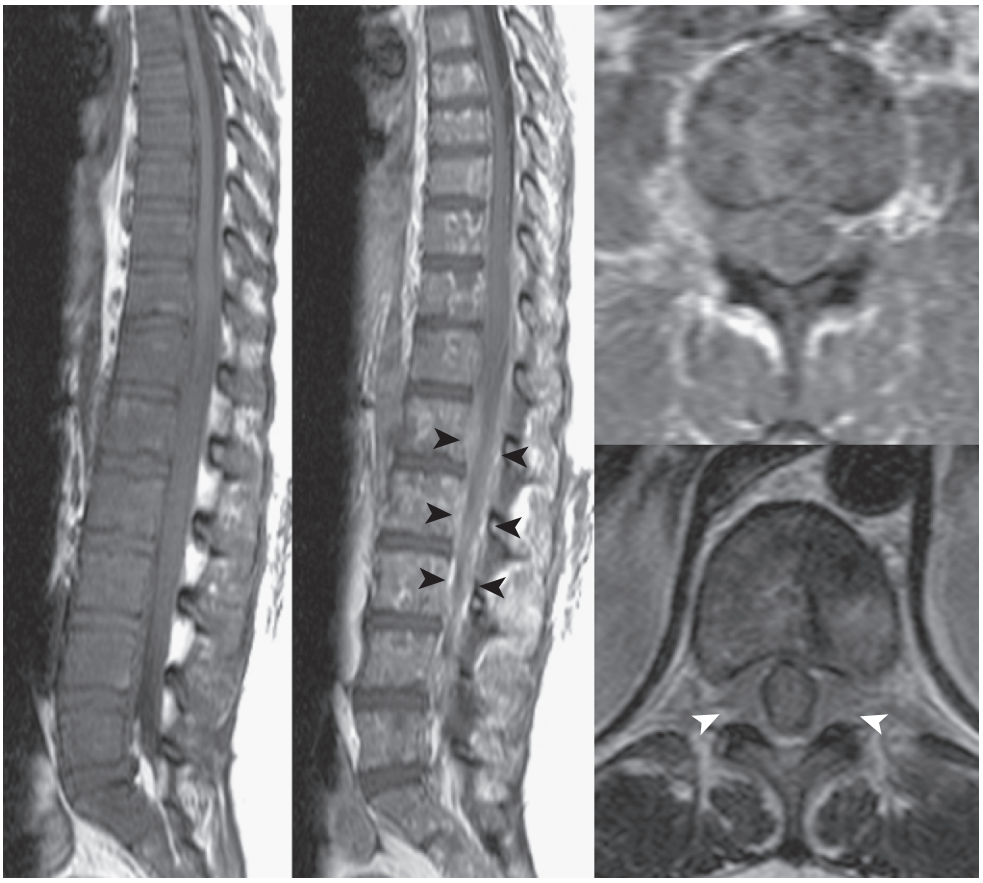


FIGURE 7-25 Epidural lymphoma—conus compression. Sagittal pre- and postgadolinium T1-weighted images *(left)* show an enhancing extradural mass *(black arrowheads)* that surrounds the conus medullaris in a patient with acquired immunodeficiency syndrome. An axial postgadolinium T1-weighted image *(upper right)* and T2-weighted image *(lower right)* show tumor filling the neural foramina *(white arrowheads)* and causing mild compression of the conus.

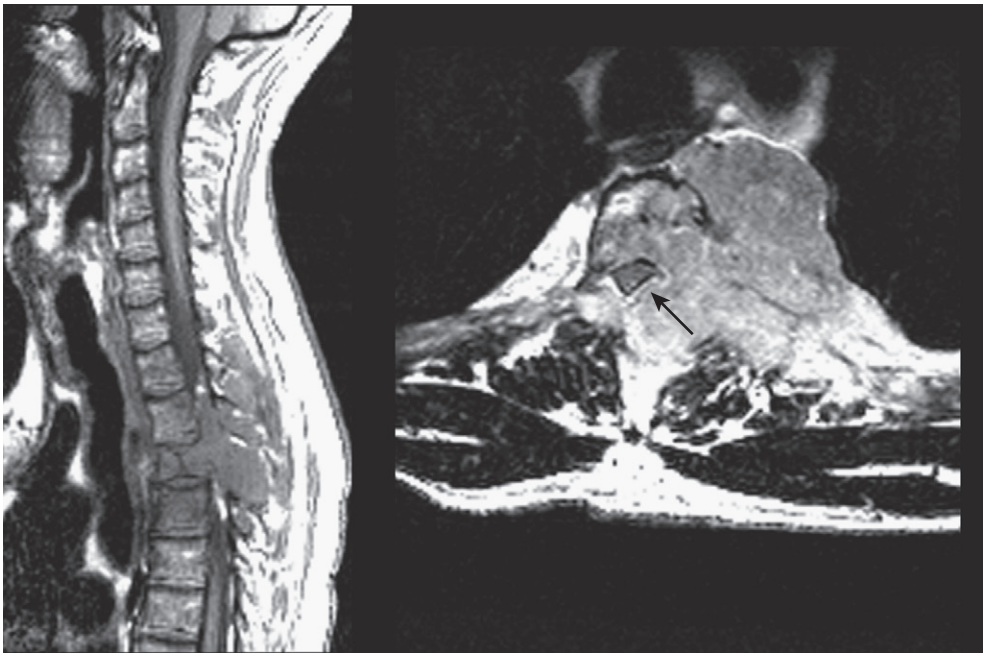


FIGURE 7-26 Multiple myeloma—cord compression. Sagittal pre- and axial postgadolinium T1-weighted images show a large mass arising within an upper thoracic vertebra with extraosseous extension that results in cord compression. Note the diamond shape of the cord *(arrow)*.



FIGURE 7-27 Ependymoma. A sagittal T2-weighted image and postgadolinium T1-weighted image show a multiseptate fluid collection that expands the thoracic cord with a solid enhancing nodule *(arrow)*. This 45-year-old woman presented with progressive difficulty with ambulation.



FIGURE 7-28 Multiple sclerosis. Sagittal and axial T2-weighted images show patchy hyperintensities throughout the entire spinal cord. None of the spine lesions showed abnormal enhancement. The postgadolinium axial T1-weighted image of the brain in the same patient shows an enhancing plaque in the periventricular white matter *(arrows)*.

and have associated cystic changes or syrinx formation (Fig. 7-27). Ependymomas have a predilection for the conus medullaris and a tendency to bleed. Slow-growing primary lesions may cause expansion of the spinal canal, scalloping of the posterior margins of the vertebral bodies, and pressure atrophy of pedicles. Other intramedullary tumors include hemangioblastoma, medulloblastoma, and metastatic disease from pineal or other intracranial sites.

Inflammation/Demyelination

Multiple sclerosis may be the first disorder that comes to mind in the category of inflammation/demyelination. The cause of this disorder, characterized by breakdown of the myelin sheath and inflammation, is unknown. Spinal cord plaques tend to occur most frequently in the cervical region and show imaging features similar to those found in the brain—T1 isointense to hypointense, T2 hyperintense—and may enhance after administration of contrast material (Fig. 7-28). The cord may be swollen as a result of active inflammation. Lesions in different states of activity and the presence of lesions in the brain add to confidence in the diagnosis of multiple sclerosis. Cord atrophy and lack of enhancement may be expected in the chronic phase.

Imaging features of myelitis are nonspecific and include T2 hyperintensity, swelling, and variable enhancement. Idiopathic inflammation of the cord (transverse myelitis) or inflammation as a result of connective tissue disorders (e.g., lupus and rheumatoid arthritis) may have the same appearance. Postinfectious demyelination is sometimes the cause. Follow-up may be necessary to differentiate these disorders from a spinal cord neoplasm.

Sarcoidosis is a noncaseating, granulomatous disease that may affect the brain and spinal cord. Simultaneous involvement of the cord and meninges may help to distinguish it from other causes of myelitis. Of course, other granulomatous processes such as tuberculosis would have to be considered.

Guillain-Barré syndrome, which is an acute inflammatory demyelinating neuropathy, as well as a chronic form (chronic inflammatory demyelinating polyneuropathy), may present with ascending progressive muscle weakness, areflexia, and other symptoms including cranial neuropathy. Enhancement of lumbosacral roots, especially isolated involvement of ventral roots, may be detected by MRI.

Infection

Abscess formation within the spinal cord (intramedullary) is extremely uncommon and usually occurs as a result of spread from another location. Intravenous drug use and human immunodeficiency virus infection are risk factors.

On the other hand, meningitis is extremely common. Of the infectious cases, viral infection is most common, with bacterial, fungal, and parasitic infections making up the remainder. Noninfectious causes include nonsteroidal antiinflammatory medications and antibiotics. Neoplastic causes are mentioned in the following text. Imaging is generally reserved for complex cases, such as those with



FIGURE 7-29 An epidural abscess. A sagittal postgadolinium T1-weighted image *(left)* shows abnormal enhancing soft tissue *(arrow)* in the epidural space. The axial postgadolinium T1-weighted image *(right)* more clearly shows a nonenhancing fluid collection *(arrow)* in this patient with recent intravenous drug use and sciatica.

localizing neurologic deficits or those that do not respond to therapy, in order to locate a parameningeal focus of infection. Thickened enhancement of meninges and nerve roots may be seen.

An epidural (bacterial) abscess may arise via a hematogenous route or from direct extension of diskitis/osteomyelitis or another paraspinal source (Fig. 7-29). *Staphylococcus aureus* is the most common organism, and risk factors include spinal instrumentation, intravenous drug use, immunodeficiency, diabetes, renal failure, alcoholism, and malignancy. Because of the loose connection of the dura to the spine, infection may spread to multiple contiguous levels. Lumbar and cervical regions are most commonly affected. On MRI, this appears as a rim-enhancing, tapered fluid collection that displaces the dura. The collection may be located anteriorly, posteriorly, or circumferentially around the thecal sac and may cause compression of the spinal cord or cauda equina. The term "phlegmon" may be applied to an enhancing inflammatory mass without a central fluid collection. Definitive treatment is surgical, although mild cases without a focal neurologic deficit may be treated with antibiotics and careful monitoring. Determination of the cranial and caudal extent of the infection is imperative prior to any planned intervention.

Pyogenic diskitis/osteomyelitis may be suspected based on abnormal T2 hyperintensity and contrast enhancement of the disk and adjacent portions of the vertebral bodies. Because degenerative changes, such as a Schmorl node, may produce identical imaging findings, clinical context is important. Sometimes, percutaneous CT-guided needle aspiration is required to confirm the diagnosis.

Tuberculous spondylitis has a preference for spreading along the anterior longitudinal ligament, affecting multiple vertebral bodies with relative sparing of the intervertebral disks. Posterior vertebral body and posterior element involvement are more common than with pyogenic infections. These features are in concert with an indolent course and may make this process indistinguishable from malignancy. Needle aspiration/biopsy is often required for definitive diagnosis because the treatment is not trivial. Other nonbacterial infections such as cysticercosis and schistosomiasis may develop in patients from endemic regions; the features are nonspecific and can be quite complex, eventually resulting in arachnoiditis, myelomalacia, and syrinx formation.

Vascular

Infarction of the spinal cord is rare and may be due to a large variety of causes such as atherosclerotic disease of the aorta, hypotension, dissection of the aorta or vertebral arteries, and compromise of spinal arteries resulting from emboli, sickle cell disease, or vasculitis. Imaging findings may be subtle, including T2 hyperintensity and enlargement of the cord. Several reports have been made of the value of diffusion-weighted imaging, but technical issues have limited widespread application in this setting. Venous obstruction/infarct as a result of cord compression is one possible mechanism of SCI. Infarcts can affect any portion of the cord, with extensive infarcts occurring as a result of occlusion of the artery of Adamkiewicz (most commonly arising from the aorta between T8 – L1 levels).

Spinal dural arteriovenous fistula is a rare vascular disorder that may lead to the development of venous congestion of the cord and present with slowly progressive myelopathy affecting the lower extremities in older adults. T2 hyperintensity, possible enlargement of the cord, and dilated subarachnoid vessels are the clues to diagnosis. MR angiography or CT angiography may be helpful, with conventional angiography as the gold standard for confirmation and possible endovascular treatment.

Cavernous malformation (cavernous angioma) less commonly occurs in the spinal cord than in the brain but has the same imaging characteristics. A mulberry shape, internal mixed T1- and T2-weighted hyperintensity as a result of blood products of different ages, along with a complete hemosiderin rim, are classic. Minimal (if any) mass effect, lack of surrounding edema, and variable enhancement are typical and help with the diagnosis. However, acute hemorrhage may cause expansion of the cord and associated edema, sometimes raising concern for neoplasm.

This concludes the brief review of radiologic findings of traumatic and nontraumatic emergencies involving the spine. Hopefully it has covered more than just the tip of the iceberg and has provided a useful framework for your future practice.

SUGGESTED READINGS

Blackmore CC, Emerson SS, Mann FA, et al. Cervical spine imaging in patients with trauma: determination of fracture risk to optimize use. *Radiology*. 1999;211:759–765.

Blake SP, Connors AM. Sacral insufficiency fracture. *Br J Radiol*. 2004;77:891–896.

Boldin C, Raith J, Fankhauser F, et al. Predicting neurologic recovery in cervical spinal cord injury with postoperative MR imaging. *Spine (Phila Pa 1976)*. 2006;31(5):554–559.

Bono CM, Vaccaro AR, Fehlings M, et al. Measurement techniques for lower cervical spine injuries: consensus statement of the Spine Trauma Study Group. *Spine (Phila Pa 1976)*. 2006;31(5):603–609.

Capone C, Burjonrappa S. Congenital spine deformities: a new screening indication for blunt cerebrovascular injuries after cervical trauma? *J Pediatr Surg*. 2010;45(12):2444–2446.

Chang W, Alexander MT, Mirvis SE. Diagnostic determinants of craniocervical distraction injury in adults. *AJR Am J Roentgenol*. 2009;192(1):52–58.

Chen Y, Zhuang Z, Qi W, et al. A three-dimensional study of the atlantodental interval in a normal Chinese population using reformatted computed tomography. *Surg Radiol Anat*. 2011;33(9):801–806.

Como JJ, Diaz JJ, Dunham CM, et al. Practice management guidelines for identification of cervical spine injuries following trauma: update from the Eastern Association for the Surgery of Trauma practice management guidelines committee. *J Trauma*. 2009;67(3):651–659.

Como JJ, Samia H, Nemunaitis GA, et al. The misapplication of the term spinal cord injury without radiographic abnormality (SCIWORA) in adults. *J Trauma Acute Care Surg*. 2012;73(5):1261–1266.

Darouiche RO. Spinal epidural abscess. *N Engl J Med*. 2006;355:2012–2020.

Deliganis AV, Baxter AB, Hanson JA, et al. Radiologic spectrum of craniocervical distraction injuries. *Radiographics*. 2000;20(spec No.):S237—S250. Erratum in *Radiographics*. 2001;21(2):520.

Denis F. Spinal instability as defined by the three-column spine concept in acute spinal trauma. *Clin Orthop*. 1984;189:65–76.

Diaz Jr JJ, Cullinane DC, Altman DT, et al. Practice management guidelines for the screening of thoracolumbar spine fracture. *J Trauma*. 2007;63(3):709–718.

Dreizin D, Letzing M, Sliker CW, et al. Multidetector CT of blunt cervical spine trauma in adults. *Radiographics*. 2014;34(7):1842–1865.

Duane TM, Dechert T, Wolfe LG, et al. Clinical examination and its reliability in identifying cervical spine fractures. *J Trauma*. 2007;62(6):1405–1408.

Fehlings MG, Furlan JC, Massicotte EM, et al. Interobserver and intraobserver reliability of maximum canal compromise and spinal cord compression for evaluation of acute traumatic cervical spinal cord injury. *Spine (Phila Pa 1976)*. 2006;31(15):1719–1725.

Flanders AE, Spettell CM, Friedman DP, et al. The relationship between the functional abilities of patients with cervical spinal cord injury and the severity of damage revealed by MR imaging. *AJNR Am J Neuroradiol*. 1999;20(5):926–934.

Flanders AE, Spettell CM, Tartaglino LM, et al. Forecasting motor recovery after cervical spinal cord injury: value of MR imaging. *Radiology*. 1996;201(3):649–655.

Goradia D, Linnau KF, Cohen WA. Correlation of MR imaging findings with intraoperative findings after cervical spine trauma. *Am J Neuroradiol*. 2007;28:209–215.

Hale DF, Fitzpatrick CM, Doski JJ, et al. Absence of clinical findings reliably excludes unstable cervical spine injuries in children 5 years or younger. *J Trauma Acute Care Surg*. 2015;78(5):943–948.

Harris JH, Carson GC, Wagner LK, et al. Radiologic diagnosis of traumatic occipitovertebral dissociation: 2. Comparison of three methods of detecting occipitovertebral relationships on lateral radiographs of supine subjects. *AJR Am J Roentgenol*. 1994;162:887–892.

Harris Jr JH. The cervicocranium: its radiographic assessment. *Radiology*. 2001;218:337–351.

Harris Jr JH, Mirvis SE, eds. *The Radiology of Acute Cervical Spine Trauma*. 3rd ed. Baltimore, MD: Lippincott, Williams and Wilkins; 1996.

Hogan GJ, Mirvis SE, Shanmuganathan K, et al. Exclusion of unstable cervical spine injury in obtunded patients with blunt trauma: is MR imaging needed when multidetector row CT findings are normal? *Radiology*. 2005;237:106–113.

Jain NB, Ayers GD, Peterson EN, et al. Traumatic spinal cord injury in the United States, 1993-2012. *JAMA*. 2015;313(22):2236–2243.

Katzberg RW, Benedetti PF, Drake CM, et al. Acute cervical spine injuries: prospective MR imaging assessment at a level 1 trauma center. *Radiology*. 1999;213:203–212.

Khurana B, Sheehan SE, Sodickson A, et al. Traumatic thoracolumbar spine injuries: what the spine surgeon wants to know. *Radiographics*. 2013;7:2031–2046.

Koeller KK, Rosenblum RS, Morrison AL. Neoplasms of the spinal cord and filum terminale: radiologic-pathologic correlation. *Radiographics*. 2000;20:1721–1749.

Kwon BK, Hilibrand AS. Management of cervical fractures in patients with diffuse idiopathic skeletal hyperostosis. *Curr Opin Orthop*. 2003;14:187–192.

Labler L, Eid K, Platz A, et al. Atlanto-occipital dislocation: four case reports of survival in adults and review of the literature. *Eur Spine J*. 2004;13:172–180.

Lad SP, Patil CG, Lad EM, et al. Trends in pathological vertebral fractures in the United States: 1993 to 2004. *J Neurosurg Spine*. 2007;7(3):305–310.

Leone A, Cerase A, Colosimo C, et al. Occipital condylar fractures: a review. *Radiology*. 2000;216:635–644.

Liu K, Xie F, Wang D, et al. Reference ranges for atlantodental interval in adults and its variation with age and gender in a large series of subjects on multidetector computed tomography. *Acta Radiol*. 2015;56(4):465–470.

Lustrin ES, Karakas SP, Ortiz AO, et al. Pediatric cervical spine: normal anatomy, variants, and trauma. *Radiographics*. 2003;23:539–560.

Munday TL, Johnson MH, Hayes CW, et al. Musculoskeletal causes of spinal axis compromise: beyond the usual suspects. *Radiographics*. 1994;14:1225–1245.

Munera F, Rivas LA, Nunez Jr DB, et al. Imaging evaluation of adult spinal injuries: emphasis on multidetector CT in cervical spine trauma. *Radiology*. 2012;263(3):645–660.

National Spinal Cord Injury Statistical Center. *Spinal cord injury facts and figures at a glance*; 2015. https://www.nscisc.uab.edu/Public/Facts%202015%20Aug.pdf.

National Trauma Data Bank. National Trauma Data Bank 2014 Annual Report. https://www.facs.org/~/media/files/quality%20programs/trauma/ntdb/ntdb%20annual%20report%202014.ashx.

Patel MB, Humble SS, Cullinane DC, et al. Cervical spine collar clearance in the obtunded adult blunt trauma patient: a systematic review and practice management guideline from the Eastern Association for the Surgery of Trauma. *J Trauma Acute Care Surg*. 2015;78(2):430–441.

Platzer P, Jaindl M, Thalhammer G, et al. Clearing the cervical spine in critically injured patients: a comprehensive C-spine protocol to avoid unnecessary delays in diagnosis. *Eur Spine J*. 2006;15:1801–1810.

Pollack Jr CV, Hendey GW, Martin DR, et al. Use of flexion-extension radiographs of the cervical spine in blunt trauma. *Ann Emerg Med*. 2001;38:8–11.

Radcliff KE, Ben-Galim P, Dreiangel N, et al. Comprehensive computed tomography assessment of the upper cervical anatomy: what is normal? *Spine J*. 2010;10(3):219–229.

Rojas CA, Bertozzi JC, Martinez CR, et al. Reassessment of the craniocervical junction: normal values on CT. *AJNR Am J Neuroradiol*. 2007;28(9):1819–1823.

Rojas CA, Hayes A, Bertozzi JC, et al. Evaluation of the C1-C2 articulation on MDCT in healthy children and young adults. *AJR Am J Roentgenol*. 2009;193(5):1388–1392.

Rojas CA, Vermess D, Bertozzi JC, et al. Normal thickness and appearance of the prevertebral soft tissues on multidetector CT. *AJNR Am J Neuroradiol*. 2009;30(1):136–141.

Samuel S, Lin JL, Smith MM, et al. Subaxial injury classification scoring system treatment recommendations: external agreement study based on retrospective review of 185 patients. *Spine (Phila Pa 1976)*. 2015;40(3):137–142.

Schuster R, Waxman K, Sanchez B, et al. Magnetic resonance imaging is not needed to clear cervical spines in blunt trauma patients with normal computed tomographic results and no motor deficits. *Arch Surg*. 2005;140:762–766.

Schwartz ED, Flanders AE, eds. *Spinal Trauma*. Philadelphia, PA: Lippincott Williams and Wilkins; 2007.

Sixta S, Moore FO, Ditillo MF, et al. Screening for thoracolumbar spinal injuries in blunt trauma: an Eastern Association for the Surgery of Trauma practice management guideline. *J Trauma Acute Care Surg*. 2012;73(5 suppl 4):S326–S332.

Sklar EM, Post JM, Falcone S. MRI of acute spinal epidural hematomas. *J Comput Assist Tomogr*. 1999;23:238–243.

Swischuk L. *Imaging of the Cervical Spine in Children*. 2nd ed. New York, NY: Springer Science+Business Media; 2013.

Tahvonen P, Oikarinen H, Pääkkö E, et al. Justification of CT examinations in young adults and children can be improved by education, guideline implementation and increased MRI capacity. *Br J Radiol*. 2013;86(1029). 20130337.

Talbott JF, Whetstone WD, Readdy WJ, et al. The Brain and Spinal Injury Center score: a novel, simple, and reproducible method for assessing the severity of acute cervical spinal cord injury with axial T2-weighted MRI findings [published online ahead of print July 10, 2015]. *J Neurosurg Spine*.

Tat ST, Mejia MJ, Freishtat RJ. Imaging, clearance, and controversies in pediatric cervical spine trauma. *Pediatr Emerg Care*. 2014;30(12):911–915.

Tomycz ND, Chew BG, Chang YF, et al. MRI is unnecessary to clear the cervical spine in obtunded/comatose trauma patients: the four-year experience of a level I trauma center. *J Trauma*. 2008;64(5):1258–1263.

Vaccaro AR, Hulbert RJ, Patel AA, et al. The subaxial cervical spine injury classification system: a novel approach to recognize the importance of morphology, neurology, and integrity of the disco-ligamentous complex. *Spine (Phila Pa 1976)*. 2007;32(21):2365–2374.

Vaccaro AR, Lehman Jr RA, Hurlbert RJ, et al. A new classification of thoracolumbar injuries: the importance of injury morphology, the integrity of the posterior ligamentous complex, and neurologic status. *Spine (Phila Pa 1976)*. 2005;30(20):2325–2333.

Vilela MD, Kim LJ, Bellabarba C, et al. Blunt cerebrovascular injuries in association with craniocervical distraction injuries: a retrospective review of consecutive cases. *Spine J*. 2015;15(3):499–505.

Wang YF, Teng MM, Chang CY, et al. Imaging manifestations of spinal fractures in ankylosing spondylitis. *Am J Neuroradiol*. 2005;26:2067–2076.

World Health Organization. Spinal cord injury. www.who.int/mediacentre/factsheets/fs384/en/#2013.

Chapter 8

Nontraumatic Emergency Radiology of the Thorax

Alejandra Duran-Mendicuti, Scott White, Salvatore G. Viscomi, Michael Stella, and Aaron D. Sodickson

An emergency medicine physician once told a bright-eyed medical student on the first clinical shift, "All kinds of problems bring people in to see us with chest complaints. But just remember this—your job is to make sure nobody leaves the emergency department with any of only four entities undiagnosed, and those four entities are pneumothorax, aortic dissection, pulmonary embolism, and myocardial infarction. Now repeat that list to me four times. [The medical student regurgitates the list four times.] Good. Beyond these four entities, anything that's causing their problem won't cause you much of a problem."

Although that synopsis of nontraumatic thoracic disease encountered in the emergency department (ED) is rather spartan, the underlying tenet stands up well in the practical evaluation of ED patients presenting with chest pain and other symptoms. Accordingly, this chapter on nontraumatic emergency thoracic radiology is organized primarily around evaluation of these entities, beginning with a review of chest radiography technique and followed by sections on the pleura/mediastinum, aortic diseases, pulmonary embolism (PE), and acute coronary syndrome (ACS). Lung parenchymal findings are covered with less emphasis, but they are readily available with greater detail in other texts, such as *Thoracic Radiology: The Requisites.*

Multidetector computed tomography (MDCT) technique deserves and receives special emphasis in this chapter because it has overtaken and continues to overtake other imaging modalities for chest evaluation in ED patients. The ready availability of CT and its high sensitivity and specificity, matched with a rapid scan performance, have made it the test of choice for a broad range of thoracic diagnoses. Aside from issues of health care costs, perhaps the only significant counterbalance to increased utilization is the concern for population radiation exposure and the associated risk of cancers induced by ionizing radiation. Radiologists should be familiar with and sensitive to these concerns and be readily able to advise clinicians and protect patients by being good stewards of radiation safety.

CHEST RADIOGRAPHY

Chest pain is one of the most common patient presentations in the ED. Despite widespread availability of "high-tech" CT scanners, it remains vital to develop the knowledge and skills needed for expert chest radiograph interpretation, because the chest radiograph remains the mainstay of first-line imaging for many ED patients with chest-related symptoms. The emergency radiologist needs to have highly developed interpretive skills for chest radiography. Detailed instruction on chest radiograph interpretation is beyond the scope of this chapter, but many excellent sources are available, including the Requisites text on thoracic radiology.

One principle that serves radiologists well is the establishment of a systematic pattern through which the interpreter progresses as he or she reads a chest radiograph. Although one is naturally drawn to look at the lungs—and although evaluation of pulmonary parenchyma is paramount—the interpreter must unerringly include assessment of extrapulmonary anatomy on every chest radiograph. The evaluation should include anatomy below the diaphragm, lung parenchyma posterior to the diaphragm, the bony thorax, spine, shoulders, and chest wall soft tissues, the heart contours, mediastinum, and pulmonary hila, pleural surfaces and interfaces, and complex areas such as the pulmonary apices. Establishing a pattern of evaluation that systematically includes all of the anatomy encountered on a chest radiograph will help prevent unfortunate errors of chest radiograph interpretation (Fig. 8-1).

Pulmonary disease is detected primarily by changes in pulmonary parenchymal density, with either a decrease (e.g., cystic lung diseases and pneumothorax) or an increase (e.g., masses, fluid, infection, fibrosis, or atelectasis) in density.

Pneumonia

On a chest radiograph, pneumonia manifests as areas of increased density within the pulmonary parenchyma as a result of alveolar consolidation. The increased density can be focal, multifocal, or diffuse. Depending on the causative organism and the immune status of the patient, the density may appear as confluent parenchymal consolidation (with vessels obscured within the density), hazy ground glass density (with vessel margins able to be detected within the density), or coarse reticular or reticulonodular opacities. Air bronchograms may be present when the alveolar opacities accentuate the airways. These densities may be marginated by pleural or fissural boundaries. The use of both frontal and lateral projections is helpful in detecting, confirming, and localizing the areas of pneumonia (Figs. 8-2 and 8-3).

Heart Failure

Progression or exacerbation of congestive heart failure can cause dyspnea as a result of pulmonary vascular

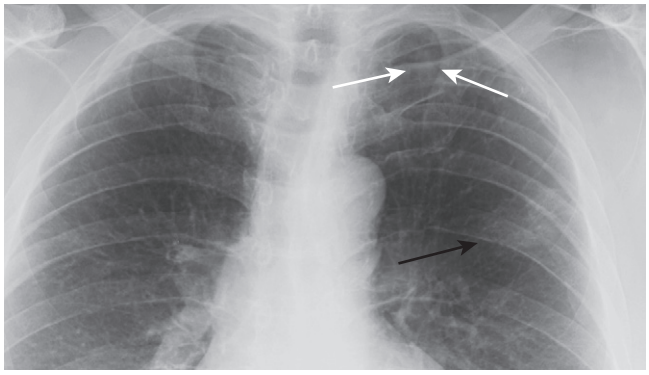


FIGURE 8-1 Chest radiograph of a patient presenting with cough and fever. A faint area of opacification within the left midlung proved to be pneumonia *(black arrow)*. Additionally, a small left apical carcinoma was detected *(white arrows)*. Because of multiple overlying structures, including the first ribs and the clavicles, the pulmonary apices are a "danger" area in terms of risk of missed findings on chest radiographs. Close inspection of the apices is warranted on every chest radiograph.

congestion or its more advanced form, pulmonary edema. Pulmonary edema can be classified as hydrostatic origin (with increased intravascular pressure, as in left ventricular failure or volume overload) due to altered permeability (with increased permeability of the pulmonary alveolar-capillary membrane, as in acute respiratory distress syndrome [ARDS]). Although some overlap in the pathophysiology likely exists, the cause of pulmonary edema cannot routinely be distinguished by chest radiographs.

The sequence by which congestive heart failure leads to pulmonary edema and may manifest on a chest radiograph is familiar. Left ventricular failure results in increased pressure within the pulmonary venous system, leading to pulmonary venous distention. The increased size of pulmonary veins on a chest radiograph, particularly in the upper lobes, manifests as "cephalization," which can be relatively subjective at imaging. As pulmonary venous capacitance is exceeded, pulmonary vessels begin to leak transudative

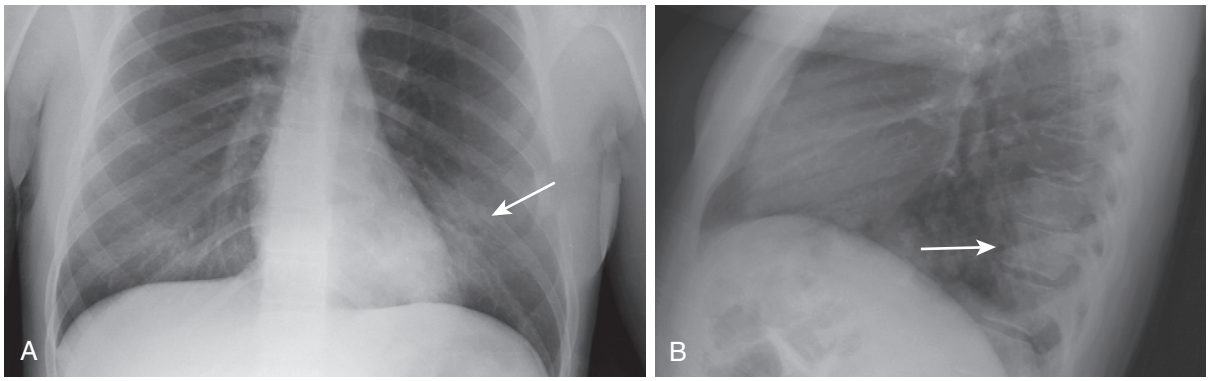


FIGURE 8-2 Chest radiograph of a patient with pneumonia. **A,** A posteroanterior view reveals a patchy opacity overlying the left lung base *(arrow)*. Note that the left cardiac border is preserved, indicating that the pneumonia is more likely in the left lower lobe. If it were lingular and abutting the left cardiac border, the left cardiac border would be obscured (the "silhouette" sign). **B,** The lateral view confirms the left lower lobe location of the pneumonia, as indicated by increased density of the lower thoracic vertebral bodies *(arrow)*. Normally, on a lateral chest radiograph, the thoracic vertebral bodies become increasingly lucent from superior to inferior. Increased density of lower thoracic vertebral bodies indicates the presence of radiodense material (in this case, a left lower lobe pneumonia) attenuating the x-ray beam.

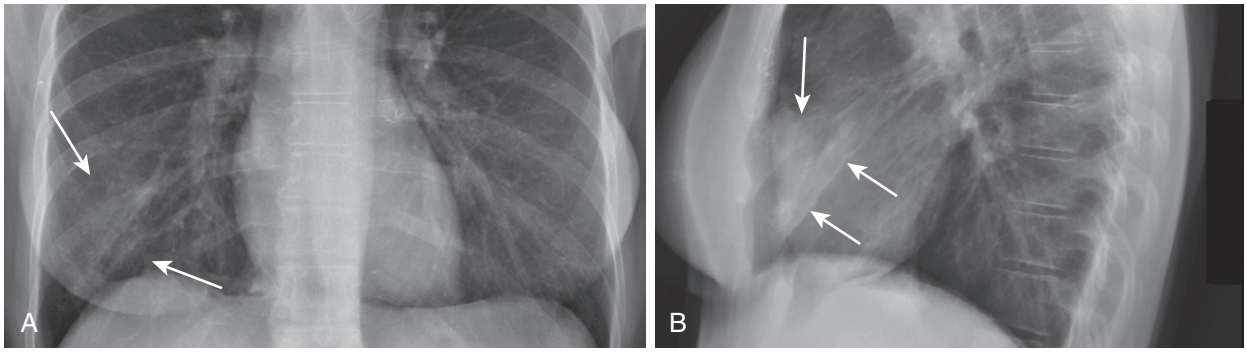


FIGURE 8-3 A chest radiograph of another patient with pneumonia. **A,** A posteroanterior view reveals a faint opacity overlying the right lung base *(arrows)*. The density does not abut the right heart or diaphragm, and thus the "silhouette" sign is of no help in determining whether the pneumonia is located in the middle versus lower lobe. **B,** The lateral view reveals increased density overlying the heart *(longer arrow)*, confined by the major fissure *(shorter arrows)*, indicating that the pneumonia is located in the right middle lobe. Note that the vertebral bodies become more lucent from superior to inferior, indicating the absence of lower lobe processes overlying the vertebrae.

fluid into the pulmonary interstitium, including the septal, peribronchial, and perivascular spaces, and into the pleural space. The chest radiograph correlates include septal lines (or "Kerley B" lines), peribronchial cuffing, indistinctness of vessel margins, and pleural effusions, respectively. With further progression, fluid begins to accumulate in the alveolar spaces, resulting in more confluent density that obscures vessel margins (Fig. 8-4).

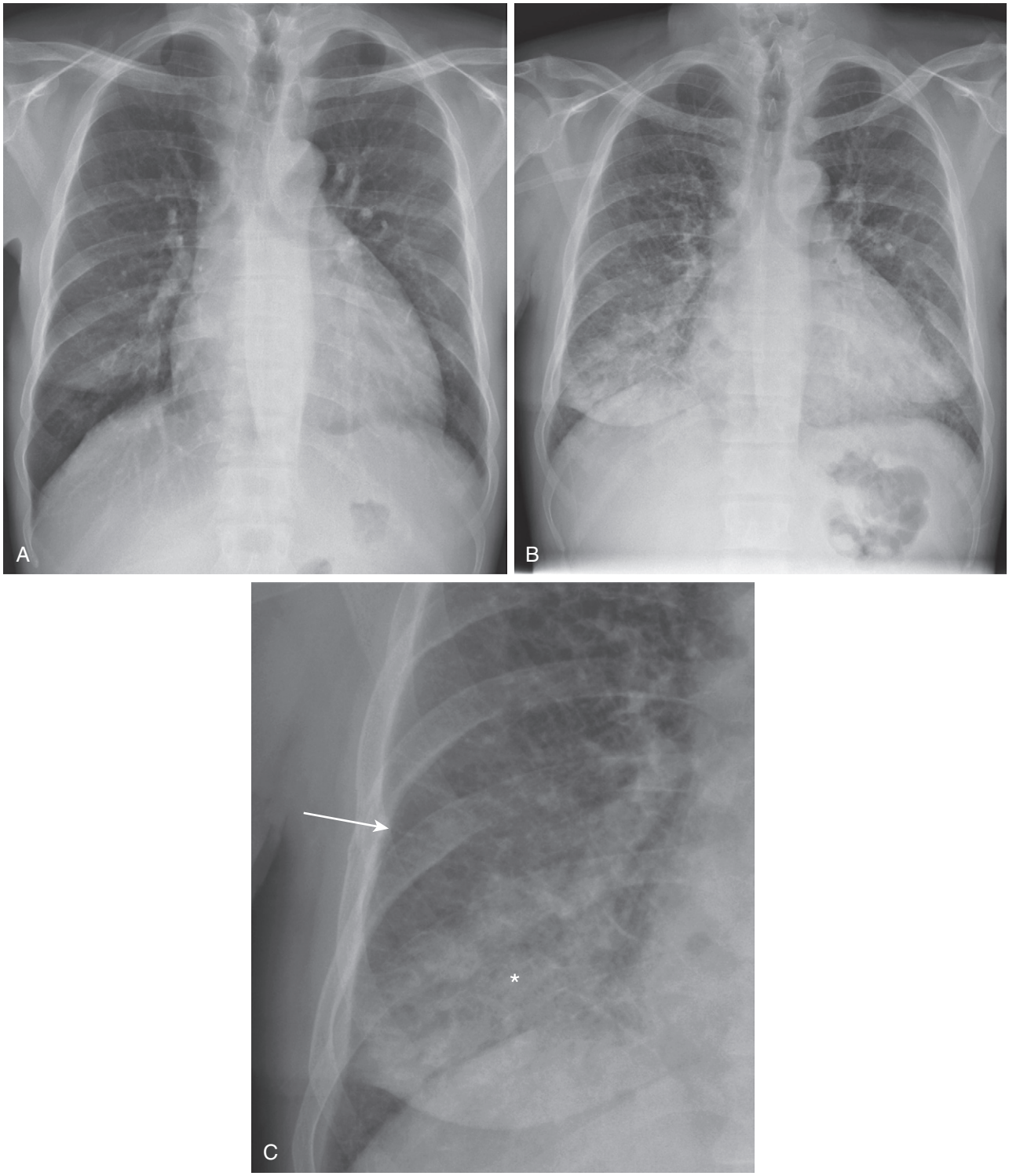


FIGURE 8-4 A patient with cardiomegaly and recurrent episodes of congestive heart failure. **A,** A posteroanterior view obtained when the patient was otherwise healthy reveals grossly clear lungs and mild cardiomegaly. There is a normal paucity of lung markings at the periphery of the lungs near the pleural margins. **B,** A posteroanterior view obtained when the patient was in congestive heart failure with pulmonary edema reveals diffusely increased lung markings and faint opacification at the bases. **C,** A magnified view of the right lung base reveals prominent septal markings in the subpleural lung periphery, or "Kerley B" lines *(arrow)*, as well as more consolidated density overlying the right lung base *(asterisk)*.

COMPUTED TOMOGRAPHY

Computed Tomography of the Pulmonary Parenchyma

CT allows for more refined analysis of the pulmonary parenchyma. In a similar manner to a chest radiograph, pulmonary parenchymal disease is detected by changes in parenchymal density and architecture. Axial images with section thicknesses of 2 mm or less permit evaluation of pulmonary parenchymal architecture at the level of the secondary pulmonary lobule, the smallest unit of lung structure marginated by connective tissue septa. The secondary pulmonary lobule consists of small and terminal bronchioles (accompanied by terminal arterioles) along with their associated acini (usually 12 or fewer in number). This complex of terminal bronchovascular structures and their associated acini is confined by interlobular septae. The interlobular septae contain pulmonary veins and pulmonary lymphatics, with the latter also found along the bronchovascular complex. Changes to the architecture of the secondary pulmonary lobule occur in a multitude of disease processes, and characterization of the architectural changes allows for refinement of differential diagnostic considerations. Of course, larger-order anatomic features are clearly defined by CT as well.

Changes to the architecture and density of the secondary pulmonary lobule can be organized according to the structures involved, including peripherally located septal structures, centrally located bronchovascular structures, and more generalized abnormalities affecting both. A detailed instruction on CT of pulmonary parenchyma is beyond the scope of this chapter, but several excellent resources are available on this subject, including the Requisites text on thoracic radiology. However, a general overview of the differential considerations associated with the previously described architectural derangements is useful, and a brief synopsis is provided in the following text.

Septal thickening may be smooth, nodular, or irregular. Differential considerations for smooth septal thickening include pulmonary edema (with septal thickening being the equivalent of "Kerley B" lines seen on a chest radiograph), ARDS, pneumonia, or pulmonary hemorrhage(Fig. 8-5). Septal thickening seen with these entities may be associated with "ground glass" density, the so-called "crazy paving" pattern, which also has been described as characteristic of alveolar proteinosis. Nodular septal thickening may be seen in lymphangitic metastases, as well as in sarcoidosis and silicosis. Nodules seen in sarcoidosis are characterized as perilymphatic and thus may be centrilobular or septal (lymphatics are associated with both the septae and bronchovascular structures). Pulmonary fibrosis can cause irregular septal thickening and may be associated with other common findings of fibrosis, such as traction bronchiectasis and honeycombing.

Centrilobular opacities or nodules generally imply abnormalities of the small airways or vascular diseases and are usually related to bronchiolitis of varying causes. The combination of centrilobular opacities/nodules with dilated/opacified bronchioles has been termed the "tree-in-bud" sign (Fig. 8-6). In the ED, centrilobular opacities/nodules may indicate an infectious bronchiolitis. Pulmonary aspiration can give a similar appearance. Other differential considerations for centrilobular opacities/nodules include pulmonary edema and hemorrhage, vasculitis, bronchoalveolar cell carcinoma, acute or subacute hypersensitivity pneumonitis, noninfectious bronchiolitis (as can be seen in smoking-related interstitial lung disease/respiratory bronchiolitis), and panbronchiolitis.

More generalized (panlobular) processes may lead to either ground glass or more consolidated opacities. If ground glass opacities are detected, the differential diagnosis is assisted by identification of ancillary findings. Ground glass opacities in the presence of honeycombing

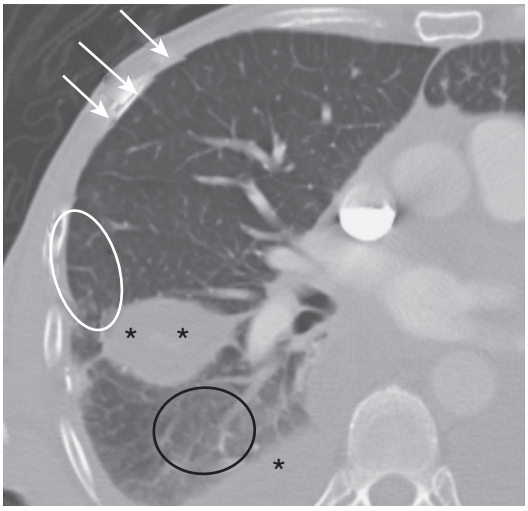


FIGURE 8-5 A patient with congestive heart failure and pulmonary edema. Thickened interlobular septae *(arrows)* define the borders of the intervening secondary pulmonary lobules. Additional findings that may be seen in congestive heart failure/pulmonary edema are shown, including centrilobular opacities *(white oval)*, ground glass opacity *(black oval)*, and pleural fluid seen posteriorly *(single asterisk)* and within the major fissure *(double asterisks)*.

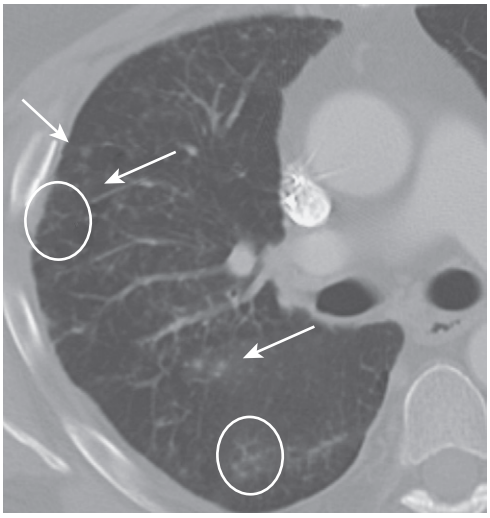


FIGURE 8-6 Examples of centrilobular opacities *(arrows)* and the "tree-in-bud" sign *(ovals)* in a patient with a history of nonspecific interstitial lung disease who presented with an acute cough. A subsequent computed tomography scan (images not provided) showed resolution of the centrilobular opacities, which were therefore presumed infectious (bronchiolitis or bronchopneumonia) in etiology.

or other findings of fibrosis should point toward differential considerations among fibrotic lung diseases. Ground glass opacities in the presence of septal thickening (the "crazy paving" pattern) should raise differential considerations including pulmonary edema, pneumonias of varying causes, and pulmonary hemorrhage, as well as entities less commonly encountered in the ED, including hypersensitivity pneumonitis, ARDS, and alveolar proteinosis. If ground glass opacities are encountered in the absence of ancillary findings, the differential considerations become even broader and include pneumonia and drug reaction, in addition to the entities previously listed (Fig. 8-7). Differential considerations for more consolidated densities include entities such as pneumonia, pulmonary edema, ARDS, and pulmonary hemorrhage, as well as acute eosinophilic pneumonia, masses, and fibrotic processes. Familiarity with the concept of evaluating pulmonary parenchyma based on analysis of the structures of the secondary pulmonary lobule will serve emergency radiologists well in their approach to formulating differential diagnoses for parenchymal disease.

Chest Computed Tomography Techniques and Protocols

This section outlines general principles guiding the selection of CT techniques and scan parameters. Although wide variability can exist between scanner types and manufacturers with regard to technological capabilities, nomenclature, and technical detail, the basic underlying considerations are applicable across these platforms. A working knowledge of these considerations can aid the radiologist in optimizing CT scan performance while remaining good stewards of radiation safety.

Patient Screening

Intravenous Contrast Material. All patients must be screened for allergy to intravenous contrast material (IVCM). Although IVCM is a critical part of evaluation for pulmonary embolus and aortic dissection, it can be omitted if the clinical indication is primarily for abnormalities of the lungs. Although protocols vary by institution, all policies should include screening for a history of allergy to contrast material and risk factors for contrast-induced nephropathy.

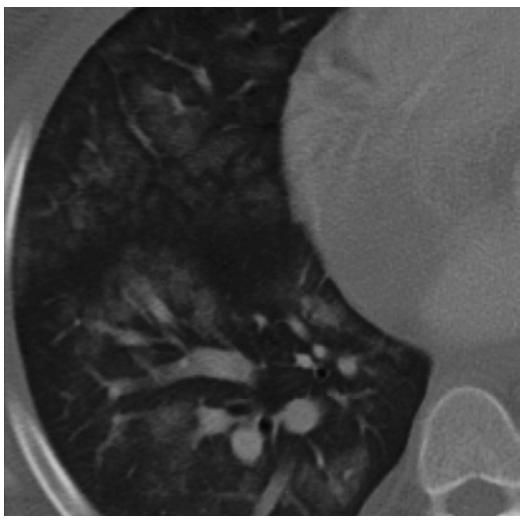


FIGURE 8-7 Example of ground glass opacities due to pulmonary edema in a postpartum patient with a history of preeclampsia, who presented with leg swelling and shortness of breath. Note that the patchy hazy density that does not obscure the underlying vascular structures.

Pregnancy. Women of child-bearing age should be screened, because concerns regarding the use of ionizing radiation during pregnancy must be weighed against medical necessity (e.g., pretest probability and urgency), examination performance characteristics (e.g., sensitivity and specificity), and alternative methods of imaging (e.g., magnetic resonance imaging [MRI] and ultrasound [US]). Alternative imaging methods with similar examination performance characteristics should be used when they are available. For properly shielded chest radiographs or CT scans of the chest collimated to avoid direct irradiation of the gravid uterus, fetal radiation exposures are extremely low, and as such, concerns about fetal radiation exposure, in general, should not affect decisions to perform medically warranted chest imaging. Although data quantifying increased risk to the maternal breast during pregnancy are lacking, theoretical concerns do prompt some practitioners to prefer nuclear scintigraphy rather than CT for evaluation of pulmonary embolus in pregnant women (the fetal doses relating to these methods have been similarly small for both modalities but have continued to decrease as CT technology advances). When CT is performed, the number of nondiagnostic scans should be minimized by taking proactive steps to optimize CT scan quality (e.g., patient coaching for breathing and motion and excellent IV line placement), thereby reducing the need for repeat scanning.

Patient Preparation

Intravenous Line Placement. Whenever possible, contrast-enhanced chest CT studies should be performed using a 20-gauge or larger peripheral IV line, preferably located in a right antecubital location. An 18- to 20-gauge size will easily allow for power-injected flow rates of 3 to 6 mL per second. Right-sided IV line placement reduces streak artifact over the anterior superior mediastinum compared with left-sided placement because of elimination of dense IV contrast material passing through the left brachiocephalic vein. Antecubital placement results in more reproducible contrast material inflow characteristics and a reduced rate of infiltration compared with more peripheral placement.

Heart Rate Control. Cardiac gated protocols (coronary CT angiography [CTA] for gated aortic dissection) generally require a regular cardiac rhythm. With current single-source 64-MDCT techniques, coronary CTA is best performed with heart rate controlled to 65 beats or less per minute. However, further advances such as quicker gantry rotation, greater numbers of detector rows, and/or dual x-ray source scanners are likely to lessen or obviate the current requirement for lower or regular heart rates.

Scan Protocol Considerations

Contrast Material Timing Principles and Techniques. Care must be taken to optimize the timing of the CT scan relative to the injection rate, injection profile, and

duration of IVCM administration. The specific timing details vary greatly depending on the duration of the scan (which depends on the CT technology in use) and on the flow rate and quantity of injected contrast material. As a general rule of thumb, IVCM should be injected at a minimum rate of 4 mL per second for CT evaluation of pulmonary embolus, aortic dissection, or traumatic aortic injury. Higher flow rates shorten the duration of the contrast bolus. As a result, scan timing must be scrutinized to ensure that contrast material opacification remains adequate throughout all portions of the scan.

Three techniques are commonly used to determine the initial scan delay after the start of the IVCM injection:

- Fixed or empiric delay. The time delay is selected based on scanner speed, experienced best estimates of the time required to reach the vascular bed of interest, and, if applicable, patient factors such as cardiac output and IV line location.
- Automated contrast bolus detection, or bolus tracking. A monitoring scan is repeated at a fixed scan position, and the acquisition scan is triggered when the contrast density exceeds a preset threshold in a vessel selected as the region of interest.
- Timing bolus. The transit time from the injection site to the vascular bed of interest is directly observed by repeat scanning at a fixed position after administration of 10 to 20 mL of IVCM (followed by a saline solution flush). The time to peak enhancement is determined on the basis of the timing bolus plus a recirculation delay, and the corresponding timing delay is subsequently used for IVCM during the acquisition scan.

Radiation Exposure and Techniques for Dose Reduction. Emergent (and overall) CT utilization has risen rapidly as a result of technological advances, a broad range of clinical applications, and widespread availability of CT. This phenomenon has raised concerns about associated radiation risks both to individuals and to the population as a whole and has increased scrutiny regarding CT use. Radiologists must do their part to optimize techniques that will reduce radiation exposure while maintaining high-quality imaging. Likewise, medical vendors have continued to advance their imaging technologies with tools that reduce radiation exposure. A variety of techniques exist to control patient exposure to radiation during CT. Radiologists should have a working knowledge of these techniques.

Most current CT scanners (and virtually all new scanners) include the capacity for automatic tube current modulation, also called *dose modulation*. These functions should be configured when available. Tube current modulation adjusts the overall x-ray tube current to a predetermined image quality or noise index or adjusts it based on a reference tube current time product (ref mAs) that would be warranted for a patient of the defined reference size. These techniques adjust x-ray tube output during the scan, either along the long axis of the patient (longitudinal modulation) or during the gantry rotation around the patient (angular modulation) as the patient's x-ray attenuation varies in these directions. Additionally, scanners intended for cardiac CT offer the capability for electrocardiographic (ECG) dose modulation or prospective scanning, in which x-ray tube output is greatly reduced or eliminated during systole.

Imaging of structures with a high degree of intrinsic tissue contrast material can tolerate a higher level of noise than imaging structures of near-uniform CT density. Both routine chest CT and CTA often involve inherently high-contrast structures, permitting lower dose techniques to be used. Administration of lower doses may be accomplished by reducing mAs through appropriate configuration of scanner-specific tube current modulation techniques. Reducing the x-ray tube peak kilovoltage (kVp) further provides opportunities not only to reduce radiation dose but also to increase vascular enhancement for the same contrast bolus, or alternatively, to maintain contrast enhancement with reduced contrast volume.

Manufacturers of CT equipment have recently developed iterative reconstruction techniques. Although the underlying algorithms vary by manufacturer and continue to evolve, these techniques are all designed to reduce image noise (and certain imaging artifacts) that occur after a certain CT acquisition. If a reduced dose acquisition is performed, iterative reconstruction may then be used to maintain the desired level of image quality. Because the appearance of the resultant image may vary in subtle ways from traditional filtered back-projection, many manufacturer software versions permit configuration of the iterative reconstruction strength so that practices can find the right balance between noise reduction and image appearance. Resultant dose reductions on the order of 30% to 50% are frequently achieved with these techniques, and even greater dose reductions are becoming more widespread as the technology advances.

Bismuth breast and thyroid shields are used in some facilities to reduce radiation dose to these organs, but they are not currently recommended by the American Association of Physicists in Medicine because they introduce artifacts throughout the image, and comparable dose reductions can be achieved through use of other methods. If these shields are used, it is important to apply them after acquisition of the planning projection radiographs and to use them only on scanners that do not incorporate real-time mA adjustments that can paradoxically increase the dose to better penetrate through the shields.

Image Reconstruction. The following image reconstructions should be performed routinely:

- 3- to 5-mm axial lung algorithm images
- Axial soft tissue algorithm images:
  Routine chest: 3 to 5 mm
  Dissection CTA: 3 mm or thinner
  Pulmonary embolus CTA: 2.5 mm or thinner—preferably 1 to 1.5 mm

Coronal and/or sagittal multiplanar reformations (MPRs) have become routine at many institutions. MPRs are particularly useful in the assessment of vascular anatomy and osseous structures, but they also can be helpful in localizing parenchymal lesions relative to the fissures and confirming motion artifacts or anatomic pitfalls on PE or dissection CTA. Routine sagittal oblique ("candy cane") MPRs are often added to aorta evaluations. Thick maximum intensity projection (MIP) images may be added to aid in PE or lung nodule detection. Minimum intensity projection images are occasionally useful in evaluation of the airways.

Indication-Specific Computed Tomography Protocol Techniques

Routine Chest Computed Tomography. Routine chest CT often is performed without IVCM to further assess a radiographic parenchymal abnormality (e.g., a pulmonary nodule). However, IVCM is helpful for assessment of empyema or mediastinal or hilar abnormalities.

Pulmonary Embolus Computed Tomography Angiography. A typical PE CTA protocol includes bolus monitoring on the main pulmonary artery, followed after a breath hold delay by scanning from lung apices to bases. For scan durations less than approximately 10 seconds, high-quality PE CTA may be performed with 50 to 75 mL of IVCM injected at 4 to 5 mL per second, depending on the kVp used.

Upper Extremity Deep Venous Thrombosis or Superior Vena Cava Syndrome. Compression and Doppler US is the test of choice for both lower and upper extremity deep venous thrombosis. For high clinical suspicion of central venous thrombosis causing superior vena cava (SVC) syndrome, CT may be performed with a venous phase timing (typically 50 to 60 seconds) that achieves more uniform venous opacification and reduces the mixing artifacts that are typically observed when dense IVCM injected through one arm mixes in the SVC with the non-opacified blood arriving from the other arm (Fig. 8-8). Coronal reformations greatly aid diagnosis.

Aortic Dissection Computed Tomography Angiography. Traditional dissection CTA protocols include the following elements:

- A noncontrast scan of the chest
- An arterial phase scan through the chest (± the abdomen and pelvis) performed either with or without cardiac gating
- A delayed phase scan through the chest, abdomen, and pelvis

The initial noncontrast scan is used to assess for a thrombosed false lumen or isolated intramural hematoma, both of which appear denser than the non-opacified blood in the aortic lumen.

The arterial phase scan is often performed with cardiac gating to reduce pulsation artifact, which can mimic focal aortic dissection at the aortic root. However, this artifact has a characteristic appearance on axial and MPR images and typically can be differentiated from aortic dissection (Fig. 8-9). If the radiologist is readily familiar with this diagnostic pitfall, a nongated arterial phase scan can be used to reduce radiation exposure and to simplify scan acquisition because cardiac gating is more challenging in this frequently tachycardic patient population. Recently developed high-pitch scan modes allowing scan durations through the entire chest on the order of 1 second have also been used successfully to eliminate aortic root pulsation artifacts without the need for cardiac gating.

A CT scan through the abdomen and pelvis is performed to assess distal extension of the intimomedial flap, involvement of visceral or iliac arteries, and end-organ ischemia. Therefore, it should be prescribed routinely in high-risk patients or in those with known aortic dissection presenting with acute symptoms.

More streamlined examinations with reduced anatomic coverage, fewer scan phases, and a drastically reduced radiation dose can be successfully implemented in low-risk patients (including most of the ED patients who undergo imaging for possible aortic dissection). For patients with a low pretest probability of aortic dissection and a low incidence of significant atherosclerotic disease, screening is performed with a non-gated contrast enhanced chest CTA, with direct monitoring by a radiologist at the scanner. If aortic dissection is detected during this chest CTA, scanning is extended through the abdomen and pelvis

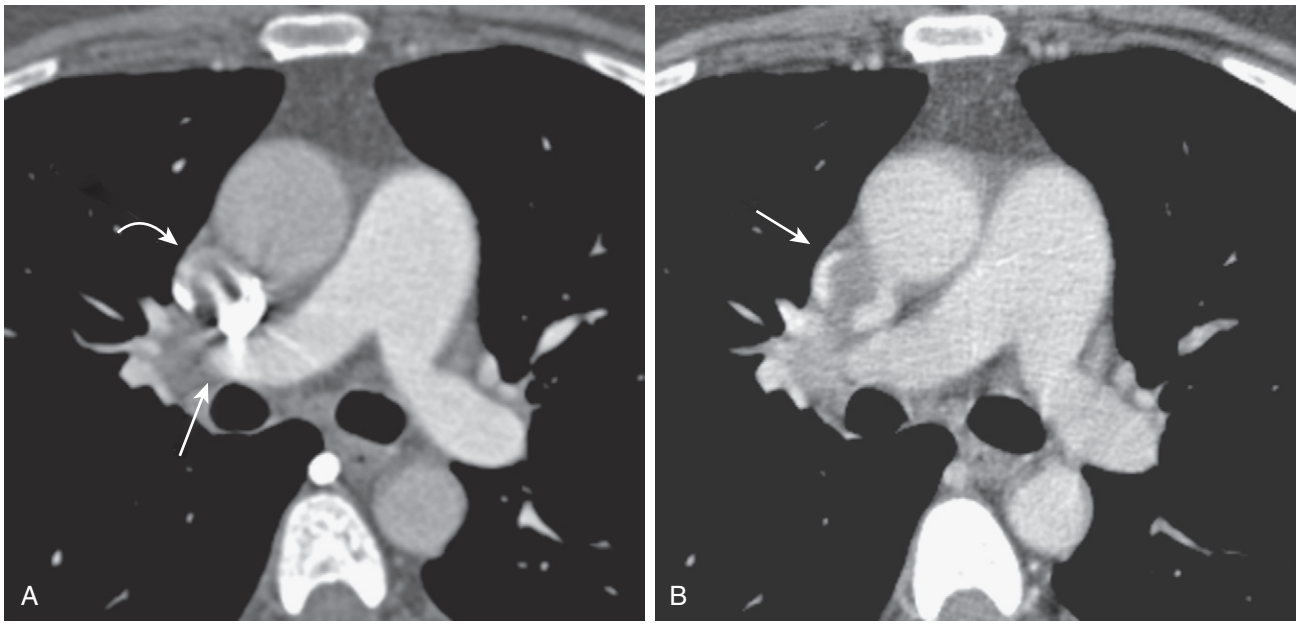


FIGURE 8-8 Superior vena cava (SVC) thrombus after recent central line removal. **A,** An early phase axial image. Dense contrast material in the SVC *(curved arrow)* produces a streak artifact that partially obscures the SVC thrombus *(arrow)* and makes it difficult to differentiate the streak artifact from a mixing artifact with unopacified blood from the left brachiocephalic vein. **B,** A delayed (90 seconds) phase axial image eliminates streak and mixing artifacts better delineating thrombus in the SVC *(arrow)*.

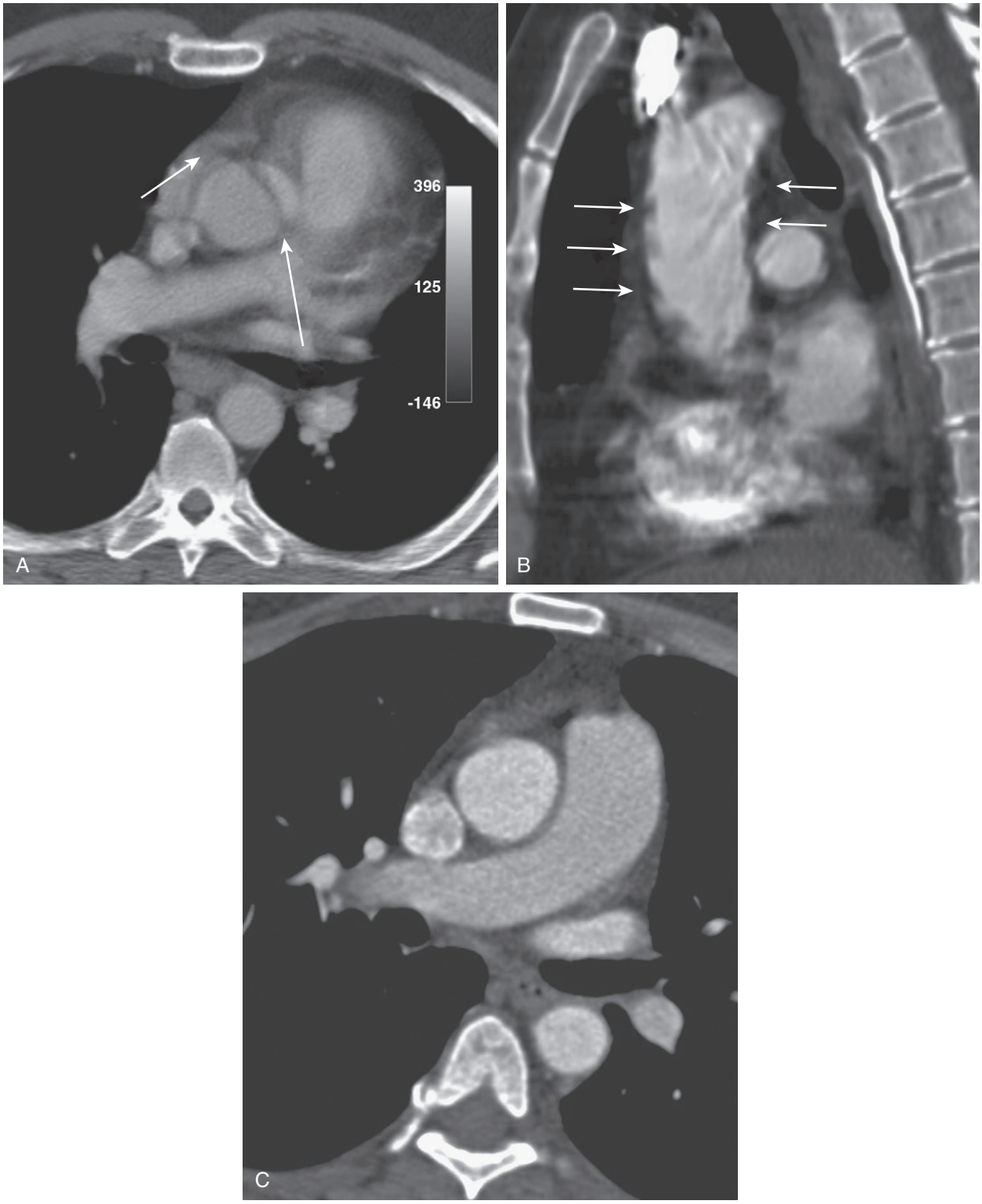


FIGURE 8-9 Pulsation artifact: a typical aortic root pulsation artifact from a nongated study, not to be confused with aortic dissection. **A,** A sharply defined band of low-density artifact *(longer arrow)* extends across the left side of the proximal ascending aorta. The artifact extends beyond the aortic margin to the right atrial appendage *(shorter arrow)*, helping to confirm its artifactual nature. **B,** Sagittal reformation showing motion artifacts *(arrows)* arising in each cardiac cycle. **C,** A repeat study performed the following day with cardiac gating, eliminating the cardiac motion artifact.

to capture the full extent of the dissection in an arterial phase. (In practice, the extended scan region is prescribed up front, and a real-time decision is made to either stop at the chest or continue through the abdomen.) Although it is rarely needed, further scanning is then performed to problem solve; delayed imaging of the abdomen and pelvis may be performed as needed to clarify end-organ perfusion. If the CTA raises suspicion for an isolated intramural hematoma but is not sufficiently diagnostic for the radiologist, a 5- to 10-minute delayed postcontrast scan is added, because IVCM will have adequately cleared the intravascular space. Even more infrequently, a repeat chest CTA with cardiac gating may be performed if a pulsation artifact cannot be differentiated from subtle ascending aorta disease. This approach requires a practice model in which radiologists can actively monitor CT acquisitions while the patient is on the Gantry table. Although the 24-hours-a-day, 7-days-a-week operations of the ED can make this procedure particularly challenging to implement "after hours," greater organization around the practice of emergency radiology is likely to make it more feasible in the future.

Pneumomediastinum and/or Evaluation of Esophageal Injury. In the ED, CT is often used rather than fluoroscopy to assess for a possible esophageal injury. The scan protocol typically includes an initial low-dose scan without use of either oral contrast material or IVCM. Subsequently, the patient takes a few swallows of enteric contrast material, and a repeat scan (with or without IVCM, depending on the indication) is performed. The "scout" noncontrast scan is included to readily differentiate enteric contrast extravasation from soft tissue calcification or a small foreign body (e.g., a fish bone). Because both gas and contrast material extravasation are intrinsically high-contrast evaluations, reduced-dose techniques are used to reduce radiation exposure on this initial scan phase.

Coronary Computed Tomography Angiography. Significant variability can exist in CT scan technique depending on local CT scanner technology and institutional decisions about whether to perform a focused coronary CTA only or a "triple rule-out" procedure that simultaneously assesses the aorta and pulmonary and coronary arteries. The numerous variables and technical details are beyond the scope of this chapter. Briefly, however, the study may be prescribed from a topogram or a low-dose unenhanced chest CT performed for calcium scoring. The CTA is then either initiated by automated bolus monitoring or after a scan delay derived from a test bolus. Cardiac gating is required, preferably with a heart rate equal to or less than 65 beats per minute. Tube current dose modulation schemes are recommended to reduce the associated radiation exposure using ECG dose modulation or prospective scanning, in which x-ray tube output is greatly reduced or eliminated during systole. Images are reconstructed at multiple intervals of the cardiac cycle to permit identification of image sets free of cardiac motion artifacts.

THE PLEURA, PERICARDIUM, AND MEDIASTINUM

Pleura

The pleura is a specialized tissue layer covering the lungs and the internal surface of the chest cavity. The visceral and parietal components form a continuous layer and create a potential cavity, the pleural space, which is generally visualized radiographically only when local or systemic disease develops. A small amount of fluid (15 to 20 mL) normally lies in each pleural cavity and lubricates the sliding lung surface during the respiratory cycle. Pleural fluid originates in the interstitium and is drawn away from the pleural space along a gradient toward the low-pressure pleural capillaries, ultimately draining into the pulmonary venous system. Pleural fluid is continuously secreted and absorbed; disruption of this equilibrium leads to effusion.

The pleural space is maintained below ambient pressure by chest wall recoil, the actions of gravity, and muscular contraction of the diaphragm. Loss of vacuum integrity leads to rapid collapse of the lung airspaces.

Pneumothorax

Pneumothorax is the presence of air within the pleural space. The causes of pneumothorax are multifactorial (Table 8-1).

Spontaneous pneumothorax occurs more frequently in smokers, persons with asthma, and thin young men. The relative risk for male smokers is up to 20 times higher than for nonsmoking males. Risk increases in a linear relationship to the amount of smoking. Blebs are often found at thoracoscopy of patients presenting with spontaneous pneumothorax and can be visualized by CT in up to 89% of patients. For this reason, chest CT is often ordered as a follow-on study to a chest radiograph showing an unexpected spontaneous pneumothorax.

Primary spontaneous pneumothorax is differentiated from secondary spontaneous pneumothorax by the absence of underlying lung disease. Secondary spontaneous pneumothorax is due to underlying pleural or parenchymal disease, usually in the form of blebs or cysts. These blebs or cysts may result from disease entities such as emphysema, *Pneumocystis carinii* pneumonia infection, or lymphangioleiomyomatosis. Spontaneous pneumothorax is sufficiently common as a component of the differential diagnosis for chest pain and dyspnea that a high index of suspicion should be maintained when evaluating routine chest radiographs for these indications. The frequency of central line placement in the ED is another reason to maintain a high index of suspicion for pneumothorax when evaluating all ED chest radiographs.

The most common imaging test performed to assess for pneumothorax is the chest radiograph. Ideally, the chest

TABLE 8-1 Etiologies of Pneumothorax

Etiology	Types
Trauma	Penetrating or blunt; barotrauma
Idiopathic	Primary or secondary
Iatrogenic	Following biopsy, surgery, central line placement, thoracentesis, mechanical ventilation, bronchoscopy
Infection	*Pneumocystis carinii*, necrotizing pneumonia
Neoplastic	Langerhans cell histiocytosis, sarcoma, lung cancer, various others
Congenital/acquired	Emphysema, congenital bullae, lymphangioleiomyomatosis

radiograph is performed with upright patient positioning so that the air–pleural interface can be readily identified toward the apices. It is seen as a thin white line where the outer margin of the visceral pleura and lung is separated from the parietal pleura and the chest wall, with lack of vessel markings beyond the pleural line. Expiratory imaging may accentuate the contrast between lung tissue and intrapleural gas. This method may be particularly helpful for smaller pneumothoraces but is generally not required. The presence of pneumothorax is often more subtle on radiography performed in the supine position, because small pneumothoraces can be easily overlooked from the air collecting anterior and medially.

Additional radiographic signs of pneumothorax seen on the supine radiograph include the deep costophrenic sulcus sign and the "double diaphragm" sign caused by nondependent air outlining the anterior diaphragmatic attachment.

A tension pneumothorax occurs when air enters but cannot exit the pleural space, which can occur when the pleural defect allowing air to pass into the pleural cavity functions mechanically like a ball valve, resulting in unidirectional air transit. The increasing intrapleural gas creates mass effect and eventually can displace the mediastinum and compromise venous blood return to the heart. Progressive accumulation of air in the pleural cavity can lead to cardiovascular impairment and, if left untreated, death. Imaging findings of tension pneumothorax include mediastinal shift away from the side of the pneumothorax, widening of the ipsilateral rib spaces, and/or relative compression of the contralateral lung.

Several estimation methods for pneumothorax size are based on chest radiograph measurements, but these methods are subject to wide interobserver variations in practice. If ambiguity exists about whether an apical lucency represents intrapleural air or a large bulla, CT is generally definitive. Chest CT also permits volumetric or percent measurements of pneumothorax size that are more precise, although intervention usually occurs prior to CT evaluation.

Small pneumothoraces are usually monitored radiographically until they resolve. Failure to resolve and interval enlargement are common indications for invasive management. The treatment for a large pneumothorax (generally 15% or more of the hemithorax) is air aspiration or evacuation by intercostal chest tube or catheter. The radiologist should be familiar with the normal locations for appropriately inserted chest tubes. Intraparenchymal, extrathoracic, and interlobar placements should be communicated to the treating physician to allow for repositioning. The multiple side ports of the chest tube should all lie within the thoracic cavity. Increasing subcutaneous emphysema on repeat chest radiographs is a clue to the potential presence of an extrathoracic side port and the need for repositioning of the chest tube.

Many possible mimics of pneumothorax exist, including overlying sheets, clothing, medical equipment, or skin folds. Repeat chest radiography after rearranging or removing the external structures can be performed to exclude pneumothorax.

Bedside US in expert hands is a rapid assessment tool that can detect pneumothorax more accurately than a supine chest radiograph, making it especially useful in acutely ill patients after line placement or trauma. The four sonographic signs described in the literature to assess for pneumothorax include the lung sliding sign (regular rhythmic movement synchronized with respiration between the visceral and parietal pleura), the lung pulse (subtle rhythmic movement of the visceral pleura upon the parietal pleura with cardiac oscillations), presence of B lines (indicating that the visceral pleura is opposing the parietal), and the lung point (absence of any sliding or B lines, indicating the presence of pneumothorax). Traumatic pneumothorax is discussed in greater detail in Chapter 2, but in brief, penetrating injury easily breaks the seal of the pleural space, which is vulnerable because of its large surface area. Significant blunt trauma is estimated to cause pneumothorax in up to 30% to 40% of cases. Pneumothorax can occur when broken ribs or other sharp structures expose the pleural space to atmospheric pressure or when a preexisting bleb is ruptured. Fractured ribs on imaging should prompt a secondary search for pneumothorax. Barotrauma related to positive pressure ventilation can lead to pneumothorax, particularly in patients with relatively noncompliant lung tissue (e.g., persons with ARDS or interstitial lung disease). Barotrauma also may occur during sport diving or from nonpenetrating blast injuries resulting from explosive devices.

Pleural Effusion

Pleural effusion, defined as abnormally increased fluid within the pleural space, may be transudative or exudative in cause. Transudative fluid is generally low in protein and typically develops in the setting of left heart failure, decreased oncotic pressure, or another systemic abnormality. Exudative fluid is often a consequence of breakdown of the barrier function of the pleura, leading to leakage of macromolecules and proteins.

Pleural fluid volume as low as 5 mL can be visualized on decubitus chest radiograph imaging. Approximately 200 mL is required to blunt the costophrenic sulcus on upright radiography. Small fluid collections can routinely be characterized on CT, US, and MRI. The CT appearance of pleural fluid varies depending on the density. Transudative effusions are near water density (i.e., approximately 0 Hounsfield units [HU]); hemorrhage and pus typically demonstrate increased density, often with a hematocrit effect in the case of hemorrhage. Low density on CT does not, however, exclude exudate. Long-standing effusions can become loculated, with an irregular pleural contour. US is a very useful tool to further characterize the effusion by showing areas of loculation and septation, and it is also commonly used for drainage guidance.

Pleural effusions also may be seen in the setting of malignancy, often related to pleural metastatic deposits. Meigs syndrome is a rare benign condition that causes pleural effusion and ascites in the setting of a benign ovarian fibroma, although other ovarian neoplasms are now commonly invoked as well. Meigs syndrome is uncommon and the pathophysiology is unclear, although it is often believed that the fluid is generated by the tumor itself and is most commonly a transudate.

Hemothorax

Traumatic hemothorax can occur after blunt or penetrating trauma. Blunt trauma may cause direct venous or

arterial rupture or may disrupt vessels as a result of rib fracture. Penetrating trauma can cause mediastinal, intercostal, substernal, or diaphragmatic vascular injury with resultant intrapleural hemorrhage.

Intrapleural blood may manifest on a chest radiograph as a localized collection or as diffuse relative opacification of one or both hemithoraces. Much smaller collections can be detected on CT with the added certainty of density characterization allowed by evaluation of HUs in a region of interest. CT, particularly when performed during IVCM administration, may identify active extravasation from an arterial injury. Progressive enlargement of hemothorax is likely due to arterial injury, whereas venous hemorrhage is more likely to stabilize. An unevacuated hemothorax, particularly if it is large, can lead to adhesions and fibrothorax, potentially restricting lung function.

Empyema

Empyema refers to abscess formation in the pleural space. Although usually a result of adjacent pneumonia, it is also known to develop after hematogenous seeding, trauma, or iatrogenesis. In the setting of suspected empyema, chest CT should be performed with administration of IVCM. The presence of a "split pleura" sign (i.e., enhancement of the visceral and parietal pleura) is strongly suggestive of empyema. Several studies have shown improved health outcomes with early evacuation of empyema, often in conjunction with fibrinolytic therapy.

Chylothorax

Chylothorax is the development of effusion containing lymphatic fluid, most often as a result of a thoracic duct injury or malignant invasion. The thoracic duct drains into the junction of the left axillary and internal jugular veins, with the majority of the course from the cisterna chyli lying on the right. Consequently, most chylous effusions are right-sided. CT is helpful in the diagnosis, because chylous fluid contains fat, which manifests as Hounsfield units (HU) measurements less than zero.

Pericardium

The pericardium is an investing connective tissue layer that covers the heart and proximal great vessels, separating the cardiac structures from the remainder of the middle mediastinum.

Pericardial Effusion

Pericardial effusion has many causes, and imaging is often nonspecific in this regard. Pericardial effusion may be idiopathic, drug-induced, or radiation-induced, or it may be the result of collagen vascular diseases, malignancy, hypothyroidism, chylous effusion, infection (pericarditis), or cardiac and renal failure.

Hemopericardium

Hemopericardium is usually the result of acute blunt or penetrating trauma from direct pericardial damage, myocardial contusion, or a proximal aortic injury. Hemorrhage into the pericardial sac can rapidly lead to tamponade and circulatory collapse. In the absence of a history of trauma, type A aortic dissection, coronary artery aneurysm rupture, or postinfarct cardiac rupture must be considered. However, a dense pericardial effusion is not a sine qua non of hemopericardium or incipient tamponade.

Cardiac Tamponade

Cardiac tamponade is a potentially life-threatening restriction of cardiac function due to rapid influx of fluid or gas into the pericardial space, regardless of its source or nature. CT findings that are worrisome for cardiac tamponade in the presence of a pericardial effusion include distention of the SVC and inferior vena cava (IVC), reflux of IVCM into the azygos vein and IVC, compression of the cardiac chambers, and angulation or bowing of the intraventricular septum. Cardiac findings can be associated with lung parenchymal findings of pulmonary edema. Imaging findings must be interpreted in conjunction with history and physical examination findings. Echocardiography should be performed if features suggest hemodynamic compromise (Fig. 8-10).

Pneumopericardium

Pneumopericardium can result, uncommonly, from blunt trauma or penetrating injury, or it may develop after positive pressure ventilation, often in association with pneumothorax. Pneumopericardium has also been associated with illicit drug use, particularly crack cocaine inhalation, which maybe related to repeated Valsalva maneuvers. Although pneumopericardium generally resolves with withdrawal of the causative insult, tension pneumopericardium can develop and should be suspected if the cardiac contour is abnormally diminished, known as the "small heart" sign.

Malignancy

Metastatic involvement of the heart and pericardium occurs in 10% to 12% of all patients with cancer and 30% of those with lung malignancy. Symptoms such as dyspnea, cough, and chest pain are potential clues to cardiac

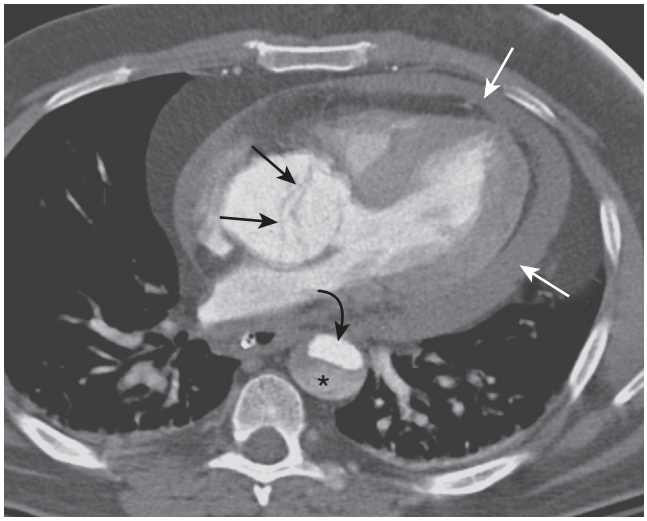


FIGURE 8-10 Axial computed tomography images showing hemopericardium *(white arrows)* resulting from type A aortic dissection (*black arrows* indicate a type A dissection flap within the ascending aorta; apparent duplication of the flap may be due to motion). Dissection extending into the descending thoracic aorta, with a hyperdense true lumen *(curved arrow)* and hypodense false lumen *(asterisk),* is noted.

or pericardial spread, although these symptoms are quite nonspecific. Contrast-enhanced chest CT to exclude PE is a common initial evaluation for oncology patients presenting to the ED with new chest-related symptoms. Foreknowledge of a patient history of malignancy, particularly lung cancer, should prompt careful visual review of the heart and pericardium for an alternative or additional explanation of symptoms.

Other pericardial diseases include pericarditis and constrictive pericarditis. Pericarditis may cause a pericardial effusion and/or pericardial thickening.The normal pericardial thickness varies from 1 to 3 mm, depending on the location and cardiac phase. Constrictive pericarditis may or may not be associated with pericardial thickening.

Mediastinum

Anatomy

The mediastinum is the space within the central chest cavity bounded laterally by the medial pleural surfaces, anteriorly by the sternum, and posteriorly by the spinal column. The inferior margin is bounded by the diaphragm, whereas the superior limit is usually arbitrarily defined by a line drawn horizontally from the manubriosternal joint to the T4 vertebra.

Several methods may be used to perform anatomic segmentation of the mediastinum. The simplest method trisects the intrathoracic structures into anterior, middle, and posterior mediastinal compartments based on location relative to the heart.

Because the three main mediastinal compartments contain very different structures, localization of a lesion to one of the mediastinal compartments considerably aids the differential diagnosis for most abnormalities. The anterior compartment normally contains thymus (or a thymic remnant), lymph nodes, and fat. During embryonic development, pluripotent germ cells migrate inferiorly through this region. The middle mediastinum contains the heart and pericardium, great vessels, tracheal bifurcation, phrenic nerves, and lymph nodes. The posterior mediastinum contains the esophagus, thoracic duct, vagus nerve and sympathetic chain branches, the azygos and hemiazygos veins, and the descending aorta.

Masses

The previously described anatomic compartmentalization of the mediastinum helps the radiologist formulate differential diagnostic considerations for mediastinal masses. Mediastinal masses may be detected as incidental findings in ED patients undergoing chest imaging, or they may be the cause of the patients' presenting symptoms, such as chest pain, dysphagia or dyspnea, cough, hemoptysis, or SVC syndrome.

Pneumomediastinum

Typical causes of pneumomediastinum include trauma, asthma, drug use (Valsalva-induced), infection, and spontaneous pneumomediastinum. Traumatic causes (other than typical blunt or penetrating external trauma) may be the result of endoscope, tube, or line insertion (i.e., iatrogenic), positive pressure ventilation, internal barotrauma related to vomiting (Boerhaave syndrome) or coughing against a closed glottis (Fig. 8-11). Pneumomediastinum generally requires no treatment apart from addressing the underlying cause.

Infection

Acute mediastinitis is a relatively rare entity, most commonly (in 90% of cases) related to esophageal rupture. Other causes include tumor necrosis, spread of infection from adjacent compartments (e.g., descending cervical infection due to spread of oropharyngeal or deep neck infection along fascial planes), and infection resulting from procedures (e.g., sternotomy and mediastinoscopy). Signs and symptoms are nonspecific and include fever, tachycardia, and chest pain. Dysphagia is often noted in cases related to esophageal perforation. Conventional radiography may reveal tracking of air along the mediastinal planes, with variable extension into the soft tissues of the neck or through the diaphragmatic hiatus into the retroperitoneum. CT lung windows are much more sensitive than radiography in detecting small amounts of mediastinal gas.

SVC Syndrome

SVC syndrome refers to the development of facial and upper extremity edema, swelling, and collateral venous engorgement as a result of SVC obstruction. Associated findings include upper body erythema, confusion, chest pain, and hoarseness. In the developed world, most cases are related to malignant invasion of the SVC. Historically, tuberculous infection and syphilitic aneurysm were more common causes. Indwelling central catheters have come to play a larger role in recent years and can lead to SVC syndrome via stricture and thrombosis. Other causes of SVC syndrome include extrinsic compression by aneurysm or lymphadenopathy and fibrosing mediastinitis, usually as a result of the inflammatory response elicited by infection with *Histoplasmosis capsulatum.* In younger patients, benign causes predominate. Malignancy is the most common cause in persons older than 40 years.

Because SVC obstruction impairs venous drainage of the head and neck, cerebral and laryngeal edema may occur. For these reasons, the development of SVC



FIGURE 8-11 A computed tomography image showing spontaneous pneumomediastinum *(black and white arrows)* in an asthmatic patient.

syndrome is considered a medical emergency, although only a minority of patients are at risk of death from cerebral edema.

A chest radiograph may reveal a mediastinal abnormality in patients with clinically suspected SVC syndrome, such as a mediastinal mass or lymphadenopathy. Contrast-enhanced CT and MR angiography are the most reliable noninvasive methods of definitive diagnosis. CT is generally preferred as the initial study because of the prevalence of lung cancer and lymphoma as causative factors in the adult population and the ease and accuracy with which CT delineates these findings (Fig. 8-12).

THE THORACIC AORTA

Relevant Computed Tomography Anatomy

On axial sections, the aorta is generally round, and its diameter should gradually taper more distally as vessels branch from its lumen, although some notable exceptions exist that represent normal variants in its size and shape. It is important to be familiar with the appearance of these variants at imaging so that they are not mistaken for disease.

Normal variants of the aortic contour identified on CTA are best recognized on MPR or three-dimensional (3D) images; these variants include the aortic spindle, ductus diverticulum, branch vessel diverticula, and pseudocoarctation. The aortic spindle is a smooth circumferential bulge below the region of the isthmus, representing normal mild dilation of the region of the posterior arch. The ductus diverticulum is a focal convex bulge along the anterior undersurface of the aortic isthmus. The obtuse angles it forms with the aorta can be used to distinguish it from a posttraumatic pseudoaneurysm, which more characteristically forms acute angles with the aortic wall. Branch vessel diverticula show smooth obtuse margins with a branch vessel emanating from the apex of the infundibulum, and can be mistaken for a posttraumatic pseudoaneurysm at a branch vessel origin. Recognition is aided by their tendency to occur in characteristic locations, such as the left subclavian artery and the third right intercostal artery. Pseudocoarctation results from elongation of the aortic arch, which characteristically results in kinking at the site where the aorta is tethered by the ligamentum arteriosum. Imaging of healthy adults has shown that normal aortic wall thickness is less than 1 mm or imperceptible on axial CTA images.

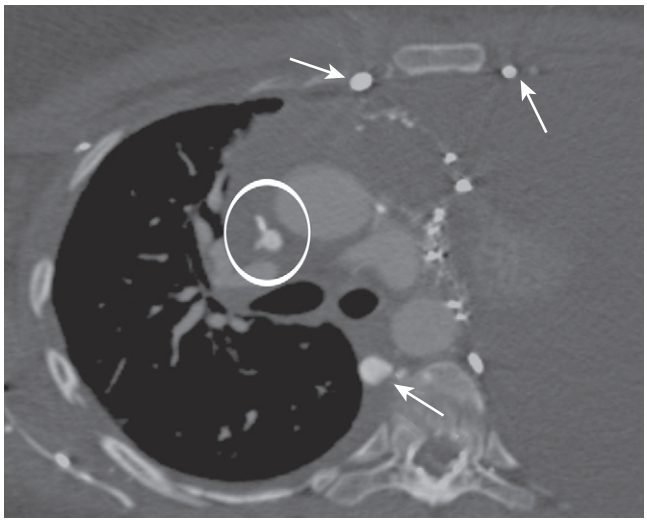


FIGURE 8-12 Superior vena cava (SVC) syndrome: axial and coronal contrast-enhanced computed tomography. Multiple collaterals and dilatation of azygos and internal mammary veins *(arrows)* in a patient with severe SVC narrowing due to tumor mass encasement *(oval)*.

Aneurysm

Thoracic aortic aneurysm is defined as a permanent abnormal dilatation of the aorta. The normal diameter of the mid ascending aorta should always be less than 4 cm, and the descending thoracic aorta should measure no more than 3 cm, even considering a slight increase in the aortic diameter with age. Distal aortic segments generally should be smaller in diameter than more proximal segments except for the previously noted anatomic variants. If this relationship is reversed, aortic monitoring for aneurysm development should be considered. CT can characterize thoracic aneurysms by their location and shape. Three fourths of aortic aneurysms are atherosclerotic in cause and fusiform in shape. Approximately 20% of atherosclerotic aneuryms are saccular, particularly in the arch and descending aorta. The incidence of aortic rupture is related to aneurysm size. An important goal for imaging is to provide accurate measurements. Conventional catheter-based aortography underestimates true aortic diameter, because it reflects only the size of the patent lumen and does not include contributions from intraluminal thrombus or mural thickening. CT accurately evaluates aneurysm dimensions, the extent of mural thickening and thrombus, the integrity of the aortic wall, and its relationship with contiguous structures. Thoracic and abdominal aortic aneurysms are discussed in detail in the chapter on vascular emergencies of this textbook. Thoracic aortic aneurysms carry a high incidence of concomitant abdominal aortic aneurysms, and thus screening of the abdomen with CT or US is generally warranted when a thoracic aneurysm is detected.

Infectious Aortitis

An infected aorta, whether of normal caliber or aneurysmal, can represent a diagnostic challenge, because patients may be asymptomatic until late stages or may present with nonspecific clinical symptoms. Nearly 50% of infected aneurysms occur in the thoracic or thoracoabdominal aorta, a significantly higher-than-expected rate given the distribution of atherosclerotic aortic aneurysms. More than 90% show a saccular structure, often lobulated. Early detection by CT can permit intervention before a rapidly progressive course with sepsis and/or rupture. CT may reveal subtle periaortic edema, stranding, and fluid in the initial stages. Rim enhancement of periaortic soft tissues followed by disruption or loss of intimal calcifications often precedes aortic enlargement. Close follow-up CT is advised because development of large aneurysms and marked growth may occur in short intervals. An infected aorta also may maintain a normal caliber. Periaortic gas and gas within the

aortic wall are specific findings but are seen in fewer than 10% of cases. Lack of mural calcification within an aneurysm suggests a nonatherosclerotic cause and therefore raises greater concern for infection. Nuclear scintigraphy with labeled leukocytes or gallium-67, when correlated with CT findings, can increase confidence in this diagnosis.

Syphilis, a now infrequent cause of infectious aortitis, has a typical course that can be assessed by CT. CT demonstrates enlargement of the aorta, which progresses to aneurysm formation that most commonly involves the ascending portion or arch. Most syphilitic aneurysms are saccular, but about 25% are fusiform. The pattern of fine and pencil-line dystrophic calcification is characteristically seen. However, this finding is often obscured by thick, irregular, coarse calcifications of secondary atherosclerosis.

Aortic Dissection

Aortic dissection occurs when intravascular blood breaches the intima and dissects within the media of the aortic wall. Imaging is critical for establishing this diagnosis and for guiding medical or surgical intervention. Chest radiography continues to play a role in the initial assessment of patients with suspected aortic dissection, principally because it provides readily available diagnostic information that helps exclude other differential considerations (e.g., pneumothorax). Its value is otherwise limited, because a normal chest radiograph cannot exclude, nor can an abnormal chest radiograph confirm, aortic dissection. Findings of aortic and/or mediastinal widening lack specificity and require further evaluation with cross-sectional imaging. Conversely, up to 25% of dissection cases will appear normal at radiography. Patients for whom radiography provides an insufficient alternate explanation of their symptoms and for whom aortic dissection remains a diagnostic consideration must undergo cross-sectional imaging to exclude dissection.

CT, MRI, and transesophageal echo have all been used for the diagnosis of acute dissection. CT compares well with MRI and transesophageal echo. Although all three modalities have been reported to have 100% sensitivity, specificity is highest for CT, approaching 100%. Aortography has a sensitivity of only 88%, with false-negative diagnoses often related to thrombosed or faint opacification of the false lumen, equal opacification of true and false lumen, unusual intimal tears, and intimal tears proximal to the catheter tip. CT is effective in identifying the entry site of the primary intimal tear and the location and extension of the intimomedial flap and in assessing the presence of thoracic and abdominal complications.

The principal criterion for CT diagnosis of aortic dissection is the presence of an intimomedial flap separating the true lumen from the false lumen. After administration of intravenous contrast, the false lumen may opacify completely, partially, or, if thrombosed, not at all. Secondary findings, which are less specific but may be helpful in equivocal cases, include displacement of intimal calcifications toward the lumen, aortic widening, and mediastinal and pleural hemorrhage. Calcification of neointimized mural thrombus can occasionally mimic displaced intimal calcifications and lead to a false-positive diagnosis if not recognized.

CTA reliably classifies aortic dissection based on the location and extension of the intimomedial flap irrespective of the site of the primary intimal tear. The Stanford classification grades the dissection as type A (ascending aortic involvement) or type B (no ascending aortic involvement; Fig. 8-13; see also Fig. 8-10), the principal criterion for determining surgical (type A) versus medical (type B) treatment. Stanford type B dissection involves the descending thoracic aorta distal to the subclavian artery.

CTA can reliably differentiate the true from false lumen, which is particularly important when endovascular management is contemplated. Although the configuration of aortic dissection can be quite variable, the false lumen is most commonly located in the right anterolateral position of the ascending aorta, the superior aspect of the arch, and the left lateral position of the descending aorta. The most reliable imaging criteria are continuity of the true lumen with the nondissected portion of the normal aorta either proximally or distally and identification of the false lumen's termination into a blind sac. Establishing continuity can be more difficult for dissections that involve the aortic root, originate at the aortic arch, or involve the entire aorta. An acute angle between the dissection flap and outer wall on an axial CT image (the "beak" sign) and a larger luminal cross-sectional area are two of the most useful indicators of the false lumen in both acute and chronic dissections. The false lumen can be filled with either contrast-enhanced blood or thrombus. "Cobwebs," which represent thin radiolucent filling defects attached to the aortic wall, from incompletely detached media, are also highly specific for the false lumen but are seen infrequently. Outer wall calcifications are useful for indicating the true lumen in acute dissection but are unreliable in chronic dissection because neointima within a false lumen may calcify. Although the direction of flap curvature is not a useful indicator, direct visualization of intimomedial rupture, seen as intimal discontinuity, evaginating intraluminal flap, and communication of the two lumina, can reliably identify the direction of entrance tear and differentiate true from false lumen. Identification of the tear site is important because both surgical and endovascular treatment aim to occlude the tear and induce thrombosis of the false lumen. In patients with aortic arch involvement, one lumen often spirals around the other, resulting in the appearance of three lumens on an axial CT image, with the central lumen invariably representing the true lumen. Enhanced CT typically shows either isodensity or hyperdensity of the true lumen (see Fig. 8-13).

Type A aortic dissection is a surgical emergency given its high mortality if not promptly treated. Blood can extend to the pericardial space through the diseased wall even without frank rupture, causing tamponade; the dissection also can compromise the great vessels and coronary arteries (see Fig. 8-13), causing myocardial ischemia.

A notable advantage of CT is the detection and characterization of thoracic and abdominal complications. Irregularity of the aortic wall, extravasation of contrast material, hemomediastinum, hemopericardium, and hemothorax are signs that raise concern for aortic rupture. Other possible complications may include distal end-organ malperfusion as a result of true lumen collapse or rapid false lumen expansion. The number of abdominal organs demonstrating decreased parenchymal enhancement has been shown to be a strong factor in outcome for patients with acute aortic dissection.

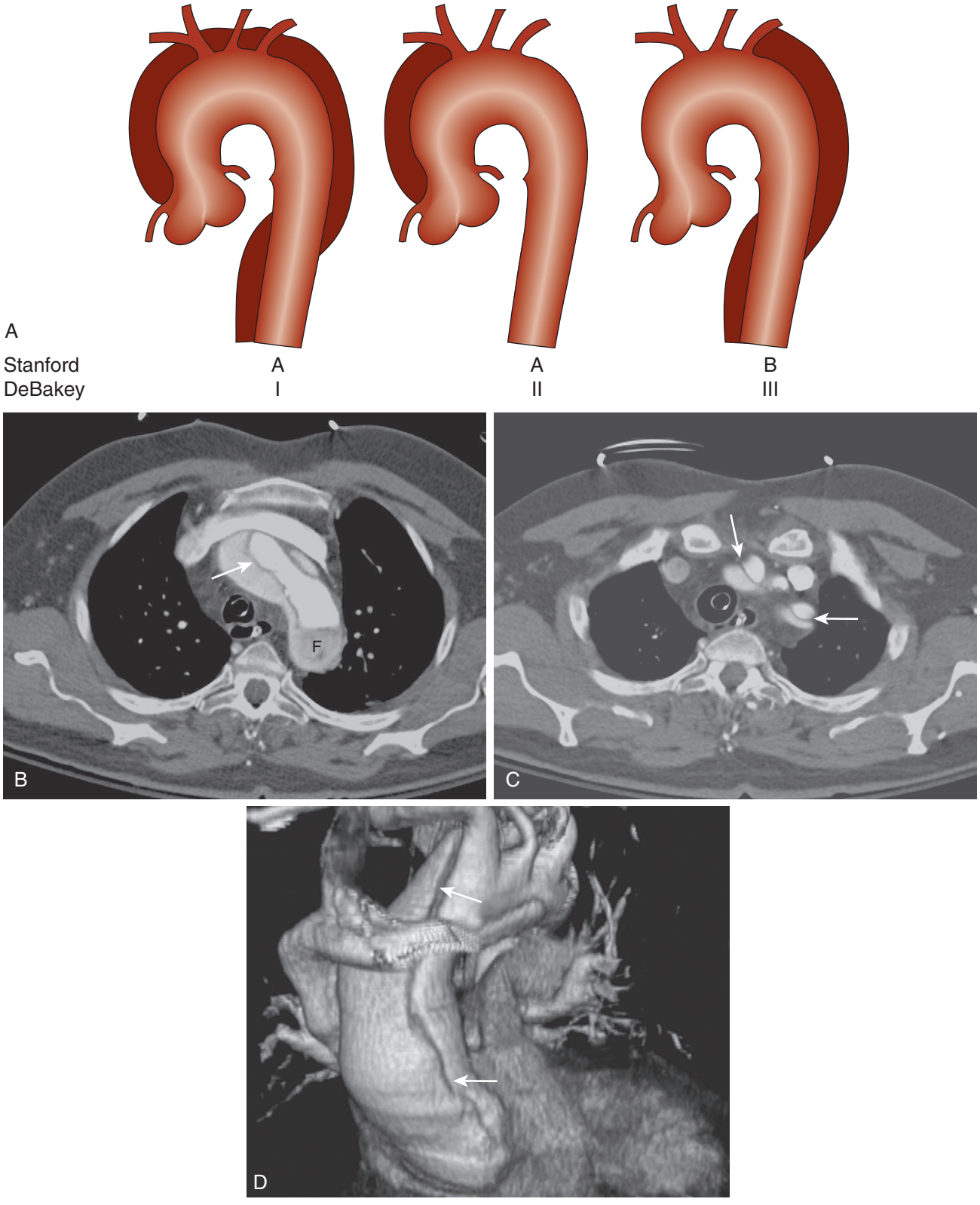


FIGURE 8-13 Aortic dissection. **A,** A diagram of Stanford aortic dissection classification. Type A dissections involve the ascending aorta, whereas type B dissections involve the descending aorta only. Although no longer in common clinical use, the older DeBakey classification scheme is included for reference. **B,** An axial image of the patient shown in Figure 8-10 at the level of the aortic arch shows an intimal flap *(arrow)*. The false lumen is hypoattenuating as a result of slow flow *(F)*. **C,** An axial image at a level just above the arch shows involvement of the origin of the great vessels *(arrows)*. **D,** A three-dimensional image with volume rendering clearly reveals the extent of dissection from proximal ascending thoracic aorta to the aortic arch *(arrows)*.

Chronic dissections should be closely monitored for aneurysmal formation, which occurs in about one third of cases. These aneurysms are prone to rupture and are the most frequent cause of late death after dissection.

Acute Intramural Hematoma

Intramural hematoma (IMH) constitutes 10% to 20% of acute aortic syndromes. Acute IMH may be the result of rupture of the vasa vasorum, with hypertension proposed as the most frequent risk factor. An alternative hypothesis is that IMH is the result of microscopic intimal tears. Hematoma accumulates within the aortic media and cannot be differentiated on imaging from a traditional dissection with a thrombosed false lumen. The clinical presentation of patients with acute IMH is quite similar to that of other acute aortic syndromes. Therefore, CT has a major role in the initial diagnosis of IMH and in the detection of early complications (e.g., ulceration, saccular aneurysm, and dissection) and late complications (e.g., fusiform aneurysm and rupture).

CT is the study of choice for making the initial diagnosis and has a reported accuracy of 100%. In the acute stage, unenhanced axial images reveal a hyperdense, smooth crescentic collection located eccentrically in the aortic wall, often without significant narrowing of the adjacent aortic lumen (Fig. 8-14). Internal displacement of intimal calcifications toward the lumen may be seen. The ascending aorta and proximal descending aorta are most frequently involved. CTA images show no enhancement within the area of the IMH, and typically no branch vessel occlusion occurs.

Intramural blood pool (IBP) is a characteristic CT finding in patients with IMH. IBPs are seen as small focal intramural puddles of contrast with a tiny intimal orifice and/or a connection with an intercostal or lumbar artery originating in the location of the IMH (Fig. 8-15). These IBPs are morphologically distinct from penetrating ulcers that have a wider communication to the aortic lumen. IBPs may resolve over time or appear on follow-up CT studies and are not thought to be associated with a poor prognosis.

It is important to recognize the potential pitfalls in the diagnosis of IMH. If an unenhanced CT scan is not obtained, contrast material in the aortic lumen can diminish its conspicuity (see Fig. 8-14). Acute IMH is not to be confused with chronic mural thrombus, which is often associated with atheromatous plaque or aneurysm and is typically irregular and low in attenuation. The distinction is best appreciated on noncontrast axial CT images, in which calcifications are frequently a marker of the intima. Mural thrombus layers on the luminal side of the calcified intima, whereas IMH is subintimal.

IMH is classified as type A or B using the same criteria as the Stanford classification based on the presence or absence of ascending aorta involvement. Type A IMH has been shown to have high risk of early complications, such as progression to dissection, aneurysmal dilatation, or aortic rupture, and therefore these patients undergo treatment with surgery. IMH localized in the descending thoracic aorta without an associated ulcer demonstrates less frequent complications on CT follow-up. In addition, a maximum aortic diameter greater than 5 cm on the initial CT imaging has been shown to be an independent predictor of progression of type A IMH.

IMH can occur with or without any other aortic abnormality. Although most IMHs resolve on follow-up CT, follow-up imaging is still important in the acute stages to assess for the development of ulcers. Ulcers can lead to saccular aneurysms and, less frequently, to overt dissection. Expansion of the hematoma may be a sign of impending rupture and is readily identified by CT. Although many cases of IMH not associated with an ulcer have a stable early radiographic and clinical course, long-term follow-up may be indicated because fusiform aneurysm formation can be a common late complication in these patients.

Penetrating Atherosclerotic Ulcer

Penetrating atherosclerotic ulcers are defined as ulcers of the inner lining of the aorta that penetrate through the internal elastic lamina into the aortic media and can result

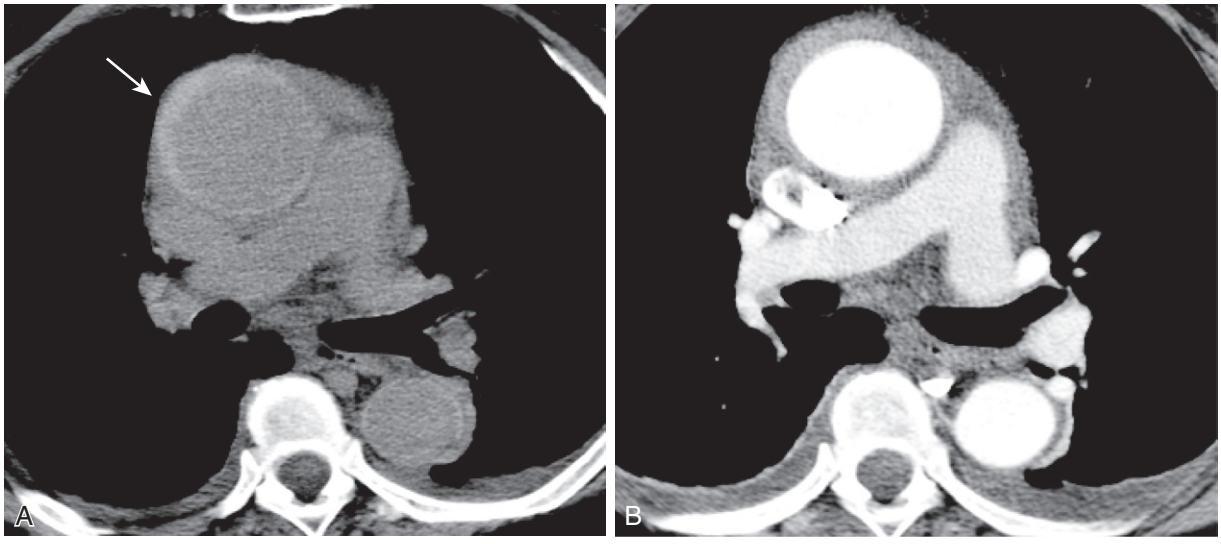


FIGURE 8-14 An intramural hematoma (IMH) involving the ascending aorta (therefore type A IMH). **A,** An axial nonenhanced CT image shows a hyperdense crescentic collection in the ascending aorta *(arrow)*. **B,** An axial contrast-enhanced image at that same level shows no intimomedial flap and decreased conspicuity of the IMH. Note small amount of fluid in the superior pericardial recess and small bilateral pleural effusions.

in focal IMH or aortic rupture (free rupture or contained in a pseudoaneurysm), if it penetrates through the entire aortic wall. The CTA finding is an aortic ulcerlike lesion that protrudes beyond the aortic circumference and can be associated with focal IMH or signs of aortic rupture in the presence of advanced atherosclerotic aortic disease (Figs. 8-16 and 8-17). Clinical presentation varies from asymptomatic to acute chest pain similar to that of aortic dissection. Location can be helpful clue to the diagnosis, because most cases of penetrating atherosclerotic ulcers are identified in the middle and distal thirds of the descending thoracic aorta.

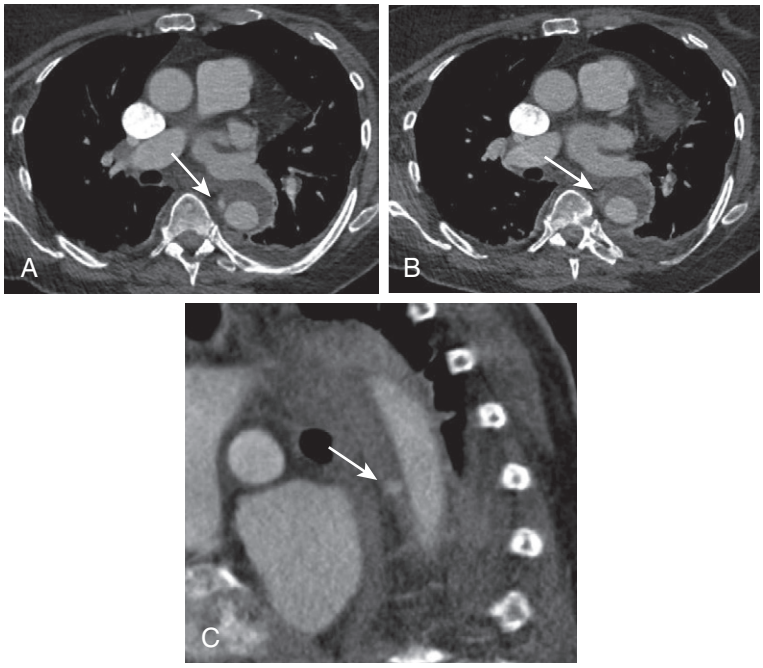


FIGURE 8-15 Intramural blood pool. **A,** An axial enhanced computed tomography (CT) image shows a focal blood pool in a patient with intramural hematoma *(arrow)*. **B,** Note the thin subtle connection of the intramural blood pool with the adjacent intercostal artery *(arrow)*. **C,** CT sagittal reformation showing the intramural blood pool *(arrow)*.

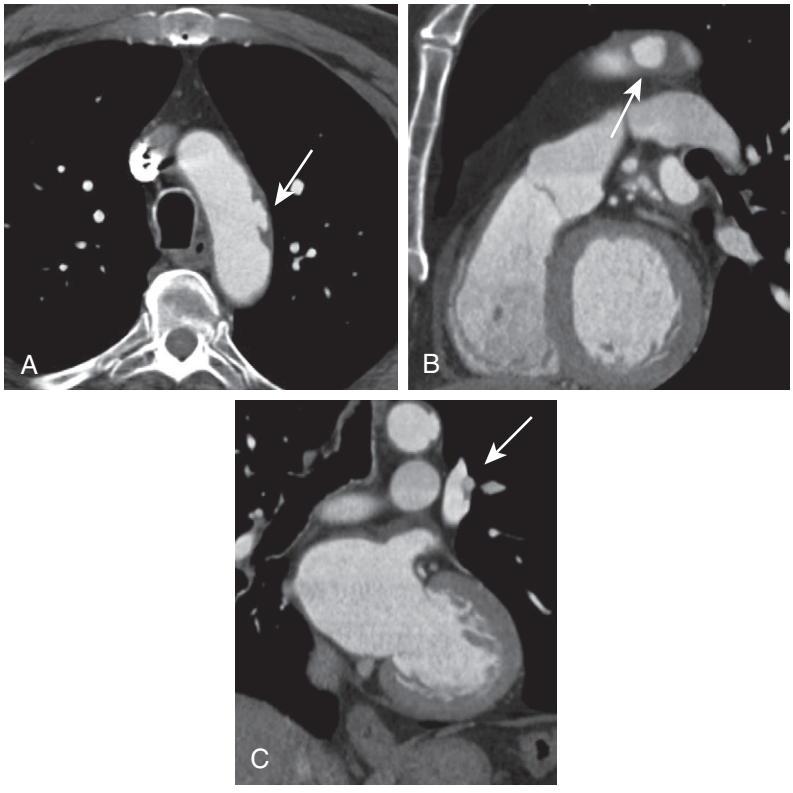


FIGURE 8-16 A penetrating atherosclerotic ulcer. **A,** An axial contrast-enhanced computed tomography (CT) image shows focal contrast outpouching at the level of the aortic arch *(arrow)* with an associated small intramural hematoma. **B** and **C,** Sagittal and coronal CT reformations at the level of the ulcer *(arrows)*.

Clinical presentation is the most important factor in patient management. Ulcerlike lesions are a common incidental finding in asymptomatic patients. If the patient is asymptomatic with no associated IMH, these ulcerlike lesions can represent either a benign ulcerated atherosclerotic plaque that does not penetrate into the media or a chronic healed ulcer. Incidentally identified ulcers show a generally benign course, whereas those initially diagnosed in symptomatic patients show an unpredictable course with frequent clinical and radiographic progression. Because neither the presence nor absence of subsequent clinical symptoms in an initially symptomatic patient is a reliable predictor of clinical course, serial CT is recommended to document resolution or progression and help determine whether patients should be managed conservatively or surgically. Interval change in ulcer size and structure can be helpful in determining a prognosis. Ulcers that demonstrate a diameter of greater than 20 mm and a depth of greater than 10 mm have a very high risk of progression. In the early follow-up period, CT identifies frequent progression of ascending aorta and arch ulcerations to saccular aneurysm formation, rupture, and dissection. Aneurysms that develop from incorporation of the ulcer into the aortic lumen are further characterized by a faster than average growth rate. Overt aortic dissection generally occurs within the first month of follow-up, and a 38% rupture rate has been reported during the initial hospital admission. Finally, the presence and interval increase of pleural effusions on serial CT have been found to be an independent factor for clinical and radiographic progression. If surgery is required, the preferred treatment is endovascular repair with stent grafting.

Postoperative Thoracic Aorta

Grafts and stents can be used for thoracic aortic surgical repair. Two widely performed techniques utilize prosthetic grafts or homografts for thoracic aortic repair or replacement. In the interposition graft technique, the diseased segment of native aorta is totally excised with graft anastomoses to the proximal and distal excision sites. The inclusion graft technique implies closure of the remaining diseased aorta around the graft, thus creating a potential space between the graft and the native aortic wall that can contain thrombus, flowing blood, or both.

Normal Graft Postoperative Findings

Expected postoperative CTA findings in all types of open repair include perigraft fluid and perigraft soft tissue attenuation. Postoperative gas, which is normal, should resolve. In some patients, low-density material surrounding or adjacent to the aortic graft (including the anterior mediastinum for ascending grafts and extrapleural for descending grafts) may remain unchanged, possibly representing a hematoma that evolved into fibrous tissue. The presence of such material on postoperative CT studies should be confirmed to be of low density and should not be mistaken for evidence of leak or infection.

In aortic graft interposition, felt strips are used to buttress the anastomosis in patients with dissection or other disease of the aortic wall. Felt pledgets are often used to repair the bypass cannulation site in the native aorta and the air evacuation needle site in the graft. Potential pitfalls can occur with felt strips and felt pledgets, because these

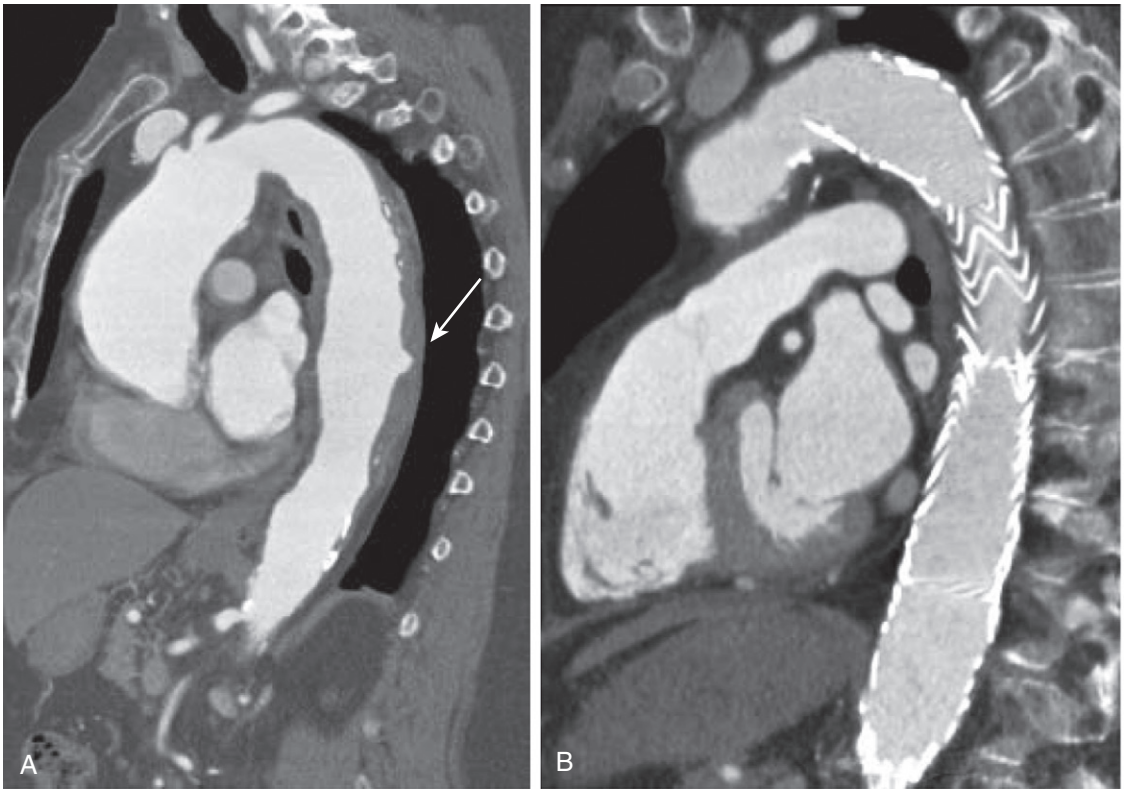


FIGURE 8-17 **A,** A penetrating atherosclerotic ulcer *(arrow)* in the descending thoracic aorta, where significant atherosclerotic changes are present. **B,** An image from a follow-up study after successful stent graft placement.

high-density structures simulate contrast material or a contained leak. Knowledge of the operative material used and acquisition of routine initial noncontrast CT can assist in avoiding these potential pitfalls. Furthermore, the high density of the felt strips helps to readily detect the anastomotic site on CT.

Another potential pitfall lies in the variable appearances of coronary artery anastomoses after aortic arch reconstruction. The coronary artery grafts may be anastomosed with a button of native aortic root, which, when conspicuous, can simulate a pseudoaneurysm at the proximal graft anastomosis. Total arch replacement with reimplantation of the head and neck vessels into the graft also can result in complex appearances on enhanced CT. In cases of type A dissection repair, small outpouchings at the anastomotic site can develop when a perfused false lumen is present distal to the anastomotic site. Another postoperative appearance that should be recognized occurs when a stage 1 "elephant trunk" technique is performed to replace the ascending aorta and arch in patients with diffuse aneurysmal process. The presence of a free segment of graft material projecting into the proximal descending aorta identifies patients who may require subsequent repair of the descending aorta.

In aneurysm repair, the length of the graft does not always match the extent of the aneurysm, with persistent dilation of the remaining native aorta. With chronic dissection repair, a double-channel aorta distal to the site of repair is an expected finding and is deliberately preserved to ensure perfusion of the organs that are dependent on the false lumen for their blood supply.

Graft Complications

CT can identify important early mediastinal complications related to the grafting procedure, such as mediastinal abscess, anastomotic dehiscence, or postoperative bleeding. Delayed complications detected by CT include anastomotic dehiscence and leakage, pseudoaneurysm formation (Fig. 8-18), infection, and new or progressing disease of the native aorta. Paravalvular leaks also can be seen after aortic valve repair.

CT is recognized as the most sensitive method of detecting a leak. A leak is confidently diagnosed when extravasation of contrast material is identified. To avoid pitfalls, an unenhanced scan may be performed in postoperative patients to obtain an unequivocal baseline appearance of the postoperative repair for comparison with the contrast-enhanced CTA images. Leaks can originate at both the proximal and distal ends of the graft and are referred to as *perigraft leaks*. Leakage at the proximal end of the graft seams to predispose to aortic rupture and underscores the importance of adequate follow-up imaging and early diagnosis.

Pseudoaneurysm formation is a major complication of the graft-interposition techniques that results from partial dehiscence of one of the suture lines and is not surrounded by any layer of the native aorta. CT is a sensitive method for the diagnosis of anastomotic pseudoaneurysm after aortic reconstruction. A pseudoaneurysm is identified as an outpouching of the graft contour and is usually partially thrombosed. Perigraft flow seen after the graft inclusion technique is performed can be considered a "protected" pseudoaneurysm. However, the presence of perigraft flow after interposition techniques is more ominous because no jacket of native aorta is present to confine the flow of blood.

When the possibility of aortic graft infection is a concern, CT should be the first imaging modality performed because of its high sensitivity and specificity. However, it can be difficult to distinguish normal postoperative findings from signs of infection in the early postoperative period. Infection or fistulization with adjacent bronchi or esophagus should be suspected if gas persists longer than 6 weeks after the surgical procedure or if new or increasing gas is present, along with increasing fluid collection or enhancement. After the early postoperative period, axial images show a ring of fat density around the graft. Perigraft fluid that persists beyond 6 to 12 weeks after surgery should lead to a strong suspicion of infection.

Thoracic Aortic Stent-Grafts

The main goals of endovascular repair, as demonstrated by CT, include absence of flow in the excluded aneurysm sac and cessation of aneurysmal growth. In the immediate posttreatment phase of thoracic aneurysms, slight expansion of the aneurysm diameter, presumably related to inflammatory changes, has been reported in up to 30% of

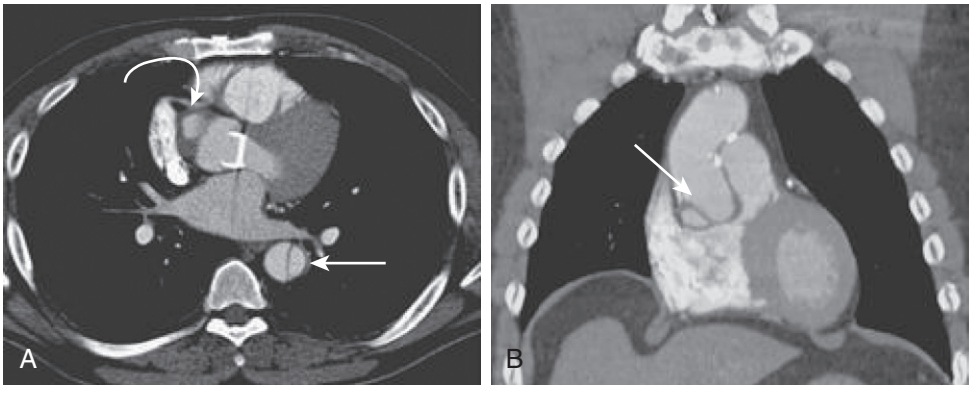


FIGURE 8-18 Postoperative complications from type A repair. **A,** An electrocardiography-gated axial computed tomography angiography image reveals outpouching of contrast *(curved arrow)* consistent with a pseudoaneurysm in the ascending aorta that was not apparent on nongated images. A dissection flap in the descending aorta is noted *(arrow)*. **B,** A coronal reformatted image better displays the pseudoaneurysm *(arrow)*.

patients. CT volumetric measurements have been shown to be more sensitive and less variable when compared with maximal diameter measurements. Cross-sectional diameter may not accurately reflect all the changes in the shape of thoracic aortic aneurysms, which can have irregular fusiform or bizarre saccular configurations.

In successful endovascular treatment of dissection, CTA immediately demonstrates obliteration of the entry tear, exclusion of flow through the intimal tear and redirecting flow exclusively into the true lumen. Follow-up CT demonstrates an interval decrease in the mean diameter of the false lumen and an increase in the caliber of the true lumen. The false lumen also demonstrates partial or complete thrombosis.

Stent-Graft Complications

CTA can accurately identify and classify endoleaks. Five described types of endoleaks include type I, flow around the graft attachment sites (proximal or distal); type II, retrograde flow from side branches into the excluded aneurysm sac; type III, graft disruption or graft malfunction; type IV, graft leaking or porosity; and type V, endotensive enlargement of the aneurysm sac without a visualized leak. An initial unenhanced scan is typically performed to avoid mistaking high-density mineralization or postoperative materials for contrast material leakage. In addition to an arterial phase, a delayed acquisition is also often performed, particularly for detecting type II endoleaks, because retrograde filling of the sac may be apparent only on the delayed phase. In addition, narrow display windows are recommended to detect subtle endoleaks. Interval increase in aneurysm diameter or sac volume can be an indirect sign of an endoleak. Axial CTA images can then confirm the presence and indicate the cause of the endoleak based on the configuration and location of the leakage in relation to the stent-graft. Type I endoleaks are readily detectable (Fig. 8-19) and can cause a substantial increase in aneurysm size and lead to rupture if undetected or untreated. However, in the early postoperative period, CTA can detect very small type I endoleaks that have a tendency to seal spontaneously. Serial CTA can be used to monitor these cases for persistent leakage and associated interval increase in aneurysm dimensions.

Type I endoleaks in thoracic aneurysms have been reported to occur when the proximal neck length is less than 2 cm, emphasizing the importance of accurate initial CT dimensional criteria. Late endoleaks typically result from dilation of the aortic neck, which should be measured on each follow-up CT scan to anticipate a potential endoleak. An interval increase usually occurs in the proximal and distal neck diameter in the first year of follow-up, but no further increases generally occur afterward. Stent migration is a less common cause of type I leak and is best depicted on orthogonal images.

Type II endoleaks result from an incompletely thrombosed aneurysm sac with retrograde perfusion by a feeding vessel, typically an intercostal artery. Serial CT usually shows spontaneous sealing or no increase in aneurysm dimensions. However, continued CT surveillance is generally recommended because of the potential risk of expansion and rupture.

Thrombosis of the stent-graft can complicate endovascular repair of the aorta. CT identifies partial thrombosis within the aortic stent-graft as nonenhancing peripheral circular or semicircular filling defects. Short-interval CT follow-up is warranted, because prognosis varies from interval resolution to complete thrombosis. Shortening in the craniocaudal axis of thetreated aneurysm, and, less commonly, stent migration, can result in kinking of the unsupported portion of the graft. MIP and MPR images are superior to axial sections in demonstrating a kink and planning repair.

Additional potentially fatal complications identified by CT are dissection and pseudoaneurysm formation. Introduction of the graft delivery system can cause iatrogenic intimal injury and a resulting false lumen. In endovascular repair of type B dissection, extension of the dissection to the ascending aorta, originating from the proximal uncovered part of

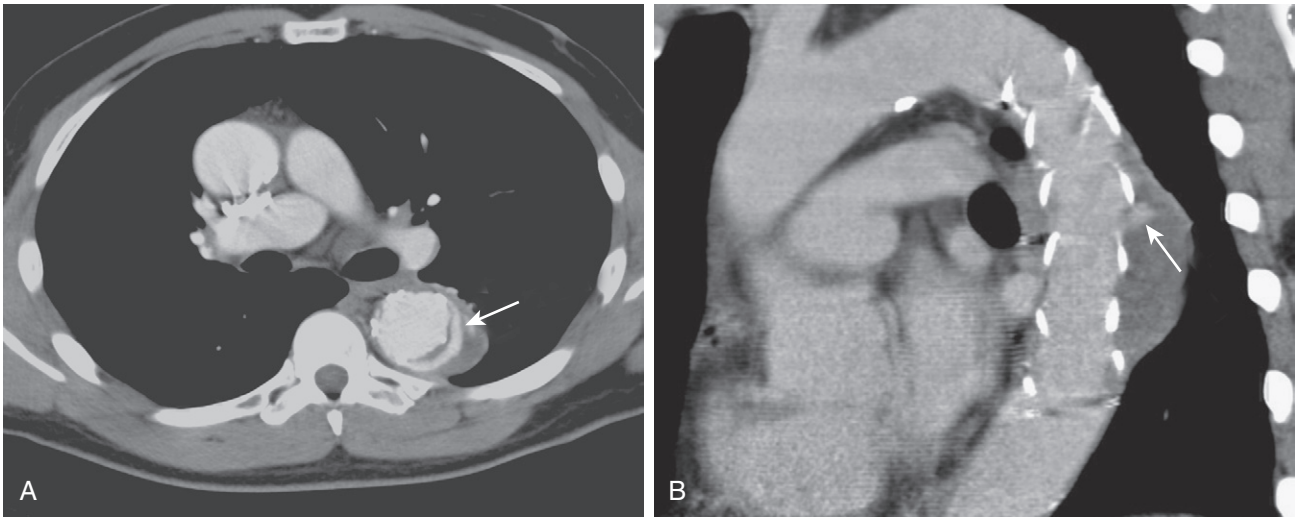


FIGURE 8-19 Endoleak after endovascular repair of enlarging penetrating aortic ulcer. **A,** An axial computed tomography angiography image shows extravasation of contrast material adjacent to the proximal edge of the stent *(arrow)*. **B,** A sagittal reformatted image shows a focal area of high density in the mid portion of the stented descending aorta, not present on precontrast images, consistent with Type III endoleak.

the stent-graft, is readily detected by CTA. Pseudoaneurysms at the anastomotic site are rarely seen with endografts but, when present, they are often detected far from the free edge of the stent-graft, possibly related to hydraulic stresses or intimal defects associated with deployment.

IMAGING EVALUATION OF PULMONARY EMBOLISM

Clinical Considerations

PE is the third most common acute cardiovascular disease after myocardial infarction (MI) and stroke and is associated with a high mortality rate. The risk of death is particularly high during the acute phase but then decreases over time. Mortality due to PE can be reduced by prompt diagnosis and treatment in the ED, as well as early prognostic stratification and identification of patients at high risk for hemodynamic deterioration.

The difficulty of diagnosing acute PE based on clinical and laboratory findings alone is why imaging studies play such a key role in the diagnostic algorithm for PE evaluation. After a brief review of the epidemiology and pathophysiology of this disease and discussion of relevant clinical findings, the different imaging modalities commonly used for evaluation are described. CT pulmonary angiography is emphasized, given its clear advantages in the ED setting. The rapid examination time afforded by CT, its widespread availability, and, perhaps most importantly, its accuracy in evaluating PE and detecting other emergent thoracic abnormalities all make it the imaging examination of choice.

Epidemiology

The incidence of venous thromboembolism (VTE; both deep venous thrombosis and PE) increases exponentially with age for both men and women. Incidence rates are somewhat higher in women of childbearing age, whereas after age 45 years, incidence rates are generally higher for men. VTE recurs frequently; about 30% of patients experience recurrence within the next 10 years. The hazard of recurrence is highest within the first 6 to 12 months.

Independent risk factors include patient age, surgery, trauma, hospital or nursing home confinement, active malignancy with or without concurrent chemotherapy, central vein catheterization or transvenous pacemaker, prior superficial vein thrombosis, varicose veins, and neurologic disease with extremity paresis. Among women, additional risk factors include oral contraceptive use, hormone therapy, pregnancy, and the postpartum period.

Pathophysiology

Thrombi present in the deep veins of the upper and, more commonly, lower extremities may dislodge and embolize to the pulmonary arteries. An increase in pulmonary vascular resistance occurs that is caused by mechanical obstruction and vasoconstriction. The alveolar dead space is increased and impairs gas exchange. As right ventricular afterload and pressure increase, right ventricular failure may ensue. Paradoxical embolism to the systemic circulation can occur in the presence of a patent foramen ovale or atrial septal defect. Pulmonary emboli are often multiple and have a predilection for the lower lobes, likely related to increased pulmonary blood flow to the lung bases. Only a minority of pulmonary emboli result in lung infarction because of the bronchial arterial collateral circulation.

Clinical Findings

Objective assessment of the clinical probability of PE should be made prior to imaging. Examples of indices used include the Wells and Geneva scores. High-sensitivity D-dimer testing has improved the specificity in the diagnosis of PE. The Prospective Investigation of Pulmonary Embolism Diagnosis (PIOPED) II investigators have published recommendations regarding the diagnostic pathways for PE, by which a normal D-dimer precludes the need for further testing in a patient with a low or moderate pretest probability of PE by clinical assessment. D-dimer testing is not called for in high-risk patients who warrant further testing. However, because D-dimer is an acute phase reactant, it has poor specificity for PE, limiting its value as a screening test during pregnancy, postoperative periods, or trauma.

Imaging Techniques

In the next sections, the imaging techniques for PE are discussed.

Chest Radiograph

Although the chest radiograph is a poor predictor of PE, it remains one of the initial steps in the workup of ED patients who present with chest pain and for whom there is clinical suspicion for PE. The chest radiograph can demonstrate other causes for presenting symptoms that mimic PE, such as pneumothorax, pneumonia, and pulmonary edema. Chest radiography plays an essential role if a ventilation-perfusion (VQ) scan is chosen as the imaging modality to confirm or exclude PE.

In the observations from the PIOPED study, the most common radiographic findings in patients with PE were atelectasis and/or parenchymal areas of increased opacity in the lower lung zones and pleural effusions. Negative findings of a chest radiograph had a negative predictive value of only 74%. Although infrequently observed, some chest radiograph findings have been described as more suggestive of PE. The Hampton sign refers to a well-defined pleural-based area of increased opacity with a convex medial border and signifies pulmonary infarction. It can help differentiate a pulmonary infarct from pleural thickening or effusion (Fig. 8-20). The Westermark sign, which refers to an area of oligemia distal to a large vessel that is occluded by PE, was found to be an uncommon but highly specific radiographic finding of PE in the PIOPED study. The Fleischner sign refers to a prominent central pulmonary artery, caused either by pulmonary hypertension resulting from peripheral emboli or by distention of the vessel by a large clot (Fig. 8-21). However, the PIOPED study concluded that no differences existed between patients with PE and those without PE with regard to most chest radiographic findings. Thus the chest radiograph cannot accurately exclude

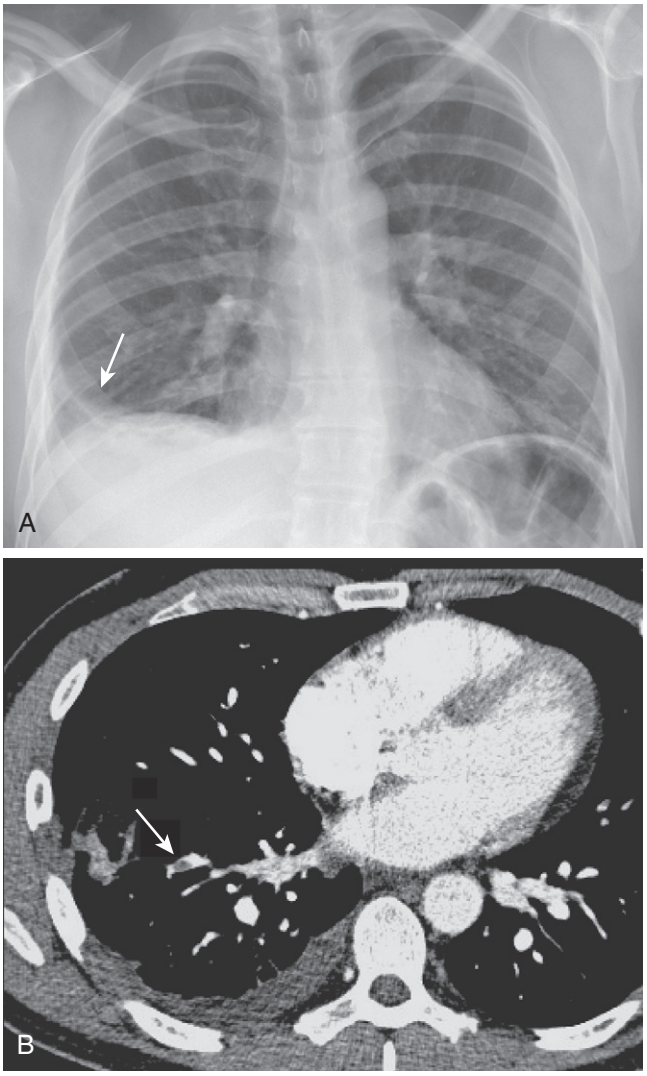


FIGURE 8-20 Atelectasis versus infarcts (Hampton sign). **A,** A posteroanterior view of the chest shows right base peripheral opacities *(arrow)* and a small right pleural effusion. **B,** Contrast-enhanced computed tomography reveals segmental and subsegmental filling defects *(arrow)* in the right lower lobe.

or confirm the presence of PE but is most useful for demonstrating alternate chest diseases and as a correlate examination for a VQ examination.

CT Pulmonary Angiography and CT Venography

CT Pulmonary Angiography. In routine practice, CTPA is considered the imaging modality of choice for evaluation of PE in an emergent setting. Multiple studies have shown it to be highly sensitive and specific for PE diagnosis, with even higher accuracy when combined with clinical assessment and D-dimer testing. It is therefore a very valuable tool for the evaluation of patients presenting to the ED in whom clinical suspicion for PE warrants imaging.

The benefits of CTPA include evaluation of the lung parenchyma, mediastinal structures, and chest wall, along with direct visualization of pulmonary emboli. Thus, in addition to high accuracy for pulmonary emboli diagnosis, CTPA can accurately detect numerous alternative or concurrent diseases such as aortic dissection, pneumothorax, pneumonia, or malignancy. For ED patients who often present with nonspecific chest complaints, this is one of the most compelling benefits of CT—the ability to broadly assess and exclude not just one but most diagnoses under clinical consideration.

Technical Factors in CTPA. When interpreting a CTPA examination, the quality of the study should be assessed and reported, because it influences diagnostic confidence. Adequate contrast opacification is essential at all levels of the pulmonary arterial tree (Fig. 8-22) to confidently assess and exclude the presence of PE. A careful and systematic evaluation at the main, segmental, and subsegmental pulmonary arterial branches is required. Volumetric acquisition and multidetector-row technology allow a relatively facile cine mode review of hundreds of images. Appropriate windowing is necessary to optimize emboli detection. With a window width too narrow, small nonocclusive emboli can be obscured. The window width and level can be appropriately adjusted until the thin pulmonary valve is visible within the contrast-opacified pulmonary artery. When it is suspected that motion artifact is simulating PE, further review in lung windows is helpful.

Diagnostic Criteria for CTPA. The following CTPA findings are used as diagnostic criteria for acute PE:

1. Complete arterial occlusion by thrombus with lack of enhancement of the lumen, with or without distension of the vessel (Fig. 8-23).
2. A partial filling defect of the vessel surrounded by contrast material, evident as the "polo mint" sign if the vessel is imaged in cross-section and as the "railway track" sign if the vessel travels within the image plane (Fig. 8-24).
3. A peripheral intraluminal filling defect that forms acute angles with the arterial wall (Figs. 8-25 and 8-26).
4. Ancillary lung parenchymal findings of acute PE, although not specific, include peripheral wedge-shaped areas suggestive of lung infarct and linear bands.
5. Ancillary cardiac findings include signs of right heart strain with right ventricular enlargement or interventricular septal bowing, as well as reflux of contrast material into the IVC and hepatic veins.

The following CTPA findings are used as diagnostic criteria for old/chronic PE:

1. Complete occlusion of the vessel (by thrombus) with vessel diameter retraction smaller than that of adjacent patent vessels.
2. A peripheral, crescent-shaped intraluminal defect that forms obtuse angles with the vessel wall.
3. Contrast-opacified, thick-walled vessels (due to recanalization), with affected vessels that may be smaller than adjacent nondiseased vessels.
4. A web or flap within a contrast-opacified vessel (Fig. 8-27).
5. Calcification within eccentric vessel thickening.
6. Ancillary lung findings that may be seen include an accompanying mosaic pattern of parenchymal perfusion, prominent bronchial or other systemic collateral vessels, pulmonary infarct, or bronchiectasis.
7. An ancillary cardiac finding is right ventricular enlargement with wall hypertrophy.

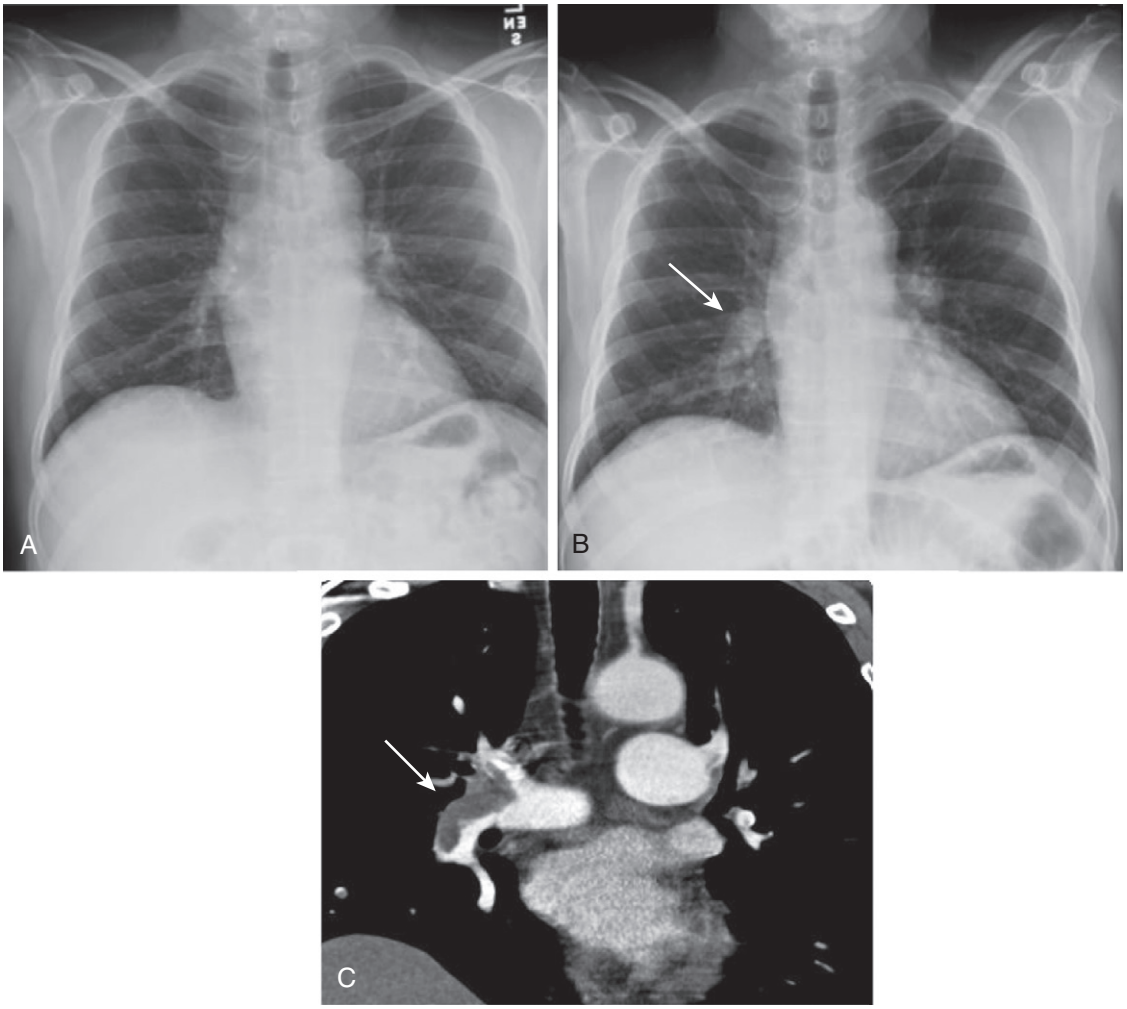


FIGURE 8-21 The Fleischner sign in a patient with acute pulmonary embolism. **A,** A frontal baseline chest radiograph. **B,** The same patient presents with acute chest pain, and a chest radiograph shows interval enlargement of the right main pulmonary artery *(arrow)*. **C,** Computed tomography angiography shows a large clot in the right main pulmonary artery expanding the vessel *(arrow)*.

CTPA Interpretation Errors. The interpreting radiologist must be aware of several potential pitfalls that can occur with CTPA, including technical, anatomic, and physiologic categories. Knowledge of these pitfalls will improve the radiologist's performance and confidence in the interpretation of CTPA.

Technique-related pitfalls include breathing artifacts and suboptimal arterial opacification resulting from an inappropriate scan delay, poor delivery of contrast material, or contrast extravasation. Knowledge of the bronchovascular segmental anatomy is mandatory to avoid anatomic pitfalls, such as mistaking a poorly enhanced pulmonary vein for an occluded artery. Segmental arteries are always seen near the accompanying branches of the bronchial tree. Knowledge of the size and location of hilar lymph nodes is of great importance because they can mimic the appearance of PE. Coronal reformations are helpful in avoiding this anatomic pitfall.

The quality of arterial enhancement in CTPA depends highly on the physiologic conditions under which the study is performed. Abnormalities of venous inflow, extrapulmonary shunts, and intrapulmonary shunts can adversely influence pulmonary arterial enhancement. Another physiologic artifact that may occur is the transient interruption of the contrast column in the pulmonary arteries, a result of increased venous return of non-opacified blood from the IVC. This phenomenon occurs in the setting of a pressure gradient from increased abdominal pressure due to the Valsalva maneuver in combination with negative intrathoracic pressure generated by deep inspiration immediately prior to imaging. Non-opacified blood enters the right atrium, diluting and potentially disrupting the contrast column in the pulmonary arteries, and even potentially simulating PE. Clues to help identify this artifact include greater opacification of both the SVC and aorta compared with the main pulmonary artery and dilution of SVC contrast material by unopacified IVC blood in the right heart. Valsalva artifact can be reduced through gentle breath-hold instructions and patient coaching. When recognized in a nondiagnostic scan, expiratory phase imaging may be performed (requiring a second bolus of contrast material) if renal function permits.

Prognostic Factors for CTPA. The main cause of 30-day mortality after acute PE is right ventricular failure. Therefore, identifying patients at high risk of right ventricular failure is important to guide appropriate treatment.

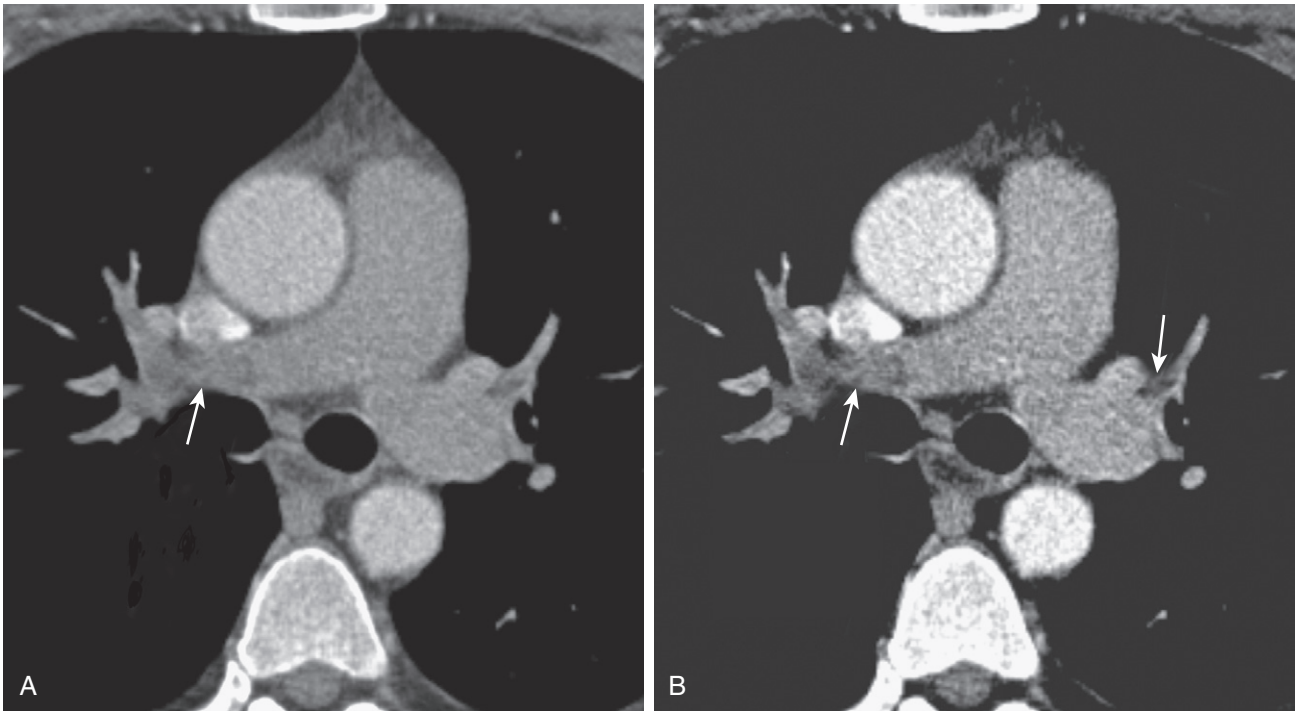


FIGURE 8-22 Poor opacification of the pulmonary arteries as a result of delayed imaging relative to the contrast bolus enhancement peak. **A,** The aorta is much more densely opacified than the pulmonary artery. Thrombus in the right main pulmonary artery *(arrow)* is difficult to discern. **B,** Using a narrower window improves visualization of the right main pulmonary thrombus *(arrow at left),* as well as a thrombus within the anterior left upper lobe segmental artery *(arrow at right).*

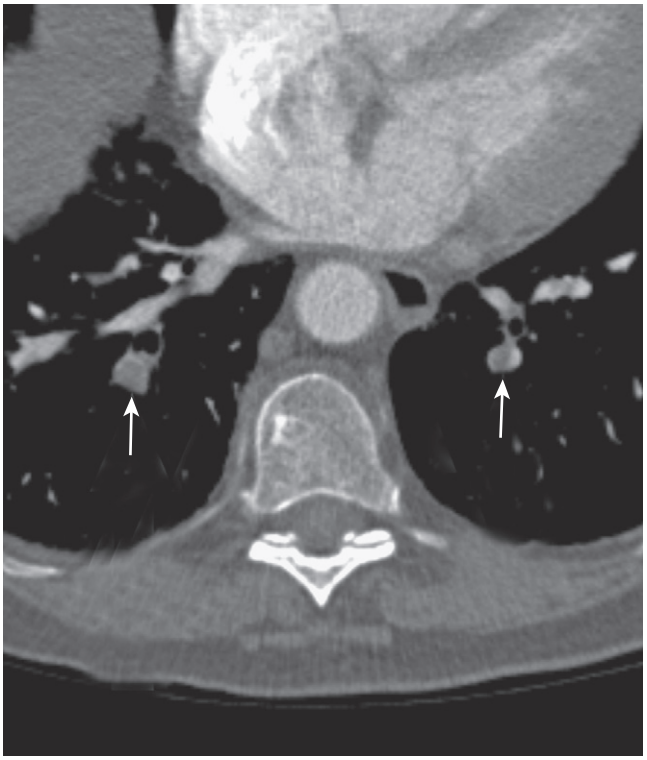


FIGURE 8-23 Acute pulmonary embolism. A right lower lobe segmental artery reveals complete occlusion by thrombus *(arrow at left).* This vessel is enlarged compared with the contralateral left lower lobe segmental artery *(arrow at right),* which also contains a large but nonoccluding thrombus.

Thrombolysis and surgical or catheter embolectomy may be performed as adjuncts to anticoagulation and may reverse right ventricular failure and reduce the risk of recurrence and death. Right ventricle enlargement in the setting of acute PE correlates with right ventricle dysfunction by echocardiography and is suspected with use of CT when the ratio of the right to left ventricular diameters exceed 0.9. The ventricular diameters are measured by identifying the maximal distance between the ventricular endocardium of the free wall and of the intraventricular septum, parallel to the tricuspid and mitral valves (Fig. 8-28). Other CTPA findings suggestive of right heart strain include reflux of contrast material into the IVC, convex bowing of the interventricular septum into the left ventricle, and increased diameter of the azygos vein and SVC.

CT Venography. Lower extremity CT venography (CTV) can provide direct imaging of the IVC, pelvic veins, and lower extremity veins immediately after CTPA. Technical limitations are not uncommon and include poor venous enhancement, mixing artifacts, and streak artifacts from orthopedic hardware.

The drawbacks of combining CTV with CTPA include a much higher volume of IVCM required to produce adequate vein opacification and the additional radiation exposure to the pelvis. As a result, most practices have abandoned CTV in favor of compression and Doppler US.

Ventilation-Perfusion Scan

VQ scan is the second-choice modality when PE is suspected, especially when IVCM administration is contraindicated as a result of allergy or renal insufficiency. For pregnant

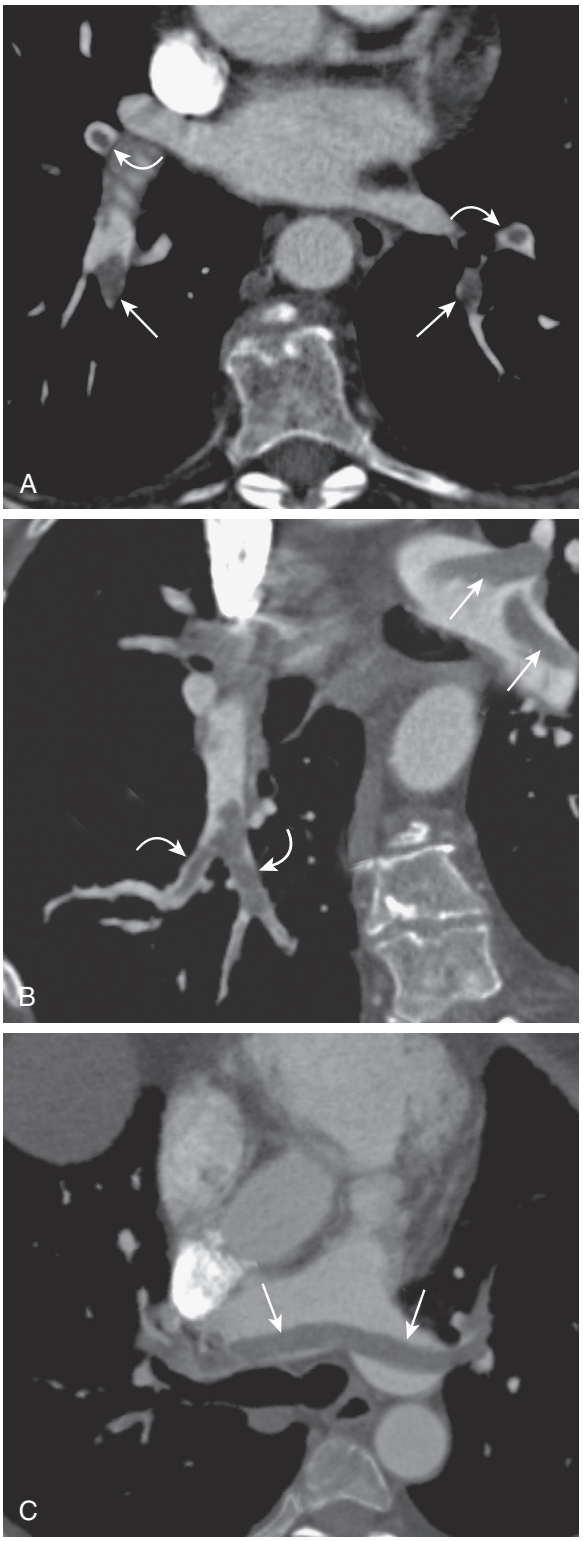


FIGURE 8-24 Acute pulmonary embolism. **A,** Bilateral lower lobe emboli exhibit the "polo mint" sign *(curved arrows)*. Partial filling defects within the vessels are surrounded by contrast material. More occlusive thrombi are seen in nearby arteries *(arrows)*. **B,** An oblique coronal reformatted image of right lower lobe pulmonary embolism showing the "railway track" sign *(curved arrows)*, the longitudinal axis equivalent of the "polo mint" sign. Left-sided emboli are also seen *(arrows)*. **C,** An oblique axial reformatted image showing a "saddle" embolus, with right and left main pulmonary emboli straddling the bifurcation *(arrows)*.

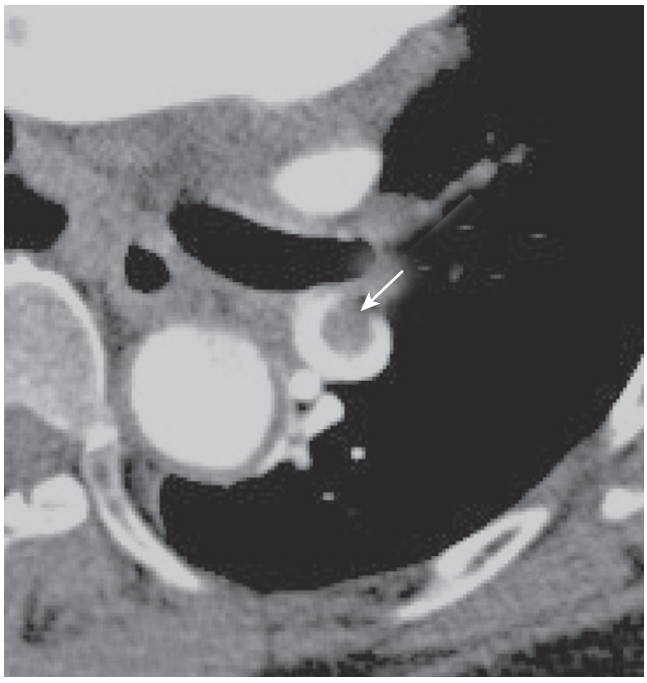


FIGURE 8-25 Acute pulmonary embolism. An axial contrast-enhanced computed tomography image showing an eccentrically positioned partial filling defect in the left interlobar artery *(arrow)*, forming acute angles with the arterial wall.

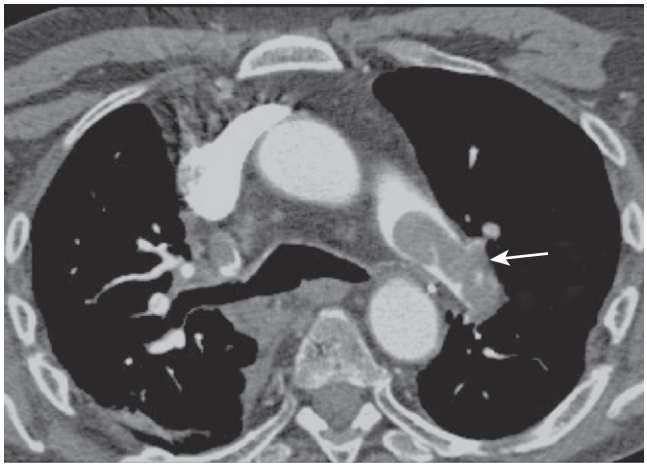


FIGURE 8-26 Acute pulmonary embolism. An axial computed tomography image shows a massive clot in the left main pulmonary artery *(arrow)*.

patients, some clinicians favor use of a VQ scan rather than CT given theoretical concerns of increased risk from maternal breast radiation.

Technetium 99m macroaggregate albumin, the radiopharmaceutical agent used for pulmonary perfusion, is injected intravenously with the patient in a supine position. If the perfusion images and the chest film are normal, the study is of low probability and the examination may be concluded. Otherwise, ventilation imaging is performed with xenon-133. The scintigraphic hallmark of PE is a perfusion defect corresponding to a bronchopulmonary segment that displays normal ventilation and with no correlating abnormality in the chest film. The modified PIOPED criteria are used for interpretation, determining

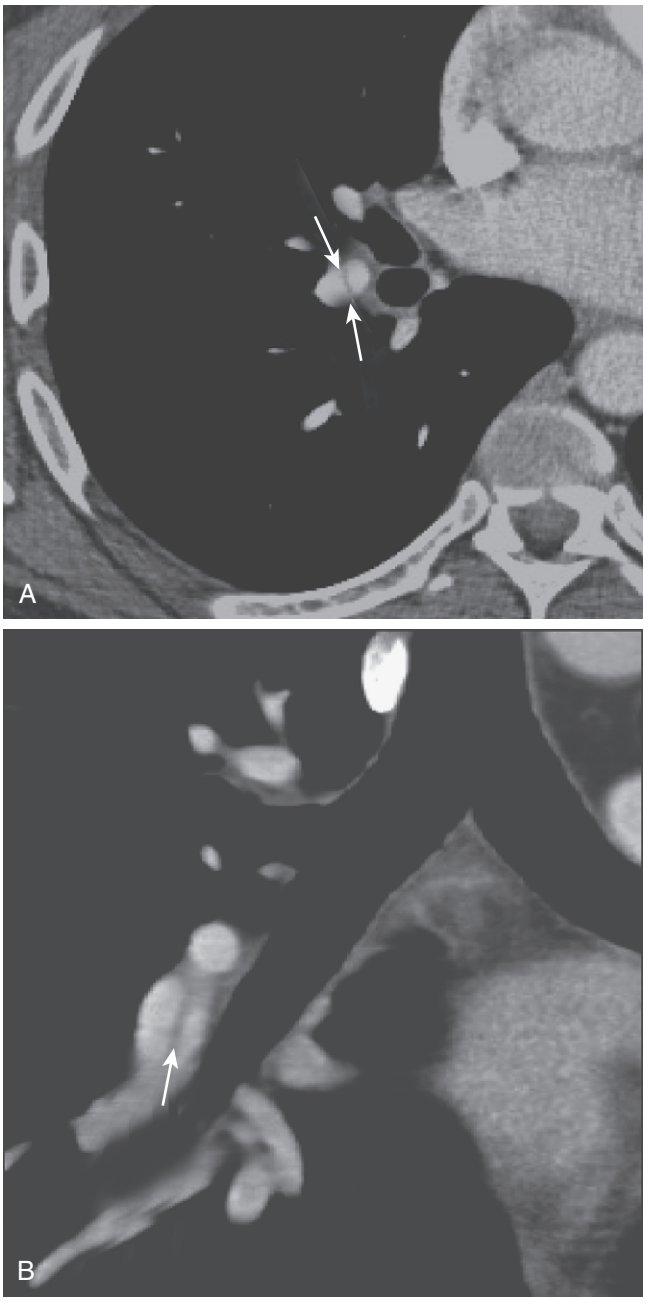


FIGURE 8-27 Chronic pulmonary embolism. **A,** An axial contrast-enhanced computed tomography image shows a linear filling defect in the right interlobar artery *(arrows)* consistent with a web in a patient with prior pulmonary embolism. **B,** Coronal reformation displays the extension of the web *(arrow)*.

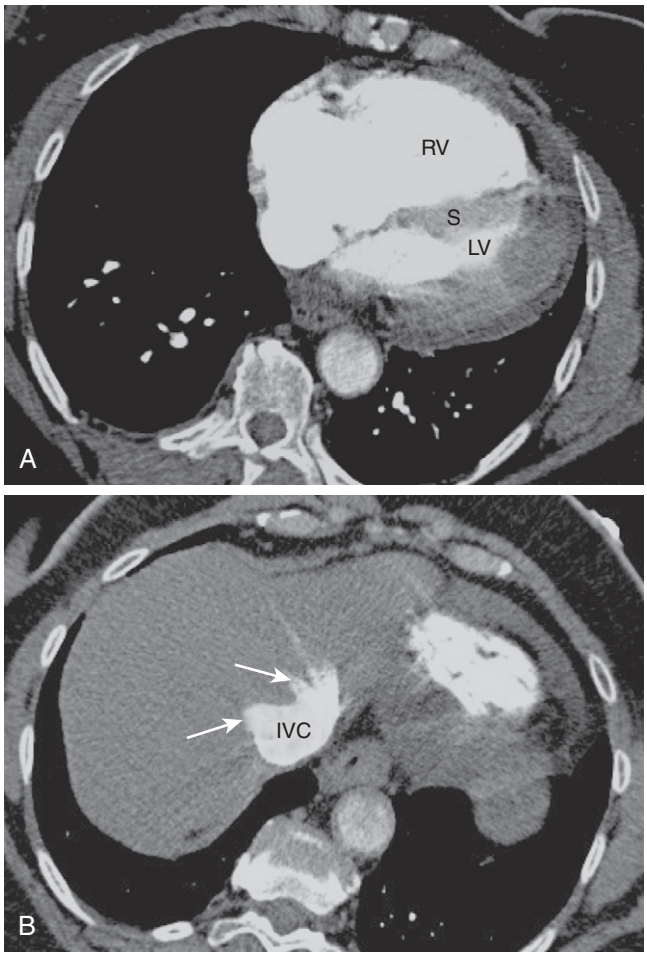


FIGURE 8-28 Right heart strain in patient with bilateral pulmonary emboli. **A,** An axial computed tomography image showing right ventricle enlargement *(RV)*. Note also straightening or leftward bowing of the interventricular septum *(S)*, with a resultant diminutive-appearing left ventricular cavity *(LV)*. **B,** An axial image at the level of the liver reveals reflux of contrast material into the inferior vena cava *(IVC)* and hepatic veins *(arrows)*.

BOX 8-1 Pulmonary Imaging Techniques

1. Chest radiograph
2. Ventilation-perfusion scan
3. Computed tomography (CT) pulmonary angiography and CT venography
4. Magnetic resonance (MR) pulmonary angiography and MR venography
5. Conventional pulmonary angiography

if the study is normal, and determining if it is of low, intermediate, or high probability (Box 8-1). This subject is discussed in depth in *Nuclear Medicine: The Requisites* and in Chapter 12.

MR Pulmonary Angiography and MR Venography

MR pulmonary angiography (MRPA) and MR venography (MRV) are considered second-line diagnostic tools (particularly in the ED) in the evaluation of PE. Practical considerations include their higher cost, limited availability, longer examination times, and reduced performance compared with MDCT. As these techniques improve further, MR imaging may play a greater role in the evaluation of patients with venous thromboembolic disease, particularly in patients who have allergies to iodinated contrast material.

MR Pulmonary Angiography. The routine use of MRPA in the evaluation of PE has been limited by technical and practical factors. Image degradation from respiratory and cardiac motion is common. High spatial resolution is necessary because of the small diameter of the pulmonary arterial branch vessels. High temporal resolution is required to produce arterial-phase-only images, thus avoiding the pulmonary venous enhancement that can obscure the evaluation of the arteries. MRPA studies are typically

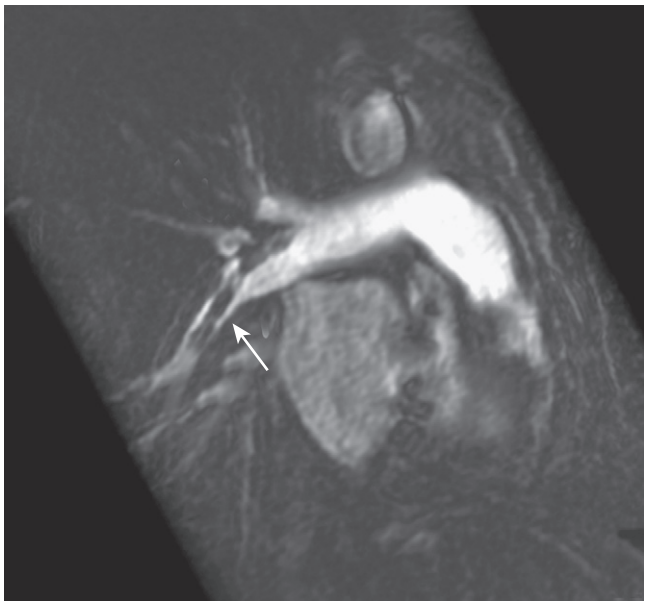


FIGURE 8-29 Acute pulmonary embolism *(arrow)*. A 56-year-old man presented with chest pain and shortness of breath. An axial oblique maximum intensity projection image of three-dimensional dynamic contrast-enhanced magnetic resonance acquisition.

performed during suspended respiration. The timing of the acquisition with respect to the gadolinium-based contrast injection can be crucial if one is to capture the pulmonary arterial phase.

According to the IRM-EP studies, MRI technology demonstrates high specificity and high sensitivity for proximal PE but limited sensitivity for distal PE and 30% are inconclusive results. Although a positive result can aid in clinical decision making, MRI cannot be used as a stand-alone test to exclude PE. The PIOPED III study concluded that MRA should be performed only in centers that routinely perform it well and in patients with contraindications for other imaging modalities. This study group also noted that a higher sensitivity was achieved when combining MRA and MRV. Emboli are detected as intraluminal filling defects or vascular cutoffs, just as in CTPA (Fig. 8-29). Major drawbacks for pulmonary MRA include cardiac and respiratory motion artifacts, losses of signal in the presence of complex blood flow patterns, and magnetic susceptibility effects from air contained in the lungs.

MR Venography. MRV, like CTV, is superior to venous US in the task of delineating the IVC and pelvic veins.

MRV can be performed without IVCM agents through use of time-of-flight MRA techniques, although gadolinium-enhanced techniques tend to provide faster acquisitions, better signal-to-noise ratio, and greater accuracy in states of slow flow or tortuous venous anatomy. Gadolinium-enhanced MRV is performed as two large field of view coronal two-dimensional (2D) or 3D gradient-echo volumes encompassing deep veins of the abdomen and pelvis, and then the thighs. The reported sensitivity and specificity of MRV in the pelvis and thighs are 100% and 95%, respectively. In the calf, the sensitivity and specificity reported are lower—87% and 97%, respectively. The combination of MRA and MRV in a single examination stands up as a strong diagnostic modality in the evaluation of thromboembolic disease.

Conventional Pulmonary Angiography

At most institutions, percutaneous, catheter-based pulmonary angiography has been replaced by CTPA as the reference standard for PE evaluation. In the emergency setting, the greater accessibility of MDCT at all times of day, along with excellent noninvasive diagnostic performance coupled with the added value of a complete assessment of the entire thorax, including most other differential diagnostic considerations, has firmly positioned it as the modality of choice. The criteria for the diagnosis of PE at conventional pulmonary angiography are similar to those at CTPA and include the findings of an intravascular filling defect or an abrupt vessel cutoff. Pulmonary angiography maintains a role in planning for catheter-based embolectomy and in some cases for surgical planning of chronic PE as a treatable cause for pulmonary hypertension.

CORONARY COMPUTED TOMOGRAPHY ANGIOGRAPHY IN THE EMERGENCY DEPARTMENT

Evaluation of Chest Pain for Exclusion of Acute Coronary Syndrome

For patients presenting to the ED with chest pain, medical imaging has been established as a primary means of delineating life-threatening entities such as acute aortic syndromes, PE, and pneumothorax. This section defines the evolving role of coronary CT angiography (CCTA) in evaluating ED patients who have chest pain potentially as a result of acute coronary syndrome (ACS) and provides a review of CT-based coronary artery anatomy, anomalies, and findings in coronary disease.

Acute Coronary Syndrome

The American Heart Association defines coronary heart disease (CHD) as a category that includes acute MI, other acute ischemic (coronary) heart disease, angina pectoris, atherosclerotic cardiovascular disease, and all other forms of chronic ischemic heart disease. The term *acute coronary syndrome* describes patients who present with either acute MI or unstable angina.

Conventional, catheter-based coronary angiography allows identification of significantly narrowed coronary arteries, or stenotic "culprit lesions," to which targeted revascularization therapy can be directed. The need for revascularization therapy of a particular culprit lesion should be supported by evidence of myocardial ischemia (using ECG, cardiac biomarkers, perfusion imaging, and stress testing, for example).

More recently, the concept of "vulnerable plaque" has gained favor; this term refers to a soft, inflammatory atherosclerotic plaque with a thin or discontinuous fibrous cap. These plaques are at risk for rupture or thrombosis, leading to coronary luminal compromise or occlusion. As a result of positive (outward) remodeling, vulnerable plaques may not be stenotic and therefore may be occult when evaluated by conventional angiography because this visualizes only the patent vessel lumen. This concept also is in evolution in that vulnerable plaques are likely numerous rather than solitary and in that disrupted, unstable, and/or ulcerated plaques extend beyond the culprit

lesion. Thus the concept of a vulnerable plaque may in fact extend further to the concept of a "vulnerable artery" or even a "vulnerable patient."

With the advent of ECG-gated multidetector and multisource CCTA, noninvasive visualization and analysis of the coronary arterial system has become feasible. CCTA has shown high accuracy in defining significant (greater than 50%) coronary stenoses, as well as the ability to detect and characterize soft and calcific plaques. Scanner technology and radiation dose reduction techniques continue to evolve, buoying the potential of CCTA as an ED triage tool for discriminating between patients with ACS and those with chest pain of other causes.

Clinical Considerations

The triage of patients who present with acute chest pain is a common task performed in the ED. Clinical findings, ECG changes, and cardiac biomarkers (troponin or creatine kinase-myocardial bound) are the current standard of care tools used to exclude ACS in these patients. Unfortunately, triage decisions based on these indices are often ineffective. Normal cardiac biomarkers upon ED presentation do not exclude ACS, and serial testing at intervals requiring up to 6 to 10 hours of hospital time is necessary to exclude MI. Furthermore, reported rates of missed ACS have ranged from 2% to 8%. Missed ACS carries a twofold increase in mortality and accounts for 20% of ED malpractice dollar losses.

Concern for missing ACS in ED patients with chest pain often prompts admission (or at least prolonged observation and testing with delayed cardiac biomarkers, stress testing, or perfusion imaging in the ED or an observation unit) of approximately 2.8 million such patients per year in the United States, at a cost of $6 to $12 billion annually. Up to 60% of these patients do not have an ACS and may be eligible for early discharge, thus highlighting the need for a rapid and more accurate triage tool for this patient population. Changes in process, technology, and staffing are being considered to improve ED throughput, but diagnostic imaging will surely continue to play a key role in achieving this goal.

CCTA shows utility as a tool that can rapidly exclude ACS in low- or intermediate-risk ED patients presenting with chest pain. CCTA has proved to be effective in visualizing calcific and soft atherosclerotic plaques, as well as in identifying significant (greater than 50%) coronary stenoses. Moreover, CCTA has shown a high negative predictive value in excluding significant coronary artery disease (CAD) and stenoses in normal or insignificantly diseased coronary arteries.

Because of its high negative predictive value, CCTA is well suited to rapidly and safely exclude CAD in low- or intermediate/indeterminate-risk patients presenting to the ED with nonspecific chest pain. Multiinstitutional trials have shown good performance of CCTA for this application, with a negative CCTA accurately indicating the absence of ACS and an extremely low risk of near-term cardiac events after ED discharge. Although CCTA is not currently in widespread clinical practice in the management of ED patients with chest pain, many sites utilize this technique, and the evolving significance of CCTA in this application warrants review in this chapter.

Coronary Artery Anatomy

The coronary arteries are the first branch vessels from the ascending aorta, located immediately above the aortic valve. The sinuses of Valsalva are three focal outpouchings between the aortic valve and the sinotubular ridge. In usual anatomy, the right coronary artery (RCA) ostium arises from the right sinus of Valsalva, and the left main coronary artery (LMA) ostium arises from the left sinus of Valsalva. The posterior or noncoronary sinus normally has no coronary ostium.

The word *coronary* is derived from the Latin *coronalis,* which means "of, relating to, or resembling a crown." The coronary arteries can be envisioned as a set of two crossing rings which encircle (or "crown") the heart, with the rings defined by the intersecting atrioventricular (AV) sulcus and interventricular septum (Fig. 8-30). Respectively, the RCA and left circumflex (LCX) arteries mirror one another and course within the right and left hemi rings of the AV sulcus, whereas the left anterior descending (LAD) artery and posterior descending artery (PDA) course within the anterior and posterior hemi rings formed over the interventricular septum (Figs. 8-31 and 8-32).

"Coronary dominance" describes which artery supplies the PDA, as well as the posterolateral left ventricular branch and the artery to the AV node. In persons with right coronary dominance (approximately 85% of the population), the RCA supplies the PDA, along with the left posterolateral branches and AV nodal artery. In persons with left coronary dominance (approximately 8% of the population), these vessels are supplied by the LCX. In codominant coronary circulation (approximately 7% of the population), both the LCX and RCA contribute to these vessels.

Right Coronary Artery

After arising from the right (or anterior) sinus of Valsalva, the RCA courses deep to the right atrial appendage within the right AV groove, following the AV groove until it intersects with the posterior interventricular septum, at the "crux" of the heart (see Fig. 8-30). For the purposes of clinical description of lesion location, the RCA is often divided into proximal (ostium to first main right ventricular branch), mid (first main branch to the acute margin), and distal (acute margin to the crux) regions. Usually, the first branch off the RCA is the conus branch; however, the conus branch often (in 23% to 51% of cases) has a separate ostium off the right sinus of Valsalva. The conus branch courses anteriorly in an arc over the conus or infundibulum and may form a collateral bridge to LAD branches (the "arc of Vieussens"), thus offering protection in cases of proximal RCA or LMA/LAD disease. The sinoatrial nodal branch/artery most commonly arises from the proximal RCA (60%) but often originates from the LCX (40%). This branch extends posteriorly along the interatrial groove and supplies branches to both atria, as well as the sinoatrial node. The right ventricular, or acute marginal, branches emerge at right or acute angles from the RCA and vary in size and number as they supply the right ventricular myocardium. In right dominant circulations, the RCA continues in the AV sulcus until it intersects with the posterior interventricular septum at the crux, where the RCA gives off the PDA branch that courses along the posterior interventricular septum, supplying

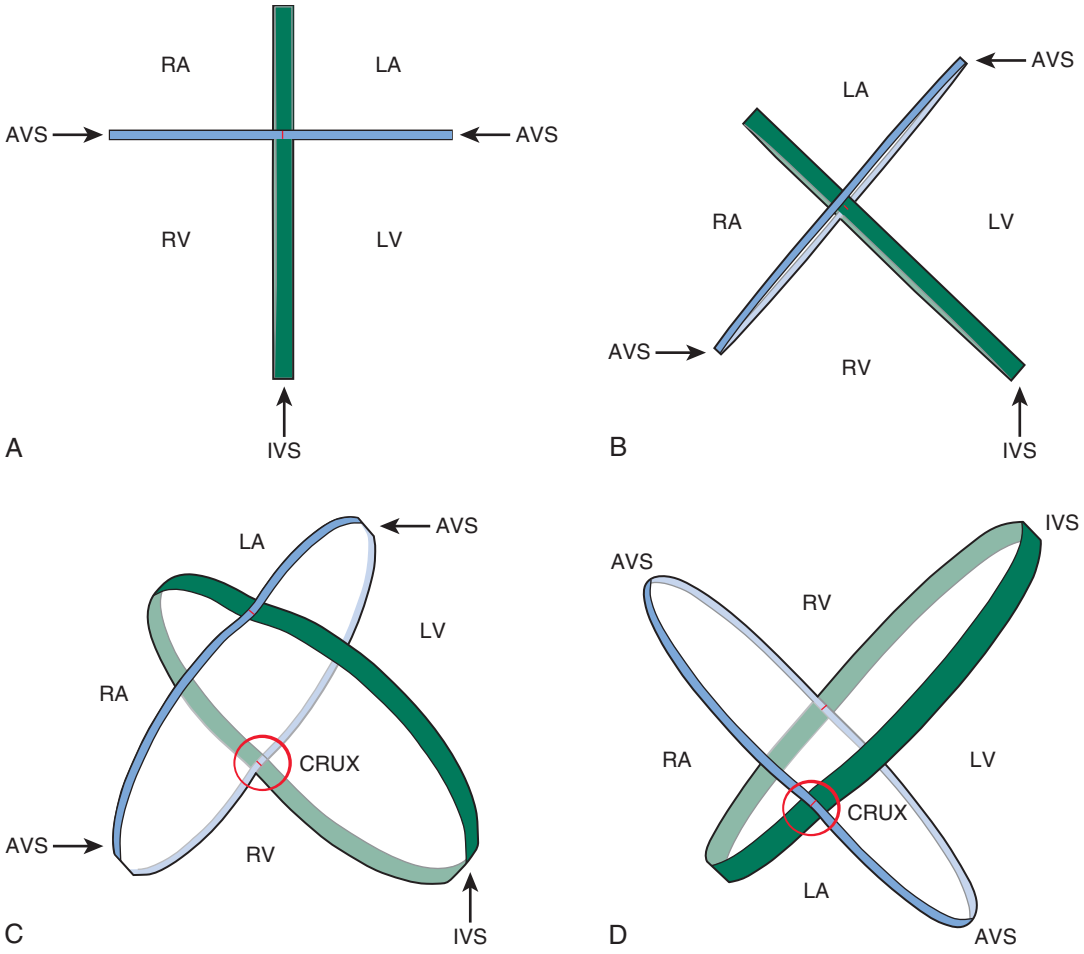


FIGURE 8-30 Crossing ring diagrams of the coronary arteries. **A,** The architectural skeleton of the heart and coronary arteries can be envisioned as a set of "crossing rings," with the atrioventricular sulci *(AVS)* and interventricular septum *(IVS)* defining the planes within which the crossing rings (and coronary arteries) lie. **B,** As viewed from the front, the heart is "tilted" within the thorax, or oriented such that the IVS points inferolaterally toward the left. **C,** When viewed from the front, the heart is rotated about the IVS long axis such that the right atrium *(RA)* and right ventricle *(RV)* are positioned more anteriorly relative to the left atrium *(LA)* and left ventricle *(LV)*. **D,** Finally, viewed inferiorly, as in a standard axial computed tomography image, the RV is positioned relatively anterior, the LA relatively posterior, and the LV and RA toward the patient's left and right, respectively. The right coronary artery (RCA) and left circumflex arteries course within the right and left atrioventricular sulci, respectively. The left anterior descending and the posterior descending arteries (PDA) course over the anterior and posterior aspects of the interventricular septum, respectively. The posterior junction of the AVS and IVS is termed the "crux" and is the point where the RCA (in a right dominant circulation) takes a downward turn to supply the PDA.

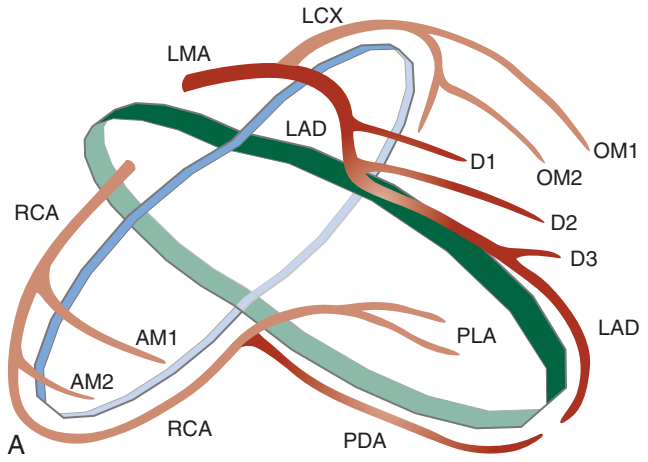
the lower third of the interventricular septum, as well as posterolateral branches (which supply the inferior wall of the left ventricle and the interventricular septum) and the AV nodal branch (which extends cephalad from the crux to the AV node).

Left Main Coronary Artery

The LMA arises from the left sinus of Valsalva and follows a short (usually 1- to 2-cm) course between the pulmonary trunk anteriorly and left atrial appendage posteriorly (Fig. 8-33). It normally bifurcates into the LAD and LCX arteries but may trifurcate with a third intermediate artery arising between the LAD and LCX. This intermediate artery has various names, including "ramus intermediate" or "ramus medians," "median artery," "left diagonal artery," and "straight left ventricular artery," and it supplies different portions of the anterolateral left ventricular wall.

Left Anterior Descending

The LAD arises from the LMA and courses around the left side of the pulmonary trunk toward the proximal interventricular septum, where it takes a roughly 90-degree downward turn and courses over the interventricular septum toward the apex (see Fig. 8-33). This downward turn over the proximal interventricular septum has clinical significance, because this is the point where the LAD becomes amenable to surgical bypass. The second diagonal branch often originates near this downward turn. By convention, the LAD is divided into three segments: proximal (LAD origin to first septal perforator), middle (first septal perforator to downward turn along interventricular sulcus/origin of second diagonal), and distal (second diagonal origin to vessel end). The LAD provides two major types of branches: the septal perforators, which generally arise at 90-degree angles from the LAD and penetrate into the



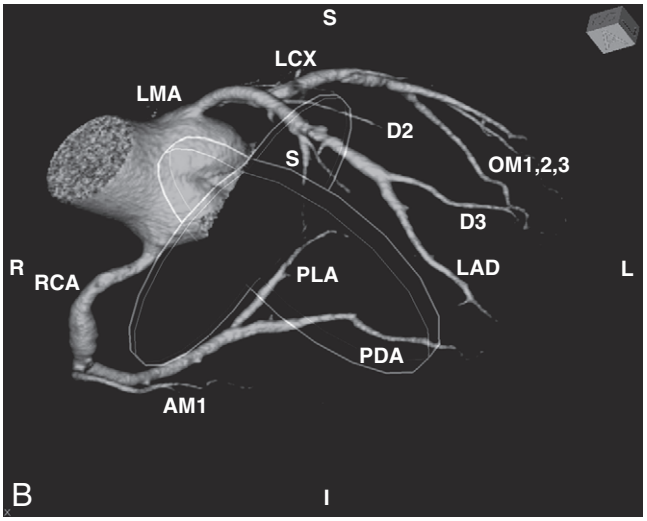


FIGURE 8-31 Coronary arteries applied to the crossing ring diagram. **A,** A diagram of the coronary arterial tree (right dominant circulation) superimposed on a frontal view of the "crossing ring" atrioventricular sulci *(AVS)* and interventricular septum *(IVS)* architectural skeleton. The right coronary artery *(RCA)* arises from the aortic right sinus of Valsalva and courses within the right AVS to the crux, where it gives off the posterior descending artery *(PDA)* branch (which travels under the inferior margin of the IVS), as well as posterolateral branches (posterolateral artery *[PLA]*, which supply the inferior and inferolateral left ventricle walls). The acute marginal (*AM1, AM2,* and so on) branches off the RCA supply the right ventricle walls. The left circumflex artery *(LCX)* arises from the left main coronary artery *(LMA)* and mirrors the RCA as it courses within the left AVS. It supplies obtuse marginal (*OM1, OM2,* and so on) branches, which perfuse the lateral wall of the left ventricle. The LMA arises from the left sinus of Valsalva. The left anterior descending *(LAD)* artery (essentially a continuation of the LMA) turns to course over the anterior aspect of the IVS and usually continues over the cardiac apex. The LAD supplies diagonal branches (*D1, D2, D3,* and so on), which perfuse the anterior, and anterolateral, walls of the left ventricle. **B,** A three-dimensional reformatted image of coronary computed tomography angiography superimposed on a frontal view of the "crossing ring" architectural skeleton. Vessels are labeled as in Figure 31, *A*. D1 is very small and not labeled, seen just above D2. The vessel labeled "S" is a large septal perforator arising from the LAD. The three OM branches are prominent, and the LCX is not seen beyond the OM3 origin. In a left dominant circulation, the LCX would continue to the crux to supply the PLA and PDA branches.

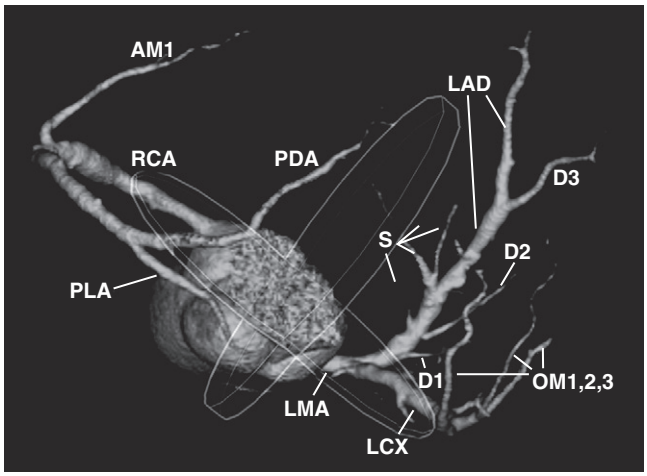


FIGURE 8-32 An axial view of the coronary arteries. A three-dimensional reformatted image of coronary computed tomography angiography as viewed from the inferior aspect of a patient, as in a standard axial computed tomography image, superimposed on a diagram of the architectural skeleton of the atrioventricular sulci *(AVS)* and interventricular septum *(IVS)*. The right coronary artery *(RCA)* arises from the right sinus of Valsalva at approximately the 10- to 12-o'clock position, and the left main coronary artery *(LMA)* arises from the left sinus of Valsalva generally at the 2- to 5-o'clock position. The RCA and left circumflex artery *(LCX)* course within the right and left AVS, respectively, and the left anterior descending *(LAD)* artery and posterior descending artery *(PDA)* course over the anterior and inferior borders of the IVS, respectively. On an axial image, the diagonal branches (*D1, D2,* and so on) extend toward the patient's left from the LAD, and the septal perforators *(S)* extend toward the patient's right from the LAD. *AM,* Acute marginal; *OM,* obtuse marginal.

interventricular septum to supply the upper two thirds of the septum, and the diagonal (D) branches, which arise at acute angles from the LAD to course over and supply the anterior/anterolateral wall of the left ventricle. The number of diagonal arteries varies, and they are named in order of their origin from the LAD (e.g., D1, D2, and so on). The LAD usually extends over the apex to supply the distal inferior wall and interventricular septum, but the PDA may supply these regions as well, and this distal LAD-PDA confluence is a source of potential collateralization in cases of RCA or LAD disease.

Left Circumflex

The LCX arises from the LMA, and its course mirrors that of the RCA as it courses under the left atrial appendage to follow the left AV sulcus toward the crux. The major branches off the LCX are the marginal (or obtuse marginal) branches, which vary in size and number. The obtuse marginal (OM) branches overlie and supply the lateral wall of the left ventricle and are labeled according to the order of their origin off the LCX (e.g., OM1, OM2, and so on). For clinical description, the LCX is divided into three segments: proximal (from the LCX ostium to the first major obtuse marginal branch [OM1]); mid (between OM1 and OM2); and distal (vessel distal to OM2). In a right dominant circulation, the LCX will terminate short of the crux, whereas in codominant and left dominant circulations, the LCX will make respectively greater contributions to the PDA, posterolateral artery, and AV nodal circulations.

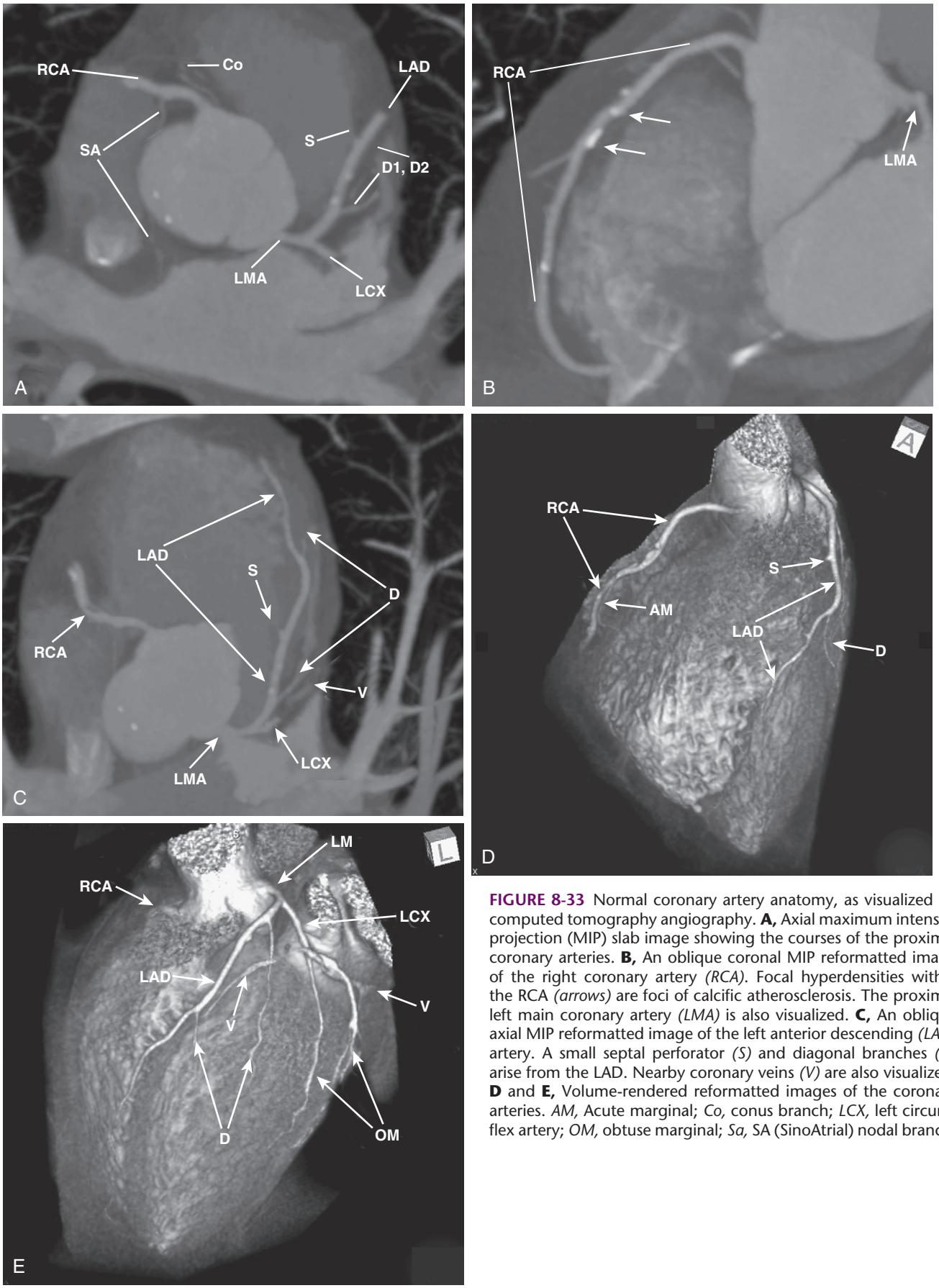


FIGURE 8-33 Normal coronary artery anatomy, as visualized by computed tomography angiography. **A,** Axial maximum intensity projection (MIP) slab image showing the courses of the proximal coronary arteries. **B,** An oblique coronal MIP reformatted image of the right coronary artery *(RCA)*. Focal hyperdensities within the RCA *(arrows)* are foci of calcific atherosclerosis. The proximal left main coronary artery *(LMA)* is also visualized. **C,** An oblique axial MIP reformatted image of the left anterior descending *(LAD)* artery. A small septal perforator *(S)* and diagonal branches *(D)* arise from the LAD. Nearby coronary veins *(V)* are also visualized. **D** and **E,** Volume-rendered reformatted images of the coronary arteries. *AM,* Acute marginal; *Co,* conus branch; *LCX,* left circumflex artery; *OM,* obtuse marginal; *Sa,* SA (SinoAtrial) nodal branch.

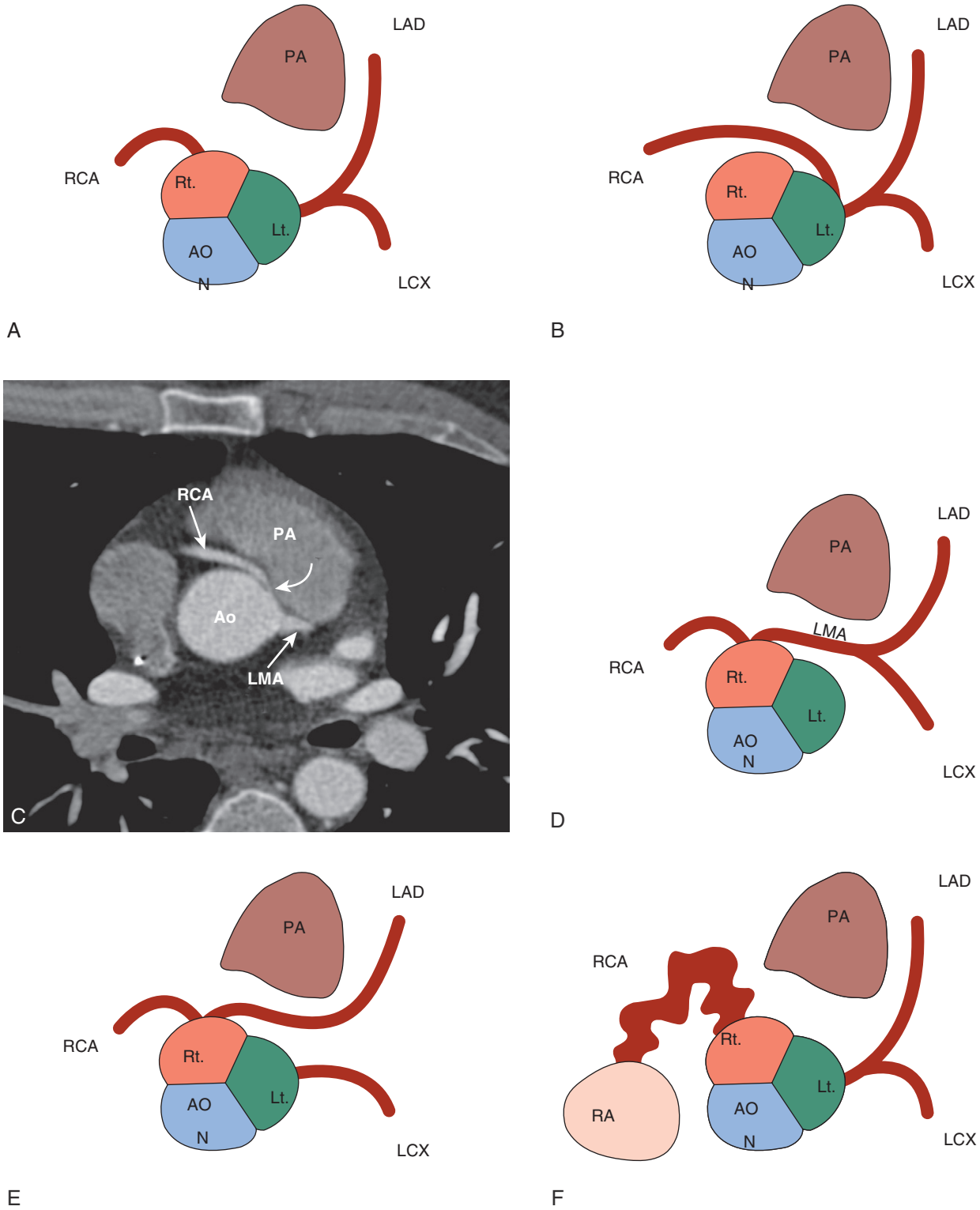


FIGURE 8-34 Diagrams of coronary artery variants, as they would be visualized on axial computed tomography images. **A,** Diagram of normal proximal coronary artery anatomy. Normally, the right coronary artery *(RCA)* arises from the right coronary sinus *(Rt)*, and the left main coronary artery *(LMA)* (which supplies the left circumflex artery *[LCX]* and left anterior descending *[LAD]* artery) arises from the left coronary sinus *(Lt)* of the aorta *(Ao)*. **B–F,** Examples of malignant "interarterial" anatomic variants. These variants portend increased risk for clinical symptoms or sudden cardiac death. The RCA may arise from the left sinus of Valsalva and course between the aorta and pulmonary artery *(PA)* **(B)** to achieve its normal right AVS position. **C** is an axial source image from a patient with this variant. Note the acute angle take-off and narrow ostial area of the anomalous RCA *(curved arrow)* compared with the normal LMA. The position of the anomalous interarterial RCA between the aorta and pulmonary artery also results in increased risk of RCA compression, especially during exercise. Conversely, either the LMA **(D)** or the LAD **(E)** may arise from the right sinus of Valsalva and follow an interarterial course. Coronary anomalies resulting in a shunt **(F)** include coronary atrioventricular (AV) fistulas and coronary artery origins from the PA. These variants predispose to ischemia or symptoms/sudden death and are thus considered *malignant*. **F** is a diagram of an AV fistula, with dilated RCA draining to the right atrium *(RA)*, rather than draining normally into the coronary sinus and left atrium. *N,* Non-coronary cusp.

Coronary Artery Anomalies

Coronary artery anomalies are a heterogeneous constellation of anatomic variants (Fig. 8-34). Although relatively uncommon (occurring in 0.46% to 5.6% of the normal population), certain forms carry elevated risk, making it important for the radiologist to detect and accurately define these variants. In particular, coronary anomalies cause up to 19% to 30% of sudden deaths in athletes. CCTA is superior to conventional angiography in delineating the ostial origin and proximal path of anomalous coronary arteries. Anomalies may be classified by the presence or absence of a shunt, or they may be classified as "malignant" or "nonmalignant" depending on their course and propensity to cause clinical symptoms or sudden death.

Anomalies not resulting in a shunt include anomalous coronary artery origins (e.g., origin from another coronary artery, another sinus of Valsalva or above the sinotubular ridge, and independent branch origins from the sinus of Valsalva), myocardial bridges, congenital aneurysms, and hypoplasia/atresia. Anomalies resulting in a shunt include artery origin from the pulmonary artery (called *Bland-White-Garland syndrome* for the LMA) and fistulas.

Malignant variants (associated with an increased risk of MI and sudden death) primarily consist of anomalous artery origins that result in an interarterial course, with the anomalous artery coursing between the aorta and pulmonary artery (see Fig. 8-34). Several factors contribute to jeopardizing the anomalous vessel in this position, including compression of the vessel between the aorta and pulmonary artery, especially during exercise, and acute-angle takeoff and narrow ostial area of the proximal vessel, resulting in diminished flow or occlusion. The most common interarterial variant is the RCA arising from the left sinus of Valsalva and coursing between the aorta and pulmonary artery to reach the right AV sulcus, although an LMA or LAD arising from the right sinus of Valsalva with an interarterial course may pose a higher risk to the patient. Anomalous coronary artery origin from the pulmonary artery is also considered malignant and is associated with myocardial ischemia and sudden death in early childhood.

Myocardial bridging occurs when a coronary artery (usually the middle third of the LAD) deviates from a normal epicardial course to reside under superficial myocardial fibers for a short distance before reemerging to a normal epicardial position (Fig. 8-35). The prevalence and clinical significance of myocardial bridging are nebulous. Whereas angiographic series report prevalence between 0.5% and 2.5%, pathologic series have reported prevalence between 15% and 85%. Generally thought to be benign, any specific case of myocardial bridging may have clinical significance, and cases have been associated with angina, myocardial ischemia and infarction, and sudden death. CCTA is effective

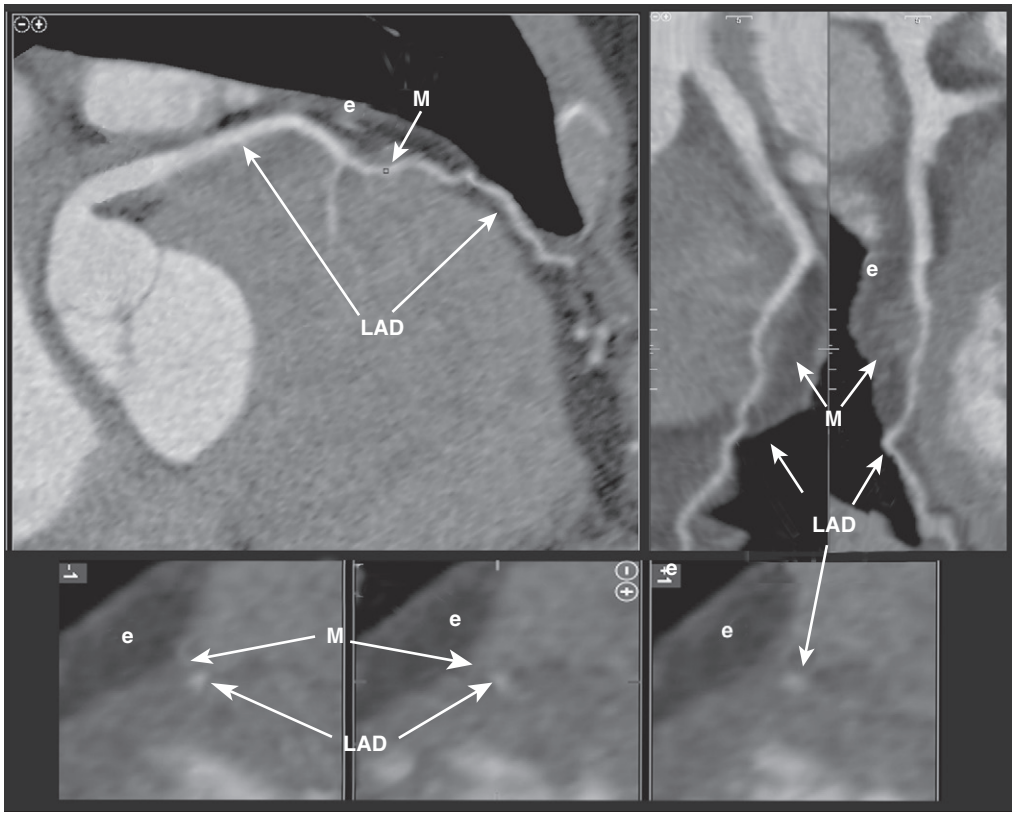


FIGURE 8-35 Example of myocardial bridging of the left anterior descending *(LAD)* artery. Long axis maximum intensity projection *(top left)*, long axis curved multiplanar reformatted images *(two top right images)*, and cross-section reformatted images *(bottom row of three images)* of the LAD. The proximal LAD is in its normal position within the epicardial fat *(e)* overlying the interventricular septum. However, the LAD deviates from its normal epicardial course to course under superficial myocardial fibers *(M)* for a short distance before reemerging to assume its normal epicardial course. The bottom row of cross-section reformatted images shows a "bridge" of myocardial fibers overlying the LAD at the level of the myocardial bridging. The myocardial fibers separate the LAD from the epicardial fat.

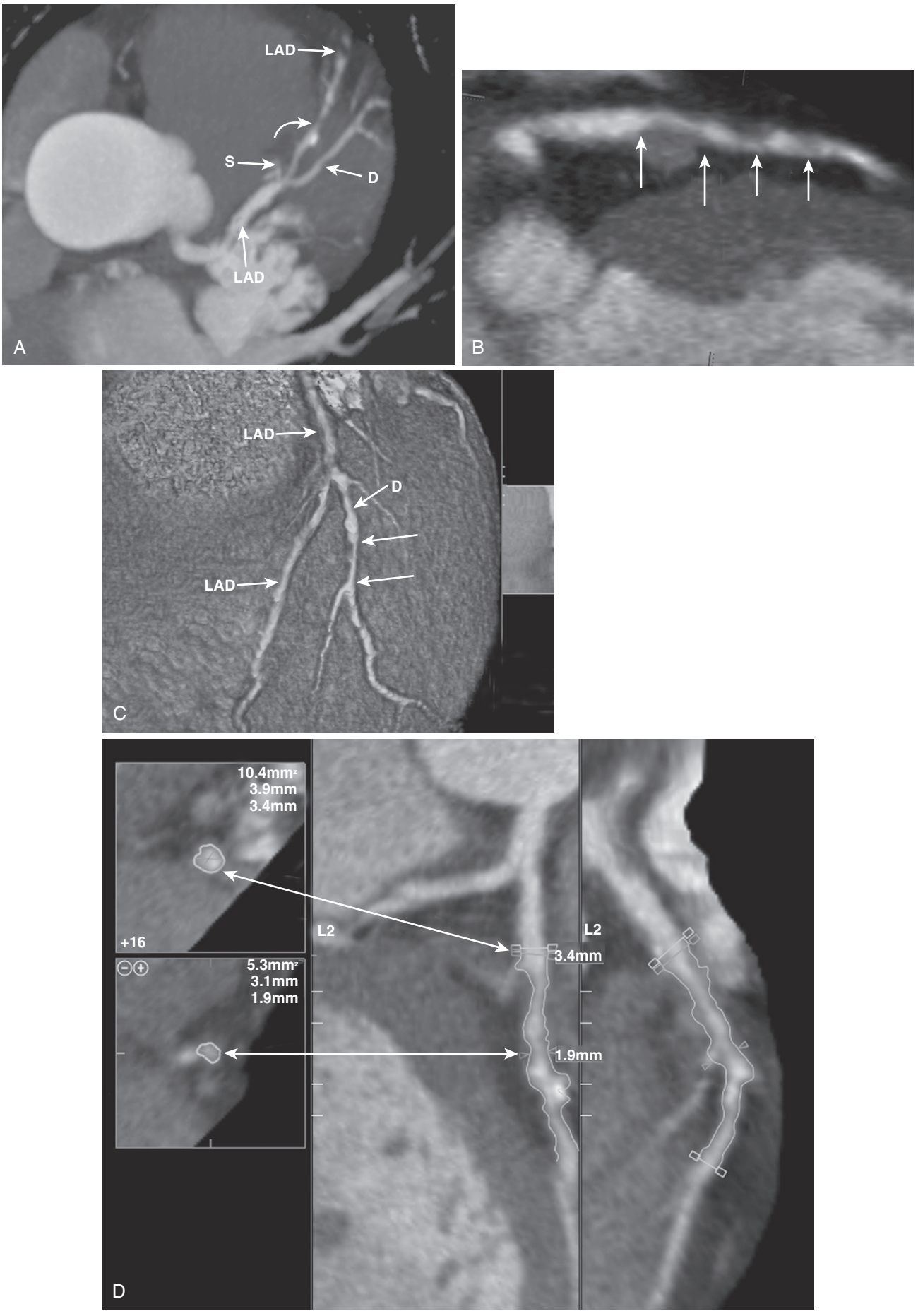

LAD
S
D
LAD
A
B
LAD
D
LAD
C
10.4mm²
3.9mm
3.4mm
+16
5.3mm²
3.1mm
1.9mm
L2
L2
3.4mm
1.9mm
D

FIGURE 8-36 Examples of coronary artery stenosis. **A,** An oblique axial maximum intensity projection reformatted image of the left anterior descending *(LAD)* artery reveals disease beyond the origins of septal *(S)* and diagonal *(D)* branches. A significant appearing stenosis is noted *(curved arrow)*. **B,** An oblique long axis reformatted image through a diagonal artery in another patient shows a severe stenosis *(between the two long arrows)*. Areas of apparent stenosis or occlusion are artifactual, related to volume averaging with adjacent epicardial fat *(small arrows)*. **C,** Volume-rendered reconstruction of the diagonal artery stenosis *(between long arrows)* seen in **B. D,** An example of software-assisted quantitative assessment of coronary stenosis. Middle and right images are orthogonal long-axis curved multiplanar reformatted images through the vessel (LAD in this case), and the two left images are short-axis cross-sectional reformatted images through the vessel. Double-headed arrows indicate the levels of the cross-section reformatted images relative to the long-axis images. The software can automatically detect the "edge" of the coronary artery (based on a threshold of attenuation or attenuation difference) and draw a line at the detected borders. With the vessel borders defined, the diameters and cross-sectional areas at any particular point can be calculated, and with these values the severity of stenosis can be quantified.

at diagnosing myocardial bridging because of its ability to visualize the myocardium and the coronary arteries. The ability to image in diastolic and systolic phases may help gauge the clinical significance by defining the severity of luminal compromise during systole. Interestingly, the bridged segment is often free of atherosclerotic disease. Because of this potential for clinical significance, myocardial bridging warrants reporting when encountered.

Coronary artery fistulas are abnormal communications between a coronary artery and another vascular structure such as the right ventricle (45%), the right atrium (25%), a pulmonary artery (15%), or the SVC, left atrium, or left ventricle (in less than 10% of cases; Fig. 8-35). The involved coronary is often dilated and tortuous, and the anomalous connection may result in a left-to-right shunt, a hemodynamic steal phenomenon, and hypoperfusion or ischemia of the myocardium normally perfused by the involved vessel.

Image Evaluation

The function of CCTA is to detect or exclude the presence of CAD in a patient with chest pain, a potentially important triage tool in the ED. CCTA detects CAD primarily by defining two findings: coronary artery stenoses and mural atherosclerotic plaque. These two findings permit the radiologist to exclude or confirm CAD in ED patients. Ancillary evaluation depends on scanning technique and software availability and includes evaluation of left ventricular wall motion and function (which bestows important physiologic/functional correlation with coronary artery findings) and possibly evaluation of myocardial perfusion defects (scar/ischemia imaging) or delayed enhancement (scar/viability imaging). This section focuses on coronary stenosis and mural atherosclerotic plaque.

Coronary Artery Stenosis

Because neither CCTA nor conventional angiography can measure the hemodynamic effect of a particular lesion, the degree of stenosis is used as a surrogate to determine lesion significance. The CCTA threshold most often used to define a significant stenosis is 50% or greater luminal narrowing, using a nearby "normal" segment of the vessel as a reference. A 50% stenosis by CCTA corresponds to approximately 70% stenosis on conventional planimetric angiography.

While acquiring an ECG-gated CCTA examination, images are obtained in each of (generally) 10 to 20 phases throughout the cardiac cycle. Images from the (usually diastolic) phase in which the least coronary motion artifact is present are then used for image analysis. To evaluate CCTA images, review of the axial images, as well as MPR and MIP images, is performed (Figs. 8-36 and 8-37). Although reformatted images are valuable in defining and delineating stenoses, the axial images remain the cornerstone of the evaluation, because virtually all diseases can be identified on the axial images. Once a stenosis is detected on the axial images, further evaluation of the lesion is best performed with two long-axis reformats through the vessel. Generally, 3- to 5-mm thin-slab MIP images are also useful for evaluating lesions in the long axis, and interactive evaluation is facilitated with sliding or rotating thin-slab MIP images. The interpreter should be aware that when using MIP images, stenoses may be masked or obscured by volume averaging.

Once detected, a stenosis can be visually measured, or estimated, using a nearby "normal" segment of the vessel as a reference, or software-assisted quantitative assessment of the stenosis may be used (Fig. 8-36). Comparison of the visual estimate/measurement method versus quantitative software-assisted assessment of stenoses has revealed that software-assisted assessment provides higher accuracy for about the same user time required for visual estimation. However, although 64-slice CCTA has shown high accuracy in detecting 50% or greater stenoses, the ability to provide exact, quantitative measures of stenosis severity is hampered by current limits in spatial resolution. As a result, the severity of stenoses is often classified in quartiles (0% to 25%, 26% to 50%, 51% to 75%, and 76% or greater) or tertiles (0% to 30%, 31% to 70%, and 71% to 99%), or some other variant, depending on local radiologist/cardiologist preferences.

Despite this relative lack of quantitative accuracy, CCTA has proven highly accurate in detecting 50% or greater stenoses and has shown high negative predictive values (generally 95% to 100%) in excluding significant coronary disease. Because the ED chest pain patient population evaluated by CCTA should have a low prevalence of disease (i.e., patients with low or intermediate risk of ACS who have normal cardiac biomarkers and ECGs), the majority of CCTA scans performed for ED patients should be essentially normal, which should facilitate more rapid image evaluation/interpretation and thus more rapid discharge or appropriate treatment for non-ACS ED patients with chest pain.

Atherosclerotic Plaque Imaging

The presence of coronary artery plaque increases ACS risk even in the absence of coronary artery stenoses. Although

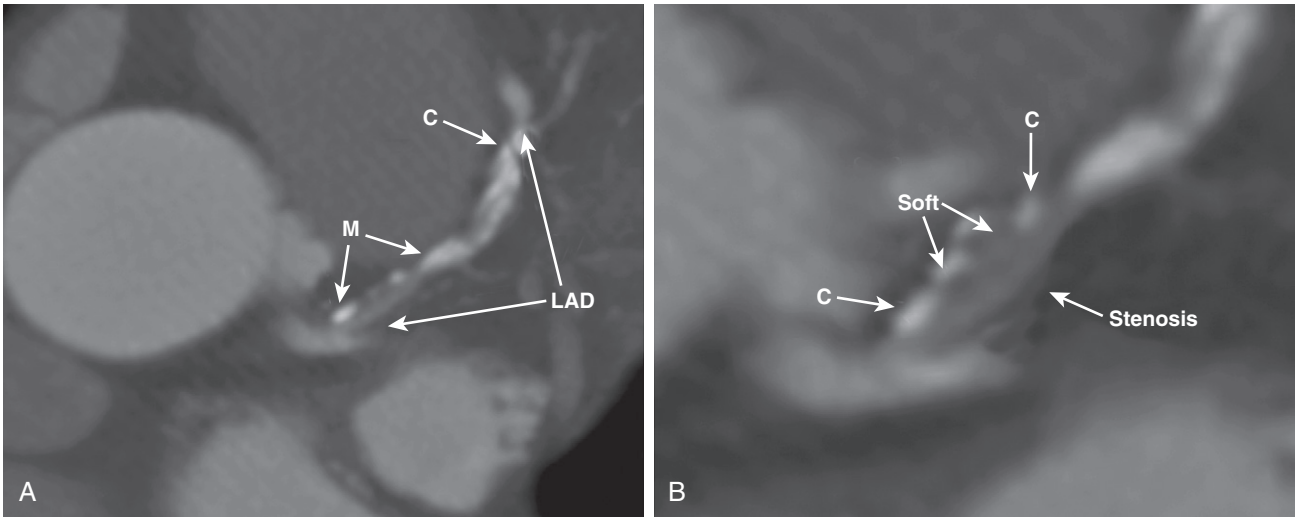


FIGURE 8-37 Coronary artery atherosclerotic plaque, as visualized by computed tomography angiography. **A,** A diffusely diseased left anterior descending *(LAD)* artery reveals hyperdense calcific *(C)* atherosclerotic plaque, as well as mixed *(M)* "soft" and calcific atherosclerotic plaque. The mixed plaque appears to be causing stenosis. **B,** A magnified image of **A,** showing components of the mixed plaque. Calcific components *(C)* appear as hyperdense relative to the opacified vessel, whereas the "soft" components *(Soft)* are hypodense. The mixed plaque is causing stenosis of the vessel.

a higher total volume or burden of atherosclerotic plaque carries a higher ACS risk, different types of plaque also impart different levels of ACS risk, because plaque vulnerability varies depending on plaque composition. Histologically, atherosclerotic plaque consists of numerous components, including calcification (generally calcium hydroxyapatite), fibrous tissue, inflammatory cells (predominantly macrophages and monocytes), smooth muscle, lipid components (such as lipid-laden macrophages and necrotic lipid cores), and hemorrhagic foci.

Both major and minor histologic criteria for defining plaque vulnerability have been described. Major histologic criteria include active inflammation, a thin cap with a large lipid-necrotic core, endothelial denudation with platelet aggregation, fissured plaques, and stenosis larger than 90%. Minor histologic criteria include superficial calcified nodules, glistening yellow plaque (seen at angioscopy), intraplaque hemorrhage, endothelial dysfunction, and positive (outward) remodeling.

For coronary plaque analysis, CCTA has inherent limits in spatial and contrast resolution that prevent discernment of many of the components of plaque. However, calcium is well defined by CCTA and can be distinguished from "soft" plaque components (Fig. 8-37). Coronary calcium scoring, or quantification of calcific coronary atherosclerotic plaque utilizing electron beam and MDCT, has been in use for more than a decade. Generally, a threshold of 130 HUs is used to define calcified atherosclerotic plaque. "Soft" or noncalcified plaque can be discerned from calcified plaque on CCTA in this manner. Noncalcified soft plaque is heterogeneous in composition, consisting of various quantities of components as previously described. On CCTA, soft coronary artery plaque is visualized as a structure that can be clearly assignable to the vessel wall (in at least two views) with densities less than the intraluminal contrast (Fig. 8-37). On CCTA, plaque is generally classified as calcified, noncalcified, or mixed.

Whereas CCTA has only limited ability to define the specific composition of noncalcified plaque, lower CT density generally indicates a greater lipid concentration, and, in fact, larger lipid pools or lipid cores (larger than 2 mm) may be visualized within the plaque of larger coronary arteries as hypodense spots demonstrating a density of at least 20 HUs less than the average surrounding noncalcified plaque tissue. Thus, despite inherent limitations, CCTA may be able to identify some of the major and minor plaque vulnerability criteria. CCTA findings associated with "high risk" vulnerable plaque include positive remodeling, low-density plaque or low-density cores, and spotty calcifications.

With regard to calcium scoring, both electronic beam CT and gated MDCT have been shown to be reliable methods of quantifying coronary calcified plaque. However, with CCTA (using intravascular ultrasound as a gold standard), plaque volume per vessel tends to be underestimated for mixed and noncalcified plaque and overestimated for calcified plaque. Despite these limits, it remains true that an individual's ACS risk will increase with both increasing total plaque volume/burden and increasing plaque vulnerability, as defined by the characteristics previously described. Although the relevance and clinical significance of CCTA-detected nonstenotic coronary plaque in ED patients with chest pain is not currently well defined, knowledge of the presence, type, and general burden of coronary plaque might in the future aid in further refining treatment pathways by better stratifying patient risk for ED physicians treating patients with chest pain (and potentially with ACS).

Combined Evaluation of the Aorta and Pulmonary and Coronary Arteries

The combined evaluation for aortic dissection, PE, and ACS has been seductively coined the "triple rule-out" examination. Indeed, several investigations have confirmed that "triple rule-out" technique examinations can reliably match

the performance of dedicated CCTA technique examinations in accuracy for detecting and negative predictive value for excluding CAD. While the potential that "triple rule-out" CT holds for rapid comprehensive evaluation and triage of ED patients with chest pain is appealing, valid impediments to implementation exist. The primary concern relates to the likely 50% or greater increase in radiation dose resulting from the requisite extension of Z axis coverage of the thorax inherent with the triple rule-out examination, compared with the dedicated CCTA examination.

Unfortunately, no clear advantage of "triple rule-out" technique compared with dedicated CCTA technique has been demonstrated. Direct comparison of the techniques has failed to reveal improved diagnostic yield, reduced clinical events, diminished resource utilization (including length of stay or subsequent testing), or reduced costs with the "triple rule-out" technique compared with the dedicated CCTA technique. As a result, "triple rule-out" CT has currently not gained widespread acceptance as an appropriate test for patients presenting with acute chest pain.

One must remember that the place held by CCTA within the chest pain evaluation algorithm is at present unclear. According to the American College of Radiology Appropriateness Criteria, in patients presenting with acute nonspecific chest pain (with a low probability of coronary disease), CCTA receives an appropriateness rating of 7 ("usually appropriate"), whereas in patients presenting with chest pain suggestive of acute coronary syndrome, CCTA receives an appropriateness score of 6 ("may be appropriate"). Despite these uncertainties, the rapid evolution of CT technology and the clear advantages it holds over current management strategies suggest that MDCT (using either dedicated CCTA or more comprehensive "triple rule-out"-type protocols) will likely become an integrated part of the clinical algorithm in the evaluation of ED patients presenting with acute chest pain.

SUGGESTED READINGS

Achenbach S. Computed tomography coronary angiography. *J Am Coll Cardiol*. 2006;48:1919–1928.

Agarwal PP, et al. Multidetector CT of thoracic aortic aneurysms. *Radiographics*. 2009;29(2):537–552.

American Association of Physicists in Medicine. AAPM position statement on the use of bismuth shielding for the purpose of dose reduction in CT scanning. http://www.aapm.org/publicgeneral/BismuthShielding.pdf. 2012.

American College of Radiology. American College of Radiology ACR appropriateness criteria: acute nonspecific chest pain—low probability of coronary artery disease. http://www.guideline.gov/content.aspx?id=35136. Reviewed 2014.

American College of Radiology. American College of Radiology ACR appropriateness criteria: chest pain suggestive of acute coronary syndrome. https://acsearch.acr.org/docs/69403/Narrative/. Reviewed 2014.

American College of Radiology. American College of Radiology ACR appropriateness criteria: clinical condition: acute chest pain—suspected pulmonary embolism. http://www.acr.org/~/media/ACR/Documents/AppCriteria/Diagnostic/AcuteChestPainSuspectedPulmonaryEmbolism.pdf. Reviewed 2011.

Ayaram D, et al. Triple rule-out computed tomographic angiography for chest pain: a diagnostic systematic review and meta-analysis. *Acad Emerg Med*. 2013;20:861–871.

Bae KT. Intravenous contrast medium administration and scan timing at CT: considerations and approaches. *Radiology*. 2010;256:32.

Berrington de Gonzalez A, Mahesh M, Kim KP, et al. Projected cancer risks from computed tomographic scans performed in the United States in 2007. *Arch Intern Med*. 2009;169:2071e7.

Becattini C, Agnelli G. Acute pulmonary embolism: risk stratification in the emergency department. *Intern Emerg Med*. 2007;2:119–129.

Brenner DJ, Hall EJ. Computed tomography: an increasing source of radiation exposure. *N Engl J Med*. 2007;357:2277e84.

Busch S, Johnson TR, Nikolaou K, et al. Visual and automatic grading of coronary artery stenoses with 64-slice CT angiography in reference to invasive angiography. *Eur Radiol*. 2007;17:1445–1451.

Centers for Disease Control and Prevention. National Hospital Ambulatory Medical Care Survey. 2010 Emergency department summary tables. http://www.cdc.gov/nchs/data/ahcd/nhamcs_emergency/2010_ed_web_tables.pdf

Chin A, Fleischmann D. State-of-the-art computed tomography angiography of acute aortic syndrome. *Semin Ultrasound CT MRI*. 2012;33:222–234.

Dake MD, Miller DC, Semba CP, et al. Descending thoracic aortic aneurysm: CT findings after endovascular stent-graft placement. *Radiology*. 1999;212:169–174.

Elefteriades JA. Natural history of thoracic aortic aneurysms: indications for surgery, and surgical versus nonsurgical risks. *Ann Thorac Surg*. 2002;74:1877–1880.

Ersoy H, Goldhaber SZ, Cai T, et al. Time-resolved MR angiography: a primary screening examination of patients with suspected pulmonary embolism and contraindications to administration of iodinated contrast material. *AJR Am J Roentgenol*. 2007;188:1246–1254. 2007.

Froehner SC, Wagner M, Brunn J, et al. CT angiography for assessment of coronary artery anomalies. In: Schoepf UJ, ed. *CT of the Heart: Principles and Applications*. Totowa, NJ: Humana Press; 2004.

Ganaha F, Miller DC, Sugimoto K, et al. Prognosis of intramural hematoma with and without penetrating ulcer: a clinical and radiological analysis. *Circulation*. 2002;106:342–348.

Ghaye B, Ghuysen A, Willems V, et al. Severe pulmonary embolism: pulmonary artery clot load scores and cardiovascular parameters as predictors of mortality. *Radiology*. 2006;239:884–891.

Ghaye B, Remy J, Remy-Jardin M. Non-traumatic thoracic emergencies. CT diagnosis of acute pulmonary embolism: the first 10 years. *Eur Radiol*. 2002;12:1886–1905.

Giuntini C, Di Ricco G, Marini C, et al. Pulmonary embolism: epidemiology. *Chest*. 1995;107(suppl 1):3S–9S.

Goldstein S, et al. Multimodality imaging of diseases of the thoracic aorta in adults: from the American Society of Echocardiography and the European Association of Cardiovascular Imaging: endorsed by the Society of Cardiovascular Computed Tomography and Society for Cardiovascular Magnetic Resonance. *J Am Soc Echocardiogr*. 2015;28:119–182.

Gorich J, Rilinger N, Sokiranski R, et al. Leakages after endovascular repair of aortic aneurysms. *Radiology*. 1999;213:767–772.

Gosselin MV, Rassner UA, Thieszen SL, et al. Contrast dynamics during CT pulmonary angiogram: analysis of an inspiration associated artifact. *J Thorac Imaging*. 2004;19:1–7.

Gottschalk A, Sostman HD, Coleman RE, et al. Ventilation-perfusion scintigraphy in the PIOPED study. Part II: evaluation of the scintigraphic criteria and interpretations. *J Nucl Med*. 1993;34:1119–1126.

Gottschalk A, Stein PD, Goodman LR, Sostman HD. Overview of prospective investigation of pulmonary embolism diagnosis II. *Semin Nucl Med*. 2002;32:173–182.

Gruettner J, et al. Coronary computed tomography and triple rule out CT in patients with acute chest pain and an intermediate cardiac risk profile. Part 1: impact on patient management. *Eur J Radiol*. 2013;82:100–105.

Hazirolan T, Canyigit M, Karcaaltincaba M, et al. Myocardial bridging on MDCT. *AJR Am J Roentgenol*. 2007;188:1074–1080.

Hell MM, et al. Prospectively ECG-triggered high-pitch coronary angiography with third-generation dual-source CT at 70 kVp tube voltage: feasibility, image quality, radiation dose, and effect of iterative reconstruction. *J Cardiovasc Comput Tomogr*. 2014;8:418–425.

Hoffmann U, Pena AJ, Cury RC, et al. Cardiac CT in emergency department patients with acute chest pain. *Radiographics*. 2006;26:963–980.

Kim SY, Leo JB, Do KH, et al. Coronary artery anomalies: classification and ECG-gated multi-detector row CT findings with angiographic correlation. *Radiographics*. 2006;26:317–334.

Ko SM, Kwon JH. Multidetector-row CT coronary angiographic finding of myocardial bridging. *Int J Card Imaging*. 2007;23:71.

Leung AN, Bull TM, Jaeschke R, et al. An official American Thoracic Society/Society of Thoracic Radiology clinical practice guideline: evaluation of suspected pulmonary embolism in pregnancy. *Am J Respir Crit Care Med*. 2011;184(10):1200–1208.

Madder RD, et al. Comparative diagnostic yield and 3-month outcomes of "triple rule-out" and standard protocol coronary CT angiography in the evaluation of acute chest pain. *J Cardiovasc Comput Tomogr*. 2011;5:165–171.

Mita T, Arita T, Matsunaga N, et al. Complications of endovascular repair for thoracic and abdominal aortic aneurysm: an imaging spectrum. *Radiographics*. 2000;20:1263–1278.

PIOPED Investigators. Value of the ventilation/perfusion scan in acute pulmonary embolism: results of the prospective investigation of pulmonary embolism diagnosis (PIOPED). *JAMA*. 1990;263:2753–2759.

Prescott-Focht JA, et al. Ascending thoracic aorta: postoperative imaging evaluation. *Radiographics*. 2013;33:73–85.

Puchner SB, et al. High-risk plaque detected on coronary ct angiography predicts acute coronary syndromes independent of significant stenosis in acute chest pain: results from the ROMICAT-II Trial. *J Am Coll Cardiol*. 2014;64(7):684–692.

Quint LE, Francis IR, Williams DM, et al. Synthetic interposition grafts of the thoracic aorta: postoperative appearance on serial CT studies. *Radiology*. 1999;211:317–324.

Raja AS, Ip IK, Prevedello LM, et al. Effect of computerized clinical decision support on the use and yield of CT pulmonary angiography in the emergency department. *Radiology*. 2012;262(2):468–474.

Ravel MP, et al. Diagnostic accuracy of magnetic resonance imaging for an acute pulmonary embolism: results of the IRM-EP study. *J Thromb Haemost*. 2012;10(5):743–750.

Remy-Jardin M, Bahepar J, Lafitte JJ, et al. Multi-detector row CT angiography of pulmonary circulation with gadolinium-based contrast agents: prospective evaluation in 60 patients. *Radiology*. 2006;238:1022–1035.

Riley P, Rooney S, Bonser R, Guest P. Imaging the post-operative thoracic aorta: normal anatomy and pitfalls. *BJR*. 2001;74:1150–1158.

Rofsky NM, Weinreb JC, Grossi EA, et al. Aortic aneurysm and dissection: normal MR imaging and CT findings after surgical repair with the continuous-suture graft-inclusion technique. *Radiology*. 1993;186:195–201.

Rogers IS, et al. Usefulness of comprehensive cardiothoracic computed tomography in the evaluation of acute undifferentiated chest discomfort in the emergency department (CAPTURE). *Am J Cardiol*. 2011;107:643–650.

Santiago Restrepo C, et al. Imaging findings in cardiac tamponade with emphasis on CT. *Radiographics*. 2007;27(6):1595–1610.

Schlett CL, et al. Prognostic value of CT angiography for major adverse cardiac events in patients with acute chest pain from the emergency department: 2-year outcomes of the ROMICAT trial. *JACC Cardiovasc Imaging*. 2011;4(5):481–491.

Schoepf UJ, Costello P. CT angiography for diagnosis of pulmonary embolism: state of the art. *Radiology*. 2004;230:329–337.

Schoepf UJ, Goldhaber SZ, Costello P. Spiral computed tomography for acute pulmonary embolism. *Circulation*. 2004;109:2160–2167.

Schoepf UJ, Kucher N, Kipfmueller F, et al. Right ventricular enlargement on chest computed tomography: a predictor of early death in acute pulmonary embolism. *Circulation*. 2004;110:3276–3280.

Schoepf UJ, Zwerner PL, Savino G, et al. How I do it: coronary CT angiography. *Radiology*. 2007;244:48–63.

Sodickson A. Strategies for reducing radiation exposure from multidetector computed tomography in the acute care setting. *Can Assoc Radiol J*. 2013;64(2):119–129.

Sodickson A, Baeyens PF, Andriole KP, et al. Recurrent CT, cumulative radiation exposure, and associated radiation-induced cancer risks from CT of adults. *Radiology*. 2009;251:175e84.

Sodickson A, Weiss M. Effects of patient size on radiation dose reduction and image quality in low-kVp CT pulmonary angiography performed with reduced IV contrast dose. *Emerg Radiol*. 2012;19(5):437–445.

Stein PD, et al. Gadolinium enhanced magnetic resonance angiography for pulmonary embolism: a multicenter prospective study (PIOPED III). *Ann Intern Med*. 2010;152(7):434–443.

Stein PD, Woodard PK, Hull RD, et al. Gadolinium-enhanced magnetic resonance angiography for detection of acute pulmonary embolism: an in-depth review. *Chest*. 2003;124:2324–2328.

Stein PD, Woodard PK, Weg JG, et al. Diagnostic pathways in acute pulmonary embolism: recommendations of the PIOPED II investigators. *Radiology*. 2007;242:15–21.

Tatli S, Yucel EK, Lipton MJ. CT and MR imaging of the thoracic aorta: current techniques and clinical applications. *Radiol Clin North Am*. 2004;42:565–585.

Van Guens RJM, Cademartiri F. Anatomy of the coronary arteries and veins in CT imaging. In: Schoepf UJ, ed. *CT of the Heart Principles and Applications*. Totowa, NJ: Humana Press; 2004.

Van Marrewijk C, Buth J, Harris PL, et al. Significance of endoleaks after endovascular repair of abdominal aortic aneurysms. *J Vasc Surg*. 2002;35:461–473.

Volpicelli G, et al. International evidence-based recommendations for point-of-care lung ultrasound. *Intensive Care Med*. 2012;38:577–591.

Wang ZJ, Reddy GP, Gotway MB, et al. CT and MR imaging of pericardial disease. *Radiographics*. 2003;23(special issue):S167–S180.

Webb RW, Muller NL, Naidich DP. *High-Resolution CT of the Lung*. 3rd ed. Philadelphia, PA: Lippincott Williams & Wilkins; 2001:49–192.

Wittram C, Yoo AJ. Transient interruption of contrast on CT pulmonary angiography: proof of mechanism. *J Thorac Imaging*. 2007;22(2):125–129.

Worsley DF, Alavi A, Aronchick JM, et al. Chest radiographic findings in patients with acute pulmonary embolism: observations from the PIOPED study. *Radiology*. 1993;189:133–136.

Wu M-T, et al. Intramural blood pools accompanying aortic intramural hematoma: CT appearance and natural course. *Radiology*. 2011;258(3):705–713.

Chapter 9

Nontrauma Abdomen

Stephan W. Anderson, Brian C. Lucey, and Jorge A. Soto

Nontraumatic acute abdominal pain may have a wide variety of causes. When diagnostic imaging is clinically indicated in the evaluation of these patients, localizing the signs and symptoms is critical to properly triage the patient so that the correct imaging modality is used. For example, in women with pelvic pain, ultrasonography is the imaging modality of choice for the initial evaluation. For abdominal pain, ultrasonography or computed tomography (CT) is typically used, possibly preceded by plain radiography, depending on the patient's presentation.

In patients with acute abdominal pain, one may consider broad categories of disease, including inflammatory, infectious, obstructive, and vascular conditions. In the following sections, these broad categories should be remembered as the various locations of acute abdominal pain are discussed, including bowel, pancreaticobiliary system, liver, genitourinary system, and spleen. Finally, nonspecific emergent imaging findings with a host of underlying causes, often requiring urgent clinical intervention, are discussed.

BOWEL DISEASE

Disease related to the bowel, including the small bowel and colon, represents a significant percentage of acute abdominal pain. Again, one may consider the underlying causes of bowel disease in the categories of obstructive, infectious, inflammatory, and vascular. Often, plain radiographs of the abdomen are acquired when underlying bowel disease is suspected, commonly followed by CT for more definitive characterization.

Diseases Causing Bowel Obstruction

Diseases causing bowel obstruction include gastric outlet obstruction and volvulus, peptic ulcer disease, mechanical small bowel obstruction, small bowel volvulus, colonic obstruction and volvulus, and adynamic ileus. These conditions are covered in the following sections.

Gastric Outlet Obstruction

Gastric outlet obstruction refers to any entity causing a mechanical obstruction to gastric emptying. Differential considerations are broad and include malignant causes such as pancreatic cancer, gastric cancer, and ampullary and duodenal cancer, as well as cholangiocarcinoma. Benign causes of gastric outlet obstruction in adults include peptic ulcer disease, gastric polyps, bezoars, caustic ingestion, gallstones (Bouveret syndrome), and pancreatic pseudocysts. Secondary inflammation or spasm resulting from pancreatitis or acute cholecystitis can cause gastric outlet obstruction. Infectious causes of gastric outlet obstruction include abdominal tuberculosis. Gastroduodenal intussusception is a rare cause of mechanical obstruction, typically related to an underlying lead point, which includes benign and malignant neoplasms.

Patients with gastric outlet obstruction present with nausea and vomiting, the hallmark symptoms. Normally these symptoms are temporally related to recent ingestion of a meal, and the vomitus often consists of undigested food. In more chronic cases, weight loss may be described, and in severe cases, patients may present with dehydration and electrolyte imbalances.

Imaging Findings. Plain radiographs may demonstrate a markedly dilated stomach, which may be filled with either air or fluid. Infrequently, plain radiography may suggest an underlying diagnosis—for example, an irregular mass lesion identified as a filling defect in cases of malignancy such as gastric cancer. Filling defects also may be identified on plain radiographs in cases of bezoar obstruction. In patients with Bouveret syndrome, a calcified gallstone may be identified in the duodenal bulb.

In patients presenting with acute symptoms of nausea and vomiting, a CT scan may be performed for further evaluation. Similar to radiography, CT clearly demonstrates the often marked distention of the stomach. CT is also helpful in characterizing the underlying causes of obstruction. Malignant causes are seen as enhancing soft tissue mass lesions arising in the stomach in cases of gastric cancer, or slightly more distally around the pancreatic head or ampulla in cases of pancreatic cancer, cholangiocarcinoma, and ampullary and duodenal cancers. Distinction among the latter can be difficult because the area of origin contains quite a bit of overlap.

In cases in which peptic ulcer disease (PUD) obstructs the stomach, the ulcer may rarely be identified, but the secondary CT findings of gastritis are typically seen as focal thickening of the gastric wall with hyperenhancement of the mucosa related to the inflammation. In these cases, the focal area of inflammation should be scrutinized for a central ulcer seen in PUD. Often, on the basis of CT, the distinction between PUD and underlying carcinoma is difficult to ascertain. Similar to PUD, in cases of obstruction resulting from inflammatory causes such as pancreatitis or cholecystitis, the epicenter of inflammation will be seen around the respective organs, but the secondary inflammation of the stomach may be identified on CT as mural thickening, possibly with hyperenhancement of the mucosa.

Gastric outlet obstruction resulting from various benign causes is often apparent, as in cases of pancreatic pseudocyst obstruction. Hyperplastic polyps, the most common form of gastric polyp, may rarely cause gastric obstruction and may be seen in the region of the prepyloric antrum because they cause obstruction by prolapse into the pyloric

channel. On CT, the appearance is that of a pedunculated, soft-tissue attenuation filling defect. In cases of Bouveret syndrome, the obstructing gallstone may be identified as a calcified filling defect in the duodenal bulb. Bezoars are seen at CT as mottled-appearing filling defects within the stomach, although they may be seen more distally within the gastrointestinal tract and have been reported to cause small bowel obstructions.

Gastric Volvulus

Gastric volvulus—an abnormal rotation of the stomach around its axis—represents a surgical emergency in its acute form. Gastric volvulus may be classified as one of two forms, mesenteroaxial or organoaxial, or a combination of the two. In the mesenteroaxial form, the less common form, the stomach rotates around the axis, bisecting both the lesser and greater curvatures of the stomach. In the organoaxial form, the stomach rotates around the axis, connecting the gastroesophageal junction (GEJ) and the pylorus.

In cases of gastric volvulus, the Borchardt triad of upper abdominal pain, retching without vomiting, and inability to pass a nasogastric tube may be present. This triad is reported in up to 70% of acute cases of gastric volvulus.

Imaging Findings. The most common causative factor of gastric volvulus in the adult population is diaphragmatic defects, and thus plain radiographs may demonstrate an intrathoracic, gas-filled viscus. In cases of mesenteroaxial volvulus, supine radiographs may demonstrate typical findings of a spherical lucency with a characteristic "beak" in the region of the distal stomach. Upright radiographs show differential air–fluid levels at different heights in cases of mesenteroaxial volvulus. Organoaxial volvulus, on the other hand, characteristically reveals a single air–fluid level in an abnormally transversely oriented stomach.

In patients presenting with a clinical suspicion of a gastric volvulus, an urgent upper gastrointestinal series can secure a prompt diagnosis. In cases of gastric volvulus, an obstruction may be identified at the site of volvulus. Mesenteroaxial volvulus demonstrates a barium-filled stomach with the GEJ below the antrum and with the typical "beak" seen in the region of the distal stomach, as on radiography. If barium gets past the GEJ, an "upside-down" stomach is seen. Transverse position of the stomach and an abnormal inferior location of the GEJ suggest organoaxial volvulus.

Because of the multiplanar capabilities of multidetector CT (MDCT) scanners, patients with suspected gastric volvulus may undergo a CT scan in the initial diagnostic evaluation. As on radiography, CT typically demonstrates the presence of a hiatal hernia, commonly the paraesophageal type, or diaphragmatic eventration, which increases the likelihood of organoaxial gastric volvulus. Multiplanar reformations are particularly useful in precisely defining the anatomy of the volvulus. Like fluoroscopy, CT demonstrates the abnormally positioned gastric antrum located superior to the GEJ—an "upside-down" stomach when the rotation is complete. Organoaxial volvulus demonstrates an abnormally transverse lie of the stomach and an inferiorly positioned GEJ given its axis of rotation. Because organoaxial volvulus is more often associated with diaphragmatic defects, the stomach is often identified in the thorax at the time of volvulus.

In cases of gastric volvulus on CT, especially the organoaxial type, complications of ischemia may be identified, including pneumatosis and portomesenteric vein gas. Mesenteroaxial volvulus, unlike organoaxial volvulus, is more frequently incomplete and less likely to cause acute complications such as necrosis.

Peptic Ulcer Disease

Peptic ulcer disease, most commonly resulting from *Helicobacter pylori,* rarely presents acutely; however, complications relating to PUD, such as acute hemorrhage or gastroduodenal perforation, may present acutely. Additionally, the somewhat more subacute presentation of gastric outlet obstruction may require imaging evaluation, as previously detailed. Causes of peptic ulcers other than *H. pylori* include use of nonsteroidal antiinflammatory drugs, Zollinger-Ellison syndrome, chemotherapy, radiation, and various infections such as cytomegalovirus. Bleeding complications related to PUD usually do not require imaging evaluation.

Epigastric to left upper quadrant burning pain and bloating, temporally related to meals and possibly radiating to the back, are the common description of PUD-related pain. Nausea, vomiting, and anorexia may be described. A sudden onset of pain suggests perforation. Patients with acute hemorrhage often present with hematemesis.

Imaging Findings. In patients with acute perforation related to PUD, pneumoperitoneum may be identified on initial plain radiographs. Like plain radiography, a CT scan may identify findings of pneumoperitoneum in cases of ulcer perforation. Often, the underlying ulcer or mural rent is not clearly identified. Small foci of air may be seen around the area of perforation in the stomach or duodenum and suggest the underlying cause. Focal wall thickening may be present in the region of the ulcer in the stomach or duodenum. When oral contrast material is administered in cases of unsuspected hollow viscus perforation, extravasation of contrast material into the peritoneal cavity is often identified. A CT scan may characterize underlying PUD in cases of gastric outlet obstruction, as previously detailed.

Mechanical Small Bowel Obstruction

Mechanical small bowel obstruction represents a relatively common cause of abdominal pain and is a frequent indication for abdominal imaging. The most common cause of mechanical small bowel obstruction is adhesions from prior surgical intervention. Other common causes include malignancy, acute inflammatory processes, and hernias. Less common causes include a gallstone ileus and small bowel intussusception.

Patients with mechanical small bowel obstruction typically present with abdominal pain, nausea, vomiting, abdominal distention, and constipation. Commonly, the abdominal pain is colicky or intermittently cramping. Initially it may be mild, with progression of symptoms as the duration increases. Vomiting initially consists of gastric contents, followed by more distal bowel contents, including bile and finally feculent material. The temporal relationship between the onset of bowel obstruction and symptoms of vomiting is related to the position of the obstruction, with more proximal causes presenting with vomiting earlier in the episode of obstruction. The vomiting may result in dehydration and electrolyte imbalances. Compared with

colonic obstruction, vomiting occurs earlier and commonly precedes constipation.

Imaging Findings. The initial imaging evaluation of patients with suspected mechanical small bowel obstruction often includes plain radiographs. The diagnosis of small bowel obstruction on plain radiography involves the visualization of distended loops of small bowel filled with air or fluid. The differentiation of small bowel loops from the colon is achieved by identifying the valvulae conniventes, also known as *plicae circulares*, of the small bowel, which are thin, mucosal folds extending across the entire small bowel loops. The haustral folds of the colon, on the other hand, are thicker bands alternating with the thick folds termed *plicae semilunares*, which do not cross the entire lumen of the colon. The small bowel loops are more central in the abdomen, with the colon seen along the periphery. Typically, 3 cm is accepted as the upper limit of normal for the diameter of the small bowel. The presence of a hernia as the cause of a small bowel obstruction may be suggested by plain radiographs based on the presence of small bowel loops in unusual locations, such as the inguinal canal, distal to dilated loops of small bowel. Alternatively, radiographs demonstrating protrusion of a segment of small bowel, as evidenced by a short segment of bowel clearly outlined by air outside the abdominal wall, again distal to dilated loops of small bowel, may indicate a hernia as the underlying cause.

CT is often used for further characterization in patients with suspected mechanical small bowel obstruction. Similar to radiography, the diagnosis on CT involves identifying distended air- and fluid-filled loops of small bowel, typically greater than 3 cm in diameter. The small bowel "feces" sign, which is the presence of air and particulate matter resembling feces within loops of small bowel, is a finding commonly seen in small bowel obstruction; its diagnosis is helpful because it suggests increased bowel transit time. Often, CT allows for the diagnosis of the exact point of transition between distended loops of small bowel and the more normal collapsed loops of small bowel and possibly for identifying the underlying cause of the small bowel obstruction (Fig. 9-1).

Closed loop obstructions are a subset of mechanical small bowel obstructions that demand acute clinical intervention. The term *closed loop obstruction* signifies the presence of two transition points, one of which is found at the proximal extent of the closed loop and the other at its distal extent. The vascular supply of these segments of small bowel is often compromised in this setting, and ischemia and necrosis may quickly ensue. Although the diagnosis of a closed loop obstruction might be suggested on plain radiographs by the presence of a short segment of distended small bowel, as well as transition points that may or may not be visualized, this diagnosis is typically confirmed by CT. The CT imaging findings include a sharp transition point, or "beak," at the proximal and distal extent of the closed loop. CT findings suggesting ischemia, including vascular engorgement, and ascites, as well as abnormally decreased enhancement after intravenous administration of contrast material, often require emergent intervention. More ominous CT imaging findings, including pneumatosis intestinalis, also may be seen and are discussed in the following text.

As noted, adhesions from prior surgical intervention are the most common cause of small bowel obstruction and are notoriously difficult to directly visualize with imaging; the diagnosis often remains one of exclusion. However, secondary signs such as abrupt angulation of small bowel loops and adherence of small bowel loops to nondependent surfaces such as the anterior parietal peritoneum lend credence to a diagnosis of adhesions as the underlying cause, especially when they are found at the transition between distended and normal small bowel loops.

Hernias are a second common cause of small bowel obstruction. CT is used to further characterize these hernias, which may be complex in some cases. Inguinal, umbilical, incisional, and Spigelian hernias in the location of the linea semilunaris are common types of hernias (Fig. 9-2). Among less common causes of mechanical small bowel obstruction are internal hernias, including congenital or surgically acquired rents within the mesentery, as well as a myriad of other named internal hernias that have been described. CT images, including multiplanar reformations, are often used to further characterize these complex hernias.

A gallstone ileus is a rare but interesting form of mechanical small bowel obstruction. In this case, a gallstone erodes into the adjacent duodenum and proceeds to obstruct the small bowel, most commonly at the ileocecal valve. Typical imaging findings include the presence of air within the gallbladder or bile ducts, as well as dilated loops of small bowel, often with a calcified gallstone at the distal extent. These findings may be seen on plain radiographs, as well as on CT. If the gallstone erodes more proximally and obstructs the duodenal bulb, similar imaging appearances of biliary gas, obstruction, and often visualization of the calcified gallstone are seen and are termed *Bouveret syndrome*.

Although more common in the pediatric population, small bowel intussusception also may be seen in adults and can cause obstruction of small bowel loops proximally. In adults, one must always consider the possibility of a lead point such as a neoplasm. Other causes of small bowel intussusception in adults include Meckel diverticulum and postoperative states, especially after gastric bypass. With the increasingly widespread use of CT, transient small bowel intussusceptions are more commonly seen. The diagnosis of a transient intussusception may be suggested on the basis of location and length, as well as the absence of proximal small bowel dilatation (Fig. 9-3).

Small Bowel Volvulus

Although small bowel volvulus is often considered a pediatric diagnosis, adults also may present acutely with this condition. Small bowel volvulus can be categorized as either primary or secondary; persons with secondary volvulus have an underlying condition predisposing to volvulus, such as pregnancy, a gastrointestinal tumor, small bowel diverticulum, or intraperitoneal adhesions. A form of small bowel volvulus that often presents within the first month of life is *midgut volvulus*. It is a result of malrotation and also may affect adult patients. In these cases, a lack of rotation or incomplete rotation of the gut around the axis of the superior mesenteric artery during embryogenesis, termed *midgut malrotation*, may lead to acute volvulus of the entire midgut.

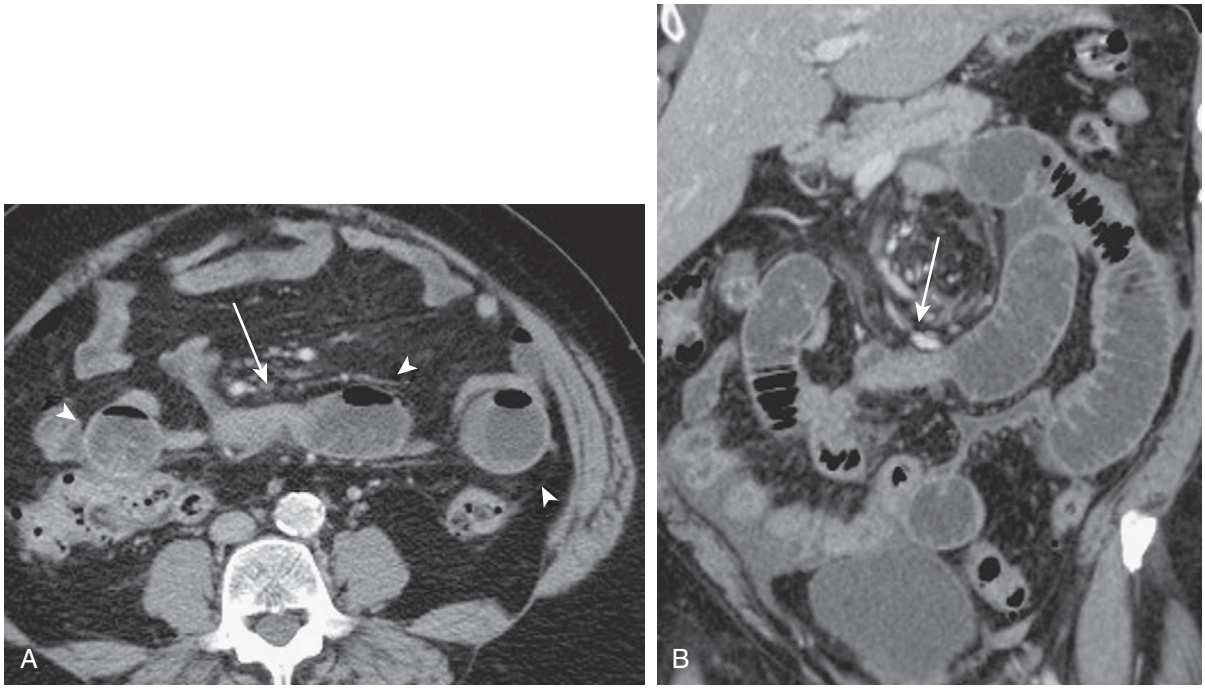


FIGURE 9-1 A 76-year-old woman with mechanical small bowel obstruction. Axial **(A)** and coronal **(B)** portal venous phase computed tomography images demonstrate multiple dilated loops of small bowel (*arrowheads*, **A**) with rapid transition from dilated loops to more normal appearing, collapsed loops *(arrows)* identified as a result of postsurgical adhesions on operative repair.

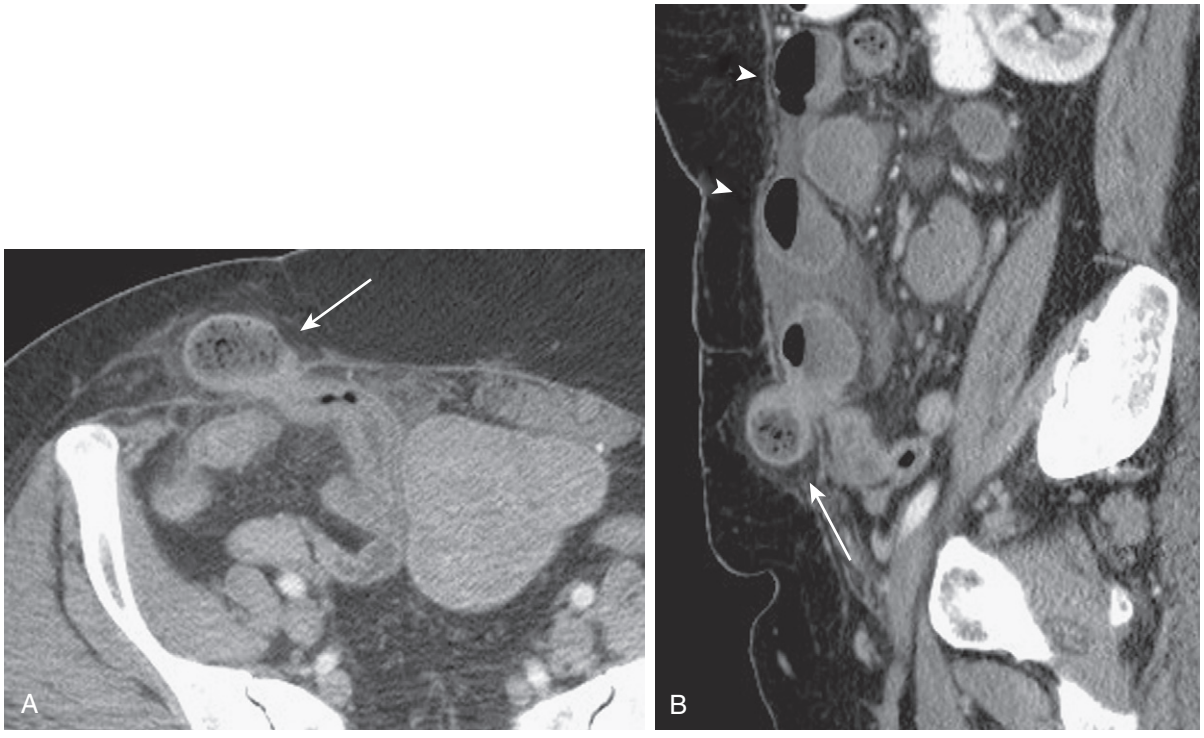


FIGURE 9-2 A 32-year-old woman with an incarcerated incisional hernia. Axial **(A)** and sagittal **(B)** portal venous phase images demonstrate an incarcerated loop of small bowel *(arrows)* demonstrating fecalization with proximally obstructed loops of small bowel identified (*arrowheads*, **B**).

Clinical findings are often nonspecific and include abdominal pain, nausea, and vomiting. More specific clinical histories include those in which the patient describes intermittent epigastric pain, possibly related to meals.

Imaging Findings. Plain radiographs are also nonspecific in patients with small bowel volvulus but may demonstrate proximal small bowel obstruction. In cases of midgut volvulus related to underlying malrotation, plain radiographs may demonstrate partial duodenal

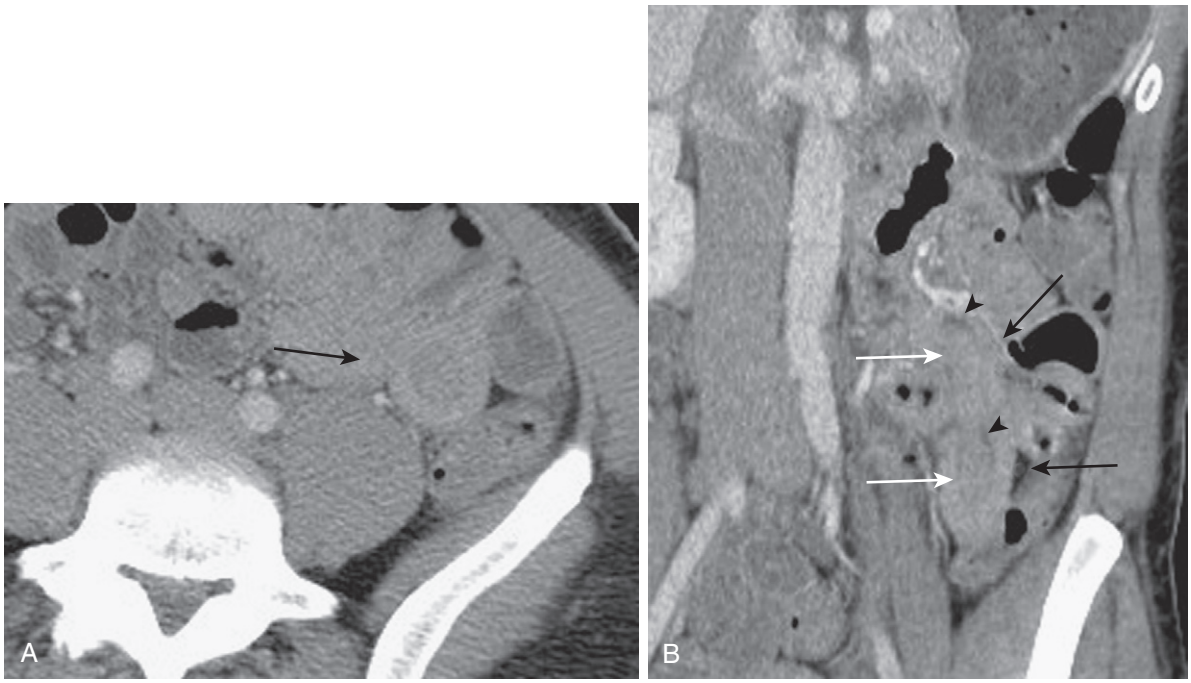


FIGURE 9-3 A 30-year-old woman with transient intussusception. An axial portal venous phase image **(A)** reveals the presence of a small bowel intussusception *(arrow)*. A coronal image **(B)** clearly shows the intussusceptum *(white arrows)* within the receiving loop of small bowel and the intussuscipiens *(black arrows)*, surrounded by small amounts of mesenteric fat *(arrowheads)*.

obstruction with a dilated, air-filled stomach and a proximal duodenum.

Currently, CT is the imaging modality of choice in diagnosing small bowel volvulus. As on plain radiographs, secondary small bowel obstruction may be identified proximal to the volvulus. The CT "whirl" sign is often associated with volvulus of the bowel and is seen as a swirling of mesenteric vessels, strands of soft tissue, and loops of bowel. Although sensitive in the diagnosis of small bowel volvulus, the finding lacks specificity, in that most patients demonstrating this finding have been shown not to have a diagnosis of small bowel volvulus. Nevertheless, the "whirl" sign of twisting mesenteric structures, including loops of small bowel, should raise suspicion of a volvulus, and other CT findings such as infiltration of the mesentery and proximal small bowel dilatation may increase specificity. Small bowel volvulus can rapidly lead to vascular compromise, and the CT images should be scrutinized for findings of ischemia, such as abnormal hypoenhancement of the small bowel. As in cases of small bowel volvulus, the "whirl" sign, in which the superior mesenteric vein and loops of bowel are seen to rotate around the superior mesenteric artery, may be demonstrated on CT in cases of midgut volvulus.

Colonic Obstruction

In the adult population, the most common consideration in colonic obstruction is malignancy, specifically adenocarcinoma. Other causes include diverticulitis, volvulus, intussusception, ischemia, adhesions, fecal impaction, and strictures from a number of prior insults, including radiation. Another possible cause of dilated loops of colon is acute or chronic megacolon. When underlying severe inflammation of the colon is present, acute megacolon is referred to as "toxic" megacolon. When no underlying colonic abnormality is present, this condition is referred to as *Ogilvie syndrome*. Ogilvie syndrome typically presents in hospitalized patients with significant underlying medical illnesses. The acute forms of megacolon are medical emergencies, given the risks of complication, which include sepsis, ischemia, and perforation. The risks of perforation increase significantly when the diameter of the cecum exceeds 12 cm. The cecum is the most likely portion of the colon to perforate, based on Laplace's law.

Patients with colonic obstruction typically present with abdominal distention, pain, nausea, and vomiting. Constipation commonly precedes vomiting in cases of colonic obstruction. Depending on the underlying cause, presentation may be acute or more chronic, possibly with changes in the caliber of stool in the case of colonic malignancy. Peritoneal signs are an ominous finding and suggest the possibility of perforation.

Imaging Findings. Typically, plain radiographs demonstrate evidence of air- and fluid-filled loops of dilated colon. A diameter of 8 cm is considered the upper limit of normal for the cecum, whereas 5 cm is considered the upper limit of normal for the remainder of the colon. When acute, colonic obstruction is a medical emergency, given the potential for rapidly developing ischemia, sepsis, or perforation.

CT demonstrates dilated loops of air- or fluid-filled colon proximal to the site of obstruction and is accurate in determining the cause of the obstruction. The CT scans should be scrutinized for signs of perforation, such as free intraperitoneal fluid or air, as well as for signs of ischemia, such as abnormal hypoenhancement of the colon. Unlike in the pediatric population, colonic obstruction as a result of intussusception is generally managed surgically, as opposed to radiologically, with reduction via air enema, for example,

given the high likelihood of an underlying malignancy. On CT, toxic megacolon demonstrates dilation of air- or fluid-filled colon with wall thickening and a distorted colonic contour or a lack of the expected haustral pattern. Because Ogilvie syndrome lacks the colonic inflammation, CT is unlikely to demonstrate a similar degree of wall thickening and submucosal edema as toxic megacolon. The chronic form of megacolon represents a functional failure of the colon as a result of various underlying causes, including chronic constipation. In these patients, when prior radiographs are available for comparison, it is often helpful to exclude acute colonic obstruction or megacolon.

Colonic Volvulus

Sigmoid volvulus is the most common form of gastrointestinal volvulus. Cecal volvulus is also a relatively common form of colonic volvulus. Sigmoid volvulus represents twisting of the sigmoid colon around its mesenteric axis. Three forms of cecal volvulus are described: the axial torsion type, loop type, and cecal bascule. The axial torsion and loop types represent the most common forms. In the axial torsion type, the cecum rotates around its long axis, appearing in the right lower quadrant. In the loop type, the cecum twists and then inverts, ending in the left upper quadrant. In the cecal bascule, the cecum simply folds medially to the descending colon, producing an occlusion at the site of flexion.

Colonic volvulus typically presents with an acute abdomen with sudden onset of colicky pain. Abdominal distention with a tympanitic abdomen may be appreciated. Constipation with inability to pass flatus or stool accompanies cases of colonic volvulus. Borborygmus is frequently seen in cases of colonic volvulus.

Imaging Findings. Plain radiographs demonstrate the beaked tapering of the efferent and afferent limbs of the dilated loop of sigmoid colon. The classic plain radiograph description of the sigmoid volvulus is that of a coffee-bean–shaped collection of air-filled bowel occupying the left upper quadrant. In cases of axial torsion–type cecal volvulus, a markedly distended loop of large bowel may be identified that extends from the right lower quadrant to the epigastrium or left upper quadrant. The distended cecum may be identified anywhere in the abdomen, depending on the mobility of the right colon. The cecal bascule is generally identified as an air-filled structure occupying the mid abdomen on plain radiography.

CT demonstrates similar beaking, as well as the "whirl" sign of bowel around mesenteric vasculature common to all types of volvulus. CT has been shown to be accurate in diagnosing cecal volvulus and in differentiating between the various subtypes based on the location of the cecum. Less common forms of colonic volvulus are also encountered, including volvulus of the splenic flexure, as well as various segments of the transverse colon.

Adynamic Ileus

Another cause for bowel dilatation, including small bowel and colon, is adynamic ileus. Adynamic ileus, also termed *paralytic ileus*, has numerous causes, including recent surgery, use of drugs (including opiates), sepsis, intraabdominal infection or inflammation, trauma, and central nervous system injuries, among others. The typical symptoms of ileus are mild abdominal pain, nausea, vomiting, and constipation. In contradistinction to mechanical causes of obstruction, adynamic ileus demonstrates diffuse mild dilatation of bowel loops. Focal ileus, the so-called "sentinel loop" sign, may be identified around areas of inflammation within the abdomen and may be helpful in localizing disease on radiography.

Patients with adynamic ileus typically present with mild abdominal pain, constipation, and bloating. Nausea and vomiting may be associated with adynamic ileus.

Imaging Findings. Plain radiographs demonstrate dilated bowel loops, often diffusely when the cause is systemic. When it is a result of focal inflammation such as pancreatitis, a more localized ileus may be identified and may be useful in localizing intraabdominal disease.

CT has been shown to have a high diagnostic accuracy in distinguishing paralytic ileus from mechanical causes. The CT findings typical of a mechanical cause of obstruction such as a distinct transition point will not be identified in cases of adynamic ileus, which demonstrate mildly dilated loops of bowel diffusely.

Infectious and Inflammatory Diseases

Infectious and inflammatory diseases of the bowel are discussed in the following sections. They include infectious small bowel enteritis, Crohn disease and diverticulitis of the small bowel, appendicitis, epiploic appendagitis, omental infarction, diverticulitis, inflammatory bowel disease of the colon, infectious colitis, and foreign bodies.

Infectious Small Bowel Enteritis

Small bowel enteritis may be the result of a multitude of infectious causes, including viral causes such as rotavirus, norovirus, and adenovirus, bacterial causes such as *Campylobacter jejuni,* and parasites, including *Giardia lamblia,* all of which may affect the immunocompetent host. Common infectious agents of small bowel enteritis in the immunocompromised host include cytomegalovirus, cryptosporidiosis, and *Mycobacterium avium intracellulare.*

Nonspecific signs and symptoms of infectious enteritis include abdominal cramping, vomiting, and diarrhea. Although the abdomen may be distended with gas, borborygmi are present, distinguishing this condition from ileus. Patients may be febrile, and leukocytosis may be present. Especially in immunocompetent hosts, the disease is often self-limited, lasting up to several days. When infectious enteritis is severe, dehydration is a relatively common complication of infectious small bowel enteritis. Currently, fecal testing and, increasingly, immunoassays are used in the clinical diagnosis.

Imaging Findings. Plain radiographs are often nonspecific but may demonstrate mildly dilated loops of small bowel, similar to adynamic ileus. In more severe cases, the degree of small bowel dilatation may approach the appearance of a small bowel obstruction.

CT imaging, when acquired, is also often nonspecific and may demonstrate mild to moderate small bowel dilatation and mural thickening (Fig. 9-4). Often, the small bowel is diffusely affected; however, certain infections may present in more specific locations such as the proximal small bowel in cases of giardiasis. In the immunocompromised host, a myriad of other infectious causes should be considered, as previously noted. Typically, nonspecific small bowel

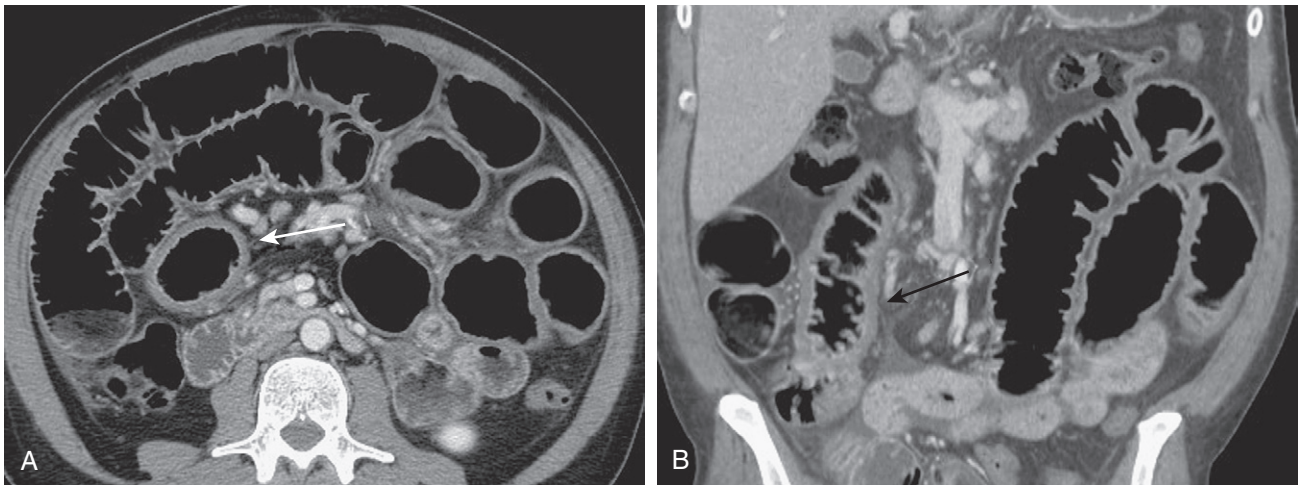


FIGURE 9-4 A 40-year-old man with viral gastroenteritis. Axial **(A)** and coronal **(B)** portal venous phase computed tomography images reveal diffuse small bowel dilatation, as well as mural thickening *(arrows)*.

wall thickening and mucosal irregularity are identified in cases of cytomegalovirus and cryptosporidium. In patients affected by *Mycobacterium avium intracellulare,* hepatic and splenic enlargement, jejunal wall thickening, and enlarged soft tissue attenuation or, less commonly but more characteristically, low-attenuation lymphadenopathy are described.

Crohn Disease, Small Bowel

Although Crohn disease can affect any portion of the gastrointestinal tract, the terminal ileum portion of the small bowel is the most commonly involved. Crohn disease may affect isolated segments of small bowel proximal to the terminal ileum. Usually, however, in cases of small bowel involvement, the colon is also affected.

Common gastrointestinal symptoms include abdominal pain, diarrhea, and weight loss. The crampy abdominal pain associated with Crohn disease may be temporarily relieved after defecation. The area of bowel involved may determine the nature of the diarrhea, with persons affected by ileitis presenting with watery, large-volume stools.

Imaging Findings. In patients presenting with acute abdominal symptoms related to Crohn disease of the small bowel, plain radiographs may demonstrate dilatation of proximal bowel loops because of a functional mechanical obstruction resulting from enteritis. Mural thickening of the affected small bowel loops also may be visualized on plain radiographs.

The manifestations of Crohn disease of the small bowel typically demonstrate nonspecific CT signs of inflammation such as mural thickening. However, more specific findings are often identified. These findings include isolation to the terminal ileum, hypervascularity and prominence of the vasa recta, the "comb" sign, increased mesenteric fat surrounding loops of small bowel, and "creeping" fat, as well as intraabdominal fistulae and abscesses (Fig. 9-5).

Small Bowel Diverticulitis

Meckel diverticulum, the most common congenital anomaly of the gastrointestinal tract, remains asymptomatic in most patients. However, various complications can ensue, including inflammation, termed *Meckel diverticulitis*. Although it is less commonly seen in other locations than in the colon, diverticula formation may affect any portion of the small bowel from the duodenum to the ileum. Potential complications include bacterial overgrowth and malabsorptive states. Diverticulitis also may affect the small bowel.

Patients with small bowel diverticulitis may present with localized tenderness in the region that is affected; however, no specific signs and symptoms are pathognomonic for this diagnosis. Often, these patients are febrile and may present with a leukocytosis. Moreover, malabsorptive states may develop, and patients may present with diarrhea and weight loss. Although these secondary findings are unrelated to diverticulitis, they may add credence to a consideration of small bowel diverticulitis. Plain radiographs, which are not typically used in the diagnosis of small bowel diverticulitis, may show a focal ileus or "sentinel loop" sign in the area of inflammation.

Imaging Findings. Meckel diverticulitis may be diagnosed by CT. A Meckel diverticulum is evident as a blind-ending pouch of variable length containing fluid, air, or particulate debris, often located near the midline but seen anywhere from the right lower quadrant to the mid abdomen. When the diverticulum is inflamed, mural thickening and surrounding inflammatory stranding may be identified (Fig. 9-6) and might be complicated by frank perforation, possibly yielding an intraabdominal abscess. In cases of diverticulitis unrelated to Meckel diverticulum, CT demonstrates focal luminal outpouchings with surrounding inflammatory changes. Again, gross perforation with abscess formation also may be seen.

Appendicitis

Appendicitis is a common clinical concern in patients presenting to the emergency department with abdominal pain. In patients presenting with the classic signs and symptoms, including right lower quadrant pain, leukocytosis, and fever, imaging may not be necessary in making the diagnosis of appendicitis. However, in patients with atypical presentations or those requiring further characterization of the suspected diagnosis, imaging is often used. Initially, the appendiceal lumen occludes as a result of a number of causes, including fecaliths and lymphoid hyperplasia. Once occluded, intraluminal fluid continues

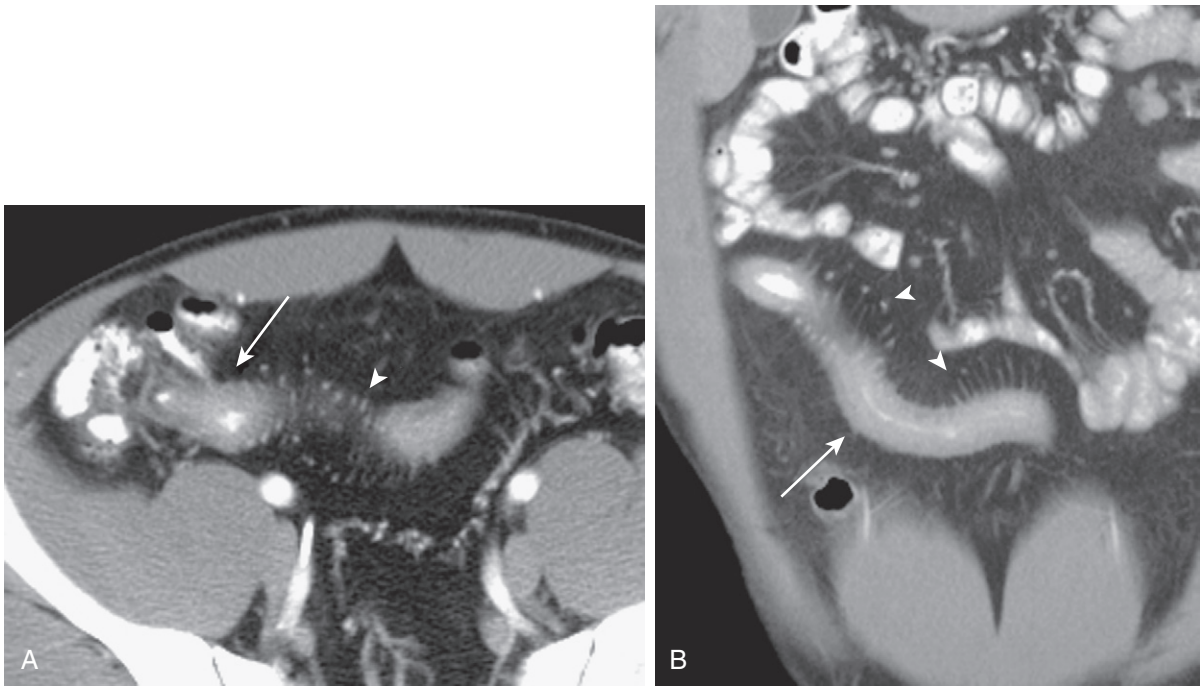


FIGURE 9-5 A 24-year-old man with Crohn disease. Axial **(A)** and coronal **(B)** portal venous phase computed tomography images demonstrate thickening of the terminal ileum *(arrows)* with prominence of the vasa recta along the mesenteric border *(arrowheads)*, the so-called "comb" sign.

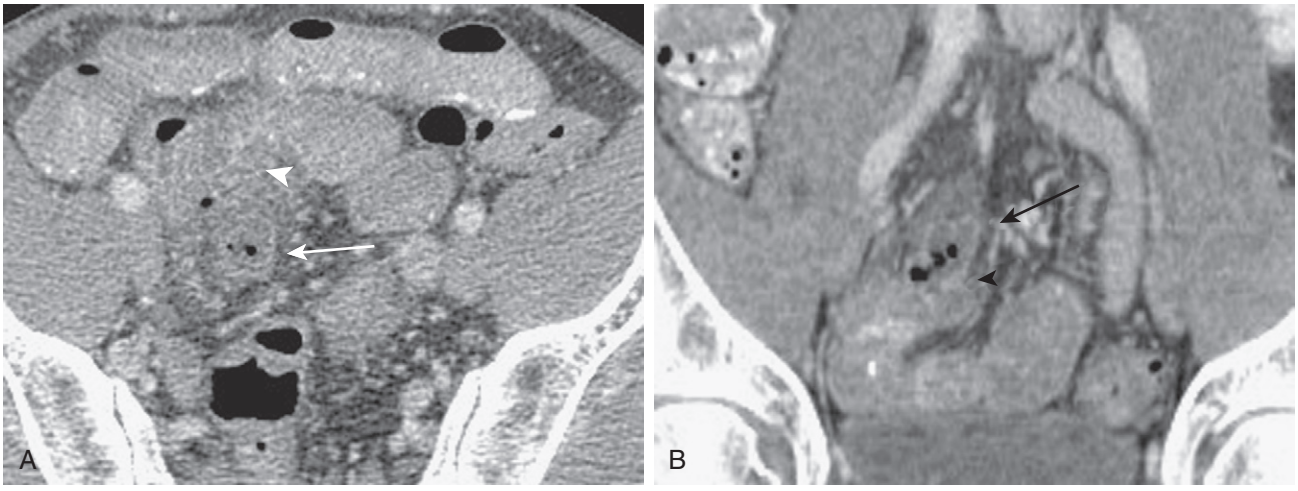


FIGURE 9-6 A 38-year-old man with Meckel diverticulitis. Axial **(A)** and coronal **(B)** portal venous phase images reveal a tubular, blind-ending pouch *(arrows)* emanating from adjacent small bowel *(arrowheads)* with surrounding inflammatory changes—findings consistent with Meckel diverticulitis.

to accumulate, distending the appendix and eventually increasing the intraluminal and intramural pressures to the point of vascular and lymphatic obstruction. Ineffective venous and lymphatic drainage allows bacterial invasion of the appendiceal wall and lumen. If untreated, perforation of the appendix may be a complication.

As noted, the classic description of patients presenting with appendicitis includes right lower quadrant pain, leukocytosis, and fever. Classically, these findings are preceded by anorexia and periumbilical pain. The migration of pain from the periumbilical region to the right lower quadrant is both sensitive and specific in the diagnosis of appendicitis. However, given the normal range of locations of the appendix, as well as varying degrees of appendiceal inflammation, patients often present with atypical signs and symptoms.

Imaging Findings. Abdominal radiographs have been shown to have little clinical utility in patients with suspected appendicitis; therefore, cross-sectional imaging may be the initial diagnostic examination of choice. In a minority of cases, a calcified fecalith may be identified in the right lower quadrant. Also, the "sentinel loop" sign may be identified in relation to appendiceal inflammation.

In the younger population, and especially in females, ultrasonography may be used as an initial imaging evaluation given radiation concerns involved with CT. Ultrasound has been shown to have a high diagnostic accuracy in the evaluation for suspected appendicitis. Typical findings

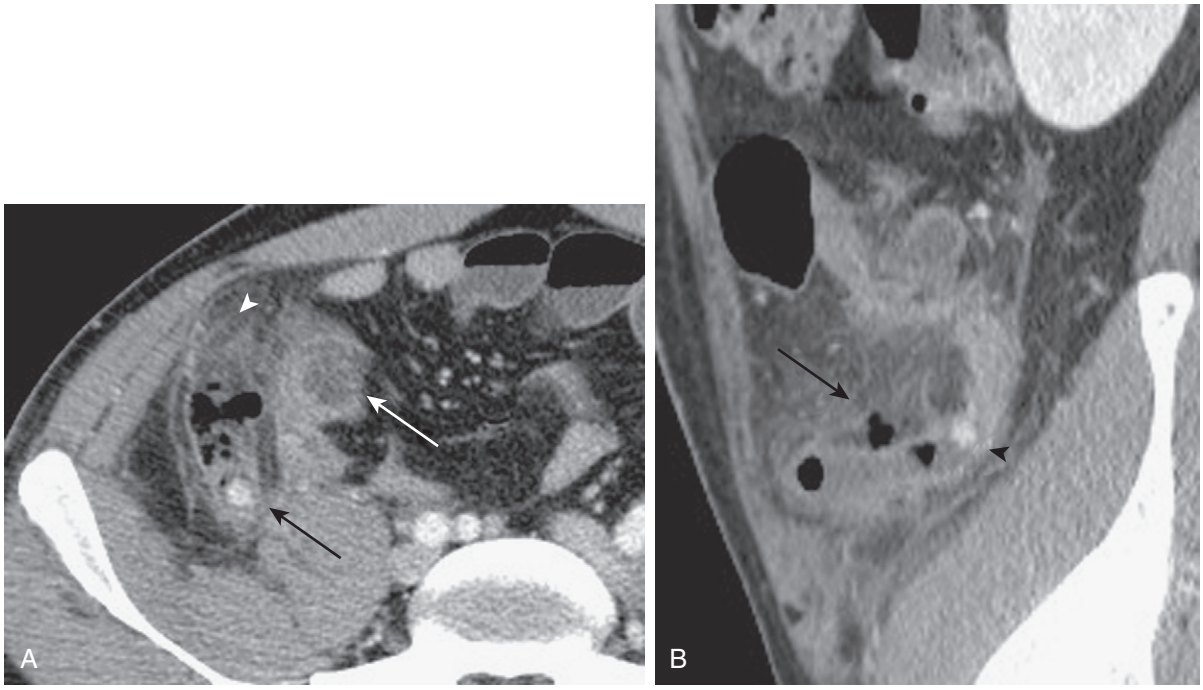


FIGURE 9-7 A 46-year-old man with a perforated appendicitis. An axial portal venous phase computed tomography (CT) image **(A)** demonstrates an inflamed appendix with periappendiceal fat stranding *(arrowhead)* and phlegmon *(white arrow)*, as well as an appendicolith at the appendiceal base *(black arrow)*. A sagittal portal venous phase CT image **(B)** demonstrates extraluminal air *(black arrow)* consistent with perforation, as well as the appendicolith *(arrowhead)*.

include the visualization of a blind-ending tubular structure measuring greater than 6 mm in diameter during graded compression. When present, an appendicolith also may be identified as an echogenic, shadowing focus within the lumen of the appendix. Secondary signs of active inflammation, including free intraperitoneal fluid, may be seen. The complications of appendicitis, which include rupture and abscess formation, also may be detected using ultrasound. Technical limitations of ultrasound include patients with an obese body habitus; moreover, given the wide variety of locations of the normal appendix, those located more posteriorly within the peritoneal cavity pose increased difficulty for evaluation.

Pregnant women often pose a diagnostic challenge when presenting with suspected appendicitis. Typically, ultrasound examination is completed to rule out other causes of abdominal pain in this patient population, such as ectopic pregnancy or ovarian torsion. However, as the gravid uterus enlarges, the appendix becomes displaced from its expected location in the right lower quadrant, and it may be difficult to visualize. Unfortunately, the normal appendix is highly unlikely to be visualized by ultrasonography in pregnant women, and further imaging is often requested to definitively exclude appendicitis. However, when the appendix is visualized on ultrasound, the findings of acute appendicitis are similar to those in nonpregnant patients and include the visualization of a blind-ending tubular structure measuring greater than 6 mm in diameter using a graded compression technique.

When the ultrasound results are equivocal or the appendix is not visualized, CT is often used in patients with suspected appendicitis. In older or significantly obese patients, CT may be the initial imaging examination. CT has been shown to have a very high diagnostic accuracy in the diagnosis of appendicitis. In patients with appendicitis, the appendix appears enlarged, often with surrounding inflammatory changes, including the free intraperitoneal fluid. When present, appendicoliths are readily identified on CT (Fig. 9-7). The diameter of the appendix varies widely in typical patients, with sizes ranging up to 1 cm. However, mean values range between 5 and 7 mm depending on whether the appendix is distended with air. Therefore, in a patient with an appendix measuring slightly greater than the standard cutoff value of 6 mm, secondary signs of inflammation should be sought, such as hyperenhancement, periappendiceal fat stranding or fluid, fascial thickening, or edema at the origin of the appendix as evidenced by thickening of the adjacent cecum, the so-called "arrowhead" sign (Fig. 9-8). Filling of the appendix by orally or rectally introduced positive contrast material is a useful means of excluding obstruction of the appendix and, therefore, acute appendicitis. When the appendix is not visualized, this finding, in the absence of right lower quadrant inflammation, carries a high negative predictive value of appendicitis.

In pregnant patients, ultrasonography is typically used initially, given risks of ionizing radiation. However, in patients with an inconclusive ultrasound examination, both CT and, with increasing frequency, magnetic resonance imaging (MRI) are often used. The findings of acute appendicitis on CT in pregnant patients are similar to those in the nonpregnant population.

Given concerns regarding radiation dose to the fetus, MRI is frequently used to evaluate pregnant patients for suspected appendicitis. MRI offers high diagnostic accuracy and is an excellent modality for excluding appendicitis.

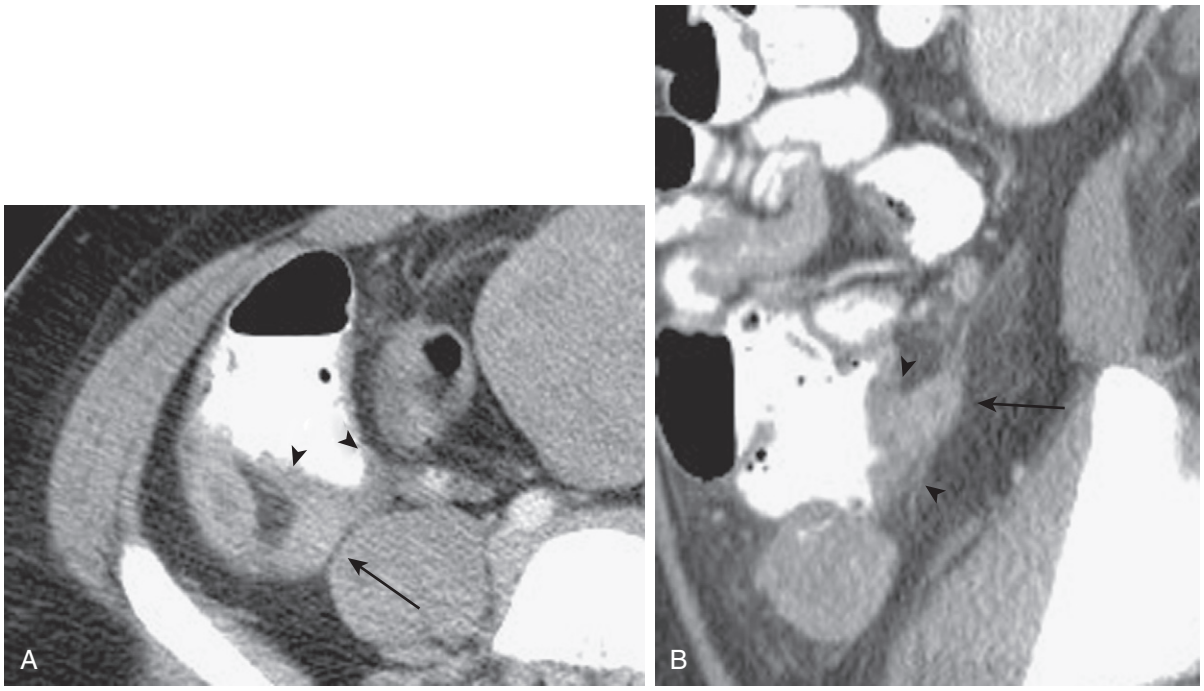


FIGURE 9-8 A 20-year-old woman with appendicitis. Axial **(A)** and sagittal **(B)** portal venous phase computed tomography images demonstrate a dilated appendix consistent with appendicitis *(arrows)*. Although not necessary in this case given the significant appendiceal dilatation, secondary signs of adjacent cecal wall thickening (*arrowheads*, **B**), the so-called "arrowhead" sign, may be useful in equivocal cases.

The appendix is considered normal when it is less than or equal to 6 mm in diameter or is filled with air or contrast material. As on CT, secondary findings such as periappendiceal inflammation are used to increase specificity when the appendix is at the upper limits of normal size. As the gravid uterus enlarges, the cecum and therefore the appendix may be in atypical locations, displaced superiorly by the uterus. Therefore, it is helpful to identify the landmarks of the terminal ileum and cecum in attempting to localize the appendix on MRI in pregnant patients.

Epiploic Appendagitis

Epiploic appendages are small fat-containing, serosal-covered outpouchings of the colon that project into the peritoneal cavity. Appendagitis represents torsion of these outpouchings with subsequent inflammation and thrombosis of the venous supply located centrally. Alternatively, spontaneous venous thrombosis has been described to increase the predilection of subsequent torsion.

Prior to the increasing utilization of CT, epiploic appendagitis was often misdiagnosed as acute appendicitis or diverticulitis given similar clinical presentations. Typically, symptoms include rapid onset of localized pain in the right or left flank, although more chronic torsion of the appendages may result in minimal or no symptoms. The pain is usually constant, and rebound tenderness is often elicited. Patients may present with low-grade fever and leukocytosis.

Imaging Findings. Given the increasingly routine use of CT imaging in patients with abdominal pain, the imaging manifestations of epiploic appendagitis have been well described. The characteristic imaging findings include an ovoid lesion containing fat, abutting the colon, with surrounding inflammatory stranding (Fig. 9-9). A central high-attenuation focus has been described and is thought to be related to a thrombosed vein. Although this finding is helpful when it is seen, the absence of this finding does not exclude the diagnosis.

Although epiploic appendagitis is typically a CT diagnosis, findings have been well described using both ultrasonography and MRI. The diagnosis using these modalities also includes the demonstration of the ovoid fatty lesion with surrounding inflammatory changes.

Omental Infarction

The cause of omental infarction is often idiopathic. It has been hypothesized that some patients may have a congenital anomalous, atypically tenuous blood supply to the omentum. However, a significant portion of cases are related to recent intraabdominal surgery. Other associations include strangulation of the omentum, such as in inguinal hernias that include portions of the omentum.

Omental infarction may present with acute abdominal pain; however, as in epiploic appendagitis, it typically represents a benign, self-limited disease process. Patients present with acute or subacute focal abdominal pain that may mimic the acute pain of appendicitis and diverticulitis. Again, patients may present with low-grade fever and leukocytosis. Occasionally, the area of infarction may be palpated as an intraabdominal mass lesion. In some cases, especially those with more severe and prolonged symptoms, operative management is successful.

Imaging Findings. Omental infarction is an alternative diagnosis that often presents with imaging features somewhat similar to those of epiploic appendagitis. CT reveals an ill-defined focal area of fat with evidence of inflammation and heterogeneous attenuation that may appear somewhat masslike. Follow-up CT imaging often

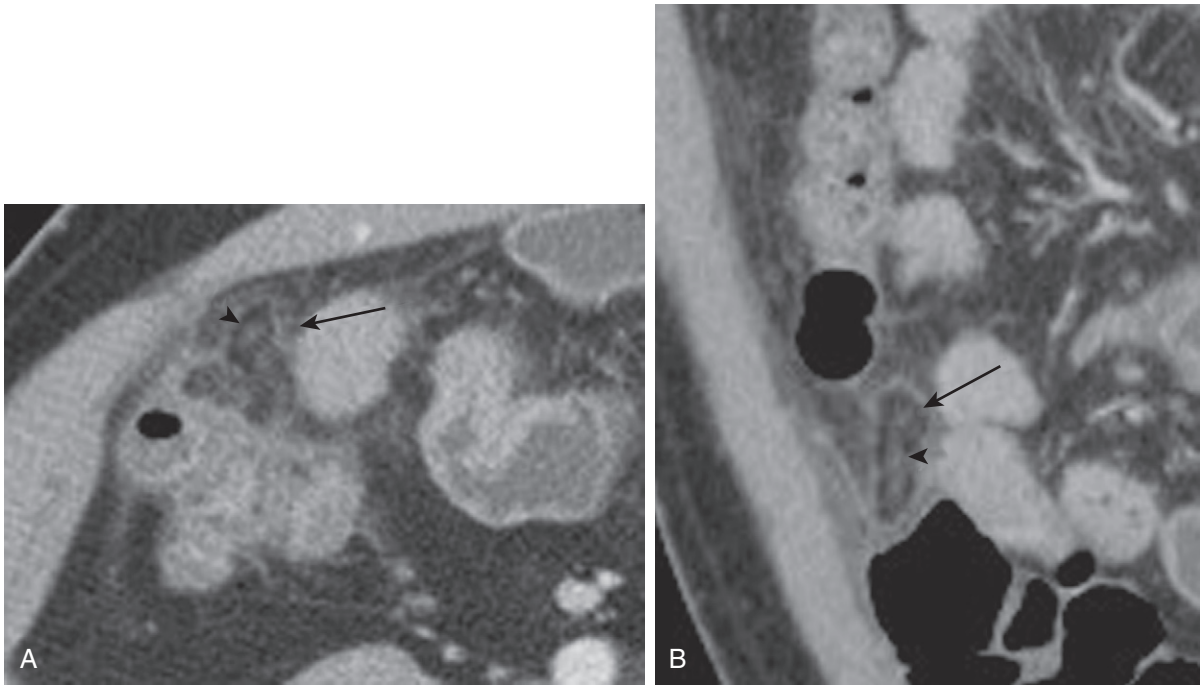


FIGURE 9-9 A 42-year-old man with epiploic appendagitis. Axial **(A)** and coronal **(B)** portal venous phase computed tomography images demonstrate a pericolonic, ovoid, fat-containing lesion *(arrows)* with a central high-attenuation focus *(arrowheads)* consistent with epiploic appendagitis.

demonstrates a more well-defined area of fat attenuation with heterogeneous attenuation throughout.

Like epiploic appendagitis, omental infarction can be readily diagnosed with ultrasound. Ultrasonography may identify the findings of a lesion that contains fat, as evidenced by a hyperechoic, noncompressible lesion in the region of the omentum.

Diverticulitis

Diverticulitis is a relatively common cause of abdominal pain and predominantly affects the colon. Diverticulitis represents the inflammation of small outpouchings, known as pulsion diverticula or pseudodiverticula of mucosa and submucosa through the regions of the underlying muscularis propria penetrated by the vasa recta. Diverticulitis is commonly a result of raised intraluminal pressures common in Western, low-fiber diets and constipation; the sigmoid colon is postulated to be most commonly affected, because it has the smallest diameter, leading to the greatest intraluminal pressures. Diverticulitis typically presents as localized, usually left-sided, abdominal pain. More severe disease, especially with the presence of complicating abscesses, may present with systemic symptoms such as fever, and leukocytosis may develop. These patients also may present with anorexia, nausea, and vomiting. Signs of peritonitis may develop with cases of more gross perforation.

Imaging Findings. Although ultrasound has been shown to be accurate in the diagnosis of acute diverticulitis, this disease is more commonly diagnosed using CT. CT scans typically involve the use of oral and intravenous contrast material. Left-sided diverticulitis predominates with the typical CT imaging findings, including colonic wall thickening and pericolonic fat stranding seen in close proximity to a diverticulum. Typically, diverticulosis is noted throughout a longer segment of adjacent colon, although only a single diverticulum is necessary to cause acute diverticulitis. Often, several small foci of extraluminal gas may be identified in the region of inflammation.

Multiple complications are associated with acute diverticulitis, including intramural sinus tracts or abscess, as well as extracolonic phlegmon or abscess formation (Fig. 9-10). Frank perforation with gross free intraperitoneal air also may be encountered in patients with diverticulitis. Other complications include the formation of fistulae that are most commonly colovesicular but may be colovaginal, coloenteric, and colouterine as well. In patients with a CT diagnosis of diverticulitis, follow-up colonoscopy is normally advised to rule out underlying malignancy masquerading as diverticulitis.

Inflammatory Bowel Disease, Colon

Inflammatory causes of colitis include Crohn disease and ulcerative colitis, both of which may present with acute signs and symptoms. Crohn disease represents granulomatous, transmural inflammation of the bowel with skip lesions in which noncontiguous segments of bowel are affected. Skip lesions are not present in ulcerative colitis. Crohn disease most commonly demonstrates an ileocolic distribution, affecting both the colon and ileum, followed by disease isolated to the ileum, typically in its distal portion, or disease limited to the colon. Ulcerative colitis, on the other hand, involves the rectum with continuous involvement of more proximal bowel, and, unlike the transmural involvement of Crohn disease, it is limited to the mucosa and submucosa with formation of crypt abscesses and mucosal ulceration.

Typical clinical presentations in Crohn disease and ulcerative colitis include abdominal pain, tenesmus, and diarrhea. A distinguishing feature may be the presentation of bloody diarrhea in patients with ulcerative colitis, a finding

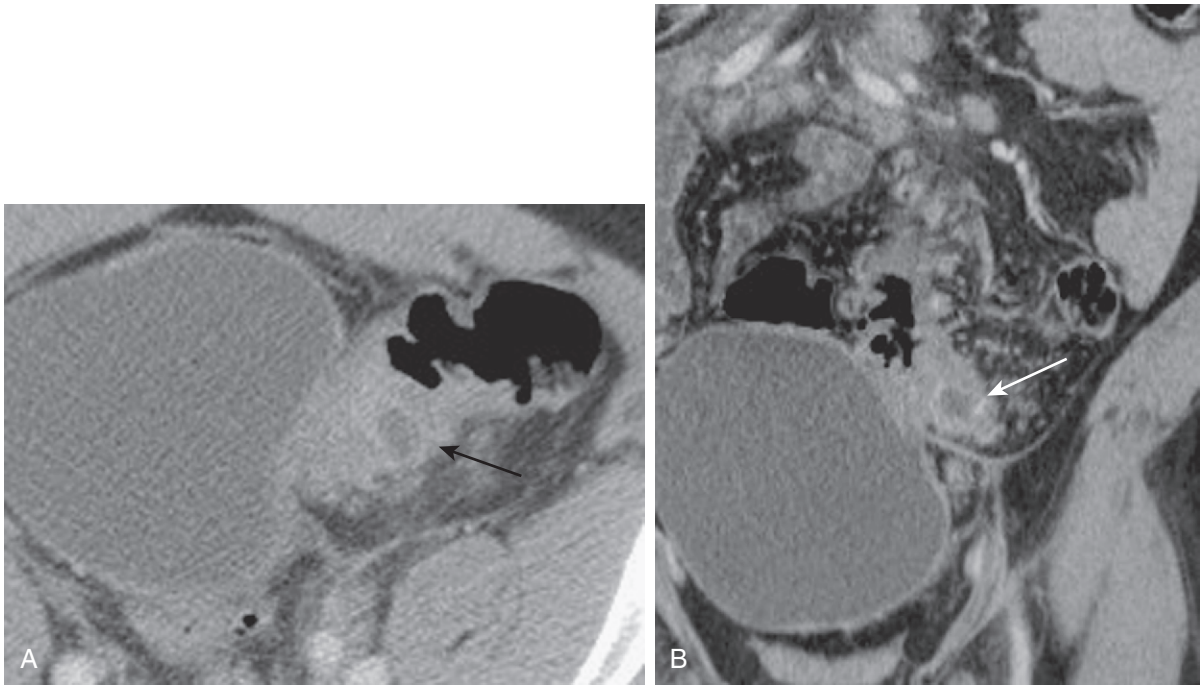


FIGURE 9-10 A 50-year-old man with diverticulitis. Axial **(A)** and coronal **(B)** portal venous phase computed tomography images reveal thickening of the sigmoid colon with a central low-attenuation focus consistent with an intramural abscess *(arrows)*.

rarely seen in Crohn disease. Especially with more severe disease, systemic symptoms such as nausea and vomiting, along with malaise and low-grade fever, may develop. Typically, Crohn disease presents somewhat more insidiously and symptoms may have persisted for several years prior to diagnosis. Also, patients with Crohn disease often have perianal disease in the form of fistulae and sinus tracts. Whereas ulcerative colitis rarely involves the small bowel, Crohn disease more commonly causes weight loss as a result of malabsorption related to small bowel involvement.

Imaging Findings. In patients with inflammatory bowel disease and acute abdominal pain, intramural edema may be identified as "thumb printing" of the colonic wall. In patients with ulcerative colitis, the colon should be evaluated for signs of toxic megacolon as evidenced by a long segment of air-filled, significantly distended colon, often greater than 6 cm in diameter. Also, dilatation of the bowel proximal to areas of active inflammation or stricture may be identified. Secondary findings in patients with inflammatory bowel disease include extraintestinal manifestations such as sacroiliitis, cholelithiasis, and renal stones that may be identified on plain radiography.

Typically, in patients presenting acutely, a CT scan is acquired in the emergency department setting. Crohn disease demonstrates bowel wall thickening in the affected segments, which are most commonly right-sided; diffuse colitis also may be seen, although isolated left-sided involvement with Crohn disease is atypical (Fig. 9-11). Ulcerative colitis, unlike Crohn disease, demonstrates contiguous involvement of the bowel from the rectum proximally. Therefore, the CT findings are usually isolated to the left side. The bowel wall may demonstrate stratification, also known as the "water halo" sign, in which the bowel wall consists of two or three symmetrically thickened layers. In the case of three symmetrically thickened layers, also known as the "target" sign, the inner hypoattenuating layer is thought to represent edema within the submucosa. In patients with chronic inflammation, as in Crohn disease or ulcerative colitis, a pattern known as the "fat halo" sign may be seen in which there is three-layer stratification, with the middle layer demonstrating fat attenuation (Fig. 9-12). The finding of a "fat halo" sign is more commonly associated with ulcerative colitis. Although these signs are nonspecific, taken in context with the remainder of the imaging findings, as well as the clinical presentation, they may suggest a potential diagnosis of inflammatory bowel disease. Also, hyperenhancement of the bowel after administration of contrast material is useful in differentiating between chronically thickened loops of bowel as a result of fibrosis and those with active inflammation.

Another classic finding in patients with Crohn disease is the so-called "creeping" fat, which represents fibrofatty proliferation of the mesenteric fat. Also, the vasa recta may be engorged in cases of acute inflammation, the so-called "comb" sign. Again, taken in isolation, this is not a specific finding for Crohn disease, because it can be seen in any hypervascular inflammation of the colon. Because the rectum is typically involved in patients with ulcerative colitis, the chronic inflammation causes proliferation of the perirectal fat, resulting in an increase in the presacral space.

Abscess and phlegmon formation are commonly encountered complications in patients with Crohn disease, given its transmural nature. Abscesses can be successfully managed percutaneously to avoid unnecessary surgery. Another complication given the transmural extent of Crohn disease is the formation of sinus tracts and fistulae. Fistulae commonly are enteroenteric and enterocolonic and also may be found within the urinary system (Fig. 9-13). Other commonly encountered fistulae are perianal and

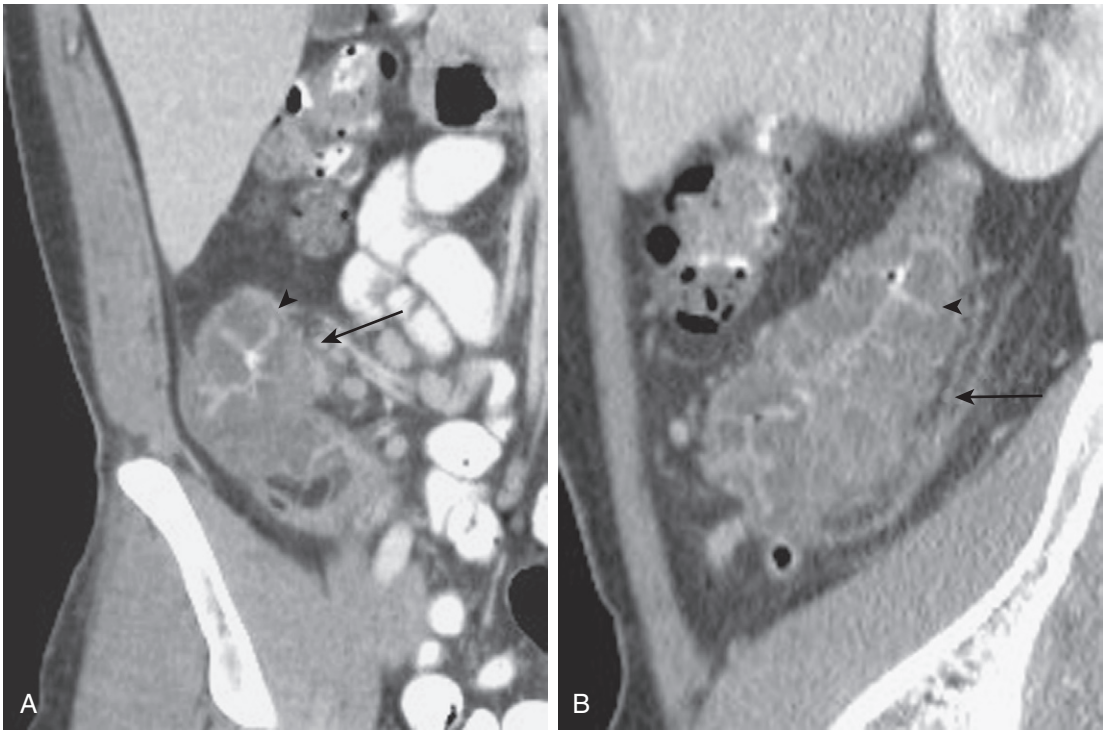


FIGURE 9-11 A 38-year-old man with Crohn disease. Coronal **(A)** and sagittal **(B)** portal venous phase images demonstrate significant cecal wall thickening *(arrows)*, with oral contrast material identified between the thickened haustra *(arrowheads)*, the so-called "accordion" sign.

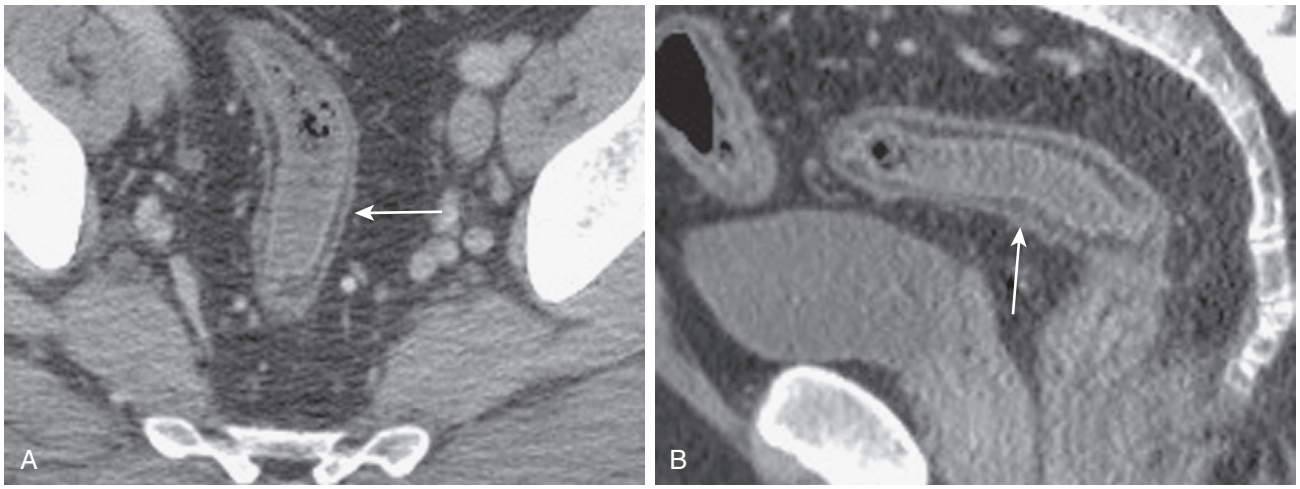


FIGURE 9-12 A 44-year-old man with chronic ulcerative colitis. Axial **(A)** and sagittal **(B)** portal venous phase computed tomography images reveal fat attenuation within the wall of the sigmoid *(arrows)*, the so-called "fat halo" sign.

enterocutaneous fistulae. Although less common, fistulae also may be encountered in patients with ulcerative colitis.

Unlike ulcerative colitis, Crohn disease affects the colon somewhat asymmetrically, because the mesenteric side may be more severely affected than the antimesenteric portion of the colon. This characteristic may result in the formation of sacculations, also known as *pseudodiverticula*.

Extracolonic manifestations of inflammatory bowel disease may be identified on abdominal CT and add specificity to a presumed diagnosis. These manifestations include sacroiliitis, which may be seen in up to 30% of patients with Crohn disease. These changes may result in eventual fusion around the sacroiliac joints in this patient population.

Another manifestation of inflammatory bowel disease that may be seen on abdominal CT is primary sclerosing cholangitis. Although more commonly associated with ulcerative colitis, primary sclerosing cholangitis also may be seen in association with Crohn disease. When primary sclerosing cholangitis is present, the typical CT findings include pruning, beading, or skip dilatations of the bile ducts. Additionally, the bile duct walls may be thickened on CT; expected normal bile duct wall thickness is approximately 1 to 2 mm. When incidentally identified, these extraintestinal manifestations of inflammatory bowel disease may increase confidence in the diagnosis in patients presenting with acute abdominal pain.

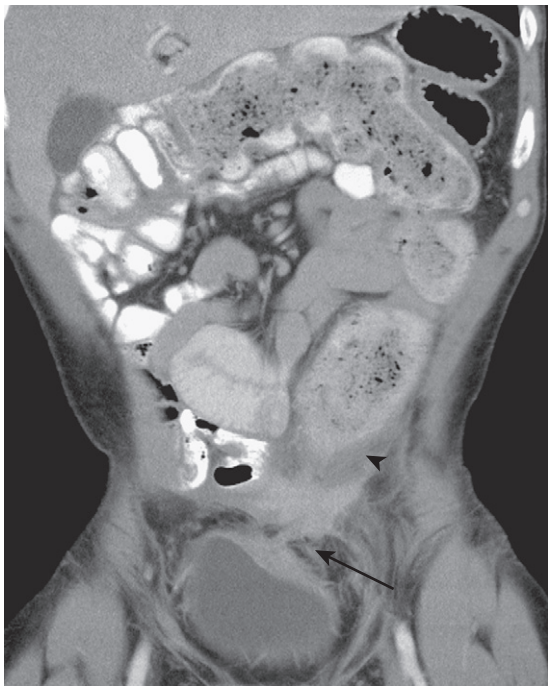


FIGURE 9-13 A 47-year-old man with Crohn disease. A coronal portal venous phase computed tomography image reveals a colovesical fistula *(arrow)* with obstruction of the colon proximally *(arrowhead)* as a result of the inflammation related to the patient's Crohn disease.

In patients with known inflammatory bowel disease who present acutely with pain, MRI is being used more frequently given concerns of ionizing radiation associated with CT. Like CT, MRI may demonstrate focal bowel wall thickening associated with hyperenhancement after administration of contrast material, as well as surrounding inflammatory changes. Associated findings previously described, such as engorgement of the vasa recta, also may be identified on MRI, as may complications of inflammatory bowel disease, including abscess or fistula formation. Perianal disease in patients with Crohn disease, in particular, is elegantly delineated with the soft tissue contrast afforded by MRI.

Infectious Colitis

Commonly encountered infectious etiologies of colitis include pseudomembranous colitis as a result of proliferation of *Clostridium difficile* related to antibiotic use, salmonella, *Shigella, Yersinia*, tuberculosis, amebiasis, schistosomiasis, *E. coli,* and cytomegalovirus, among others. The diagnosis of pseudomembranous colitis is often suspected because it is temporally related to antibiotic use. Another infectious cause of colitis is tuberculosis. Although the diagnostic dilemma may be somewhat simplified when patients display concurrent pulmonary tuberculosis, the abdominal manifestations may be seen in the absence of pulmonary infection. Neutropenic colitis or typhlitis typically affects the cecum and ascending colon, although the terminal ileum and appendix also may be affected.

The clinical presentation of infectious colitis is somewhat dependent on the underlying cause, although patients generally present with diffuse, crampy abdominal pain and diarrhea, which may be profuse and bloody. Fever and leukocytosis also may be associated with infectious colitis. In some cases, the diarrhea may be persistent, prompting the presentation.

Imaging Findings. Plain radiographs are nonspecific, but mural edema may be identified within the colon. Again, as in cases of inflammatory bowel disease, one should consider and evaluate for the complication of toxic megacolon.

The CT imaging appearances of the infectious colitides are nonspecific, and considerable overlap exists among the various causes. The CT findings typically demonstrate pancolitis with marked colonic wall thickening, approaching the severity of Crohn disease (Fig. 9-14). The "accordion" sign may be seen as edematous haustral folds, separating the oral contrast–filled lumen into narrow ridges, similar in appearance to an accordion. Although originally described as specific for patients with pseudomembranous colitis, this finding may be seen in any cause of severe colonic wall edema.

Tuberculous infection of the colon may have a somewhat more specific CT imaging appearance. In these patients, severe colonic wall thickening may be seen, commonly along with thickening of the terminal ileum, because the ileocecal area is the most frequently affected. Lymphadenopathy is classically described as low attenuation as a result of necrosis; calcification also may be seen. Like Crohn disease, tuberculosis is a well-known cause of intraabdominal fistulae, as well as sinus tracts. Tuberculosis is also one of the causes of the cone-shaped cecum. Peritoneal thickening and ascites are common manifestations of intraabdominal tuberculosis. Shallow mucosal ulcers may lead to significant gastrointestinal hemorrhage in patients with colonic involvement by tuberculosis.

The imaging characteristics of neutropenic colitis on CT are fairly nonspecific, demonstrating segmental bowel wall thickening, adjacent fat stranding, and fluid. The diagnosis of typhlitis should be entertained given these nonspecific imaging findings involving the cecum and/or descending colon in the immunocompromised patient population. Rapid diagnosis is critical to avoid complications of frank bowel necrosis and perforation.

Foreign Bodies

Foreign bodies within the gastrointestinal tract are an uncommon cause of complications. However, in cases of bowel perforation without apparent alternative causes, foreign bodies should be a consideration. In more proximal portions of bowel, the foreign bodies are typically ingested. However, more distally in the rectum, foreign bodies also are often inserted anally. Patients who ingest foreign bodies orally often have a mental disorder; patients in penitentiaries are also a frequent subset of this population. The ingested foreign bodies may include various household items, including metallic objects. The intentional ingestion of illicit narcotics may be seen in attempts to transport the narcotics. In addition, foodstuffs, including bones or the pits from fruits, may cause bowel injury. Various anally inserted foreign objects have been described, including glass and metallic objects.

Patients with complications related to orally ingested foreign bodies may present with acute abdominal pain. If bowel perforation has occurred, the signs and symptoms of peritonitis may ensue. Other complications include mechanical bowel obstruction with patients presenting with abdominal pain and distention, and possibly with nausea

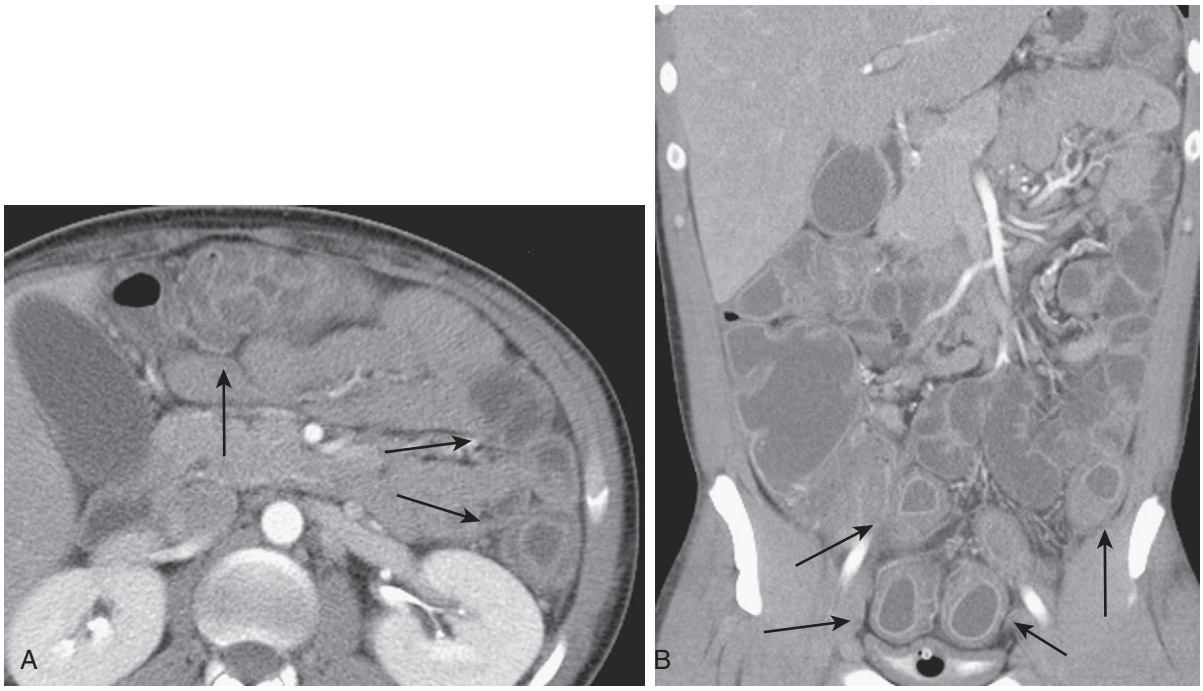


FIGURE 9-14 A 34-year-old man with fever and diarrhea as a result of *Clostridium difficile* colitis from recent antibiotic use. Axial **(A)** and coronal **(B)** portal venous phase computed tomography images demonstrate multiple thickened loops of colon *(arrows)*. Note the relative hypoattenuation of the thickened colon, well visualized on the axial image, consistent with submucosal edema.

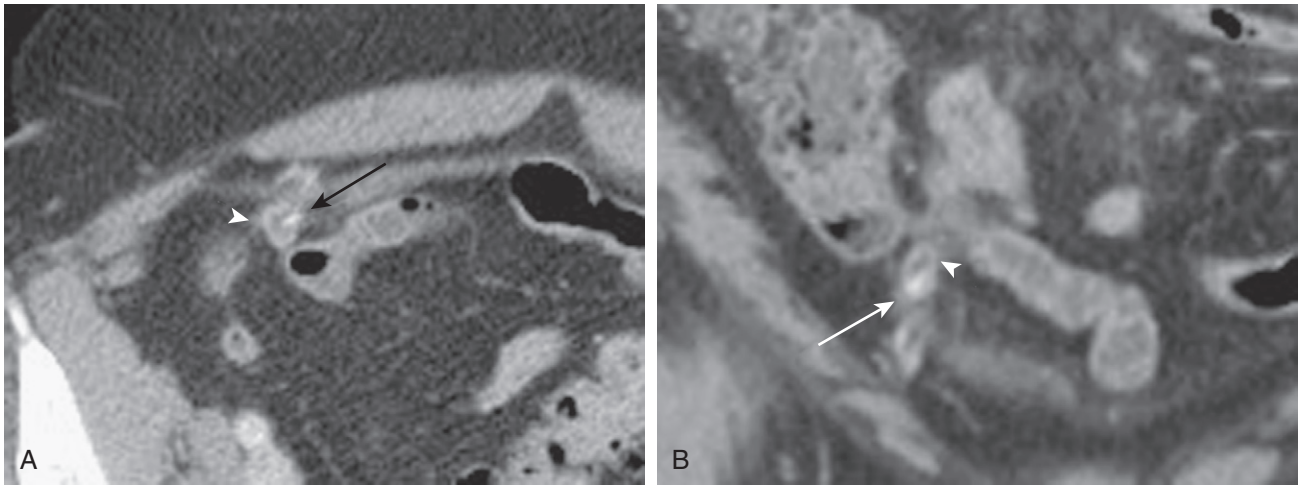


FIGURE 9-15 A 52-year-old woman with perforated Meckel diverticulum as a result of ingestion of a fish bone. Axial **(A)** and coronal **(B)** portal venous phase computed tomography images reveal a linear, hyperattenuating structure *(arrows)* consistent with a foreign body, which, in this case, happens to be located within a blind-ending tubular pouch *(arrowheads)*. Operative repair revealed a fish bone perforating the patient's Meckel diverticulum.

and vomiting. Patients with anally inserted foreign bodies may present with pain or may present to the emergency department because they are unable to extract the intentionally placed foreign body.

Imaging Findings. Foreign bodies, depending on their composition, may be radiopaque and readily identified on plain radiographs. However, smaller foreign bodies, as well as those of radiolucent composition, are not identified, although secondary findings of the related complications may be seen. These findings include evidence of free intraperitoneal air or possibly bowel obstruction. Plain radiographs may be obtained for patients with anally inserted foreign bodies to localize the foreign body prior to definitive management. Intentionally ingested illicit narcotics, which are often wrapped in various protective covers such as balloons or condoms, may be radiographically apparent.

In patients with known foreign body ingestion, CT is infrequently used for localization and evaluation of potential complications. Also, in patients with bowel perforation, and even in cases of obstruction, one may consider the possibility of a foreign body as the underlying cause. The foreign bodies, depending on the composition, also may be subtle on CT (Fig. 9-15). However, when complications ensue, they may be helpful in localizing the foreign body.

In cases of anally introduced foreign bodies, CT is particularly useful in identifying rectal injuries as evidenced by rectal wall thickening, surrounding fat stranding, and possibly free extra- or intraperitoneal air. CT is also rarely used in the evaluation of illicit narcotic ingestion.

Vascular Diseases

Vascular diseases of the bowel include acute gastrointestinal bleeding and mesenteric ischemia.

Acute Gastrointestinal Bleeding

Acute gastrointestinal bleeding is often classified into upper and lower gastrointestinal categories based on the site of hemorrhage. Noninvasive imaging is uncommonly indicated in upper gastrointestinal hemorrhage, and thus only a discussion of lower tract bleeding follows. Acute lower gastrointestinal hemorrhage is a common cause of hospital admission with significant associated morbidity and mortality. The most common colonic causes of bleeding include diverticulosis, ischemic and infectious colitis, colonic neoplasm, benign anorectal disease, and arteriovenous malformations (AVMs). Small bowel causes are much less frequent and are most commonly the result of diverticulosis, AVM, and neoplasm.

Consensus has not been reached regarding the initial imaging evaluation of patients presenting with acute lower gastrointestinal bleeding. Colonoscopy, technetium 99m (^{99m}Tc) red blood cell scintigraphy, CT, and conventional mesenteric angiography are all successfully applied, depending on the given scenario. Because colonoscopy may be limited in cases of severe, massive hemorrhage as a result of obscured visualization, alternate imaging for localization of the bleeding site is often required prior to possible operative intervention.

Patients with acute lower gastrointestinal hemorrhage report maroon stools or possibly bright red blood in the rectum, depending on the location of the hemorrhage. The signs and symptoms somewhat depend on the underlying cause. Abdominal pain and diarrhea may be associated with infectious and inflammatory colitis. Severe gastrointestinal hemorrhage may result in hemodynamic instability and shock.

Imaging Findings. Both ^{99m}Tc-labeled erythrocytes and ^{99m}Tc sulfur colloid are applied in the evaluation of acute gastrointestinal hemorrhage. However, ^{99m}Tc-labeled erythrocytes offer the possibility for delayed imaging in cases of intermittent bleeding. Nuclear scintigraphy has been demonstrated to be sensitive in the detection and accurate in the localization of the source of acute gastrointestinal hemorrhage. The diagnosis of gastrointestinal bleeding on nuclear scintigraphy depends on the visualization of an area of tracer localization that persists and is identified to move through the lumen of the bowel as a result of peristalsis. The transit within the bowel may be observed to be antegrade or retrograde; however, localization depends on the initial area of visualization.

Recently, CT has been shown to have a high diagnostic accuracy in both the detection and localization of massive gastrointestinal bleeding. Optimal results necessitate the distention of the bowel with a low-attenuation contrast agent, including water. Both unenhanced and arterial-phase intravenous contrast-enhanced images should be acquired. CT diagnosis relies on the visualization of an area of active arterial contrast extravasation. In some cases, CT may diagnose the underlying cause of acute hemorrhage, such as in the case of colonic neoplasms.

Currently, given the noninvasive alternatives, the use of conventional mesenteric angiography as the initial imaging examination has decreased. However, catheter-directed therapy such as vasopressin and, more currently, super selective embolization techniques have been shown to be effective methods of treatment.

Mesenteric Ischemia

Mesenteric ischemia most commonly occurs as a result of long-standing atherosclerotic disease, with secondary acute or chronic thrombosis or embolization, as well as any cause of hypotension resulting in hypoperfusion on a background of narrowed mesenteric arteries. Other common causes occur in patients with embolization from proximal sources such as the heart as a result of mechanical heart valves or atrial fibrillation. Various other causes of mesenteric ischemia include vasculitides, bowel obstruction, radiation, corrosive ingestion, and drugs, including immunosuppressive drugs and agents involved in treating leukemia, lymphoma, and severe inflammation within the peritoneal cavity. Typically, depending on the cause, segmental portions of the bowel are affected, although more diffuse involvement also may be seen.

The classic description of acute mesenteric ischemia is that of severe abdominal pain out of proportion to findings on physical examination. Typically, the pain is visceral and poorly localized. Nausea, vomiting, and diarrhea are associated. In severe cases, abdominal distention and peritonitis may ensue. In the minority of patients, gastrointestinal hemorrhage may occur.

Imaging Findings. The diagnosis of mesenteric ischemia may be suggested on plain radiographs by the presence of dilated loops of bowel demonstrating wall thickening, which may be seen as "thumb printing," as well as more specific signs such as pneumatosis intestinalis, or air within the bowel wall, and portomesenteric venous gas. Alternatively, the area of bowel ischemia may cause a functional obstruction and the more proximal loops of bowel may become dilated.

On CT, similar findings of dilatation and mural thickening are seen. Other findings, including abnormal decreased enhancement and ascites, as well as later findings of pneumatosis, are also clearly seen on CT. CT also offers the possibility of evaluating both the arterial and venous supply of the small bowel and may directly visualize vascular thrombosis. Therefore, in cases of suspected bowel ischemia, the administration of intravenous contrast material is of significant potential benefit. Currently, postprocessing options such as multiplanar reformations afforded by MDCT technology offer a great benefit in evaluation of the mesenteric vasculature in cases of mesenteric ischemia.

PANCREATICOBILIARY DISEASE

Pancreaticobiliary disease is commonly related to inflammatory causes, including acute and chronic pancreatitis and obstruction that is often related to biliary stone disease. Usually the clinical diagnosis and management of uncomplicated pancreatitis do not rely on imaging diagnosis;

however, the various complications of pancreatitis are typically identified and characterized on imaging. Also, biliary obstruction and the various complications of stone disease are a frequent cause of abdominal pain, and imaging is often used in its diagnostic evaluation.

Acute Pancreatitis

Inflammation of the pancreas as a result of injury to the pancreatic parenchyma from release of pancreatic enzymes is a common cause of abdominal pain and may be associated with significant morbidity and mortality. In developed countries, the most common cause of pancreatitis is alcohol abuse. Another frequent cause is biliary stone disease, which is obstruction of the pancreas by a stone lodging in the pancreatic duct, distal common bile duct, or ampulla of Vater. Other causes have been reported, including various medications such as steroids and nonsteroidal antiinflammatory drugs, infectious causes including bacterial and viral pathogens, iatrogenic causes such as endoscopic retrograde cholangiopancreatography (ERCP), direct trauma, obstructing malignancies, hypertriglyceridemia, and ischemia, usually related to surgery. Congenital anomalies such as pancreas divisum also have been implicated in an increased incidence of pancreatitis. CT or MRI imaging of pancreas divisum includes the visualization of a dominant dorsal duct without evidence of communication between the dorsal and ventral ducts.

Patients with acute pancreatitis present with epigastric pain that is typically constant but may improve when the patient is supine. Patients commonly report anorexia, possibly with accompanying nausea and vomiting. Also, patients with acute pancreatitis may be febrile. Bowel sounds are often hypoactive as a result of an ileus related to the local inflammation.

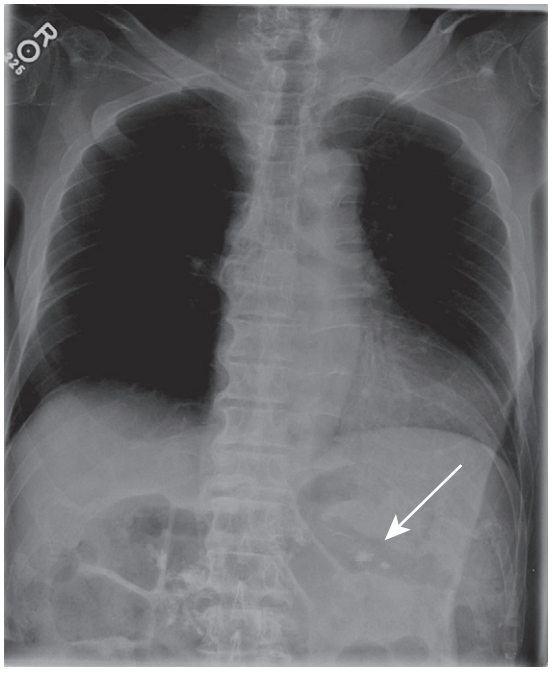


FIGURE 9-16 A 51-year-old man with chronic pancreatitis. A plain radiograph demonstrates multiple punctate foci of calcification overlying the expected location of the pancreas *(arrow)*, a finding consistent with chronic pancreatitis.

Imaging Findings

Plain radiographs may demonstrate a focal ileus as a result of the local inflammation related to the pancreas. Also, in patients with acute or chronic pancreatitis, the secondary signs of chronic pancreatitis as evidenced by parenchymal calcification may be identified.

Although imaging is not typically acquired in uncomplicated cases of acute pancreatitis, it does play a significant role in this disease process. Initial plain radiographs in patients with acute pancreatitis may demonstrate a local ileus as a result of inflammation, the so-called "sentinel loop" sign. Other findings may include the visualization of calcifications within the pancreatic parenchyma in patients presenting with acute or chronic pancreatitis (Fig. 9-16). The main role of ultrasonography in relation to acute pancreatitis is in patients with suspected gallstone pancreatitis; ultrasound may be used for confirmation of the presence of gallstones. Ultrasound also may be able to identify evidence of choledocholithiasis, although the examination of the distal aspect of the common duct is often limited on ultrasonography. Ultrasound may demonstrate the findings of acute pancreatitis because it affects the pancreatic parenchyma and surrounding peripancreatic tissues. Often, diffuse or focal enlargement of the pancreas is identified, along with evidence of edema seen as abnormally hypoechoic parenchyma. Peripancreatic fluid also may be identified on ultrasonography. Although not required for the diagnosis of uncomplicated acute pancreatitis, when they are seen, typical CT findings include focal or diffuse enlargement of the gland and edema, identified as abnormal hypoattenuation of the parenchyma and stranding along with free fluid in the peripancreatic tissues (Fig. 9-17).

In patients suspected of having complicated acute pancreatitis, CT is usually the modality of choice. The use of CT, including the Balthazar CT severity index, has been shown to be valid in prognosticating acute pancreatitis based on the degree of CT findings of peripancreatic inflammation, phlegmon, and necrosis. Necrosis is evidenced by the absence of enhancement of the affected parenchyma when compared with adjacent areas of more normally enhancing pancreatic parenchyma. Therefore, when complicated pancreatitis is of clinical concern, CT scans are typically acquired, both with and without intravenous administration of contrast material, to evaluate for degrees of enhancement within the pancreatic parenchyma. The pancreatic necrosis may be seen to affect anywhere from small areas of the pancreatic parenchyma to virtually the entirety of the gland. If these patients receive follow-up CT examinations, the areas of necrosis typically do not regain enhancement and, when treated nonoperatively, they may resorb, forming a focal cleft within the gland. If, on follow-up examinations, the initial area of pancreatic necrosis is noted to have increased in size, then these patients are more likely to undergo necronectomy. In a smaller subset of patients pancreatic necrosis will develop after an initially unremarkable CT examination. Recent evidence suggests that these patients may be subject to a particularly high morbidity and mortality. Recently, novel techniques including perfusion CT have been described in the application to acute pancreatitis and may be clinically useful in

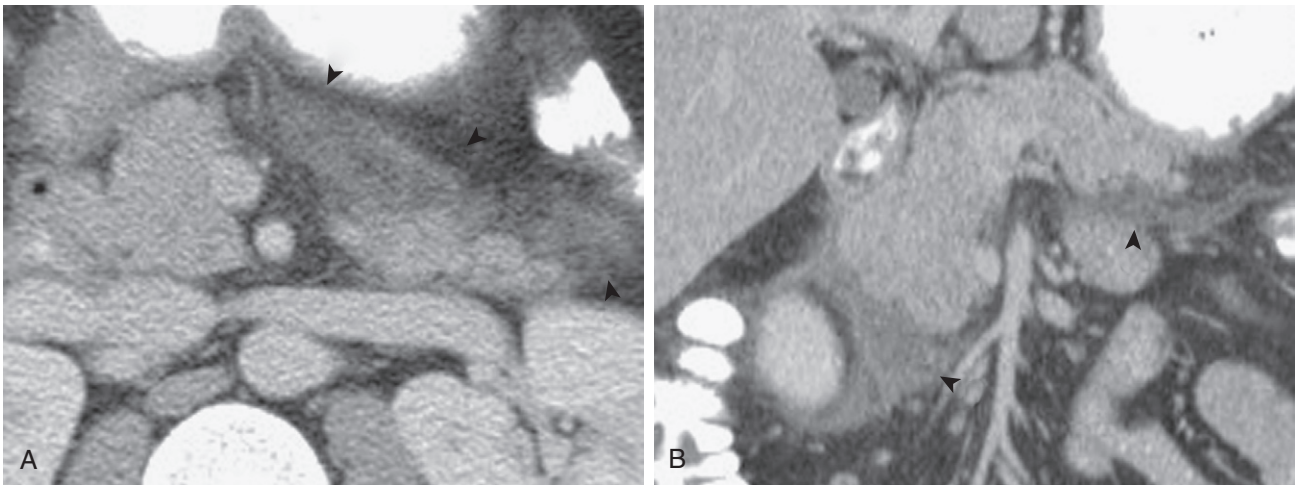


FIGURE 9-17 A 34-year-old man with acute pancreatitis. Axial **(A)** and coronal **(B)** portal venous phase computed tomography images reveal diffuse enlargement of the pancreas with peripancreatic fluid and stranding *(arrowheads)* consistent with uncomplicated pancreatitis.

assessing the status of pancreatic perfusion and possibly in predicting more severe ischemia and necrosis. Areas of pancreatic necrosis may become infected; these patients experience significant increases in morbidity and mortality. Although CT findings, such as gas bubbles within necrotic parenchyma, may be highly suggestive of infected pancreatic necrosis, patients typically undergo ultrasound or CT-guided fine needle aspiration for confirmation.

Patients with severe cases of acute pancreatitis often have increased peripancreatic fluid as a result of inflammation. Recently these findings have been shown to prognosticate both disease severity and 24-hour mortality, based on the findings of pleural effusions, ascites, or retroperitoneal fluid collections. Typically, pancreatic fluid collections are identified along the anterior or anterolateral aspect of the gland. Other common locations include the anterior pararenal space either bilaterally or asymmetrically, depending on the precise location of pancreatic inflammation, as well as within the lesser sac. Less commonly, fluid collections are identified in the posterior pararenal space, as well as within the peritoneum around the liver and spleen. These fluid collections also may dissect into the thorax, including the mediastinum.

Other complications that may be identified by CT in patients with acute pancreatitis include sequelae of injury to the splenic vasculature. These sequelae include splenic vein thrombosis, splenic infarction or subcapsular hemorrhage, and splenic artery pseudoaneurysm formation (Fig. 9-18). Rarely, pseudoaneurysms may communicate with the pancreatic duct in a condition known as *hemosuccus pancreaticus*, in which bleeding occurs into the pancreatic duct and out of the ampulla of Vater to exit into the duodenum (Fig. 9-19). Treatment of splenic artery pseudoaneurysms may be accomplished successfully via transcatheter embolization, as well as with use of percutaneous techniques.

In the minority of patients with acute pancreatitis who have pancreatic fluid collections, the fluid collections may proceed to form pseudocysts. Typically, the acute fluid collections are resorbed; however, when encapsulated and well defined in shape, they are termed *pseudocysts*. Acute pancreatitis usually causes small ductal disruption as a result of necrosis of the parenchyma, which allows the fluid collections, and eventually pseudocysts, to form. Pseudocysts typically require at least 3 to 4 weeks to form after an episode of acute pancreatitis—usually up to 6 weeks. Because they are formed from pancreatic secretions, these collections are normally amylase and lipase rich. Even when the prototypical encapsulated pseudocyst is formed, the smaller collections are highly likely to undergo complete involution with conservative management. Specifically, pseudocysts greater than 6 cm in diameter have been shown to have a significantly higher rate of operative management than do smaller lesions. For the most part, pseudocysts are treated when they are symptomatic, cause abdominal pain, are noted to enlarge on serial imaging, are noted to have become infected, or cause hemorrhage or obstruction of adjacent bowel or bile ducts.

Chronic Pancreatitis

Chronic pancreatitis represents continued, irreversible inflammation that leads to fibrosis and calcification. Eventually, endocrine and exocrine insufficiency may develop. The patient typically presents with chronic abdominal pain and, unlike with acute pancreatitis, the pancreatic enzyme levels may be either normal or only mildly elevated. The most common cause of chronic pancreatitis, as with acute pancreatitis, is alcohol abuse. Other causes include hyperlipidemia, hypercalcemia, medications, cystic fibrosis, hereditary metabolic disorders, obstruction from congenital (pancreas divisum) or acquired (e.g., posttraumatic) causes, autoimmune pancreatitis, and idiopathic pancreatitis in up to 30% of cases. The role of gallstones in chronic pancreatitis remains controversial.

Patients with chronic pancreatitis describe intermittent bouts of epigastric abdominal pain that may radiate to the back. The pain may be induced by meals or occur independently of food intake. With ongoing chronic pancreatitis, exocrine insufficiency may result in diarrhea and weight loss. Endocrine insufficiency also may develop.

Imaging Findings

As noted, plain radiographs may demonstrate the pancreatic parenchymal calcifications associated with chronic pancreatitis.



FIGURE 9-18 A 45-year-old woman with acute pancreatitis. Axial **(A)** and coronal **(B)** portal venous phase computed tomography images demonstrate complete thrombosis of the splenic, superior mesenteric, and portal veins *(arrows)*.

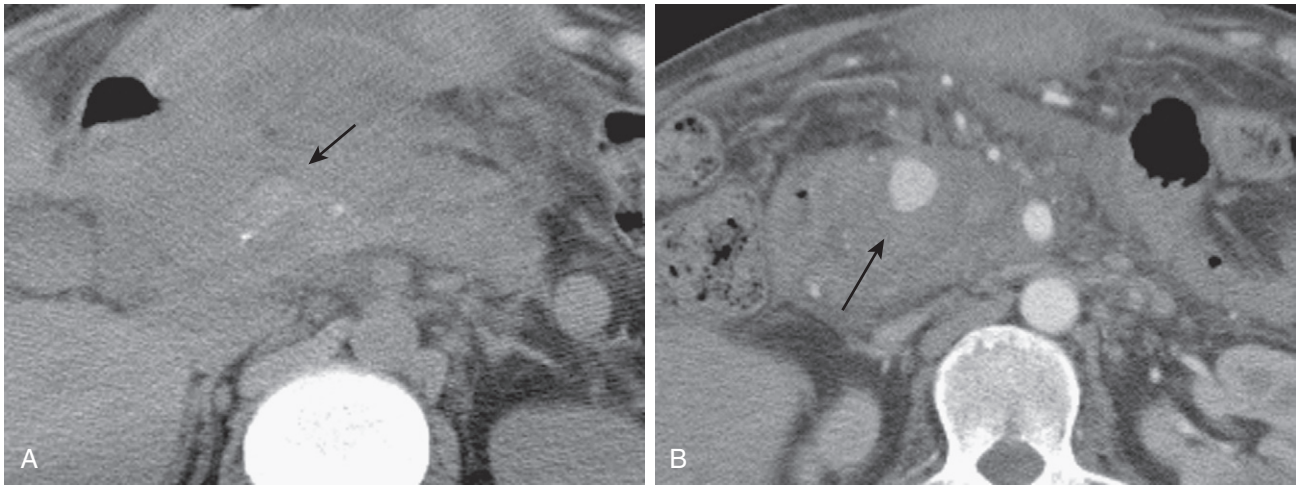


FIGURE 9-19 A 27-year-old man with a history of pancreatitis and known gastroduodenal pseudoaneurysm after attempted coil embolization with hemosuccus pancreaticus. An axial unenhanced **(A)** computed tomography (CT) image demonstrates hyperattenuation within the main pancreatic duct *(arrow)*, consistent with hemosuccus pancreaticus, confirmed on subsequent endoscopic retrograde cholangiopancreatography. An axial arterial phase CT image **(B)** demonstrates round, hyperattenuating focus *(arrow)* consistent with a gastroduodenal artery pseudoaneurysm resulting from the patient's history of pancreatitis.

On CT, the findings of chronic pancreatitis include atrophy of the parenchyma, parenchymal calcifications, and dilatation of the pancreatic duct. Pseudocysts may also be visualized in patients with chronic pancreatitis.

The findings of pancreatic parenchymal calcification as echogenic, shadowing foci, as well as the secondary ductal dilatation seen in chronic pancreatitis, are well visualized by ultrasonography. Secretin-enhanced MR cholangiopancreatography provides a functional assessment of pancreatic exocrine function and has been shown to be useful in diagnosing early stages of chronic pancreatitis prior to the morphologic changes previously noted.

Cholelithiasis/Choledocholithiasis

Gallstone disease is one of the most common gastrointestinal disorders and is estimated to have a prevalence of between 10% and 15% in the United States. Although most patients with gallstone disease remain asymptomatic, symptoms develop in approximately 20%, which

represents a significant disease burden in the adult population. The prevalence increases with increasing age and is more common in females. Additionally, increased rates of obesity in Western countries will likely further increase rates of gallstone disease. Most commonly in developed countries, gallstones are composed primarily of cholesterol, with calcium and pigments, including bilirubin and bilirubinate, composing the remaining minority of stones.

Patients with gallstone disease frequently describe symptoms of biliary colic. Generally, patients describe intermittent bouts of pain localized to the epigastrium or right upper quadrant that are gradual in onset and last up to several hours. Fatty meals may inconsistently be associated with bouts of biliary colic. Complications of gallstone disease, including cholecystitis, may infrequently be the initial presentations.

Imaging Findings

In a minority of patients, gallstones are identified on plain radiographs as calcified foci overlying the expected location of the gallbladder in the right upper quadrant.

Ultrasound is the method of choice for the noninvasive diagnosis of gallstones. Typically, gallstones are identified as freely mobile, echogenic foci demonstrating posterior acoustic shadowing. A small portion of gallstones may be affixed to the gallbladder wall and do not demonstrate mobility during the examination. The absence of posterior acoustic shadowing decreases the specificity of the ultrasound examination; however, discrete echogenic foci without shadowing most commonly represent gallstones. When the gallstones are seen within a contracted gallbladder, the wall echo shadow triad may be identified; the gallbladder mucosa is seen as a thin echogenic line anterior to a second echogenic line corresponding to the anterior wall of the gallstones with complete posterior acoustic shadowing of the more posterior aspect of the gallstones and gallbladder wall. This triad is helpful in differentiating the findings of gallstones from adjacent loops of air-filled bowel.

Although CT is not indicated in the primary detection of patients with suspected gallstone disease, gallstones may be identified incidentally on CT. Gallstones have various appearances on CT based on their composition; cholesterol stones have a range of attenuation values from 0 to several hundred Hounsfield units (HUs), although most have attenuation values less than 100 HU. Pigmented stones have slightly higher attenuation values, although they also demonstrate a wide range of values. Recently, changing peak voltage settings during CT examination has been shown to significantly increase the detection rates of gallstones.

Cholecystitis

Cholecystitis represents the sequela of obstruction of the cystic duct, most commonly by a gallstone, followed by biliary stasis and secondary infection. In a minority of patients, acute cholecystitis occurs in the absence of gallstones, termed *acalculous cholecystitis*. These patients, who represent approximately 5% to 10% of all cases of acute cholecystitis, are generally critically ill with significant, prolonged bile stasis.

Patients with cholecystitis present with right upper quadrant pain as a result of peritoneal irritation from the inflamed gallbladder. Pain is typically described as severe and constant. Nausea and vomiting are associated, and a minority of patients present with fever. Murphy's sign, which is an inspiratory pause with palpation of the right upper quadrant, may be elicited.

Imaging Findings

In patients with suspected acute cholecystitis, ultrasonography is typically used in the initial diagnostic evaluation. The ultrasound criteria for diagnosing acute cholecystitis include evidence of gallstones, gallbladder wall thickening, and distention, as well as elicitation of a sonographic Murphy's sign. To elicit a sonographic Murphy's sign, the patient is asked to breathe out with the ultrasound probe placed over the right upper quadrant. Upon the subsequent inspiration, if the patient halts the inhalation as the gallbladder passes beneath the ultrasound probe and is visualized, it is considered to be a positive sonographic Murphy's sign (Fig. 9-20). The normal gallbladder wall is typically 2 to 3 mm in diameter; gallbladder wall thickness greater than 3 mm is considered abnormal in patients with suspected acute cholecystitis. A caveat in evaluating gallbladder wall thickness is that a thickened gallbladder wall can have numerous causes. Gallbladder wall thickening can be seen in common systemic diseases such as cirrhosis, acute hepatitis, hypoproteinemia, renal failure, and congestive heart failure. Often, in patients with gallbladder wall thickening as a result of acute cholecystitis, areas of lucency corresponding to subserosal edema may be seen within the wall. Finally, in patients with acute cholecystitis, the gallbladder is typically significantly distended because of obstruction. A measurement of greater than 10 cm in the long axis of the gallbladder or 5 cm in the transverse or anterior-posterior axis is normally used to signify abnormal distention. Complications include gangrenous cholecystitis, which may demonstrate a striated pattern of gallbladder wall thickening with alternating hyperechoic and hypoechoic layers. Increasingly specific signs in more severe cases include the presence of sloughed mucosa seen within the gallbladder lumen as demonstrated by thin hyperechoic bands. In some cases of severe cholecystitis, hemorrhage may be present within the lumen, termed *hemorrhagic cholecystitis*. In these cases, ultrasound commonly demonstrates the findings of gangrene, in addition to nonshadowing intraluminal echoes, which may entirely fill the lumen of the gallbladder. Finally, emphysematous cholecystitis represents a rare but life-threatening complication, often associated with diabetes, in which foci of air are identified within the wall and/or lumen of the gallbladder. On ultrasound, echogenic foci or bands are seen with posterior ring-down artifact, or "dirty shadowing." Often, the presence of the gas obscures actual visualization of the gallbladder wall.

CT is often used for patients with nonspecific clinical presentations of abdominal pain or equivocal findings on the initial ultrasound examination. The findings of acute cholecystitis, including its complications, should be recognized on CT. As on ultrasound, CT demonstrates gallbladder wall thickening, pericholecystic fluid, and possibly pericholecystic fat stranding. In most cases, the obstructing gallstone may be identified, although this identification is less likely with CT than with ultrasound, as previously discussed. When intravenous contrast material is

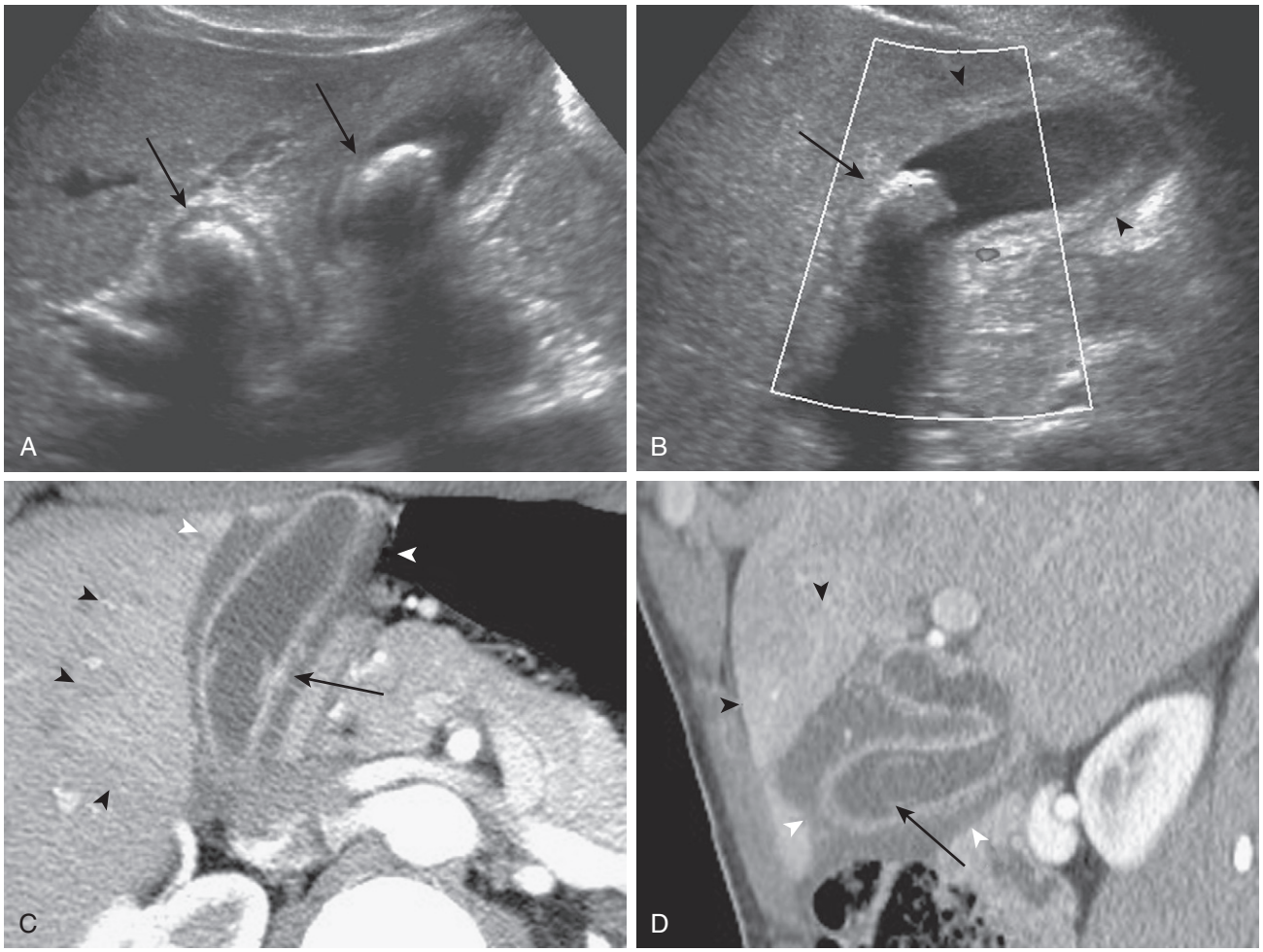


FIGURE 9-20 A 43-year-old man with acute cholecystitis. Ultrasound images **(A** and **B)** demonstrate echogenic, shadowing gallstones *(arrows)* with gallbladder wall thickening *(arrowheads)* in a patient in whom a sonographic Murphy's sign was elicited. Axial **(C)** and sagittal **(D)** portal venous phase computed tomography images reveal a gallstone *(arrows),* as well as a thickened gallbladder wall *(white arrowheads)*. Although not acquired in the arterial phase of contrast, hepatic hyperenhancement consistent with secondary inflammation is nevertheless seen *(black arrowheads)*.These findings are specific for this life-threatening complication and should be recognized and treated urgently.

administered, especially when imaging occurs during an arterial phase of enhancement, evidence may be seen of secondary inflammation of the liver around the gallbladder fossa (see Fig. 9-20). This finding is seen as relative hyperenhancement of this portion of the liver parenchyma. CT also may demonstrate the complications of acute cholecystitis. In patients with gangrenous cholecystitis, the most specific CT imaging findings are shown to be direct evidence of the sloughed membranes within the lumen, irregularity of the gallbladder wall, and perforation, including a pericholecystic abscess. Hemorrhage is also clearly identified on CT, as evidenced by increased attenuation of the intraluminal bile. Finally, emphysematous cholecystitis is also demonstrated on CT by direct evidence of air within the gallbladder wall and/or lumen.

Hepatobiliary scintigraphy is also a common modality in assessing patients with acute cholecystitis. The examination requires the services of a nuclear medicine technologist, who may not be available at all hours, and depends on on the length of the examination itself, so typically it is not used as a first-line modality. The technologist administers a radionuclide in the form of a ^{99m}Tc-labeled iminodiacetic acid derivative, which is taken up by hepatocytes and excreted into the bile ducts. This technique offers a functional assessment of the patency of the cystic duct. Normally, the radionuclide is seen within the bile ducts and gallbladder lumen before being excreted into the duodenum and proximal small bowel. Obstruction of the cystic duct eliminates visualization of the gallbladder lumen. This technique offers very high diagnostic accuracy in the assessment of acute cholecystitis. Increased specificity and the diagnosis of more severe or gangrenous cases of acute cholecystitis are achieved by the visualization of a "rim" sign of relatively increased tracer localization to the hepatic parenchyma surrounding the gallbladder fossa.

Choledocholithiasis

Common bile duct stones typically occur as a result of passage from the gallbladder and represent a cause of increased morbidity and mortality in persons with gallstone disease. Less commonly, the stones may form within the common duct itself. The classic presentation includes colicky right upper quadrant pain, which may be associated

with jaundice as a result of biliary obstruction. Alternatively, obstructing common bile duct stones may be complicated by infection, and the classic Charcot triad of fever, right upper quadrant pain, and jaundice may be the initial presentation. Common bile duct stones are also a significant cause of pancreatitis.

As in patients with cholelithiasis, biliary colic is a common presenting symptom in patients with choledocholithiasis. Less frequently, complications of choledocholithiasis, including biliary obstruction with possible cholangitis, may be the initial presenting clinical scenario.

Imaging Findings

In patients with a clinical presentation suggestive of choledocholithiasis, ultrasound may be used initially to confirm the presence of gallstones, as well as to evaluate for the secondary signs of common duct stones such as the presence of biliary dilatation. The common duct stone itself may be directly visualized by ultrasound as an echogenic, shadowing, intraluminal filling defect; however, in the majority of cases, the stones are not directly visualized.

In the acute setting, especially in patients presenting with nonspecific signs and symptoms, CT may be one of the initial imaging modalities used. Similar to gallstones, common duct stones display a wide range of attenuation values, from isoattenuating to bile to heavily calcified, and thus the diagnostic accuracy of routine CT techniques in detecting choledocholithiasis is limited. Optimal protocols for the detection of common bile duct stones are usually considered to include imaging in the absence of oral or intravenous contrast material to limit interference with the visualization of the hyperattenuating common duct stones. Recently, MDCT has demonstrated moderate sensitivity and specificity in this diagnosis, using routine CT protocols that include intravenous and oral contrast material in patients with nonspecific abdominal pain. CT findings of choledocholithiasis include the direct visualization of the common duct stone, often surrounded by lower attenuating bile, the so-called "target" sign. Other common imaging findings include the presence of a hyperattenuating stone seen eccentrically located within the bile duct surrounded by a crescent of lower attenuating bile, termed the "crescent" sign.

In patients with symptoms that lead to a moderate or high clinical suspicion of common duct stones, MR cholangiopancreatography (MRCP) and/or ERCP may be used initially, depending on the degree of clinical confidence. With MRCP, choledocholithiasis is diagnosed by the direct visualization of the common duct stones as low-signal, intraluminal filling defects. Biliary calculi are readily identified as low-signal filling defects surrounded by hyperintense bile using MRCP techniques. Differential considerations for intraluminal filling defects on MRCP include pneumobilia, blood clots, vascular pulsation artifact, and susceptibility artifact from adjacent cholecystectomy clips, among others. Pneumobilia is differentiated by its nondependent location within the bile ducts.

Hepatolithiasis

The presence of intrahepatic bile duct stones proximal to the confluence of the left and right intrahepatic bile ducts is termed *hepatolithiasis*. This entity is particularly prevalent in East Asia and is thought to be related to bile stasis and recurrent bacterial infections. Typically, the stones are pigment stones with a significant cholesterol component as well. Parasite infection by *Ascaris lumbricoides, Clonorchis sinensis,* or *Opisthorchis viverrini* has been implicated as the initial insult followed by recurrent pyogenic seeding of the susceptible bile ducts. Other initial insults include malnutrition. The cycle of recurrent bacterial infections is termed *recurrent pyogenic cholangitis*.

Patients with recurrent pyogenic cholangitis may present with signs and symptoms of acute cholangitis: right upper quadrant pain, fever, and jaundice. Also, patients may present with complications related to recurrent infection of the bile ducts, including bacteremia or sepsis, focal hepatic abscess, or, eventually, cholangiocarcinoma.

Imaging Findings

Interestingly, ultrasound has demonstrated difficulty in detecting the biliary stones associated with recurrent pyogenic cholangitis because of the soft, "mudlike" consistency of the stones. In some cases, ultrasound may directly visualize parasites within the biliary ducts.

The typical CT findings of hepatolithiasis include direct visualization of the intrahepatic stones, as well as intra- and extrahepatic biliary dilatation and stricture formation (Fig. 9-21). Hepatic parenchymal atrophy also may be identified. During the acute stages, recurrent pyogenic infections demonstrate the typical findings of inflammation on CT, including bile duct wall enhancement and adjacent hepatic parenchymal hyperenhancement. Complications of the acute disease include intrahepatic abscess and biloma formation. The dreaded long-term complication of recurrent pyogenic cholangitis is the development of cholangiocarcinoma, which typically develops in atrophic, stone-containing segments of the hepatic parenchyma and is usually associated with narrowing of the adjacent portal vein. As with ultrasound, the presence of intrabiliary parasites may be directly identified with CT.

DISEASES OF THE LIVER

Hepatitis is a relatively common clinical presentation, and the diagnosis and management of this disease typically does not require imaging. However, in unsuspected cases imaging may be performed, and the radiologist should be aware of the typical imaging characteristics and associated findings of the various hepatitides. Focal hepatic infections, on the other hand, often require imaging both in the diagnosis and in the characterization of the underlying cause. In addition, image-guided therapies are often used in the management of focal hepatic infections.

Focal Hepatic Infections

Pyogenic hepatic abscesses account for the majority of hepatic abscess cases in the United States. Pyogenic hepatic abscess formation is most commonly associated with cryptogenic, posttraumatic, and biliary causes. Portal venous seeding as a result of infections drained by the portal venous vasculature, such as appendicitis or diverticulitis, accounts for approximately 10% of cases.

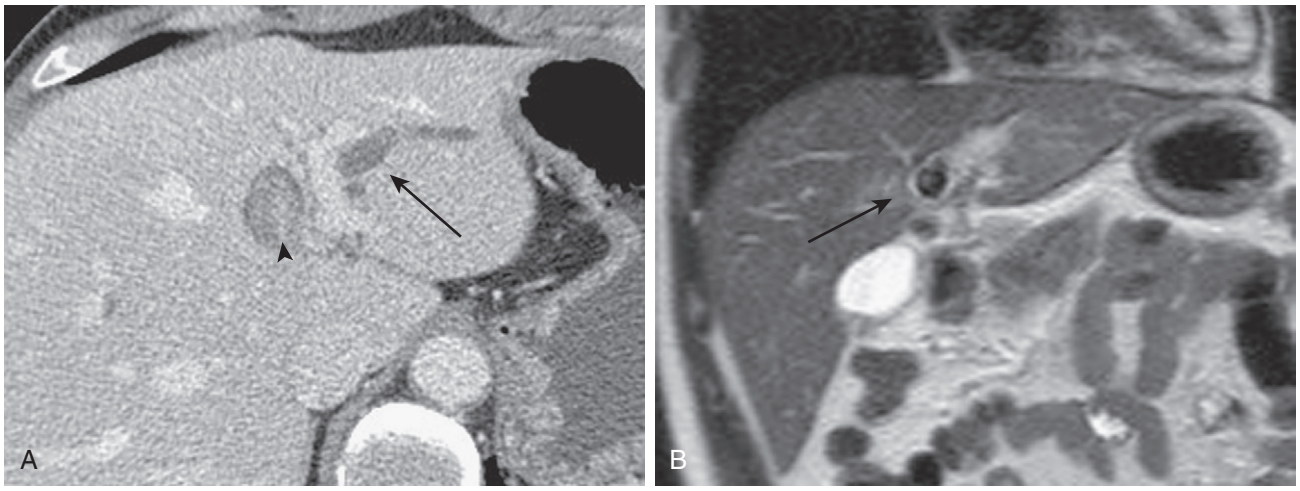


FIGURE 9-21 A 42-year-old man with a history of chronic recurrent cholangitis. An axial portal venous phase computed tomography image **(A)** demonstrates the presence of hepatolithiasis *(arrowhead)*, as well as intraductal biliary dilatation *(arrow)* as a result of a stricture related to recurrent infection. A coronal T2-weighted magnetic resonance image **(B)** confirms the presence of an intrahepatic bile duct stone *(arrow)*.

Although bacterial infections are the most common cause of hepatic abscess in the United States, worldwide, *Entamoeba histolytica* is a cause of significant morbidity and mortality. Amebic liver abscess is a common extraintestinal manifestation of *E. histolytica,* an infection with a prevalence of approximately 10% worldwide. This infection is rare in the United States; the affected patients are typically from countries where the infection is more common, including Africa, Central and South America, and India, as well as East Asian countries, or they have recently traveled to these areas. Classically, gross pathologic findings show that these collections are filled with blood products, forming a brown, thick consistency described as "anchovy paste."

Finally, *Echinococcus granulosus* is a common parasitic infection that may result in focal hepatic infection. Like amebiasis, infection of the liver occurs through the invasion of the mucosa of the bowel followed by the portal venous system. Although rare in the United States, echinococcal disease is common in the Mediterranean region, as well as in areas where raising of sheep is more common. The composition of the hydatid cyst results in its characteristic imaging features. At histopathology, it is composed of three layers: the outer pericyst and the inner endocyst, separated by a thin membrane termed the ectocyst. The outer pericyst is actually composed of compressed liver parenchyma and fibrosis.

Patients with pyogenic hepatic abscesses typically present with right upper quadrant pain, fever, and malaise. Depending on the size and number of abscesses, the presentation may be acute or more chronic and indolent with weight loss or fever of unknown origin. When irritation of the right hemidiaphragm is associated with the hepatic abscess, patients may report having referred pain to the right shoulder. Patients with amebic liver abscesses also typically report having right upper quadrant pain, and most patients present with fever. The presentation of a hydatid cyst involving the liver is variable and may be due to reports of a mass in the right upper quadrant or upper abdominal discomfort. Cyst rupture may result in a more acute presentation of pain with peritonitis.

Imaging Findings

Ultrasonography may be used in the diagnosis of pyogenic liver abscess. The typical imaging findings are of a relatively hypoechoic, heterogeneous collection surrounded by normal-appearing liver parenchyma. Often, internal echoes are identified as a result of debris and pus. However, early in the development of these infections, they may be of a more phlegmonous nature and appear ill-defined and hyperechoic relative to the hepatic parenchyma. As they mature, they take on the more classic cystic-appearing features. These collections also may contain air as a result of the presence of gas-forming organisms, and the typical hyperechoic foci demonstrating ring-down artifact are seen on ultrasound. Amebic liver abscesses demonstrate findings similar to findings of pyogenic infections on ultrasonography; hypoechoic, intraparenchymal collections often demonstrate homogeneous, low-level echoes internally. The typical imaging appearance of echinococcal disease of the liver may be identified on ultrasonography, as well as CT; uni- or multilocular collections with possible identification of smaller daughter cysts are common.

On CT, the abscesses are relatively hypoattenuating with the surrounding liver parenchyma (Fig. 9-22). Often, surrounding, smaller collections are identified in the vicinity of the largest abscess cavity. Hyperenhancement of the surrounding liver parenchyma may be identified, possibly related to local portal venous obstruction as a result of the acute inflammation. As on ultrasound, direct evidence of air may be observed within the collection. Complications of liver abscesses, including venous thrombosis, are seen in up to half of patients. The hepatic venous system is affected nearly as often as the portal veins. Contrast-enhanced CT demonstrates the nonenhancing hypoattenuating tubular structures of the thrombosed veins.

CT findings of amebic liver abscesses are similar to pyogenic liver abscesses in that a well-defined, hypoattenuating, peripherally enhancing collection is typically identified. Serologic testing, in the appropriate patient population with typical CT findings, often solidifies the diagnosis. Extrahepatic extension of the infection is relatively common, a possible discriminating imaging finding

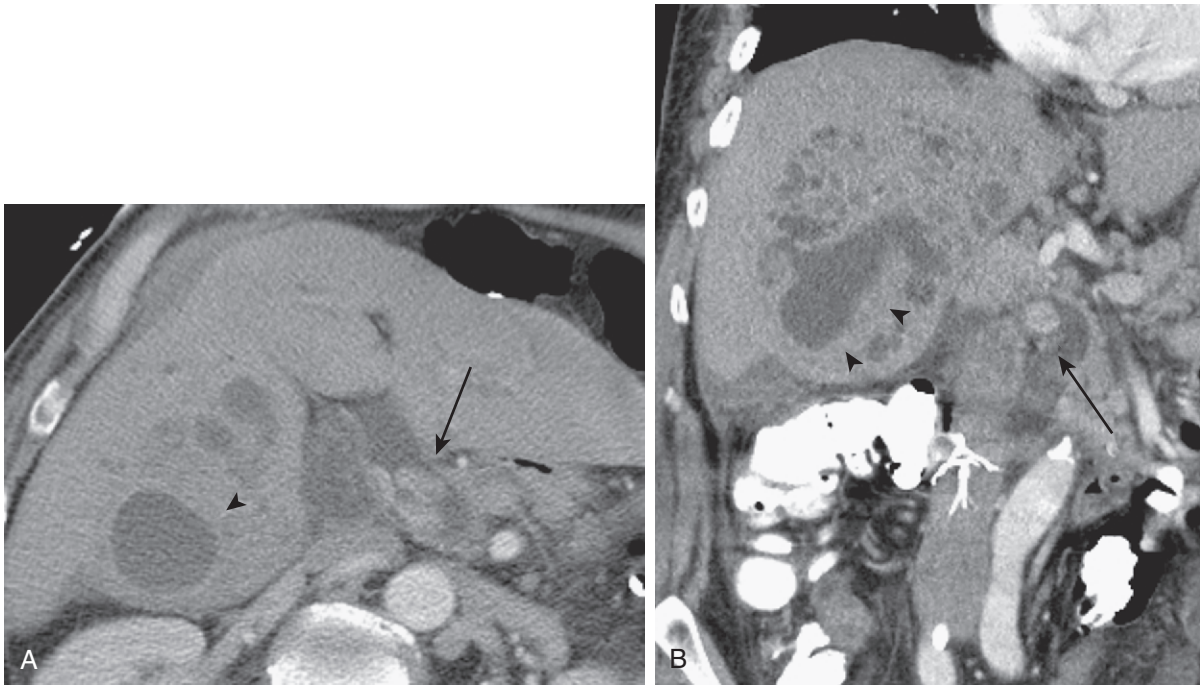


FIGURE 9-22 A 70-year-old man with choledocholithiasis and a hepatic abscess. Axial **(A)** and coronal **(B)** portal venous phase computed tomography images demonstrate large bile duct stones *(arrows)* with a focal intrahepatic fluid collection *(arrowheads)* consistent with the patient's known pyogenic abscess.

when considering this diagnosis. Extension into the pleural space, chest wall, pericardium, bile ducts, bowel, and surrounding viscera has been described.

Both ultrasound and CT may diagnose the findings of echinococcal disease within the liver. Typically, these cystic lesions are identified as uni- or multilobular collections. Often, small daughter cysts are seen within the larger lobules, a finding highly specific for echinococcal disease. Another fairly specific sign for echinococcal disease is the so-called "water lily" sign, in which the endocyst ruptures and is seen floating dependently within the outer layers of the cyst. Complications, when affecting the liver, include rupture into the peritoneal cavity or into the biliary tracts.

In all three of the aforementioned focal hepatic infections, radiology may play a role in management. In patients presenting with pyogenic abscesses, ultrasound or CT-guided percutaneous needle aspiration or catheter placement combined with antibiotic therapy results in a definitive treatment for most patients. In patients with amebic liver abscess, medical management with metronidazole is successful in the majority of patients. However, persons with more severe disease burden may benefit from percutaneous drainage using ultrasound or CT guidance. Finally, in patients with echinococcal liver disease, surgery remains the cornerstone of treatment. However, percutaneous therapy has been shown to be successful, often in conjunction with scolicidal agents. Typically, patients are treated with albendazole prior to intervention to avoid the risk of anaphylaxis by causing the cyst material to become nonantigenic.

Hepatitis

A myriad of underlying causes exist for acute hepatitis, including toxic causes such as alcohol and various medications, infectious causes, and autoimmune causes, among others. Typically, imaging is not used in the evaluation and diagnosis of hepatitis, although the findings of hepatitis should be recognized if imaging is acquired for another indication or if the diagnosis of hepatitis is not suspected.

Patients with diffuse inflammation of the liver or acute hepatitis may present with a wide range of clinical signs and symptoms, from mild forms to fulminant hepatic failure. Often, abdominal discomfort, anorexia, nausea, and vomiting, as well as jaundice, may be associated with acute hepatitis.

Imaging Findings

Two distinct ultrasound patterns have been described in patients with acute hepatitis: the "bright liver" and the "starry sky" appearance. The bright liver refers to increased parenchymal echogenicity and attenuation of sound as it passes through the abnormal liver parenchyma. This pattern is nonspecific and can be seen in patients with acute alcoholic hepatitis, cirrhosis, chronic hepatitis, and diffuse fatty infiltration of the liver. The second pattern, called "starry sky," refers to a diffuse decrease in echogenicity of the liver as a result of edema of the hepatocytes, causing the walls of the portal venules to be seen as echogenic areas on the dark background of the edematous hepatic parenchyma. This finding is also nonspecific and has been described in other diseases involving the liver, including Burkitt lymphoma and in fasting patients. Another finding that may be identified on ultrasound in patients with acute hepatitis is diffuse gallbladder wall thickening. Viral hepatitides are associated with gallbladder wall thickening, and fairly significant periportal lymphadenopathy may be seen.

Typical CT findings of acute hepatitis are nonspecific and may include findings of periportal edema, also known as a periportal "collar," hepatomegaly, and ascites.

As on ultrasound, gallbladder wall thickening and lymphadenopathy may be identified in patients with viral hepatitides.

DISEASES OF THE GENITOURINARY TRACT

Genitourinary disease, especially nephrolithiasis and its complications, represents a significant cause of abdominal pain and commonly requires imaging to be diagnosed. Infectious genitourinary diseases, such as pyelonephritis, less commonly require imaging diagnosis; however, the complications of the various genitourinary infections may necessitate an imaging evaluation. Finally, acute vascular insults of the kidney, including infarcts and renal vein thrombosis, are commonly diagnosed using cross-sectional imaging.

Nephrolithiasis

Renal calculi are usually caused by crystallization of the supersaturated stone-forming materials from urine. Calcium is the most common stone-forming material, with uric acid constituting the second largest component. Numerous other less common components are described, including xanthine, cystine, struvite, and precipitation of medications such as protease inhibitors in the human immunodeficiency virus (HIV) population, among others. Alternatively, renal disease may initiate the formation of crystals within the renal tubules that are extruded into the renal collecting system to undergo further growth. Ureteral calculi are most commonly a consequence of renal calculi passing distally into the ureters.

Nephrolithiasis and ureterolithiasis present with pain in the region of the flanks, which may radiate into the groin, especially with distal progression of the stones into the ureter. Costovertebral tenderness is commonly elicited in patients with nephrolithiasis. Also, hematuria is often associated with nephrolithiasis.

Imaging Findings

Nephrolithiasis may be identified as focal calcific densities projecting over the renal shadows. The expected course of the ureters should be analyzed for evidence of ureteral calculi. Bladder calculi also may be identified on plain radiographs. In patients with a known history of renal calculi who have undergone lithotripsy, plain radiographs may be used to evaluate for residual renal or ureteral calculi. When multiple ureteral calculi are identified after lithotripsy, it is termed *Steinstrasse*. The translation of this German term is "stone street."

Ultrasound is often used in patients presenting with acute renal failure and may demonstrate findings of nephrolithiasis, possibly with signs of obstruction. Renal calculi are seen as echogenic foci, typically demonstrating posterior acoustic shadowing. Also, signs of hydronephrosis and hydroureter may be identified on ultrasound in patients with acute obstruction. Proximal and distal ureteral stones may be clearly identified on ultrasonography; however, ultrasound is limited in the evaluation of the entirety of the ureter, and therefore sensitivity in detecting ureteral calculi is significantly less than with CT.

Renal stone CT protocols are usually acquired without the use of oral or intravenous contrast material, which may obscure the underlying stones. CT has a high diagnostic accuracy in the detection of renal and ureteral calculi and may be used to differentiate among stones of various chemical compositions. Recently, ultra-low-dose CT with a radiation dose equivalent to an x-ray examination of the kidneys, ureters, and bladder has been shown to be diagnostically sufficient in evaluating renal and ureteral calculi. Renal stones are most commonly composed of calcium in the form of calcium oxalate, calcium phosphate, and calcium urate. Other common stones are struvite, uric acid, and cystine stones. These most common forms of renal stones are all readily identified by routine CT techniques (Fig. 9-23). However, in patients with HIV who have a clinical suspicion of nephrolithiasis, protease-inhibitor induced stones, because they are not routinely identified on CT, should be a consideration.

Secondary signs of acute ureteral obstruction include enlargement of the kidney, which often demonstrates diffusely decreased attenuation secondary to edema, perinephric stranding, and dilatation of the ureter and collecting system. Three areas of narrowing in the course of the ureter are common areas for the identification of obstructing ureteral stones. These areas include the ureteropelvic junction, the pelvic brim as the ureter crosses into the pelvis, and the ureterovesical junction. Ureteral stones, when identified in the pelvis, may demonstrate a soft tissue "rim" sign surrounding the calculus, distinguishing a ureteral calculus from adjacent pelvic vein phleboliths.

Pyelonephritis

Pyelonephritis is typically caused by *E. coli* or *Enterococcus faecalis* in the outpatient community population. In patients who do not respond to therapy, or in whom symptoms progress, ultrasound or CT may be used to evaluate the various complications of pyelonephritis.

Patients with pyelonephritis may describe a preceding lower urinary tract infection including dysuria, frequency, and lower abdominal pain. Subsequently, patients often experience flank pain, which may be either unilateral or bilateral. Fever and leukocytosis may be associated with pyelonephritis.

Imaging Findings

Uncomplicated pyelonephritis may demonstrate an enlarged, swollen kidney with areas of increased or decreased renal parenchymal echogenicity. More so in children, power and color Doppler techniques have been used to diagnose pyelonephritis based on focal areas of hypovascularity.

On CT, simple pyelonephritis may demonstrate a striated nephrogram, as well as ill-defined hypoattenuating areas within the parenchyma. These findings are caused by the decreased excretory function of the renal tubules as a result of obstruction by inflammatory debris, vasospasm, and surrounding parenchymal edema. Delayed enhancement as a result of vasospasm may be identified on the affected side. Other findings associated with pyelonephritis on CT may be thickening and hyperenhancement of the urothelium. Perinephric stranding also may be identified.

Renal Abscess

Renal abscess formation is a potential complication of pyelonephritis, the suspicion of which typically entails the use of imaging for characterization. The imaging

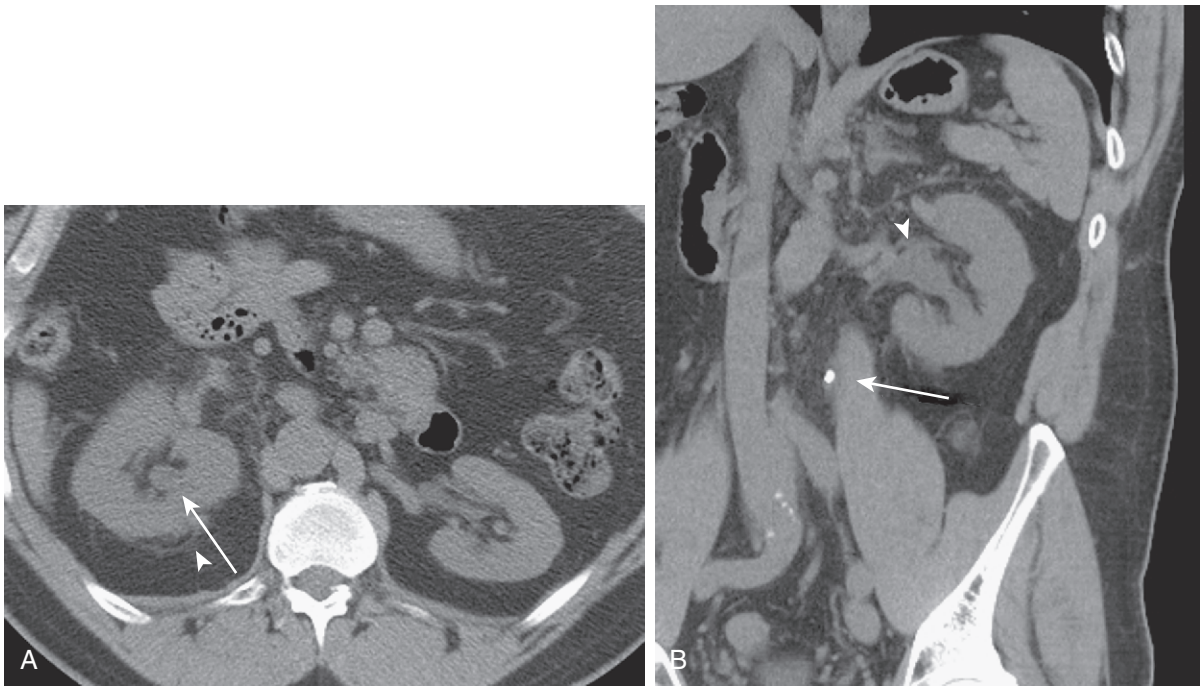


FIGURE 9-23 A 59-year-old woman with obstructing ureteral calculus. An axial unenhanced computed tomography (CT) image **(A)** demonstrates mild diffuse enlargement of the right kidney with hydronephrosis *(arrow)* and mild perinephric stranding *(arrowhead)*. A coronal unenhanced CT image **(B)** demonstrates hydronephrosis *(arrowhead)* and the ureteral stone *(arrow)*.

characteristics of the abscess, when identified, are used for planning management.

Patients with a renal abscess commonly present with fever, chills, and abdominal pain. Associated urinary tract symptoms also may be reported. Leukocytosis is typically associated with a renal abscess.

Imaging Findings

The distinction between a focal renal abscess and acute focal bacterial nephritis has important implications for subsequent management. Renal abscesses usually demonstrate ultrasound findings of a complex, focal, hypoechoic region within the parenchyma, often with internal echotexture but with evidence of increased through-transmission (Fig. 9-24). It has been reported that focal bacterial nephritis lacks the increased through-transmission of a renal abscess.

CT demonstrates focal, low-attenuation areas that may extend into the perirenal soft tissues. These areas are more readily identified with intravenous contrast material, thereby increasing the attenuation differences between normally enhancing renal parenchyma and the nonenhancing abscess collection. Often, secondary CT signs of inflammation accompany a renal abscess, including perinephric fat stranding.

In patients with a renal abscess, percutaneous drainage via ultrasound or CT guidance may be used to successfully manage patients, an approach that has been shown to have outcomes similar to those of surgical management. However, smaller abscess collections may be treated successfully with use of intravenous antibiotics.

Emphysematous Pyelonephritis

Emphysematous pyelonephritis represents a severe renal parenchymal infection that is almost exclusively encountered in diabetic patients. The most commonly cultured organism in patients with emphysematous renal tract disease is *E. coli.* Because this entity results in significant increases in morbidity and mortality, emphysematous pyelonephritis should be considered in all diabetic patients with signs and symptoms of pyelonephritis.

Patients with emphysematous pyelonephritis often present with fever and flank pain. In severe cases, crepitus may be appreciated. Also, given the severity of the infection, a significant portion of patients may present with frank septic shock.

Imaging Findings

CT is primarily used as the initial imaging modality for evaluating complicated pyelonephritis, including emphysematous infections. CT clearly demonstrates gas within the renal parenchyma that may extend into the perirenal soft tissues. A classification system based on imaging has been shown to have prognostic implications. Two types of emphysematous pyelonephritis are described: type I without and type II with associated renal or perirenal fluid collections. Persons with associated fluid collections have a more favorable prognosis, which is hypothesized to be a result of a more favorable immune response as evidenced by the presence of fluid collections. The diagnosis of emphysematous pyelonephritis is a medical emergency and typically requires emergent nephrectomy, although successful management has been described using percutaneous drainage or medical therapy.

Xanthogranulomatous Pyelonephritis

Xanthogranulomatous pyelonephritis (XGP) represents a chronic inflammatory condition of the renal parenchyma.

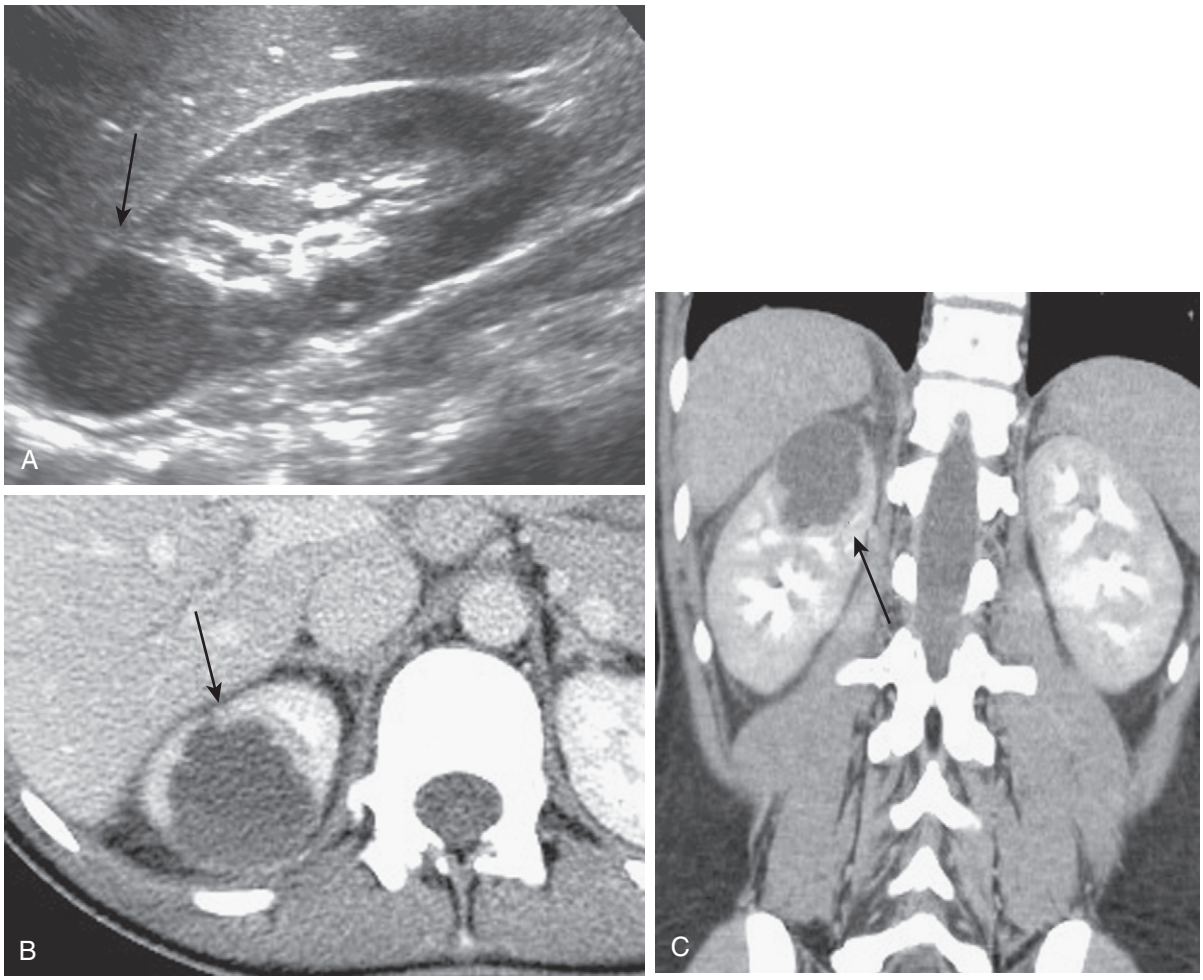


FIGURE 9-24 A 37-year-old woman with renal abscess. An ultrasound image **(A)** reveals a focal hypoechoic area within the renal parenchyma with scattered internal echoes *(arrow)*. Axial **(B)** and coronal **(C)** portal venous phase computed tomography images reveal a corresponding focal hypoattenuating area within the parenchyma of the right kidney, findings consistent with a renal abscess.

XGP has been associated with urinary tract infections as a result of *E. coli* and *Proteus mirabilis* and is almost exclusively seen in patients with underlying urinary tract obstruction, commonly as a result of stone disease. Histopathologically, lipid-laden "foamy" macrophages accompany both acute and chronic inflammatory cells. Most commonly, the kidney is affected diffusely, although focal involvement of a portion of the parenchyma also may be identified. CT and ultrasound demonstrate the findings of XGP, although, usually, definitive preoperative diagnosis is difficult because renal malignancy remains on the list of differential diagnoses in most cases.

Patients with XGP present with signs and symptoms of a chronic illness: anorexia, weight loss, fevers, and flank pain. Because XGP may create a fistula with adjacent soft tissues, patients initially may present with cutaneous fistulas.

Imaging Findings

Few ultrasound imaging characteristics are available to distinguish XGP from a renal tumor because the most common ultrasound finding is that of a circumscribed, solid renal mass, which may be hyperechoic, isoechoic, or hypoechoic with respect to the renal cortex. Hydronephrosis and renal calculi are commonly identified on ultrasound.

CT demonstrates renal enlargement with fluid-filled cavities replacing the renal parenchyma, often with extension into the perinephric tissues, findings suggestive of XGP. Again, hydronephrosis and renal calculi may be identified in patients with XGP (Fig. 9-25). CT evidence of fistula formation with surrounding tissues, including bowel or skin, lends credence to a suspected diagnosis of XGP.

Pyonephrosis

In patients with fever, chills, and flank pain, as well as obstruction of the urinary tract established on imaging, pyonephrosis should be highly suspected. Pyonephrosis represents infection of an obstructed urinary tract and is a medical emergency. Because this scenario of infection within the obstructed collecting system represents "pus under pressure," the condition of these patients can rapidly deteriorate and septic shock can develop, along with possible irreversible deterioration of renal function.

Imaging Findings

Typically, ultrasound is indicated to demonstrate obstruction of the affected urinary system as evidenced by hydronephrosis and possibly hydroureter. Also, fluid–fluid levels

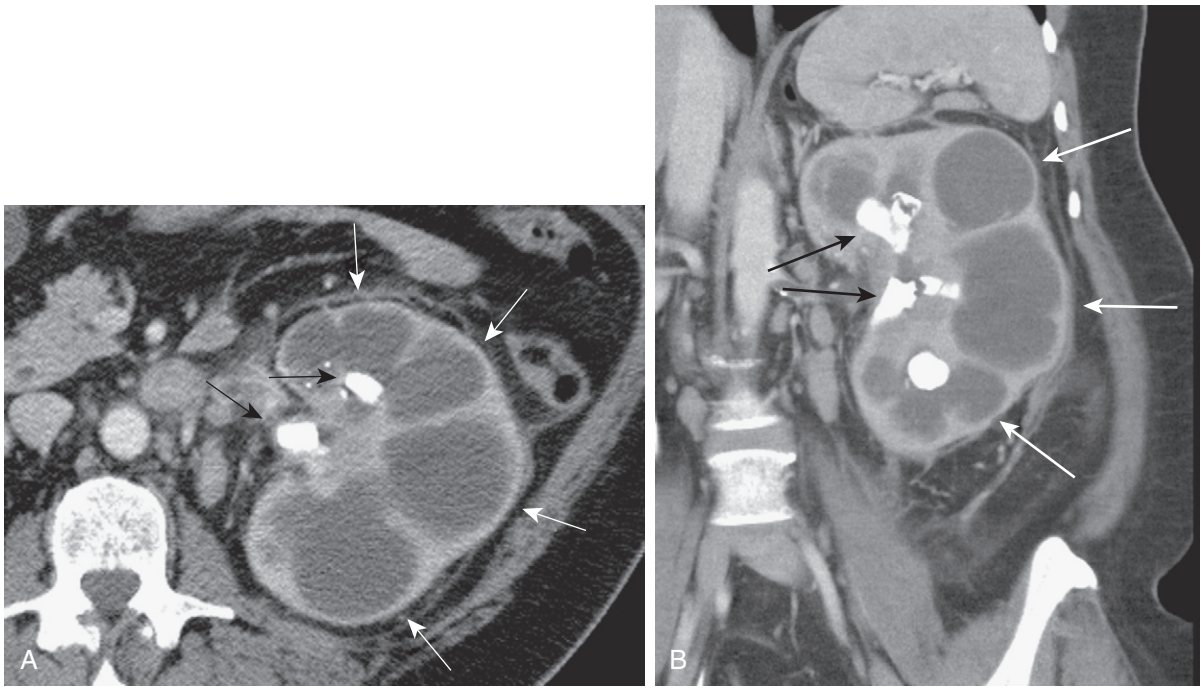


FIGURE 9-25 A 50-year-old woman with xanthogranulomatous pyelonephritis (XGP). Axial **(A)** and coronal **(B)** portal venous phase computed tomography images demonstrate significant enlargement of the left kidney with large renal calculi *(black arrows)* and large, low attenuation infiltration of the renal parenchyma *(white arrows)*, characteristic of XGP.

and coarse or possibly low-level echoes are described in pyonephrosis.

On CT, the findings of renal obstruction as evidenced by hydronephrosis are identified. The obstructing lesion also may be characterized with CT. CT findings of inflammation may be identified, including inflammatory fat stranding around the collecting system and ureter, as well as hyperenhancement of the urothelium. Thickening of the urothelium of the renal pelvis also may be identified.

Prompt placement of a percutaneous nephrostomy tube is indicated in these patients with pyonephrosis, who often eventually require subsequent definitive management to treat the underlying obstruction.

Emphysematous Cystitis/Pyelitis

Emphysematous cystitis represents a rare, fulminant infection of the bladder, again associated with underlying diabetes. Repeated urinary tract infections, neurogenic bladder, and bladder outlet obstruction have also been described in association with emphysematous cystitis. Commonly isolated organisms include *E. coli* and *Enterobacter aerogens.* Common causes of air within the bladder should be considered and excluded, such as recent instrumentation—for example, Foley catheter placement or cystoscopy. Less common alternative causes of air within the bladder include fistulas with adjacent loops of bowel. Clinical history is often helpful in excluding these considerations. Unlike emphysematous pyelonephritis, conservative treatment with antibiotics is usually successful in treating emphysematous cystitis.

Emphysematous pyelitis refers to gas within the renal collecting system. Typically, the gas is a result of emphysematous infections of the bladder and kidney, although primary infection of the urothelium is a less common cause. Again, other causes of air within the bladder and collecting system should be excluded as previously detailed. Emphysematous pyelitis, because it is most commonly a result of infection of the bladder or kidney, is normally managed by treating the underlying abnormality.

Patients with emphysematous cystitis often have fairly subtle clinical presentations, and therefore a high clinical suspicion is necessary in the appropriate patient population. Complaints include dysuria, fever, and hematuria. Although not sensitive, a report of pneumaturia is highly specific to this diagnosis.

Imaging Findings

Plain radiographs may demonstrate mottled or curvilinear lucencies overlying the expected location of the bladder wall. Also, an air–fluid level may be identified in patients with intraluminal air; this level is noted to change position with the patient. The intraluminal air also may outline the irregular mucosal surface, distorted by submucosal blebs, termed the *beaded necklace* appearance.

In patients with emphysematous cystitis, CT is highly sensitive for the finding of air localized within the bladder lumen or wall. It is important to exclude air within the renal parenchyma in these cases.

Renal Infarct

Nontraumatic renal infarcts are typically a result of embolic phenomena, which may be secondary to atrial fibrillation, left ventricular thrombus in patients with prior myocardial infarction, and atherosclerotic disease in the aorta. Other considerations in cases of renal infarction include infective endocarditis and vasculitides, overwhelming shock and hypoperfusion, sickle cell disease, and iatrogenic injury.

Patients with renal infarction usually present with nonspecific signs and symptoms. Acute onset of low back pain in patients with risk factors of thromboembolic disease has been described as suggestive of renal infarction. Patients may present with fever and leukocytosis, as well as hematuria and proteinuria.

Imaging Findings

Most patients with renal infarction demonstrate peripheral, wedge-shaped areas of decreased attenuation on contrast-enhanced CT. Smaller subsets of patients have multifocal areas of low attenuation or global infarction. Persons with sickle cell disease may demonstrate multiple "slitlike" areas of infarction, possibly as a result of thrombosis of small venous channels. In cases of global renal infarction, the cortical "rim" sign is seen as a hyperattenuating rim around the cortex as the cortical tissue remains perfused by proximal branches of the renal artery and collateral vessels. Because the majority of renal infarcts have embolic sources, the remainder of the abdomen, including the spleen and bowel, should be scrutinized for further complications of embolic phenomena.

Renal Vein Thrombosis

The most common cause of renal vein thrombosis is nephrotic syndrome, which leads to a hypercoagulable state with systemic effects and a predilection for renal vein thrombosis. Another relatively frequent cause of renal vein thrombosis is a result of extension of renal cell carcinoma. Less likely causes are in patients with renal transplants or hypercoagulability as a result of causes other than nephrotic syndrome. Although it is usually asymptomatic, renal vein thrombosis may present with acute flank pain and hematuria, similar to nephrolithiasis.

Imaging Findings

Ultrasound can demonstrate enlargement of the affected kidney and may demonstrate direct evidence of the thrombus within the renal vein, as evidenced by an echogenic intraluminal filling defect. Unlike in the renal transplant population, intrarenal arterial Doppler studies in native kidneys have shown inadequate sensitivity and specificity for diagnosing renal vein thrombosis.

CT clearly demonstrates thrombus within the renal vein and may aid in characterizing the underlying cause, especially in cases of renal cell carcinoma. Other CT findings in renal vein thrombosis include an enlarged kidney with a prolonged corticomedullary phase and delayed nephrogenic and excretory phases. Also, significant prolongation of parenchymal enhancement may be seen on follow-up examinations up to many hours later. Because complications include the potential for pulmonary embolism, extension of the thrombus into the inferior vena cava should be evaluated using ultrasound or CT.

DISEASES OF THE SPLEEN

The overwhelming majority of splenic abnormality identified on imaging is benign and represents an incidental finding. However, several splenic abnormalities may present with acute abdominal symptoms, including focal infections of the spleen. Also, vascular insults such as splenic infarcts and torsion related to a "wandering" spleen may present acutely and require imaging to be diagnosed.

Splenic Abscess

Patients with splenic abscesses commonly have an underlying predisposition to infection, such as diabetes mellitus, leukemia, intravenous drug abuse, or HIV positivity. Other associations include endocarditis and recent splenic infarction from various causes. A variety of bacteria are commonly isolated in these cases, including *E. coli, Pseudomonas aeruginosa, Staphylococcus aureus,* streptococcus, *Mycobacterium* organisms such as tuberculosis, and fungal organisms. Unilocular abscesses are typically a result of pyogenic abscesses.

Patients with splenic abscesses typically present with fever and abdominal pain that is often localized to the left upper quadrant. Diaphragmatic irritation can cause referred pain in the shoulder, called the *Kehr sign*. Patients also report pleuritic chest pain.

Imaging Findings

When seen on ultrasound, splenic abscesses appear as focal, hypoechoic areas, often with internal echoes or debris. Rarely, gas may be identified as focal echogenic areas with posterior "dirty shadowing."

Splenic abscesses are for the most part low attenuation on CT. They may demonstrate peripheral rim enhancement and possibly contain gas. Mycobacterial and fungal abscesses typically demonstrate several or many small, hypoattenuating ovoid lesions throughout the splenic parenchyma. *Echinococcus* is another relatively common cause of splenic abscess. As in other areas of involvement, echinococcal disease of the spleen demonstrates the typical multiloculated cystic appearance, possibly with more specific visualization of daughter cysts.

In cases of pyogenic abscess, management may include splenectomy; however, percutaneous ultrasound or CT-guided drainage has been demonstrated as a viable alternative in selected patients.

Splenic Infarction

Splenic infarction is a cause of acute abdominal pain and fever in patients who commonly have underlying hematologic or thromboembolic disorders. However, a small subset of patients remains asymptomatic, and splenic infarction is often incidentally identified on imaging studies obtained for other reasons. Hematologic disorders include both benign diseases such as sickle cell disease and malignant lymphoproliferative disorders, including lymphoma and leukemia. Thromboembolic causes typically include atherosclerotic disease or emboli originating from the heart, as in endocarditis or atrial fibrillation, or are secondary to prosthetic mitral valves. Splenic vein thrombosis as a result of a variety of causes, including pancreatitis, may result in splenic infarction. As detailed in the following text, a dramatic cause of splenic infarction is torsion of a "wandering" spleen.

Splenic infarction is often incidentally identified on imaging for unrelated clinical indications. However, especially when larger, splenic infarction can cause abdominal pain, typically in the left upper quadrant. These patients also may be febrile.

Imaging Findings

The findings of splenic infarction can be seen as peripheral on both ultrasound and CT, hypoechoic in the case of ultrasound, and hypoattenuating wedge-shaped defects in the case of CT.

Less classic appearances of splenic infarction include multiple focal, heterogeneous areas of infarction, as well as massive areas involving significant portions of the splenic parenchyma. In contrast to unenhanced CT, intravenous contrast enhanced CT has been shown to improve detection of splenic infarcts significantly. Complications in cases of splenic infarction are secondary infection and abscess formation, as well as pseudocyst formation, hemorrhage, and even rupture. In cases of chronic splenic infarcts, as seen in patients with sickle cell disease, the spleen appears atrophic and diffusely calcified, a finding that may be apparent on plain radiographs as focal calcification in the left upper quadrant.

One consideration in patients with sickle cell disease is the possibility of splenic sequestration, which might have a somewhat similar imaging appearance to splenic infarction in some cases. Although splenic sequestration is typically a clinical diagnosis based on hematocrit decrease and splenic enlargement, imaging may provide a diagnosis in unsuspected cases. In splenic sequestration, CT findings of multiple, peripheral, nonenhancing areas or diffuse low attenuation involving the majority of the splenic parenchyma are identified.

Splenic Torsion

Splenic torsion occurs as a result of twisting of the spleen around its vascular pedicle and is associated with the rare condition of a "wandering" spleen. The term is used when the spleen is not identified in its expected location but is seen elsewhere in the abdomen or pelvis. The underlying cause for the ectopic location is hyperlaxity or abnormal development of the supportive ligaments of the spleen. Although it is more commonly seen in children, wandering spleen has been identified in adults, most commonly women. Patient presentation in cases of splenic torsion varies from acute to chronic, intermittent pain. An even less common cause of acute abdominal pain that demonstrates similar imaging appearances, although on a somewhat smaller scale, is acute torsion of an accessory spleen, or splenule.

Patients with splenic torsion typically present with acute abdominal pain. Because these cases are associated with a wandering spleen, patients may report a more prolonged history of intermittent abdominal pain. Less commonly, splenic torsion may be asymptomatic with clinical presentation prompted by a palpable abdominal mass caused by the torsed spleen.

Imaging Findings

In cases of torsion related to a wandering spleen, a hypovascular or avascular mass is identified in the peritoneal cavity on ultrasound. In cases of torsion of a splenule, a smaller hypovascular mass is identified adjacent to the normal-appearing spleen.

CT also demonstrates a hypoenhancing or nonenhancing mass in cases of complete infarction, usually surrounded by inflammatory changes. CT may be used to directly identify the twisted vascular pedicle, which is described as having a whorled appearance. In cases of torsion of a splenule, a hypovascular soft tissue mass is identified on CT in the left upper quadrant adjacent to a normal spleen.

EMERGENT IMAGING FINDINGS

Several imaging findings are considered emergent findings because they suggest underlying disease requiring urgent intervention. These findings include pneumoperitoneum, which, although possibly suggested clinically, is typically an imaging diagnosis. The findings of pneumoperitoneum demand urgent attention, even though various underlying causes exist, some of which are benign, as discussed in the next section. Additionally, intraabdominal hemorrhage also warrants urgent attention both in acute clinical management and in imaging evaluation to diagnose the underlying cause. Acute urinary and biliary obstruction both have various underlying causes, and although the uncomplicated obstruction does not usually represent an emergent, life-threatening situation, various complications of the obstructions may indeed represent true emergencies as detailed in the following text.

Pneumoperitoneum

Pneumoperitoneum refers to free air within the peritoneal cavity. Common causes include perforation of a hollow viscus and iatrogenic causes such as recent surgery and orogenital insufflations, which are the most common cause overall, and extension from other compartments of the body, including pneumomediastinum. In cases of pneumoperitoneum resulting from surgery, one should expect appropriate resolution during the postoperative period. The majority of cases are noted to resolve within 2 days based on radiography; however, many patients have minute areas of free air for several days and even up to several weeks on CT scans postoperatively.

Because the signs and symptoms of pneumoperitoneum are usually related to the underlying cause, clinical presentations are myriad. When perforation of a hollow viscus occurs, peritonitis may ensue, which might be preceded by focal abdominal pain, based on the underlying etiology. Benign causes of pneumoperitoneum, such as those resulting from orogenital insufflations, may be asymptomatic and only incidentally identified on imaging.

Imaging Findings

Plain radiographs are often used initially to detect free intraperitoneal air. Typically, a supine radiograph, in addition to an upright view of the chest, is acquired to evaluate for free intraperitoneal air (Fig. 9-26). Left lateral decubitus views of the abdomen and lateral chest radiographs are further options. In cases of upright radiographs or left lateral decubitus views, acquisition with the central ray of the x-ray beam at the highest level of the peritoneal cavity has been shown to increase sensitivity. Various signs of pneumoperitoneum on abdominal radiographs have been described: they include the Rigler sign, in which air is seen on both sides of the bowel wall; the falciform ligament sign, in which air outlines the falciform ligament; the "football" sign, in which air outlines the confines of

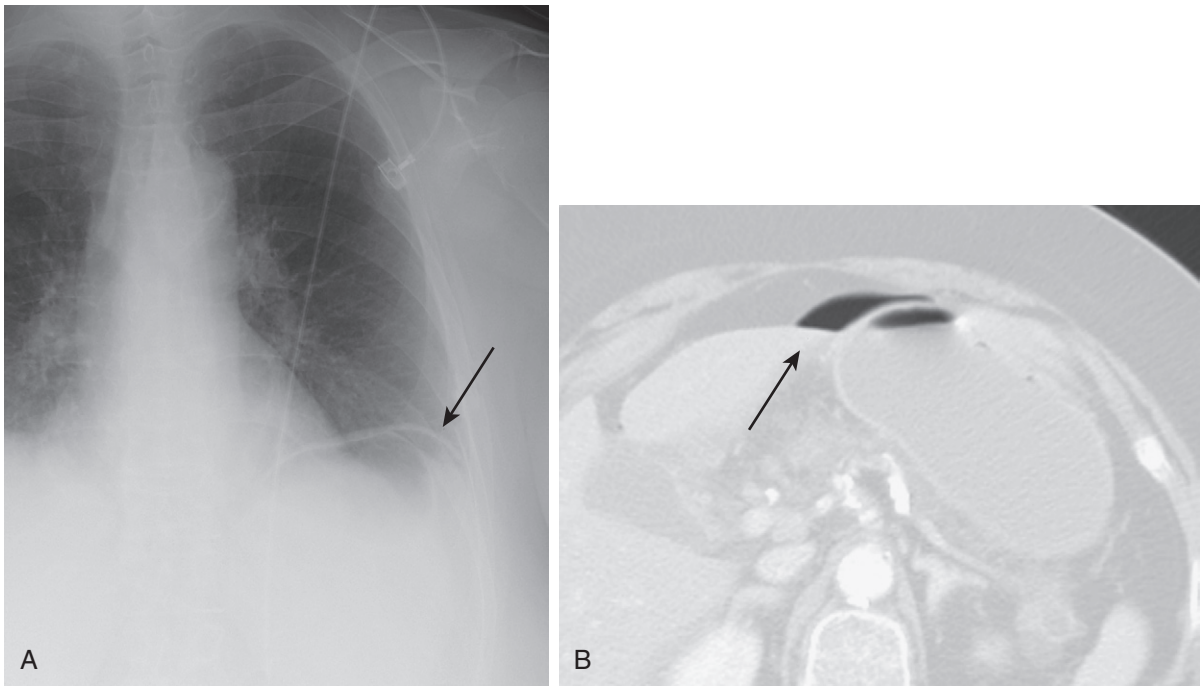


FIGURE 9-26 A 76-year-old woman with a perforated duodenal ulcer and free intraperitoneal air. A plain upright chest radiograph **(A)** demonstrates lucency *(arrow)* beneath the diaphragm on the left, adjacent to the air-filled stomach, consistent with free intraperitoneal air. Axial computed tomography **(B)** using lung windows clearly demonstrates free intraperitoneal air *(arrow)* adjacent to the stomach, as on the radiograph.

the peritoneal cavity; the "inverted V" sign, in which air outlines the medial umbilical folds; and the right upper quadrant air sign, in which a focal, typically triangular, collection of gas is seen in the right upper quadrant. At least one of these signs has been reported in slightly more than half of patients with pneumoperitoneum on supine abdominal radiographs. The "cupola" sign of air outlining the median subphrenic space has also been described in a minority of patients with pneumoperitoneum on supine radiographs.

CT is the most sensitive modality for detecting small volumes of pneumoperitoneum. In cases of hollow viscus perforation, it has been shown to be highly accurate in the localization of the site of perforation, especially when thin collimation images and multiplanar reformations are viewed. The findings of focal bowel wall thickening, localized air bubbles, and direct visualization of a rent within the wall of the bowel have been shown to be accurate predictors of the site of perforation.

Spontaneous Hemoperitoneum

Spontaneous hemoperitoneum, in the absence of trauma, may be seen as a result of a variety of causes, including splenic, hepatic, vascular, coagulopathic, and gynecologic. Typically a patient presents with acute symptoms, including abdominal pain possibly associated with hypotension. Spontaneous splenic hemorrhage may be a result of underlying lymphoproliferative disease, infection, or rupture of a splenic artery pseudoaneurysm commonly caused by pancreatitis, among a myriad of other underlying causes. Ruptured splenic artery aneurysm, which represents the most common splanchnic vessel aneurysm territory, is also a potential cause of spontaneous splenic hemorrhage.

Spontaneous hemorrhage originating from the liver is usually associated with hepatic tumors, both benign and malignant. As in any splanchnic vascular territory, rupture of hepatic arterial aneurysms or pseudoaneurysms may cause spontaneous hemorrhage. Benign hepatic tumors predisposing to spontaneous hemorrhage include adenomas, whereas hepatocellular carcinoma and, less likely, metastases account for the malignant etiologies (Fig. 9-27). Spontaneous hemorrhage as a result of other benign hepatic lesions, including focal nodular hyperplasia and cavernous hemangioma, has been described but is much less frequently observed.

Another significant cause of spontaneous intraabdominal hemorrhage, affecting both intraperitoneal and retroperitoneal compartments, is coagulopathy, including medical anticoagulation. Hemorrhage resulting from coagulopathy most commonly involves the rectus sheath, iliopsoas, and retroperitoneal compartments. Less commonly, the hemorrhage is within the peritoneum, and rarely it involves a solid visceral organ, such as the spleen or liver. Patients often present with acute abdominal pain and, because the majority of cases involve anticoagulant or antiplatelet administration, they are generally known to be coagulopathic.

Patients with spontaneous retroperitoneal hemorrhage often present with acute abdominal pain. When the hemorrhage is extensive, patients may present with hypotension and even frank shock.

Imaging Findings

In these cases, ultrasound can identify hemoperitoneum as free fluid with homogeneous internal echoes. Additionally,

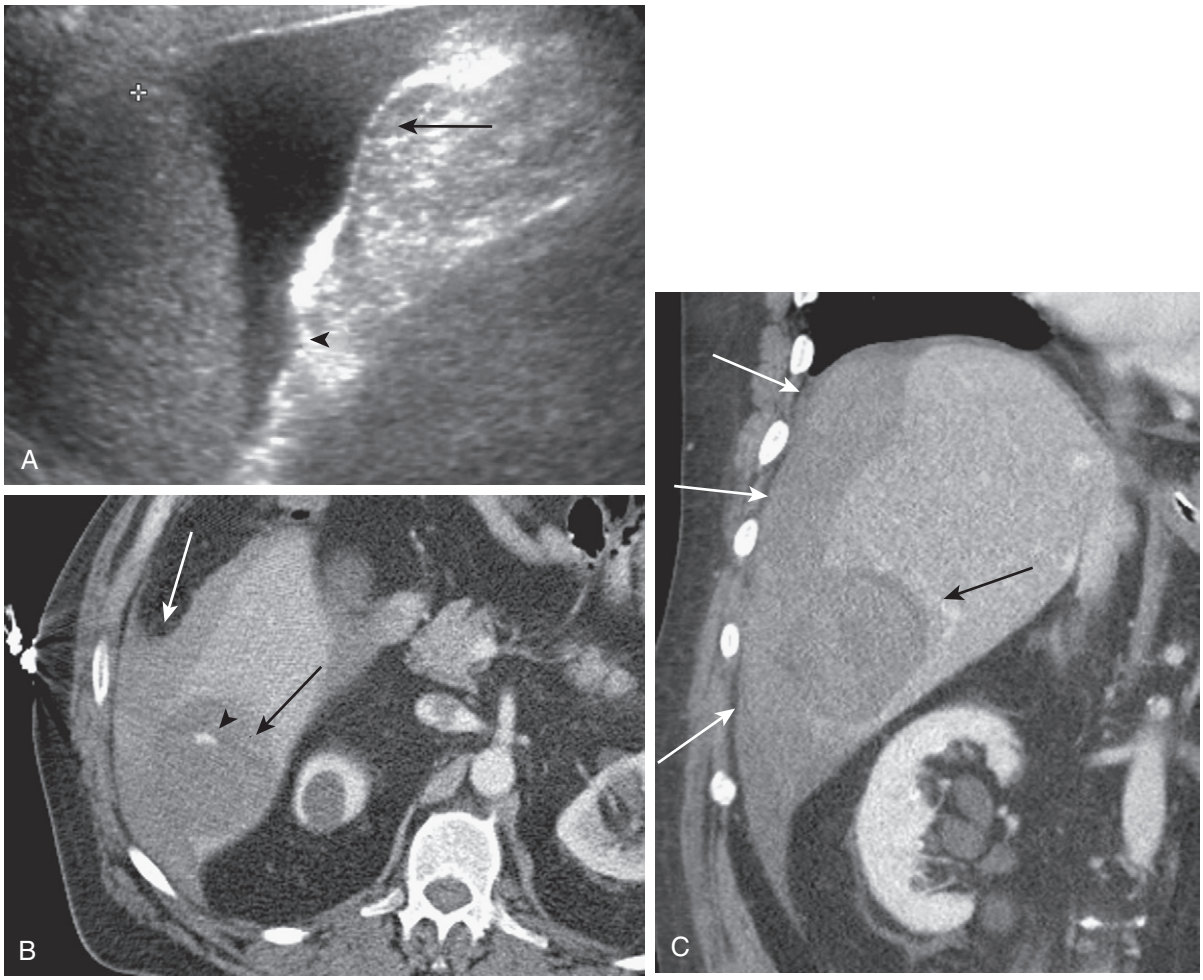


FIGURE 9-27 A 57-year-old woman with a ruptured hepatocellular carcinoma. An ultrasound image **(A)** demonstrates free intraperitoneal fluid *(arrow)* with evidence of dependently layering debris *(arrowhead)* consistent with hemoperitoneum. Axial **(B)** and coronal **(C)** portal venous phase images demonstrate the patient's hepatoma *(black arrows)* with a central hyperattenuating focus *(arrowhead)* seen on the axial image consistent with active hemorrhage. Perihepatic hemorrhage is also seen on the computed tomography images *(white arrows)*.

a clot may appear as a focal heterogeneous collection, which might seem to be masslike but demonstrates no internal vascularity.

CT is often used as the initial imaging modality in cases of suspected hemoperitoneum or to evaluate for the underlying cause when hemoperitoneum is identified on ultrasound. On CT, a focal region of high-attenuation clotted blood, known as the "sentinel clot" sign, is useful in localizing the underlying cause of hemorrhage.

On CT, in cases of spontaneous splenic hemorrhage, the underlying cause may be clearly visualized as a focal or infiltrative mass lesion in cases of malignancy, as diffuse enlargement with or without focal hypoattenuating areas in the case of infection, or as a pseudoaneurysm. In these cases, the CT protocol should include intravenous contrast material to allow characterization of intraparenchymal abnormalities and clear visualization of the splenic artery. CT affords potential characterization of the etiology of spontaneous hepatic hemorrhage; however, the hemorrhage may obscure the underlying cause in some cases. In this subset of patients, short-term follow-up CT or MRI is typically used to evaluate the cause once the hemorrhage has organized or resolved.

In coagulopathic patients, CT demonstrates the hematoma in the various intraabdominal compartments, and, in the majority of cases, a hematocrit effect, or the separation of the cellular components from the plasma, is visualized. This sensitive and specific finding suggests underlying coagulopathy.

Spontaneous Retroperitoneal Hemorrhage

In addition to rupture of the various visceral organ-related aneurysms and pseudoaneurysms, a significant cause of spontaneous retroperitoneal hemorrhage is rupture of an abdominal aortic aneurysm (AAA). Although less commonly encountered than spontaneous hemorrhage from underlying hepatic and splenic disease, spontaneous renal and pancreatic hemorrhage can be severe and life-threatening. The most common causes of spontaneous renal hemorrhage include benign and malignant lesions, commonly renal angiomyolipoma and renal cell carcinoma, respectively. Other causes of renal hemorrhage include vasculitides such as polyarteritis nodosa and Wegener granulomatosis.

Similar to patients with intraperitoneal hemorrhage, patients with spontaneous retroperitoneal hemorrhage

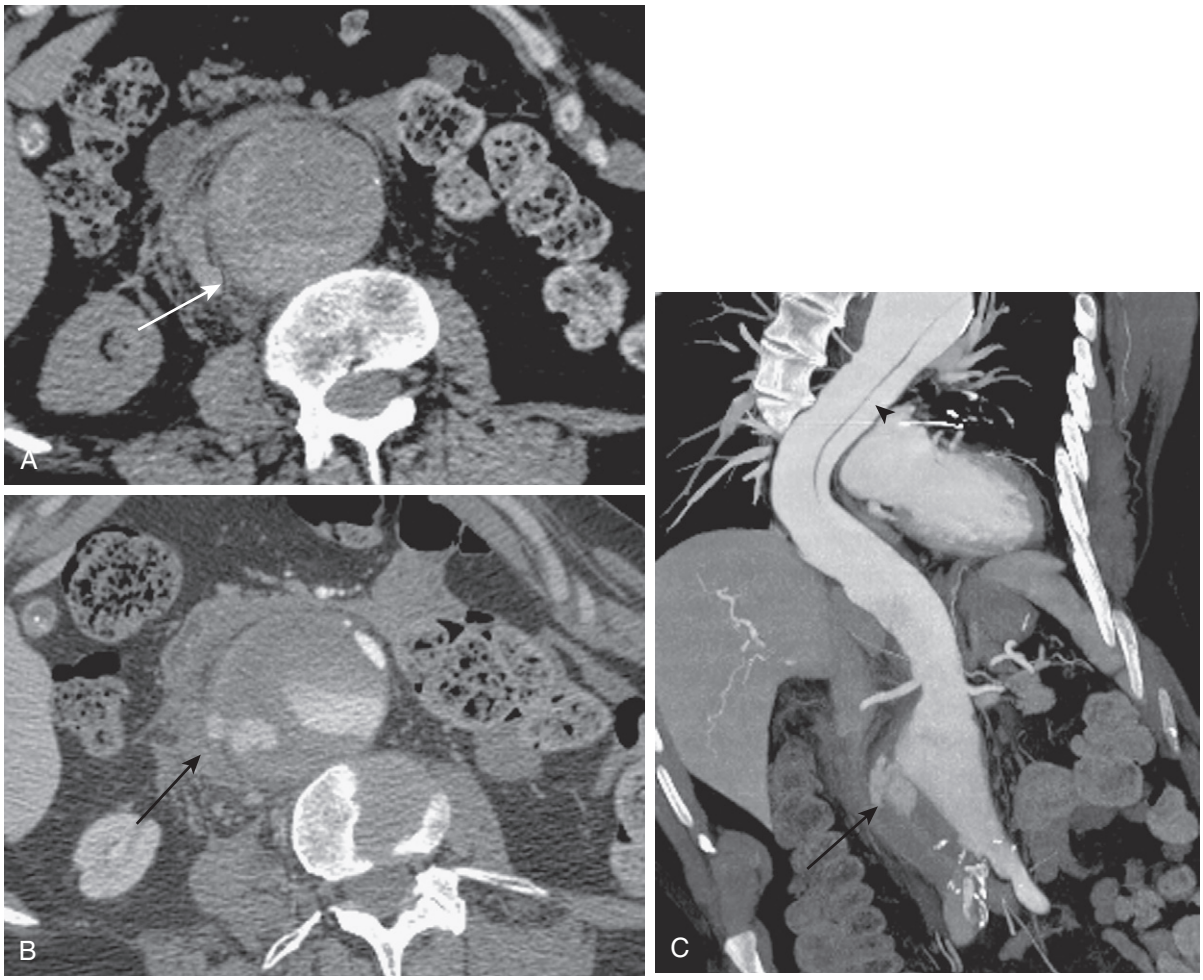


FIGURE 9-28 A 68-year-old man with a ruptured abdominal aortic aneurysm. An axial unenhanced computed tomography (CT) image **(A)** reveals hyperattenuation within the wall of the aorta *(arrow)*, the so-called "crescent" sign. An axial arterial phase CT image **(B)** reveals extravasation of contrast material beyond the confines of the aortic wall *(arrow)*. A coronal maximum intensity projection image **(C)** reveals extraluminal extravasation of contrast material *(arrow)*, as well as an incidentally noted thoracic aortic dissection *(arrowhead)*.

often present with acute abdominal pain. When the hemorrhage is severe and massive, patients may present with hypotension and possibly even shock. In cases related to underlying renal disease, hematuria may be associated.

Imaging Findings

Ultrasound may identify the retroperitoneal hemorrhage and possibly characterize the underlying cause, as in the case of the renal tumors previously mentioned; however, CT is often used.

In cases of ruptured AAA, CT is often the first-line imaging modality (Fig. 9-28). CT protocols may include the use of intravenous contrast material to evaluate for active extravasation, although unenhanced CT may readily identify cases of AAA rupture. In cases of rupture, CT demonstrates hematoma within the retroperitoneum, contiguous with the aorta. Often, when large, the hemorrhage is identified within multiple retroperitoneal compartments. CT findings that increase the specificity of the diagnosis of ruptured AAA include the "crescent" sign, which refers to hyperattenuating clefts within mural thrombus or the aneurysmal wall itself; a "draped" aorta, which refers to displacement of the aorta onto the spine with lateral "draping" over a vertebral body; discontinuity of the aortic wall; and frank active contrast extravasation. Ruptured AAA represents a surgical emergency that warrants rapid intervention. In cases of renal tumors, specific findings of angiomyolipoma may be identified, such as areas of macroscopic focal fat. However, these findings can become somewhat obscured by hemorrhage. Also, in cases of renal malignancy, the underlying mass may become obscured, and follow-up imaging by CT and MRI may be necessary for identification and characterization of the mass lesion. The spatial resolution and multiplanar capabilities of the current generation of CT scanners offer the ability to accurately diagnose vascular abnormalities resulting from vasculitis, such as the multiple small aneurysms characteristic of polyarteritis nodosa. The common causes of spontaneous hemorrhage specific to the pancreas include hemorrhage related to pseudocysts that cause pseudoaneurysm formation in the surrounding arteries as a result of exposure to the various pancreatic enzymes. Other causes include pancreatic malignancies, which are rare.

In cases of spontaneous hemorrhage within the abdomen, conventional angiography may demonstrate ongoing

active arterial hemorrhage, and percutaneous transcatheter embolization can be used as definitive treatment of the hemorrhage. However, given the myriad of causes of hemorrhage, its underlying cause often remains to be definitively managed.

Biliary Obstruction

Patients with acute biliary obstruction may present acutely with abdominal pain, possibly with associated jaundice, depending on the chronicity of the underlying cause. Biliary obstruction has both intrahepatic and extrahepatic causes; common intrahepatic causes of cholestasis include hepatitis (previously discussed) and cirrhosis. Typically, these processes are chronic and are usually diagnosed clinically without the use of imaging. Intrahepatic mass lesions, both primary and secondary to the hepatic parenchyma, may cause focal intrahepatic biliary obstruction. Extrahepatic causes of biliary obstruction include both those extrinsic and intrinsic to the bile duct. The most common cause is intrinsic obstruction related to choledocholithiasis. However, other intrinsic causes are neoplasia, including cholangiocarcinoma; infectious causes; and inflammatory causes such as primary sclerosing cholangitis and HIV cholangiopathy. Extrinsic causes of extrahepatic biliary obstruction include neoplasm, commonly pancreatic adenocarcinoma, and inflammation as a result of pancreatitis. Additionally, metastatic lymphadenopathy in the porta hepatis may result in an extrinsic compression and secondary obstruction of the extrahepatic bile ducts.

Mirizzi syndrome is an uncommon cause of extrahepatic biliary obstruction. In this case a gallstone becomes lodged in the cystic duct and the inflammation surrounding this process creates a functional stricture of the common hepatic duct.

In patients with uncomplicated biliary obstruction, typical presentations include signs and symptoms of jaundice, dark urine, and pale stools. Icterus also may be seen, as well as pruritus. Depending on the underlying cause, as well as the acuity of the obstruction, abdominal pain may be associated with uncomplicated biliary obstruction.

Imaging Findings

In cases of biliary obstruction, ultrasonography may identify evidence of biliary dilatation, although it may not be present in early obstruction. In some cases, the underlying cause can be identified as an intraluminal filling defect or an extrinsic mass, such as in pancreatic neoplasia or pseudocysts resulting from pancreatitis.

In patients with nonspecific clinical presentation, CT initially may be performed in cases of biliary obstruction. In cases of intrinsic causes of biliary obstruction, the intraductal filling defect may be identified, such as in the case of choledocholithiasis or neoplasm. In cases of *Ascaris lumbricoides* infection, the organisms themselves can be visualized as tubular intrahepatic filling defects causing the biliary obstruction. Inflammatory causes such as HIV cholangiopathy demonstrate concentric biliary ductal wall thickening, resulting in a functional stricture. Similar findings are seen in primary sclerosing cholangitis, with areas of beading affecting both intrahepatic and extrahepatic bile ducts. Extrinsic causes of extrahepatic biliary obstruction, although they may be identified on ultrasonography, are typically readily identified on CT and MRI (Fig. 9-29).

In cases of Mirizzi syndrome, both ultrasound and CT may demonstrate the typical findings of an impacted stone within the cystic duct, which often demonstrates an abnormally low insertion into the common hepatic duct. Classification of Mirizzi syndrome is based on the absence (type I) or presence (types II to IV, depending on size) of a cholecystocholedochal fistula.

In patients with high clinical suspicion of biliary obstruction, MRCP is typically the initial noninvasive imaging examination. MRCP demonstrates intraluminal filling defects of choledocholithiasis as low-signal foci within surrounding hyperintense bile, as previously described. As on CT, obstructing neoplasms, including cholangiocarcinoma or pancreatic neoplasms, may be identified. Infectious and inflammatory causes of biliary obstruction are also well characterized, demonstrating findings similar to those on CT, including biliary ductal wall thickening and hyperenhancement during stages of active inflammation.

Urinary Obstruction

Nephrolithiasis is the most common cause of acute urinary tract obstruction. Other common causes of obstruction include prostatic enlargement in men by compression of the urethra and compression by gynecologic malignancies or the gravid uterus in women. Also, malignancies of the urothelium, most commonly transitional cell carcinoma, may obstruct the ureters when they occur within the bladder, obstructing the ureterovesical junction, or within the ureter itself. Retroperitoneal fibrosis may cause obstruction of

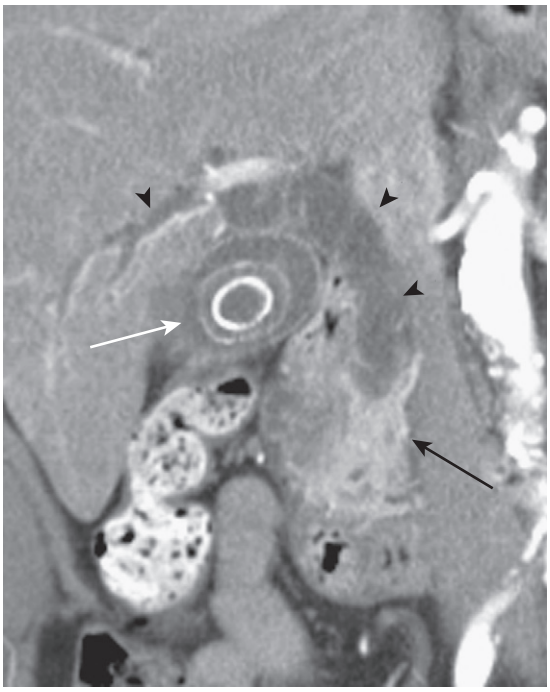


FIGURE 9-29 A 76-year-old woman with biliary obstruction resulting from a cholangiocarcinoma. A coronal portal venous phase computed tomography image demonstrates significant intrahepatic and extrahepatic biliary dilatation *(arrowheads)* with abrupt narrowing resulting from a malignant stricture that demonstrates enhancing thickened bile duct walls *(black arrow)*. Incidental note is made of a lamellated gallstone *(white arrow)*.

the ureters, which are also typically displaced medially in this condition.

Patients with acute urinary obstruction often present with acute, often excruciating, abdominal pain referred to as "renal colic." However, more chronic causes of urinary obstruction may be relatively pain free with presentations related to changes in urine output, possibly even anuria. Hematuria may be associated, depending on the underlying cause. Also, patients with urinary obstruction may present with multiple urinary tract infections.

Imaging Findings

Ultrasound is typically used as the initial imaging modality to diagnose acute urinary tract obstruction. In these cases, hydronephrosis, as evidenced by prominence of the collecting system and displacement of the renal sinus fat, may be identified on ultrasound. In some cases, ultrasound can directly demonstrate the cause of obstruction, especially when the cause is proximal, around the ureteropelvic junction or proximal ureter, or within the pelvis, such as in the case of obstruction by benign prostatic hyperplasia or gynecologic malignancies. Also, given the acoustic window of the bladder, intraluminal bladder lesions causing obstruction are readily identified on ultrasound, as in the case of transitional cell carcinoma.

CT is often used for further characterization in cases of urinary obstruction or in cases in which the cause of obstruction is not identified on the ultrasound examination. As noted, CT clearly identifies renal and ureteral calculi, the most common causes of acute urinary obstruction. Pelvic abnormalities including an enlarged prostate in males or gynecologic malignancies in females may be identified on CT. Retroperitoneal fibrosis, characterized by irregular soft tissue attenuation within the retroperitoneum, often surrounding or abutting the aorta and inferior vena cava, is readily seen on CT. The ureters, when involved, are typically medially displaced and demonstrate abnormal surrounding soft tissue attenuation. The bladder should be scrutinized for filling defects, including neoplasms, which may be identified on unenhanced CT images but are more readily seen if the bladder is distended with iodinated contrast material.

CONCLUSION

Patients presenting with nontraumatic abdominal pain present a challenging diagnostic dilemma given the breadth of possible underlying diagnoses. However, the imaging workup may be tailored to the individual patient based on the signs and symptoms of the clinical presentation. Significant overlap often occurs in the clinical presentations of the various intraabdominal diseases, and thus imaging is crucial in clinical management decisions. With a thorough understanding of intraabdominal disease and the ability to triage among the various imaging modalities based on specific clinical concerns, the radiologist plays an integral role in the efficient, successful care of patients with acute abdominal pain.

SUGGESTED READINGS

Artigas JM, Martí M, Soto JA, Esteban H, Pinilla I, Guillén E. Multidetector CT angiography for acute gastrointestinal bleeding: technique and findings. *Radiographics*. 2013;33:1453–1470.

Hines J, Rosenblat J, Duncan DR, Friedman B, Katz DS. Perforation of the mesenteric small bowel: etiologies and CT findings. *Emerg Radiol*. 2013;20:155–161.

Lubarsky M, Kalb B, Sharma P, Keim SM, Martin DR. MR imaging for acute nontraumatic abdominopelvic pain: rationale and practical considerations. *Radiographics*. 2013;33:313–337.

Maddu KK, Mittal P, Arepalli CD, Shuaib W, Tewari A, Khosa F. Colorectal emergencies and related complications: a comprehensive imaging review—noninfectious and noninflammatory emergencies of colon. *AJR Am J Roentgenol*. 2014;203:1217–1229.

Mortelé KJ, Segatto E, Ros PR. The infected liver: radiologic-pathologic correlation. *Radiographics*. 2004;24:937–955.

Patel NB, Oto A, Thomas S. Multidetector CT of emergent biliary pathologic conditions. *Radiographics*. 2013;33:1867–1888.

Santillan CS. Computed tomography of small bowel obstruction. *Radiol Clin North Am*. 2013;51:17–27.

Stoker J, van Randen A, Laméris W, Boermeester MA. Imaging patients with acute abdominal pain. *Radiology*. 2009;253:31–46.

Taourel P, Thuret R, Hoquet MD, Doyon FC, Merigeaud S, Delabrousse E. Computed tomography in the nontraumatic renal causes of acute flank pain. *Semin Ultrasound CT MR*. 2008;29:341–352.

Thoeni RF. The revised Atlanta classification of acute pancreatitis: its importance for the radiologist and its effect on treatment. *Radiology*. 2012;262:751–764.

Thoeni RF, Cello JP. CT imaging of colitis. *Radiology*. 2006;240:623–638.

Tkacz JN, Anderson SA, Soto J. MR imaging in gastrointestinal emergencies. *Radiographics*. 2009;29:1767–1780.

Watanabe Y, Nagayama M, Okumura A, et al. MR imaging of acute biliary disorders. *Radiographics*. 2007;27:477–495.

Zissin R, Hertz M, Osadchy A, Even-Sapir E, Gayer G. Abdominal CT findings in nontraumatic colorectal perforation. *Eur J Radiol*. 2008;65(1):125–132.

Chapter 10

Pelvic Emergencies

Brian C. Lucey

Many diseases that affect the abdomen may also extend to involve the pelvis. These diseases are described in Chapter 9. In addition, trauma does not respect anatomic boundaries, and pelvic injuries that occur as a result of trauma are described in Chapter 3. This chapter covers conditions that, for the most part, are confined to the pelvis, and a great number of them are related to the genitourinary tract. Although some overlap occurs, many of these disease entities are gender specific. In the male, these entities primarily consist of diseases of the testes and prostate and include testicular torsion, orchitis, epididymitis, maldescended testis, and prostatitis. In the female, the entities primarily affect the ovaries and uterus and include ovarian cysts, endometriosis, ovarian torsion, tubo-ovarian abscess, and ectopic pregnancy. The most frequent presentation in the male is testicular pain, and in the female the most frequent presentation is either pelvic pain or dysfunctional uterine bleeding. The imaging modalities used to investigate these entities include sonography, computed tomography (CT), and magnetic resonance imaging (MRI); however, in the emergency department setting, sonography is the first-line modality of choice for many of these pelvic conditions.

MALE DISORDERS

Testicular Torsion

The testis and epididymis attach to the inner scrotal wall via a broad attachment. When this attachment is too narrow, it may function as a pedicle around which the testis may twist. This twisting, or torsion, compromises the blood supply to the testis, which may lead to infarction of the testis. Males with testicular torsion often present with acute scrotal pain, and this condition requires emergent treatment to maintain viability of the affected testis. Testicular salvage rates are greatest when surgery is performed within 6 hours of the onset of symptoms. After 24 hours the testis is usually no longer salvageable. Patients with the "bell clapper" deformity, in which the tunica vaginalis joins high on the spermatic cord, are more prone to testicular torsion compared with the general population.

Sonography is the preferred imaging examination for the diagnosis of testicular torsion because of its high sensitivity and specificity. Gray-scale ultrasound findings are often completely normal when torsion is present, and the testes may appear symmetric with respect to both size and echogenicity. A small hydrocele may be present on the affected side. Within a few hours of the onset of symptoms, the scrotal wall will appear thickened, and the testis and epididymis will appear enlarged and hypoechoic as a result of inflammation and/or hemorrhage. Color Doppler imaging is crucial for the diagnosis of torsion. The lack of demonstrable blood flow to the affected testis, assuming appropriate ultrasound settings are used, is virtually pathognomonic for torsion (Fig. 10-1). In prepubertal patients, demonstrating the presence of blood flow often is difficult even in normal testes. Two potential false-negative scenarios must be considered when evaluating for torsion. First, a twisted testis may untwist spontaneously with resultant hyperemia on color Doppler imaging, and thus testicular torsion can be mistaken for epididymo-orchitis; and second, incomplete torsion may result in venous occlusion without arterial occlusion, which may result in arterial flow being detected in the testis despite the presence of torsion.

Testicular scintigraphy is often used as an adjunct to ultrasound when a diagnosis of torsion cannot be made with certainty. Given the added delay of scintigraphic examinations, however, some surgeons operate when findings of an ultrasound are equivocal. The treatment for testicular torsion is detorsion of the affected testicle and orchiopexy—that is, with fixture of the testis to the scrotal wall to prevent torsion from recurring.

Torsion of the Testicular Appendages

Although males have four testicular appendages, only two, the appendix testis and appendix epididymis, are commonly visible with ultrasound imaging. These appendages are remnants of embryonic ducts and serve no real function. Because they are attached by a small pedicle, they are prone to torsion. Torsion of these appendages is one of the most common causes of acute scrotal pain in children. The appendix testis is more commonly affected than the appendix epididymis, although it is often difficult to identify the offending appendage. Patients are usually young, prepubertal males who report acute-onset scrotal pain. Clinical examination may reveal a bluish discoloration of the skin at the site of pain, which is called the "blue dot" sign and is pathognomonic. Upon ultrasound imaging the twisted appendix is often identified as a round, extratesticular, extraepididymal mass lacking color Doppler flow (Fig. 10-2). A reactive hydrocele may be present, along with scrotal wall skin thickening.

Epididymitis and Orchitis

Epididymitis or epididymo-orchitis is an infection of the epididymis and/or testis and is a common cause of acute-onset scrotal pain. Typically, scrotal pain associated with epididymitis or epididymo-orchitis is relieved when the testes are elevated over the symphysis pubis, a maneuver called the *Prehn sign*. In contradistinction, the pain associated with testicular torsion is not relieved by this

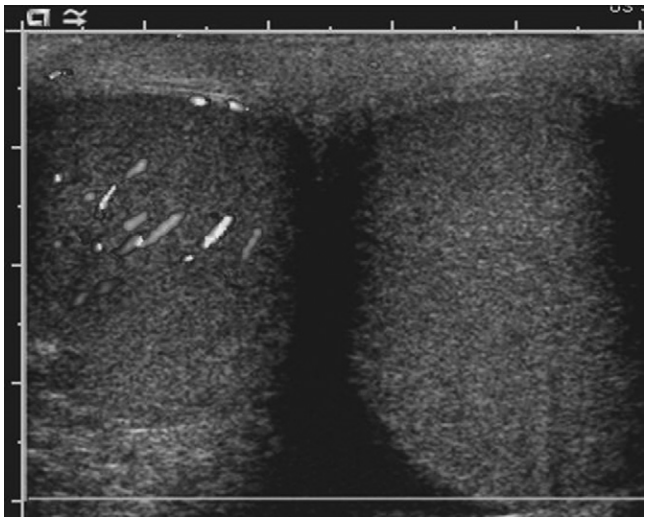


FIGURE 10-1 Sonographic image of a 19-year-old patient with testicular torsion. No flow is identified in the left testis.

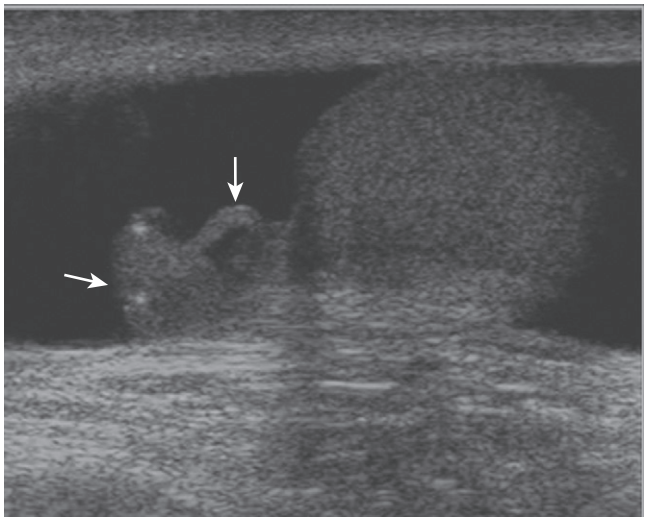


FIGURE 10-2 Sonographic image of the testis of a 9-year-old patient showing torsion of the testicular appendix. The *arrows* show an enlarged swollen appendix testis.

maneuver. Although the causative agent in epididymitis is usually not identified in young children, the infection usually originates in the prostate gland or bladder and spreads to the epididymis and testis via the vas deferens and spermatic cord lymphatics. A congenital anomaly of the urinary tract may be present. In adolescents, the cause is usually a sexually transmitted infection.

Ultrasound examination of a patient with epididymitis demonstrates enlargement of the epididymis, primarily the head, with heterogeneous echotexture. Color Doppler evaluation shows increased blood flow to the epididymis and/or testis (Fig. 10-3). A reactive hydrocele may be an associated finding. When the entire testis is involved, it often is enlarged and has altered echogenicity. On gray-scale imaging findings alone, the appearance of the testis may mimic a diffusely infiltrative disease such as leukemia or lymphoma, although the clinical presentation should suggest the correct diagnosis. Untreated epididymo-orchitis may progress to formation of a scrotal abscess or may

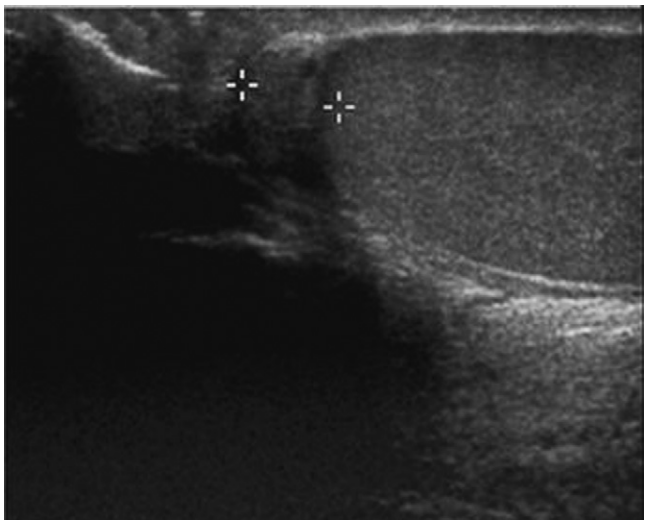


FIGURE 10-3 Sonographic image of a 32-year-old patient with acute epididymitis of the contralateral epididymis. The epididymis is swollen and shows increased vascularity with color Doppler imaging.

result in testicular infarction, which may lead to testicular atrophy. In patients with epididymo-orchitis, a follow-up sonogram performed 4 to 6 weeks after the initial event is advised in all cases to ensure complete resolution of the imaging findings after appropriate interval therapy. A follow-up sonogram is important to exclude an underlying tumor as the cause for the patient's symptoms. It is uncommon for a testicular tumor to present with acute scrotal pain; the accepted figure is that acute pain is a symptom in less than 10% of tumors. When such pain occurs, it is usually due to acute hemorrhage or infarction of the testis that contains the tumor. Orchitis as a result of infection with mumps occurs in approximately 25% of patients who contract the disease. The sonographic findings include an enlarged hypoechoic testis, a small hydrocele, and sometimes thickening of the scrotal wall. Infertility occasionally may result as a consequence of mumps orchitis. Severe scrotal infection may result in the rare condition called *Fournier gangrene*, which is a fulminant infectious process involving the scrotal wall and skin of the perineum that is in essence a fasciitis. The severe infection may result in gas formation along the fascial planes of the scrotal wall. Sonographic findings include the findings of epididymo-orchitis along with small echogenic ill-defined foci within the scrotal wall. These foci represent gas, and this finding requires urgent communication to the referring physician because surgical debridement may be required. In questionable cases, CT may be performed, which will clearly show the presence of any gas as hypoattenuating foci within the scrotal wall (Fig. 10-4).

Inguinal Scrotal Hernia

An uncommon cause of acute scrotal pain is incarceration of an inguinal hernia that extends into the scrotum. Indirect inguinal hernias are not uncommon; however, extension into the scrotal sac is rare. The clinical findings are usually obvious with a large swelling in the scrotum, although the mass may not be easily reduced. Sonographically, the appearance may be nonspecific, with a heterogeneous mass

identified in the scrotum. It is usually easy to identify the mass as being separate from the testis, although following the mass along the inguinal canal may not be easy. The presence of bowel may be detected if the two walls and lumen are clearly visible; however, it is not always clear that the mass represents bowel. Often the mass may merely be omental fat that has herniated into the scrotum. The presence of peristalsis may confirm the diagnosis. In cases in which doubt exists, a CT scan could be performed, which would show the hernia and its contents extending into the scrotum. Signs of incarceration on sonography include the absence of color flow on color Doppler evaluation. Although this sign may be easy to elicit in identifiable bowel wall, if the hernia consists of omental fat alone, it may be an unreliable sign. On CT, signs of incarceration include edema of the adjacent fat around the hernia and, possibly, decreased enhancement of the bowel wall of any bowel loops that may be present in the hernia.

Testicular Trauma

Trauma to the testis may be either penetrating or blunt. Penetrating trauma to the testis, as in many other locations, usually requires immediate surgical exploration. Blunt trauma to the testis in a hemodynamically stable patient should be evaluated with sonography. The key diagnosis to make after testicular trauma is the presence or absence of testicular rupture. A ruptured testicle requires immediate surgical repair, and early diagnosis is required to maximize the chances of testicular salvage. A ruptured testicle that is operated on within 72 hours of the trauma has a salvage rate approaching 80%, but this rate drops to 30% with subsequent delay. The sonographic findings suggesting testicular rupture include loss of clarity of the margins of the testis and abnormal structure of the testis; on occasion, testicular parenchyma protruding beyond the testicular capsule may be identified. Sonographic findings seen after trauma to the testes that does not result in testicular rupture include altered echogenicity with loss of the normal homogeneity and alternating foci of either increased or decreased echogenicity. Depending on the degree of trauma, the heterogeneity may be focal or more generalized. A focal area of heterogeneity may be mistaken for epididymo-orchitis or even tumor, and thus an accurate history of testicular trauma is required to help differentiate these conditions. Despite having an accurate history, when focal heterogeneity is seen as a result of trauma, a follow-up scan is advised in 4 to 6 weeks to ensure complete resolution. As with many testicular conditions, after trauma to the scrotum, a secondary hydrocele is commonly observed, which appears as a hypoechoic fluid collection within the scrotum. An associated scrotal hematoma may be present, which also may appear as a hypoechoic fluid collection when it is hyperacute. As the hematoma resolves, more complex elements may develop within the scrotum, and the presence of complex fluid in the scrotum after trauma represents a resolving hematoma. The long-term sequelae of testicular trauma include complete or incomplete infarction with a resultant smaller testicle, chronic fibrosis, and even calcification.

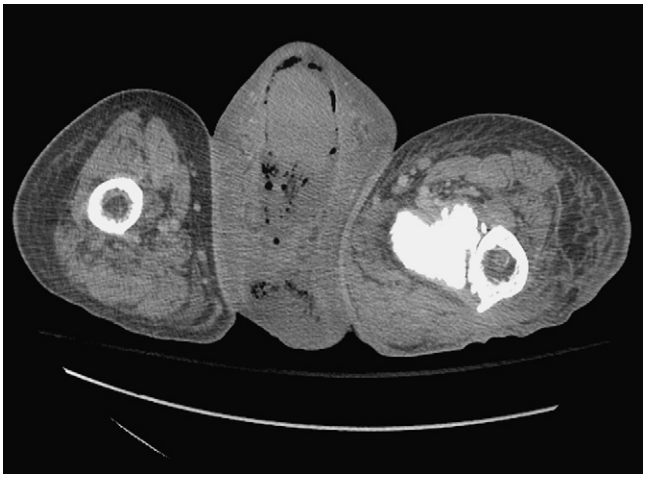


FIGURE 10-4 A computed tomography image of a 65-year-old male patient with Fournier gangrene. The image shows gas within the scrotum with a hydrocele and extensive subcutaneous edema.

Cryptorchidism

The arrest in the descent of the testis along its normal path is one of the most common disorders of the genitourinary tract. This phenomenon occurs in up to 3% of term infants, although in the majority of these infants the testis will descend naturally during the first few months of life. Nearly four out of five maldescended testes in adults are located at or below the level of the inguinal canal. Although maldescended testes are associated with a host of congenital syndromes, the condition also may occur in isolation. The most damaging consequence of maldescended testes is infertility; infertility rates in persons with unilateral maldescent are reported to be close to 20%, but this rate rises to 75% in cases in which the maldescent is bilateral. Maldescended testes have a high rate of germ cell tumors, and this risk extends to the contralateral descended testis as well. Maldescended testes are also at increased risk of both torsion and trauma and hence should be considered in any patient presenting with pelvic or scrotal pain in which both testes are not clearly palpable. Because the majority of maldescended testes are found in the inguinal canal, the testis may usually be identified by sonography. Maldescended testes appear as small, usually hypoechoic, rounded or oval structures along the line of the inguinal canal (Fig. 10-5). Care should be taken not to confuse the small testis with a lymph node. Any focal areas of heterogeneity within the testis could represent malignant degeneration. The sensitivity of sonography for detecting maldescended testis varies between 75% and 97% and depends on whether the testis is palpable. A maldescended testis that lies higher than the inguinal canal becomes difficult to locate with sonography. Other imaging modalities that may be used to locate the testis include CT and MR. With multidetector CT, the small soft tissue mass of the maldescended testis is usually identifiable, which was not always the case in the era of large slice thickness CT. T2-weighted MRI may be useful to locate the high signal testis, which may be best identified using coronal plane imaging along the plane of the gonadal vessels.

Prostatitis

Acute prostatitis is, in essence, a clinical diagnosis, and imaging is rarely required to make the diagnosis. It is most

commonly caused by recent instrumentation or surgery; however, infection also may spread from the urinary tract. Untreated or inadequately treated prostatitis may lead to formation of a prostate abscess. Performing transrectal sonography in patients with acute prostatitis may help make the diagnosis even before imaging, because the passage of the probe may be exquisitely painful. The sonographic appearance of acute prostatitis is primarily of a heterogeneous prostate gland that may show focal areas of hypoechogenicity with demonstrable increased vascularity, usually within the peripheral zone. In severe cases, the hypoechogenicity may be more diffuse and the increased vascularity may be seen throughout the gland. Chronic prostatitis usually appears as bands of increased echogenicity representing areas of fibrosis. Usually little evidence of increased vascularity is found. A prostatic abscess appears as a well-defined walled collection that contains hypoechoic fluid (Fig. 10-6). The fluid is usually somewhat complex, with foci of increased echogenicity within it as well. Gas present in the abscess is seen as irregular foci of increased echogenicity with so-called "dirty" shadowing behind it.

Female Disorders

Pelvic conditions that affect women who present to the emergency department may be divided into those causing pelvic pain and those causing dysfunctional uterine bleeding. Conditions that cause pelvic pain include ovarian cyst with rupture, endometriosis, tubo-ovarian abscess, and ovarian torsion. Causes of dysfunctional uterine bleeding include spontaneous abortion, an endometrial polyp, endometrial hyperplasia, and endometrial cancer. An ectopic pregnancy may present with a combination of these symptoms. Congenital uterine anomalies and cystic lesions of the lower genitourinary tract may be symptomatic but are more commonly incidental findings. The imaging appearance of these anomalies and lesions are described in the Requisites Series book on ultrasound.

Human chorionic gonadotropin results are critical for the accurate interpretation of a pelvic ultrasound examination in a sexually active female with pelvic pain. Pregnancy status alters the potential diagnosis in many cases; patients presenting with pelvic pain with or without bleeding and who have a positive pregnancy test and an empty uterus should be considered to have an ectopic pregnancy until proven otherwise. Sonography is the imaging modality of choice in the evaluation of pelvic pain and dysfunctional bleeding. MRI is a favored complementary modality, although with the proliferation of CT imaging in the emergency department setting, particularly in patients presenting with abdominal pain, radiologists are seeing conditions on CT imaging with increasing frequency that once were the preserve of sonography. It is important to recognize these entities for what they are when using CT.



FIGURE 10-5 A computed tomography image of a 22-year-old patient with bilateral maldescended testes that are seen as bilateral oval soft tissue masses in the inguinal canals.

Hemorrhagic Ovarian Cyst

Although hemorrhagic ovarian cysts are common, their imaging appearance is widely variable. Hemorrhagic cysts develop at the time of ovulation when vessels surrounding a corpus luteal cyst rupture, giving rise to hemorrhage within the corpus luteum. As the cyst evolves over time, the sonographic features change with the stage of clot retraction. Patients may present with acute onset adnexal pain that can be severe.

Physiologic ovarian follicles measure less than 3.0 cm in diameter. Most hemorrhagic cysts measure 3.0 to 3.5 cm in diameter, have a thin outer wall, and demonstrate posterior acoustic through-transmission. Fine, reticular septations resembling a fishnet pattern are a common finding

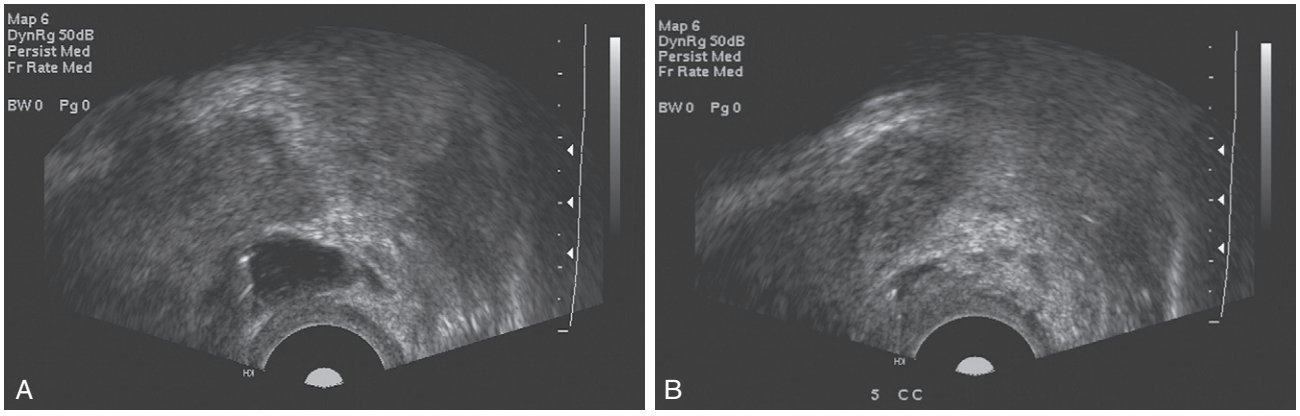


FIGURE 10-6 **A,** A Transrectal sonographic image of a 68-year-old patient with a prostatic abscess that is seen as an irregular hypoechoic collection. **B,** A transrectal sonographic image of the prostate after transrectal drainage of the abscess. The echogenic needle may be seen.

at ultrasound. These septations represent fibrin strands that do not contain blood flow. In some patients the hemorrhagic cyst contains a retracting clot. Although a large portion of the cyst appears anechoic, the retracting clot appears as an adherent, echogenic structure within the cyst that contains no blood flow. In rare cases, when the clot becomes very small, it can simulate a mural nodule and raise concern for an ovarian neoplasm. Fluid–fluid or fluid–debris levels also can be demonstrated within a hemorrhagic cyst. Hemorrhagic cysts can be complicated by rupture, with free spill of hemorrhagic contents into the pelvis. When this phenomenon occurs, echogenic fluid will be demonstrated within the pelvis surrounding the uterus and adnexa. In some cases, the hemoperitoneum may be massive. Although the sonographic features are well described, given that many patients with a ruptured hemorrhagic cyst present with pelvic pain, in the emergency department setting this pain is often interpreted as abdominal pain, and CT imaging may be the first modality used. We are seeing CT imaging of ovarian cysts, hemorrhagic cysts (Fig. 10-7), and ruptured cysts (Fig. 10-8) with increasing frequency. Normal ovaries may be difficult to identify on CT imaging, and identification often depends on the hormonal status. When the ovaries are larger, as in younger women of childbearing age, they are more likely to be identified. Similarly, in patients with little pelvic fat, the ovaries may be difficult to distinguish from loops of unopacified bowel in the pelvis. Often the position of the ovaries is assumed, and the usual location is either side of the uterus along the margin of the round ligament. In young patients with a malignancy that requires pelvic radiation therapy, the ovaries are frequently surgically sutured to the superolateral aspect of the pelvic wall to move the ovaries out of the path of the treating radiotherapy beam. In these cases, the ovaries appear as solid masses, with cystic components located superiorly and laterally to their usual position. These masses should not be mistaken for disease, particularly tumor, and knowledge of the prior procedure is useful to avoid confusion. The findings of a simple ovarian cyst are similar to those of a cyst located elsewhere—namely, a well-defined round or oval mass in the location of the ovary with an imperceptible wall and containing simple fluid with Hounsfield unit (HU) values of 10 or less. A hemorrhagic cyst might be identified as a mass similar to a simple cyst, but an irregular enhancing ring may be seen within the cyst that represents the enhancing involuting wall of the cyst. The CT findings of a ruptured cyst are more variable. Often the cyst itself can no longer be identified because the contents have spilled into the peritoneal cavity. What may be seen is free fluid in the cul-de-sac or even in the location of one of the adnexa. This fluid is frequently of slightly higher attenuation than simple fluid and may have an HU value of 60 to 80; it represents the blood from the ruptured cyst. Active extravasation occasionally may be seen as a line of high density representing administered intravenous contrast material being lost into the peritoneal cavity.

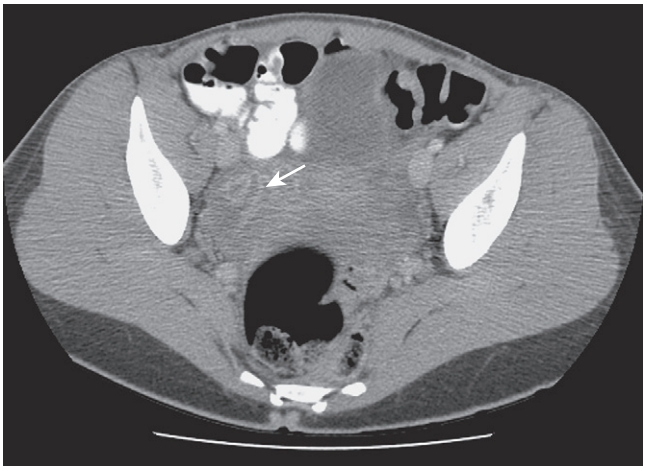


FIGURE 10-7 A computed tomography image of a 32-year-old patient with a hemorrhagic ovarian cyst *(arrow)*. The linear high-attenuation foci in the right adnexa represents the blood.



FIGURE 10-8 A computed tomography image of a 27-year-old patient with a ruptured hemorrhagic cyst. The active bleeding into the peritoneum is seen as an irregular focus of high attenuation in the left adnexa.

Ovarian Torsion

Acute onset of adnexal pain in a female raises concern for ovarian torsion. The Fallopian tubes are relatively long in children and the ovaries are hypermobile, which increases their susceptibility to torsion. Although normal ovaries may twist, usually an ovarian or paraovarian cyst or mass is present that predisposes the ovary to torsion by functioning as a fulcrum around which the ovary can twist. The ovary becomes twisted around its pedicle, leading to various degrees of hemorrhagic infarction. If surgery is not performed expeditiously, future fertility and hormonal regulation may be compromised. There is a slight predilection for torsion to involve the right ovary. When the right ovary is affected, the diagnosis is more difficult to establish given the number of other conditions that present with right lower quadrant or pelvic pain such as appendicitis, Meckel diverticulitis, and inflammatory bowel disease. The median age of patients with ovarian torsion is 11 years.

Pelvic ultrasound is the study of choice for evaluation of ovarian torsion. Normal ovaries often appear hypoechoic relative to the adjacent pelvic tissue and have an ovoid or ellipsoid shape. Microcystic follicles are routinely identified in normal ovaries. When the ovaries demonstrate normal gray-scale imaging characteristics and have a normal size and shape, color Doppler evaluation is usually

not necessary. If, however, one ovary appears abnormally large relative to the other side, torsion may be present. In nearly all cases of ovarian torsion, the affected ovary is massively enlarged and has a round or globular configuration. In neonates and young girls, ovarian torsion is commonly seen as a large cystic mass with fluid–debris levels. In young or adolescent girls, the more classic imaging appearance is an enlarged, echogenic ovary with multiple enlarged peripheral follicles. In other cases, the ovary may appear as a complex cystic mass as a result of the presence of an underlying cyst or tumor (Fig. 10-9). Color Doppler evaluation of the ovary often reveals an absence of blood flow, a finding classically associated with ovarian torsion. However, torsion may be present even if arterial waveforms are demonstrated because the ovary has a dual blood supply (from both the uterine and ovarian arteries). The presence of arterial waveforms within the ovary should not sway the diagnosis away from ovarian torsion if the gray-scale imaging findings and physical examination are consistent with torsion.

Endometriosis

Endometriosis is a condition defined as the presence of endometrial tissue outside of the uterus. The condition may be localized or widespread. Widespread endometriosis may result in extensive endometrial implants throughout the abdomen and pelvis, and the diagnosis may be extremely difficult to make. Sonography is of limited value in making this diagnosis, and CT and MR also have both poor sensitivity and poor specificity for diagnosing endometriosis. All three imaging modalities, however, are useful in identifying localized disease. The most frequently encountered presentation of endometriosis is a single or multiple small adnexal masses called *endometriomas*, which have been referred to as "chocolate cysts" in the past. Patients may present with acute pelvic pain. Sonography is the normal first-line imaging modality, and the sonographic findings are usually diagnostic. On sonography, an endometrioma appears as a complex cystic mass in the adnexa that lies outside of the ovary. The mass is well defined and contains homogeneous low-level echoes throughout the mass. Endometriomas range in size from 1 cm to more than 15 cm, although the vast majority lie in the 3- to 6-cm range. Rarely, a thin septation may be identified within the endometrioma. The sonographic features are classic, although the potential differential diagnosis includes a hemorrhagic cyst and, rarely, an ovarian neoplasm in cases in which the classic features are not easily identified. On CT imaging, an endometrioma appears as a well-defined cystic mass that has a uniform HU value greater than that of a simple cyst, usually in the range of 30 to 60 HU. On MRI, endometriomas show high signal on T1-weighted imaging with a classic "shading" appearance on T2-weighted imaging. The "shading" appearance is a progressive change from high signal at one side of the mass to low signal on the opposite side with varying levels of intermediate signal between them. This pattern of signal intensity is caused by the high level of iron within the endometrioma. Both CT and MRI may show evidence of the complications of long-standing endometriosis, which include obstruction to either the ureter or bowel. Endometriosis should be considered in unusual cases of ureteric or bowel obstruction of unknown cause in females of childbearing age who present to the emergency department.

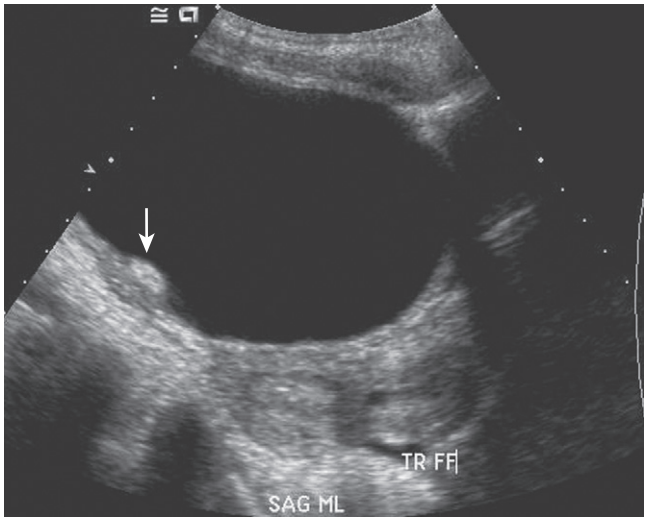


FIGURE 10-9 A sonographic image of a 48-year-old patient with a cystic ovarian mass that underwent torsion. The solid mural nodule is identified *(arrow)*.

Disorders of the Fallopian Tubes

Disorders of the Fallopian tubes include hydrosalpinx, pyosalpinx, and tubo-ovarian abscess. Hydrosalpinx is seldom an acute condition and is usually an incidental finding. It results from occlusion of the Fallopian tube and is often bilateral. The most common cause, infection, often follows instrumentation. The obstruction leads to dilatation of the Fallopian tube, which becomes filled with serous fluid. Although hydrosalpinx can present with acute pelvic pain, the condition may remain asymptomatic; however, long-term consequences include infertility. Sonographic findings are usually characteristic, and a dilated tubular cystic structure with anechoic fluid within is usually found. When a hydrosalpinx becomes secondarily infected, the condition is known as *pyosalpinx*, which presents as acute pelvic pain with the signs and symptoms of acute infection, including elevated fever and white blood cell count. The fluid within the Fallopian tube will no longer be anechoic on sonography, indicating the presence of pus within the tube (Fig. 10-10). Aggressive antibiotic therapy is indicated, but when the tube is extremely distended, percutaneous or transvaginal drainage may be required.

A condition that overlaps pyosalpinx and one that occurs more frequently is tubo-ovarian abscess formation. This condition in essence has a similar etiology to pyosalpinx in that the most common cause is a sexually transmitted disease. The infection travels along the Fallopian tube and results in formation of an abscess in the adnexa. The clinical presentation usually leads to suspicion of the diagnosis. Sonography is again the imaging modality of choice. A complex mass may be identified in the adnexa, and the mass may be shown to lie outside of the ovary. On transvaginal sonography, gentle pressure placed directly over this mass will be exquisitely painful and may help confirm the diagnosis, because other causes of complex adnexal masses tend not to cause such discomfort. As with other pelvic diseases, the presentation may be

interpreted as abdominal pain, rather than pelvic pain, and CT may be the first-line imaging modality used. In this case, a tubo-ovarian abscess may be seen as a pelvic abscess with thick walls and may contain fluid and/or solid components (Fig. 10-11). The presence of a dilated tubular structure on the ipsilateral side representing a hydro- or pyosalpinx may help to distinguish this abscess as a tubo-ovarian abscess rather than an appendiceal or diverticular abscess.

Endometritis

Endometritis, which is defined as inflammation of the endometrium, may be acute or chronic. Endometritis may extend to involve the myometrium or even the parametrium. The most common cause is infection. Most causative agents are staphylococcus or streptococcus, and it usually occurs after procedures entailing instrumentation are performed, such as delivery or abortion. The clinical presentation typically includes fever and purulent vaginal discharge and may be associated with vague lower abdominal pain. Chronic endometritis is usually the result of chlamydia, tuberculosis, or chronic pelvic inflammatory disease and usually presents as a bloody discharge. The presence of pus within the endometrial canal is called *pyometra*.

From an imaging perspective, given that lower abdominal pain or pelvic pain is a frequent cause for presenting to the emergency department, sonography is usually the first imaging modality used. The sonographic appearance of acute endometritis may be normal in the early stages. The endometrium also may appear to be thickened and heterogeneous, and hypoechoic fluid may be identified in the endometrial canal. Occasionally gas is present and can be identified on sonography as hyperechoic foci with "dirty" posterior shadowing. Given that endometritis is frequently seen in the presence of retained products of conception, signs of these products also may be present. These products include the presence of a hematoma seen as a heterogeneous intrauterine mass with debris and fluid. Increased vascularity occasionally may be seen with endometritis, although this finding is inconsistent.

CT also may be the first-line imaging modality used, depending on the patient's presenting symptoms. If the gynecologic symptoms of discharge and pelvic pain predominate, it is likely that sonography will be requested initially. If pain is the predominate symptom and abdominal pain rather than pelvic pain is suggested, then CT may be requested first. The findings of endometritis on CT are somewhat nonspecific and include the presence of fluid within the endometrial canal. The canal may be widened because of the presence of fluid, hematoma, and debris. This widening might be less easy to appreciate on conventional axial imaging but easier to appreciate when reviewing the images in the sagittal plane. Gas is also identified on occasion and is seen on CT as tiny black bubbles within the endometrial canal. When endometritis is diagnosed with imaging, care should be taken to exclude further foci of inflammation or infection such as salpingitis or oophoritis, because these associations of endometritis are common.

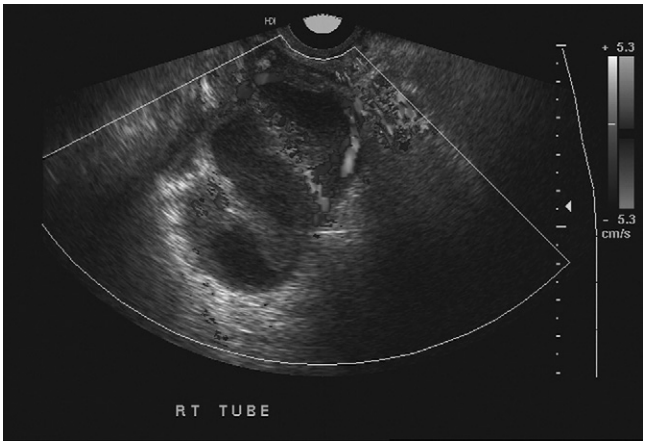


FIGURE 10-10 A sonographic image of a 38-year-old patient with a pyosalpinx. The tubular nature of the hypoechoic lesion may be appreciated. The hypoechoic fluid contains multiple low-level echoes, indicating that this entity is not a hydrosalpinx.

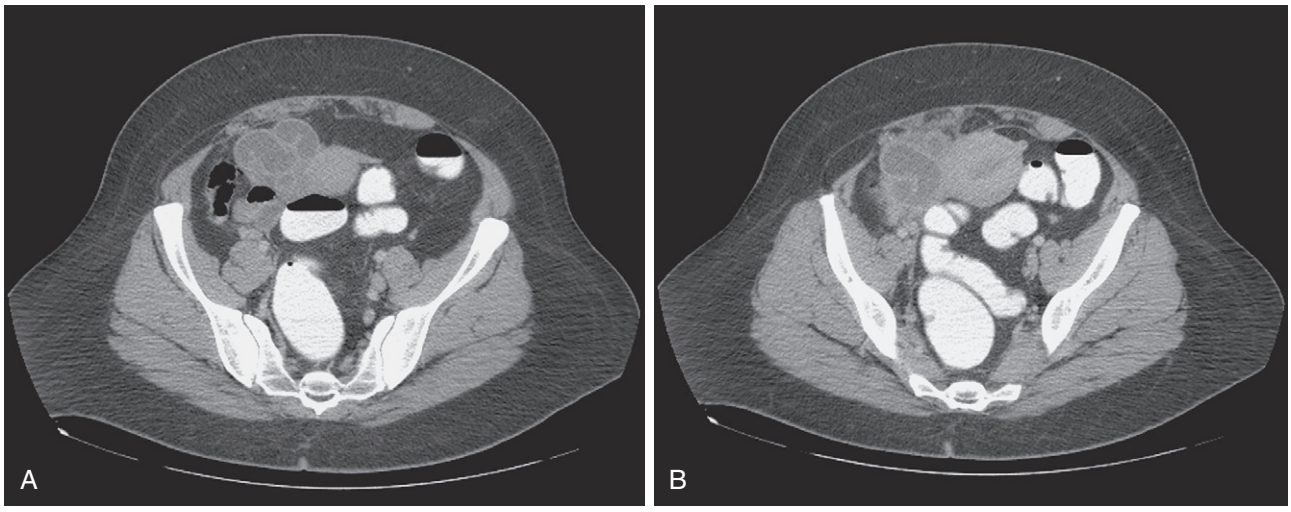


FIGURE 10-11 **A,** A computed tomography (CT) image of a 27-year-old patient with a pyosalpinx. The tubular nature of the lesion in the right adnexa may be appreciated. **B,** Another CT image of the same patient. Some inflammatory changes have occurred in the fat adjacent to the Fallopian tube. This pyosalpinx has progressed to form a tubo-ovarian abscess.

Ectopic Pregnancy

Ectopic pregnancy is a common condition that may result in death if it is not adequately diagnosed and treated, and thus missing the diagnosis has far greater consequences than making a false-positive diagnosis. Ectopic pregnancies are responsible for up to 15% of maternal deaths. By definition, any female patient with a positive pregnancy test and an empty uterus should be regarded as having an ectopic pregnancy until otherwise proven. It is not always possible to identify the ectopic pregnancy directly, and failure to identify it should never be taken as evidence that the patient does not have an ectopic pregnancy. Ectopic pregnancy usually presents with pelvic pain and may well be associated with bleeding. On imaging, the best way to determine that an ectopic pregnancy is not present is to identify an appropriately positioned gestational sac. In women with an ectopic pregnancy, the sloughing of the decidua may result in the appearance of a pseudogestational sac. This sac can be differentiated from a gestational sac in that it is a fluid collection within the endometrial canal surrounded by a single decidual layer, unlike the gestational sac, which appears as a fluid collection within the decidua that abuts the endometrium or as concentric rings, the so-called "double decidual" sign. The most specific sonographic sign confirming ectopic pregnancy is the identification of a live embryo that lies outside the uterus, usually in the adnexa (Fig. 10-12). This sign is positively identified in only approximately 20% to 25% of cases of ectopic pregnancy and therefore cannot be relied on to make the diagnosis. A nonspecific complex adnexal mass in a patient with a positive pregnancy test is strong evidence to support the presence of an ectopic pregnancy. Complex free fluid in the pelvis is also a good indicator in the correct clinical setting (Fig. 10-13). The presence of an adnexal mass in association with complex free

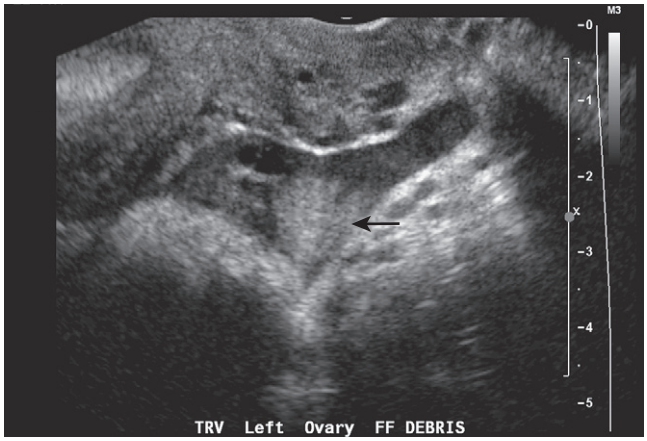


FIGURE 10-12 A sonographic image of a 23-year-old patient with a ruptured ectopic pregnancy. The free fluid containing echogenic debris representing blood is seen in the cul-de-sac *(arrow)*.

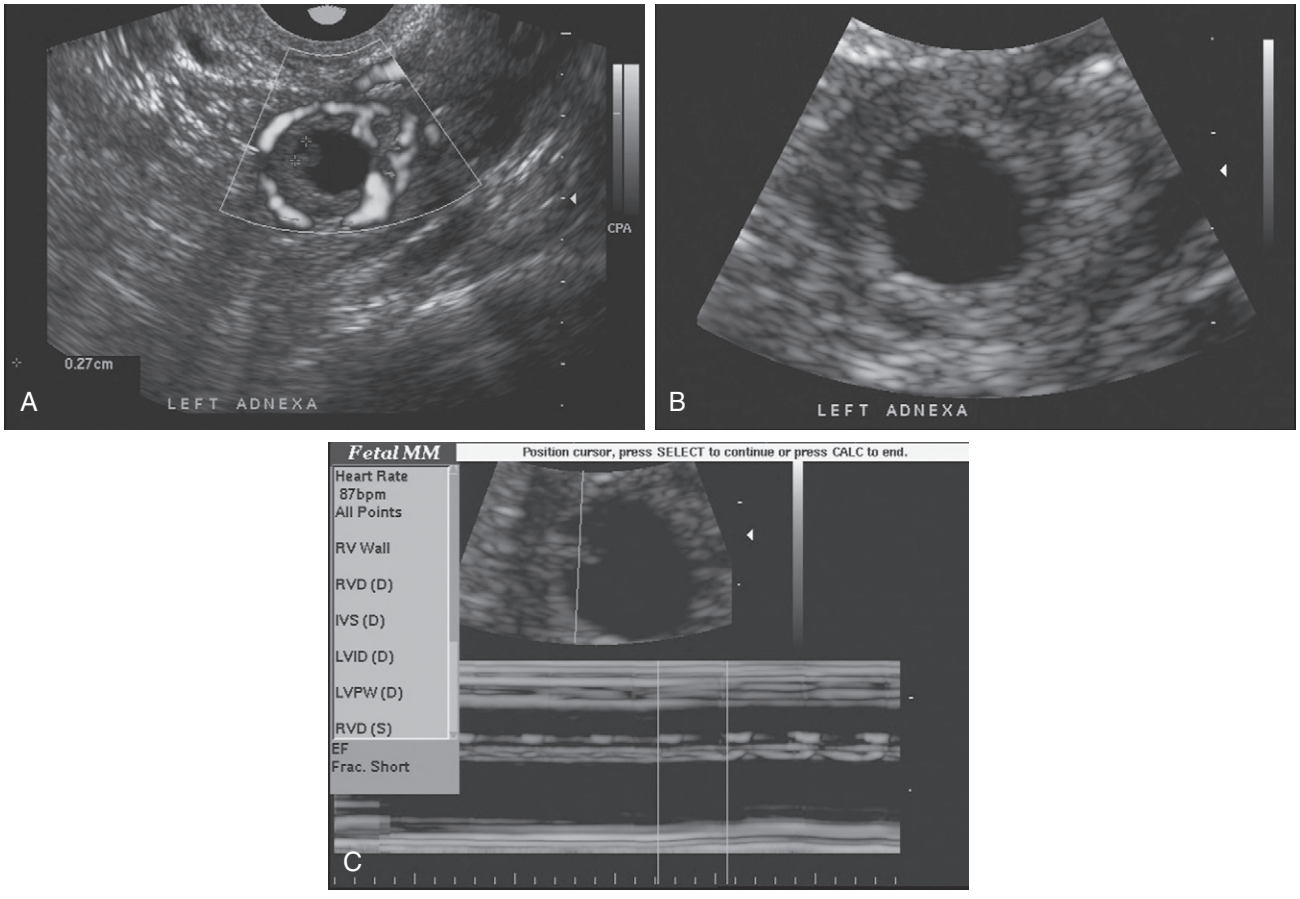


FIGURE 10-13 **A,** A sonographic image of a 27-year-old patient showing an ectopic pregnancy located in the left adnexa. The classic "ring of fire" is well shown. **B,** Another image of the same patient shows an ectopic pregnancy with a clearly identifiable yolk sac. **C,** Another image from the same patient shows a documented fetal heartbeat with the ectopic pregnancy.

fluid has a sensitivity of close to 40% but a specificity of 99% for the detection of an ectopic pregnancy. It is important to remember that up to one third of patients with an ectopic pregnancy may have a completely normal sonogram—hence the importance of the mantra "positive pregnancy test with an empty uterus equals ectopic pregnancy until proven otherwise."

Another condition that may present with pelvic pain associated with bleeding is early pregnancy failure. This condition may be characterized by a positive pregnancy test with no demonstrable intrauterine pregnancy and hence may have an appearance similar to ectopic pregnancy. Fluid usually will be present within the endometrial canal, and a gestational sac may be present. The gestational sac will be abnormal and may be enlarged, with no evidence of a developing fetus within it. In cases in which it is not easy to distinguish between early loss of pregnancy and ectopic pregnancy, the key is to monitor the level of human chorionic gonadotropin. This level will continue to rise in patients with an ectopic pregnancy but will start to fall if the pregnancy fails.

Postpartum Bleeding

Patients with postpartum bleeding often first present to the emergency department. The most common cause of postpartum bleeding is retained products of conception (RPOC). It is important to differentiate RPOC from the presence of a simple hematoma within the endometrial canal. Both conditions have similar sonographic appearances, characterized by the presence of a heterogeneous, predominantly echogenic mass located within the endometrial cavity. The most specific sonographic sign that may distinguish these two entities is the presence of vascularity in the RPOC, with demonstrable blood flow when using color Doppler imaging. A simple hematoma will not have any blood flow within it. Separating these entities may not be possible using CT imaging alone, because the hematoma will be of high attenuation in the acute setting, just as RPOC will appear as a high-density focus within the uterus. CT is unlikely to be sensitive enough to detect the attenuation difference because of the small degree of vascular enhancement that is present with RPOC. It is important to attempt to differentiate these entities when the patient presents to the emergency department, because the management is considerably different. The presence of a hematoma within the endometrial cavity often may be treated conservatively and frequently will resolve spontaneously. RPOC, on the other hand, usually requires evacuation of the endometrial cavity to arrest the bleeding and permit normal uterine contraction.

Ovarian Vein Thrombosis

Ovarian vein thrombosis is a relatively uncommon condition that is diagnosed in up to 0.2% of deliveries. It is unilateral in approximately 85% of cases, with a right to left predominance of 12:1. It also may result from pelvic inflammatory disease, malignancy, or pelvic surgery. Morbidity is associated not only with the thrombosis but also with any superimposed infection, resulting in septic thrombophlebitis. The thrombus may propagate to involve the inferior vena cava or renal veins and may result in a pulmonary embolus. The clinical presentation is pelvic pain and fever. Imaging modalities that may be used to make the diagnosis are sonography, CT, and MRI. The imaging modality that is first used depends on how the patient presents and the degree of suspicion for the diagnosis. Ovarian vein thrombosis often is not suspected at the time of diagnosis, and thus the onus is very much on the radiologist to suspect and make the diagnosis, particularly when conducting imaging for a postpartum patient who has either fever or pain.

The diagnosis of ovarian vein thrombosis by sonography is often limited by the presence of overlying bowel gas. The characteristic finding is that of a tubular hypoechoic structure extending from the adnexa cranially. No blood flow may be identified within this structure when it is interrogated with color Doppler imaging. Associated enlargement of the ovary on the affected side may be present, although frequently, identifying this enlargement with certainty is difficult. It may be difficult to definitively distinguish ovarian vein thrombosis from hydronephrosis or thrombosis of the inferior mesenteric vein. CT is the most likely imaging modality to be used in the emergency department, particularly if the patient presents with fever and abdominal pain. Appendicitis is frequently the suspected diagnosis. The CT finding that enables the diagnosis is the identification of an enlarged ovarian vein that contains either occlusive or nonocclusive thrombus (Fig. 10-14). This thrombus may be identified as a focus of hypoattenuation within the enhancing vein or as an abruptly occluded vessel that is dilated distally. Some nonspecific stranding of the fat is usually present adjacent to the vessel as a result of the thrombosis. This nonspecific inflammatory stranding may be exuberant if there is superimposed infection resulting in septic thrombophlebitis (Fig. 10-15).

Dysfunctional Uterine Bleeding

A number of conditions result in dysfunctional uterine bleeding (DUB). The most common entities include a submucosal fibroid, an endometrial polyp, endometrial hyperplasia, and an endometrial carcinoma. Fibroids are a ubiquitous finding on sonographic imaging of the uterus. A small number of fibroids may be located in the submucosa, with greater than 50% of their circumference projecting into the endometrial canal. These submucosal fibroids are usually asymptomatic but may cause pelvic pain or DUB. Defining a fibroid as submucosal on sonography alone is not always easy, and hysterosonography may be required. Similarly, endometrial polyps may be difficult to identify on sonography alone, and hysterosonography also may be required. On sonography, the presence of a polyp is often suspected by the presence of an abnormal-appearing endometrial stripe. The heterogeneous polyp may be indistinguishable from the endometrial stripe, and the appearances may suggest abnormal enlargement of the stripe. Instilling saline solution into the endometrial canal for the hysterosonogram clearly distinguishes the polyp from the endometrium. Endometrial hyperplasia and, more rarely, an endometrial carcinoma also may present with DUB. Both of these entities will appear as irregular thickening of the endometrial stripe, with carcinoma having a more aggressive and extensive appearance. Again, with hysterosonography, these entities are usually

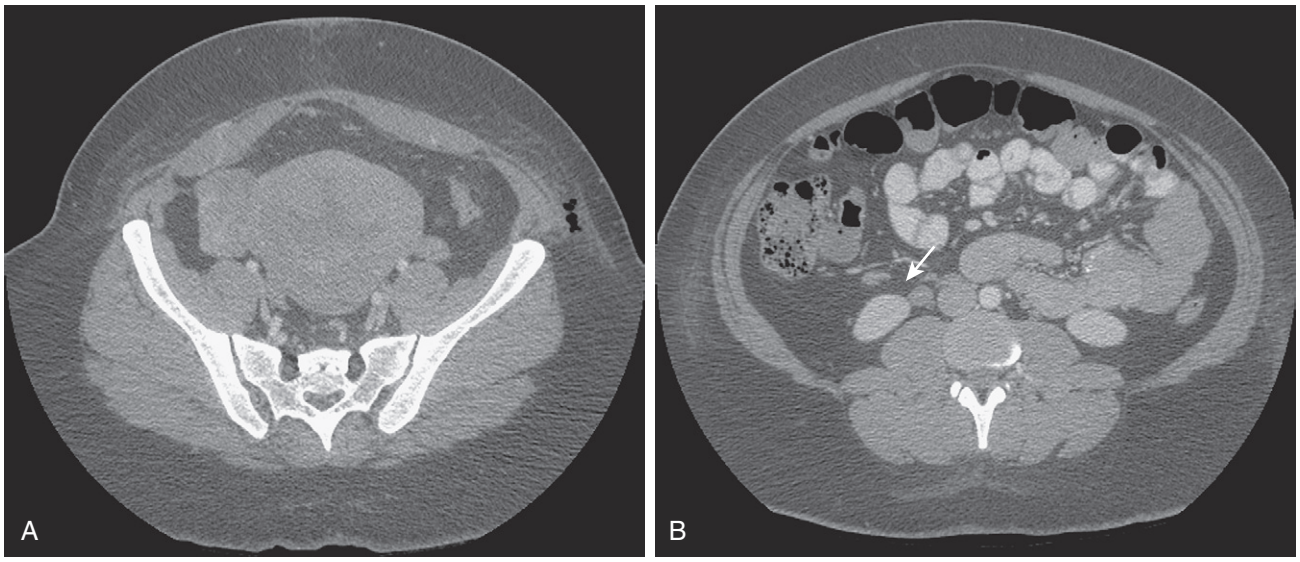


FIGURE 10-14 **A,** A computed tomography (CT) image of a 34-year-old postpartum patient shows a large mass in the right adnexa representing a dilated ovary resulting from gonadal vein thrombosis. **B,** A CT image shows a dilated thrombosed right gonadal vein *(arrow)*.

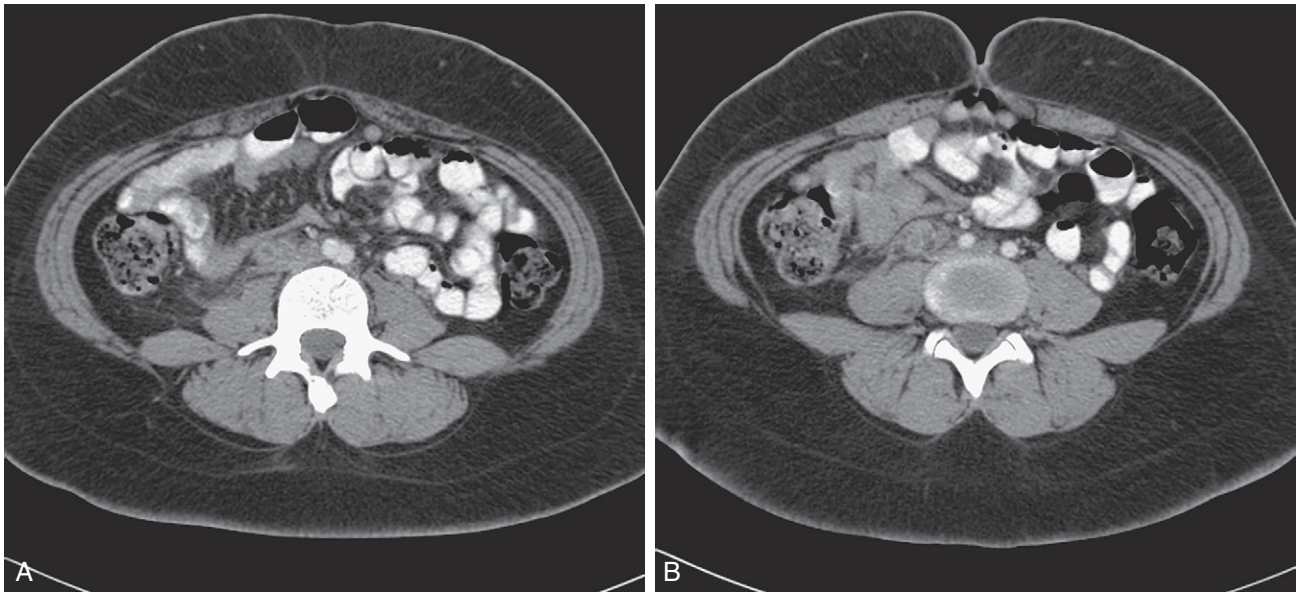


FIGURE 10-15 **A** and **B,** Computed tomography images of a 29-year-old patient showing a distended right ovarian vein. The vessel has an enhancing wall and contains thrombus. Inflammatory changes are identified around the vessel, better seen in **B**. This presentation represents septic thrombophlebitis.

clearly distinguished and may certainly be distinguished from submucosal fibroids or polyps.

Conclusion

Sonography is the mainstay imaging modality for much pelvic disease in both male and female patients and is often used to make a definitive diagnosis. In the male, sonography should be used for imaging the testes, scrotum, and prostate. In the female patient, sonography is the preferred imaging modality for gynecologic disease. However, given that many such diseases present with abdominal pain, in today's climate, CT imaging may be the modality that is first used. It is becoming increasingly important to be able to recognize the CT findings of many of the conditions traditionally imaged using sonography. MRI has a large role to play, particularly in the imaging of gynecologic disease; however, in the emergency department setting, MRI is seldom the imaging modality first used. MRI is more frequently used as a further tool for more complete evaluation of the patient, either after admission or on an outpatient basis, rather than from the emergency department. The role of MRI from the emergency department may well increase over time as more emergency departments acquire MRI equipment for the exclusive use of the emergency department.

SUGGESTED READINGS

Bennett GL, Slywotzky CM, Giovanniello G. Gynecologic causes of acute pelvic pain: spectrum of CT findings. *Radiographics*. 2002;22:785–801.

Bignardi T, Alhamdan D, Condous G. Is ultrasound the new gold standard for the diagnosis of ectopic pregnancy? *Semin Ultrasound CT MR*. 2008;29:114–120.

Gjelsteen AC, Ching BH, Meyermann MW, et al. CT, MRI, PET, PET/CT, and ultrasound in the evaluation of obstetric and gynecologic patients. *Surg Clin North Am*. 2008;88:361–390.

Guichard G, El Ammari J, Del Coro C, et al. Accuracy of ultrasonography in diagnosis of testicular rupture after blunt scrotal trauma. *Urology*. 2008;71:52–56.

Kalish GM, Patel MD, Gunn ML, Dubinsky TJ. Computed tomographic and magnetic resonance features of gynecologic abnormalities in women presenting with acute or chronic abdominal pain. *Ultrasound Q*. 2007;23:167–175.

Lambert MJ, Villa M. Gynecologic ultrasound in emergency medicine. *Emerg Med Clin North Am*. 2004;22:683–696.

Lee JC, Bhatt S, Dogra VS. Imaging of the epididymis. *Ultrasound Q*. 2008;24:3–16.

Lin EP, Bhatt S, Rubens DJ, Dogra VS. Testicular torsion: twists and turns. *Semin Ultrasound CT MR*. 2007;28:317–328.

Pearl MS, Hill MC. Ultrasound of the scrotum. *Semin Ultrasound CT MR*. 2007; 28:225–248.

Umeoka S, Koyama T, Togashi K, et al. Vascular dilatation in the pelvis: identification with CT and MR imaging. *Radiographics*. 2004;24:193–208.

Van Dyck P, Vanhoenacker P, Goris H, D'Haenens P. Puerperal ovarian vein thrombophlebitis. *JBR-BTR*. 2002;85:168–169.

Chapter 11

Vascular Emergencies

Russ Kuker, Carlos A. Anaya, Ana Maria Gomez, and Felipe Munera

The term *vascular emergency* carries a critical sense of urgency given that the integrity of the vascular system is crucial to maintain the vital blood supply to the various organ systems. Consequently, certain clinical scenarios demand immediate action to determine whether a blood vessel is intact or damaged and if it is able to maintain adequate perfusion. A broad spectrum of conditions fit the criteria to be considered vascular emergencies, including the various degrees of vascular trauma, spontaneous aneurysm rupture, acute dissection, acute thromboembolic disease, and surgical or interventional procedural complications. A prompt and accurate diagnosis is indispensable to allow the treating physician to determine the best therapeutic approach.

ARTERIAL EMERGENCIES

Improved diagnostic methods and increasing specialization have enhanced our ability to treat vascular emergencies. The treatment of patients experiencing these emergencies has changed radically in recent years; it has become increasingly complex and involves a team approach, with diagnostic and interventional radiologists being essential members of the team. In the evaluation of vascular emergencies, the role of catheter angiography as a diagnostic tool increasingly is being replaced by computed tomographic angiography (CTA) and sometimes magnetic resonance angiography (MRA). With technological advances, these modalities, particularly multidetector CTA (MD-CTA), have become an integral part of the initial assessment of acute vascular insults because they are minimally invasive techniques that are currently available in most emergency departments and trauma centers and permit a prompt and accurate diagnosis within a short period. These modalities are the methods of choice for the diagnosis of patients who do not have an indication for immediate surgical exploration. In addition, patients with direct signs of vascular injury on CTA (Box 11-1) can be taken to surgery without diagnostic angiography, given the high sensitivity of CTA for the detection of vascular injuries. Furthermore, computed tomography (CT)/CTA can be safely performed in patients with metallic fragments from bullets or other foreign objects, as opposed to magnetic resonance imaging (MRI)/MRA. MD-CTA has become the mainstay for diagnosing arterial injuries from blunt and penetrating trauma, not only to the chest and abdomen, but also to the neck and extremities.

BOX 11-1 Direct Signs of Vascular Trauma on Computed Tomographic Angiography

Irregular arterial margins
Filling defects
Contrast extravasation
Lack of vascular enhancement
Sudden or abrupt vascular caliber changes

Arterial Emergencies of the Neck

Trauma of the Extracranial Carotid and Vertebral Arteries

Vascular injuries to the neck are frequently the result of penetrating trauma and are seen in 25% of such cases. They also can result from blunt trauma, hyperextension, and blast injuries. CTA has proved to be extremely valuable in the evaluation of patients with these injuries because it provides simultaneous information about cervical spine and aerodigestive tract injuries. The full spectrum of vascular injuries can be identified, ranging from spasm to vessel transection. Most arterial injuries involve the carotid arteries, although vertebral arteries can be injured in up to 4% of cases.

Classically, the neck is divided into three zones for injury classification and management purposes. Zone 1 is from the clavicles to the cricoid cartilage, zone 2 is from the cricoid to the angle of the mandible, and zone 3 is from the angle of the mandible to the skull base. Zones 1 and 3 are extremely difficult to approach surgically. Injuries to zone 2 are the most common (60% to 70%), which represents a clinical advantage because they are readily accessible for physical examination and surgery. The management of unstable patients who have sustained a penetrating neck injury is emergency surgical exploration. Some controversy still exists regarding the treatment of hemodynamically stable patients who present with a wound that penetrates the platysma, because the local standards of care and resources may vary (Fig. 11-1). In general, surgeons opt for a conservative approach, starting with CT/CTA, and they use additional diagnostic studies or perform surgery when it is medically indicated. CTA has high sensitivity and specificity, with reported values for the diagnosis of cervical vascular injuries ranging between 90% and 100%, respectively. The routine use of conventional angiography has been discouraged because of the high number of examinations with negative findings and the potential risk for complications as a result of its invasive nature. Nevertheless, the presence of any indirect sign around the carotid artery (Box 11-2) should warrant a correlation with angiography given the potential catastrophic consequences of missing a lesion in this location.

Blunt traumatic injuries of the extracranial carotid and vertebral arteries may have devastating consequences, with an incidence that oscillates between 0.33% and 2.7%,

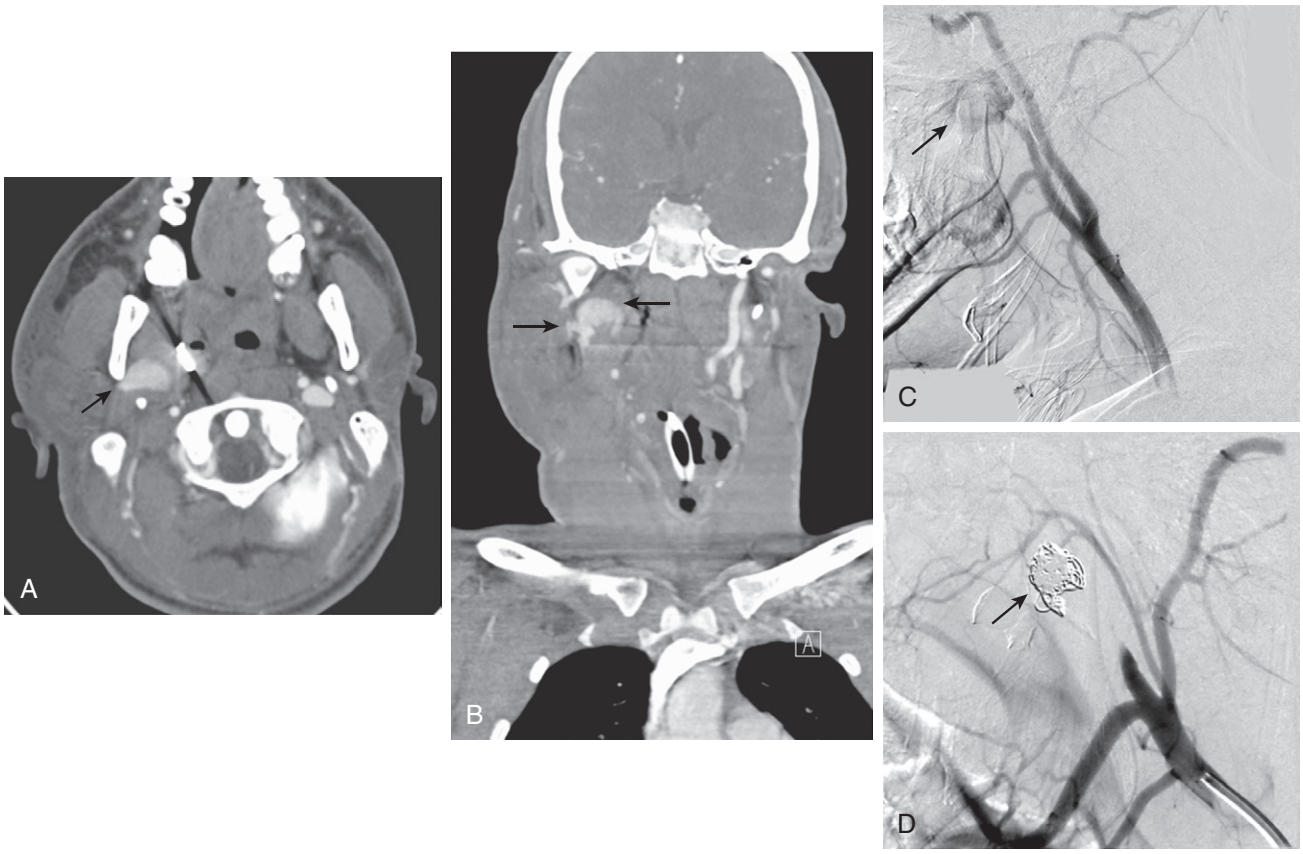


FIGURE 11-1 A 23-year-old man with a ballistic injury. **A** and **B,** Computed tomographic angiography images demonstrate a pseudoaneurysm and transection/injury to the right external carotid artery at the bifurcation into the internal maxillary and superficial temporal arteries *(arrows)*. **C** and **D,** The patient subsequently underwent conventional angiography and embolization of the pseudoaneurysm *(arrows)*. (Courtesy Dr. Charif Sidani, University of Miami, Miami, FL.)

BOX 11-2 Indirect Signs of Vascular Trauma on Computed Tomographic Angiography

Indistinctness of perivascular fat planes
Perivascular hematoma
Bone or bullet fragment less than 5 mm away from a major vessel

according to reports from centers that perform aggressive angiographic screening. Although CTA and MRA have great potential as screening tools in patients who have a blunt cerebrovascular injury, catheter angiography is still considered the gold standard. Intimal dissection and occlusion are more common with blunt trauma than with penetrating injuries (Fig. 11-2). Approximately 10% of patients have focal neurologic findings on initial presentation, and in two thirds of the patients, symptoms develop within 24 hours. The remaining patients may present with neurologic findings weeks to months later.

The type of intervention performed for carotid and vertebral injuries is determined by the nature of the lesion, the symptoms and clinical condition of the patient, and the feasibility of accessing the injured segment either with open surgery or with an endovascular approach. In general, intimal flaps and nonocclusive dissections are managed with anticoagulation, provided there are no

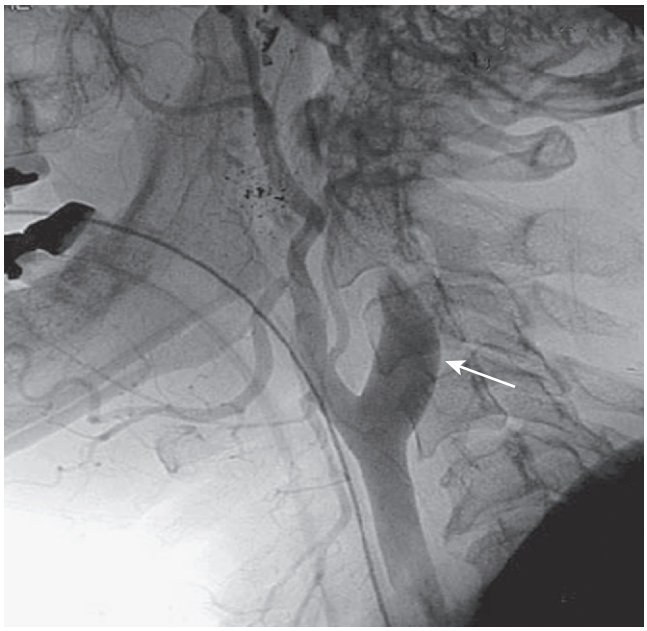


FIGURE 11-2 A conventional angiogram obtained after a gunshot wound to the neck shows complete occlusion of the internal carotid artery as a result of occlusive dissection with the characteristic flame-shaped appearance *(arrow)*. (Courtesy Dr. F. Gomez, Cali, Colombia.)

contraindications. Stent placement is reserved for flow-limiting dissections, whereas covered stents (stent grafts) have been used successfully to treat pseudoaneurysms and arteriovenous (AV) fistulas with good immediate results and patency rates (see Fig. 11-1). Embolization is another alternative for cases of vascular transection in which surgical or endovascular vessel wall reconstruction cannot be achieved and adequate collateral pathways are demonstrated.

Nontraumatic Emergencies of the Carotid and Vertebral Arteries

Carotid and Vertebral Artery Dissection. Spontaneous dissection of the carotid or vertebral arteries in the absence of trauma is rare and usually occurs in patients with an underlying history of hypertension or fibromuscular dysplasia or an underlying collagen disorder such as Marfan or Ehlers-Danlos syndrome. It can occur at any age. Clinical manifestations are variable, including neck pain or ipsilateral headache, Horner syndrome (i.e., ptosis, myosis, and unilateral anhydrosis), and acute or chronic focal neurologic events either in the form of a transient ischemic attack or as a permanent neurologic deficit. All imaging modalities, including ultrasound, CT, and MRI, can be used to demonstrate the intimal flap, a compressed true lumen, slow flow in the false lumen, or even thrombus formation. Catheter angiography is generally indicated to better assess flow patterns or to confirm the absence of flow (see Fig. 11-2). Most patients are successfully treated with anticoagulation, but stent placement in the true lumen may be necessary to maintain or restore cerebral perfusion.

Aortic Emergencies. Acute aortic syndromes encompass a spectrum of aortic emergencies that include traumatic aortic injury (TAI), aortic dissection, penetrating atherosclerotic ulcer of the aorta, intramural hematoma, and aortic aneurysm rupture. Chapter 2 covers the topics of aortic dissection, intramural hematoma, and penetrating ulcer. This section focuses on traumatic aortic injuries.

TAI is a novel term that encompasses a spectrum of injuries characterized by a variable degree of aortic wall laceration and that include intimal tear, intramural hematoma, traumatic dissection, traumatic pseudoaneurysm, and, in the most severe form, aortic transection. TAI may result from rapid decelerations, crush injuries, penetrating wounds, and surgical or angiographic instrumentation. Blunt trauma is the most frequent cause of TAI, usually as the result of shearing, hydrostatic forces, and/or torsion forces applied along the aortic arch during a motor vehicle accident and falls from heights. Less common causes include displaced clavicular and thoracic vertebral fractures with entrapment of the aorta between the anterior chest wall and the spine. The overall mortality at the scene of the accident has been reported to be as high as 80% in autopsy series, with only 10% to 20% of victims surviving the initial trauma. Bleeding from a laceration or rupture can be controlled by the aortic adventitia or the periaortic tissues, which can help the patient survive the initial injury; however, the end result is pseudoaneurysm formation, which, because of its instability, requires prompt diagnosis and treatment (Fig. 11-3). The region of the aorta most susceptible to blunt injury is the isthmus, where the relatively mobile proximal thoracic aorta and arch join the fixed distal arch at the insertion of the ligamentum arteriosum, just distal to the left subclavian artery origin (Fig. 11-4). This area is involved in as many as 90% to 95% of cases. Other common areas of injury are the aortic root and the diaphragmatic hiatus. Injuries to the ascending aorta are uncommon (5% to 9%) and usually lethal because of the lack of surrounding connective tissue, resulting in rapid death as a result of exsanguination or cardiac tamponade. Clinical suspicion, as well as prompt diagnosis and treatment, are of crucial importance in persons with a TAI, given that 30% of the victims will die within 6 hours and 40% to 50% will die within 24 hours.

Plain radiographs are used for the initial imaging screening of trauma patients because they are readily available and have the capacity to quickly assess injuries such as pneumothorax, hemothorax, mediastinal hematoma (Fig. 11-5), and fractures. Clinical signs and symptoms found in patients with TAI include chest pain, back pain, dyspnea, cough, hoarseness, hypotension, pulse discrepancy, shock, and coma; as many as 30% to 50% of these patients may not show external signs of trauma.

A normal upright chest radiograph has a negative predictive value of 98% when evaluating patients for aortic injury; however, such a radiograph rarely can be obtained for patients with severe multitrauma. In such patients a frontal poorly inspired film tends to be obtained with which mediastinal abnormalities frequently cannot be adequately assessed. Indirect signs for possible TAI on a chest radiograph include widening of the mediastinum, tracheal shift, deviation of the nasogastric tube or endotracheal tube to the right of the T3-T4 spinous processes, widening of the left or right paraspinal lines, apical cap, increased density of the aortopulmonary window, hemothorax, depression of the left main stem bronchus, and an ill-defined aortic arch. Mediastinal widening has reported sensitivities ranging between 81% and 100%, with a specificity of 60%; however, significant interreader variability exists when using this sign to predict aortic injury.

A catheter aortogram has long been considered the gold standard for the diagnosis of TAI, with reported sensitivities and specificities approaching 100%. However, MD-CTA has become the preferred method for screening patients with major traumatic and nontraumatic aortic emergencies because of its improved spatial and contrast resolution and supplemental postprocessing techniques (thin sections, multiplanar reformations, and three-dimensional volume-rendered images), with a performance that rivals that of catheter angiography. MD-CTA has helped to better characterize the location and extent of TAI and other vascular injuries, thus allowing for faster diagnosis and treatment planning. In addition, MD-CTA also can recognize a greater number of normal variants of the vascular anatomy and subtle vascular injuries that were less likely to be seen with conventional CT scans (Fig. 11-6). Furthermore, the need to perform aortography to confirm the diagnosis of TAI is eliminated when direct signs of injury are present on CTA. Direct signs of TAI on CTA include active extravasation of contrast material, pseudoaneurysm formation, irregularity of the aortic wall, abrupt change in the caliber of the aorta, aortic dissection, intimal flaps,

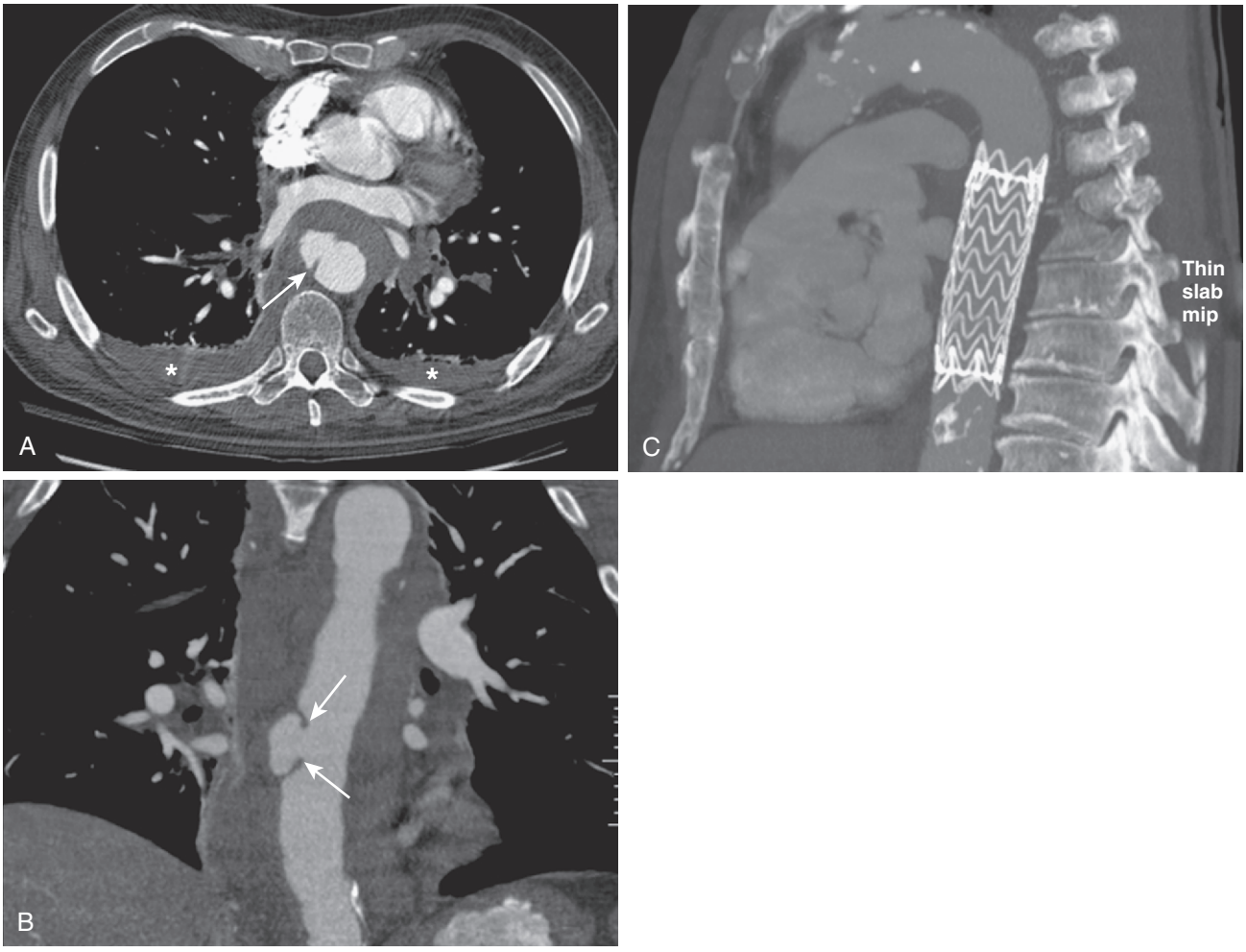


FIGURE 11-3 Traumatic aortic injury in the mid descending aorta after blunt trauma. Axial **(A)** and coronal reformat **(B)** images demonstrate a localized complete rupture of the aortic wall that led to mediastinal periaortic hematoma leaking into both pleural spaces *(asterisks)*. A pseudoaneurysm *(arrows)* has developed at the rupture site. **C,** Thin maximal intensity projection *(mip)* showing complete pseudoaneurysm occlusion after repair with a stent graft. (Courtesy Dr. Daniel J.A. Margolis, David Geffen School of Medicine, University of California–Los Angeles, Los Angeles, CA.)

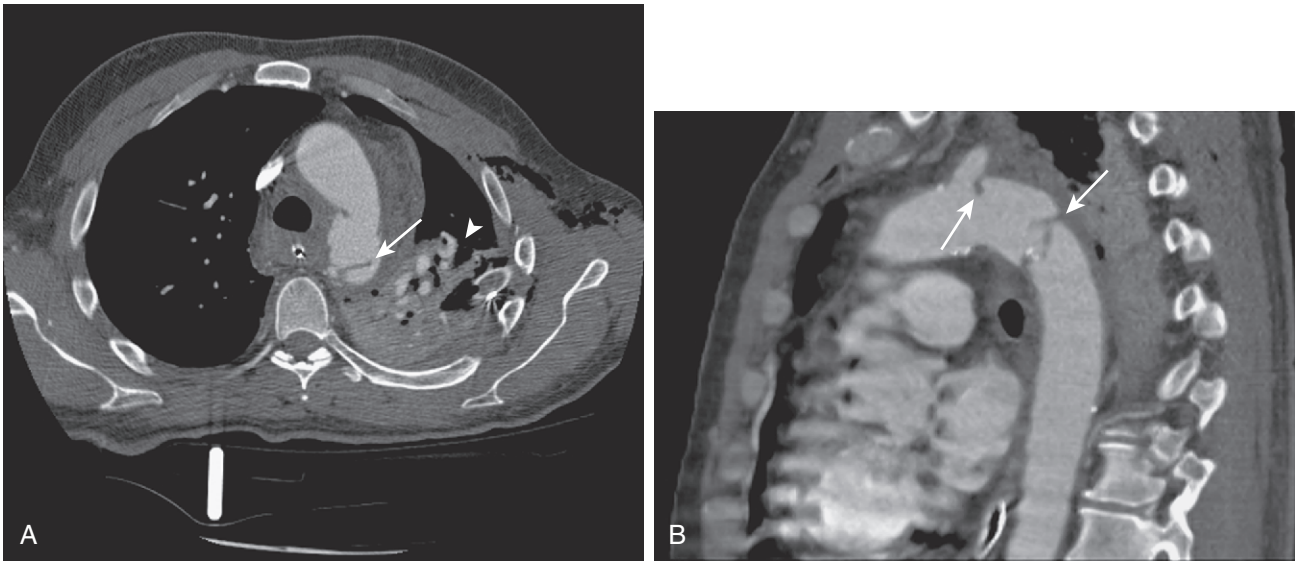


FIGURE 11-4 Axial computed tomographic angiography **(A)** and sagittal reformat **(B)** demonstrate a traumatic aortic injury with an intimal tear *(arrows)* distal to the left subclavian artery origin and surrounding hematoma consistent with a contained aortic rupture. Also seen are partially visualized left rib fractures, subcutaneous emphysema, and an atelectatic left lung *(arrowhead)*. (Courtesy Dr. Daniel J.A. Margolis, David Geffen School of Medicine, University of California–Los Angeles, Los Angeles, CA.)

and filling defects. Indirect signs of possible aortic injury include periaortic hematoma and mediastinal hematoma (Fig. 11-7).

Catheter angiography can accurately demonstrate abnormalities affecting the aortic lumen; however, it is a time-consuming, invasive procedure that may require higher doses of contrast material and is limited in diagnosing concurrent injuries in multitrauma patients, risking a delay in management of other potentially lethal injuries. A minority of patients may still require catheter angiography when MD-CTA examinations are nondiagnostic or show equivocal or indirect signs of TAI. The decision to perform a catheter angiogram for patients with indirect findings depends on the experience of the interpreter, the quality of the scan, and the clinical condition of the patient. Angiographic diagnosis of intimal injury is demonstrated by the presence of intimal irregularity, linear defects, or filling defects caused by an intimal flap. The presence of contrast material outside the lumen is consistent with active extravasation. The contrast material can be contained or free; both presentations are consistent with a transmural laceration and require immediate attention. The current complication rate for angiography is less than 1%, and complications include aortic rupture, acute renal failure, anaphylaxis, and entry site hematoma.

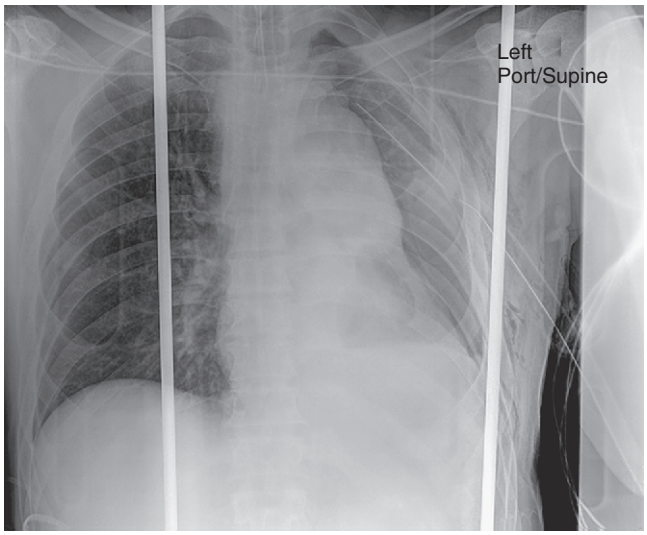


FIGURE 11-5 A portable radiograph demonstrates multiple signs of traumatic aortic injury, including a widened mediastinum, slight tracheal shift, widening of the right paratracheal stripe, left apical cap, obliteration of the aortopulmonary window with poorly defined aortic arch, and a left hemothorax with a chest tube in place and rib fractures.

Transesophageal echocardiography (TEE) is another imaging modality that can provide detailed real-time images of the aorta, heart, and pericardium and can be performed at the patient's bedside. Studies have shown sensitivity ranging between 63% and 100% and specificity ranging between 84% and 100% for the detection of aortic rupture. The wide range of these results is explained by the fact that TEE is operator dependent. Direct signs of aortic injury include an intimal flap, intraluminal thick stripes, a pseudoaneurysm, aortic occlusion, and an aortic wall hematoma. The main limitation of TEE is its "blind spot," which represents the lack of visualization of a 3- to 5-cm segment in the distal ascending aorta and proximal arch that can be the site for TAI in 10% to 20% of patients. TEE is an alternative for the evaluation of unstable patients. However, negative findings of TEE in the setting of suspicious clinical or radiologic findings warrant further investigation.

Currently MRA is not considered the imaging technique of choice for the evaluation of TAI because of the relatively long acquisition times, the limited access to manage and control hemodynamically unstable patients, and the difficulties in scanning patients with metallic fragments or devices that may preclude the examination.

Treatment. Immediate surgical intervention is the treatment of choice in patients with TAI who are hemodynamically unstable, have persistent bleeding, or have evidence of an expanding hematoma. Surgical repair is usually a major intervention requiring thoracotomy, aortic cross-clamping, partial cardiopulmonary bypass, suturing or prosthetic grafting of the aorta, and treatment of concomitant injuries such as the evacuation of pericardial tamponade or a

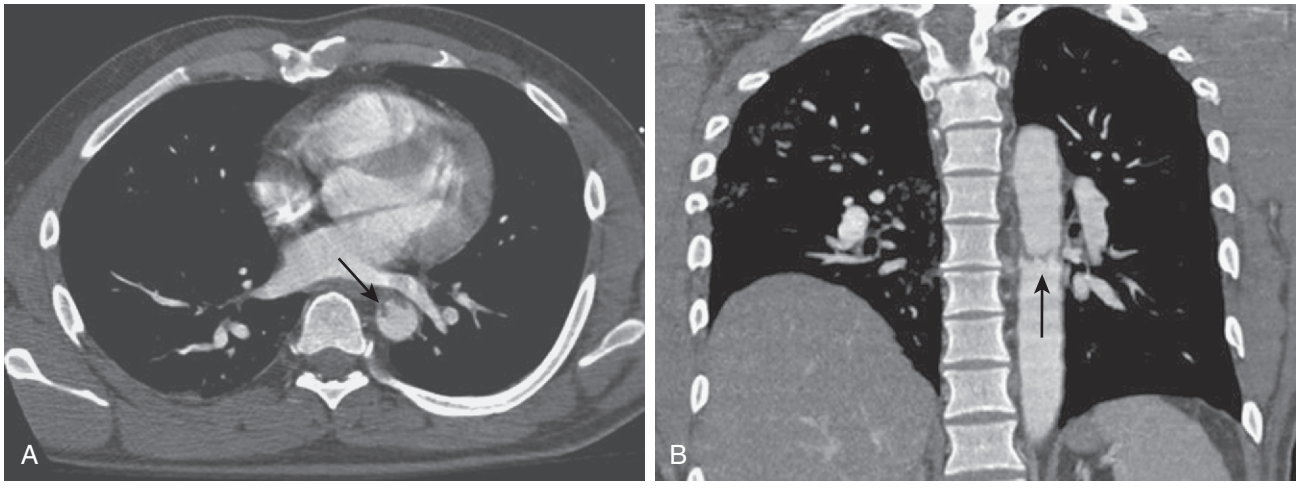


FIGURE 11-6 **A** and **B,** Computed tomographic angiography images in the axial and coronal plane obtained after blunt chest trauma demonstrate an intimal tear *(arrows)* in the mid descending aorta without extravasation or surrounding hematoma. (Courtesy Dr. Daniel J.A. Margolis, David Geffen School of Medicine, University of California–Los Angeles, Los Angeles, CA.)



FIGURE 11-7 A contrast-enhanced computed tomographic image obtained in a patient who sustained a motor vehicle accident demonstrates a concentric paraaortic hematoma *(arrowheads)* without active extravasation or obvious wall defects that was managed with medication and followed up until resolution. (Courtesy Dr. Daniel J.A. Margolis, David Geffen School of Medicine, University of California–Los Angeles, Los Angeles, CA.)

large hemothorax. The operative mortality of open thoracotomy ranges between 9% and 28%, with a high rate of major morbidities, including paraplegia (up to 20%) as a result of spinal cord ischemia and stroke. Patient triage and selection are essential to perform a successful thoracotomy because open thoracotomy can worsen the clinical condition of severely injured patients who may not be able to tolerate this procedure.

Alternative management of TAI consists of delayed operative intervention or no operative intervention at all while the patient is closely monitored and blood pressure (BP) is controlled to reduce the risk of free rupture. The mainstay of treatment is to maintain systolic BP below 120 mm Hg (mean arterial pressure below 80 mm Hg) and allow patients who have sustained associated severe trauma to stabilize before undergoing surgical repair. This approach is indicated in hemodynamically stable patients with small aortic tears or those with associated injuries such as significant head, cardiac, or pulmonary trauma, large body surface burns, contaminated wounds, large retroperitoneal hematomas, or other high-risk medical comorbidities. Some of these aortic injuries may develop into a chronic pseudoaneurysm (Fig. 11-8), and others may even resolve during the period of observation. Close clinical and imaging follow-up is imperative to detect injury progression or aortic rupture.

More recently, endovascular treatment of TAI using stent grafts has been introduced as an alternative in the management of hemodynamically stable patients and patients with contraindications to cardiopulmonary bypass, such as severe coagulopathy, extensive additional injuries, and severe underlying cardiac or pulmonary disease. Mortality and morbidity with use of stent grafts appear to be lower than with surgery, most likely because of the less invasive nature of the procedure, a shorter operation time, and lack of surgery-related comorbidities. The stent grafts are delivered via a common femoral artery cut-down procedure and positioned with angiographic and fluoroscopic guidance. The left subclavian artery origin often must be covered with the endograft to provide adequate proximal support without significant clinical consequence in many patients. A significant number of patients with TAI are young, and the aortas of young patients are small; however, most stent grafts available today are made for the treatment of larger aortas affected by degenerative aortic aneurysms. Although it is usually recommended that the size of the stent graft be increased by 10% to 20% to ensure an adequate seal, an excessive increase in the size of the stent graft has been associated with type I endoleaks (Table 11-1) and stent graft collapse. Complications related to the endovascular repair include hematomas in the groin, iliofemoral dissection, endoleaks, graft migration, and arterial rupture. The overall morbidity rate has been found to be approximately 12%, with a mortality rate of 4%. Clinical and imaging follow-up of patients who receive either surgical and endovascular treatment is required to ensure early identification of posttreatment complications.

Minor Aortic Injury. With the increased utilization and improved sensitivity of MDCT in evaluating patients with blunt thoracic trauma, a greater number of minor aortic injuries (MAIs) are being diagnosed. An MAI has been described as a posttraumatic abnormality of the internal contour of the aorta wall, an intimal flap, an intraluminal filling defect, or an intramural hematoma. In a retrospective review of 81 patients by Gunn and colleagues, MAI occurred in approximately 28% of cases of blunt TAI. The majority of MAI cases in this series occurred in the descending thoracic aorta (69%) and were treated conservatively (83%) with antihypertensive drugs, anticoagulant agents, or both. The patients in this series who were treated without operative or endovascular repair were followed up for a mean of 466 days, with no reports of death or complications as a result of MAI. In another retrospective review of 115 patients, Forman and colleagues included in their definition of MAI small pseudoaneuryms of less than 10% of the normal aortic diameter as measured at the level of the pseudoaneurysm. In their study, in about one third of patients with MDCT-diagnosed blunt TAI, the injuries were minor. Although the absence of a mediastinal hematoma nearly excluded the possibility of major TAI, approximately 21% of cases of MAI occurred without evidence of a mediastinal hematoma. About 62% of patients in this series who met the definition of MAI were treated with medication and did not show evidence of progression of TAI at the last imaging follow-up. These studies indicate that MAI is identified by MDCT in more than a quarter of the cases of blunt TAI, MAI has a low mortality, and most of the time MAI can be managed conservatively with excellent outcomes.

Penetrating Aortic Injury. Penetrating injuries to the intrathoracic great vessels are uncommon, with an incidence of 1%; they have a high mortality rate that ranges between 50% and 85%, despite advances in trauma care and prehospital resuscitation. These types of injuries can be caused by gunshot wounds (GSWs) or stab wounds that traverse the chest or the base of the neck (Fig. 11-9). Overall, GSWs are more common and more lethal than stab wounds. Penetrating injuries to the thoracic aorta often occur along the ascending aorta and the arch branches, with a documented low incidence of descending thoracic injuries. These types of lesions are commonly associated with coexisting lethal intrathoracic

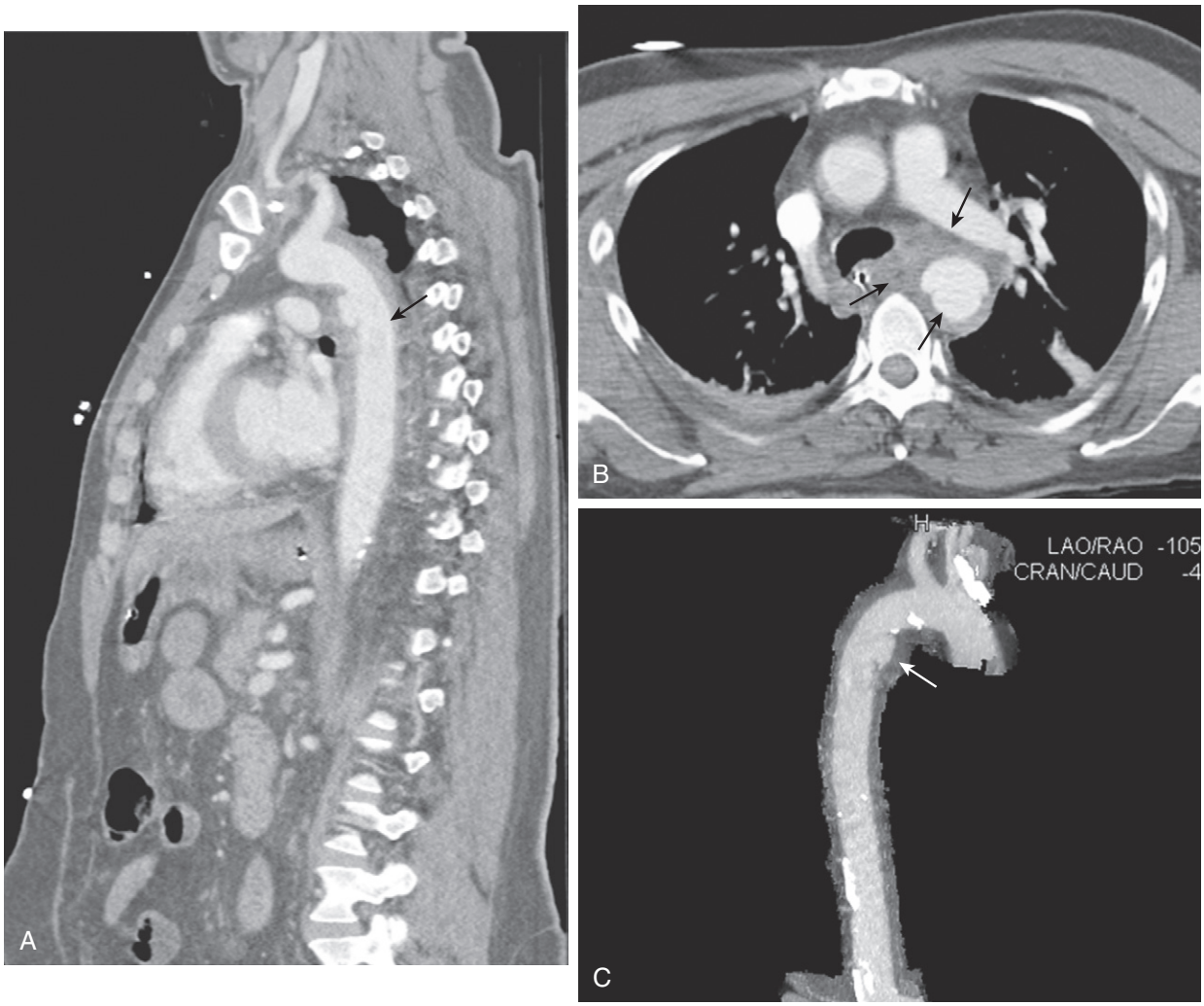


FIGURE 11-8 A 50-year-old man on a moped who was hit by a car. **A** and **B**, Computed tomographic angiography images show a traumatic pseudoaneurysm at the aortic isthmus with a periaortic hematoma/contained rupture *(arrows)*. **C,** A three-dimensional reconstructed image of the thoracic aorta confirms the location of the pseudoaneurysm *(arrow)*.

TABLE 11-1 Endoleak Classification

Endoleak type I	Inadequate seal around the proximal or distal end of the stent graft
Endoleak type II	Retrograde flow from branch vessels (intercostal, lumbar, inferior mesenteric, and gonadal arteries) resulting in persistent filling of aneurysm
Endoleak type III	Stent graft laceration or fabric tears and dislodgment of modular graft devices
Endoleak type IV	Porosity of the graft fabric and diffuse leakage through interstices
Endotension	Excluded sac continues to enlarge without apparent endoleak formation

injuries, which worsen the patient's prognosis. Although the aorta is protected by osseous structures, a laceration in this large-caliber vessel with high intraluminal pressure can cause rapid exsanguination. Thoracic aortic injuries have a worse prognosis than injuries to the abdominal aorta, probably because of the retroperitoneal location of the abdominal aorta, which can slow the rate of exsanguination. Thoracic aortic injuries usually manifest as hemorrhage into the mediastinum or pleural cavity presenting as hemothorax, cardiac tamponade, or mediastinal hematoma.

A portable supine chest radiograph continues to be the best initial imaging modality to screen for chest trauma. Radiopaque markers should be placed at the entry and exit sites of the wounds to provide a guide to the possible wound trajectory and the organs that might have been injured. Penetrating vascular lesions are suggested by a large hemothorax, widened mediastinum, foreign bodies in the proximity of the great vessels, or a bullet in a position different from its predicted course, suggesting bullet embolism, also known as "missing missile."

MDCT/CTA has become an integral part of the assessment of aortic injury resulting from blunt trauma, and its role in penetrating injuries to the aorta continues to expand because of its availability, short acquisition time, and ability to identify vascular lesions. MDCT/CTA is also able to locate bullets and fragments, document the wound tract and bullet path, visualize associated fractures, and evaluate internal organ injuries. MDCT/CTA continues to have

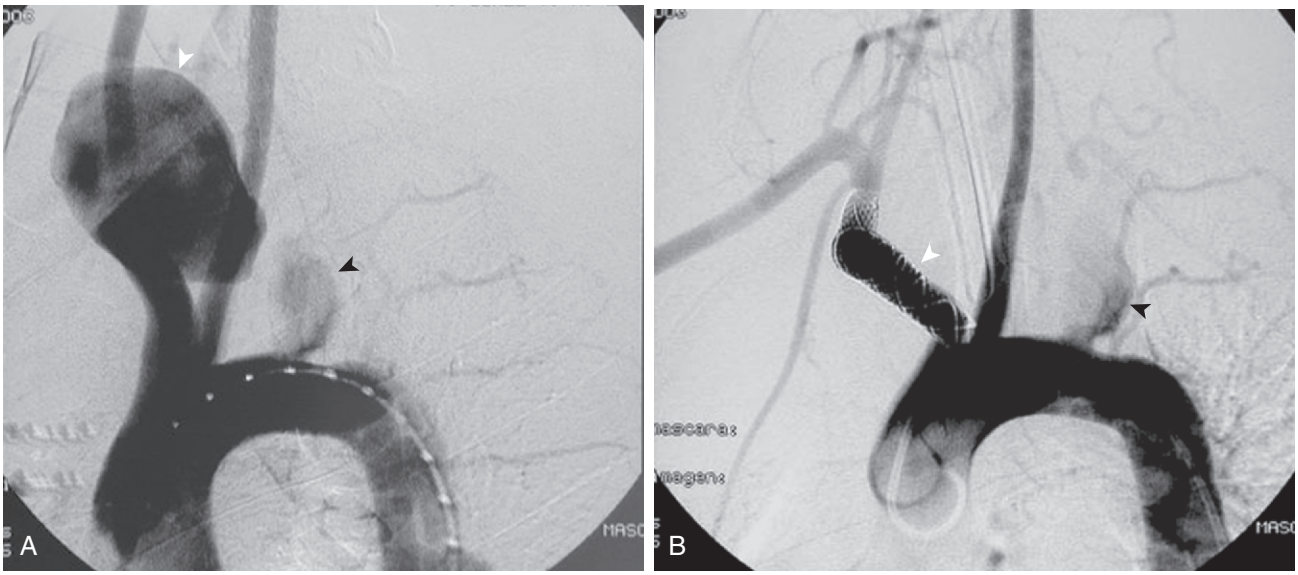


FIGURE 11-9 **A,** An arch angiogram obtained after a stab wound to the neck. A large pseudoaneurysm is present at the level of the distal brachiocephalic trunk *(white arrowhead)* and a second pseudoaneurysm is present that involves the arch and possibly the left subclavian artery origin *(black arrowhead).* Neither one of the subclavian arteries is visualized. **B**, After treatment with a covered stent *(white arrowhead)* the large brachiocephalic aneurysm has been occluded, preserving the right carotid and reestablishing flow in the right subclavian. The aortic pseudoaneurysm *(black arrowhead)* required surgical repair. (Courtesy Dr. W. Escobar, Cali, Colombia.)

a major role in hemodynamically stable patients who have GSWs that are suspected to have transversed the mediastinum, because MDCT/CTA can define the wound tract and its relationship with vascular and aerodigestive structures, thus helping plan further treatment.

Aortic angiography remains the gold standard for the diagnosis of vascular lesions because of its ability to show pseudoaneurysm formation, active extravasation, and arteriovenous fistulas. However, fewer catheter aortograms are being performed because of the previously mentioned benefits of noninvasive imaging with MD-CTA. In the case of a penetrating injury to the major vessels, lesions in the central venous structures such as the innominate veins can be simultaneously present in up to one fourth of patients, and they account for nearly 22% of fatalities in penetrating chest trauma. When catheter angiography is performed, a venous phase should be carried out in all arteriograms, and if venous injury is suspected, use of conventional venograms should be considered.

Penetrating injuries to the thoracic aorta are usually treated with urgent surgical repair via an anterolateral thoracotomy. Endovascular repair with stent grafts may be possible for penetrating injuries in some patients (see the section on TAI).

Nontraumatic Aneurysms of the Thoracic and Abdominal Aorta

Thoracic Aortic Aneurysms. Thoracic aortic aneurysms (TAAs) are often the result of atherosclerotic disease or cystic medial degeneration with subsequent weakening and dilatation of the aortic wall. The development of TAAs is usually a silent process, it is seen less commonly than abdominal aortic aneurysms, and it generally occurs in older men in their sixth and seventh decades. Based on their structure, aneurysms are classified as either fusiform aneurysms, which involve the full circumference of the vessel wall, or saccular aneurysms that involve only a focal portion. Thoracic aneurysms occur in the ascending aorta in 40% to 60% of cases, in the descending aorta in 30% to 40% of cases, and in the aortic arch and thoracoabdominal aorta in 10% of cases. The incidence and prevalence of thoracic aortic disease, including TAA, are steadily increasing because of the aging population and improved diagnostic techniques. The reported incidence of TAA ranges from 6 to 10 cases per 100,000 patients per year. The natural history of untreated TAA is progressive expansion of the aneurysm and, ultimately, rupture (Fig. 11-10).

Given that most patients are asymptomatic, TAAs are commonly diagnosed as an incidental finding on imaging studies. However, they also can present with signs and symptoms related to compression of adjacent structures. Ascending aortic aneurysms can compress the coronary arteries or the origins of the great vessels, causing myocardial or cerebral ischemia. Together with arch aneurysms, they can erode into the mediastinum and compress the left recurrent laryngeal nerve, causing hoarseness, or the phrenic nerve, leading to hemidiaphragmatic paralysis. They also can press on (1) the tracheobronchial tree, causing wheezing, dyspnea, cough, hemoptysis, and pneumonitis; (2) the esophagus, resulting in dysphagia; and (3) the superior vena cava (SVC), causing SVC syndrome. Mural thrombus from the aneurysms can be a source of emboli and cause strokes, as well as renal, mesenteric, or limb ischemia. Heart failure can result from aortic root aneurysms, leading to aortic regurgitation, or from the rupture of a sinus of Valsalva aneurysm into the right side of the heart. Chest and back pain are rare symptoms associated with compression of intrathoracic structures or erosion into adjacent bones (Fig. 11-11).

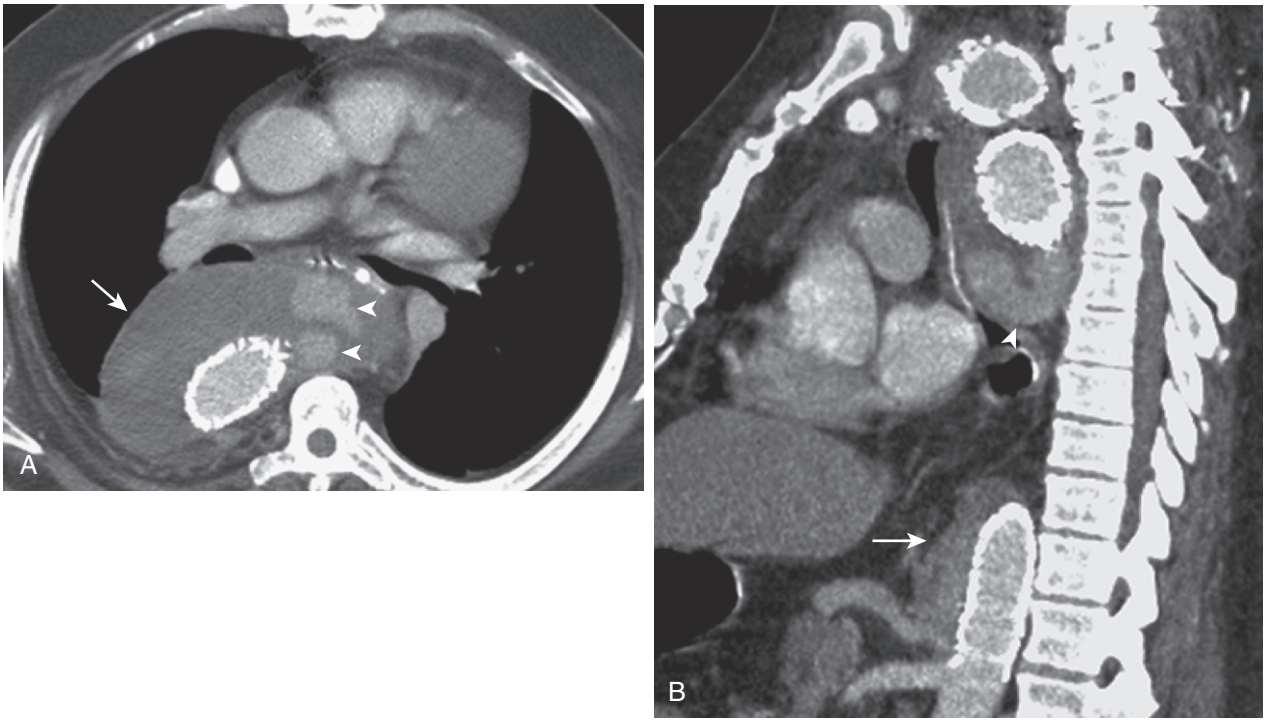


FIGURE 11-10 **A** and **B,** A patient with a large thoracic aortic aneurysm *(arrows).* This patient had a right arch and aberrant left subclavian artery origin. After treatment with an endograft, an endoleak developed where the endograft overlapped the celiac trunk *(arrowheads).*

The most feared complications of TAAs are aneurysm dissection and rupture. Dissection can lead to arterial occlusion and end-organ ischemia, and rupture can cause massive hemorrhage that usually cannot be contained by adjacent structures and therefore is considered a surgical emergency. Patients present with hypotension and acute onset of chest pain, abdominal pain, back pain, or neck pain. Rupture occurs more commonly into the left pleural space, but it also can occur into the pericardium, causing pericardial tamponade (Fig. 11-12), or into the esophagus, resulting in an aortoesophageal fistula and dramatic upper gastrointestinal (GI) bleeding.

The risk of rupture and dissection of TAAs increases with aneurysm size. The mean rate of rupture or dissection for small aneurysms is around 2%; it increases to 3% for aneurysms measuring 5.0 to 5.9 cm and to 7% in patients with aneurysms 6 cm in diameter or larger. The mean aortic growth rate has been estimated to be 0.1 cm per year. Greater growth rates are seen in patients with Marfan syndrome, aneurysms of the descending aorta, and dissecting aneurysms. Although men are more prone to the development of thoracic aneurysms, women have a higher likelihood of rupture and dissection.

Multiple causes have been associated with thoracic aortic aneurysms, and they differ depending on their location within the thoracic aorta. Aneurysms of the ascending aorta and aortic arch are more commonly seen in elderly patients as a result of atherosclerosis or aortic valve stenosis, leading to poststenotic dilatation. The younger patient population presenting with thoracic aneurysms in the ascending aorta and aortic arch (Tables 11-2 and 11-3) usually have a connective tissue disorder such as Marfan syndrome (mutation of the fibrillin-1 gene), Ehlers-Danlos syndrome (a defect in type III collagen), Loeys-Dietz syndrome, or Turner syndrome (which is associated with bicuspid aortic valves). Other infrequent causes include mycotic and syphilitic aneurysms. Aneurysms of the sinus of Valsalva can be congenital, infectious, or postsurgical in origin and are seen as dilatations in connection with the aortic root. Vasculitis can affect all portions of the thoracic aorta. One of the most striking entities is Takayasu arteritis, which is characterized by a chronic inflammatory process of unknown cause that affects the aorta, its major branches, and the pulmonary arteries. Takayasu arteritis affects the vessel wall, causing obliterative luminal changes, occlusion, or dilatation. Aneurysm formation can be a fatal complication of this disease because it may lead to heart failure as a result of aortic valve regurgitation or aortic rupture.

Aneurysms of the descending thoracic aorta are also most commonly degenerative in origin; they are caused by atherosclerosis and usually are associated with hypertension, hypercholesterolemia, and smoking. These aneurysms are generally fusiform with significant intimal calcifications and demonstrate associated tortuosity and mural thrombus. Other causes include chronic aortic dissection (Stanford type A or B), which can dilate over time as the wall of the false lumen weakens, creating a dissecting aneurysm with a high risk of rupture. Injuries to the descending thoracic aorta associated with blunt trauma can result in the formation of pseudoaneurysms, which are characteristically located near the aortic isthmus distal to the subclavian artery and have a high risk of rupture (these pseudoaneurysms are discussed in the TAI section). As with ascending thoracic aneurysms, younger patients with descending thoracic aortic aneurysms usually have an underlying connective tissue disorder (Table 11-4) or vasculitis. Mycotic aneurysms also can affect this segment.

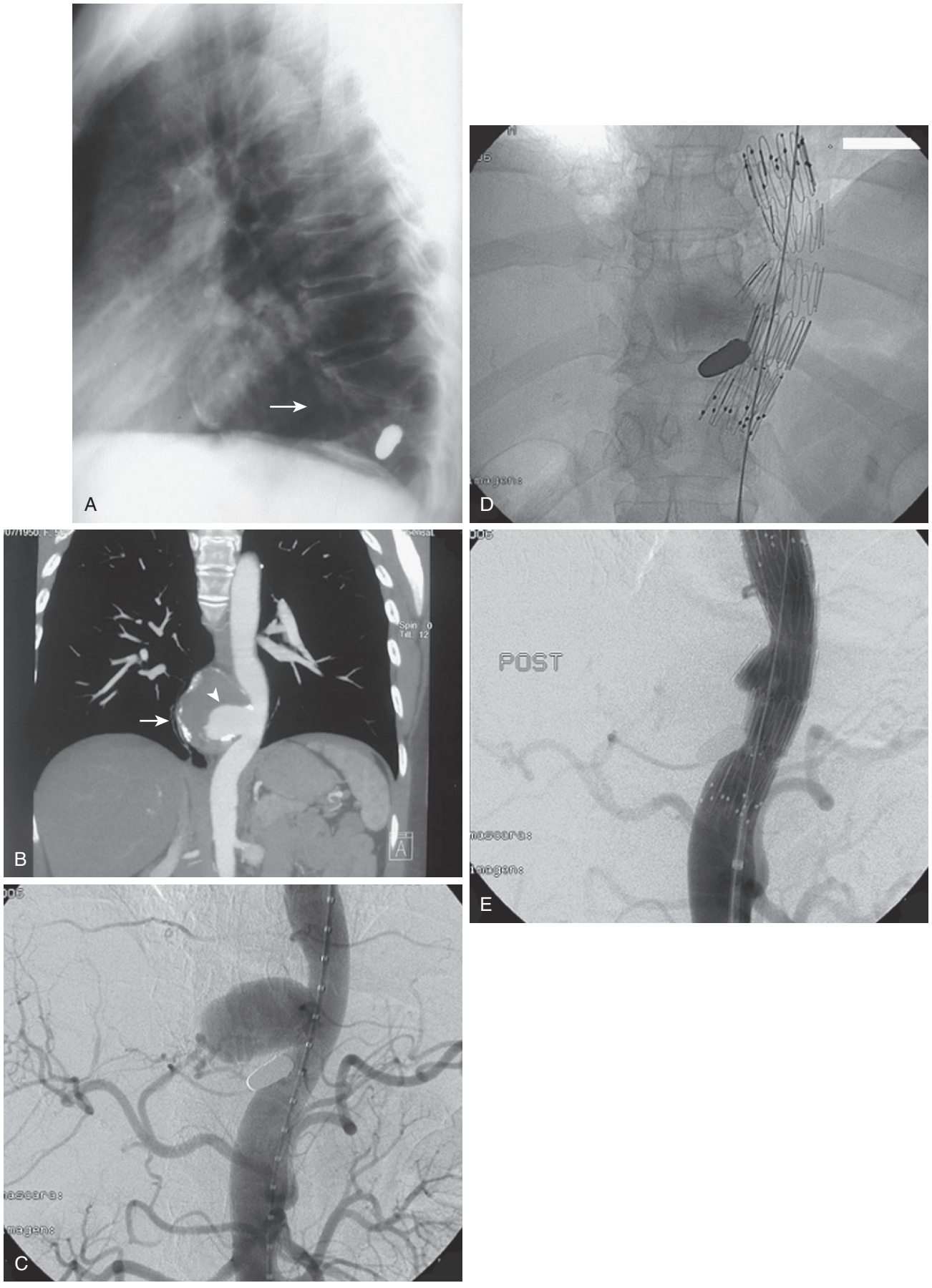


FIGURE 11-11 A 40-year-old patient with back pain and a history of a gunshot wound 15 years earlier. **A,** A lateral radiograph demonstrates the projectile overlying the spine and an anterior wedge-shaped lytic defect involving T11-T12 *(arrow)*. **B,** Computed tomographic angiography shows a large chronic saccular pseudoaneurysm with peripheral calcifications *(arrow)* and the patent inner lumen *(arrowhead)*. **C,** Catheter angiography shows the thoracoabdominal aneurysm with preserved upper abdominal branches. **D** and **E,** After repair with an endograft, complete exclusion of the aneurysm is achieved. (Courtesy Dr. W. Escobar, Cali, Colombia.)

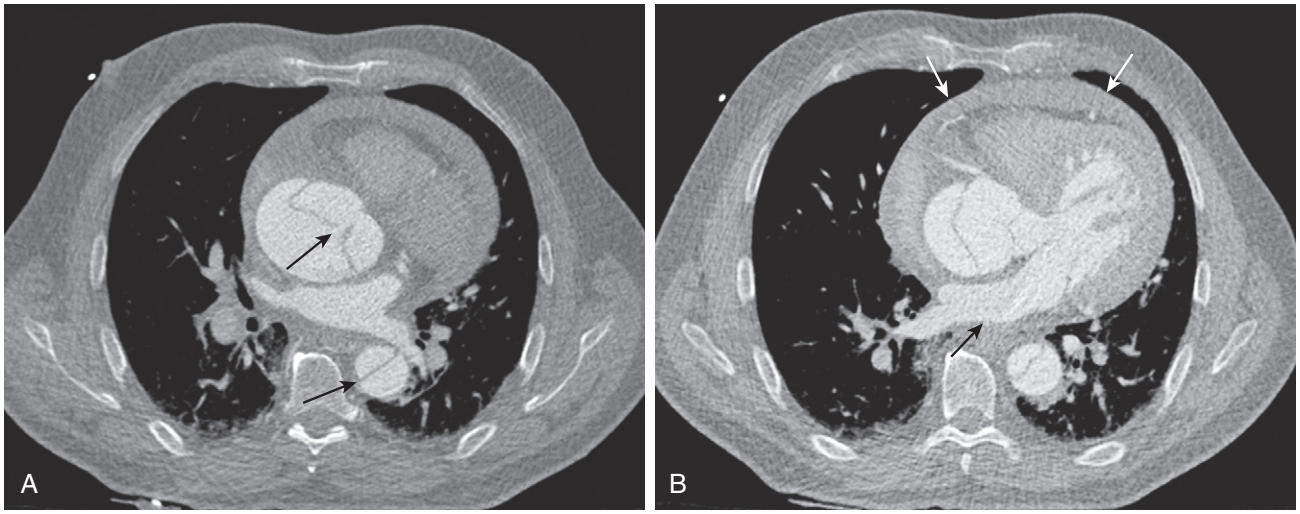


FIGURE 11-12 A 59-year-old man with chest pain and hypotension. Computed tomographic angiography images show a type A dissection complicated by hemopericardium compressing the left atrium (*black arrow* in **B**). Note the displaced intimal flap in the ascending and descending portions of the aorta (*black arrows* in **A**) and a high attenuation pericardial effusion consistent with blood (*white arrows* in **B**).

TABLE 11-2 Ascending Thoracic Aortic Aneurysms

Degenerative	Associated with atherosclerosis
Inheritable/connective tissue	Marfan syndrome
	Ehlers-Danlos syndrome
	Loeys-Dietz syndrome
	Turner syndrome
	Osteogenesis imperfecta
	Rheumatoid arthritis
	Bicuspid aortic valve
	Aneurysm of sinus of Valsalva
Arteritis	Giant cell
	Takayasu
	Behcet disease
	Relapsing polychondritis
Infectious	Syphilis
	Mycotic aneurysms

TABLE 11-3 Aortic Arch Aneurysms

Degenerative	Resulting from atherosclerosis
Arteritis	Giant cell
	Takayasu
	Behcet disease
Infectious	Syphilis

Aneurysms located in the thoracoabdominal aorta appear less frequently than abdominal or thoracic aneurysms, which is fortunate, because these lesions are difficult to treat as a result of the numerous visceral branches that arise along this segment. Aneurysms located in the thoracoabdominal aorta are divided into four types according to the Crawford classification (Table 11-5). Types II and III are the more complex aneurysms, with type II having the highest risk of treatment-induced spinal cord infarction and renal failure.

TABLE 11-4 Descending Thoracic Aortic Aneurysm

Degenerative	Resulting from atherosclerosis
	Focal pseudoaneurysm resulting from a penetrating aortic ulcer
Arteritis	Giant cell
	Takayasu
	Behcet disease
Inherited/connective tissue	Marfan syndrome
	Ductus aneurysm
	Loeys-Dietz syndrome
Infectious	Mycotic aneurysms
Traumatic	Posttraumatic pseudoaneurysms
	Chronic aortic transection

TABLE 11-5 Crawford Classification of Thoracoabdominal Aneurysms

I	Descending thoracic aorta to suprarenal aorta
II	Proximal descending thoracic aorta to infrarenal aorta (below the diaphragm)
III	Mid descending thoracic aorta to infrarenal aorta
IV	Supravisceral aorta to infrarenal aorta

Diagnosis. Thoracic aortic aneurysms are usually seen on a routine chest radiograph as an incidental finding. Common findings include a widened mediastinum, enlarged aortic knob, tracheal deviation, aortic kinking, and blunted aortopulmonary window. However, a chest radiograph is limited in the diagnosis of thoracic aneurysms because it cannot accurately differentiate a tortuous aorta from an aortic aneurysm, and small aortic aneurysms can easily be missed.

CTA provides sufficient information to diagnose and follow up on the progression of a TAA; angiographic

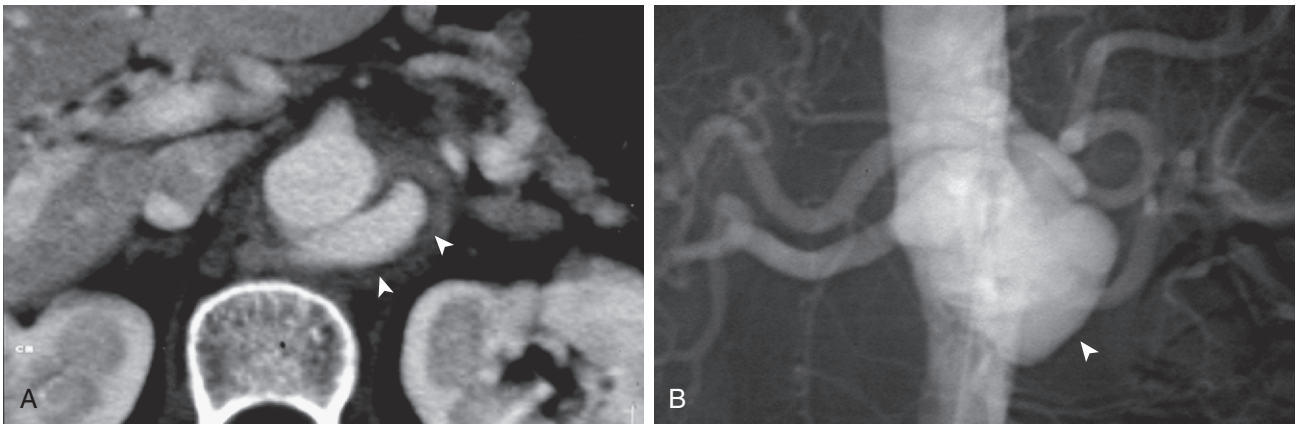


FIGURE 11-13 **A**, Contrast-enhanced computed tomography shows an avidly enhancing posterior aortic wall saccular aneurysm at the level of the celiac trunk *(arrowheads)*; note the absence of atherosclerotic plaque. **B**, A conventional angiogram shows the size of the aneurysm and the proximity to the celiac trunk and renal arteries *(arrowhead)*. Salmonella was found on the specimen. (Courtesy Dr. Javier Casillas, University of Miami, Miami, FL.)

sequences allow for precise delineation of the extension of the aneurysm, involvement of the great vessels, and other associated thoracic disease (see Fig. 11-11). Unenhanced CT is used to identify areas of aortic calcification, mural thrombus, acute wall hematoma (circumferential or crescentic), and recent hemorrhage. Administration of contrast material helps differentiate the patent lumen from a mural thrombus and demonstrates an intimal flap and a false lumen in areas of aortic dissection. CT also shows the relationship of the aneurysm to the adjacent structures and helps correlate associated patient symptomatology with imaging findings. Mycotic aneurysms can affect any portion of the aorta and are seen as saccular dilatations with multilobulated contours (Fig. 11-13). Cross-sectional CT imaging features include a perianeurysmal soft tissue mass, fluid collection, and occasionally gas-forming inflammation. Syphilitic aortic aneurysms are rarely seen these days, but when they are encountered, they usually demonstrate extensive aortic calcification or linear calcifications with longitudinal wrinkling of the wall, causing a "shaggy tree bark" pattern; approximately 75% of the cases exhibit a saccular structure.

Both CTA and MRA can be used successfully as preprocedural imaging techniques to plan surgical or endovascular repair, because they are both able to measure the dimensions of the aneurysm and detect the involved vessels. Accurate measurements are crucial when selecting the appropriate stent graft diameter for endovascular procedures to minimize stent-related complications such as endoleak, stent migration, and branch occlusion. CTA with multiplanar reconstruction and digital subtraction angiography are considered the most useful techniques to depict structural characteristics of the aneurysm, as well as to detect graft complications.

Contrast-enhanced MRA (CE-MRA) can provide exquisite detail of the aneurysm and associated dissection or branch involvement. Sometimes it also can visualize small vascular structures in greater detail, such as the Adamkiewicz artery, providing valuable information in the planning of surgical repair and helping to avoid postoperative neurologic deficits. However, CE-MRA cannot visualize aortic calcification, which can be important during treatment planning. These two modalities continue to complement each other, because one may show certain characteristics that cannot be shown by the other.

In either case, serial imaging studies are usually required in this patient population to monitor aneurysm size. A repeat study can be obtained 6 months after the initial diagnosis, and if the aneurysm is stable, imaging follow-up can be obtained annually.

Treatment. TAA repair depends on its location. Aneurysms located in the ascending aorta are usually treated surgically via a median sternotomy with aneurysm resection and prosthetic tube graft placement. Surgical treatment is recommended for patients who are symptomatic, present with large aneurysms, have a high aneurysmal growth rate, or have associated complications. The best time to treat patients with TAA is still uncertain given the limited understanding of its natural history. Nonetheless, for most ascending thoracic aneurysms, repair is considered in patients with aneurysms that are 5.5 cm in diameter or larger. The decision to intervene is made depending on the patient's operative risks versus the risk of developing an aneurysm-related complication such as dissection or rupture (e.g., patients with Marfan syndrome have their aneurysms repaired earlier because of the high risk of dissection and valvular insufficiency). Mortality of elective surgical repair in ascending aortic aneurysms ranges from 3% to 5%, and it carries a high risk of postsurgical morbidity, including paraplegia, stroke, and bleeding; however, successful repair practically eliminates the risk of rupture. Lesions that are not treated with a surgical approach can have a mortality rate as high as 74%. Repair of arch aneurysms is even more challenging because of the high risk of stroke during replacement of the abnormal arch and reimplantation of the brachiocephalic vessels. Elective surgical repair for descending thoracic and thoracoabdominal aortic aneurysms has an associated mortality rate of 5% to 14% and a significant risk of paraplegia as a result of occlusion of the spinal cord blood supply; the risk has decreased with the implementation of protective techniques such as regional epidural hypothermic protection and cerebrospinal fluid drainage. Indications for surgical repair of descending

BOX 11-3 Signs of Impending Aneurysm Rupture on Computed Tomography/Computed Tomographic Angiography

Enlarging aneurysm
Low thrombus/lumen ratio
Hemorrhage into mural thrombus (seen as hyperdense crescents on unenhanced computed tomography)

aortic aneurysms include diameter equal to or larger than 6.5 cm, a patent primary entry site, expanding false lumen of either a dissection or aneurysm, symptomatic patients, or signs of impending rupture (Box 11-3).

Endovascular treatment of aortic arch aneurysms requires surgical transposition of supraaortic vessels and is currently used in select cases to help reduce the risk inherent in surgical repair. Patients with descending thoracic aortic aneurysms also can be offered endograft repair as an alternative to surgical treatment, in particular patients with high operative risk. Endografts successfully exclude the aneurysm sac in most patients, with an apparent lower rate of persistent neurologic deficits in the range of 2% to 3% (versus 5% to 6% for patients treated with surgery). Nevertheless, stent grafts are also associated with complications such as stroke, paraplegia, and device-related complications such as endoleaks and graft migration. Long-term studies are being performed to assess the durability of endograft aneurysm repair (see Fig. 11-10).

Abdominal Aortic Aneurysms. Abdominal aortic aneurysms (AAAs) are fusiform or saccular dilatations of the abdominal aorta that often form as a consequence of degeneration of the media from atherosclerotic disease, which causes weakening of the wall and widening of the luminal diameter. Degenerative aneurysms are more frequent in the elderly population, whereas in younger patients, abdominal aneurysms are usually a result of inheritable diseases such as Marfan syndrome and Ehlers-Danlos syndrome. Predisposing factors that have been associated with AAA include advanced age, family history, male gender, tobacco use, and white race, with a lower incidence found in patients of Asian descent. Patients with AAA have a higher incidence of hypertension, atherosclerosis, myocardial infarction, heart failure, and peripheral vascular disease than do control subjects matched for age and gender.

Other types of AAA include inflammatory and infectious aneurysms. Inflammatory aneurysms, as their name indicates, show an increased inflammatory reaction in the aneurysm wall and surrounding tissues and present with a triad of chronic abdominal pain, weight loss, and elevated erythrocyte sedimentation rate. Infectious or mycotic aneurysms are more frequently associated with transient bacteremia with *Staphylococcus* or *Salmonella*, which leads to infection of the vessel wall or an atherosclerotic plaque by hematogenous spread. Rarely, aneurysms caused by tuberculosis infection have been reported.

Patients with AAA are usually asymptomatic, and aneurysms often are detected as an incidental finding on radiologic studies. Sometimes clinical examination can detect an AAA if a pulsatile abdominal mass or an abdominal bruit is present; unfortunately, physical examination sensitivity among studies varies widely, and confirmatory imaging is usually required. Symptomatic patients usually report lower back pain or abdominal pain that can be nonspecific and easily confused with other disease processes. Patients with acute rupture present with abrupt-onset pain in the lower back or abdomen that can be associated with a pulsatile abdominal mass and hypotension. The natural history of abdominal aortic aneurysms is usually characterized by gradual expansion of the aneurysm sac with mural thrombus formation lining the inner surface. The aneurysm may then cause compression of adjacent structures, thromboembolic events, erosion into neighboring structures (e.g., the duodenum or iliac vein), and, ultimately, rupture.

AAA rupture is a catastrophic complication with a reported mortality of up to 90%. It usually occurs in the posterolateral aspect of the aorta, causing retroperitoneal hemorrhage. Less commonly, it ruptures in the anterolateral aspect, causing intraperitoneal bleeding and quick exsanguination. Contained ruptures in the form of retroperitoneal hematomas may be associated with ecchymosis of the flanks, otherwise known as *Grey-Turner syndrome*. In general, the larger the aneurysm, the higher the risk for spontaneous rupture, and the faster it tends to expand. The average expansion rate for aortic aneurysms 4.0 cm in diameter is 1 to 4 mm per year, followed by 4 to 5 mm per year for aneurysms measuring 4.0 to 6.0 cm, and 7 to 8 mm per year in larger aneurysms. The lifetime risk of rupture of abdominal aneurysms larger than 5.0 cm in diameter is 20%; it then increases to 40% for aneurysms that measure more than 6.0 cm, and to more than 50% for aneurysms that exceed 7.0 cm. The corresponding estimated annual rupture rates are 4%, 7%, and 20%, respectively.

Other AAA complications that may require immediate treatment are those related to compression or erosion of adjacent structures, as seen in large degenerative AAA, or inflammatory or mycotic aneurysms. Some examples include gastric outlet syndrome as a result of compression of the duodenum, aortoenteric fistula formation causing massive upper GI bleeding, and venous fistula formation in the inferior vena cava (IVC), the left renal vein, or the common iliac vein. These fistulae can have high flow rates and result in acute congestive heart failure or in hematuria and flank pain.

Diagnosis. Early AAA detection is imperative to reduce patient morbidity and mortality as a result of this silent disease. The most common site of arterial aneurysms is the abdominal aorta, especially along its infrarenal segment. Abdominal aneurysms are diagnosed when the aorta is 1.5 times greater that the diameter of the normal aorta or when the minimum anteroposterior diameter is greater than 3.0 cm, irrespective of age and gender.

Imaging techniques are currently relied on for the diagnosis and follow-up of aortic aneurysms. Real-time ultrasonography is a noninvasive and cost-effective modality useful for screening for AAA, with an accuracy that approaches 100% in the diagnosis of infrarenal aortic aneurysms. Its accuracy in measuring the aortic diameter below the level of the renal arteries has been shown to correlate well with direct intraoperative measurements. The size of the aneurysm is calculated by measuring the maximum anteroposterior aortic diameter or the largest transverse diameter measured in a plane perpendicular to the luminal arterial axis to avoid overestimation of the aneurysm size. AAA is seen as a dilated vessel with irregular lumen and eccentric echogenic thrombus material. Although ultrasound

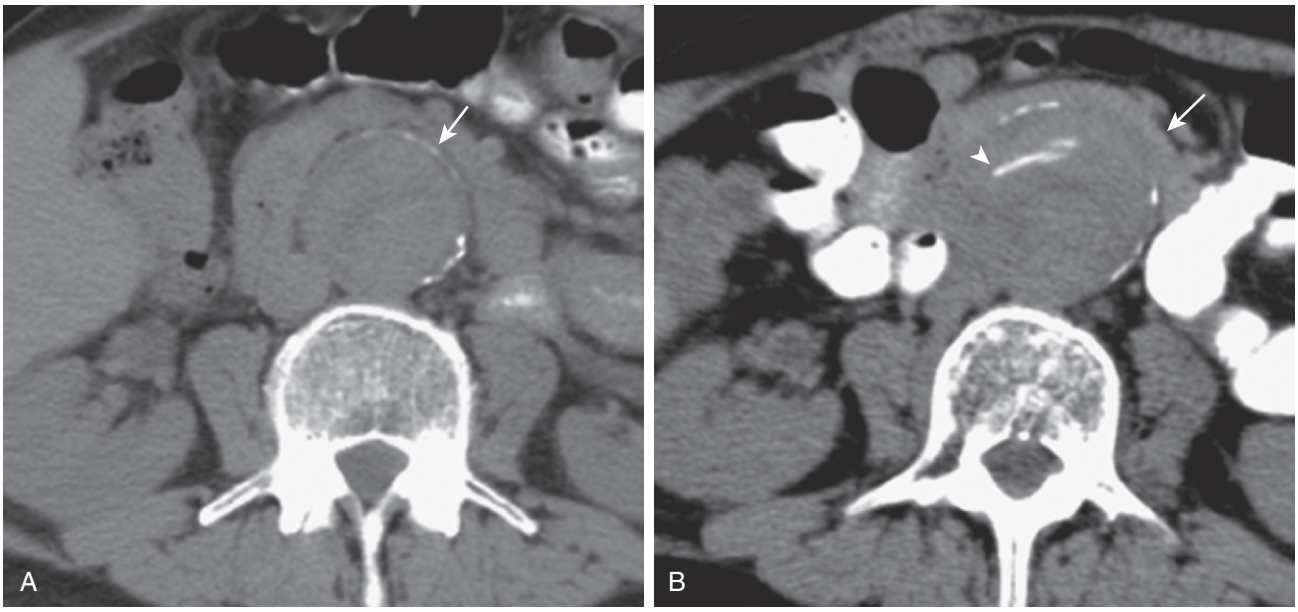


FIGURE 11-14 **A** and **B,** Noncontrast computed tomography images obtained 1 year apart. The first image **(A)** shows an abdominal aortic aneurysm with peripheral plaque and mural thrombus *(arrow)*; 1 year later **(B),** the aneurysm *(arrow)* has increased in size, and intramural crescents have developed *(arrowhead)*, raising concern for an impending rupture of the aneurysm.

is a convenient procedure, it is limited by the patient's body habitus and the interposition of bowel gas that obscures visualization of the deeper structures. Likewise, it is not as reliable as CTA for detecting complications such as rupture, aneurysm extension into the suprarenal aorta, and detection of posttherapeutic complications such as endoleaks.

MD-CTA has emerged as the new gold standard for the diagnosis of AAAs, replacing catheter arteriography. MD-CTA offers high-resolution imaging and shorter scan times, allowing the detection and characterization of aneurysms and related complications, including impending rupture and contained or complete rupture. Several signs of impending rupture have been identified on CT (see Box 11-3), including increased aneurysm size, a low thrombus-to-lumen ratio, and mural thrombus hemorrhage that is usually identified as high-attenuation crescents in the wall of the aortic aneurysm on unenhanced CT images (Fig. 11-14). Various signs suggest a contained AAA rupture, including loss of definition of the posterior aortic wall, the presence of an organized hematoma with contour abnormalities of the vessel wall, interruption of a continuous ring of aortic wall calcification, and a posterior wall of the aorta following the contour of the vertebra with or without associated vertebral erosion (a sign known as a "draped" aorta). A ruptured AAA is determined by the presence of hemorrhage contiguous to the aorta that almost always involves the retroperitoneal space and rarely involves the iliopsoas compartment. Periaortic blood might be seen in the pararenal space, perirenal space, or both; a hematocrit sign (cellular-fluid level) and rectus sheath bleeds are rarer but are helpful when they are present and tend to be associated with coagulopathic hemorrhage (Fig. 11-15).

CT is also useful in differentiating between different types of aortic aneurysms. Mycotic aneurysms are usually seen as saccular-shaped collections with a lobulated contour; other features may include a periaortic soft tissue mass with stranding, retroperitoneal paraaortic fluid collection, vertebral erosion, gas-forming inflammation around the aneurysm, intraaortic air pockets, and thrombus formation within a false lumen after aneurysmal rupture (see Fig. 11-13). In inflammatory aneurysms, CT and MRI can detect the cuff of soft tissue inflammation surrounding the aneurysm, thickening of the aneurysm wall, perianeurysmal and retroperitoneal fibrosis, and adherence of the anterior aneurysm wall to adjacent structures (Fig. 11-16). On precontrast CT images, the thickened aortic wall has soft tissue attenuation that enhances after intravenous administration of contrast material. The arterial wall may become indistinguishable from periaortic fibrosis. Periaortic fibrotic tissue can adhere to the ureters, small bowel, duodenum, and IVC, causing entrapment of these structures and further complicating surgical repair. Preoperative imaging is of great importance in the planning of surgical and endovascular treatment of patients with AAA. Important preoperative features and measurements performed on CTA include the maximum transverse aneurysm diameter, relation of the aneurysm to the renal arteries, presence of a proximal neck (renals to aneurysm distance), presence of a distal neck (aneurysm to aortic bifurcation distance), extension of the aneurysm into the iliac arteries, identification of concomitant aneurysms, and appearance of the access pathway, including femoral and iliac arteries. Some conditions that limit the delivery of an endograft include a very large AAA, a markedly tortuous aorta, pelvic arteries with abrupt angles, and extensive calcification causing luminal narrowing. Any of these factors can represent an exclusion criterion depending on the specific anatomy and the degrees of angulation and stenosis. They determine the suitability or unsuitability for endovascular treatment, and cautious analysis of the images in conjunction with the surgical/interventional team is crucial to decrease the risk of endoleaks, attachment failures, graft migration,

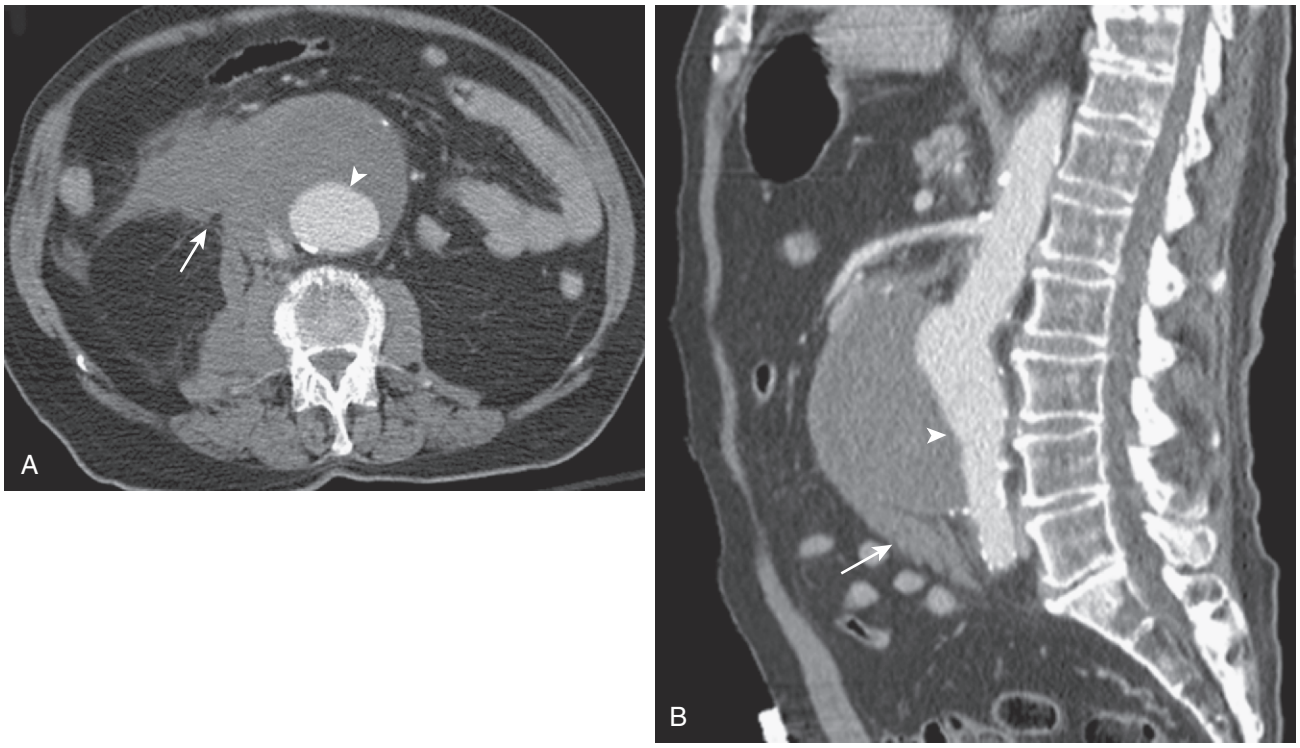


FIGURE 11-15 **A** and **B,** Computed tomographic angiography images demonstrating a large infrarenal aortic aneurysm *(arrowheads)* with rupture *(arrows)*. (Courtesy Dr. Daniel J.A. Margolis, David Geffen School of Medicine, University of California–Los Angeles, Los Angeles, CA.)

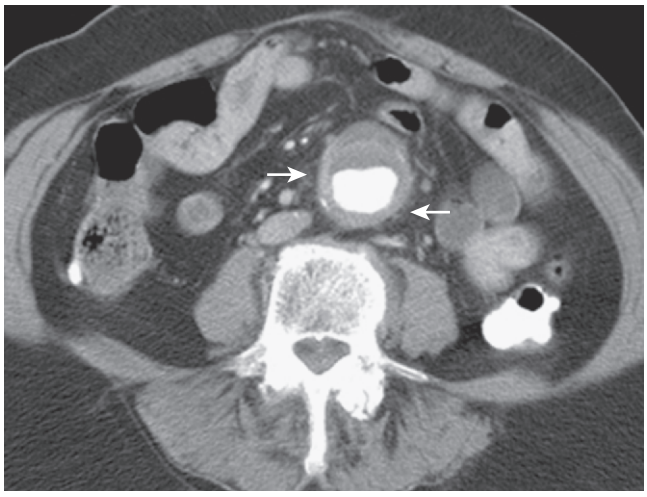


FIGURE 11-16 Computed tomographic angiography demonstrates an aortic aneurysm *(arrows)* with an enhancing aortic wall, ill-defined margins, and mild stranding of the adjacent fat compatible with an inflammatory aortic aneurysm. (Courtesy of Dr. Daniel J.A. Margolis, David Geffen School of Medicine, University of California–Los Angeles, Los Angeles, CA.)

and conversion to open repairs. MRA has shown properties similar to those of CTA for diagnosing and performing preoperative planning for AAA; it provides precise information about the location and extent of the aneurysm. Conventional arteriography is currently used as an adjunct imaging modality for evaluating patients with complex vascular anatomy, for evaluating aneurysms that could not be fully characterized with CTA and MRA, and for intraprocedural graft positioning.

Treatment. Treatment is usually recommended for AAAs measuring 5.5 cm or larger to eliminate the risk of rupture and for symptomatic AAAs regardless of their diameter. Ruptured aneurysms with hemodynamic compromise require immediate surgical repair. In select cases, endovascular intervention might be indicated for the management of ruptured aneurysms that remain hemodynamically stable. Patients with aneurysms 4.0 to 5.4 cm in diameter should undergo imaging follow-up every 6 to 12 months for early detection of expansion. Currently, elective repair is not recommended in patients with asymptomatic aneurysms that measure less than 5.0 cm in men, or less than 4.5 cm in women. Higher mortality rates are seen in patients who have emergent repair rather than elective surgery, and for this reason, early detection and surveillance of high-risk populations remain crucial in the treatment of AAAs.

Open surgical treatment is usually offered to hemodynamically unstable patients and to patients who want an elective surgical repair. Such treatment involves a midline transabdominal incision or left retroperitoneal flank access with subsequent clamping of the aorta, excision of the aneurysm, and placement of a synthetic graft. Aortic clamping can be linked to the development of significant morbidities such as ischemia of the lower extremities or bowel or paraplegia.

Postoperative complications related to an elective open surgical approach vary between 0.4% and 10% and include pseudoaneurysm formation, graft infection, enteric fistulas, and graft limb occlusion.

Treatment of pararenal and suprarenal aortic aneurysms is more complex because it requires cross-clamping of the aorta above the visceral arteries and sometimes branch vessel reimplantation, thus increasing operative morbidity

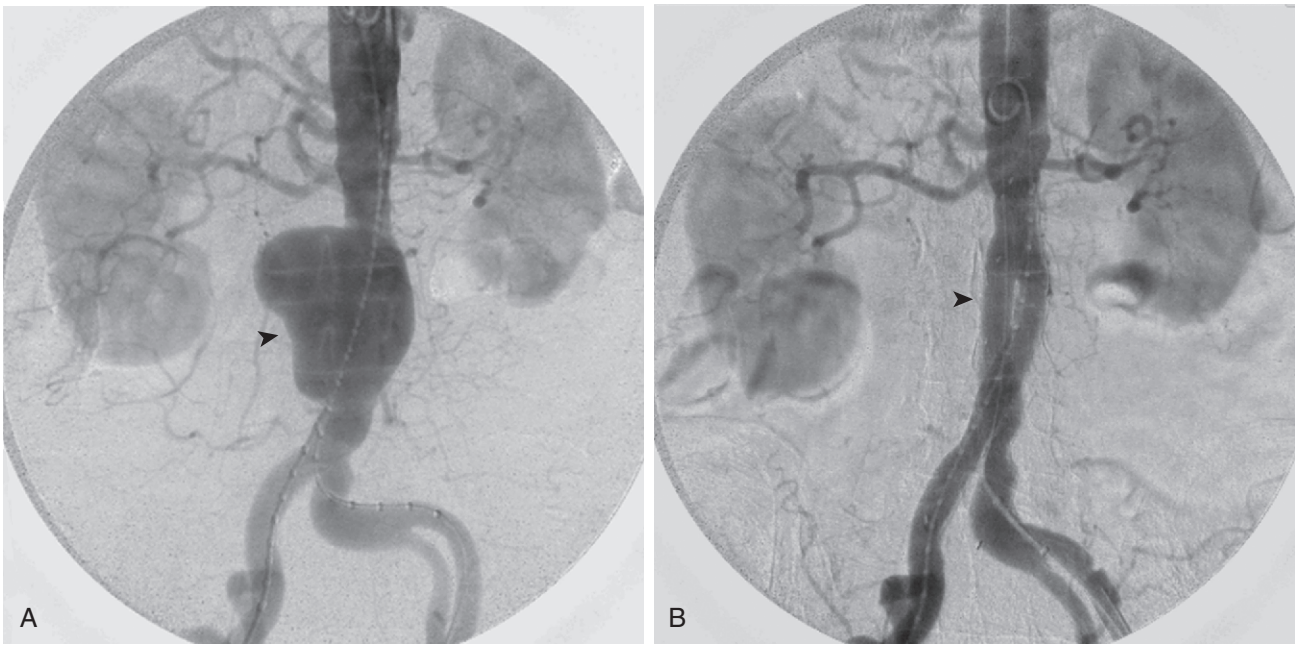


FIGURE 11-17 **A,** Conventional catheter angiography with bilateral marked catheters in place demonstrates a large lobulated infrarenal aortic aneurysm *(arrowhead)* with a 4-cm proximal neck suitable for endovascular repair. **B,** An image after endovascular repair image demonstrates complete exclusion of the aneurysm *(arrowhead)* with no endoleak and preservation of the renal and hypogastric arteries.

and mortality, with up to 15% of patients requiring temporary dialysis and 5% experiencing permanent renal failure. The overall 5-year survival rate among these patients is 40% to 50%.

Endovascular aortic aneurysm repair (EVR) offers a less invasive approach to reduce the operative morbidity and mortality. Blood losses are significantly reduced because the graft is placed intravascularly via femoral access, and likewise, the risk for lower limb and visceral ischemia is lower because aortic clamping is not performed. EVR is offered to patients who are undergoing repair for asymptomatic AAA or symptomatic nonruptured AAA or to patients who are at high risk surgically and have significant comorbidities. The role of the endograft is to exclude the aneurysmal sac from the arterial circulation and decrease the mechanical stress over the vessel wall (Fig. 11-17). Studies have shown benefits in the perioperative mortality and a 30-day morbidity and mortality rate of less than 3% with EVR. However, despite its short-term advantages, long-term survival and quality-adjusted life expectancy do not seem to vary significantly when compared with open surgery repair.

A common complication related to stent graft placement is the development of endoleaks (Fig. 11-18). An endoleak is defined as an incomplete exclusion of the aneurysmal sac. The estimated incidence oscillates in the 10% to 45% range, and currently lifelong imaging follow-up is recommended to detect endoleaks and other graft-related complications. Delayed rupture is rare (0.1% to 1% per year) and has been associated with type I and type III endoleaks, graft migration, and endograft kinking. When type I or type III endoleaks are recognized, immediate treatment is indicated through graft extension, reintervention, or conversion to open repair. Other serious complications include graft infection and occlusion (Fig. 11-19). Occlusion is usually due to distortion of one of the graft limbs and can cause lower extremity ischemia if it is not promptly treated. Continuous aortic expansion at the "neck" can cause endograft migration and delayed type I endoleak, but this occurrence is rare because endografts are oversized at the time of placement by up to 20% to ensure an adequate seal.

Traumatic Abdominal Aortic Injury

Traumatic abdominal aortic injuries are relatively rare, accounting for only 4% to 6% of all aortic injuries. Despite medical advances, these injuries remain one of the most lethal causes of early death in persons who experience trauma, with a mortality rate that ranges between 50% and 80%. Penetrating injuries to the abdominal aorta that cause complete transection are not often seen in the hospital setting because of rapid exsanguination. The most common causes of traumatic penetrating injuries to the aorta include GSWs and stab wounds. Besides the obvious risk that a direct aortic injury implies, the high mortality is also linked to the high incidence of associated injuries to other organs. Abdominal aortic injuries resulting from penetrating trauma have lower mortality rates compared with thoracic aortic injuries because of the compartmental retroperitoneal location of the abdominal aorta. However, when the aortic rupture extends beyond the retroperitoneum into the suprarenal segment or intraperitoneally, the protective effect of retroperitoneal tamponade is lost and the risk of death increases. Common complications seen in patients who survive penetrating injuries include arteriovenous fistula and pseudoaneurysm formation (see Fig. 11-11).

Blunt abdominal aortic injuries are due to direct forceful compression of the aorta against the spine, as seen with fast deceleration seat belt injuries. These injuries more frequently result in intimal tears or traumatic dissection, but pseudoaneurysms, thrombosis of the aorta, and aortic

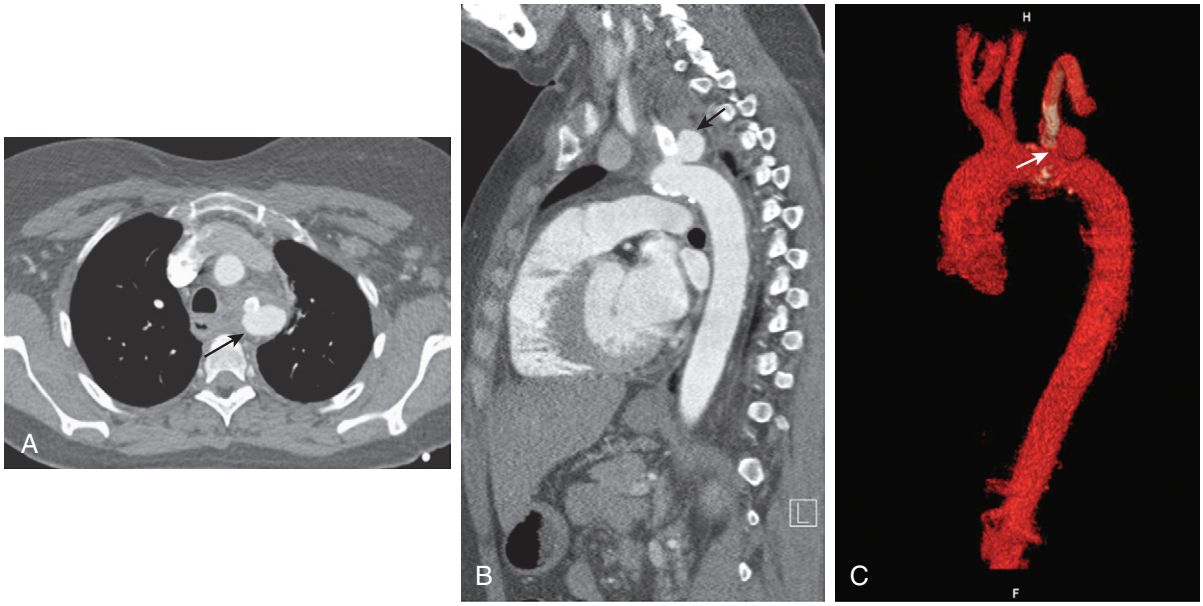


FIGURE 11-18 A 48-year-old woman with a left subclavian artery aneurysm underwent stenting and has a type 1 endoleak. Computed tomographic angiography images demonstrate extravasation of intravenous contrast material as a result of an incomplete seal at the proximal end of the stent graft, causing leakage into the pseudoaneurysm sac (*arrows* in **A** and **B**). The location of the endoleak was confirmed with a three-dimensional reconstruction (*arrow* in **C**).

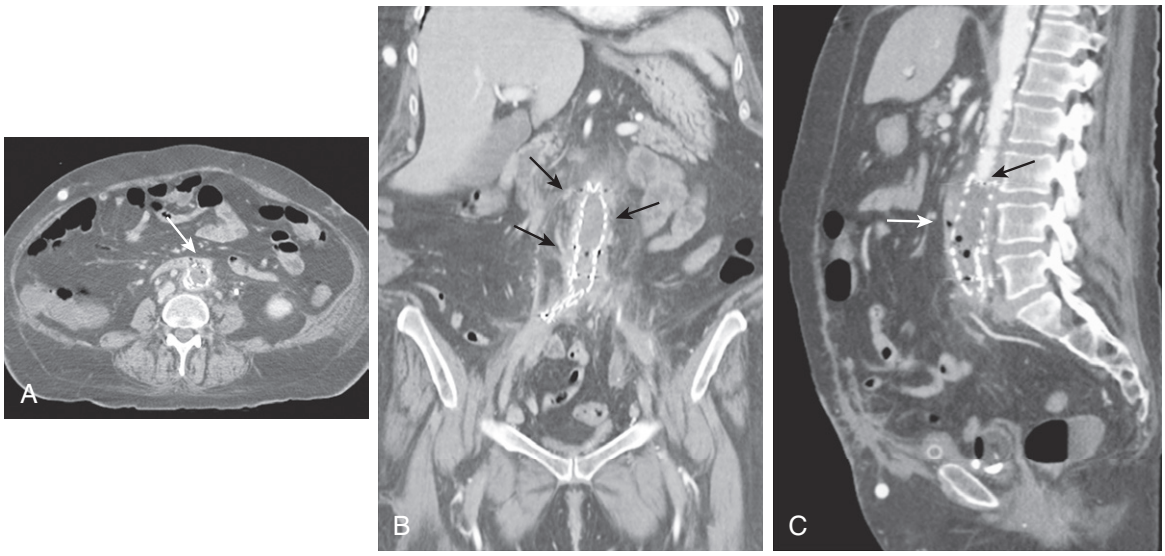


FIGURE 11-19 A 63-year-old man with an infected and thrombosed aortic stent graft with an aortoduodenal fistula. Computed tomographic angiography images demonstrate an abrupt cut-off of the contrast material in the abdominal aorta (*black arrow* in **C**). The duodenum is inseparable from the aorta (*white arrows* in **A** and **C**). Air is present in the lumen of the aorta with enhancement of the walls and adjacent fat stranding with reactive lymph nodes (*black arrows* in **B**).

rupture also may occur. Traumatic abdominal injuries account for 17% of abdominal aortic dissections, which can lead to other serious comorbidities in up to 60% of cases, such as branch vessel occlusion with visceral or limb ischemia and paraplegia. Because of its high mortality, a high clinical suspicion index is required to make a timely diagnosis. Acute manifestations include acute abdomen (abdominal pain and peritoneal signs), neurologic deficits, and acute arterial insufficiencies. MD-CTA is currently the imaging technique of choice. CTA can detect multiple organ and vascular injuries and can characterize aortic dissections and recognize associated complications such as aortic thrombosis, false aneurysm formation, and aortic rupture. Indirect findings of aortic rupture and dissection are retroperitoneal hematoma and abnormal opacification of the aortic lumen. A small amount of peritoneal fluid and hemoperitoneum can be detected easily with MDCT in cases of trauma, and therefore close attention must be directed to the dependent portions of the peritoneal cavity such as Morrison's pouch, paracolic gutters, areas adjacent to the bladder, and pelvis and perihepatic and perisplenic spaces. Attenuation measurements can be

obtained for all areas of fluid accumulation to help differentiate between simple fluid, blood (hematoma), and active bleeding. CT attenuation values for free blood measure between 20 and 40 Hounsfield units (HUs), whereas clotted blood measures between 40 and 70 HUs and active bleeding in contrast-enhanced images shows density measurements within 10 HUs of the density of vascular contrast material seen within an adjacent major vessel. Thrombosis of the false lumen and aortic aneurysm formation may mask aortic dissection in CT imaging. Catheter angiography of the abdominal aorta is indicated if questions persist after MD-CTA has been performed. The thoracic aorta must always be examined as well to rule out serious injuries at this level.

The management of traumatic aortic injuries varies depending on the specific lesion, the clinical condition of the patient, and the available resources. Traumatic aortic injury is frequently associated with other significant injuries, and a delay in treatment can be detrimental.

Emergency surgery is recommended in patients with medically uncontrolled hemodynamic shock and lower limb or other end-organ acute ischemia.

Endovascular treatment using stent grafts and noncovered stents has been widely reported as a treatment option in patients with acute traumatic abdominal aortic injuries and dissections. Stent graft placement is usually performed in hemodynamically stable patients with viable extremities. This therapeutic method is less invasive than other procedures, offers a shorter time of surgical intervention, and avoids aortic cross-clamping. Because open surgical exposure is not required, blood loss is reduced to a minimum, and the risk of infection and contamination of the graft as a result of peritoneal soiling from intestinal injury decreases dramatically. If endograft repair is being considered, precise measurements of the aorta are obtained from the MD-CTA images to ensure that the proper stent graft size is selected. Grafts must be placed to cover the entire extent of the injury, whether dealing with pseudoaneurysm or a dissection. Sparing of the ostia is preferred to avoid inducing visceral ischemia. Associated arteriovenous fistulas or pseudoaneurysms of branch vessels can be treated at the same time with coil embolization if permitted by the patient's hemodynamic condition. In cases of extensive flow-limiting aortic dissection causing infradiaphragmatic ischemia, percutaneous balloon fenestration of the dissection flap to reestablish flow is a therapeutic alternative.

Nontraumatic Aortic Dissection

Spontaneous isolated dissection of the abdominal aorta is a rare event with an estimated incidence of 2% to 4% and is more frequently the extension of a thoracic aortic dissection. It is caused by a tear in the intima, usually associated with degeneration of the media or cystic medial necrosis. Blood separates the intima from its surrounding media, creating a false lumen filled with blood, which can propagate distal or proximal to the initial tear. Isolated abdominal aorta dissections often originate below the renal arteries, with some originating even lower, near the inferior mesenteric artery. Propagation of the dissection can involve branch vessels, including the renal arteries and the celiac and mesenteric arteries, or can extend into the iliac arteries (Fig. 11-20). The renal arteries are most frequently involved. The most common predisposing factors to abdominal aortic dissection are hypertension and atherosclerosis. Other causes include a penetrating atherosclerotic ulcer, aortic aneurysms, trauma, Marfan syndrome, fibromuscular dysplasia, and iatrogenic causes as a result of surgical or angiographic procedures. Clinical presentation is usually characterized by sudden-onset abdominal or back pain, but it may vary from completely asymptomatic to frank visceral or limb ischemia. MD-CTA allows a fast, accurate, and precise diagnosis. CTA findings of aortic dissection include visualization of an intimal flap separating the true and false lumen, inhomogeneous enhancement of the aortic lumen, the presence of a double channel in the aorta, and asymmetric vessel wall thickening. Unenhanced images can help identify internal displacement of the intimal calcifications. The imaging findings that help distinguish the false lumen from the true lumen include the "beak" sign, which represents a wedge-shaped area of the false lumen at the edge of the dissection; the "cobweb" sign, manifested as low-attenuation linear densities that represent residual strands of medial tissue that did not separate completely from the intima during the dissection and are floating in the false lumen; and a relatively larger cross-sectional area of the false lumen with respect to the true lumen. CT also can assess the extent of the dissection and possible involvement of visceral and iliac vessels (see Fig. 11-20). MRA is a highly accurate diagnostic tool that has the advantage of showing different sequences and can even demonstrate flow dynamics with the implementation of flow-enhanced sequences and cine images. In addition, some of the noncontrast MRA sequences offer an alternative for patients in whom the use of contrast material is limited because of severe impairment of renal function or an iodine allergy. Unfortunately, MRI/MRA has restricted availability in the emergency setting, is usually more time-consuming, and has limited applicability in emergency patients who may have noncompatible implants and metallic fragments and are attached to numerous monitoring devices. MRI is thus usually reserved for stable patients to confirm the diagnosis after equivocal imaging findings of previous examinations.

Conservative treatment of spontaneous abdominal dissection is usually administered in cases of asymptomatic chronic dissection and includes antihypertensive medication, as well as close clinical and imaging follow-up. Treatment of spontaneous abdominal dissection is necessary in the presence of associated rupture, lower extremity ischemia, unremitting pain, and associated aneurysms with a high risk of rupture. Surgical treatment in patients with a ruptured abdominal aorta consists of emergent aortic repair with tube grafts or aortobifemoral bypass grafts. The objective of surgical treatment is to create a reentry point that decompresses the false lumen and allows perfusion of the major branches.

Endovascular treatment of aortic abdominal dissection has been successfully reported in several cases. In short-segment dissection, the rationale is to bring the intimal flap back to the aortic wall and compress it to close the false lumen. An uncovered stent can be used to maintain the false lumen compressed and excluded from the systemic circulation.

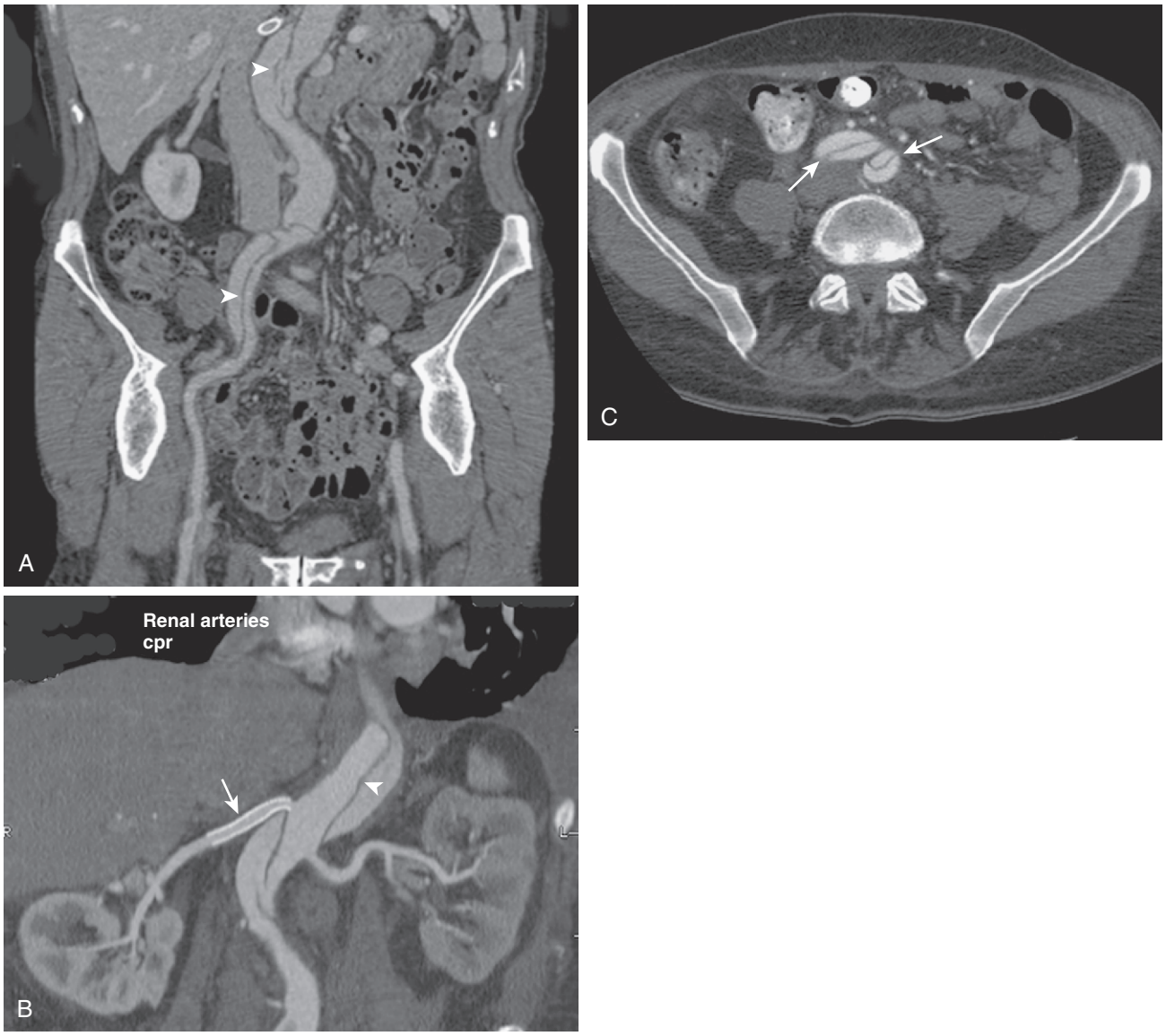


FIGURE 11-20 **A** to **C,** Computed tomographic angiography images demonstrate a complex dissection flap extending from the thoracic aorta along the abdominal aorta *(arrowheads)* and into the iliac arteries *(arrows)*. The right renal artery had previously undergone stenting, and the renal flow is preserved.

Acute Abdominal Aortic Occlusion

Acute aortic occlusion (AAO) usually results from thrombosis or embolism into a previously diseased aorta. Differentiating between embolus and thrombus can be difficult. Acute thrombosis is the most common cause of acute aortic occlusion and usually results from end-stage atherosclerotic aortoiliac disease in association with low flow states as a result of cardiac dysfunction or dehydration.

Emboli also can be the source of acute occlusion, more frequently originating from the heart in patients with a history of arrhythmia, myocardial infarction, endocarditis, or cardiac tumors. Emboli from thoracic aortic aneurysms and ulcerated plaques also have been described, along with, rarely, paradoxical embolization from a deep venous thrombus in patients with atrial septal defects or other causes of right to left shunt.

It is rare for acute thrombosis of an AAA to cause AAO. Aortic dissection also can cause AAO by propagation of the dissection to the aortic bifurcation and compression of the true lumen by the false lumen. This event also is rare and is considered an emergency, requiring urgent surgical repair or fenestration of the dissection. Less common causes of acute aortic thrombosis include trauma, iatrogenic injuries, and hypercoagulable states (antithrombin III, protein C/protein S deficiencies, and lupus, among others). AAO is usually preceded by a progressive stenosis with associated signs and symptoms of chronic ischemia, such as lower extremity claudication pain at rest. A partial occlusion allows collateral circulation to build over time and maintain blood supply even in the setting of a superimposed acute event; these patients present with worsening claudication or pain at rest. However, the presentation may be more severe, because symptoms typically get aggravated with development of cyanosis below the level of the umbilicus, pallor and coldness of the lower extremities, absent femoral pulses, and neurologic symptoms ranging from numbness and weakness to complete anesthesia and paralysis. The diagnosis of AAO can be made with ultrasound,

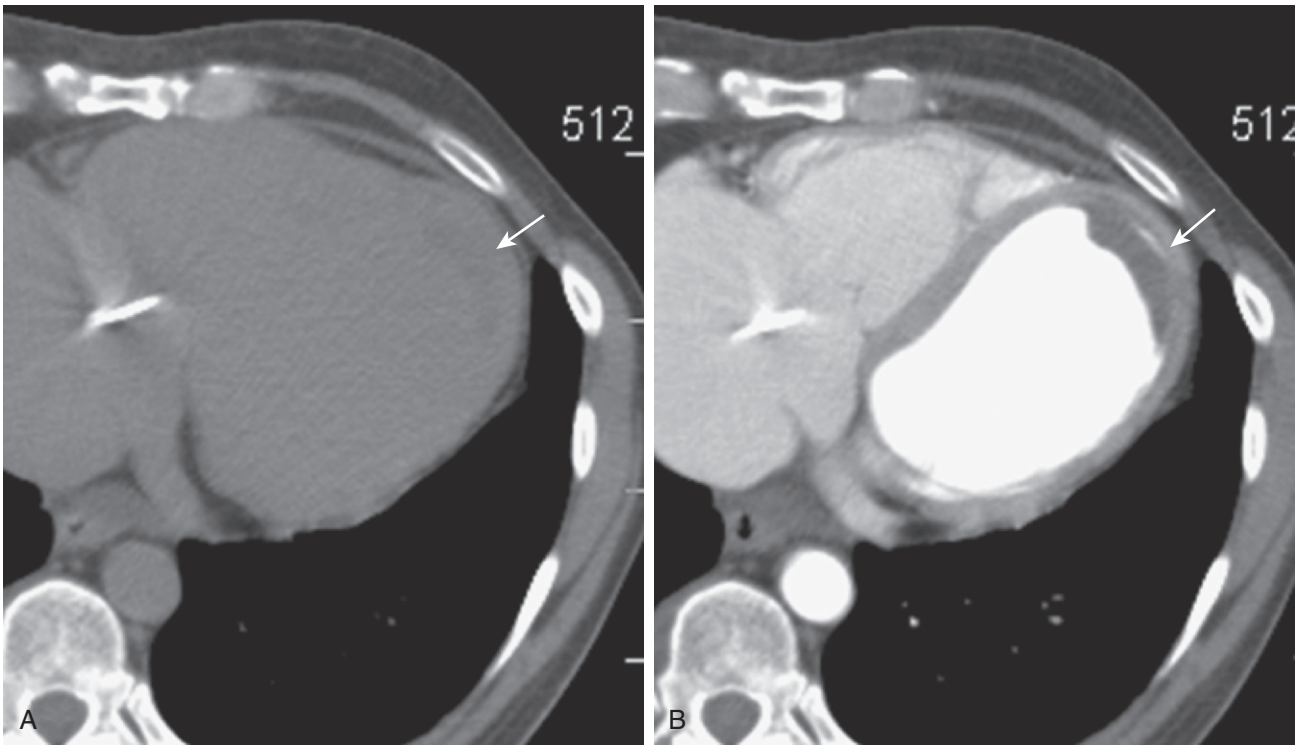


FIGURE 11-21 **A** and **B,** Pre- and postcontrast computed tomography (CT) images show an intraventricular apical hypodensity *(arrows)* surrounded by contrast material in the contrast-enhanced CT image, consistent with an intraventricular apical thrombus.

CTA, and catheter angiography. The use of MRA is limited for the various reasons previously cited but can be used if it is readily available. All cross-sectional modalities can also detect branch vessel involvement and determine the extent of the thrombus; however, ultrasound is operator dependent and can be limited by the patient's habitus and bowel gas interposition. MD/CTA scanning can evaluate the complete thoracoabdominal aorta and the cardiac chambers when a cardiac source of emboli is sought (Fig. 11-21). The treatment of AAO requires immediate systemic anticoagulation to prevent thrombus propagation, hydration, and optimization of cardiac and renal function. As previously mentioned, surgery is the first treatment option and should be performed promptly. A delay in treatment can predispose to the development of limb ischemia, compartment syndrome, thrombus propagation to renal and mesenteric arteries, reperfusion syndrome, limb loss, and even death. Surgery usually involves an attempt to repair the aorta, aortobifemoral bypass, or, in patients with high surgical risk, an axillobifemoral bypass. Despite surgical intervention, acute abdominal aortic occlusion has a high mortality rate of approximately 50%. In select patients, catheter angiography may provide a therapeutic alternative if a realistic probability of reestablishing patency exists and signs of irreversible ischemia are not yet present (Fig. 11-22).

Abdominal Compartment Syndrome

Compartment syndrome is defined as an increased pressure in a body compartment that causes deficient tissue perfusion and risks tissue and organ viability. Abdominal compartment syndrome (ACS) is a critical condition characterized by a continuous elevation of the intraabdominal pressure (IAP; normal, 0 to 5 mm Hg) associated with abdominal distention and leading to respiratory insufficiency with decreased lung capacity, increased airway pressure, hypoxia, hypercarbia, reduced cardiac output, oliguria, and eventually multiorgan failure. Increased intracranial pressure and impairment of the portosystemic circulation also can result from the rise in central venous pressure. Abdominal trauma with hepatic, vascular, and/or splenic injury is the most common cause of acute ACS. Other causes are massive fluid resuscitation and packing for uncontrolled hemorrhage. Ruptured aortic aneurysms can cause ACS by increasing abdominal fluid volume (Box 11-4).

CT findings of ACS include compression of the IVC, hemoperitoneum or acute ascites, bowel wall thickening with increased wall enhancement, and massive abdominal distention with an increased anteroposterior/transverse abdominal diameter ratio (greater than 1:0.80), also known as the "round belly" sign. The most accurate way to diagnose ACS is to measure IAP, which can be performed directly through insertion of a catheter into the peritoneal cavity or indirectly through the bladder. When IAP measurements are consistently above 20 to 25 mm Hg, ACS is diagnosed and immediate decompression is mandatory. Abdominal decompression also can be performed prophylactically after laparotomy when evidence of massive edema, tight closure, packing, and hemodynamic instability exists. In the case of ACS, abdominal decompression should bring immediate clinical improvement. The mortality rate is high, approximating 70%.

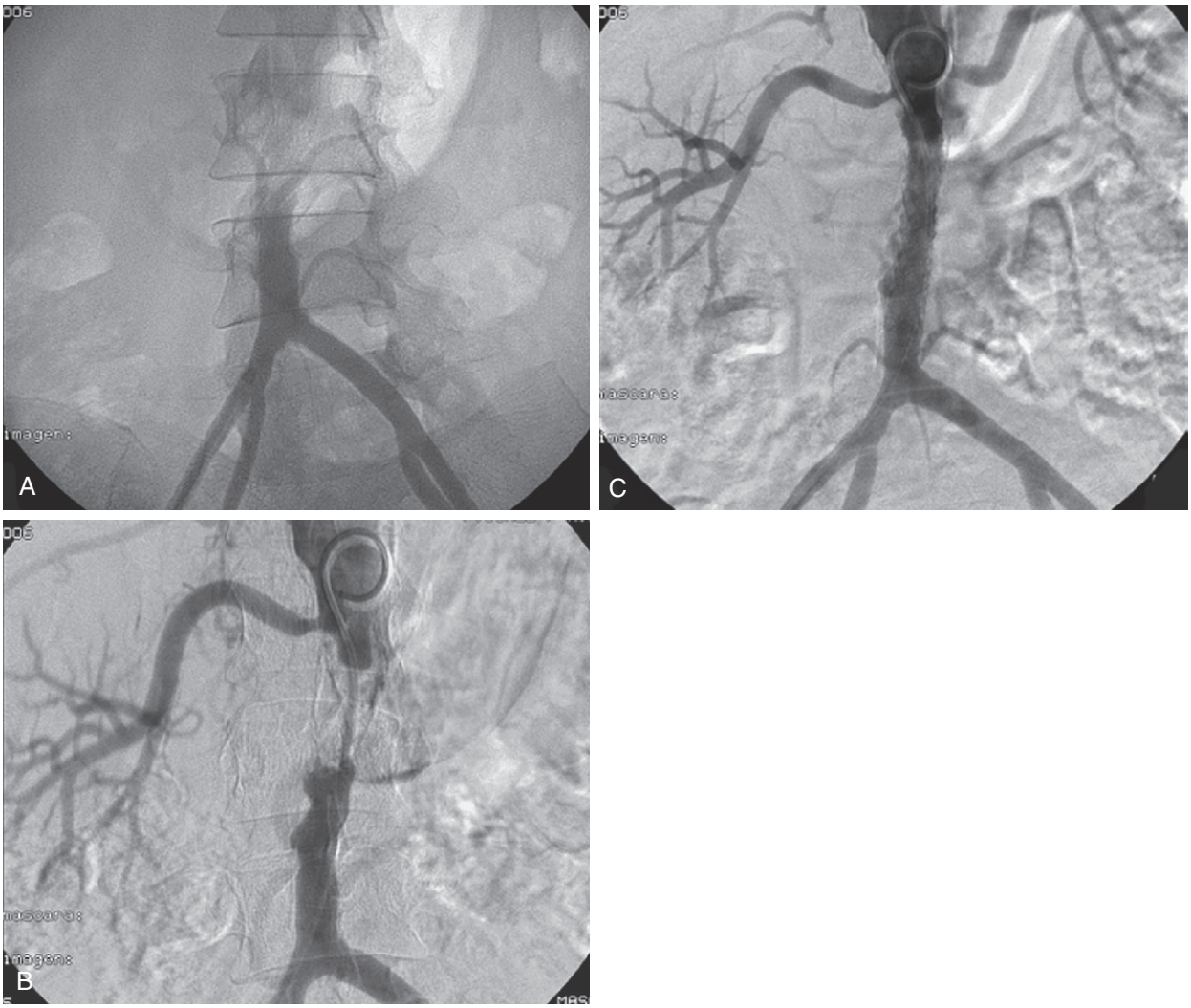


FIGURE 11-22 **A** to **C,** A 52-year-old female patient with diabetes who presented with unstable angina. A conventional angiogram demonstrates abdominal aortic occlusion. After crossing the occlusion, simultaneous injection via a "pigtail" catheter and access sheath better shows the length of the occluded segment. After stent placement, patency was reestablished.

BOX 11-4 Risk Factors for the Development of Acute Abdominal Compartment Syndrome

Penetrating or blunt trauma
Retroperitoneal hemorrhage
Ruptured abdominal aortic aneurysm
Pancreatitis
Massive ascites
Neoplasm
Pneumoperitoneum
Burns of the abdominal wall—extrinsic compression
Massive fluid resuscitation
Postoperative forced closure of abdominal wall
Bowel edema
Postoperative ileus
Liver transplantation
Intraabdominal packing

Vascular Emergencies of the Mesenteric-Visceral Arteries

Splanchnic Vascular Trauma

When penetrating or blunt abdominal trauma occurs, a patient can experience isolated vascular injuries, isolated visceral injuries, or a combination of both. Unstable patients with extensive visceral organ and vascular involvement are taken directly to surgery. When arterial and vascular injuries are suspected, patients with a suitable hemodynamic status can undergo CT and then angiography for embolization. Patients who have a history of previous liver trauma, biopsy, or another interventional procedure and who present with delayed hemobilia constitute a separate group who will also require angiography to evaluate for the presence of an arterial to biliary fistula that can be treated with embolization.

The spleen is a solid visceral organ that is commonly affected when abdominal trauma occurs. The spleen is well vascularized, and in cases of severe trauma, splenic injury

can lead to hemodynamic instability as a result of continuing hemorrhage. In the case of severe trauma, immediate surgery for splenic repair or resection may be required. When clinically feasible, CT evaluation is the ideal modality to characterize the degree of splenic injury. Embolization is a management alternative in patients with an injured but viable spleen. Both selective embolization of focal areas of extravasation and embolization of the main splenic artery have been described. Selective embolization carries a risk of focal infarcts and abscess formation. Embolization of the main splenic artery decreases the overall flow to the spleen, allowing the clotting mechanisms to stop the bleeding but without creating an infarction, as collateral flow via short gastric arteries is maintained.

Nontraumatic Emergencies of the Mesenteric and Visceral Vasculature

Acute Mesenteric Ischemia. Acute mesenteric ischemia is a critical condition that is poorly tolerated, with high mortality rates even in the setting of early intervention. A delayed diagnosis further complicates the overall prognosis of the patient and is almost always lethal. More than 50% of cases are embolic in origin; 20% are due to thrombosis of preexisting stenotic lesions, 20% are related to low flow states (nonocclusive mesenteric ischemia), and 10% are due to portomesenteric venous thrombosis. The classic presentation is generalized abdominal pain out of proportion to the physical findings. However, because this disease process is identified predominantly in elderly persons, the presentation can be more subtle, with minimal findings on physical examination and vague pain.

The classic plain film findings of gas in the wall of the affected bowel loops (pneumatosis intestinalis) and in the portal vein occur late in the process, once bowel infarction has already occurred. Early signs are nonspecific and include bowel thickening and dilatation. CT/CTA is the preferred initial imaging modality to evaluate for suspected bowel ischemia, because it allows visualization of the mesenteric arteries, veins, bowel luminal diameter, and wall thickness.

Catheter angiography remains an important diagnostic modality. Mesenteric embolic occlusion characteristically appears as convex filling defects outlined by contrast material. Most of the emboli are identified in the proximal segment of the superior mesenteric artery, resulting in profound ischemia in the absence of collateral flow. The standard management is surgical embolectomy or bypass with resection of the nonviable bowel segment. If no signs of irreversible bowel ischemia are present, endovascular intervention may be indicated. Catheter embolectomy with or without thrombolysis can be attempted.

In the absence of an embolic source, arterial thrombosis resulting from an underlying stenotic lesion is the most frequent cause. Usually patients have an associated history of peripheral vascular disease. Catheter thrombolysis followed by treatment of the underlying stenosis with angioplasty and stenting is the preferred approach, provided that the patient has no signs of irreversible bowel ischemia.

Nonocclusive mesenteric ischemia is a syndrome characterized by low flow in the superior mesenteric artery without evidence of embolus, thrombus, or any other fixed lesion. It is more frequently encountered in hypotensive patients undergoing infusion of vasopressor agents.

Acute Gastrointestinal Bleeding. Acute GI bleeding is classified into upper and lower causes based on its origin proximal or distal to the ligament of Treitz. Upper GI bleeds are approximately five times more common than lower GI bleeds, and lower GI bleeding originates in the colon in approximately 80% of cases. Localization of the bleed is critical to determine management. Upper GI bleeds usually occur as a result of gastritis and gastric or duodenal ulcers, whereas the most common cause of lower GI bleeds is colonic diverticulosis followed by angiodysplasia. Depending on the site of origin (proximal or distal) and the severity of the hemorrhage, a GI bleed will manifest as hematemesis, melena, and/or hematochezia (Fig. 11-23).

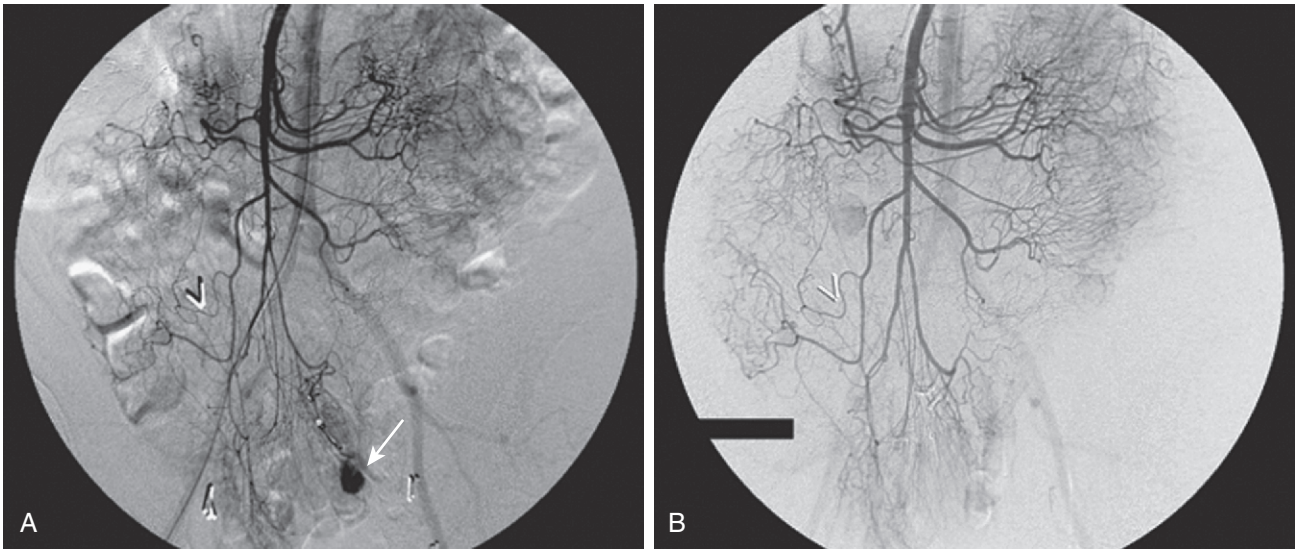


FIGURE 11-23 **A** and **B,** A 75-year-old patient with recurrent lower gastrointestinal hemorrhage. Superior mesenteric artery catheter angiography shows a focal area of abnormal contrast pooling fed by one of the distal ileal branches *(white arrow)* most consistent with a small bowel hemangioma that caused recurrent bleeding episodes. After coil embolization, the abnormal enhancement was no longer identified and the symptoms resolved.

A positive nasogastric aspirate and lavage is an effective way to determine if a patient has an upper GI bleed. In these patients, the initial evaluation is performed with endoscopy, which not only confirms the diagnosis and identifies the source in more than 95% of cases but also can offer therapy with sclerotherapy, clipping, cauterization, or banding. With lower GI bleeds, identification of the bleeding site with colonoscopy is more difficult, with an overall reported success rate of 70%. More than 85% of lower GI bleeds resolve spontaneously with supportive therapy alone. It is crucial that all patients with GI bleeding be stabilized, with large bore venous access for fluid resuscitation and transfusion as needed.

If endoscopy and colonoscopy do not reveal the source of the bleeding, various diagnostic imaging alternatives are available. One option is to perform a tagged red blood cell nuclear scan, which can detect bleeding rates as low as 0.1 mL/min; however, the ability of this scan to localize the bleeding to a particular segment of bowel is limited. Catheter angiography, which detects a bleeding rate of approximately 0.5 to 1 mL/min, is another option. Given the often intermittent nature of GI bleeds and the time required to stabilize and transfer the patient, angiograms are positive in only about 50% of the cases. However, if an angiogram is performed immediately after positive results of a tagged red blood cell scan are identified, or when the angiogram is obtained during an episode of active bleeding, the likelihood of finding the source increases.

MD-CTA is a promising noninvasive first-line diagnostic modality that offers fast scanning times that vary between 6 and 20 seconds and provides accurate diagnosis or exclusion of active GI hemorrhage by comparing pre- and postintravenous contrast images and identifying abnormal hyperattenuating areas of extravasated contrast material within the bowel lumen. The anatomic coverage usually includes from the diaphragm to the inferior pubic rami to encompass the entire rectum. No oral contrast material or fluid is administered. The preliminary unenhanced examination is performed to depict any preexisting intraluminal hyperattenuating material (such as suture material, clips, foreign bodies, orally administered pharmaceutical drugs, and retained contrast material within a diverticulum, which can serve as potential pitfalls) and can be performed using a low radiation dose technique. The initial scan is followed by a biphasic acquisition in the arterial and portal venous phases. The isotropic data set obtained in current generation CT scanners allows the routine generation of multiplanar reformations and three-dimensional reconstructions. Active extravasation of contrast material is seen as an intraluminal focal collection or linear "jet" visible in the arterial and/or portal venous phase but not on the unenhanced scan. MD-CTA is increasingly being used in this setting; a recent meta-analysis showed that the sensitivity of MD-CTA for detecting active acute GI hemorrhage was 85.2%, and the overall specificity was 92.1% (Fig. 11-24).

During catheter angiography, it is important to first study the vessel that has the highest likelihood of being the source of bleeding with selective angiograms. Visualization of both the arterial and venous phases is required, because some bleeds may be caused by varices related to portal hypertension or thrombosis. The presence of contrast extravasation into the bowel is diagnostic. Extravasation is usually seen during the arterial phase and persists after venous washout before slowly dissipating. Catheter-directed therapy options include embolization and vasopressin infusion. When subselective catheterization of the bleeding branch is possible, it can be followed by embolization with GELFOAM (Pfizer Inc., New York, NY), large particles (polyvinyl alcohol or spheres), and microcoils to stop the bleeding. When the bleeding is diverticular, postpolypectomy, or mucosal in origin, intraarterial vasopressin infusion is an effective alternative. Vasopressin is not effective for bleeding that results from pseudoaneurysms or arteriovenous malformations, and it is contraindicated in cases of bleeding as a result of an ischemic bowel. After embolization, patients should be monitored closely, because approximately 20% may have recurrent bleeding, and bowel ischemia may develop in some patients.

Aneurysms of the Visceral Arteries. Aneurysms of the visceral arteries are rare compared with aortoiliac and femoropopliteal aneurysms. The most commonly affected vessels are the splenic, hepatic, and superior mesenteric arteries. The most frequent causes of true aneurysms are atherosclerosis and vasculitis, and the most frequent causes of pseudoaneurysms are pancreatitis, trauma, and infection. Most of these aneurysms are asymptomatic and are discovered as incidental findings, but some aneurysms may present with rupture.

Splenic artery aneurysms are the third most common intraabdominal aneurysm, after aortic and iliac aneurysms, and account for 60% of the cases of visceral aneurysms (Fig. 11-25). Most splenic artery aneurysms are saccular, single, and less than 3 cm in diameter. As with other intraabdominal aneurysms, common causes include pancreatitis, atherosclerosis, trauma, and fibrodysplastic disease. Interestingly, these aneurysms are four times more prevalent in females than males, with a higher incidence among pregnant and multiparous women. The catastrophic complication of rupture in pregnancy results in high mortality rates in the order of 70% to 90% for both the mother and fetus. Treatment options include surgical resection and embolization. Endovascular stent graft placement can be another option in select cases.

Hepatic artery aneurysms represent approximately 20% to 40% of all splanchnic artery aneurysms. They can be extrahepatic or intrahepatic, with the former representing about two thirds of the cases. The causes of hepatic aneurysms include atherosclerosis and trauma. Less common causes include pancreatitis, vasculitis, hereditary telangiectasias, cystic medial necrosis, liver abscess, and tuberculosis.

The superior mesenteric artery is the third most common location for visceral artery aneurysms. The frequency of these aneurysms is estimated at 5.5% of all splanchnic aneurysms and less than 0.5% of all intraabdominal aneurysms. In the past, it was believed that most of these aneurysms had an infectious cause; however, more recent reports have suggested that most cases are due to atherosclerosis. Collagen vascular disorders and polyarteritis nodosa have also been implicated. These aneurysms usually manifest with severe mid-epigastric pain.

Aneurysmal involvement of the celiac, ileocolic, and gastroduodenal arteries has also been described. Aneurysms of the gastroduodenal artery are often associated with pancreatic disease and can cause bleeding in the peritoneal or

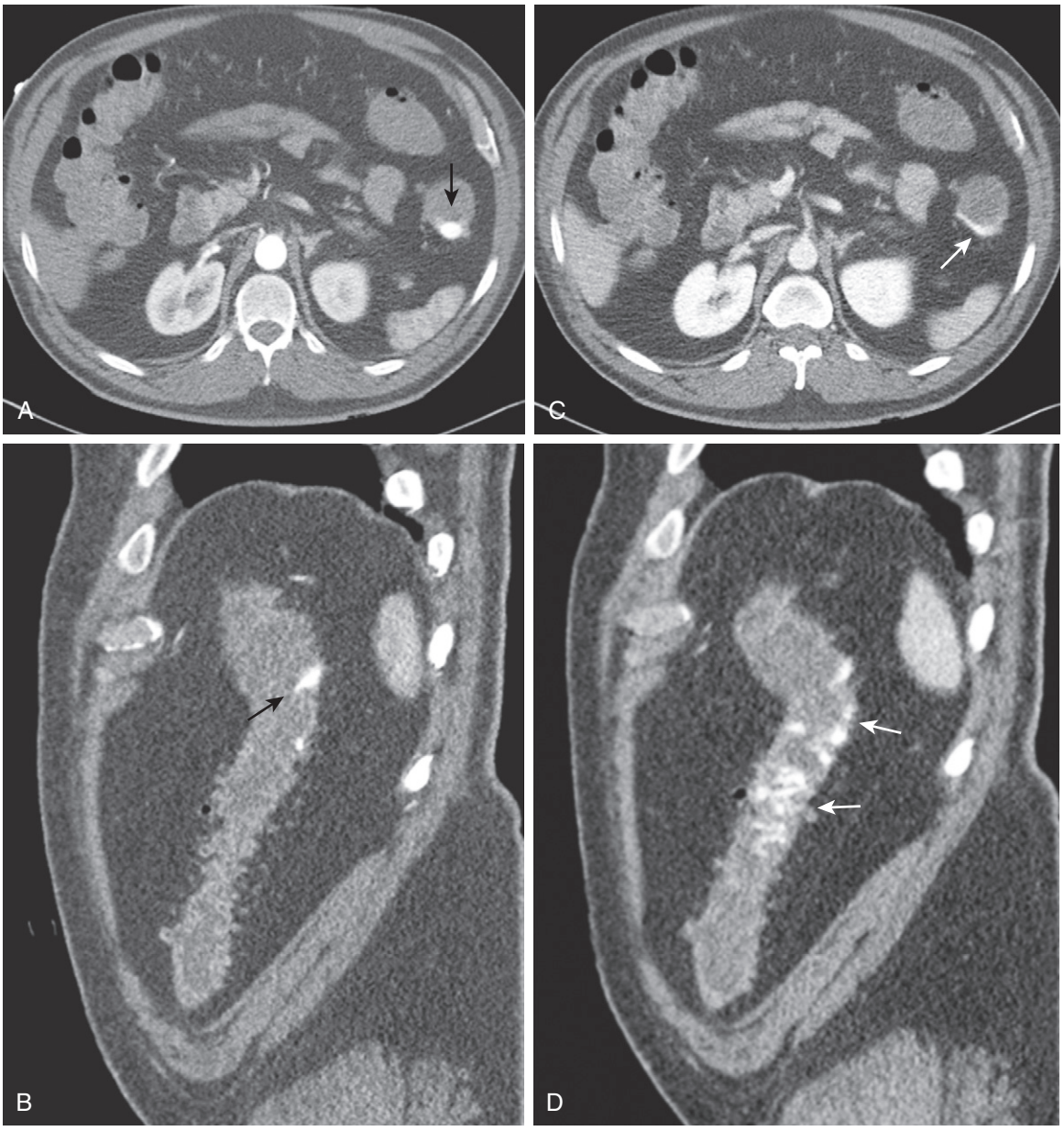


FIGURE 11-24 A 56-year-old man with lower gastrointestinal bleeding. Computed tomographic angiography images show an active arterial blush originating from a diverticulum at the splenic flexure (*black arrows* in **A** and **B**) with increased accumulation and pooling on the portal venous phase (*white arrows* in **C** and **D**).

retroperitoneal space and more rarely into the portal vein or into a pancreatic pseudocyst (Fig. 11-26). In general, elective repair is recommended for splanchnic aneurysms when they reach a size greater than 2 to 2.5 cm. Pseudoaneurysms are always considered to carry a high risk of rupture, and thus repair is recommended upon detection regardless of their size.

Traumatic Injury of the Renal Arteries

The renal arteries are the most frequently injured branch vessels of the abdominal aorta during blunt trauma. More than 80% of renal injuries are mild, and patients present with stable hematomas or hematuria without visible injury and can be managed conservatively. On the other end of the spectrum are the completely shattered kidney and avulsion of the vascular pedicle with complete devascularization, which requires emergent surgery. Patients with intermediate-grade injuries usually can be managed with angiographic interventions, although surgical repair may be necessary if the patient experiences hemodynamic compromise that requires rapid control of hemorrhage.

Upon CT/CTA, a nonenhancing kidney, a large perirenal hematoma, and active contrast extravasation are all signs of severe renal trauma with vascular involvement. A nonenhancing renal artery or vein is a critical finding that indicates thrombosis, and dissection or transection must be considered in the diagnosis. Extravasation and pseudoaneurysm formation are usually seen in patients with penetrating trauma. Angiography is indicated when the diagnosis of a vascular injury is uncertain (a rarity with current CT technology) or when a vascular injury can be treated by endovascular means.

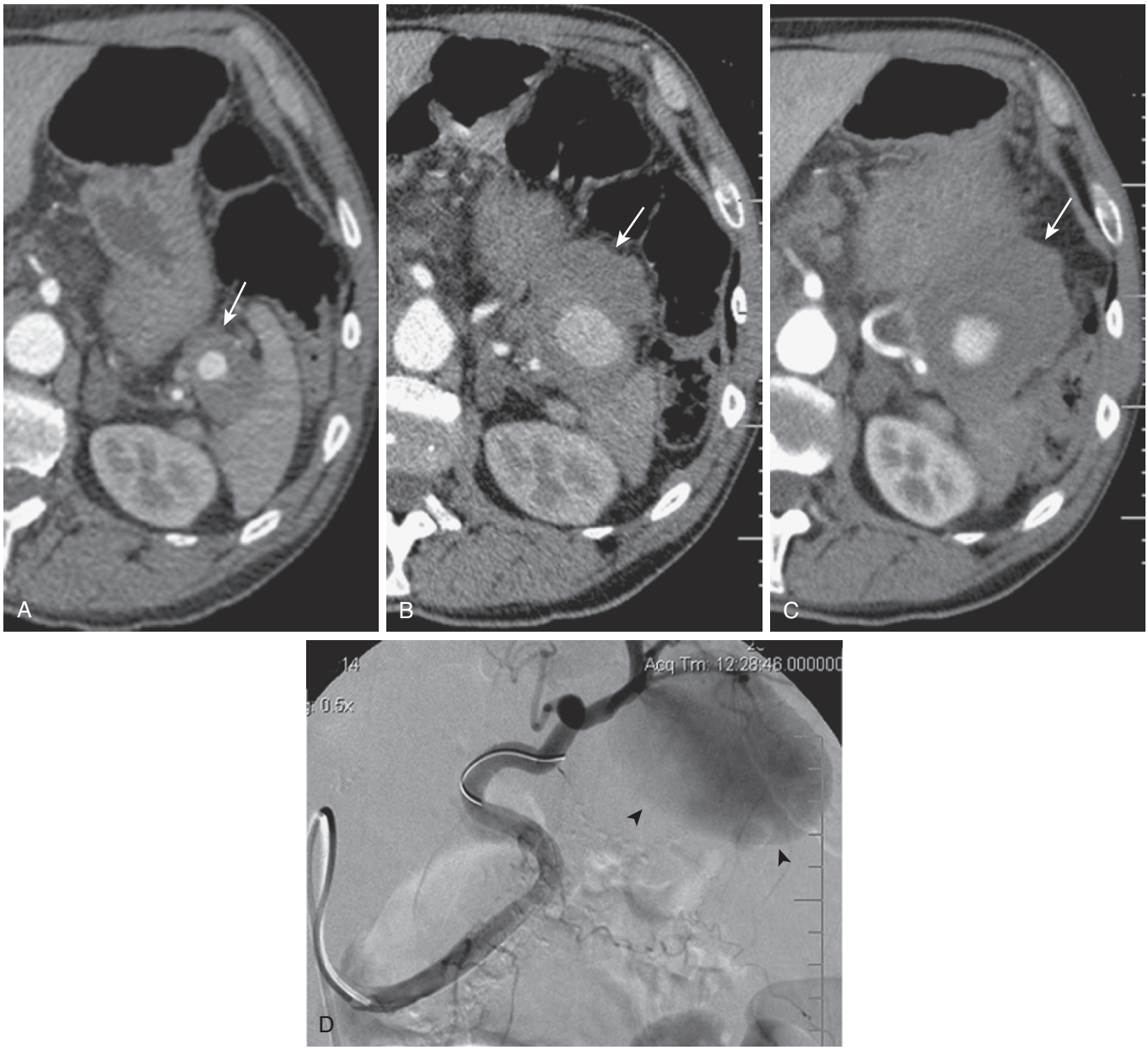


FIGURE 11-25 A to **D,** A patient with chronic pancreatitis and an enlarging splenic artery pseudoaneurysm. The patient did not want to undergo any invasive procedures, so he was followed up with serial computed tomographic angiography every 6 months, which demonstrated progressive enlargement of the aneurysm *(arrows)*; in the most recent follow-up evaluation, dense crescents worrisome for impending rupture were identified. Catheter angiography **(D)** showed that the aneurysm *(arrowheads)* had increased further in size. The patient then underwent surgery for aneurysm resection.

Iatrogenic renal vascular injuries also can be included in this category, because biopsies, ablations, and partial nephrectomies can lead to bleeding or pseudoaneurysms and formation of AV fistulas. These renal vascular injuries may result in active extravasation into the perirenal space or the renal collecting system (Fig. 11-27).

Nontraumatic Renal Arterial Emergencies

Acute Renal Ischemia. Normal kidneys have no significant collateral blood supply, and acute occlusion will lead to rapid loss of kidney function if the kidney is not effectively revascularized within 1 to 2 hours. The most common cause of acute occlusion in middle-aged and elderly patients is embolic disease of a cardiac source, whereas in the young patient population the most common cause is trauma. Other causes include aortic or renal artery dissection, thrombosis of a focal stenosis, thromboembolism from a renal artery aneurysm, and procedural complications (Fig. 11-28). Patients with acute renal artery ischemia classically present with flank pain and hematuria. Occlusion in the setting of progressive renal artery stenosis is less likely to end in acute ischemia because collateral flow usually via capsular, adrenal, or gonadal arteries will have developed. Both CT and MRI are useful to demonstrate the areas of asymmetric renal perfusion, with generalized lack of enhancement seen with complete arterial occlusion or

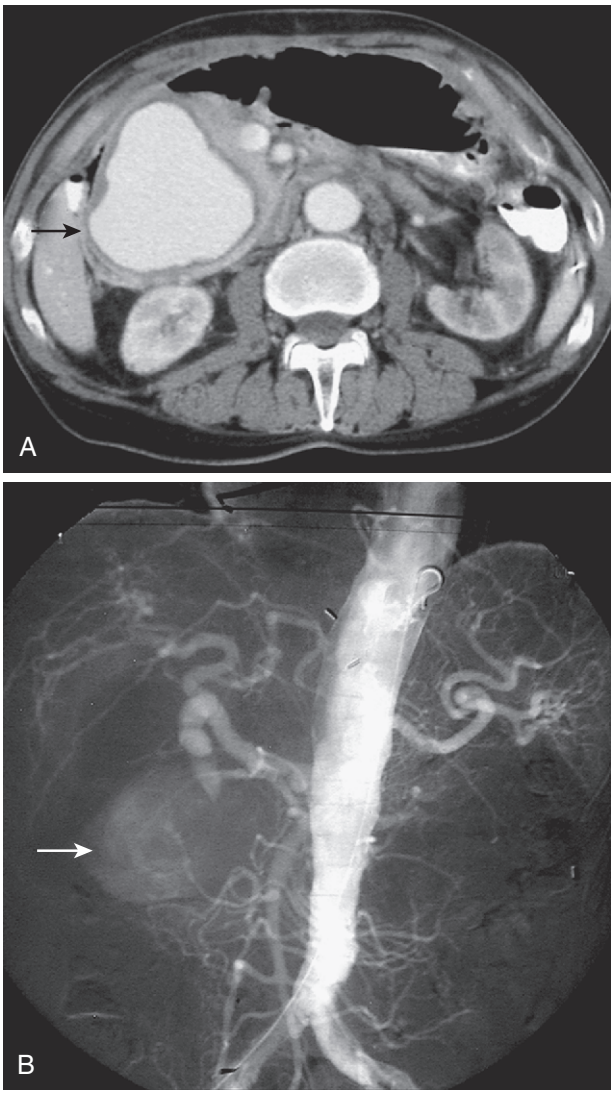


FIGURE 11-26 A, A contrast-enhanced computed tomography image through the level of the pancreas demonstrates a large heterogeneous mass with an enhancement pattern similar to the aorta and located lateral to the head of the pancreas *(arrow)*. The duodenum is not visualized. Findings correspond to a large pseudoaneurysm as a result of pancreatitis. **B,** Conventional angiography demonstrates an enlarged gastroduodenal artery feeding a very large aneurysm *(arrow)*. (Courtesy Dr. Javier Casillas, University of Miami, Miami, FL.)

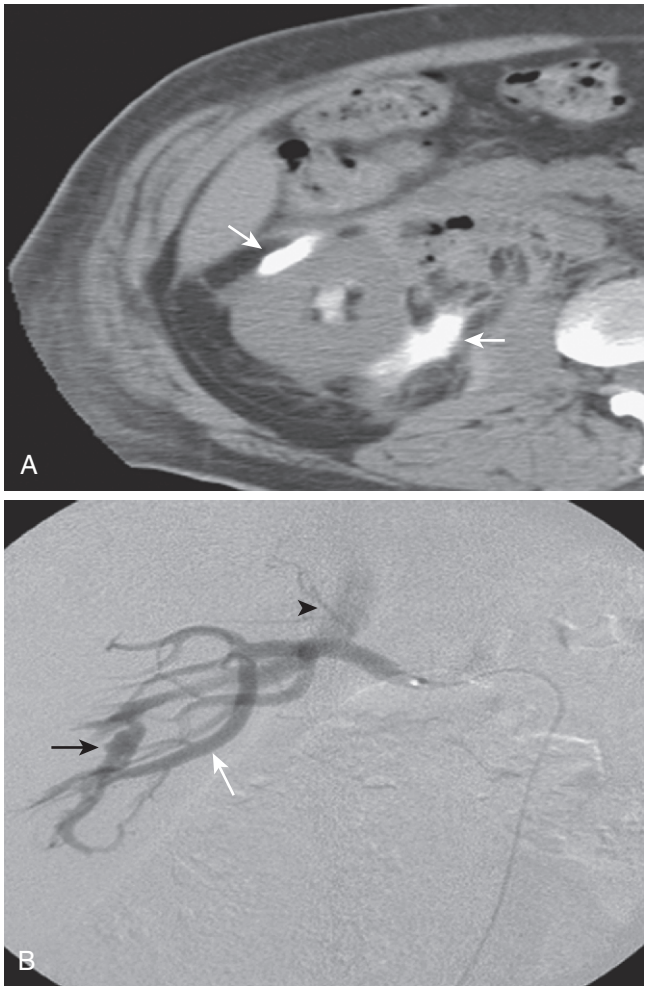


FIGURE 11-27 A, After a transjugular kidney biopsy, gross hematuria developed. Computed tomography was performed, which demonstrates contrast extravasation into the perirenal space resulting in a urinoma *(white arrows)*. The patient was initially managed conservatively, but heavy hematuria recurred. **B**, A preembolization angiogram shows an arteriovenous fistula *(black arrow)* fed by the lower polar renal artery *(white arrow)* and early venous drainage with prompt visualization of the inferior vena cava *(arrowhead)*.

areas of segmental infarction as a result of smaller emboli. CTA and MRA can demonstrate renal artery stenosis, arterial dissection, and other renal artery anomalies, as well as accessory arteries or collateral flow. Revascularization of acute renal artery occlusion is difficult because of the narrow time window before irreversible changes develop. If an occlusive dissection develops during renal artery angioplasty, stenting is indicated; if the occlusion is a result of thrombosis, then treatment is undertaken with thrombolysis, and thrombectomy or surgical revascularization is indicated.

Aneurysms of the Renal Artery. Aneurysms of the renal arteries are rare. Causes include degenerative aneurysms, which are usually asymptomatic, fibromuscular dysplasia, infection, trauma, and idiopathic and iatrogenic causes. Other causes such as polyarteritis nodosa tend to involve small peripheral intraparenchymal branches. The risk of rupture increases when the aneurysm diameter exceeds 2 cm, and this risk has been found to be higher in pregnant patients. These aneurysms also may be complicated by renal infarction, hypertension, and spontaneous fistula formation. The decision to treat depends on aneurysm size and clinical presentation. Minimally invasive angiographic alternatives such as coil embolization and stent graft placement are effective techniques; however, these alternatives cannot always be implemented, and surgical reconstruction or bypass may be required.

Renal Neoplasm–Related Vascular Emergencies. Some benign and malignant renal neoplasms can be the source of acute clinical symptoms, including pain, hemorrhage, and gross hematuria. Angiomyolipomas are benign renal neoplasms that contain fat, smooth muscle, and blood vessels. They are well known for their association with tuberous sclerosis and their tendency to bleed, particularly when they are larger than 4 cm. Ultrasound or CT evaluation is usually performed in the emergency setting

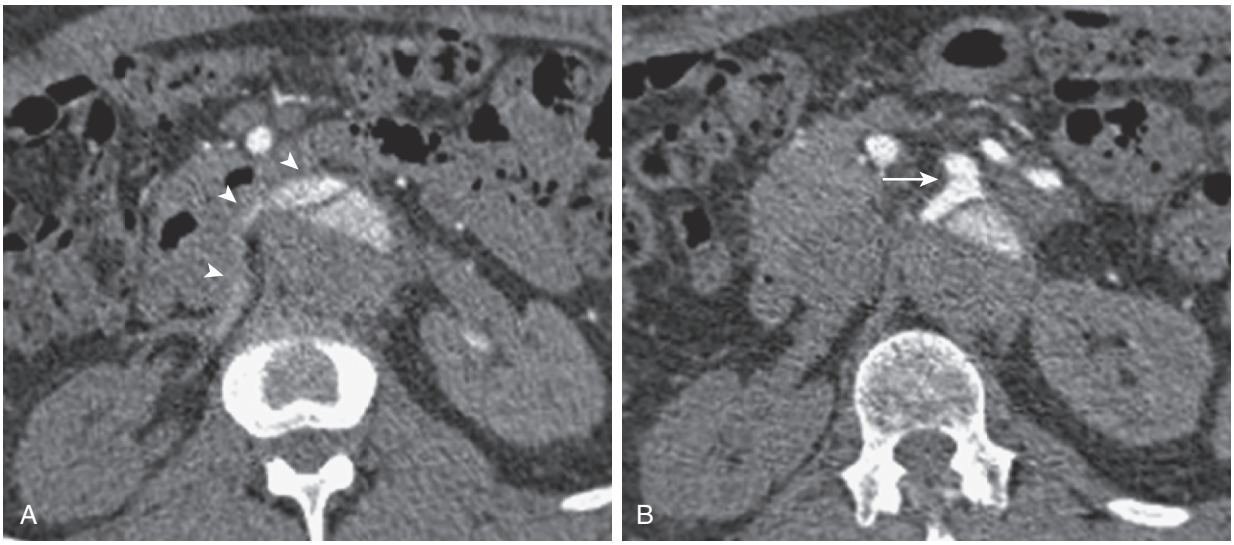


FIGURE 11-28 **A** and **B,** Computed tomographic angiography of a complex aortic dissection. Part of the aortic false lumen in the posterior aspect of the aorta has thrombosed. The dissection flap is partially involving the origin of the right renal artery, causing flow impairment (**A,** *arrowheads*); compare with the preserved celiac trunk origin (**B,** *arrow*).

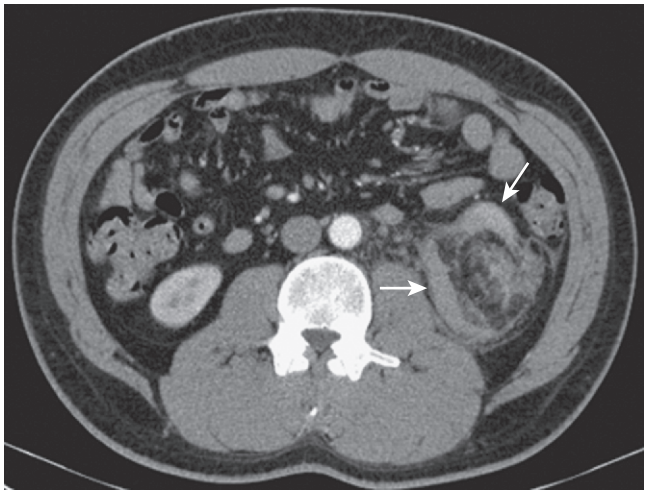


FIGURE 11-29 A 35-year-old patient presented with sudden left flank pain. Contrast computed tomography shows a fatty mass lesion in the lower pole of the left kidney in addition to perirenal fluid *(arrows)*; findings are consistent with left renal angiomyolipoma complicated by acute hemorrhage.

as a result of acute flank pain that may be associated with hemodynamic changes. Images will demonstrate the acute renal and perirenal hemorrhage with or without contrast extravasation. The mass itself, as well as the characteristic intralesional fat, usually can be identified, although identification can be difficult in the setting of acute hemorrhage (Fig. 11-29). The presence of other angiomyolipomas can help in the diagnosis. These lesions are usually treated with percutaneous embolization using a combination of particles, coils, and sometimes alcohol. Follow-up scans are performed to document resolution of the hematoma and shrinkage of the lesion.

Renal cell carcinomas are the most common malignant renal neoplasm in adults. The so-called classic triad of flank pain, hematuria, and mass is present in only one third of patients. Percutaneous embolization for tumor control is generally not indicated except in select cases in which the tumor size is too large for resection and embolization may help control operative bleeding. Other indications for percutaneous embolization include severe gross or recurrent hematuria or perirenal hemorrhage.

Vascular Emergencies of the Pelvis

Trauma of the Pelvic Arteries

Traumatic injury to the vascular structures of the pelvis is frequently the result of pelvic fractures in combination with violent shear and traction forces. Pelvic vascular injuries can lead to rapid hypovolemic shock and death from exsanguination if not treated promptly. Most pelvic fractures are a consequence of lateral compression, and the majority of those fractures are successfully stabilized with pelvic fixation. Unstable pelvic fractures that result from more complex forces do not respond well to pelvic fixation and can be aggravated by associated coagulopathy and cancellous bone bleeding. If the patient is hemodynamically stable, an expedited MD-CTA can be quite helpful in characterizing the fracture and assessing the location and degree of vascular involvement. When both intraabdominal hemorrhage and pelvic fractures are present, the patient is taken directly to the operating room for repair of the abdominal injuries and pelvic fixation. Endovascular intervention is usually postponed until the more emergent conditions are treated, unless CT/CTA determines that the more ominous finding can be best approached with endovascular techniques (Fig. 11-30). Angiography in hemodynamically unstable patients should be directed first to a rapid evaluation of the source of bleeding and then expeditiously to embolization. A previous CT/CTA helps to direct the angiogram and possibly obviate the need for an initial nonselective pelvic angiogram, because the absence of abnormal findings in nonselective angiography does not exclude an active bleed, and selective internal and external iliac angiograms are still mandated. It is important to note, however, that an initial pelvic angiogram can be useful to identify massive extravasation and depict the patient's specific anatomy. Also, one should not confuse the

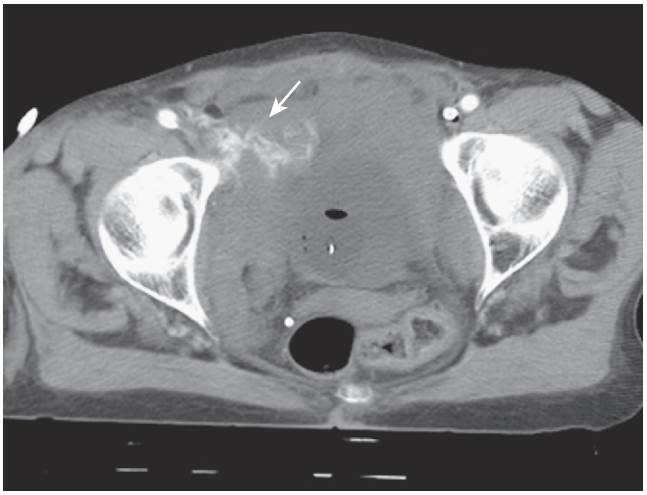


FIGURE 11-30 The patient was in a motor vehicle accident and sustained a pelvic fracture. After initial stabilization, computed tomographic angiography demonstrated active contrast extravasation adjacent to the right superior pubic ramus *(arrow)*; the patient underwent angiography for embolization.

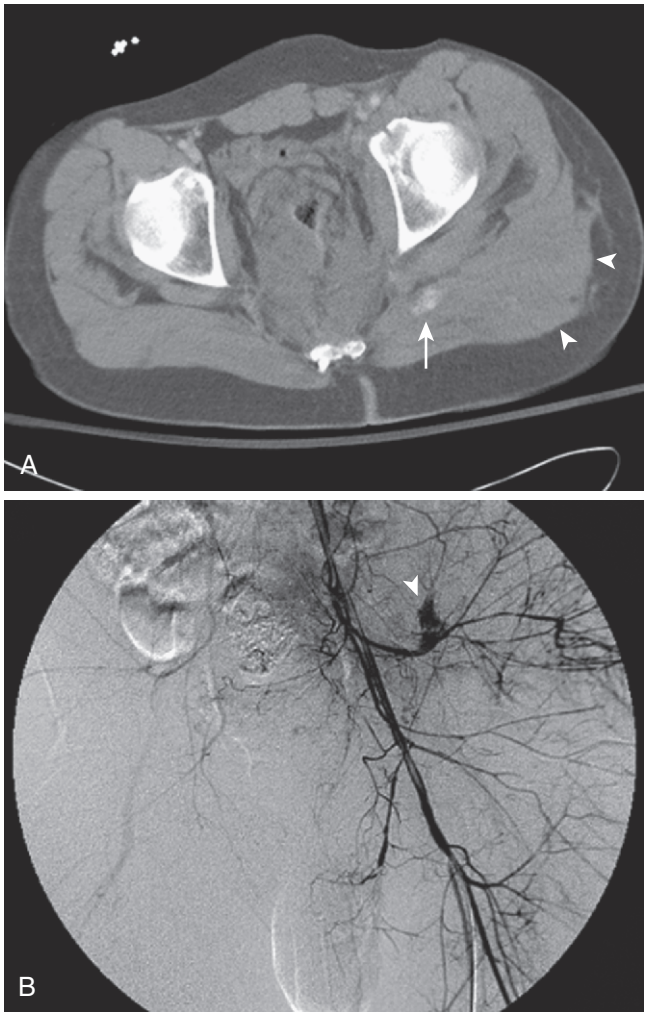


FIGURE 11-31 **A,** The patient sustained blunt trauma with fracture of the pelvis. A large left gluteal hematoma is present *(arrowheads)*, and active extravasation is identified in the same area *(arrow)*. **B,** Catheter angiography shows the extravasation arising from the superior gluteal artery *(arrowhead)*, which was embolized using GELFOAM pledgets.

normal cavernosal blush at the penoscrotal junction with an area of extravasation. The primary goal of embolization in patients with pelvic fractures is to promptly stop the hemorrhage and decrease the arterial flow to the injured vessel. GELFOAM pieces are mixed with contrast material, and vessel embolization is performed until no further extravasation is identified (Fig. 11-31). In stable patients, subselective embolization can be performed, and other embolic agents such as coils and glue can be used. The use of covered stents has also been described with great success, but it is recommended that a specialist familiar with their use be the person performing the procedure. Both coil embolization and stent graft placement have been used successfully to treat traumatic pseudoaneurysms (Fig. 11-32). After embolization, completion of angiography is important to exclude other sources of bleeding.

Nontraumatic Emergencies of the Iliac Arteries

Iliac Occlusive Disease. Atherosclerosis is the most common cause of iliac occlusive disease and frequently involves the distal aorta. Patients tend to present with unilateral or bilateral leg claudication or ischemia depending on the level of obstruction and the presence of collateral circulation; bilateral symptoms suggest aortic involvement. Aortoiliac occlusive disease is part of the lower extremity peripheral vascular disease spectrum (see the section covering the lower extremities), and as such it can lead to loss of the extremity or even the loss of life when it becomes acute. Causes for acute presentation include embolism, thrombosis, dissection, trauma, low cardiac output states, and hypotension. Emboli are the most common cause of sudden lower extremity ischemia, with 80% originating in the heart as a result of atrial fibrillation, valvular disease, or recent myocardial infarction. Emboli also can originate in the peripheral circulation proximal to the occlusion as a consequence of irregular or ulcerated plaque, aneurysms, and previous interventions such as stent grafts. Emboli tend to get wedged at bifurcation points or in areas where vessels narrow abruptly. The iliac arteries and the aorta are involved in 18% and 15% of cases of acute ischemia of the lower extremities, respectively. Emboli tend to have a more acute and severe presentation because of the lack of collateral circulation. Occlusive thrombosis is caused by the disruption of an atheromatous plaque that leads to exposure of its core products with subsequent activation of the coagulation cascade (Fig. 11-33). In patients who present with acute ischemic symptoms, a history of thigh or buttock claudication is suggestive of underlying iliac atherosclerotic disease. Leriche syndrome is described as the combination of intermittent claudication, impotence, and significantly decreased or absent femoral pulses. This syndrome can be identified in approximately one third of male patients with aortoiliac occlusive disease and indicates chronic peripheral arterial insufficiency as a result of narrowing of the distal aorta. Iliac occlusive disease can also present as "blue toe" syndrome when it causes distal emboli.

Examination will reveal the absence of femoral pulses and a decreased ankle brachial index (ABI). Ultrasound evaluation with Doppler of the iliac arteries is difficult; however, the analysis of the duplex spectral waveforms demonstrating spectral broadening and the absence of a

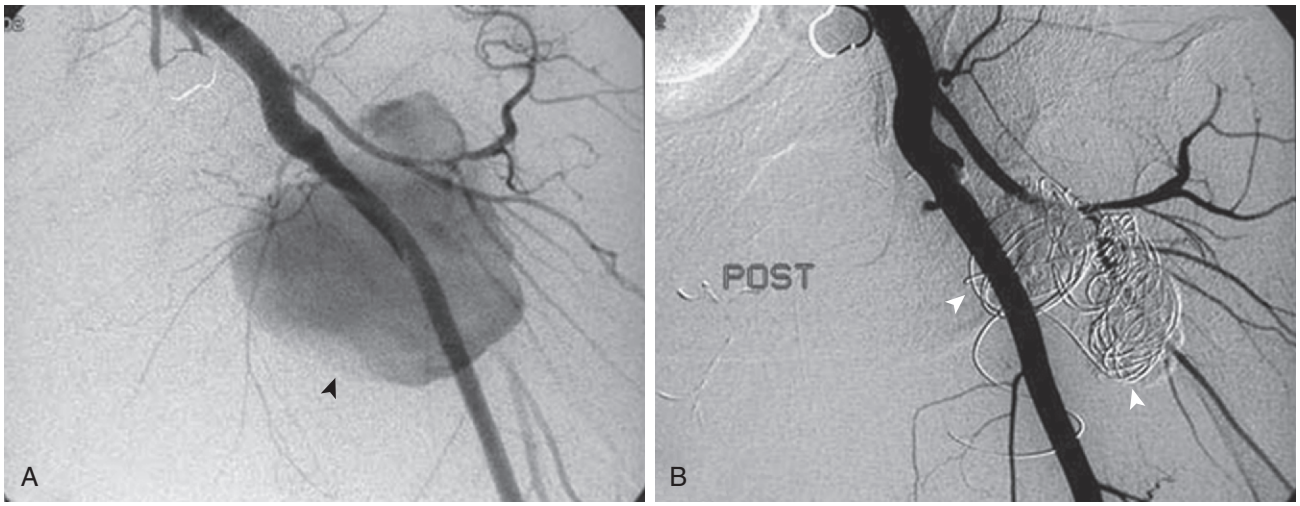


FIGURE 11-32 The patient sustained a gunshot wound to the pelvis. **A,** Catheter angiography shows a large pseudoaneurysm arising from a hypogastric artery branch *(arrowhead)*. **B,** After subselective coil embolization, the aneurysm has been completely occluded *(arrowheads)*. (Courtesy Dr. W. Escobar, Cali, Colombia.)

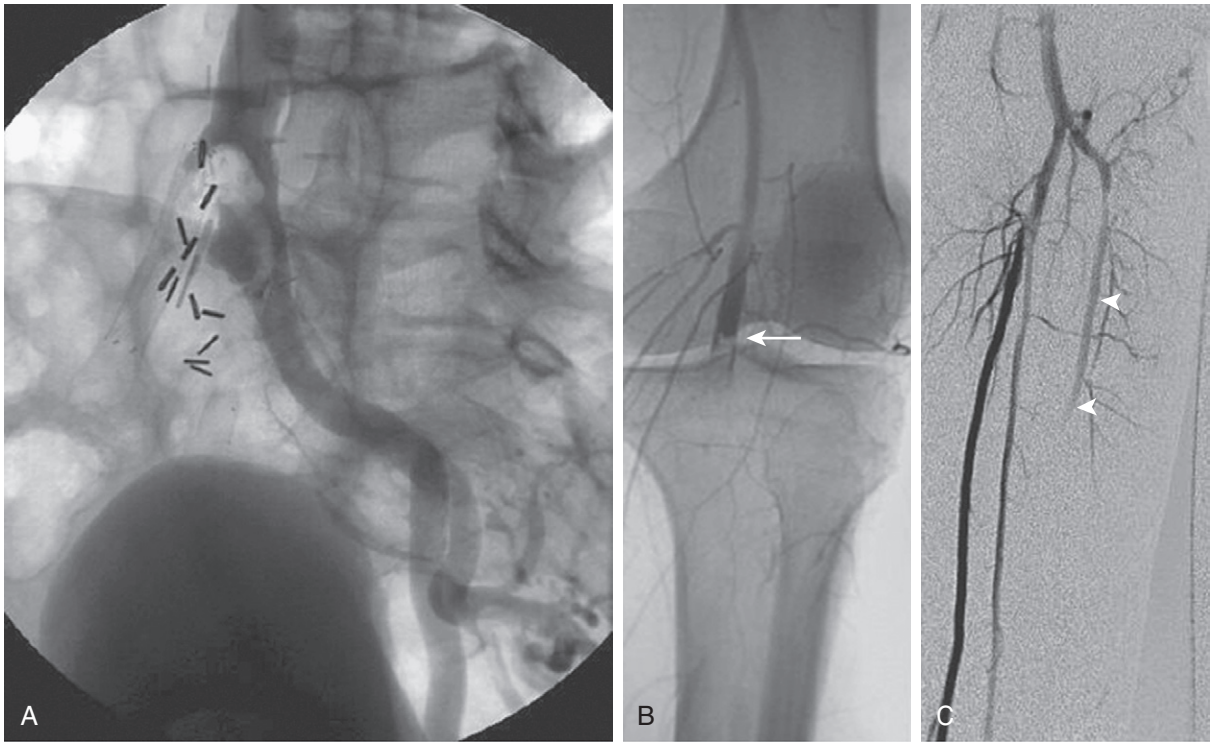


FIGURE 11-33 The patient presented with sudden onset of a painful, cold left foot. **A,** Catheter angiography shows a large thrombus developing from an occluded right iliac artery stent and extending into the left common iliac artery. **B,** A left lower extremity angiogram shows complete occlusion at the level of the popliteal artery as a result of an embolus *(arrow)*. **C,** After catheter-directed thrombolysis, patency of the popliteal, posterior tibial, and peroneal arteries was reestablished, and the anterior tibial artery flow is partially restored *(arrowheads)*.

normal triphasic pattern can provide valuable information about proximal disease.

CE-MRA and CTA can both detect aortoiliac disease with great sensitivity and specificity and allow for adequate therapeutic planning. CT tends to overestimate the degree of stenosis, particularly in the presence of calcification. MRA offers limited evaluation of segments containing stents because of the metal-induced susceptibility artifact.

In general, both CTA and MRA provide excellent characterization of the aortoiliac vasculature for diagnosis, follow-up, and therapeutic planning. Occasionally, both are used in cases of conflicting results or when assessment of the calcified wall is important for therapeutic planning.

Catheter angiography is usually reserved for cases in which intervention is anticipated or to answer specific inquiries regarding pressure gradient measurements and

information on flow dynamics. Definitive treatment of hemodynamically significant aortoiliac disease is usually aortobifemoral bypass, with a 5-year patency rate of approximately 90%. Patients in whom aortoiliac disease becomes symptomatic but who have comorbidities that increase the operative risk may benefit from a less invasive approach such as endovascular repair with angioplasty and stenting, axillary-femoral bypass, or femoro-femoral bypass. Focal concentric iliac artery stenosis usually responds well to angioplasty, with a more than 60% primary patency rate at 4 years; however, because stents are approved for iliac use, most iliac lesions are now treated with primary stenting, with a 4-year patency rate of almost 80% for stenotic lesions and 60% for recanalized occlusions. Minimally invasive treatment of bilateral common iliac artery occlusive disease will require placement of bilateral stents, also known as "kissing" stents when they touch each other at the aortoiliac confluence. When dealing with patients who report acute or recent onset of symptoms and a fresh thrombus is suspected, thrombolysis is an excellent recanalization alternative (see Fig. 11-33).

Iliac Aneurysms. Degenerative aneurysms of the iliac arteries tend to involve the common iliac artery (CIA) and are frequently seen in association with AAAs or dissection (Fig. 11-34). External and internal iliac artery aneurysms are rare. As with AAAs, the most feared complication is aneurysm rupture, which can be free, contained, or into a venous structure. Findings of rupture can be subtle with only mild perivascular stranding noticed, or they can be dramatically florid with retroperitoneal and/or intraperitoneal hemorrhage. Rupture into venous structures causes high output congestive heart failure. Chronic ruptures usually contain thrombus associated with saccular dilatation and disruption of intimal calcification. Isolated CIA aneurysms warrant repair when they reach 2.5 to 3.0 cm in diameter, and they can be managed with stent graft placement provided there is an adequate access pathway and sufficient landing zones to allow appropriate attachment of the graft.

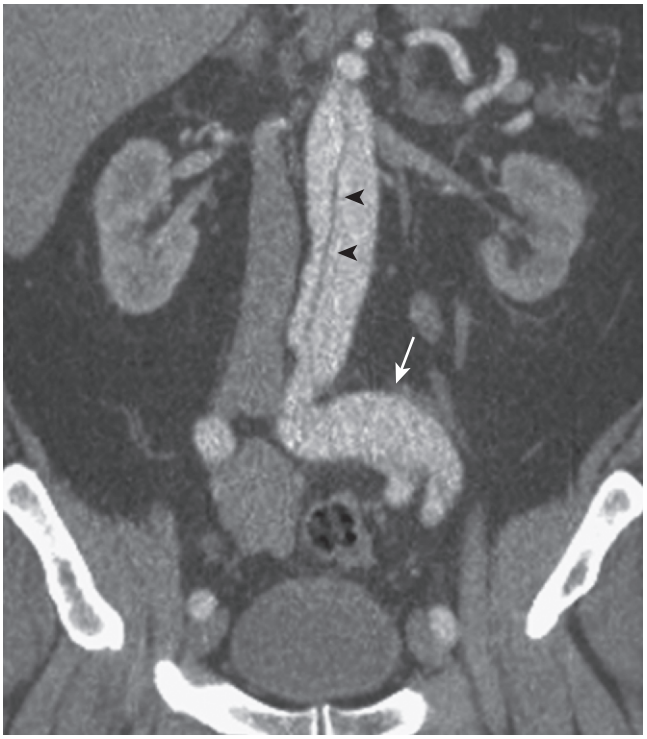


FIGURE 11-34 Coronal computed tomographic angiography reconstruction demonstrates a 3.5-cm aneurysmal dilatation of the left common iliac artery *(arrow)*. An abdominal aorta dissection flap *(arrowheads)* is also present that extends into the iliac (not shown).

Iliac Artery Dissection. Dissection of the iliac arteries is usually an extension of thoracoabdominal aortic dissection. Primary iliac artery dissection is relatively rare and has been described in association with fibromuscular dysplasia and vigorous training in professional athletes. Both CTA and MRA are excellent for the evaluation of thoracoabdominal and iliac dissection (see Fig. 11-20).

Vascular Emergencies of the Extremities

Arterial Injury of the Upper Extremities

Traumatic vascular lesions in the upper extremities can occur in as many as 40% to 50% of patients with penetrating trauma when "hard" (or direct) clinical signs are present. Hard clinical signs include pulsating hemorrhage, expanding hematoma, presence of a thrill or bruit, pulse deficit, and extremity ischemia (Box 11-5). Indirect (or "soft") signs include stable hematoma, extensive soft tissue injury, adjacent fracture or adjacent nerve injury, nonpulsatile bleeding, and delayed capillary refill (Box 11-6). In the absence of hard clinical signs, the patients can be treated conservatively, and noninvasive imaging modalities play a major role in their evaluation and follow-up. Besides the conventional penetrating and blunt traumatic injuries that any vessel is subject to, the arteries of the upper extremity are also at risk for unique injuries because of the major functional role they play in our lives. Among them are stretch injuries that occur during extreme traction when attempting to stop a fall. The subclavian-axillary segment is particularly at risk, and associated brachial plexus injuries are common. Intimal tears and disruption of the media can then lead to thrombosis and distal embolization (Fig. 11-35). Other injuries include blunt trauma from incorrect use of crutches, affecting the axillary-brachial segment, iatrogenic injuries during central venous access procedures, and injuries related to self-administered drugs.

BOX 11-5 Hard Clinical Signs of Arterial Trauma

Pulsating hemorrhage
Expanding hematoma
Presence of a thrill or bruit
Pulse deficit
Extremity ischemia

BOX 11-6 Soft Clinical Signs of Arterial Trauma

Stable hematoma
Extensive soft tissue injury
Adjacent fracture
Adjacent nerve injury
Nonpulsatile bleeding
Delayed capillary refill

CTA is the preferred imaging modality to emergently assess the arteries of the proximal upper extremities, with catheter angiography reserved for patients who have equivocal diagnoses or when therapeutic interventions are required. CTA offers the advantage of simultaneously assessing for additional nonvascular injuries, whereas conventional angiography offers the advantage of diagnosing and treating at the same time. Both modalities can identify any of the vascular injuries, including intimal tear, occlusion, pseudoaneurysm, active extravasation, complete transection, and arteriovenous fistulas. Branch vessel extravasation and pseudoaneurysms can be treated with coil embolization. Main arterial pseudoaneurysms and fistulas also can be treated with embolization or covered stents (Fig. 11-36).

Nontraumatic Arterial Emergencies of the Upper Extremities

Acute upper extremity ischemia most frequently presents with hand and digit symptoms and can vary from mild coldness to complete necrosis. On occasion, digital ischemia can occur in the presence of normal palpable pulses. The location of symptoms depends on the level of occlusion. The most common cause of acute nontraumatic upper extremity ischemia is embolization of cardiac origin and is suggested by recurrent ischemic events that may affect the extremity or the central nervous system. Other possible causes include trauma, aortic dissection, and the steal phenomenon in patients with a recent history of surgical AV shunting for dialysis access. Malignancy

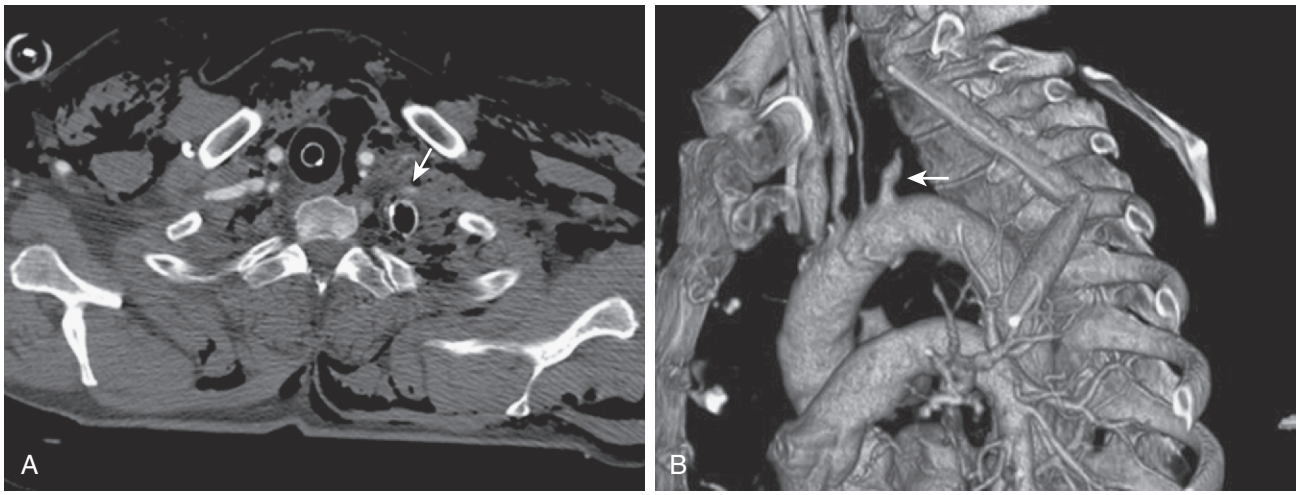


FIGURE 11-35 This patient sustained blunt chest trauma during a motor vehicle accident. **A,** Computed tomographic angiography shows a thinned left subclavian artery origin *(arrow)*. **B,** Volume-rendered reconstruction better shows the left subclavian artery occlusive dissection *(arrow)*.

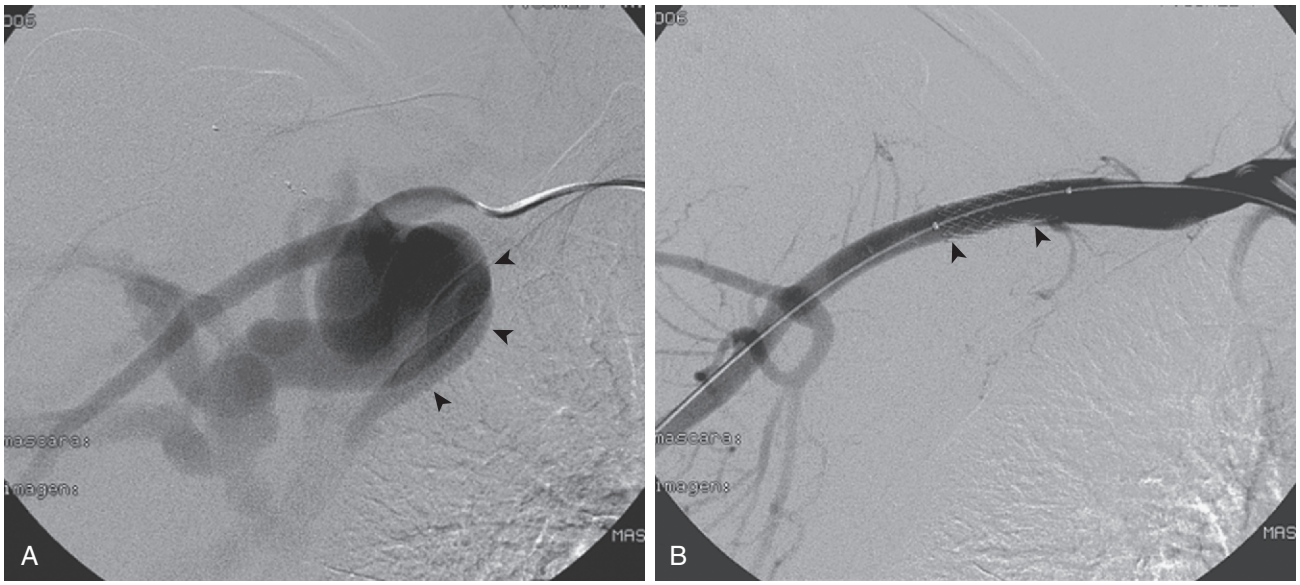


FIGURE 11-36 This 25-year-old male patient sustained a gunshot wound to the right shoulder area 5 years earlier and now presented with congenital heart failure. **A,** A selective angiogram of the right subclavian artery shows a high flow arteriovenous subclavian fistula with large aneurysmal dilatation of the vein *(arrowheads)*. **B,** After endovascular treatment with a covered stent, the fistula is completely occluded and the subclavian artery is preserved *(arrowheads)*. (Courtesy Dr. W. Escobar, Cali, Colombia.)

and hypercoagulable states also can present with acute digit ischemia. Recurrent events limited to one arm are compatible with a source localized proximally within that extremity, like an aneurysm or stenosis in the subclavian artery, in which case thoracic outlet syndrome with arterial involvement must be considered. Thoracic outlet syndrome is defined as the symptomatic extrinsic compression of the neurovascular structures of the upper extremities as they exit the upper thorax. Neural and venous compressions represent the majority of the cases, and arterial compressions are rare; however, embolic events can occur in as many as 40% of patients. Arterial compression usually occurs at the scalene triangle as a result of anomalous osseous or ligamentous structures or muscle hypertrophy. The arterial pulsation causes repetitive focal trauma that results in development of focal narrowing and poststenotic dilatation, where thrombus may form and cause distal embolization. Imaging should evaluate not only the arterial lumen but also the surrounding structures to detect anatomic anomalies causing the compression. CTA and MRA are both useful for depiction of the vessel lumen and surrounding tissues.

One of the most expeditious ways to obtain an objective imaging evaluation of the upper extremity circulation is through ultrasound imaging. However, the subclavian artery cannot always be visualized in its entirety, and in the emergency setting, obtaining a full arterial duplex examination may prove to be too time consuming if the operator is not well familiarized with the examination. In the setting of nontraumatic upper extremity ischemia, the most accurate imaging modality remains conventional catheter angiography because the location of the disease can be as distal as the digit level, and noninvasive imaging modalities may not yet provide sufficient resolution or detail to accurately evaluate all cases. Angiographic evaluation of critical hand ischemia as a result of embolic disease usually demonstrates the embolus within the brachial artery; however, magnification views of the hand and digits may be required to distinguish between distal emboli and other causes, such as vasculitis.

Any of the systemic vasculitides can affect the upper extremities and present as an acute event. By characterizing the distribution pattern, one may contribute to narrowing the differential diagnosis. Takayasu arteritis usually causes stenosis and occlusion of the proximal subclavian artery, giant cell arteritis tends to involve the subclavian and brachial arteries, and Buerger disease (thromboangiitis obliterans) causes occlusion of the main arteries and induces hypertrophy of small perineural collaterals that give the characteristic "corkscrew" angiographic appearance. Finally, systemic lupus erythematosus, rheumatoid arthritis, scleroderma, and mixed connective tissue disorder are likely to cause multiple occlusions of the small arteries, particularly at the digit level.

Critical hand ischemia resulting from embolic disease is usually treated with surgical embolectomy. Thrombolysis should be considered when an extensive distal thrombus is present. After recanalization, if the source of embolization is a focal atherosclerotic lesion or an aneurysm, treatment with balloon dilatation or stenting can be attempted accordingly.

Upper Extremity Aneurysms. Upper extremity artery aneurysms are rare; causes include atherosclerosis, acute or repetitive trauma, chronic dissection, connective tissue disorders, and, in cases of distal ulnar artery aneurysms, hypothenar hammer syndrome. Aneurysms of the intrathoracic subclavian artery are usually atherosclerotic in nature, whereas aneurysms in the extrathoracic segment are usually a result of thoracic outlet syndrome. Atherosclerotic aneurysms can present with pain, hoarseness, distal embolization, stroke, and rupture. Occasionally, the dilated origin of an aberrant subclavian artery known as the *diverticulum of Kommerell* can evolve into a true aneurysm that can be associated with pain, dysphagia, and dissection. CTA and MRA can provide a complete aneurysm characterization that allows for safer therapeutic planning.

Arterial Trauma of the Lower Extremities

Vascular injuries of the lower extremities are a serious complication of both penetrating and blunt trauma. The rate of limb loss with major injuries is approximately 15%, and 25% of the patients eventually experience some degree of limb dysfunction as a result of related osseous or nerve injuries. As mentioned previously, clinical signs of arterial injury are divided into "hard" and "soft" signs (see Boxes 11-5 and 11-6). Patients with a profoundly ischemic limb or active hemorrhage from the wound have emergent surgery, whereas stable patients with viable limbs should undergo a complete limb and pulse examination. A quick determination of the ABI can be helpful, because the incidence of vascular injury in patients with a normal ABI and normal examination findings is less than 10%. This number can increase to 20% when "soft" signs are present and the ABI is less than 1, and it increases to 40% when the ABI is less than 1 and the mechanism is a gunshot wound or the patient has an associated pulse deficit or neurologic deficit.

In the setting of normal findings of a physical examination, a penetrating wound in proximity to vascular structures is considered to be an indication for angiography only in cases in which the bullet tract follows the course of a major artery over a long segment. In the past, some practices called for angiography to be performed for every patient with a penetrating injury in proximity to a runoff vessel and when the overall identification of clinically relevant vascular injuries was less than 10%. CTA has become a useful minimally invasive tool in this scenario, with the ability to accurately diagnose the type of injury, as well as its extent and location. CTA can depict injuries that do not routinely require surgical intervention, such as intimal flaps, branch vessel occlusions, and partial luminal narrowing with preservation of distal flow. Catheter angiography remains a useful examination for patients with nonconclusive CTA findings and whenever endovascular transcatheter therapy is indicated. In general, partial injuries (such as intimal flaps) are managed conservatively, branch vessel extravasation may require embolization with coils (Fig. 11-37), and pseudoaneurysms are treated with embolization or stent grafts. Major injuries demand open surgical repair when extensive reconstruction or bypass is required.

Knee Dislocation. Knee dislocation can cause arterial injuries in approximately 40% of cases. Most patients are young and have limited collateral flow, which makes them highly vulnerable to popliteal occlusion, and a delay in diagnosis and treatment can lead to amputation as a result of irreversible ischemic changes. Physical

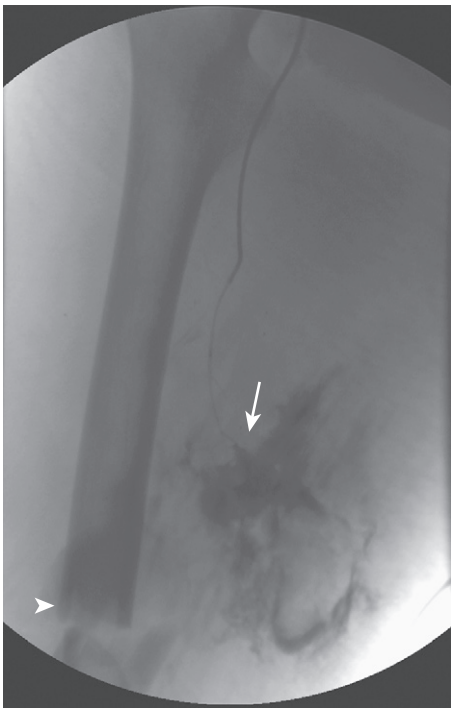


FIGURE 11-37 After a motorcycle accident, the patient was noticed to have an enlarging right thigh. A selective angiogram shows a large area of contrast extravasation arising from one of the femoral profunda branches *(arrow)*. Notice the femoral fracture *(arrowhead)*. The extravasation was treated with a combination of GELFOAM and coils.

examination with emphasis on the distal pulses and associated signs of vascular injury is crucial for a prompt diagnosis; however, an abnormal pedal pulse as an isolated finding on the initial examination of patients with knee dislocations is not sensitive enough to detect an injury that invariably requires vascular intervention. Patients with signs of an ischemic limb should proceed directly to surgery, and if it is required, intraoperative angiography can be performed for confirmation. Catheter angiography should include multiple projections to exclude intimal tears, spasm, and partial thrombosis. Small and nonocclusive lesions are managed conservatively. Patients who have been treated with prompt reduction and those with normal findings of vascular examinations can be further evaluated with CTA to determine the integrity of the popliteal artery.

Femoral Artery Pseudoaneurysm. Pseudoaneurysm of the femoral artery is often the result of an arterial puncture to perform cardiac or peripheral angiography and occurs in 1% to 5% of the cases. Patients may present with a large inguinal hematoma or a pulsatile mass. Most pseudoaneurysms thrombose spontaneously, but up to 3% to 5% may persist, increase in size, or rupture. Because of their location, these aneurysms are generally diagnosed with duplex ultrasound. Occasionally MRA or CTA is required when these asneurysms cannot be adequately characterized with ultrasound because of their large size or multilobulated characteristics, because of the inability of ultrasound to visualize the pedicle, or when they persist despite an initial attempt to treat them. Most femoral pseudoaneurysms can be treated with ultrasound-guided compression of the pedicle (or neck) to interrupt the flow and induce thrombosis; when this treatment fails, thrombin injection can be performed under direct ultrasound visualization to control the aneurysm flow as the thrombin is being administered (Fig. 11-38).

Nontraumatic Acute Lower Extremity Limb Ischemia

Acute lower limb ischemia is usually the result of atherosclerosis that gradually progresses to the point of complete occlusion; it manifests with insufficient limb perfusion and worsening pain that may acutely become exacerbated. The level of arterial compromise correlates closely with the location of ischemic symptoms; aortoiliac disease manifests as pain in the thigh and buttock, whereas femoral-popliteal disease manifests as pain in the calf. Symptoms of chronic peripheral vascular disease are precipitated by walking a predictable distance and are relieved by rest (claudication). Ischemic pain at rest is more worrisome; it can be partially relieved by placing the extremity in a dependent position, so that perfusion is facilitated by the effect of gravity. An acute, profoundly ischemic leg is a surgical emergency. Among the causes for acute limb ischemia are emboli, plaque disruption and thrombosis, dissection, trauma, and low cardiac output states. Among the various causes of acute limb ischemia, the major diagnostic goal is to differentiate embolic from thrombotic occlusion. Emboli are the most common cause of sudden lower extremity ischemia, and approximately 80% originate in the heart as a result of atrial fibrillation, valvular disease, or recent myocardial infarction. Emboli also can originate in the peripheral circulation (proximal to the level of occlusion) as a consequence of irregular or ulcerated plaques, aneurysms, dissection flaps, previous interventions, or stent grafts (Fig. 11-39). Emboli tend to get wedged at bifurcation points or stenotic areas; the femoral artery bifurcation is the most common site (40%), followed by the iliac arteries (20%), the aorta (15%), and the popliteal arteries (15%). Acute thrombosis occurs more often in the setting of established atherosclerotic disease, where the disruption of an existing atheromatous plaque leads to exposure of its core products and subsequent activation of the coagulation cascade.

The classic signs of acute limb ischemia are the "5 Ps": pulselessness, pallor, pain, paresthesias, and paralysis. Although not included in the "5 Ps," coldness of the extremity is an additional valuable sign. Muscle weakness and paresthesia are signs of limb-threatening ischemia, whereas paralysis and anesthesia are signs of irreversible ischemia, and thrombolysis is contraindicated. Patients with acute limb ischemia should undergo emergent evaluation via vascular surgery.

In addition to the routine physical examination, the degree of ischemia can be easily and promptly assessed with the ABI. The ABI is obtained by measuring blood pressure at the ankle and the arm using a conventional blood pressure cuff and Doppler ultrasound (because the pulse frequently is not palpable in this setting); the ankle pressure is then divided by the brachial pressure. A normal ABI value is 1 or slightly above 1, and, in general, an ABI value less than 0.5 is an indication of severe disease. However, results should be interpreted with caution, because these values may not reflect the acuity of

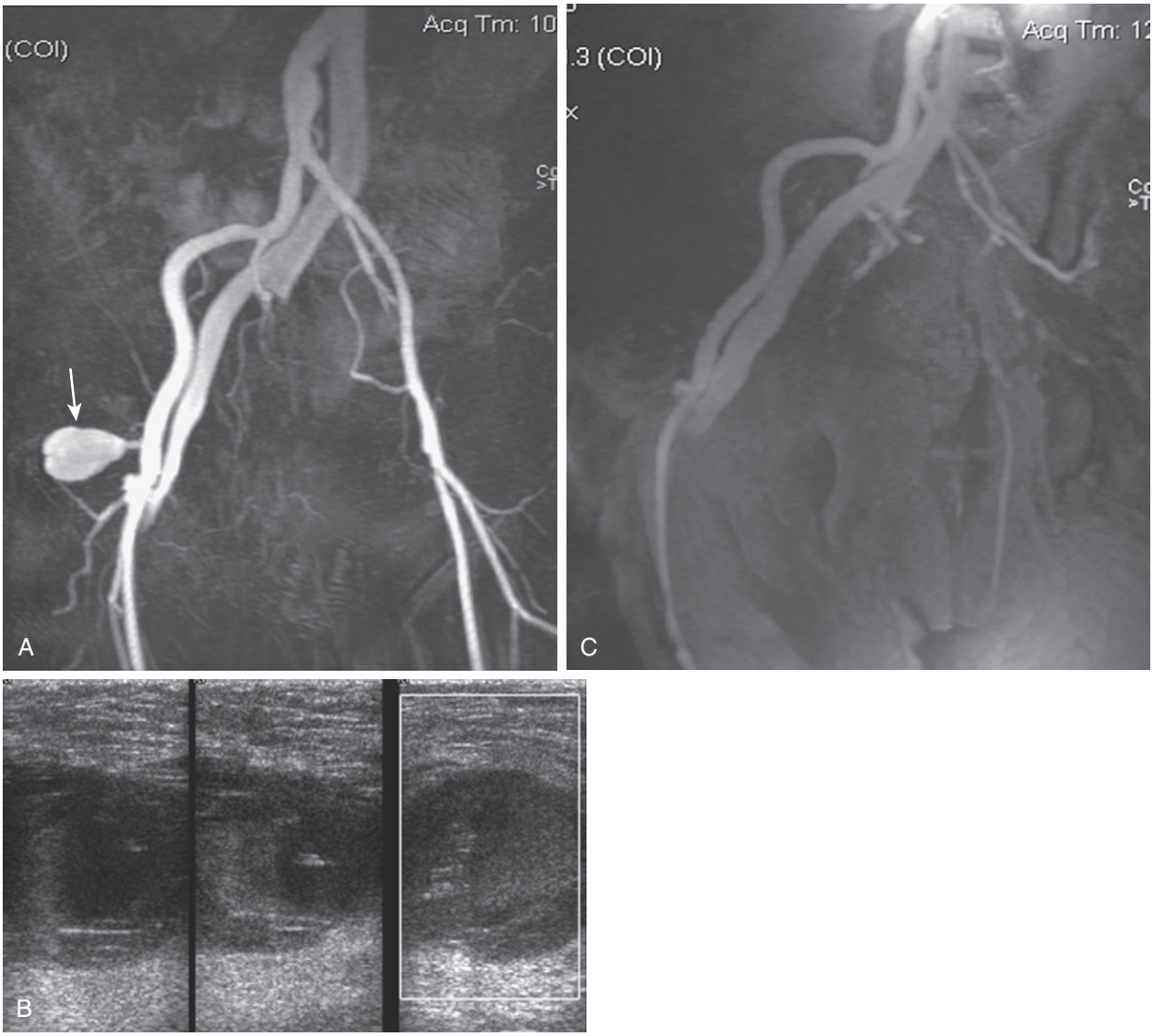


FIGURE 11-38 **A,** Contrast-enhanced magnetic resonance angiography (MRA) demonstrates a large pseudoaneurysm *(arrow)* of the right common femoral artery that occurred as a complication of catheterization for coronary angiography. In addition, prompt enhancement of the common femoral vein, iliac vein, and inferior vena cava is observed consistent with an arteriovenous fistula. **B,** Under ultrasound guidance a 22-gauge needle is advanced into the aneurysm lumen, and thrombin is slowly injected under constant monitoring until complete thrombosis of the sac is achieved. **C,** After thrombin therapy, MRA demonstrates complete thrombosis of the pseudoaneurysm and a persistent arteriovenous fistula.

the condition, and in the setting of small vessel disease (e.g., diabetes), the ABI value may be elevated, giving a false impression of normality.

Patients with critical ischemia due to an embolus or graft thrombosis should undergo immediate surgical exploration for embolectomy or bypass. If an angiography team works in close conjunction with the vascular surgeons, the patient can undergo angiography promptly to determine the site and cause of the occlusion, as well as the presence of distal runoff; the absence of patent distal vasculature decreases the likelihood of successful thrombectomy and thrombolysis might be favored, provided the patient has no signs of irreversible ischemia. Alternatively, if a patient presents with acute ischemia but without limb-threatening signs, the vascular team may opt to administer heparin and perform a more complete but still expeditious diagnostic workup to better plan the therapeutic strategy.

Duplex ultrasound is useful as a primary noninvasive study to determine flow status. The lower extremities are evaluated over the distal external iliac, femoral, popliteal, posterior tibial, and dorsalis pedis arteries. Duplex ultrasound can provide an accurate evaluation of the vasculature and flow pattern using gray scale and color images, as well as analysis of flow velocities and spectral waveforms. MRA and CTA can be used in this situation, but they have drawbacks that must be kept in mind: routine MRI/MRA cannot identify vascular calcifications, and vessel lumen evaluation can be difficult with CTA as well because of artifact in heavily calcified arteries.

Catheter angiography is indicated when emergent surgical revascularization is not required to salvage a viable

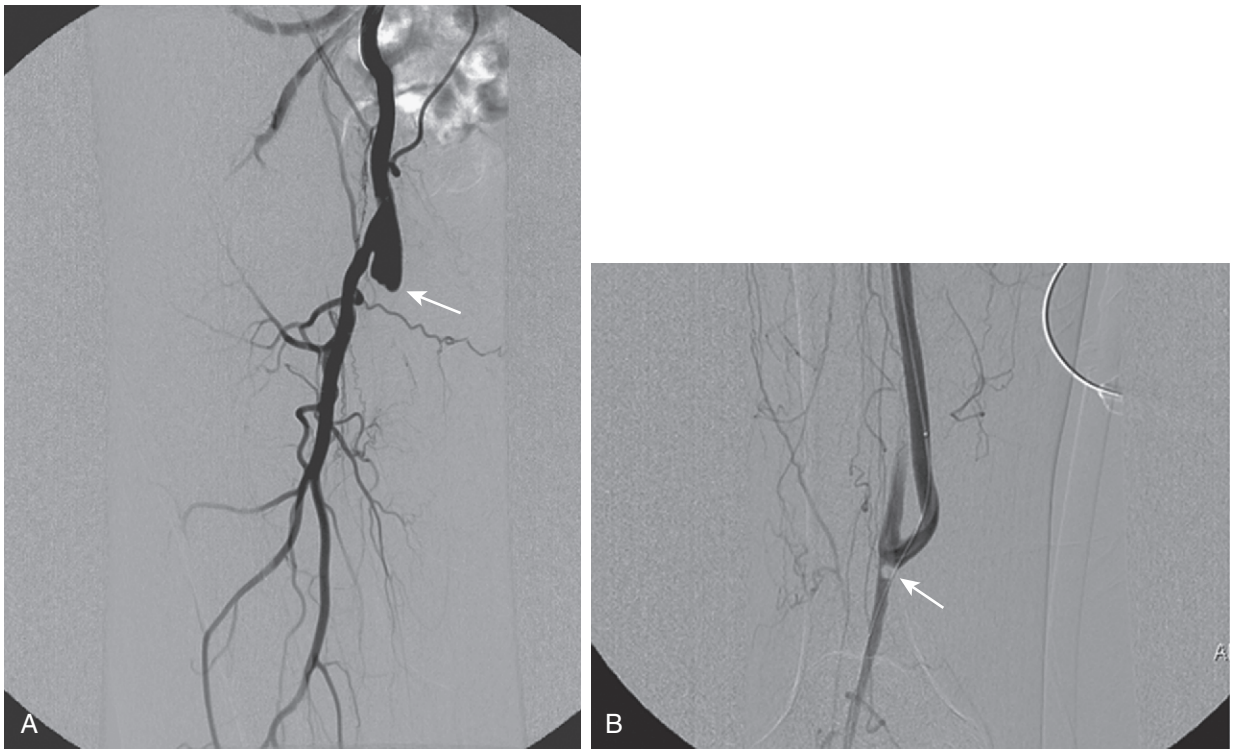


FIGURE 11-39 A patient with a known femoropopliteal bypass who presents with acute limb ischemia. **A,** A selective angiogram confirms a bypass occlusion *(arrow).* The bypass was selectively catheterized and thrombolysis was performed using tissue plasminogen activator via an infusion catheter. **B,** After 24 hours, bypass patency has been reestablished; there is a focal round filling defect in the popliteal artery just distal to the anastomosis *(arrow)*, consistent with the embolus that triggered the graft occlusion and for which further lysis was performed.

BOX 11-7 Major Contraindications for Thrombolysis

Major surgery within the past 2 weeks
Hemorrhagic cerebrovascular accident within the past 2 months
Suspected aortic dissection
Intracranial tumor or arteriovenous malformation
Active internal or gastrointestinal bleeding

BOX 11-8 Relative Contraindications for Thrombolysis

Gastrointestinal bleeding within the past 6 months
Heavy vaginal bleeding
Head injury (e.g., a subdural hematoma) within the previous 4 weeks
Ischemic cerebrovascular accident within the past 2 months
Active ulcer
Severe hypertension
Traumatic cardiopulmonary resuscitation
Pregnancy
Diabetic retinopathy with hemorrhage, retinal neoplasm, or a recent laser procedure
Therapeutic international normalized ratio greater than 3

extremity and is generally reserved for cases in which endovascular intervention is anticipated. The evaluation should include the aortic bifurcation and runoff vessels if CTA or MRA has not been performed. If indicated, thrombolysis can be performed (see Fig. 11-39). Thrombolytic therapy is contraindicated in the presence of an intracranial tumor, recent surgery, intracranial bleed, severe hypertension, bleeding at a noncompressible site, and GI hemorrhage. Contraindications for thrombolysis have been further subdivided into absolute and relative, understanding that clinical judgment for each patient and careful evaluation of the risks and benefits are crucial in the decision-making process (Boxes 11-7 and 11-8). Follow-up angiograms are obtained in patients treated with thrombolytic infusion to reassess patency and determine the underlying cause for the occlusion.

Aneurysms of the Lower Extremities

True aneurysms of the lower extremities are less frequent than AAA. They can be found at the popliteal and common femoral levels and are bilateral in 60% to 70% of patients. Most are degenerative or atherosclerotic in origin and occur in association with AAA in more than 50% of cases. These aneurysms are often asymptomatic and rarely rupture. The most frequent and feared complications are thrombosis and distal embolization. Imaging evaluation should always include the opposite lower extremity and the abdominal aorta. Ultrasound is a useful initial modality, but full characterization with MRA or CTA is often required. Popliteal artery aneurysms usually warrant treatment once they are diagnosed because of the high incidence of distal embolization. Common femoral artery aneurysms are usually treated once they reach a diameter of 2.5 cm. Standard treatment is surgical excision and bypass.

VENOUS EMERGENCIES

Traumatic Injury of the Internal Jugular Vein

As previously mentioned, the traditional approach to surgical exploration of all penetrating neck injuries has greatly evolved in the past few years as a result of, among other reasons, the advent of MDCT. However, it has also remained clear that if these patients are hemodynamically unstable or demonstrate direct signs of vascular trauma such as pulsatile bleeding, pulsatile or expanding hematoma, hematemesis, hemoptysis, stridor, or air leak, they should undergo immediate surgical exploration without imaging workup. When these signs are not present, patients can undergo imaging evaluation. Although both duplex ultrasound and conventional angiography have been used to assess penetrating neck injuries, MD-CTA appears to be the most suitable initial evaluation tool because of its availability, speed, and capability of providing information regarding associated injuries. Internal jugular (IJ) vein injuries occur in 15% to 20% of penetrating neck trauma cases. They can be identified as hematoma surrounding or compressing the jugular vein; an occasional contrast extravasation also can be identified if images are obtained in a delayed phase. This consideration is also important during angiography, where acquisition must be carried into the venous phase if venous injuries are to be identified. In patients who require surgery, ligation and repair of the IJ vein has proved to be of no clinical consequence. In patients with no other indication for emergent surgical exploration, IJ vein injuries identified with MD-CTA have been successfully managed nonoperatively. Endovascular treatment for the management of actively bleeding IJ vein injuries has also been described but is rarely required and remains experimental.

Venous Emergencies of the Chest

Superior vena cava syndrome (SVCS) represents a constellation of signs and symptoms that occur as a consequence of the occlusion of the SVC and constitutes a medical emergency. Clinical manifestations are dramatic and include severe edema and venous distention of the face and upper extremities with facial swelling, headache, impaired vision, nausea, mental status changes, chest pain, orthopnea, cough, hoarseness, and stridor. The syndrome can lead to respiratory failure, brain edema, and death. The SVC is a thin-walled, low-pressure venous structure that can be obstructed by neoplastic invasion associated with intravascular thrombosis or by extrinsic compression alone. More than 80% of cases of SVC syndrome are caused by mediastinal tumors, with bronchogenic carcinomas accounting for 75% to 80% of cases and non-Hodgkin lymphoma accounting for 10% to 15% of cases. Nonmalignant conditions also can cause SVCS, including mediastinal fibrosis (e.g., tuberculosis and histoplasmosis), thrombosis related to central venous catheters (which is becoming more common with the increasing use of catheters for dialysis or other medications), aortic aneurysms, vasculitis, and benign mediastinal tumors such as teratoma, cystic hygroma, and thymoma. Malignant causes of SVCS are predominantly observed in persons aged 40 to 60 years, whereas benign causes account for most of the cases in younger persons. The clinical diagnosis is generally quite apparent. A chest radiograph is the initial modality of choice and generally reveals a widened mediastinum as a result of the presence of an underlying mass. Clues of previous granulomatous infection include parenchymal changes and calcified mediastinal lymph nodes.

Contrast-enhanced CT has the advantage of providing more accurate information on the location and type of obstruction. It also provides information about other critical structures such as the heart, pericardium, and bronchi. MRI and MR venography can delineate the venous system and the areas of obstruction. Direct contrast venography is performed if percutaneous intervention is being considered. In general, patients with SVCS demonstrate significant clinical improvement after treatment with conservative measures such as elevation of the head of the bed and supplemental oxygen. Aggressive emergency treatment is indicated when brain edema or a threatened upper airway is present. Treatment alternatives include radiotherapy, chemotherapy, or both. Radiation therapy successfully palliates SVC obstruction in 70% of patients with lung carcinoma and in more than 95% of patients with lymphoma, even before tumor shrinkage is identified on plain films. Chemotherapy has also proved to be quite effective and may be preferable for patients with chemosensitive tumors.

Venous Emergencies of the Abdomen

Inferior Vena Cava Obstruction

Causes of IVC obstruction can be intrinsic or extrinsic. IVC obstruction most commonly occurs as a result of extension of iliac vein thrombosis and involves predominantly the infrarenal segment. Some conditions that predispose to IVC thrombosis include a central line extending into the IVC, previous surgery, trauma, and the presence of a caval filter. Direct involvement of the IVC lumen can occur by direct invasion of a renal cell carcinoma or hepatocellular carcinoma. Extrinsic obstruction of the IVC causing luminal compression can be caused by hepatomegaly, tumors, massive lymphadenopathy, retroperitoneal fibrosis, or a large AAA.

The clinical presentation of IVC obstruction varies. A slow, progressive occlusion allows for the development of collateral flow, whereas a more acute occlusion causes edema of the lower extremities and even hypotension from decreased blood return. Ultrasonography, CT, and MRI can be useful in identifying IVC occlusion, thrombosis, and extrinsic compression by surrounding structures or tumor (Fig. 11-40). Acute thrombus may appear hyperdense on unenhanced CT. Direct IVC venography is rarely required for diagnosis and is usually obtained only if a filter is being considered or if thrombolysis is to be performed.

The standard treatment of IVC thrombosis is anticoagulation. If pulmonary emboli are a concern (and they usually are), a filter can be placed above the thrombus, usually in the suprarenal segment of the IVC. Catheter-directed thrombolysis also can be performed for rapid relief of symptoms, for prevention of thrombus extension into side branches such as the renal veins, or for prevention of chronic occlusion-related complications. In addition, a stent can be placed if an area of stenosis is identified during thrombolysis.

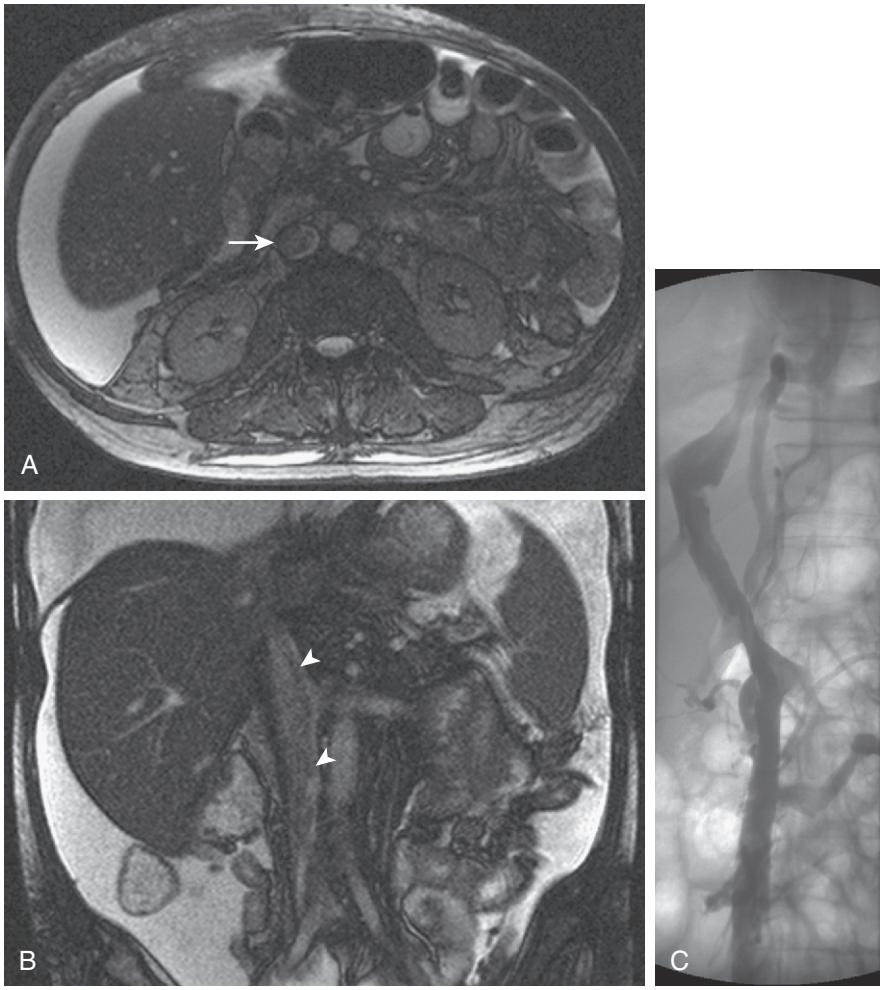


FIGURE 11-40 This patient had worsening ascites and pleural effusion after recent liver transplantation. Magnetic resonance axial (A) and coronal (B) True fast imaging with steady-state precession (true FISP) show a filling defect along the inferior vena cava (IVC) consistent with caval thrombosis (*arrow* in **A** and *arrowheads* in **B**). A large amount of ascites is identified. **C,** After catheter-directed thrombolysis, conventional venography shows a patent IVC with a focal stenosis at the suprahepatic IVC anastomosis site. This stenosis was treated with balloon angioplasty.

Inferior Vena Cava Trauma

Although the IVC is a low-pressure system, injuries can cause significant blood loss, leading to hemodynamic compromise, and more than 50% of patients with a caval injury die before arriving at the hospital. Surgical treatment of IVC injuries is difficult, and intraoperative mortality is high. Whenever possible, supportive management is preferred to promote tamponade of the bleed through constriction by the hematoma and surrounding structures.

Renal Vein Thrombosis

Acute renal vein thrombosis (RVT) is a relatively common complication of nephrotic syndrome (especially when caused by membranous glomerulonephritis) that occurs in as many as 10% of cases. RVT also can develop as a consequence of thrombus extension from the IVC and the iliofemoral veins. Common signs and symptoms include flank pain, hematuria, and impaired renal function; some patients can be asymptomatic. Ultrasound can detect renal vein thrombosis, but visualization can be limited. Confirmation with CT or MRI is useful to further characterize the thrombosis and its extent, but the underlying impairment of renal function may limit the use of intravenous contrast material with both modalities.

Acute bland thrombus usually causes renal vein expansion, lack of enhancement of the renal vein, and asymmetric renal enhancement on the postcontrast images. When renal vein thrombosis is identified, tumor thrombus should be kept in mind as a possible differential diagnosis, but tumor thrombus tends to enhance with use of contrast material.

As with other deep vein thromboses, the standard treatment for RVT is anticoagulation. Systemic thrombolysis also has been described; however, hemorrhagic complications are seen in 15% to 40% of cases, and therefore systemic thrombolysis is not routinely used. Recent studies in patients who presented with symptomatic RVT and renal dysfunction have shown good outcomes with marked improvement of renal function after treatment with catheter-directed thrombolysis and thrombectomy.

Portal Vein Thrombosis

Portal vein thrombosis is often chronic in nature and results from a focal occlusion that leads to the development

of collateral pathways, known as *cavernous transformation of the portal vein*. Eventually, portal hypertension and portosystemic collateral veins develop, which may cause variceal GI bleeding. Acute thrombosis of the portal vein is rare and usually occurs in patients with underlying hypercoagulable states or severe trauma. It may induce thrombosis of the superior mesenteric vein and cause intestinal ischemia. Endovascular recanalization with thrombolysis and thrombectomy can be attempted from a transjugular or transhepatic approach in select cases (Fig. 11-41).

Mesenteric Venous Thrombosis

Acute superior mesenteric vein (SMV) thrombosis is an uncommon and insidious disease that is potentially lethal. Acute mesenteric thrombosis will cause congestion of the bowel wall and may result in intestinal ischemia. Signs and symptoms may overlap with those of many other diseases, and thus diagnosis and treatment can be delayed. Mesenteric venous thrombosis accounts for 5% to 15% of all mesenteric ischemic events. The main predisposing factor is underlying hypercoagulability. Other clinical conditions associated with SMV thrombosis include abdominal trauma, abdominal surgery, pancreatitis, sepsis, portal hypertension, underlying malignancies, and use of estrogens.

Contrast-enhanced MDCT establishes the diagnosis with a sensitivity of 90%. Findings include lack of venous enhancement, expansion of the mesenteric vein, mesenteric stranding, and bowel edema.

In general, anticoagulation is the first line of therapy for SMV thrombosis if no peritoneal signs are present. On the other hand, if signs of peritonitis are present, management should be surgical. The 30-day mortality for SMV thrombosis varies from 15% to 50% with traditional anticoagulation and resection of the infarcted bowel. Catheter-directed thrombolysis also has been proposed as an alternative therapeutic modality.

Hepatic Vein Obstruction

Acute thrombotic occlusion of the main hepatic veins (Budd-Chiari syndrome) can occur as a result of hypercoagulable states, underlying blood dyscrasias, malignancy, oral contraceptive use, or suprahepatic IVC webs. Acute Budd-Chiari syndrome typically causes hepatosplenomegaly,

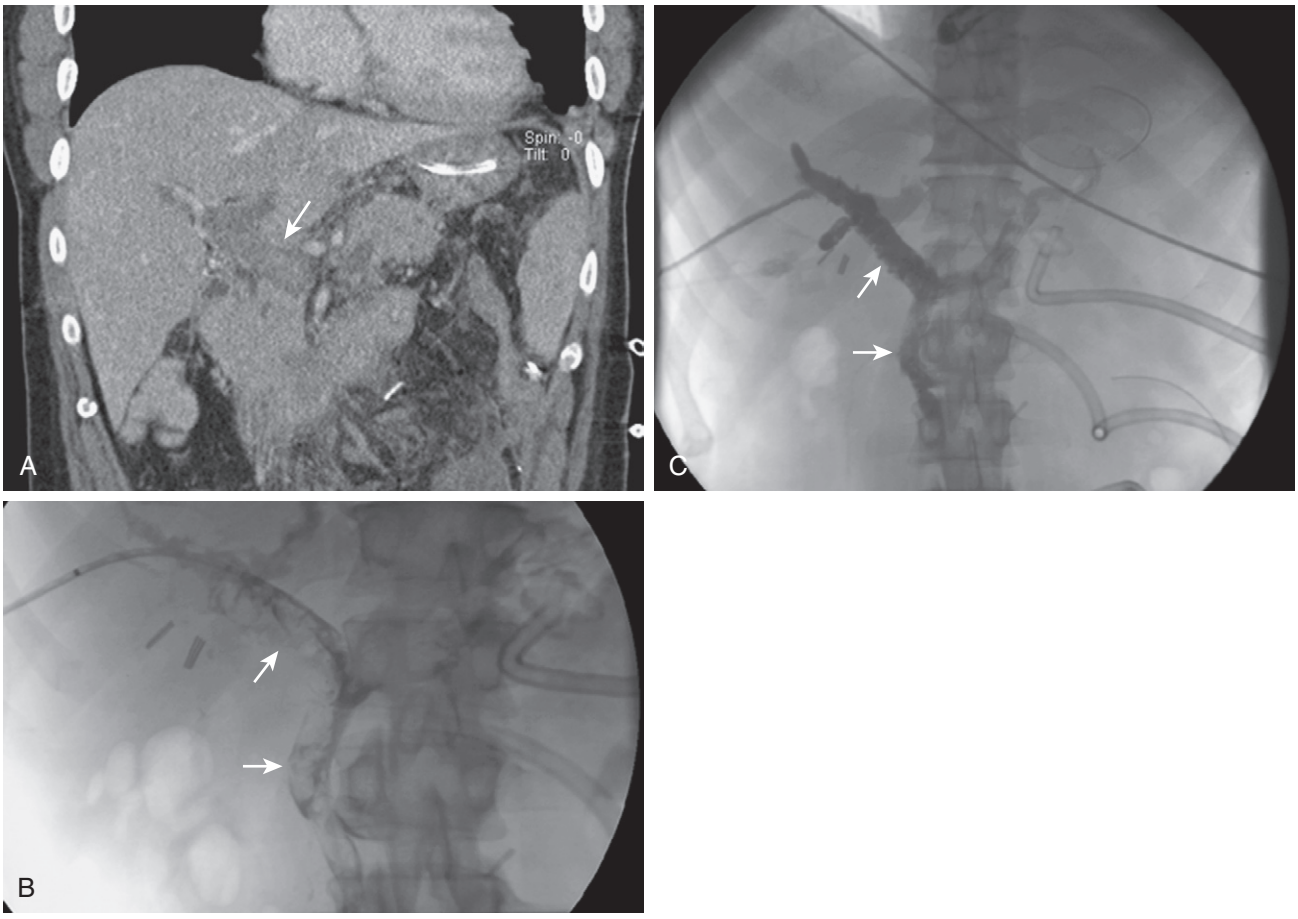


FIGURE 11-41 **A,** A patient with blunt abdominal trauma who subsequently developed bowel ischemia and required extensive bowel resection. Portal vein thrombosis was found on contrast-enhanced computed tomography *(arrow)*. **B,** Using a transhepatic approach, the portal vein was accessed; a portal venogram confirms a large thrombus burden involving the portal vein and superior mesenteric vein *(arrows)*. **C,** After 48 hours of catheter-directed thrombolysis, flow has been reestablished and much of the thrombus has decreased *(arrows)*; anticoagulation therapy was then begun.

abdominal pain, massive ascites, and signs of liver dysfunction. Ultrasound demonstrates absence of flow in the hepatic veins and heterogeneous liver echotexture. CT and MR can identify the lack of enhancement of the hepatic veins and heterogeneous, patchy enhancement of the liver parenchyma ("nutmeg" liver) with sparing of the caudate lobe, which maintains a normal enhancement pattern as a result of its separate, direct drainage into the IVC. Acute occlusion can be treated with catheter-directed or systemic thrombolysis. If a weblike stenosis is identified, angioplasty or stenting can be attempted as well. Chronic anticoagulation is usually required when no underlying anatomic abnormality is identified. Transjugular intrahepatic portosystemic shunt creation is a therapeutic alternative to treat massive ascites resulting from hepatic venous outflow obstruction.

Venous Emergencies of the Upper Extremities

Venous Thrombosis

Acute thrombosis of superficial veins of the upper extremities is a common complication in patients who undergo multiple attempts at intravenous access and in intravenous drug abusers. Central venous catheters are the most common cause of central upper extremity and jugular vein thrombosis, with approximately 50% of patients experiencing some thrombus around the catheter, although fewer than 5% become symptomatic. Upper extremity edema is generally associated with thrombosis of the central veins at the axillary, subclavian, or brachiocephalic levels. Venous expansion can cause dull pain that may extend to the neck if the jugular vein is also involved. The overall rate of pulmonary embolism originating from upper extremity thrombosis is less than 10%; however, 15% to 30% of cases of central upper extremity venous thrombosis may be complicated by pulmonary embolism. Acute thrombosis is characterized by the presence of an intraluminal filling defect that expands the vein and reduces or completely occludes its flow. Ultrasound, CT, and MRI can all demonstrate these changes. Ultrasound is the preferred modality for initial evaluation, but it has limited capability to directly interrogate the central veins, and further evaluation with MR venography or CT with use of contrast material is usually necessary. As with other types of venous thrombosis, treatment usually requires anticoagulation and, in specific cases, thrombolysis.

Thoracic Outlet Syndrome

Venous thoracic outlet syndrome frequently presents first as acute thrombosis of the upper extremity. Frequently an underlying anatomic variant causes central venous obstruction, such an anomalous muscle or ligament or a cervical rib. The term "effort thrombosis" or *Paget-Schroetter syndrome* is essentially the same phenomenon of subclavian vein thrombosis occurring in athletic patients, probably as a result of repetitive venous compression secondary to muscle training and hypertrophy. The stenosis induced by progressive intimal hyperplasia leads to the development of collateral flow. Pulmonary embolus is infrequent because the underlying condition is a fixed venous stenosis. Evaluation with ultrasound is helpful in demonstrating the thrombus, but further assessment with CT or MRI can demonstrate the underlying anomaly, the extent of the occlusion, and the amount of collateral flow. Venograms are generally reserved for patients undergoing evaluation for thrombolysis, which is frequently effective in controlling the symptoms and revealing the underlying venous lesion. Patients can then undergo surgical decompression, and further catheter interventions such as balloon venoplasty and stenting are reserved for a significant residual or recurrent postsurgical stenosis.

Venous Emergencies of the Pelvis and Lower Extremities

Deep venous thrombosis (DVT) of the lower extremities is a common disorder. Predisposing factors include immobilization, previous DVT, previous surgery (e.g., orthopedic surgery of the pelvis or knee and neurosurgical procedures), hypercoagulability syndromes, use of central venous catheters, use of oral contraceptives, iliac vein compression (May-Thurner syndrome or pelvic tumors), and use of IVC filters. Thrombosis originates more frequently in the calf veins, which are involved in more than 90% of cases. Approximately 25% to 50% progress centrally toward the thigh and pelvis. Thrombosis of the iliac veins is identified and is usually a result of extension of a more distal thrombus. Acute DVT presents with lower extremity edema, congestion, and pain. Pulmonary embolism can occur in up to 50% of patients. The risk of embolism is much higher when the DVT extends above the popliteal vein. Clinically, acute DVT can be difficult to differentiate from entities such as cellulitis, a ruptured Baker cyst, superficial thrombophlebitis, chronic thrombosis, venous insufficiency, and other entities causing lower extremity edema. Serum d-dimer has become a popular screening test with a high negative predictive value when results are within normal limits. However, the specificity of this test is limited, and imaging is usually required to confirm the diagnosis. Ultrasound is by far the most frequently used imaging technique to identify lower extremity DVT, with sensitivity and specificity for detection of thrombus at the popliteal level and above higher than 95%. These numbers drop to 80% for veins in the calf region. Noncompressibility of the affected vein remains the single most reliable diagnostic criterion. Additional criteria include intraluminal thrombus visualization, vein enlargement, absent color flow signal, absent Doppler signal, absent respiratory variation and augmentation, and absent response to the Valsalva maneuver.

The widespread use of CT to identify pulmonary emboli has led researchers to look for DVT during the same examination. Results demonstrate that thrombus can be identified in up to 10% of the lower extremity and pelvis scans obtained during the venous phase of enhancement of pulmonary CTA. MR venography has a sensitivity and specificity greater than 95% for the detection of DVT; however, its current use in the acute setting remains limited (Fig. 11-42). Conventional catheter venography has been practically abandoned for the diagnosis of DVT. Today, catheter venography is used only in patients who represent a diagnostic dilemma or in those who require a therapeutic intervention. Thrombi are seen as filling defects outlined by contrast material. Differentiation of acute and chronic DVT sometimes can be challenging, but the presence of collateral veins is a helpful sign of

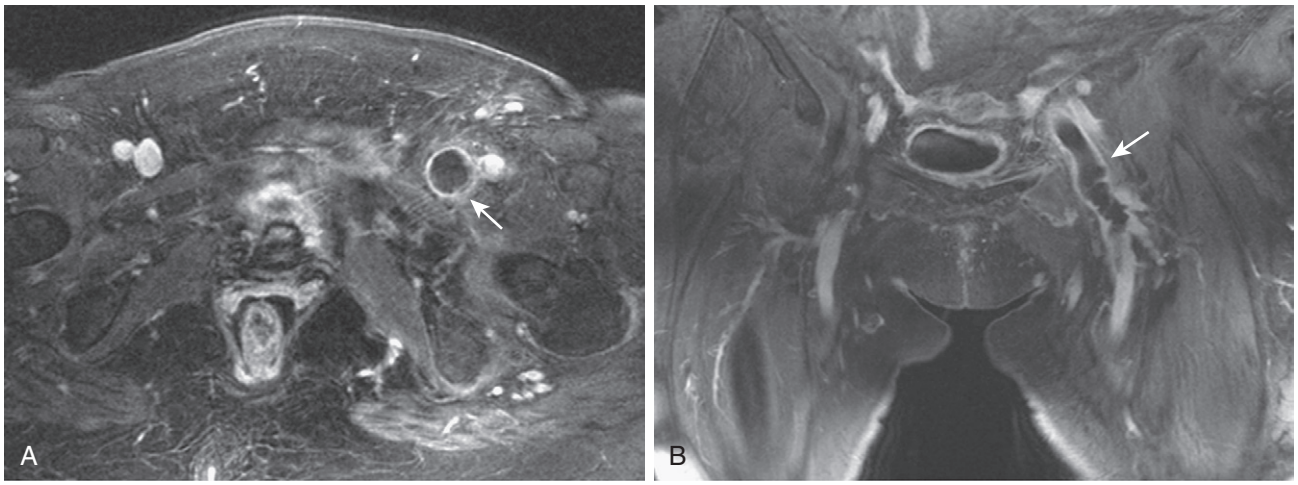


FIGURE 11-42 **A** and **B,** Axial and coronal fat-suppressed, contrast-enhanced, magnetic resonance venography images show a large filling defect in the left common femoral and external iliac veins *(arrows)* with contrast material surrounding the thrombus and venous enlargement consistent with acute deep vein thrombosis. Because of severe lower extremity edema and functional impairment, the patient subsequently underwent treatment with catheter-directed thrombolysis.

chronicity. The traditional treatment of acute DVT is anticoagulation to prevent extension of the thrombus while the endogenous mechanisms progressively lyse the clot and reestablish patency. With this approach, complete resolution of the thrombosis is achieved in up to 50% of cases. Thrombolysis and mechanical thrombectomy can be performed as well. The principle is to macerate the thrombus to expose greater portions of the thrombus to the lytic agent and at the same time facilitate its removal or breakdown by endogenous mechanisms. The great majority of patients have prompt relief of their symptoms, and venous patency at 1 year is maintained in more than 70% of patients. Thrombolytic therapy has many contraindications, mostly involving factors that increase the risk of serious bleeding, such as recent surgery, upper GI bleeding, recent CVA, and a central nervous system tumor or trauma. Bleeding requiring transfusion was reported in 11% of patients in the national venous thrombolysis registry, and the rate of intracranial bleeding was only 0.2%. Venous stent placement after venous thrombolysis is usually reserved for patients with underlying stenosis of a large vein.

SUGGESTED READINGS

AbuRahma AF. Fate of endoleaks detected by CT angiography and missed by color duplex ultrasound in endovascular grafts for abdominal aortic aneurysms. *J Endovasc Ther*. 2006;13:90–95.

Ahrar K, Smith DC, Bansal RC, et al. Angiography in blunt thoracic aortic injury. *J Trauma*. 1997;42:665–669.

Al-Bahrani AZ, Abid GH, Sahgal E, et al. A prospective evaluation of CT features predictive of intra-abdominal hypertension and abdominal compartment syndrome in critically ill surgical patients. *Clin Radiol*. 2007;26:676–682.

Asensio JA, Chahwan S, Hanpeter D, et al. Operative management and outcome of 302 abdominal vascular injuries. *Am J Surg*. 2000;180:528–534.

Atar E, Belenky A, Hadad M, et al. MR Angiography for abdominal and thoracic aortic aneurysms: assessment before endovascular repair in patients with impaired renal function. *AJR Am J Roentgenol*. 2006;186:386–393.

Attia C, Villard J, Boussel L, et al. Endovascular repair of localized pathological lesions of the descending thoracic aorta: midterm results. *Cardiovasc Intervent Radiol*. 2007;30:628–637.

Berthet JP, Marty-Ane CH, Veerapen R, et al. Dissection of the abdominal aorta in blunt trauma: endovascular or conventional surgical management? *J Vasc Surg*. 2003;38:997–1004.

Bhalla S, Menias CO, Heiken JP. CT of acute abdominal aortic disorders. *Radiol Clin North Am*. 2003;41:153–169.

Biffi WL, Ray Jr CE, Moore EE, et al. Noninvasive diagnosis of blunt cerebrovascular injuries: a preliminary report. *J Trauma*. 2002;53:850–856.

Bolognesi R, Manca C, Tsialtas D, et al. Aortic intramural hematoma: an increasingly recognized aortic disease. *Cardiology*. 1998;89:178–183.

Branchereau A, Jacobs M, eds. *Vascular Emergencies*. Elmsford, NY: Wiley-Blackwell; 2003.

Brandt M, Walluscheck KP, Jahnke T, et al. Endovascular repair of ruptured abdominal aortic aneurysm: feasibility and impact on early outcome. *Vasc Interv Radiol*. 2005;16:1309–1312.

Castaner E, Andreu M, Gallardo X, et al. CT in nontraumatic acute thoracic aortic disease: typical and atypical features and complications. *Radiographics*. 2003; 23(suppl):S93–S110.

Chan FY, Crawford ES, Coselli JS, et al. In situ prosthetic graft replacement of mycotic aneurysm of the aorta. *Ann Thorac Surg*. 1989;47:193–203.

Demers P, Miller DG, Mitchell RS, et al. Stent-graft repair of penetrating atherosclerotic ulcers in the descending thoracic aorta: mid-term results. *Ann Thorac Surg*. 2004;77:81–86.

Deree J, Shenvi E, Fortlage D, et al. Patient factors and operating room resuscitation predict mortality in traumatic abdominal aortic injury: a 20-year analysis. *J Vasc Surg*. 2007;3:493–497.

Dogra VS, Bhatt S, eds. *Emergency Cross-Sectional Imaging*. Philadelphia, PA: Elsevier Saunders; 2007.

Dyer S, Moore EE, Ilke DN, et al. Thoracic aortic injury: how predictive is mechanism and is chest computed tomography a reliable screening tool? A prospective study of 1,561 patients. *J Trauma*. 2000;48:673–683.

Evangelista A, Mukherjee D, Mehta RH, et al. Acute intramural hematoma of the aorta: a mystery in evolution. *Circulation*. 2005;111:1063–1070.

Faggioli G, Stella A, Freyrie A, et al. Early and long-term results in the surgical treatment of juxtarenal and pararenal aortic aneurysms. *Eur J Vasc Endovasc Surg*. 1988;15:205–211.

Fang JF, Wong YC, Lin BC, et al. Usefulness of multidetector computed tomography for the initial assessment of blunt abdominal trauma patients. *World J Surg*. 2006;30:176–182.

Farber A, Wagner WH, Cossman DV, et al. Isolated dissection of the abdominal aorta: clinical presentation and therapeutic options. *J Vasc Surg*. 2002;36:205–210.

Fattori R, Napoli G, Lovato L, et al. Descending thoracic aortic disease: stent-graft repair. *Radiology*. 2003;229:176–183.

Federle MP, Pan KT, Pealer KM. CT criteria for differentiating abdominal hemorrhage: anticoagulation or aortic aneurysm rupture? *AJR Am J Roentgenol*. 2007;188:1324–1330.

Fishman JE. Imaging of blunt aortic and great vessel trauma. *J Thorac Imaging*. 2000;15:97–103.

Fishman JE, Nunez Jr D, Kane A, et al. Direct versus indirect signs of traumatic aortic injury revealed by helical CT: performed characteristics and interobserver agreement. *AJR Am J Roentgenol*. 1999;172:1027–1031.

Forman M, Mirvis S, Hollander D. Blunt thoracic aortic injuries: CT characterization and treatment outcomes of minor injury. *Eur Radiol*. 2013;23:2988–2995.

García-Blázquez V, Vicente-Bártulos A, Olavarria-Delgado A, et al. Accuracy of CT angiography in the diagnosis of acute gastrointestinal bleeding: systematic review and meta-analysis. *Eur Radiol*. 2013;23:1181–1190.

Garzon G, Fernandez-Velilla M, Marti M, et al. Endovascular stent-graft treatment of thoracic aortic disease. *Radiographics*. 2005;25(suppl):S229–S244.

Gavant ML. Helical CT grading of traumatic aortic injuries: impact on clinical guidelines for medical and surgical management. *Radiol Clin North Am*. 1999;37: 553–573.

Görich J, Asquan Y, Seifarth H, et al. Initial experience with intentional stent-graft coverage of the subclavian artery during endovascular thoracic aortic repairs. *J Endovasc Ther*. 2002;9(suppl 2):II-39–II-43.
Gunn M, Campbell M, Hoffer EK. Traumatic abdominal aortic injury treated by endovascular stent placement. *Emerg Radiol*. 2007;13:329–331.
Gunn M, Lehnert B, Lungren R, et al. Minimal aortic injury of the thoracic aorta: imaging appearances and outcome. *Emerg Radiol*. 2014;21:227–233.
Hallet JW. Splenic artery aneurysms. *Semin Vasc Surg*. 1995;8:321–326.
Halliday KE, al-Kutoubi A. Draped aorta: CT sign of contained leak of aortic aneurysms. *Radiology*. 1996;199:1–3.
Hellmann DB, Grand DJ, Freischlag JA. Inflammatory abdominal aortic aneurysm. *JAMA*. 2007;297:395–400.
Hermsen K, Chong WK. Ultrasound evaluation of abdominal aortic and iliac aneurysms and mesenteric ischemia. *Radiol Clin North Am*. 2004;42:365–381.
Hillemanns P, Knitza R, Muller-Hocker J. Rupture of splenic artery aneurysm in a pregnant patient with portal hypertension. *Am J Obstet Gynecol*. 1996;174: 1665–1666.
Hirsch AT, Haskal ZJ, Hertzer NR, et al. ACC/AHA 2005 practice guidelines for the management of patients with peripheral arterial disease (lower extremity, renal, mesenteric, and abdominal aortic): a collaborative report. *Circulation*. 2006;113:e463–e654.
Hollerman JJ, Fackler ML, Coldwell DM, Ben-Menachem Y. Gunshot wounds: 2. Radiology. *AJR Am J Roentgenol*. 1990;155:691–702.
Hovsepian DM, Hein AN, Pilgram TK, et al. Endovascular abdominal aortic aneurysm repair in 144 patients: correlation of aneurysm size, proximal aortic neck length, and procedure-related complications. *J Vasc Interv Radiol*. 2001;12:1373–1382.
Inaba K, Munera F, McKenney MG, et al. The nonoperative management of penetrating internal jugular vein injury. *J Vasc Surg*. 2006;43:77–80.
Ishida M, Kato N, Hirano T, et al. Endovascular stent-graft treatment for thoracic aortic aneurysms: short- to midterm results. *J Vasc Interv Radiol*. 2004;15:361–367.
Isselbacher EM. Thoracic and abdominal aortic aneurysms. *Circulation*. 2005;15(111):16–28.
Iyer VS, MacKenzie KS, Tse LW, et al. Early outcomes after elective and emergent endovascular repair of the thoracic aorta. *J Vasc Surg*. 2006;43:677–683.
Kaji S, Nishigami K, Akasaka T, et al. Prediction of progression or regression of type A aortic intramural hematoma by computed tomography. *Circulation*. 1999;100(suppl 2):II-281–II-286.
Kasirajan K, Heffernan D, Langsfeld M. Acute thoracic aortic trauma: a comparison of endoluminal stent grafts with open repair and nonoperative management. *Ann Vasc Surg*. 2003;17:589–595.
Kaufman JA, Lee MJ. *Vascular and Interventional Radiology: The Requisites*. Philadelphia, PA: Elsevier; 2004.
Kerwin AJ, Bynoe RP, Murray J, et al. Liberalized screening for blunt carotid and vertebral artery injuries is justified. *J Trauma*. 2001;51:308–314.
Kieffer E, Bahnini A, Koskas F, et al. In situ allograft replacement of infected infrarenal aortic prosthetic graft: results in forty-five patients. *J Vasc Surg*. 1993;17:349–356.
Kim HS, Fine DM, Atta MG. Catheter-directed thrombectomy and thrombolysis for acute renal vein thrombosis. *J Vasc Interv Radiol*. 2006;17:815–822.
Kim HS, Patra A, Khan J, et al. Transhepatic catheter-directed thrombectomy and thrombolysis of acute superior mesenteric venous thrombosis. *J Vasc Interv Radiol*. 2005;16:1685–1691.
Laffargue G, Taourel P, Saguintaah M, et al. CT diagnosis of abdominal compartment syndrome. *AJR Am J Roentgenol*. 2002;178:771–772.
Laing CJ, Tobias T, Rosenblum DI, et al. Acute gastrointestinal bleeding: emerging role of multidetector CT angiography and review of current imaging techniques. *Radiographics*. 2007;27:1055–1070.
Lamah M, Darke S. Value of routine computed tomography in the preoperative assessment of abdominal aneurysm replacement. *World J Surg*. 1999;23: 1076–1080. discussion 1080-1081.
LaRoy LL, Cormier PJ, Matalon TA, et al. Imaging of abdominal aortic aneurysms. *AJR Am J Roentgenol*. 1989;152:85–92.
LeBlang SD, Dolich MO. Imaging of penetrating thoracic trauma. *J Thorac Imaging*. 2000;15:28–35.
Lettinga-van de Poll T, Schurink GW, De Hann MW, et al. Endovascular treatment of traumatic rupture of the thoracic aorta. *Br J Surg*. 2007;94:525–533.
Levy JR, Heiken JP, Gutierrez FR. Imaging of penetrating atherosclerotic ulcers of the aorta. *AJR Am J Roentgenol*. 1999;173:151–154.
Lohan DG, Saleh R, Nael K, et al. Contrast-enhanced MRA versus nonenhanced MRA: pros and cons. *Appl Radiol*. 2007;36(suppl):S3–S15.
Makaroun MS, Dillavou ED, Kee ST, et al. Endovascular treatment of thoracic aortic aneurysms: results of the phase II multicenter trial of the GORE TAG thoracic endoprosthesis. *J Vasc Surg*. 2005;41:1–9.
Manghat NE, Morgan-Hughes GJ, Roobottom CA. Multi-detector row computed tomography: imaging in acute aortic syndrome. *Clin Radiol*. 2005;60:256–267.
Mark A, LePage MA, Quint LE, Sonnad SS. Aortic dissection: CT features that distinguish true lumen from false lumen. *AJR Am J Roentgenol*. 2001;177:207–211.
Marti M, Artigas JM, Garzon G, et al. Acute lower intestinal bleeding: feasibility and diagnostic performance of CT angiography. *Radiology*. 2012;262:109–116.
Mattox KL. Injury to the thoracic great vessels. In: Moore EE, Mattox KL, Feliciano DV, eds. *Trauma*. 2nd ed. Norwalk, CT: Appleton & Lange; 1991:393.
May J, White GH, Waugh R, et al. Improved survival after endoluminal repair with second-generation prostheses compared with open repair in the treatment of abdominal aortic aneurysms: a 5-year concurrent comparison using life table method. *J Vasc Surg*. 2001;33(suppl 2):S21–S26.
McKenney KL, McKenney MG, Cohn SM, et al. Hemoperitoneum score helps determine need for therapeutic laparotomy. *J Trauma*. 2001;50:650–654.
Miller LA, Shanmuganathan K. Multidetector CT evaluation of abdominal trauma. *Radiol Clin North Am*. 2005;43:1079–1095.
Mirvis SE, Shanmuganathan K, Miller BH, et al. Traumatic aortic injury: diagnosis with contrast-enhanced thoracic CT—five-year experience at a major trauma center. *Radiology*. 1996;200:13–22.
Moizumi Y, Komatsu T, Motoyoshi N, Tabayashi K. Clinical features and long-term outcome of type A and type B intramural hematoma of the aorta. *J Thorac Cardiovasc Surg*. 2004;127:421–427.
Munera F, Soto JA, Palacio D, et al. Diagnosis of arterial injuries caused by penetrating trauma to the neck: comparison of helical CT angiography and conventional angiography. *Radiology*. 2000;216:356–362.
Munera F, Soto JA, Palacio D, et al. Penetrating neck injuries: helical CT angiography for initial evaluation. *Radiology*. 2002;224:366–372.
Nienaber CA, Kische S, Ince H. Thoracic aortic stent-graft devices: problems, failure modes, and applicability. *Semin Vasc Surg*. 2007;20:1–9.
Noel AA, Gloviczki P, Cherry Jr KJ, et al. Ruptured abdominal aortic aneurysms: the excessive mortality rate of conventional repair. *J Vasc Surg*. 2001;34:41–46.
O'Sullivan GJ, Lohan DG, Gough N, et al. Pharmacomechanical thrombectomy of acute deep vein thrombosis with the trellis-8 isolated thrombolysis catheter. *J Vasc Interv Radiol*. 2007;18:715–724.
Pamela T, Johnson PT, Chen JK, Loey BL. Loeys-Dietz syndrome: MDCT angiography findings. *AJR Am J Roentgenol*. 2007;189:29–35.
Parellada JA, Palmer J, Monill JM, et al. Mycotic aneurysm of the abdominal aorta: CT findings in three patients. *Abdom Imaging*. 1997;22:321–324.
Patel NH, Stephens KE, Mirvis SE, et al. Imaging of acute thoracic aortic injury due to blunt trauma: a review. *Radiology*. 1998;209:335–348.
Pauls S, Orend KH, Sunder-Plassmann L, et al. Endovascular repair of symptomatic penetrating atherosclerotic ulcer of the thoracic aorta. *Eur J Vasc Endovasc Surg*. 2007;34:66–73.
Peterson AH, Williams DM, Rodrigues JL, Francis IR. Percutaneous treatment of a traumatic aortic dissection by balloon fenestration and stent placement. *AJR Am J Roentgenol*. 1995;164:1274–1276.
Picard E, Marty-Ane CH, Vernhet H, et al. Endovascular management of traumatic infrarenal abdominal aortic dissection. *Ann Vas Surg*. 1998;12:515–521.
Pickhard PJ, Shimony JS, Heiken JP, et al. The abdominal compartment syndrome: CT findings. *AJR Am J Roentgenol*. 1999;173:575–579.
Quint LE, Williams DM, Francis IR, et al. Ulcerlike lesions of the aorta: imaging features and natural history. *Radiology*. 2001;218:719–723.
Rakita D, Newatia A, Hines JJ, et al. Spectrum of CT findings in rupture and impending rupture of abdominal aortic aneurysms. *Radiographics*. 2007;27:497–507.
Rivas LA, Munera F, Fishman JE. Multidetector-row computerized tomography of aortic injury. *Semin Roentgenol*. 2006;41:26–36.
Saletta S, Lederman E, Fein S, et al. Transesophageal echocardiography for the initial evaluation of the widened mediastinum in trauma patients. *J Trauma*. 1995;39:137–142. discussion 141-142.
Sanchez-Ross M, Anis A, Walia J, et al. Aortic rupture: comparison of three imaging modalities. *Emerg Radiol*. 2006;13:31–33.
Schoder M, Grabenwoger M, Holzenbein T, et al. Endovascular stent-graft repair of complicated penetrating atherosclerotic ulcers of the descending thoracic aorta. *J Vasc Surg*. 2002;36:720–726.
Schwartz SA, Taljanovic MS, Smyth S, et al. CT findings of rupture, impending rupture, and contained rupture of abdominal aortic aneurysms. *AJR Am J Roentgenol*. 2007;188:W57–W62.
Sebastià C, Pallisa E, Quiroga S, et al. Aortic dissection: diagnosis and follow-up with helical CT. *Radiographics*. 1999;19:45–60.
Shanmuganathan K. Multi-detector row CT imaging of blunt abdominal trauma. *Semin Ultrasound CT MR*. 2004;25:180–204.
Shanmuganathan K, Mirvis SE, Sover ER. Value of contrast-enhanced CT in detecting active hemorrhage in patients with blunt abdominal and pelvic trauma. *AJR Am J Roentgenol*. 1993;161:5–9.
Shiga T, Wajima Z, Apfel CC, et al. Diagnostic accuracy of transesophageal echocardiography, helical computed tomography, and magnetic resonance imaging for suspected thoracic aortic dissection. *Arch Intern Med*. 2006;166:1350–1356.
Sicard GA, Zwolak RM, Sidawy AN, et al. Endovascular abdominal aortic aneurysm repair: long-term outcome measures in patients at high risk for open surgery. *J Vasc Surg*. 2006;44:229–236.
Sommer T, Fehske W, Holzknecht N, et al. Aortic dissection: a comparative study of diagnosis with spiral CT, multiplanar transesophageal echocardiography, and MR imaging. *Radiology*. 1996;199:347–452.
Soto JA, Munera F, Cardoso N, et al. Diagnostic performance of helical CT angiography in trauma to large arteries of the extremities. *J Comput Assist Tomogr*. 1999;23:188–196.
Soto JA, Munera F, Morales C, et al. Focal arterial injuries of the proximal extremities: helical CT arteriography as the initial method of diagnosis. *Radiology*. 2001;218:188–194.
Stone DH, Brewster DC, Kwolek CJ. Stent-graft versus open-surgical repair of the thoracic aorta: mid-term results. *J Vasc Surg*. 2006;44:188–197.
Suzuki T, Mehta RH, Ince H, et al. Clinical profiles and outcomes of acute type B aortic dissection in the current era: lessons from the International Registry of Aortic Dissection (IRAD). *Circulation*. 2003;108(suppl 2):II-312–II-317.
Symbas PN, Sherman AJ, Silver JM, et al. Traumatic rupture of the aorta: immediate or delayed repair? *Ann Surg*. 2002;235:796–802.
Tespili M, Banfi C, Valsecchi O, et al. Endovascular treatment of thoracic aortic disease: mid-term follow-up. *Catheter Cardiovasc Interv*. 2007;70:595–601.
Teufelsbauer H, Polterauer P, Lammer J, et al. Repair of abdominal aortic aneurysms: the benefits of offering both endovascular and open surgical techniques. *Perspect Vasc Surg Endovasc Ther*. 2006;18:238–246.

Thanila A, Macedo TA, Stantson AW, Oderich GS. Infected aortic aneurysms: imaging findings. *Radiology*. 2004;231:250–257.

Thomas TT, Evangelist A, Nienaber CA, et al. Long-term survival in patients presenting with type A acute aortic dissection: insights from the International Registry of Acute Aortic Dissection (IRAD). *Circulation*. 2006;114: 350–356.

Tsai TT, Nienaber CA, Eagle KA. Acute aortic syndromes. *Circulation*. 2005;112: 3802–3813.

Veith FJ, Baum RA, Ohki T, et al. Nature and significance of endoleaks and endotension: summary of opinions expressed at an international conference. *J Vasc Surg*. 2002;35:1029–1035.

Vernhet H, Marty-Ane CH, Lesnik A, et al. Dissection of the abdominal aorta in blunt trauma: management by percutaneous stent placement. *Cardiovasc Intervent Radiol*. 1997;20:473–476.

von Kodolitsch Y, Nienaber CA, Dieckmann C, et al. Chest radiography for the diagnosis of acute aortic syndrome. *Am J Med*. 2004;116:73–77. A-40.

Weigel S, Tombach B, Waintz D, et al. Thoracic aortic stent graft: comparison of contrast-enhanced MR angiography and CT angiography in the follow-up: initial results. *Eur Radiol*. 2003;13:1628–1634.

White GH, Yu W, May J, et al. Endoleak as a complication of endoluminal grafting of abdominal aortic aneurysms: classification, incidence, diagnosis, and management. *J Endovasc Surg*. 1997;4:152–168.

Willens HJ, Kessler KM. Transesophageal echocardiography in the diagnosis of diseases of the thoracic aorta: Part 1. Aortic dissection, aortic intramural hematoma, and penetrating atherosclerotic ulcer of the aorta. *Chest*. 1999;116:772–779.

Won JY, Lee DY, Shim WH, et al. Elective endovascular treatment of descending thoracic aortic aneurysms and chronic dissections with stent-grafts. *J Vasc Interv Radiol*. 2001;12:575–582.

Yang CY, Liu KL, Lee CW, et al. Mycotic aortic aneurysm presenting initially as an aortic intramural air pocket. *AJR Am J Roentgenol*. 2005;185:463–465.

Yeh TS, Jan YY, Jeng LB, et al. Massive extra-enteric gastrointestinal hemorrhage secondary to splanchnic artery aneurysms. *Hepatogastroenterology*. 1997;44:1152–1156.

Chapter 12

Emergency Nuclear Radiology

Anna K. Chacko and Rashmikant B. Shah

Advances in the understanding and knowledge of disease and the development of newer treatment methods, along with the increasing skill of health care providers and their expanding ability to treat disease, have made medicine a rapidly expanding frontier. The increasing availability of multiple modes of transport and increasing mobility, an aging population, armed conflicts worldwide, increasing communicability and spread of disease, and complications from complex medical and/or surgical interventions have all combined to increase the incidence of emergency medical situations. Timely intervention could, in most instances, halt or forestall dangerous disease conditions, which has required increasing support of imaging services to diagnose disease and evaluate the efficacy of treatment.

The staple of imaging support has long been conventional radiography. However, newer modalities have made inroads into the use of plain film. These modalities are interventional radiology, computed tomography (CT), magnetic resonance imaging (MRI), ultrasound, and nuclear medicine.

The development and refinement of CT, MRI, and ultrasound to bring superlative anatomic resolution, as well as their ease of access and availability, have produced changes in the utility and utilization of nuclear medicine in the arena of emergency medicine.

Significant delays in the acquisition of nuclear medicine images are imposed by the incorporation/inclusion of the radiopharmaceutical agent into a metabolic/functional process. This delay places nuclear medicine imaging at a disadvantage and delegates it to the position of being a second-line study in most instances. To assess the use of a nuclear medicine procedure, it is helpful to review the advantages and disadvantages of the modality, which can be accomplished by assessing the characteristics of the modality using a SWOT (strength, weaknesses, opportunities, and threats) overview:

- The strength of nuclear medicine imaging lies in the ability to analyze and evaluate physiologic processes and, thereby, function. Nuclear medicine procedures allow imaging of physiologic or pathophysiologic processes that generally have long turnover cycles. However, emergency situations develop rapidly and must be resolved rapidly, which restricts the use of nuclear medicine imaging to a select few situations.
- Some pathologic processes, such as gastrointestinal (GI) bleeding, occur intermittently or sporadically. Nuclear medicine imaging procedures are advantageous in such instances because they do not add further radiation exposure with repeated and or delayed imaging.
- Nuclear medicine procedures provide invaluable sensitivity and specificity. Scintigraphic techniques are inherently exquisitely sensitive. Metabolic changes invariably precede the appearance of anatomic changes. This feature is fundamental to nuclear medicine and consequently provides the information sought much earlier along the course of the disease.
- Scintigraphy highlights disease in an entire organ system, such as in skeletal scanning. This property is not easily obtained with other modalities. For example, with bone scanning, scintigraphy provides the ability to assess the skeletal system without additional radiation, allowing detection of unsuspected distant metastases, metabolic bone disease, and nonaccidental injuries (as in child abuse).
- Scintigraphy offers a high signal-to-noise ratio. The accumulation of the administered radiopharmaceutical agent in an area of disease (such as in bone turnover) or its conspicuous absence from a normal physiologic process (such as with pulmonary emboli in pulmonary vasculature) utilizes this characteristic effectively.
- Nuclear medicine procedures provide an alternative when other procedures are contraindicated, as in patients with compromised renal function or in patients with sensitivity to contrast material.
- Flow and/or perfusion studies followed by delayed static images are achieved with relative ease and without the use of additional radiation, as is well illustrated in the evaluation of osteomyelitis.
- The portability of a gamma camera is a great asset when performing imaging of patients in an intensive care unit, when transportation may be logistically challenging.

A similar SWOT analysis of other modalities such as sonography, CT, angiography, or MRI also may be of some value:

- CT and MRI offer superlative spatial resolution that cannot be achieved with scintigraphy.
- CT and MRI allow the visualization of structures in the proximity of the area of concern. For example, in the setting of trauma, the development of surgical complications such as biliary leakage and abscess formation allow the radiologist to view other or adjacent organs.
- Sonography is an extremely useful modality because it is easily available and is portable. This feature is valuable when it might be difficult to transport the patient to the imaging suite.

However, these modalities also have disadvantages:

- With conventional radiography, CT, or angiography, the issue of radiation exposure both to the patient and to the operator can be problematic, particularly when the procedures must be repeated frequently. With the easy availability of these modalities, it can become logistically easier to repeat the studies in order to evaluate progression of the disease process and thus easier to disregard the issue of exposure of the patient to unnecessary and additional radiation.
- Repeated imaging using radiographic procedures is undesirable when intermittent, recurring, or sporadic events are part of the spectrum of the disease.
- Reliance on the skill of the operator is a major issue in sonography, because the skill of the operator may not always be consistent.
- Degradation of images by inherent issues, such as the presence of fat or air, can interfere with the quality of the images.

With the development of sophisticated fusion technology, it has become common to combine the high sensitivity of nuclear medicine with the superlative resolution of other imaging modalities.

To fully exploit the use of radionuclides in the emergent or urgent situation, it is essential to understand the basic premise and promise of the modality, the physics of the modality, and the kinetics and chemistry of the tracers used.

RADIONUCLIDES

The radionuclides used in nuclear medicine are produced by artificial means in either a nuclear reactor or a particle accelerator. Both production methods involve the bombardment of a target nucleus with high-energy particles, which results in the transformation of stable nuclides into radionuclides.

In a reactor, the target is bombarded with neutrons, producing radioactive products with an excess of neutrons. By contrast, in a cyclotron, the target is bombarded with charged particles such as protons, producing radioactive species whose nuclei contain a deficit of neutrons or an excess of protons. Whereas reactor-produced radionuclides emit β− particles and cyclotron-produced radionuclides emit β+ particles, some of these products emit gamma rays, which makes them useful in nuclear medicine imaging.

P.J. Ell and S.S. Gambhir provide an elegant and concise explanation of how reactors and cyclotrons work in the third edition of *Nuclear Medicine in Clinical Diagnosis and Treatment* (see Suggested Readings).

Radionuclides used for imaging must possess certain characteristics that make them suitable for imaging, including the following properties:

- Gamma emission
- Short half-life (minutes to hours)
- High tissue penetration
- High specific activity

In addition, when used in tagged (as a radiopharmaceutical) or untagged form, these radionuclides must provide useful clinical information while exposing the patient to minimal radiation.

The chemical properties of the radionuclide should allow for its incorporation into the tracer of choice. The physical half-life of the radionuclide and the biologic and effective half-life of the tracer must effectively allow the study of the organ/metabolic/pathologic process under consideration. Ideally, the emission should be a single gamma ray in the range of 100 to 250 keV, allowing good detection efficiency with the thallium-doped sodium iodide (NaI) crystal that is used in conventional nuclear medicine cameras.

Several of the radionuclides that are made in accelerators or nuclear reactors have half-lives long enough to allow shipment to distant health care facilities. When a long-lived radionuclide decays to a shorter-lived radionuclide, the parent nuclide can become a transportable source for the production of the daughter nuclide. Because the parent and daughter radionuclides are chemically different, the daughter can be extracted either for direct use or for tagging. The device for transporting and extracting the daughter radionuclide is the generator.

The most widely used radionuclide in nuclear medicine is technetium-99m (^{99m}Tc). Some of the other radionuclides used for clinical emergency situations include xenon-133 and indium-111.

Technetium-99m

Technetium exists only in the form of radioactive isotopes. The first ^{99m}Tc generator was developed in 1958. The ability to conveniently transport the radionuclide using a generator ushered in an explosion in the development of medical applications of ^{99m}Tc.

^{99m}Tc is the most widely used tracer in nuclear medicine, accounting for more than 85% of routine diagnostic procedures in a nuclear medicine department. The following radiation characteristics of ^{99m}Tc make it an ideal agent (Fig. 12-1):

- 140.5-keV gamma emissions provide ideal tissue penetration, allowing easy collimation and excellent absorption in the thallium-doped NaI crystal.
- ^{99m}Tc decays to technetium-99, which has a half-life of 21,000 years! However, ^{99}Tc is a low-energy beta emitter.
- Gamma emission allows the use of higher doses, while absorbed radiation dose is maintained at acceptable levels.

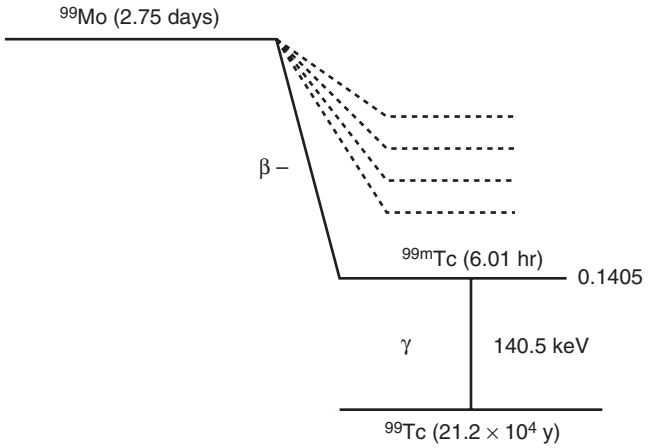


FIGURE 12-1 Decay scheme showing the isomeric transition of technetium-99m (^{99m}Tc). *^{99}Mo,* Molybdenum-99.

Gamma rays are attenuated both in tissue and in detector material (thallium-doped NaI). Compton scatter is the predominant interaction in tissue, while the photoelectric effect is the interaction occurring in the detector. Radionuclides emitting low-energy gamma rays are likely to be absorbed by photoelectric effect within the tissue and will not reach the detector. This phenomenon leads to poor-resolution images, often requiring larger doses than those with higher-energy gamma rays, which will make it through to the detector.

^{99m}Tc is obtained from "milking" a molybdenum-99 (^{99}Mo) generator (Fig. 12-2). ^{99}Mo is obtained as a by-product from the fission of uranium. ^{99}Mo is chemically separated from the other radionuclides in the reactor product. Purified ^{99}Mo as anionic molybdate solution is loaded onto the generator column, which contains alumina. The alumina, which is positively charged, is able to adsorb ^{99}Mo ions. The assembly is then autoclaved. Several normal saline solution washings of the column yield eluate-containing ^{99m}Tc. These washings are subjected to several quality control tests to determine eluate volume, radionuclide purity ("moly" breakthrough), radiochemical purity (proper chemical form of technetium as pertechnetate), pyrogenicity, sterility, and/or alumina breakthrough. The half-life of ^{99}Mo is 66 hours, allowing for weekly delivery of the generator to elute ^{99m}Tc.

The eluted technetium can now be tagged to the appropriate pharmaceutical agent for use. When radionuclides such as technetium are tagged to specific pharmaceutical agents, they are called *radiopharmaceuticals*. The pharmaceutical portion of the diagnostic radiopharmaceutical is present in very small amounts and will not elicit any pharmacologic response in the patient. The radioactive component is present in even smaller amounts. The ^{99m}Tc radiopharmaceuticals for use in emergency situations are listed in Box 12-1.

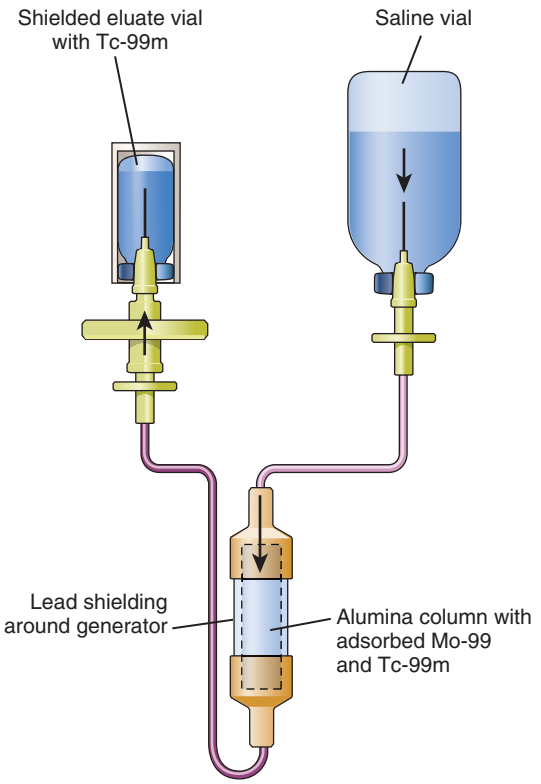


FIGURE 12-2 Molybdenum-technetium generator. Tc-99m, Technetium-99m; Mo-99, molybdenum-99.

The radiopharmaceuticals are made from "cold kits" supplied by manufacturers. With the exception of hexamethylpropyleneamine oxime (HMPAO), the kits are generally stable for up to 12 months. These kits provide a very convenient method of preparing radiopharmaceuticals in facilities that may not be close to laboratories. ^{99m}Tc can assume oxidation states ranging from I to VII based on the number of electrons available for reaction with ligands. The lower the oxidation state, the less stable it is and the most likely it is to react with ligands. The most stable electronic configuration for technetium is the state with the value of VII where it is present as the pertechnetate ion and unlikely to tag to a ligand. Consequently, to produce a ^{99m}Tc-labeled radiopharmaceutical, the technetium first must be reduced to a lower oxidation state. This reduction is most commonly accomplished through the addition of tin. Some cold kits contain antioxidants such as ascorbic acid or gentisic acid, which not only retard oxidation of the radiolabeled product but also improve the stability of the kit. Tin II (stannous) supplies electrons and in the process becomes oxidized to tin V (stannic) ion. The various oxidation states of technetium allow the formation of a variety of different radiopharmaceuticals, which adds to the value of technetium as a nuclear medicine staple.

Reagents in the "kit" vial are generally freeze dried and packed under vacuum. Alternatively, they may be combined with an inert gas such as nitrogen, which ensures that the tin in stannous form will not undergo oxidization to the stannic form by exposure to the atmosphere. The amount of tin in the reagent vial is critical to the preparation of the radiopharmaceutical. Inadequate amounts of tin allow the oxidation of free pertechnetate, which ultimately degrades the image obtained and could render a study nondiagnostic.

Indium-111

Indium-111 (^{111}In) is produced in a cyclotron from parent Cd and has a half-life of 67 hours (2.8 days). The principal photons are 171 keV and 247 keV. The relatively long half-life of ^{111}In allows sequential imaging (Fig. 12-3).

^{111}In has the following medical diagnostic applications:

- ^{111}In oxine for isotopic labeling of blood cell components such as platelets for detection of thrombi
- ^{111}In-labeled leukocytes for localization of inflammation and abscesses

BOX 12-1 Technetium-99m Radiopharmaceuticals

- ^{99m}Tc pertechnetate for scrotal scanning
- ^{99m}Tc macroaggregated albumin for perfusion lung scans
- ^{99m}Tc sulfur colloid for gastrointestinal bleeding
- ^{99m}Tc diethylene triamine pentaacetic acid
- ^{99m}Tc methylene diphosphonate for bone scanning
- ^{99m}Tc pertechnetate
- ^{99m}Tc hexamethylpropyleneamine oxime (exametazime) or technetium-99m ethyl cysteinate dimer
- ^{99m}Tc mercaptoacetyltriglycine (MAG3) for renal scanning
- ^{99m}Tc-labeled red blood cells for gastrointestinal bleeding

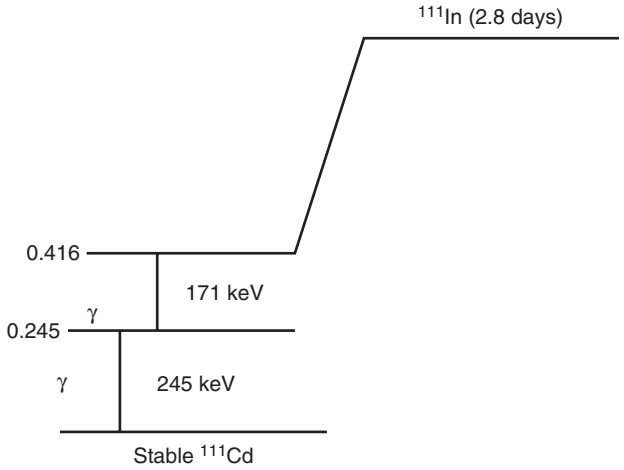


FIGURE 12-3 Decay scheme for indium-111 (^{111}In)—electron capture. *^{111}Cd,* Cadmium-111.

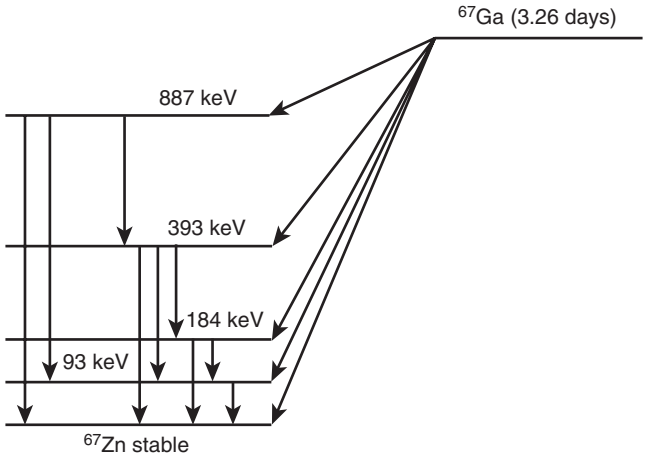


FIGURE 12-4 Decay scheme for gallium-67 (^{67}Ga). *^{67}Zn,* Zinc-67.

- ^{111}In-labeled leukocytes are also used for evaluation of leukocyte kinetics
- ^{111}In used in labeling peptides for diagnosis of certain neoplastic disorders such as ^{111}In octreotide for carcinoids, paragangliomas, and pheochromocytomas

Ordinarily, the uses of indium such as for tumor detection are not considered emergency procedures. ^{111}In-labeled leukocytes can be used for localizing abscesses and other inflammatory procedures. Although CT, MRI, and sonography may be the first-line modalities for investigation of infections, scintigraphy is an excellent adjunct not only for detecting the inflammatory/infectious processes but also for verifying if the abnormality noted on the other studies is indeed an inflammatory process.

Xenon-133

Xenon is an inert and relatively insoluble gas produced by the fission of uranium-235. Xenon is used in its radioactive form most commonly for ventilation studies. Xenon-133 (^{133}Xe) has a physical half-life of 5.3 days and, in the face of normal pulmonary function, a biologic half-life of approximately 30 seconds.

The main disadvantages of ^{133}Xe are the low photon abundance (36%) and low tissue penetration of the 81-keV gamma ray. The low photon energy generally mandates the initial use of the xenon—that is, before the administration of the technetium lung perfusion agent. Overlying soft tissue, such as breast tissue, can produce artifacts on the xenon images.

Gallium-67

Gallium-67 (^{67}Ga) is used as gallium citrate. Although ^{67}Ga citrate cannot be used for an emergent situation requiring a diagnostic test within a few hours of requisition, it is an important radionuclide for the workup of infection, which constitutes an emergency of sorts.

^{67}Ga is produced in a cyclotron from the parent zinc-68. ^{67}Ga decays by electron capture to stable zinc-67 in 3.26 days (Fig. 12-4). The transition energy, which is 0.997 MeV, is dissipated by several electron capture transitions. Several gamma photons are emitted that are used for imaging. The principal ones are 93 keV with 37% abundance, 185 keV with 20% abundance, 300 keV with 17% abundance, and 394 keV with 5% abundance.

The exact mechanism of uptake of ^{67}Ga citrate is not precisely known. After intravenous administration of ^{67}Ga, the complex dissociates to become bound to transferrin.

The principal organs that localize gallium are the liver, spleen, and bone marrow. The excretion of gallium is bimodal, initially through the kidneys and later through the GI tract. Persistence of gallium activity in the kidneys beyond 24 hours should be cause for further workup. Some uptake occurs in the lachrymal and salivary glands and the lactating breast, which is attributed to the high concentration of lactoferrin in these tissues. Both transferrin and lactoferrin are metabolized in the liver, which accounts for the uptake in the liver. Gallium is believed to behave like iron; it utilizes the transferrin mechanism and responds to procedures such as total body irradiation in a manner similar to iron saturation of transferrin.

IMAGING EQUIPMENT

The components of the detection system/gamma camera (Fig. 12-5) include the following:

- Collimator
- Scintillation crystal and optical coupling
- Array of photomultiplier tubes
- Signal processor, which analyzes the X-Y position of the signal
- Pulse height analyzer
- Computer integrated into the camera

Gamma rays emitted from the patient enter the NaI crystal after passing through the collimator. The collimator used varies with the situation. Gamma rays are converted into light within the crystal. An array of photomultiplier tubes is coupled to the scintillation crystal. The light from the crystal is converted into an electric signal, which is proportional to the amount of light generated in the crystal. The electric signals from the photomultiplier tubes are processed by the circuitry to generate position signals and the energy signal. The latter is proportional to the energy of the gamma ray emitted by the radionuclide. The pulse height analyzer analyzes and selects only the signals,

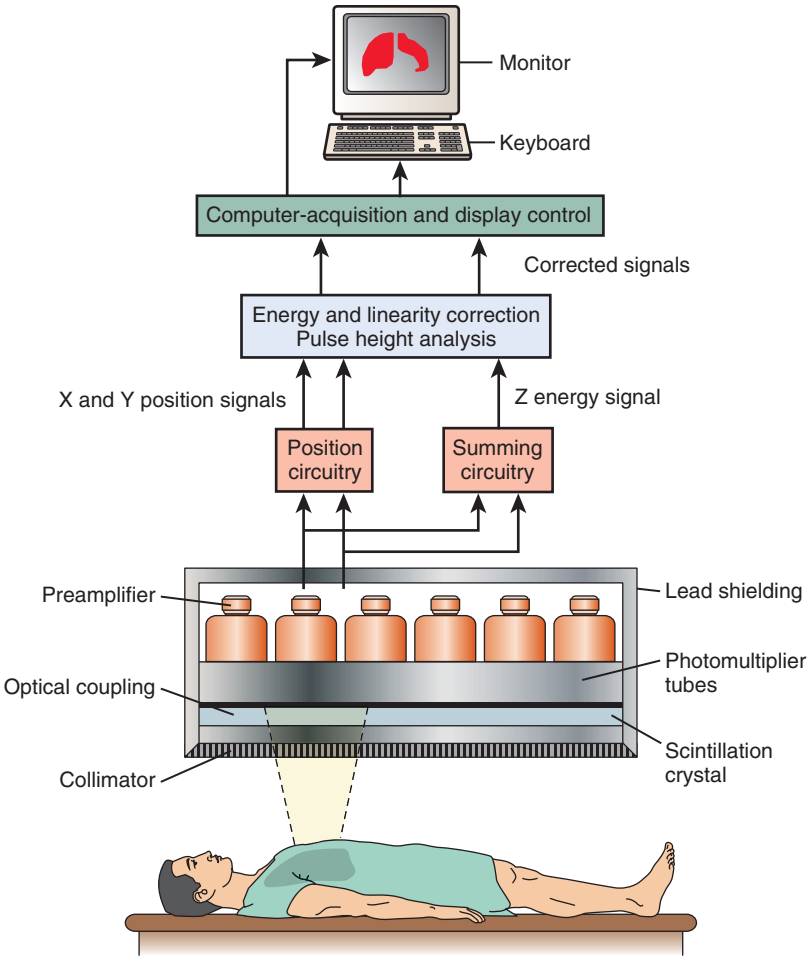


FIGURE 12-5 Components of a gamma camera.

which fall in the energy range preset for the radionuclide under consideration. The correction of the X and Y position of the signal, as well as the energy discrimination/pulse height analysis, is performed in the memory of the computer, which is integrated into the gamma camera. The information is recorded as an image in the memory of the computer and displayed on a color or black and white monitor. Each study (which could be composed of several images) is stored to be retrieved for review and reporting.

LUNG SCINTIGRAPHY

The most common indication for lung scintigraphy is to determine the likelihood of pulmonary embolism. Less common indications include lung transplantation, perioperative evaluation, and evaluation of right-to-left shunt.

Pulmonary Embolism

The incidence of pulmonary embolism (PE) and its detection have increased with the increasing frequency of long-distance travel and the consequent loss of mobility. Aging of the population and the increasing incidence of comorbidities such as cardiac and peripheral vascular (including venous) disease increase the likelihood of the occurrence of PE. There are many risk factors for deep vein thrombosis (DVT) and PE. It is well known that, among these risk factors, prolonged immobility, recent surgery, pregnancy, and underlying malignancy may actually initiate DVT.

PE is the third most common cause of death in the United States, with 650,000 instances of PE occurring each year. PE seems to present with a greater preponderance in hospitalized patients. Given the high prevalence of the condition, its lethality, and the fact that a large number of patients with PE have atypical presentations, it is recommended that every patient with chest pain undergo testing for PE.

Venous thrombosis, in contrast to arterial thrombosis, is caused by problems with the plasma clotting system. Minimal platelet participation is present in the venous versus the arterial process. Increasing evidence shows that an underlying coagulopathy may be responsible for spontaneous DVT and PE. Hypercoagulability may be congenital or acquired. Primary or acquired deficiencies in protein C, protein S, or antithrombin III are known to be common causes of DVT and PE.

Radiopharmaceuticals and Techniques

The major function of the lungs is to effect the exchange of carbon dioxide (CO_2) for oxygen (O_2) from the blood. This exchange is accomplished by perfusion of the capillaries in the walls of the alveoli, where inspired air brings in O_2 and is exchanged for CO_2 in the deoxygenated blood.

The CO_2 in the alveoli is then discharged to the outside of the body via expiration. Both of these aspects of the respiratory anatomy and physiology are assessed in nuclear medicine. Pulmonary perfusion is assessed by the intravenous administration of ^{99m}Tc macroaggregated albumin, whereas the various phases of ventilation are studied using gases or aerosols.

In pregnant women, a perfusion-only lung scan should be considered if a chest radiograph is normal and the patient has no history of smoking or lung disease. Because ^{99m}Tc is excreted in breast milk, the patient should be encouraged to express and store breast milk for 2 days until the radionuclide has decayed sufficiently.

Perfusion

^{99m}Tc macroaggregated albumin (MAA) is the agent of choice for assessing pulmonary perfusion. The mechanism of accumulation with this agent is the blockade of capillaries in the pulmonary arterial circulation.

A minimum of 100,000 particles is necessary to obtain readable images. To obtain optimal images, approximately 200,000 to 600,000 particles are required. The size of the particles ranges from 5 μ to 100 μ, with the majority measuring around 30 μ. The desired particle concentration can be obtained by diluting the kit with normal saline solution. It is important to check the particle size using a microscope or a hemocytometer. Smaller fragments enter into the general circulation and are phagocytized by the liver and spleen.

Approximately 0.1% of capillaries are blocked with one injection. Ordinarily this degree of blockade is of little or no consequence. However, in patients whose pulmonary arterial circulation is tenuous, such as patients with pulmonary hypertension, blockade of the reduced capillary bed can precipitate cardiac complications or exacerbate the underlying condition. In patients with right-to-left shunts, transfer of particles into the systemic arterial circulation could cause adverse coronary or cerebral events. For these patients, as well as pediatric patients, we recommend administration of a lower dose of particles (100,000 to 200,000).

^{99m}Tc MAA is produced by the addition of ^{99m}Tc pertechnetate to a sterile "cold kit" containing stannous albumin aggregates as lyophilized powder. ^{99m}Tc pertechnetate is added to the cold kit. The tagged kit is allowed to stand at room temperature for 15 minutes to ensure maximum tagging. The usual administered activity in adults is 3 to 5 mCi (111-185 MBq). The pediatric dose is 25 to 50 mCi/kg of body weight. The lung is the critical organ in this procedure, receiving an absorbed radiation dose of 0.22 rad/mCi.

^{99m}Tc MAA is administered intravenously in a peripheral vein. Withdrawal of blood back into the syringe could produce clots, which could appear as "hot spots" on the lung scans. Injection into sites of central venous access, such as Swan-Ganz catheters, should be avoided. The syringe should be gently agitated to prevent the MAA particles from settling out. Injecting the dose slowly over three to five deep breaths, as well as having the patient supine, will ensure the even distribution of particles.

The patient undergoes imaging in a sitting position, although images could be obtained with the patient supine. Ideally, the patient undergoes imaging with a large field-of-view gamma camera using a parallel-hole collimator. A diverging collimator may be necessary in larger patients to encompass both lungs on the anterior and posterior views. The standard views are the anterior, posterior, right and left laterals, both right and left posterior oblique, and both right and left anterior oblique (Fig. 12-6). Generally, a minimum of 500,000 counts is accumulated per image.

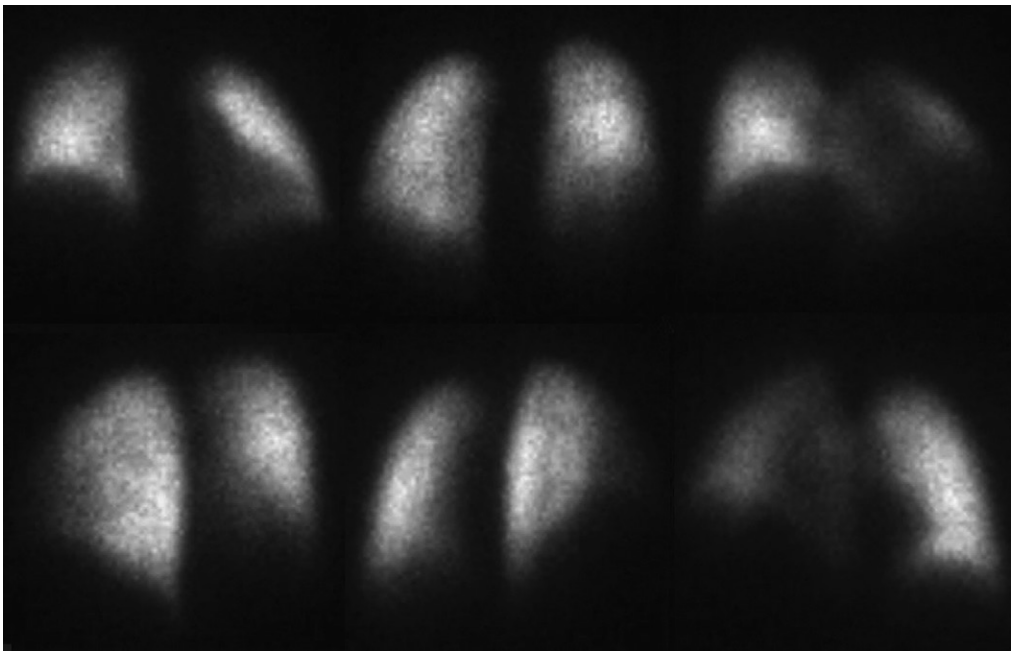


FIGURE 12-6 Normal findings of a technetium-99m perfusion lung scan. Images show a standard six-view study: anterior, posterior, and left anterior oblique views *(top row, left to right)*, and left posterior oblique, right posterior oblique, and right anterior oblique views *(bottom row, left to right)*.

In our institution, we have found single photon emission CT (SPECT) to be of use in determining whether the perfusion defect is segmental or nonsegmental.

Ventilation

Inert gases can be used to perform ventilation studies of the lung in tandem with technetium perfusion studies. Their short biologic half-life allows relatively complete clearance of the lung, providing a clean slate, so to speak, for lung imaging with a longer-lived perfusion agent.

Xenon-133. ^{133}Xe is relatively inexpensive and is the most commonly used agent for ventilation. Overlying soft tissue easily attenuates the principal gamma emission of 81 keV. Consequently, images of the lungs are generally obtained in the posterior projection. Additional images may be obtained in the posterior oblique projections. Images are rarely obtained in the anterior, anterior oblique, and lateral projections because of the degradation caused by overlying soft tissues such as breast tissue. Consequently, any abnormalities that are seen only in the anterior areas of the lungs will be missed. Exhausting the xenon is a cumbersome and complex process requiring a charcoal trap or a venting system. To avoid contamination with xenon, which is heavier than air, a negative pressure room is required. Furthermore, xenon is fat soluble and will adhere to plastic drapes, floor wax, and instrument grease. Consequently, the background level will gradually rise during the workweek.

Xenon can be used to assess all phases of ventilation. The most commonly used technique involves having the patient breathe xenon through a spirometer. The patient exhales as deeply as possible and then inhales 10 to 20 mCi of ^{133}Xe. The respiration is suspended at the end of the inhalation for 15 seconds while the first image is obtained. The patient breathes xenon out into a spirometer, which constitutes a closed system. Approximately 2 L of O_2 are used to dilute the expired xenon (Fig. 12-7). The patient rebreathes this mixture for 2 to 3 minutes, at which time another static image is obtained, which constitutes the equilibrium image. After equilibrium has been reached, fresh air is breathed in until the xenon is completely washed out. Images are obtained every 15 seconds for 2 to 3 minutes. For patients with chronic obstructive pulmonary disease (COPD), the washout phase may be delayed up to 5 minutes to image areas of regional airway trapping. This entire process presupposes that the patient is able to perform the necessary breathing into a spirometer or a closed system.

The initial/single breath reflects the regional ventilatory rate. The equilibrium phase depicts the aerated volume of the lungs, and the washout phase delineates trapping. Xenon is fat soluble and partially soluble in blood, which will cause deposition in the liver, particularly in patients with fatty replacement in the liver.

Krypton-81m. Krypton-81m (^{81m}Kr) also has been used for ventilation imaging. The photon emissions of 176 and 192 keV and the short half-life of 13 seconds allow equilibrium imaging of the lungs in multiple projections. However, the short half-life precludes the ability to obtain single-breath and washout images. ^{81m}Kr is obtained from rubidium-81 (^{81}Rb), which has a half-life of 4.6 hours. Although krypton generators are available, the cost of the generator can be quite high because of the short half-life of ^{81}Rb. The activity administered is 1 to 10 mCi.

Radiolabeled Aerosols. Radiolabeled aerosols are the agents most often used to study ventilator function. Aerosol studies do not allow dynamic imaging. Although dynamic imaging may be of value in studying airways disease, it is not required in the suspected clinical setting of PE.

The most commonly used aerosol is ^{99m}Tc diethylene triamine pentaacetic acid (DTPA) in a volume of 2 mL put into the nebulizer of an aerosol delivery system. The aerosol is prepared by injecting 30 mCi of ^{99m}Tc DTPA into the nebulizer of the delivery system. Side tubing in the system

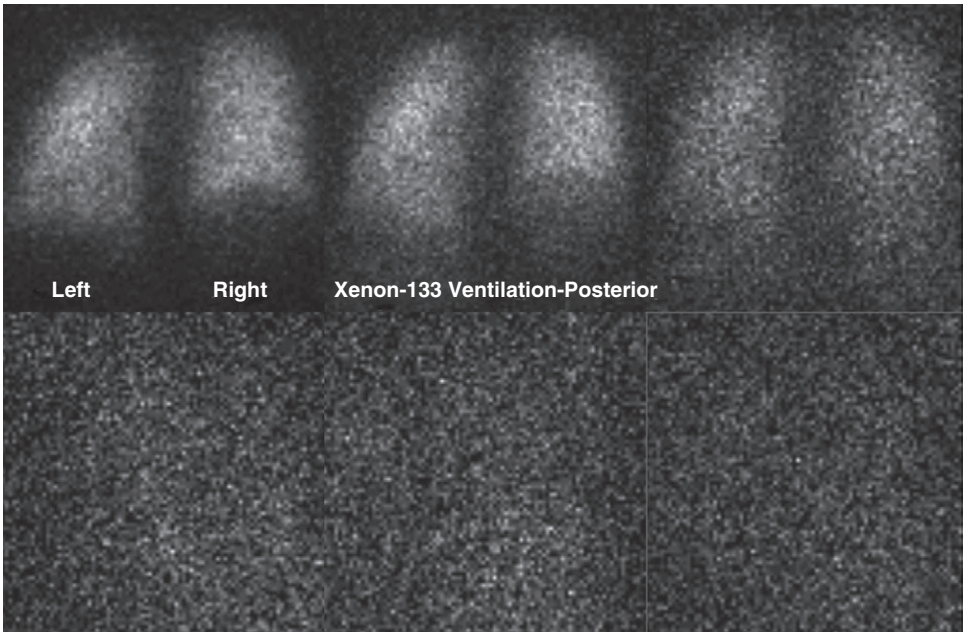


FIGURE 12-7 Normal findings of a xenon-133 (^{133}Xe) ventilation lung scan. The ventilation is usually performed before the perfusion study. Because of the rapid clearance of lung activity of ^{133}Xe, a posterior view study is performed to maximize the area of the lung seen. Comparison with perfusion is less than optimal.

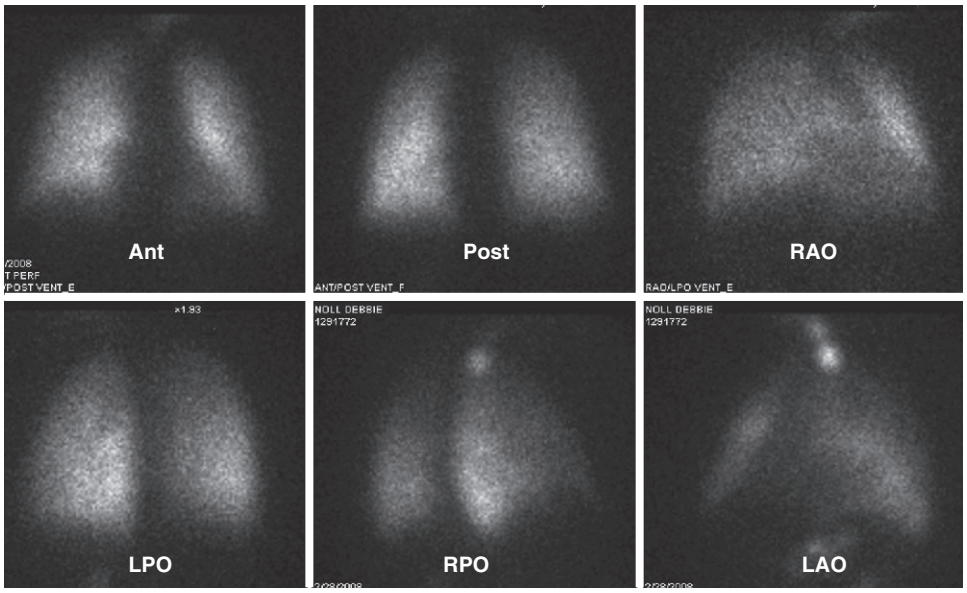


FIGURE 12-8 Technetium-99m diethylene triamine pentaacetic acid aerosol images. Normal study findings show six views, and corresponding six views are obtained for perfusion. Comparable images make interpretation of a lung scan much easier than with a single posterior (Post) view xenon-133 study. *Ant,* Anterior; *LAO,* left anterior oblique; *LPO,* left posterior oblique; *RAO,* right anterior oblique; *RPO,* right posterior oblique.

allows oxygen to flow through a flow meter at the rate of 8 to 10 L/min. Generally, only a small amount of activity (1 to 2 mCi) is delivered. The trachea is the critical organ in the aerosol ventilation study. One of the major advantages of this system is that it can be attached to an endotracheal or tracheostomy tube. In patients without airway tubing, the aerosol is inhaled through the mouth while a nose clip is applied. In either circumstance, little or no patient effort or cooperation is required to deliver the aerosol into the airway. The aerosol is usually delivered with the patient in a supine position so that it is distributed evenly. No special venting is required with ^{99m}Tc DTPA as it is with xenon. The second major advantage of using ^{99m}Tc DTPA is that the imaging characteristics are ideal. Therefore, the ^{99m}Tc DTPA study can be performed either before or after the ^{99m}Tc MAA study. If the ventilation study is performed before the perfusion study, the amount of activity required is between 1 and 2 mCi. However, if the perfusion study is performed first, the number of counts accumulated for the ventilation study must be three to four times greater than for the perfusion study.

In the workup for PE, use of ^{99m}Tc DTPA aerosol is ideal, because images can be obtained in projections to match the ventilation images. After inhalation, aerosol particles are deposited in the distal airways and not the alveoli. After inhalation, the technetium DTPA particles dissolve in the fluids within the alveoli and ultimately diffuse across the epithelial barrier into the circulation. As long as the epithelial barrier is intact, the aerosol diffuses relatively slowly into the circulation. The half-time disappearance of the aerosol from the alveoli is about 80 minutes, and it is much faster in patients whose epithelial barrier may be deficient, as in patients with COPD or in smokers. The technetium DTPA that has entered into the circulation is cleared via the kidneys. Larger particles are deposited in the central airways, the mouth, and the alimentary tract (from swallowed particles; Fig. 12-8).

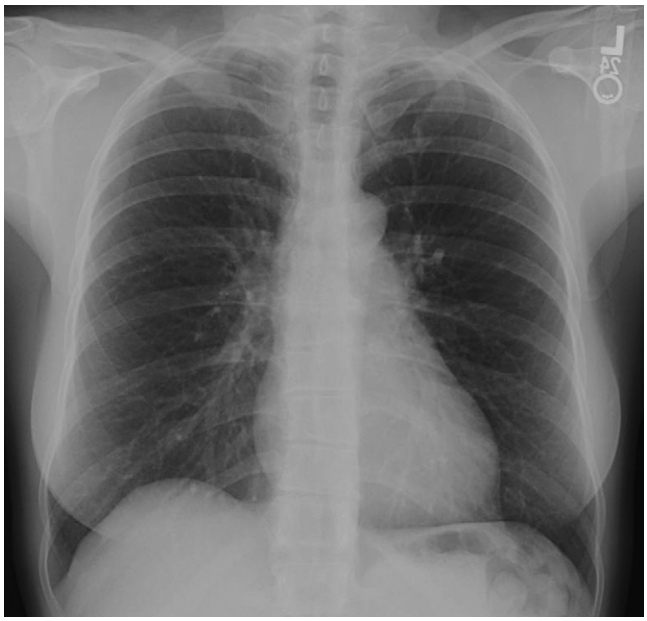


FIGURE 12-9 A normal chest radiograph. Interpretation of the ventilation-perfusion study for pulmonary embolism.

Technegas. Technegas is composed of ultrafine particles of ^{99m}Tc-labeled carbon produced by combustion of pertechnetate at 2500°C in a graphite crucible. A Technegas generator is portable and produces fine images. The smaller particle size makes Technegas a better agent than technetium DTPA aerosol, particularly in patients with COPD.

Chest Radiograph. It is good practice to obtain a radiograph within 24 hours of performing the ventilation-perfusion (VQ) scan. It is preferable to have a chest radiograph for evaluation before performing the VQ scan (Fig. 12-9). Having a full-inspiration posteroanterior (PA) and lateral chest radiograph available for interpretation

would be ideal. However, a large percentage of the patients who are at risk for PE in the hospital or intensive care unit setting may be experiencing several other cardiopulmonary pathologic processes that could interfere with the reading of the VQ scan.

Symptomatology and chest radiograph findings in patients with PE are often nonspecific. Although Hampton's hump and the Westermark sign, when found, are pathognomonic of PE; their absence on a chest radiograph does not denote the absence of pulmonary embolic. Additionally, in patients who are in intensive care, a portable chest radiograph is the first diagnostic procedure to be performed, but these radiographs do not have the quality of standing PA and lateral chest radiographs.

With the introduction of multidetector CT scanners, the majority of patients who need a PE workup undergo direct imaging with CT pulmonary angiography. In patients with impending renal compromise, CT angiography with use of contrast material may be risky. Increasingly, the CT angiogram has become the gold standard for diagnosis of PE. Clinical suspicion of PE is the most common indication for lung scanning. Although CT angiography has become the first method used in diagnosing PE, pulmonary scintigraphy is the method of choice for patients who are allergic to iodinated contrast material.

The Prospective Investigation of Pulmonary Embolism Diagnosis (PIOPED) study, completed in the 1990s, provided a comprehensive look at the value of ventilation and perfusion scans in persons with acute PE. The PIOPED criteria were based on the use of xenon ventilation scans. With the development of CT pulmonary angiography, the algorithms proposed by the PIOPED study have had to be modified. Several guidelines have been used for interpreting VQ scintigraphy in the setting of increased risk for PE, including the McNeill, Biello, and PIOPED methods. The results of the VQ scan are reported as the probability of PE being present on the information used as a basis for the study—that is, high, intermediate/indeterminate, and low probability. William Klingensmith and Steve Holt (see Suggested Readings) have proposed a physiologic approach to the interpretation of VQ scans that has the advantage of being intuitive, as opposed to other approaches.

The most important diagnostic feature of PE on VQ scans is the mismatched defect, when there is a perfusion defect but no abnormality on the ventilation scan. The finding of segmental perfusion defects is characteristic of a PE.

The following outline is a practical and simple algorithm for use in the workup of PE:

The *first step* is to obtain a chest radiograph for comparison with the VQ scans.

The *second step* is to scrutinize the perfusion scan for perfusion defects. These defects should be characterized on the basis of whether they are segmental/subsegmental or nonsegmental. Nonsegmental defects do not correspond anatomically to a segment and therefore are unlikely to be the result of a PE. If the defect appears to conform to a segment or a portion of a segment, we proceed to the next step.

The *third step* is to determine the size of the segmental perfusion defect. A classic segmental perfusion defect corresponds anatomically to a bronchopulmonary segment; these are pleural based and wedge shaped. The defect is categorized as large when it occupies 75% or more of the segment, moderate when it occupies 25% to 75% of the segment, and small when it occupies less than 25% of the segment.

The *fourth step* is to ascertain whether the segmental or subsegmental defects observed on the perfusion scan are matched on the ventilation study and the chest radiograph.

The *fifth step* is to discuss the likelihood of PE based on the scans in light of the pretest likelihood of PE. If no abnormalities are noted on the perfusion study, the study is considered normal. The likelihood of PE is less than 5%.

Unmatched perfusion defects are likely a result of acute or chronic PE. PEs are multiple in 90% of cases and bilateral in 85% of cases. In the first few days, the defects may disappear or become smaller. New defects may occur because of fragmentation. Changes in regional perfusion pressure could transform a partially obstructing clot into a fully obstructing clot.

The methods for ascertaining the likelihood of PE based on abnormal examinations have undergone changes, modifications, and iterations over the years. The probability of having a PE is determined by the size and the number of perfusion abnormalities and concomitant abnormalities (or absence of abnormalities) on the ventilation scan and chest radiographs. The following system of classification is used:

A *high-probability scan* has two or more large, mismatched segmental defects (or equivalents in moderate/large defects) with no abnormality on the ventilation study (Fig. 12-10). In the clinical setting in which PE is highly likely, a high-probability VQ scan indicates a probability of PE greater than 90%. If the mismatched perfusion defects should resolve within days or weeks, the probability of a recent embolism is higher.

In a *low-probability scan,* the perfusion scans are smaller than 25% of a segment regardless of the results of the ventilation scan or appearance of the chest radiograph (Fig. 12-11).

An *intermediate-probability scan* is one that does not fit into the high or low categories.

A description of the abnormalities and whether they are accompanied by matched defects on the ventilation scan and correlate with the chest radiograph would make interpretation much easier. The descriptions we propose are as follows:

- *Mismatched abnormality*—a defect observed on the perfusion scan is not seen on the ventilation study, and there is no corresponding abnormality on a chest radiograph. This presentation is characteristic of an uncomplicated PE in which the ventilatory architecture remains intact in the presence of a perfusion abnormality. A caveat to this presentation is when the vascular occlusion is incomplete. A partial occlusion may present as a mildly decreased perfusion, which is then labeled (erroneously) as a nonspecific finding. Additionally, the size of the vessel can affect the perfusion scan.
- *Complete match*—a defect on the perfusion scan is matched by a defect on the ventilation scan without the presence of an infiltrate on the chest radiograph. The complete match of VQ abnormalities is commonly seen in patients with obstructive lung disease.

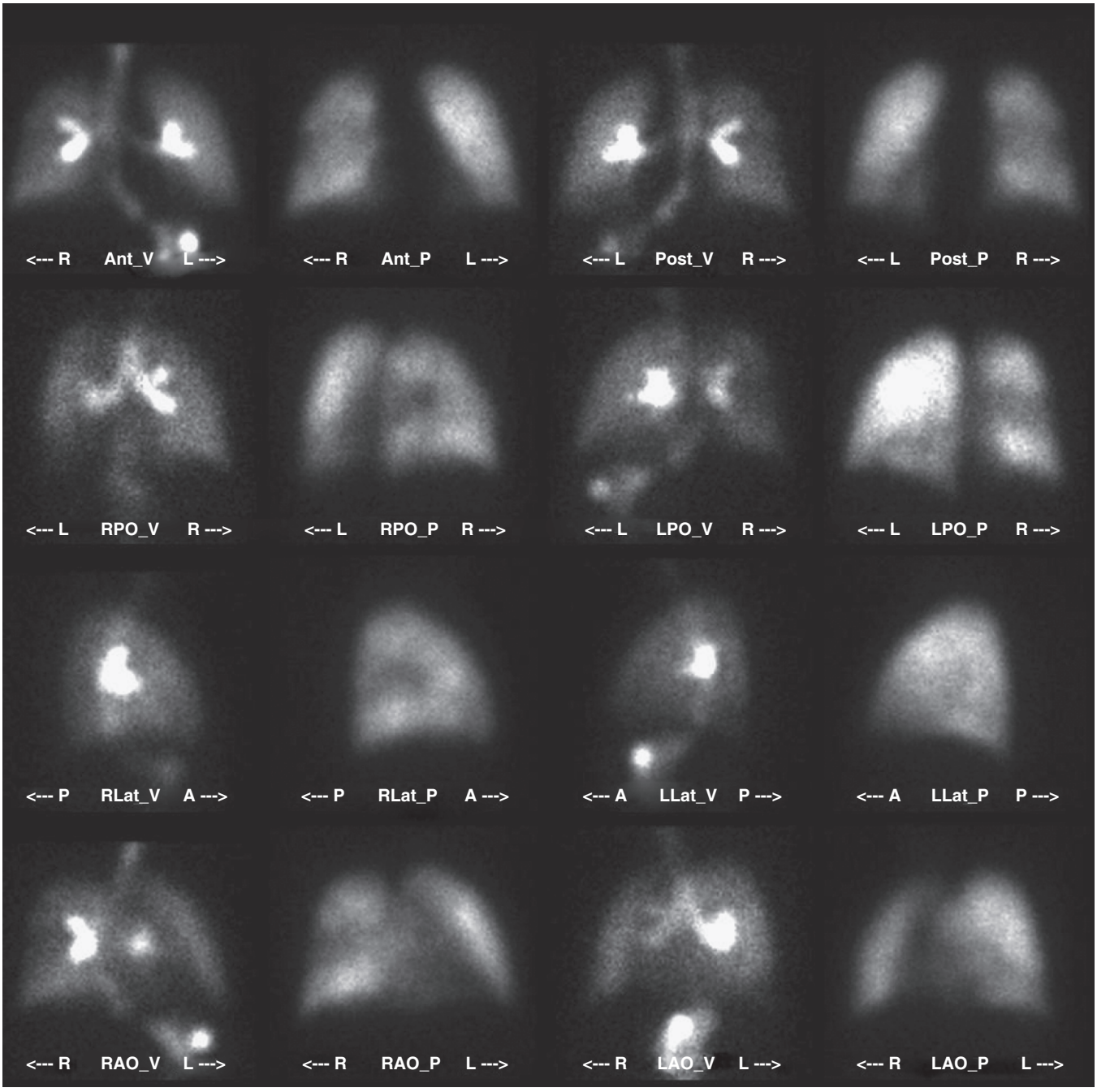


FIGURE 12-10 A high-probability lung scan with technetium-99m diethylene triamine pentaacetic acid aerosol and macroaggregated albumin. The superior segment of the right lower lobe and a major portion of the left lower lobe show perfusion deficit with good ventilation, a ventilation perfusion mismatch. *Ant,* Anterior; *LAO,* left anterior oblique; *Lat,* lateral; *LPO,* left posterior oblique; *Post,* posterior; *RAO,* right anterior oblique; *RPO,* right posterior oblique.

- *Triple match*—there is complete matching of the VQ defects and a corresponding abnormality on the radiograph.
- *Reverse mismatch*—the ventilatory abnormality is worse than the perfusion abnormality. This presentation can be seen with mucus plugging of the airways, atelectasis, and a right-to left shunt.
- *Circumferential and perifissural hypoperfusion*—this presentation is seen with microemboli.

Repeat Scans. Because the perfusion picture can evolve over the ensuing weeks or months, it is advisable to repeat the study after 3 weeks. Defects persisting at 3 months are unlikely to resolve. The larger the defect and the older the patient, the less likely it is that the perfusion scan will revert to normal. In patients with diffuse lung disease, emboli are less likely to resolve completely. Patients with high-probability or intermediate-probability scans who have been treated for PE should undergo follow-up imaging after 3 months.

Lung scans are also of value in patients with a lung transplant to ascertain if the venous anastomosis has been compromised, especially while the patient is restricted to the intensive care unit.

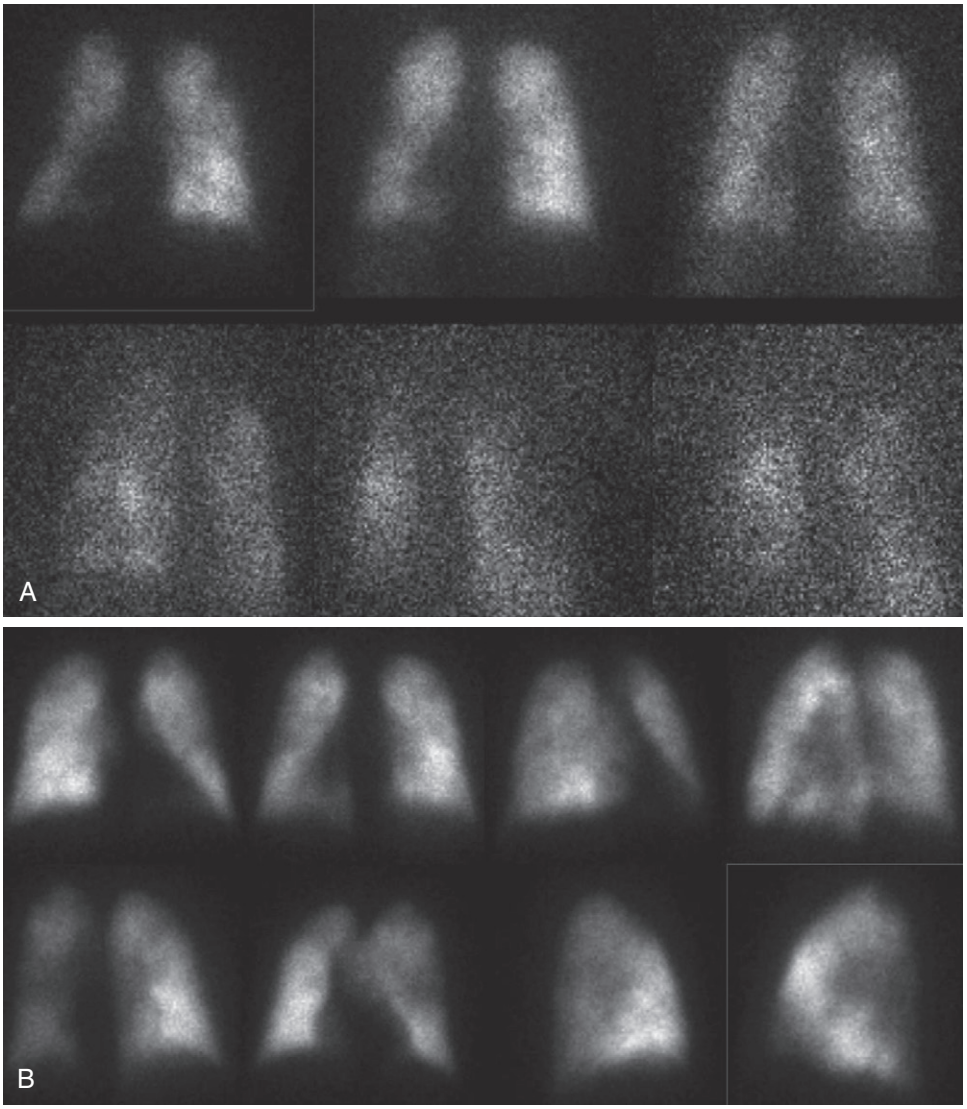


FIGURE 12-11 A xenon-133 ventilation study **(A)** and technetium-99m macroaggregated albumin study **(B)** show nonsegmental matching abnormalities, suggesting a low probability for pulmonary embolism.

BRAIN DEATH

CT and MRI are the modalities of choice for studying acute events involving the central nervous system. Scintigraphic brain perfusion studies are usually reserved for assessment of whether perfusion of the brain is effective. The harvesting of organs for transplantations requires that the diagnosis of irreversible cessation of brain function be made accurately and quickly. The requirement for alacrity of diagnosis is to prevent the organ degradation that occurs with death.

A second use of scintigraphy is to establish cerebrospinal fluid shunt patency, although establishing this patency rarely qualifies as an absolute emergency.

The diagnosis of brain death is primarily a clinical one; clinicians frequently rely on the patient being in a coma with a total absence of brainstem reflexes and spontaneous respiration, along with electrocerebral silence. The findings of death must be present for a finite period of observation (6 to 24 hours). States that mimic brain death include alcohol and barbiturate intoxication, sedative overdose, hypothermia, and hypoglycemic coma. In these instances, electrocerebral activity may drop to a level so low as to be undetectable. Additionally, the Lazarus sign (spinal reflexes and spontaneous movement of arms and shoulders that may be present after cessation of ventilation) may cause some confusion.

Confirmation of absent intracranial perfusion offers confirmation of brain death. This confirmation can be obtained by demonstrating the absence of intracranial perfusion and the absence of sagittal sinus activity after intravenous administration of tracer material. Occasionally the sagittal sinus may be perfused from the external carotid circulation (Fig. 12-12).

Brain death is diagnosed primarily clinically. However, complicating situations such as hypothermia and drug overdose may make a clinical or electroencephalogram (EEG) diagnosis difficult or impossible. Scintigraphic examinations are not affected by these conditions. Lack of perfusion on a radionuclide study is considered compatible with a diagnosis of brain death, more so than an isoelectric EEG. However, the actual pathophysiologic process producing the lack of cerebral perfusion on a scan is due to cerebral edema, which occurs because of elevation of intracranial pressures above systemic arterial pressure.

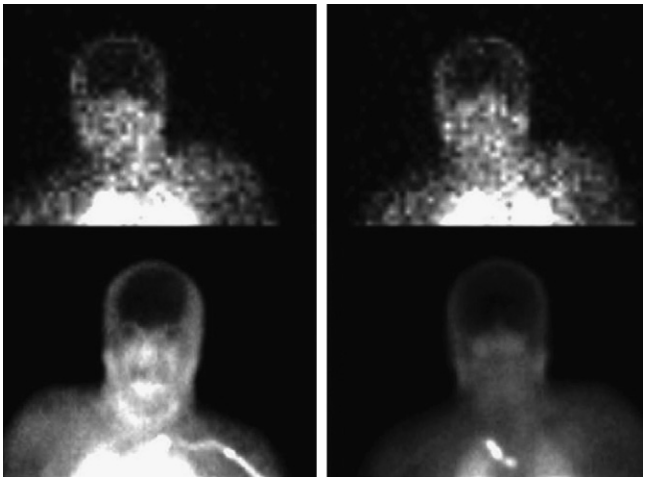


FIGURE 12-12 Technetium-99m ethyl cysteinate dimer planar imaging study shows no perfusion and no delayed activity in the skull—the "empty skull" appearance. These findings are better seen with single photon emission computed tomography imaging of the brain if clinically feasible.

It must be noted that the degree of cerebral edema from increased intracranial pressure that causes an absence of perfusion in itself carries a grave prognosis.

Patients being evaluated for brain death are usually in the intensive care unit. Transferring these patients to the imaging suite is often extremely difficult and quite labor intensive. Hence the use of scintigraphy for evaluation of brain perfusion, which can be obtained with ease at the patient's bedside, is the first-line option.

Radiopharmaceuticals

The radiopharmaceutical agents used for the diagnosis of brain death are ^{99m}Tc DTPA and ^{99m}Tc HMPAO or ethyl cysteinate dimer (ECD). ^{99m}Tc DTPA is used on the premise that it provides a radionuclide angiogram. We prefer using ^{99m}Tc HMPAO or ECD because they are brain perfusion agents and will not be picked up in a nonperfused brain. Furthermore, a nuclide angiogram can be performed dynamically while injecting the ^{99m}Tc HMPAO or ECD and additionally followed up with planar static or SPECT images.

^{99m}Tc DTPA, a hydrophilic radiopharmaceutical, does not cross the blood–brain barrier and can be used for the radionuclide angiographic portion of the study. This agent is commonly used for planar scintigraphy.

^{99m}Tc HMPAO (hexamethyl-propylene oxime or exametazime) is a lipophilic agent, which is ideal for SPECT imaging of the brain; it can be prepared with or without stabilizer for brain imaging. The brain preferentially retains the ^{99m}Tc HMPAO because it is converted in vivo by glutathione to the hydrophilic complex. The ^{99m}Tc pertechnetate should be fresh and not more than 30 minutes from eluting. The stabilizer used is methylene blue, which acts as a free-radical scavenger.

Technique

In some nuclear medicine laboratories, a scalp tourniquet is applied to minimize the external carotid perfusion. This measure also reduces scalp perfusion, which could be mistaken for cerebral perfusion. The most commonly used tourniquet is an elastic band placed above the level of the orbits. This technique is not recommended in children because application of the tourniquet may increase intracranial pressure.

In most instances the use of ^{99m}Tc DTPA will suffice. It is injected intravenously as a bolus, and dynamic images may be obtained with the camera centered over the face. Occasionally, it may be difficult to administer a good-quality intravenous bolus. In this case, using ^{99m}Tc DTPA is convenient, in that a repeat injection can be performed.

The use of ^{99m}Tc HMPAO or ECD is recommended in difficult cases. Because the uptake of these agents relies on both perfusion and active uptake by a viable brain, a dynamic flow study may not be necessary and delayed static images will suffice, particularly if the intravenous injection of bolus was unsatisfactory and subsequent dynamic images could not be obtained for a variety of reasons, including malfunctioning of the computer.

Because both dynamic flow and static images are used in this study, we prefer to use the low-energy all-purpose collimator, which can be used in both the dynamic and static studies. With ^{99m}Tc DTPA, 10 mCi are given intravenously, whereas with ^{99m}Tc HMPAO, 15 to 20 mCi of activity are administered. Because both sets of compounds are tagged with ^{99m}Tc, the window setting is at 15% at a 140-keV peak. The flow study involves obtaining 1- to 2-second images for 30 seconds. Immediate or early planar static images are acquired for 500k to 750k counts in the standard anterior and posterior projections and both lateral projections. It is vital to perform imaging over the injection site to verify that the dose has not been infiltrated. With ^{99m}Tc HMPAO, delayed static images are obtained 2 hours after injection in the standard projections.

Interpretation

On the radionuclide angiogram, flow will be seen in the common carotid arteries. The flow will not be seen beyond the base of the skull. If there is no cerebral blood flow, no uptake will be seen in the brain.

^{99m}Tc DTPA is used strictly as a blood pool agent in the documentation of brain death. It does not cross the blood–brain barrier and remains in the blood pool even on delayed static images. Consequently, the delayed static images, which are obtained 5 to 10 minutes after completion of the "flow" study, will not reveal any activity in the territory of the cerebral arteries.

On HMPA and ECD studies, in a normal, viable brain, uptake of radionuclide will occur in the brain—preferentially in the cortex. With brain death, no activity will be seen in the brain. Occasionally, increased uptake of the radionuclide is noted on the immediate static images in the nasopharyngeal region. Mishkin originally described this appearance, which was subsequently eponymously labeled the "hot nose sign of Mishkin." However, it has been documented in other instances, such as internal carotid occlusion without brain death, which is attributed to the shunting of blood flow into the external carotid circulation. In the presence of clinical signs of brain death, the "hot nose" sign could be used as a secondary or corroborative finding. The sagittal sinus may be

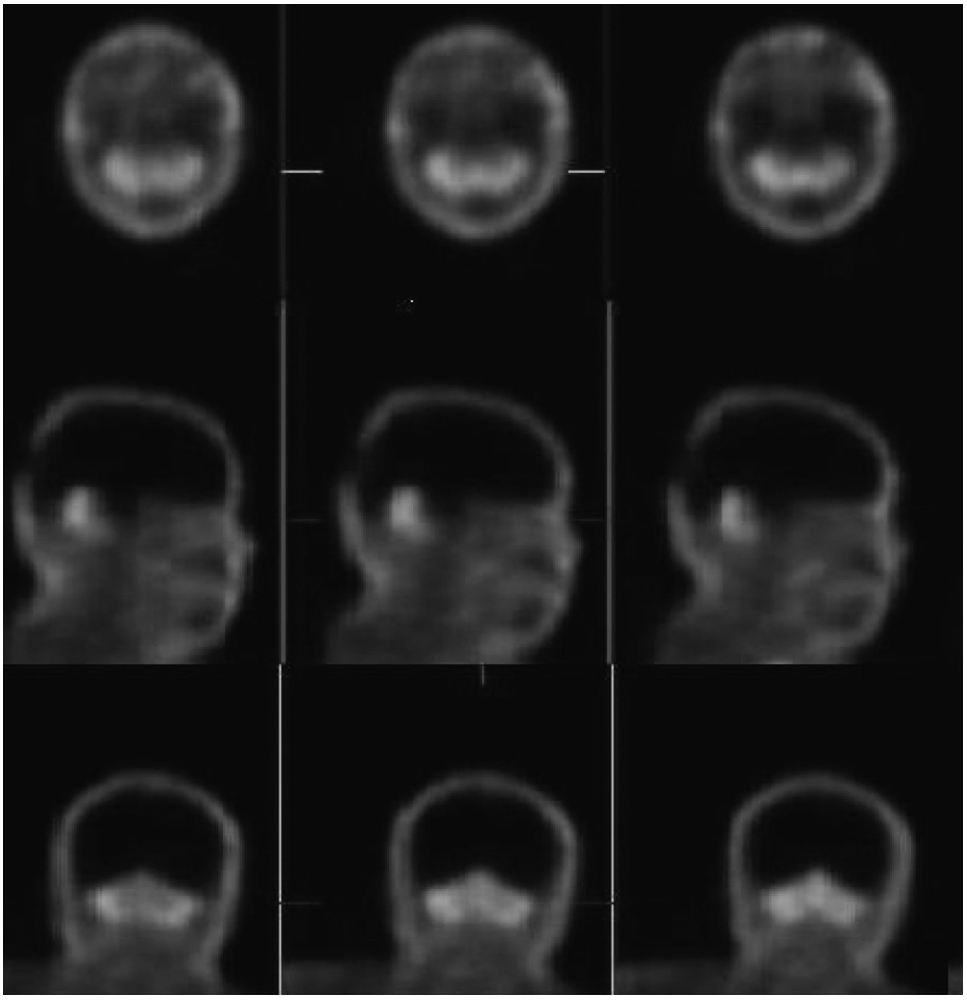


FIGURE 12-13 Technetium-99m ethyl cysteinate dimer brain perfusion single-photon emission computed tomography imaging shows complete absence of perfusion in the cerebral hemispheres and minimal uptake in the brainstem and cerebellum. The brainstem and cerebellar activity usually disappears within 24 hours, and a second study is required to confirm complete absence of perfusion.

visualized faintly as a result of filling from the external carotid circulation.

With brain death, there is no uptake of HMPAO or ECD radiopharmaceuticals in nonviable brain tissue. If necessary, this outcome can be further verified by obtaining SPECT images, which will show an "empty skull."

Tomographic SPECT images allow better visualization of activity distribution within the skull and allow visualization of brainstem and cerebellar activity that is difficult to see with the planar imaging previously discussed. Figure 12-13 shows the same patient as in Figure 12-12 with SPECT imaging clearly demonstrating activity in the brainstem and cerebellum. The cerebellar and brainstem activity usually clears in 24 to 36 hours and confirms diagnosis of brainstem death as well. The patient in Figures 12-12 and 12-13 showed no activity in the cerebellum or brainstem when the study was repeated after 20 hours.

INFECTION

Although nuclear medicine plays a very important role in the detection of infection, several barriers exist to the implementation and incorporation of nuclear medicine into the algorithm for the workup of infection, not the least of which is the time it takes to arrive at an answer. Radionuclide imaging is often complementary to CT, which is ideal for fusion or simultaneous imaging.

Several agents are available for the workup of infection; the choice varies widely with the situation involved.

Radiopharmaceuticals

The radiopharmaceuticals used include ^{99m}Tc methylene diphosphonate for part of the workup of musculoskeletal infection, ^{67}Ga citrate, and ^{111}In oxime and ^{99m}Tc HMPAO for autologous leukocytes.

Leukocyte Labeling

Leukocytes can be labeled with ^{111}In oxime or with ^{99m}Tc HMPAO. Infections that mount a neutrophilic response are best visualized with the leukocyte label. Opportunistic infections, however, are not associated with neutrophilic response, and hence these infections are not ideal for imaging with radionuclide-labeled leukocytes.

The labeling process is performed in vitro, is cumbersome, and requires meticulous attention to detail.

Furthermore, the in vitro process carries with it the risk to personnel of handling blood products. The process itself takes 2 to 3 hours. First, 40 mL of blood is drawn into a syringe that contains anticoagulant. The syringe is kept upright for 1 to 2 hours to allow the red blood cells (RBCs) to form sediment. This process is further accelerated by the addition of hydroxyethyl starch and the hypotonic lysis of the RBCs. The next step is to separate the leukocytes from platelets by centrifugation. The leukocyte pellet that forms after the separation of the RBCs and platelets is incubated with the radiopharmaceutical agent, washed, and injected into the patient. The doses of ^{99m}Tc HMPAO–labeled and ^{111}In-labeled leukocytes are 5 to 10 mCi and 300 to 500 μCi, respectively.

A total white blood cell (WBC) count of at least 2000/mL is essential to obtain satisfactory images. Neutrophils are the majority of WBCs labeled; hence, the images obtained reflect neutrophil-mediated response. Mature granulocytes are highly specialized, short-lived, nondividing cells. They generally measure around 12 to 15 microns and possess a multilobulated nucleus and multiple cytoplasmic granules. These neutrophils mature in the bone marrow for about 15 days and then reside in the circulation for 10 hours. If they migrate into tissues, they survive about 4 days.

Images obtained with leukocytes labeled with indium or technetium immediately after injection show intense pulmonary activity that clears rapidly. This phenomenon is believed to be due to leukocyte activation during labeling, which slows their movement through the pulmonary vasculature.

^{99m}Tc HMPAO–labeled WBC studies, on the other hand, can be performed within a few hours of imaging, making this study more desirable for "emergency" purposes. The advantages and disadvantages of each of these techniques are discussed in a later section.

In some conditions that present as emergencies in the workup of infection, particularly osteomyelitis, the labeling of autologous leukocytes could present a problem. The first of these conditions is sickle cell crises. Here the sickling RBCs cannot effectively be separated from WBCs. The second condition is leukemia, in which the WBCs encountered are abnormal and functionally are not responsive to infection.

Indium-Labeled Leukocytes

A large field-of-view gamma camera is used with a medium-energy parallel-hole collimator. A 15% window is centered on the 174-keV photopeak, and a 20% window is centered on the 245-keV photopeak.

With ^{111}indium-labeled WBC studies, images are obtained 24 hours after injection, by which time the pulmonary activity would have already cleared. It is important to note that the 24-hour time lag required for indium-labeled infection imaging would remove it from consideration as a "true emergency." At 24 hours after injection, normal distribution occurs through the spleen, liver, and bone marrow (Fig. 12-14).

One disadvantage of ^{111}In imaging is that the amount of radioactivity administered—0.3 to 0.5 mCi of indium—results in low photon flux and makes it more difficult to accumulate the necessary number of counts to achieve a satisfactory image. Furthermore, the photopeaks are not optimal in comparison with ^{99m}Tc.

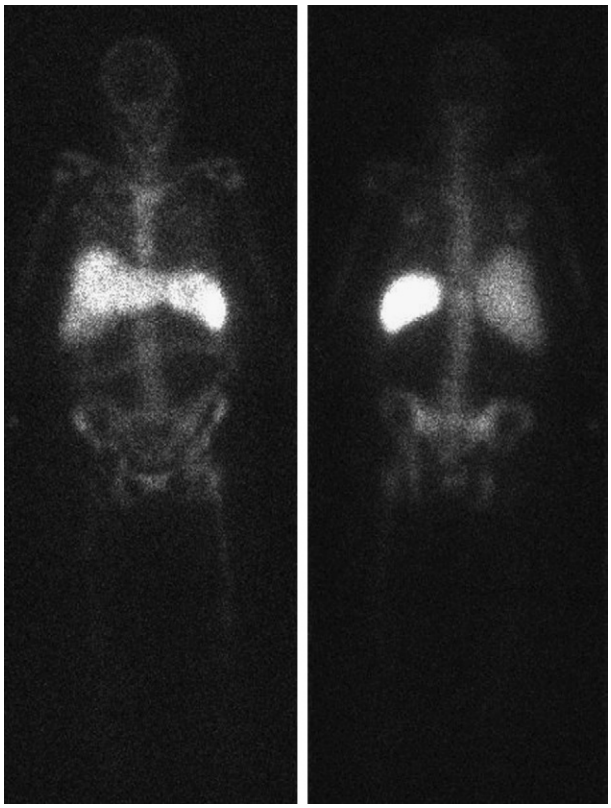


FIGURE 12-14 Normal distribution of indium-111 oxine-labeled leukocytes. A large portion of the activity is sequestered in the liver and spleen.

The advantages of using the indium label are its long half-life and the fact that the label is stable. Another advantage is that indium can be used in conjunction with other radionuclides such as ^{99m}Tc sulfur colloid bone marrow imaging, particularly with musculoskeletal infection. Here simultaneous dual isotope scans can be acquired, or, alternatively, they can be acquired in tandem. Because some infections can be indolent, such as those involving joint prostheses, the longer half-life of indium makes it a much more useful compound.

Technetium-Labeled Leukocytes

A low-energy, all-purpose, high-resolution collimator is used with a 15% window centered on the 140-keV photopeak of ^{99m}Tc. Granulocyte labeling is selective with the ^{99m}Tc HMPAO complex. Urinary activity and renal parenchymal activity appear soon after injection. Biliary activity is seen in a variable number of patients as early as 3 hours after injection, which accounts for bowel activity appearing at 4 hours. Bone marrow uptake is also seen with ^{99m}Tc-labeled leukocytes, although none is seen in normal bone. Images are routinely obtained at 2 and 4 hours after injection, although 45-minute and 24-hour images also may be obtained if they are needed (Fig. 12-15).

Technetium Methylene Diphosphonate

^{99m}Tc methylene diphosphonate (MDP) is one of the agents of choice for the evaluation of osteomyelitis. This agent is used for the triple-phase bone scan. It is injected intravenously, and flow/perfusion studies of the affected part are obtained at one image per second for a total of 30

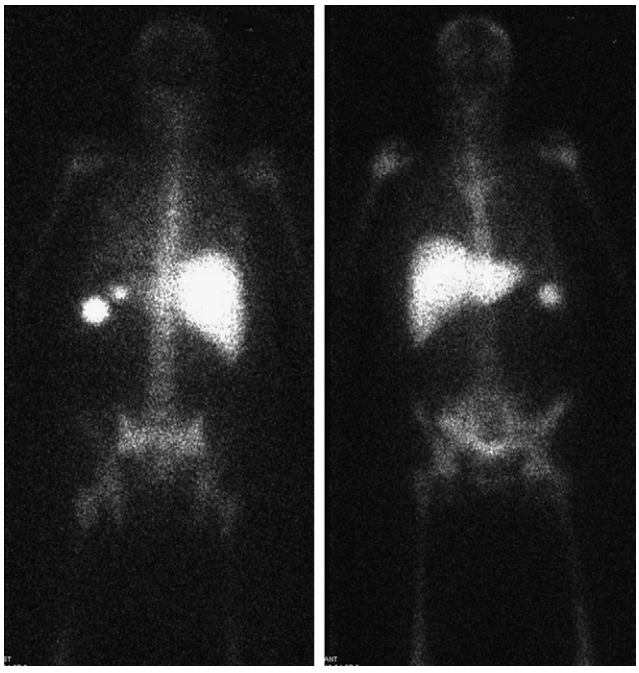


FIGURE 12-15 Technetium-99m hexamethylpropyleneamine oxime white blood cell imaging shows two foci of collection in the left upper quadrant of the abdomen corresponding to a suspected abscess on a computed tomography scan of the abdomen.

seconds. For a perfusion study, ideally a high-sensitivity collimator is used. This procedure is followed by the acquisition of "blood pool" images or immediate static images of the area in question. Two to 4 hours after intravenous administration of the ^{99m}Tc MDP, delayed static images are acquired for 500 K counts per projection utilizing a high-resolution collimator (Fig. 12-16). In smaller nuclear medicine departments, it is not uncommon to use a low-energy all-purpose collimator for both the perfusion and the static images.

Technetium Sulfur Colloid

^{99m}Tc sulfur colloid traditionally has been used as a liver–spleen scan agent. Because it is picked up by the reticuloendothelial system, it also serves as a bone marrow agent. Approximately 3 to 10 mCi of ^{99m}Tc sulfur colloid are used intravenously for imaging the bone marrow. The critical organ is the liver, with a radiation absorbed dose of 0.34 rad (cGy)/mCi.

When ^{99m}Tc- or ^{111}In-labeled WBC scans are used to evaluate for osteomyelitis, abnormal uptake in infection foci must be differentiated from normal WBC uptake in the reticuloendothelial elements in bone marrow. When technetium agents are used, they must be injected in tandem one after the other. However, when indium and technetium are used, they can be used simultaneously, and a dual isotope study can be performed.

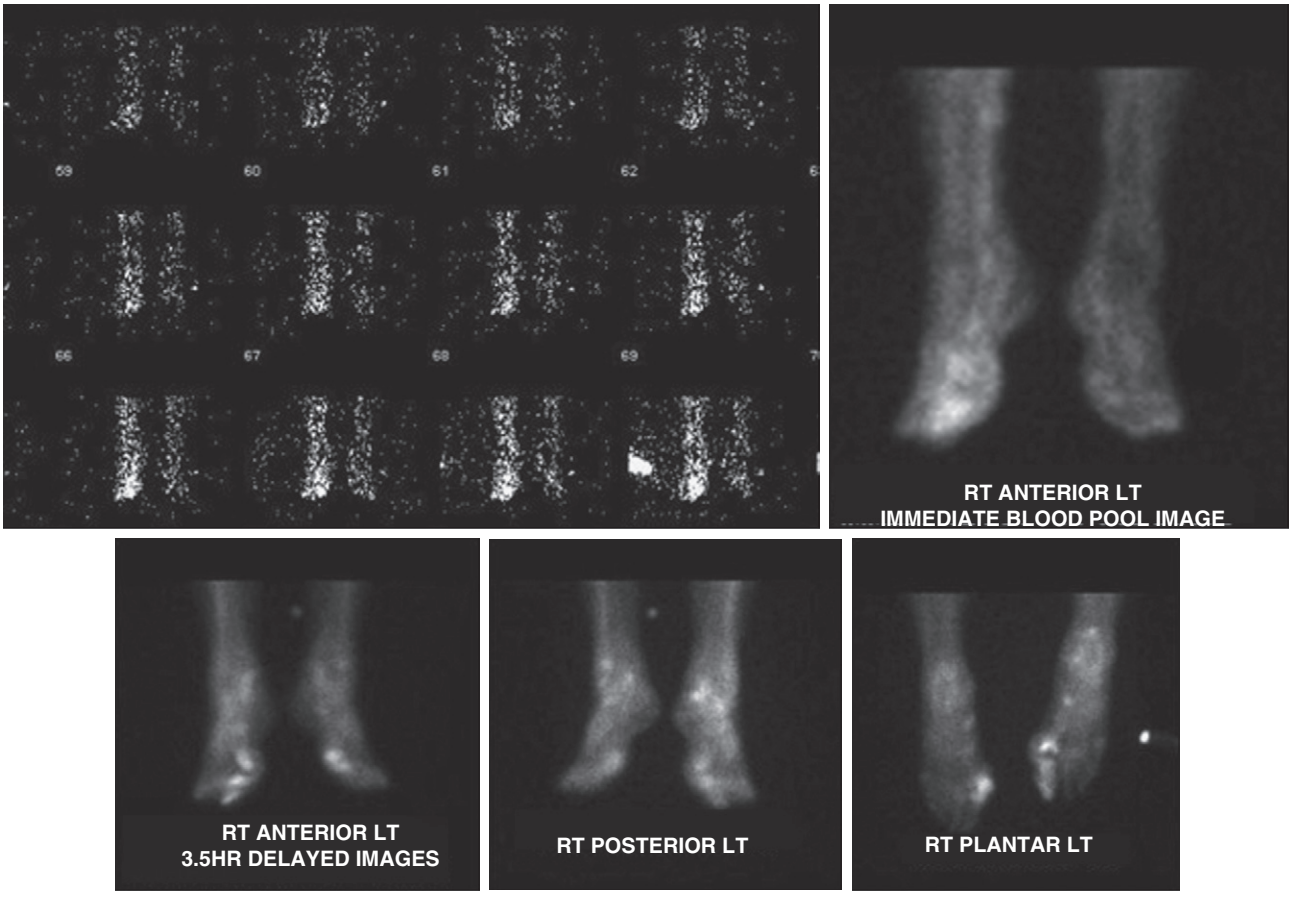


FIGURE 12-16 A technetium-99m methylene diphosphonate scan shows increased flow, blood pool, and delayed activity in the right first metatarsophalangeal (MTP) joint and great toe region, suggesting osteomyelitis. Increased delayed activity in the left MTP region is due to osteoarthritis and does not show increased flow or blood pool counts.

Gallium-67 Citrate

The uptake of gallium in infection is multifactorial. Approximately 90% of the circulating gallium is bound to transferrin. The increased vascularity and increased membrane permeability in inflammatory foci result in the increased deposition of gallium in areas of inflammation. Some of the gallium is delivered through the leukocytes, which bind the radionuclide. A third mechanism is the formation of siderophores by certain bacteria and fungi. These iron-chelating compounds are secreted by microorganisms, which dissolve Fe-3^+ ions by chelation and take up the iron by active transport. Because gallium is handled similarly to iron, siderophore–^{67}Ga complex is transported into the bacterium, where it stays until the bacterium is phagocytosed by macrophages.

At 24 to 72 hours after the intravenous injection of ^{67}Ga citrate, images are obtained. Multichannel analyzers on modern gamma cameras allow the inclusion of many of the photopeaks of gallium—93, 184, 296, and 388 keV. A medium-energy collimator is recommended to improve the resolution.

Gallium is best utilized in the workup of chronic osteomyelitis and infected joint prostheses. As the infection becomes more chronic, neutrophils are no longer recruited into the process and WBC-labeled imaging agents become decreasingly useful. Gallium then becomes the agent of choice. In acute osteomyelitis, increased gallium uptake frequently precedes the ^{99m}Tc MDP accumulation because osteomyelitis is initially an involvement of the bone marrow. Gallium is also useful in infants younger than 6 months of age for whom ^{99m}Tc MDP scans are likely to be negative.

Newer Agents

Because it is cumbersome to label leukocytes in vitro, significant effort has been expended in developing in vivo methods for labeling WBCs. These methods include the labeling of leukocytes in vivo, use of peptides, and use of antigranulocyte antibodies/antibody fragments. Until recently, ^{99m}Tc-labeled monoclonal murine M class immunoglobulins that bind to cluster designation 15 receptors on the surfaces of leukocytes had been the subject of clinical trials. This (fanolesomab) is labeled with ^{99m}Tc pertechnetate. After approximately 10 to 20 mCi are injected intravenously, the agent is distributed in the vasculature, and it is retained in the spleen and liver. The ease of in vivo labeling, the lack of risk of handling blood products by technologists, and the rapid and intense accumulation in regions of infection make quite a compelling case for pursuing these avenues further.

Indications

Infections generally tend to be indolent and rarely present as emergencies. However, when a postsurgical patient presents with symptoms suggestive of infection, an excellent case is to be made for using nuclear medicine in the workup. The accuracy of WBC-labeled studies in abdominal abscesses is greater than 85%, which is comparable with CT.

With the advent of fusion imaging or SPECT CT, the work of the diagnostician is easier and the results are far more valuable. The complementary use of the anatomic strengths of CT with the metabolic sensitivity of nuclear medicine will serve to vastly and incrementally increase the usefulness of each of these modalities by overcoming the limitations of each modality.

Abdominal Abscesses

Abdominal abscesses are a common and difficult to diagnose problem in postsurgical patients. Although ultrasound is probably the easiest and the most expedient method of diagnosis, surgical dressings, wounds, edema, and the patient's body habitus often become deterrents to diagnosis using this modality. Although CT provides exquisite resolution, it includes the inconvenience of administration of oral contrast material and the risk of precipitating or worsening renal compromise with the administration of intravenous contrast material. Furthermore, the radiation exposure with multidetector CT is not trivial, particularly in patients who may need repeated studies. In this case, nuclear medicine with the use of radiolabeled WBCs can prove invaluable in pinpointing the disease. The additional advantage of using nuclear medicine procedures is that the entire body can be imaged without additional radiation exposure.

The following causes of intraabdominal abscesses are the most common:

1. Perforation of a diseased viscus—peptic ulcer, inflamed appendix, or diverticulum
2. Gangrenous cholecystitis
3. Mesenteric ischemia with bowel infarction
4. Pancreatic necrosis or pancreatic abscess progressing to abscess formation
5. Penetrating abdominal trauma
6. Postoperative complications such as anastomotic leaks

The most commonly encountered organism is *Escherichia coli.* Skin flora may cause abscesses after penetrating wounds to the abdomen. *Neisseria gonorrhoeae* and chlamydia are commonly involved in pelvic abscesses in females who might have pelvic inflammatory disease. Microbial flora of the GI tract varies from the proximal to the distal sites, with small numbers of aerobic streptococci in the stomach and proximal small bowel and large numbers of these organisms, as well as large numbers of anaerobic gram-negative bacilli and anaerobic gram-positive flora, in the terminal ileum and colon. The differences in the types and concentrations of these microorganisms partially account for differences in septic complications based on the location of the injury or disease. Septic complications from upper GI perforations are far less ominous than those from colonic insults.

With indium-labeled WBC scans, whole-body imaging is recommended 4 and 24 hours after intravenous administration of the agent, and with ^{99m}Tc-labeled WBC studies, imaging is performed at 1 and 4 hours. Abscesses demonstrate progressively increasing activity, often greater than the liver and outside areas of normal accumulation.

In the case of hepatic abscesses, indium-labeled WBCs are preferred because the biliary excretion seen with ^{99m}Tc-labeled WBCs could complicate the interpretation of the image. It is important to note that activity in an abscess will increase on delayed images, whereas normal uptake regresses. Hence, when searching for hepatic abscesses, we recommend that ^{111}In-labeled WBCs be used. Analysis of the images definitely should not be made on the basis of the early images alone.

Pancreatic abscesses are best studied with ^{111}In-labeled studies because of the increased likelihood of spontaneous communication of the abscess with the gut. As a note of caution, unfortunately, WBC scans are positive with pancreatic abscesses and fat necrosis, as well as with pancreatic pseudocysts.

In patients with catheter tunnel infection who are undergoing peritoneal dialysis, nuclear medicine provides the ability to distinguish between early peritonitis and exit site infection, which is of special importance when the clinical management is different based on the site of the infection.

Six functional compartments are present within the peritoneal cavity:

1. Pelvis
2. Right paracolic gutter
3. Left paracolic gutter
4. Infradiaphragmatic spaces
5. Lesser sac
6. Interloop potential spaces of the small intestine

Inflammatory Bowel Disease

^{99m}Tc-labeled WBC studies are believed to be useful in the diagnosis of inflammatory bowel disease (IBD). Early views of the abdomen supply the diagnosis, with uptake in the diseased bowel greater than that noted in the spleen. Delayed images are less reliable, because with ^{99m}Tc-labeled WBC studies, ^{99m}Tc-labeled secondary complexes may be excreted into the bowel. The configuration of the uptake in the bowel is usually sufficient to distinguish IBD from abdominal abscesses.

Musculoskeletal Infections

The major problems of imaging for osteomyelitis with WBC-labeled studies are that (1) osteomyelitis is frequently more chronic and (2) WBCs normally accumulate in the bone marrow, where they are destroyed by the reticuloendothelial system. In the imaging of a prosthesis, nuclear medicine imaging is not affected by the prosthesis, whereas the prosthesis is a deterrent to imaging with any of the other imaging modalities. Bone scintigraphy is useful, in that a negative scan essentially excludes a prosthetic complication. Adding ^{67}Ga citrate increases the accuracy of bone scintigraphy. The combination of leukocyte labeling combined with marrow imaging is believed to have the highest accuracy of all the imaging studies available (Fig. 12-17).

Joint Prostheses

Infection and loosening are the most frequent complications of joint replacement. It is vital to be able to differentiate between these entities, especially because the management strategy is totally different in each case. With aseptic loosening, the patient requires a single hospital admission for single-stage revision joint replacement. With an infected prosthesis, multiple hospital admissions are required, initially to perform an excisional arthroplasty, then for a prolonged course of antibiotic therapy, and eventually for a revision arthroplasty.

When no ^{99m}Tc MDP uptake is identified in and around the prosthesis, the possibility of any actual abnormality is remote. Diffuse periprosthetic uptake is seen in cases of infection, as well as in cases of aseptic loosening. With the new porous-coated prostheses, periprosthetic bony ingrowth is stimulated; therefore, diffuse periprosthetic uptake is seen because of programmed bony ingrowth and is not necessarily indicative of disease. This type of uptake, when seen in nonporous prosthetics, is associated with increased blood flow, and osteolysis is seen with infection. ^{99m}Tc MDP imaging is of tremendous value because of its high negative predictive value.

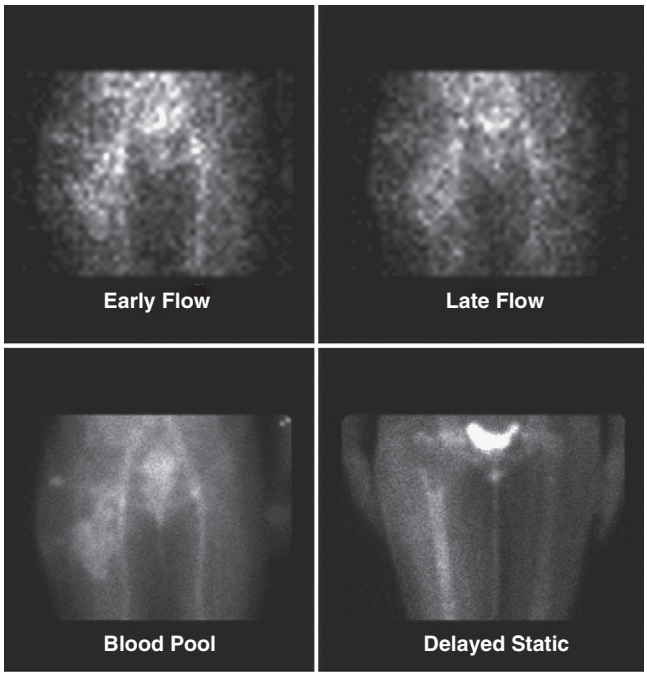


FIGURE 12-17 A technetium-99m methylene diphosphonate bone scan shows soft tissue infection but no evidence of osteomyelitis. The patient underwent removal of a right hip prosthesis.

The most important differentiator between the two clinical entities—loosening and infection—is the level of neutrophils, which are always present in large numbers in infection and absent in loosening. Therefore, ^{99m}Tc-labeled leukocytes intuitively would seem to be the agent of choice. However, because leukocytes are also present in the bone marrow, one must search for concordance and discordance with accompanying ^{99m}Tc sulfur colloid images. For instance, when the WBC-labeled images show more activity than the ^{99m}Tc sulfur colloid, the discordance is due to infection. The combined technique has an accuracy of greater than 90%.

^{67}Ga citrate imaging is also useful because of the high negative predictive value. Gallium uptake is related to inflammation and not necessarily infection alone, which makes this a less specific test. However, ^{67}Ga may prove to be more useful if the infection is believed to be more chronic and therefore less likely to be mediated by granulocytes.

Osteomyelitis

Osteomyelitis can present after trauma, as a consequence of bacteremia, or as a result of vascular insufficiency, such as in a diabetic foot. The common organisms vary with the age of the patient: *Staphylococcus aureus* and *Streptococcus* in neonates and infants, *S. aureus* in

adults, and gram-negative bacteria in elderly persons. With the changing face of disease, immune status of patients, and exposure to "exotic" microorganisms from previously inaccessible geographic locations, the list of organisms producing osteomyelitis has become much more extensive.

In children, osteomyelitis is often hematogenous. Because the epiphyses and metaphyses have separate blood supplies in children, it is common to have only metaphyseal involvement with sparing of the epiphysis. In most instances, accumulation of the radionuclide (^{99m}Tc MDP) increases on all three phases, with the accumulation increasing and becoming more focal on the delayed images. Ewing's sarcoma can mimic osteomyelitis on scans. Consequently, clinical correlation is important to differentiate one entity from the other.

In patients with diabetes, infection is often complicated by neuropathy. ^{99m}Tc MDP scans are used for anatomic localization. WBC-labeled agents are invaluable in the diagnosis of infection. Because there is uptake of WBC label in the bone marrow, one looks for discordant versus concordant uptake to make the diagnosis. ^{99m}Tc sulfur colloid is used to locate the position of the bone marrow. With the use of SPECT, we can anticipate that the use of a single radiopharmaceutical agent and anatomic correlation with CT will make the diagnosis and follow-up of osteomyelitis easier.

Septic Arthritis

Septic arthritis tends to be monoarticular and shows increased uptake with ^{99m}Tc MDP, WBC-labeled scanning, and ^{67}Ga. This uptake, however, is nonspecific and can be seen in instances of gout, which can manifest as a monoarticular, sterile inflammatory arthropathy. Uptake is seen on both sides of the joint. With associated cellulitis, radionuclide uptake may be detected in areas around the joint or adjacent soft tissues.

Septic arthritis in pediatrics is a true emergency and often affects the hip. The most common mode of presentation with imaging is as a photopenic defect with a normal radiograph. The diagnosis is made after hip aspiration.

Transient synovitis can affect the hip in children with a fair degree of frequency. Bone scans are often negative or only mildly positive in this entity.

Infection in Immunocompromised Patients

Imaging of infection in immunocompromised patients is best performed using ^{67}Ga citrate rather than labeled WBCs. Normal findings of a chest radiograph with normal findings of a gallium scan exclude the presence of infective disease in the chest. Normal findings of a gallium scan in the face of an abnormal chest radiograph is indicative of the inability of the patient to mount a response and carries a poor prognosis. *Pneumocystis carinii* and/or bacterial pneumonia show diffuse intense uptake of gallium. Faint uptake in the chest may be seen in mycobacterial or cytomegalovirus infections. Lymph node uptake is seen most often with mycobacterial infection or lymphoma. Kaposi sarcoma will not take up gallium; hence, in the absence of ^{67}Ga uptake, an abnormal chest radiograph should raise the suspicion of Kaposi sarcoma.

Infections in the Lung and Other Regions

Pulmonary Disease

^{99m}Tc HMPAO–labeled WBC scans are ideal to detect lung abscesses. Surprisingly, lobar pneumonia is usually negative on WBC scanning except early in the course of the pneumonia. This phenomenon is believed to be due to early termination of WBC migration in the disease. In acute respiratory distress syndrome, persistent increasing WBC uptake occurs in the lungs, such that delayed images will present with increasing uptake as opposed to the normal transient early uptake described previously in this section.

Infection associated with obstruction in bronchogenic carcinoma and with bronchiectasis shows abnormal uptake with labeled WBCs.

TRAUMA AND BONE INFARCTION

Avascular necrosis of the femoral head is quite common and is seen in several disease states, such as trauma, chronic steroid use, and sickle cell crises. Initial photopenia is present as a result of decreased vascularity followed by increased activity that reflects new remodeling. Although bone scanning with ^{99m}Tc MDP is far more sensitive than conventional radiography, magnetic resonance is by far the best imaging modality for the workup of infarction.

Accessory ossicles are very easily differentiated from new bone fragments on conventional radiographs. However, in the rare instance in which the patient reports pain, citing a possible injury, bone scanning may be of some use in the investigation of the pain. For instance, an inexpert golfer may report pain in the region of the hook of the hamate. Radiographs occasionally may be of dubious value in differentiating an os hamuli proprium from an old fracture versus reinjury of the hook of the hamate. Bone scans performed using high-resolution or converging collimators will show increased activity with bony injury.

The pediatric skeleton responds to bony injury much differently than does the mature skeleton because in early childhood the skeleton is more porous and elastic. The thicker periosteum limits fractures from extending through the entire thickness of the bone. Ligaments and tendons are stronger than physes and will resist stress and torque forces, which results in fractures of the growth plate in the setting of trauma. As the child matures and reaches puberty, the increased growth and muscle strength result in avulsion fractures. Although the pediatric skeleton has a higher likelihood for repair and healing, the potential exists for interruption of the vascular supply, which can be catastrophic for achieving complete and normal growth. Fifteen percent of growth plate injuries result in shortening. Avulsion-type injuries occur where there is attachment of large muscle groups. This type of injury is seen with sports activity. Although CT and MRI provide exquisite images and the ability to evaluate chondral injury and disruption, bone scans allow evaluation of the entire skeleton, which can be used to direct focused utilization of any of the other modalities mentioned.

Nonaccidental injury (NAI) in children constitutes part of the spectrum of abuse, including physical abuse, sexual abuse, psychological abuse, and neglect. Four million children each year are abused in the United States, and 200 children die as a result. Radiologic evaluation of NAI is of

tremendous importance in the diagnosis of child abuse. It is important to remember that not all children present with a high clinical suspicion of abuse. The child may present with some other reason for evaluation, which reveals lesions suspicious of NAI. Although opinion is divided among radiologists about the use of conventional radiography and survey of the entire skeleton versus bone, we believe that bone scans, when positive, can provide enough information to preclude exposing the child to a complete skeletal survey. The skeletal lesions can be classified as high-, moderate-, and low-specificity fractures and should lead to a high degree of suspicion for NAI, as follows:

1. Corner or bucket handle fractures are considered the most highly specific.
2. Moderate-specificity lesions include multiple fractures, fractures of different ages, epiphyseal separations, vertebral body fractures, and subluxations.
3. Low-specificity lesions include clavicular fractures, long bone shaft fractures, linear skull fractures, and subperiosteal new bone formation.

A skeletal survey and bone scintigraphy are complementary, and we recommend that both be performed in suspected NAI.

GASTROINTESTINAL BLEEDING

The causes of GI bleeding are classified into upper and lower GI bleeding. Upper GI bleeding comes from the esophagus, stomach, or duodenum. The most common causes of upper GI bleeding include ingestion of caustic substances, gastric malignancy, peptic ulcers, gastritis, esophageal varices, and Mallory-Weiss tears.

Lower GI bleeding originates from the jejunum, ileum, and the large bowel. Some of the common causes include diverticular disease, angiodysplasia, polyps, hemorrhoids, cancers, IBD, infectious colitis, and anal fissure.

Endoscopy is the first line of diagnostic evaluation when a patient presents with melena. Nuclear medicine studies are fairly innocuous and noninvasive.

The false-positive conditions include intramural hematomas and hemangiomas, which concentrate the radiopharmaceutical agent in the wall of the bowel. This presentation can be distinguished from bleeding into the lumen of the GI tract by the fact that repeated images would not show any progression through the bowel.

Bleeding from ectopic gastric mucosa into a reduplication enteric cyst also can produce a false-positive finding. In this instance as well, the tagged RBCs will not progress.

Radiopharmaceuticals

An ideal agent for GI bleeding would be one that quickly accumulates extravascularly at the bleeding site. The ideal agent also would be rapidly cleared from the blood pool, providing good target-to-background ratios (TBRs). Because GI bleeding in most instances is slow and intermittent, the ideal agent would detect slow bleeding and allow for reimaging without reinjection.

The two agents that are used for detection of the source of GI bleeding are ^{99m}Tc-labeled RBCs (Fig. 12-18) and ^{99m}Tc sulfur colloid. Neither of these agents is ideal, and each agent has advantages and disadvantages that the other may not possess.

^{99m}Tc-labeled RBCs remain in the vascular compartment, which allows repeated imaging of the GI tract. However, it is the very persistence of the agent in the blood pool that precludes the ability to obtain an optimal TBR. With the more popular but technically more challenging in vitro technique, the appearance of free pertechnetate can be avoided with meticulous attention to washing. The presence of free pertechnetate can present a problem because it is picked up by the gastric mucosa and can obscure bleeding in the gastric cavity, as well as the overlying transverse colon. Because the ^{99m}Tc RBCs stay in the blood pool, images are generally difficult to read because of the presence of the tagged RBCs in the large and capacitance vessels.

^{99m}Tc sulfur colloid is picked up by the reticuloendothelial system and shows uptake in the liver, spleen, and bone marrow. The advantage of the technetium sulfur colloid is that the high TBR allows the detection of active bleeding at low bleeding rates of 0.5 to 0.1 mL per minute. If the patient is not bleeding at the time of the injection and for the next 15 minutes, and bleeds later, no technetium sulfur colloid will remain in the blood pool to allow reimaging. Furthermore, the normal uptake in the liver and spleen also can obscure the flexures should they be the sites of bleeding.

Technique

The patient is positioned supine with the camera positioned to include the entire abdomen. If ^{99m}Tc sulfur colloid is being used, a dynamic study is performed immediately after the intravenous injection of the ^{99m}Tc sulfur colloid. Static images are obtained every 10 minutes up to 30 minutes. If ^{99m}Tc-labeled RBC scanning is performed, dynamic images are obtained immediately after intravenous injection of the radiolabeled RBCs. Five-minute images are acquired for a total of 1 hour. If no bleeding is detected, then images are obtained every hour for 4 hours and again at 6 and 24 hours, which should help in detecting intermittent bleeding.

Meckel Scan

Meckel diverticulum is the most common GI anomaly, occurring in approximately 2% of the population. It is more common in men than in women. Ectopic gastric mucosa is contained in 5% to 7% of these diverticula, which can present with bleeding. Most of these patients present with rectal bleeding. The diverticula vary in position and are frequently located approximately 2 feet from the ileocecal junction. They are most frequently visualized in the suprapubic region as a small focus of intense ^{99m}Tc uptake.

Technique

Ectopic gastric mucosa, whether in a Meckel diverticulum or in a reduplication cyst, can be detected with ease after the administration of up to 10 mCi of ^{99m}Tc injected intravenously as pertechnetate. "Dynamics" are obtained every 5 minutes for 30 minutes after intravenous injection. Static images can be acquired after the dynamic phase is completed, with images taken at 40, 50, and 60 minutes. Oblique views are helpful in localizing the site of the diverticulum. It is important to note that ectopic gastric mucosa will behave similarly to regular gastric mucosa, becoming equally intense.

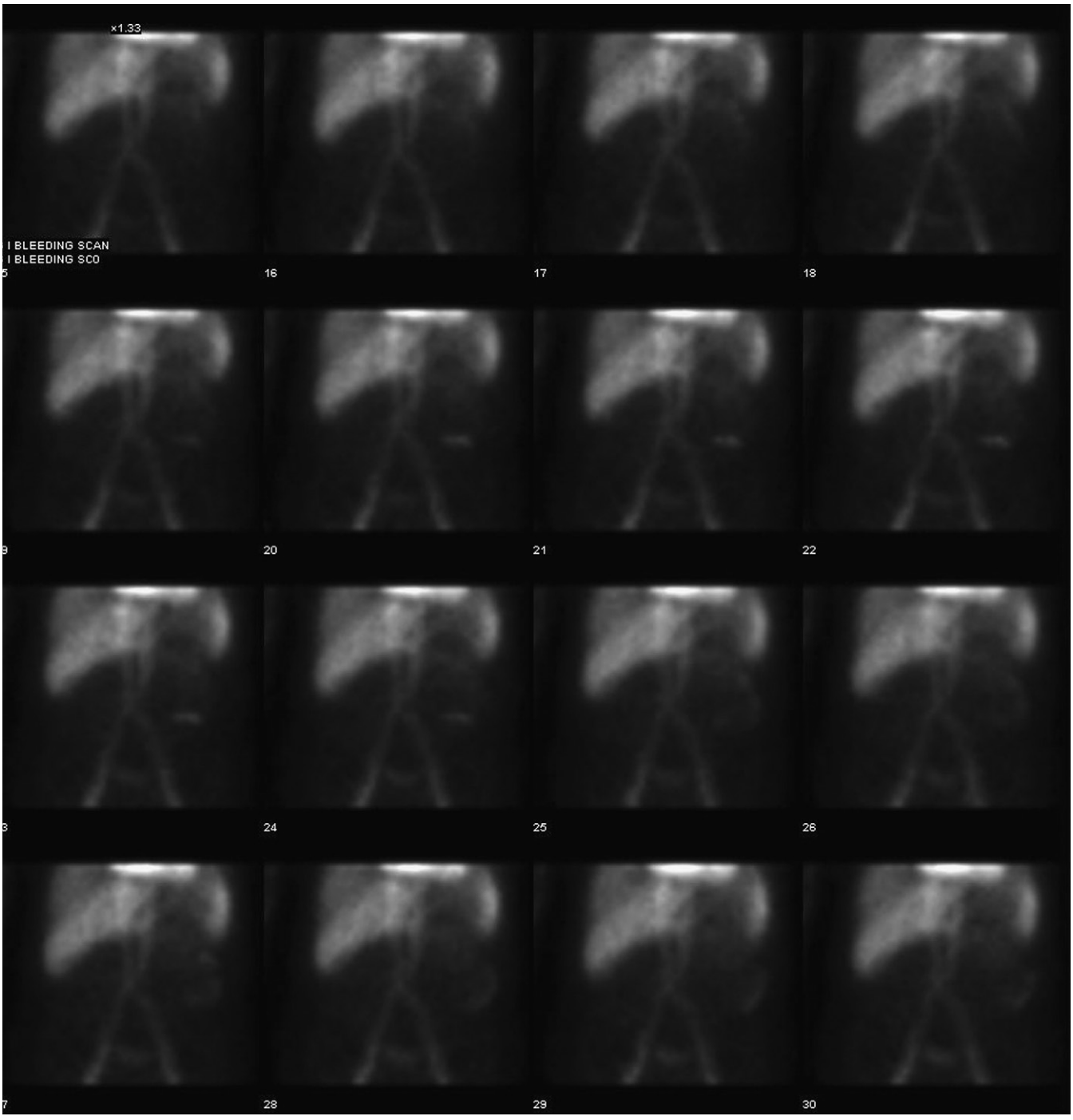


FIGURE 12-18 A technetium-99m red blood cell study shows significant progressive accumulation of activity in the descending colon as a result of bleeding.

HEPATOBILIARY SCINTIGRAPHY

Hepatobiliary scintigraphy is one of the most important studies performed in the nuclear medicine department on an emergency basis. The most common indications for emergency hepatobiliary scintigraphy are acute cholecystitis and bile leaks.

Patients presenting with right upper quadrant pain are generally evaluated for acute cholecystitis. Ultrasound in this instance generally is not useful. However, with chronic cholecystitis, ultrasound would be the preferred method of investigation. A significant percentage of the patients who are liable to be candidates for chronic cholecystitis are also relatively obese, which presents a challenge for ultrasound evaluation. Because chronic cholecystitis is associated with flatulence, bowel gas also can prove to render an ultrasound examination difficult if not impossible to perform.

Hepatobiliary Agents—Mechanism

Bile is produced by the hepatocytes, and approximately two thirds of bile is excreted into the duodenum via the common bile duct. The remaining one third flows via

the cystic duct into the gallbladder, where it is stored. When a cholecystagogue (CCK) is administered or is produced in response to a fatty meal, the gallbladder contracts and bile is emptied into the duodenum. If the patient has recently had a meal, the endogenous CCK will prevent the gallbladder from filling. Therefore, the patient is encouraged to not eat for 4 hours before the test. If the patient has been fasting for more than 24 hours, the gallbladder is generally full of viscous bile, which prevents accumulation of tracer. In contrast to bilirubin, the hepatobiliary agents are not conjugated; therefore, abnormalities of the conjugation mechanism are not a contraindication to the use of the hepatobiliary iminodiacetic acid (HIDA) scan or the diisopropyl iminodiacetic acid (DISIDA) scan.

The hepatobiliary agents used most commonly are ^{99m}Tc mebrofenin (HIDA) or ^{99m}Tc disofenin (DISIDA). These radiopharmaceutical agents are taken up by the hepatocytes and excreted into the biliary tract. Elevated levels of bilirubin associated with hepatocyte dysfunction may preclude the use of DISIDA because retention of the tracer in the liver may be prolonged. After intravenous administration of 3 to 5 mCi of the tracer (HIDA), initial visualization of the cardiac blood pool is noted. Within 5 minutes, the agent appears in the liver. During the next 5 to 7 minutes, images of the liver can be obtained in multiple projections. The agent then enters into the biliary tract with "opacification" of the major bile ducts and the common bile duct. At this time, the tracer appears in the duodenum. The cystic duct and gallbladder are the next to fill. Similar to the bile previously mentioned, some of the tracer enters into the gallbladder as long as the cystic duct is patent.

Acute Cholecystitis

The vast majority of patients with acute cholecystitis have cystic obstruction, and thus hepatobiliary scintigraphy is used for the diagnosis of acute cholecystitis. Absence of visualization of the gallbladder for up to 4 hours after injection of the radiotracer is considered diagnostic for acute cholecystitis (Fig. 12-19). The appearance of the tracer in the gallbladder effectively excludes the presence of acute cholecystitis. However, in some cases of acalculous cholecystitis, filling of the gallbladder may occur. Additionally, the presence of an accessory cystic duct can cause a filling of the gallbladder through an "alternate" route. Structures that simulate a gallbladder can produce false-negative results; these structures include duodenal diverticula and biliary duplication cysts.

Not infrequently in a person with chronic cholecystitis, tracer may not accumulate in the gallbladder. Some pharmaceutical interventions may actually prompt the filling of the gallbladder.

If the patient has fasted for a prolonged period, the gallbladder may be full of viscous bile. In this case, the administration of CCK prior to or early in the study (while tracer is still available in the liver) will make the gallbladder contract and empty its contents. If the cystic duct is not obstructed, then tracer will enter the gallbladder, effectively excluding the diagnosis of acute cholecystitis.

Intravenous administration of morphine (0.04 mg/kg diluted in 10 mL of normal saline solution administered over 5 minutes) causes constriction of the sphincter of Oddi, raising intraductal pressure and forcing the filling of the gallbladder (Fig. 12-20). Occasionally there may not be enough tracer in the liver or the biliary tree to fill the gallbladder, which may necessitate a second injection of the tracer. Administration of morphine is a measure that should be used with caution where there is obstruction to the proximal portion of the cystic duct, as evidenced by the "cystic duct" sign. Enough pressure may be generated in the system to force the tracer into the gallbladder, producing a false-negative study.

An important note of caution is that CCK should not be used after administration of morphine. The CCK causes the gallbladder to contract, while the morphine raises the intraductal pressure, which can result in severe pain.

Certain ancillary signs are of use in the diagnosis of cholecystitis:

1. The "rim" sign is a crescentic accumulation of a radiopharmaceutical agent within the parenchyma of the liver, along the inferior margin of the liver above the "empty" gallbladder fossa. Pericholecystic hyperemia associated with acute cholecystitis is believed to be the mechanism producing this finding. The "rim" sign is often but not invariably associated with acute cholecystitis. At least half of these patients may have a perforated or gangrenous gallbladder.
2. The "cystic duct" sign is defined as a small nubbin of activity in the cystic duct proximal to the site of obstruction. This sign is believed to be diagnostic of acute cholecystitis.
3. ^{99m}Tc HIDA/DISIDA scans are paramount in the detection of postsurgical or post-traumatic biliary leaks (Fig. 12-21). These agents are highly sensitive in detecting biliary leaks, which are not seen with other modalities. Additional views of the paracolic gutter and the pelvis must be obtained. A thorough knowledge of the anatomy of the peritoneal spaces is useful in helping the surgeon with the postoperative care of the patient.

Biliary Atresia Versus Neonatal Hepatitis

Hepatobiliary scintigraphy is useful in the differential diagnosis of biliary atresia versus neonatal hepatitis. Preparation of the patient by prescribing phenobarbital (2.5 mg/kg orally twice a day) for a week will stimulate the uptake of the tracer, allowing visualization of a patent biliary tree, which will help rule out atresia.

Biliary atresia occurs after birth in very young infants or neonates. This condition is characterized by the development of progressive inflammation in the biliary tract, causing irreversible damage and disappearance of the bile ducts. The neonate appears normal at birth and then obstructive jaundice starts to develop 2 to 3 weeks after birth. Distinguishing between biliary atresia and neonatal hepatitis is critical because early surgical intervention is mandatory in effecting a good outcome. The Kasai procedure is a roux-en-Y or hepatoportojejunostomy. The chances of success are greatly diminished after the infant is older than 3 months. Hence, every infant with jaundice in the neonatal period should be

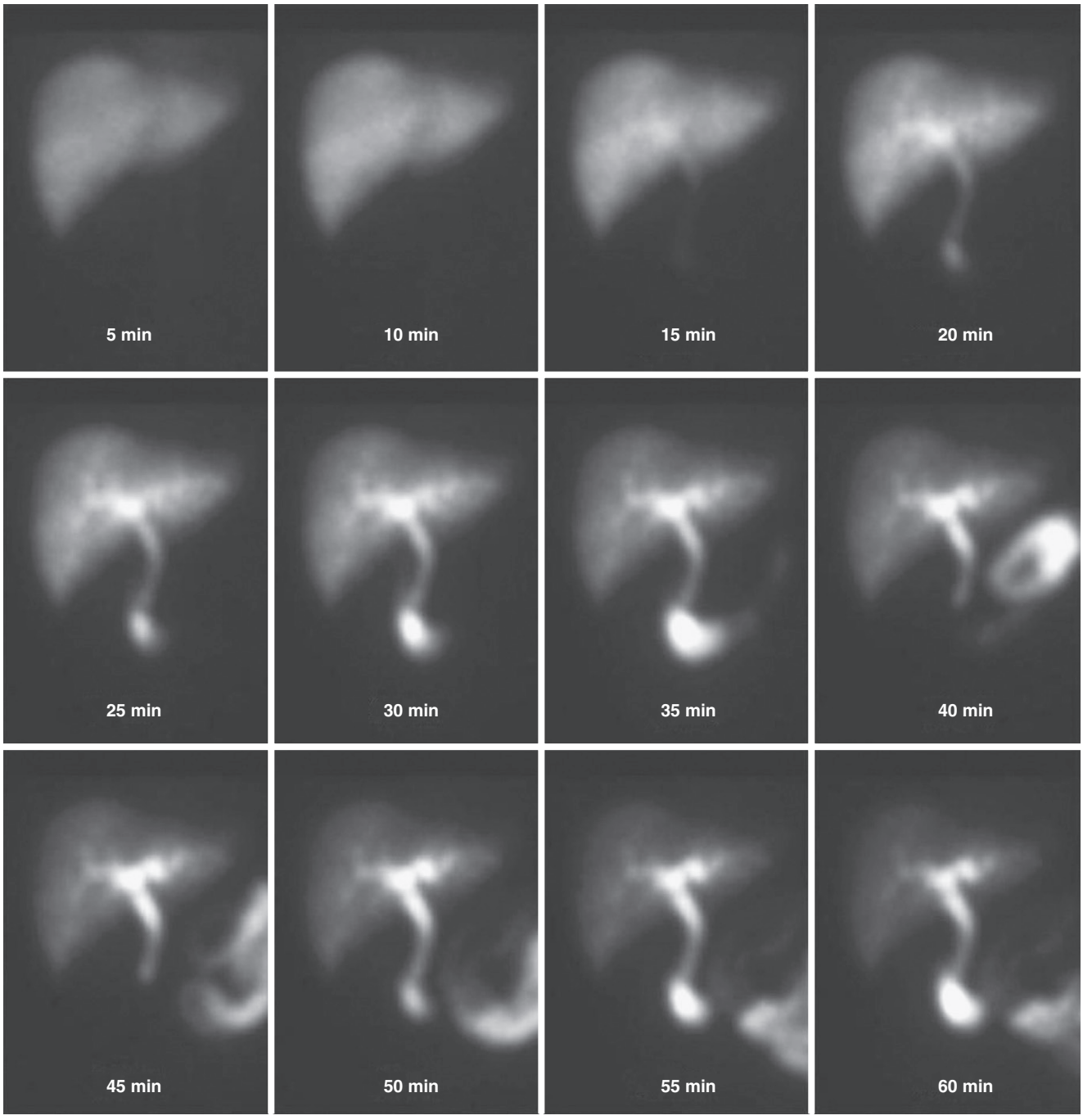


FIGURE 12-19 Acute cholecystitis. Nonvisualization of the gallbladder for 60 minutes (min) with technetium-99m choletech. The gallbladder fossa is empty, without any activity. The appearance of the common bile duct and duodenum is normal.

studied with ^{99m}Tc hepatobiliary agents (HIDA/DISIDA) to ensure that the surgical treatment is instituted before it is too late.

SCROTAL SCANNING

In the setting of testicular pain, the working diagnosis is either testicular torsion or epididymo-orchitis. Testicular scans and Doppler ultrasound have a high degree of sensitivity in detecting testicular torsion. Because testicular torsion is a surgical emergency, a rapid and accurate diagnosis is paramount.

Radiopharmaceuticals and Technique

The patient is placed in a frog-leg position with the scrotum supported on a sling made by using a towel straddled across the front of the patient's thighs. A conventional flow study with dynamic images is obtained after the intravenous administration of 5 to 10 mCi of ^{99m}Tc pertechnetate or ^{99m}Tc DTPA, which are essentially "blood pool" agents. After the dynamic study is completed, blood pool static images are obtained in the anterior projection. Delayed static images are obtained, which will provide additional confirmation of the lack of vascularity to the affected testis in

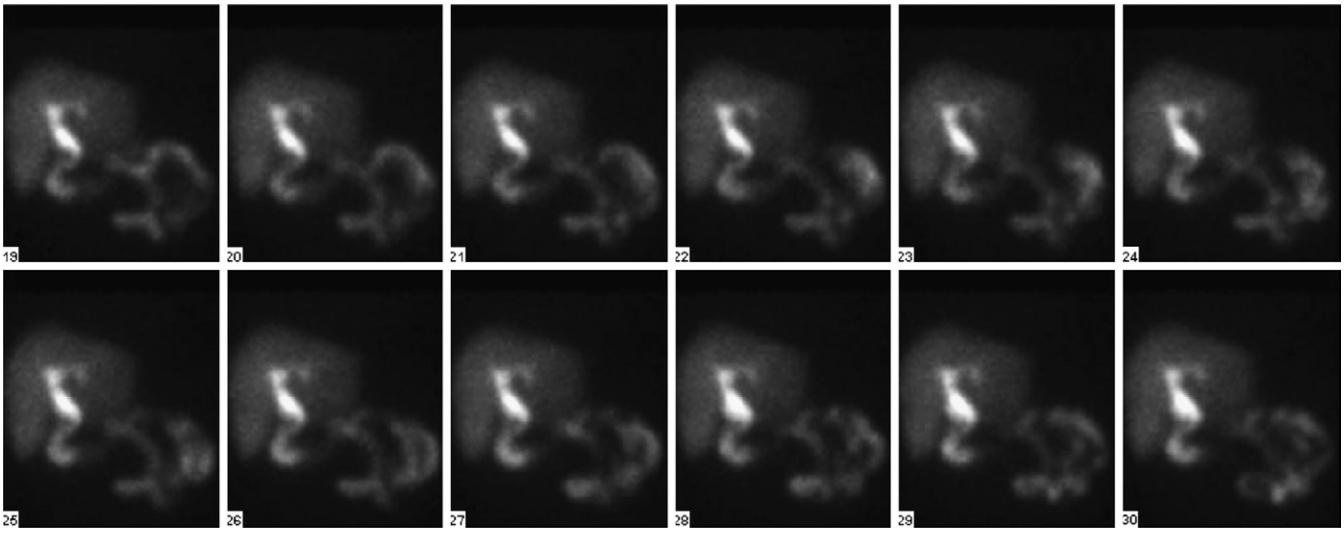


FIGURE 12-20 A scan after the administration of morphine shows that the gallbladder is not filled, indicating complete cystic duct obstruction. Retention of activity in the common bile duct is due to contraction of the sphincter of Oddi.

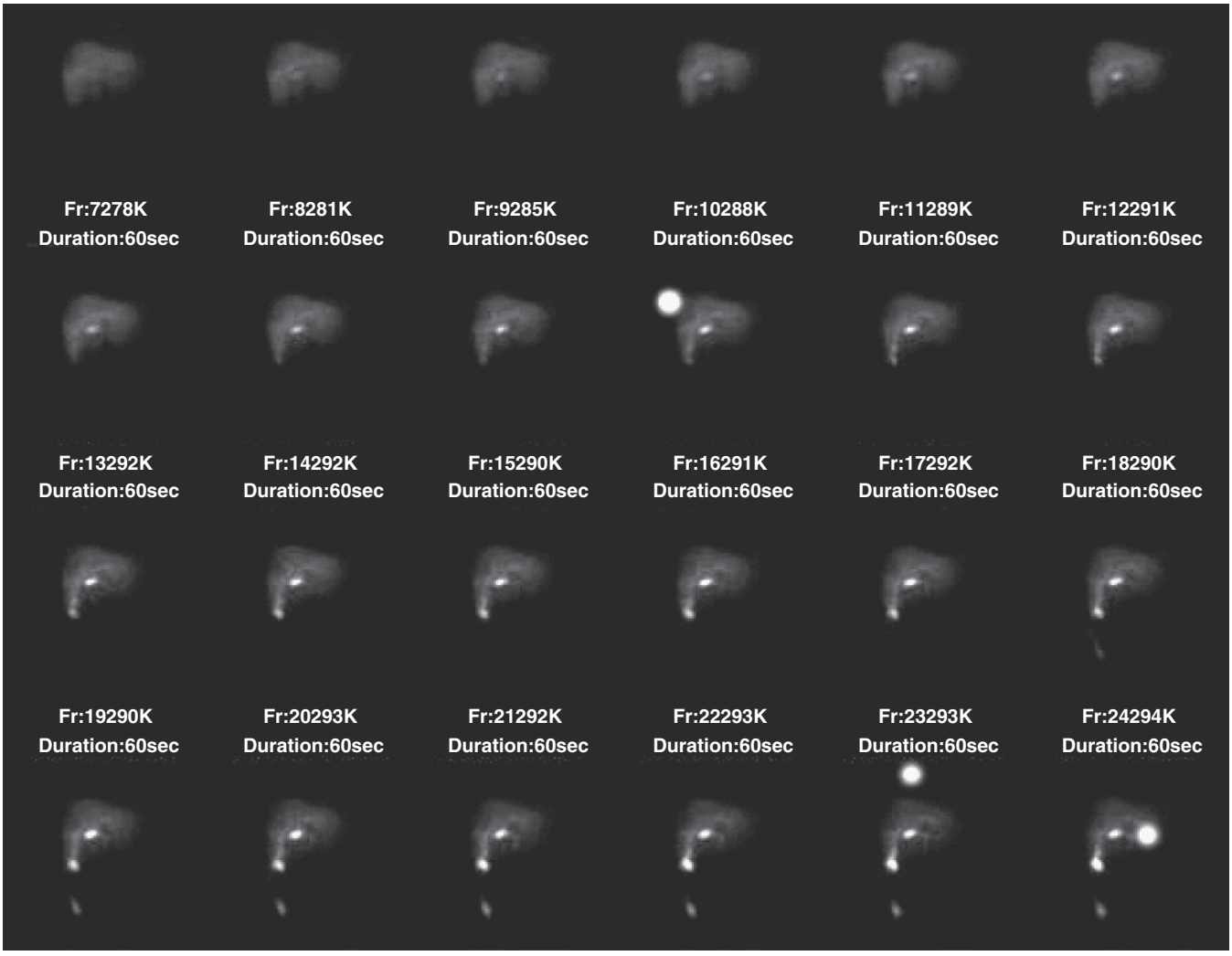


FIGURE 12-21 A technetium-99m diisopropyl iminodiacetic acid study shows a biliary leak with tracer along the right paracolic gutter.

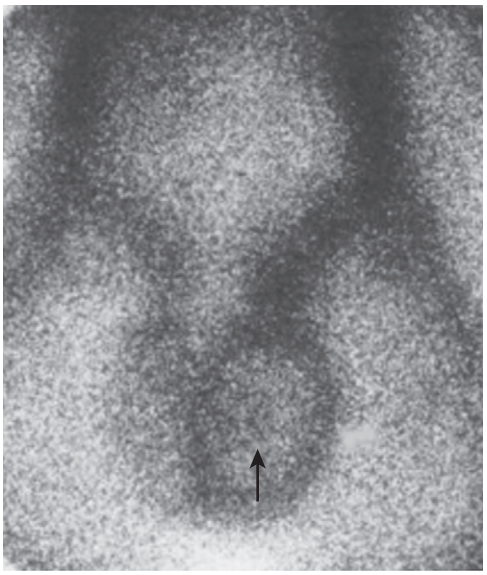


FIGURE 12-22 Left testicular torsion *(arrow)* shows increased peripheral flow and absence of central activity (the "halo" sign) consistent with testicular torsion. Minimal activity is noted in the right testicle, which was normal.

torsion. It is extremely important to have the technologist mark the side of symptomatology distinctly on the images submitted to the picture archiving and communication system. Personally, we prefer to use a converging collimator to obtain the images.

Interpretation

Testicular Torsion

In the early stage of torsion, the perfusion to the affected side may be normal. A "nubbin" sign is believed to be pathognomonic for torsion and represents the site of the actual torsion of the testicular vessels. This sign is due to visualization of the spermatic artery, which is being filled by the iliac artery (Fig. 12-22). In the later stages of the torsion—that is, 24 hours later—the relative avascular testis is thrown into high relief by the increased flow through the pudendal vessels to the scrotal sac. The now perfused scrotal sac with the absent vascularity in the testis provides a "halo" sign.

Epididymo-orchitis

Epididymo-orchitis is usually a viral or bacterial condition. Associated with increased vascularity to the affected testis, it typically shows up as increased blood flow to the testicle. In some instances in which edema of the testicle may be present, Doppler ultrasound is invaluable in showing preservation of blood flow, even though the testis may appear to be relatively photopenic on the scan.

CONCLUSION

A downward trend in the use of nuclear medicine as an emergency imaging modality occurred in the past decade, particularly with the development of the exquisite anatomic resolution provided by CT, the additional physiologic imaging provided by MRI, and the convenience of ultrasound. However, with the increasing development of newer agents and a better understanding of metabolic processes, combined with fusion of more than one modality, nuclear medicine is again being recognized as a valuable imaging modality that provides both primary and complementary workups in the diagnosis of disease and the evaluation of treatment efficacy.

Nuclear medicine places an additional onus on the diagnostician to learn not just the appearance of the disease process but also the fundamental physics of the subspecialty, as well as to gain a better understanding of the pathophysiology and the molecular basis of disease. Most importantly, it is imperative that practitioners become familiar with the pitfalls, false-positive findings, and false-negative findings so that they do not place the patient or the referring clinician in harm's way.

SUGGESTED READINGS

Bar-shalom R, Yefremov N, Guralnik L, et al. SPECT/CT using Ga 67 and 111 in labeled leukocyte scintigraphy for diagnosis of infection. *J Nucl Med*. 2006;47:587–594.

Burke J. *Advances in 99mTc radiopharmaceutical chemistry*. San Francisco, CA: Paper presented at: 148th Annual Meeting of the American Pharmaceutical Association; March 2001.

Carvalho PA, Anthony PJ. Evaluation of GI bleeding with Tc 99m RBC. http://www.med.harvard.edu/JPNM/TF95_96/Feb13/WriteUp.html. Published February 13, 1996. Accessed October 14, 2015.

Curtin K, Fitzgerald SW, Nemcek Jr AA, et al. CT diagnosis of acute appendicitis: imaging findings. *AJR Am J Roentgenol*. 1995;164:905.

Ell PJ, Gambhir SS. *Nuclear Medicine in Clinical Diagnosis and Treatment*. 3rd ed. Philadelphia, PA: Churchill Livingstone; 1980.

Fayad LM, Johnson P, Fishman EK. Multidetector CT of musculoskeletal disease in the pediatric patient: principles, techniques, and clinical applications. *Radiographics*. 2005;25:603–618.

Feied CF. Pulmonary embolism. In: 4th ed. Rosen P, Barkin RM, eds. *Emergency Medicine Principles and Practice*. Vol 3. St Louis, MO: Mosby Year-Book; 1998:3.

Heytens L, Verlooy J, Gheuens J, Bossaert L. Lazarus sign and extensor posturing in a brain-dead patient. *J Neurosurg*. 1989;71:449–451.

Hoffer PB. *Gallium 67 Imaging*. New York, NY: Wiley; 1978.

Huang AH. The hot nose sign. *Radiology*. 2005;235:216–217.

Hussain HM, Barnes CE. Pediatric skeletal trauma: plain film to MRI. *Appl Radiol*. 2007;36:8.

Kao SC, Smith WL. Skeletal injuries in the pediatric patient. *Radiol Clin North Am*. 1997;35:727–746.

Klingensmith 3rd WC, Holt SA. Lung scan interpretation: a physiologic, user-friendly approach. *J Nucl Med*. 1992;33(7):1417–1422.

Kowalsky RJ, Falen SW. *Radiopharmaceuticals in Nuclear Pharmacy and Nuclear Medicine*. Washington, DC: American Pharmaceutical Association; 2004.

Lew DP, Waldvogel FA. Current concepts: osteomyelitis. *New Engl J Med*. 1997;336:999–1007.

Love C, Palestro CJ. Radionuclide imaging of infection. *J Nucl Med Technol*. 2004;32:47–57.

Love C, Tomas MB, Marwin SE, et al. Role of nuclear medicine in diagnosis of the infected joint replacement. *Radiographics*. 2001;21:1229–1238.

Mandelstam SA, Cook D, Fitzgerald M, et al. Complementary use of radiological skeletal survey and bone scintigraphy in detection of bony injury in suspected child abuse. *Arch Dis Childhood*. 2003;888:387–390.

McGlone BS, Balan KK. The use of nuclear medicine techniques in the emergency department. *Emerg Med J*. 2001;18:424–429.

Mettler FA, Guiberteau MJ. *Essentials of Nuclear Medicine Imaging*. 5th ed. Philadelphia, PA: WB Saunders; 2005.

Mishkin FS, Dyken ML. Increased early radionuclide activity in the nasopharyngeal area in patients with internal carotid artery obstruction: hot nose. *Radiology*. 1970;96:77–80.

Oyen WJ, Boerman OC, Corstens FH. Imaging acute appendicitis: invited commentary. *J Nucl Med*. 2000;41:456.

PIOPED Investigators. *Technescan MAA kit [package insert]*. St. Louis, MO: Mallinckrodt; 2001.

PIOPED Investigators. Value of the ventilation/perfusion scan in acute pulmonary embolism: results of the prospective investigation of pulmonary embolism diagnosis. *JAMA*. 1990;263:2753–2759.

Runge MS, Patterson C. *Principles of Molecular Medicine*. 2nd ed. Washington, DC: Humana Press; 2006.

Saber AA, LaRaja RD. Abdominal abscesses. http://emedicine.medscape.com/article/189468-diagnosis. Updated September 28, 2015. Accessed October 14, 2015.

Sharp PF, Gemmell HG, Murray AD. *Practical Nuclear Medicine*. 3rd ed. Washington, DC: Springer; 2005.

Society of Nuclear Medicine. *Society of Nuclear Medicine Procedure Guideline for Hepatobiliary Scintigraphy,* version 3.0, approved; June 23, 2001. http://interactive.snm.org/docs/pg_ch11_0703.pdf.

Tofe AJ, Francis MD. In vitro stabilization of low-tin bone imaging agent (^{99m}Tc-Sn-HEDP) by ascorbic acid. *J Nucl Med*. 1976;17:820–825.

Tucker WD, Greene MW, Weiss AJ, Murrenhoff AP. Methods of preparation of some carrier-free radioisotopes involving sorption on alumina. *U.S. Army Environmental Command Report BNL-3746, Brookhaven National Laboratory*. May 29, 1958.

Uliel L, Mellnick VM, Menias CO, Holz AL, McConathy J. Nuclear medicine in the acute clinical setting. *Radiographics*. 2013;33:375–395.

Zeissmann HA. Clinical scintigraphy: genitourinary system. In: O'Malley JP, Thrall JH, eds. *The Requisites: Nuclear Medicine*. 3rd ed. Philadelphia, PA: Mosby; 2005.

This page intentionally left blank

Index

A
AAST trauma classification
  in liver injuries, 85–86, 86t
  in renal injuries, 102–103, 103t
  in splenic injuries, 90–91, 91t
Abdomen, venous emergencies of, 362–365, 363f
Abdominal abscess, radionuclide scans in, 384–385
Abdominal pain, nontraumatic, 281–315
  in bowel disease, 281–296
  in genitourinary tract disease, 305–309
  in liver diseases, 302–305
  in pancreaticobiliary disease, 296–302
  in spleen disease, 309–310
Abdominal trauma, 81–114
  of adrenal gland, 105–106
  bladder, 106–109
  blunt, 81–85
    computed tomography for, 81–85, 83f–84f
    sonography for, 81, 82f
  of bowel and mesentery, 95–100
  computed tomography in. *see* Computed tomography (CT), in abdominal trauma
  of gallbladder and bile duct, 88–89
  of kidneys, 102–104
  of liver, 85–88
  of pancreas, 92–95
  of pelvis, 106–111, 107f
  penetrating, 111–113
    computed tomography in, 112–113, 112f–114f
    ultrasonography in, 112
  peritoneal fluid in, 100–102
  of rectum, 110–111, 111f
  of spleen, 89–92
  ultrasonography in. *see* Ultrasonography, in abdominal trauma
  of ureter, 104–105, 105f
  of urethra, 109–110
Abscess
  abdominal, radionuclide scans in, 384–385
    of liver, radionuclide scans in, 384
  brain, 28–30, 30f–31f
    pyogenic, 29f
  of liver, 302, 304f
  peritonsillar, 46
  of prostate, 318–319, 319f
  renal, 305–306, 307f
    in children, 198, 199f
  retropharyngeal, 48f
    in children, 206–207, 206f–207f
  of soft tissues, 178, 179f–180f
  in spinal cord, 240, 241f
  of spleen, 309
  superficial, 50, 50f
  tubo-ovarian, 321–322, 322f
Acetabular fractures, 143–144, 143b, 144f
  associated both column, 144
  Judet-Letournel classification of, 143
  posterior wall, 143
  transverse, 143
    plus posterior wall, 143
  T-shaped, 144
Acquired immunodeficiency syndrome (AIDS), abscess and, 28
Acromioclavicular joint
  osteoarthritis of, 169
  trauma of, osteolysis in, 168–169, 169f
Acromioclavicular joint injuries, 116–117, 117b, 118f
Acute coronary syndrome
  anatomy in, 270–272
  clinical considerations in, 270
  coronary computed tomography angiography in, 269–270
  evaluation of chest pain for exclusion of, 269
Acute disseminated encephalomyelitis (ADEM), 34, 36f
Adenitis, in children
  cervical, 214
  mesenteric, 196, 197f
Adenoids, enlargement of, in children, 207, 207f
Adhesive capsulitis, of glenohumeral joint, 170
Adrenal trauma, 105–106
  CT in, 105–106, 106f
Airway injuries, 45, 47f
Alberta Stroke Program, early CT score, 14
American Association for the Surgery of Trauma (AAST) trauma classification. *see* AAST trauma classification
Amyloid angiopathy, cerebral, as intracranial hemorrhage cause, 12–14
Aneurysms, 20–21
  of abdominal aorta, 339–342
    diagnosis of, 339–341, 340f–341f
    endovascular repair of, 342, 342f
    retroperitoneal hemorrhage in, 312, 313f
    treatment of, 341–342, 342f–343f
  of aortic arch, 335
  of gastroduodenal arteries, 349–350, 352f
  of iliac arteries, 356, 356f
  in intracranial hemorrhage, 2
  of lower extremities, 361
  mycotic, of aorta, 337–339, 338f
  of renal artery, 352
  of thoracic aorta, 255, 334–342, 335f, 337t
    causes of, 335, 337t
    computed tomography angiography in, 335f, 337–338
    diagnosis of, 337–338
    dissection and rupture in, 335, 337f, 339b
Aneurysms *(Continued)*
    endovascular repair of, 261–262, 335f, 339
    graft repair in, 261
    treatment of, 338–339
  of thoracoabdominal aorta, 336f, 337, 337t
  of upper extremity, 358
  of visceral arteries, 349–350
Angina, in acute coronary syndrome, 269
Angioedema, 51
Angiography
  in acute coronary syndrome, 269
  in carotid artery injuries, 327, 328f
  catheter, 22–23
  computed tomography. *see* Computed tomography angiography (CTA)
  magnetic resonance. *see* Magnetic resonance angiography
  in pulmonary embolism, 269
Angioma, cavernous, 241
Angiomyolipoma, renal, 352–353, 353f
Ankle brachial index, 354–355, 359–360
Ankle injuries, fractures in, 154, 156b, 157f–158f
  rotational malleolar, 154
  tibial plafond (pilon), 154–156, 155f
  triplane, 156, 159f
Ankylosing spondylitis
  of cervical spine, 228, 228f
  of hip, 177f
Antibiotic-associated colitis, 294, 295f
Aorta
  abdominal
    acute occlusion of, 345–346, 347f
    aneurysm of. *see* Aneurysms, of abdominal aorta
    dissection of, nontraumatic, 344
    traumatic injury of, 342–344
  arch of, aneurysm of, 335, 337t
  computed tomography angiography of. *see* Computed tomography angiography (CTA), of aorta
  dissection of
    abdominal nontraumatic, 344
    computed tomography angiography in, 249–251, 256, 278–279
    differentiated from pulsation artifact, 249, 250f
    endovascular repair of, 262, 344
    graft repair of, 261
    thoracic, 256–258, 257f
    type of, 256, 257f
  mycotic aneurysm of, 337–339, 338f
  stent placement in
    in aneurysm, 339, 342, 343f
    in traumatic injury, 332, 334f
  thoracic, 255–263
    anatomy of, 255
    aneurysm of. *see* Aneurysms, of thoracic aorta

Note: Page numbers followed by "b", "f" and "t" indicate boxes, figures and tables respectively.

Aorta *(Continued)*
dissection of, 256–258, 257f
hematoma of, intramural, 258, 258f–259f
infectious, 255–256
interposition graft, 260–261
penetrating atherosclerotic ulcer of, 258–260, 259f–260f
postoperative, 260
stent-grafts in, 261–262
thoracoabdominal aneurysm of, 336f, 337, 337t
traumatic injury of, 62–64, 65f, 327–329, 330f
blunt, 327–328, 330f
common locations of, 327
computed tomography angiography in, 329–331, 330f–332f, 333–334, 336f
hematoma in, 329, 330f
intimal flap in, 63, 65f
intimal tear in, 63, 65f, 330f–331f
penetrating, 332–334, 334f
pseudoaneurysm in, 63–64, 66f–68f, 329, 330f, 334f
signs of, 329–331, 331f
transesophageal echocardiography in, 331
treatment of, 331–332, 333t, 334
Aortitis, infectious, 255–256
Aortoiliac disease, 354
Appendicitis, 287–290, 289f–290f
"arrowhead" sign in, 289, 290f
in children, 194–195, 195f
during pregnancy, 289
Appendix epididymis, torsion in, 201–202
Appendix testis, torsion in, 201–202
Arterial emergencies, 327–361
of aorta, 329–332, 330f
computed tomography angiography in, 327
signs of vascular trauma in, 327, 327b–328b
of lower extremity, 358–359, 359f
of mesenteric-visceral arteries, 347–353
of neck, 327–346
of pelvis, 353–356
of upper extremity, 356–357, 356b, 357f
Arterial spin labeling (ASL), 17
Arteriovenous fistula, spinal dural, 241
Arthritis
infectious, 178–180, 181f
septic, 178–179, 386. *see also* Septic arthritis
rheumatoid
of glenohumeral joint, 170, 170f
of hip, 175, 177f
of spine, 237
Arthropathies
of glenohumeral joint, 169–170
of hip, 174–176
of spine, 237, 237f–238f
Arthroplasty, orthopedic hardware infections in, 184
Articular facet fracture, 230f
Aspiration
of foreign bodies, 208, 209f
of meconium, 206, 206f
Astrocytoma, 33f
Atherosclerosis
aortic ulcer in, 258–260, 259f–260f
coronary. *see* Coronary arteries, atherosclerosis of
of iliac arteries, 354
lower extremity ischemia in, 359
spontaneous cervical dissection and, 21–22
Atlantoaxial dissociation, 225–226, 227f
Atlanto-occipital dislocation, 225, 226f–227f
Atlas (C1)
in atlantoaxial dissociation, 225
fractures of, 225, 226f
Jefferson, 225, 226f
Atresia
biliary, differentiated from hepatitis, 389–390
in children
colonic, 188
duodenal, 186–187, 187f
esophageal, 188, 188f
ileal, 187, 187f
Avulsion injuries
cervical root, 234, 235f
of gallbladder, 89f
of knee, 154, 155f
pelvic, 140, 140f
Axial loading, in cervical spine injury, 224b, 228–230
Axis (C2)
in atlantoaxial dissociation, 225
fractures of, 226, 228f–229f
dens, 226, 229f
hangman, 226, 228f
Axonal injury, diffuse, 8–10, 10f

B

Bankart lesion, in anterior dislocation, 118, 119f
Barton fracture, 129–130, 131f–132f
Baseball fractures, of hand, 139, 139f
Bennett fracture, 136–137, 137f
reverse, 138
Bile duct, trauma to, 88–89
bilomas in, 89, 90f
scintigraphy in, 89, 90f
Bile duct stones
common, 301–302
intrahepatic, 302
Biliary obstruction, 314, 314f
abdominal pain in, 314
in choledocholithiasis, 314
Biliary tract disorders
atresia, 389–390
in cholecystitis, radionuclide scans in, 389, 390f–391f
Bilomas, in abdominal trauma, 89, 90f
Bladder
cystography in, 107
CT, 107–108, 108f
infection of, emphysematous, 308
posterior urethral valves in, 197
rupture of, 108–109
extraperitoneal, 108–109, 108f–109f
intraperitoneal, 109, 110f
trauma of, 106–109
Bleeding
gastrointestinal, acute, 296
mesenteric injury with, 101f
in pelvic trauma, 106, 107f
Blunt trauma, of abdomen, 81–85
computed tomography for, 81–85, 83f–84f
sonography for, 81, 82f
Bolus tracking techniques, 22
Bone marrow edema, of hip, transient, 172–173, 173f
Boutonniere deformity, 140
Bowel disease, 281–296. *see also* Gastrointestinal disorders
appendicitis, 287–290, 289f–290f
colitis
infectious, 294, 295f
ulcerative, 291, 293f
diverticulitis
of colon, 291, 292f
of small bowel, 287, 288f
enteritis, 286–287
epiploic appendagitis, 290
in foreign bodies, 294–296, 295f
gastrointestinal bleeding, acute, 296
ileus
adynamic, 286
gallstone, 283
Meckel diverticulum, 287, 288f
obstruction
of colon, 285–286
of gastric outlet, 281–282
of small bowel, 282–283, 284f–285f
omental infarction, 290–291
peptic ulcer disease, 282
volvulus. *see* Volvulus
Bowel injury, 95–100
hematomas in, 96–98, 98f
hypovolemic shock in, 101–102, 102f
intraperitoneal air in, 99b
laceration in, 100f
locations of, 98b
in penetrating trauma, 111
peritoneal fluid in, 100–102, 102f
Boxer's fracture, 138, 139f
Brain
abscess, 28–30, 30f–31f
pyogenic, 29f
contusion in, 7–8, 9f
diffuse axonal injury in, 8–10, 10f
herniation of, 10–11
in hydrocephalus, 211
hypoxic ischemic injury in children, 211
parenchymal infection of, 27–28, 28f
trauma of, in children, 210–211
traumatic and nontraumatic emergencies of, 1–60
tumors of, 30–32, 32f–34f
vascular disorders of. *see* Cerebrovascular disorders
Brain death, radionuclide scans in, 379–381, 380f
Branchial cleft cysts, 49, 49f
Bronchiolitis, in children, 208–209, 210f
Buckle fractures, 216–217
of radius, 131–132, 131f–132f
Budd-Chiari syndrome, 364–365
Bullet wounds, skull fracture caused by, 38–39
Bursitis, of shoulder, calcific, 165
Burst fracture, of thoracolumbar spine, 231, 233f
Burst injury, to bowel and mesentery, 96

C
Calcaneal fractures, 159–161, 231, 232f
Calcific bursitis/tendinitis, of shoulder, 165, 166f
Calcification
  in pancreatitis, 297, 297f
  in subdural hematoma, 4–5, 6f
  of tumors, 30–32
Calcium hydroxyapatite deposition disease, of shoulder, 165, 166f
Calcium pyrophosphate disease, of spine, 238f
Calculi
  choledocholithiasis and, 302
  genitourinary tract, 305, 306f
  urinary tract, in children, 200
Capsulitis, adhesive, of glenohumeral joint, 170
Carcinoma
  endometrial, 324–325
  renal cell, 353
Cardiac injuries, in chest trauma, 62
Cardiovascular disorders
  of aorta. *see* Aorta
  arterial emergencies in, 327–361. *see also* Arterial emergencies
  venous emergencies in, 362–366. *see also* Venous emergencies
Carotid arteries
  dissection of, spontaneous, 329
  nontraumatic emergencies of, 329–334
  pseudoaneurysm of, 328–329, 328f
  trauma of, extracranial, 327–329, 328f
Carpal bones, 134–135
  dislocations of, 134–135, 136b
    lunate, 135, 135f
    perilunate, 134–135, 135f
  hamate fracture of, 133, 134f
  instability of, 135f, 136
    scapholunate dissociation in, 135f, 136
  lunate fracture of, 134
  scaphoid fracture, 132–133, 133f
  triquetral fracture of, 133, 134f
Carpometacarpal joint dislocation, 137–138, 138f
Catheter angiography, 22–23
Cellulitis, 177
  cobblestone appearance in, 177
  of foot, 177f
  of leg, 177f–178f
Central nervous system disorders, in children, 210–214
Central nervous system-immune reconstitution inflammatory syndrome (CNS-IRIS), 34–35
Cerebellitis, in children, 211–212
Cerebral blood flow (CBF), magnetic resonance perfusion imaging of, 17
Cerebral edema, in children, 211
Cerebral venous infarction, 20, 20f
Cerebritis, 27–28
Cerebrovascular disorders
  acute, 11–20
    cerebral venous infarction and sinus thrombosis, 20, 20f
    cortical laminar necrosis, 19–20, 19f
    hemorrhagic transformation, 19, 19f
    ischemic stroke, acute, 14–19. *See also* Ischemic stroke, acute
    parenchymal hemorrhage, spontaneous, 12–14, 12f–13f
  infarction in. *see* Infarction, cerebral
Cervical dissection, spontaneous, 21–22
Cervical root avulsion, 234, 235f
Cervical spine
  ankylosing spondylitis of, 228, 228f
  discitis and osteomyelitis of, 47, 48f
  rheumatoid arthritis of, 237
  trauma of
    atlantoaxial dissociation, 225–226, 227f
    atlanto-occipital dislocation, 225, 226f–227f
    axial loading, 228–230
    C1 fractures, 225, 226f
    C2 fractures, 226, 228f–229f
    in children, 212
    hyperextension, 228, 228f, 230f
    hyperflexion, 226–228, 229f
    lateral bending, 230
    mechanisms of injury in, 224b
    occipital condyle fractures in, 225, 225f
    patterns of injury in, 223
Cervicocerebral arterial injuries, 21–24
  spontaneous cervical dissection, 21–22
  spontaneous intracranial dissection, 24
  traumatic, 22–24, 23f–24f
Chance fracture, of thoracolumbar spine, 231–233, 233f
Chauffeur fracture, 130–131, 131f–132f
Chest pain, 243. *see also* Thoracic disorders
Chest trauma, 61–80
  aortic injuries in, 62–64. *see also* Aorta, traumatic injury of
  cardiac injuries in, 62, 64f
  diaphragmatic injuries in, 71–74
  esophageal injuries in, 62
  fractures in, 75
  lung contusion in, 64–65, 69f
  lung laceration in, 65–67
  multidetector computed tomography protocol in, 61
  pleural space injuries in, 61
  thoracic skeleton injuries in, 75–79
  tracheobronchial injuries in, 67–71
Chiari malformations, 211
Chiari I malformation, 237
Children
  air block complications in, 204–205, 204f–205f
  appendicitis in, 194–195, 195f
  bronchiolitis in, 208–209, 210f
  cervical adenitis in, 214
  cervical spine injury in, 212
  croup in, 207, 208f
  cryptorchidism in, 318
  elbow injuries in
    fat pad sign in, 122–123, 123f, 127f
    fractures in, 123f, 124–125, 124b
  epididymitis in, 201, 201f
  epiglottitis in, 207, 207f
  esophageal atresia in, 188, 188f
  foreign body in, 207–208, 209f
  fractures in
    elbow, 216–217, 217f
    plastic bending, 215–216, 216f
    Salter-Harris, 214–215, 214f–215f
    skull, 210–211, 210f–211f
  glottic/subglottic masses in, 207, 208f
  hematocolpos/hematometrocolpos in, 203–204, 204f
  hemorrhagic ovarian cyst in, 203, 203f
Children *(Continued)*
  hip pain in, 217–218, 217f–218f
  hydrocephalus in, 211
  hydronephrosis in, 198–199
  hypertrophic pyloric stenosis in, 190–191, 190f–191f
  hypoxic ischemic injury in, 211
  intussusception in. *see* Intussusception, in children
  malrotation in, 191–193, 192f
  mastoiditis in, 212–214, 213f
  Meckel diverticulum in, 195–196, 196f
  meconium aspiration syndrome in, 206, 206f
  meningitis/encephalitis in, 211–212, 213f
  mesenteric adenitis in, 196
  necrotizing enterocolitis in, 188–190, 189f–190f
  neonatal. *see* Neonates
  nonaccidental injury in, 218–219, 218f–219f
    metaphyseal fractures in, 218, 219f
    radionuclide scans in, 386–387
    rib fractures in, 218, 218f
    skull fractures in, 210–211, 211f
  omental infarction in, 197, 197f
  ovarian torsion in, 320
  pneumonia in, 208, 209f
  pneumothorax in, 209–210, 210f
  respiratory emergencies in, 206–210
  retropharyngeal abscess in, 206–207, 206f–207f
  scrotal hernia in, 200–201, 201f
  stridor in, 206
  surfactant deficiency disease in, 204, 204f
  testicular appendage torsion in, 316
  torsion in
    adnexal, 202–203, 203f
    testicular, 202, 202f
    testicular appendages, 201–202, 202f
  transient tachypnea in, 205
  unicameral bone cyst in, 214f
  ureteropelvic junction obstruction in, 199–200, 199f
  urethral valves in, posterior, 197, 198f
  urinary tract infection in, 197–198, 199f
  urolithiasis in, 200, 200f
  venous sinus thrombosis in, 211, 212f
Cholangiocarcinoma, biliary obstruction in, 314, 314f
Cholangiopancreatography, endoscopic retrograde
  in bile duct injury, 89, 90f
  in pancreatic injury, 95, 96f
Cholangitis, recurrent pyogenic, 302, 303f
Cholecystagogue (CCK), in hepatobiliary scintigraphy, 388–389
Cholecystitis, 300–301, 301f
  acute, radionuclide scans in, 389, 390f–391f
  Murphy's sign in, 300, 301f
  radionuclide scan in, 301
Choledocholithiasis, 301–302
  biliary obstruction in, 314
  pancreatitis in, 297
Cholelithiasis, 299–300
Chondromatosis, synovial, of hip, 175–176
Chylothorax, 253
Clavicle fractures, 115–116, 117f, 117b

Clay shoveler fracture, 226–228
Clostridium difficile colitis, 294, 295f
Coccygeal fractures, 234
Colic artery, laceration of, 102f
Colitis
  infectious, 294, 295f
  ulcerative, 291, 293f
    "fat halo" sign in, 292, 293f
Colles fracture, 129, 130f
Colon
  atresia in, 188
  diverticulitis of, 291, 292f
  inflammatory bowel disease of, 291–294, 293f–294f, 385
  injury to, 95–96, 98b, 100f
  obstruction of, 285–286
  volvulus of, 286
Colpocephaly, 26
Common bile duct stones, 301–302
Compartment syndrome, abdominal, 346, 347b
Compression fractures, in thoracolumbar spine, 231, 232f
Computed tomography (CT)
  in abdominal trauma
    blunt, 81–85, 83f–84f
    of bowel and mesenteric injuries, 96, 98b, 100f
    delayed images in, 82–84, 84f
    of gallbladder, 88–89, 89f
    of liver, 85–88, 86f–88f
    multidetector scanning in, 81
    of pancreas, 93–95, 94f–97f
    penetrating, 112–113, 112f–114f
    portal venous-phase imaging in, 82–84, 83f–84f
    in renal injury, 103–104, 104f–105f
    of spleen, 91–92, 92f–94f
  in aneurysms, 20, 21f
  angiography in. *see* Computed tomography angiography (CTA)
  contrast agents in. *see* Contrast agents, in computed tomography
  in extremity trauma, 163
    angiography technique, 163
    volumetric reconstruction and image post-processing in, 163
  in intracranial hemorrhage, 2
    contrast agents in, 2
    in contusion, 7–8, 9f
    in diffuse axonal injury, 8–10, 10f
    epidural, 2, 3f–4f
    extraaxial hematomas, 2
    intra-axial, 2
    subarachnoid, 6, 8f, 20–21, 21f
    subdural, 5–6, 5f
  in ischemic stroke, acute, 14, 15f
    perfusion imaging in, 17–19, 18f
  in sinus disease, 51–52
  in spine injury, 221
  in thoracic disorders, 246–251
    coronary angiography in, 251
    heart rate control in, 247
    image reconstruction in, 248
    multidetector technique, 243
    patient preparation for, 247
    radiation exposure in, 248
    routine chest, 249
    techniques and protocols in, 247–251
  in thoracic injury, multidetector protocol, 61
Computed tomography angiography (CTA), 17
  in abdominal trauma, 82
  of aorta
    anatomy in, 255
    in dissection, 249–251, 256, 278–279
    in stent-graft, 262, 262f
    in thoracic aneurysm, 335f–336f, 337–338
    in traumatic injuries, 330f–332f, 333–334, 336f
    in "triple rule-out", 251, 278–279
  application of, 20–21
  in arterial emergencies, 327
    signs of vascular trauma in, 327, 327b–328b
  coronary, 251, 269–279
    anatomy in, 270–272, 271f–272f
    anomalies in, 275–277, 275f
    image evaluation in, 277–278
    plaque imaging in, 277–278, 278f
    predictive value of, 270
    stenosis in, 276f–278f, 277
    in "triple rule-out", 251, 278–279
  heart rate control in, 247
  in pulmonary embolism, 249, 264–266, 278–279
    chronic, 264, 268f
    diagnostic criteria for, 264, 266f–268f
    interpretation errors in, 265
    prognostic factors for, 265–266
    technical factors in, 264, 266f
    in "triple rule-out" examination, 278–279
    venography in, 264–266
  pulsation artifact in, 249, 250f
  for traumatic cervicocerebral injuries, 22
  "triple rule-out", 251
Congenital disorders, of spine, 237
Contrast agents, in computed tomography, in intracranial hemorrhage, 2
Contrast material, in computed tomography, 247
  in abdominal trauma, 84, 84f
    penetrating, 112
  in pulmonary embolism, 264, 267f
  in renal trauma, extravasation of, 104
  timing principles and techniques, 247–248
Contusions
  of bowel wall, 96–98
  cardiac, 62
  of gallbladder, 88
  intra-axial hemorrhage, 7–8, 9f
  of kidneys, 102–103, 103t
    computed tomography in, 103–104, 104f
  of liver, 85
  of lung, 64–65, 69f
  of pancreas, 94–95, 94f
Coronary arteries
  anatomy of, 270–272, 271f–272f
  anomalies of, 275–277, 275f
  atherosclerosis of, plaque imaging in, 277–278, 278f
  computed tomography angiography of. *see* Computed tomography angiography (CTA), coronary
  fistulas of, 275f, 277
  image evaluation in, 277–278
Coronary arteries *(Continued)*
  left anterior descending
    anatomy of, 271–272, 272f–274f
    anomalies of, 275–277, 275f
    myocardial bridging of, 275–277, 275f
  left circumflex, 272, 272f–274f
  left main
    anatomy of, 271, 272f–274f
    anomalies of, 275, 275f
  right
    anatomy of, 270–271, 271f–274f
    anomalies of, 275, 275f
  stenosis in, 276f–278f, 277
Coronoid process fractures, 125, 128f
Cortical laminar necrosis, 19–20, 19f
Costochondral fractures, lung herniation in, 75–77, 77f
Cranial sutures, skull fractures and, 210–211
Craniofacial dissociations, 41
Craniopharyngioma, 33f
Crohn disease
  abscess and fistula in, 292–293, 294f
  "accordion" sign in, 293f
  of colon, 291, 293f–294f
  comb sign in, 287, 288f, 292
  of small bowel, 287, 288f
Croup, 51, 51f
  in children, 207, 208f
Cruciate ligament avulsion injuries, posterior, 154, 155f
Crush injury, to bowel and mesentery, 96
Cryptorchidism, 200–201, 318, 319f
Cyst
  branchial cleft, 49, 49f
  ovarian, hemorrhagic, 319–320, 320f
    in children, 203, 203f
  thyroglossal duct, 49
Cystitis
  in children, 197–198
  emphysematous, 308
Cystography, in bladder trauma, 107
  CT, 107–108, 108f
Cystourethrogram, voiding, in posterior urethral valves, 197, 198f

D

Dancer's fracture, 162–163
Dandy-Walker malformations, 211
Degenerative disease, of spine, 237
Dens fracture, 226, 229f
Dental disease, complicated, 57–58, 58f
"Dependent viscera" sign, in diaphragmatic injuries, 74, 74f, 76f
Desmoteplase, 17
Diaphragmatic injuries, 71–74
  collar sign in, 72–74, 75f–76f
  dependent viscera sign in, 74, 74f, 76f
  mediastinal shift in, 76f
  in penetrating abdominal trauma, 113f
Diastasis, 37–38
Digital subtraction angiography (DSA), 19
  for vascular lesions, 20–21
Discitis, of cervical spine, 47, 48f
Dislocations
  of ankle, 154–156, 156b
  atlanto-occipital, 225, 226f–227f
  of carpal bones, 134–135, 136b
    lunate, 135, 135f
    perilunate, 134–135, 135f

Dislocations *(Continued)*
of carpometacarpal joint, 137–138, 138f
of elbow, 122–126, 123f
in foot, 156–163, 161b
of glenohumeral joint, 118–119, 118b
anterior, 118, 119f
posterior, 118, 120f
in hand, 136–140, 136b
of interphalangeal joints, 140
of metacarpophalangeal joint, 139
of hip, 144–145, 145f
of knee, 148, 148f, 150f
arterial injuries in, 358–359
of patella, 148, 151f–152f
of sternoclavicular joint, 77, 78f
subtalar, 156
in thumb, 136–137
Dissection, spontaneous
cervical, 21–22
intracranial, 24
Diverticulitis
of colon, 291, 292f
of small bowel, 287, 288f
Diverticulum, Meckel
in children, 195–196, 196f
radionuclide scans in, 387
of small bowel, 287, 288f
Duodenum
atresia or stenosis, in children, 186–187, 187f
peptic ulcer disease of, 282
trauma of, laceration of, 100f

E

Ear infections, 55–57, 55f–56f
Gradenigo syndrome in, 56–57, 56f
mastoiditis in, 55–56, 55f
in children, 212–214, 213f
otitis externa in, malignant, 56–57
otitis media in , in children, 212–214, 213f
Ear pain, mastoiditis and, in children, 212–214
Echocardiography, transesophageal, in aortic traumatic injury, 331
Ectopic pregnancy, 323–324, 323f
Edema
of hip bone marrow, transient, 172–173, 173f
pulmonary, 246f
ground glass opacities in, 247f
of spinal cord, 234
Effusion
pericardial, 253
pleural, 252
Ehlers-Danlos syndrome, spontaneous cervical dissection and, 21–22
Elbow injuries
in children
fat pad sign in, 122–123, 123f, 127f
fractures in, 124–125, 124b, 216–217, 217f
in coronoid process fractures, 125, 128f
dislocations in, 124b, 125–126
fat pad sign in, 122–123, 123f
in children, 122–123, 123f, 127f
humerus fractures in, 126f–127f
olecranon process fractures in, 127f
radius fractures in, 129–132
Elderly
acetabular fractures in, 172f
aortic aneurysm in, 339
femoral fractures in, proximal, 145
Embolic phenomena, renal infarct in, 308
Embolism
in aorta, 345
chest radiography in, 376–378, 376f
computed tomography angiography of. *see* Computed tomography angiography (CTA), in pulmonary embolism
in iliac arteries, 354
lower extremity ischemia in, 358, 359f
lung scintigraphy in, 373
PIOPED study of, 377
pulmonary, 263–269
chest radiography in, 263–264, 264f–265f
chronic, 264, 268f
clinical considerations in, 263
conventional pulmonary angiography in, 269
CT venography in, 264–266
diagnostic criteria for, 264, 266f–268f
epidemiology of, 263
Fleischner sign in, 263–264, 265f
Hampton sign in, 263–264, 264f
imaging techniques in, 263–269
in lower extremity venous thrombosis, 365
MR pulmonary angiography in, 268–269, 269f
MR venography in, 269
pathophysiology of, 263
PIOPED study of, 263
"railway track" sign in, 264, 267f
right ventricular enlargement in, 265–266, 268f
ventilation-perfusion scan in, 266–268, 268b
upper extremity ischemia in, 357–358
Embolization
in hepatic vascular injuries, 85, 87f
in pelvic artery trauma, 353–354, 354f–355f
Emergency nuclear radiology. *see* Nuclear radiology
Emphysema
pulmonary interstitial, 204–205, 204f
subcutaneous, in tracheobronchial injuries, 67–68, 72f–73f
Empyema, 253
Encephalitis, 27–28
in children, 211–212, 213f
herpes, 28f
Encephalomeningitis, 26–27
Encephalopathy
posterior reversible, 35–36, 37f
toxic, 36–37, 38f
Endometrial carcinoma, 324–325
Endometrial polyps, 324–325
Endometriosis, 321
Endometritis, 322
Endovascular repair
in aneurysm, 261–262
in aortic aneurysm
abdominal, 341–342, 342f–343f
thoracic, 335f, 339
in aortic dissection, 261–262, 344
Endovascular repair *(Continued)*
in aortic traumatic injuries, 332, 334
endoleaks in, 332, 333t
Enteritis, infectious, 286–287, 287f
Enterocolitis, necrotizing
in neonates, 188–190, 189f–190f
Rigler sign of, 188–189, 189f
Ependymomas, 238, 240f
Epididymitis, 316–317, 317f
in children, 201, 201f
Epididymo-orchitis, radionuclide scans in, 392
Epidural hemorrhage, 2, 3f–4f
Epiglottitis, 51, 52f
in children, 207, 207f
Epiploic appendagitis, 290, 291f
ERCP (endoscopic retrograde cholangiopancreatography)
in bile duct injury, 89, 90f
in pancreatic injury, 95, 96f
Erythrocytes, ^{99m}Tc-labeled, in gastrointestinal bleeding, 296
Esophageal injury, 251
Esophagus
atresia in, 188, 188f
foreign body in, 208, 209f
trauma to, 62
Essex-Lopresti fracture, 125
Extraaxial hemorrhage, 1–6
epidural, 2, 3f–4f
intraventricular, 1, 6, 9f
subarachnoid, 6, 7f–8f
subdural, 3–4, 5f
calcification in, 4–5, 6f
computed tomography in, 5–6, 5f
magnetic resonance imaging of, 3–4
Extracranial herniation, 11
Extremity trauma, 115–164
computed tomography in, 115
angiography technique, 163
with volumetric reconstruction and image post-processing, 163
of lower extremity, 140–142, 140b
arterial injuries in, 358–359, 359f
steps for interpretation of, 115, 116b
of upper extremity, 115
arterial injuries in, 356–357, 356b, 357f

F

Facial smash, 42
Falciform ligament, in necrotizing enterocolitis, 188–189, 189f
Fallopian tube, disorders of, 321–322, 322f
tubo-ovarian abscess in, 321–322, 322f
Fasciitis, necrotizing, 178, 179f
FAST (focused abdominal sonography for trauma), 81, 82f
Fat blood interface (FBI) sign in knee injuries, 147
Fat pad sign in elbow injuries, 122–123, 123f
in children, 123f, 127f, 216–217, 217f
Female genitourinary disorders. *see* Genitourinary diseases, in female
Femoral artery aneurysm and pseudoaneurysm, 359, 360f
Femur
avascular necrosis of head, radionuclide scans in, 386
dislocations of, 144–147
fractures of

Femur *(Continued)*
arterial injuries in, 360f
distal, 147–148, 149f
floating knee in, 147–148, 149f
Garden classification of, 145–147
intertrochanteric, 147
in neck, 145–147
proximal, 144–147, 145f
in shaft, 147
subcapital, 145–147
subtrochanteric, 147
trochanteric, 146f, 147
osteonecrosis of head, 173–174, 173t, 174f–175f
double line sign, 173–174
Ficat classification of, 173, 173t
transient bone marrow edema and osteoporosis of, 172–173, 173f
Fibroids, uterine, 324–325
Ficat classification, of femoral head osteonecrosis, 173, 173t
Fistula
arteriovenous, spinal dural, 241
of coronary artery, 275f, 277
in Crohn disease, 292–293, 294f
Flail chest, 75, 77f
Fleischner sign, in pulmonary embolism, 263–264, 265f
Flexor digitorum profundus tendon injuries, 140
Floating knee, 147–148, 149f
Floating shoulder, 117–118
Fluoroscopic image, in intussusception, 194, 195f
Foot
cellulitis of, 177f
trauma of
calcaneal fractures in, 159–161, 160f
in forefoot, 162–163
in hindfoot, 156–161, 160f, 161b
metatarsal fractures in, 162–163, 162f
metatarsophalangeal, 163
in midfoot, 161–162
phalangeal fractures in, 163
subtalar dislocation in, 160f
talus fractures in, 156–159
tarsometatarsal, 161–162
Foreign bodies, 183–184, 183f
aspiration of, 208, 209f
in children, 207–208, 209f
gastrointestinal, 294–296, 295f
Fournier gangrene, 317, 318f
Fractures, 116
of acetabulum. *see* Acetabular fractures
of ankle, 154, 156b, 157f–158f
rotational malleolar, 154
tibial plafond (pilon), 154–156, 155f
Tillaux, 156, 159f
triplane, 156, 159f
around the elbow, 122–126, 123f
of calcaneus, 159–161, 160f
in chest trauma, 75
in children
in elbow injuries, 123f, 124–125, 124b, 216–217, 217f
plastic bending, 215–216, 216f
radionuclide scans in, 386
Salter-Harris, 214–215, 214f–216f
skull, 210–211, 210f–211f
Fractures *(Continued)*
of clavicle, 115–116, 117f, 117b
description of, 116b
of femur. *see* Femur, fractures of
of foot, 161b
of hamate, 133, 134f
of hand, 136b
of humerus. *see* Humerus fractures
of knee, 151b
in lower extremity, 140–142, 140b
of lunate, 134
metacarpal, 138, 139f
of thumb, 137f
metatarsal, 162–163, 162f
of occipital condyle, 225, 225f
of patella, 148–151, 151f–152f
pelvic. *see* Pelvic fractures
phalangeal. *see* Phalangeal fractures
of proximal femur, 145–147, 146f
of radius. *see* Radius, fractures of
of ribs. *see* Rib, fractures of
sacral, 142, 142f
of scaphoid, 132–133, 132b, 133f
of scapula, 115, 116f, 117b
of skull. *see* Skull fractures
of sternum, 77, 78f–79f
of talus, 156–159
of temporal bone. *see* Temporal bone fractures
terminology related to, 116b
of thoracic spine, 79
of thumb, 136–137
of tibia. *see* Tibia fractures
triquetral, 133, 134f
of ulna
distal and shaft, 126–132
pronator quadratus sign in, 126–128
"Frozen shoulder", 170

G
Galeazzi fracture-dislocation, 128–129, 129f
Gallbladder
cholecystitis of, 300, 301f
Murphy's sign in, 300, 301f
radionuclide scan in, 301, 389, 390f–391f
trauma to, 88–89
avulsion in, 89f
computed tomography in, 88–89, 89f
ultrasonography in, 88
Gallium-67 citrate imaging, 372, 372f
in infections, 384
in orthopedic hardware, 184
in joint prostheses, 385
Gallstone, 299–300
ileus in, 283
pancreatitis in, 297
Gamekeeper's thumb, 137, 138f
Gangrene, Fournier, 317, 318f
Garden classification, of femoral fractures, 145–147
Gastric outlet obstruction, 281–282
Gastroduodenal artery aneurysm and pseudoaneurysm, 349–350, 352f
in pancreatitis, 351f
Gastroduodenal artery pseudoaneurysm, in pancreatitis, 299f
Gastroenteritis, viral, 287f
Gastrointestinal disorders. *see also* Bowel disease
bleeding, 348–349, 348f, 350f
radionuclide scans in, 387
in children, 186–197
appendicitis, 194–195, 195f
enterocolitis, necrotizing, 188–190, 189f–190f
esophageal atresia, 188, 188f
intussusception, 193–194, 193f–195f
malrotation, 191–193, 192f
Meckel diverticulum, 195–196, 196f
mesenteric adenitis, 196
inflammatory bowel disease. *see* Inflammatory bowel disease
intussusception. *see* Intussusception
Meckel diverticulum, 387
obstruction, neonatal, 186–188, 187f
high, 186–187, 187f
low, 187–188, 187f–188f
omental infarction, 197, 197f
pyloric stenosis, hypertrophic, 190–191, 190f–191f
volvulus. *see* Volvulus
Genitourinary diseases, 305–309
abdominal pain in, 305
biliary obstruction, 314, 314f
in children, 197–204
adnexal torsion and, 202–203, 203f
epididymitis, 201, 201f
hematocolpos/hematometrocolpos, 203–204, 204f
hemorrhagic ovarian cyst, 203, 203f
hydronephrosis, 198–199
posterior urethral valves in, 197, 198f
scrotal hernia, 200–201, 201f
testicular torsion, 202, 202f
torsion of the testicular appendages, 201–202, 202f
ureteropelvic junction obstruction, 199–200, 199f
urinary tract infection, 197–198, 199f
urolithiasis, 200, 200f
in female, 319
in dysfunctional uterine bleeding, 324–325
in ectopic pregnancy, 323–324, 323f
in endometriosis, 321
in endometritis, 322
in fallopian tube disorders, 321–322, 322f
in hemorrhagic ovarian cyst, 319–320
in ovarian torsion, 320–321, 321f
in ovarian vein thrombosis, 324, 325f
pelvic pain in, 319, 323–324
in postpartum bleeding, 324
uterine bleeding in, 319
in male, 316–325
in cryptorchidism, 318, 319f
in epididymitis, 316–317, 317f
in prostatitis, 318–319, 319f
scrotal scanning in, 390–392, 392f
in testicular appendage torsion, 316
in testicular torsion, 316, 317f
in testicular trauma, 318
nephrolithiasis, 305, 306f
obstruction in, 314–315
pyelonephritis. *see* Pyelonephritis
pyonephrosis, 307–308

Genitourinary diseases *(Continued)*
renal abscess, 305–306, 307f
renal infarct, 308–309
urinary obstruction, 314–315
in nephrolithiasis, 314–315
Glenohumeral joint
adhesive capsulitis of, 170
dislocations of, 118–119, 118b
anterior, 118, 119f
inferior subluxation in, 119
posterior, 118, 120f
pseudosubluxation in, 119
rheumatoid arthritis of, 170, 170f
Glioblastoma multiforme, 33f
Glottic masses, in children, 207, 208f
Gradenigo syndrome, 56–57, 56f
Graft
aortic interposition, 260–261
complications of, 261, 261f
Great vessel, injuries of, 62–64
Greenstick fractures, 215–216
Guillain-Barré syndrome, 240
Gunshot wounds
aortic injury in, 332–333
penetrating abdominal trauma from, 111

H
Hamate fractures, 133, 134f
Hampton sign, in pulmonary embolism, 263–264, 264f
Hand injuries
carpometacarpal dislocations in, 137–138, 138f
foreign bodies in, 183f
metacarpal fractures in, 138, 139f
of thumb, 137f
phalangeal fractures, in thumb, 139–140, 139f
of thumb, 136–137
carpometacarpal dislocation in, 137–138, 138f
metacarpal fracture in, 138, 139f
phalangeal fracture in, 139–140
Hawkins classification, of talus fractures, 156–159
Head and neck region
infections in, 45–58
trauma of, 37–45
airway and pharyngeal injuries in, 45, 47f
cervical spine injuries in. *see* Cervical spine, trauma of
contusion in, 7–8, 9f
diffuse axonal injury in, 8–10, 10f
Le Fort fractures, 41, 41f
mandibular, 42–43, 43f–44f
maxillofacial fractures in, 39
nasal fractures, 40
orbital blow-out fractures, 39–40, 39f
skull fractures in. *see* Skull fractures
smash fractures, 42, 42f
temporal bone fractures, 43–45, 45f–46f
zygomaticomaxillary complex fractures, 40, 41f
vascular disorders in. *see also* Cerebrovascular disorders
of carotid and vertebral arteries, 327–329, 328f
in traumatic injuries, 327–329, 328f
zones of injury in, 327
Heart
injuries in chest trauma, 62, 64f
metastatic involvement of, 253–254
Heart failure
chest radiography in, 243–245, 245f
computed tomography in, 246f
Heart rate, in computed tomography angiography, 247
Hello sign, in testicular torsion, 392, 392f
Hemangioblastoma, 32f
Hemangioma
in abdominal trauma, 84f
of small bowel, 348f
of spine, 238
Hemarthrosis in knee injuries, 147, 148f
Hematocele, in lung laceration, 65
Hematochezia, 348, 348f
Hematocolpos, in children, 203–204, 204f
Hematoma
acute intramural, 258, 258f–259f
in adrenal trauma, 105–106
of bowel wall, 96–98, 98f
epidural, 2, 3f, 235
extraaxial, 2. *see also* Extraaxial hemorrhage
in hepatic trauma, 85
classification of injury in, 86t
mesenteric, 99f–101f
of pancreas, 94–95, 95f
in renal trauma, 103, 103f
spinal, 234–236, 235f–236f
in splenic trauma
computed tomography of, 91–92, 92f–93f
ultrasonography of, 91, 91f
subdural, 3–4, 5f, 235
calcification in, 4–5, 6f
Hematometrocolpos, in children, 203–204, 204f
Hematuria, in bladder trauma, 107
Hemopericardium, 62, 64f, 253, 253f
Hemoperitoneum, spontaneous, 311–312, 312f
Hemorrhage, 1
in aortic traumatic injury, 329
gastrointestinal, 348–349, 348f, 350f
radionuclide scans in, 387
general imaging characteristics of, 2
hemoperitoneum in, 311, 312f
in hepatic vascular injuries, 86
intracranial, 1–2. *see also* Intracranial hemorrhage
in ovarian cyst, 203, 203f, 319–320, 320f
in pelvic trauma, 353–354, 354f–355f
peritoneal, in abdominal trauma, 81
pituitary, 6
postpartum, 324
retroperitoneal, 312–314, 313f
in spinal cord trauma, 234, 236f
uterine, 319, 324–325
postpartum, 324
Hemorrhagic transformation, 19, 19f
Hemothorax, 252–253
in chest trauma, 61, 62f
Hepatic artery
aneurysm of, 349
trauma to, 86–87, 88f
Hepatic vein obstruction, 364–365
Hepatitis, 304–305
neonatal, differentiated from biliary atresia, 389–390
Hepatobiliary scintigraphy, 388–390
in acute cholecystitis, 389, 390f–391f
agents for, mechanisms of, 388–389
in cholecystitis, 301
in differentiation of neonatal biliary atresia and hepatitis, 389–390
in liver trauma, 89, 90f
Hepatolithiasis, 302, 303f
Herniation
brain. *see* Brain, herniation of
of lung, in costochondral fractures, 75–77, 77f
scrotal
in children, 200–201, 201f
inguinal, 317–318
small bowel obstruction in, 283, 284f
Herpes encephalitis, 28f
Highly active antiretroviral therapy (HAART), 34
Hill-Sachs fracture, 118, 119f
Hip
ankylosing spondylitis of, 175, 177f
arthropathies and, 174–176
bone marrow edema of, transient, 172–173, 173f
dislocations of, 144–145, 145f, 145b
insufficiency fractures of, 171–172, 171f
osteoarthritis of, 175, 176f
osteonecrosis of femoral head, 173–174, 174f–175f
osteoporosis of, transient, 172–173, 173f
pain in, 170–176
in children, 217–218, 218f
rheumatoid arthritis of, 175, 177f
septic arthritis of, in children, 386
Hirschsprung disease, in children, 188, 188f
Humerus fractures, 119–122, 120b, 123f
distal, 125, 126f–127f
lateral condylar, 124–125, 124f
proximal, 119–122, 121f–122f
in shaft, 120b, 122, 123f
supracondylar, 123f
Hutchinson fracture, of radius, 130–131, 131f–132f
Hydrocele, 200–201, 317, 318f
Hydrocephalus, 25–26, 26f
Hydrocephalus, in children, 211
Hydronephrosis, in children, 198–199
Hydrosalpinx, 321
Hygroma, subdural, 5–6
Hymen, imperforate, 203
Hyperextension injuries
of cervical spine, 224b, 228, 230f
of thoracolumbar spine, 233
Hyperflexion injuries, of cervical spine, 224b, 226–228, 229f
Hypovolemic shock, in bowel injuries, 101–102, 102f
Hypoxic ischemic injury, in children, 211

I
Ileocolic intussusception, 193–194, 193f–195f
Ileum
atresia of, 187, 187f
injury to, 99f–100f

Ileus
adynamic, 286
gallstone, 283
meconium, 187
Iliac artery, nontraumatic emergencies of, 354–356, 355f
aneurysm, 356, 356f
dissection, 345f, 356
occlusive, 354–356, 355f
Immunocompromised patients, infections in, 386
in enteritis, 286
Impingement, of rotator cuff, 166–168
Incisional hernias, small bowel obstruction in, 283, 284f
Indium-111, 371–372, 372f
leukocytes labeled with
in infections, 382
normal distribution of, 382, 382f
Infarction
acute ischemic, 14, 15f. *see also* Ischemic stroke, acute
cerebral venous, 20, 20f
lacunar, 14–15, 16f
omental, 290–291
in children, 197, 197f
renal, 308–309
of spinal cord, 241
splenic, 309–310
Infections
aortitis in, 255–256
arthritis in, 178–180
septic. *see* Septic arthritis
colitis in, 294, 295f
cystitis in
in children, 197–198
emphysematous, 308
of ear. *see* Ear infections
endometritis in, 322
enteritis in, 286–287, 287f
epididymitis in, 316–317, 317f
in children, 201
fasciitis in, necrotizing, 178, 179f
of head and neck region, 45–58
hepatic abscess in, 302, 304f
in immunocompromised patients, 386
enteritis in, 286
in joint prostheses, 385
mediastinal, 254
musculoskeletal, 176–185
radionuclide scans in, 385, 385f
as nontraumatic intracranial emergencies, 26–30
nuclear radiology in. *see* Nuclear radiology, in infections
in orthopedic hardware, 184–185
osteomyelitis. *see* Osteomyelitis
pyelonephritis. *see* Pyelonephritis
sinusitis in. *see* Sinusitis
of soft tissue, 177–178
in spinal cord, 240–241, 241f
of urinary tract in children, 197–198, 199f
Infectious diseases, of bowel, 286–296
Inflammatory bowel disease, 286–296
abscess and fistula in, 292–293, 294f
"accordion" sign in, 293f
of colon, 291–294, 293f–294f
comb sign in, 287, 288f, 292
"fat halo" sign in, 292, 293f
radionuclide scans of, 385
Inguinal scrotal hernia, 317–318
in children, 200–201
Instability
carpal, 135f, 136
dorsal intercalated segmental, 136
scapholunate dissociation in, 135f, 136
volar intercalated segmental, 136
in traumatic spine injury, 221, 223
Insufficiency fractures of hip, 171–172, 171f
Intertrochanteric fractures, of femur, 147
Intestinal disorders. *see* Gastrointestinal disorders
Intra-axial hemorrhage, 1, 7–10
contusion in, 7–8, 9f
diffuse axonal injury in, 8–10, 10f
Intracranial dissection, spontaneous, 24
Intracranial hemorrhage, 1–2. *see also* Extraaxial hemorrhage, Intra-axial hemorrhage
contrast agents, computed tomography in, 2
in contusion, computed tomography in, 7–8, 9f
in diffuse axonal injury
computed tomography in, 8–10, 10f
magnetic resonance imaging in, 8–10, 10f
epidural, 2, 3f–4f
computed tomography in, 2, 3f–4f
extraaxial, 2–6
computed tomography in, 2
intra-axial, 1, 7–10
subarachnoid. *see* Subarachnoid hemorrhage
subdural, 3–4, 5f
computed tomography in, 5–6, 5f
magnetic resonance imaging in, 3–4
Intramural hematoma, 24, 25f
Intraoral trauma, 22
Intraperitoneal air, in bowel injury, 96–98, 99f, 99b
Intraperitoneal fluid, in bowel and mesenteric trauma, 98, 102f
Intraperitoneal hemorrhage, in abdominal trauma, 82f
Intraventricular hemorrhage, 1, 6, 9f
Intussusception
in children, 193–194, 193f–195f
small bowel obstruction in, 283, 285f
Ischemia
lower extremity, 359–361, 361f
mesenteric, 296, 348
myocardial, coronary computed tomography angiography in, 269
renal, 351–352, 353f
upper extremity, 357–358
Ischemic stroke, acute, 14–19
computed tomography, 14, 15f
perfusion imaging in, 17–19, 18f
magnetic resonance angiography, 16–17
magnetic resonance imaging
diffusion-weighted, 14–16, 15f–16f
perfusion, 17
Isotropic voxel scanning , in abdominal trauma, blunt, 84–85

J

Jefferson burst fracture, of atlas, 225, 226f
Jejunum, laceration in, 100f
John Cunningham (JC) virus, 34
Judet-Letournel classification, of acetabular fractures, 143
Jugular vein
thrombosis of, 365
traumatic injury of, 362

K

Kidneys
neoplasm-related vascular emergencies of, 352–353, 353f
pyelitis of, emphysematous, 308
pyelonephritis of. *see* Pyelonephritis
renal artery injuries in, 350–351, 352f
renal vein thrombosis of, 363
trauma of, 102
urinary tract infection and, in children, 197–198, 198f
Kienbock disease, in lunate fracture, 134
Knee injuries
avulsion, 154, 155f
dislocation in, arterial injuries in, 358–359
dislocations in, 148, 151b
fat blood interface, 147
floating knee in, 147–148, 149f
hemarthrosis and lipohemarthrosis in, 147, 148f
patellar fractures in, 151f–152f
tibial plateau fractures in, 151–154, 153f
Krypton-81m, 375

L

Lacerations
of bowel, 98–99, 100f
duodenal, 100f
of gallbladder, 88
of liver, 85
classification of injury in, 86t
computed tomography in, 85–86, 86f–88f
ultrasonography in, 85, 85f
of lung. *see* Lungs, laceration of
mesenteric, 99–100, 101f
of pancreas
computed tomography in, 94–95, 95f–96f
magnetic resonance imaging in, 95, 97f–98f
renal, 102–103, 103t
computed tomography in, 103–104, 104f
ultrasonography in, 103
of spleen, 91, 92f, 94f
of trachea, 68
Lacunar infarcts, 14–15, 16f
"Ladd" bands, 191–192
Ladd procedure, 193
Laparotomy, in penetrating abdominal trauma, 111
Laryngotracheobronchitis, 51. *see also* Croup
in children, 207, 208f
Lateral bending, in cervical spine injury, 230
Lateral flexion injuries, of cervical spine, 224b
Lavage, peritoneal, in penetrating abdominal trauma, 112
Le Fort fractures, 41, 41f
Leukocytes, radionuclide-labeled, in infection imaging, 381–384
in infectious arthritis, 179

Leukoencephalopathy, progressive multifocal, 34–35, 37f
Lipohemarthrosis, in knee injuries, 147, 148f
Lisfranc injuries, 161–162, 162f
Liver, 302–305
  abscess of, 302, 304f, 384
  hepatitis of, 304–305
  laceration in. *see* Lacerations, of liver
  radionuclide scans of, 388–390
    in abscess, 384–385
  trauma of, 85–88
    AAST classification of, 85–86, 86t
    computed tomography in, 85–88, 86f–88f
    contusions in, 85
    hematomas in, 85
    lacerations in, 85, 85f
    in penetrating injury, 113f
    scintigraphy in, 89, 90f
    ultrasonography in, 85, 85f
    vascular injuries in, 86, 86t, 87f–88f
  tumors of, hemoperitoneum in, 311, 312f
Lower extremity
  trauma of, arterial injuries in, 358–359, 359f
  vascular emergencies of
    nontraumatic, 359–361, 361f
    traumatic, 358–359, 359f
Ludwig's angina, 58f
Lumbar compression fracture, 232f
Lunate
  dislocation of, 135, 135f
    spilled teacup sign in, 135, 135f
  in dorsal intercalated segmental instability, 136
  fractures of, 134
    Kienbock disease in, 134
  idiopathic avascular osteonecrosis of, 134
  in scapholunate dissociation, 135f, 136
  in volar intercalated segmental instability, 136
Lungs
  carcinoma of, metastatic, to brain, 34f
  chest radiography of, 243
    in pneumonia, 244f
  computed tomography of
    centrilobular opacities in, 246, 246f
    "tree-in-bud" sign in, 246, 246f
  contusion of, 64–65, 69f
  foreign body in, 208
  herniation of, in costochondral fractures, 75–77, 77f
  laceration of, 65–67
    compression rupture in, 65, 71f
    nodular appearance in, 67, 71f
    pneumatocele and hematocele in, 65, 70f
    types of, 65, 70f
  radionuclide scans of, 386
    ventilation-perfusion. *see* Ventilation-perfusion scan
Lung scintigraphy, 373–378
  aerosol studies in, 375, 376f
  in pulmonary embolism, 373
    high-probability scan in, 377, 378f
    low-probability scan in, 377, 379f
    repeat scans in, 378
  radiopharmaceuticals and techniques for, 373–378
    perfusion in, 374–375, 374f
    ventilation in, 375–378
Luxatio erecta, 119
Lyme disease, 27
Lymphadenitis, mesenteric, in children, 196
Lymphadenopathy, 50–51
Lymphoma, 238, 239f

M

Magnetic resonance angiography
  in aortic aneurysm, 338
  in arterial emergencies, 327
  in ischemic stroke, 16–17
  in pulmonary embolism, 268–269, 269f
    venography in, 269
Magnetic resonance imaging (MRI)
  angiography. *see* Magnetic resonance angiography
  in intracranial hemorrhage, 2
    in diffuse axonal injury, 8–10, 10f
    signal characteristics of, 2t
    subarachnoid, 6
    subdural, 3–4
  in ischemic stroke, acute, diffusion-weighted imaging, 14–16, 15f–16f
  of pancreas, 95, 97f–98f
  in sinus disease, 51–52
  in spine injury, 222f
  in traumatic cervicocerebral injuries, 24, 25f
Maisonneuve fracture, 154, 157f–158f
Male genitourinary disorders. *see* Genitourinary diseases, in male
Malgaigne fractures, 142
Mallet finger fractures, of hand, 139, 139f
Malrotation, 191–193, 192f
  intestinal, 283
Mandibular trauma, 42–43, 43f–44f
Mastoiditis, 55–56, 55f
  in children, 212–214, 213f
  septic thrombophlebitis and, 57f
Maxillofacial fractures, 39
Meckel diverticulum
  in children, 195–196, 196f
  radionuclide scans in, 387
  of small bowel, 287, 288f
Meconium aspiration syndrome, 206, 206f
Meconium ileus, 187
Mediastinitis, 254
Mediastinum, 254–255
  anatomy of, 254
  diseases of
    infection, 254
    masses, 254
    pneumomediastinum, 254, 254f
    in superior vena cava syndrome, 254–255, 255f
Megacolon, 285
Meigs syndrome, 252
Meningiomas, of spine, 238
Meningitis, 26–27, 27f–28f, 240–241
  in children, 211–212, 213f
Meningoencephalitis, 26–27
Mesenteric arteries
  aneurysm of, 349
  vascular emergencies of, 347–353
Mesenteric injury, 95–100
  bleeding in, 101f
  CT of, 98b
  hematoma in, 99–100, 99f, 101f
  lacerations in, 99–100, 101f
  peritoneal fluid in, 100–102
  stranding in, 99–100
Mesenteric ischemia, 296, 348
Mesenteric lymphadenitis, in children, 196
Mesenteric venous thrombosis, 364
Metacarpal fracture, 138, 139f
  of thumb, 138, 139f
Metastasis
  to heart and pericardium, 253–254
  of lung carcinoma to brain, 34f
Metatarsal fractures, 162–163, 162f
Metatarsophalangeal injuries, 163
Microcolon, in children, 187, 187f
Mirizzi syndrome, 314
Monteggia fracture-dislocation, 128, 128f
Morphine, in hepatobiliary scintigraphy, 389, 391f
Multiple sclerosis, 34, 35f
  in spinal cord, 240, 240f
Mumps orchitis, 317
Murphy's sign, in cholecystitis, 300, 301f
Musculoskeletal disorders
  in children, 214–219, 214f
  fractures. *see* Fractures
Musculoskeletal infections
  appendicular, 176–185
  radionuclide scans in, 385, 385f
Myeloma, multiple, 238, 239f

N

Nasal fractures, 40
Navicular fractures, 161
Neck. *see* Head and neck region
Necrosis
  avascular, radionuclide scans in, 386
  in pancreatitis, 297–298
Neonates
  air block complications in, 204–205
  biliary atresia in, 389–390
  emphysema in, pulmonary interstitial, 204–205, 204f
  enterocolitis in, necrotizing. *see* Enterocolitis, necrotizing, in neonates
  hepatitis in, 389–390
  intestinal obstruction in, 186–188, 187f
    high, 186–187, 187f
    low, 187–188, 187f–188f
  meconium aspiration syndrome in, 206, 206f
  meningitis in, 26–27, 27f
  pneumomediastinum in, 204–205, 205f
  pneumonia in, 205–206
  pneumopericardium in, 204–205, 205f
  pneumothorax in, 204–205, 205f
  respiratory distress in, 204–206
  surfactant deficiency disease in, 204, 204f–205f
  tachypnea in, transient, 205
  urethral valves in, posterior, 197, 198f
Neoplasms, of kidney, vascular emergencies in, 352–353, 353f
Nephrolithiasis, 305, 306f
  urinary obstruction in, 314–315
Neurocysticercosis, 28–30, 31f
Neurocytoma, central, 33f
Neutropenic colitis, 294
Nonaccidental injury, in children, 218–219, 218f–219f
  metaphyseal fractures in, 218, 219f
  radionuclide scans in, 386–387
  rib fractures in, 218, 218f
  skull fractures in, 210–211, 211f

Nuclear radiology, 369–393
in brain death diagnosis, 379–381, 380f
equipment used in, 372–373, 373f
in gastrointestinal disorders
in bleeding, 387
in inflammatory bowel disease, 385
hepatobiliary. *see* Hepatobiliary scintigraphy
in infections, 381–386
in abdominal abscess, 384–385
indications for, 384
in joint prosthesis, 385
in lung, 386
musculoskeletal, 385, 385f
in osteomyelitis, 383f, 385–386
radiopharmaceuticals in, 381
in inflammatory bowel disease, 385
lung scintigraphy in, 373–378
in pulmonary embolism, 373
high-probability scan in, 377, 378f
low-probability scan in, 377, 379f
repeat scans in, 378
radionuclides used in, 370–372
scrotal scanning, 390–392, 392f
in trauma, 386–387

O
Occipital bone, occipital condyle fractures of, 225
Occipital condyle fractures, 225, 225f
Occipitomastoid suture, 44–45, 47f
Odontoid process, fracture of, 226
Ogilvie syndrome, 285
Olecranon process fractures, 125
Omental infarction, 290–291
in children, 197, 197f
Orbital blow-out fractures, 39–40, 39f
Orbital infections, 51–55, 52f–54f
Orbital roof fracture, 40
Orchitis, 316–317
Orthopedic hardware infections, 184–185
Os odontoideum, 231, 232f
Osteoarthritis
of acromioclavicular joint disease, 169
of hip, 175, 176f
Osteomyelitis, 47, 48f, 182f
acute, 180–183
radionuclide scans in, 385–386
of spine, 241
technetium-99m methylene diphosphonate (MDP) for, 383f, 386
Osteonecrosis, avascular
of femoral head, 173
double line sign, 173–174
Ficat classification of, 173, 173t
idiopathic, of lunate, 134
Osteoporosis
of hip
fractures in, 172–173, 173f
transient, 172–173, 173f
thoracolumbar spine injuries in, 234
Otitis externa, malignant, 56–57
Otitis media, in children, 212–214, 213f
Ovarian vein thrombosis, 324, 325f
Ovary
cyst of, hemorrhagic, 203, 203f, 319–320, 320f
torsion of, 320–321, 321f
in children, 202, 203f
in tubo-ovarian abscess, 321, 322f

P
Pachymeningitis, 27, 28f
Pain
abdominal, 281. *see also* Abdominal pain
in chest, 243. *see also* Thoracic disorders
in hip, 170–176
pelvic, 319
in pregnancy, 319, 323–324
scrotal. *see* Scrotal pain
in shoulder, 165–170
Pancreas
abscess of, 385
inflammation of, 297
trauma of, 92–95
contusions in, 94–95, 94f
CT in, 94–95, 94f–97f
differentiated from retroperitoneal fluid, 95, 97f
hematomas in, 94–95, 95f
lacerations in. *see* Lacerations, of pancreas
MR in, 95, 97f–98f
pseudoaneurysms in, 94–95, 97f
transection in, 94–95
Pancreatitis
acute, 297–298, 298f–299f
necrosis in, 297–298
calcification in, 297, 297f
chronic, 297f, 298–299
gastroduodenal artery pseudoaneurysm in, 299f
splenic artery pseudoaneurysm in, 351f
Parenchymal hemorrhage, spontaneous, 12–14, 12f–13f
Parenchymal infection, of brain, 27–28, 28f
Patella
alta, 148
baja, 148–151, 151f–152f
dislocations of, 148, 151f–152f
fractures of, 151f–152f
Pediatric emergencies, 186–220. *see also* Children, Neonates
Pelvic disorders, 316–326
in female, 319
fractures. *see* Pelvic fractures
in male, 316–325
traumatic, 106–111, 107f, 353–354
bladder injuries in, 106–109
bleeding in, 106
hemorrhage in, 142, 353–354, 354f
pseudoaneurysms in, 353–354, 355f
rectal injury in, 110–111, 111f
urethral injury in, 109–110
vascular emergencies in, 353–356
Pelvic fractures, 106, 141f
with bleeding, 107f, 353–354, 354f
classification of, 140–141
with hemorrhage, 142
with pelvic ring disruption, 140–142, 140f
Penumbral imaging, 19
Peptic ulcer disease (PUD), 282
gastric outlet obstruction in, 281
Perfusion imaging, in acute ischemic stroke
computed tomography, 17–19, 18f
magnetic resonance imaging, 17
Pericardial injuries, in chest trauma, 62
Pericarditis, 254
Pericardium diseases, 253–254
effusion, 253
hemopericardium, 253, 253f
in malignancy, 253–254
pneumopericardium, 253
Perilunate dislocation, 134–135, 135f
Perimandibular abscess, 58f
Peritoneal cavity, contrast material in, 98–99, 100f
Peritoneal fluid, in bowel and mesenteric trauma, 100–102, 102f
Peritoneal hemorrhage, in abdominal trauma, 81
Peritoneal lavage, in abdominal trauma, 112
Peritonsillar abscess, 46
Phalangeal fractures
of foot, 163
of hand, 139–140
Pharyngitis, 46
Phenobarbital, in hepatobiliary scintigraphy, 389
Phlegmon, 178
Pillar fracture, of cervical spine, 226, 228, 230f
PIOPED study. *see* Prospective Investigation of Pulmonary Embolism Diagnosis (PIOPED) study
Pituitary hemorrhage, 6
Plasminogen activator, recombinant tissue, in ischemic stroke, acute, 14
Plastic bending fractures, in children, 215–216, 216f
Pleura, 251–253
diseases of
chylothorax, 253
effusion, 252
empyema, 253
hemothorax, 252–253
pneumothorax. *see* Pneumothorax
Pleural space, injuries of
in chest trauma, 61
hemothorax, 61, 62f
pneumothorax. *see* Pneumothorax
Pneumatocele, in lung laceration, 65, 70f
Pneumatosis intestinalis, in necrotizing enterocolitis, 188–189, 189f
Pneumohemarthrosis, in knee injuries, 147, 148f
Pneumomediastinum, 254
in children, neonatal, 204–205, 205f
computed tomography in, 251, 254f
in tracheobronchial injuries, 67–68, 72f–73f
Pneumonia
chest radiography in, 244f
in children, neonatal, 204–205, 208, 209f
Pneumopericardium, 253
in children, neonatal, 204–205, 205f
Pneumoperitoneum, 310–311, 311f
in necrotizing enterocolitis, 188–189
Pneumothorax, 251–252
in chest trauma, 61, 63f
in children, neonatal, 204–205, 205f, 209–210, 210f
etiologies of, 251, 251t
spontaneous, 251
tension, 252
Polyps, endometrial, 324–325
Popliteal artery aneurysm, 361

Portal vein
thrombosis of, 363–364, 364f
trauma to, 86–87, 88f
Posterior reversible encephalopathy syndrome, 35–36, 37f
Postpartum period
hemorrhage in, 324
retained products of conception in, 324
Pott's puffy tumor, 52–54, 53f
Pregnancy
appendicitis during, 289
computed tomography in, 247, 319
ectopic, 323–324, 323f
pelvic pain in, 319, 323–324
pulmonary embolism in, 373
Prevertebral infection/inflammation, 47, 48f
Progressive multifocal leukoencephalopathy, 34–35, 37f
Pronator quadratus sign, in radius and ulna injuries, 126–128
Prospective Investigation of Pulmonary Embolism Diagnosis (PIOPED) study, 377
Prospective Investigation of Pulmonary Embolism Diagnosis (PIOPED) II study, 263
Prostate abscess, 318–319, 319f
Prostatitis, 318–319, 319f
Pseudoaneurysm, 22–23
in aortic injuries, 63–64, 66f–68f, 329, 333f–334f
in aortic reconstruction, 261–263
of carotid artery, 328–329, 328f
of femoral artery, 359, 360f
of gastroduodenal artery, 299f
in hepatic arterial injuries, 86–87, 88f
in pancreatic trauma, 94–95, 97f
in pancreatitis, 298, 299f
in pelvic trauma, 353–354, 355f
of splenic artery, 351f
in splenic trauma, 92
Pseudocysts, pancreatic, 298
Pseudogout, of spine, 238f
Pseudomeningocele, 234, 235f, 237, 237f
Pseudosubluxation, of glenohumeral joint, 119
Pulmonary artery computed tomography angiography, in "triple rule-out", 251, 278–279
Pulmonary disease, radionuclide scans in, 386
Pulmonary parenchyma, computed tomography of, 246–247, 246f–247f
Pulsation artifact, in computed tomography angiography, 249, 250f
Pyelitis, emphysematous, 308
Pyelonephritis, 305
in children, 197–198
emphysematous, 306
renal abscess in, 305–306
xanthogranulomatous, 306–307, 308f
Pyloric stenosis, hypertrophic, 190–191, 190f–191f
"string sign" of, 191, 191f
Pyonephrosis, 307–308
Pyosalpinx, 321, 322f

R

Radiation exposure, in computed tomography, 248
Radiography
abdominal, in intussusception, 193, 193f
in aortic traumatic injury, 329
chest, in pulmonary embolism, 263–264, 264f–265f
conventional
in extremity trauma, 115
in pulmonary embolism, 376–378, 376f
Radiology, nontraumatic emergency, of thorax, 243–280, 244f
in heart failure, 243–245, 245f
interpretation of, 243, 244f
in pneumonia, 244f
Radionuclides. *see* Nuclear radiology
Radioulnar joint, distal, in Galeazzi fracture dislocation, 129f
Radius
fractures of
buckle, 131–132, 131f–132f
distal and shaft, 126–132
in Galeazzi fracture-dislocation, 129–132, 131f–132f
pronator quadratus sign in, 126–128
proximal, 125, 127f
in ulnar styloid, 129
in Monteggia fracture-dislocation, 128, 128f
Rectal injury, 110–111, 111f
Red blood cells (RBCs), technetium-99m (^{99m}Tc) labeled, in gastrointestinal bleeding, 296, 387, 388f
Reflux, vesicoureteral, 197
Renal abscess, 305–306, 307f
Renal artery disorders
aneurysm, 353–354
ischemic, 351–352, 353f
traumatic, 350–351, 352f
iatrogenic, 351, 352f
Renal injury, 102–104
AAST classification of, 102–103, 103t
computed tomography in, 103–104, 104f–105f
contrast extravasation in, 104
fracture in, 104
ultrasonography in, 103, 103f
urine leak in, 103–104, 104f
vascular pedicle injury in, 104, 105f
Renal vein thrombosis, 309, 363
Respiratory distress, neonatal, 204–206
Respiratory emergencies, in children, 206–210
bronchiolitis, 208–209, 210f
croup, 207, 208f
epiglottitis, 207, 207f
foreign body, 207–208, 209f
glottic/subglottic masses, 207, 208f
pneumonia. *see* Pneumonia
pneumothorax, 209–210, 210f
retropharyngeal abscess, 206–207, 206f–207f
stridor, 206
Retained products of conception, 324
Retroperitoneal fluid, differentiated from pancreatic injury, 95, 97f
Retroperitoneal hemorrhage, 312–314, 313f
Retropharyngeal abscess, in children, 206–207, 206f
Retropharyngeal infection, 46–47, 48f
Rheumatoid arthritis
of glenohumeral joint, 170, 170f
of hip, 175, 177f
of spine, 237
Rib
dislocation of, 234
fractures of, 75
flail chest in, 75, 77f
lung herniation in, 75–77, 77f
Rolando fracture, of thumb, 136–137, 137f
Rotator cuff abnormalities/disorders
calcific tendinitis, 165
critical zone in, 166–167
impingement, 166–168, 167f
spectrum of, 168f–169f
ultrasonography in, 165

S

Sacral fractures, 142, 142f, 234
Sail sign, elbow fractures and, 216–217, 217f
Salivary gland disorders, 47–48, 49f
Salter-Harris fractures, in children, 214–215, 214f–216f
Sarcoidosis, 240
Scaphoid
fractures of, 132–133, 132b, 133f
rotatory subluxation of, 135f, 136
Scapholunate dissociation, 135f, 136
Terry Thomas sign in, 135f, 136
Scapula fractures, 115, 116f, 117b
Schatzker classification, of tibial plateau fractures, 151–154
Scintigraphy. *see* Nuclear radiology
Scrotal hernia, in children, 200–201, 201f
Scrotal pain
in epididymitis, 316–317, 317f
in inguinal scrotal hernia, 317–318
in orchitis, 317, 392, 392f
in testicular appendage torsion, 316
in testicular torsion, 316, 317f, 392
Segond fracture, 154, 155f
Septic arthritis, 178–179, 181f
of hip, in children, 217–218, 386
radionuclide scans in, 386
of shoulder, 181f
Septic emboli, abscess from, 28, 31f
Septic thrombophlebitis
mastoiditis and, 57f
of ovarian vein, 324, 325f
Shearing injury, to bowel and mesentery, 96
Shock, hypovolemic, in bowel injuries, 101–102, 102f
Shoulder
acromioclavicular joint injuries of, 116
calcific bursitis/tendinitis, 165
calcium hydroxyapatite deposition disease of, 165, 166f
floating, 117–118
frozen, 170
glenohumeral joint disorders of, 169–170. *see also* Glenohumeral joint
impingement in, 166–168, 166f
osteoarthritis of, 169
pain in, 165–170
rheumatoid arthritis of, 170
rotator cuff disorders of. *see* Rotator cuff abnormalities/disorders

Sickle cell disease
pneumonia and, 208
spleen in, 309
Sinus infections, 51–55, 52f–54f. *see also* Sinusitis
Sinus thrombosis, 20, 20f
venous, in children, 211, 212f
Sinusitis, 52f
complications of, 54–55, 54f
Pott's puffy tumor and, 53f
subdural empyema and, 53f
Skier's thumb, 137, 138f
Skull fractures, 37–39, 38f–39f
in children, 210–211, 210f–211f
Slipped capital femoral epiphysis (SCFE), 218, 218f
Small intestine
Crohn disease of, 287, 288f
diverticulitis of, 287, 288f
enteritis of, 286–287, 287f
injury to, 98b
intussusception of, 283, 285f
obstruction of, 282–283, 284f–285f
closed loop, 283
volvulus of, 283–285
Smash fractures, 42, 42f
Smith fracture, 129, 130f
Soft tissue infections, 177–178
cellulitis in, 177. *see also* Cellulitis
necrotizing fasciitis in, 178
Sonography. *see* Ultrasonography
Spine
nontraumatic, 236–241
congenital disorders and, 237
degenerative disease/arthropathy and, 237, 237f–238f
infection in, 240–241, 241f
inflammation/demyelination and, 240, 240f
neoplasms and, 237–240, 239f–240f
tumorlike conditions and, 237–240, 239f–240f
vascular, 241
thoracic fractures in, 79
traumatic, 221–236
background and imaging algorithms on, 221–223, 222f
cervical. *see* Cervical spine, trauma of
cervical, patterns of, 223, 224b
cervicocranium and, 223–224, 224t
imaging, pitfalls in, 231, 231f–232f
prevertebral soft tissues and, assessment of, 225
severity, stability, and treatment decisions in, 230–231
by site, 225–226
soft tissue, evaluation of, 234–236
subaxial cervical, 226–230
thoracolumbar. *see* Thoracolumbar spine injuries
Splanchnic vascular trauma, 347–348
Spleen, 309–310
abscess of, 309
infarction of, 309–310
in sickle cell disease, 309
torsion of, 310
trauma of, 89–92, 347–348
AAST classification of, 90–91, 91t
Spleen *(Continued)*
computed tomography in, 91–92, 92f–94f
hematomas in, 91, 91f
lacerations in, 91, 92f, 94f
pseudoaneurysm in, 92, 94f
shattered tissue in, 92f
ultrasonography in, 91, 91f
Splenic artery aneurysm, 349, 351f
Spondylitis
ankylosing
of cervical spine, 228, 228f
of hip, 175, 177f
tuberculous, 241
Spondyloarthropathies, seronegative, of hip, 175
Stab wounds
aortic injury in, 332–333, 334f, 342
penetrating abdominal trauma from, 111
"Steeple" sign, 51
Stent placement
in aorta
in aneurysm, 339, 342, 343f
in traumatic injury, 332, 334, 334f, 344
in carotid artery pseudoaneurysm, 328–329, 328f
in hepatobiliary injuries, 89, 90f
in ureteral trauma, 105f
Stent-grafts, in thoracic aorta, 261–262
Sternal fractures, 77, 78f–79f
Sternoclavicular dislocation, 77, 78f
Stomach
injury to, 95–96, 98b
peptic ulcer disease of, 282
pyloric stenosis in, hypertrophic, 190–191, 190f
volvulus of, 282
Stress fracture, of hip, 171
Stridor, in children, 206
Stroke. *see also* Cerebrovascular disorders
hemorrhagic, 12–14
ischemic, acute, 14–19. *see also* Ischemic stroke, acute
Subarachnoid hemorrhage, 6, 7f–8f, 235, 236f
computed tomography in, 6, 20–21, 21f
magnetic resonance imaging in, 6
Subaxial cervical spine, injury of, 226–230
axial loading, 228–230
hyperextension, 228, 228f, 230f
hyperflexion, 226–228, 229f
lateral bending, 230
Subclavian artery disorders, 357f
Subdural hematoma (SDH), 3–4, 5f
calcification in, 4–5, 6f
computed tomography in, 5–6, 5f
magnetic resonance imaging of, 3–4
Subfalcine herniation, 11
Subglottic masses, in children, 207, 208f
Subluxation
of glenohumeral joint
inferior, 119
pseudosubluxation in, 119
of scaphoid, rotatory, 135f, 136
Submillimeter, for vascular evaluation, 22
Subtalar dislocation, 160f
Superficial abscesses, 50, 50f
Suppurative thyroiditis, 48–49
Supracondylar fractures, in children, 216–217
Supraspinatus tendon, critical zone of, 166–167
Surfactant deficiency disease, in neonates, 204, 204f–205f
Susac syndrome, 34
Synovitis, pigmented villonodular, of hip, 175–176
Syphilis
aortic aneurysm in, 337–338
aortitis in, 256

T

Tachypnea, in neonates, transient, 205
Talus, fracture of, Hawkins classification of, 156–159
Tamponade, cardiac, 253
Tarsometatarsal joint injuries, 161–162
Teardrop fracture, of cervical spine, 226–228, 230f
Technegas, 376
Technetium-99m (^{99m}Tc), 370–371, 370f–371f
in aerosol studies, 375–376, 376f
in brain death diagnosis, 380, 380f–381f
interpretation of, 380–381
radiopharmaceuticals in, 380
technique for, 380
diethylene triamine penta-acetic acid (DTPA)
in brain death diagnosis, 380
in lung scintigraphy, 375–376, 376f, 378f
disofenin (DISIDA), 389
ethyl cysteinate dimer, in brain death diagnosis, 379, 380f
in hepatobiliary scans, 389, 390f–391f
hexamethyl-propylene oxime or exametazime (HMPAO)
in brain death diagnosis, 380
leukocytes labeled with, in infections, 382, 383f
in infections, 382
macroaggregated albumin (MAA) in, 374, 378f–379f
methylene diphosphonate (MDP)
in infections, 382–383, 383f
in musculoskeletal infections, 385, 385f
in osteomyelitis, 383f, 386
in orthopedic hardware infections, 184
in perfusion, 374–375, 374f
pharmaceuticals tagged with, 371b
in pulmonary embolism, 267–268, 374, 374f, 378f
red blood cells labeled with, in gastrointestinal bleeding, 296, 387, 388f
in scrotal scans, 390–392
sulfur colloid
in gastrointestinal bleeding, 296, 387
in infection, 383
Temporal bone fractures, 43–45, 45f–46f
Tendinitis, of rotator cuff, calcific, 165
Teratoma, ovarian, 203f
Testicular appendage torsion, 316, 317f
in children, 201–202, 202f, 316, 317f
Testis
in cryptorchidism, 318, 319f
cryptorchidism in, 200–201
radionuclide scans of, 392, 392f
torsion of, 316, 317f, 392, 392f
hello sign in, 392f
radionuclide scans of, 392, 392f

Testis *(Continued)*
torsion of, in children, 202, 202f
trauma of, 318
Thoracic aorta, 255–263. *see also* Aorta, thoracic
Thoracic disorders
of aorta, 255–263. *see also* Aorta, thoracic
computed tomography in. *see* Computed tomography (CT), in thoracic disorders
nontraumatic emergency radiology of, 243–280
radiography in, 243–245, 244f
in heart failure, 243–245, 245f
interpretation of, 243, 244f
in pneumonia, 243, 244f
in trauma, 61–80. *see also* Chest trauma
in vena cava syndrome, superior, 362
Thoracic injury, in chest trauma, 61
Thoracic outlet syndrome, 365
Thoracic spine fractures, 79
Thoracolumbar spine injuries, 222–223, 230–234, 232f–233f
burst fracture in, 231, 233f
Chance fracture in, 231–233, 233f
compression fractures in, 231, 232f
Thrombectomy, mechanical, 18f
Thrombolysis, 17
in deep vein thrombosis, 365–366
in lower extremity ischemia, 360–361, 361f
contraindications to, 361b
Thrombolytic therapy, in iliac artery thrombosis, 360–361
Thrombophlebitis, septic, of ovarian vein, 324, 325f
Thrombosis
aortic, 262, 345–346, 346f
cerebral venous. *see* Cerebral venous infarction
deep venous, 365, 366f
pulmonary embolism in, 263. *see also* Embolism, pulmonary
iliac artery, 354, 355f
mesenteric venous, 364
ovarian vein, 324, 325f
portal vein, 363–364, 364f
renal vein, 309, 363
sinus, 20, 20f
upper extremity, deep venous, 249
vena cava obstruction in, inferior, 362, 363f
venous, 365
venous sinus, 55
in children, 211, 212f
Thumb injuries
carpometacarpal dislocation in, 138f
metacarpal fracture in, 138, 139f
phalangeal fracture in, 139–140, 139f
Thyroglossal duct cyst, 49
Thyroid-related disorders, 48–49
Tibia fractures
plafond (pilon), 154–156, 155f
in plateau, 151–154, 153f
Schatzker classification of, 151–154
Segond, 154, 155f
triplane, 156, 159f
Tillaux fractures, 156, 159f, 214–215, 216f
Toddler's fractures, 215–216
Tonsillar herniation, 11, 12f
Tonsils, enlargement of, in children, 207, 207f
Torsion
adnexal, in children, 202–203, 203f
ovarian, 320–321, 321f
splenic, 310
testicular, 316, 317f, 392, 392f
in children, 202, 202f
hello sign in, 392f
radionuclide scans of, 392, 392f
testicular appendage, 316, 317f
in children, 201–202, 202f, 316, 317f
Torus fractures, 215–216
of radius, 131–132, 131f–132f
Toxic encephalopathy, 36–37, 38f
Toxoplasmosis, abscess and, 28, 30f
Trachea, lacerations of, 68
Tracheobronchial injuries, 67–71, 72f–73f
Transalar herniation, 11
Transient ischemic attack (TIA), 12
Transtentorial herniation, 11
Trauma
abdominal, 81–114. *see also* Abdominal trauma
of acromioclavicular joint, osteolysis in, 168–169, 169f
of aorta. *see* Aorta, traumatic injury of
of chest, 61–80. *see also* Chest trauma
of cranial arteries, extracranial, 327–329
to esophagus, 62
of foot. *see* Foot, trauma of
fractures in. *see* Fractures
of hand. *see* Hand injuries
of head and neck. *see* Head and neck region, trauma of
of kidneys. *see* Kidneys, trauma of
of knee. *see* Knee injuries
of liver. *see* Liver, trauma of
of lower extremity, arterial injuries in, 358–359, 359f
mesenteric. *see* Mesenteric injury
of pancreas. *see* Pancreas, trauma of
radionuclide scans in, 386–387
of renal arteries, 350–351, 352f
in spine injury, 221–236
background and imaging algorithms on, 221–223, 222f
cervical, patterns of, 223, 224b
cervicocranium and, 223–224, 224t
imaging, pitfalls in, 231, 231f–232f
prevertebral soft tissues and, assessment of, 225
severity, stability, and treatment decisions in, 230–231
by site, 225–226
soft tissue, evaluation of, 234–236
subaxial cervical, 226–230
thoracolumbar, 231–234, 232f–233f
of spleen. *see* Spleen, trauma of
testicular, 318
of upper extremity, arterial injuries in, 356–357, 356b, 357f
of urethra. *see* Urethral injury
of vena cava, inferior, 363
Traumatic cervicocerebral injuries, 22–24, 23f–24f
Triplane fractures, of tibia, 156, 159f
Tripod fracture, 40
Triquetral fracture, 133, 134f
Trochanteric fractures of femur, 147
Tuberculosis, colitis in, 294
Tuberculous spondylitis, 241
Tumors
of brain, 30–32, 32f–34f
of liver, hemoperitoneum in, 311, 312f
of spine, 237–240, 239f–240f
Tympanosquamous suture, 44–45, 47f
Typhlitis, 294

U
Ulcer
aortic, 258–260, 259f–260f
endovascular repair of, 262f
of stomach and duodenum, in peptic ulcer disease, 282
Ulcerative colitis, 291, 293f
"fat halo" sign in, 292, 293f
Ulna
fractures of
distal and shaft, 126–132
in Galeazzi fracture-dislocation, 129, 130f
pronator quadratus sign in, 126–128
in Monteggia fracture-dislocation, 128, 128f
Ulnar styloid process fractures, of radius, 129
Ultrasonography, 369
in abdominal trauma
blunt, 81, 82f
FAST, 81, 82f
of gallbladder, 88
of liver, 85, 85f
penetrating, 112
of renal injury, 103, 103f
of spleen, 91, 91f
in intussusception, in children, 193f–194f
in rotator cuff disorders, 165
Ultrasound. *see* Ultrasonography
Uncal herniation, 11
Upper extremity
arterial injuries in, 356–357, 356b, 357f
thrombosis in, 249
vascular emergencies of
aneurysms, 356, 356f
nontraumatic, 357–358
traumatic, 356b, 357f
venous, 365
Ureteral calculus, in children, 198–199
Ureteral injury, 104–105, 105f
Ureterolithiasis, 305
Ureteropelvic junction obstruction, 199–200, 199f
Ureters, calculi in, 305, 306f
Urethral injury, 109–110
retrograde urethrogram in, 109–110, 110f
Urethral valves, posterior, in children, 197, 198f
Urethrography, retrograde, in urethral injury, 109–110, 110f
Urography, intravenous, in ureteral injury, 104–105
Urolithiasis, in children, 200, 200f
Uterus
bleeding from, 324–325
postpartum, 324
endometrial carcinoma of, 324–325
endometrial polyps of, 324–325
endometriosis of, 321
endometritis of, 322
fibroids of, 324–325

V
Vascular diseases, of bowel, 296
Vascular emergencies, 327–368
  arterial, 327–361. *see also* Arterial emergencies
  venous, 362–366. *see also* Venous emergencies
Vascular injuries, 20–21
Vascular malformations, 20–21
Vasospasm, posttraumatic, 24
Vena cava
  inferior
    obstruction of, 362
    trauma of, 363
  superior, syndrome of, 254–255, 255f, 362
    computed tomography in, 249, 249f, 255, 255f
Venography
  computed tomography, 20
    in pulmonary embolism, 264–266
  magnetic resonance, 20
    in pulmonary embolism, 269
Venous emergencies, 362–366
  of abdomen, 362–365
  of chest, 362
Venous emergencies *(Continued)*
  in jugular vein trauma, 362
  of pelvis and lower extremities, 365–366, 366f
  of upper extremities, 365
Venous sinus thrombosis, 55
  in children, 211, 212f
Ventilation-perfusion scan, in pulmonary embolism, 266–268, 268b
Ventricles, cardiac, right, enlargement in pulmonary embolism, 265–266, 268f
Vertebral arteries
  dissection of, spontaneous, 329
  nontraumatic emergencies of, 329–334
  trauma of, extracranial, 327–329
Visceral arteries
  aneurysms of, 349–350
  vascular emergencies of, 347–353
Volar plate injury, of hand, 139–140, 139f
Volvulus
  of colon, 286
  midgut, 191–193, 283
  of small intestine, 283–285
  of stomach, 282

W
"Wet readings", 1
White blood cells, radionuclide-labeled, in infections, 184, 382
White matter disorders, 32–37
  multiple sclerosis as, 34, 35f
  posterior reversible encephalopathy syndrome as, 35–36, 37f
  progressive multifocal leukoencephalopathy as, 34–35, 37f
  toxic encephalopathy as, 36–37, 38f

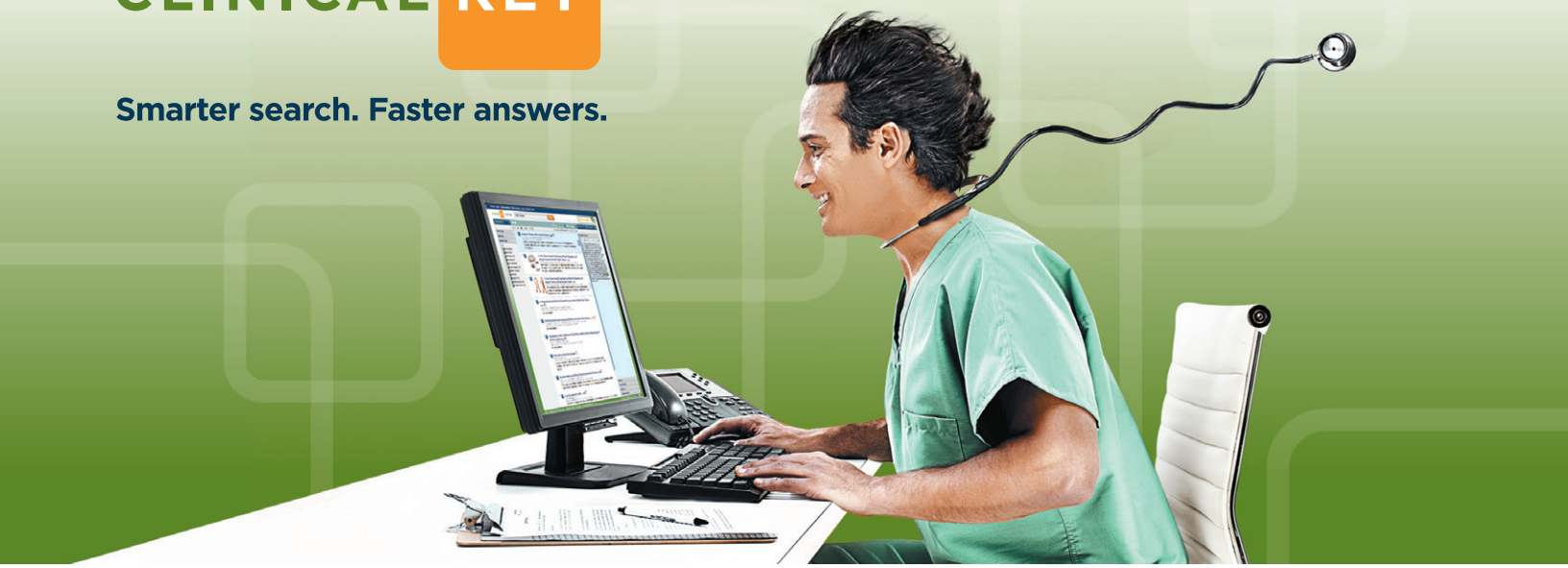
X
Xenon-133 scans, 372
  of lungs, in pulmonary embolism, 267–268, 375, 375f, 379f

Y
Young-Burgess classification, of pelvic fractures, 142

Z
Zygomaticomaxillary complex fractures, 40, 41f

CLINICAL KEY™

Smarter search. Faster answers.



Smarter, Faster Search for Better Patient Care

Unlike a conventional search engine, ClinicalKey is specifically designed to serve doctors by providing three core components:

1 Comprehensive Content

The most current, evidence-based answers available for every medical and surgical specialty.

2 Trusted Answers

Content supplied by Elsevier, the world's leading provider of health and science information.

3 Unrivaled Speed to Answer

Faster, more relevant clinical answers, so you can spend less time searching and more time caring for patients.

Start searching with ClinicalKey today!

Visit ***ClinicalKey.com*** for more information and subscription options.

ELSEVIER